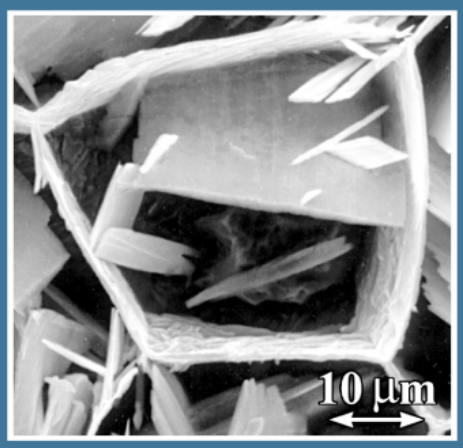
WOODHEAD PUBLISHING IN MATERIALS



Phase transformations in steels

Volume 1: Fundamentals and diffusion-controlled transformations

Edited by Elena Pereloma and David V. Edmonds

WP
WOODHEAD PUBLISHING

Phase transformations in steels

© Woodhead Publishing Limited, 2012

Related titles:

Phase transformations in steels Volume 2: Diffusionless transformations, high strength steels, modelling and advanced analytical techniques
(ISBN 978-1-84569-971-0)
Edited by two leading experts in the field, and with contributions from some of the most distinguished figures in steel research, this two-volume work summarises the vast amount of recent research on phase transformations in steels. The book covers both fundamental aspects (thermodynamics, diffusion, etc.) and more particular features (bainite, martensite, etc.). Volume 2 discusses diffusionless transformations and phase transformations in high strength steels as well as modelling and advanced analytical techniques.

Microstructure evolution in metal forming processes: Modelling and applications
(ISBN 978-0-85709-074-4)
Metal forming processes involve varying degrees of deformation to the metal substrate. This deformation results in changes to the microstructure of the metal. These microstructural changes need to be monitored and controlled. This book looks at the evolution of microstructure during metal forming processes and its modelling and control to produce steels and other metals with the right properties.

Nanostructured metals and alloys: Processing, microstructure, mechanical properties and applications
(ISBN 978-1-84569-670-2)
Nanostructured metals and alloys have enhanced tensile strength, fatigue strength and ductility and are suitable for use in applications where strength or strength-to-weight ratios are important. Part I of this important book reviews processing techniques for bulk nanostructured metals and alloys. Parts II and III discuss microstructure and mechanical properties, whilst Part IV outlines applications of this new class of material.

Details of these and other Woodhead Publishing materials books can be obtained by:

- visiting our web site at www.woodheadpublishing.com
- contacting Customer Services (e-mail: sales@woodheadpublishing.com; fax: +44 (0) 1223 832819; tel.: +44 (0) 1223 499140 ext. 130; address: Woodhead Publishing Limited, 80 High Street, Sawston, Cambridge CB22 3HJ, UK)
- contacting our US office (e-mail: usmarketing@woodheadpublishing.com; tel. (215) 928 9112; address: Woodhead Publishing, 1518 Walnut Street, Suite 1100, Philadelphia, PA 19102-3406, USA)

If you would like e-versions of our content, please visit our online platform: www.woodheadpublishingonline.com. Please recommend it to your librarian so that everyone in your institution can benefit from the wealth of content on the site.

© Woodhead Publishing Limited, 2012

Phase transformations in steels

Volume 1: Fundamentals and diffusion-controlled transformations

Edited by

Elena Pereloma and David V. Edmonds



Oxford Cambridge Philadelphia New Delhi

© Woodhead Publishing Limited, 2012

Published by Woodhead Publishing Limited,
80 High Street, Sawston, Cambridge CB22 3HJ, UK
www.woodheadpublishing.com
www.woodheadpublishingonline.com

Woodhead Publishing, 1518 Walnut Street, Suite 1100, Philadelphia, PA 19102-3406, USA

Woodhead Publishing India Private Limited, G-2, Vardaan House, 7/28 Ansari Road,
Daryaganj, New Delhi – 110002, India
www.woodheadpublishingindia.com

First published 2012, Woodhead Publishing Limited
© Woodhead Publishing Limited, 2012. Chapter 1 which was prepared by a US government employee and is therefore in the public domain and cannot be copyrighted. The authors have asserted their moral rights.

This book contains information obtained from authentic and highly regarded sources. Reprinted material is quoted with permission, and sources are indicated. Reasonable efforts have been made to publish reliable data and information, but the authors and the publishers cannot assume responsibility for the validity of all materials. Neither the authors nor the publishers, nor anyone else associated with this publication, shall be liable for any loss, damage or liability directly or indirectly caused or alleged to be caused by this book.

Neither this book nor any part may be reproduced or transmitted in any form or by any means, electronic or mechanical, including photocopying, microfilming and recording, or by any information storage or retrieval system, without permission in writing from Woodhead Publishing Limited.

The consent of Woodhead Publishing Limited does not extend to copying for general distribution, for promotion, for creating new works, or for resale. Specific permission must be obtained in writing from Woodhead Publishing Limited for such copying.

Trademark notice: Product or corporate names may be trademarks or registered trademarks, and are used only for identification and explanation, without intent to infringe.

British Library Cataloguing in Publication Data
A catalogue record for this book is available from the British Library.

Library of Congress Control Number: 2012934584

ISBN 978-1-84569-970-3 (print)
ISBN 978-0-85709-610-4 (online)

The publisher's policy is to use permanent paper from mills that operate a sustainable forestry policy, and which has been manufactured from pulp which is processed using acid-free and elemental chlorine-free practices. Furthermore, the publisher ensures that the text paper and cover board used have met acceptable environmental accreditation standards.

Typeset by Replika Press Pvt Ltd, India
Printed by TJI Digital, Padstow, Cornwall, UK

© Woodhead Publishing Limited, 2012

Contents

Contributor contact details *xi*
Foreword *xv*
Introduction *xvii*

Part I Fundamentals of phase transformations 1

1 The historical development of phase transformations understanding in ferrous alloys 3
R. E. Hackenberg, Los Alamos National Laboratory, USA

1.1 Introduction 3
1.2 The legacy of ferrous technology, characterization, and understanding prior to 1880 5
1.3 The recognition of ferrous phase transformations in the first period (1880–1925) 8
1.4 The consolidation of ferrous phase transformations in the second period (1925–1970) 21
1.5 Conclusion 37
1.6 Bibliography 38
1.7 References 40

2 Thermodynamics of phase transformations in steels 56
J. Ågren, Royal Institute of Technology (KTH), Sweden

2.1 Introduction: the use of thermodynamics in phase transformations 56
2.2 External and internal variables 57
2.3 The state of equilibrium 60
2.4 The combined first and second law – its application 62
2.5 The calculation of thermodynamic properties and equilibrium under fixed T, P and composition 72
2.6 Gibbs energy of phases in steel – the Calphad method 74

© Woodhead Publishing Limited, 2012

2.7	Various kinds of phase diagrams	80
2.8	Effect of interfaces	85
2.9	Thermodynamics of fluctuations in equilibrium systems	91
2.10	Thermodynamics of nucleation	92
2.11	References	93
3	Fundamentals of diffusion in phase transformations M. Hillert, Royal Institute of Technology (KTH), Sweden	94
3.1	Introduction	94
3.2	Driving forces of simultaneous processes	96
3.3	Atomistic model of diffusion	98
3.4	Change to a new frame of reference	101
3.5	Evaluation of mobilities	113
3.6	Trapping and transition to diffusionless transformation	119
3.7	Future trends	123
3.8	Acknowledgement	124
3.9	References	125
4	Kinetics of phase transformations in steels S. Van Der Zwaag, Delft University of Technology (TU Delft), The Netherlands	126
4.1	Introduction	126
4.2	General kinetic models	128
4.3	Geometrical/microstructural aspects in kinetics	129
4.4	Nucleation	132
4.5	Growth	139
4.6	Experimental methods	141
4.7	Industrial relevance	150
4.8	Acknowledgements	151
4.9	References	152
5	Structure, energy and migration of phase boundaries in steels M. Enomoto, Ibaraki University, Japan	157
5.1	Introduction	157
5.2	Atomic structure of phase boundaries	158
5.3	Free energies of phase boundaries	163
5.4	Migration of phase boundaries	171
5.5	Conclusions and future trends	177
5.6	References	179

© Woodhead Publishing Limited, 2012

Part II Diffusion-controlled transformations 185

6 Fundamentals of ferrite formation in steels 187
M. Strangwood, The University of Birmingham, UK

6.1 Introduction 187
6.2 Crystallography 189
6.3 Transformation ranges 193
6.4 Nucleation 198
6.5 Growth 208
6.6 Conclusions 216
6.7 References 216

7 Proeutectoid ferrite and cementite transformations in steels 225
M. V. Kral, University of Canterbury, New Zealand

7.1 Introduction 225
7.2 Temperature-composition range of formation of proeutectoid ferrite and cementite 227
7.3 The Dubé morphological classification system 229
7.4 Three-dimensional morphological classifications 233
7.5 Crystallographic orientation relationships with austenite 255
7.6 Habit plane, growth direction and interfacial structure of proeutectoid precipitates 258
7.7 Future trends 266
7.8 Sources of further information and advice 266
7.9 Acknowledgements 267
7.10 References 267

8 The formation of pearlite in steels 276
D. Embury, McMaster University, Canada

8.1 Introduction 276
8.2 An overview of the pearlite reaction 278
8.3 Crystallographic aspects of the reaction 285
8.4 The role of alloying elements 291
8.5 The deformation of pearlite 298
8.6 Future trends in pearlitic steels 303
8.7 Sources of further information and advice 306
8.8 Acknowledgements 307
8.9 References 307

© Woodhead Publishing Limited, 2012

9 Nature and kinetics of the massive austenite-ferrite phase transformations in steels 311
Y. Liu, Max Planck Institute for Intelligent Systems, Germany and Tianjin University, P. R. China, F. Sommer, Max Planck Institute for Intelligent Systems, Germany and E. J. Mittemeijer, Max Planck Institute for Intelligent Systems, Germany and University of Stuttgart, Germany

9.1 Introduction 311
9.2 Kinetic information based on thermal analysis 314
9.3 Modular phase transformation model 315
9.4 Characteristics of normal and abnormal transformations 320
9.5 Kinetics of the normal transformation 332
9.6 Kinetics of the abnormal transformation 338
9.7 Transition from diffusion-controlled growth to interface-controlled growth 345
9.8 Transition from interface-controlled growth to diffusion-controlled growth 360
9.9 Massive transformation under uniaxial compressive stress 367
9.10 Conclusion 377
9.11 References 377

Part III Bainite and diffusional-displacive transformations 383

10 Mechanisms of bainite transformation in steels 385
S. B. Singh, Indian Institute of Technology Kharagpur, India

10.1 Introduction 385
10.2 Bainite: general characteristics 386
10.3 Diffusion-controlled growth mechanism 391
10.4 Displacive mechanism of transformation 396
10.5 Summary and conclusion 411
10.6 References 412

11 Carbide-containing bainite in steels 417
T. Furuhara, Tohoku University, Japan

11.1 Definitions of bainite structure 417
11.2 Crystallography and related characteristics of ferrite in bainite 423
11.3 Characteristics of carbide precipitation in bainite structure 429
11.4 Future trends 433
11.5 References 433

© Woodhead Publishing Limited, 2012

12 Carbide-free bainite in steels 436
F. G. Caballero, National Center for Metallurgical Research (CENIM-CSIC), Spain

12.1 Introduction 436
12.2 Influence of silicon on cementite precipitation in steels 442
12.3 Carbon distribution during the carbide-free bainite reaction 446
12.4 Microstructural observations of plastic accommodation in carbide-free bainite 456
12.5 Conclusions 461
12.6 Acknowledgement 462
12.7 References 463

13 Kinetics of bainite transformation in steels 468
A. Borgenstam and M. Hillert, Royal Institute of Technology (KTH), Sweden

13.1 Introduction 468
13.2 Transformation diagrams 470
13.3 Nucleation and growth of bainite 477
13.4 Start temperature of bainite 485
13.5 Effect of alloying elements 491
13.6 Overall kinetics 494
13.7 Conclusions 499
13.8 Acknowledgement 499
13.9 References 499

Part IV Additional driving forces for transformations 503

14 Nucleation and growth during the austenite-to-ferrite phase transformation in steels after plastic deformation 505
J. Sietsma, Delft University of Technology, The Netherlands and Ghent University, Belgium

14.1 Introduction 505
14.2 Background 506
14.3 Experiments and simulations on the effect of plastic deformation on ferrite formation 516
14.4 Future trends and conclusion 523
14.5 References 524

15 Dynamic strain-induced ferrite transformation (DSIT) in steels 527
P. D. Hodgson and H. Beladi, Deakin University, Australia

15.1 Introduction 527

© Woodhead Publishing Limited, 2012

15.2 What limits grain refinement in conventional static transformation? 528
15.3 Ultrafine ferrite formation in steels 532
15.4 Nature of the transformation 536
15.5 Modelling 543
15.6 Can grain sizes less than 1 μm be achieved? 546
15.7 Industrial implementation 548
15.8 Future trends 548
15.9 Conclusions 550
15.10 Acknowledgements 550
15.11 References 550

16 The effect of a magnetic field on phase transformations in steels 555
Y. Zhang and C. Esling, Université de Lorraine, France

16.1 Introduction 555
16.2 Evolution of the magnetic field generators 556
16.3 Basic mechanisms of field influence on a phase transformation in steels 557
16.4 Effect of magnetic field on phase equilibrium and transformation 560
16.5 Future trends and conclusions 577
16.6 References 577

17 The effect of heating rate on reverse transformations in steels and Fe-Ni-based alloys 581
Yu. Ya. Meshkov, Institute for Metal Physics, National Academy of Sciences, Ukraine and E. V. Pereloma, University of Wollongong, Australia

17.1 Introduction 581
17.2 Effect of heating rate on austenite formation in steels 582
17.3 Effect of heating rate on austenite microstructure after $\gamma \rightarrow \alpha(\alpha') \rightarrow \gamma$ phase transformations in quenched steels 592
17.4 Effect of rapid heating on mechanical properties of steels and its applications 600
17.5 Effect of heating rate on the reverse austenite transformation in Fe-Ni-based alloys 602
17.6 Conclusions 612
17.7 References 613

Index *619*

© Woodhead Publishing Limited, 2012

Contributor contact details

(* = main contact)

Editors

Professor Elena Pereloma*
Faculty of Engineering
University of Wollongong
Northfields Avenue
Wollongong
NSW 2522
Australia

E-mail: elenap@uow.edu.au

Professor David Edmonds
Institute for Materials Research
School of Process, Environmental and Materials Engineering
University of Leeds
Leeds LS2 9JT
UK

E-mail: d.v.edmonds@leeds.ac.uk

Chapter 1

Robert E. Hackenberg
Los Alamos National Laboratory
Materials Science and Technology Division (MST-6)
Mail Stop G770
P.O. Box 1663
Los Alamos, NM 87545
USA

E-mail: roberth@lanl.gov

Chapter 2

John Ågren
Division of Physical Metallurgy
Royal Institute of Technology (KTH)
SE-100 44 Stockholm
Sweden

E-mail: john@kth.se

Chapter 3

M. Hillert
Division of Materials Science and Engineering
Royal Institute of Technology (KTH)
Brinellv. 23
SE-100 44 Stockholm
Sweden

E-mail: mats@mse.kth.se

© Woodhead Publishing Limited, 2012

Chapter 4

Sybrand van der Zwaag
Novel Aerospace Materials Group
Faculty of Aerospace Engineering
Delft University of Technology (TU Delft)
2629 HS Delft
The Netherlands

E-mail: S.vanderZwaag@tudelft.nl

Chapter 5

Masato Enomoto
Department of Materials Science and Engineering
Ibaraki University
4-12-1, Nakanarusawa
Hitachi-city
316-8511 Japan

E-mail: enomotom@mx.ibaraki.ac.jp

Chapter 6

M. Strangwood
Phase Transformations and Microstructural Modelling Group
The University of Birmingham
School of Metallurgy and Materials
Elms Road
Edgbaston
Birmingham B15 2TT
UK

E-mail: m.strangwood@bham.ac.uk

Chapter 7

Professor Milo V. Kral
Department of Mechanical Engineering
University of Canterbury
P.O. Box 4800
Christchurch
New Zealand 8140

E-mail: milo.kral@canterbury.ac.nz

Chapter 8

David Embury
Department of Materials Science and Engineering
McMaster University
Hamilton
Ontario
L8S 4L7
Canada

E-mail: emburyd@mcmaster.ca

Chapter 9

Yongchang Liu
Max Planck Institute for Intelligent Systems (formerly Max Planck Institute for Metals Research)
Heisenbergstr 3,
D-70569 Stuttgart
Germany

and

School of Materials Science & Engineering
Tianjin University
300072 Tianjin
P. R. China

© Woodhead Publishing Limited, 2012

Ferdinand Sommer
Max Planck Institute for Intelligent Systems (formerly Max Planck Institute for Metals Research)
Heisenbergstr 3,
D-70569 Stuttgart
Germany

Eric Jan Mittemeijer*
Max Planck Institute for Intelligent Systems (formerly Max Planck Institute for Metals Research)
Heisenbergstr 3,
D-70569 Stuttgart
Germany

and

Institute for Materials Science
University of Stuttgart
Germany

E-mail: e.j.mittemeijer@mf.mpg.de

Chapter 10

S. B. Singh
Department of Metallurgical and Materials Engineering
Indian Institute of Technology Kharagpur
Kharagpur 721302
India

E-mail: sbs22@metal.iitkgp.ernet.in

Chapter 11

Tadashi Furuhara
Institute for Materials Research
Tohoku University
Sendai 980-8577
Japan

E-mail: furuhara@imr.tohoku.ac.jp

Chapter 12

Francisca G. Caballero
National Center for Metallurgical Research (CENIM-CSIC)
Av. Gregorio del Amo, 8
E-28040 Madrid
Spain

E-mail: fgc@cenim.csic.es

Chapter 13

Annika Borgenstam* and Mats Hillert
Division of Physical Metallurgy
Department of Materials Science and Engineering
Royal Institute of Technology (KTH)
Stockholm
Sweden

E-mail: annika@mse.kth.se; mats@mse.kth.se

© Woodhead Publishing Limited, 2012

Chapter 14

Jilt Sietsma
Department of Materials Science and Engineering
Delft University of Technology
Mekelweg 2
2628 CD Delft
The Netherlands

E-mail: J.Sietsma@tudelft.nl

and

Department of Materials Science and Engineering
Ghent University
Technologiepark 903
B-9052 Gent-Zwijnaarde
Belgium

Chapter 15

P. Hodgson* and H. Beladi
Institute for Frontier Materials
Deakin University
Geelong
Victoria 3217
Australia

E-mail: peter.hodgson@deakin.edu.au; hossein.beladi@deakin.edu.au

Chapter 16

Yudong Zhang* and Claude Esling
Laboratoire d'Étude des Microstructures et de Mécanique des Matériaux
LEM3 CNRS UMR 7239 (former LETAM CNRS FRE 3143)
Université de Lorraine
57045 Metz
France

E-mail: yudong.zhang@univ-metz.fr; esling@letam.sciences.univ-metz.fr; claude.esling@univ-metz.fr

Chapter 17

Yu.Ya. Meshkov
Institute for Metal Physics
National Academy of Sciences
36 Vernadsky St
Kiev 252142
Ukraine

E-mail: zimina@imp.kiev.ua; kotr@imp.kiev.ua

E.V. Pereloma*
Faculty of Engineering
University of Wollongong
Northfields Avenue
Wollongong
NSW 2522
Australia

E-mail: elenap@uow.edu.au

© Woodhead Publishing Limited, 2012

Foreword

A new and comprehensive book on phase transformations in steels is both timely and welcome. It is gratifying near the beginning of a new, technology-dominated, century to see a group of experts and well accomplished researchers, some of whom have devoted major parts of their professional activities to this area, as well as a group of younger researchers and steel users, all willing to assemble together a new two-volume publication on steels.

Strikingly, unlike many other groups of important metallic materials, it is the onset of transformations in steels resulting from the various thermal and mechanical treatments that make steels so special. This is possible mainly because of the unique properties of iron (Fe) which exhibits three different simple crystal structures: bcc, fcc and bcc again, as temperature rises. Even more unique is the fact that, contrary to the usually observed order of the sequence of phase changes observed with temperature, the gamma phase at higher temperatures is the 'more open' phase than the bcc alpha phase, and hence more able to absorb substantial amounts of alloying element additions. As a result, on quenching or cooling, and other heat treatments, all kinds of phase transformations can take place, and their understanding, manipulation, and utilization constitutes the essence of the importance that steels have exhibited in the past in the development of civilizations and related technologies.

The various chapters bring nicely up to date the vast assembled knowledge of steel transformations in the literature: from the more basic aspects (thermodynamics, diffusion, kinetics, etc.), through the more particular transformation features (nucleation and growth, bainite, martensite, massive, shape memory, etc.), to some aspects of the more recent and advanced analytical possibilities (synchrotron, atom probe, etc.).

Perhaps it is fitting also to mention that the bewildering role of magnetism in iron is the basis of much of this behavior. It is well documented that the ferromagnetic transition in the bcc-Fe phase makes the bcc phases more stable at lower temperatures than the fcc-gamma phase, but still too few people realize that it is the anti-ferromagnetic transition in the gamma phase at temperatures near 0 K that makes the crystalline closed-packed (therefore

© Woodhead Publishing Limited, 2012

'wrong') gamma phase return to stability on heating. Without these unusual features of iron, phase transformations in steels would not take place and the enormous versatility and benefits of steels in the progress of society would be lost.

It may also be time to admit that the ferromagnetic alpha phase has actually a bc-tetragonal symmetry due to the magnetic moments, if the more modern standards of phase definition are adopted, and so the bcc (and paramagnetic) beta phase which has been banished from the iron phase diagrams since the 1920s should be rightfully restored to its original position.

Undoubtedly, research on transformations in steels will continue in the future, as more sophisticated heat treatments are devised and more advanced techniques are brought into use to study the results, particularly at the micro and nano scales. The present book is likely to serve here as a good basis for future advances.

Ted Massalski
Professor of Materials Science, Engineering and Physics
Carnegie Mellon University

© Woodhead Publishing Limited, 2012

Introduction

Steel has been available as a high tonnage engineering material for nearly two centuries. During this time it has had a very creditable track record and one which is crucial to engineering progress, especially in providing the infrastructure in underdeveloped and developing parts of the world, which still dwarf in size and population the more developed nations. This is why the volume of steel production continues to increase, leading to the continual need to consider more economic ways of manufacturing using steel in order to minimise energy consumption and preserve natural resources.

Despite commendable efforts by scientists and engineers to understand fully the processing-microstructure-property relationships in steels, these continue to present new challenges to researchers because of the complexity of the phase transformation reactions and the wide spectrum of microstructures and properties achievable. Thus, an important theme and objective of this book is to follow the development of our understanding of phase transformations in iron alloys and steels through to the development of modern commercial steels, and in particular to highlight the clear connection between phase transformation studies, no matter how isolated and remote they may seem at the outset, to the emergence of new steels with enhanced engineering properties.

Unlike many other metals, the combination of several characteristics, such as magnetism, allotropic phase changes and the different solubility and diffusion behaviour of interstitial and substitutional elements, makes iron-based alloys unique and is responsible for a diversity of phase transformations. The first chapter of this book provides a historical perspective on the first pioneering attempts to gain insight into the complexity of these reactions. All aspects of phase transformations (thermodynamics, diffusion, kinetics and crystal structure) must be properly understood in order to develop a complete picture of the transformation reactions in steels. Thus it was deemed necessary to devote the first section of the book to the fundamental principles of thermodynamics, diffusion and kinetics, and in addition, owing to its growing importance in helping to understand transformations, the phase boundary interface separating parent and product, now much more amenable to observation and analysis using the increased power of modern metallographic instrumentation, as well as modelling.

© Woodhead Publishing Limited, 2012

Starting from the earliest studies on phase transformations in steels, a large number of theories and definitions have emerged leading to continual debates amongst researchers. Only with the development of more advanced experimental capabilities have some of these issues been satisfactorily resolved while others still provoke conflicting opinions. This book aims to represent the current status of knowledge on steel phase transformations whilst also highlighting the challenges facing future researchers in this field.

As mentioned in the Foreword, and demonstrating how the Fe-C system continues to generate important issues, magnetism plays an important role in the phase transformations of iron and steels due to the ferromagnetic and anti-ferromagnetic transitions that take place. Thus it is suggested that paramagnetic beta phase should be restored to the Fe-C phase diagram.

The most important transformations in steels, and the area where almost all research has been concentrated, are those which result in the final microstructure and properties. These involve decomposition of the high temperature γ-phase, austenite, which takes place on cooling and, dependent upon steel alloying and cooling conditions and also whether mechanical working occurs, could follow different paths resulting in a large diversity of lower temperature phase types and their mixtures. These phase transformations could be classified based upon microstructure, thermodynamics or mechanisms and in the present book the phase transformations are classified according to their mechanism. In this scheme the phase transformations in steels are customarily divided into two major groups, which are named according to whether long-range diffusion of atoms occurs or not, namely diffusional or non-diffusional (diffusionless). Each type of phase transformation is then characterised by a set of specific features, including but not limited to composition, crystal structure, shape change and carbon mobility.

It is generally accepted that the formation mechanisms of proeutectoid grain boundary allotriomorphs (of α-ferrite and cementite) and pearlite are diffusional. These reactions take place within the higher temperature region of the low temperature phase field with slow kinetics and generally do not require significant undercooling below the $\gamma \rightarrow \alpha$ transition temperature. In contrast, the formation of martensite with a structure change but composition inherited from parent austenite occurs by a diffusionless transformation at rapid cooling and/or large undercoolings. In-depth presentations of the current state of phase transformation theory for the former type of reactions are given in Volume 1, Part II, whereas the latter is addressed in Volume 2, Part I. These constitute the more traditional microstructures which have long been studied; Henry Clifton Sorby, for example, first identified pearlite around the middle of the 19th century. Moreover, they have long provided the properties of the high-tonnage carbon and alloy steels used in construction and many engineering applications. Nevertheless, as described in these sections, significant progress has been made in understanding their

© Woodhead Publishing Limited, 2012

formation, both for ferrite/pearlite and for basic martensite, in the latter case the *phenomenological theory of martensite crystallography* and, more recently, the proposals deriving from interface mechanics embodied in the so-called *topological model*, which attempt to describe the mechanistic aspects of the transformation. This demonstrates the rich variety of transformations in iron-based alloys, especially when one also adds the shape memory effect, which is of immense interest and commercialisation in non-ferrous systems.

Although significant advances have been made in developing a basic understanding of the nucleation and growth processes, and in validation of various theories, questions still remain due to the limitations of even the most powerful experimental techniques and the complexities of multiphase microstructures forming under a variety of conditions, generally at elevated temperatures. Examples include: elucidating the exact path for carbon diffusion; determining the embryo structure, location and evolution; measuring the effect of so-called 'solute drag' on interface migration; determining the diffusivities and binding energies of elements in multi-component systems; accurately measuring interfacial and strain energies; providing explanations on the differences between the predicted rates of diffusion of substitutional elements at low temperatures and the observed solute clustering. Proving again the complexity, even previously well-accepted ideal cases of partitioning of alloying elements under local equilibrium (LE) or paraequilibrium (PE) conditions for diffusional transformations are now challenged by assumption of negligible partitioning of substitutional elements under local equilibrium (NP-LE).

However, the issues most difficult to resolve, not unexpectedly, have been related to the intermediate products formed between the classical diffusional (e.g. ferrite/pearlite) and diffusionless (e.g. martensite) ones. A variety of morphologies of these products including Widmanstätten ferrite, upper bainite, lower bainite and carbide-free bainite, as well as granular bainite and the so-called 'acicular ferrite microstructures', are considered to exhibit a mixture of characteristics familiar to both classes of transformation, which has fuelled continuous debate regarding the exact formation mechanisms. Perhaps the main discord concerned with the fundamentals of the reaction mechanism has been related to the nature of the bainite transformation (Volume 1, Part III), which essentially reduces to the behaviour and location of carbon during the formation of the bainitic ferrite crystals. As mentioned above, better resolution of such questions might evolve from real-time measurement of carbon concentrations in parent austenite and product ferrite during transformation at elevated temperatures.

Nevertheless, there have been significant positive advances in these phase transformation studies. In this quest for greater understanding of the bainite reaction mechanism, experimental steels have been developed which contain untransformed austenite, useful for studying features of the

© Woodhead Publishing Limited, 2012

transformation mechanism, but which have subsequently been shown can impart valuable properties to a new generation of formable high strength steels for automotive use that has eventually led to commercialisation, e.g. transformation induced plasticity (TRIP) steels. Chapters on these new steels can be found in Volume 2, Part II, alongside comparative chapters on the new twinning induced plasticity (TWIP) steels and high alloyed maraging steels.

Almost all modern high-volume metal production processes are continuous, involving continuous cooling, often associated with mechanical forming, such that complex dynamic changes are more often the norm and sometimes even difficult to simulate in a laboratory environment. Thus, near-equilibrium microstructures are not always the ones which could lead to commercial success. Consequently, given the different industrial processes required in the production of steel in all its various forms, which are continually being updated or modified, a section dealing with parameters involved in transformation other than temperature was considered necessary. External factors, such as deformation, heating rate or application of electromagnetic field could either accelerate or retard the phase transformations depending upon the chosen set of conditions (Volume 1, Part IV). Although a significant body of evidence has been accumulated over time on the effects of these parameters, the underlying mechanisms are not yet fully understood. The phenomenon of restoration of prior austenite morphology and orientation at slow or fast heating rates and absence of it at intermediate heating rates continues to puzzle physical metallurgists. The explanations put forward for this structural inheritance also lack direct and comprehensive experimental evidence.

Many of the significant advances to our understanding of phase transformations in the evolution of steel microstructure during the last 50 years would not have been possible without the parallel development of higher resolution microscopes and related techniques. In the last two decades significant advances have been made in many characterisation techniques (Volume 2, Part IV) and microstructure observations have moved from only *ex-situ* to also *in-situ* ones. It is now possible using *in-situ* transmission electron microscopy, neutron and synchrotron scattering or electron backscattering diffraction coupled with energy dispersive X-ray spectroscopy, to observe the progress of phase transformations not only on heating or cooling, but under external load too. Recent leaps in the development of atom probes and aberration corrected transmission electron microscopes enable the collection of compositional and crystallographic information with atomic resolutions (<0.1 nm). The ability to gather microanalytical data at high resolutions has become increasingly important with the realisation that relatively low bulk concentrations of alloying elements can have disproportionately large effects on transformation behaviour. The exact structure of grain and interphase

© Woodhead Publishing Limited, 2012

boundaries and solute segregation to them can now be revealed more clearly. The improved resolution limit is especially valuable with the increased trend towards production of steels with ultrafine and nano-sized grains and precipitates. Perhaps it should be mentioned that more and more use of 3D techniques in addition to more customarily utilised 2D provides invaluable information on the morphology and distribution of various phases and their crystallography, which helps to fine-tune existing theories and indicates the route for other experiments. But whilst researchers should remain vigilant to artefacts related to each technique and continue to analyse data diligently, these newly developed techniques will allow gathering of the essential information for advancement or validation of existing theories and models, as well as provide the necessary input data for rapidly developing modelling methodologies.

However, we must remain mindful that these instruments and their applications, as will be evident from this section in the book, have become extremely specialised and expensive, and are not widely available, and consequently much of the metallographic work on commercial steel microstructures is still conducted at much lower resolutions by more conventional microscopy. This emphasises the need for consistent descriptions and classifications of microstructure and transformation behaviours across the length scales. As far as has been possible, we have tried to maintain a similar nomenclature throughout the book.

The major new inclusion in this book derives from probably the most significant and totally new topic or field of activity in phase transformations to emerge during the latter part of the main period covered, namely phase transformations modelling. A full section (Volume 2, Part III) has been devoted to this fairly embryonic but rapidly growing field, including all of the well-known approaches: first principles, phase field, molecular dynamics, neural networks. The models provide qualitative and semi-quantitative insight into phase transformations. Some good examples of the preliminary applications to ferrous transformations will be found, some of which have already produced useful advances whilst others are meeting the extensive challenges arising from the complexity of the subject. The hope exists that eventually steels may be designed from first principles taking into account the complexities of phase change associated with those of processing on a large scale, so often difficult to reproduce accurately in the laboratory, or alternatively to study during commercial production. However, it is clear that despite the progress made, the lack of reliable experimental data for input into the models hinders their development. For first principles models reliable experimental data are needed for validation of the potentials. As mentioned previously, quantitative interfacial and strain energy data, data on diffusivities and nucleation, are urgently required to further advance modelling and the theories of ferrous phase transformations.

© Woodhead Publishing Limited, 2012

Finally, the success of applying the knowledge of phase transformations to design of advanced high strength steels should be acknowledged (Volume 2, Part II). This part begins with a chapter on high strength low alloy (HSLA) or microalloyed steels which have probably been the category of steels that have seen the most resource-intensive development during the latter part of the period covered by this book, and still do, driven mainly by the ever more stringent engineering requirements for steels needed in the recovery and transmission of oil and gas. In the quest for greater strength and toughness combined with weldability, extensive data and understanding have been accumulated on the influence of alloying and controlled deformation processing and cooling on the phase transformation and precipitation reactions.

The pathway from the development of quenched and tempered steels and HSLA steels to dual phase, transformation-induced plasticity, nanostructured bainitic ('Nanobain'), twinning-induced plasticity and quenched and partitioned steels is marked by gradual increase in complexity of processing schedules and the microstructures formed. In the latter steels, the direct application of phase transformation sequences in the design of processing schedules led to either significant strength advantage or desirable combinations of high strength/high ductility in formable steels. These manipulations of steel microstructures also enable the achievement of cost savings due to leaner steel compositions and consequently the reduced use of natural resources, coupled with socio-economic benefits.

This project would not have been possible without support from Woodhead Publishing staff and the enthusiasm and co-operation of authors and co-authors in joining us in this task – which apart from confirming our inception of the idea, has made it a more worthwhile and also an enjoyable activity over the last two years. Our authors must also be congratulated on their efforts to produce comprehensive overviews of the topics, including fair and balanced treatments of various theories and models where appropriate. There can be no doubt that it has been an immense task and we can attest to the considerable work which has gone into the production of the manuscript for this book. It will always be a snapshot of where we have reached in this discipline by the year of publication, but it will also, we hope and because of the quality of the chapters provided, stand as a useful source for reference, advanced teaching and learning for a long time to come. In particular, it is hoped that this book will inspire a young generation of scientists and engineers to further advance the knowledge on phase transformations in steels, which remains a fascinating and significant field to explore.

Elena Pereloma
University of Wollongong
David Edmonds
University of Leeds

© Woodhead Publishing Limited, 2012

1

The historical development of phase transformations understanding in ferrous alloys

R. E. HACKENBERG, Los Alamos National Laboratory, USA

Abstract: This chapter reviews the historical evolution of phase transformations understanding as it was developed in steels and other ferrous alloys. The focus is on the discoveries, dead ends, confusions, controversies, and achievements in the 1880–1925 period when the age-old 'hardening problem' in steel was pursued using metallography, thermal analysis, and the Gibbs phase rule. The shift in paradigm regarding metal structure and phase transformations was completed in the following period, 1925–1970, when breakthroughs afforded by X-ray diffraction and other techniques shed new light on all transformations. The evolving interactions of physical metallurgy with chemistry, physics, and other fields will be highlighted.

Key words: history, kinetics, metallography, microstructure, X-ray diffraction.

1.1 Introduction

1.1.1 The importance and variety of ferrous phase transformations

The technological importance of steels and other ferrous alloys is beyond doubt. Iron is abundant, constituting 4.2% of the earth's crust. Over millennia iron ore has been reduced to metal and altered by heat treatment and metalworking. The core structural applications of steel stem from a combination of high strength, good ductility, and low cost. The diverse uses of ferrous alloys in applications requiring tailored electrochemical, magnetic, thermal expansion, and other functional properties testify to their tremendous versatility.

Phase transformations are the most potent means of tailoring the microstructure and properties of ferrous alloys. The rich variety of phase

Los Alamos National Laboratory is operated by the Los Alamos National Security LLC for the National Nuclear Security Administration of the US Department of Energy. Los Alamos National Laboratory does not endorse the viewpoint of this publication or guarantee its technical correctness.

Published by Woodhead Publishing Limited, 2012

transformations stems from several fortuitous characteristics specific to iron (Leslie and Hornbogen, 1996):

- allotropic phase changes between face-centered-cubic (FCC) γ-austenite and body-centered cubic (BCC) α- and δ-ferrites,
- ferromagnetic ordering, whose thermodynamics give rise to this anomalous allotropy of iron,
- high solubility of carbon and other elements in γ,
- carbon's anisotropic distortion of supersaturated α, giving the extremely hard body-centered tetragonal (BCT) α'-martensite,
- vastly different diffusion rates of interstitial and substitutional solutes, and
- reasonable mobility of substitutional solutes at subcritical temperatures where α is stable.

1.1.2 Scope of this review

The historical development of phase transformations understanding will be reviewed through the lens of ferrous alloys. The origin and evolution of the major concepts that shaped this sub-field of physical metallurgy will be brought into focus. In many ways, iron and steel affords a privileged vantage point from which to survey the history of phase transformations:

- Ferrous alloys have been the dominant metallic materials available for practical applications for a very long time – over many centuries – during which time different conceptions of metal structure and the scientific method more generally have evolved. Many of the same questions, experiments and theories first posed to understand ferrous alloys were applied to newer alloys such as aluminum, nickel, titanium, and uranium.
- The allotropy of iron afforded a variety of very distinct first-order phase changes, ones capable of altering 100% of the starting microstructure, which as a consequence were more readily measured by length and property changes as compared with other alloys that transformed in more subtle ways via evolution of much smaller volume fractions of clusters and precipitates that were more difficult to measure.
- The ferromagnetism of iron provided an additional, perhaps crucial, window into measuring the phase transformations behavior.

This scientific history is intertwined with technological change. The development of inexpensive, high-tonnage methods of ironmaking and steelmaking in the mid-19th century vastly expanded the applications of steel. This in part explains why phase transformation studies began when they did, around 1880, as a scientific response to the needs of steel production and use

Published by Woodhead Publishing Limited, 2012

in railroads, building construction, naval armor and automotive applications (Misa, 1995). Section 1.2 covers the 'pre-history' of phase transformation studies prior to 1880.

Two major periods of development followed. The first period, 1880–1925, will be surveyed in Section 1.3. Researchers worked to answer the major question of the day: how does steel harden, and why? This was a period of evolving and conflicting ideas, originating from disparate perspectives: classical chemistry and physics, extractive and process metallurgy, geology, engineering, mechanics, and metallurgical craft traditions. The question had not been answered by 1925, though significant progress had been made.

Studies of steel by X-ray diffraction opened the second period, 1925–1970 (Section 1.4). X-ray and electron microscopy freed phase transformations understanding from the limitations of its progenitor disciplines (especially chemistry) and opened it up to the influence of more suitable concepts originating in solid state physics. Advances in understanding diffusion, defects, and crystallography were pivotal in completing this paradigm shift. The normative concepts and methods of phase transformations developed in this period set the research agenda and approach for the post-1970 era. Brief concluding remarks (Section 1.5) and a bibliography of key technical, historical, and biographical literature will round out this survey (Section 1.6).

1.2 The legacy of ferrous technology, characterization, and understanding prior to 1880

1.2.1 Iron and steel in technological history

Iron-based materials have a long historical pedigree. The first man-made irons and steels date from about 2500 BC. Historical ironmaking centers in pre-Roman times include Anatolia, Mesopotamia, East Africa, India, and China (Raymond, 1984). Iron was obtained in small quantities from charcoal smelting methods. Given its scarcity and superior strength when hardened ('steeled') relative to other materials such as bronze, it was a valuable material. Iron displaced bronze for utilitarian applications during 1200–900 BC in the eastern Mediterranean region – the dawn of the Iron Age (Maddin, 1992). Quenching from high temperatures was a known condition for this hardening, but the other variables remained a mystery, confined to the realm of serendipity, and later the craftsman's specialization (and secrecy). Depending on the smelting and metalforming route, the conversion of iron to quality steel required either carburization or decarburization to attain a carbon concentration suitable for hardening. More sophisticated objects took advantage of spatial gradients in carbon and/or cooling rate. For example,

Published by Woodhead Publishing Limited, 2012

swords had hard, high-carbon surface regions supported by tougher, lower-carbon interiors. But this gets ahead of the story: the critical roles of carbon and cooling rate would not be explicitly recognized until the end of the 18th and 19th centuries, respectively.

Technological progress in this new Iron Age was slow. Bronze Age metallurgical skills did not translate to iron, a more challenging material to smelt and work. Iron's high melting point made it difficult to purify in a completely molten condition or cast into shape. The alternative approach was to work out the slag and form to shape through redundant forging steps, a time-consuming process that in the hands of the expert ironworker could result in exquisite decorative patterns such as those seen in Damascus steel blades (Durand-Charre, 2004). Over time, the temperature of iron reduction furnaces increased through improvements in insulation, forced air convection, and the transition from wood-based to coal-based fuels (Raymond, 1984), an evolutionary progression culminating in the modern blast furnace. A steelmaking revolution occurred in the 1860s with the introduction of the Bessemer–Kelly pneumatic process and Siemens–Martin open hearth process. By contrast, legacy crucible and puddling steelmaking methods were low-volume, time-consuming, difficult-to-control, energy-inefficient, and required expert knowledge (Misa, 1995).

Now available in large amounts, iron and steel were used in more demanding, engineered systems such as bridges and railroads. This benefited from and spurred further development of the discipline of solid mechanics, which saw rapid progress in the early 19th century (Timoshenko, 1953). The physical origin of the strength of materials still lay hidden in the microstructure, though. The present materials science paradigm of processing-microstructure-properties-performance was still unknown, and would not be fully articulated for another century.

1.2.2 Early metallographic studies

The perception of internal structure would require the invention or adaptation of characterization techniques never before applied to metals. Prior to 1863, any examination by unaided eye or low-power light optical microscopy (LOM) was carried out on *unprepared* surfaces (intact or fractured), the result of corrosion, overheating, wear, etc. This method concealed more than it revealed. A notable advance was the direct (unmagnified) prints of polished and etched meteoric iron made in 1808 by Aloys von Widmanstätten, revealing to the unaided eye the distinctive microstructure that bears his name.

The direct observation of microstructure took a major step forward in 1863 when Henry Clifton Sorby examined a carburized Swedish iron by a *reflected* light microscopy method. This involved an adaptation of his *transmitted* light microscope that he had developed for his earlier geology researches. In

Published by Woodhead Publishing Limited, 2012

doing so, Sorby became the first to apply a microscopy method to reveal a bulk metallic microstructure (Smith, 1960, 1965b; Higham, 1965). However, Sorby published this work only in abstract form in 1864, and did not pursue the topic further. The time was not ripe for the adoption of light microscopy to the study of metals, and Sorby himself had other interests to pursue (Humphries, 1965). As late as the 1870s, the craft tradition centered around individual iron- and steel-masters was still strong (especially in Sheffield), with its attendant lore and secrecy. Furthermore, science was still thought of as an occupation of the leisured classes (Sorby himself was of independent means), not an enabler of industrial and technological advance.

1.2.3 Prior understandings of metal structure

The interpretative frameworks prior to 1880 were ill-suited to understand metals. Paradigmatic understandings from chemistry and other disciplines such as mineralogy were ready at hand, but of limited applicability for metals. The following are several elements of the mid-19th century understanding of metals and alloys (Smith, 1960, 1965a, 1968; Servos, 1990; Cahn, 2001):

- *Bonding and phase stoichiometry*. Atoms bonded with one another to form discrete molecules. From classical (Daltonian) chemistry, discrete valence states and stoichiometric ratios governed all elemental combinations. This would soon clash with emerging evidence of (1) intermetallic compounds having the 'wrong' proportions in relation to classical valence states and (2) solid solutions having constant crystal structure over a continuously variable range of compositions. Claude Berthollet, a contemporary of John Dalton, held views more consonant with the idea of nonstoichiometric solid solutions, but these views did not gain a foothold.
- *Crystallinity and geometric packing*. Crystallinity was viewed with reference to externally observable facets common to minerals, and had little to do with the internal geometric packing of the molecules. Furthermore, amorphous structures were considered just as common as crystalline ones. Speculations on the origin of hardening of steel, fracture, or other changes otherwise inexplicable by chemical arguments alone were frequently made in terms of amorphous↔crystalline transitions. The intergranular appearance of brittle fracture surfaces, as contrasted with the fibrous appearance of ductile fracture surfaces, lent credence to the popular view that deformation, fracture and failure are caused by vibration-induced crystallization.
- *Microstructure*. The discrete atom or molecule was the locus of structure, consistent with Daltonian chemistry. This was not always the case. An alternative 'corpuscular' understanding focused on multiple levels of

inter-related organization – one that might be described as particles (and pores) encompassed within larger particles, and so on – circulated widely in the scientific thought world in the 1600s and early 1700s. This adumbrates the modern understanding of microstructure as a complex, hierarchical organization of phases modified on various length scales by crystallographic and chemical defects. The qualitative nature of these theories and the inability of experimental methods to test and refine them placed corpuscular understanding at a disadvantage with respect to the more quantitative approaches of the ascendant Newtonian mechanics (manifested in theories of elasticity and strength of materials) and Daltonian chemistry.

- *Properties*. Solid mechanics had developed a remarkable level of mathematical sophistication, but this idealized 'strength of materials' did not require any knowledge of the internal structure of the material. Furthermore, it was widely held that externally visible features – Damascus steel patterns being the most prominent example – indicated the quality of steel.

This established understanding proved inadequate to address the hardening problem, which was about to be examined with new approaches that would call into question this earlier paradigm.

1.3 The recognition of ferrous phase transformations in the first period (1880–1925)

1.3.1 The hardening of steel, the central problem

Understanding (and controlling) the hardening of steel was the defining problem of this formative period, 1880–1925. This problem was by no means simple: it touches upon just about every phase, constituent, and transformation in steel. The pioneering generation of researchers (Table 1.1) would have to grapple with the complexity arising from the following issues:

- the key role of carbon and the influences of alloy and impurity elements,
- the structural state of carbon (aggregation or solution),
- differing phases and microconstituents,
- the path dependence of first-order phase transformations, and
- competing modes of austenite decomposition resulting in heterogeneous microstructures.

This was a period of evolving and conflicting ideas derived from and examined against the data from the new methods of thermal analysis and LOM.

Published by Woodhead Publishing Limited, 2012

Table 1.1 First-generation ferrous phase transformations researchers (born prior to 1870)

Name	Lifespan	Location	Contributions and notable monographs
Henry Clifton Sorby	1826–1908	Sheffield	LOM of steel (1863–64, 1885–87) Identified pearlite (1886)
Josiah Willard Gibbs	1839–1903	New Haven	Phase equilibrium theory (1876–78)
Dmitri K. Chernov	1839–1921	St. Petersburg	Identified the critical temperature required to harden steel (1868)
William C. Roberts-Austen	1843–1902	London	Fe-C phase diagram (1899) *An Introduction to the Study of Metallurgy* (1891)
Henry Marion Howe	1848–1922	Boston New York	Systematized nomenclature (1912) *Metallography of Steel and Cast Iron* (1916)
Floris Osmond	1849–1912	Creusot Paris	Identified critical points (1886) Identified alpha, beta, and gamma allotropes of iron (1890)
Johan A. Brinell	1849–1925	Sweden	Identified critical points (1885)
Adolf Martens	1850–1914	Berlin	LOM of cast irons (1878)
Henri Le Chatelier	1850–1936	Paris	Invented Pt/Pt-Rh thermocouple, for quantitative thermal analysis (1886)
John E. Stead	1851–1923	Sheffield	Drew attention to the crystalline nature of iron and steel (1898) Studied eutectics and effects of phosphorus
Hendrik W.B. Roozeboom	1854–1907	Amsterdam	Fe-C phase diagram consistent with Gibbs Phase Rule (1900)
John O. Arnold	1858–1930	Sheffield	Systematic studies of alloy elements (1894) and diffusion (1899)
Robert A. Hadfield	1858–1940	Sheffield	Fe-13Mn-1C, austenitic alloy (1882) Fe-3Si soft magnet alloy (1899)
Nikolai S. Kurnakov	1860–1941	St. Petersburg	Thermal analysis and phase equilibria
Gustav H.J.A. Tammann	1861–1938	Dorpat Göttingen	Nucleation and growth concepts (1922) Systematic phase diagram studies *Lehrbuch der Metallographie* (1st edn, 1914)
Albert Sauveur	1863–1939	Chicago Boston	Surveyed nomenclature (1938) and hardening theories (1896, 1926) *Metallography and Heat Treatment of Iron and Steel* (1st edn, 1916)
Emil Heyn	1867–1922	Berlin	Popularized LOM in Germany Founded Deutsche Gesellschaft für Metallkunde

Published by Woodhead Publishing Limited, 2012

1.3.2 The state of carbon

The 'hardening problem' is recounted in various sources, including Smith (1960, 1964, 1965a, 1965b, 1968, 1992), Vanpaemel (1982), Maddin (1992), and Stubbles (1998). It will be briefly summarized. The Greeks and Romans were aware that iron could be hardened by heating and quenching, but little progress was made until chemists studied the problem with their analytical methods in the 17th and 18th centuries. Rene de Reaumur was the key figure that invigorated these studies, and in the 1720s, he inverted the ancient understanding that steel is purified iron, instead proposing that the hardness in iron arose from some particulate matter acquired by iron ('sulfurs and salts', in the terminology of the time) that could be manipulated by heat treatment.

In 1774 the Swedish chemist Sven Rinman identified the role of a special substance in iron which he termed 'plumbago' (later to be renamed carbon in 1800). This substance was later investigated by another Swedish chemist, Tobern Bergman, and at the time was considered to be a type of phlogiston, a term which roughly translates as 'fire-substance'. (This view was a relatively minor addition or corollary to the phlogiston theories of combustion and rusting which dominated 18th century thinking on chemical changes more broadly.) The volume increase on quenching (identified by Charles Perrault in 1680) was a key observation that these theories sought to explain. The identification of carbon in iron, and its implied connection to hardening is a major stepping stone. But the advance was limited:

> the [quench-hardening] models from the 17th and 18th centuries were purely academic and in fact, useless for practice. None of these models could account for the relation between the final quenching product and the quenching temperatures or the various quenching agents. The models were largely qualitative in nature and of unlimited flexibility so no quantitative use or verification was possible (Vanpaemel, 1982).

Around 1790 the phlogiston theory was replaced with an atomic understanding of oxidation and other chemical changes by Antoine Lavoisier, Joseph Priestley and others. Oxygen and carbon were recognized as distinct elements as part of this paradigm shift into classical chemistry. Resolution of the hardening problem required recognition of both the chemical state of carbon and the allotropy of iron. Analytical chemistry methods allowed the carbon question to be examined first, in the early to mid-1800s; recognition of iron's allotropy would come later.

In 1865, L. Rinman (no apparent relation to Sven Rinman) chemically dissolved in acid steel specimens having the same chemistry but different heat treatments after austenitizing: a slow-cooled steel yielded a hard carbon-rich residue, whereas a quenched steel yielded no residue at all.

Published by Woodhead Publishing Limited, 2012

On this basis Rinman (1865) coined the terms 'cement carbon' for the soft residue-yielding sample and 'hardening carbon' for the hardened, residue-free sample. In modern parlance, 'hardening carbon' is carbon in solid solution while 'cement carbon' is that sequestered in a carbide phase. This 'cement carbon' residue would later be identified as the Fe_3C compound by Abel (1881) and Muller (1888), and christened 'cementite' by Floris Osmond in the same decade.

These concepts of carbon aggregation would play a significant role in the first theories of hardening that were proposed in the 1890s. These analytical chemistry methods helped focus attention on finding exactly what was different about two steels that had the same chemical composition but widely different properties. The answer was about to be revealed by LOM and thermal analysis, a combination used by the pioneering generation of ferrous phase transformations researchers (Table 1.1) to mount the first serious attack on the 'hardening' problem.

1.3.3 Thermal analysis and the allotropy of iron

The allotropic changes in iron and steel provided the other half of the picture needed to explain hardening, and thermal arrest measurements were the defining method of their study. Aspects of this are reviewed by Smith (1960, 1992), Cohen (1962), Sadovsky (1965), Thompson (1965), Cohen and Harris (1965), and Kelly (1976).

The critical points in iron were discovered by Dmitri Chernov[1] in 1868, though his results would not be available in English for another decade. He demonstrated two basic criteria that had to be met for carbon steels to be hardened:

1. The steel had to be heated above a critical temperature, which he labeled 'a'. (In 1894 this would be capitalized to A, with this particular temperature called the A_1.)
2. It then had to be cooled at a sufficiently high rate to below 200°C (now known as M_s).

Chernov also identified another threshold temperature, labeled 'b' and now associated with the A_3 critical temperature, above which austenite grain growth significantly accelerated.

Similar results came from the studies of Johan Brinell (1885). He described the hardening process as one of converting 'cement carbon' into 'hardening carbon' once the critical ('a') temperature was attained on heating, a process which occurred virtually instantaneously. On cooling, however, the reverse

[1]The surnames 'Chernov' and 'Tschernoff' are used interchangeably in the English-language literature.

Published by Woodhead Publishing Limited, 2012

process – 'hardening carbon' being converted back to 'cement carbon' – showed cooling-rate-dependent behavior: it was completed over a long time on slow cooling (to the product later identified as pearlite), whereas negligible conversion occurred at fast cooling rates (forming what is now known as martensite). Several thermal arrests (Table 1.2). were identified as a result of these studies. Burgess and Crowe (1913) provide an interesting compilation of early measurements of these critical temperatures by techniques other than thermal analysis; Cohen and Harris (1965) re-presented this data with commentary. Magnetic measurements were particularly important, and later played a key role in the determination of ternary phase diagrams (Honda, 1918).

By 1885 the converging evidence had reached critical mass. Chernov and Brinell had correlated the hardening of iron to certain heat treatments, though the temperatures could only be qualitatively measured by visual or other indirect means. Sorby (who presented his paper at a meeting that year) and Adolf Martens (Section 1.3.5) had demonstrated the possibilities of LOM, though without advancing a new interpretative understanding. It was Floris Osmond who deployed (and improved on) all these experimental techniques to purposely advance a theory of hardening. First, he replaced fractography with metallography as the preferred window into microstructure. He then seized upon Henri Le Chatelier's newly invented Pt/Pt-Rh thermocouple to precisely measure temperatures and thermal arrests, which he did at Louis-Joseph Troost's laboratory at the Sorbonne (Osmond, 1886, 1890). Previous methods and protocols of thermal analysis were inaccurate and cumbersome; Kayser and Patterson (1998) review this. Osmond demonstrated that these thermal arrests on cooling reappeared on heating, but at slightly higher temperatures. He added the subscripts c ('chauffage' or heating) and r ('refroidissement' or cooling) to the symbols, giving the nomenclature of Ac and Ar that are still used today.

Osmond's basic approach of quantitative thermal analysis, metallography, and chemical analysis (and urged on by his single-minded focus on steel) launched a wave of systematic research geared toward theorizing and understanding. The combination of these and other methods were on display in the first paper (Osmond and Werth, 1885; commentary by Bastien, 1965). These studies were international in scope, with correspondence and conference interactions among all the major researchers (Table 1.1). By the mid 1890s, the expanding metallographic and thermal arrest observations prompted a flowering of hardening hypotheses. These were surveyed by Albert Sauveur (1896), which generated 100 pages of discussion from the leaders in the field (AIME, 1898).

The evidence for the allotropic transitions in iron and steel provided substance for the 'Allotropist' theory. They held that the hardening was due to a high-temperature superhard allotrope of iron, soon identified as

Published by Woodhead Publishing Limited, 2012

Published by Woodhead Publishing Limited, 2012

Table 1.2 Critical points (thermal arrests) in the Fe-C binary system and their associated phase transitions (Sauveur, 1896; Kennon, 1999b)

Symbol	Reaction	Temperature range	Thermodynamic order	Description
A_4	$\delta \leftrightarrow \gamma$	1394–1495°C [1667–1768 K]	1st	Precipitation of austenite from δ-ferrite
A_3	$\gamma \leftrightarrow \beta$	768–912°C [1041–1185 K]	1st	Ferrite precipitation when it occurs above the A_2. This pertains to carbon contents below ~0.45 wt%
A_2	$\beta \leftrightarrow \alpha$	768°C [1041 K]	2nd	Paramagnetic (β)-ferromagnetic (α) ordering transition in ferrite
A_{32}	$\gamma \leftrightarrow \alpha$	727–768°C [1000–1041 K]	1st	Ferrite precipitation when it occurs below the A_2. This pertains to carbon contents between ~0.45 and 0.77 wt%
A_{cm}	$\gamma \leftrightarrow \theta_p$	727–1148°C [1000–1421 K]	1st	Precipitation of paramagnetic cementite in hypereutectoid steels
A_1	$\gamma \leftrightarrow \alpha + \theta_p$	727°C [1000 K]	1st	Eutectoid reaction in hypoeutectoid and eutectoid steels
A_{13} (or A_{321})	$\gamma \leftrightarrow \alpha + \theta_p$	727°C [1000 K]	1st	Eutectoid reaction in hypereutectoid steels
A_0	$\theta_p \leftrightarrow \theta_f$	215°C [488 K]	2nd	Paramagnetic-ferromagnetic ordering transition in cementite

θ is the symbol for cementite; the subscripts p and f refer to paramagnetic and ferromagnetic ordering in this compound. The other Greek letters identify iron's allotropes. The symbols A_{13} and A_{32} appear less frequently in modern usage, where they are lumped together with A_1 and A_3, respectively.

beta-iron (Table 1.2), which was retained on rapid quenching. The physical origin of beta's remarkable hardness could only be speculated upon, though. On this view, carbon had no special role other than enabling the retention of beta. Osmond and William Chandler Roberts-Austen were the major Allotropists.

An opposing view of hardening, the Carbonist theory, was promoted by Sheffield metallurgists Robert Hadfield and John Oliver Arnold (1894, 1896). They held that the hardening was due to the amount and state of aggregation of carbon. They postulated a hardening constituent – a specific molecular or colloidal arrangement of iron and carbon that they variously termed 'martensite' or 'hardenite' – that altered its arrangement upon quenching. Arnold in fact insisted that the high-temperature constituent was the stoichiometric chemical compound, named hardenite, that decomposed on quenching according to the eutectoid reaction: $Fe_{24}C \rightarrow 21Fe + Fe_3C$. This is referred to as Arnold's 'sub-carbide' theory. A 'carbo-allotropic' theory that incorporated elements of both theories was proposed by Henry Marion Howe (1895), a central figure who corresponded widely with all the major researchers. His hybrid theory never caught on, and his inclinations were Carbonist in any event.

Walter Rosenhain entered the debate in 1909 with at-temperature measurements of the relative slip behavior of alpha, beta, and gamma iron (Rosenhain and Humfrey, 1909), which strongly supported the hard-beta tenet of the Allotropist position. Later measurements of at-temperature tensile behavior demonstrating that gamma was actually harder than beta threw the earlier conclusions into doubt (Rosenhain and Humfrey, 1913); vigorous, even vitriolic discussion followed this paper. Rosenhain ended up re-interpreting both experiments in terms of a third view that martensite is the hard amorphous phase created by the breakup of the austenite crystal structure by the interstitial carbon movements during its decomposition; Howe (1916, p. 190) summarizes this. When this took place at a low enough temperature during cooling, the amorphous product would not be able to (re)-crystallize into a softer phase. These ideas had their roots in the amorphous-cement theory of grain boundaries first proposed by George Beilby around 1903; Rosenhain would be an untiring advocate for this view until his death in 1934. These major hardening theories as well as several lesser-known ones based on grain size, residual stresses, and even phlogiston are presented in accessible prose penned by Sauveur in the 1930s and republished more recently (Sauveur, 1981).

In so far as an allotropic phase change (FCC→BCC/BCT) *and* dissolved carbon in austenite are required to harden steel, both the Carbonist and Allotropist theories were partly right, but they missed the bigger picture. This is understandable in view of the limitations of experimental methods and the inadequacy of the paradigms in circulation. The widely-held misperception

Published by Woodhead Publishing Limited, 2012

that iron's allotropy was a molecular or colloidal phenomenon was not soon relinquished (Cohen and Harris, 1965). For example, the discussions in both of Albert Sauveur's surveys of hardening theories (Sauveur, 1896; AIME, 1898; Sauveur, 1926) are shot through with molecule-based reasoning. The sway that the concept of a superhard allotrope had on the thinking at the time is understandable in light of the best-known example of allotropy: the graphite and diamond forms of carbon, with their striking differences in properties. This reasoning was a dead end when applied to iron, as X-ray diffraction would later demonstrate that beta and alpha are crystallographically identical in terms of atom positions, differing only in magnetic order. Beta was ultimately dropped from the nomenclature of iron phase diagrams in the 1930s and 1940s. However, the philosophical issue as to whether beta-iron constitutes a phase thermodynamically distinct from alpha-iron occasionally merits attention (Cohen and Harris, 1965; Massalski, 2010).

1.3.4 Phase equilibria and alloy additions

Phase diagrams were the key theoretical innovation of this period, and are reviewed by Smith (1992) and Kayser and Patterson (1998). Josiah Willard Gibbs (1875–78) published his far-reaching theory of heterogeneous phase equilibria in a little-read journal where this dense, inaccessible work would lie dormant for a quarter-century. James Clerk Maxwell, who had corresponded with Gibbs, appreciated the significance of his work. Just before Maxwell's death in 1879, he discussed Gibb's work with Johannes van der Waals, who in turn brought it to the attention of Hendrik W.B. Roozeboom. (Had Maxwell lived longer he would have publicized it more widely.)

It was Roberts-Austen (1899) who drew the first Fe-C phase diagram, a nearly-correct one at that. This prompted Roozeboom (1900) to re-formulate the Fe-C diagram consistent with the Gibbs Phase Rule. This was a major advance, in the sense of constraining the bounds of what was thermodynamically permissible. However, the practical delineation of distinct phases continued to be challenging owing to the limitations of characterization methods and the kinetic complexities of steels.

Metal alloy additions also generated considerable interest in this period. High-alloy steels containing Cr, Ni, W, and other elements had been produced throughout the 1800s, but fresh understandings provided by thermal analysis, metallography and phase diagrams gave new impetus to these studies. The 1880s and 1890s saw initial successes with Robert Hadfield's development of the first austenitic steel, Fe-13Mn-1C, for wear-resistance applications, and soft magnetic Fe-3Si alloy used in electrical transformers (recounted by Main, 1965, and Bechtold and Wiener, 1965). Hadfield undertook systematic studies of numerous alloying elements, and collaborated with James Dewar,

Published by Woodhead Publishing Limited, 2012

Heike Kammerlingh-Onnes and others to measure low-temperature properties in alloy steels as well (Main, 1965).

As another example, Fe-1.8C-9W-2.5Mn air-hardening steels were invented by Robert Mushet in 1868 and were initially applied to the low-speed cutting of other hard steels, such as for gun barrels. Starting in 1894 Frederick Taylor and Maunsel White applied this material with remarkable success to high-speed machining of softer mild steels, ushering in the modern age of 'high-speed' or 'red-hard' tool steels.[2] More broadly, stainless steels and other alloys rich in Cr and Ni underwent significant development during 1900–1920 in France, England, and Germany, recounted by Bastien (1965).

The science had not developed well enough to predict the response from adding any given element. Something of a false start came from Osmond's (1890) classification of alloy elements based on Roberts-Austen's view that the strength of an alloy was determined by the atomic volume of the solute. This was based on empirical observations that alloy additions to gold having higher atomic volumes weakened the alloy, while those with comparable or lower volumes had little effect. This theory did not translate to iron; Arnold (1894) happily demonstrated inconsistencies in his Allotropist rival's hypothesis. In any event, a better grouping into austenite-stabilizers and ferrite-stabilizers emerged after ternary Fe-C-M phase diagrams were studied in depth starting in the 1920s, where M represents substitutional, typically metallic, alloy element(s).

1.3.5 Constituents, microstructure, and reaction sequences

Sorby is credited with the first examination of metallic microstructure via LOM. Two decades after his initial report of 1864, Sorby briefly reappeared onto the scene, prompted by the recent work published by Martens and Osmond. Sorby (1886) reported the discovery of a 'pearly compound', enabled by improvements in the resolving power of his microscope lenses. Although he provided no micrographs in this paper, his description of pearlite is quite accurate: alternating plates of a hard carbon-rich constituent and a soft carbon-poor constituent, the ratio of which increases with the bulk carbon content; furthermore, the 'pearly compound' forms from the decomposition of a homogeneous constituent stable at higher temperatures. A related paper displayed a variety of micrographs from various iron and steel grades in addition to meteoric iron that first drew his interest to metals (Sorby, 1887).

[2]Taylor would become even more widely known in the business world for his views on workplace 'scientific management'. This was inspired by his systematic, empirical approach to tool steel research and development which was first tested when he reorganized the Bethlehem Steel machine shops, a saga recounted by Misa (1995).

Published by Woodhead Publishing Limited, 2012

However astute these observations were on pearlite, he did not offer much in the way of interpretation, and furthermore could not resolve the details of quench-hardened microstructures that were the main focus of attention. These were Sorby's last original research papers on iron and steel, and he turned his attention to other topics. By this time, an ever-growing number of researchers knew of Sorby's innovation and had the means and motivation to apply LOM to a broader range of ferrous microstructures.

The application of metallography and thermal analysis, in addition to the established chemical analysis of dissolved residues, defined the normative pattern of research in this period. This combination motivated the development of hardening theories, which were about much more than just hardening, narrowly considered. In the most illuminating studies (Sauveur, 1896), thermal arrest and microstructural data were systematically quantified as a function of carbon content and annealing (austenitizing) temperature. The theories would have to account not only for the hard constituent present at ambient temperature (martensite) but also all of the other constituents that appeared in the microstructures, now made visible by LOM – a tall order. Such studies provided the essential data on the phases present at various temperatures and compositions that enabled the first Fe-C phase diagrams to be drawn around 1900 (see Section 1.3.4).

It was a tortuous path to the modern microstructural nomenclature, of which pearlite, bainite, martensite, and proeutectoid ferrite/carbide are the major constituents. Half a century passed between the discovery of the first clearly recognizable constituent, pearlite, and the establishment of modern nomenclature. Sorby had described the structure and constitution of coarse pearlite remarkably well. The coarseness of this product lent it to LOM investigations, which resulted in the early work on stereology (Belaiew, 1922) and considerations of 3D structure (Belaiew, 1925). The other constituents, an ever-shifting, sometimes overlapping list of names and definitions, would not fare so well, as their fine structure was beyond the resolution of LOM. Prior to the application of X-ray diffraction in the 1920s and electron microscopy in the 1950s and 1960s, the internal arrangement of the phases constituting these outwardly visible constituents could only be speculated upon. Phase-diagram lever-rule analyses of mesoscale metallographic data provided useful insight, while the molecular-based theories of the constituents' chemical arrangements at finer length scales continued to be a distraction.

The hard constituent in steel was named 'martensite' in 1895 by Osmond in recognition of Adolf Martens, a bridge engineer with the Prussian State Railway who took up the metallography of cast irons (Martens, 1878,1893) in his spare time. Smith (1960) notes: 'Martens' initial article (published in the *Zeitschrift des Vereines deutscher Ingenieure* in January 1878) is the first paper on microstructure of metals to be widely noted by both scientists and industrial metallurgists alike, and it marks the transition from

Published by Woodhead Publishing Limited, 2012

sporadic observations of structure to a planned attempt to study it in relation to properties.' Martens was dedicated to accuracy of observation, as his published sketches of iron-carbon eutectic mixtures show. Martens and his later collaborator Emil Heyn popularized metallography but did not relate their careful observations to any metallurgical theory or view of hardening. Osmond originally had 'martensite' in mind for the high temperature parent phase, but switched this to 'austenite' after Roberts-Austen published the first Fe-C phase diagram in 1899. The term 'martensite' was then redeployed to name the hard product itself.

Howe took up the task of systematizing the names and understandings of microstructure. He proposed the terms eutectoid, ferrite, cementite and pearlite which were endorsed by Osmond in 1893. Howe corresponded widely with the other major researchers and organized an international effort to systematize nomenclature in 1910–1912 (Howe *et al.*, 1912). He knew that names conveyed meanings, and did not propose these terms lightly. Howe continued to coin geologic-sounding names, a pattern that made sense to the practitioners of this era and which most likely originated with Sorby. More examples of Howe's unique terminology are scattered throughout his major monograph (1916). The researchers of the time had to contend not only with the proeutectoid, pearlite, bainite, and martensite constituents of prime interest today, but also a wider array of microstructural constituents related to slag, inclusions, eutectics, and other features related to gross chemical inhomogeneities and uncontrolled temperature excursions. It was not always clear which constituents resulted from solid-solid transformations and which originated in liquid reactions. Albert Sauveur was still early in his career (Sauveur, 1896) when he began to assume Howe's role of the consolidator and redactor of the burgeoning ferrous researches from the first and second generations (Tables 1.1 and 1.3). He continued in this role for over four decades (Sauveur, 1916, 1926, 1935, 1938, 1939).

A variety of other terms were in circulation that described products now known as medium-to-fine-spacing pearlite, bainite (in its many variations), tempered martensite, and spheroidite. Names were assigned to these products early on, prior to a fuller understanding of their internal structures (which in any event was still several decades in the future). This would pose difficulties in view of an ever-expanding body of data and theories. Sorbite, troostite, and osmondite were the most notable of the terms no longer in circulation. Different researchers used these terms to describe different, or at least, incompletely overlapping products that at best appeared outwardly the same at LOM resolutions. Sorbite and troostite were coined by Howe in honor of Sorby and Troost, respectively, but these terms would ultimately get dropped after the 1930s (Vilella *et al.*, 1936).

In descriptive terms, sorbite was the most straightforward of these terms since it described products having LOM-resolvable ferrite-carbide mixtures:

Published by Woodhead Publishing Limited, 2012

Table 1.3 Second-generation ferrous phase transformations researchers (born 1870–1895)

Name	Lifespan	Location	Contributions and notable monographs
Kotaro Honda	1870–1954	Sendai	Magnetic alloys Phase diagrams
Harry Brearley	1871–1948	Sheffield	Invented stainless steel (1913)
Leon Guillet	1873–1946	Paris	Stainless and other alloy steels
Carl Benedicks	1875–1958	Stockholm	LOM of troostite Founded Swedish Institute for Metallography (1920)
Walter Rosenhain	1875–1934	London	Theories of slip, (re)-crystallization, and phase diagrams *Introduction to Physical Metallurgy* (1914)
Nicholas T. Belaiew	1878–1955	St. Petersburg London Paris	Widmanstatten structures Pearlite stereology Carbides in Damascus steel
Albert Portevin	1880–1962	Paris	Stainless steel Tempering
William H. Hatfield	1882–1943	Sheffield	Invented 18Cr-8Ni stainless steel (1924)
Heinrich Hanemann	1883–1960	Berlin	*Atlas Metallographicus* (1927)
Axel Hultgren	1886–1974	Stockholm	Ortho- and para-equilibrium concepts for ferrite and carbide formation (1947)
Pierre Chevenard	1888–1960	Decazeville Saint Etienne	Ni-rich, Invar, creep- and oxidation-resistant steels Precision dilatometry
Zay Jeffries	1888–1965	Cleveland	Red hardness of tool steels Grain size quantification Theory of work hardening
Arne Westgren	1889–1975	Stockholm	X-ray diffraction determinations of iron's allotropes (1921) and many other phases in ferrous and nonferrous alloys
Marcus A. Grossmann	1890–1952	Cleveland Pittsburgh	Hardenability *Principles of Heat Treatment* (1st edn, 1935)
Edgar C. Bain	1891–1971	Cleveland New York Kearny, NJ Pittsburgh	Solid solutions (1923) Isothermal transformations, TTT diagrams, reaction sequences (1930) Identified bainite and re-systematized nomenclature (1936) *Alloying Elements in Steel* (Bain and Paxton, 1966)

Published by Woodhead Publishing Limited, 2012

spheroidite and very coarse pearlite. Although sorbitic microstructures possess the same phases at comparable length scales, the distinction between the phase transformation reaction paths by which they evolved – some passing through martensite and others passing more directly from pearlite – had yet to be recognized. The other two terms were more difficult to define since they described products having internal structures not resolvable by LOM. Osmondite, the least used of these three terms, was proposed three times without being formally adopted. It referred to martensite after light to medium amounts of tempering. Probably the most elastic and troubled of these terms was troostite (Benedicks, 1905; Howe, 1907; Sauveur, 1935). Bullens' (1912) survey of troostite definitions gives some idea of their variability and the interpretative views in circulation at the time:

- Finely divided graphite (Breuil)
- Pure beta-iron (Boynton)
- Carbide-saturated beta-iron (Fletcher)
- Elementary carbon/carbide in alpha-iron (Kourbatoff; Sauveur)
- Pearlite with ultra-microscopic (colloidal) cementite (Benedicks)
- Supersaturated solid solution of carbide in alpha iron, part of which is under stress (Campbell)
- Ferrite + cementite + saturated austenite (Rogers)
- Deposited 'solvite' – cementite saturated with austenite (Kroll).

The best definition of troostite in modern parlance includes bainite and medium- to fine-spacing pearlite. Given the sub-micron length scales of these microstructures that would not be rendered visible until many decades later with the advent of electron microscopy, it is not difficult to see why the troostite definitions of 1912 varied so widely. Kennon (1999a) provides a thorough listing of both obsolete and currently used nomenclature and terminology.

The sequences by which these various constituents were thought to have formed were quite different in relation to the modern understanding. The prevailing idea at the time was that martensite was a transition state located in a chain of decomposition reactions represented, for example, by Howe (1907):

$$\text{austenite} \leftrightarrow \text{martensite} \leftrightarrow \text{troostite} \leftrightarrow \text{osmondite} \leftrightarrow \text{sorbite} \leftrightarrow \text{pearlite} \qquad [1.1]$$

In this scheme, a continuous, uninterrupted slow cool would realize the entire chain of reactions, resulting in the end-state of pearlite. A cooling path interrupted by a quench would preserve the condition that existed at the time of the quench, which could result in martensite, troostite, osmondite, or sorbite; these were 'spontaneously caught in transit' (Howe, 1916, p. 78). So

Published by Woodhead Publishing Limited, 2012

on this view martensite served as a transition state or precursor (remote or proximate) for all the remaining constituents, including pearlite. There were different versions of the sequential 'decomposition-chain'. Early evidence to the contrary was provided by Portevin and Garvin (1919) and Chapin (1922). However, the modern view of kinetically competitive products, all of which form directly from the starting austenite, would not gain wide acceptance until after the first isothermal transformation studies in the 1930s.

1.3.6 The first period in perspective

Physical metallurgy was in its formative years during this period, driven on by the needs of steel producers and users. The burgeoning data being gathered from LOM, thermal analysis and other new methods like magnetometry and dilatometry called out for an interpretative framework that would bring order and understanding. Most notable of the first-period accomplishments was the development of the first accurate iron-base phase diagram, which organized ferrite allotropes and carbides with the constraints imposed by the Gibbs phase rule.

The understanding of kinetics, microstructural development, and the hardening problem benefited from fresh influxes of data but was still a work in progress at the close of the first period around 1925. Sorby's application of LOM to steels finally opened the door to the unexplored world of microstructure, but only pearlite had been clearly identified. The other microstructural constituents were all given names without fundamental, direct understanding of their internal structures or kinetic modes of formation, resulting in confusion that only compounded the difficulties of formulating a robust hardening theory; Sauveur (1896, 1926) found little progress in a 30-year span. The experimental methods were approaching their asymptotic limits as they were incapable of revealing the details of atomic arrangements. Lacking this crucial information, the old molecular paradigm maintained its hold on the interpretative imagination.

1.4 The consolidation of ferrous phase transformations in the second period (1925–1970)

1.4.1 Overview

This impasse was broken when Max von Laue discovered X-ray diffraction (XRD) by solid crystals in 1912. The basic structure of metals and alloys was finally revealed to be overwhelmingly crystalline, packed as atoms not molecules, and possessing defects. This breakthrough ushered in the second period, one of paradigm building on sounder physical foundations (Cahn,

1999). The application of XRD to steels in the 1920s and early 1930s had an immediate impact on ferrous phase transformations. The pioneering X-ray studies of Westgren (1921) and Westgren and Phragmen (1922, 1924) revealed several key points:

- The alpha, beta, and delta allotropes of iron are crystallographically identical, BCC.
- Gamma iron has an FCC structure, which expands with dissolved carbon.
- Carbon atoms in the austenite do not substitute for iron atoms.
- Carbide phases other than cementite are present in certain alloy steels, such as M_6C.

Edgar Collins Bain realized the potential of XRD early on. He reproduced some of Westgren and Phragmen's results while informing topics such as:

- understanding solid solutions in terms of an atomic, not molecular basis (Bain, 1923),
- identifying the $(Fe,W)_6C$=M_6C phase as responsible for the red hardness in tool steels (Bain and Jeffries, 1923), and
- revealing key aspects of stainless steels, including the Fe-Cr gamma loop and relating carbide precipitation to stainless steel corrosion (Bain *et al.*, 1933).

Besides the obvious crystal structure information, XRD also provided evidence of crystal imperfections that anticipated the proposal of dislocations and other crystalline defects in the 1930s. Fortuitously, solid-state physics began its emergence into a recognizable field during the second period (Hoddeson *et al.*, 1992), the same time that physical metallurgy was doing the same. Diffraction methods and the problems in crystal and defect structure they illuminated offered a point of commonality between metallurgical phase transformations and solid state physics. XRD was augmented by transmission electron microscopy (TEM) in the 1950s and microanalysis in the 1960s; each new technique caused a fresh reconsideration of older data and inspired new theories and approaches. This would drastically shift the paradigm for understanding solids, one rooted in crystalline phases, defects, and kinetic processes governing microstructural evolution.

Bolstered by these new methods, second and third generations of researchers (Tables 1.3 and 1.4) would obtain a satisfactory answer to the hardening problem, with advances in store for all phase transformations.

1.4.2 Martensite

Among all phase transformations, martensite advanced the most rapidly in the second period. This is perhaps due to its relative simplicity of involving

Published by Woodhead Publishing Limited, 2012

Table 1.4 Third-generation ferrous phase transformations researchers (born 1895–1920)

Name	Lifespan	Institutional Affiliations	Research Areas
Robert F. Mehl	1898–1976	Juniata College Naval Research Laboratory American Rolling Mill Co. Carnegie Institute of Technology US Steel	Crystallography of precipitation Diffusion mechanism Pearlite formation Overall nucleation and growth kinetics
Zenji Nishiyama	1901–1991	Tohoku University Osaka University Nippon Steel Co.	Martensite, tempering, and aging Recrystallization and deformation
Carl Wagner	1901–1977	Technische Hochschule Darmstadt Massachusetts Institute of Technology Max Planck Institute of Physical Chemistry (Göttingen)	Thermodynamics of solutions and defects Diffusion Oxidation kinetics
Georgii V. Kurdjumov	1902–1996	Institutes in Moscow and Kiev	Martensite formation, tempering, and aging
Cyril Stanley Smith	1903–1992	American Brass Co. Los Alamos Scientific Laboratory University of Chicago Massachusetts Institute of Technology	Crystallography of precipitation and pearlite Grain and phase morphology History of metallurgy
Clarence Zener	1905–1993	Washington University of St. Louis City College of New York Washington State University Watertown Arsenal University of Chicago Westinghouse Electric Co. Texas A&M University Carnegie Mellon University	Diffusional growth theory applied to precipitation, pearlite, bainite, grain coarsening, and creep Diffusion mechanism and internal friction Zener diode Geometric programming Oceanic thermal energy harvesting
Alexander R. Troiano	1908–2002	Notre Dame University Case Institute of Technology	Crystallography and growth of martensite and bainite Hydrogen effects and corrosion

Published by Woodhead Publishing Limited, 2012

Table 1.4 (Continued)

Name	Lifespan	Institutional Affiliations	Research Areas
Lawrence S. Darken	1909–1978	US Steel Brooklyn Polytechnic Institute Pennsylvania State University	Diffusion mechanism Thermodynamics of alloys Thermochemistry of steelmaking Growth of pearlite and tin whiskers
Morris Cohen	1911–2005	Massachusetts Institute of Technology	Martensite formation, tempering, and aging Thermodynamics Diffusion Materials education and public policy
Thomas A. Read	1913–1966	Frankford Arsenal Oak Ridge National Laboratory Columbia University University of Illinois	Martensite crystallography Internal friction Deformation Corrosion
David Turnbull	1915–2007	Case Institute of Technology General Electric Co. Harvard University	Nucleation theory and experiment Diffusion Cellular and recrystallization reactions Amorphous materials
Norman J. Petch	1917–1992	Cambridge University Leeds University University of Newcastle-Upon-Tyne Strathclyde University	Crystallography: carbon positions in cementite, austenite, and martensite Grain size effects on mechanical response

Published by Woodhead Publishing Limited, 2012

a change in crystal structure but not composition. XRD yielded the first wave of improved martensite understanding. Westgren and Phragmen's (1922) high-temperature diffraction studies effectively spelled the end of beta-iron theories of hardening. X-rays provided clear evidence that martensite is in fact a distorted form of BCC alpha iron. Bain (1924) proposed an illustrative picture of a homogeneous deformation of an FCC austenite unit cell to create the BCC unit cell, now called the 'Bain Strain' (reviewed by Bowles and Wayman, 1972, and Wayman, 1990). Shortly thereafter, Fink and Campbell (1926) provided clear evidence that martensite had a tetragonal distortion that was related to the carbon content. This tetragonality was soon related to the anisotropic distortion of trapped carbon atoms and FCC-BCC crystallographic relationships by Kurdjumov and others in the 1920s and 1930s; for more, see Kurdjumov (1960) and Roytburd (1999). Once mechanical strength was related to the inhibition of dislocation and twin activity in the 1930s, 1940s and 1950s, it became clear that the severe distortions of the BCC/BCT lattice by misfitting carbon atoms gave the remarkable hardness of ferrous martensite; Cohen (1962) surveys the evolution in this understanding.

The concept of an FCC-BCT lattice correspondence that was consistent with these notions gained acceptance, and were soon measured, resulting in the well-known Kurdjumov–Sachs, Nishiyama–Wasserman, and Greninger–Troiano orientation relationships (recounted by Wayman, 1990). The development of the concepts of dislocation and twinning defects in the 1930s and beyond provided the means to understand the self-accommodation of crystallographic variants. The adoption of a micromechanical outlook (strain energy minimization) led to the major martensite development of this period: the Phenomenological Theory of Martensite Crystallography (PTMC), developed independently by Weschler, Lieberman and Read (1953) and Bowles and Mackenzie (1954). The PTMC and related understandings were shortly thereafter used (Bilby and Christian, 1956) to explain earlier habit plane and crystallographic observations in ferrous martensite (Greninger and Troiano, 1940, 1949) and were extensively tested against habit plane and other measurements in a wide variety of ferrous and non-ferrous systems in the following decades.

The advent of TEM allowed the fine structure of martensite's internal defects and external interfaces to be examined in great detail. Martensite studies in the 1940s and 1950s focused heavily on model alloys having high carbon and alloy contents, especially Fe-30Ni-(C). When low-carbon, low-alloy martensites received increasing attention in the 1960s (Marder and Krauss, 1967, 1969) there was a recognition of two distinct classes of ferrous martensite. Most of the terms in use related to the martensite morphology, though others focused on the lattice invariant deformation type (dislocation vs twin), composition (low-carbon vs high-carbon) or even relative speed of martensite growth (Schiebung vs Umklapp). To resolve the confusion

Published by Woodhead Publishing Limited, 2012

stemming from the large number of terms in use at the time, Krauss and Marder (1971) polled the martensite community and settled on the terms 'lath' and 'plate' martensite.

In the 1950s the nucleation of martensite became a focus of study that still remains at the frontier of research. Homogeneous nucleation processes were ruled out early on, from observations of martensite forming at 4 K, where thermal activation was not feasible (Kaufman and Cohen, 1956). Small-particle experiments that effectively subdivided the nucleating heterogeneities into hermetically-sealed compartments, originally used for solidification studies (Vonnegut, 1948; Turnbull, 1949), bolstered the evidence for heterogeneous nucleation (Cech and Turnbull, 1956; Magee, 1971).

There has been considerable theoretical work since the late 1940s (Fisher and Hollomon, 1949) to identify the appropriate defect structure (dislocation array) of a martensite embryo and critical nucleus (Kaufman and Cohen, 1958). Martensite nucleation and growth problems are examples where theory outpaced experiment, in view of the ~1000 m/s rate of propagation of a martensite unit (Forster and Scheil, 1940; Bunshah and Mehl, 1953). Zener (1948) proposed the first theory predicated on elastically soft phonon modes that caused the resistance to shearing of the parent lattice into product lattice to diminish as the M_s was approached.

Time was added as a variable with the discovery of isothermal martensites (Kurdjumov and Maksimova, 1948; Shih *et al*., 1955), as contrasted with the more typical athermal variety. Isothermal martensite highlighted the alteration of martensite formation and subsequent aging by incidental interactions with diffusive processes such as stabilization, autotempering, Zener ordering, spinodal decomposition, chemical ordering, or segregation of carbon and other interstitials (Harris and Cohen, 1949; Kinsman and Shyne, 1967); these are reviewed by Kurdjumov and Khachaturyan (1972) and Taylor and Cohen (1992). Additionally, alternate driving forces for martensite formation were also identified, including stress (Patel and Cohen, 1953), strain (Olson and Cohen, 1972), and magnetic field (Korenko and Cohen, 1974). The shape memory effect had been identified in a variety of ferrous alloys in the 1970s and 1980s (reviewed by Maki, 1990).

1.4.3 Precipitation and tempering

The modification of ferrous alloys due to minor second phase particles, whether carbonitrides, intermetallics, or oxides, became increasingly well known and understood in the second period. This was exploited for both dispersion hardening and for austenite grain size control purposes. The awareness of optimal particle size and spacing relationships, and the kinetics of the Ostwald ripening (second-phase particle coarsening) of such dispersions provided a key understanding that gave focus for optimal alloy and processing design.

Published by Woodhead Publishing Limited, 2012

Speich and Clark (1965) and Edmonds and Honeycombe (1978) survey the entire range of precipitation in ferrous alloys.

Martensite tempering provides an example of the variety of decomposition paths available when starting from highly supersaturated, highly defective microstructures. The three classical stages of tempering – (1) transition carbide formation, (2) decomposition of retained austenite, and (3) further relief of martensite's carbon supersaturation to form cementite in a BCC matrix – were illuminated by a series of systematic studies (Roberts *et al*., 1953; Lement *et al*., 1954, 1955; Werner *et al*., 1957). A fourth stage of tempering, alloy carbide precipitation, was identified in 'secondary-hardening' steels (Kuo, 1953, 1956). Other subtle phenomena have been observed that alter the condition of martensite during the quench or natural aging, such as autotempering, Zener ordering, clustering, segregation, and spinodal decomposition (reviewed by Cohen, 1962, Owen, 1992 and Taylor and Cohen, 1992).

Classical precipitation hardening was first observed in an aluminum alloy by Wilm in 1906. Once Merica *et al*. (1920) identified the phase diagram prerequisite (decreasing solid solubility with decreasing temperature), a plethora of other alloys had been successfully precipitation hardened (Newkirk, 1968). Age-hardening in dozens of iron-based alloys had been identified by the early 1950s (Geisler, 1951; Hardy and Heal, 1954). The nature of the precipitating particles and their cluster and transition-phase precursors became clearer with the advent of TEM in the 1950s and atom probe two decades later. Two instances of precipitation in ferrous alloys will be briefly mentioned.

Classical continuous precipitation from alpha-iron solid solutions has been demonstrated in many systems such as Fe-Mo (Geisler, 1951; Speich and Clark, 1965). Studies of Fe_3C and Fe_4N precipitation from alpha-iron (Wert, 1949) using internal friction helped motivate the first quantitative theories of precipitation kinetics (Zener, 1949; Wert and Zener, 1950; Ham, 1958, 1959).

Maraging steels first emerged around 1960 (Decker and Floreen, 1988). Since they are hardened by intermetallic precipitation instead of carbide precipitation, these alloys are compositionally distinct from other high-strength steels by their negligibly low level of carbon and their high alloy content (~18 wt% Ni, in addition to Mo, Ti, Co, and W). Fine-scale Guinier–Preston zones and intermetallic particles evolve out of the supersaturated martensitic matrix during aging, producing an extraordinary combination of ultrahigh strength and toughness. Since these precipitates are composed solely of slower-diffusing substitutional elements, they resist coarsening much better than carbides. Moreover, dimensional stability and weldability are robust from an industrial perspective.

Published by Woodhead Publishing Limited, 2012

1.4.4 Microconstituents and overall kinetics in transformations involving diffusion

Resolution of the hardening problem required two understandings to emerge: the physical origin of the intrinsic hardness of martensite (Section 1.4.2), and how martensite is obtained on cooling vis-à-vis all the alternative austenite decomposition reaction products that compete with martensite. The modern view of kinetically competitive products, each of which originated directly from austenite (and not via intermediate products, notably martensite), was prefigured by Portevin and Garvin (1919), but would not be accepted until the pioneering isothermal transformation studies of Robertson (1929), Davenport and Bain (1930) and Vilella *et al*. (1936). Like many major shifts in understanding, remnants of the old 'decomposition-chain' view (Eq. [1.1]) would appear in the literature for another decade or two (Sauveur, 1935, 1938, 1939; Honda, 1926, 1935, 1949).

Bain and co-workers experimentally determined time-temperature-transformation (TTT) diagrams in a large number of steels throughout the 1930s (Davenport, 1939), and recognized the critical importance of grain size in addition to alloy chemistry on the overall kinetics (Bain, 1932a, 1932b, 1938). The concept of hardenability now began to mature (Grossmann, 1935). Isothermal studies were rapidly adopted by researchers worldwide, and by the 1940s the first TTT diagram compilations were being published. Likewise, the burgeoning LOM observations were organized into large 'metallographic atlases' (Hanemann and Schrader, 1927; Habraken *et al*., 1966). A key aspect of Bain's approach was to determine the kinetics of austenite decomposition reactions from direct LOM observations. These isothermal studies revealed a new microconstituent, bainite, named in Bain's honor by his colleagues. This prompted the sorting out of microstructural nomenclature into its modern groupings (Vilella *et al*., 1936). Mehl (1948) further discusses these developments.

Indirect techniques such as dilatometry, resistivity, magnetometry, XRD, and hardness measurements continued to be used in addition to the more time-intensive LOM, and notably, all these gave different answers to the question 'when does the transformation start?' (Smith, 1935). This highlights the underappreciated role of 'pre-transformation phenomena'. These might be pragmatically defined as the changes taking place in a system prior to the visible appearance or other distinct signal indicating the 'official start' of transformation. This has been a topic of some interest for martensitic transformations (Tanner and Wayman, 1981; Tanner and Soffa, 1988), tempering (Krauss and Speich, 1983; Taylor and Cohen, 1992), and age-hardening alloys (Haasen *et al*., 1984).

Semi-empirical theories of overall reaction kinetics were developed independently by many workers (Cahn, 2001), including Johnson and

Published by Woodhead Publishing Limited, 2012

Mehl (1939), Avrami (1939, 1940, 1941), and Kolmogorov (1937). Pearlite formation in eutectoid steels proved to be an early test case (Mehl and Hagel, 1956). The overall kinetics were separated out into the more fundamental rates of nucleation and growth that were measured independently (Hull *et al.*, 1942). The adoption of Arrhenius temperature dependencies into overall reaction rates and their interpretation in terms of activation energies of more fundamental diffusive processes evolved over several decades; see Laidler (1993) and Philibert (2006) for more on this.

1.4.5 Morphology and crystallography of transformations involving diffusion

By the late 1930s, isothermal transformations, XRD, and LOM were established as the preferred approach for the study and interpretation of phase transformations. The product morphologies and their connection to the crystallographic relations between phases became of interest. The initial impetus had been a landmark series of nine studies of Widmanstatten morphologies by Mehl and colleagues during 1930–37 (e.g., Mehl *et al.*, 1933). The strikingly faceted, directional morphology of Widmanstatten ferrite and carbide precipitates (whether in their proeutectoid or bainitic forms) suggested a crystallographic relationship between the precipitate and the austenite matrix. The measurement of definite ferrite-austenite orientation relationships that were correlated with good matching along low-index, close-packed crystallographic planes further accentuated this view.

Bainite has been viewed as encompassing the broad category of ferritic reaction products described as having, in some way, a 'Widmanstatten' morphology, which might include any elongated shape, such as plates, laths, or rods. Over time, 'bainite' assumed almost as elastic a definition as troostite had back in the first period. Bainite came to be defined negatively: for practical purposes bainite included all products that were not proeutectoid grain boundary allotriomorphs, pearlite, or martensite (all of which are more easily recognized). This confusion can be attributed in part to its nonlamellar morphologies and in part to its transformation kinetics that vary widely from alloy to alloy.

This morphological variability (ISIJ, 1995; Kennon, 1999a) coupled with related formation mechanism disputes stretched the definitions of bainite to their breaking point and prompted reconsiderations of the morphological varieties and bounding definitions of bainite, starting at the end of the second period (Aaronson, 1969; Hehemann, 1970; Hehemann *et al.*, 1972; Aaronson *et al.*, 1990a,b; Christian and Edmonds, 1984; Bhadeshia and Christian, 1990; Bramfitt and Speer, 1990; Hillert, 1995). The mechanistic debate arose out of observations that bainite exhibited characteristics consistent with a displacive, martensite-like mechanism:

Published by Woodhead Publishing Limited, 2012

1. surface relief (Ko and Cottrell, 1952; Christian and Edmonds, 1984; Aaronson and Hall, 1994),
2. substructure of slightly misoriented subunits (Oblak and Hehemann, 1967; Kinsman and Aaronson, 1967; Bhadeshia, 1981; Bhadeshia and Edmonds, 1979, 1980),
3. ferrite-carbide crystallography (Bhadeshia, 1980),
4. upper limiting temperature B_s (Zener, 1946),
5. incomplete reaction phenomena (Hehemann, 1970; Aaronson *et al.*, 2006), and
6. stabilization (Hehemann and Troiano, 1954, 1956).

Bainite, however, does have distinct diffusional aspects (or at least appeared to violate one or more of the strict criteria for a displacive transformation). Not fitting neatly into diffusional or displacive categories, bainite became the occasion for controversy as to its formation mechanism. The major points of disagreement concern the following areas:

- *Crystallography*: Whether the mechanism of FCC→BCC lattice change is 'military' (displacive) or 'civilian' (diffusive) (Christian, 1965), with the attendant consequences for the structure of the austenite-bainite transformation interface (glissile vs. sessile) and the nature and meaning of surface relief.
- *Kinetics*: The fundamental reason why the overall kinetics vary by orders of magnitude between different alloys, and why in many instances the incomplete reaction phenomenon and an upper limiting temperature (B_s) are observed.
- *The fate of carbon*: Whether the freshly formed ferritic component of bainite is completely, partially, or negligibly carbon-supersaturated.

Several major exchanges of view on these and other bainite-related topics were published in the literature in the 1980s. A bainite study in an Fe-C-Mn-Si steel by Bhadeshia and Edmonds (1979) generated several discussions (Liu *et al.*, 1985; Aaronson *et al.*, 1989a; Enomoto, 1989) and authors' replies (Bhadeshia and Edmonds, 1985, 1989a,b). Likewise, Christian and Edmonds (1984) prompted several rounds of critiques (Aaronson and Reynolds, 1988a,b; Aaronson *et al.*, 1989b) and authors' replies (Christian and Edmonds, 1988a,b, 1989).

The debates on these topics, although made more difficult by semantic issues, did center on substantive technical points of disagreement that were unable to be resolved, partly due to experimental limitations. Since that time, the 'bainite debate' (as it were) continues to simmer, with continuing work being done with advanced experimental methods and modeling approaches that inform topics such as interfacial structure, solute effects, and carbon supersaturation. In recent years, several varieties of diffusional-displacive

Published by Woodhead Publishing Limited, 2012

theories of bainite have emerged, which attempt to reconcile the diffusional and displacive aspects and enable quantitative kinetic modeling of this transformation.

Bainite's long history of confusion and controversy should not obscure the many ways in which it has become a technologically relevant microstructure that is critical to the superior strength, toughness, and weldability of many advanced steels (see, for example, Bhadeshia, 2001, 2004). Bainite's finer scale offers many advantages in comparison with ferrite-pearlite microstructures on which more conventional steels are based.

Crystallographic insights resulted from studies of the morphology of the more uniform (and less controversial) transformation products that form at lower supersaturations than Widmanstatten and bainite products. Allotriomorphic precipitates and pearlite nodules exhibit rounded interfaces with the austenite that suggested a lack of crystallographic constraint with respect to the parent austenite. The ferrite-cementite crystallography *within* pearlite was recognized, though. Proeutectoid ferrite and cementite morphologies were classified by a scheme that recognized the determining roles of nucleation site and interfacial structure (Dube *et al.*, 1958; Aaronson, 1962). These observations were generalized in a theory of precipitate morphology whose interpretative key was interfacial structure vis-à-vis the ledge mechanism of solid-solid precipitate growth (Aaronson *et al.*, 1970), a concept that originated in the vapor-solid and liquid-solid crystal growth literature in the 1930s. This was but one area that benefited from the understanding of partially coherent boundaries in terms of misfit dislocation arrays (Frank and van der Merwe, 1949; van der Merwe, 1950).

The 'active nucleus' of pearlite became of interest in view of its two-phase structure. Hull and Mehl (1942) proposed cementite as the active nucleus; further, the cementite had to repeatedly re-nucleate as the pearlite colony expanded outward during growth. Mehl and Hagel (1956) and Howell (1998) review these topics. Serial sectioning and polarized light metallography by Hillert (1962) prompted a new model of pearlite evolution, based on the gradual development of cooperation between ferrite and cementite, which formed interpenetrating single crystals. Pearlite and bainite/Widmanstatten ferrite were placed at opposite ends of the crystallographic spectrum in terms of parent-product orientation relationship and interfacial structure. Pearlite adopts no reproducible relation to the parent austenite, while the bainite/Widmanstatten ferrite evolves under considerable crystallographic constraint by the austenite. This was supported by XRD (Mehl and Smith, 1935; Smith and Mehl, 1942) and LOM (Hultgren and Ohlin, 1960) studies. The observation of the faceting of bainite/Widmanstatten ferrite and a rounded, nodular growth front for pearlite reinforced this understanding. It was concluded that the pearlite grew with a disordered or incoherent interface (Smith, 1953; Hillert, 1962).

Published by Woodhead Publishing Limited, 2012

1.4.6 Kinetic theories of diffusional nucleation and growth

Systematic isothermal transformation studies starting in the 1930s clearly outlined the time- and temperature-dependence of overall reaction rates of non-martensitic transformation products. The concepts of nucleation and growth (N&G) as the fundamental processes governing the overall rate had been around for some time (see Cahn's 1987 retrospective). For example, Gustav Tammann (1922) sketched the undercooling dependence of nucleation and growth rates in solidification that translated well to solid state transformations; Fine (1996) reviews this. The application of N&G theory to solids had three major tasks:

1. understanding solid state diffusion,
2. deriving solute flux-growth rate equations for specific processes of embryo development or precipitate growth, and
3. obtaining thermodynamic and other ancillary quantities that entered into these kinetic equations.

These will be considered in turn.

The very idea of solid state diffusion was in itself a paradigm shift from an older 'inert view' of solid matter (see Cahn, 1999). Diffusion was first observed in the Pb-Au system by Roberts-Austen (1896), who had benefited from working as assistant to diffusion pioneer Thomas Graham (Barr, 1997). Extensive diffusion measurements in steel were soon made by Arnold and McWilliam (1899), and it became widely recognized that both carbon and substitutional alloying elements diffused in solid iron and steel. An Arrhenius temperature-dependence of diffusion was first proposed by Dushman and Langmuir (1922), though it had been prefigured by Roberts-Austen. This development was pivotal for understanding the temperature-dependence of diffusional transformation kinetics.

Interstitial diffusion was conceived in the 1930s and probed with internal friction measurements (Zener, 1948); Wert (1986) reviews these studies. Diffusion couple methods were also used (Wells *et al.*, 1950). The specific mechanism of substitutional diffusion took longer to work out. The direct exchange and ring mechanisms were widely held views prior to the discovery and later acceptance of a vacancy-mediated mechanism by Smigelskas and Kirkendall (1947). This mechanism meshed well with statistical thermodynamic understandings of vacancy and other defect concentrations developed two decades prior by Schottky *et al.* (1929). Radiotracer methods enabled the diffusivities for all major elements in ferrite and austenite to be determined by the end of this period (Fridberg *et al.*, 1969).

Darken (1948) recast Fick's continuum diffusion flux equations in terms of the chemical potentials rather than concentrations. This was soon confirmed in

Published by Woodhead Publishing Limited, 2012

observations of uphill carbon diffusion in Fe-C-Si diffusion couples (Darken, 1949). It laid the foundation for solving the classic diffusion problems in steel, those involving simultaneous migration of fast-diffusing carbon and slow-diffusing substitutional elements. Another important phenomenon, short-circuit diffusion along defects, was recognized in the 1950s (see Mehrer, 2006) and would be a key factor in theories of lamellar and grain boundary, precipitation (Cahn and Hagel, 1962; Aaronson and Domian, 1966).

Placing N&G on a quantitative basis suitable for experimental testing required that these rates be expressed in terms of fundamental thermodynamic and kinetic quantities. Diffusional solid-solid nucleation theory was adapted from statistical fluctuation-based nucleation theories of condensation from vapor or liquid (Volmer and Weber, 1925; Becker and Doring, 1935). A kinetic rate equation of unit atom additions (or removals) from a growing (or dissolving) embryo formed the basis of the classical solid-solid nucleation theory that emerged (Turnbull, 1948, Fisher *et al.*, 1948; Turnbull and Fisher, 1949). The competition between chemical driving forces and strain and surface energy retarding forces allowed the calculation of the nucleation barrier ΔG^*. The basic concepts were in place by the mid 1950s (Hollomon and Turnbull, 1953). Theoretical evaluations of ΔG^* and other factors in a variety of homogeneous and heterogeneous nucleation circumstances then followed; see Lee and Aaronson (1975) and Kelton and Greer (2010) for more details.

Continuum diffusional growth rate theories based on a sharp-interface model were first formulated in a seminal paper by Zener (1946). It outlined a quantitative approach to diffusion-limited kinetics, based on simple physical principles and mathematics, which set the standard for the work that followed (Zener, 1949, Hillert, 1957; Ham, 1959). Its basic premise was that the diffusional flux was the rate-limiting step in precipitate growth; the change in crystal structure was faster and would proceed as quickly as the diffusion flux allowed. Differential equations coupling growth rate and solute flux were formulated and solved for a variety of precipitate geometries, including the cooperative growth of pearlite and cellular colonies (Turnbull, 1955; Cahn, 1959). Characteristic growth rate time exponents were predicted for allotriomorphic/equiaxed precipitates, Widmanstatten plate/lath/rod precipitates, pearlite, and cellular forms. These growth exponents were confirmed by experimental measurements in standard N&G experiments (Mehl and Hagel, 1956; Speich and Cohen, 1960; Kinsman and Aaronson, 1967) as well as in carburization/decarburization experiments where the nucleation step was factored out (Purdy and Kirkaldy, 1963). Hillert (1986) recounts how the research into problems of precipitate morphology, instability, size-scaling, and pattern selection grew out of Zener's new approach.

The differential equations for growth required the specification of boundary conditions at the migrating interface. These models usually made the assumption

that chemical local equilibrium (LE) obtained at the interface (modified by interfacial curvature), and that the interface structure itself posed negligible impediment to its migration. The application of LE to the ternary diffusion case was first developed by Kirkaldy and others (Kirkaldy, 1958; Purdy *et al*., 1964; Coates, 1973). LE and the related theory of paraequilibrium (PE) growth (Hultgren, 1947; Hillert, 1953) made specific predictions about the growth rate and elemental partitioning that were tested against growth kinetics measurements on ferrite or cementite precipitates. The added complexities of coupled two-phase growth were elucidated in Cahn and Hagel's (1962) in-depth survey of ferrous pearlite N&G kinetics, which established itself as a key point of reference for later studies.

The electron microprobe allowed direct measurements of substitutional element partitioning, providing early tests of LE and PE theories of proeutectoid ferrite (Aaronson and Domian, 1966; Gilmour *et al*., 1972; Sharma and Kirkaldy, 1973). Good-to-fair agreement with LE/PE treatments obtained at low supersaturations in both partitioning and growth rate measurements. The deviations from local equilibrium found at higher supersaturations were thought to arise from solute-drag forces acting to retard the interfacial motion (Kinsman and Aaronson, 1967; Hillert, 1969). These solute-drag theories (reviewed by Hillert, 1999, and Aaronson *et al*., 2004) were adapted from treatments originally developed for recrystallization and grain growth (Cahn, 1962).

Thermodynamic functions and phase diagrams were key inputs in the kinetic N&G equations. The various modeling approaches adopted were predicated on energetic competition between phases (Kaufman *et al*., 1962; Aaronson *et al*., 1966a,b; McLellan and Dunn, 1969). This was generalized as the Calphad method that became dominant (Kaufman and Bernstein, 1970; Saunders and Miodownik, 1998). This is quite different from the Hume-Rothery (1926) approach, with its focus on the electron/atom ratio in substitutional solid solution systems.

1.4.7 Unusual kinetic behavior and morphologies

Steels abound with transformation products deviating from the 'classical' ones. Two will be cited. Divergent pearlite in Fe-C-Mn and Fe-C-Si does not fit the textbook picture since its growth rate decreases and its interlamellar spacing increases with isothermal reaction time (Cahn and Hagel, 1962, 1963; Fridberg and Hillert, 1970). This highlights the interactions of long range interstitial volume diffusion and interphase boundary diffusion of substitutional elements. An ever-decreasing driving force for growth vs time at constant temperature slows the growth and widens the interlamellar spacing. Divergent pearlite has also been observed above the upper Ae1, where ferrite is not an equilibrium phase; Cahn and Hagel (1962) demonstrated the

Published by Woodhead Publishing Limited, 2012

temperature-composition domain where this is thermodynamically possible. This product was first observed by Hultgren and Edstrom (1937), who called it 'porous cementite'; this was later reinterpreted as being divergent pearlite (Fridberg and Hillert, 1970; Hillert, 1982).

Interphase precipitation is a technologically important nonclassical austenite decomposition product. It consists of the cooperative growth of ferrite with nonlamellar carbides such as MC, M_2C, M_6C, or $M_{23}C_6$. It was first observed in low-carbon steels containing 13 wt% Cr (Mannerkoski, 1964) or 2 wt% Mo (Relander, 1964). It was named interphase precipitation by Davenport *et al*. (1968) and Berry *et al*. (1969). Interphase precipitation is a technologically important strengthening mechanism; scientifically, it lent insight into the structure and migration of ledged interfaces (Honeycombe, 1976).

1.4.8 Spinodal decomposition, order-disorder, and magnetic transitions

The transformations reviewed up to this point have been of the first order N&G variety, the major ones governing the behavior of steel. A different set of continuous and/or second-order transformations has also been observed. The best known of these is spinodal decomposition (Hillert, 1961; Cahn, 1961, 1968). This required the development of the concept of chemically diffuse interfaces (Cahn and Hilliard, 1958, 1959). Spinodal decomposition has been observed both for carbon and substitutional elements like Cr and Be. Atom probe field-ion microscopy has been the key technique in these studies; see reviews by Haasen (1985), Taylor and Cohen, (1992), and Miller (2012).

Chemical order-disorder transformations were discovered early in the second period (Bain, 1923; Johansson and Linde, 1925; Nix and Shockley, 1938). The first quantitative order-disorder model by Bragg and Williams (1934) laid the path for later developments in continuous and/or second-order transformations, much in the way that seminal papers by Zener (1946) and Turnbull (1948) set the course for diffusional first-order N&G transformations a decade later.

Fe-Al has been a model system for testing the approaches to antiphase boundary migration kinetics and decomposition paths more broadly in systems undergoing both chemical and magnetic ordering (Cahn and Allen, 1977; Allen and Cahn, 1976, 1979). This work resulted in the Allen–Cahn equation governing the evolution of nonconserved order parameters in phase field models.

The second-order magnetic transition in iron was recognized early on and figured into the beta-iron controversies of the first period. Fe-Si soft magnet alloys developed by Hadfield around 1900 were soon put to use in

electrical transformers (Main, 1965; Bechtold and Wiener, 1965). Rapid development of iron-containing hard magnetic materials took place starting in the 1930s, such as Alnico alloys, whose superior properties derived from their fine precipitate structure; these are reviewed by de Vos (1969) and Haasen (1985).

1.4.9 The second period in perspective

The discovery of XRD and its application to metals and alloys in the 1920s was a pivotal turning point in the modern history of phase transformations. The first period confusions were resolved and its data re-interpreted in light of this new paradigm of crystalline solids and their defects. The revelation of these hitherto unknown patterns of structure raised new questions and opened up fresh avenues of inquiry.

At the same time, solid state physics also began coalescing out of previously isolated lines of research into a recognizable field, a process that took several decades (Hoddeson *et al*., 1992; Smith, 1965a). This was beneficial for the advance of metallurgical phase transformations in view of the useful physical notions it brought to bear on understanding microstructural changes. The synergy between these two fields would reach its zenith around 1950. The support of open-ended, fundamental, interdisciplinary research at major government and corporate research laboratories contributed significantly to this milieu (Turnbull, 1987; Cahn, 1987, 2001). Many of these institutions were founded in the first period to support the growing chemical, electrical, and telecommunications industries (Servos, 1990). The technical imperatives of two world wars prompted a considerable expansion in the number, size, and overall funding of these institutes, from which physical metallurgy greatly benefited.

The old paradigm rooted in classical chemistry was shed in the second period. However, chemistry had also been changing. Physical chemistry emerged as a distinct field during 1880–1930 (Servos, 1990; Laidler, 1993; Cahn, 2001). Some of the pioneers in physical metallurgy (e.g., Kurnakov and Tammann) had physical chemistry backgrounds and were contemporaries of the founders of physical chemistry: Wilhelm Ostwald, Svante Arrhenius, and Jacobus van't Hoff. However, metallurgy and chemistry interacted only peripherally with one another in spite of their common interests in the Gibbs phase rule, solution thermodynamics, and thermally activated reaction kinetics. Simply put, chemistry never focused significant attention on crystalline structures and their imperfections, unlike solid state physics.

By the 1960s, the major phenomena and topical areas of phase transformations had been identified: thermodynamics, crystallography, defects, diffusion, nucleation, and growth. These data were rationalized in terms of the new paradigm centered on microstructure and its control through alloy chemistry

Published by Woodhead Publishing Limited, 2012

and processing. By the end of the second period around 1970, solid-solid phase transformations had matured to the point where the outstanding research problems could be described (Cohen *et al.*, 1963), several major conferences had been convened, and a major monograph (Christian, 1965) and the first textbooks (Fine, 1964; Burke, 1965; Shewmon, 1969) had been published.

This new phase transformations understanding had technological impacts when combined with insights about defect interactions that determine strength and ductility; the latter advanced rapidly in this period with the elucidation of dislocations and twins. This was a far cry from the beta-iron, amorphous-layer and 'knot' theories of hardening in earlier circulation as late as the 1920s. The ever-more ingenious use of phase transformations to attain optimal microstructures led to improvements in strength-ductility-cost metrics for steels. The path to high strength, ductile, weldable structural steels, continues to lie in fine-scale precipitates, grain size, and defect structures. Phenomena unforeseen at the start of the second period such as TRIP (Transformation Induced Plasticity) and interphase precipitation added new strategies for materials innovation in the 1960s. Similar possibilities implicit in ferrous alloys are far from being exhausted.

1.5 Conclusion

Research since 1970 has generally involved a working out of the understandings established by this point in time. For example, N&G theories were tested, thermodynamic databases were systematized, and kinetic equations of continuous transformations were generalized into phase-field approaches. With the help of ever-faster computers, theory, modeling, and simulation have become more sophisticated, but share the same physical basis (e.g., multicomponent diffusion, continuum elasticity) as the simpler theories first formulated in the 1950s.

However, there remains far-from-complete closure of experimental observation with theory, with serious discrepancies in many instances, such as nucleation, where accurate measurement of absolute interfacial energies remains the biggest source of uncertainty (Lange *et al.*, 1989), not to mention the continuing inability to directly observe nucleation at the atomic scale. The complexity of real microstructures – multiscale arrangements of crystals and defects – still eludes the rigorous quantitative description satisfying to the physicist, and may have been the major factor contributing to the divergence of solid state physics and physical metallurgy in the 1960s. The growing specialization of both disciplines, segregation into academic departments, and the closure or retrenchment of major industrial and government laboratories were also important factors. The overlap between the two fields receded to topics such as martensite, second-order transformations, and electronic structure.

Published by Woodhead Publishing Limited, 2012

The irreducible complexity of actual microstructures continues to challenge understandings of diffusional transformations. The variability of transformation products carrying the same name is not just a problem for bainite; it affects all nonmartensitic transformation products. The ever-growing list of adjectival modifiers to classical transformation product names (Kennon, 1999a) are testament to this problem. Diffusional transformations still are at the stage of qualitative or semi-quantitative explanation. Robust quantitative prediction of kinetics and microstructural development from first principles was recognized as a distant goal several decades ago (de Fontaine, 1981; Cohen, 1984) and remains so today. For their part, martensitic transformations met with many early successes in the second period, though its nucleation is still an outstanding challenge. Phase transformations remain at the frontier of materials research; discoveries and surprises still await the patient and perceptive researcher.

Phase transformations and physical metallurgy were in their infancy in the 1880s when Sorby and the first generation began to lift the veil on metallic microstructure, starting with steel. A half-century later, the field realized a fruitful synergy with solid state physics, as the rate of discovery of the key physical phenomena, theorizing, and paradigm building hit a peak in the 1950s (Cahn, 1999). These physical understandings and intuitions, still with us today, enabled the long run of remarkable improvements of ferrous alloys and materials more broadly, stretching to the present time. So much remains to be uncovered under the many levels of complexity in real microstructure – and the varied and often subtle kinetic paths by which the material reached such a state. In this sense phase transformations is still a young field, inviting researchers to stretch their approaches and imaginations, just as it once beckoned the earlier generations on whose achievements we stand.

1.6 Bibliography

1.6.1 Key technical literature

Phase transformations conference proceedings, special journal issues, and monographs began appearing in the middle of the second period (c. 1950); they will be listed through to the present time. Book format proceedings citations are listed by the editor; if no editors were listed, then by the publisher. Journal citations are given by the editors or symposium organizers.

The present series of Solid-Solid Phase Transformations (PTM) proceedings can be found in Aaronson *et al.* (1982), Lorimer (1988), Johnson *et al.* (1994), Koiwa *et al.* (1999), Howe *et al.* (2005), and Bréchet *et al.* (2011). Other broad-spectrum proceedings of similar scope include Smoluchowski *et al.* (1951), Institute of Metals (1956), Nicholson *et al.* (1969), ASM

Published by Woodhead Publishing Limited, 2012

(1970), Smith *et al*. (1979), and Tsakalakos (1984). Interest in martensitic transformations warranted a dedicated series of International Conferences on Martensite (ICOMATs): Suzuki (1976), Naukova Dumka (1978), Owen *et al*. (1979), Delaey and Chandrasekaran (1982), JIM (1987), Muddle (1990), Wayman and Perkins (1993), Gotthardt and Van Humbeek (1995), Ahlers *et al*. (1999), Pietikainen and Soderberg (2003), Ko *et al*. (2006), and Olson *et al*. (2009).

There have been a number of ferrous-specific proceedings. The *Decomposition of Austenite* series includes Zackay and Aaronson (1962), Marder and Goldstein (1984), Damm and Merwin (2003) and Clarke *et al*. (2011). Others of general interest include Speich and Clarke (1965), Climax Molybdenum (1967), Wayman (1972), and Doane and Kirkaldy (1978).

Those specific to bainite and related issues of morphology and interfacial structure include Smith (1987), Cohen (1990), Aaronson and Howe (1991), Wayman *et al*. (1994), ISIJ International (1995), Hillert (2002), and Bhadeshia (2004). Martensite and tempering are covered in Kinsman and Magee (1971), Krauss and Speich (1983), Olson *et al*. (1990), Krauss and Repas (1992), Olson and Owen (1992), and Chen (1998).

1.6.2 Key historical and biographical literature

Volumes of a historical nature include Mehl (1948, 1965), Smith (1960, 1965b), and Cahn (2001). The origins of solid-state physics are surveyed in Mott (1980) and Hoddeson *et al*. (1992). The paradigms that shaped solid-solid phase transformations were examined by Cahn (1999). Barr (1997), Tuijn (1997), and Mehrer (2006) review historical topics in diffusion. Laidler (1993) traced the lineage of major concepts and personalities in thermodynamics and kinetics, from a physical chemistry perspective.

The quarterly periodical *Metallographist* is a key primary reference containing lively discussions and biographical information from a formative decade in the first period. It was founded and edited by Albert Sauveur in 1898, and after having been renamed *Iron and Steel Magazine* in 1904, ceased publication in 1906 (Smith, 1960). Personal reflections on the first period developments and personalities were penned by Sauveur in the 1930s and later re-issued (Sauveur, 1981).

Extended commentaries and retrospectives on the contributions of key ferrous phase transformations researchers can be found in the following articles, proceedings, and festschrifts:

- Various chapters in Smith (1965b) for JO Arnold, EC Bain, RA Hadfield, HM Howe, Z Jeffries, H Le Chatelier, A Martens, F Osmond, HC Sorby, JE Stead, and DK Chernov.
- Austin (1970) and Stubbles (1998) for HM Howe.

- Wayman (1972) for EC Bain.
- Kelly (1976) for W Rosenhain.
- Hillert (1986) for C Zener.
- Cargill *et al*. (1987) for D Turnbull.
- Kayser and Patterson (1998) for WC Roberts-Austen.
- Ahlers *et al*. (1999) for GV Kurdjumov.
- Cahn (2001) for K Honda, GV Kurdjumov, RF Mehl, W Rosenhain, CS Smith, G Tammann, and many others.
- Pietikainen and Soderberg (2003) for GV Kurdjumov and Z Nishiyama.
- Ko *et al*. (2006) for M Cohen.
- Olson *et al*. (2009) for TA Read and several other martensite researchers.

The *Dictionary of Scientific Biography* (Gillespie, 1970–1980) has entries for the following: NT Belaiew, C Benedicks, JA Brinell, DK Chernov, P Chevenard, JW Gibbs, NS Kurnakov, L Guillet, RA Hadfield, E Heyn, Z Jeffries, H Le Chatelier, A Martens, F Osmond, A Portevin, RAF de Reaumur, WC Roberts-Austen, HWB Roozeboom, W Rosenhain, A Sauveur, HC Sorby, JE Stead and G Tammann.

1.7 References

Aaronson HI (1962), 'The Proeutectoid Ferrite and Proeutectoid Cementite Reactions', in Zackay VF and Aaronson HI, *Decomposition of Austenite by Diffusional Processes*, New York, Interscience, pp. 387–546.

Aaronson HI (1969), 'On the Problem of the Definitions and the Mechanisms of the Bainite Reaction', *The Mechanism of Phase Transformations in Crystalline Solids*, London, Institute of Metals, pp. 270–281.

Aaronson HI and Domian HA (1966), 'Partition of Alloying Elements between Austenite and Proeutectoid Ferrite or Bainite', *Trans. TMS-AIME*, 236, 781–796.

Aaronson HI and Hall MG (1994), 'A History of the Controversy over the Roles of Shear and Diffusion in Plate Formation above M_d and a Comparison of the Atomic Mechanisms of these Processes', *Metall. Mater. Trans. A*, 25A, 1797–1819.

Aaronson HI and Howe JM, organizers (1991), 'The Role of Ledges in Phase-Transformations', *Metall. Trans. A*, 22A, 1137–1390.

Aaronson HI and Reynolds WT, Jr (1988a), 'Reply to a Discussion by J.W. Christian and D.V. Edmonds of Papers by Aaronson and Co-Workers on the Proeutectoid Ferrite and Bainite Reactions', *Scripta Metall.*, 22, 567–572.

Aaronson HI and Reynolds WT, Jr (1988b), 'Rejoinder to Comments by J.W. Christian and D.V. Edmonds', *Scripta Metall.*, 22, 575–576.

Aaronson HI, Domian HA and Pound GM (1966a), 'Thermodynamics of Austenite → Proeutectoid Ferrite Transformation I. Fe-C Alloys', *Trans. TMS-AIME*, 236, 753–767.

Aaronson HI, Domian HA and Pound GM (1966b), 'Thermodynamics of Austenite → Proeutectoid Ferrite Transformation II. Fe-C-X Alloys', *Trans. TMS-AIME*, 236, 768–781.

Aaronson HI, Laird C and Kinsman KR (1970), 'Mechanisms of Diffusional Growth of Precipitate Crystals', *Phase Transformations*, Metals Park, OH, ASM, pp. 313–396.

Aaronson HI, Laughlin DE, Sekerka RF and Wayman CM, eds. (1982), *Proc. Int. Conf. Solid-Solid Phase Transformations*, Warrendale, PA, TMS-AIME.

Aaronson HI, Reynolds WT, Hu H and Liu SK (1989a), 'Further Comments on "The Bainite Transformation in a Silicon Steel" ', *Metall. Trans. A*, 20A, 324–330.

Aaronson HI, Rigsbee JM, Furuhara T, Prabhu N, Reynolds WT, Jr and Howe JM (1989b), 'Further Rebuttal to J.W. Christian and D.V. Edmonds', *Scripta Metall.*, 23, 279–284.

Aaronson HI, Reynolds WT, Jr, Shiflet GJ and Spanos G (1990a), 'Bainite Viewed Three Different Ways', *Metall. Trans. A*, 21A, 1343–1380.

Aaronson HI, Furuhara T, Rigsbee JM, Reynolds WT, Jr and Howe JM (1990b), 'Crystallographic and Mechanistic Aspects of Growth by Shear and by Diffusional Processes', *Metall. Trans. A*, 21A, 2369–2409.

Aaronson HI, Reynolds WT and Purdy GR (2004), 'Coupled-Solute Drag Effects on Ferrite Formation in Fe-C-X Systems', *Metall. Mater. Trans. A*, 35A, 1187–1210.

Aaronson HI, Reynolds WT and Purdy GR (2006), 'The Incomplete Transformation Phenomenon in Steel', *Metall. Mater. Trans. A*, 37A, 1731–1745.

Abel FA (1881), 'Memorandum on Results of Preliminary Experiments Made with Thin Discs of Steel', *Proc. Inst. Mech. Engrs.*, 696–705. See also (1883) *Proc. Inst. Mech. Engrs.*, 70–71 and (1885) *Proc. Inst. Mech. Engrs.*, 30–57.

Ahlers M, Kostorz G and Sade M, eds. (1999), 'Proceedings of ICOMAT-98', *Mater. Sci. Eng.*, A273–275, 1–839.

AIME (1898), 'The Microstructure of Steel and the Current Theories of Hardening (Discussion)', *Trans. AIME*, 27, 846–944.

Allen SM and Cahn JW (1976), 'Mechanisms of Phase Transformations within the Miscibility Gap of Fe-Rich Fe-Al Alloys', *Acta Metall.*, 24, 425–437.

Allen SM and Cahn JW (1979), 'A Microscopic Theory for Antiphase Boundary Motion and Its Application to Antiphase Domain Coarsening', *Acta Metall.*, 27, 1085–1095.

Arnold JO (1894), 'The Physical Influence of Elements on Iron', *J. Iron Steel Inst.*, 45, 107–155; 181–251.

Arnold JO (1896), 'The Influence of Carbon on Iron', *Proc. Instn. Civil Engrs.*, 123, 127–162.

Arnold JO and McWilliam A (1899), 'The Diffusion of Elements in Iron', *J. Iron Steel Inst.*, 55, 85–129.

ASM (1970), *Phase Transformations*, Metals Park, OH, ASM.

Austin, JB (1970), 'Henry Marion Howe', *Metall. Trans.*, 1, 1795–1803.

Avrami M (1939), 'Kinetics of Phase Change. I. General Theory', *J. Chem. Phys.*, 7, 1103–1112.

Avrami M (1940), 'Kinetics of Phase Change. II. Transformation-Time Relations for Random Distribution of Nuclei', *J. Chem. Phys.*, 8, 212–224.

Avrami M (1941), 'Kinetics of Phase Change. III. Granulation, Phase Change, and Microstructure', *J. Chem. Phys.*, 9, 177–184.

Bain EC (1923), 'Crystal Structure of Solid Solutions', *Trans. AIME*, 68, 625–639.

Bain EC (1924), 'The Nature of Martensite', *Trans. AIME*, 70, 25–46.

Bain EC (1932a), 'On the Rates of Reaction in Solid Steel', *Trans. AIME*, 100, 13–46.

Bain EC (1932b), 'Factors Affecting the Inherent Hardenability of Steel', *Trans. Am. Soc. Steel Treat.*, 20, 385–428.

Bain EC (1938), 'Grain Size and Hardenability of Steels to be Heat Treated', *J. Iron Steel Inst.*, 138, 33–56.
Bain EC and Jeffries Z (1923), 'The Cause of Red Hardness of High Speed Steel', *Iron Age*, 112, 805–810.
Bain EC and Paxton HW (1966), *Alloying Elements in Steel*, Metals Park, OH, ASM.
Bain EC, Aborn RH and Rutherford JJB (1933), 'The Nature and Prevention of Intergranular Corrosion in Austenitic Stainless Steels', *Trans. Am. Soc. Steel Treat.*, 21, 481–509.
Barr LW (1997), 'The Origin of Quantitative Diffusion Measurements in Solids: A Centenary View', *Defect and Diffusion Forum*, 143–147, 3–10.
Bastien PG (1965), 'The Beginnings of Microscopic Metallography in France and Its Effect on the Physical Chemistry of Alloy Steels, Prior to 1920', in Smith CS, *The Sorby Centennial Symposium on the History of Metallurgy*, New York, Gordon and Breach, pp. 171–188.
Bechtold JH and Wiener GW (1965), 'The History of Soft Magnetic Materials', in Smith CS, *The Sorby Centennial Symposium on the History of Metallurgy*, New York, Gordon and Breach, pp. 501–518.
Becker R and Doring W (1935), 'Kinetic Treatment of Nucleus Formation in Supersaturated Vapors' [In German], *Annalen der Physik*, 24, 719–752.
Belaiew NT (1922), 'The Inner Structure of the Pearlite Grain', *J. Iron Steel Inst.*, 105, 201–239.
Belaiew NT (1925), 'On the Inner Crystalline Structure of Ferrite and Cementite in Pearlite', *Proc. Roy. Soc. London*, A108, 295–306.
Benedicks C (1905), 'The Nature of Troostite', *J. Iron Steel Inst.*, 2, 352–370.
Berry FG, Davenport AT and Honeycombe RWK (1969), 'The Isothermal Decomposition of Alloy Austenite', *The Mechanism of Phase Transformations in Crystalline Solids*, London, Institute of Metals, pp. 288–292.
Bhadeshia HKDH (1980), 'The Lower Bainite Transformation and the Significance of Carbide Precipitation', *Acta Metall.*, 28, 1103–1114.
Bhadeshia HKDH (1981), 'A Rationalisation of Shear Transformations in Steels', *Acta Metall.*, 29, 1117–1130.
Bhadeshia HKDH (2001), *Bainite in Steels*, 2nd edn, London, IOM Communications.
Bhadeshia HKDH, organizer (2004), 'Bainite Transformations', *Current Opinion in Solid State and Materials Science*, 8, 211–311.
Bhadeshia HKDH and Christian JW (1990), 'Bainite in Steels', *Metall. Trans. A*, 21, 767–797.
Bhadeshia HKDH and Edmonds DV (1979), 'The Bainite Transformation in a Silicon Steel', *Metall. Trans. A*, 10A, 895–907.
Bhadeshia HKDH and Edmonds DV (1980), 'The Mechanism of Bainite Formation in Steels', *Acta Metallurgica*, 28, 1265–1273.
Bhadeshia HKDH and Edmonds DV (1985), 'Reply to Discussion of "The Bainite Transformation in a Silicon Steel" ', *Metall. Trans. A*, 16A, 466–468.
Bhadeshia HKDH and Edmonds DV (1989a), 'Further Reply to Comments on "The Bainite Transformation in a Silicon Steel" ', *Metall. Trans. A*, 20A, 330–332.
Bhadeshia HKDH and Edmonds DV (1989b), 'Reply to Discussion of the Criticism of Heat Treatment of an Fe-C-Si Alloy', *Metall. Trans. A*, 20A, 333–334.
Bilby BA and Christian JW (1956), 'Martensitic Transformations', in *The Mechanism of Phase Transformations in Metals*, London, Institute of Metals, pp. 121–172.

Published by Woodhead Publishing Limited, 2012

Bowles JS and Mackenzie JK (1954), 'The Crystallography of Martensite Transformations', *Acta Metall.*, 2, 129–137, 138–147, 224–234.

Bowles JS and Wayman CM (1972), 'The Bain Strain, Lattice Correspondence, and Deformations Related to Martensitic Transformations', *Metall. Trans.*, 3, 1113–1121.

Bragg WL and Williams EJ (1934), 'The Effect of Thermal Agitation on Atomic Arrangement in Alloys', *Proc. Roy. Soc. London*, A145, 699–730.

Bramfitt BL and Speer JG (1990), 'A Perspective on the Morphology of Bainite', *Metall. Mater. Trans. A*, 21A, 817–829.

Bréchet Y, Clouet E, Deschamps A, Finel A and Soisson F, eds. (2011), 'Solid-Solid Phase Transformations in Inorganic Materials (PTM 2010)', *Solid State Phenomena*, 172–174, 1–1463.

Brinell J (1885), 'The Changes in the Texture in Steel on Heating and Cooling' [In Swedish], *Jernkontorets Annaler*, 40, 9–38. Full German text in (1885), *Stahl und Eisen*, 11, 611–620. English abstracts in (1886), *J. Iron Steel Inst.*, (i), 365–367; (1898), *J. Iron Steel Inst.*, 53, 145–189; and (1899), *The Metallogrophist*, 2, 129–136.

Bullens DK (1912), 'Mechanism of the Formation of Troostite', *Metallurgical and Chemical Engineering*, 10, 205–207.

Bunshah RF and Mehl RF (1953), 'Rate of Propagation of Martensite', *Trans. AIME*, 197, 1251–1258.

Burgess GK and Crowe JJ (1913), 'The Critical Ranges A2 and A3 of Pure Iron', *Trans. AIME*, 47, 665–739.

Burke JE (1965), *The Kinetics of Phase Transformations in Metals*, Oxford, Pergamon.

Cahn JW (1959), 'Kinetics of Cellular Segregation Reactions', *Acta Metall.*, 7, 18–28.

Cahn JW (1961), 'On Spinodal Decomposition', *Acta Metall.*, 9, 795–801.

Cahn JW (1962), 'Impurity-Drag Effect in Grain Boundary Motion', *Acta Metall.*, 10, 789–798.

Cahn JW (1968), 'Spinodal Decomposition', *Trans. TMS-AIME*, 242, 166–180.

Cahn JW (1987), 'The Emergence of Modern Nucleation Theory', in Cargill GS, Spaepen F and Tu KN, *Phase Transitions in Condensed Systems*, MRS Symp. Proc. 57, Warrendale, PA, MRS, pp. 41–55.

Cahn JW (1999), 'Challenges of Paradigm Building for Solid-State Transformations', in Koiwa M, Otsuka K and Miyazaki T, *Proc. Int. Conf. Solid-Solid Phase Transformations*, Sendai, Japanese Institute of Metals, pp. 3–14.

Cahn RW (2001), *The Coming of Materials Science*, New York, Pergamon.

Cahn JW and Allen SM (1977), 'Microscopic Theory for Domain Wall Motion and its Experimental Verification in Fe-Al Alloy Domain Growth Kinetics', *J. Physique Colloque*, 38-C7, 51–54.

Cahn JW and Hagel WC (1962), 'Theory of the Pearlite Reaction', in Zackay VF and Aaronson HI, *Decomposition of Austenite by Diffusional Processes*, New York, Interscience, pp. 131–192.

Cahn JW and Hagel WC (1963), 'Divergent Pearlite in Manganese Eutectoid Steel', *Acta Metall.*, 11, 561–574.

Cahn JW and Hilliard JE (1958), 'Free Energy of a Nonuniform System 1. Interfacial Free Energy', *J. Chem. Phys.*, 28, 258–267.

Cahn JW and Hilliard JE (1959), 'Free Energy of a Nonuniform System 3. Nucleation in a 2-Component Incompressible Fluid', *J. Chem. Phys.*, 31, 688–699.

Cargill GS, Spaepen F and Tu KN (1987), *Phase Transitions in Condensed Systems*, MRS Symp. Proc. 57, Warrendale, PA, MRS.

Published by Woodhead Publishing Limited, 2012

Cech RE and Turnbull D (1956), 'Heterogeneous Nucleation of the Martensite Transformation', *Trans. AIME*, 206, 124–132.

Chapin WR (1922), 'Properties of Some Steels in the Hardening Range', *Trans. Am. Soc. Steel Treat.*, 2, 507–515.

Chen HS, ed. (1998), *Proceedings of an International Conference on Displacive Phase Transformations and their Applications in Materials Engineering*, Warrendale, PA, TMS.

Chernov DK (1868), 'Critical Review of Lavroff's and Kalakutsky's Articles on Steel and Steel Guns and D.K. Chernov's Personal Investigations on the Same Subject' (in Russian), *Notes of the Russian Engineering Society*, July 1868, pp. 339–440. English translation in (1880), *Trans. Inst. Civil Eng.*, pp. 286–307.

Christian JW (1965), *The Theory of Transformations in Metals and Alloys*, 1st edn, Oxford, Pergamon.

Christian JW and Edmonds DV (1984), 'Bainite Transformation', in Marder AR and Goldstein JI, *Phase Transformations in Ferrous Alloys*, Warrendale, PA, TMS-AIME, pp. 293–325.

Christian JW and Edmonds DV (1988a), 'Reply to comments by H.I. Aaronson and W.T. Reynolds Jr.', *Scripta Metall.*, 22, 573–574.

Christian JW and Edmonds DV (1988b), 'Final Response to H.I. Aaronson and W.T. Reynolds Jr.', *Scripta Metall.*, 22, 577–580.

Christian JW and Edmonds DV (1989), 'Refutation of "Further Rebuttal" by Aaronson and Co-workers', *Scripta Metall.*, 23, 285–290.

Clarke AJ, Caballero FG and Hackenberg RE, organizers (2011), 'Austenite Formation and Decomposition IV', *Metall. Mater. Trans. A.*, 42A, 3590–3751.

Climax Molybdenum (1967), *Transformation and Hardenability in Steels*, Ann Arbor, MI, Climax Molybdenum.

Coates DE (1973), 'Diffusional Growth Limitation and Hardenability', *Metall. Trans.*, 4, 2313–2325.

Cohen M (1962), 'Strengthening of Steel', *Trans. TMS-AIME*, 224, 638–657.

Cohen M (1984), 'Ferrous Phase Transformations – Some Comments and Directions', in Marder AR and Goldstein JI, *Phase Transformations in Ferrous Alloys*, Warrendale, PA, TMS-AIME, pp. 403–406.

Cohen M, organizer (1990), 'International Conference on Bainite', *Metall. Trans. A*, 21A, 765–893 and 1341–1556.

Cohen M and Harris JM (1965), 'The Beta Iron Controversy', in Smith CS, *The Sorby Centennial Symposium on the History of Metallurgy*, New York, Gordon and Breach, pp. 209–233.

Cohen M, Cahn JW, Christian JW, Flinn PA, Hillert M, Kaufman L and Read TA (1963), 'Phase Transformations in the Solid State', in Himmel L, Harwood JJ and Harris WJ, *Perspectives in Materials Research*, Washington DC, Office of Naval Research.

Damm EB and Merwin MJ, eds. (2003), *Austenite Formation and Decomposition*, Warrendale, PA, TMS and ISS.

Darken LS (1948), 'Diffusion, Mobility and their Interrelation through Free Energy in Binary Metallic Systems', *Trans. AIME*, 175, 184–201.

Darken LS (1949), 'Diffusion of Carbon in Austenite with a Discontinuity in Composition', *Trans. AIME*, 180, 430–38.

Davenport AT, Berry FG and Honeycombe RWK (1968), 'Interphase Precipitation in Iron Alloys', *Metal Science*, 2, 104–106.

Davenport ES (1939), 'Isothermal Transformation in Steels', *Trans. ASM*, 27, 837–886.

Published by Woodhead Publishing Limited, 2012

Davenport ES and Bain EC (1930), 'Transformation of Austenite at Constant Subcritical Temperatures', *Trans. AIME*, 90, 117–154.

de Fontaine D (1981), 'Thermodynamics and Kinetics of Phase Separation', in Tien JK and Elliott JF, *Metallurgical Treatises*, Warrendale, PA, TMS-AIME, pp. 423–444.

de Vos KJ (1969), 'Alnico Permanent Magnet Alloys', in Berkovitz AE and Kneller E, *Magnetism and Metallurgy*, New York, Academic Press, pp. 473–512.

Decker RF and Floreen S (1988), 'Maraging Steels – The First Thirty Years', in Wilson RK, *Maraging Steels: Recent Developments and Applications*, Warrendale, PA, TMS, pp. 1–38.

Delaey L and Chandrasekaran M, eds. (1982), 'Proceedings of ICOMAT-82', *J. Physique Colloque*, 43-C4, 1–865.

Doane DV and Kirkaldy JS, eds. (1978), *Hardenability Concepts with Application to Steel*, Warrendale, PA, TMS-AIME.

Dube CA, Aaronson HI and Mehl RF (1958), 'La Formation de la Ferrite Proeutectoide dans les Aciers au Carbone', *Revue de Metallurgie*, 55, 201–210.

Durand-Charre M (2004), *Microstructure of Steels and Cast Irons*, Berlin, Springer.

Dushman S and Langmuir I (1922), 'The Diffusion Coefficient in Solids and its Temperature Coefficient', *Phys. Rev.*, 20, 113.

Edmonds DV and Honeycombe RWK (1978), 'Precipitation in Iron-Base Alloys', in Aaronson HI and Russell KC, *Precipitation Processes in Solids*, Warrendale, PA, TMS-AIME, pp. 121–160.

Enomoto M (1989), 'Discussion of the Criticism of Heat Treatment of an Fe-C-Si alloy', *Metall. Trans. A*, 20A, 332–333.

Fine ME (1964), *Phase Transformations in Condensed Systems*, New York, Macmillan.

Fine ME (1996), 'Phase Transformations in Condensed Systems Revisited: Industrial Applications', *Metall. Mater. Trans. A*, 27A, 2397–2418.

Fink WL and Campbell ED (1926), 'Influence of Heat Treatment and Carbon Content on the Structure of Pure Iron-Carbon Alloys', *Trans. Am. Soc. Steel Treat.*, 9, 717–754.

Fisher JC and Hollomon JH (1949), 'Kinetics of the Austenite-Martensite Transformation', *Trans. AIME*, 185, 691–700. Discussion (1950), *Trans. AIME*, 188, 1065–1066.

Fisher JC, Hollomon JH and Turnbull D (1948), 'Nucleation', *J. Appl. Phys.*, 19, 775–784.

Forster F and Scheil E (1940), 'Untersuhung des Zeitlichen Ablaufes von Umklappvorgangen in Metallen', *Z. Metallkunde*, 32, 165–173.

Frank FC and van der Merwe JH (1949), 'One-Dimensional Dislocations', *Proc. Roy. Soc. London*, 198A, 205–216; 216–225.

Fridberg J and Hillert M (1970), 'Ortho-Pearlite in Silicon Steels', *Acta Metall.*, 18, 1253–1260.

Fridberg J, Torndahl LE and Hillert M (1969), 'Diffusion in Iron', *Jernkontorets Annaler*, 153, 263–276.

Geisler GH (1951), 'Precipitation from Solid Solutions of Metals', in Smoluchowski R, Mayer JE and Weyl WA, *Phase Transformations in Solids*, New York, Wiley, pp. 387–544.

Gibbs JW (1875–78), 'On the Equilibrium of Heterogeneous Substances', *Trans. Connecticut Academy of Sciences*, 3, 108–248; 343–524.

Gillespie CC, ed. (1970–1980), *Dictionary of Scientific Biography* (in 16 volumes), New York, Scribner's.

Gilmour JB, Purdy GR and Kirkaldy JS (1972), 'Partition of Manganese during the Proeutectoid Ferrite Transformation in Steel', *Metall. Trans.*, 3, 3213–3222.

Gotthardt R and Van Humbeek J, eds. (1995), 'Proceedings of ICOMAT-95', *J. Physique IV Colloque*, 5-C8, 1–1264.

Greninger AB and Troiano AR (1940), 'Crystallography of Austenite Decomposition', *Trans. AIME*, 140, 307–336.

Greninger AB and Troiano AR (1949), 'The Mechanism of Martensite Formation', *Trans. AIME*, 185, 590–598.

Grossmann MA (1935), *Principles of Heat Treatment*, Metals Park, OH, ASM. The fifth edition (1964) was revised by EC Bain.

Haasen P (1985), 'The Early Stages of the Decomposition of Alloys', *Metall. Trans. A*, 16A, 1173–1184.

Haasen P, Gerold V, Wagner R and Ashby MF, eds. (1984), *Decomposition in Alloys: The Early Stages*, New York, Pergamon.

Habraken L, De Brouwer JL, Schrader A, Rose A and Pokorny A (1966), *De Ferri Metallographia: Metallographic Atlas of Iron, Steels and Cast Irons*, Philadelphia, PA, WB Saunders.

Ham FS (1958), 'Theory of Diffusion-Limited Precipitation', *J. Phys. Chem. Solids*, 6, 335–351.

Ham FS (1959), 'Diffusion-Limited Growth of Precipitate Particles', *J. Appl. Phys.*, 30, 1518–1525.

Hanemann H and Schrader A, eds. (1927), *Atlas Metallographicus*, Berlin, Borntraeger.

Hardy HK and Heal TJ (1954), 'Report on Precipitation', *Prog. Met. Phys.*, 5, 143–278.

Harris WJ and Cohen M (1949), 'Stabilization of the Austenite-Martensite Transformation', *Trans. AIME*, 180, 447–470.

Hehemann RF (1970), 'The Bainite Transformation', *Phase Transformations*, Metals Park, OH, ASM, pp. 397–432.

Hehemann RF and Troiano AR (1954), 'Stabilization of Bainite Reaction', *Trans. AIME*, 200, 1272–1280.

Hehemann RF and Troiano AR (1956), 'The Bainite Transformation', *Metal Progress*, 70, 97–104.

Hehemann RF, Kinsman KR and Aaronson HI (1972), 'Debate on the Bainite Reaction', *Metall. Trans.*, 3, 1077–1094.

Higham N (1965), 'Sorby – The Man and His Background', in Smith CS, *The Sorby Centennial Symposium on the History of Metallurgy*, New York, Gordon and Breach, pp. 17–41.

Hillert M (1953), 'Paraequilibrium', Internal Report, Stockholm, Swedish Institute for Metals Research. Reprinted in Agren J, Brechet Y, Hutchinson C, Philibert J and Purdy G (2006), *Thermodynamics and Phase Transformations: The Selected Works of Mats Hillert*, Les Ulis Cedex A, EDP Sciences, pp. 9–24.

Hillert M (1957), 'Role of Interfacial Energy during Solid State Phase Transformations', *Jernkontorets Annaler*, 141, 757–789.

Hillert M (1961), 'Solid-Solution Model for Inhomogeneous Systems', *Acta Metall.*, 9, 525–535.

Hillert M (1962), 'The Formation of Pearlite', in Zackay VF and Aaronson HI, *Decomposition of Austenite by Diffusional Processes*, New York, Interscience, pp. 197–237.

Published by Woodhead Publishing Limited, 2012

Hillert M (1969), 'The Role of Interfaces in Phase Transformations', *The Mechanism of Phase Transformations in Crystalline Solids*, London, Institute of Metals, pp. 231–247.

Hillert M (1982), 'An Analysis of the Effects of Alloying Elements on the Pearlite Reaction', in Aaronson HI, Laughlin DE, Sekerka RF and Wayman CM, *Proc. Int. Conf. Solid-Solid Phase Transformations*, Warrendale, PA, TMS-AIME, pp. 789–806.

Hillert M (1986), 'Impact of Clarence Zener upon Metallurgy', *J. Appl. Phys.*, 60, 1868–1876.

Hillert M (1995), 'The Nature of Bainite', *ISIJ International*, 35, 1134–1140.

Hillert M (1999), 'Solute Drag, Solute Trapping and Diffusional Dissipation of Gibbs Energy', *Acta Mater.*, 47, 4481–4505.

Hillert M, organizer (2002), 'Viewpoint Set on Bainite', *Scripta Materialia*, 47, 137–212.

Hoddeson L, Braun E, Teichmann J and Weart S, eds. (1992), *Out of the Crystal Maze: Chapters from the History of Solid State Physics*, Oxford, Oxford University Press.

Hollomon JH and Turnbull D (1953), 'Nucleation', *Prog. Met. Phys.*, 4, 333–388.

Honda K (1918), 'On Magnetic Analysis as a Means of Studying the Structure of Iron Alloys', *J. Iron Steel Inst.*, 97, 375–419.

Honda K (1926), 'Is the Direct Change from Austenite to Troostite Theoretically Possible?', *J. Iron Steel Inst.*, 114, 417–422.

Honda K (1935), 'Austenite, Martensite, Pearlite. Classical View', *Metal Progress*, 28, 34–35.

Honda K (1949), 'Mechanism of the Formation of Pearlite in Steels', *Nature*, 164, 229–230.

Honeycombe RWK (1976), 'Transformation from Austenite in Alloy Steels', *Metall. Trans. A*, 7A, 915–936.

Howe HM (1895), 'The Hardening of Steel', *J. Iron Steel Inst.*, 48, 258–309.

Howe HM (1907), 'The Iron-Carbon Phase, "Osmondite"', *Electrochemical Industry*, 5, 347–350.

Howe HM (1916), *The Metallography of Steel and Cast Iron*, New York, McGraw-Hill.

Howe HM, Osmond F, Carpenter HCH, Campbell W, Benedicks C, Wust F, Stansfield A, Stead JE, Guillet L, Heyn E, Rosenhain W and Sauveur A (1912), 'Report of Committee 53 on the Nomenclature of the Microscopic Substances and Structures of Steel and Cast Iron', *Proc. 6th Congress of the Int. Association for Testing Materials*. See footnote 4 in Vilella *et al.* (1936) for other reprintings of this report.

Howe JM, Laughlin DE, Lee JK, Dahmen U and Soffa WA, eds. (2005), *Proc. Int. Conf. Solid-Solid Phase Transformations in Inorganic Materials (PTM 2005)*, Warrendale, PA, TMS.

Howell PR (1998), 'The Pearlite Reaction in Steels: Mechanisms and Crystallography Part I. From HC Sorby to RF Mehl', *Materials Characterization*, 40, 227–260.

Hull FC and Mehl RF (1942), 'Structure of Pearlite', *Trans. ASM*, 30, 381–421.

Hull FC, Colton RA and Mehl RF (1942), 'Rate of Nucleation and Rate of Growth of Pearlite', *Trans. AIME*, 150, 185–207.

Hultgren A (1947), 'Isothermal Transformation of Austenite', *Trans. ASM*, 39, 915–1005.

Hultgren A and Edstrom O (1937), 'Om en speciell struktur hos cementit, som utskilts ur austenit', *Jernkontorets Annaler*, 121, 163–176.

Hultgren A and Ohlin H (1960), 'Nucleation and Growth of Pearlite', *Jernkontorets Annaler*, 144, 356–391.

Hume-Rothery W (1926), 'Researches on the Nature, Properties, and Conditions of Formation of Intermetallic Compounds, with Special Reference to Certain Compounds of Tin', *J. Inst. Metals*, 35, 295–361.

Humphries DW (1965), 'Sorby: The Father of Microscopical Petrography', in Smith CS, *The Sorby Centennial Symposium on the History of Metallurgy*, New York, Gordon and Breach, pp. 17–41.

Institute of Metals (1956), *The Mechanism of Phase Transformations in Metals*, London, Institute of Metals.

ISIJ International (1995), Special Issue on New Aspects of Microstructure in Modern Low Carbon High Strength Steels', *ISIJ International*, 35, 937–1041.

JIM (1987), *Proceedings of ICOMAT-86*, Sendai, Japanese Institute of Metals.

Johansson CH and Linde JO (1925), 'Röntgenographische Bestimmung der Atomanordnung in den Mischkristallreihen Au-Cu und Pd-Cu', *Ann. Physik*, 78, 439–460.

Johnson WA and Mehl RF (1939), 'Reaction Kinetics in Processes of Nucleation and Growth', *Transactions AIME*, 135, 416–422 and 442–458.

Johnson WC, Howe JM, Laughlin DE and Soffa WA, eds. (1994), *Proc. Int. Conf. Solid-Solid Phase Transformations*, Warrendale, PA, TMS.

Kaufman L and Bernstein H (1970), *Computer Calculation of Phase Diagrams*, New York, Academic Press.

Kaufman L and Cohen M (1956), 'Martensitic Transformation in Iron-Nickel System', *Trans. AIME*, 206, 1393–1401.

Kaufman L and Cohen M (1958), 'Thermodynamics and Kinetics of Martensitic Transformations, *Prog. Met. Phys.*, 7, 165–246.

Kaufman L, Radcliffe SV and Cohen M (1962), 'Thermodynamics of the Bainite Reaction', in Zackay VF and Aaronson HI, *Decomposition of Austenite by Diffusional Processes*, New York, Interscience, pp. 313–352.

Kayser FX and Patterson JW (1998), 'Sir William Chandler Roberts-Austen – His Role in the Development of Binary Diagrams and Modern Physical Metallurgy', *J. Phase Equilibria*, 19, 11–18.

Kelly A (1976), 'Walter Rosenhain and Materials Research at Teddington', *Phil. Trans. Roy. Soc. London*, A282, 5–36.

Kelton KF and Greer AL (2010), *Nucleation in Condensed Matter*, Amsterdam, Elsevier.

Kennon NF (1999a), 'Nomenclature of Phases and Constituents', in Samuels LE, *Light Microscopy of Carbon Steels*, Materials Park, OH, ASM, pp. 5–27.

Kennon NF (1999b), 'Phase Transformations', in Samuels LE, *Light Microscopy of Carbon Steels*, Materials Park, OH, ASM, pp. 29–37.

Kinsman KR and Aaronson HI (1967), 'Influence of Molybdenum and Manganese on the Kinetics of the Proeutectoid Ferrite Reaction', *Transformation and Hardenability in Steels*, Ann Arbor, MI, Climax Molybdenum, pp. 39–55.

Kinsman KR and Magee CL, organizers (1971), 'Formation of Martensite in Iron Alloys', *Metall. Trans.*, 2, 2326–2462.

Kinsman KR and Shyne JS (1967), 'Thermal Stabilization of Austenite in Iron-Nickel-Carbon Alloys', *Acta Metall.*, 15, 1527–1543.

Kirkaldy JS (1958), 'Diffusion in Multicomponent Metallic Systems: I and II', *Canadian Journal of Physics*, 36, 899–906; 907–916.

Ko T and Cottrell SA (1952), 'The Formation of Bainite', *J. Iron Steel Inst.*, 172, 307–313.

Ko T, Hsu TY and Zhao LC, eds. (2006), 'Proceedings of ICOMAT-05', *Mater. Sci. Eng.*, A 438–440, 1–1180.

Published by Woodhead Publishing Limited, 2012

Koiwa M, Otsuka K and Miyazaki T, eds. (1999), *Proc. Int. Conf. Solid-Solid Phase Transformations*, Sendai, Japanese Institute of Metals.

Kolmogorov AN (1937), 'Statistical Theory for the Recrystallization of Metals' (in Russian), *Izv. Akad. Nauk SSSR. Materm.*, 3, 355–359.

Korenko MK and Cohen M (1974), 'Some Martensitic Embryo Experiments Using High Magnetic Fields', *Scripta Metall.*, 8, 751–754.

Krauss G and Marder AR (1971), 'The Morphology of Martensite in Iron Alloys', *Metall. Trans.*, 2, 2343–2357.

Krauss G and Repas PE, eds. (1992), *Fundamentals of Aging and Tempering in Bainitic and Martensitic Steel Products (Speich Symposium)*, Warrendale, PA, ISS.

Krauss G and Speich GR, organizers (1983), 'Peter G. Winchell Symposium on the Tempering of Steel', *Metall. Trans. A*, 14A, 988–1133.

Kuo K (1953), 'Carbides in Chromium, Molybdenum, and Tungsten Steels', *J. Iron Steel Inst.*, 173, 363–375.

Kuo K (1956), 'Alloy Carbides Precipitated During the Fourth Stage of Tempering', *J. Iron Steel Inst.*, 184, 258–268.

Kurdjumov GV (1960), 'Phenomena Occurring in the Quenching and Tempering of Steels', *J. Iron Steel Inst.*, 195, 26–48.

Kurdjumov GV and Khachaturyan AG (1972), 'Phenomena of Carbon Atom Redistribution in Martensite', *Metall. Trans.*, 3, 1069–1076.

Kurdjumov GV and Maksimova OP (1948), 'Kinetics of Austenite to Martensite Transformation at Low Temperatures', *Doklady Akademii nauk SSSR*, 61 (No. 1), 83.

Laidler KJ (1993), *The World of Physical Chemistry*, Oxford, Oxford University Press.

Lange WF, Enomoto M and Aaronson HI (1989), 'Precipitate Nucleation Kinetics at Grain Boundaries', *Int. Mater. Rev.*, 34, 125–150.

Lee JK and Aaronson HI (1975), 'The Kinetic Equations of Solid-Solid Nucleation Theory', in Aaronson HI, *Lectures on the Theory of Phase Transformations*, 1st edn, pp. 83–115.

Lement BS, Averbach BL and Cohen M (1954), Microstructural Changes on Tempering Iron-Carbon Alloys', *Trans. ASM*, 46, 851–881.

Lement BS, Averbach BL and Cohen M (1955), 'Further Study of Microstructural Changes on Tempering Iron-Carbon Alloys', *Trans. ASM*, 47, 291–319.

Leslie WC and Hornbogen E (1996), 'Physical Metallurgy of Steels', in Cahn RW and Haasen P, *Physical Metallurgy*, 4th edn, Amsterdam, North-Holland, pp. 1555–1620.

Liu SK, Reynolds WT, Hu H, Shiflet GJ and Aaronson HI (1985), 'Discussion of "The Bainite Transformation in a Silicon Steel" ', *Metall. Trans. A*, 16A, 457–466.

Lorimer GW, ed. (1988), *Phase Transformations '87*, London, Institute of Metals.

Maddin R (1992), 'A History of Martensite: Some Thoughts on the Early Hardening of Iron', in Olson GB and Owen WS, *Martensite*, Materials Park, OH, ASM, pp. 11–19.

Magee CL (1971), 'The Kinetics of Martensite Formation in Small Particles', *Metall. Trans.*, 2, 2419–2430.

Main SA (1965), 'The Contributions of Sir Robert Hadfield to Metallurgical Science and Technology', in Smith CS, *The Sorby Centennial Symposium on the History of Metallurgy*, New York, Gordon and Breach, pp. 81–98.

Maki T (1990), 'Microstructure and Mechanical Behavior of Ferrous Martensite', *Mater. Sci. Forum*, 56–58, 157–168.

Published by Woodhead Publishing Limited, 2012

Mannerkoski M (1964), On the Decomposition of Austenite in a 13 Per Cent Chromium Steel', *Acta Polytech. Scand.*, Ch. 26.
Marder AR and Goldstein JI, eds. (1984), *Phase Transformations in Ferrous Alloys*, Warrendale, PA, TMS-AIME.
Marder AR and Krauss G (1967), The Morphology of Martensite in Fe-C Alloys', *Trans. ASM*, 60, 651–660.
Marder AR and Krauss G (1969), 'Formation of Low-Carbon Martensite in Fe-C Alloys', *Trans. ASM*, 62, 957–964.
Martens A (1878), 'Über die mikrokopische Untersuchung des Eisens', *Zeitschrift des Vereines deutscher Ingenieure*, 22, 11–18. English translation in (1879) *Engineering*, 28, 88–90.
Martens A (1893), 'The Microstructure of Ingot Iron in Cast Ingots', *Trans. AIME*, 23, 37–63.
Massalski TB (2010), 'Comments Concerning Some Features of Phase Diagrams and Phase Transformations', *Materials Transactions (JIM)*, 51, 583–596.
McLellan RB and Dunn WW (1969), 'A Quasi-Chemical Treatment of Interstitial Solid Solutions: Its Application to Carbon Austenite', *J. Phys. Chem. Solids*, 30, 2631–2637.
Mehl RF (1948), *A Brief History of the Science of Metals*, New York, AIME.
Mehl RF (1965), 'The Historical Development of Physical Metallurgy', in Cahn RW, *Physical Metallurgy*, Amsterdam, North-Holland, pp. 1–31.
Mehl RF and Hagel WC (1956), 'The Austenite-Pearlite Reaction', *Prog. Met. Phys.*, 6, 74–134.
Mehl RF and Smith DW (1935), 'Orientation of Ferrite in Pearlite', *Trans. AIME*, 116, 330–341.
Mehl RF, Barrett CS and Smith DW (1933), 'Studies upon Widmanstatten Structure IV. Iron-Carbon Alloys', *Trans. AIME*, 105, 215–258.
Mehrer H (2006), 'Pioneers and Landmarks of Diffusion', *Defect and Diffusion Forum*, 258–260, 1–14.
Merica PD, Waltenberg RG and Scott H (1920), 'Heat Treatment and Constitution of Duralumin', *Trans. AIME*, 64, 41–77.
Miller MK (2012), 'Atom Probe Tomography for Studying Phase Transformations in Steels', in Pereloma E and Edmonds DV (eds), *Phase Transformations in Steels. Volume 2: Diffusionless Transformations, High Strength Steels, Modelling and Advanced Analytical Techniques*, Cambridge: Woodhead Publishing.
Misa TJ (1995), *A Nation of Steel: The Making of Modern America 1865–1925*, Baltimore, MD, Johns Hopkins University Press.
Mott N, organizer (1980), 'The Beginnings of Solid State Physics', *Proc. Royal Soc. London*, 282A, 1–177.
Muddle BC, ed. (1990), 'Proceedings of ICOMAT-89', *Mater. Sci. Forum* 56–58, 1–778.
Muller FGC (1888), 'Grundzuge einer Theorie des Stahls', *Stahl und Eisen*, 8, 281–297.
Naukova Dumka (1978), *Martensite Transformations, Proceedings of the International Conference ICOMAT-77*, Kiev, Naukova Dumka.
Newkirk JB (1968), 'Commentary on "Heat Treatment and Constitution of Duralumin," by P.D. Merica, R.G. Waltenberg and H. Scott, *Trans. AIME* 64 (1920) 41', *Trans. ASM*, 61, 367–419.
Nicholson RB, Christian JW, Greenwood GW, Nutting J and Smallman RE, organizers

(1969), *The Mechanism of Phase Transformations in Crystalline Solids*, London, Institute of Metals.
Nix FC and Shockley W (1938), 'Order-Disorder Transformations in Alloys', *Rev. Mod. Phys.* 10, 1–71.
Oblak JM and Hehemann RF (1967), 'Structure and Growth of Widmanstatten Ferrite and Bainite', *Transformation and Hardenability in Steels*, Ann Arbor, MI, Climax Molybdenum, pp. 15–38.
Olson GB and Cohen M (1972), 'A Mechanism for the Strain-Induced Nucleation of Martensitic Transformations', *J. Less-Common Metals*, 28, 107–118.
Olson GB and Owen WS, eds. (1992), *Martensite*, Materials Park, OH, ASM.
Olson GB, Azrin M and Wright ES, eds. (1990), *Innovations in Ultrahigh-Strength Steel Technology: 34th Sagamore Army Research Conference Proceedings*, New York, US Army Laboratory Command.
Olson GB, Lieberman DS and Saxena A, eds. (2009), *Proceedings of ICOMAT-08*, Warrendale, PA, TMS.
Osmond F (1886), 'Transformation of Iron and Carbon in Irons, Steels, and White Cast Irons' (in French), *Comptes Rend. Acad. Sci. (Paris)*, 103, 743–1135.
Osmond F (1890), 'On the Critical Points of Iron and Steel', *J. Iron Steel Inst.*, 1, 38–80.
Osmond F and Werth J (1885), 'Theorie Cellulaire des Proprietes de l'Acier', *Annales des Mines*, 8, 5–84.
Owen WS (1992), 'The Strength of Ferrous Martensite', in Olson GB and Owen WS, *Martensite*, Metals Park, OH, ASM, pp. 277–293.
Owen WS *et al.*, organizers (1979), *Proceedings of ICOMAT-79*, Cambridge, MA, MIT Press.
Patel JR and Cohen M (1953), 'Criterion for the Action of Applied Stress in the Martensitic Transformation', *Acta Metall.*, 1, 531–538.
Philibert J (2006), 'Some Thoughts and/or Questions about Activation Energy and Pre-Exponential Factor', *Defect and Diffusion Forum*, 249, 61–72.
Pietikainen J and Soderberg O, eds. (2003), 'Proceedings of ICOMAT-02', *J. Physique IV Colloque*, 112, 1–1229.
Portevin AM and Garvin M (1919), 'The Experimental Investigation of the Influence of the Rate of Cooling on the Hardening of Carbon Steels, *J. Iron Steel Inst.*, 99, 459–563.
Purdy GR and Kirkaldy JS (1963), 'Kinetics of Proeutectoid Ferrite Reaction at an Incoherent Interface, as Determined by a Diffusion Couple', *Trans. TMS-AIME*, 227, 1255–1256.
Purdy GR, Weichert DH and Kirkaldy JS (1964), 'Growth of Proeutectoid Ferrite in Ternary Iron-Carbon-Manganese Austenites', *Trans. TMS-AIME*, 230, 1025–1034.
Raymond R (1984), *Out of the Fiery Furnace: The Impact of Metals on the History of Mankind*, Melbourne, Macmillan Australia.
Relander K (1964), 'Austenitzerfall eines 0.18%C-2%Mo-Stahles im Temperaturbereich der Perlitstufe', *Acta Polytech. Scand.*, ch 34.
Rinman L (1865), 'Investigations on the Nitrogen Content of Steel and Cast Iron and on the Form of Carbon in Hardened and Unhardened Steel' (in Swedish), *Ofversigt af K. Vetenskaps-akademiens Forhandlingar*, Stockholm, 22, 443–450.
Roberts CS, Averbach BL and Cohen M (1953), 'The Mechanism and Kinetics of the First Stage of Tempering', *Trans. ASM*, 45, 576–604.
Roberts-Austen WC (1891), *An Introduction to the Study of Metallurgy*, Charles Griffin, London.

Published by Woodhead Publishing Limited, 2012

Roberts-Austen WC (1896), 'On the Diffusion of Metals', *Phil. Trans. Roy. Soc. London A*, 187, 383–415.
Roberts-Austen WC (1899), 'Fifth Report to the Alloys Research Committee', *Trans. Inst. Mech. Eng.*, pp. 31–100.
Robertson JM (1929), 'The Microstructure of Rapidly Cooled Steel', *J. Iron Steel Inst.*, 119, 391–419.
Roozeboom HWB (1900), 'Iron and Steel from the Point of View of the Phase-Doctrine' (in German), *Z. Physikalische Chemie*, 34, 437–487. English translation in (1900), *J. Iron Steel Inst.*, 58, 311–316.
Rosenhain W (1914), *An Introduction to the Study of Physical Metallurgy*, London, Constable.
Rosenhain W and Humfrey JCW (1909), 'The Crystalline Structure of Iron at High Temperature', *Proc. Roy. Soc. London A*, 83, 200–209.
Rosenhain W and Humfrey JCW (1913), 'The Tenacity, Deformation, and Fracture of Soft Steel at High Temperatures', *J. Iron Steel Inst.*, 87, 219–314.
Roytburd AL (1999), 'Kurdjumov and His School in Martensite of the 20th Century', *Mater. Sci. Eng.*, A273–275, 1–10.
Sadovsky VD (1965), 'Tschernoff and the Development of the Theory of Heat Treatment of Steel', in Smith CS, *The Sorby Centennial Symposium on the History of Metallurgy*, New York, Gordon and Breach, pp. 189–207.
Saunders N and Miodownik AP (1998), *CALPHAD: A Comprehensive Guide*, Oxford, Pergamon.
Sauveur A (1896), 'The Microstructure of Steel and Current Theories of Hardening', *Trans. AIME*, 26, 863–906.
Sauveur A (1916), *Metallography and Heat Treatment of Iron and Steel*, 1st edn, New York, McGraw-Hill.
Sauveur A (1926), 'The Current Theories of the Hardening of Steel Thirty Years Later', *Trans. AIME*, 73, 859–908.
Sauveur A (1935), *Metallography and Heat Treatment of Iron and Steel*, 4th edn, New York, McGraw-Hill.
Sauveur A (1938), 'Wanted: International Committee on Nomenclature', *Metals and Alloys*, 9, 137.
Sauveur A (1939), 'Some Things We Do Not Know about Steel', *Metal Progress*, 35, 555–559.
Sauveur A (1981), *Metallurgical Reminiscences and Dialogue [A Collection of Two Works]*, Metals Park, OH, ASM.
Schottky W, Ulich H and Wagner C (1929), *Thermodynamik, die Lehre von den Kreisprozessen, den physikalischen und chemischen Veränderungen und Gleichgewichten*, Berlin, Verlag Julius Springer.
Servos JW (1990), *Physical Chemistry from Ostwald to Pauling: The Making of a Science in America*, Princeton, NJ, Princeton University Press.
Sharma RC and Kirkaldy JS (1973), 'Thermodynamics and Kinetics of the Proeutectoid Ferrite Reaction in Fe-C-Ni in the Vicinity of 730°C', *Can. Met. Quart*, 12, 393–401.
Shewmon PG (1969), *Transformations in Metals*, New York, McGraw-Hill.
Shih CH, Averbach BL and Cohen M (1955), 'Some Characteristics of Isothermal Martensitic Transformation', *Trans. AIME*, 203, 183–187.
Smigelskas AD and Kirkendall EO (1947), 'Zinc Diffusion in Alpha Brass', *Trans. AIME*, 171, 130–142.

Published by Woodhead Publishing Limited, 2012

Smith CI, Taunt RJ, Edmonds DV, Doherty RD and Williamson J, organizers (1979), *Phase Transformations*, London, Institution of Metallurgists.
Smith CS (1953), 'Microstructure', *Trans. ASM*, 45, 533–575.
Smith CS (1960), *A History of Metallography*, Chicago, IL, University of Chicago Press.
Smith CS (1964), 'The Discovery of Carbon in Steel', *Technology and Culture*, 5, 149–175.
Smith CS (1965a), 'The Prehistory of Solid State Physics', *Physics Today*, 18, 18–30.
Smith CS, ed. (1965b), *The Sorby Centennial Symposium on the History of Metallurgy*, New York, Gordon and Breach.
Smith CS (1968), 'Matter Versus Materials: A Historical View', *Science*, 162, 637–644.
Smith CS (1992), 'Early Ideas on the Structure of Steel', in Olson GB and Owen WS, *Martensite*, Metals Park, OH, ASM, pp. 21–39.
Smith DA, organizer (1987), 'Viewpoint Set #11: Interface Motion and the Mechanism of Phase Transformation', *Scripta Metall.*, 21, 1009–1038.
Smith GV and Mehl RF (1942), 'Lattice Relationships in Decomposition of Austenite to Pearlite, Bainite, and Martensite', *Trans. AIME*, 150, 211–226.
Smith HA (1935), 'Reactions in the Solid State, I. Initial Course of Subcritical Isothermal Diffusion Reactions in Austenite in an Alloy Steel', *Trans. AIME*, 116, 342–362.
Smoluchowski R, Mayer JE and Weyl, WA, eds. (1951), *Phase Transformations in Solids*, New York, Wiley.
Sorby HC (1886), 'On the Application of Very High Powers to the Study of the Microscopical Structure of Steel', *J. Iron Steel Inst.*, 1, 140–147.
Sorby HC (1887), 'On the Microscopical Structure of Iron and Steel', *J. Iron Steel Inst.*, 1, 255–288.
Speich GR and Clark JB, eds. (1965), *Precipitation from Iron Base Alloys*, New York, Gordon and Breach.
Speich GR and Cohen M (1960), 'Growth Rate of Bainite', *Trans. TMS-AIME*, 218, 1050–1059.
Stubbles JR (1998), 'Who Was Henry Howe?', *Metall. Mater. Trans. B*, 29B, 5–16.
Suzuki H, ed. (1976), *Proceedings of the 1st JIM International Symposium on New Aspects of Martensitic Transformations (ICOMAT-76)*, Sendai, Japanese Institute of Metals.
Tammann G (1914), *Lehrbuch der Metallographie*, 1st edn, Leipzig, Voss.
Tammann G (1922), *Aggregatzustände*, translated by Mehl RF (1925), *States of Aggregation*, New York, Van Nostrand.
Tanner LE and Soffa WA, organizers (1988), 'Pretransformation Behavior Related to Displacive Transformations in Alloys', *Metall. Trans. A*, 19A, 760–796.
Tanner LE and Wayman CM, organizers (1981), 'Pretransformation Phenomena, Fluctuations and Related Effects', *Metall. Trans. A*, 12A, 558–605.
Taylor KA and Cohen M (1992), 'Aging of Ferrous Martensites', *Prog. Mater. Sci.*, 36, 225–272.
Thompson FC (1965), 'The John Oliver Arnold, 1858–1930', in Smith CS, *The Sorby Centennial Symposium on the History of Metallurgy*, New York, Gordon and Breach, pp. 99–108.
Timoshenko SP (1953), *History of Strength of Materials: With a Brief Account of the History of the Theory of Elasticity and Theory of Structures*, New York, McGraw-Hill.

Published by Woodhead Publishing Limited, 2012

Tsakalakos T, ed. (1984), *Phase Transformations in Solids*, MRS Symp. Proc. 21, New York, North-Holland.
Tuijn C (1997), 'On the History of Models for Solid-State Diffusion', *Defect and Diffusion Forum*, 143–147, 11–20.
Turnbull D (1948), 'Transient Nucleation', *Trans. AIME*, 175, 774–783.
Turnbull D (1949), 'The Subcooling of Liquid Metals', *J. Appl. Phys.*, 20, 817.
Turnbull D (1955), 'Theory of Cellular Precipitation', *Acta Metall.*, 3, 55–63.
Turnbull D (1987), 'Autobiography', in Cargill GS, Spaepen F and Tu KN, *Phase Transitions in Condensed Systems*, MRS Symp. Proc. 57, Warrendale, PA, MRS, pp. 1–29.
Turnbull D and Fisher JC (1949), 'Rate of Nucleation in Condensed Systems', *J. Chem. Phys.*, 17, 71–73.
van der Merwe JH (1950), 'On the Stresses and Energies Associated with Inter-Crystalline Boundaries', *Proceedings of the Physical Society*, 63A, 616–637.
Vanpaemel J (1982), 'A History of the Hardening of Steel: Science and Technology', *J. Physique Colloque*, C4-43, 847–854.
Vilella JR, Guellich GE and Bain EC (1936), 'On Naming the Aggregate Constituents in Steel', *Trans. ASM*, 24, 225–261.
Volmer M and Weber A (1925), 'Nucleus Formation in Supersaturated Structures' (in German), *Z. Physik Chemie*, 119, 227–301.
Vonnegut B (1948), 'Variation with Temperature of the Nucleation Rate of Supercooled Liquid Tin and Water Drops', *J. Colloid Science*, 3, 563–569.
Wayman CM, organizer (1972), 'Phase Transformations and Related Phenomena (Bain Symposium)', *Metall. Trans.*, 3, 1030–1121.
Wayman CM (1990), 'The Growth of Martensite Since E.C. Bain (1924) – Some Milestones', *Materials Science Forum*, 56–58, 1–32.
Wayman CM and Perkins J, eds. (1993), *Proceedings of ICOMAT-92*, Carmel, CA, Monterey Institute for Advanced Studies.
Wayman CM, Aaronson HI, Hirth JP and Rath BB, organizers (1994), 'Proceedings of the Pacific Rim Conference on the Roles of Shear and Diffusion in the Formation of Plate-Shaped Transformation Products', *Metall. Mater. Trans. A*, 25A, 1785–2016 and 2553–2673.
Wells C, Batz W and Mehl RF (1950), 'Diffusion Coefficient of Carbon in Austenite', *Trans. AIME*, 188, 553–560.
Werner FE, Averbach BL and Cohen M (1957), 'The Tempering of Iron-Carbon Martensite Crystals', *Trans. ASM*, 49, 823–841.
Wert CA (1949), 'Precipitation from Solid Solutions of C and N in Alpha-Iron', *J. Appl. Phys.*, 20, 943–949.
Wert CA (1986), 'Internal Friction in Solids', *J. Appl. Phys.*, 60, 1888–1895.
Wert CA and Zener C (1950), 'Interference of Growing Spherical Precipitate Particles', *J. Appl. Phys.*, 21, 5–8.
Weschler MS, Lieberman DS and Read TA (1953), 'On the Theory of the Formation of Martensite', *Trans. AIME*, 197, 1503–1515.
Westgren A (1921), 'Roentgen Spectrographic Investigations of Iron and Steel', *J. Iron Steel Inst.*, 207, 303–337.
Westgren A and Phragmen G (1922), 'X-Ray Studies on the Crystal Structures of Steel', *J. Iron Steel Inst.*, 105, 241–273.
Westgren A and Phragmen G (1924), 'X-Ray Studies on the Crystal Structure of Steel, Part II', *J. Iron Steel Inst.*, 109, 159–174.

Published by Woodhead Publishing Limited, 2012

Zackay VF and Aaronson HI, eds. (1962), *Decomposition of Austenite by Diffusional Processes*, New York, Interscience.

Zener C (1946), 'Kinetics of Decomposition of Austenite', *Trans. AIME*, 167, 550–595.

Zener C (1948), *Elasticity and Anelasticity of Metals*, Chicago, IL, University of Chicago Press.

Zener C (1949), 'Theory of Growth of Spherical Precipitates from Solid Solution', *J. Appl. Phys.*, 20, 950–953.

Published by Woodhead Publishing Limited, 2012

2

Thermodynamics of phase transformations in steels

J. ÅGREN, Royal Institute of Technology (KTH), Sweden

Abstract: The basics of thermodynamics are reviewed with special attention to phase transformations. The distinction between internal and external variables is emphasized and the general equilibrium conditions are derived from the combined first and second law. The concepts of entropy production and driving force as well as stability are discussed. The calculation of thermodynamic properties and phase equilibria is considered and the Calphad method is briefly reviewed, including modeling of substitutional and interstitial disorder. The thermodynamic bases of phase diagrams are examined, and finally, the effect of interfaces, fluctuations and thermodynamics of nucleation are reviewed.

Key words: internal and external variables, entropy production, Gibbs energy, driving force, Le Chatelier's Principle, phase diagrams, interfacial energy, fluctuations, nucleation.

2.1 Introduction: the use of thermodynamics in phase transformations

It is often taken for granted in textbooks that thermodynamics only applies at equilibrium, i.e. the condition when nothing more can change. From the viewpoint of analyzing phase transformations, where the change itself is of primary interest, thermodynamics would then seem rather useless. However, it is easy to demonstrate that such a conclusion is incorrect. At equilibrium, various properties of the system can be measured experimentally, e.g. volume, temperature, composition, amount and composition of the different phases present, etc. A liquid may be supercooled substantially below its solidification point and kept there long enough to allow various thermodynamic measurements. The properties of cementite in plain carbon steel may be evaluated although it is not an equilibrium phase. The decomposition into iron and graphite is simply too sluggish and occurs only for very high carbon contents and long heat treatment times. These examples hold for metastable equilibria where the stable conditions have not yet been reached due to the finite rate of kinetics. The fact that one can perform exactly the same thermodynamic measurements a little bit outside equilibrium and extrapolate these measurements rather far into the non-equilibrium regime indicates that

© Woodhead Publishing Limited, 2012

thermodynamics would also apply considerably outside equilibrium. But how far outside would it apply? In this chapter we will demonstrate how thermodynamics may be applied as far as needed to solve certain problems. We shall also state the rules which must be obeyed for a sound analysis.

Once we have accepted that thermodynamics may be applied regardless of whether there is equilibrium or not, we have to consider the concept of local behavior, i.e. thermodynamics may be applied locally in a small volume element. This has as a consequence that, even though it is fruitless to apply thermodynamics to a complex body as a whole, it may still be helpful to apply thermodynamics locally to its parts and thus attach certain properties to each point in the body. Sometimes it is necessary to also include some influence of non-local effects, i.e. the thermodynamic properties may depend on neighboring regions and gradients have to be taken into account.

The concepts of non-equilibrium states and local behavior (possibly including some non-local behavior) serve as the basis for thermodynamics of phase transformations. As we shall see, it allows the calculation of driving forces for various changes of a non-equilibrium system.

A modern and thorough treatise of the thermodynamic basis of phase transformations is found in the recent book by Hillert (2008). The present chapter is largely inspired by that book and personal experience in teaching phase transformations and thermodynamics to graduate research students.

2.2 External and internal variables

2.2.1 Action and reaction

A given system may be influenced from the outside in several different ways. These interactions involve

- heat
- work
- composition change.

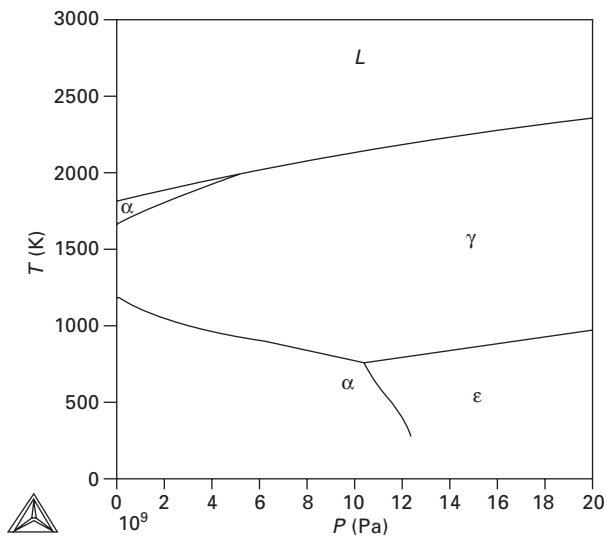
A system with constant composition is called a closed system. If the composition may be changed it is called an open system. A closed system that is also thermally isolated, i.e. no heat is exchanged with the outside, is left completely alone and is called adiabatic or isolated. We may change the composition by adding (or removing) certain components. The definition of components is somewhat arbitrary but should reflect all possible composition changes we are interested in. In physical metallurgy it is usually most convenient to use the chemical elements as components but it may sometimes be more convenient to choose stoichiometric compounds, like oxides. The system Fe-O could thus be fully represented by the components Fe and O but FeO and Fe_2O_3 are also possible, although we would then have to accept the

© Woodhead Publishing Limited, 2012

possibility of negative concentrations outside the interval between FeO and Fe_2O_3. Although this is perfectly thermodynamically consistent, it may lead to some difficulties when plotting phase diagrams using potentials as axes.

In a system with c components we may thus perform the external actions in $c + 2$ different ways. These external actions can generally be characterized by well-defined variables, for example the volume and the amount of a certain component. As these variables are controlled from the outside by the experimentalist or the processing conditions they are called external variables. Thus, generally there will be $c + 2$ external variables.

Once the external action is over and the external conditions are kept constant, the reactions inside the system will proceed until a new state of equilibrium is established and there will be no more changes unless there are new external actions on the system. The equilibrium state of the system is thus a function of $c + 2$ external variables which can be chosen in many different ways. We may thus call these variables external state variables. For example, the equilibrium state of a piece of iron would be a function of three external state variables, i.e. the number of moles of iron, pressure and temperature. As far as the properties of a material are concerned the absolute amount of a substance is not of interest and without loss of generality we may consider 1 mol of iron and only two variables, e.g. pressure and temperature, are then needed to uniquely define the equilibrium state. This fact is expressed by Gibbs phase rule, discussed in Section 2.4.5, and it is reflected in the phase diagram of pure iron which is shown in Fig. 2.1. All phase diagrams in the present chapter have been calculated using the Thermo-Calc code (Andersson *et al.*, 2002).



2.1 Phase diagram of pure iron.

© Woodhead Publishing Limited, 2012

In a system that is not yet in equilibrium, more variables are usually needed to characterize it completely. These variables cannot be controlled directly from the outside but their values evolve as a consequence of internal reactions in the system. Consequently they are called internal variables. Familiar examples in an alloy are the fraction and composition of different phases, the number or fraction of vacancies, the state of chemical and magnetic order, etc. At equilibrium the internal variables attain certain values which depend on the given external conditions. As these variables characterize the state of the system at a given instant, they are called internal state variables.

The distinction between external and internal variables is essential but is unfortunately not always fully appreciated. As a simple example, one may consider the thermal vacancies of a pure metal at elevated temperatures. Suppose a piece of pure iron is taken from room temperature up to close to the melting point at atmospheric pressure and kept there for some time. In this case it is natural to consider the temperature T, pressure P and number of moles of iron N_{Fe} of the piece as the external variables. At the beginning there are few vacancies but their number will gradually increase and level out at a much higher value corresponding to equilibrium at the high temperature. The number N_{Va} of vacancies is an internal variable. In principle it can have any value depending on the history of the material but for given P, T and N_{Fe} it has a well-defined value at equilibrium, i.e. $N_{Va}^{eq} = N_{Va}^{eq}(P,T,N_{Fe})$

2.2.2 Extensive and intensive variables

In the example of thermal vacancies, the total number of vacancies was considered. However, provided that the system is sufficiently large to have reasonable statistics, the total number of vacancies will be proportional to the size of the system. It is thus rather inconvenient to use N_{Va} as an internal variable. It is more convenient to consider the fraction of lattice sites that will be vacant, i.e. the so-called site fraction y_{Va} which is given by $y_{Va} = N_{Va}/(N_{Va} + N_{Fe})$ and, for a given value of the site fraction, N_{Va} is thus proportional to, N_{Fe}, i.e. $N_{Va} = N_{Fe}y_{Va}/(1 - y_{Va})$ Thus y_{Va} is an example of an intensive variable because its value will not change if a larger or smaller part of an equilibrium system is considered. On the other hand N_{Va} is an extensive variable and so also is the system size defined as N_{Fe}. An extensive variable can thus be external or internal and the same holds for an intensive variable. In the above case T and P are both intensive and external variables.

There are two kinds of intensive variables: potentials and densities. The first type will be discussed in more detail in Section 2.4. The second type is obtained by normalizing an extensive variable to the size of the system. The customary term density stems from the important example of mass density which is given by the mass of the system divided by its volume. Some examples are given in Table 2.1. Molar quantities are particularly useful

© Woodhead Publishing Limited, 2012

Table 2.1 Examples of intensive variables obtained by normalizing extensive quantities to the system size

System size as	Mass m	Volume V	Number of moles of j, N_j	Internal energy U
Volume V	Density $\rho = m/V$	1	Concentration $c_j = N_j/V$	Energy density $U_V = U/V$
Number of moles N	Molar mass m/N	Molar volume $V/N = V_m$	Mole fraction $x_j = N_j/N$	Molar energy $U_m = U/N$

examples of densities and are denoted by a lower index or subscript m, e.g. the molar volume V_m. Traditionally the molar content is called mole fraction and denoted x_j rather than N_{jm} which would be more logical. There are many more possibilities and Table 2.1 lists only a few common examples.

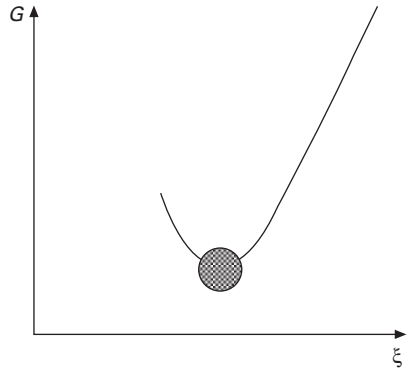
It is inconvenient to use extensive variables when we consider the local thermodynamic behavior because we would then have to specify the size of each volume element considered. On the other hand, we will not have that difficulty if we use intensive variables because we may imagine that these generally would vary with location in a system, i.e. they would be field variables. Integration over the whole system of a density-type of variable would then give the corresponding quantity for the whole system, e.g. its total energy or mass.

2.3 The state of equilibrium

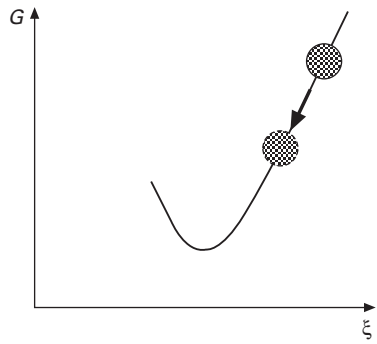
When the external conditions are kept constant, systems usually evolve towards stationary states where the internal variables no longer change. Such a state is an equilibrium state provided that the external conditions do not impose a constant flow of matter or energy. The latter would be the case, for example, if different sides of the system are kept at constant but different temperatures. In that case equilibrium can never be attained and the stationary state rather corresponds to a steady-state solution of the appropriate transport problem. It should be mentioned, though, that in systems which are far from equilibrium sometimes not even stationary solutions are possible, but there will be solutions with oscillatory time dependence.

As we shall explain in Section 2.4, the equilibrium state fulfills well-defined thermodynamic criteria. For given external conditions equilibrium is obtained for the combination of internal variables that gives an extremum in the appropriate thermodynamic function. For simplicity we shall here first consider external conditions where P, T and composition are kept constant. In that case we shall see in Section 2.4 that the appropriate thermodynamic function is Gibbs energy G. For an internal variable ξ, equilibrium is then given by the minimum in G (see Fig. 2.2).

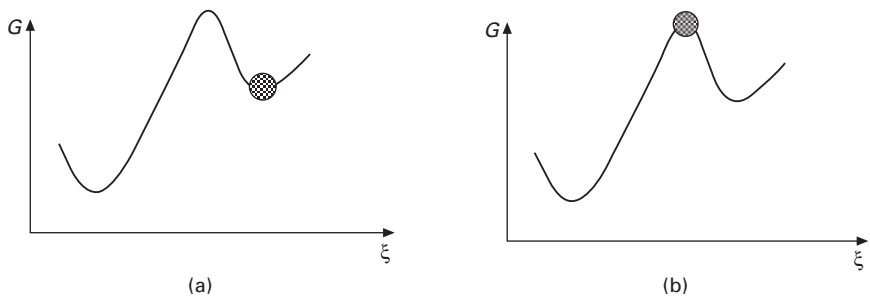
© Woodhead Publishing Limited, 2012



2.2 Equilibrium for the value of the internal variable ξ that gives the lowest Gibbs energy.



2.3 Change in Gibbs energy during a phase transformation.



2.4 (a) Metastable equilibrium, (b) unstable equilibrium (critical state).

According to the second law of thermodynamics, see Section 2.4, an ongoing spontaneous process is characterized by a steady decrease in Gibbs energy (see Fig. 2.3). On the other hand the situation may be as in Fig. 2.4(a). The equilibrium state is only a local minimum and there is a deeper minimum at

© Woodhead Publishing Limited, 2012

another value of ξ. However, in order to reach that value, the system would first have to pass a maximum, Fig. 2.4(b), before it could steadily decrease its Gibbs energy towards the more stable equilibrium. The required increase in Gibbs energy violates the second law of thermodynamics and could only happen by means of a sufficiently large fluctuation (see Section 2.8). The system thus has some stability and the equilibrium in Fig. 2.4(a) is said to be metastable. The maximum in Fig. 2.4(b) is an unstable equilibrium because even an infinitely small fluctuation would lead to a decrease in Gibbs energy. An unstable equilibrium is often called a critical state.

2.4 The combined first and second law – its application

2.4.1 First and second laws of thermodynamics

At a given instant the internal energy of a system U depends only on its internal state. Such a quantity is called a state quantity. Of course the internal state may depend on the history unless the system is at equilibrium, and thus U may indirectly depend on the history of a non-equilibrium system. For example, a highly deformed piece of steel will have a higher concentration of defects and, before these have been annealed out, U indirectly depends on the thermo-mechanical history. The first law states that U is a conserved quantity and thus obeys a conservation equation. In a closed system its value may be changed by adding or removing heat and work to or from the system. This is usually written

$$dU = \delta Q + \delta W \qquad [2.1]$$

Here δQ and δW stand for amount of heat and work added. If we consider pressure-volume work only, the work addition is expressed as $\delta W = -PdV$. This is positive for $P > 0$ and $dV < 0$, i.e. when work is added to the system.

In the second law another state function, the entropy S, is introduced. However, the entropy is not a conserved quantity and may thus be produced inside the system, but can never be consumed according to the second law. For a closed system the change in entropy S is thus given by

$$dS = \delta Q/T + d_iS \qquad [2.2a]$$

$$d_iS \geq 0 \qquad [2.2b]$$

The first term $\delta Q/T$ is the entropy exchanged with the outside and may be positive or negative depending on whether heat is added to or removed from the system. It vanishes for an adiabatic system. The second term d_iS is called the internal entropy production and is always positive for spontaneous processes inside the system. As mentioned, this is the essence of the second law. Such processes are usually called irreversible processes because they

© Woodhead Publishing Limited, 2012

always take the system towards equilibrium. They never occur in the reverse way which would take the system further away from equilibrium. If $d_iS = 0$ there can be no internal reactions. This may be the case if the system is at equilibrium or if the kinetics are so sluggish that no reactions occur during the observation. In the latter case the system is said to be frozen-in. It should be observed that the entropy change could have any sign because it also depends on the sign and magnitude of dQ. S has to increase by an internal process only if the system is adiabatic.

2.4.2 The combined law

The combined law is obtained by combination of Eqs [2.1] and [2.2]. i.e.

$$dU = TdS - PdV - Td_iS \qquad [2.3]$$

If the system is open, i.e. there is exchange of matter with the outside, Eq. [2.3] is modified

$$dU = TdS - PdV + \sum \mu_k dN_k - Td_iS \qquad [2.4]$$

where N_k denotes the number of moles of component k inside the system. The new quantity μ_k is called the chemical potential for component k and will be discussed in more detail shortly. Equation [2.4] is the combined law in its general form. Suppose that the internal reactions can be described with internal variables ξ_j. We can then express the internal entropy production by

$$d_iS = \frac{1}{T} \sum D_j d\xi_j \qquad [2.5]$$

The quantity D_j is called the driving force for the jth internal process. It is defined as positive for spontaneous increase in ξ_j. The introduction of the driving force allows the distinction between equilibrium, $D_j = 0$, and frozen-in state $d\xi_j = 0$. Thus we can write the combined law as

$$dU = TdS - PdV + \sum \mu_k dN_k - \sum D_j d\xi_j \qquad [2.6]$$

2.4.3 Natural variables

Equation [2.6] implies that the internal energy is a function $U(S, V, N_k, \xi_1, \xi_2 \ldots)$. However, the internal energy is also a physical quantity which in principle can be measured under various conditions, e.g. at different T and P, and we could thus express it as another function having the external variables T and P rather than S and V. Nevertheless, in thermodynamics it is generally acceptable to use the same symbol to denote a given quantity although it may refer to completely different mathematical functions. We can thus write $U(T,P)$ and $U(S,V)$ but always keep in mind that they are completely different functions. The variables S, V, N_k are called the natural

© Woodhead Publishing Limited, 2012

variables of the internal energy because they appear as differentials in the combined law. Using the natural external variables we immediately find the following partial derivatives:

$$\frac{\partial U}{\partial S} = T \qquad [2.7a]$$

$$\frac{\partial U}{\partial V} = -P \qquad [2.7b]$$

$$\frac{\partial U}{\partial N_k} = \mu_k \qquad [2.7c]$$

$$\frac{\partial U}{\partial \xi_j} = -D_j \qquad [2.7d]$$

Each derivative tells how much the internal energy changes per unit amount of an extensive quantity, i.e. entropy, volume or number of moles of k, added to the system. In physics such derivatives are called potentials. The potential μ_k is called the chemical potential. It should be emphasized that the potential corresponding to volume is $-P$. We also note that the driving force D_j should be regarded as a potential. If the natural variables are not used, one has to state what variables were kept constant during the differentiation. For example, the heat capacity at constant volume is defined as

$$\left(\frac{\partial U}{\partial T}\right)_{VN_k} = c_V \qquad [2.8]$$

As T is not a natural variable for the internal energy, one cannot be certain what the other variables are and thus it is necessary in this case to include the suffices V and N_k to denote that U is considered as a function $U(T,V,N_k)$. Observe that the same derivative taken under constant pressure, i.e. using a function $U(T,P,N_k)$, is a completely different quantity.

2.4.4 Different forms of the combined law

We can generalize the combined law to include more types of interactions thus:

$$dU = \sum Y_j dX_j - \sum D_j d\xi_j \qquad [2.9]$$

Here Y_j denotes the potential which corresponds to the external extensive variable X_j. For example, we may consider X_j as the electric charge and Y_j would then be the electric potential. The variables X_j and Y_j are conjugated to each other and are called a conjugated pair. For a system where all X_j are kept constant the energy will be constant at equilibrium because the last

© Woodhead Publishing Limited, 2012

summation in Eq. [2.9] will vanish. If we consider the internal process of moving X_j from one part of the system to another we find by applying Eq. [2.9] to each part that the potential Y_j must be the same in both parts. This leads to the important conclusion that a system in equilibrium must have the same value of a given potential over the whole system. For a system at equilibrium with all X_j kept constant, all imaginable internal changes would lead to an increase in internal energy, i.e. the equilibrium state is a minimum in internal energy. For example, a system with fixed entropy, volume and composition has its lowest possible internal energy. All non-equilibrium states would have a higher energy.

We may rearrange Eq. [2.4] to obtain

$$dS = \frac{1}{T}\, dU + \frac{P}{T}\, dV - \frac{1}{T} \sum \mu_k dN_k + d_i S \qquad [2.10]$$

We can thus conclude that a system at fixed energy, volume and composition has maximum entropy at equilibrium.

Usually it is difficult to arrange an experiment in order to keep the entropy constant. It is somewhat easier to arrange for a fixed volume or energy. We may rearrange Eq. [2.6]:

$$d(U - TS) = -\, SdT - PdV + \sum \mu_k dN_k - \sum D_j d\xi_j \qquad [2.11]$$

The function $U - TS$ is called the Helmholtz energy and is usually denoted with F. Again we immediately obtain the partial derivatives

$$\frac{\partial F}{\partial T} = -S \qquad [2.12a]$$

$$\frac{\partial F}{\partial V} = -P \qquad [2.12b]$$

$$\frac{\partial F}{\partial N_k} = \mu_k \qquad [2.12c]$$

$$\frac{\partial F}{\partial \xi_j} = -D_j \qquad [2.12d]$$

For the Helmholtz energy the natural variables are obviously T, V and N_k, and we may conclude that at equilibrium under fixed temperature, volume and composition we will have a minimum in Helmholtz energy.

In experiments it is usually more convenient to control pressure and temperature and we may rearrange Eq. [2.11] to obtain

$$d(U - TS + PV) = -\, SdT + VdP + \sum \mu_k dN_k - \sum D_j d\xi_j \qquad [2.13]$$

The function $G = U - TS + PV$ is called the Gibbs energy and has T, P and N_k as natural variables. Again we obtain the partial derivatives

© Woodhead Publishing Limited, 2012

$$\frac{\partial G}{\partial T} = -S \qquad [2.14a]$$

$$\frac{\partial G}{\partial P} = V \qquad [2.14b]$$

$$\frac{\partial G}{\partial N_k} = \mu_k \qquad [2.14c]$$

$$\frac{\partial G}{\partial \xi_j} = -D_j \qquad [2.14d]$$

We also conclude that at equilibrium under fixed temperature, pressure and composition there will be a minimum in Gibbs energy.

Consider now an infinitely small subsystem of a larger equilibrium system and then let that subsystem grow by moving its imaginary boundary. During that imaginary growth there is no entropy production because nothing is really happening inside the system and the internal energy change becomes

$$dU = (TS_m - PV_m + \sum \mu_k x_k)\, dN \qquad [2.15]$$

where N is the size of the subsystem. At equilibrium all potentials are constant and so are the molar quantities and we may directly perform an integration to obtain U.

$$U = TS - PV + \sum \mu_k N_k \qquad [2.16]$$

We thus find that

$$G = U - TS + PV = \sum \mu_k N_k \qquad [2.17]$$

In a similar way we may introduce other thermodynamic functions having other natural variables that may be convenient for other experimental conditions. One may mention, for example, the Grand potential $-PV$, sometimes called the Landau free energy after the Russian physicist L. Landau (see Landau and Lifshitz, 1970):

$$d(U - TS - \sum \mu_k N_k) = d(-PV) = -SdT - PdV - \sum N_k d\mu_k - \sum D_j d\xi_j \qquad [2.18]$$

This function is useful when one considers equilibrium at fixed temperature, volume and chemical potentials.

2.4.5 Gibbs–Duhem relation and the phase rule

If one tries to replace also the volume with pressure in Eq. [2.18] one obtains for a system at equilibrium

© Woodhead Publishing Limited, 2012

$$d(-PV + PV) = 0 = -SdT + VdP - \sum N_k d\mu_k \quad [2.19]$$

This equation is called the Gibbs–Duhem relation and reveals the fact that there are only $c + 1$ independent potentials in a system with c components. Moreover, it is clear that Eq. [2.19] can be applied to each phase and it has its own values of S, V and N_k. We have already concluded that each potential is constant at equilibrium. If there are several phases present, they must thus all have the same value of T and P, etc., if equilibrium is to be maintained. In a one-phase system there are $c + 1$ independent potentials. For each additional phase there is an additional Gibbs–Duhem relation and for p phases there are thus $c + 1 - (p - 1) = c - p + 2$ independent potentials. The number of independent potentials is called the number of degrees of freedom f and the relation $f = c - p + 2$ is called the Gibbs phase rule.

2.4.6 Equilibrium conditions

From the different forms of the first law we see directly which function should be minimized under given external conditions. The most common examples are summarized in Table 2.2. At equilibrium nothing is happening, i.e. everything is constant. One may then question how one could know what was kept constant before equilibrium was established and what function was minimized. For example, at equilibrium there is some pressure and volume which are both constant. Was the Gibbs energy or the Helmholtz energy minimized? The answer is that it does not matter which variables were kept constant as long as the same equilibrium state is approached. Provided that all calculations are performed correctly the minimization of the different functions would all give the same result. If we know the volume and the temperature of the system it is certainly most convenient to use the Helmholtz energy but we could equally well use any other function, e.g. Gibbs energy. However, if we use Gibbs energy we have to perform the calculation iteratively and find the pressure for which the derivative $\partial G/\partial P = V$ agrees with the fixed volume.

It should be emphasized that Table 2.2 lists only the most commonly used

Table 2.2 Functions to be minimized at equilibrium for various external conditions

Fixed variables	Function to be minimized	Name
U, V, N_k	$-S$	Negative entropy
S, V, N_k	U	Internal energy
T, V, N_k	$F = U - TS$	Helmholtz energy
T, P, N_k	$G = U - TS + PV = F + PV$	Gibbs energy
S, P, N_k	$H = U + PV$	Enthalpy
U, V, μ_k	$-PV = U - \sum N_k \mu_k$	Grand potential
T, P, N_k, μ_j	$G - \sum N_j \mu_j$	

© Woodhead Publishing Limited, 2012

conditions and corresponding functions. There are many more possibilities that are all derived from the various forms of the combined law but most of them have limited use. However, the last possibility in Table 2.2, which does not have a name, is actually quite useful. It can be used to calculate the equilibrium state of a system under fixed temperature and pressure where the potentials of some of the elements, but not all, are fixed. For the remaining elements their content is fixed. This may be the situation when a certain steel is equilibrated in an atmosphere of given nitrogen, oxygen or carbon activity.

2.4.7 Evaluation of the driving force

In Section 2.4.4 different expressions for the driving force D_j were derived from the various forms of the combined law. Its use will now be demonstrated for the case of constant T, P and composition, which is most important from the practical point of view. For a non-equilibrium system, Eq. [2.13] then reads:

$$dG = -\sum D_j d\xi_j \qquad [2.20]$$

Consider now a process where the ξ variables change from an initial state to a final state. Even though the driving forces may vary in a complicated way during the integration, the integral

$$-\sum \int_{\text{start}}^{\text{final}} D_j d\xi_j = G^{\text{final}} - G^{\text{start}} \qquad [2.21]$$

is easily evaluated as the difference in Gibbs energy between the two states. We call this quantity the integrated driving force.

As another example of the use of Eq. [2.20], we now consider the formation of a β particle in an α matrix. We consider dN_k moles of element k taken from α and transferred to β, i.e. $dN_k = -dN_k^\alpha = dN_k^\beta$. In principle, one or several elements may be transferred. The Gibbs energy of the whole system which has a fixed overall composition is given by

$$G = G^\alpha + G^\beta \qquad [2.22]$$

We chose as our single internal variable the number of moles of β that has formed and the driving force from Eq. [2.14d] thus yields

$$D = -\frac{\partial G}{\partial \xi} = -\frac{\partial G}{\partial N^\beta} = -\sum_k \left(\frac{\partial G^\alpha}{\partial N_k^\alpha} \frac{\partial N_k^\alpha}{\partial N^\beta} + \frac{\partial G^\beta}{\partial N_k^\beta} \frac{\partial N_k^\beta}{\partial N^\beta} \right) \qquad [2.23]$$

From Eq. [2.14c] we introduce the chemical potentials and applying $dN_k = -dN_k^\alpha = dN_k^\beta$ we can write Eq. [2.23] as

© Woodhead Publishing Limited, 2012

$$D = \sum_k (\mu_k^\alpha - \mu_k^\beta) \frac{\partial N_k}{\partial N^\beta} \quad [2.24]$$

It remains to be discussed what the composition of the material transferred from α to β is. In the special case where the composition of β cannot change, the transferred composition must be the same as in β and $N_k = x_k^\beta N^\beta$, i.e.

$$D = \sum_k (\mu_k^\alpha - \mu_k^\beta) x_k^\beta \quad [2.25]$$

Applying Eq. [2.17], Eq. [2.25] may also be written $D = \sum_k x_k^\beta \mu_k^\alpha - G_m^\beta$. This well-known relation or Eq. [2.25] can be found in many textbooks, e.g. the very recent and extensive treatise by Aaronson *et al*. (2010).

2.4.8 Stability conditions

The different types of equilibrium were discussed in Section 2.3. They can be stated in a more precise mathematical form by investigating the combined law. For example, at given T, P and composition we use the Gibbs energy and apply Eq. [2.20]. However, at equilibrium all driving forces vanish and we have to perturb the system in order to check the stability. Consider first a case with a single internal variable which is only perturbed a small amount $\Delta\xi$ from equilibrium. We find

$$\Delta G = \frac{1}{2} \frac{\partial^2 G}{\partial \xi^2} (\Delta\xi)^2 \quad [2.26]$$

For stable equilibrium the perturbation must lead to an increase in Gibbs energy, i.e. the second derivative must be positive. We can apply Eq. [2.26] to a case where we consider as an internal process the transfer of component k from one part of the system to another. In Section 2.4.4 we used this 'thought experiment' to show that a potential must have the same value everywhere in an equilibrium system. Now we also ask under what conditions such an equilibrium is stable. We identify ξ with N_k and find immediately that for a stable system the second derivative of G with respect to N_k must be positive. From the expression for the chemical potential we find that this condition may be written

$$\left(\frac{\partial \mu_k}{\partial N_k}\right)_{P,T,N_j} > 0 \quad [2.27]$$

The chemical potential has no natural variables and thus we have added what variables are fixed as suffices. In a stable system at fixed temperature and pressure the chemical potential of a component must always increase

© Woodhead Publishing Limited, 2012

when it is added to the system. By looking at Eq. [2.9], which concerns U as a function of all extensive variables X_i, we may by similar considerations deduce that the following more general condition

$$\left(\frac{\partial Y_k}{\partial X_k}\right)_{X_j} > 0 \qquad [2.28]$$

must be obeyed in a stable system. Starting with Eq. [2.9] we can now exchange an extensive variable with the corresponding potential and we find stability conditions of the type

$$\left(\frac{\partial Y_k}{\partial X_k}\right)_{Y_i X_j} > 0 \qquad [2.29]$$

In the above derivative Y_i denotes the potentials and X_j the extensive quantities, which are kept constant during the differentiation. We thus find that, regardless of whether potentials or extensive quantities are constant, a potential has to increase when the conjugated extensive quantity is added to a stable system.

For example, we may immediately write the following stability criterion

$$\left(\frac{\partial T}{\partial S}\right)_{P, X_j} > 0 \qquad [2.30]$$

where X_j represents all the components. This may be written in a more transparent form in terms of c_P, the heat capacity at constant pressure and defined as $(\partial H/\partial T)_P$. From Table 2.2 we see that the enthalpy H may be written as a function of T and P, although these are not its natural variables, if we use the relation $H = G + TS$ and the fact that $S = -\partial G/\partial T$ (see Eq. [2.14a]), then

$$c_P = \left(\frac{\partial H}{\partial T}\right)_P = T\frac{\partial S}{\partial T} \qquad [2.31]$$

$$\left(\frac{\partial T}{\partial S}\right)_P = \frac{1}{\left(\frac{\partial S}{\partial T}\right)_P} = \frac{T}{c_P} > 0 \qquad [2.32]$$

In a closed stable system the heat capacity is positive. Another condition is

$$\left(\frac{\partial - P}{\partial V}\right)_T > 0 \qquad [2.33]$$

© Woodhead Publishing Limited, 2012

By introducing the isothermal compressibility defined as

$$\kappa_T = -\frac{1}{V}\left(\frac{\partial V}{\partial P}\right)_T \qquad [2.34]$$

Eq. [2.33] may be rephrased into its more familiar form

$$\frac{1}{V\kappa_T} > 0 \qquad [2.35]$$

Thus the compressibility must be positive in a stable material. It should be observed that the stability criteria only involve conjugated variables. Consequently there is no requirement on, for example, the thermal expansion which is defined as $\alpha = (\partial V/\partial T)/V$ because V and T are not conjugated. In fact, although the thermal expansion is usually positive, there are important examples of substances with negative values, e.g. rubber (see, for example, Pellicer *et al.*, 2001).

The following general relation may be shown

$$\left(\frac{\partial Y_k}{\partial X_k}\right)_{Y_1 Y_2 \ldots Y_{k-1} X_{k+1} \ldots} \leq \left(\frac{\partial Y_k}{\partial X_k}\right)_{Y_1 Y_2 \ldots X_{k-1} X_{k+1} \ldots} \qquad [2.36]$$

If a potential is fixed rather than the conjugated extensive variable, the system is closer to instability. In a system with c components the most sensitive stability condition is thus given by, for example

$$\left(\frac{\partial \mu_c}{\partial N_c}\right)_{TP\mu_2 \ldots \mu_{c-1} N_1} \geq 0 \qquad [2.37]$$

If also μ_1 is kept constant, the derivative will vanish due to the Gibbs–Duhem relation. For alloys, Eq. [2.37] may be given in a more convenient form. Introducing G_m as a function of the independent mole fractions x_2, x_3, etc., taking x_1 as a dependent quantity and defining

$$\phi_i = \mu_i - \mu_1 = \left(\frac{\partial G_m}{\partial x_i}\right)_{PTx_j} \qquad [2.38]$$

the limit of stability is written using the determinant

$$\begin{vmatrix} \phi_{22} & \cdots & \phi_{2C} \\ \vdots & \ddots & \vdots \\ \phi_{C2} & \cdots & \phi_{CC} \end{vmatrix} = 0 \qquad [2.39]$$

where

$$\phi_{ij} = \left(\frac{\partial \phi_i}{\partial x_j}\right) \qquad [2.40]$$

© Woodhead Publishing Limited, 2012

For a binary system this gives the well-known expression defining the so-called spinodal (see, for example, Cahn, 1961):

$$\frac{d^2G_m}{dx_{B^2}} = 0 \qquad [2.41]$$

Inside the composition and temperature regime where this second derivative is negative, an initially homogeneous alloy may decompose by means of a spinodal mechanism.

2.4.9 Le Chatelier's Principle

Equation [2.36] has some quite interesting consequences. It was already pointed out that the driving force should be regarded as a potential conjugated to some internal variable. We could then write Eq. [2.36] as:

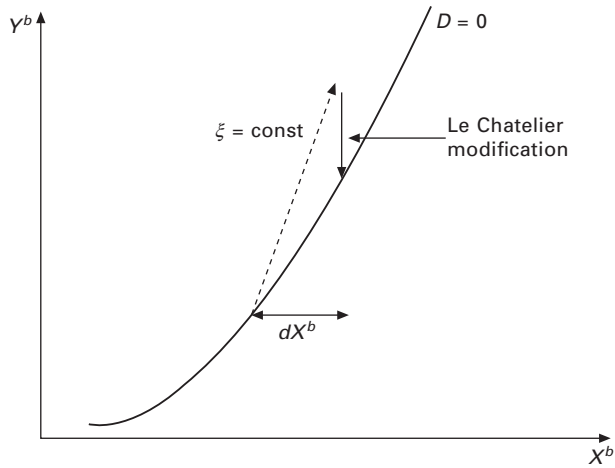
$$\left(\frac{\partial Y_k}{\partial X_k}\right)_{D_j} \leq \left(\frac{\partial Y_k}{\partial X_k}\right)_{\xi_j} \qquad [2.42]$$

We have considered a stable system and so both derivatives are thus positive. The derivative on the left-hand side is taken under a constant driving force, e.g. $D_j = 0$, which corresponds to equilibrium. The derivative on the right-hand side is taken under constant ξ_j, i.e. under frozen-in conditions. The important interpretation of Eq. [2.42] is as follows. If an equilibrium system is exposed to an infinitesimal change dX_k of an external condition such that there is no time for internal reactions, i.e. frozen-in conditions, the conjugated potential Y_k will increase accordingly. When equilibrium is established the initial increase has diminished. For example, if the volume is suddenly compressed pressure will increase, but as equilibrium is approached pressure will decrease and approach a constant value which is larger than the original value. Equation [2.41] may be regarded as a mathematical formulation of Le Chatelier's Principle. A graphical illustration is given in Fig. 2.5. For a more thorough discussion the reader is referred to Hillert (1995).

2.5 The calculation of thermodynamic properties and equilibrium under fixed *T, P* and composition

In order to perform thermodynamic calculations for real materials it is necessary to know how their thermodynamic properties vary with internal and external conditions. In the previous section it was demonstrated that both equilibrium and non-equilibrium properties, driving forces and stability may be derived from a thermodynamic state function, such as Gibbs energy. In most cases it does not matter what function one chooses but since the

© Woodhead Publishing Limited, 2012



2.5 Graphical illustration of Le Chateliers principle. The solid curve marks the relation between Y^b and X^b under equilibrium.

majority of practical problems involve temperature, pressure and composition as external conditions, Gibbs energy is most useful. Nevertheless, it should be emphasized that some special problems cannot be analyzed with all state functions. For example, the critical point in the temperature-pressure diagram of a fluid cannot be very well handled using the Gibbs energy but needs a function that has volume as a natural variable, e.g. internal energy, entropy or Helmholtz energy.

In the following we will limit the discussion to problems where Gibbs energy is sufficient. We thus need a function: $G_m = G_m(T, P, x_1, x_2 \ldots \xi_1, \xi_2 \ldots)$, where the xs denote the mole fractions and the ξs are various internal variables. From such a function we may derive all thermodynamic quantities of interest (see Eq. [2.14]). For example, $V_m = \partial G_m/\partial P$, $S_m = \partial G_m/\partial T$ $\alpha = (\partial^2 G_m/\partial P \partial T)/\partial G_m/\partial P$, $c_P = -T\partial^2 G_m/\partial T^2$, etc.

The chemical potential is obtained as

$$\mu_k = G_m + \frac{\partial G_m}{\partial x_k} - \Sigma\, x_j \frac{\partial G_m}{\partial x_j} \qquad [2.43]$$

and the driving forces

$$D_j = -\frac{\partial G_m}{\partial \xi_j} \qquad [2.44]$$

Here we have assumed that the ξs are given as intensive variables.

The above equations hold for a one-phase as well as a multi-phase system. In a database it is most flexible to store a function $G_m^\alpha = G_m^\alpha(T, P, T, P, x_1^\alpha, x_2^\alpha \ldots \xi_1^\alpha, \xi_2^\alpha \ldots)$ for each separate phase α. The Gibbs energy of a multiphase system is then obtained as

© Woodhead Publishing Limited, 2012

$$G = \sum_{\alpha} N^{\alpha} G_m^{\alpha}(T, P, x_1^{\alpha}, x_2^{\alpha} \ \ldots \ \xi_1^{\alpha}, \xi_2^{\alpha} \ldots) \qquad [2.45]$$

where the summation is performed over all phases in the system and N^{α} is the number of moles of atoms in each phase. The mole fractions x, the ξs and the N^{α}s are now all internal variables. However, they are not independent because the overall composition of the system is fixed as expressed by the mass balances

$$N_k = x_k N = \sum_{\alpha} N^{\alpha} x_k^{\alpha} \qquad [2.46]$$

The mole fractions are also related because for each phase α

$$\sum_{k=1}^{c} x_k^{\alpha} = 1 \qquad [2.47]$$

The equilibrium is now calculated by finding the minimum in Eq. [2.45] under the constraints given by Eqs [2.46] and [2.47]. It should be noted that often there are constraints on some or all of the ξ values. The minimization can be performed with many different methods and we shall not discuss these further in this chapter.

2.6 Gibbs energy of phases in steel – the Calphad method

In order to find expressions for the Gibbs energy of the individual phases the so-called Calphad method (Saunders and Miodownik, 1998; Lukas *et al.*, 2007) has been found most valuable. In this method one formulates models for the individual phases. Such models can have varying degree of sophistication, ranging from simple regular solutions to cluster methods. So-called Monte Carlo methods should also be mentioned although they are somewhat different in character as they are not based on expressions of suitable state functions. Nevertheless, they are very powerful for some problems but due to laborious computations they are typically applied to very simple alloy systems and they will not be discussed further here. As a rule, the simpler a model is, the more complex alloys, in terms of number of elements and phases, may be analyzed.

2.6.1 Modeling of disorder and entropy

All methods based on mathematical expressions for a state function have Boltzmann's classical expression for the entropy as a starting point:

$$S = k_B \ln W \qquad [2.48]$$

© Woodhead Publishing Limited, 2012

Here W is the number of different ways a system can arrange itself under given external conditions and k_B is Boltzmann's constant. For example, in a crystal with N atoms and N_{Va} vacant lattice sites, there is $N + N_{Va}$ lattice sites and the vacancies may be distributed on those sites in

$$W = \frac{(N + N_{Va})!}{N!N_{Va}!} \quad [2.49]$$

different ways if they are randomly distributed. Inserting Eq. [2.49] into Eq. [2.48] and applying Stirling's approximation $\ln(x!) \cong x \ln x - x$, which is justified because N and N_{Va} are typically very large, we obtain

$$S \cong -\frac{Nk_B}{(1 - y_{Va})}((1 - y_{Va}) \ln (1 - y_{Va}) + y_{Va} \ln y_{Va}) \quad [2.50]$$

where y_{Va} is the fraction of vacant lattice sites. The quantity $N/(1 - y_{Va})$ is thus the number of lattice sites including the vacant ones. The entropy per mole of lattice sites is thus

$$S_m = -R((1 - y_{Va}) \ln (1 - y_{Va}) + y_{Va} \ln y_{Va}) \quad [2.51]$$

where R, the gas constant, is simply k_B multiplied by the Avogadro number.

The Gibbs energy for a system with vacancies should also contain the extra energy associated with formation of a vacancy as well as the pressure volume work to expand the lattice and some changes in vibrational modes around the vacancy. We may lump all these contributions in a parameter ${}^\circ G_{Va}$ which we could formally define as the change in Gibbs energy to form the first vacancy counted per mole of vacancies. If we assume that it is constant we obtain for a system with 1 mole of lattice sites

$$G_m = y_{Va} {}^\circ G_{Va} + RT((1 - y_{Va}) \ln(1 - y_{Va}) + y_{Va} \ln y_{Va}) \quad [2.52]$$

In order to use the Gibbs energy to find the equilibrium state we have to consider a fixed number of atoms rather than lattice sites and we should thus look at the Gibbs energy per mole of atoms which is $G_m/(1 - y_{Va})$. The equilibrium fraction of vacancies is thus obtained as

$$\frac{\partial[G_m/(1 - y_{Va})]}{\partial y_{Va}} = \frac{1}{(1 - y_{Va})} \frac{\partial G_m}{\partial y_{Va}} + \frac{G_m}{(1 - y_{Va})^2} = 0 \quad [2.53]$$

Equation [2.53] may be rewritten

$$G_m + \frac{\partial G_m}{\partial y_{Va}} - y_{Va} \frac{\partial G_m}{\partial y_{Va}} = 0 \quad [2.54]$$

By comparison with Eq. [2.42] we find that the expression on the left-hand side is actually the chemical potential of vacancies, i.e. $\mu_{Va} = (\partial G/\partial N_{Va})$

© Woodhead Publishing Limited, 2012

$_{T,P,N}$. At equilibrium the chemical potential of vacancies thus vanishes. By applying Eq. [2.54] to Eq. [2.52] we find

$$\mu_{Va} = {}^{\circ}G_{Va} + RT \ln y_{Va} \qquad [2.55]$$

and the equilibrium fraction of vacancies is thus

$$y_{Va}^{eq} = \exp(-{}^{\circ}G_{Va}/RT) \qquad [2.56]$$

In fact, Eq. [2.51] may be applied to any system where there is a random mixture of constituents. The only problem is to define the constituents, i.e. to find those things that mix randomly. From Eqs [2.44] and [2.53] it is clear that $\mu_{Va} = (\partial G/\partial N_{Va})_{T,P,N} = -D_{Va}$ serves as the driving force for creation or annihilation of vacancies and we may express it in terms of the equilibrium vacancy content by combining Eqs [2.55] and [2.56] as $D_{Va} = -RT \ln(y_{Va}/y_{Va}^{eq})$. The entropy production $D_{Va}dy_{Va}$ is thus always positive as the system approaches equilibrium.

2.6.2 Regular solution type models

Consider, for example, a substitutional alloy, where one may assume a random mixture of its c components. Expressed per mole of atoms we would then have

$$G_m = \sum_{k=1}^{c} x_k {}^{\circ}G_k + RT \sum_{k=1}^{c} x_k \ln x_k + {}^{E}G_m \qquad [2.57]$$

If we consider only two components and replace x with y and set the last term ${}^{E}G_m = 0$, we recover as a special case the expression for thermal vacancies. We have an expression like Eq. [2.56] for each phase in the system and indicate the phase with an upper index, e.g. for the phase α we write G_m^{α}, ${}^{\circ}G_m^{\alpha}$, ${}^{E}G_m^{\alpha}$.

The last quantity ${}^{E}G_m^{\alpha}$ is called the excess energy and takes into account contributions which are not included in the first two sums and, like the mixing entropy, it vanishes for a pure component. The quantity ${}^{\circ}G_k^{\alpha}$ thus denotes the Gibbs energy of pure k in the α phase. The simplest expression for the excess energy is called the regular solution and is given by

$${}^{E}G_m^{\alpha} = \sum_{k} \sum_{j>k} x_k x_j L_{kj}^{\alpha} \qquad [2.58]$$

Of course, the regular solution parameters L_{kj}^{α} are zero when $k = j$ and we also obviously have $L_{kj}^{\alpha} = L_{jk}^{\alpha}$. When experimental data are analyzed they are usually found to be functions of temperature and it is common to apply expansions of the type $a + bT + cT \ln T + \ldots$ where the coefficients a, b and c are fitted to experimental data. However, often experimental data cannot be fitted satisfactorily unless L_{kj}^{α} is allowed to vary also with composition. The

© Woodhead Publishing Limited, 2012

most commonly used method is to expand L_{kj}^{α} in a so-called Redlich–Kister polynomial

$$L_{kj}^{\alpha} = {}^{0}L_{kj}^{\alpha} + {}^{1}L_{kj}^{\alpha}(x_k - x_j) + {}^{2}L_{kj}^{\alpha}(x_k - x_j)^2 \ldots = \sum_{\ell=0}^{m} {}^{\ell}L_{kj}^{\alpha}(x_k - x_j)^{\ell} \quad [2.59]$$

When ℓ is uneven, we have ${}^{\ell}L_{kj}^{\alpha} = -{}^{\ell}L_{jk}^{\alpha}$ and otherwise ${}^{\ell}L_{kj}^{\alpha} = {}^{\ell}L_{jk}^{\alpha}$. Such a model is usually referred to as being of the regular solution type. In the special case where only the first two terms are non-zero, it is referred to as a subregular solution.

If the experimental information is such that many terms in the expansion are needed to have a good fit to experimental data, it is a strong indication that the model, i.e. Eq. [2.57], is not realistic. Even though higher-order expansions may represent the experimental information satisfactorily, they will lead to difficulties when extrapolating the data and usually one only uses terms up to the second order.

For a binary regular solution phase α with components A and B, Eq. [2.43] yields the following expressions for the chemical potentials of A and B, respectively.

$$\mu_A = {}^{\circ}G_A^{\alpha} + RT\ln(1 - x_B) + x_B^2 L_{AB}^{\alpha} \quad [2.60a]$$

$$\mu_B = {}^{\circ}G_B^{\alpha} + RT\ln x_B + (1 - x_B)^2 L_{AB}^{\alpha} \quad [2.60b]$$

2.6.3 Phases with substitutional and interstitial components

Interstitially dissolved atoms do not occupy normal lattice sites and consequently they do not mix with substitutional atoms. It is more reasonable to assume that they mix randomly with vacant interstices or with other types of interstitial atoms. We should thus regard such a phase as consisting of two sublattices, one where the substitutional atoms mix and one where the interstitials and vacant sites mix. It should be emphasized, as discussed in the previous section, that the substitutional atoms also mix with vacancies but usually their fraction is so low that it can be neglected except in those cases when one is particularly interested in the vacancy content.

We write a formula unit of such a phase $(M_1M_2\ldots)_a(C, D \ldots Va)_c$ and Eq. [2.57] is thus modified into

$$G_m = \sum_M \sum_C y_M y_C {}^{\circ}G_{MC} + RT\left[a\sum_M y_M \ln y_M + c\sum_C y_C \ln y_C\right] + {}^{E}G_m \quad [2.61]$$

© Woodhead Publishing Limited, 2012

The *y*s stand for the fraction of lattice sites, substitutional or interstitial, that is occupied by a certain component *M* or *C*, and *a* and *c* are the number of moles of each type of lattice site. In FCC there is one interstitial site per substitutional site and $a = c = 1$. In BCC there are three interstitial sites per substitutional and $a = 1$, $c = 3$. The suffix *m* in Eq. [2.61] stands for 1 mole of formula units and *MC* stands for the real or hypothetical compound corresponding to the formula unit $(M)_a(C)_c$, often called an end member. In particular, the formula unit $(M)_a(Va)_c$ means that all interstitials are vacant and it thus corresponds to pure *M*. It is straightforward to show that Eq. [2.43] is then modified into

$$\mu_{M_aC_c} = G_m + \frac{\partial G_m}{\partial y_M} + \frac{\partial G_m}{\partial y_c} - \sum_{j=1}^{C} y_j \frac{\partial G_m}{\partial y_j} \qquad [2.62]$$

The summation is taken over all components, i.e. over both sublattices including the vacancies. The expression for the chemical potential of *M* thus becomes

$$\mu_M = \frac{1}{a}\left[G_m + \frac{\partial G_m}{\partial y_M} + \frac{\partial G_m}{\partial y_{Va}} - \sum_{j=1}^{C} y_j \frac{\partial G_m}{\partial y_j}\right] \qquad [2.63]$$

The chemical potential for an interstitial component *C* is obtained from

$$\mu_{M_aC_c} = a\mu_M + c\mu_C \qquad [2.64]$$

and becomes

$$\mu_C = \frac{1}{c}\left[\frac{\partial G_m}{\partial y_C} - \frac{\partial G_m}{\partial y_{Va}}\right] \qquad [2.65]$$

The excess energy term is usually expressed as a regular solution type on each sublattice leading to expressions of the type

$${}^{E}G_m^a = \sum_j \sum_k \sum_{i>k} y_k y_i y_j L_{kij}^{\alpha} \qquad [2.66]$$

where *k* and *i* refer to components on the same sublattice and *j* is on the other sublattice. As an example, we give the expression for Fe-Mn-C in austenite (FCC).

$$\begin{aligned} G_m^{\gamma} = {} & y_{Fe}y_C\,{}^{\circ}G_{FeC}^{\gamma} + y_{Mn}y_C\,{}^{\circ}G_{MnC}^{\gamma} + y_{Fe}y_{Va}\,{}^{\circ}G_{Fe}^{\gamma} + y_{Mn}y_{Va}\,{}^{\circ}G_{Mn}^{\gamma} \\ & + RT\,[y_{Fe}\ln y_{Fe} + y_{Mn}\ln y_{Mn} + y_C \ln y_C + y_{Va}\ln y_{Va}] \\ & + y_{Fe}\,y_{Mn}y_C\,{}^{\circ}L_{Fe,Mn:C}^{\gamma} + y_{Fe}\,y_{Mn}\,y_{Va}\,{}^{\circ}L_{Fe,Mn:Va}^{\gamma} \\ & + y_{Fe}y_C\,y_{Va}\,{}^{\circ}L_{Fe:C,Va}^{\gamma} + y_{Mn}y_C\,y_{Va}\,{}^{\circ}L_{Mn:C,Va}^{\gamma} \end{aligned} \qquad [2.67]$$

In Eq. [2.67] we have used the facts that ${}^{\circ}G_{FeVa}^{\gamma} = {}^{\circ}G_{Fe}^{\gamma}$ and ${}^{\circ}G_{MnVa}^{\gamma} = {}^{\circ}G_{Mn}^{\gamma}$. It

© Woodhead Publishing Limited, 2012

should also be observed that the parameters $L^{\gamma}_{Fe,Mn:Va}$, $^{\circ}G^{\gamma}_{FeC}$, $^{\circ}G^{\gamma}_{MnC}$, $L^{\gamma}_{Fe:C,Va}$ and $L^{\gamma}_{Mn:C,Va}$ refer to the binary Fe-Mn, Fe-C and Mn-C systems, respectively. Moreover, two y fractions may be eliminated because $y_{Fe} + y_{Mn} = 1$ and $y_C + y_{Va} = 1$. Only the parameter $L^{\gamma}_{Fe,Mn:C}$ represents a ternary effect.

By means of Eq. [2.63] it is straightforward to derive the expression for the chemical potentials. The leading terms are

$$\mu_{Fe} = {}^{\circ}G^{\gamma}_{Fe} + y_{Mn}y_C\,{}^{\circ}\Delta G^{\gamma}_{MnC} + RT\,[\ln(1 - y_{Mn}) + \ln(1 - y_C)] + \ldots \quad [2.68a]$$

$$\mu_{Mn} = {}^{\circ}G^{\gamma}_{Mn} - (1 - y_{Mn})y_C\,{}^{\circ}\Delta G^{\gamma}_{MnC} + RT\,[\ln y_{Mn} + \ln(1 - y_C)] + \ldots \quad [2.68b]$$

$$\mu_C = {}^{\circ}G^{\gamma}_C + y_{Mn}\,{}^{\circ}\Delta G^{\gamma}_{MnC} + RT\ln[y_C/(1 - y_C)] + \ldots \quad [2.68c]$$

where we have introduced

$${}^{\circ}\Delta G^{\gamma}_{MnC} = {}^{\circ}G^{\gamma}_{Fe} + {}^{\circ}G^{\gamma}_{MnC} - {}^{\circ}G^{\gamma}_{FeC} - {}^{\circ}G^{\gamma}_{Mn} \quad [2.69a]$$

$${}^{\circ}G^{\gamma}_C = {}^{\circ}G^{\gamma}_{FeC} - {}^{\circ}G^{\gamma}_{Fe} + L^{\gamma}_{Fe:C,Va} \quad [2.69b]$$

The parameter $^{\circ}\Delta G^{\gamma}_{MnC}$ represents the effect of Mn content on the carbon chemical potential and the interaction between carbon and manganese in iron. The parameter $^{\circ}G^{\gamma}_C$ represents the reference state for carbon in austenite.

2.6.4 Activity and reference states

The activity a^{ref}_j of a component j is defined relative to a chosen reference state from the chemical potential μ_j by means of

$$\mu_j = \mu^{\text{ref}}_j + RT\ln a^{\text{ref}}_j \quad [2.70]$$

Thus the activity is unity in the chosen reference state. For a binary regular solution, with components A and B, combination of Eqs [2.60] and [2.70] yields

$$a^{\text{ref}}_B = x_B \exp(({}^{\circ}G^{\alpha}_B - \mu^{\text{ref}}_B + (1 - x_B)^2 L^{\alpha}_{AB})/RT) \quad [2.71]$$

In metallurgy several choices of reference states are common. For example, one may choose pure B in the phase and at the temperature under consideration. This is called the Raoultian reference and in a binary regular solution the Raoultian activity is given by

$$a_B = x_B \exp((1 - x_B)^2 L^{\alpha}_{AB}/RT) \quad [2.72]$$

Evidently the B activity approaches the mole fraction x_B in the neighborhood of pure B. This fact is referred to as Raoult's law. On the other hand, for sufficiently low B contents the activity will be proportional to x_B, with a

© Woodhead Publishing Limited, 2012

proportionality factor $\exp(L^{\alpha}_{AB}/RT)$ which may be larger or smaller than unity depending on the sign of the regular solution parameter. The proportionality factor is called the activity coefficient and the behavior at low B contents is referred to as Henry's law.

Another possibility is to take as reference the most stable state of the component under the temperature of interest, for example, β. In that case the proportionality factor becomes $\exp((^{\circ}G^{\alpha}_{B} - {}^{\circ}G^{\beta}_{B} + (1 - x_B)^2 L^{\alpha}_{AB})/RT)$. This has the consequence that the activity of pure B in α will be larger than unity if it is not the most stable state at the temperature of interest.

Still another possibility, which is sometimes used in steel refining, is to prescribe that the activity of a certain alloy element is unity when there is 1 mass% of the element in the molten steel. Its activity, close to the composition of 1 mass%, will then simply be equal to the content expressed in mass%.

Actually, the issue of reference state must be considered even when the activity has not yet been introduced. This is because there is no unique zero level for the energy and consequently not for the thermodynamic functions that depend on the energy either. According to the third law of thermodynamics, all substances have the same value of entropy at 0 K and by convention it is set to 0. There is no such natural choice of reference for the energy, and for each component one may choose any reference that is convenient provided that all subsequent calculations are performed consistently and based on the chosen references. In the above discussion we considered various choices of reference for expressing the activity. They all had in common that we considered references at the same temperature and pressure as the conditions of interest, i.e. the reference varies with temperature. If such a reference is chosen, it is not possible to represent the temperature dependencies of individual phases but only the temperature dependence relative to the reference. In order to represent temperature dependencies, e.g. entropy and heat capacity, one needs to use temperature independent references. The most common choice is the so-called stable element reference (SER). In this reference, the reference for entropy is taken as 0 at 0 K and for enthalpy it is the enthalpy of the most stable phase at 25°C (298.15 K), i.e. $\mu_k^{\mathrm{ref}} = H_k^{\mathrm{SER}}$.

2.7 Various kinds of phase diagrams

Phase diagrams play a very important role when interpreting phase transformations in steel and, in fact, many conclusions can be drawn directly from the phase diagram. A phase diagram indicates which phase or phases are thermodynamically stable in the different areas of the diagram. A phase diagram may be plotted with different quantities on the axes and for each particular problem a certain set of axes is usually most convenient. The simplest phase diagram is one with potential quantities on all axes. However, the Gibbs phase rule (see Section 2.4.5), reveals that the number of potentials

© Woodhead Publishing Limited, 2012

that can be varied independently is $f = c - p + 2$ which has its largest value $f = c + 1$ when $p = 1$, i.e. when there is only one phase. This would thus be the dimensionality of the full phase diagram if all phase regions should be represented. Usually one wants to plot two-dimensional diagrams and thus, except for the case of a pure element where $c = 1$, it is necessary to reduce the dimensionality by sectioning or projections. Some important aspects of phase diagrams will be discussed in this section.

2.7.1 Potential diagrams

For a pure element like Fe the Gibbs phase rule yields $f = 3 - p$ and the full phase diagram is two-dimensional (see the phase diagram for pure Fe depicted in Fig. 2.1). Pressure and temperature have been chosen as potential axes but one could also have chosen pressure and chemical potential or temperature and chemical potential. The topology of such a diagram is simple and given by the phase rule. Regions with two coexisting phases have $f = 1$ and are lines, and regions with three coexisting phases $f = 0$ are represented by points. From the meaning of the diagram it is self-evident that such a three-phase point appears where two two-phase lines meet and a third two-phase line will then leave the point. According to the phase rule, four phases cannot coexist because they would require $f = -1$.

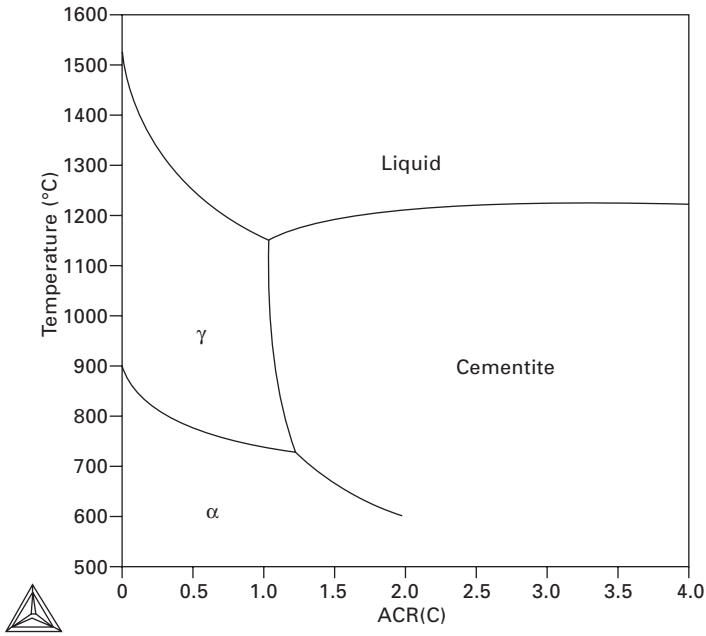
For a binary system the phase rule gives $f = 4 - p$ and the full potential phase diagram will be three dimensional. We may lower the dimensionality by sectioning the full diagram at a given potential. For that case we will write the phase rule

$$f = c - p + 2 - n_s \qquad [2.73]$$

where n_s is the number of potentials that have been given a fixed value. Usually one considers the phase diagram at atmospheric pressure. From Eq. [2.73] it is obvious that from a topological point of view sectioning by keeping one of the potentials fixed is equivalent with having one component less. A binary potential phase diagram at a fixed pressure would thus have the same topology as the diagram for a pure element. This is demonstrated by Fig. 2.6 which shows the metastable Fe-C phase diagram plotted at $P =$ 1 atm with temperature and C activity as axes. The reference state for C is graphite at the temperature under consideration. Equilibrium with graphite is thus represented by a vertical line at ACR(C) = 1.

In many practical situations the potential diagram in Fig. 2.6 may be more instructive than the conventional diagram. One example is when iron is in contact with a carbon-rich atmosphere having a certain carbon activity and one would like to know what phase will form in contact with the gas. From Eq. [2.73] it also follows that the topology of the Fe-C-N potential diagram would look the same if sectioned at $P = 1$ atm and a certain N activity.

© Woodhead Publishing Limited, 2012



2.6 The metastable Fe-C phase diagram plotted at P = 1 atm with temperature and C activity as axes. The reference state for C is graphite at the temperature under consideration.

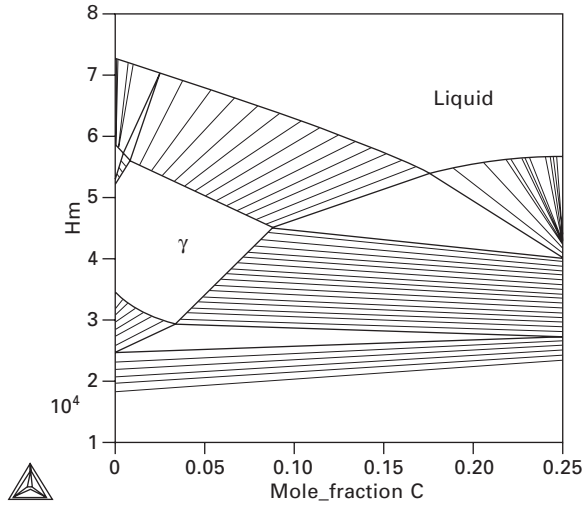
2.7.2 Molar diagrams and mixed diagrams

Although two phases in equilibrium have the same values of the potentials, they usually have different values of the molar quantities, e.g. the mole fractions. In a stable system a potential must increase when the amount of the corresponding component increases (see Section 2.4.8). Along a two-phase line in a potential phase diagram the phase corresponding to the higher chemical potential thus must have a larger value on the corresponding molar quantity. If a potential axis is replaced with the corresponding mole fraction, the two-phase line in the potential diagram opens up into a two-phase field. The two points representing two phases in equilibrium may be tied together with a straight line, a tie-line. An example is shown in Fig. 2.7, where the binary Fe-C system is plotted with molar enthalpy instead of temperature on one axis. A number of tie-lines have been included in the figure.

This type of diagram is useful to show how much heat needs to be added in order to reach a certain part of the phase diagram. The reference temperature for enthalpy is 25°C (298 K). For example, a steel with eutectoid composition, i.e. x_C = 0.034, needs at least 30 kJ mol^{-1} to be austenitized and c. 70 kJ mol^{-1} to be fully molten.

If we want to exchange carbon content in Fig. 2.7 to carbon activity,

© Woodhead Publishing Limited, 2012



2.7 The metastable Fe-C phase diagram plotted at P = 1 atm with molar enthalpy and C mole fraction as axes.

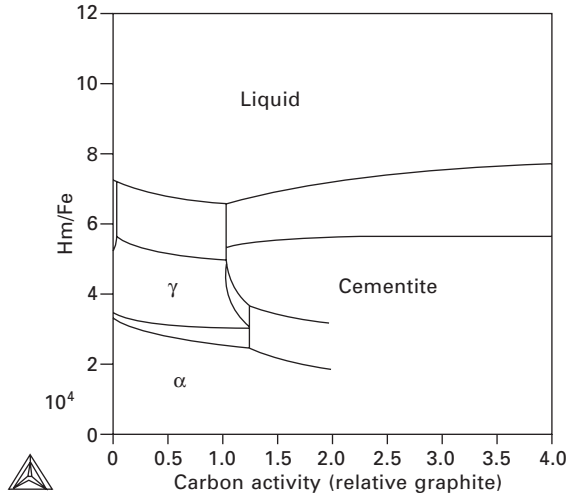
certain measures have to be taken in order to obtain a true phase diagram, i.e. a diagram where each point corresponds to a well-defined set of phases. This is discussed in detail by Hillert (2008) and in the present case it turns out that we have two choices. Either we may keep the molar enthalpy on the y-axis and instead plot a_C/a_{Fe} on the x-axis, or we may plot the enthalpy per mole of iron atom on the y-axis and the carbon activity on the x-axis. The latter diagram is shown in Fig. 2.8. As can be seen it has the same topology as a usual binary phase diagram but we have exchanged the potential and molar quantities.

From Eq. [2.73] we may calculate the dimensionality of a phase-field also when we have exchanged some potentials with molar quantities. If there are no molar quantities, the dimensionality is directly given by Eq. [2.73] but with each potential that is exchanged with a molar quantity increased by one until it is the same as the dimensionality d of the diagram, usually two, i.e.

$$f = c - p + 2 - n_s + n_m \qquad [2.74]$$

where n_m is the number of molar quantities introduced. If the calculated f is larger than d, the dimensionality of a phase field will simply be d. For the binary system sectioned once at P = 1 atm, we find $f = 3 - p + n_m$. Thus a three-phase region will be a point in the diagram with only potentials, a line if one potential is exchanged with a molar variable, and an area if both potentials are exchanged with molar quantities.

© Woodhead Publishing Limited, 2012



2.8 The metastable Fe-C phase diagram plotted at P = 1 atm with enthalpy per mole of Fe and carbon activity relative graphite as axes.

2.7.3 Sections

For steels with two alloy elements the complete potential phase diagram will be three dimensional even if it is sectioned at P = 1 atm. In order to have a two-dimensional diagram we may then section it at constant value of another potential, usually the temperature. As discussed earlier, it would then have the same topological properties as a unary system. The most common way to plot ternary systems is the isobaric, isothermal sections with molar quantities on the axes. They then have the same topology as Fig. 2.7. All phase fields are then areas. At equilibrium a potential has the same value in all phases. If only potentials have been sectioned, all tie-lines will then lie in the plane of the phase diagram. When the tie-lines are in the plane, one may apply the well-known lever rule to evaluate the fraction of the different phases from the average value of the molar quantity. This useful property is lost when the tie-lines are not in the plane. The latter situation is the case if a ternary system is sectioned in a different way which will now be discussed.

Consider a ternary system sectioned at atmospheric pressure and at a given mole fraction of one of the components. If one plots temperature on the y-axis and the molar content of one of the other elements on the x-axis, one obtains a so-called isoplethal section, sometimes called vertical section. Such isopleths are common in the literature. In this case we have $n_s = 2$, $n_m = 2$, and $f = 5 - p$ and consequently all one-, two- and three-phase regions will be areas in a two-dimensional diagram. However, in this case it is evident that the tie-lines are generally out of plane because the diagram is sectioned at a constant molar quantity and the lever rule cannot be applied.

© Woodhead Publishing Limited, 2012

An example is shown in Fig. 2.9 showing an isopleth for the Fe-Cr-C system sectioned at $x_{Cr} = 0.05$ and $P = 1$ atm. According to Eq. [2.74] a four-phase equilibrium is given by a line, see the horizontal line representing the four-phase equilibrium $\gamma + \alpha + M_7C_3 +$ Cementite at 757°C in Fig. 2.9.

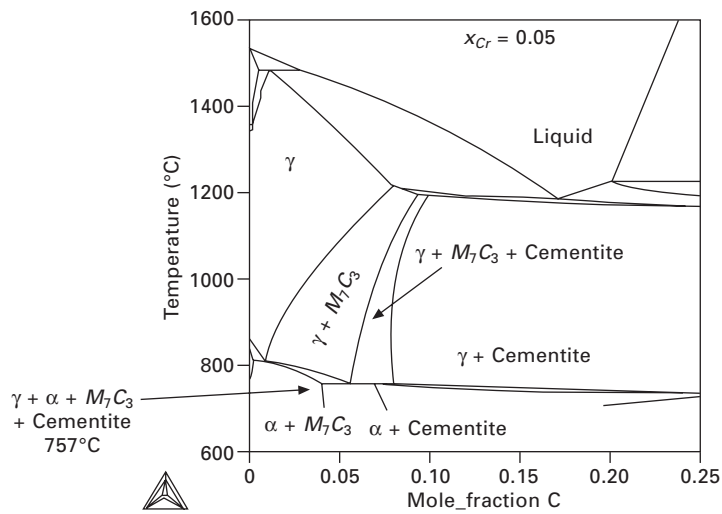
2.8 Effect of interfaces

2.8.1 Surface energy and surface stress

The surface energy is related to the physical process of changing the interfacial area in a system, for example during growth of a particle. In the simplest case only the interfacial area is changed and all other quantities stay constant. This is generally not the case during a precipitation process where both volume fraction of the precipitated phase and the interfacial area increase. It is approximately the case during coarsening where small particles dissolve and large particles grow leaving the volume fraction approximately constant but decreasing the total interfacial area. It is also the case during grain growth in a one-phase material where the total grain boundary area decreases leaving everything else unchanged.

Already Gibbs (1875) and more recently Cahn (1980) pointed out that the surface of a solid can have its physical area changed by either of two different processes when an external force is applied:

- creation or destruction of surface area without changing surface structure and properties per unit area;



2.9 Isopleth at $x_{Cr} = 0.05$ of Fe-Cr-C phase diagram plotted at $P = 1$ atm. The tie-lines are not in plane.

© Woodhead Publishing Limited, 2012

- elastic deformation ε_{ij} of the surface layer, keeping the number of surface lattice sites constant while changing the form, physical area and properties.

They defined the surface energy σ as the work of *creating* a new unit area of the surface and the surface stress f_{ij} as related to the work of *elastically deforming* the surface. If dA_0 denotes the area change due to the creation of new surface we have for the total area change dA:

$$dA = A_0(d\varepsilon_{11} + d\varepsilon_{22}) + dA_0 \quad [2.75]$$

The change in internal energy caused by the area change may then be written

$$dU = A_0(f_{11}\, d\varepsilon_{11} + f_{22}\, d\varepsilon_{22} + f_{12} d\varepsilon_{12}) + \sigma\, dA_0 \quad [2.76]$$

and the surface stresses and surface energy are thus defined as

$$f_{ij} = \frac{1}{A_0}\left(\frac{\partial U}{\partial \varepsilon_{ij}}\right)_{A_0} \quad [2.77a]$$

and

$$\sigma = \left(\frac{\partial U}{\partial A_0}\right)_{\varepsilon_{ij}} \quad [2.77b]$$

The surface stress thus is a tensorial quantity and it follows that

$$\left(\frac{\partial \sigma}{\partial \varepsilon_{ij}}\right) = f_{ij} \quad [2.78]$$

For the sake of simplicity the following discussion will be limited to cases with isotropic surface properties. Thus the surface energy is constant and does not depend on the orientation of the surface and the only non-zero surface stresses are $f_{11} = f_{22} = f$. Even though Gibbs called f surface tension, this term should be avoided. The reason is that the term surface tension is often misused for surface energy and it only has a meaning for the isotropic case, whereas both surface stress (a 2*2 tensor) and surface energy (a scalar) are generally applicable.

Consider a β-particle in a matrix α assumed to have a constant hydrostatic pressure, equal to the external pressure. Strictly speaking, we thus exclude cases where the matrix is solid and has been deformed elastically. This assumption will be strictly valid when the matrix is liquid or gaseous. Suppose the particle and the matrix are at equilibrium and the total volume is kept constant. Allow the volume of the particle to change by elastic compression or expansion without any transfer of atoms between the two phases under adiabatic conditions. We then have $dU = 0$, i.e.

© Woodhead Publishing Limited, 2012

$$dU = dU^{\alpha} + dU^{\beta} + dU^{\sigma} = 0 \qquad [2.79]$$

The first two terms represent the change in internal energy of the α matrix and the β particle respectively, whereas the last term represents the change caused by the change in interfacial area. Under the present assumptions the result becomes particularly simple because the only contribution to the change in internal energy of α and β stems from the pressure volume work and deformation of the interface. We thus have

$$dU = P^{\alpha}dV^{\beta} - P^{\beta}dV^{\beta} + f\,dA^{el} = 0 \qquad [2.80]$$

where $dA^{el} = A_0(d\varepsilon_{11} + d\varepsilon_{22})$ and $dV = dV^{\alpha} + dV^{\beta} = 0$ have been used. It thus follows that at equilibrium the particle will be under a compressive pressure given by

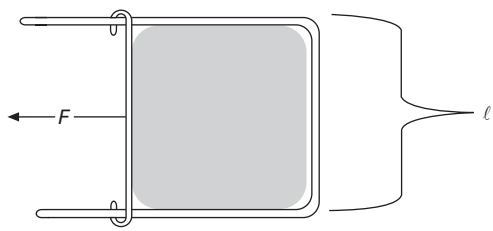
$$P^{\beta} - P^{\alpha} = f\,dA^{el}/dV^{\beta} \qquad [2.81]$$

For a spherical particle with radius r we have $dA^{el}/dV^{\beta} = 2/r$ and the familiar condition for mechanical equilibrium is obtained

$$P^{\beta} - P^{\alpha} = 2f/r \qquad [2.82]$$

We may thus note the compressive internal stress of the β particle is goverened by the surface stress rather than the surface energy. The relation between surface stress and internal pressure is quite general and may be used to calculate, for example, the critical size during nucleation if the internal pressure is known.

If a thin film of a liquid in contact with a large reservoir of the same liquid is slowly expanded a distance dx by pulling the bar in Fig. 2.10, the new interfacial area, upper and lower side, will be formed by transferring atoms from the reservoir to the film. The elastic deformation of the interface will not change and thus $dU = 2\sigma\,\ell dx$. This quantity must equal the work performed on the system by opposing the surface stress $Fdx = 2\ell f\,dx$ because these are the only tensile forces that a liquid can support. If β is a liquid, the surface stress thus has the same value as the surface energy. If the experiment is performed by pulling the bar very quickly, or if the liquid is very viscous,



2.10 The thin-film experiment to measure surface stress between liquid and atmosphere.

© Woodhead Publishing Limited, 2012

there will not be time enough for the liquid to relax and tensile stresses will build up both at the interface and in the bulk between the two interfaces. As equilibrium is approached the stresses in the bulk will vanish and the surface stress will relax to the equilibrium value being equal to the surface energy.

The important conclusion is thus that, if the β phase is a liquid droplet, we could as well calculate the internal pressure from the surface energy. In general, however, the surface energy and the surface stress will be different and the internal pressure must be calculated from the surface stress. However, this does not mean that the surface energy is less important. As we shall see, the interfacial energy plays the major role in the effect of interfaces on phase equilibria whereas the internal pressure caused by the surface stress is of secondary importance.

2.8.2 Effect on phase equilibria – isotropic case

We shall consider the simple case of a β phase inclusion in an α matrix. The β phase is assumed to be gaseous or liquid and we shall thus assume isotropic properties. The effect of capillarity can then be treated with any one of the characteristic state functions but it is most convenient to choose the function that has as its natural variables those state variables that will be kept constant for the system under consideration. From a practical point of view it thus seems convenient to keep temperature, the external pressure and the content of matter in the system constant and one should then use the Gibbs energy. The total Gibbs energy of a two-phase system consisting of the β inclusion in the α matrix is given by:

$$G = G^{\beta} + G^{\alpha} + G^{\sigma} \qquad [2.83]$$

G^{σ} is the contribution from surface free energy of the α/β interface. Due to capillarity, the internal pressure in the particle may be higher than in the α matrix. It is thus convenient to write G^{β} as

$$\begin{aligned} G^{\beta} &= N^{\beta}\left[U_m(P^{\beta}) - TS_m(P^{\beta}) + PV_m(P^{\beta})\right] \\ &= G(P^{\beta}) + (P - P^{\beta})V(P^{\beta}) \end{aligned} \qquad [2.84]$$

The values of T and P in Eq. [2.84] are those in the surroundings, according to the definition of Gibbs energy. In the present case the same value of P holds in the α matrix that is supposed to be liquid or gaseous but not to the β phase if the α/β interface is curved.

Consider the transfer of dN_j^{β} atoms of component j from α to β in a multicomponent system, and the total change of Gibbs energy is obtained after first inserting Eq. [2.84] in Eq. [2.83]. The transfer may cause a change of P^{β} and we thus obtain

© Woodhead Publishing Limited, 2012

$$dG = G_j^\beta(P^\beta)dN_j^\beta + (\partial G^\beta/\partial P)dP^\beta - V^\beta dP^\beta - (P^\beta - P)dV^\beta$$
$$- G_j^\alpha(P)dN_j^\beta + dG^\sigma = G_j^\beta(P^\beta)dN_j^\beta - (P^\beta - P)dV^\beta$$
$$- \mu_j^\alpha(P)\ dN_j^\beta + dG^\sigma \qquad [2.85]$$

We have here inserted the symbol for chemical potential, $\mu_j^\alpha(P)$, instead of the partial Gibbs energy for the α matrix, $G_j^\alpha(P)$. We have not done so for the partial Gibbs energy of β because we hesitate to consider the chemical potential as identical to the partial Gibbs energy for a phase not under the same pressure as the surroundings. Moreover, we see no need to do so. For a spherical particle of radius r and isotropic interfacial energy σ, the last term in Eq. [2.85] is $dG^\sigma = (2\sigma/r)V_j^\beta dN_j^\beta$, where V_j^β is the partial molar volume of β. Of course σ may contain an entropy contribution and is thus a surface Gibbs energy. From Eq. [2.85] the equilibrium conditions thus become

$$\mu_j^\alpha = G_j^\beta(P^\beta) + (2\sigma/r - (P^\beta - P))V_j^\beta \qquad [2.86]$$

For the case when β is liquid and the surface energy and surface stress are identical we simply obtain,

$$\mu_j^\alpha = G_j^\beta(P^\beta) \qquad [2.87]$$

This condition may be interpreted in terms of a normal common tangent construction with a Gibbs energy curve for the β phase corresponding to the pressure $P^\beta = P + 2\sigma/r$. On the other hand, if β is a solid we may not assume that the surface stress and surface energy are identical but it may be a reasonable approximation that the β phase is incompressible. If this is the case then

$$G_j^\beta(P^\beta) = G_j^\beta(P) + (P^\beta - P)V_j^\beta \qquad [2.88]$$

and the equilibrium conditions are obtained as

$$\mu_j^\alpha = G_j^\beta(P) + 2\sigma/rV_j^\beta \qquad [2.89]$$

This condition may be interpreted in terms of a normal common tangent construction with a Gibbs energy curve for the β phase displaced upwards by a distance $2\sigma/rV_j^\beta$. Under both those simplifying but still reasonable approximations we find that the surface energy is the important quantity and not the surface stress.

An expression for the critical size may be obtained by considering the growth of a β-phase particle without changing its composition, i.e. transfer of balanced amounts of all the components. Then we have $dN_j^\beta = x_j^\beta dN^\beta$ and obtain

$$dG = [G_m^\beta(P^\beta) - (P^\beta - P)V_m^\beta - \sum x_j^\beta \mu_j^\alpha(P)]\ dN^\beta + dG^\sigma \qquad [2.90]$$

For a spherical particle and balanced transfer we have $dG^\sigma = (2\sigma/r)V_m^\beta dN^\beta$ and the critical size may be obtained from $dG = 0$ yielding

© Woodhead Publishing Limited, 2012

$$-[G_m^{\beta}(P^{\beta}) - (P^{\beta} - P)V_m^{\beta} - \sum x_j^{\beta}\mu_j^{\alpha}(P)] = (2\sigma/r)V_m^{\beta} \quad [2.91]$$

It is instructive to consider two extremes, either the β phase may be approximated as incompressible or compressible as an ideal gas. Both extremes may serve as reasonably good approximations for many cases of practical importance.

For the case when β is incompressible, Eq. [2.91] becomes

$$-[G_m^{\beta}(P) - \sum x_j^{\beta}\mu_j^{\alpha}(P)] = (2\sigma/r)V_m^{\beta} \quad [2.92]$$

The quantity inside the square brackets is the driving force for initial precipitation (see Eq. [2.25]), and is often denoted ΔG_m. We thus arrive at the familiar textbook expression

$$r_c = 2\sigma/(-\Delta G_m/V_m^{\beta}) \quad [2.93]$$

This is a reasonable approximation if β is a condensed phase.

When β is an ideal gas we have

$$G_m^{\beta}(P^{\beta}) = G_m^{\beta}(P) + RT \ln \frac{P^{\beta}}{P} \quad [2.94]$$

Using $(P^{\beta} - P) = 2f/r, f = \sigma$ and Eq. [2.94], we may rewrite Eq. [2.91] as

$$[G_m^{\beta}(P) - \Sigma x_j^{\beta}\mu_j^{\alpha}(P)] = -RT \ln \frac{P^{\beta}}{P} \quad [2.95]$$

The quantity $\Delta^{\circ}\mu = [G_m^{\beta}(P) - \sum x_j^{\beta}\mu_j^{\alpha}(P)]$ is obviously a characteristic thermodynamic function for the gas and the α phase under consideration. Then, again using $P^{\beta} - P = 2\sigma/r$, one can write

$$P\left(\frac{P^{\beta}}{P} - 1\right) = P(e^{-\Delta^{\circ}\mu/RT} - 1) = \frac{2\sigma}{r} \quad [2.96]$$

For the critical radius of a bubble it then follows that

$$r_c = \frac{2\sigma}{P(e^{-\Delta\mu^{\circ}/RT} - 1)} \quad [2.97]$$

A pore may nucleate even if there is no gas at all provided that there is an external hydrostatic tension, i.e. $P < 0$. For a pore without gas $P^{\beta} = 0$ and the mechanical equilibrium gives directly

$$r_c = -\frac{2f}{P} \quad [2.98]$$

Since the surface energy is equal to the surface stress when α is a liquid, we may also write

$$r_c = -\frac{2\sigma}{P} \quad [2.99]$$

© Woodhead Publishing Limited, 2012

2.9 Thermodynamics of fluctuations in equilibrium systems

The second law states that all spontaneous processes have a positive entropy production. When equilibrium has been established all imaginable processes would cause a negative entropy production and the second law will then reverse them and drive the system back to the equilibrium state by spontaneous processes. However, the second law does not prohibit processes with negative entropy production. In fact, there is always a probability for such processes by means of fluctuations in a system at equilibrium. In order to understand this, we may first note that the internal entropy production Td_iS may be given a straightforward meaning by the following argument. Consider our system, which we assume to be at equilibrium, together with its surroundings which we assume have the same temperature T as the system. We further consider the new system formed by our initial system and its surroundings as a closed isolated system, i.e. its energy, volume and composition are fixed. The entropy change of this new system is then $TdS_{tot} = dS - \delta Q/T = Td_iS$. As already mentioned, the equilibrium state is then the state that maximizes the entropy of the new system comprised of the surroundings and our initial system. According to Boltzmann's relation, the entropy of that system is $S_{tot} = k_B \ln W$, where W is the number of ways in which the system can arrange its state. $1/W$ may thus be regarded as the probability that the system is arranged in one particular way. The probability of a fluctuation may be estimated as w/W, where w is the number of ways in which the system can arrange the particular fluctuation. The entropy change in the new system caused by the fluctuation would thus be $\Delta S_{tot} = k_B \ln w/W$, i.e.

$$p = w/W = \exp(\Delta S_{tot}/k_B) \qquad [2.100]$$

But $\Delta S_{tot} = \Delta_iS$ and we have thus shown that Boltzmann's relation permits violations of the second law. It should be noted that if Δ_iS is positive, the system is not in equilibrium and the above reasoning does not apply.

In order to see how likely a fluctuation is, we shall thus calculate the entropy production caused by the fluctuation, i.e. Δ_iS, which will actually be a 'consumption' as it is negative for a system at equilibrium. Consider a fluctuation in some internal variable ξ. We take the average of ξ as zero, i.e. $\overline{\xi} = 0$ which must also be the equilibrium value if the system is at equilibrium. Δ_iS may be expanded around $\overline{\xi} = 0$. The first derivative is zero due to the equilibrium condition $\partial\Delta_iS/\partial\xi|_{\xi=\overline{\xi}} = 0$ and we thus have $\Delta_iS = -a\xi^2/2 + \ldots$, where $a = \partial^2\Delta_iS/\partial\xi^2 > 0$ due to stability requirements. The probability that ξ will take a value in the range ξ to $\xi + d\xi$ thus is

$$p(\xi)d\xi = A \exp(-a\xi^2/2k_B)d\xi \qquad [2.101]$$

A is determined from the normalization condition and we thus have

© Woodhead Publishing Limited, 2012

$$p(\xi)d\xi = \sqrt{\frac{a}{2\pi}}\exp(-a\xi^2/2k_B)d\xi \qquad [2.102]$$

This is a Gaussian distribution and the mean square fluctuation $\overline{\xi^2} = 1/a$.

In a system with constant T and P we find from the fundamental equation that $T\Delta_i S = -\Delta G$ and the constant a thus is

$$a = \frac{1}{T}\frac{\partial^2 \Delta G}{\partial \xi^2} \qquad [2.103]$$

For example, as one approaches the limit of stability, where $a = 1/T\partial^2\Delta G/\partial\xi^2 \rightarrow 0$ and the mean square fluctuation $1/a \rightarrow \infty$, the fluctuations become much more likely.

2.10 Thermodynamics of nucleation

The entropy production Td_iS is very important in order to understand fluctuations of a system at equilibrium. The probability p of having a negative $T\Delta_i S$ by a fluctuation is $p = \exp(\Delta_i S/k_B)$, i.e. violations of the second law are possible but there is a penalty which makes them very unlikely as soon as $\Delta_i S$ becomes much bigger than Boltzmann's constant k_B. It is thus evident that the quantity $-T\Delta_i S$ is precisely the one we usually call the activation barrier for nucleation.

We shall now evaluate $\Delta_i S$ for the formation of a critical spherical nucleus under fixed temperature, pressure and composition and one should thus consider Gibbs energy. We obtain the activation barrier by integrating Gibbs energy from the size 0 to the critical size, which is now easy because G is a state function and we obtain directly

$$\begin{aligned} -T\ \Delta_i S &= G^{\text{final}} - G^{\text{initial}} = n^\beta G_m^\beta + A\sigma - \Sigma\, n_i^\beta \mu_i^\alpha \\ &= n^\beta [G_m^\beta(P^\beta) - (P^\beta - P)V_m^\beta - \Sigma\, x_i^\beta \mu_i^\alpha] + 4\pi\, r^2\sigma \end{aligned} \qquad [2.104]$$

where $n^\beta = V^\beta/{V_m}^\beta$. As already mentioned, we usually call the quantity inside the square bracket the driving force for initial precipitation. It is interesting to notice that this quantity also appeared in our derivation of the equilibrium equations for the unstable nucleus. We may combine Eq. [2.104] with the equilibrium condition, Eq. [2.91], and obtain

$$-T\Delta_i S = \frac{4}{3}\pi\, r_c^2\sigma \qquad [2.105]$$

It should be noticed that this is a quite general result and it holds regardless of whether or not β is incompressible. We can thus use Eq. [2.104] to calculate the probability of reaching a critical size r_c by means of a fluctuation if we apply Eq. [2.100]. The result is

© Woodhead Publishing Limited, 2012

$$p = \exp\left(-\frac{4}{3}\,\pi\, r_c^2 \sigma / k_B T\right) \qquad [2.106]$$

For an interfacial energy of 1 Jm^{-2} and a temperature of 1000 K, we find that the probability is negligible until the size comes down to the size of one or two atoms. The result depends very much on the value of the interfacial energy and a different interfacial energy would give a quite different result.

Using the expression $r_c = 2\sigma/(-\Delta G_m/V_m^{\beta})$ for incompressible β, we obtain the classic textbook result:

$$-T\Delta_i S = \frac{16}{3}\,\pi\, \sigma^3/(\Delta G_m/V_m^{\beta})^2 \qquad [2.107]$$

2.11 References

Aaronson H. I., Enomoto M. and Lee J. K., 2010. *Mechanism of Diffusional Phase Transformations in Metals and Alloys*, Boca Raton, FL: CRC Press.

Andersson J.-O., Helander T., Höglund L., Shi P. and Sundman B., 2002. Thermo-Calc & DICTRA, computational tools for materials science. *CALPHAD* 26, 273–312.

Cahn J. W., 1961. On spinodal decomposition. *Acta Metallurgica* 9, 795–801.

Cahn J. W. 1980. Surface stress and the chemical equilibrium of small crystals – I. the case of the isotropic surface. *Acta Metallurgica* 28, 1333–1338.

Gibbs J. W., 1875 [1948]. In *Collected Works*, 1. New Haven, CT: Yale University Press, pp. 215–331.

Hillert M., 1995. Le Chatelier's Principle – restated and illustrated with phase diagrams. *Journal of Phase Equilibria,* 16, 403–410.

Hillert M., 2008. *Phase Equilibria, Phase Diagrams and Phase Transformations: Their Thermodynamic Basis*, 2nd edn, Cambridge: Cambridge University Press.

Landau L. D. and Lifshitz E. M., 1970. *Statistical Physics*, Oxford: Pergamon Press.

Lukas H. L., Fries S. G. and Sundman B., 2007. *Computational Thermodynamics – the Calphad Method,* Cambridge: Cambridge University Press.

Pellicer J., Manzanares J. A., Zúñiga J., Utrillas P. and Fernández J., 2001. Thermodynamics of rubber elasticity. *Journal of Chemical Education* 78, 263–267.

Saunders N. and Miodownik A. P., 1998. *CALPHAD*, Oxford: Pergamon Press.

© Woodhead Publishing Limited, 2012

3
Fundamentals of diffusion in phase transformations

M. HILLERT, Royal Institute of Technology, (KTH) Sweden

Abstract: An atomistic model in the lattice-fixed frame of reference is the basis for the present discussion of the fundamentals of diffusion. It is shown that cross terms appear when gradients of some composition variable are introduced. It is demonstrated that an equation describing the movement of Kirkendall markers must be included in the new set of flux equations when the frame of reference is changed. It is argued that one should store information of mobilities rather than diffusivities and one should make calculations of diffusion in the lattice-fixed frame.

Key words: frame of reference, driving force for diffusion, evaluation of mobilities, Kirkendall shift, deviation from local equilibrium.

3.1 Introduction

This chapter discusses some fundamental aspects on diffusion that the author, having a basic training as a chemical engineer, has found important in his work in the field of materials science and engineering. Many sections of the chapter are based on previous publications by the author. A wider coverage of the field, but still with an emphasis on materials, can be found in Kirkaldy and Young (1987) and Borg and Dienes (1988).

Diffusion in a crystalline solution phase occurs by atoms jumping into vacant lattice sites. The fundamentals of diffusion are thus based on a lattice-fixed frame of reference. However, in the laboratory one studies diffusion relative to the length dimension of the specimens and one takes measurements relative to a frame of reference that is regarded as the volume-fixed frame. As an alternative, one may evaluate the experimental results in the number-fixed frame. Furthermore, in practical applications one is interested in making predictions in any of these frames. When discussing the fundamentals of diffusion, it is thus necessary to consider all frames and, in particular, to transfer information from one frame to another.

Fundamentally, one may regard diffusion in the lattice-fixed frame as driven by thermodynamic forces and the kinetic coefficient is regarded as the mobility of the diffusing atom. The thermodynamic force for diffusion

© Woodhead Publishing Limited, 2012

and its application to basic kinetic equations for diffusion, referred to the lattice-fixed frame, will be discussed in the first few sections.

The kinetic equation is usually transferred to one of the other frames and at the same time one usually introduces a composition gradient instead of the thermodynamic force. The influence of the thermodynamic properties of the system will thus be included in the kinetic coefficients which change character drastically. They are then regarded as diffusion coefficients but in the present chapter they are called diffusivities for conformity with mobilities and the relationship between diffusivities and mobilities is discussed in detail.

Due to the thermodynamic properties, the diffusivities may vary with composition much more than the mobilities which do not depend on the thermodynamic properties. Experimental information on diffusion in the volume-fixed or number-fixed frame is thus difficult to rationalize without considering the 'thermodynamic factor' separately. It may seem convenient to interpret experimental information directly in terms of parameters defined for the lattice-fixed frame, i.e. mobilities, and to save them in databases instead of diffusivities. The stored mobilities can then be used for practical applications either by continuously evaluating the required diffusivities in the volume- or number-fixed frame or directly in the lattice-fixed frame. In both cases one must have access to stored information on the thermodynamic properties.

When calculating the progress of diffusion in a phase during a phase transformation, one must take into account the boundary conditions at the phase interface. It is the movement of the phase interface that represents the phase transformation and it is often assumed that phase interfaces are very mobile. In that case one can apply the approximation of local equilibrium between two phases where they meet at an interface and the boundary conditions for the diffusion inside the phases are given by the thermodynamics properties of the adjoining phases. For a binary system they are obtained directly from the phase diagram or they can be calculated directly under the assumption of local equilibrium between the two phases. However, in higher order systems there is a multitude of possible tie-lines because there is one more degree of freedom for each additional component. The correct tie-line can be found only together with the solution of the diffusion equation for the phases. That is usually done by some iteration process applied for each step in time when the process of diffusion is treated numerically. This may be avoided by modelling the transfer of atoms across the interface. Such a model can be based on an absolute reaction rate approach and will be discussed.

Several factors that affect the progress of a diffusional phase transformation are connected to the moving phase interface. In general they will displace the local equilibrium between the two phases or even cause a deviation from local equilibrium. Such factors will be sketched or just mentioned in the last

© Woodhead Publishing Limited, 2012

few sections. Already the transfer of atoms across the interface will dissipate Gibbs energy which may become important at very high velocities. There may be a local volume change at the moving interface, which will cause a local build-up of high pressures if the material does not yield. Furthermore, there are factors that depend upon what happens inside the moving interface. They may be described with models that are based on the distribution of the components inside the interface. However, in this chapter the phase interface has only been modelled without descriptions of local properties or composition as a function of the position in the interface. Such models are regarded as sharp interface models.

3.2 Driving forces of simultaneous processes

We shall start by reviewing the basis of Gibbs' thermodynamics in a way that leads directly to the definition of thermodynamic driving force for diffusion and other processes. The discussion is based on Chapter 1 in Hillert (2008). The second law of thermodynamics states that the entropy S of an isolated system can never decrease but it can increase by spontaneous internal processes. For each process the extent will be denoted by ξ_i and for an isolated system with a number of simultaneous processes one has

$$dS = d_{ip}S = \sum A_i d\xi_i > 0 \qquad [3.1]$$

The subscript *ip* stands for 'internal process'. For a system open to exchange of heat, Q, and matter, N, with the surroundings, one has

$$dS = dQ/T + S_m dN + \sum A_i d\xi_i \qquad [3.2]$$

S_m is the molar entropy of the system and it is here assumed that any addition of matter is made without changing the composition, i.e., with balanced amounts of various components. The coefficient A_i is regarded as the affinity of the process i and is sometimes regarded as its thermodynamic force. The addition of heat, dQ, enters into the first law which defines the change of internal energy, U:

$$dU = dQ + dW + H_m dN \qquad [3.3]$$

At this stage we shall simply regard H_m as a coefficient related to the increase of the content of matter. dW is the work done on the system. By only considering compression work, $dW = -PdV$, we obtain by combination of the two laws,

$$TdS = dU - (H_m - TS_m)dN + PdV + T\sum A_i d\xi_i \qquad [3.4]$$

Introducing the notation $G_m = H_m - TS_m$, without yet discussing its interpretation, we can express Eq. [3.4] as

© Woodhead Publishing Limited, 2012

$$dU = TdS - PdV + G_m dN - T\sum A_i d\xi_i \quad [3.5]$$

Equations [3.4] and [3.5] are two different ways of expressing the combined law but they are of limited use because the variations of S and U are given as combinations of variables some of which are often difficult to control experimentally. The most practical form of the combined law is obtained as follows, because T and P are convenient experimental variables and they are often kept constant. It introduces a new quantity, $G = U - TS + PV$:

$$dG = d(U - TS + PV) = - SdT + VdP + G_m dN - T\sum A_i d\xi_i \quad [3.6]$$

G is called Gibbs energy and G_m is thus the molar Gibbs energy, obtained as a partial derivative under constant T, P and ξ_i. By regarding the addition of individual amounts of the components we instead write

$$dG = d(U - TS + PV) = - SdT + VdP + \sum G_i dN_i - T\sum A_i d\xi_i \quad [3.7]$$

G_i is defined as the partial derivative $\partial G/\partial N_i$ when all the other variables are kept constant including the amounts of the other components. It is also regarded as the chemical potential of component i and is then denoted by μ_i. It is also convenient to define a quantity called enthalpy, $H = U + PV$, for which we find

$$dH = d(U + PV) = TdS + VdP + \sum \mu_i dN_i - T\sum A_i d\xi_i \quad [3.8]$$

The production of entropy by internal processes is given by Eq. [3.1] and for the rate of internal production of entropy we find

$$\sigma = \frac{\partial_{ip} S}{\partial t} = \sum A_i \frac{\partial \xi_i}{\partial t} > 0 \quad [3.9]$$

Under constant T and P it is more convenient to consider the rate of Gibbs energy dissipation

$$d(-G)/dt = T\sum A_i \partial \xi_i/\partial t = \sum X_i \partial \xi_i/\partial t = T\sigma > 0 \quad [3.10]$$

$\partial \xi_i/\partial t$ is regarded as the flux of process i, and is denoted J_i. This term makes most sense for processes of transportation, e.g. diffusion, but is used more generally. For convenience we have changed the notation of TA_i to X_i. This quantity is regarded as the driving force for the process i under constant T and P. It is the partial derivative of G, $\partial G/\partial \xi_i$, when the other variables are kept constant. Under constant T and P one may write the rate of dissipation of Gibbs energy as

$$- dG/dt = T\sigma = \sum X_i J_i > 0 \quad [3.11]$$

It should be emphasized that there is no rule requiring that $X_i J_i > 0$ for each of a number of simultaneous processes.

For a system with several internal processes, it is possible to consider other aspects and to find that it is more convenient to consider a different set of

© Woodhead Publishing Limited, 2012

processes, all of which are linear combinations of the initial ones. This new way of looking at the system does not change what actually happens in the system. One may thus assume that the overall dissipation of Gibbs energy is the same and the value of $\sum X_i J_i$ must be the same. This criterion can be used to derive the driving forces for the new processes from the driving forces for the initial ones.

3.3 Atomistic model of diffusion

Diffusion can be treated mathematically by starting with Fick's law for diffusion and expressing material properties through diffusion coefficients. However, in ternary and higher order systems, one may need a large number of such coefficients. It may be difficult both to determine them experimentally and to handle them in calculating the progress of diffusion. By accepting an atomistic model one may considerably reduce the number of independent coefficients and may relate the diffusion coefficients to the thermodynamic properties; this procedure considerably decreases their remaining dependence on composition. In this section we shall thus develop an atomistic model which will then be used throughout the chapter. The discussion is based on Section 17.1 in Hillert (2008).

The rate of many internal processes depends on the possibility of crossing an energy barrier, e.g. in the narrow passage between other atoms when an atom jumps from one lattice site into the neighbouring one in diffusion. The extra energy, Q, is provided by thermal fluctuations and the probability is proportional to $\exp(-Q/RT)$ according to Boltzmann statistics. However, the requirement is decreased by the driving force, and the flux may thus be represented by

$$J = K \exp - \frac{Q - X/2}{RT} \qquad [3.12]$$

From this equation it is evident that Q as well as X are expressed as J/mol if the gas constant R is given as J/mol,K. It is here assumed that the reaction path can be regarded as a distance between the initial and final states and also that the driving force is caused by a continuous change of the Gibbs energy of the system along the path. If X is the total Gibbs energy change between the two states then only half will be available at the top of the barrier if it is situated in the middle between the two states. According to the philosophy of the absolute reaction rate approach, originating from Eyring (Glasstone *et al.*, 1941, ch. 9), one should also consider the rate of the reverse process and for the net rate we obtain

© Woodhead Publishing Limited, 2012

$$J = K\left(\exp -\frac{Q - X/2}{RT} - \exp -\frac{Q + X/2}{RT}\right)$$
$$= K \exp -\frac{Q}{RT} \cdot \left(\exp \frac{-X}{2RT} - \exp \frac{X}{2RT}\right)$$
$$= K \exp -\frac{Q}{RT} \cdot 2\sinh \frac{X}{2RT} \cong \frac{K}{RT} \exp -\frac{Q}{RT} \cdot X \qquad [3.13]$$

This is a good approximation when $X << 2RT$. We can express the result with a so-called phenomenological L coefficient,

$$J = L \cdot X \qquad [3.14]$$

where $L = (K/RT) \exp(-Q/RT)$ according to this model. When introducing the absolute reaction rate approach, Glasstone *et al.* proposed that the K coefficient should contain a frequency factor that is proportional to the absolute temperature which will balance T in the denominator. The temperature dependence of the L coefficient should then be given by the exponential factor alone.

Consider diffusion in a binary, crystalline phase where the A and B atoms occupy the same kind of lattice sites. First we shall make the unrealistic assumption that they diffuse by exchanging positions with each other. We shall estimate the probability of such an exchange between two neighbouring sites, situated on two adjacent planes in the lattice. We shall assume that there is a composition gradient and represent the compositions with the mole fractions x'_A, x'_B and x''_A, x''_B. The probability that there actually is a B atom on the site in the first plane and an A atom on the site in the second plane is $x'_B x''_A$ and the probability that there will be a thermal fluctuation strong enough to overcome the barrier will then be proportional to $x'_B x''_A \exp(-(Q - X/2)/RT)$. There will also be a probability of exchange in the opposite direction and the net flux of B atoms should thus be

$$J_{BA} = K\left(x'_B x''_A \exp -\frac{Q - X/2}{RT} - x'_A x''_B \exp -\frac{Q + X/2}{RT}\right)$$
$$= K \exp -\frac{Q}{RT}\left(x'_B x''_A \exp \frac{X}{2RT} - x'_A x''_B \exp -\frac{X}{2RT}\right) \qquad [3.15]$$

The driving force for the exchange depends on the difference in the chemical potentials between the two planes,

$$X = -\Delta(\mu_B - \mu_A) \qquad [3.16]$$

Important parts of the chemical potentials originate from the statistics of the mixing of the A and B atoms in the solution phase and for ideal mixing

$$-\Delta(\mu_B - \mu_A)^{\text{ideal}} = RT \ln(x'_A x''_B / x''_A x'_B) \qquad [3.17]$$

© Woodhead Publishing Limited, 2012

However, the effect of composition is already accounted for by the pre-exponential factors $x'_A x''_B$ and $x''_A x'_B$. It seems that, when applying the absolute reaction rate approach for modelling a process, one should avoid counting this factor twice (Hillert, 2001). By only keeping the part of the driving force that originates from the excess Gibbs energy, we obtain

$$\begin{aligned} J_{BA} &= K \exp - \frac{Q}{RT} \left(\begin{array}{l} x''_A x'_B \exp \dfrac{X + RT \ln(x'_A x''_B / x''_A x'_B)}{2RT} \\ - x'_A x''_B \exp - \dfrac{X + RT \ln(x'_A x''_B / x''_A x'_B)}{2RT} \end{array} \right) \\ &= KRT \exp(-Q/RT) \sqrt{x''_A x'_B x'_A x''_B} \cdot 2 \sinh(X/2RT) \\ &\cong x_A x_B K \exp(-Q/RT) \cdot X \end{aligned} \qquad [3.18]$$

We have used the approximation $F << 2RT$ and $x'_B \cong x''_B$. One may regard $x_A x_B K \exp(-Q/RT)$ as a phenomenological coefficient L in Eq. [3.14]. The driving force was defined by Eq. [3.16] but in diffusion it is more common to consider the negative of a potential gradient, $-d\mu_i/dz$, rather than of the difference $\Delta\mu_i$. The jump distance in the direction of the flux, Δz, will thus be included in the coefficient. It is also common to express the result with a mobility M defined through the following expression:

$$J_{BA} = - x_A x_B M \cdot \frac{d(\mu_B - \mu_A)}{dz} \qquad [3.19]$$

As already emphasized, this derivation was based on an unrealistic assumption of a direct exchange of positions between A and B atoms. It is accepted that the diffusion of atoms in substitutional solutions in metallic materials occurs by a vacancy mechanism based on the presence of thermal vacancies. Atoms jump into vacant sites in the lattice. It is thus necessary to consider two separate processes, diffusion of A atoms and diffusion of B atoms, and one should distinguish between two fluxes, J_A and J_B. For each one the derivation will be very similar to the previous derivation but will now concern the exchange of positions between an atom and a vacancy. The driving force will thus be $-d(\mu_B - \mu_{Va})/dz$. However, there is an important difference, because the number of vacancies is not preserved but may change by generation and condensation of vacancies at dislocations, crystal boundaries and surfaces. We shall simplify the result by optimistically assuming that there is sufficient time for the equilibrium number of vacancies to be established always and everywhere. The potential gradient of vacancies will thus vanish and the driving force for a B atom to jump into an adjacent vacant site is $-d(\mu_B - \mu_{Va})/dz \cong -d\mu_B/dz$. In principle, one should consider another effect of the vacancies. The fraction of atoms will be less than unity due to the presence of thermal vacancies. It should thus be more correct to express the content of a component through its site fraction, defined as $y_j = N_j/(\sum N_i + N_{Va})$.

© Woodhead Publishing Limited, 2012

This is only slightly less than the ordinary mole fraction. Furthermore, it is common to include the fraction of vacancies in the mobility. Considering vacancies instead of *A* atoms in Eq. [3.19], we may approximate the flux equation as follows,

$$J_B = -y_{Va}y_B M_B d\mu_B/dz \cong -x_B M_B d\mu_B/dz \qquad [3.20]$$

The driving force is usually defined in units of J mol^{-1} m^{-1} and the flux in units of mol m^{-2} s^{-1}. The rate of dissipation of Gibbs energy in Eq. [3.11] will thus be in units of J m^{-3} s^{-1} and the mobility will be in units of mol^2 J^{-1} m^{-1} s^{-1}. In formal treatments of diffusion without any model one prefers to work with the flux proportional to concentration, $c_B = x_B/V_m$. The new mobility is then expressed in units of mol,m^2/J,s.

Without any model one should be prepared to find cross effects, i.e., the flux of one component may also depend on the driving forces of other components. However, we shall simply use the phenomenological equation, Eq. [3.14], without cross terms, and with the present model the phenomenological coefficient will be $L_i = c_i M_i = (x_i/V_m)M_i$. For simplicity the derivative of the driving force will be expressed with the ∇ operator, $X_i = -\nabla\mu_i$, yielding

$$J_i = L_i X_i = -c_i M_i \nabla\mu_i = -(x_i/V_m)M_i \nabla\mu_i \qquad [3.21]$$

This will be the mathematical formulation of our atomistic model.

3.4 Change to a new frame of reference

It was emphasized already by Darken (1948) that one needs different frames of reference when discussing various aspects of diffusion. It is often necessary to change a flux equation for diffusion from one frame to another. Section 3.4 is concerned with such changes and the discussions were inspired by Ågren (1982) and Andersson and Ågren (1992). In order to distinguish between quantities, when they are referred to different frames of reference, we shall use an asterisk for the lattice-fixed frame. Using the lattice-fixed frame of reference one can always write $\sum J_i^* = 0$ for diffusion inside a phase. J_i^* represents all the diffusing species that reside in lattice sites including the vacancies. To make this fact evident one could instead write $\sum J_i^* - J_{Va}^* = 0$ where J_i^* only represents the atomic species. From each J_i^* one can evaluate the change of the local content of component *j* using Fick's second law but that does not apply to the vacancies because we have already seen that they can be generated or condensed locally, e.g. by some dislocation mechanism. As an approximation we shall accept the extreme case where the number of vacancies is immediately and everywhere adjusted to the equilibrium value and, neglecting the possible variation with composition, one treats the equilibrium site fraction as constant, $y_{Va} = y_{Va}^{eq}$. Without this approximation there would be a so-called correlation effect which will thus be neglected in

© Woodhead Publishing Limited, 2012

the present treatment. Correlation, treated as a secondary effect, will decrease the rate of diffusion by an appreciable factor but the practical importance is not as high as one may think, first because experimental data on diffusion are rarely very accurate and, secondly, because the experimental values of mobilities or diffusivities may have been evaluated without considering the correlation effect in the first place.

The net transportation of atoms through the lattice will be $\sum J_i^*$ and the flux of vacancies through the material should be $J_{Va}^* = -\sum J_i^*$. This is sometimes regarded as the vacancy wind. The net transportation of atoms through the lattice can be studied experimentally by inserting small inert particles in any position in the material, so-called Kirkendall markers. They will be fixed to the lattice and one may study how the amount of material changes on the two sides of a band of particles. However, it will appear as if the markers are travelling through the material and this movement is called the Kirkendall shift. Measured in mole of atoms m^{-2} s^{-1}, it will be

$$J_K = -\sum J_i^* \qquad [3.22]$$

J_K is here expressed in the same units as the fluxes but it can be changed to m/s by multiplying by the molar volume, V_m. Due to the adjustment of the local content of vacancies, lattice planes gradually disappear on one side of the particles and new lattice planes are constructed on the other side. If the piece of material was lying on a board and was fixed to the board by very thin nails, penetrating the material in the position of the markers, then one should actually be able to see the whole piece of material slowly gliding on the board while the nails are stationary. It will thus be interesting to consider a new frame of reference that moves with the piece of material. Relative to the markers, i.e., relative to the lattice-fixed frame, the new frame will move with a velocity $\sum J_j^*$ mol of atoms m^{-2} s^{-1}. This frame is thus regarded as the number-fixed frame and fluxes will be denoted J_j when given relative to that frame. All quantities will be identified with an asterisk when their values are given relative to the lattice-fixed frame.

A fraction x_j of those atoms is j atoms and they will not cross a plane that originally was at the markers but is now regarded as moving with the new frame. The net diffusion of j atoms relative to the new frame will thus be

$$J_j = J_j^* - x_j \sum_{i=1}^{n} J_j^* = \sum_{i=1}^{n} (\delta_{ji} - x_j) J_{\mathrm{i}}^* \qquad [3.23]$$

where δ_{ji} is the Kronecker symbol, having the value 1 for $i = j$ and otherwise 0. As an alternative, we may consider the rate of material crossing the plane of the markers through the effect the diffusing atoms have on the volume. It will be $\sum V_i J_i^*$, where V_i is the partial molar volume of component i. The unit will be m/s and is thus a real velocity, v. It may be changed into mole

© Woodhead Publishing Limited, 2012

of atoms m^{-2} s^{-1} by dividing by the molar volume, V_m. The fraction x_j is j atoms and the net flux of j atoms will be

$$J_j = J_j^* - x_j v/V_m = J_j^* - x_j \sum (V_i J_i^*/V_m) \quad [3.24]$$

We can represent Eqs [3.23] and [3.24] by one equation:

$$J_j = J_j^* - x_j \sum a_i J_i^* = \sum_{i=1}^{n} (\delta_{ji} - x_j a_i) J_i^* = \sum_{i=1}^{n} \alpha_{ji} J_i^* \quad [3.25]$$

where $a_i = V_i/V_m$ and $a_i = 1$ in the number-fixed frame according to Eq. [3.23]. The symbol α_{ji} was introduced in order to simplify the final result. Multiplying Eq. [3.25] by a_j and adding the contributions for all the components, we obtain:

$$\sum a_j J_j = \sum a_j J_j^* - \sum a_j x_j \sum a_i J_i^* = \sum a_j J_j^* - \sum a_i J_i^* = 0 \quad [3.26]$$

since $\sum a_j x_j = \sum V_j x_j / V_m = V_m/V_m = 1$. We have thus found that $\sum V_i J_i = 0$ and the flux in Eq. [3.24] is thus given in the volume-fixed frame.

According to the linear version of thermodynamics of simultaneous processes, usually called irreversible thermodynamics, one may consider the behaviour of a system as the result of a new set of n processes if all the new fluxes are linear combinations of the initial ones. However, the new fluxes are related through Eq. [3.26] and there are only $n - 1$ independent fluxes. We must add an additional, linear combination in order not to lose any information. We find such a combination in the Kirkendall shift and shall thus add it as the flux of the new nth process (Hillert, 2008, p. 102). It was given for the number-fixed frame by Eq. [3.22] but we shall now generalize its definition to be suitable also for the volume-fixed frame. Let v_K be the rate of the Kirkendall markers in m/s:

$$v_K/V_m = J_K = -\sum V_i J_i^*/V_m = -\sum a_i J_i^* \quad [3.27]$$

3.4.1 Driving forces for new frames of reference

We have thus seen how the flux of a component j relative to a number- or volume-fixed frame of reference can be evaluated from the fluxes of all the components relative to the lattice-fixed frame. In principle, we could directly obtain the flux of j relative to a new frame if we knew the thermodynamic driving force in that frame but we would also need to know a new set of phenomenological coefficients. It will now be demonstrated how this can be accomplished. In principle, the new driving forces can be obtained through the condition that the net effect on the dissipation of Gibbs energy must be the same when described in a new frame, $T\sigma = \sum X_i^* J_i^* = \sum X_j J_j$. See the discussion following Eq. [3.11]. Remembering that the nth flux is now the Kirkendall shift, we can write

© Woodhead Publishing Limited, 2012

$$T\sigma = \sum_{h=1}^{n} (X_i^* J_i^*) = \sum_{j=1}^{n-1} (X_j J_j) + X_K J_K$$
$$= \sum_{j=1}^{n-1} \left(X_j \left(J_j^* - x_j \sum_{i=1}^{n} a_i J_i^* \right) \right) + X_K \left(- \sum_{i=1}^{n} a_i J_i^* \right) \quad [3.28]$$

Comparing the coefficients for each J_i^* term we find

$$X_i^* = X_i + \sum_{j=1}^{n-1} (X_j(-x_j a_i)) + X_K(-a_i) \quad \text{for } i \le n \quad [3.29]$$

$$X_n^* = \sum_{j=1}^{n-1} (X_j(-x_j a_n)) + X_K(-a_n) \quad [3.30]$$

Eliminating X_K between Eqs [3.29] and [3.30], we obtain the driving force for the diffusion of the components relative to the new frame of reference:

$$X_i = X_i^* - (a_i/a_n)X_n^* \text{ for } i < n \quad [3.31]$$

Inserting this result as X_j in Eq. [3.30] and completing the summations to n terms we find the driving force for the Kirkendall shift.

$$X_K(-a_n) = X_n^* - \sum_{j=1}^{n-1} (X_j(-x_j a_n)) = X_n^* + \sum_{j=1}^{n-1} x_j a_n (X_j^* - (a_j/a_n)X_n^*)$$
$$= X_n^* + \sum_{j=1}^{n} x_j a_n X_j^* - x_n a_n X_n^* - X_n^* \sum_{j=1}^{n} x_j a_j + X_n^* x_n a_n$$
$$= -a_n \sum_{j=1}^{n} x_j X_j^* = a_n \sum_{j=1}^{n} x_j d\mu_j/dz = 0$$

[3.32]

because $\sum x_j a_j = \sum x_j V_j / V_m = 1$ by definition and $\sum x_i d\mu_i = 0$ according to the Gibbs–Duhem relation. The driving force for the Kirkendall shift is thus zero in the number- and volume-fixed frames (Hillert, 2008, p. 103) and it has to be driven by the other driving forces through cross terms, as we shall soon see. It is interesting that one usually introduces only $n - 1$ new fluxes, those given by Eq. [3.25]. One can still derive the same driving forces, as given here by Eq. [3.31], because by only introducing $n - 1$ new fluxes in Eq. [3.28] one has actually accepted that the driving force of the missing flux must be zero and we have now seen that the driving force for the Kirkendall shift in the last term satisfies that condition. It is evident that Eqs [3.29] and [3.30] without the last term should result in Eq. [3.31]. Finally we obtain the new driving forces in terms of the initial ones from Eq. [3.29] with $X_K = 0$. It can be written as follows:

© Woodhead Publishing Limited, 2012

$$X_i^* = \sum_{j=1}^{n-1} (\delta_{ij} - x_j a_i) X_j = \sum_{j=1}^{n-1} \alpha_{ji} X_j \quad \text{for } i \le n \qquad [3.33]$$

We should finally like to evaluate the phenomenological coefficients in the new flux equations, defined through

$$J_j = \sum_{h=1}^{n-1} L_{jh} X_h \quad \text{for } j < n \qquad [3.34]$$

$$J_K = \sum_{k=1}^{n-1} L_{Kh} X_h \qquad [3.35]$$

The full expression of Eq. [3.34] is obtained by starting from J_j as a linear function of J_i^* in Eq. [3.25] and then inserting J_i^* as $L_i^* X_i^*$ from Eq. [3.21] and finally inserting X_i^* as a linear function of X_h from Eq. [3.33]. The kinetic coefficients will thus be

$$L_{jh} = \sum_{i=1}^{n} (\delta_{ji} - x_j a_i) L_i^* (\delta_{ih} - x_h a_i) \qquad [3.36]$$

The cross terms are very important in the new frames of reference. It is interesting that there is a symmetry, $L_{jh} = L_{hj}$. That is required by Onsager's reciprocity theorem for simultaneous processes. By instead starting from Eq. [3.27] we find

$$L_{Kh} = \sum_{i=1}^{n} (-a_i) L_i^* (\delta_{ih} - x_h a_i) \qquad [3.37]$$

This gives the coefficients in the cross terms for the Kirkendall shift which is driven only by the other driving forces.

The driving force for the new flux of any component h in the number-fixed frame, where $a_i = 1$, is obtained as $-(\nabla\mu_h - \nabla\mu_n)$ by inserting $-\nabla\mu_i$ as X_i^* in Eq. [3.31]. This driving force corresponds to the Gibbs energy decrease when an h atom changes position with an atom of the omitted component n. The flux thus represents this exchange process. The flux equations for all the other components represent exchange with the omitted one.

It is evident that in order to describe the fluxes in a volume-fixed frame, one must consider a mechanism where one atom of any independent component exchanges positions with a_i/a_n atoms of the component selected to be the dependent one because $X_h = -\nabla(\mu_h - (a_h/a_n)\mu_n)$. That will be a non-physical model but is useful for describing the behaviour of the material in the volume-fixed frame.

© Woodhead Publishing Limited, 2012

3.4.2 Alternative method

From Eqs [3.36] and [3.37] we have obtained the following results for the description of the atomistic model in the number- and volume-fixed frames of reference:

$$J_j = \sum_{i=1}^{n} \sum_{h=1}^{n-1} \alpha_{ji} L_i^* \alpha_{hi} X_h \quad \text{for } j < n \qquad [3.38]$$

and

$$v_K / V_m = J_K = - \sum_{i=1}^{n} \sum_{h=1}^{n-1} a_i L_i^* \alpha_{hi} X_h \qquad [3.39]$$

where $$\alpha_{hi} = \delta_{hi} - X_h a_i \qquad [3.40]$$

We are thus able to relate J_j and v_K in the number- or volume-fixed frame to L_i^* and through Eq. [3.40] also to X_h^*, which are defined in the lattice-fixed frame. It should be noted that we could have done this directly, obtaining much simpler expressions from Eqs [3.25] and [3.27].

$$J_j = J_j^* - x_j \Sigma a_i J_i^* = \sum_{i}^{n} \alpha_{ji} J_i^* = \sum_{i}^{n} \alpha_{ji} L_i^* X_i^* \quad \text{for } j < n \qquad [3.41]$$

$$v_K / V_m = J_K = - \Sigma a_i J_i^* = - \Sigma a_i L_i^* X_i^* \qquad [3.42]$$

In Eq. [3.38] there is a symmetry relation, $\alpha_{ji} L_i^* \alpha_{hi} = \alpha_{hi} L_i^* \alpha_{ji}$, in agreement with Onsager's reciprocity theorem but in Eq. [3.41] $\alpha_{ji} L_i^* \neq \alpha_{ij} L_j^*$ because there the driving forces were not defined for the same frame of reference as the fluxes. Their product does not give the correct dissipation of Gibbs energy which is a necessary condition for Onsager's reciprocity theorem to apply. However, there is no reason why Eq. [3.41] could not be used in practical applications. It seems evident that one should get the same result and that has been confirmed analytically (Andersson and Ågren, 1992). It may be more complicated to write a program for calculations based on Eq. [3.38] but, once the programming has been done, one may expect that it makes only a slight practical difference what method has been used. Equations [3.41] and [3.42] may give quicker results for analytical work. That method will thus be used in the next few sections. On the other hand, for more complicated applications it may be safer to keep the condition of symmetric cross coefficients by using Eqs [3.38]–[3.40].

3.4.3 Diffusivities in lattice- and number-fixed frames

From a practical point of view it may often be convenient to regard the composition gradients as the driving forces for diffusional fluxes. The

© Woodhead Publishing Limited, 2012

constant of proportionality is then called the diffusion constant or diffusion coefficient but will here be called diffusivity for conformity with mobility. It can be introduced by expressing the potential gradient as a function of some composition variable. The molar Gibbs energy of simple metallic solution phases is generally given as a function of the mole fractions, x_i, and they will be our first choice as composition variables:

$$d\mu_j = \sum_{k=1}^{n} \frac{\partial \mu_j}{\delta x_k} dx_k \qquad [3.43]$$

With n components there will be only $n - 1$ independent mole fractions because there is a relation between them, written as $\sum x_i = 1$ for mole fractions and as $\sum V_i c_i = 1$ for concentrations. We shall now see how diffusivities are related to mobilities by first defining diffusivities for the n components and then eliminating one of them to obtain diffusivities for $n - 1$ independent components.

Direct approach in lattice-fixed frame

The present work is based on the general assumption that there are no cross terms in the phenomenological flux equations for diffusion with a vacancy mechanism, as given in Eq. [3.21]. Applying Eq. [3.43] to Eq. [3.21] for the lattice-fixed frame, we obtain

$$J_j^* = -L_j^* \frac{d\mu_j}{dz} = -L_j^* \sum_{k=1}^{n} \frac{\partial \mu_j}{\partial x_k} \frac{dx_k}{dz} \quad \text{for } j \le n \qquad [3.44]$$

Equation [3.44] defines n diffusivities instead of a single mobility because it has $n - 1$ cross terms. It is interesting that the mere change of expression for the gradient has introduced cross terms but also that Onsager's reciprocity theorem does not apply because $J_j^* \cdot (-\partial \mu_j / \partial x_k)$ does not represent dissipation of Gibbs energy as a term $J_j X_j$ would.

Elimination of a dependent composition variable

It is possible to redefine the diffusivities in Eq. [3.44] because only $n - 1$ of the composition variables are independent. By selecting the nth variable as the dependent one, we obtain $dx_n = -\sum dx_k$ from $\sum x_i = 1$ and can eliminate the nth variable as follows:

$$\frac{d\mu_j}{dz} = \sum_{k=1}^{n} \frac{\partial \mu_j}{\partial x_k} \frac{dx_k}{dz} = \sum_{k=1}^{n-1} \frac{\partial \mu_j}{\partial x_k} \frac{dx_k}{dz} + \frac{\partial \mu_j}{\partial x_n} \sum_{k=1}^{n-1} \frac{-dx_k}{dz}$$

$$= \sum_{k=1}^{n-1} \left(\frac{\partial \mu_j}{\partial x_k} - \frac{\partial \mu_j}{\partial x_n} \right) \frac{dx_k}{dz} \qquad [3.45]$$

© Woodhead Publishing Limited, 2012

Inserting this in Eq. [3.44] we obtain

$$J_j^* = -L_j^* \frac{d\mu_j}{dz} = -L_j^* \sum_{k=1}^{n-1} \left(\frac{\partial \mu_j}{\partial x_k} - \frac{\partial \mu_j}{\partial x_n} \right) \frac{dx_k}{dz} = -\sum_{k=1}^{n-1} \frac{D_{jk}^{n*}}{V_m} \frac{dx_k}{dz} \quad \text{for } j \le n \tag{3.46}$$

where

$$D_{jk}^{n*} = V_m L_j^* \left(\frac{\partial \mu_j}{\partial x_k} - \frac{\partial \mu_j}{\partial x_n} \right) = x_j M_j^* \left(\frac{\partial \mu_j}{\partial x_k} - \frac{\partial \mu_j}{\partial x_n} \right) \quad \text{for } k < n \tag{3.47}$$

V_m was introduced here in order to express D_{jk}^{n*} in m^2/s. The superscript n in D_{jk}^{n*} indicates what composition variable has been chosen as dependent. The new diffusivities are defined only for the $n-1$ components chosen to be regarded as independent. If applied to $k = n$ it would yield $D_{jn}^{n*} = 0$.

Use of number-fixed frame

Inserting Eq. [3.44] in Eq. [3.25] we obtain

$$J_j = \sum_{i=1}^{n} \alpha_{ji} J_i^* = -\sum_{i=1}^{n} \alpha_{ji} L_i^* \frac{d\mu_i}{dz} = -\sum_{i=1}^{n} \alpha_{ji} L_i^* \sum_{k=1}^{n} \frac{\partial \mu_i}{\partial x_k} \frac{dx_k}{dz} \quad \text{for } j \le n \tag{3.48}$$

In connection to Eq. [3.25], it was emphasized that $\alpha_{ji} = \delta_{ji} - x_j$ for the number-fixed frame. Inserting Eq. [3.45] in Eq. [3.48] we again eliminate one composition variable, obtaining

$$\begin{aligned} J_j &= -\sum_{i=1}^{n} \alpha_{ji} L_i^* \frac{d\mu_i}{dz} = -\sum_{i=1}^{n} \alpha_{ji} L_i^* \sum_{k=1}^{n-1} \left(\frac{\partial \mu_i}{\partial x_k} - \frac{\partial \mu_i}{\partial x_n} \right) \frac{dx_k}{dz} \\ &= -\sum_{k=1}^{n-1} \frac{D_{jk}^{n}}{V_m} \frac{dx_k}{dz} \quad \text{for } j < n \end{aligned} \tag{3.49}$$

where

$$D_{jk}^{n} = V_m \sum_{i=1}^{n} \alpha_{ji} L_i^* \frac{d\mu_i}{dz} = \sum_{i=1}^{n} \alpha_{ji} x_i M_i^* \left(\frac{\partial \mu_i}{\partial x_k} - \frac{\partial \mu_i}{\partial x_n} \right) \quad \text{for } k < n \tag{3.50}$$

We started from n independent flux equations in the lattice-fixed frame of reference but for all the other frames there are only $n - 1$ independent flux equations. This was found already in Section 3.4 and it was concluded that, in order not to lose any information when changing to a new frame of reference, it is necessary to add a flux equation for the Kirkendall shift using Eq. [3.22]. For that flux we obtain

$$J_K = -\sum_{i=1}^{n} J_i^* = \sum_{i=1}^{n} L_i^* \frac{d\mu_i}{dz} = \sum_{i=1}^{n} \frac{x_i}{V_m} M_i^* \sum_{k=1}^{n} \frac{d\mu_i}{dx_k} \frac{dx_k}{dz} \tag{3.51}$$

© Woodhead Publishing Limited, 2012

3.4.4 Application of lattice and number-fixed frames for binary systems

For the binary *A*-*B* system we shall select *B* as the *n*th component and can make the following simplification.

$$\frac{d\mu_A}{dz} = \left(\frac{\partial \mu_A}{\partial x_A} - \frac{\partial \mu_A}{\partial x_B}\right)\frac{dx_A}{dz} = \frac{d\mu_A}{dx_A}\frac{dx_A}{dz} \qquad [3.52]$$

Let us first consider the lattice-fixed frame. There will be only one term in the summations in Eq. [3.46] when $n = 2$. Using Eq. [3.52] it will yield:

$$J_A^* = -L_A^*\left(\frac{\partial \mu_A}{\partial x_A} - \frac{\partial \mu_A}{\partial x_B}\right)\frac{dx_A}{dz} = -\frac{x_A}{V_m}M_A^*\frac{d\mu_A}{dx_A}\frac{dx_A}{dz} = -\frac{D_{AA}^{B*}}{V_m}\frac{dx_A}{dz} \qquad [3.53]$$

This diffusivity may be regarded as the individual or intrinsic diffusivity, D_A^*. Equation [3.47] yields

$$D_A^* \equiv D_{AA}^{B*} = V_m L_A^* \frac{d\mu_A}{dx_A} = x_A M_A^* \frac{d\mu_A}{dx_A} = M_A^* RT\frac{d\ \ln a_A}{d\ \ln x_A} \qquad [3.54]$$

The activity was here introduced through its definition $\mu_i = {}^\circ\mu_i + RT \ln a_i$. One regards $x_A d\mu_A/dx_A = RTd \ln a_A/d \ln x_A$ as the thermodynamic factor and for very dilute or ideal systems it is equal to 1 due to Henry's law, yielding $D_A^* \cong RTM_A$. This relation also a pplies to the major component in very dilute solutions due to Raoult's law. By instead eliminating component *A* we obtain a corresponding result for *B*, $D_B^* = x_B M_B^* d\mu_B/dx_B \cong RTM_B^*$. It should be noticed that $d \ln a_B/d \ln x_B = d \ln a_A/d \ln x_A$ in a binary system due to the Gibbs–Duhem relation. It should again be emphasized that these diffusivities are defined for the lattice-fixed frame.

Let us now turn to the number-fixed frame and again applying Eq. [3.52], we obtain from Eq. [3.50]:

$$\begin{aligned} D_{jk}^n &= V_m \sum_{i=1}^{n} \alpha_{ji}\frac{x_i}{V_m}M_i^*\left(\frac{\partial \mu_i}{\partial x_k} - \frac{\partial \mu_i}{\partial x_n}\right) \\ &= \alpha_{AA}x_A M_A^*\frac{d\mu_A}{dx_A} + \alpha_{AB}x_B M_B^*\frac{d\mu_B}{dx_A} \\ &= \alpha_{AA}x_A M_A^*\frac{d\mu_A}{dx_A} - \alpha_{AB}x_A M_B^*\frac{d\mu_A}{dx_A} \\ &= (\alpha_{AA}M_A^* - \alpha_{AB}M_B^*)\frac{d\mu_A}{d\ \ln x_A} \quad \text{for } k < n \end{aligned} \qquad [3.55]$$

We have here used the Gibbs–Duhem relation, $x_A d\mu_A = -x_B d\mu_B$. For $j = A$

© Woodhead Publishing Limited, 2012

and $i = 1 = A$ we obtain from Eq. [3.23] $\alpha_{AA} = 1 - x_A = x_B$ and for $i = n = B$ we obtain $\alpha_{AB} = - x_A$. We thus find

$$J_A = -(1 - x_A)\frac{x_A}{V_m} M_A^* \frac{d\mu_A}{dx_A}\frac{dx_A}{dz} + x_A \frac{x_B}{V_m} M_B^* \frac{d\mu_B}{dx_A}\frac{dx_A}{dz}$$
$$= -\left(x_B x_A M_A^* \frac{d\mu_A}{dx_A} + x_A x_B M_B^* \frac{d\mu_B}{dx_B} \right) \frac{dx_A}{V_m dz} \quad [3.56]$$

Introducing the individual diffusivity defined by Eq. [3.54], we write this result as

$$J_A = -(x_B D_A^* + x_A D_B^*) \frac{dx_A}{V_m dz} \quad [3.57]$$

One may introduce a new symbol $\widetilde{D}_{AB} = x_B D_A^* + x_A D_B^*$ which is regarded as the interdiffusivity or chemical diffusivity and in that connection one often writes

$$J_A = -(x_B D_A^* + x_A D_B^*) \frac{dx_A}{V_m dz} = - \frac{\tilde{D}_{AB}}{V_m}\frac{dx_A}{dz} = - J_B \quad [3.58]$$

This is the most common form of Fick's law but $\widetilde{D}_{AB}$ is usually denoted D_A. It should be remembered that it applies to the number-fixed frame.

3.4.5 Use of concentration as composition variable

When using the volume-fixed frame it is natural but not necessary to use concentration as the composition variable. Then we need some relations between concentrations and mole fractions. First there is a direct relation $x_i = V_m c_i$ because the concentration is defined as $c_i = x_i/V_m$. However, the composition dependence of the molar volume may not be small enough to be neglected. The relation $dx_i = V_m dc_i$ is only approximate and should be applied with care. On the other hand, from $\sum x_i V_i = V_m$ one obtains $\sum c_i V_i = 1$, and for the more reasonable approximation that all the V_i are independent of composition we obtain $\sum V_i dc_i = 0$, which we shall apply.

Use of lattice-fixed frame

Originally, Fick's law was first formulated with a gradient of the concentration. Before applying concentration to the volume-fixed frame we shall again start with the lattice-fixed frame, obtaining instead of Eq. [3.44]:

$$J_j^* = - L_j^* \frac{d\mu_j}{dz} = - L_j^* \sum_{k=1}^{n} \frac{\partial \mu_j}{\partial c_k}\frac{dc_k}{dz} \quad \text{for } j \le n \quad [3.59]$$

© Woodhead Publishing Limited, 2012

We again eliminate one composition variable, this time using $V_n dc_n = -\sum_{k=1}^{n-1} V_k dc_k$:

$$J_j^* = -L_j^* \frac{d\mu_j}{dz} = -L_j^* \sum_{k=1}^{n} \left(\frac{\partial \mu_j}{\partial c_k} - \frac{V_k}{V_n} \frac{\partial \mu_j}{\partial c_n} \right) \frac{dc_k}{dz}$$

$$= -\sum_{k=1}^{n-1} D_{jk}^{n*} \frac{dc_k}{dz} \quad \text{for } j < n \qquad [3.60]$$

where

$$D_{jk}^{n*} = L_j^* \left(\frac{\partial \mu_j}{\partial c_k} - \frac{V_k}{V_n} \frac{\partial \mu_j}{\partial c_n} \right) = c_j M_j^* \left(\frac{\partial \mu_j}{\partial c_k} - \frac{V_k}{V_n} \frac{\partial \mu_j}{\partial c_n} \right) \quad \text{for } k \le n \qquad [3.61]$$

This time there was no need to divide by V_m because D_{jk}^{n*} is already expressed in m/s. Equations [3.59] and [3.60] are very similar to Eqs [3.44] and [3.46] and they would be identical if V_m is constant in $x_i = V_m c_i$. However, $dx_i = V_m dc_i$ is only approximately true and D_{jk}^{n*} has only approximately the same value in the lattice- and volume-fixed frames.

Use of volume-fixed frame

Inserting c_k instead of x_k in Eq. [3.44] and combining with Eq. [3.25] we obtain

$$J_j = \sum_{i=1}^{n} \alpha_{ji} J_i^* = -\sum_{i=1}^{n} \alpha_{ji} L_i^* \frac{d\mu_i}{dz}$$

$$= -\sum_{i=1}^{n} \alpha_{ji} c_i M_i^* \sum_{k=1}^{n} \frac{\partial \mu_i}{\partial c_k} \frac{dc_k}{dz} \quad \text{for } j \le n \qquad [3.62]$$

Eliminating one composition variable with the same method as before we obtain:

$$J_j = -\sum_{i=1}^{n} \alpha_{ji} c_i M_i^* \sum_{k=1}^{n-1} \left(\frac{\partial \mu_i}{\partial c_k} - \frac{V_k}{V_n} \frac{\partial \mu_i}{\partial c_n} \right) \frac{dc_k}{dz} = -\sum_{k=1}^{n-1} D_{jk}^{n} \frac{dc_k}{dz} \quad \text{for } j \le n \qquad [3.63]$$

where

$$D_{jk}^{n} = \sum_{i=1}^{n} \alpha_{ji} c_i M_i^* V_k \left(\frac{\partial \mu_i}{V_k \partial c_k} - \frac{\partial \mu_i}{V_n \partial c_n} \right) \quad \text{for } k < n \qquad [3.64]$$

This is similar to the result for the number-fixed frame and they seem to be identical for the case $V_k = V_n = V_m$ for which one can expect that V_m is

© Woodhead Publishing Limited, 2012

independent of composition, yielding $V_m dc_k = dx_k$. In that case, $\alpha_{ji} = \delta_{ji} - x_j V_i / V_m = \delta_{ji} - x_j$, which is the expression for the number-fixed frame. It should be noted that D^n_{jk} also appeared in Eq. [3.51] for the number-fixed frame. The two quantities are slightly different except when $V_k = V_n = V_m$.

For the Kirkendall shift we obtain from Eq. [3.27]:

$$v_K = J_K V_m = -\sum_{i=1}^{n} V_i J_i^* = \sum_{i=1}^{n} V_i L_i^* \frac{d\mu_i}{dz} = \sum_{i=1}^{n} V_i c_i M_i^* \sum_{k=1}^{n} \frac{\partial \mu_i}{\partial c_k} \frac{dc_k}{dz} \quad [3.65]$$

The volume-fixed frame has the advantage that experimental measurements are made in that frame. However, it is difficult to apply the equations derived in this section for the transfer of fluxes from the lattice- to volume-fixed frame because all the derivatives $\partial \mu_i / \partial c_i$ are partial derivatives and must be evaluated under constant values of all the other c_i. It is not evident how that could be done because the thermodynamic information is usually given as Gibbs energy as function of the mole fractions, x_i, and $c_j = x_j / V_m = x_j / \sum x_i V_i$. It seems that the number-fixed frame should be preferred when transferring fluxes to or from the lattice-fixed frame. It could then be transferred between the number- and volume-fixed frames using information on the molar volumes.

3.4.6 Application of the volume-fixed frame to a binary system

For a binary *A*-*B* system, Eq. [3.63] yields:

$$J_A = -D^B_{AA} \frac{dc_A}{dz} \quad [3.66]$$

D^B_{AA} can be evaluated directly from experimental values of J_A and the gradient. It is usually denoted D_A. In the volume-fixed frame, $\sum V_i J_i = 0$ by definition and inserting J_A from Eq. [3.66] and a similar expression for J_B we obtain

$$\begin{aligned} V_A J_A + V_B J_B &= -D^B_{AA} \frac{dc_A}{dz} \cdot V_A - D^A_{BB} \frac{dc_B}{dz} \cdot V_B \\ &= -(D^B_{AA} - D^A_{BB}) \frac{dc_A}{dz} \cdot V_A = 0 \end{aligned} \quad [3.67]$$

We have again used $\sum V_i dc_i = 0$ and find $D^B_{AA} = D^A_{BB}$ in the volume-fixed frame, confirming that there is only one independent diffusivity in the binary system. It may be regarded as a chemical diffusivity or interdiffusivity and can be denoted $\widetilde{D}_{AB}$. It is similar to $\widetilde{D}_{AB}$ defined in Eq. [3.58] for the number-fixed frame and they are identical if $V_A = V_B = V_m$. It is advisable not to denote D^B_{AA} by D_A, nor D^A_{BB} by D_B.

© Woodhead Publishing Limited, 2012

For ternary and even higher order systems, there will be a rapidly increasing number of diffusivities due to cross terms. It is important to realize that they may become mutually dependent if some model is applied and in that case it may not be advisable to estimate their values in order to meet an immediate need. Their interdependence according to the present atomistic model is caused by their relation to the mobilities because the number of mobilities is only one for each component. The practical problem is thus to obtain values of the mobilities and also to obtain the thermodynamic information needed when applying Sections 3.4.3 and 3.4.5.

3.5 Evaluation of mobilities

For a binary system there will be only one diffusivity in the volume-fixed frame, the interdiffusivity. Without a model there will be three independent diffusivities for a ternary system due to the appearance of cross terms in the flux equations. For higher order systems the number of independent diffusivities will increase rapidly. Furthermore, the values of the diffusivities may vary with composition. It is thus a formidable task to determine the diffusivities experimentally in sufficient detail for a higher order system. However, the number of independent diffusivities may be drastically reduced by accepting some model. We shall here accept the atomistic model defined by Eq. [3.21] and we would then need to base the discussion on the lattice-fixed frame where only n mobilities are needed in an n-component system. To determine them, we need to know the fluxes in the lattice-fixed frame but they are usually determined by experiments in the volume-fixed frame. In Section 3.4 we derived expressions for fluxes in the volume-fixed frame in terms of those in the lattice-fixed frame using the relation $J_j = J_j^* - x_j \sum a_i J_i^*$ in Eq. [3.25]. However, now we need to inverse that relation and evaluate the fluxes in the lattice-fixed frame from those in the volume-fixed frame. That can be done by substituting v_K/V_m for $-\sum a_i J_i^*$ according to Eq. [3.27] and inserting $x_i = V_m c_i$.

$$J_j^* = J_j - c_j v_K \qquad [3.68]$$

It should be noticed that we have here introduced the rate of the Kirkendall markers, v_K, instead of the rate of the volume-fixed frame relative to the lattice-fixed frame used in Eq. [3.24], v, and $v_K = -v$. In the following discussion we shall assume that the fluxes in the lattice-fixed frame have been evaluated from measurements in the volume-fixed frame and application of Eq. [3.68]. If the thermodynamic properties are also known, then one can evaluate $d\mu_j/dz$ and obtain the mobility from Eqs [3.21] and [3.68]:

$$M_j^* = -\frac{J_j^*}{c_j} \Big/ \frac{d\mu_j}{dz_j} = \frac{J_j - c_j v_K}{c_j} \Big/ \frac{d\mu_j}{dz_j} \qquad [3.69]$$

© Woodhead Publishing Limited, 2012

Once the n mobilities have been determined, any diffusivity in the volume-fixed frame, including those in cross terms, i.e., all the diffusivities defined by Eq. [3.63], can be obtained through Eq. [3.64] if thermodynamic information is available. The diffusivities will be the information used for calculations by hand and in the immediate future also for calculations using a computer. However, calculations of the progress of diffusion will probably be easier if carried out in the lattice-fixed frame and it may be predicted that more and more programs for handling diffusion will be written for that frame. The mobilities together with thermodynamic information will then be applied directly in everyday work.

A classic method of evaluating mobilities avoids the necessity of measuring the Kirkendall shift and having access to the thermodynamic data. One studies the ideal binary system between an element and a radioactive isotope of the same element. That should be an ideal solution and both components should have practically the same mobility, and the measured interdiffusivity could be related directly to the diffusivity of the radioactive component. Equation [3.54] yields

$$\tilde{D}_{AB} = x_B D_A^* + x_A D_B^* = D_B^* = x_B M_B^* \frac{d\mu_B}{dx_B}$$
$$= M_B^* \frac{d\mu_B}{d \ln x_B} = RTM_B^* = RTM_A^* \qquad [3.70]$$

This method can also be applied to a system of the radioactive element in another element because that would also be very close to. As a first approach to describe the variation of the mobility with composition, one could assume a linear variation with composition of M_A^* in the A-B system. Actual study of that variation requires measurements for alloys with intermediate compositions and use of Eq. [3.69].

3.5.1 Diffusion in phases with interstitials

Phases with different kinds of sites for the atoms are described with sublattices. With two sublattices one can write the formula as $(A, B)_{b^1}(C, D)_{b^2}$. The composition is then represented by site fractions, y_i^r, being mole fractions defined for each sublattice, r, separately. The mole fraction of component j in the phase will be $x_j = b^r y_j^r/(b^1 + b^2)$ and it is easy to transform between the two methods. Often there are a majority of vacant sites in one sublattice, a so-called interstitial sublattice, e.g. in austenite and ferrite of Fe-C alloys where $b^1 = 1 = b^2$ for austenite and $b^1 = 1$ and $b^2 = 3$ for ferrite. The major sublattice is characterized as substitutional. It contains thermal vacancies but they are very few and are seldom included in the formula. On the other hand, vacancies are the major constituent in the interstitial sublattice and the

© Woodhead Publishing Limited, 2012

formula may be written as $(A, B)_{b^S}(C, Va)_{b^I}$. Those vacancies are regarded as stoichiometric.

Thermodynamic models of interstitial phases are based on site fractions but in such phases the relation to the mole fractions is more complicated because the vacancies are included in the set of site fractions but not in the set of mole fractions, $x_j = b^r y_j^r/[b^S + b^I(1 - y_{Va}^I)]$. The chemical potential of an interstitial component is intimately connected to the chemical potential of the vacancies. In a formal sense, the notation μ_I really stands for $\mu_I - \mu_{Va}$ and that is how it is evaluated from the Gibbs energy which is given as a function of site fractions, including the site fraction of vacancies. Of course, that is taken care of automatically when the chemical potential is evaluated from a computerized databank of thermodynamic properties. In turn, the chemical potential of an interstitial is also a function of all the site fractions and that must be remembered when one evaluates the gradient of a chemical potential.

The molar volume, V_m, is the volume for one mole of atoms without including the vacancies. It will thus vary with the content of interstitial solutes even if they have a very slight effect on the total volume. It may be better to use the molar volume per formula unit, V_{mf}, which does not vary as much.

The L_i coefficient in the flux equation, Eq. [3.21], was given as $(x_i/V_m)M_i$ and its value will thus decrease as x_i is decreased, an effect of the dilution when other elements are added. One may guess that the corresponding effect of interstitial elements on the diffusion of a substitutional element will be less because they will not decrease the probability that a substitutional atom has a thermal vacancy as nearest neighbour, a necessary condition for the atom to jump. We shall thus assume that such elements have a negligible effect and assume that $L_i^{S*} = b^S y_i^S M_i^*/V_{mf}$. For interstitial elements we shall use $L_i^{I*} = b^I y_i^I y_{Va}^I M_i^*/V_{mf}$ by comparing with Eq. [3.20]. For each sublattice the sum of site fractions is equal to 1. The dependent composition variable in the substitutional sublattice can be eliminated by $dy_n^S = -\sum dy_k^S$. In the interstitial sublattice we shall eliminate the vacancies and a similar relation applies to them, $dy_{Va}^I = -\sum dy_k^I$. Also for interstitial phases one can choose between the three frames of reference but we shall not discuss the volume-fixed frame for the reason explained at the end of the section.

Using lattice-fixed frame

The treatment of diffusivity in the lattice-fixed frame, given in Section 3.4.3, applies even to interstitial atoms because they jump between sites in the same lattice as the substitutional atoms, even though they reside in a different sublattice. Let there be n substitutional elements and m interstitials. However, there are $m + 1$ site fractions in the interstitial sublattice where

© Woodhead Publishing Limited, 2012

the last one is y^I_{Va}. Changing the composition variables in Eq. [3.44] to site fractions we obtain

$$J^*_j = -L^*_j X^*_j = -L^*_j \frac{d\mu_j}{dz} = -L^*_j \sum_{k=1}^{n+m+1} \frac{\partial \mu_j}{\partial y_k} \frac{dy_k}{dz} \quad \text{for } j \le n+m \quad [3.71]$$

We may eliminate the nth component in the substitutional sublattice as before and the vacancies in the interstitial sublattice, using $\sum y^S_i = 1$ and $\sum y^I_i = 1$.

$$\begin{aligned} J^*_j &= -L^*_j \frac{d\mu_j}{dz} \\ &= -L^*_j \left(\sum_{k=1}^{n-1} \left(\frac{\partial \mu_j}{\partial y^S_k} - \frac{\partial \mu_j}{\partial y^S_n} \right) \frac{dy^S_k}{dz} + \sum_{k=n+1}^{n+m} \left(\frac{\partial \mu_j}{\partial y^I_k} - \frac{\partial \mu_j}{\partial y^I_{Va}} \right) \frac{dy^I_k}{dz} \right) \\ &= -\sum_{k \neq n} \frac{D^{n,Va*}_{jk}}{V_{mf}} \frac{dy^{S,I}_k}{dz} \end{aligned} \quad [3.72]$$

$$D^{n*}_{jk} = V_{mf} L^*_j \left(\frac{\partial \mu_j}{\partial y^S_k} - \frac{\partial \mu_j}{\partial y^S_n} \right) \quad \text{for } k < n \quad [3.73]$$

$$D^{Va*}_{jk} = V_{mf} L^*_j \left(\frac{\partial \mu_j}{\partial y^I_k} - \frac{\partial \mu_j}{\partial y^I_{Va}} \right) \quad \text{for } k > n+1 \quad [3.74]$$

It should be remembered that L^*_j is equal to $b^S y^S_j M^*_j / V_{mf}$ for $j < n$ but it is equal to $b^I y^I_j y^I_{Va} M^*_j / V_{mf}$ for $j > n$, i.e., for interstitial elements.

Using the number-fixed frame

The number of atoms crossing the plane of markers is always $\sum J^*_i$ if the flux of vacancies is excluded and the fraction of j atoms in the same amount of the material is x_j. The α_{ji} factor in the number-fixed frame is thus independent of the possible existence of sublattices. We can thus use $\alpha_{ji} = \delta_{ji} - x_j$ in $J_j = \sum \alpha_{ji} J^*_j$ in the following equations. Insertion of J^*_j from Eq. [3.71] into Eq. [3.25] yields

$$J_j = \sum_{i=1}^{n+m} \alpha_{ji} J^*_i = -\sum_{i=1}^{n+m} \alpha_{ji} L^*_i \sum_{k=1}^{n+m+1} \frac{\partial \mu_i}{\partial y_k} \frac{dy_k}{dz} \quad \text{for } j \le n+m \quad [3.75]$$

Eliminating the nth component in the substitutional sublattice and the vacancies from the interstitial sublattice, we obtain

© Woodhead Publishing Limited, 2012

$$J_j = -\sum_{i=1}^{n} \alpha_{ji} L_i^* \left(\sum_{k=1}^{n-1} \left(\frac{\partial \mu_j}{\partial y_k^S} - \frac{\partial \mu_i}{\partial y_n^S} \right) \frac{dy_k^S}{dz} + \sum_{k=n+1}^{n+m} \left(\frac{\partial \mu_i}{\partial y_k^I} - \frac{\partial \mu_i}{\partial y_{Va}^I} \right) \frac{dy_k^I}{dz} \right)$$

$$= -\sum_{k \neq n} \frac{D_{jk}^{n,Va}}{V_{mf}} \frac{dy_k^{S,I}}{dz} \qquad [3.76]$$

$$D_{jk}^{n} / V_{mf} = \sum_{i=1}^{n+m} \alpha_{ji} L_i^* \left(\frac{\partial \mu_i}{\partial y_k^S} - \frac{\partial \mu_i}{\partial y_n^S} \right) \quad \text{for } k < n \qquad [3.77]$$

$$D_{jk}^{Va} / V_{mf} = \sum_{i=1}^{n+m} \alpha_{ji} L_i^* \left(\frac{\partial \mu_i}{\partial y_k^I} - \frac{\partial \mu_i}{\partial y_{Va}^I} \right) \quad \text{for } k > n \qquad [3.78]$$

Again it should be remembered that L_i^* is equal to $b^S y_i^S M_i^* / V_{mf}$ for $i < n$ but it is equal to $b^I y_i^I y_{Va}^I M_i^* / V_{mf}$ for $i > n$, i.e., for interstitial elements. Andersson and Ågren (1992) have already discussed this case but their final equations are slightly different because they used a composition variable that does not appear in the thermodynamic model of interstitial solutions.

Applications

Interstitials in steels, mainly carbon and nitrogen, are much more mobile than substitutional elements. The difference is so large that one can treat most cases as one of two extreme cases. For short times one may neglect the diffusion of substitutional elements completely but should of course take into account their effect on the chemical potential of the rapidly diffusing interstitial element. That would be a purely thermodynamic effect. After long times the rapid diffusion of the interstitial elements may have stopped but one can consider the diffusion of substitutional elements. There may be simultaneous diffusion of the interstitial elements but only due to the redistribution of the substitutional elements. At that stage it may be a good approximation to assume that there is uniform carbon or nitrogen activity and their effect on the substitutional elements can be evaluated from their activities if one has access to a thermodynamic databank.

The situation will be more complicated if there is a phase transformation controlled by long range diffusion of carbon or nitrogen. The boundary conditions at the phase interface may then be affected by very local redistribution of substitutional elements (Hillert, 1953; Kirkaldy, 1958; Hillert and Ågren, 1988). This is an important and active field of research that involves deviation from local equilibrium at phase interfaces for the substitutional elements but good local equilibrium for the interstitials. Other factors may also interact with phase interfaces and may cause deviations from

© Woodhead Publishing Limited, 2012

local equilibrium. The remainder of this chapter will discuss the boundary conditions and such factors briefly.

3.5.2 Boundary conditions at phase interfaces

In order to predict the progress of one-dimensional diffusion in a phase of limited extent, it is necessary to know the boundary conditions at the two sides of the phase. In a phase transformation there is a moving interface between the two phases and the conditions at the interface will define boundary conditions of both phases. It is very common to assume that there is local equilibrium between the two phases even though they may be separated by a moving phase interface. With that assumption one could fix the boundary conditions for a binary system for which the two-phase equilibrium at given T and P has no degrees of freedom. The compositions at the interface will then be constant during the process of diffusion. However, for each additional component there is a new degree of freedom and already for a ternary system the operating tie-line is affected by the diffusion process itself and may change with time. In computerized calculations of diffusion, one usually finds the operating tie-line by an iteration process for each step in time. Such a procedure gets more complicated for each additional component. The situation gets even more complicated if the assumption of local equilibrium at the interface could not be applied. In such a case it is necessary to define the conditions at the interface in some other way, which means that one must apply a model for the physical factor causing the deviation from local equilibrium.

If the interface is curved, as it is for a spherical inclusion, the pressure difference will affect the local equilibrium. That effect can be easily handled with a computerized program for thermodynamic calculations by assuming that the included phase is under an increased pressure, $\Delta P = 2\sigma/\rho$. If the interface experiences a resistance when moving, i.e. some kind of friction, then the effect on the included phase can be translated into a pressure increase and be treated as such. Then it is necessary to find a suitable physical model and combine it with diffusion into a kinetic model for the overall process. Simple methods that have been tried are to assume a constant friction coefficient, which results in a friction proportional to the velocity of the interface, and a constant friction that implies that there is an energy barrier that must be surmounted. A more detailed model is to assume that the atoms have to cross the interface individually and to give the atoms of each component a mobility. For that model one could apply the formalism for diffusion and assume that the interface has a fixed thickness Δz comparable to the thicknesses of the space elements into which the system is already divided for numerical treatment of diffusion inside the phases. It should be possible to apply the atomistic model derived in Section 3.3 but without using the approximation $\sqrt{x'_B x''_B} \cong x_B$ because the compositions of the two phases

© Woodhead Publishing Limited, 2012

may be too different. The following flux equation has thus been proposed for the flux across the interface:

$$J_B = -M_B\sqrt{x_B^{\alpha/\beta}x_B^{\beta/\alpha}}\ \Delta\mu_B/\Delta z = -M_B\sqrt{x_B^{\alpha/\beta}x_B^{\beta/\alpha}}\ (\mu_B^{\alpha/\beta} - \mu_B^{\beta/\alpha})/\Delta z \quad [3.79]$$

With the approximation $\sqrt{x'_B x''_B} \cong x_B$, this equation reduces to Eq. [3.21], which has often been used for numerical solutions of diffusion inside a phase, divided into thin slices. The quantity Δz is then the distance between the centres of two neighbouring slices (Larsson *et al.*, 2006). The Kirkendall shift is evaluated as $J_k = -\sum J_i = \sum M_i x_i \Delta\mu_i/\Delta z$ and according to the Gibbs–Duhem relation, $\sum x_i d\mu_i = 0$, it would be very close to zero if Δz is small and the mobilities are equal. It is evident that the Kirkendall shift is caused only by differences between the mobilities. On the other hand, if Eq. [3.79] without the approximation is applied to the two slices adjoining the interface, then the Kirkendall shift may be considerable. In that case, the interface plays the role of Kirkendall markers and the Kirkendall shift is identical to the rate of the phase transformation.

The composition at the interface and its rate of movement will thus be calculated for each time step when the progress of diffusion in the whole system is calculated. If the initial conditions at the interface, represented by the two adjoining slices, are not correct, then there may be an automatic iteration towards better values with time. The calculated conditions at the interface will approach those for local equilibrium if high values have been chosen for the mobilities of the atoms for crossing the interface. A deviation from local equilibrium will be obtained if lower values are chosen. A limitation of this method is that it can only describe such conditions at the interface when each component is transferred to the side with the lower chemical potential of the component. Cases have been observed where atoms are transferred to the side with the higher potential and will be mentioned in the next section.

3.6 Trapping and transition to diffusionless transformation

It is known that a diffusional phase transformation may become partitionless or even diffusionless if the rate can be increased enough by increasing the supersaturation. Partitionless means that the new phase forms with the same composition as the parent phase, which may occur behind a steep pile-up of the minority component in the parent phase. Diffusionless means that the result is the same but there is no diffusion of the components relative to each other. It is also known that under less drastic conditions there may be

© Woodhead Publishing Limited, 2012

trapping, which means that one component is transferred across the moving phase interface against its own driving force. Of course, the diffusionless transformation is the extreme of trapping. Certainly, such phenomena cannot be modelled with the above mechanism of individual jumps of atoms to the side with lower chemical potential. There is a need for a more general model that can also describe the transfer of atoms to a higher potential. An attempt has been made to improve the above treatment by adding a third mechanism, a cooperative transfer of the components (Larsson and Borgenstam, 2007).

There have been attempts to predict trapping on a strictly formal basis using the fact that two simultaneous processes may affect each other by cross terms in their rate equations (Baker and Cahn, 1971; Caroli *et al.,* 1986). Instead of Eq. [3.21] one should then write the flux equations as

$$J_j = L_{jj}X_j + L_{jk}X_k \qquad [3.80]$$

Trapping may occur if the two terms have different signs and the second one is larger. As demonstrated in Section 3.4.1, one may define a new set of processes and derive the driving forces for them by the criterion that the dissipation of Gibbs energy must be accounted for. In an attempt to give the introduction of cross terms a physical interpretation, a new set of processes has been introduced as linear combinations of the initial ones hoping to find a case where the cross terms have vanished. For a binary system the following new fluxes have been chosen:

$$J_A^* = J_j + J_k \qquad [3.81]$$

$$J_B^* = x_k J_j - x_j J_k \qquad [3.82]$$

If applied to diffusion processes inside a phase, the first flux gives the net flux of atoms, i.e., the Kirkendall shift and the second flux describes the mixing of the two components. This set of new processes thus happens to be the same as the set obtained when changing from lattice-fixed to number-fixed frame, although in Section 3.4 we started with fluxes without cross terms in the lattice-fixed frame. The ambition has been to find two new processes that are independent of each other, i.e. without cross terms. The coefficients for the new processes can be obtained as demonstrated in Section 3.4.1 and there is no general way to make them zero if they are zero for the initial set of processes. However, by requiring that they must be zero in the new set, one can easily derive what values they must have in the initial set. By using the initial set of processes with those values, one may thus model a transformation occurring with two independent processes without directly representing them in the computer program. Since the new set of processes is identical to the set introduced when changing from lattice- to number-fixed frame, this simply means that one would apply the alternative method described in Section 3.4.2 but with cross terms. At the same time there would

© Woodhead Publishing Limited, 2012

be no cross terms in Eqs [3.38] and [3.39]. This approach does not seem to have found much practical application.

Here we have only considered the so-called sharp interface situated between two thin space elements. Wide interface models are more powerful and can be applied to describe such phenomena as segregation and solute drag during grain growth (Cahn, 1962) and phase transformations (Hillert, 2004) and trapping (Hillert and Sundman 1977). Finally, the phase field method must be mentioned where the width is not fixed in advance (Moelans *et al.*, 2008). Instead, the interface is diffuse and the variation of the local state and composition along the direction of diffusion are optimized continuously by minimization of the overall Gibbs energy and the movement of the phase interface is obtained. This seems to be the most powerful method but requires more computing time.

3.6.1 Local change of volume at phase interface

The introduction of mobilities for diffusion in the lattice-fixed frame in Section 3.3 was straightforward, but the introduction of new frames of reference revealed a complication. Formally, the equations were correct as far as the Kirkendall shift was defined as the net amount of material that crossed the plane of the Kirkendall markers. The complication appeared when the Kirkendall shift was measured as a length in the specimen because then it had to be assumed that the cross section of the system had not changed. It may be measured either in m^2 for the volume-fixed frame or in a measure related to the number of atoms in the cross section. Primarily, one should expect that an expansion of the volume due to a Kirkendall effect should be homogeneous in all three dimensions. It may be argued that for one-dimensional diffusion, a solid piece of material should be able to change its volume only in the direction of diffusion and that requirement could only apply to the cross section measured in m^2. It is thus necessary to accept plastic deformation simultaneous to the diffusion. The situation is more complicated if there is diffusion in two or three dimensions and even more interesting if there is a diffusional phase transformation. In Section 3.5.2 it was mentioned that the movement of the interface has the same origin as the Kirkendall shift. The following discussion is similar to the one given by Hillert (2008, Section 17.4) but the method of transforming fluxes between different frames of reference will now be used.

In order to evaluate the need of local plastic deformation at the moving phase interface during a transformation, it is necessary to apply a unique lattice-fixed frame of reference for each phase and also to consider the flux of atoms across the phase interface, J_j^{trans}. That flux is defined relative to the interface, which is generally moving with different velocities relative to the two phases. Those velocities will be denoted $v^{\alpha/\beta}$ and $v^{\beta/\alpha}$ for a $\beta \rightarrow \alpha$

© Woodhead Publishing Limited, 2012

transformation. When comparing the three fluxes, it is convenient to describe them in the same frame of reference and we shall choose a frame fixed to the interface. Since the flux leaving one phase must cross the interface and be received by the other phase, the three fluxes for each element must be equal when expressed in the same frame. According to Eq. [3.24] we obtain

$$J_j^{\alpha} - x_j^{\alpha} v^{\alpha/\beta}/V_m^{\alpha} = J_j^{\text{trans}} = J_j^{\beta} - x_j^{\beta} v^{\beta/\alpha}/V_m^{\beta} \qquad [3.83]$$

$v^{\alpha/\beta}$ and $v^{\beta/\alpha}$ are generally different and there would then be a local change of volume. The lattice of the β phase will move away from the lattice of the α phase with a velocity of $\Delta v = v^{\alpha/\beta} - v^{\beta/\alpha}$. To find this quantity we shall first eliminate the flux across the phase interface, J_j^{trans}, from Eq. [3.83] and then sum over all components:

$$v^{\alpha/\beta}/V_m^{\alpha} - v^{\beta/\alpha}/V_m^{\beta} = \Sigma J_i^{\alpha} - \Sigma J_i^{\beta} \qquad [3.84]$$

We may then eliminate any one of the velocities from Eq. [3.83], obtaining

$$v^{\alpha/\beta}/V_m^{\alpha} = [J_j^{\alpha} - J_j^{\beta} - x_j^{\beta} (\Sigma J_i^{\alpha} - \Sigma J_j^{\beta})]/(x_j^{\alpha} - x_j^{\beta}) \qquad [3.85]$$

and similarly for $v^{\beta/\alpha}$. We may then take the difference and for a binary system we finally obtain

$$\Delta v = v^{\alpha/\beta} - v^{\beta/\alpha} = \lfloor (V_m^{\alpha} x_B^{\beta} - V_m^{\beta} x_B^{\alpha}) (J_A^{\alpha} - J_A^{\beta}) - (V_m^{\alpha} x_A^{\beta} - V_m^{\beta} x_A^{\alpha}) - (J_B^{\alpha} - J_B^{\beta}) \rfloor / (x_A^{\alpha} - x_A^{\beta}) \qquad [3.86]$$

In two- or three-dimensional diffusion experiments, this may cause severe deformations of the material, which may occur by several deformation mechanisms. One of them is stress-induced diffusion caused by the build-up of a high positive or negative pressure in a precipitating phase. A drastic example is the growth of a spherical nodule of graphite in a supersaturated matrix of an Fe-C solution phase (Hillert, 1957). The diffusion of carbon to the graphite would primarily dominate completely and the pressure in the graphite should build up until the hole in the matrix is expanding at the same rate. Otherwise, the diffusion of carbon has to stop due to a pressure-induced increase of the carbon potential in the graphite. In reality, a balance will be established where the diffusion of carbon is slowed down and the hole is expanded by stress-induced diffusion of iron or mechanical deformation of the matrix.

3.6.2 Composition of flux across phase interface

It is possible to derive the net composition of the material transferred across the phase interface without modelling the mechanism of transfer but

© Woodhead Publishing Limited, 2012

considering the fluxes in the two phases. Inserting Eq. [3.85] into the first part of Eq. [3.83] we obtain after some manipulations:

$$\begin{aligned} J_j^{\text{trans}} &= J_j^{\alpha} - x_j^{\alpha} v^{\alpha/\beta}/V_m \\ &= [x_j^{\alpha}(J_j^{\beta} - x_j^{\beta} \Sigma J_i^{\beta}) - x_j^{\beta} (J_j^{\alpha} - x_j^{\alpha} \Sigma J_i^{\alpha})]/(x_j^{\alpha} - x_j^{\beta}) \end{aligned} \quad [3.87]$$

By first summing Eq. [3.85] over all the components we obtain after similar manipulations:

$$\begin{aligned} \Sigma J_i^{\text{trans}} &= \Sigma J_i^{\alpha} - v^{\alpha/\beta}/V_m \\ &= [(J_j^{\beta} - x_j^{\beta} \Sigma J_i^{\beta}) - (J_j^{\alpha} - x_j^{\alpha} \Sigma J_i^{\alpha})]/(x_j^{\alpha} - x_j^{\beta}) \end{aligned} \quad [3.88]$$

The mole fraction of component j in the material crossing the interface will thus be

$$x_j^{\text{trans}} = J_j^{\text{trans}}/\Sigma J_i^{\text{trans}} = \frac{x_j^{\alpha}(J_j^{\beta} - x_j^{\beta} \Sigma J_i^{\beta}) - x_j^{\beta}(J_j^{\alpha} - x_j^{\alpha} \Sigma J_i^{\alpha})}{(J_j^{\beta} - x_j^{\beta} \Sigma J_i^{\beta}) - (J_j^{\alpha} - x_j^{\alpha} \Sigma J_i^{\alpha})} \quad [3.89]$$

From this composition one can evaluate the driving force for the transfer as $\sum x_i^{\text{trans}} \Delta\mu_i$ to be used when trying possible models for the transfer.

3.7 Future trends

Most measurements of the rate of diffusion and most practical applications of diffusion have concerned binary alloys. That activity has resulted in an impressive amount of data on diffusivities that is available in various compilations. However, most commercial alloys contain more than one alloying element and that is particularly true for steels. Then there will be cross terms in the kinetic flux equation, which define new diffusivities. To determine all of them may require too much experimental work and one should not expect to find many such values in compilations. It may thus be predicted that experimental data will in the future be analyzed in terms of mobilities that are defined in the lattice-fixed frame. It may reasonably be assumed that there should be no cross terms in the lattice-fixed frame and, thus, only one mobility for each element, although it should vary with composition. Compared to the diffusivities, the variation with composition is much smaller for the mobilities because they do not contain the composition dependence of the thermodynamic properties.

The reason is that the gradient of the chemical potential of a component is used as the driving force in the lattice-fixed frame. In order to use that formalism, it is thus necessary to have access to the thermodynamic properties of the system. In that field one encounters the same kind of problem when going to ternary and higher order systems. Binary phase diagrams are manifestations of the thermodynamic properties and are available in compilations for a large

© Woodhead Publishing Limited, 2012

number of systems. By combination with various kinds of thermodynamic measurements it has been possible to obtain reasonable descriptions of the thermodynamic properties of binary systems. This is called the CALPHAD approach (Saunders and Miodownik, 1998; Lukas *et al.*, 2007). The same holds for ternary systems, although additional parameters must be taken into account. There is an increasing complexity for each additional component in a system. The situation is similar to that in the field of diffusion, but efforts to handle that kind of situation have already started in the field of thermodynamics. There are already computerized databases available together with powerful software for the calculation of various thermodynamic quantities.

The results achieved so far in the field of thermodynamics have been made possible by an informal world-wide collaboration. Although the results are impressive and are already of considerable use, it is important that the work continues. It is evident that the same kind of effort is necessary in the field of diffusion and the experience gained in the field of thermodynamics may be useful in the field of diffusion. It is necessary to reach international agreement on each step in the work, the choice of 'model', i.e., choice of frame of reference, flux equation and kind of parameter to be evaluated and stored, e.g. diffusivity or mobility, the values of those parameters in simple systems, primarily pure elements and binary systems, and the method of describing their dependence on composition and temperature.

Since the values of diffusivities in the volume-fixed frame and the driving forces in the lattice-fixed frame depend on the thermodynamic properties, it is necessary that the future work on diffusion in alloy systems be closely connected to the development in the field of thermodynamic properties of alloy systems. Hopefully, that will come naturally because many research groups will work in both fields.

To the present author it seems that one should agree on analyzing experimental information in terms of mobilities and also to make numerical calculations in the lattice-fixed frame. The database should only contain the mobilities but that information, in combination with a thermodynamic database, will be used for evaluating diffusion coefficients for binary systems. Lists of such quantities are necessary for filling the need of making hand calculations for simple cases, but for more complicated cases it is necessary to have a powerful package of databases and programs for thermodynamics and diffusion.

3.8 Acknowledgement

The author owes much of his understanding of the fundamentals of diffusion to many discussions with Professor John Ågren, and this chapter was inspired by his paper with Dr J.-O. Andersson in 1992.

© Woodhead Publishing Limited, 2012

3.9 References

Ågren J (1982), *J. Phys. Chem. Solids*, 43, 421.
Andersson J-O and Ågren J (1992), *J. Appl. Phys.*, 72, 1350.
Baker J C and Cahn J W (1971), in *Solidification*, eds. J. Hughel and G F Bolling, Metals Park, OH, ASM, p. 23.
Borg R J and Dienes G J (1988), *Solid State Diffusion*, Boston, MA, Academic Press.
Cahn J W (1962), *Acta Metall.*, 10, 1.
Caroli B, Caroli C and Roulet B (1986), *Acta Metall.*, 34, 1867.
Darken L S, (1948), *Trans. AIME*, 175, 184.
Glasstone S, Laidler K J and Eyring H (1941), *The Theory of Rate Processes*, New York, McGraw-Hill.
Hillert M (1953), *Paraequilibrium* (Internal report), Stockholm, Swedish Inst. Metal Res. Reprinted in *Thermodynamics and phase transformations – The collected works of Mats Hillert*, (2006), Les Ulis Cedex A, France, EDP Science.
Hillert M (1957), *Jernkontorets Ann.*, 141, 67.
Hillert M (2001), *Scripta Mater.*, 44, 1095.
Hillert M (2004), *Acta Mater.*, 52, 5289.
Hillert M (2008), *Phase Equilibria, phase Diagrams and Phase Transformations – their Thermodynamic Basis*, 2nd edn, Cambridge, Cambridge University Press.
Hillert M and Ågren J (1988), Diffusional transformations under local equilibrium in Fe-C-M systems, in *Advances in Phase Transitions*, Oxford, Pergamon Press.
Hillert M and Sundman B (1977), *Acta Metall.*, 25, 11.
Kirkaldy J S (1958), *Can. J. Phys.*, 36, 907.
Kirkaldy J S and Young D J (1987), *Diffusion in the Condensed State*, London, The Institute of Metals.
Larsson H and Borgenstam A (2007), *Scripta Mater.*, 56, 61.
Larsson H, Strandlund H and Hillert M (2006), *Acta Mater.*, 54, 945.
Lukas H L, Fries S G and Sundman B (2007), *Computational Thermodynamics*, Cambridge, Cambridge University Press.
Moelans N, Blanpain B and Wollants P (2008), *CALPHAD*, 32, 268.
Saunders N and Miodownik A P (1998), *CALPHAD – Calculation of Phase Diagrams*, Oxford, Pergamon Press.

© Woodhead Publishing Limited, 2012

4

Kinetics of phase transformations in steels

S. VAN DER ZWAAG, Delft University of Technology (TU Delft), The Netherlands

Abstract: This chapter deals with the kinetics of diffusional phase transformations in steels, in particular, the formation of allotriomorphic ferrite from an fully austenitic starting condition in low alloyed steels, and focuses on the macroscopically apparent transformation kinetics as described by the well-known Johnson–Mehl–Avrami (JMA) equation. While the JMA approach is very practical from an industrial perspective, fitting experimental transformation curves to JMA equations does not lead to insight into the underlying physics of the transformation process. The actual austenite to ferrite transformation proceeds via a nucleation and growth process. Recent insights into the physical nature of both the nucleation and the growth process are discussed and remaining challenges are identified. A survey of common and less usual methods to follow the transformation kinetics of the austenite decomposition is presented. The chapter ends with a short description of the industrial relevance of a better understanding of the transformation kinetics.

Key words: transformation kinetics, nucleation, growth, diffusion, interface mobility, mixed mode, JMA kinetics, steel production.

4.1 Introduction

As is well known, and clearly presented in the other chapters in this book, lean and alloyed steels can exist in different phases or mixtures of phases depending on the chemical composition and the actual temperature. Unlike many other metallic systems, steels can undergo not only the liquid-solid phase transformation but also many solid-solid phase transformations. These solid-solid phase transformations, the nature of which depend on the cooling rate in going from one (stable or metastable) phase to another (stable or metastable) phase, offer a unique tool to tailor the microstructure of steels and thereby to tune the mechanical properties of steels of a fixed chemical composition over a wide range of strength and ductility values. Given the wide range of steel compositions in combination with the many phase transformations and resulting microstructures, it is impossible to deal with all options and conditions within the context of a single chapter. Hence, in this chapter the attention is focused on the austenite-ferrite phase transformation which plays a dominant role in any thermomechanical process route for low alloy or lean steels. This is not unreasonable because low

© Woodhead Publishing Limited, 2012

alloyed steels with either a simple or a complex multiphase microstructure form about 80% of all steels currently produced. For most of these steels the allotriomorphic ferrite forms a large fraction of the total microstructure. The treatment of just this type of transformation here is, on the one hand, specific as other solid state transformations related to austenite decomposition, such as pearlite, upper and lower bainite and martensite formation, have other specific characteristics. On the other hand, the description of this type of transformation is generic as the interacting aspects of nucleation, growth and initial microstructure will play a role in all sorts of transformations. The main purpose of this chapter is to show the complexity of the kinetics of phase transformations and to demonstrate that for seemingly identical conditions the kinetics can be rather different. Furthermore, the treatment will show that a single transformation-time curve, can never be reconstructed unambiguously into all the factors and processes which played a role in the transformation kinetics. Implicitly the treatment also explains why steels of a fixed composition made on different installations can have different microstructures and hence properties.

The chapter starts with the well-known macroscopic description of solid state phase transformations based on a sequence of nucleation and growth processes, the Johnson–Mehl–Avrami–Kolmogorov (JMAK) approach. To stay in line with the subsequent treatment of the physics of the nucleation and growth processes, attention is focused on isothermal transformations. While it is possible to derive the exact values of the key parameters in the JMA model assuming a microstructure free continuum as the starting condition for the transformation, and by making additional assumptions on the nucleation and growth processes, it is impossible to invert the process and to derive hard evidence for either the nature of the nucleation or growth process by fitting JMA equations to experimental transformation curves. In this chapter the effect of the microstructure on the apparent JMA parameters for a given transformation process is shown.

Notwithstanding its pivotal role in phase transformations, as a *conditio sine qua non*, the precise physics of the nucleation process remain rather unclear. This is partially due to the impossibility to monitor non-invasively the rearrangements of the small number of atoms (estimated at values as low as a hundred or less) making the transition of being in the parent phase to forming the nucleus in the relevant time scale (estimated at values less than a microsecond). In this chapter we will summarize a recent generic model for nucleation processes, which explains why it is impossible to quantitatively predict the nucleation kinetics for steels as a function of composition and undercooling.

While the growth of ferrite grains from the parent austenite seems easier to address as it proceeds on a larger scale (typically micron scale) and over longer time scales (seconds to minutes), exact prediction of kinetics remains

© Woodhead Publishing Limited, 2012

difficult as the growth involves both short distance atomic rearrangements at the austenite-ferrite interface, as well as long distance diffusional transport of interstitial and substitutional alloying elements with widely differing intrinsic mobilities. In this chapter we discuss recent findings on the nature of the ferrite growth suggesting that different growth mechanisms may apply to different grains in the same sample undergoing a single thermal treatment. Finally, the chapter concludes with a short section discussing the relevance of a good understanding of the transformation kinetics for the steel industry.

4.2 General kinetic models

The simplest model to predict the kinetics of solid state transformation is that of Johnson–Mehl–Avrami–Kolmogorov (JMAK) (Kolmogorov, 1937; Avrami 1939, 1940; Johnson and Mehl, 1939). This model describes solid state transformation kinetics involving nucleation and growth of a new phase out of the parent phase which disappears as a consequence of the formation of the new phase. The model, which applies to all first order phase transformations driven by nucleation and growth kinetics, leads to the following equation for the volume fraction of the new phase

$$F = 1 - \exp(-kt^n) \qquad [4.1]$$

where k is the rate constant and n is the so-called Avrami coefficient.

In his landmark papers on this subject (Cahn, 1956a, 1956b), J. W. Cahn showed how the Avrami model concept can be used to describe the kinetics of phase transformation for both isothermal transformation and during continuous cooling. He showed how the Avrami constants depend on the underlying simplifying assumptions for nucleation and growth.

In the case of interface controlled growth (such as in low carbon alloys or extra low carbon alloys, i.e. steels in which solute partitioning does not play a role and the transformation is primarily dictated by the atomic rearrangements at the interface), the growth rate is constant and the Avrami exponent attains a value of 4 for three-dimensional growth (with constant nucleation rate) and a value of 3 for two-dimensional growth. For diffusion controlled growth rate (applicable to most low alloyed steels and modest cooling rates and involving partial or complete solute partitioning), a value of 5/2 is expected for three-dimensional growth and continuous nucleation.

An interesting condition occurs when nucleation takes place on specific sites such as grain corners which rapidly saturate soon after the transformation begins. Initially, nucleation may be random and growth unhindered leading to the regular values for n ($3 < n < 4$). Once the nucleation sites are consumed, the formation of new particles will cease. In the case of primary transformations where a three-dimensional diffusion controlled growth

© Woodhead Publishing Limited, 2012

rate is expected, the minimum value is $n = 3/2$ which applies in the case of decreasing nucleation rates (Pradell *et al.*, 1988). If the distribution of nucleation sites is non-random, then the growth may be restricted to one or two dimensions. Site saturation may lead to n values of 1, 2 or 3 for surface, edge and point sites, respectively.

In a recent paper, Liu *et al.* (2007) presented an extensive and general analysis of the Avrami kinetics and the implications for both isothermal and isochronal transformations for a wide range of additional assumed conditions. Furthermore, their paper presents detailed recipes on how to correctly derive the effective activation energy and the apparent growth exponent n for isothermal and isochronal transformations.

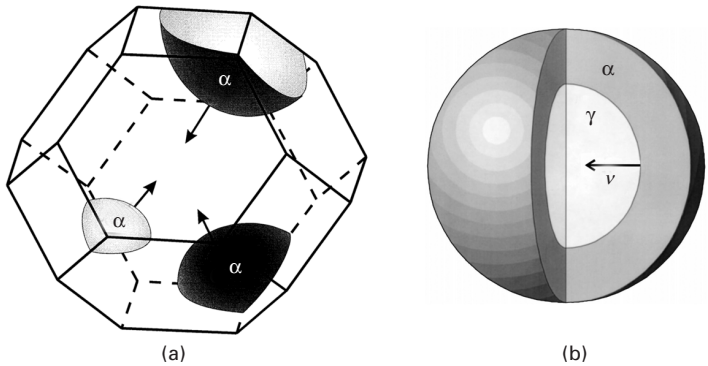
4.3 Geometrical/microstructural aspects in kinetics

While the nucleation and growth concepts and models presented above essentially consider the processes to take place in a continuous space without specific features, in reality the transformation takes place from an austenitic starting structure with grains, having a size, a shape and important features such as grain corners and grain boundaries, which often act as preferred nucleation sites. The significant effect of the geometry of the starting microstructure on the final macroscopic transformation kinetics (without varying the intrinsic kinetics of nucleation and growth processes) has been demonstrated by Van Leeuwen *et al.* (1998). To this aim they used the tetrakaidecahedron model configuration for which the presence of grain boundaries, edges, and corners allows for incorporation of realistic nucleation effects, which is shown to approximate the key feature of the more general Voronoi tessalation (Voronoi, 1907; Aurenhammer, 1991). They compared the results of their tetrakaidecahedron simulation with those for the spherical approximation of an average austenite grain (Vandermeer, 1990). The tetrakaidecahedron configuration leads to 24 grain corners, 36 edges and 14 faces. The earlier spherical geometry allows for the construction of simpler analytical models for calculating the fraction transformed as a function of the interface mobility, but does not allow for proper inclusion of localized nucleation effects. Both configurations are shown in Fig. 4.1.

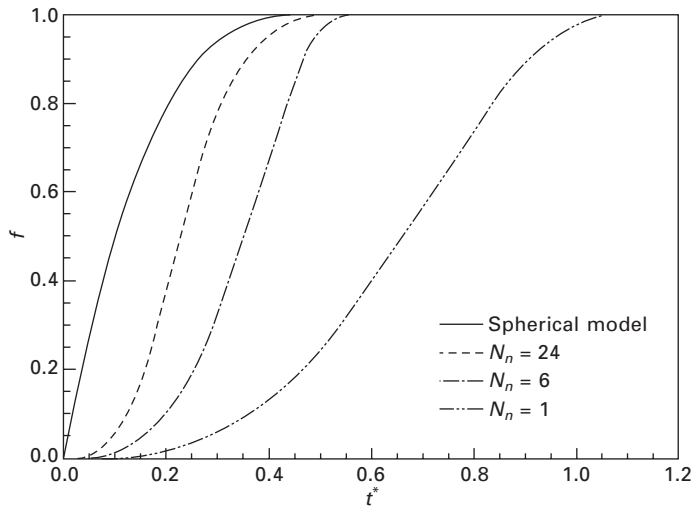
In their simulations the influence of various relevant microstructural parameters (such as the number of active nucleation sites per grain and their relative position) as well as the type of nucleation (site saturation or continuous nucleation) on the macroscopic transformation kinetics were investigated, assuming for simplicity a constant interface velocity. As indicated in the previous section, for a constant interface velocity the Avrami coefficient n obtains a value of either 3 (site saturation) or 4 (continuous nucleation).

The effect of the assumed geometry on the calculated macroscopic transformation behaviour is very large, with the spherical configuration

© Woodhead Publishing Limited, 2012



4.1 (a) Tetrakaidecahedron representation of austenite grain with some ferrite grains. (b) Spherical austenite grain showing partial transformation after uniform nucleation at the grain boundary.

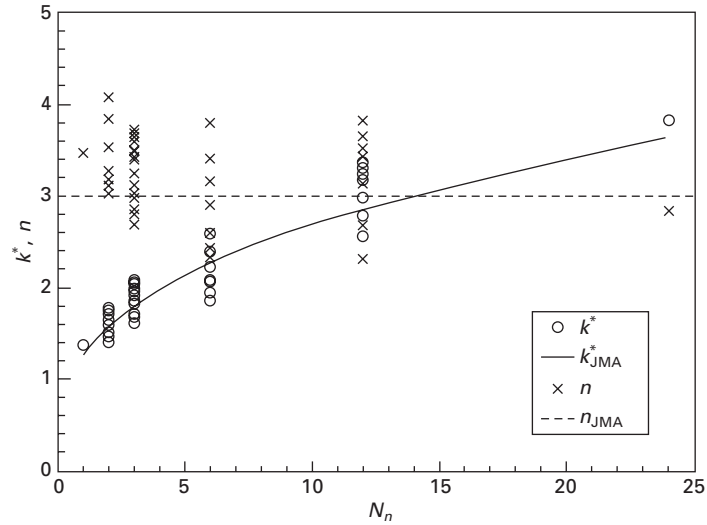


4.2 Calculated transformation curves according to the spherical model and the tetrakaidecahedron model using different values for the number of nuclei, N_n.

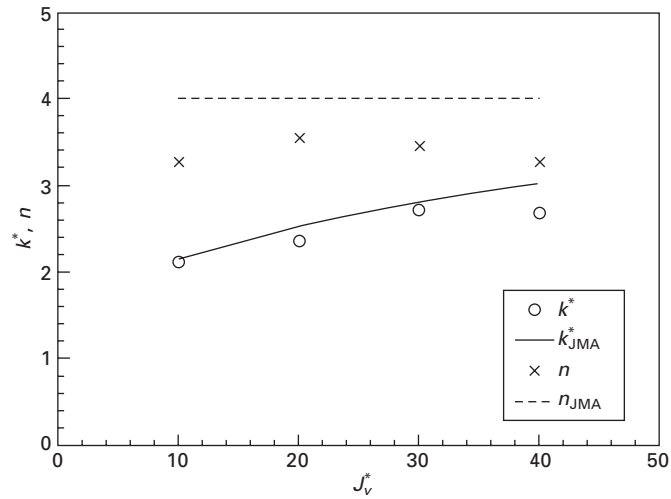
giving initially the fastest transformation rate. For discrete nucleation sites a more sigmoidal transformation behaviour is predicted (Fig. 4.2).

Using the tetrakaidecahedron configuration the effect of the number of active nucleation sites on the apparent Avrami coefficients can be calculated easily. Figure 4.3 shows the effect of the number of sites per grain on the apparent Avrami coefficients k and n in the case of instantaneous nucleation. Depending on the number of active nuclei and their configuration the Avrami coefficient can deviate significantly from the theoretical value for uniform

© Woodhead Publishing Limited, 2012



4.3 Avrami rate constant k and the Avrami constant n as a function of the number of nucleation sites (grain corners) for various configurations.



4.4 JMA fit parameters for several simulations with different nucleation rates and no active nucleation sites present at the very start of the transformation.

nucleation in a uniform space, $n = 3$. The apparent rate constant k seems to be less affected by the geometry.

Figure 4.4 shows that in the case of uniform nucleation the values for n are smaller than the estimated value of 4 and slightly decrease with increasing

© Woodhead Publishing Limited, 2012

nucleation rate J_V. Again, this can be ascribed to the finite dimensions of the starting grain. For the rate factor k^*, a good agreement between the JMA and tetrakaidecahedron kinetics is found. Note that the random nucleation used here is to ensure comparable assumptions for both the tetrakaidecahedron and the JMA model. In practice, the possibility of the tetrakaidecahedron to model heterogeneous nucleation is a step further in the direction of a reliable physical transformation model.

Both Figs 4.3 and 4.4 confirm that, while it is possible to calculate the Avrami coefficient starting with assumed conditions of nucleation and growth and a featureless homogeneous initial state, microstructural features make it impossible to deduce the nucleation and growth conditions from the Avrami coefficients derived from experimental observations.

4.4 Nucleation

During nucleation the austenite phase (γ-Fe) with a face-centred cubic (fcc) lattice structure and a high solubility of interstitial carbon transforms into the ferrite phase (α-Fe) with a body-centred cubic (bcc) lattice structure and a low solubility of interstitial carbon and in general a different solubility for substitutional alloying elements. Although seemingly simple, the nucleation process is very hard to study experimentally since the number of atoms involved in a stable nucleus is very small (of the order of 100 atoms) and the average composition of that nucleus does not deviate significantly from that of the surrounding matrix material. Furthermore, nuclei below the critical size will be short lived and nuclei above the critical size will rapidly grow to larger dimensions. Over the years a variety of idealized model geometries have been proposed (Enomoto and Aaronson, 1986; Tanaka *et al*., 1995; Huang and Hillert, 1996) to describe the initial stage of the ferrite nucleus and characterize the relevant interfacial energies. Given the experimental challenges, an understandably limited number of experimental studies have been performed to test the validity of the proposed model geometries, or the basic assumptions of the classical nucleation theory for homogeneous and heterogeneous nucleation itself. Rare examples of these studies are the *ex-situ* investigations by Crusius *et al*. (1992), Huang and Hillert (1996), Militzer *et al*. (1996) and, more recently, Enomoto and Yang (2008), Savran *et al*. (2010) and Landheer *et al*. (2009). These studies revealed that grain corners are the most favourable nucleation sites for the formation of ferrite grains and suggested that the orientation of some of the interfaces separating the ferrite nucleus from the austenite parent plays an important role. While these studies provide the most detailed knowledge to date, they do not deal with the nucleation process itself but provide information on the early growth stage from which certain aspects of the nucleation process are derived.

An alternative approach to understand the nucleation process is to use

© Woodhead Publishing Limited, 2012

colloidal model systems (Schall *et al.*, 2006; Ramsteiner *et al.*, 2010). The use of colloidal particles simulating atoms allows the direct observation of the packing of individual particles in 3D when using scanning laser confocal microscopy. Notwithstanding the beauty and elegance of such experiments, the colloidal approach is likely only to increase our understanding of the configurational effects on nucleation and not to shed too much light on the important effects of interstitial or substitutional alloying effects.

In the realization that not all factors relevant to nucleation can ever be determined experimentally, the issue of nucleation can for the time being potentially best be addressed from a thermodynamics perspective (van Dijk *et al.*, 2007). When a system is cooled below the phase transformation temperature, the Gibbs free energy of the system can be lowered by the formation of a new phase. The formation of this new phase requires the creation of a new interface between the new phase and the parent phase, which costs interfacial energy. In the case of a solid-state phase transformation in a polycrystalline material, the new phase forms preferentially at structural defects at the grain boundaries of the parent phase and, as a consequence, that distortional energy of the parent phase is released during the formation of the new phase. Generally there is a net energy barrier to form the energetically favourable new phase. The transformation rate to reach thermodynamic equilibrium strongly depends on the size of the energy barrier to form the new phase with respect to the kinetic energy of the atoms.

The change in Gibbs free energy between the new ferrite phase and the parent austenite phase, $\Delta G_{ch} = -\Delta\mu n$ is proportional to the number of atoms n in the cluster of the new phase and the difference in chemical potential $\Delta\mu = \mu_p - \mu_n$ between the chemical potential of the parent phase (μ_p) and that of the new phase (μ_n). The difference in chemical potential $\Delta\mu$ generally increases for a growing undercooling below the transformation temperature T_0. The formation of a cluster of the new phase leads to the creation of additional interface energy from the interfaces between the new phase and the parent phase, σ_{np}, and a release of grain boundary energy from the boundaries between different grains of the parent phase, σ_{pp}. The net interfacial Gibbs free energy of the cluster amounts to

$$\Delta G_s = \sum_i A^i_{np}\sigma^i_{np} - \sum_j A^j_{pp}\sigma^j_{pp} \qquad [4.2]$$

where A_{np} is the surface area of the newly formed interface between the new phase and the parent phase and A_{pp} is the surface area of the consumed boundaries between different grains of the parent phase. The interface and grain boundary energies may be different at different sides of the nucleus. Assuming that the shape of the cluster is independent of the size, the net interfacial Gibbs free energy scales with the total surface area of the cluster, and therefore as $\Delta G_s \propto n^{2/3}$. The net Gibbs free energy needed to form the

© Woodhead Publishing Limited, 2012

cluster interface of the new phase can therefore be expressed as $\Delta G_s = \Delta\Omega\, n^{2/3}$, where $\Delta\Omega$ is a proportionality constant that depends on the geometry of the cluster and the interfacial energies involved.

The total change in Gibbs free energy of the cluster $\Delta G = \Delta G_{ch} + \Delta G_s$ as a function of the size n is then given by:

$$\Delta G(n) = -\Delta\mu n + \Delta\Omega n^{2/3} \qquad [4.3]$$

This equation can be rewritten in terms of dimensionless parameters when the Gibbs free energy of the cluster is normalized by the kinetic energy $k_B T$:

$$\gamma(n) = -\alpha n + \beta n^{2/3} \qquad [4.4]$$

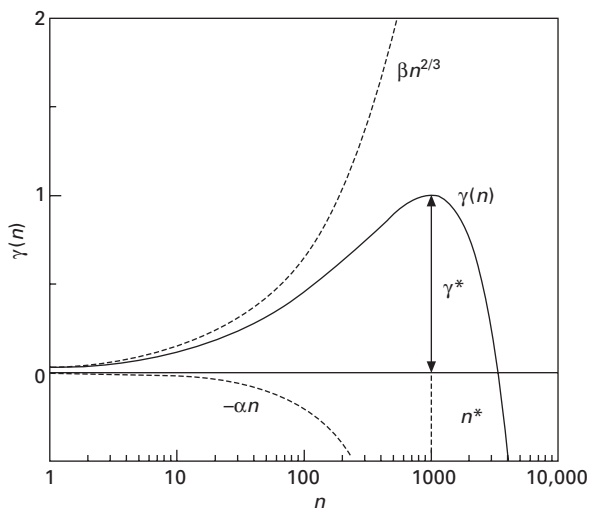
with $\gamma = \Delta G/k_B T$, $\alpha = \Delta\mu/k_B T$ and $\beta = \Delta\Omega/k_B T$. The characteristic behaviour of $\gamma(n)$ as a function of n is shown in Fig. 2.5.

For $\alpha > 0$ ($T < T_0$) and $\beta > 0$, the relative Gibbs free energy $\gamma(n)$ shows a maximum $\gamma^* = \gamma(n^*)$ at a critical cluster size n^*:

$$n^* = \frac{8\beta^3}{27\alpha^3} \qquad [4.5]$$

$$\gamma^* = \frac{\alpha n^*}{2} = \frac{4\beta^3}{27\alpha^2} > 0 \qquad [4.6]$$

A second parameter relevant for nucleation (Offerman *et al.*, 2004) is parameter Ψ, which expresses the relation between the chemical driving force per unit volume $\Delta G_v = N_0\Delta\mu$ and the activation energy for nucleation $\Delta G^* = \Psi/\Delta G_v^2 = \Psi/(N_0\Delta\mu)^2$, where N_0 is the number density of atoms (1/



4.5 Development of γ as a function of the number of atoms n.

© Woodhead Publishing Limited, 2012

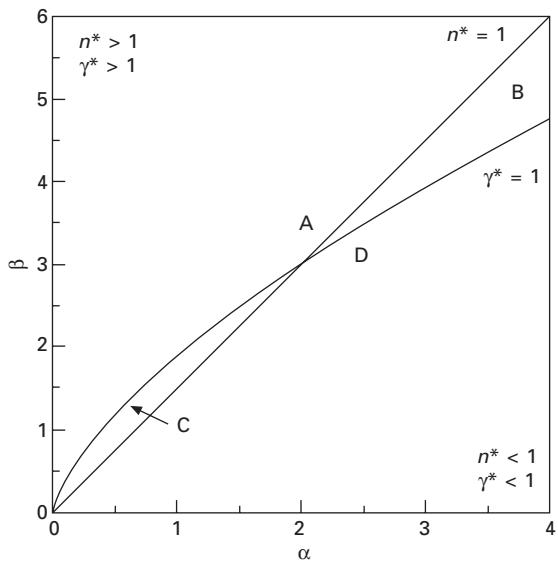
N_0 corresponds to the volume associated to a single atom). The parameter Ψ combines all the relevant information on the formed interfaces and the consumed grain boundaries of the cluster and therefore implicitly also the geometry of the cluster. From an evaluation of Eq. [4.6] we can see that Ψ is directly related to $\Delta\Omega$:

$$\Psi = (N_0 \Delta\mu)^2 \, \Delta G^* = \frac{4}{27} N_0^2 \, \Delta\Omega^3 \qquad [4.7]$$

where we have used $\Delta G^* = \gamma^* k_B T = 4\Delta\Omega^3/27\Delta\mu^2$.

The main result of the classical nucleation theory is that after an initial stage a constant (steady-state) nucleation rate is reached. This result is, however, only valid for $\gamma^* > 1$ and $n^* > 1$. For $\gamma^* < 1$ the energy barrier for the formation of stable clusters is too weak to be effective, while for $n^* < 1$ the concept of a critical cluster breaks down. In both cases there is effectively no barrier for nucleation. As a consequence, the prediction of the classical nucleation theory that, after an initial stage a stable cluster size distribution is formed that leads to the steady-state nucleation, no longer applies. It is important to note that for a solid-state phase transformation with a change in crystal structure, the minimum critical cluster size n^* for which the new phase can be distinguished from the parent phase is generally larger than 1.

The dependence of n^* and γ^* on the parameters α (related to the driving force) and β (related to the interfacial energies) is evaluated in Fig. 4.6.



4.6 Dependence of the critical cluster size n^* and the relative energy barrier for nucleation γ^* as a function of the parameters $\alpha = \Delta\mu/k_B T$ and $\beta = \Delta\Omega/k_B T$.

© Woodhead Publishing Limited, 2012

When we consider the two validity limits ($\gamma^* > 1$ and $n^* > 1$) of the classical nucleation theory independently, four different regions can be distinguished. The lines $\gamma^* = 1$ and $n^* = 1$ that separate these regions reflect a gradual cross-over between qualitatively different types of nucleation behaviour. Region A is described by the classical nucleation theory (with steady-state nucleation). The other three regions (B, C and D) correspond to *effectively* barrier-free nucleation. Region B applies for strongly undercooled systems with a high net interfacial energy $\Delta\Omega$ (Kashchiev, 2000). Region D applies to spinodal decompositions and cluster aggregations, where the net interfacial energy is very weak or absent (Yang *et al.*, 2006). Region C qualitatively differs from regions B and D as the energy barrier for nucleation is weak, while the critical cluster size is still significant. In region C the cluster growth is initially uphill ($n^* > 1$), while in regions B and D it is downhill from the start ($n^* < 1$). Region C only occurs for a limited range of parameters and has to our knowledge not been studied so far. As we will see later, this region can be relevant for heterogeneous nucleation in solid-state phase transformations where the net interfacial energy $\Delta\Omega$ is relatively low. In these systems the energy needed to form an interface between the new and the old phase is nearly compensated by the removal of the grain boundary between different grains of the parent phase for certain preferential nucleation sites (e.g. grain corners). For the barrier-free nucleation in regions B, C and D, no steady-state nucleation is found. The rate of formation of new stable clusters of the new phase is controlled by cluster dynamics and is intrinsically time-dependent.

For region A the formation rate of stable clusters ($n > n^*$) is expressed by (Kashchiev, 2000; Mutafschiev, 2001; Kelton *et al.*, 1983; Kelton, 1991):

$$\dot{N}_{ss} = N_p \omega^* Z e^{-\gamma^*} \qquad [4.8]$$

where $\dot{N}_{ss}$ is the steady-state nucleation rate for the formation of new grains per unit volume, N_p is the density of potential nucleation sites, ω^* is the rate constant, and Z is the so-called Zeldovich factor. The Zeldovich factor Z accounts for the fact that only cluster sizes with an energy within $k_B T$ from $\Delta G^* = \Delta G(n^*)$ can effectively cross the energy barrier for nucleation. For conditions in which nucleation is relatively slow compared to the growth, the potential nucleation sites are mainly consumed by growth. In this case N_p is proportional to the untransformed volume fraction. Alternatively, for relatively fast nucleation, as in austenite decomposition, growth has a negligible effect and N_p is mainly defined by the number of grains formed per unit volume N.

The rate constant for a critical nuclei of size n^* is given by the well known equation

© Woodhead Publishing Limited, 2012

$$\omega^* = (n^*)^{2/3} c_0 \nu_0 \exp(-Q/k_B T) = \left(\frac{4\beta^2}{9\alpha^2}\right) c_0 \nu_0 \exp(-Q/k_B T) \qquad [4.9]$$

The rate of formation of stable clusters of the new phase is controlled by cluster dynamics and is intrinsically time-dependent. The cluster dynamics responsible for the formation of stable grains of the new phase in the matrix of the parent phase can be characterized by the following simplified process where only single atom attachment and detachments to the cluster are considered:

$$[C(n)] \underset{k^{(n+1,n)}}{\overset{k^{(n,n+1)}}{\rightleftarrows}} [C(n+1)] \qquad [4.10]$$

where $C(n)$ is the concentration of new-phase clusters of size n and $C(n+1)$ is the concentration of clusters of size $n + 1$. The clusters of size n have a transition rate $k^{(n,n+1)}$ to clusters of size $n + 1$ and the clusters of size $n + 1$ have a transition rate $k^{(n+1,n)}$ to clusters of size n. The transition rates $k^{(n,n+1)}$ and $k^{(n+1,n)}$ are directly related to the size dependent relative Gibbs free energy of the cluster (Slezov and Schmelzer, 1994):

$$k^{(n,n+1)} = \omega \frac{e^{-\gamma(n+1)}}{e^{-\gamma(n+1)} + e^{-\gamma(n)}} = \omega \frac{e^{-W}}{1 + e^{-W}} \qquad [4.11]$$

$$k^{(n+1,n)} = \omega \frac{e^{-\gamma(n)}}{e^{-\gamma(n)} + e^{-\gamma(n+1)}} = \omega \frac{1}{1 + e^{-W}} \qquad [4.12]$$

where $W = \gamma(n + 1) - \gamma(n)$ and $\omega \propto n^{2/3}$ is the size dependent rate constant for atom attachments and detachments introduced in Eq. [4.7].

From the cluster dynamics (van Dijk *et al.*, 2007), an effective nucleation rate $\dot{N}_{\text{eff}}$ was derived that applies to both steady-state nucleation and barrier free nucleation (independent of γ^* and n^*) by considering the net number of clusters per unit of time that reaches the critical size $n = n^+$ for which the thermal energy is insufficient to dissolve the cluster:

$$\dot{N}_{\text{eff}} = [k^{(n^+,n^+ +1)} C(n^+) - k^{(n^+ +1,n^+)} C(n^+ +1)] \qquad [4.13]$$

The critical size n^+ is defined by the condition $\gamma(n^+) = \gamma^* - 1$ with $n^+ > n^*$. For nucleation regime A ($\gamma^* > 1$ and $n^* > 1$) $\dot{N}_{\text{eff}}$ approaches the steady-state nucleation rate after an initial time dependent stage.

The concepts presented above can now be applied to the kinetics for ferrite formation. The gain in chemical potential $\Delta\mu$ below the transformation temperature A_3 acts as the driving force for the heterogeneous nucleation of ferrite grains. This gain in chemical potential depends both on temperature and on the fraction transformed. The temperature dependence is to a good approximation described (Kashchiev, 2000; Mutafschiev, 2001) by:

© Woodhead Publishing Limited, 2012

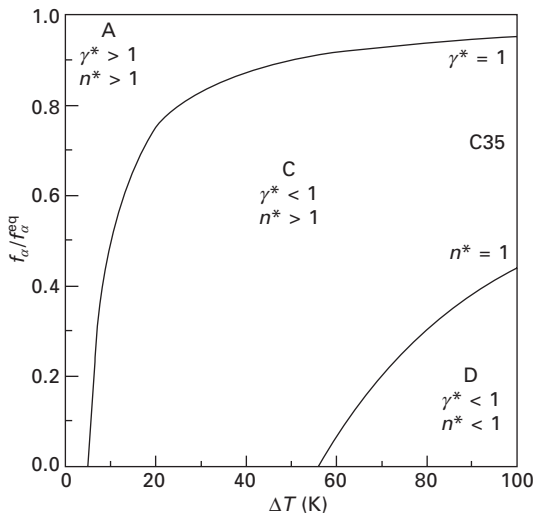
$$\Delta\mu(T) \approx \left(\frac{d\Delta\mu}{dT}\right)(A_3 - T) \propto (A_3 - T) \qquad [4.14]$$

where $(A_3 - T)$ is the undercooling with respect to the transformation temperature A_3 and $(d\Delta\mu/dT)$ is the temperature derivative of $\Delta\mu$, which is roughly constant. Once the new ferrite phase is formed, the parent austenite phase enriches in carbon due to the small solubility of carbon in ferrite ($x_C^{\alpha} \approx$ 0.022 wt%). As a consequence, the transformed fraction of ferrite f_α reduces the gain in chemical potential $\Delta\mu$. To a first approximation, the dependence of the gain in chemical potential $\Delta\mu$ on the transformed fraction of ferrite f_α can be approximated by:

$$\Delta\mu(f_\alpha) \approx \Delta\mu(f_\alpha = 0)\left(1 - \frac{f_\alpha}{f_\alpha^{eq}}\right) \propto \left(1 - \frac{f_\alpha}{f_\alpha^{eq}}\right) \qquad [4.15]$$

where f_α^{eq} is the equilibrium ferrite fraction at temperature T.

Inserting thermodynamic data and data from micro-beam diffraction experiments (Offerman *et al.*, 2002), the nucleation regimes for a typical low alloyed engineering steel C35 (0.35 wt% carbon, 0.8 wt% Mn) as a function of two control parameters, the undercooling ΔT and the fraction transformed f_α/f_α^{eq} can be calculated and results are shown in Fig. 4.7. According to the calculations, the system can be in one of three different nucleation regimes (A, C, and D), depending on the undercooling and the fraction transformed. For an undercooling ΔT smaller than $\Delta T_{\gamma^*=1}$, the system always shows an energy barrier for nucleation that is larger than the kinetic energy of the



4.7 Nucleation type as a function of the undercooling.

© Woodhead Publishing Limited, 2012

atoms (regime A). For an undercooling ΔT larger than $\Delta T_{\gamma^*=1}$ the nucleation initially shows either a weak barrier for $\Delta T < \Delta T_{n^*=1}$ (regime C) or no barrier for $\Delta T > \Delta T_{n^*=1}$ (regime D) and eventually shows a cross-over to $\gamma^* > 1$ (regime A) when the transformation proceeds. From Fig. 4.7 it is clear that essentially barrier-free nucleation is quite possible and is even the most likely mode of nucleation for many industrial applications.

Although it is clear that much more work is needed to understand and quantify the nucleation phenomena, it is also obvious that the impossibility of direct and quantitative observations of the ferrite nucleation process itself will make the chances of real progress in the coming years rather slim. However, an interesting approach to address the nucleation issue indirectly comes from a recent 3D phase field simulation study by Mecozzi *et al*. (2008). In their simulations they studied the effect of both the interfacial growth kinetics and the width of the temperature range below the A_3 temperature over which nucleation was assumed to take place on the transformation behaviour. More or less as a side effect of their simulations, they found a relation between the nucleation temperature range and the width of the final ferrite grain size distribution. Such information on the range of the nucleation temperatures may be used in fine tuning the current approximate models used in industrial processing.

4.5 Growth

The growth of ferrite out of the parent austenite phase, except for the case of pure iron or extremely dilute alloys, not only involves the displacement of the interface between the two crystal phases but also the redistribution of solute atoms as their solubility in either ferrite or austenite is never identical. So, in line with all solid state phase transformations proceeding via a sharp and well-defined interface, the growth of ferrite can be approached by focusing on the kinetics of the diffusional partitioning of the solutes and taking the intrinsic interface mobility as a kinetically non-significant parameter (diffusion controlled models) or by focusing on the intrinsic mobility of the interface and ignoring the contribution of the partitioning of the solutes (interface controlled models). The concepts of both approaches and their implications have been described in landmark papers and reviews (Zener, 1946; Purdy and Kirkaldy, 1963; van der Ven and Delaey, 1996; Hillert, 1999; Christian, 2002, Hillert and Ågren, 2004). The core element of the diffusion controlled models is that the concentrations at both sides of the interface are prescribed according to the assumed thermodynamic-thermokinetic concept with far field diffusion being described by Fickian diffusion laws. The core element of the interface controlled model is that the movement of the interface will not wait for the supply or expulsion of solute atoms and will proceed as a result of the difference in thermodynamic driving force on both sides of the interface.

© Woodhead Publishing Limited, 2012

Relatively recently, so-called mixed-mode models for the solid state phase transformations in binary alloys in which the interface mobility and the diffusional partitioning both play a role have been proposed (Krielaart *et al.*, 1997; Svoboda *et al.*, 2001; Sietsma and van der Zwaag, 2004, Bos and Sietsma, 2007). Such a combination of an intrinsic interface mobility and diffusional redistribution is also assumed in phase field models. Mixed-mode model predictions suggest that initially the phase transformation proceeds as if interface controlled conditions apply, while in later cases the diffusional character becomes more important. The original mixed-mode model was developed for systems in which only one alloying element is present and the analysis was relatively simple leading to the following equation for the interface mobility v

$$v = M\Delta G \qquad [4.16]$$

where M is the intrinsic (temperature dependent) interface mobility and ΔG the thermodynamic driving force which is the sum of the differences in thermodynamic potential for each alloying element across the interface

$$\Delta G = \sum_{i=1}^{N} x_i^{\alpha} (\mu_i^{\gamma} - \mu_i^{\alpha}) \qquad [4.17]$$

In the original treatment the initial compositions of austenite were taken to be the nominal composition and the initial composition of the ferrite was taken to be the ferrite equilibrium and the build-up of the interface concentration followed from mass-conservation considerations. The original binary mixed-mode model has recently been extended and generalized by Bos and Sietsma (2009) who considered systems with multiple partitioning elements and took the maximum rate of free energy gain as the deciding factor for the partitioning of the solute elements. Unlike the earlier models of local equilibrium (LE) or negligible-partitioning (NPLE) (see the review by Van de Ven and Delaey, 1996) in which the partitioning or non-partitioning of the solute atoms is prescribed in the model, the transition from full partitioning to negligible partitioning of substitutional alloying elements under continuous cooling conditions follows automatically from the mixed-mode negligible partitioning simulations. The transition from NPLE to LE behaviour has also been addressed by Zurob *et al.* (2008, 2009), but their approach required the introduction of an additional interfacial segregation concept.

While the Bos–Sietsma mixed-mode model provides a general and valuable framework covering both interface and diffusional transformations as well as LE and NPLE conditions without making *a priori* assumptions, it now becomes very important to determine the intrinsic interfacial mobility M with greater accuracy. The first attempts to determine the interface mobility used regular austenite to ferrite transformation curves as the fit data and, by making appropriate assumptions on the nucleation behaviour as well as

© Woodhead Publishing Limited, 2012

the grain size (Krielaart *et al.*, 1997; Wits *et al.*, 2000), there remains quite some uncertainty on the exact value of the interfacial mobility, although the original value proposed by Krielaart *et al.* (1997), $M_0 = 0.8 \exp(-140\ 10^3/RT)$ mol mJ^{-1} s^{-1}, was validated independently by Odqvist in 2011. The major reason for the uncertainty in the determination of the interfacial mobility is that the number of adjustable parameters to describe a regular transformation curve for cooling from the fully austenitic starting state to the fully transformed state is too large, and the shape of the transformation curve lacks features that can be used to discriminate between the models.

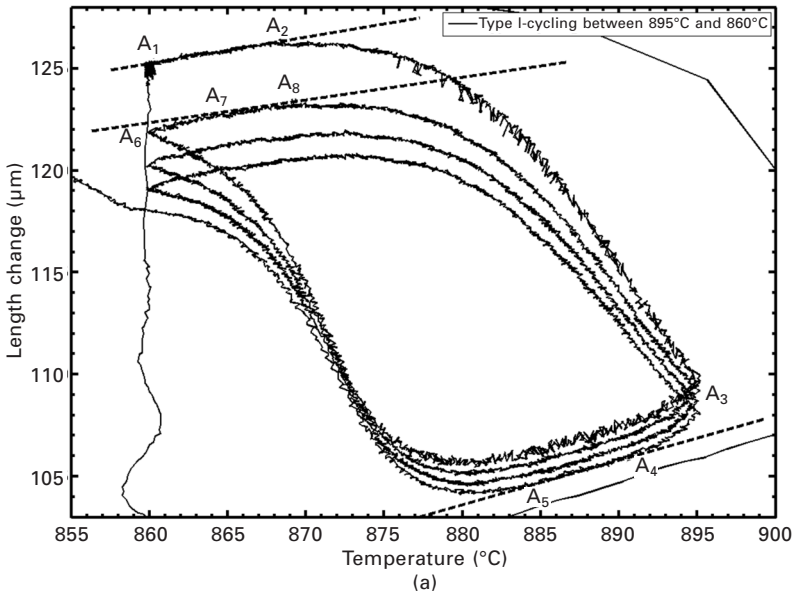
To address this issue a new experimental concept, the cyclic partial transformation, has been proposed and explored by Chen and van der Zwaag (Chen and van der Zwaag, 2010; Chen *et al.*, 2011). In this new arrangement, the material is not fully transformed but thermally cycled well within the two-phase region and making sure that ferrite and austenite are always present. For such an experiment, the effect of nucleation on the transformation curve can be excluded. Furthermore, the cyclic transformation curve shows far more features than a usual transformation curve, such as a stagnant stage, a transformation stage and an inverse transformation stage, which can be used to discriminate between the various growth modes and to allow a better estimation of the interfacial mobility value. An example of the experimental and calculated (LE and NPLE mode) transformation curves for a lean C-Mn steel is shown in Fig. 4.8. Clearly the LE model does not describe all experimentally observed features for a cyclic experiment, while both models describe the transformation curve starting from a fully austenitic state equally well.

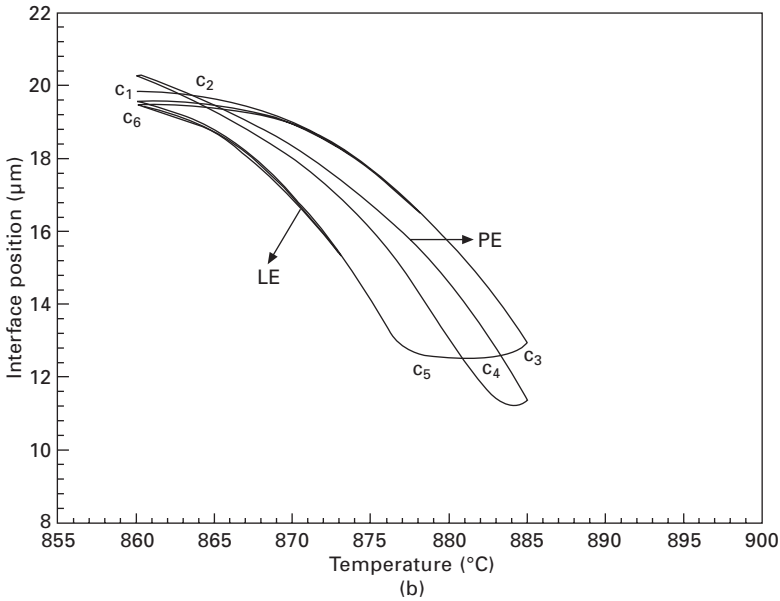
Finally, while in recent years there has been excellent progress in our understanding of the precise conditions of the growth mode of ferrite from austenite, our models remain an idealization of the real transformation behaviour. Microbeam X-ray diffraction experiments by Offerman *et al.* (2002, 2004), to follow the growth of several individual ferrite grains during a single cooling experiment, have shown that individual grains can follow growth kinetics in accordance with diffusional growth models, with mixed-mode growth models or can show features not predicted by either model. Apparently, even in a small, nominally homogeneous sample, the transformation kinetics of individual grains may be different.

4.6 Experimental methods

As the austenite decomposition is a proper phase transformation, the decomposition leads to a change in a number of physical properties of the sample. As the changes are often (linearly or non-linearly) related to the fractions of the phases present during the transformation, a number of physical characterization techniques have been developed to follow the

© Woodhead Publishing Limited, 2012





4.8 (a) Experimental dilatation signal for cyclic transformation experiment; (b) calculated transformation curves for cyclic transformation curves for the steel composition and thermal conditions as employed for the experiment in (a).

© Woodhead Publishing Limited, 2012

transformation *in-situ*. Some of the more powerful techniques to follow the austenite decomposition are described below. They make use of the change in atomic volume and hence the sample dimension, the specific heat and heat of transformation, the crystal structure, the acoustic wave velocity and the acoustic attenuation and finally the magnetic properties of the ferrite formed, respectively.

4.6.1 Dilatometry

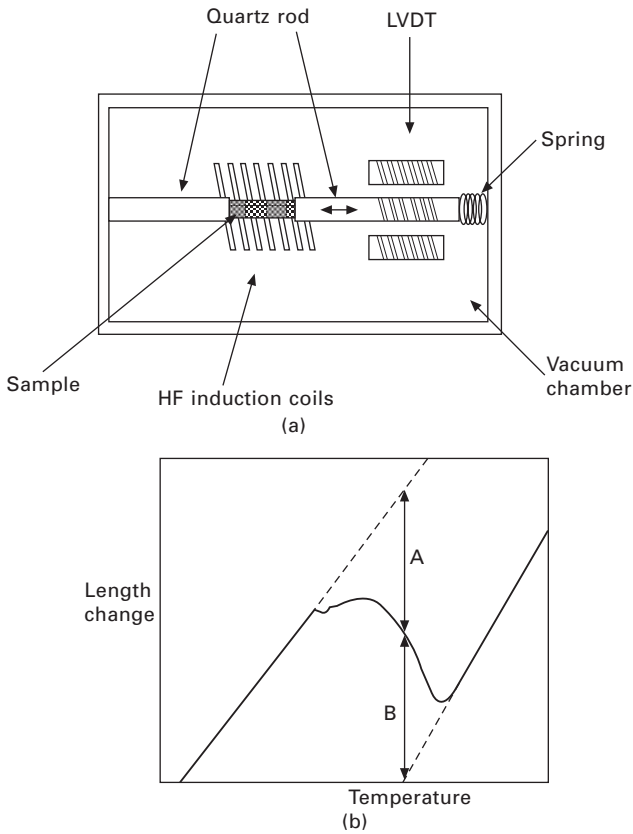
The most important and most widely used experimental method to study the kinetics of the austenite decomposition is dilatometry, i.e. the measurement of the length change as a function of temperature and time. The technique has three major advantages:

1. with modern (inductive or direct current) heating and (forced gas) cooling systems, it is possible to vary the heating and cooling rates over a very wide range from typically 1000°C/s to 0.001°C/s and to hold the temperature constant at specific temperatures during a cooling or heating cycle,
2. the recorded signal, i.e. the dilatation, is a measure of the total degree of transformation up to that point rather than a measure of the transformation rate and
3. the method is relatively cheap both from an instrument and a sample perspective.

A schematic diagram of the dilatometer and the recorded signal as a function of the temperature for normal linear cooling from the austenitic state is shown in Fig. 4.9. The dilatation curve of Fig. 4.9(b) essentially consists of three parts: a more or less linear contraction at high temperatures, with is due to the thermal contraction of the austenite, a clearly non-linear segment at intermediate temperatures reflecting the decomposition of the austenite into ferrite and perlite, and a more or less linear part at lower temperatures reflecting the thermal contraction of the reaction products ferrite and perlite. The expansion of the sample during the transformation is due to the difference in atomic volume for the initial carbon enriched austenite and that of ferrite and cementite. The atomic volume of the relevant phases V_i is linked to their lattice parameters by $V_\alpha = a_\alpha^3/2$, $V_\gamma = a_\gamma^3/4$, $V_\theta = a_\theta b_\theta c_\theta/12$, where α is ferrite, γ is austenite and θ is cementite and a, b and c are the lattice constants.

In dilatometry, it has been customary to calculate the degree of transformation by applying the so-called 'lever rule' after extrapolating the linear parts of the dilatation curves (see Fig. 4.9(b)). For the condition sketched in Fig. 4.9(b), the ferrite fraction is given by B/(A+B). It has been pointed out (Onink *et al.*, 1996; Kop *et al.*, 2001a) that, apart from microstructural features such as banding (Kop *et al.*, 2001b; Dong-Woo *et al.*, 2007) and transformation

© Woodhead Publishing Limited, 2012



4.9 (a) Schematic diagram of a dilatometer and (b) the dilatation signal for linear cooling from the austenitic state, including the procedure for the application of the 'lever rule'.

plasticity (Gautier *et al*., 1987; Zwigl and Dunand, 1999), this procedure is essentially incorrect for two reasons:

- During the ferrite formation, the carbon is expelled from the ferrite into the austenite. The resulting carbon enrichment of the austenite leads to an increase in the lattice parameter and therefore to a change in atomic volume. The temperature and carbon dependence of the austenite lattice parameter for high purity Fe-C alloys has been measured by Onink *et al*. (1993). The effect of substitutional alloying elements on the austenite lattice parameter has been compiled by van Dijk *et al*. (2005).
- The simultaneous formation of ferrite and perlite during the later stages of the transformation. The application of the lever rule can lead to significant underestimations of both the instantaneous ferrite fraction (up to 15% underestimation at the start of the pearlite formation) and a gross underestimation of the perlite fraction. The latter is due to the

© Woodhead Publishing Limited, 2012

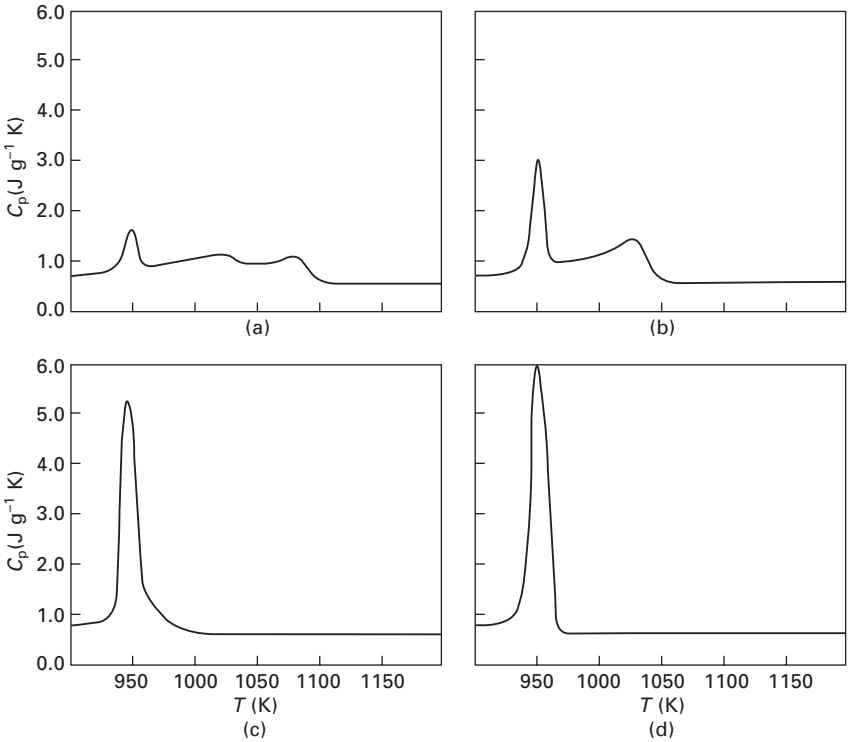
fact that the average atomic volume of perlite is about equal to that of austenite enriched up to the pearlite onset level. Hence, the formation of a substantial pearlite fraction leads to a minor length change. Various methods have been proposed to correct for these effects (Onink *et al.*, 1996; Kop *et al.*, 2001a; Choi, 2003; Lee *et al.*, 2007) to obtain more accurate estimates of the actual ferrite and pearlite fractions from the dilatational signal.

4.6.2 Differential scanning calorimetry

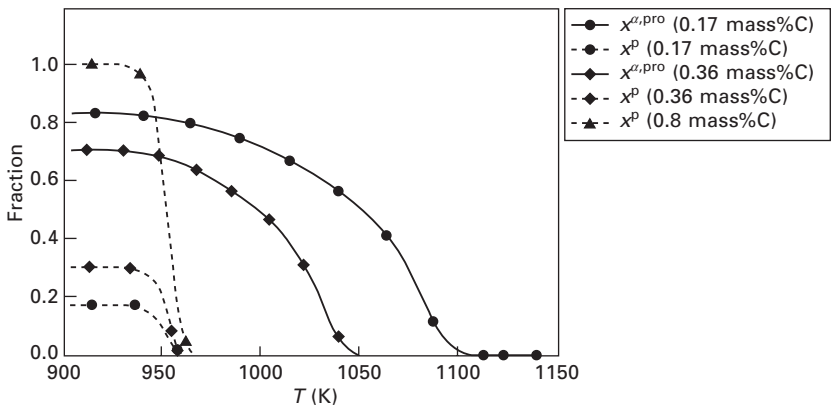
Differential scanning calorimetry (DSC) is a commonly used thermal analysis technique in the investigation of reaction and transformation kinetics in a wide range of materials and makes use of the heat effects involved in a phase change. The determination of the reaction rates and the fraction transformed involves a detailed analysis of the heat fluxes as a function of time and temperature. To determine the fraction transformed, the effects of the temperature dependence of the specific heat and the latent heats (Tajima and Umeyama, 2002; Tajima *et al.*, 2004) must be taken into account properly using procedures as defined in the textbooks (Speyer, 1994). For austenite the temperature dependence of the specific heat is relatively mild and monotonic and only weakly dependent on the carbon concentration, but the temperature dependence of the specific heat of ferrite is very strong showing a very strong peak at the Curie temperature. As a result the heat of formation of ferrite also depends strongly on the temperature at which the ferrite is formed and ranges from –20 kJ/kg at 900°C to –100 kJ/kg at 600°C. Unlike the small change in length upon the transformation of enriched austenite into pearlite, the thermal effect of this transformation is very large with an enthalpy difference of about 85 kJ/kg and hence easily detectable.

Typical examples of the effective thermal heat capacities during cooling at a constant cooling rate of 20 K/min for four binary Fe-C alloys of various C levels are shown in Fig. 4.10 (after Krielaart *et al.*, 1996). The curve for Fe-0.17 wt%C alloy shows three peaks. The peak at 1080 K is related to a high rate of ferrite formation, the peak at 1040 K is related to the magnetic peak at the Curie temperature and the peak at 950 K is related to the pearlite formation. For the Fe-0.36 wt%C alloy, only two peaks are present as the peak for the ferrite formation coincides with the Curie peak. For the Fe-0.57 wt%C curve all ferrite formation takes place below the Curie temperature and the peak related to the initial ferrite formation manifests itself as a shoulder on the pearlite peak. For the Fe-0.8 wt%C alloy the only peak is related to the pearlite formation. However, after properly correcting for the temperature dependencies of the specific heats and enthalpies, simple and continuous transformation curves are obtained as shown in Fig. 4.11 (from Krielaart *et al.*, 1996).

© Woodhead Publishing Limited, 2012



4.10 Heat capacities of high purity Fe-C alloys at a cooling rate of 20 K/min. (a) Fe-0.17 wt% C, (b) Fe-0.36 wt%C, (c) Fe-0.57 wt% C and (d) Fe-0.8 wt%C.



4.11 Calculated fractions of pro-eutectoid ferrite and pearlite as a function of temperature for three Fe-C alloys, using the raw data as presented in Fig. 4.10.

© Woodhead Publishing Limited, 2012

Similar analyses have been performed for Fe-Mn alloys (Li *et al.*, 2002), Cr steels (Tajima *et al.*, 2004) and Cr-Mo steels (Gojic *et al.*, 2004; Raju *et al.*, 2007) to determine chemical composition effects.

It should be pointed out that the applicability of DSC for austenite transformations is somewhat limited as the range of heating and cooling rates is much lower than for modern dilatometers. Furthermore, as the heat flow is directly proportional to the rate of transformation rather than the degree of transformation, the technique is also not very suitable for slow isothermal transformations. However, the information as obtained from DSC measurements is extremely valuable for designing and controlling industrial installations such as the run-out table in a hot-strip mill, in which the cooling conditions are imposed in order to obtain specific cooling rates required to generate the desired transformation product (see also Section 4.7).

4.6.3 X-ray diffraction

Given that the decomposition of austenite involves a phase change from the parent austenitic face-centred-cubic (fcc) crystal structure to the new ferrite body-centred-cubic (bcc) crystal structure, X-ray diffraction can in principle be used to monitor this transformation. However, given that for normal laboratory X-ray sources the time to record diffractograms is relatively long and only a thin surface layer is probed, the technique has been used primarily for quantification of static microstructures and not for time resolved measurements. With the advent of more powerful and hard X-ray sources such as synchrotrons, time resolved studies could be made, even for conditions as encountered in welding (Babu *et al.*, 2002; Palmer *et al.*, 2004; Komizo and Terasaki, 2011). However, for transient conditions such as in welding a quantitative analysis of the kinetics is impossible. A more informative method to follow the transformation of the decomposition of austenite, even down to the level of events taking place at the level of single grains has been developed by Offerman *et al.* (Offerman *et al.*, 2002; Offerman *et al.,* 2004; Savran *et al.*, 2010) using the instrumental methodology developed by the Reiso team (Lauridsen *et al.*, 2000; Margulies *et al.*, 2001; Poulsen, 2004). The method makes use of the high intensity of a synchrotron beam which allows collimation of the beam down to a size of $40 \times 40\ \mu m^2$, yet allowing a sufficient intensity to result in a scan time for a full 2D diffractogram of 1 second. For such a small beam size the number of grains hit by the beam is relatively small (of the order of 300–500 grains) and as a result individual diffraction spots per grain on the detector. By measuring the spot intensity as a function of time for successive recordings, the volumetric growth (or shrinkage) of individual grains can be derived. Furthermore, from the small shifts in the position of austenite spots on the detector the carbon enrichment can be followed too. A typical example of a 2D diffractogram half-way during

© Woodhead Publishing Limited, 2012

the transformation and four distinctive types of growth curves for individual ferrite grains is shown in Fig. 4.12(a) and (b), respectively. Clearly, this synchrotron based XRD technique is very powerful in unravelling details of the transformation at the level of individual grains, yet requires access to a synchrotron and dedicated software to analyse the very large data sets for a single experiment.

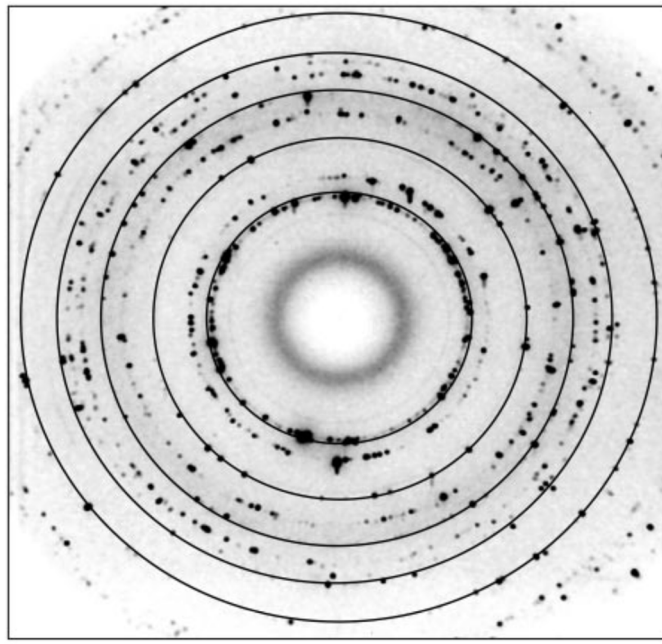
4.6.4 Laser ultrasonics

While very informative about the kinetics of the austenite decomposition and the reaction products formed, the techniques discussed above do not allow on-line determination of the transformation. A relatively new technique to measure the phase transformation kinetics as well as other structural transformations under real production conditions at a hot strip mill is laser ultrasonics (Scruby and Moss, 1993). The technique is based on creating a shock pulse in the material by applying a laser pulse (typically 2–10 ns duration and energy levels of 10^4 J/m^2) and detecting the travelling wave some distance away from the illuminated site using a second laser and laser interferometry. Using this method, both the attenuation (due to scattering at microstructural defects such as grain and phase boundaries) and changes in wave velocity (linked to phase changes and to loss of texture) can be detected. Hence, the technique has been used to monitor processes such as austenite recrystallization (Smith *et al.*, 2006), austenite grain growth (Dubois *et al.*, 2000) and ferrite recovery (Smith *et al.*, 2007). These studies focused on the link between the metallurgical process and the wave attenuation factor. Monitoring the austenite decomposition was found to be easier using the wave velocity change (Dubois *et al.*, 1998, 2001; Kruger and Damm, 2006). It was found that for C-Mn steels with carbon concentrations above 0.05 wt%, the technique could follow the decomposition process in hot-rolled steels and even distinguish between ferrite formation and pearlite formation. The measurements are affected by the occurrence of the magnetic transition at the Curie temperature and the presence of a well-developed texture. While not yet a fully quantitative technique, the laser ultrasonics method seems very promising for in-line application in hot-rolling mills.

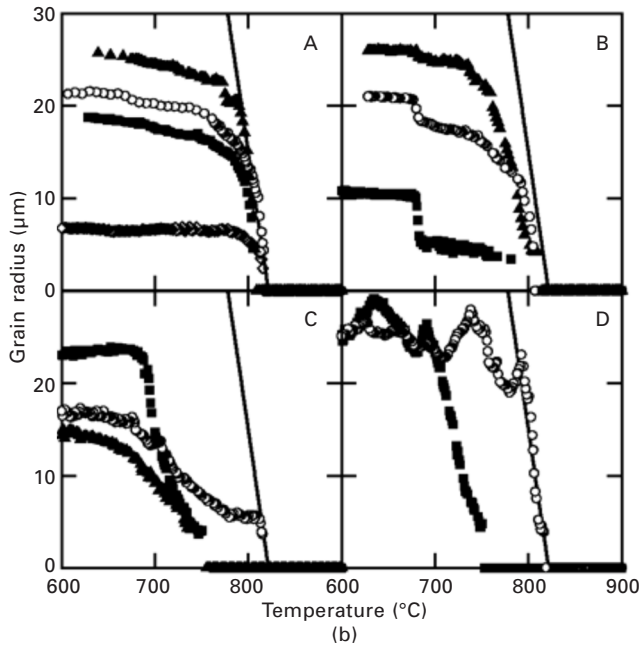
4.6.5 Neutron depolarization

A very interesting, yet rarely used method for following the formation of ferrite and pearlite is the neutron depolarization (ND) technique. This technique makes use of the fact that neutrons have a magnetic component, a spin, which probes local magnetic fields in materials. The technique has been developed at the TU Delft for the determination of domain sizes in magnetic materials, such as thin films, amorphous glasses and other materials

© Woodhead Publishing Limited, 2012



(a)



(b)

4.12 (a) Diffractograms half way during the transformation. Diffraction spots on the drawn rings correspond to ferrite grains. (b) Distinctive growth modes for four ferrite grains in a single experiment (from Offerman *et al.*, 2002).

© Woodhead Publishing Limited, 2012

(Rekveldt, 1973; Rosman and Rekveldt, 1991). Using a polarized beam and following the Larmor precession of the neutrons upon its transmission through a sample in three dimensions, information on both the magnetic fraction and the average magnetic domain size is obtained simultaneously. Realizing that ferrite formed below the Curie temperature is magnetic, the ND technique has been used successfully to follow *in-situ* the formation of ferrite and pearlite in medium carbon steels (te Velthuis *et al.*, 1997, 2000a; van Dijk *et al.*, 1999). Since the method probes both the ferrite fraction and the average ferrite grain size simultaneously, the ND measurements allow the determination of nucleation sites active during the transformation as well as the average growth of the ferrite grains. Furthermore, by carefully analysing the depolarization matrix and comparing the experimentally determined matrix with the matrix calculated for various spatial configurations of the nuclei in a representative volume of the sample, it is even possible to deduce information on the microstructure formation as such (te Velthuis *et al.*, 2000b). Although the ND technique is arguably the most informative technique to follow the austenite decomposition, its application has so far been very limited as the technique requires a powerful neutron source, extensive instrumental developments and is restricted to steel grades for which the A3 temperature is above the Curie temperature of iron (770°C) and to low cooling rates.

4.7 Industrial relevance

Steel, being one of the most important construction materials in western society since the Industrial Revolution in the 18th and 19th century, is being produced in very large quantities, with a current world capacity of 1.4 billion tons of steel per year. An increasing part of this production volume is now produced in Asia and the steel production level is a key component and requirement in the industrial growth of the region.

The net steel production rate of an integrated steel plant depends on the mass flow rate in the successive production units. For each of the production units the production rate is determined by the dimensions and layout of the installations, the kinetics of the heat transfer, the kinetics of the chemical processes and the kinetics of the metallurgical processes ultimately leading to the desired microstructures and properties. For lean steel grades, the most important metallurgical process controlling the mechanical properties is the solid state phase transformation of austenite to ferrite (and its related phases bainite and martensite). This transformation takes place on the run-out table of a strip mill, which is located in between the last stand of the finish rolling mill and the coiler. At this run-out table, cold water is sprayed in controlled quantities and at a large number of positions along the length of the run-out table to cool the steel strip from its initial high temperature of around 900°C

© Woodhead Publishing Limited, 2012

to typically 500–300°C and to remove the heat of transformation using so-called laminar cooling (Uetz *et al.*, 1991; Hollander, 1994). Traditionally, the length of the run-out table for a larger steel mill is of the order of 100–150 m and, with a typical final rolling speed of 10 m/s, this gives a maximum time for the transformation of 15 seconds or less. Apart from other constraints, this maximum available time for transformation sets the range of chemical compositions which can be rolled on a particular rolling mill. By changing the local intensity of the cooling process, a change in the balance between nucleation and growth can be adjusted leading to a change in the ferrite grain size or even in a change in reaction product. Both changes are tools to vary the mechanical properties of a steel of a given composition.

While such a long run-out table and a relatively long maximum available transformation time offer many opportunities to tune the mechanical properties, it also means that the fine details of the kinetics of the transformation need to be known quite precisely. When the composition of the steel is very lean, i.e. the concentration of alloying elements is very low, the transformation proceeds very rapidly anyway and much shorter cooling units of only 5 m effective length and higher cooling intensities of up to 750°C/s have been developed. Such compact ultra-fast cooling units lead to far more compact installations and lower capital investments and hence are being used in modern direct strip installations.

On the other side of the kinetic spectrum one finds the modern superbainite steels developed by Bhadeshia's group (Garcia-Mateo *et al.*, 2005; Hasan *et al.*, 2010) where the very slow transformation rates leading to transformation times of up to one day or more, form a major obstacle in the commercial development of these steels, notwithstanding their outstanding mechanical properties.

In conclusion, the kinetics of the austenite-ferrite transformation, or more generally, the decomposition of austenite in any of the low temperature phases, is of crucial importance for steel production. For given dimensions of a steel plant, the austenite-ferrite transformation kinetics determine the production volume, the range of steel grades that can be processed and the range of properties, for a given composition, that can be obtained.

4.8 Acknowledgements

The author gratefully acknowledges the long-standing collaboration with his research team at the Technical University Delft and their important contributions. He is particularly grateful to Drs Jilt Sietsma, Niels van Dijk, Erik Offerman, Dave Hanlon, Pina Meccozi, Yvonne van Leeuwen, Theo Kop and Hao Chen, as well as Matthias Militzer. The TU Delft research on ferrous phase transformation kinetics was initiated around 1990 by the late Dr Kees Brakman (TU Delft) and Dr Frans Hollander (Hoogovens Research).

© Woodhead Publishing Limited, 2012

It received major funding over many years from Hoogovens/Corus/Tata Steel and the Netherlands Institute for Metals Research (now M2i).

4.9 References

Aurenhammer F (1991) Vornoi Diagrams: a survey of fundamental geometric data structure. *Computing Surveys*, 23, 345–405.

Avrami M (1939) Kinetics of phase change I: General theory. *J Chem Phys*, 7, 1103–1112.

Avrami M (1940) Kinetics of phase change II: transformation-time relationships for random distributions of nuclei. *J Chem Phys*, 8, 212–224.

Babu S S, Elmer J W, Vitek J M and David S A (2002) Time resolved X-ray diffraction investigation of primary weld solidification in Fe-C-Al-Mn steels. *Acta Mater*, 50, 4763–4781.

Bos C and Sietsma J (2007) A mixed mode model for partitioning phase transformations. *Scripta Mater*, 57, 1085–1088.

Bos C and Sietsma J (2009) Application of the maximum driving force concept for solid state partitioning phase transformations in multi-component systems. *Acta Mater*, 57, 136–144.

Cahn J W (1956a) Transformation kinetics during isothermal holding. *Acta Metal*, 4, 449–459.

Cahn J W (1956b) Transformation kinetics during continuous cooling. *Acta Metal*, 4, 572–575.

Chen H and van der Zwaag S (2010) Application of the cyclic phase transformation concept for investigating growth kinetics in solid state partitioning phase transformations. *J Compu Mater Sci*, 49, 801–813.

Chen H, Appolaire B and van der Zwaag S (2011) Application of the cyclic partial phase transformations for identifying kinetic transitions during the solid-state phase transformations: experiments and modeling. *Acta Mater*, 59, 6751–6760.

Choi S (2003) Model for estimation of transformation kinetics from dilatation data during cooling of hypo-eutectoid steels. *Mater Sci Eng A*, 363, 72–80.

Christian J W (2002) *The Theory of Transformations in Metals and Alloys*. Oxford: Pergamon Press.

Crusius S, Inden G, Knoop U, Hoglund L and Agren J (1992) On the growth of ferrite allotriomorphs in Fe-C alloys. *Metallkd*, 83, 629–738.

Dong-Woo S, Chang-Seok O and Nam H H (2007) Dilatometric analysis of phase fraction during autenite decomposition into banded microstructure in low carbon steel. *Metal Mater Trans A*, 38A, 2963–2973.

Dubois M, Moreau A, Militzer M and Bussiere J F (1998) Laser ultrasonic monitoring of phase transformations in steels. *Scripta Mater*, 39, 735–741.

Dubois N, Militzer M, Moreau A and Bussiere J F (2000) A new technique for quantitative real-time monitoring of austenite grain growth in steel. *Scripta Mater*, 42, 867–874.

Dubois M, Moreau A and Bussiere J F (2001) Ultrasonic velocity measurements during phase transformations in steels using laser ultrasonics. *J Appl Phys*, 89, 6487–6495.

Enomoto M and Aaronson H I (1986) On the critical nucleus composition of ferrite in an Fe-C-Mn alloy. *Metall Trans A*, 17A, 1381–1384.

Enomoto M and Yang J B (2008) Simulation of nucleation of pro-eutectoid ferrite at austenite grain boundaries during continuous cooling. *Metall Mater Trans A Phys Metall 39A*, 5, 994–1002.

© Woodhead Publishing Limited, 2012

Garcia-Mateo C, Caballero F G and Bhadeshia H K D H (2005) Superbainite: a novel very strong bainitic microstructure. *Rev Metal*, 41, 186–193.

Gautier E, Simon A and Beck G (1987) Transformation plasticity during the pearlitic transformation of a eutectoid steel. *Acta Metal*, 35, 1367–1375.

Gojic M, Suceska M and Rajic M (2004) Thermal analysis of low alloy Cr-Mo steel. *J Therm Anal Calor*, 75, 947–956.

Hasan H S, Peet M, Bhadeshia H K D H, Wood S and Booth E (2010) Temperature cycling and the rate of the bainite transformation. *Mater Sci Tech*, 26, 4, 453–456.

Hillert M (1999) Solute drag, solute trapping and diffusional dissipation of Gibbs energy. *Acta Mater*, 47, 4481–4505.

Hillert M and Ågren J (2004) On the definition of paraequilibrium and orthoequilibrium. *Scripta Mater*, 50, 697–699.

Hollander F (1994) PhD thesis, University Twente, the Netherlands.

Huang W and Hillert M (1996) The role of grain corners in nucleation. *Metall Mat Trans A*, 27A, 480–483.

Johnson W and Mehl R (1939) Reaction kinetics in processes of nucleation and growth. *Trans AIME* 125, 416–458.

Kashchiev D (2000) *Nucleation*, *Basic Theory With Applications*. Oxford: Butterworth.

Kelton K F (1991) Crystal nucleation in liquids and glasses. *Solid State Physics*: *Adv in Res and App*, 45, 75–177.

Kelton K F, Greer A L and Thompson C V (1983) Transient nucleation in condensed systems. *J Chem Phys*, 79, 6261–6276.

Kolmogorov A (1937) Statistical theory for the recrystallization of metals. *Izv. Akademii Nauk USSR Ser Matematic*, 3, 355–359.

Komizo Y and Terasaki H (2011) *In-situ* time-resolved X-ray diffraction using synchrotron. *Sci Tech Weld Joining*, 16, 79–86.

Kop T A, Sietsma J and van der Zwaag S (2001a) Dilatometric analysis of the phase transformations in hypo-eutectoid steels. *J Mater Sci*, 36, 519–526.

Kop T A, Sietsma J and van der Zwaag S (2001b) Anisotropic dilatation behaviour during transformation of hot rolled steels showing banded structure. *Mater Sci Techn*, 17, 1569–1574.

Krielaart G P, Brakman C M and van der Zwaag S (1996) Analysis of phase transformation in Fe-C alloys using differential scanning calorimetry. *J Mater Sci*, 31, 1501–1508.

Krielaart G P, Sietsma J and van der Zwaag S (1997) Simulation of pro-eutectoid ferrite formation using a mixed control growth mode. *Mater Sci Eng*, A237, 216–222.

Kruger S E and Damm E B (2006) Monitoring austenite decomposition by ultrasonic velocity. *Mater Sci Eng A*, 425, 238–243.

Landheer H, Offerman S E, Petrov R H and Sietsma J (2009) The role of crystal misorientations during solid-state nucleation of ferrite in austenite. *Acta Mater*, 57, 1486–1496.

Lauridsen E M, Jensen D J, Poulsen H F and Lienert U (2000) Kinetics of individual grains during recrystallization. *Scripta Mater*, 43, 561–566.

Lee S J, Lusk M T and Lee Y K (2007) Conversional model of transformation strain to phase fraction in low alloy steels. *Acta Mater*, 55, 875–882.

Li C M, Sommer F and Mittemeijer E J (2002) Characteristics of the austenite to ferrite transformation in Fe-Mn alloys. *Mater Sci Eng A*, 325, 307–319.

Liu F, Sommer F, Bos C and Mittemeijer E J (2007) Analysis of solid state transformation kinetics: models and recipes. *Int Mater Rev*, 52, 193–212.

Margulies L, Winther G and Poulsen H F (2001) *In-situ* measurement of grain rotation during deformation of polycrystals. *Science 23*, 291, 2392–2394.

© Woodhead Publishing Limited, 2012

Mecozzi M G, Militzer M, Sietsma J and van der Zwaag S (2008) The role of nucleation behaviour in phase field simulations of the austenite to ferrite transformation. *Metal Mater Trans A Phys Metall*, 39A, 6, 1237–1247.

Militzer M, Pandi R and Hawbolt E B (1996) Ferrite nucleation and growth during continuous cooling. *Metal Mater Trans A Phys Metall*, 27, 1547–1556.

Mutafschiev B (2001) *The Atomistic Nature of Crystal Growth*. Berlin: Springer-Verlag.

Odqvist J (2011) KTH Stockholm, private communications.

Offerman S E, van Dijk N H, Sietsma J, Grigull S, Lauridsen E M, Margulies L and van der Zwaag S (2002) Grain nucleation and growth during phase transformations. *Science*, 298, 1003–1005.

Offerman S E, Van Dijk N H, Sietsma J, Lauridsen E M, Margulies L, Grigull S, Poulsen H F and van der Zwaag S (2004) Solid state phase transformations involving solute partitioning: modelling and measuring at the level of individual grains. *Acta Mater*, 52, 4757–4766.

Onink M, Brakman C M, Tichelaar F D, Mittemeijer E J, van der Zwaag S, Root J H and Konyer N B (1993) The lattice parameter of austenite and ferrite in Fe-C alloys as functions of carbon concentration and temperature. *Scripta Metal Mater*, 29, 1011–1016.

Onink M, Tichelaar F D, Brakman C M, Mittemeijer E J and van der Zwaag S (1996) Quantitative analysis of the dilatation by decomposition of Fe-C austenites: calculations of volume change upon transformation. *Z Metalk*, 87, 24–32.

Palmer T A, Elmer J W and Babu S S (2004) Observation of ferrite-austenite transformations in the heat affected zone of 2205 duplex stainless steel spot welds using time resolved X-ray diffraction. *Mater Sci Eng A*, 374, 307–321.

Poulsen H F (2004) *Three-dimensional X-ray Diffraction Microscopy: Mapping Polycrystals and their Dynamics*. New York: Springer.

Pradell T, Crespo D, Clavaguera N and Clavaguera-Mora M T (1988) Diffusion controlled grain growth in primary recrystallisation: Avrami exponents revisited. *J Physics: Condensed Matter*, 10, 3833–3841.

Purdy G R and Kirkaldy J S (1963) The kinetics of proeutectoid ferrite reaction at an incoherent interface as determined by a diffusion couple. *Trans. TMS-AIME*, 227, 1255–1262.

Raju S, Jeya Ganesh B, Banerjee A and Mohandas E (2007) Characterisation of thermal stability and phase transformation energetics in tempered 9Cr-1Mo steel using drop and differential scanning calorimetry. *Mater Sci Eng A*, 465, 29–37.

Ramsteiner I B, Weitz D A and Spaepen F (2010) Stiffness of the crystal-liquid interface in a hard-sphere colloidal system measured from capillary fluctuations. *Phys Rev E*, 82, 4, 041603.

Rekveldt M T (1973) Study of ferromagnetic bulk domains by neutron depolarisation in 3 dimensions. *Z Physik*, 259, 391–410.

Rosman R and Rekveldt M T (1991) Neutron depolarisation in granular materials: a review of theory and experimental results. *J Magn Magn Mater*, 95, 319–340.

Savran V I, Offerman S E and Sietsma J (2010) Austenite nucleation and growth observed on the level of individual grains by three-dimensional X-ray diffraction microscopy. *Metall Mater Trans A Phys Metall*, 41A, 3, 583–591.

Schall P, Cohen I, Weitz D A and Spaepen F (2006) Visualisation of dislocation nucleation by indenting colloidal crystals. *Nature*, 440, 7082, 319–323.

Scruby C B and Moss B C (1993) Non-contact ultrasonic measurements on steel at elevated temperatures. *NDT & E Int*, 26, 177–188.

© Woodhead Publishing Limited, 2012

Sietsma J and van der Zwaag S (2004) A concise model for mixed–mode transformations in the solid state. *Acta Mater*, 52, 4143–4152.

Slezov V V and Schmelzer J (1994) Comments on nucleation theory. *J Phys Chem Solids*, 55, 243–251.

Smith A, Kruger S E, Sietsma J and van der Zwaag S (2006) Laser ultrasonic monitoring of austenite recrystallization in C-Mn steels. *ISIJ Int*, 46, 1223–1232.

Smith A, Kruger S E, Sietsma J and van der Zwaag S (2007) Laser-ultrasonic monitoring of ferrite recovery in ultra low carbon steel. *Mater Sci Eng A*, 458, 391–401.

Speyer R F (1994) *Thermal Analysis of Materials*. New York: Marcel Dekker.

Svoboda J, Fischer F D, Fratzl P, Gamsjager E and Simha N K (2001) Kinetics of interfaces during diffusional transformations. *Acta Mater*, 49, 1249–1259.

Tanaka T, Aaronson H I and Enomoto M (1995) Calculations of the ferrite-austenite phase boundaries in Fe-C-X systems from the central atom model. *Metall Trans A*, 26A, 535–545.

Tajima M and Umeyama Y (2002) Latent heats of phase transformations in iron and steels. *High Temp High Press*, 34, 91–97.

Tajima M, Nishimoto Y and Shima K (2004) Effect of carbon and chromium contents on latent heat of pearlite transformation of steels. *J Iron Steel Inst Jap*, 90, 807–811.

te Velthuis S G E, Rekveldt M T, Sietsma J and van der Zwaag S (1997) Ferrite nucleation and growth in a medium carbon steel studied by neutron depolarisation. *Physica B*, 241, 1234–1236.

te Velthuis S G E, van Dijk N H, Rekveldt M T, Sietsma J and van der Zwaag S (2000a) Field dependent neutron depolarisation study of ferrite formation in medium-carbon steels. *Acta Mater*, 48, 1105–1114.

te Velthuis S G E, van Dijk N H, Rekveldt M T, Sietsma J and van der Zwaag S (2000b) A three-dimensional model for the development of the microstructure in steel during slow cooling. *Mater Sci Eng A*, 277, 218–228.

Uetz G, Woelk G and Bishops T (1991) Influencing the formation of steel structure by suitable temperature control in the run-out sections of hot-strip mills. *Steel Research*, 62, 216–222.

Vandermeer R A (1990) Modelling diffusional growth during austenite decomposition to ferrite in polycrystalline Fe-C alloys. *Acta Metall Mater*, 38, 2461–2470.

Van der Ven A and Delaey L (1996) Models for precipitate growth during the austenite to ferrite and austenite transformation in Fe-C and Fe-C-M alloys. *Prog Mater Sci*, 40, 181–264.

van Dijk N H, te Velthuis S G E, Rekveldt M T, Sietsma J and van der Zwaag S (1999) Neutron depolarisation study of phase transformations in steel. *Physica B – Condensed Matter*, 267, 88–91.

van Dijk N H, Butt A M, Zhao L, Sietsma J, Offerman S E, Wright J P and van der Zwaag S (2005) Thermal stability of retained austenite in TRIP steels studied by synchrotron X-ray diffraction during cooling. *Acta Mater*, 53, 5439–5447.

van Dijk N H, Offerman S E, Sietsma J and van der Zwaag S (2007) Barrier free heterogeneous grain nucleation in polycrystalline materials: the austenite to ferrite transformation in steel. *Acta Mater*, 55, 4489–4498.

van Leeuwen Y, Vooijs S, Sietsma J and van der Zwaag S (1998) The effect of geometrical assumptions in modelling solid state transformations. *Met Mater Trans A*, 29, 12, 2925–2931.

Voronoi G (1907) Nouvelles applications des paramètres continus à la théorie des formes quadratiques. *J Reine und Angewandte Mathematik*, 133, 97–178.

© Woodhead Publishing Limited, 2012

Wits J J, Kop T A, van Leeuwen Y, Sietsma J and van der Zwaag S (2000) A study on the austenite to ferrite phase transformation in binary substitutional iron alloys. *Mater Sci Engineering A*, 283, 234–241.

Yang J, McCoy B J and Madras G (2006) Cluster kinetics and dynamics during spinodal decomposition. *J Chem Phys*, 124, 024713.

Zener C (1946) Kinetics of the decomposition of austenite. *Trans Met Soc AIME*, 167, 550–595.

Zurob H S, Hutchinson C R, Beche A A, Purdy G R and Brechet Y (2008) A transition from local equilibrium to paraequilibrium kinetics for ferrite growth in Fe-C-Mn: a possible role of interfacial segregation. *Acta Mater*, 56, 2203–2211.

Zurob H S, Hutchinson C R, Brechet Y, Seyedrezai H and Purdy G R (2009) Kinetic transitions during non-partitioned ferrite growth in Fe-C-X alloys. *Acta Mater*, 57, 2781–2792.

Zwigl P and Dunand D C (1999) A numerical model of transformation plasticity for iron. *Mater Sci Eng A*, A262, 166–172.

© Woodhead Publishing Limited, 2012

5

Structure, energy and migration of phase boundaries in steels

M. ENOMOTO, Ibaraki University, Japan

Abstract: This chapter discusses the advances in recent decades of our understanding of the structure, energy and migration mechanism of interphase boundaries. Our understanding of the structure of phase boundaries, e.g. ferrite/austenite and other boundaries, has been advanced by high-resolution transmission electron microscopy studies coupled with computer modeling. Simultaneously, theories and simulation methods of phase boundary energies have been advanced considerably due to the development of interatomic potentials. The migration of phase boundaries is discussed with emphasis on the motion of ledges or disconnections under diffusional and strain field interactions.

Key words: phase boundary, ledge, disconnection, ferrite, austenite, cementite, equilibrium shape.

5.1 Introduction

Interfaces exert major influences on the behavior of materials. The theory of solid interface has been developed considerably in recent decades. In the first part of this chapter, following a brief introduction to the classification of phase boundaries, the structures of specific ferrite/austenite and cementite/austenite boundaries, as revealed by conventional and high resolution transmission electron microscopy (HRTEM) associated with computer modeling, and the edge-to-edge matching model are described. This is followed by a description of the calculation methods of phase boundary structure and energy by continuum and discrete-lattice-plane approaches, O-lattice theory and atomistic simulations using multi-body interaction potential. It is essentially important to evaluate the phase boundary energies of orientations varying in five or possibly eight degrees of freedom to understand the nucleation and growth behavior and the morphology of precipitates. In the third part, the theory of migration of disconnections and ledged phase boundaries is described. Whereas diffusional interaction among migrating ledges was the main issue in earlier theories, it is now realized that it is necessary to incorporate not only diffusion field interaction, but also stress/strain field interactions among ledges because ledges are generally associated with transformation and misfit dislocations, termed disconnections.

© Woodhead Publishing Limited, 2012

5.2 Atomic structure of phase boundaries

5.2.1 Classification of phase boundaries

Phase boundaries are the junction of two crystals which differ in lattice structure and composition. In coherent phase boundaries the atomic configuration of the two crystals are the same at the boundary plane and the lattices are continuous across the boundary. Even if the misfit is finite, forced coherency can be achieved when one crystal embedded in the other is small enough, although a substantial amount of strain energy is generated. Semi-coherent or partially* coherent boundaries occur with larger misfit and are composed of coherent regions and regions of disregistry which are relieved by dislocations and/or steps. As an example, the broad faces of Widmanstätten ferrite plates in steel belong to the class of an orientation relationship characterized by low-index conjugate planes and directions, and relatively high-index habit planes which actually decompose into a ledge structure. In incoherent boundaries, the atomic arrangement is disordered and the coordination between atoms across the boundary is believed to resemble that of a liquid. In other words, incoherent boundaries can be viewed as a boundary in which the regions of disregistry are spaced so closely that they overlapped each other. Three types of incoherent phase boundaries are recognized depending on whether the orientation relationship and the habit plane are rational or irrational (Howe *et al.*, 2000).

In general, the boundary energy increases with increasing degree of disorder and difference in composition, whereas the boundary friction (the inverse of the mobility) decreases with increasing degree of incoherency. The energy of coherent phase boundaries is usually less than ~2–300 mJ/m^2. On the other hand, the energy of incoherent boundaries is thought to be greater than several hundred mJ/m^2, and the energies of semi-coherent boundaries fall somewhere in between. The energy of a phase boundary is defined as the difference of the free energy of a system composed of abutting two crystals of different crystal structure and composition from the average of the free energies of the two phases, each occupying the same volume as that of the system containing the boundary. According to this definition the strain energy of coherent precipitates becomes a part of the interfacial energy. However, the strain field of a coherent precipitate is of long range and the total strain energy is proportional to the volume of the precipitate. Hence, as seen from the common practice of its inclusion in the volume free energy term in the equation of a nucleus free energy, it is not considered to be an interfacial energy. In contrast, the strain energy of misfit interfacial dislocations at a

* Some authors use 'partly coherent' to avoid confusion with partial dislocation (Howe *et al.*, 2000).

© Woodhead Publishing Limited, 2012

semi-coherent boundary is not far reaching and approximately proportional to the area of the boundary unless the precipitate is too small. This is considered to be a part of the interfacial energy (see Section 5.3.2).

Howe *et al*. (2000) proposed that the distinction between fully coherent and semi-coherent phase boundaries is defined by introduction of a single linear misfit compensating defect, such as a dislocation loop, because the strong diffraction contrast often associated with a fully coherent precipitate disappears when a misfit compensating dislocation loop is introduced at the precipitate boundary and this can be observed quite well under HRTEM. On the other hand, the distinction between semi-coherent and incoherent phase boundaries can be made by the absence of detectable misfit accommodating defects or misfit localization at the boundary under HRTEM, which is directly related to the definition of incoherent boundaries.

It has been reported that a strong correlation exists between the surface energies of pure metals and the heats of sublimation, and between the grain boundary energies and the heats of fusion (Hondros, 1978). These energies are influenced by the adsorption of impurity and/or solute atoms. It follows that the energy of phase boundaries, which can occur in alloys, is expected to be inevitably influenced by solute segregation, at least in semi-coherent and incoherent boundaries. Whereas a large amount of data on solute segregation at grain boundaries is available, studies of solute segregation at interphase boundaries are scarce and thus this is not discussed in this chapter.

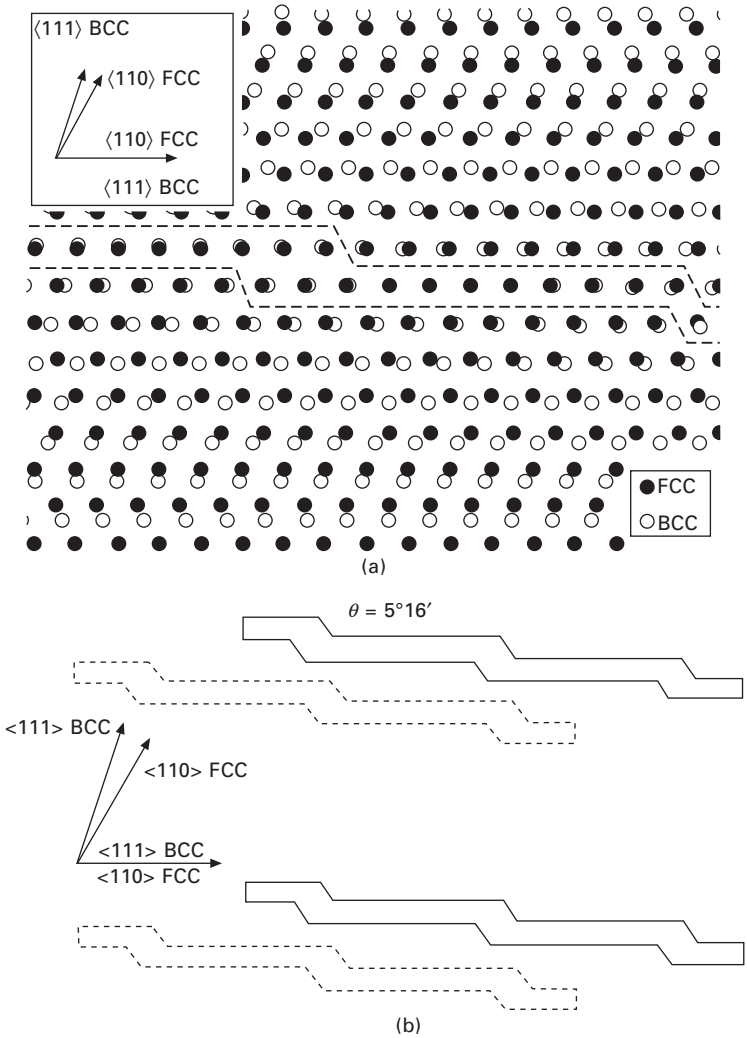
5.2.2 Ledge structure of phase boundary

The atomic structure and migration kinetics of face centered cubic/body centered cubic (fcc/bcc) boundaries are of special importance in steel because the austenite to ferrite transformation is one of the most widely used and extensively studied phase transformations. In this transformation two major morphologies of ferrite are observed, termed equiaxed (allotriomorphic) and acicular (plate-like), respectively. The latter morphology is absent at low undercoolings but becomes increasingly predominant at larger undercoolings when the alloy is cooled below a certain temperature, called W_s temperature. The formation of this morphology at large undercoolings indicates that the mobility of the broad face of a ferrite plate is low compared to that at the plate tip and thus a substantial barrier exists for migration. It should be mentioned that both equiaxed and acicular ferrite are nucleated preferentially at austenite grain boundaries. The former has a specific orientation relationship, Kurdjumov–Sachs (K-S) or Nishiyama–Wassermann (N-W) with at least one of the matrix grains (King and Bell, 1975), and the latter has a specific orientation relationship with the matrix grain into which it has grown (King and Bell, 1974).

Hall *et al*. (1972) studied the structure of the boundary between bcc Cr-rich

© Woodhead Publishing Limited, 2012

precipitates and the fcc Cu-rich matrix in a Cu-Cr alloy, which triggered a number of subsequent studies of phase boundary structure. They compared extensive TEM observations with computer plots of atom configuration at the boundaries. Figure 5.1(a) is a superimposed plot of the atom configuration in the $\{111\}_{fcc}$ and $\{110\}_{bcc}$ planes which are K-S related. Whereas a good fit is not obtained between the two planes over a large area, there are regions



5.1 (a) Atomic configuration in the $\{111\}_{fcc}$ and $\{110\}_{bcc}$ planes with Kurdjumov-Sachs orientation relationship. Dashed lines show the region of good fit. (b) Regions of good fit in the K-S related $\{111\}_{fcc}$ and $\{110\}_{bcc}$ planes. Dashed lines show the regions of good fit in the adjacent (one atom low) planes (Hall *et al.*, 1972).

© Woodhead Publishing Limited, 2012

of good fit which are spaced periodically. If the stacking of $\{111\}_{fcc}$ planes are designated A, B and C, and the stacking of $\{110\}_{bcc}$ planes by D and E, the introduction of a one-atom high step alters the combination of atom layers from A-D to B-E, etc., and as a result, the proportion of atoms of good matching increases more than a few times. This is shown in Fig. 5.1(b). The energy of the boundary can be markedly lowered by introducing an array of such steps, which were termed structural ledges or structural disconnections. Indeed, Rigsbee and Aaronson (1979a, 1979b) observed three-atom high steps at the broad face of a ferrite plate, which were ~2.2–9.0 nm apart, in an Fe-0.62mass%C–2.0mass%Si alloy. The residual misfit was accommodated by single arrays of misfit dislocations. It was also observed that the two close-packed planes were not always strictly parallel, but deviated within a few degrees and, moreover, the macroscopic habit plane was inclined to the close-packed planes from 9° to a little less than 20°. These earlier studies served as a basis for subsequent studies of phase boundary structure.

Several orientation relationships have been reported between cementite plate (or lath) and austenite, e.g. the Pitsch orientation relationship (Pitsch, 1962) and Farooque–Edmonds orientation relationship (Farooque and Edmonds, 1990) and so forth (Thompson and Howell, 1987; Zhou and Shiflet, 1992). Moreover, the habit planes of cementite plates exhibited a large scatter (Spanos and Aaronson, 1990; Spanos and Kral, 2009). Close inspection under HRTEM microscopy coupled with computer modeling (Howe and Spanos, 1999) revealed that cementite/austenite boundaries contained $(101_{cem}//(113)_{fcc}$ terraces and periodically spaced ledges with $[010]_{cem}//[110]_{fcc}$ line direction and $(001)_{cem}//(\bar{1}13)_{fcc}$ riser plane, which is analogous to the boundaries between ferrite plate and austenite. The macroscopic habit plane was deviated to the atomic habit plane, presumably depending on the density of ledges. Moreover, two sets of edge dislocations with Burgers vectors parallel and perpendicular to the terrace plane were associated with the ledges, which were presumably introduced for compensating misfits. Thus, dislocations would have to climb in the migration of cementite/austenite boundaries and they would play a major role in the partitioning of alloying elements during cementite formation. The stepped structure was also observed in other alloy systems such as the broad faces of proeutectoid α plates in a titanium alloy (Furuhara and Aaronson, 1991; Furuhara *et al.*, 1991). These features are intrinsic in nature and seem to have important implications for the energies and migration behaviors of solid-solid transformation interfaces.

5.2.3 Edge-to-edge matching model

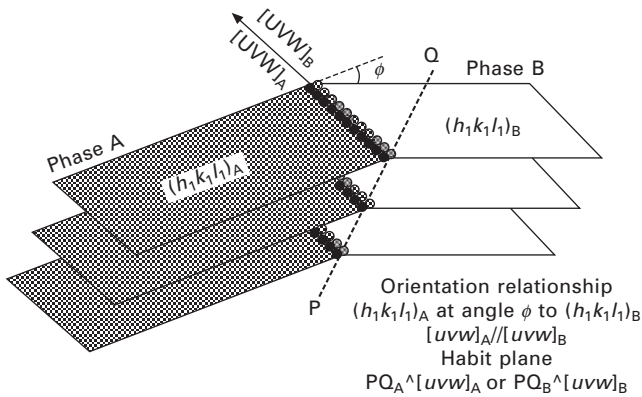
Earlier models of phase boundary structure are mostly based upon plane-to-plane matching. For example, matching between atoms in the two close-packed planes have been studied extensively in fcc/bcc phase boundaries.

© Woodhead Publishing Limited, 2012

In contrast, matching of close-packed rows at the edges of two planes in the precipitate and the matrix phases plays a major role in this model. This concept was first proposed to explain the high-index, i.e. $\{225\}\gamma$, habit plane of martensite in steel (Frank, 1953).

In this model two close-packed or nearly close-packed rows in each phase are chosen to be parallel, see Fig. 5.2 (Kelly and Zhang, 2006). Then, the planes containing a high density of these atom rows are chosen and arranged to meet edge-to-edge. The inclination angle ϕ is determined such that the boundary plane PQ achieves a maximum atom-row matching. From this procedure one can determine the orientation relationship and the habit plane between the precipitate and the matrix crystals. It is reported that by varying the lattice parameter ratio of the two crystals, one can obtain a series of orientation relationships, e.g. Pitsch, Nishiyama–Wassermann and Baker–Nutting orientation relationships and associated habit planes between bcc and fcc crystals (Kelly and Zhang, 1999). Zhang and Kelly (1998) explained the orientation relationships between Widmanstätten cementite plates and the matrix austenite by the edge-to-edge concept.

The edge-to-edge matching model has attracted attention because it seems to offer a more general approach to the structure of phase boundaries than the conventional ones. Indeed, the understanding of the structure and the energy of irrational phase boundaries have been advanced considerably. More specifically, the energy of irrational phase boundaries can be quite low when the boundary is commensurate in one direction (Reynolds and Farkas, 2006). Massalski *et al*. (2006) speculate that incoherent boundaries of the type of low-index conjugate habit planes can lower the effective phase boundary energies by forming a facet (thus decreasing the critical nucleus volume) and be involved in the nucleation of precipitate, whereas it is often considered that incoherent phase boundaries do not take part in nucleation.



5.2 Schematic illustration of edge-to-edge matching at the boundary of two phases (Kelly and Zhang, 2006).

© Woodhead Publishing Limited, 2012

As expected from the earlier work (Frank, 1953), martensite boundaries in Fe-Ni-Mn alloy (Moritani *et al.*, 2002) and Fe-Ni-Co-Ti alloys (Ogawa and Kajiwara, 2004) were understood in terms of edge-to-edge matching.

5.3 Free energies of phase boundaries

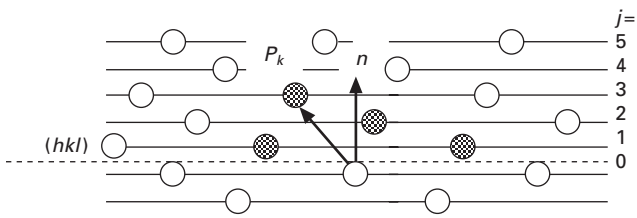
5.3.1 Chemical energy of coherent boundaries

The surface energy of a pure solid is correlated strongly with sublimation energy (Hondros, 1978) which is related to the bond strength between atoms in the crystal. Hence, Becker (1938) formulated the boundary energy between two phases differing in composition as:

$$\sigma = n_s z_s (x^\alpha - x^\beta)^2 \Delta e \qquad [5.1]$$

where $\Delta e = e_{AB} - (e_{AA} + e_{BB})/2$, e_{AB}, etc., are the bond energies between A and B atoms, etc., n_s is the atom density in the boundary plane, z_s is interfacial coordination number, and x^α and x^β are the compositions of the α and β phases, respectively. Only atoms in the plane immediately adjacent to the boundary plane are considered in this equation. When the orientation of the boundary plane is of relatively higher order, the nearest neighbors to an atom in one phase lie in the second, third and farther atom planes on the other side of the boundary (see Fig. 5.3). Indeed, a (110) type fcc/fcc boundary already has one nearest neighbor atom on the second plane from the boundary. The number of such bonds across the boundary is two because an atom in the second plane *in the first phase* has a nearest neighbor atom in the first plane of the other phase. Hence, the total number of nearest neighbor bonds across the boundary becomes $\sum_j j z_j$ and, thus, the energy of an (*hkl*) type boundary across which the nearest neighbor bonds lie over the j_{max} planes is given by

$$\sigma = n_s \left(\sum_{j=1}^{j_{max}} j z_j \right) (x^\alpha - x^\beta)^2 \Delta e \qquad [5.2]$$



5.3 Schematic illustration showing the distribution of nearest neighbor atoms to an atom A across the (*hkl*) type phase boundary. In this diagram nearest neighbor bonds exist up to the third (j_{max} = 3) plane.

© Woodhead Publishing Limited, 2012

The interfacial coordination number is calculated by the vector method (Lee and Aaronson, 1980). In this method the number j is first calculated from the equation:

$$j = \frac{\mathbf{P}_k \cdot \mathbf{m}}{d_{hkl}} \qquad [5.3]$$

where $\mathbf{P}_k$ is the position vector of the nearest neighbor atom, $\mathbf{m}$ is the unit normal vector to the boundary plane and d_{hkl} is the interplanar spacing. z_j is the number of $\mathbf{P}_k$'s which yield the same j value when Eq. [5.3] was calculated for all nearest neighbor position vectors.

It is assumed in Eq. [5.2] that the composition varies from x^α to x^β over one atom plane. Thus, it yields the interfacial energy at 0 K. At a finite temperature one calculates the atom composition of the ith plane x_i such that the total free energy of the system will become a minimum. If only the nearest neighbor interaction is considered, the sum of all bond energies, i.e. enthalpy of the system is given by:

$$\Delta H = n_s \sum_i (x_i - x^\alpha)\Delta h_i \qquad [5.4]$$

$$\Delta h_i = \Delta e \left\{ x^\alpha Z - x_i z_\ell - \sum_{j=1}^{j_{\max}} (x_{i+j} + x_{i-j}) z_j \right\} \qquad [5.5]$$

where z_ℓ (= z_0) is the number of nearest neighbor atoms in the (j =)0th plane. The positional entropy of the system is given by:

$$\Delta S = -kn_s \sum_i \left\{ x_i \ln \frac{x_i}{x^\alpha} + (1 - x_i) \ln \frac{1 - x_i}{1 - x^\alpha} \right\} \qquad [5.6]$$

where k is the Boltzmann constant. The equilibrium concentration profile which minimizes the total free energy $\Delta G = \Delta H - T\Delta S$ is obtained from the equation:

$$\frac{\partial \Delta G}{\partial x_i} = 0 \quad \text{for} \quad i = -n \sim n \qquad [5.7]$$

where n is the number of atom planes in each phase. Thus, the equilibrium concentration profile is determined by $2n$ transcendental equations. It can be shown that the concentration thus calculated varies steeply at low temperatures near the boundary plane and the profile becomes progressively broader with increasing temperature.

The phase boundary energy can be calculated with the compositions x_i which satisfy Eq. [5.7]. After manipulation, the equation of the boundary energy is obtained from the equation:

© Woodhead Publishing Limited, 2012

$$\sigma = n_s \sum_i \left[\Delta e \left\{ (x_i - x^\alpha)^2 Z + \sum_{j=1}^{j_{\max}} (x_i - x_{i-j})^2 z_j \right\} \right.$$

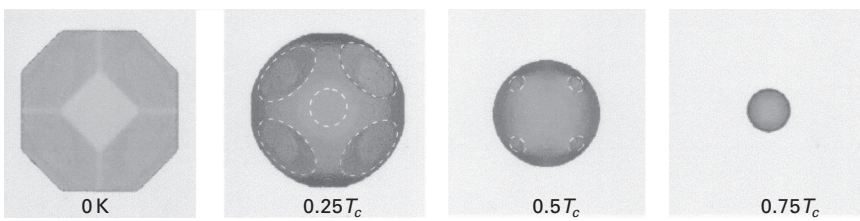
$$\left. + kT \left\{ x_i \ln \frac{x_i}{x^\alpha} + (1 - x_i) \ln \frac{1 - x_i}{1 - x^\alpha} \right\} \right] \quad [5.8]$$

Figure 5.4 shows the variation of the equilibrium shape of fcc/fcc phase boundary with temperature. At 0 K the shape is surrounded by eight {111} and six {100} facets. At $0.25T_C$, where T_C is the critical temperature of the miscibility gap, the Wulff shape is a sphere truncated with larger {111} and smaller {100} facets. The {100} facets disappear at $0.5T_C$ and both types of facet disappear until the temperature reaches $0.75T_C$. Whereas in the above treatment a planar boundary is assumed, an advanced treatment of the energy of non-planar boundary was presented (Sonderegger and Kozeschnik, 2009). This method is called the 'discrete lattice plane nearest neighbor broken bond' (DLP-NNBB) method and can be extended to an interstitial-substitutional system (Yang and Enomoto, 1999, 2001, 2002) as well as a multi-component alloy.

Cahn and Hilliard (1958) developed a continuum model of coherent interfacial energy, which is known as the theory of diffuse interface. In this method the free energy function is expanded by a Taylor series of composition variable x, its gradient $\mathrm{d}x/\mathrm{d}s$ and $\mathrm{d}^2x/\mathrm{d}s^2$, etc., where s is the distance coordinate, to express the free energy of the system as:

$$G = An_v \int_{-\infty}^{\infty} \left\{ g(x) + K_1 \frac{\mathrm{d}^2 x}{\mathrm{d}s^2} + K_2 \left(\frac{\mathrm{d}x}{\mathrm{d}s} \right)^2 \right\} \cdot \mathrm{d}s \quad [5.9]$$

where $g(x)$ is the free energy of homogeneous solid solution of composition x, K_1 and K_2 are coefficients, A is area and n_v is the number of atoms per unit volume. Performing integration by parts of the second term and considering that $\mathrm{d}x/\mathrm{d}s = 0$ as $x \to \pm\infty$,



5.4 Variation with temperature of Wulff equilibrium shape of coherent phase boundary in a binary fcc alloy. T_C is the critical temperature of the miscibility gap. LeGoues *et al.* (2006) and unpublished work by Nagano and Enomoto (2006).

© Woodhead Publishing Limited, 2012

$$G = An_v \int_{-\infty}^{\infty} \left\{ g(x) + K\left(\frac{\mathrm{d}x}{\mathrm{d}s}\right)^2 \right\} \cdot \mathrm{d}s \qquad [5.10]$$

where $K = K_2 - \mathrm{d}K_1/\mathrm{d}x$. The equilibrium concentration distribution is obtained from the Euler equation of variational principle as:

$$\Delta g(x) = K\left(\frac{\mathrm{d}x}{\mathrm{d}s}\right)^2 \qquad [5.11]$$

where $\Delta g(x) = g(x) - \{(1 - x)\mu_A + x\mu_B\}$.
Hence,

$$\sigma = 2n_v \int [K\Delta g(x)]^{1/2}\mathrm{d}x \qquad [5.12]$$

Considering nearest-neighbor interactions only, K is given by $K = (2/3)h_{0.5}^M r_0^2$ where $h_{0.5}^M$ and r_0 are, respectively, the heat of mixing and the nearest neighbor distance. Expanding $g(x)$ with respect to temperature and composition variables, the composition profile in the boundary region and the interfacial energy are given by:

$$\frac{x - x_C}{x_C - x_\alpha} = \tanh\left[\left\{\frac{\beta(T - T_C)}{2K}\right\}^{1/2} s\right] \qquad [5.13]$$

and

$$\sigma = \frac{2\sqrt{2}}{3}\frac{n_v K^{1/2}\beta^{3/2}}{\gamma}(T_C - T)^{3/2} \qquad [5.14]$$

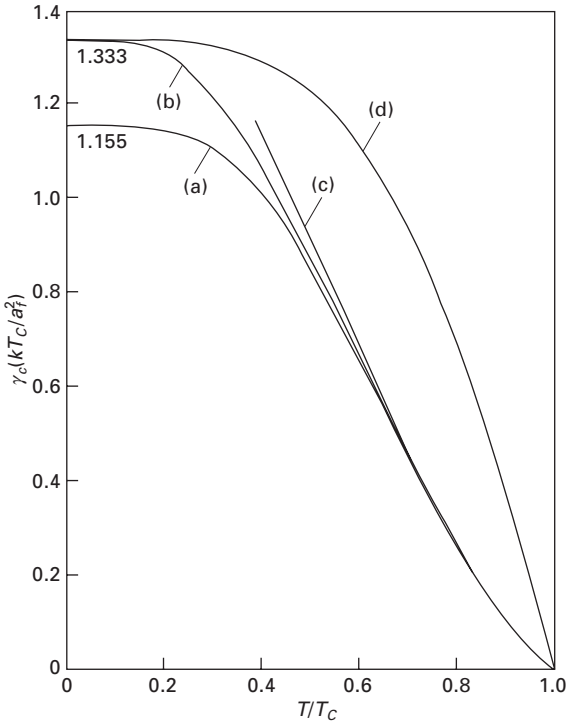
respectively, where $\beta = (\partial^3 \mathrm{g}/\partial \mathrm{T}\partial \mathrm{x}^2)/2$ and $\gamma = (\partial^4 \mathrm{g}/\partial \mathrm{x}^4)/4!$ are the coefficients of series expansion of free energy function $g(x)$ and x_C is the concentration at the critical point. The thickness of interface is given by:

$$\ell \approx 2\left\{\frac{2K}{\beta(T_C - T)}\right\}^{1/2} \qquad [5.15]$$

and thus, is inversely proportional to $(T_C - T)^{1/2}$ near the critical temperature. This accounts for the $(T_C - T)^{3/2}$ dependence of interfacial energy in the Cahn–Hilliard continuum approach, whereas in the Becker type equation the interfacial energy is proportional to $(T_C - T)$ near the critical temperature.

Figure 5.5 compares (111) and (100) fcc/fcc coherent phase boundary energies calculated from the DLP-NNBB model with that calculated from the continuum model. Whereas these energies are almost identical near T_C, the continuum model breaks down due to a large concentration gradient at low temperatures. Becker's model gives a larger energy, except at 0 K since the entropy term is ignored.

© Woodhead Publishing Limited, 2012



5.5 Comparison of coherent fcc/fcc boundary energies calculated from discrete-lattice-plane (DLP) and continuum approaches. (a) (111) type boundary from DLP, (b) (100) type from DLP, (c) from continuum approach and (d) from Becker's equation (Lee and Aaronson, 1980).

5.3.2 Energy of misfit dislocation boundaries

Since the majority of phase boundaries contain interfacial dislocations except, presumably, at the nucleation stages, more than one treatment has been proposed to evaluate the energy of misfit dislocation boundaries. The earliest equation proposed for a boundary containing an array of parallel misfit dislocations by Van der Merwe (1963a, 1963b) is:

$$\sigma_{st} = \frac{\mu b}{4\pi^2}[1 + \beta - (1 + \beta^2)^{1/2} - \beta \ln \{2\beta(1+\beta^2)^{1/2} - 2\beta^2\}] \quad [5.16]$$

where β and μ are the misfit and the shear modulus at the boundary, respectively. An equation proposed by Hirth and Lothe (1982) permits the energy of a multiple dislocation net to be calculated. To use the equation by Hirth and Lothe, the dislocation configuration needs to be determined. This can be accomplished using O-lattice theory; the intersection lines of the boundary plane, e.g. of (*hkl*) type, with the Wigner–Seitz cell of the

© Woodhead Publishing Limited, 2012

O-lattice of two abutting crystals, represent the dislocation network of the boundary. The structural energy thus calculated can be smaller or larger, depending upon the misfit, but the temperature dependence is much smaller than that of the chemical energy (Spanos, 1989). Moreover, the anisotropy of structural energy of a cube-on-cube oriented fcc/fcc boundary is less than several per cent, whereas the anisotropy of chemical energy increases up to ~15% in spite of the fact that the anisotropy of the chemical energy of fcc/fcc boundaries is one of the smallest among the metal interfaces. Thus, when the structural part is dominant over the chemical part, the equilibrium shape is surrounded by a large number of smaller facets, whereas when the chemical part is predominant the equilibrium shape tends to be surrounded by a small number of large facets.

Ecob and Ralph (1981) calculated the configuration of interfacial dislocations at fcc/bcc interfaces using O-lattice theory. These authors introduced a geometrical parameter with which one can evaluate the relative stability of a dislocation boundary. It is called the *R*-parameter and takes the form:

$$R = \sum_i \sum_j \sqrt{\frac{b_i b_j}{d_i d_j}} \qquad [5.17]$$

where b_i and b_j are the magnitude of the Burgers vectors of the dislocation network and d_i and d_j are the dislocation spacings. Using this parameter they performed a Wulff construction for the equilibrium shape of an fcc/bcc boundary and predicted the direction of elongation of the precipitate is parallel to $[\bar{1}\ 14\ 12]_{fcc}$, somewhat deviated from the close-packed $<011>_{fcc}$ direction, and the cross-sectional shape of bcc precipitates is a parallelpiped in the austenite matrix, both of which were in good agreement with those of Cr-rich precipitate in the Cu matrix in a Cu-Cr alloy. They also reported that essentially the same habit plane, i.e. $(335)_\gamma$, was obtained for a Nishiyama–Wassermann (N-W) orientated precipitate as in the Rigsbee–Aaronson approach.

5.3.3 Energy of ledged boundary

Van der Merwe and Shiflet (1994a, 1994b) and Shiflet and Van der Merwe (1994a, 1994b) evaluated the energy of phase boundaries composed of structural ledges and terrace patches forming a two-dimensional rectangular net. A sinusoidal interaction potential was employed between atoms across the boundary for calculation of the energy of terrace patches. The line energy of a ledge was calculated as the energy of a dislocation jog. They also evaluated the energy of misfit dislocations, introduced to accommodate the misfit perpendicular to the terrace. They noted that the mismatch which built up along the terrace patch was compensated by a lateral displacement

© Woodhead Publishing Limited, 2012

of atoms and proposed that ledged interfaces were energetically favored over planar ones in which misfit was compensated by dislocations. These calculations were extended to N-W and K-S oriented $\{111\}_{fcc}//\{110\}_{bcc}$ boundaries. It was concluded that stepped boundaries were more stable than planar boundaries for values of misfit ratio usually encountered in fcc/bcc systems (Shiflet and Van der Merwe, 1994b).

5.3.4 Atomistic calculation of phase boundary structure and energies

Yang and Johnson (1993) developed an embedded atom model (EAM) potential of the α and γ phases of pure iron and calculated the energy of N-W related fcc/bcc boundaries. In this model the total energy of the lattice is given by:

$$E = \sum_i F(\rho_i) + \frac{1}{2}\sum_{i \neq j} \phi(r_{ij}) \qquad [5.18]$$

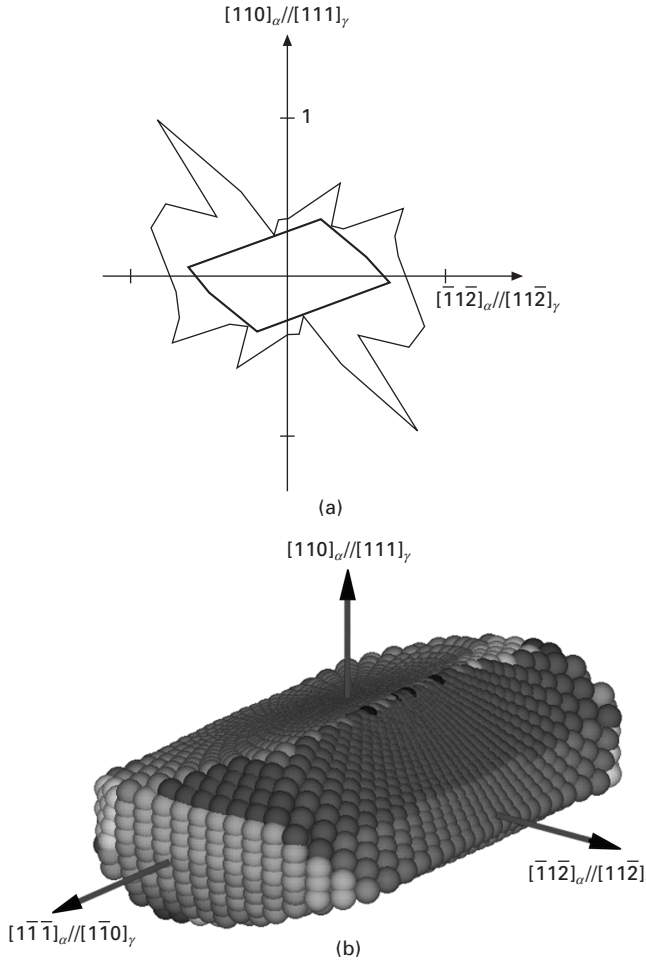
where $F(\rho_i)$ is the energy to embed an atom i into the electron gas of electron density ρ_i, which is expressed as

$$\rho_i = \sum_{i \neq j} f(r_{ij}) \qquad [5.19]$$

and $f(r_{ij})$ is the contribution to the electron density at atom i from atom j, r_{ij} is the separation between atoms i and j and $\phi(r_{ij})$ is a pair interaction energy. The lowest energy was calculated to be 240 mJ/m^2 for a boundary rotated 13° from the $\{111\}_\gamma$ and $\{110\}_\alpha$ close-packed planes. This is much smaller than that reported from dihedral angle measurement of grain boundary ferrite allotriomorphs (~760 mJ/m^2) (Gjostein *et al.*, 1966) and is much larger than those evaluated from nucleation rate measurement of grain boundary ferrite allotriomorphs (~10 mJ/m^2 or even smaller) (Lange *et al.*, 1988; Offerman *et al.*, 2002). More or less similar values have been reported for the energy of an fcc/bcc phase boundary of pure iron from an EAM potential developed by other authors (Chen *et al.*, 1994).

Nagano and Enomoto (2006) calculated the energies of K-S, Greninger–Troiano (G-T), N-W and cube-on-cube oriented α and γ phase boundaries of pure iron using the Yang and Johnson potential (1993). The cube-on-cube orientation relationship was chosen to represent the irrational orientation relationship. For each orientation relationship a few tens of boundary energies were calculated rotating the boundary planes around the axes parallel and perpendicular to the close packed planes. Figure 5.6(a) illustrates the $(\bar{1}11)_\alpha//(\bar{1}10)_\gamma$ section through the polar plot of K-S related α/γ boundary energy. The equilibrium (Wulff) shape was a plate elongated along $\{111\}_\alpha$ and $\{110\}_\gamma$ directions for the K-S relationship (Fig. 5.6(b)) whereas

© Woodhead Publishing Limited, 2012



5.6 (a) $(\bar{1}11)_\alpha//(\bar{1}10)_\gamma$ section through the polar plot of K-S related α/γ phase boundary energy calculated from the Yang and Johnson potential. (b) Wulff equilibrium shape of a precipitate of bcc iron in the fcc iron matrix (or vice versa) with K-S orientation relationship (Nagano and Enomoto, 2006).

thick square and rectangular plates were obtained for G-T and N-W relationships, respectively (Enomoto *et al.*, 2005). On the other hand, a polyhedron with numerous small facets was obtained for the cube-on-cube orientation relationship (OR). The volume of a critical nucleus in the Wulff space of ferrite, denoted V_W, in the austenite matrix was increased in the order of K-S, G-T and N-W by ~10%, whereas that for the cube-on-cube OR was nearly nine times greater than these three orientation relationships. The V_W of grain boundary allotriomorphs was also calculated and it decreased

© Woodhead Publishing Limited, 2012

to ~1/3–1/5 of the nuclei in the matrix. In classical nucleation theory the activation energy for nucleation is given by:

$$\Delta G^* = \frac{4V_W}{(\Delta G_V)^2} \quad [5.20]$$

where ΔG_V is the free energy change attending the nucleation (Aaronson and Lee, 1999). These values, however, were a few orders of magnitude greater than those evaluated from the ferrite nucleation rates by means of classical nucleation theory (Offerman *et al*., 2006).

5.4 Migration of phase boundaries

5.4.1 Mechanisms of boundary migration

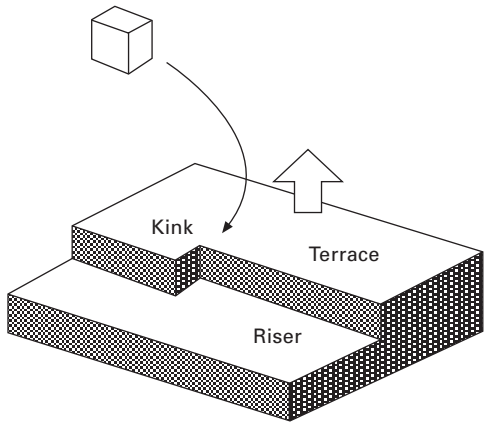
In the migration of precipitate/matrix boundaries, fully coherent boundaries are essentially immobile, semi-coherent boundaries can migrate by ledge mechanism and incoherent boundaries are thought to move by continuous random jumping of atoms across the boundary with little barrier to growth. Irrational boundaries are not always incoherent and such a boundary can move also by ledge mechanism. Martensite boundaries contain glissile disconnections (Pond *et al*., 2003), e.g. ledges associated with a screw dislocation, and move with little barrier, if they move synchronously.

Ledges or disconnections migrate under diffusion field and strain field interaction with their neighbors. In this section the characteristics of ledge motion are discussed in terms of diffusion field overlap. Indeed, the essential features of the growth and morphological evolution of Widmanstätten ferrite plates were reproduced by considering solely diffusion field overlap (Enomoto, 1991; Spanos *et al*., 1994). Then results of simulations which incorporate the strain field interaction are described.

5.4.2 Growth kinetics of a ledged boundary

Burton *et al*. (1951) proposed a terrace-ledge-kink mechanism for crystal growth from the vapor phase. Not only on the surface of crystals, but also within the solids numerous observations have been available which directly reveal that precipitates can grow by the migration of ledges. Indeed, thickening of a plate-shaped precipitate occurs by the lateral migration of ledges across the broad face of a precipitate (Aaronson, 1970, 1974). Moreover, the observation that the partially coherent structure of the leading edge of a plate with uniformly spaced ledges may indicate that plate lengthening may occur by ledge mechanism (Lee and Aaronson, 1988). When the density of kinks is large, the migration of ledges is controlled by diffusion of solute to or from the riser of a ledge (see Fig. 5.7). In terms of a coordinate system moving with the ledge,

© Woodhead Publishing Limited, 2012



5.7 Schematic illustration of terrace-ledge-kink mechanism of crystal growth.

$$x = \frac{X - Vt}{h}, \qquad y = \frac{Y}{h} \qquad [5.21]$$

where X and Y are the (stationary) coordinates in the direction of ledge motion and perpendicular to the terrace, respectively, h is the ledge height and V is the velocity of the ledge. The diffusion equation which governs the steady-state ledge motion is given by:

$$\frac{\partial^2 \Gamma}{\partial x^2} + \frac{\partial^2 \Gamma}{\partial y^2} + 2p\frac{\partial \Gamma}{\partial x} = 0 \qquad [5.22]$$

Here, $\Gamma = (c - c^0)/(c^m - c^0)$ is the normalized solute concentration, $p = Vh/2D$ is dimensionless velocity, called Peclet number, c, c^m and c^0 are the solute concentration in the matrix, the concentration in the matrix at the base of the riser and at infinity (bulk concentration), and D is the solute diffusivity. The flux balance condition at the ledge riser,

$$V = -\Omega \frac{\partial \Gamma}{\partial x}\bigg|_{x=0} \qquad [5.23]$$

governs the ledge migration rate. At the terrace no atoms are attached, namely,

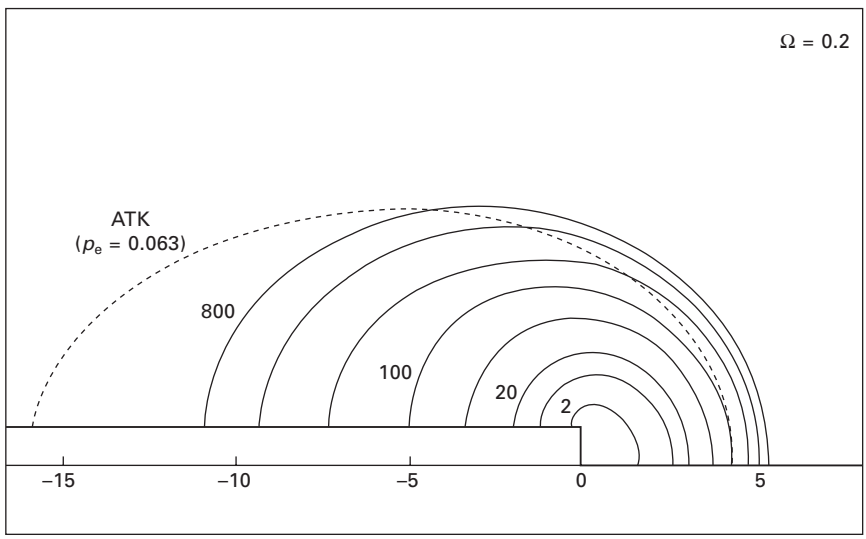
$$\frac{\partial \Gamma}{\partial x}\bigg|_{y=0} = 0 \qquad [5.24]$$

where $\Omega = (c^m - c^0)/(c^m - c^p)$ is the solute supersaturation and c^p is the solute concentration in the precipitate. Jones and Trivedi (1971) and Atkinson (1981) solved these equations analytically. These works were followed by Doherty

© Woodhead Publishing Limited, 2012

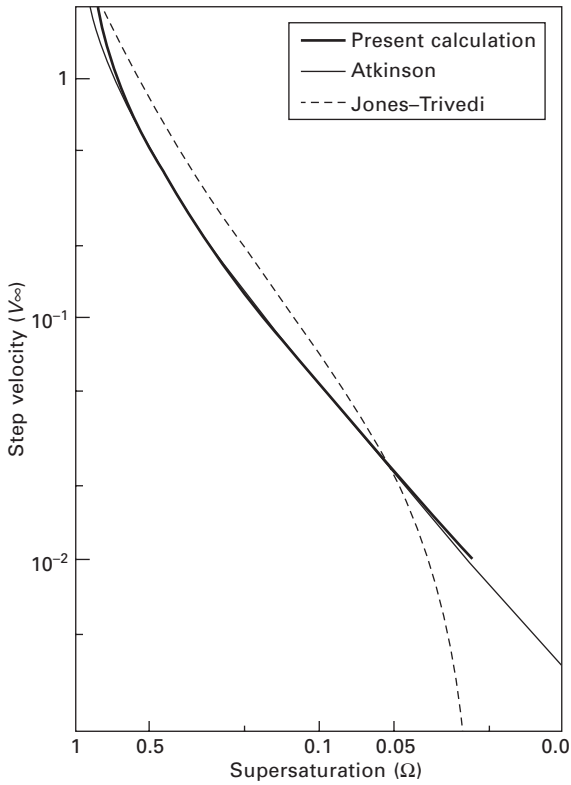
and Cantor (1982) and Enomoto (1987a) who solved the equations by finite difference numerical technique. Figure 5.8 shows the concentration contours around a ledge riser moving under the supersaturation $\Omega = 0.2$. It is seen that the diffusion field extends farther in the direction of growth initially, whereas eventually it extends farther behind the ledge at later stages. The dashed curve shows the concentration contour calculated by Atkinson (1981). Figure 5.9 compares the relationships between the velocity of a single ledge and the supersaturation. Subsequently, Atkinson (2007) incorporated the concentration dependence of diffusivity in his analysis of steady motion of a single ledge.

These authors extended their calculations to a train of ledges (Jones and Trivedi, 1975; Atkinson, 1982, 1991; Enomoto *et al.*, 1982; Enomoto, 1987b). The qualitative features of the motion of a train of ledges can be summarized as follows. In a two-ledge train of initially large separation, the leading ledge moves faster than the trailing ledge and the ledges grow apart with time at large supersaturations. As either or both of initial separation and supersaturation decreases, the trailing ledge moves faster than the leading one and they tend to coalesce. The coalesced double height ledge moves at a speed of one half the velocity before the coalescence. In a three-ledge train, the ledge velocity decreases successively from the leading end and the train expands at large supersaturations and initial ledge spacings. As one or both



5.8 Variation of isoconcentration contour with time ($\Gamma = 0.2$). The numbers indicate the dimensionless time $\tau = Dt/h^2$, where h is the ledge height. A dashed curve was calculated from Atkinson's analysis of steady-state ledge motion (Enomoto, 1987a).

© Woodhead Publishing Limited, 2012



5.9 Relationship between the step velocity and supersaturation due to analytical treatments and computer simulation (Enomoto, 1987a).

of these decreases, a ledge in the middle of the train moves at the lowest speed and coalesces with the trailing ledge. As the supersaturation and the initial spacing decrease further, all three ledges coalesce into a triple height ledge. In a multiple ledge train, an increasing number of ledges coalesce from the trailing end with the decrease in supersaturation and initial ledge spacing. Eventually all the component and coalesced ledges move at constant velocities over a sufficiently long period.

In the case where the density of kinks on the ledge riser is not large, the motion of kinks on the ledge riser is governed by diffusion in three dimensions. Atkinson and Wilmott (1991) analyzed the motion of a train of kinks and reported qualitatively similar features to those of ledges in two dimensions.

5.4.3 Ledgewise growth vs disordered growth

Doherty and Cantor (1982) and Enomoto (1987a) conducted a simulation of the motion of an infinite train of equally spaced ledges. Apart from the

© Woodhead Publishing Limited, 2012

stability of such a ledge configuration, the works aimed to answer a question as to whether the ledged boundary in which atom addition occurs only at restricted portions of the boundary, i.e. ledge risers, can grow faster than the disordered boundary in which solute atoms can be adsorbed at all positions of the boundary. The growth rate of such a ledged boundary is given by:

$$G = \frac{h}{\lambda} v \qquad [5.25]$$

where h is the ledge height and λ is the ledge spacing. In the initial period in which diffusion fields of adjacent ledges do not overlap significantly, the boundary moves following the same time law as that of a single ledge. When the time reached $\sim\lambda^2/D$, the time exponent of growth gradually reached 1/2 as the extent of diffusion field overlap increases. The growth rate in the direction *perpendicular to the terrace* can exceed the disordered boundary at small ledge spacing. However, ledged boundaries did not appear to grow faster than the disordered boundary in the direction *perpendicular to the plane of the boundary*.

These results were obtained under idealized conditions and many issues remain to be solved in order to bridge the gap between the conditions assumed in the simulations and actual conditions at solid interfaces (Atkinson *et al*., 1991). They include elaboration of a most appropriate boundary condition along the ledge riser for a solid interface, incorporation of the influence of elastic interaction between ledges on the diffusion, and use of a discrete description of atom transport for one or two atom high ledges rather than the continuum models so far developed. Indeed, Howe (1998) observed that ledges displayed a discontinuous start-stop behavior, rather than a continuous smooth movement along the broad face of a θ-plate in an Al-Cu-Mg-Ag alloy. Whereas various sources of ledges have been observed (Aaronson, 1974), the mechanism governing the nucleation rate and height of ledges are not well known. Thus, only initial attempts have been made to incorporate the nucleation and annihilation of ledges into simulation of precipitate growth (Enomoto, 1991; Spanos *et al*., 1994). It is also noted that Bréchet and Purdy (2005) incorporated effects of solute accumulation on the migration of a ledge riser.

In microalloyed steels, often characteristic arrays of carbide precipitates are observed within ferrite particles (Honeycomb, 1984). The precipitate sizes and spacings of precipitate rows are usually less than 10 nm and 10–100 nm, respectively, which become smaller as the transformation temperature is lowered. The straight rows of carbides are believed to be formed by nucleation of carbide at the low-energy terrace of a ledge at the α/γ phase boundaries, i.e. $(111)_\gamma$ and $(110)_\alpha$ close-packed planes. This type of carbide precipitation, called interphase precipitation is observed at temperatures typically higher than 700°C, whereas more irregular arrays of precipitates,

© Woodhead Publishing Limited, 2012

e.g. curved rows and precipitate sheet planes deviated from the close-packed planes, can be observed at lower temperatures (≥600°C). Okamoto and Ågren (2010) combined solute drag with ledge migration in their newly proposed model of interphase precipitation in microalloyed steel.

5.4.4 Motion of disconnections

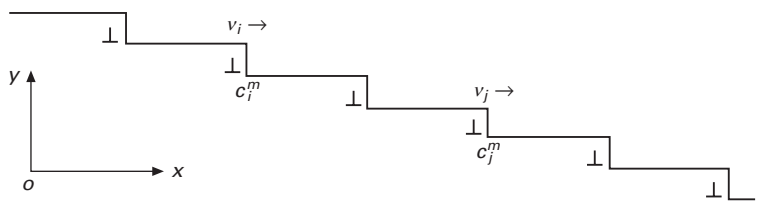
As described in an earlier section, ledges are often associated with interfacial dislocations. These defects which have both dislocation and ledge character are called disconnections. The concept of disconnection has proved useful for the discussion of interfacial phenomena in diffusional and diffusionless transformations (Hirth and Pond, 1994; Hirth, 1996; Howe *et al.*, 2009). Kamat and Hirth (1994) were the first to note this feature of interfacial ledges and discuss the condition for the formation of a multiple height ledge taking elastic interaction into account. Subsequently, Enomoto and Hirth (1996) developed a finite difference computer model which incorporated both diffusional and elastic interactions to simulate the migration of disconnections. The elastic force acting on the *i*th disconnection from the neighbors in a train of disconnections (see Fig. 5.10), is given by:

$$F_i = \sum_{j \neq i} \sigma_{xy}^{(j)} b = \frac{\mu b^2}{2\pi(1-\nu)} \sum_{j \neq i} \Phi(x_i, x_j, y_i, y_j) \qquad [5.26]$$

where $\sigma_{xy}^{(j)}$ is the stress of the *j*th disconnection acting on the *i*th disconnection, b is the Burgers vector, μ is the shear modulus, ν is the Poisson's ratio and Φ is defined by:

$$\Phi(x_i, x_j, y_i, y_j) \equiv \frac{(x_i - x_j)\{(x_i - x_j)^2 - (y_i - y_j)^2\}}{\{(x_i - x_j)^2 + (y_i - y_j)^2\}^2} \qquad [5.27]$$

The solute concentration at the riser of the *i*th disconnection is calculated from:



5.10 Ledges containing an edge dislocation (disconnections) with the Burgers vector parallel to the terrace plane (Enomoto and Hirth, 1996).

© Woodhead Publishing Limited, 2012

$$\sum_{j\neq i}\sigma_{xy}^{(j)}b+\frac{\Delta G_{th}}{V_m}h=\frac{RT}{V_m}\left\{(1-c^0)\ln\frac{1-c_i^m}{1-c^0}+c^0\ln\frac{c_i^m}{c^0}\right\} \quad [5.28]$$

where ΔG_{th} is the free energy change attending the transformation and V_m is the molar volume. The ΔG_{th} is given by:

$$\Delta G_{th}=RT\left\{(1-c^0)\ln\frac{1-c^e}{1-c^0}+c^0\ln\frac{c^e}{c^0}\right\} \quad [5.29]$$

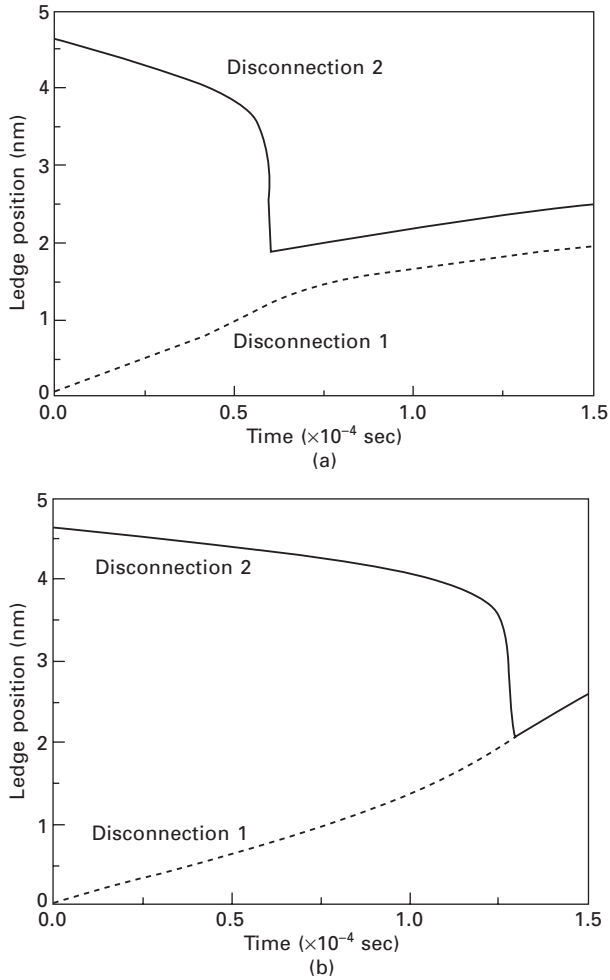
where c^e is the solute concentration in the matrix at equilibrium with the precipitate, c^0 is the bulk solute concentration, R is the gas constant and T is temperature.

So far, simulations incorporating strain field interactions were conducted in Al-Ag alloy in which two-atom high disconnections at the broad face of γ' plate contain Shockley partial dislocations. The elastic interaction force depends upon the Burgers vectors of the partial dislocations. Figure 5.11(a) and (b) show the evolution of ledge configuration in a train of two disconnections which have different Burgers vectors. The pair of disconnections in Fig. 5.11(a) migrated under a strong attractive force and thus the leading disconnection moved backward from the beginning, approached one another and stopped at a distance ~h, where the interaction became repulsive. With the assumed initial spacing (5 nm), this occurred in less than 10^{-4} sec. In contrast, the pair of disconnections in Fig. 5.11(b) coalesced to form one double height disconnection, although this occurred slowly due to weaker elastic interaction. These disconnections end up with a pile-up at the plate edge and the form of pile-up depends on the nucleation sequence of different types of Shockley partials. A remarkable difference from the ledge motion *without* elastic interaction is that the component ledges having a dislocation character can move at a constant spacing and an equal speed in a train after the initial transient period. This is in contrast to the train of ledges moving solely with diffusion field interaction which achieves steady motion with different velocities. Moreover, the pile-ups of multiple disconnections can occur readily when the elastic interaction favors the process (Kamat and Hirth, 1994).

5.5 Conclusions and future trends

The theory of phase boundaries in solids has been advanced significantly during recent decades. One of the most remarkable features is the recognition of ledged structure which lowers the free energy and increases the stability of a phase boundary. This was revealed with the boundary of ferrite plates in the austenite matrix in an Fe-C-Si alloy (Rigsbee and Aaronson, 1979b) and the boundary of cementite plates in austenite in a high manganese steel

© Woodhead Publishing Limited, 2012



5.11 Motion of disconnections on the broad face of a γ' plate in an Al-Ag alloy simulated at 350°C. Ledges 1 and 2 contain (a) Shockley partials of the Burgers (a/6)[11$\bar{2}$] and (a/6)[$\bar{2}$11], and (b) Shockley partials of the Burgers (a/6)[$\bar{2}$11] and (a/6)[1$\bar{2}$1], respectively (Enomoto and Hirth, 1996).

(Howe and Spanos, 1999) as well as in some non-ferrous alloys. In addition to the conventional approach to the structure of phase boundaries based upon plane-to-plane matching, an approach based upon edge-to-edge matching originally proposed for martensite boundary has attracted considerable attention. Using this approach, understanding of irrational boundaries, e.g. containing one-dimensional commensuration, has been advanced.

The calculation of coherent phase boundary energies has been fairly well established. The DLP-NNBB approaches permit the chemical energy

© Woodhead Publishing Limited, 2012

of coherent boundaries to be calculated for a large number of boundary orientations and thus to construct the equilibrium shape of a precipitate in three dimensions as long as the crystal structures are relatively simple. One can calculate more accurately specific boundary energies by means of atomistic calculations using multi-body interaction potential and from *ab initio* calculations as well. The energies of semi-coherent boundaries, containing misfit dislocations and/or ledges are obtained by adding the energies of these defects (termed structural parts) to the chemical part. Geometrical models such as O-lattice theory provide relative stability and morphology of semi-coherent phase boundaries (Ecob and Ralph, 1981). A significant amount of experimental data is available for the energy of incoherent phase boundaries. The values of nucleus/matrix boundary energy evaluated from measured nucleation rates are often much smaller than the calculated and measured phase boundary energy values. Further investigation of nucleus/matrix boundary energy as well as nucleation theory is needed to bridge this gap.

The structure and crystallography of transformation interfaces are described by disconnections, the motion of which dictates the growth and morphological evolution. The influences of diffusion field interaction among ledges on the migration behavior have been documented fairly well. One can expect further significant advances in the area of migration of phase transformation interfaces by incorporating elastic strain energy interactions. One would also expect further developments in these areas by large-scale computer simulation.

For recent developments of the theories of interfaces, special attention should be paid to the symposium on 'The Mechanisms of the Massive Transformation' held in 2000 and the Hume-Rothery symposium on 'Structure and Diffusional Growth Mechanisms of Irrational Interphase Boundaries' held in 2004. A number of valuable suggestions illuminating the future problems regarding ledge growth were made in the symposium on 'The Role of Ledges in Phase Transformations' held in 1989. Although the suggestions were made two decades ago, only a little progress seems to have been made since then. Sutton and Balluffi (1995) described basic principles in great detail of all aspects of interfaces in solids. Howe (1997) presented a unified description of solid-vapor, solid-liquid and solid-solid interfaces with emphasis on a nearest-neighbor bond approach and terrace-ledge-kink mechanism for the migration of phase boundaries. Readers are also referred to a comprehensive description of experimental studies of disconnection at phase boundaries by Howe *et al*. (2009).

5.6 References

Aaronson H I (1970), 'Mechanisms of diffusional growth of precipitate crystals', in Aaronson H I, *Phase Transformations*, Metals Park, OH, ASM, pp. 313–396.

© Woodhead Publishing Limited, 2012

Aaronson H I (1974), 'Observations on interphase boundary structure', *J Microscopy*, 102, 275–300.

Aaronson H I and Lee J K (1999), 'The kinetic equations of solid → solid nucleation theory and comparisons with experimental observations', in Aaronson H I, *Lectures on the Theory of Phase Transformations*, 2nd edn. Warrendale, PA, TMS, pp. 165–229.

Atkinson C (1981), 'The growth kinetics of individual ledges during solid-solid phase transformations', *Proc Roy Soc Lond*, A378, 351–368.

Atkinson C (1982), 'The growth kinetics of ledges during phase transformations: multistep interactions', *Proc Roy Soc Lond*, A384, 107–133.

Atkinson C (1991), 'A mathematical method for the calculation of ledge growth kinetics', *Metall Trans A*, 22A, 1211–1218.

Atkinson C (2007), 'The influence of concentration-dependent diffusivity on the growth kinetics of individual ledges during solid-solid phase transformations', *Acta Met*, 55, 2503–2508.

Atkinson C and Wilmott P (1991), 'Diffusion-controlled kink motion', *Metall Trans A*, 22A, 1219–1224.

Atkinson C, Enomoto M, Mullins W W and Trivedi R (1991), 'Report on panel discussion II: critical problems in the mathematics of ledgewise growth', *Metall Trans A*, 22A, 1247–1248.

Becker R (1938), 'Die Keimbuildung bei der Aussheidung in Metallishen Mischkristallen', *Annalen der Physik*, 32, 128–140.

Bréchet Y and Purdy G (2005), 'A self-consistent treatment of precipitate growth via ledge migration in the presence of interfacial dissipation', *Scripta Mater*, 52, 7–10.

Burton W K, Cabrera N and Frank F C (1951), 'The growth of crystals and the equilibrium structure of their surfaces', *Phil Trans Roy Soc*, 243, 299–358.

Cahn J W and Hilliard J E (1958), 'Free energy of a nonuniform system. I. Interfacial free energy', *J Chem Phys*, 28, 258–267.

Chen J K, Farkas D and Reynolds Jr W T (1994), 'Atomistic simulations of fcc:bcc interphase boundary structures', in Johnson W C, Howe J M, Laughlin D E, Soffa W A, *Solid→Solid Phase Transformations*, Warrendale, PA, TMS-AIME, pp. 1097–1102.

Doherty R D and Cantor B (1982), 'Computer modeling of ledge growth kinetics', in Aaronson H I, Laughlin D E, Sekerka R F, Wayman C M, *Solid→Solid Phase Transformations*, Warrendale, PA, TMS-AIME, pp. 547–553.

Ecob R C and Ralph B (1981), 'A model of the equilibrium structure of fcc/bcc interfaces', *Acta Met*, 29, 1037–1046.

Enomoto M (1987a), 'Computer modeling of the growth kinetics of ledged interphase boundaries – I. Single steps and infinite train of steps', *Acta Met*, 35, 935–945.

Enomoto M (1987b), 'Computer modeling of the growth kinetics of ledged interphase boundaries – II. Finite train of steps', *Acta Met*, 35, 947–956.

Enomoto M (1991), 'Computer simulation of morphological changes of grain boundary precipitates growing by the ledge mechanism', *Metall Trans A*, 22A, 1235–1245.

Enomoto M and Hirth J P (1996), 'Computer simulation of ledge migration under elastic interaction', *Metall Mater Trans A*, 27A, 1491–1500.

Enomoto M, Aaronson H I, Avila J and Atkinson C (1982), 'Influence of diffusional interactions among ledges on the growth kinetics of interphase boundaries', in Howe J M, Aaronson H I, Laughlin D E, Sekerka R F, Wayman C M, *Solid→Solid Phase Transformations*, Warrendale, PA, TMS-AIME, pp. 567–571.

Enomoto M, Nagano T and Yang J B (2005), 'Calculation of interfacial energy between

© Woodhead Publishing Limited, 2012

α and γ iron near a rational orientation relationship', in Howe J M, Laughlin D E, Lee J K, Dahmen U and Soffa W A, *Solid→Solid Phase Transformations in Inorganic Materials*, Warrendale, PA, TMS-AIME, pp. 67–78.

Farooque M and Edmonds D V (1990), 'The orientation relationships between widmanstätten cementite and austenite', *Proc. XIIth Intl Congress for Electron Microscopy*, Seattle, pp. 910–911.

Frank F C, (1953), 'Martensite', *Acta Metall*, 1 15–21.

Furuhara T and Aaronson H I (1991), 'Computer modeling of partially coherent bcc:hcp boundaries', *Acta Met Mater*, 39, 2857–2872.

Furuhara T, Howe J M and Aaronson H I (1991), 'Interphase boundary structures of intragranular proeutectoid α plates in a hypereutectoid Ti-Cr alloy', *Acta Met Mater*, 39, 2873–2886.

Gjostein N A, Domian H A, Aaronson H I and Eichen E (1966), 'Relative interfacial energies in Fe-C alloys', *Acta Met*, 14, 1637–1644.

Hall M G, Aaronson H I and Kinsman K R (1972), 'The structure of nearly coherent fcc:bcc boundaries in a Cu-Cr alloy', *Surf Sci*, 31, 257–274.

Hirth J P (1996), 'Dislocations, steps and disconnections at interfaces', *J Phys Chem Solids*, 10, 985–989.

Hirth J P and Lothe J (1982), *Theory of Dislocations*, New York, John Wiley and Sons.

Hirth J P and Pond R C (1994), 'Steps, dislocations and disconnections as interface defects relating to structure and phase transformations', *Acta Mater*, 44, 4749–4763.

Hondros E D (1978), 'Interfacial energies and composition in solids', in Russell K C and Aaronson H I, *Precipitation Processes in Solids*, Warrendale, PA, TMS-AIME, pp. 1–30.

Honeycomb R W K (1984), 'Carbide precipitation in ferrite', in Marder A R and Goldstein J I, *Phase Transformations in Ferrous Alloys*, Warrendale, PA, TMS-AIME, pp. 259–291.

Howe J M (1997), *Interfaces in Materials*, New York, John Wiley & Sons.

Howe J M (1998), 'Atomic structure, composition, mechanisms and dynamics of transformation interfaces in diffusional phase transformations', *Mater Trans JIM*, 39, 3–23.

Howe J and Spanos G (1999), 'Atomic structure of the austenite-cementite interface of proeutectoid cementite plates', *Phil Mag A*, 79, 9–30.

Howe J M, Aaronson H I and Hirth J P (2000), 'Aspects of interphase boundary structure in diffusional phase transformations', *Acta Mater*, 48, 3977–3984.

Howe J M, Pond R C and Hirth J P (2009), 'The role of disconnections in phase transformations', *Prog Mater Sci*, 54, 792–838.

Jones G J and Trivedi R (1971), 'Lateral growth in solid-solid phase transformations', *J Appl Phys*, 42, 4299–4304.

Jones G J and Trivedi R (1975), 'The kinetics of lateral growth', *J Crystal Growth*, 29, 155–166.

Kamat S V and Hirth J P (1994), 'The elastic stabilization of multiple-height growth ledges during diffusional phase transformations', *Acta Metall Mater*, 42, 3767–3772.

Kelly P M and Zhang M X (1999), 'Edge-to-edge matching: a new approach to the morphology and crystallography of precipitates', *Mater. Forum*, 23, 41–62.

Kelly P M and Zhang M X (2006), 'Edge-to-edge matching – the fundamentals', *Metall Mater Trans A*, 37A, 833–839.

King A D and Bell T (1974), 'Morphology and crystallography of Widmanstätten proeutectoid ferrite', *Met Sci*, 5, 253–260.

© Woodhead Publishing Limited, 2012

King A D and Bell T (1975), 'Crystallography of grain boundary proeutectoid ferrite', *Metall Trans A*, 6A, 1419–1429.

Lange III W F, Enomoto M and Aaronson H I (1988), 'The kinetics of ferrite nucleation at austenite grain boundaries in Fe-C alloys', *Metall Trans A*, 19A, 427–440.

Lee Y and Aaronson H I (1980), 'Anisotropy of coherent interphase boundary energy', *Acta Metall*, 28, 539–548.

Lee H J and Aaronson H I (1988), 'Eutectoid decomposition mechanisms in hypereutectoid Ti-X alloys', *J Mater Sci*, 23, 150–160.

LeGoues F K, Aaronson H I, Lee Y W and Fix G J (2006), 'Influence of crystallography upon critical nucleus shapes and kinetics of homogeneous fcc→fcc nucleation', in Aaronson H I, Laughlin D E, Sekerka R F and Wayman C M, *Solid→Solid Phase Transformations*, Warrendale, PA, TMS-AIME, pp. 427–431.

Massalski T B, Soffa W A and Laughlin D E (2006), 'The nature and role of incoherent interphase interfaces in diffusional solid-solid phase transformations', *Metall Mater Trans A*, 37A, 825–831.

Moritani T, Miyajima N, Furuhara T and Maki T (2002), 'Comparison of interphase boundary structure between bainite and martensite in steel', *Scripta Mater*, 47, 193–199.

Nagano T and Enomoto M (2006), 'Calculation of the interfacial energies between α and γ iron and equilibrium particle shape', *Metall Mater Trans*, 37A, 929–937.

Offerman S E, van Dijk N H, Sietsma J, Grigull S, Lauridsen E M, Margulies L, Poulsen H F, Rekveldt M Th and van der Zwaag S (2002), 'Grain nucleation and growth during phase transformations', *Science*, 298, 1003–1005.

Offerman S E, van Dijk N H, Sietsma J, Lauridsen E M, Margulies L, Grigull S, Poulsen H F and van der Zwaag S (2006), 'Phase transformations in steel studied by 3D XRD microscopy', *Nucl Instr Meth Phys Res B*, 246, 194–200.

Ogawa K and Kajiwara S (2004), 'High-resolution electron microscopy study of ledge structures and transition lattices at the austenite-martensite interface in Fe-based alloys', *Phil Mag*, 84, 2919–2947.

Okamoto R and Ågren J (2010), 'A model for interphase precipitation based on finite interface solute drag theory', *Acta Mater*, 58, 4791–4803.

Pitsch W (1962), 'Die Orientierungszusammenhang zwishen Zementie und Austenit', *Acta Met*, 10, 897–900.

Pond R C, Celoto S and Hirth J P (2003), 'A comparison of the phenomenological theory of martensitic transformations with a model based on interfacial defects', *Acta Mater*, 52, 5385–5398.

Reynolds Jr. W T and Farkas D (2006), 'Edge-to-edge interfaces in Ti-Al modeled with the embedded atom method', *Metall Mater Trans A*, 37A, 865–871.

Rigsbee J M and Aaronson H I (1979a), 'A computer modeling study of partially coherent fcc:bcc boundaries', *Acta Metall*, 27, 351–363.

Rigsbee J M and Aaronson H I (1979b), 'The interfacial structure of the broad faces of ferrite plates', *Acta Metall*, 27, 365–376.

Shiflet G J and van der Merwe J H (1994a), 'The role of structural ledges at phase boundaries – II. Fcc-bcc interfaces in Nishiyama–Wassermann orientation', *Acta Met Mat*, 42, 1189–1198.

Shiflet G J and van der Merwe J H (1994b), 'The role of structural ledges as misfit-compensating defects: fcc-bcc interphase boundaries', *Metall Mater Trans A*, 25A, 1895–1903.

Sonderegger B and Kozeschnik E (2009), 'Size dependence of the interfacial energy in the generalized nearest-neighbor broken-bond approach', *Scripta Mater*, 60, 635–638.

© Woodhead Publishing Limited, 2012

Spanos G (1989), 'The bainite and proeutectoid cementite reactions in hypereutectoid Fe-C-Mn alloys', PhD thesis, Carnegie-Mellon University.

Spanos G and Aaronson H I (1990), 'The interfacial structure and habit plane of proeutectoid cementite plates', *Acta Met Mat*, 38, 2721–2732.

Spanos G and Kral M V (2009), 'The proeutectoid cementite transformation in steels', *Int Mat Rev*, 54, 19–47.

Spanos G, Masumura R A, Vandermeer R A and Enomoto M (1994), 'The evolution and growth kinetics of precipitate plates growing by the ledge mechanism', *Acta Metall Mater*, 42, 4165–4176.

Sutton A P and Balluffi R W (1995), *Interfaces in Crystalline Materials*, Oxford, Clarendon Press.

Thompson S W and Howell P R (1987), 'The orientation relationship between intragranularly nucleated Widmanstätten cementite and austenite in a commercial hypereutactoid steel', *Scripta Metall*, 21, 1353–1357.

Van der Merwe J H (1963a), 'Crystal interfaces. Part I. Semi-infinite crystals', *J App Phys*, 34, 117–122.

Van der Merwe J H (1963b), 'Crystal interfaces. Part. Finite overgrowths', *J App Phys*, 34, 123–127.

Van der Merwe J H and Shiflet G J (1994a), 'The role of structural ledges at phase boundaries – I. Interfaces with rectangular atomic nets', *Acta Met Mat*, 42, 1173–1187.

Van der Merwe J H and Shiflet G J (1994b), 'The role of structural ledges at phase boundaries – III. Fcc-bcc interfaces in Kurdjumov–Sachs orientation', *Acta Met Mat*, 42, 1199–1205.

Yang Z G and Enomoto M (1999), 'A discrete lattice plane analysis of coherent fcc/B1 interfacial energy', *Acta Mater*, 47, 4515–4524.

Yang Z G and Enomoto M (2001), 'Calculation of the interfacial energy of B1-type carbides and nitrides with austenite', *Metall Mater Trans A*, 32A, 267–274.

Yang Z G and Enomoto M (2002), 'Discrete lattice plane analysis of Baker–Nutting related B1 compound/ferrite interfacial energy', *Mater Sci Eng*, A332, 184–192.

Yang Z and Johnson R A (1993), 'An EAM simulation of the α-γ iron interface', *Model Simul Mater Sci Eng*, 1, 707–716.

Zhang M X and Kelly P M (1998), 'Crystallography and morphology of Widmanstätten cementite in austenite', *Acta Mater*, 46, 4617–4628.

Zhou D S and Shiflet G J (1992), 'A new orientation relationship between austenite and cementite in an Fe-C-Mn steel', *Scripta Metall*, 27, 1215–1218.

© Woodhead Publishing Limited, 2012

6

Fundamentals of ferrite formation in steels

M. STRANGWOOD, The University of Birmingham, UK

Abstract: The diffusional formation of ferrite at low undercoolings has, historically, been extensively researched, which has led to well-established mechanisms for nucleation and growth. These have been verified against experimental data to allow modelling with good agreement to experiment, often as transformation diagrams. These mechanisms are summarised here and opportunities for improvement through advances in experimentation and computation are highlighted.

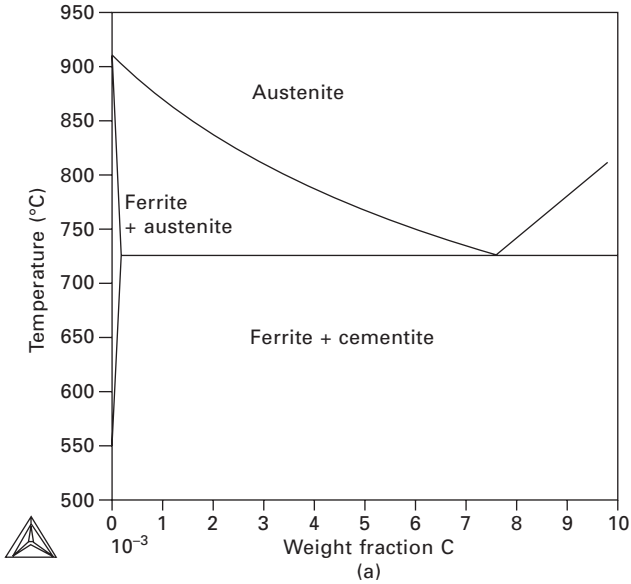
Key words: diffusional formation, ferrite, allotriomorphs, idiomorphs, partition-local equilibrium, non partition-local equilibrium, paraequilibrium.

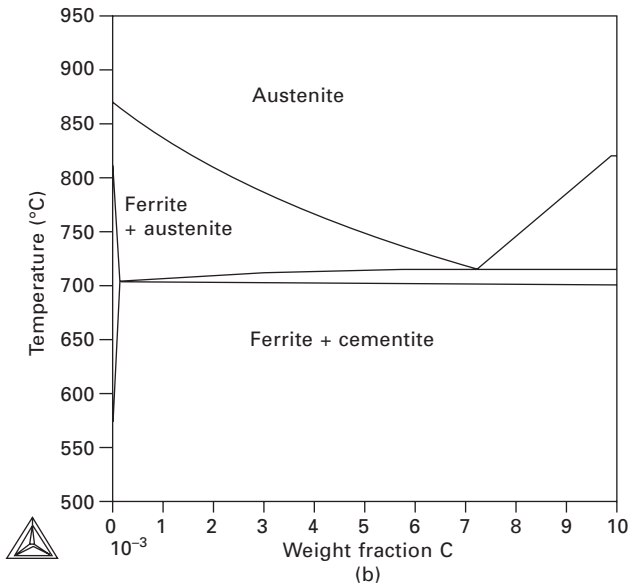
6.1 Introduction

The technical importance of ferrite in medium- to high-carbon steels throughout the 19th and early 20th centuries meant that this was one of the first phases whose transformation behaviour and mechanisms were studied in detail. The ability, since the initial developments by Sorby in the second half of the 19th century (Hammond, 1989), to distinguish and characterise this phase optically has allowed a great deal of early phase transformation work to be associated with the nucleation and growth of this phase. The subsequent use of much of this work in undergraduate and postgraduate courses has led to a familiarity with it that can often result in its complexities and remaining questions being missed.

The importance and early study of this field has led to a number of excellent books and reviews (Aaronson, 1962, 1969; Christian, 1975; Bhadeshia, 1985; Hillert, 1998; Costa e Silva *et al.*, 2007). This chapter will summarise the work carried out in this field and the current understanding and quantitative description of the formation of ferrite by diffusional mechanisms at relatively low undercoolings (Fig. 6.1) (displacive and coupled diffusional-displacive transformations at larger undercoolings are dealt with in later chapters) under thermal conditions, albeit to less depth than in the previous reviews. Despite the deep understanding of this transformation gained over the last 150 years, issues remain that need to be tackled for a more quantitative description of the transformation along with some of the subtleties shown for this phase. However, improved experimental and modelling techniques may now allow a number of remaining issues to be addressed, which will be considered here.

© Woodhead Publishing Limited, 2012





6.1 (a) Schematic Fe-C phase diagram and (b) vertical isopleth for Fe-C-Ni at 1 wt% Ni showing shifts in transformation temperatures and broadening of phase fields with addition of an austenite stabiliser. Diffusional formation of ferrite will take place from the Ae_3 temperature down to around 600°C.

© Woodhead Publishing Limited, 2012

6.2 Crystallography

6.2.1 Volume change

The transformation from austenite to ferrite involves the re-arrangement of the iron atoms in the fcc austenite structure into the ferritic bcc structure. In pure iron the lattice parameters reported are: 0.3648 nm and 0.2906 nm for austenite and ferrite, respectively, at 910°C (Basinski *et al.*, 1955; Goldschmidt, 1962; Kohlhaas *et al.*, 1967; Onink *et al.*, 1993). Alloying additions in solid solution will cause the lattice parameters of austenite and ferrite to change, often linearly with the amount of solute in solid solution (Vegard's law; Denton & Ashcroft, 1991). The room temperature lattice parameters for ferrite are readily obtained by X-ray diffraction (XRD), whereas those for austenite require high temperature XRD (Garcia de Andres *et al.*, 1998; Kop *et al.*, 2001). Applications of these techniques have resulted in identification of the lattice parameter relationships summarised in Table 6.1.

The formation of ferrite from austenite in pure iron therefore involves a volume change of –0.55%, which will change with composition as the lattice parameters change and as the transformation temperature changes. The latter factor will also vary with cooling rate as faster cooling rates tend to depress

Table 6.1 Summary of effects of alloying elements in solution on lattice parameters (nm) of austenite and ferrite

Phase	Relationship	Reference
γ at 300 K	0.3573 + 0.0033 [C] + 0.000095 [Mn] – 0.00002 [Ni] + 0.00006 [Cr] + 0.00031 [Mo] + 0.00018 [V] (wt%)	Ridley *et al.*, 1969 Dyson & Holmes, 1970
Strain-free γ at 300 K (AISI 316)	0.35965 + (0.0028 ± 9.07 × 10^{-5}) [C] (wt%) Expansion parameters reported between 0.0028 and 0.0603 for proportion of interstices filled by C and 0.0597 for interstices filled by N	Hummelshøj *et al.*, 2010
γ (C-Mn steels)	0.3577 + 0.00065 [C] + 0.0001 [Mn] – 0.00002 [Ni] + 0.00006 [Cr] + 0.00056 [N] + 0.00028 [Al] – 0.00004 [Co] + 0.00014 [Cu] + 0.00053 [Mo] + 0.00079 [Nb] + 0.00032 [Ti] + 0.00017 [V] + 0.00057 [W] at%	Lee & Lee, 2005
γ at 300 K	0.35729 + 0.0001144 [Mn] at%	Li *et al.*, 2002
α 298 K	0.28664 + 0.00006 [Mn] – 0.00003 [Si] – 0.00007 [Ni] + 0.00005 [Cr] – 0.0001 [P] – 0.00031 [Ti] + 0.00027 [Ru] + 0.00035 [Rh] + 0.00029 [Re] + 0.00037 [Ir] + 0.0004 [Pt] at%	Lee & Lee, 2005
α 298 K	0.28664 + 0.0000543 [Mn] at%	Li *et al.*, 2002

© Woodhead Publishing Limited, 2012

the transformation temperature from austenite to ferrite. The difference in molar volume between ferrite and austenite in alloy steels can be estimated using the relationships in Table 6.1, provided that amounts of solute in solution are known. This will require knowledge and/or assumptions regarding the degree of deviation from equilibrium during nucleation and growth and the extent of any precipitation. Commercial thermodynamic packages can then be used to predict the composition of the phases before and after transformation and so the molar volume change. The volume change means that the formation of ferrite in an austenitic matrix will cause some elastic straining of the surrounding austenitic matrix. Lower temperature bcc-based products, such as martensite and bainite that form by a displacive or coupled displacive-diffusional mechanism, result in potentially large shear strains in the surrounding austenitic matrix (Christian, 1965; Bhadeshia, 1985) such that externally applied strains can influence the morphology, transformation temperature and extent of transformation for these phases (Tamura & Wayman, 1992; Shipway & Bhadeshia, 1995). As for most crystalline materials, the elastic modulus of austenite decreases with increasing temperature; reports give a wide range of values, but modulus values have been reported to decrease below 50 GPa at temperatures between 600 and 800°C (Cooke, 1988). This is composition dependent and the modulus of Ni-free austenitic stainless steels decreases from 195 to 140 GPa over the range 25–700°C (Piatti & Schiller, 1986). In addition, the thermal expansivity of ferrite is greater than that for austenite (17.5×10^{-6} K^{-1} c.f. $19.5 - 24.7 \times 10^{-6}$ K^{-1}; Basinski *et al.*, 1955; Goldschmidt, 1962; Gorton *et al.*, 1965; Kohlhaas *et al.*, 1967; Onink *et al.*, 1993) so that the strain energy increases significantly as transformation temperature decreases, whilst the degree of lattice matching between the two structures decreases.

The range of values cited above treat the thermal expansion coefficient as a constant, i.e. linear expansion coefficient, whereas a number of XRD and dilatometric studies have revealed that the thermal expansivity of ferrite can be treated as a series of linear segments valid for different temperature ranges (Garcia de Andres *et al.*, 2002; Choi, 2003) or by a quadratic expression in temperature (T) with an exponential correction for the Curie temperature (Liu *et al.*, 2004). The thermal expansion coefficient for austenite is usually dealt with by a quadratic expression in T (te Velthuis *et al.*, 1998; Garcia de Andres *et al.*, 2002; Choi, 2003; Liu *et al.*, 2004). Example values for strain energy and interfacial energy vary from 400 J mol^{-1} for bainite forming between 440 and 560°C (Strangwood, 1987) to 1214 J mol^{-1} for a martensitic phase in pure iron forming at 700–750°C (Cohen *et al.*, 1949; Ackert & Parr, 1971). Theoretical predictions for the strain energy using a coherent interface are 4–5 times higher (Roitburd & Kurdjumov, 1979) indicating that relaxation in the interfacial condition is taking place. Transformation from an fcc structure to the bcc structure can be achieved through the Bain

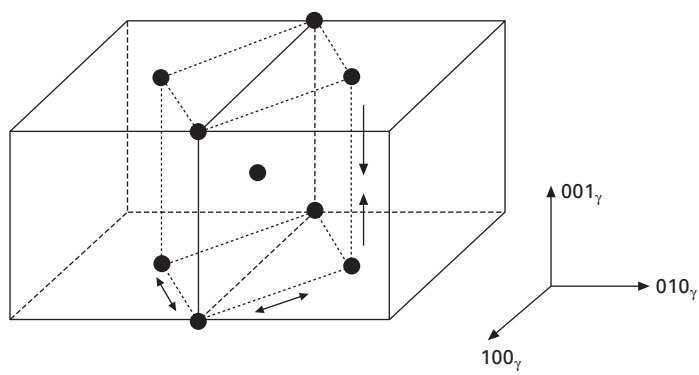
© Woodhead Publishing Limited, 2012

strain (Fig. 6.2) (Bain, 1924), and can be envisaged as a compression of 0.203 along $[001]_\gamma$ accompanied by dilation of 0.127 along $<110>_\gamma$. In the absence of long-range diffusion, this is manifested as an invariant line strain (invariant plane strain + rigid body rotation, as covered in later chapters) so that the coupling of shear and dilation components with externally applied stresses or those generated by transformation of neighbouring volumes can exert a strong influence on the transformation.

The effect of externally applied stresses is much reduced for ferrite formation at higher transformation temperatures where long-range diffusion can occur. Firstly, this is due to the reduced elastic modulus for austenite at the higher temperatures coupled with a reduced volume change reducing the elastic strain energy generated in the austenite surrounding a region of newly formed ferrite. In addition, the diffusion achieving advance of the α/γ interface into the remaining austenite (i.e. that normal to the interface plane) can be accompanied by diffusion within the interface that removes the shear strain associated with the transformation. The remaining strain is then dilatational and the strain energy can be dealt with by use of an Eshelby analysis (Eshelby, 1957, 1959), but this is usually negligible compared with the accuracy of transformation measurement techniques. Even the use of very large hydrostatic pressures (100s–1000s bar) would give little change in the transformation temperature (through a Clausius–Clapeyron treatment of the chemical driving force) for the small change in specific volume when considering diffusional transformations at low undercoolings.

6.2.2 Orientation relationships

Although elastic strain energy is not significant for diffusion-dominated formation of ferrite, the crystallography of the parent and product phases does affect the formation and morphology of ferrite. The need to minimise interfacial



6.2 The Bain strain.

© Woodhead Publishing Limited, 2012

energy in nucleation and, to a lesser extent, growth leads to the adoption of an orientation relationship (OR) between the austenite and ferrite. Reported ORs are not that predicted by the Bain strain ($[001]_\gamma \parallel [001]_\alpha$, $<110>_\gamma \parallel <100>_\alpha$), but are within 11° of it, which encompasses the Kurdjumov–Sachs (KS) (Kurdjumov & Sachs, 1930) and Nishiyama–Wasserman (NW) (Nishiyama, 1934; Wasserman, 1933) orientation relationships (Table 6.2). The deviations from the ideal orientation arise from the lack of a close packed plane in the bcc phase and so the alignment of the iron atoms from the two lattices results in elastic straining. The five orientation relationships noted in Table 6.2 can be related to each other by small rigid body rotations around common axes (Dahmen, 1982). Thus, the KS and NW/Pitsch orientation relationships can be converted into the GT and GT′ by rotations of 2.41° and 2.86° around <011> and <111>, respectively. The occurrence of a number of closely related orientation relationships would suggest that the free energy penalty associated with accommodating a common interface between fcc and bcc lattices has a number of local minima. The selection of any particular variant can be determined by small differences in composition, lattice parameter and transformation temperatures, e.g. the selection of GT′ in high nickel meteorites (He *et al.*, 2006) and stainless steels (Tsai *et al.*, 2002). Variant selection has been much more closely studied for displacive and displacive-diffusional transformations, particularly the training of shape memory alloys (Liu & Bunge, 1991; Kitahara *et al.*, 2005; Raghunathan *et al.*, 2008; Malet *et al.*, 2009). The development and widespread use of automated electron back scattered diffraction (EBSD) techniques in high resolution scanning electron microscopes (Dingley, 2004; Randle, 2009a, 2009b) should make the identification and quantification of the crystallographic relationships for ferrite formed thermally under low undercoolings much easier, allowing the assumptions about nucleation and growth to be verified.

Table 6.2 Reported ferrite/austenite orientation relationships in iron and steels

Orientation relationship	Crystallography	Comments
Kurdjumov–Sachs (KS)	$\{110\}_\alpha \parallel \{111\}_\gamma$ $<111>_\alpha \parallel <101>_\gamma$	5.6° rotation results in NW
Nishiyama–Wasserman (NW)	$\{110\}_\alpha \parallel \{111\}_\gamma$ $<001>_\alpha \parallel <101>_\gamma$	Good atomic fit for only 8% of interface area between ferrite and austenite
Greninger–Troiano (GT)	$\{110\}_\alpha$ 0.2° from $\{111\}_\gamma$ $<111>_\alpha$ 2.7° from $<101>_\gamma$	Midway between KS and NW (Greninger & Troiano, 1949)
Inverse GT (or GT′)	$\{5\ 12\ 17\}_\alpha \parallel \{7\ 17\ 17\}_\gamma$ $<111>_\alpha \parallel <101>_\gamma$	Observed in Gibeon meteorite (He *et al.*, 2006)
Pitsch	$\{101\}_\alpha \parallel \{010\}_\gamma$ $<111>_\alpha \parallel <101>_\gamma$	Pitsch (1962)

© Woodhead Publishing Limited, 2012

6.3 Transformation ranges

6.3.1 Transformation-time-temperature (TTT) and continuous cooling transformation (CCT) diagrams

The diffusional formation of ferrite ranges from 910°C (pure iron) to around 600°C depending on composition and cooling rate and involves a diffusional rearrangement of the iron atoms (pure iron) combined with a range of composition variations for steels. The effects for particular alloying elements will be cumulative, coming from their combined thermodynamic effects (α- or γ-stabilising nature as shown for Ni in Fig. 6.1(b)) and their kinetic effects, i.e. the time required for short- or long-range diffusion and partition during the transformation from austenite to ferrite. The kinetic effect due to elemental diffusion can be supplemented for strong carbo-nitride formers by M-(C,N) clustering, reducing the effective diffusivity of the interstitial elements and so slowing transformation.

Nucleation and growth rates are dealt with in greater detail later, but only alloying elements in solution have a significant effect on transformation behaviour (for transformation at low undercoolings the extent of solute trapping is limited). Thus, Ni will have the largest potential effect on depressing the Ae_3 due to its potency as a γ-stabiliser and its high solubility in austenite; kinetically it will also tend to partition to austenite and so slow transformation rates compared with Fe-C. The relatively high solubility of Mn means that it is frequently added to steels commercially to slow the ferrite formation kinetics. C and N are also potent γ-stabilisers, but their effect is limited by their generally low solubility, particularly in the presence of strong carbide formers such as Ti and Nb, which tend to precipitate carbo-nitrides in austenite removing the alloying element effects prior to temperatures at which ferrite forms. Si in solution suppresses the formation of cementite and raises the activity of carbon in solution so that it exerts the opposite effects to, for example, Nb.

Of the main microalloying element additions, V will tend to form carbides in ferrite or during the transformation (Honeycombe, 1976, 1979) so that it has a greater direct effect (as for Mo) on transformation behaviour in solution and through modifying the diffusivity of C; Nb, which is being investigated for its direct effect on the austenite-to-ferrite transformation has an indirect effect through modification of the prior austenite grain structure and hence distribution of nucleation sites for ferrite formation. The presence of vanadium in solution (the 'vanadium effect') can modify the transformation kinetics and lead to more acicular ferrite products (He & Edmonds, 2002). Cr is most effective in raising the transformation temperatures and slows the diffusion of C and N by clustering.

The effects of composition have, for many years been represented by transformation-time-temperature (TTT) or isothermal transformation (IT)

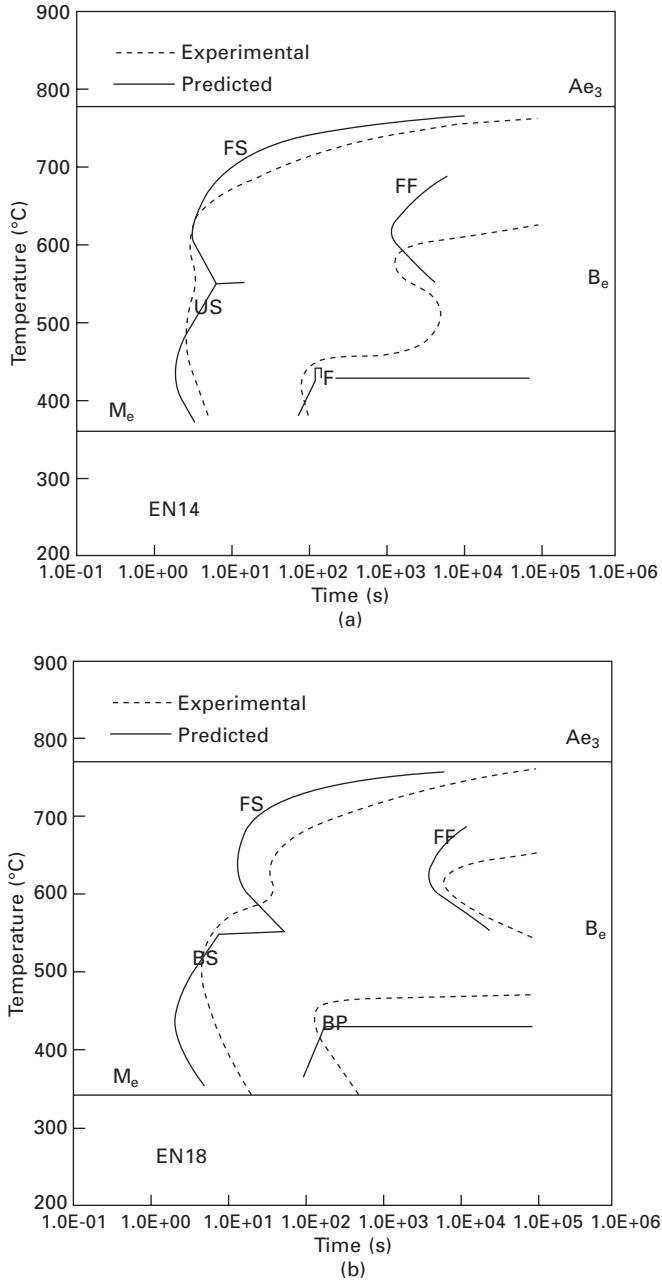
© Woodhead Publishing Limited, 2012

diagrams (Fig. 6.3), which apply strictly to instantaneous quenching to the transformation temperature and then holding at that temperature. The examples in Fig. 6.3 show the effect of increasing C and Mo (Fig. 6.3(b) compared with Fig. 6.3(a)). These additions cause slowing of both ferrite start time (FS) at temperatures between 550°C and the Ae_3 temperature (upper 'C' curves) with a much greater retardation of the ferrite finish time (FF) for the same temperature range shown by the dashed experimentally determined lines. The reduced extent of C diffusion associated with bainite start (BS) and finish (BF) gives a smaller shift in the lower 'C' curves (550°C down to M_S). Cooling rate effects are represented on continuous cooling transformation (CCT) diagrams (see Fig. 6.4 below).

The use of TTT diagrams followed the pioneering work of Davenport and Bain (1930) in studying the isothermal transformation behaviour of carbon steels. Since the 1930s a large number of TTT diagrams have been determined, mostly by microscopy and dilatometry in research papers and by steelmakers (Iron and Steel Institute, 1956; US Steel, 1963; ASM International, 1977; Akselsen *et al*., 1986; Harrison & Farrar, 1987; Paju *et al*., 1991). The accuracy of early diagrams would have been limited by the experimental techniques used; optical microscopy and point counting, XRD and dilatometry. More recently, *in-situ* studies, e.g. synchrotron studies, have been used (Poulsen, 2002; Offerman *et al*., 2005), but these studies utilise small samples (0.4–1.0 mm thick with a sample area of around 100 × 100 μm) and so may be affected by the presence or lack of segregation, which could lead to differences in overall transformation behaviour (Bhadeshia, 1983; Strangwood, 1987) compared with commercial steels. Three dimensional X-ray diffraction (3D-XRD) can be used to image individual grains, but, as with transmission electron microscopy (TEM) before it, the scaling up of the behaviour of small groups of grains to give overall steel behaviour in bulk (tonnage) quantities remains an issue. Despite the limitations of traditional and more recent techniques, published TTT diagrams are often the data used to verify transformation models for steels and iron-based systems (Kirkaldy, 1973; Kirkaldy *et al*., 1978; Bhadeshia, 1982; Umemoto *et al*., 1982; Kirkaldy, 1991; Lee & Bhadeshia, 1993).

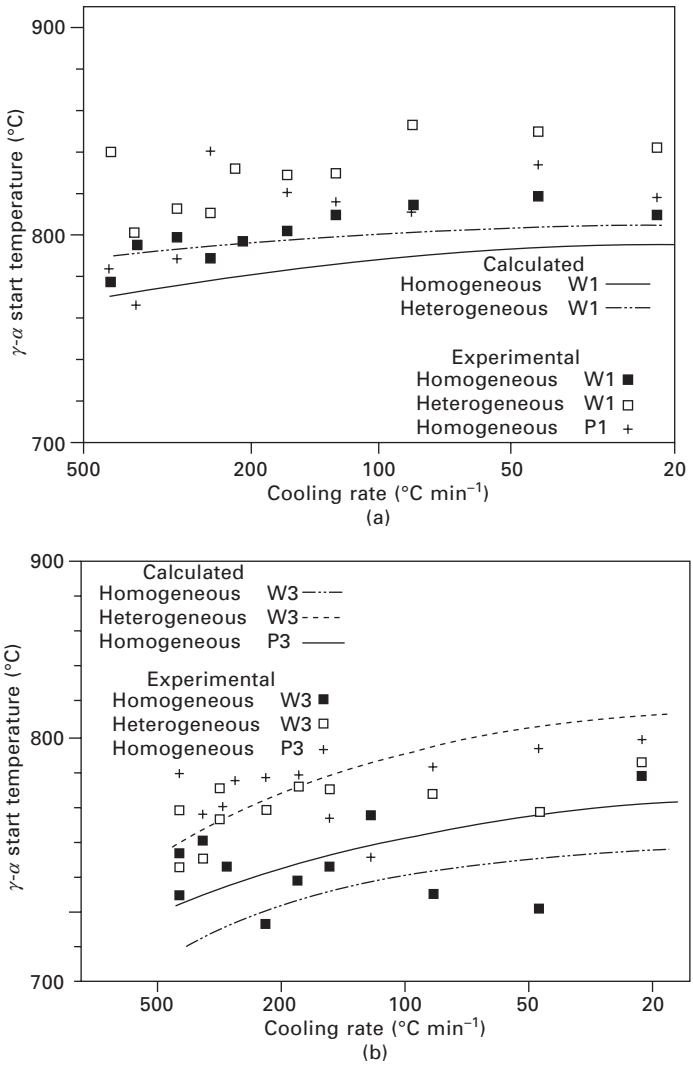
Similar techniques applied to continuously cooled samples, e.g. Jominy end quench samples, allowed CCT diagrams to be determined. The latter can be modelled for the upper 'C' curve using the additivity rule (Scheil, 1935; Homberg, 1996; Rios, 2005), i.e. if the cooling stages below the equilibrium transformation temperature are divided into a series of steps so that time t_i is spent at each temperature step, T_i, for which the incubation time is τ_i then transformation starts when pre-nucleation steps are completed, which is when:

© Woodhead Publishing Limited, 2012



6.3 Agreement between predicted and experimental TTT curves for EN14 (0.25 C-0.25 Si-1.5 Mn-0.015 S-0.015 P wt%) and EN16 (0.35 C-0.3 Si-1.5 Mn-0.03 S-0.025 P-0.25 Mo wt%) (Lee & Bhadeshia, 1993). Used with permission from Elsevier.

© Woodhead Publishing Limited, 2012



6.4 Example continuous cooling transformation (CCT) diagrams for homogenised and non-homogenised weld metal (W) and wrought (P) samples of (a) 0.1 C-0.19 Si-1.1 Mn and (b) 0.14 C-0.22 Si-1.81 Mn (wt%) steels (Strangwood, 1987).

$$\sum_i \frac{t_i}{\tau_i} = 1 \qquad [6.1]$$

This applies if the pre-nucleation steps are the same for the temperature steps considered and so the pre-nucleation steps for allotriomorphic/idiomorphic ferrite cannot be carried through to the displacive-diffusional transformations

© Woodhead Publishing Limited, 2012

of the lower 'C' curve. The 'additivity' approach in Eq. [6.1] has been used for the calculated curves in Fig. 6.4, which have been compared with experimentally (dilatometry) determined CCT curves for homogenised and nonhomogenised samples of two weld metals (W1 and W3) along with homogenised wrought material of the same compositions excluding oxygen (P1 and P3). Figure 6.4(b) shows that addition of 0.04 wt% C and 0.71 wt% Mn in W3/P3 compared with W1/P1 has results in suppression of the diffusional formation of ferrite to much lower temperatures, an effect that is more marked at faster cooling rates. The accuracy of these models will depend on a number of factors, including the theories for the stages of nucleation and growth used in the model; the data used in these theories; and the range of applicability, some of the aspects of which will be covered for nucleation and growth of ferrite at low undercoolings below.

6.3.2 Pure iron

For pure iron, with no partition required, there is no need for long-range diffusion in the parent austenite phase and the rate of transformation depends on the mobility of the α/γ interface. The transformation rate is therefore expected to be rapid, although reports of interface mobility are not readily available. The rapidity of transformation in pure iron means that it has been difficult to interrupt the transformation, although studies have revealed martensites in pure iron at cooling rates of around 3×10^3–5×10^4 K s^{-1} (Gilbert & Owen, 1962; Speich & Warlimont, 1968; Ackert & Parr, 1971; Duflos & Cantor, 1982). Additions of alloying elements – often for technological purposes to generate more useful metastable structures with improved mechanical properties – result in slowing of transformation, which has allowed the mechanisms of the transformation to be studied.

6.3.3 Carbon and alloy steels

In moving from pure iron to steels, the first compositional change is the addition of carbon, which, as an austenite stabiliser, depresses the transformation temperatures resulting in slower transformation rates. In addition, there is a need for long-range diffusion, due to the lower solubility of carbon in ferrite than in austenite. The use of medium- to high-carbon levels to achieve increased strength levels allowed empirical determination of TTT curves, as noted above, using interrupted heat treatments and optical metallography, followed by dilatometry, X-ray diffraction, electron microscopy and thermal methods such as differential scanning calorimetry (DSC) (Raju *et al.*, 2007, 2009), which is often used for phase diagram determination (Boettinger *et al.*, 2007) and differential thermal analysis (DTA) (Kempen *et al.*, 2002; Boettinger *et al.*, 2007). The experimental determination of a large number of

© Woodhead Publishing Limited, 2012

TTT diagrams (and accompanying continuous cooling transformation (CCT) curves; Figs 6.3 and 6.4) along with phase diagrams has allowed the design of improved steels along with the generation of a large body of thermodynamic data, that can be used to predict phase stability and composition as well as provide driving forces for models of nucleation and growth. Transformation theory has been verified against the data provided by the techniques above and so the agreement will be limited by the accuracy of those techniques. The continued development of experimental and analytical techniques means that continued experimental measurement is required in order to refine the theories as finer effects can be resolved (e.g. transformation products detected at levels lower than the roughly 5% achievable by, for example, XRD and dilatometry).

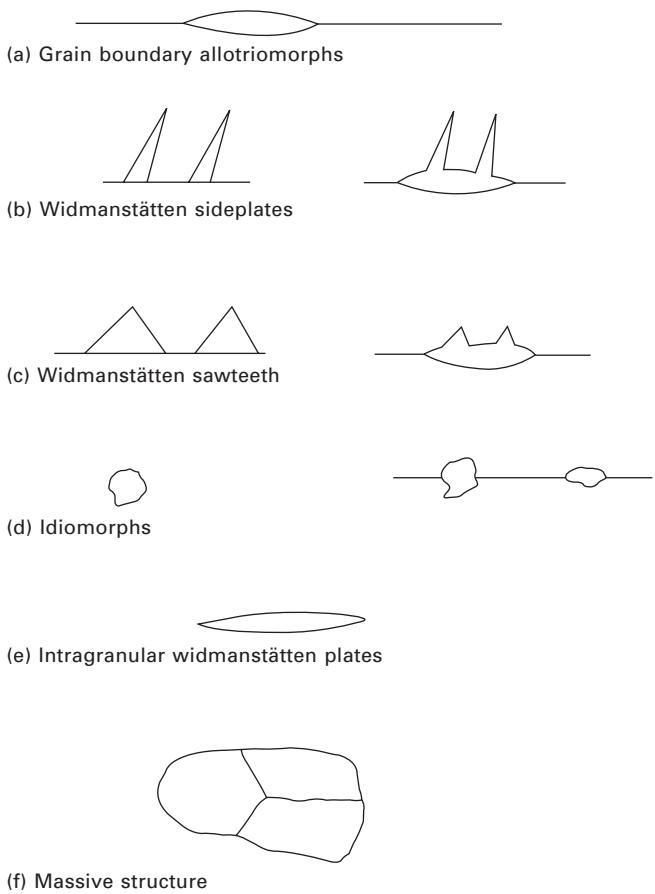
6.4 Nucleation

6.4.1 Morphology and interfaces

The Dubé morphological classification (Dubé, 1948) (Fig. 6.5) was derived for alloy steels and, for products of diffusional transformations, would include grain boundary allotriomorphs, intragranular idiomorphs, sideplates (Widmanstätten ferrite) and massive. At low undercoolings below the Ae_3 temperature, random fluctuations will lead to bcc-like clusters being present throughout the grains and at prior austenite grain boundaries. Application of classical nucleation theory, based on the Volmer (1939) and Becker and Döring (1935) approaches allows the nucleation of ferrite on prior austenite grain boundaries to be modelled. In most approaches the ferrite forms as a pillbox (Enomoto & Aaronson, 1986; Enomoto *et al.*, 1986), i.e. an orientation relationship is adopted with one of the grains that allows the formation of a broad low energy interface with one austenite grain. The α/γ interface with the other grain is generally curved and is a higher energy interface. If two low energy facets are possible, depending on the indices of the interface plane in that austenite grain, then a sawtooth ferrite grain, similar to that shown in Fig. 6.5(c), can form.

The study of these crystallographic relationships has not been undertaken for allotriomorphic ferrite in as much detail as it has been for Widmanstätten plates and bainite colonies developing from the grain boundary. Historically, this would have needed to have been carried out using TEM along with trace analysis on sufficient numbers of interfaces to identify a common interface plane normal (Purdy, 1978; Edmonds, 1979; Strangwood & Bhadeshia, 1986; Babu & Bhadeshia, 1991). Hot stage TEM has been used to determine the mobility of α/γ interfaces (Purdy, 1978), which confirmed that, for ferrite formed on prior austenite grain boundaries, low energy facetted interfaces formed between ferrite and one austenite grain with a higher energy curved

© Woodhead Publishing Limited, 2012



6.5 Summary of the Dubé classification.

interface with the neighbouring austenite grain. In these studies, the facetted interface demonstrated low mobility, whilst the curved interface moved much more rapidly. The increased automation possible with EBSD systems noted above means that this analysis can be completed much more readily as it has been for aluminium-based systems (Yuan *et al.*, 2005) and in re-constructing the prior austenite grain size and texture from transformation products, such as martensite (Miyamoto *et al.*, 2010) and pearlite (Morimoto *et al.*, 2007; Roberts, 2010).

In terms of accounting for the nucleation behaviour of ferrite in steels, this level of detail has not been necessary as the main objective has been to account for alloying element and processing effects on the transformation start line for TTT and CCT diagrams. As the latter were typically determined from dilatometry and optical metallography, nucleation rates were averaged over a large number of grain boundaries in the ensemble. Thus average

© Woodhead Publishing Limited, 2012

fitted parameters – both thermodynamic and more importantly interfacial energies – were appropriate. Experimentally, the lower carbon contents seen in more modern grade steels present problems in generating sufficiently rapid cooling rates in dilatometry experiments in terms of measuring such rapid temperature changes with traditional thermocouples, as the thermal mass of the thermocouple starts to become significant, and in ensuring uniform temperature distributions. For such grades flash annealing using laser heating and temperature monitoring may need to be used.

Similarly, whilst interfacial energies have been modelled *ab initio* from first principles calculations for a number of systems including ceramics (Si, Al_2O_3, SiC, titanates, YBCO and other superconductors), intermetallics, aluminium-based alloys, titanium-based alloys and nickel-based superalloys (Lu *et al.*, 2004; Hu *et al.*, 2009; Schwingenschlogl & Schuster, 2009; Takahashi *et al.*, 2009), this level of detail has not been applied to steels in terms of transformation behaviour. Most *ab initio* modelling in steels has been applied to mechanical properties, e.g. grain boundary segregation and embrittlement (Messmer & Briant, 1982; Braithwaite & Rez, 2005; Hackett *et al.*, 2008; Wachowicz & Kiejna, 2008). These studies consider full interatomic and atom-vacancy interactions allowing for structural relaxations with the Vienna *ab-initio* simulator package (VASP) being widely used. The coverage of full interactions places limits on the number of atoms (around 100 maximum) that are included in the model. Even with this low number of atoms, computer run times are large. However, the effects shown in terms of electron density correlate with the macroscopic embrittling effects of S and P and increased grain boundary cohesion for B and C segregation.

The increased grain boundary cohesion predicted by these models for B segregated at prior austenite grain boundaries is consistent with the effect of low levels of B on grain boundary nucleation of ferrite. Some 30–200 ppm can cause the elimination of grain boundary allotriomorphs (Thivellier *et al.*, 1978; McMahon, 1980) depending on cooling rate. This 'super-hardenability' effect would be consistent with B segregating to prior austenite grain boundaries and lowering their effective interfacial energy (by around 0.49 eV for a [210] grain boundary) (Braithwaite & Rez, 2005). This would increase the activation energy for nucleation (see next section) shifting the TTT and CCT start lines to the right.

Modelling using larger atom arrays (1000s of species) is possible using parameterised approaches, such as the embedded atom method (Foiles *et al.*, 1986) and central-force many-body potential (Finnis & Sinclair, 1984), but these do not show the fine scale effects of the full interactions. As with any modelling approach, validation against experiment is needed and, due to the small numbers of atoms involved, usually involves TEM, e.g. high resolution of grain boundary structures; high resolution composition traces across grain boundaries (Hackett *et al.*, 2008); and detailed analysis of

© Woodhead Publishing Limited, 2012

EELS line near-edge structure (ELNES) (Dennis *et al.*, 2004; Braithwaite & Rez, 2005). In general the fit can be made good (within a few percent) through judicious fitting of interaction potentials, but if this is carried out for a range of conditions, then the behaviour for steels at the mm–m scale could be covered. The linking of *ab-initio* calculations to the small volume samples during 3D-XRD for a range of conditions could be one approach to achieve this for both ferrite (room temperature) and austenite (elevated temperature) structures. One particular success of the *ab-initio* approach has been to model hydrogen embrittlement (Geng *et al.*, 2005; Tian *et al.*, 2011), the early stages of which resulted in new high strength steels with improved resistance to hydrogen cracking (Olson, 1987); the verification of this approach was the improved toughness and hydrogen cracking resistance of ultra-high (> 1500 MPa tensile strength) strength forgings.

Thus, continued development of atomic-level models with verifying experimentation can lead to more representative values for interfacial energy ranges as well as accounting for segregation effects (B) and the stability of atomic clusters.

6.4.2 Nucleation rates

Whatever the values used and their source, a number of academic and commercial packages have been developed to predict the transformation of steels under cooling situations. Apart from those that fit transformation to dilatometric (or other experimental data for given steel composition ranges, e.g. Sysweld), the basis for most models is that nucleation occurs upon prior austenite grain boundaries. The nucleation rate depends on the activation barrier for nucleation (ΔG^*_{het}) through the number density of critically sized embryos and the interfacial diffusion rate needed to add another atom to this embryo causing it to exceed the critical size (more appropriately critical number of atoms; Christian, 1975) and continue to grow as a stable nucleus. This will lead to expressions of the type:

$$I_v = Const\ N_{het}\ \nu \exp\left(\frac{-\Delta G^*_{het}}{kT}\right)\exp\left(\frac{-E_M}{RT}\right) \qquad [6.2]$$

where ν is the Debye frequency ($\sim 10^{13}$ s^{-1}), k is the Boltzmann constant, T is absolute temperature, E_M is the activation energy for interfacial diffusion and R is the universal gas constant.

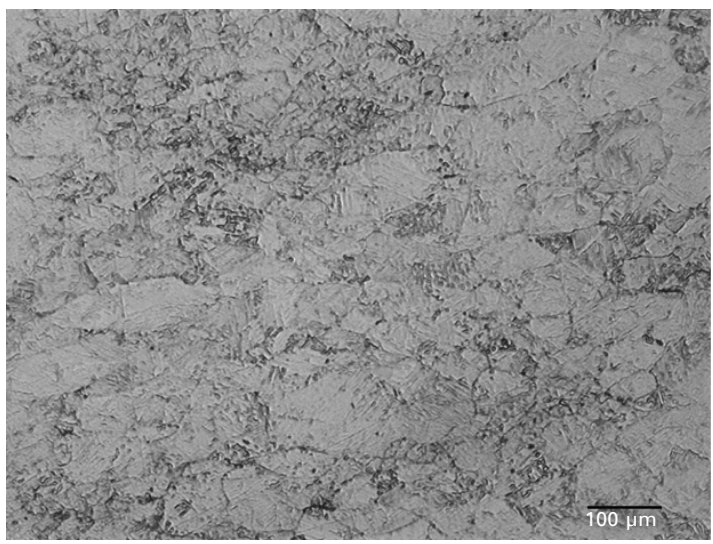
The use of equations of this type continues to make assumptions regarding the shape of the prior austenite grains and the shapes of the ferrite nuclei. The rate is dependent on the number density of nucleation sites, N_{het}, which will depend on the size of the prior austenite grains along with their shape. Commonly an average or 'mode' grain size is quoted from 2D sections used,

© Woodhead Publishing Limited, 2012

which can be corrected by stereological methods to an equivalent 3D value if the distribution is normal and isotropic (Underwood, 1970; Higginson & Sellars, 2003). This type of correction is not possible for non-equiaxed shapes and so cannot be applied to rolled and unrecrystallised austenite grains, which are usually assumed to be pancake-shaped (Fig. 6.6), whilst recrystallised austenite grains would be considered tetrakaidecahedra. Similarly, the constant in Eq. [6.2] is dependent on the shape of the nucleus; for grain boundary nucleation, a hemispherical cap is assumed with the semi-angle given by the balance of surface traction forces based on interfacial energies. In most cases, this assumption leads to a nucleus that is symmetric about the prior austenite grain boundary and so would be expected to grow into both adjacent austenite grains. As noted above, the adoption of low energy interfaces with one grain, but not the other, gives sawtooth allotriomorphs; in this case growth into one grain would be favoured over that into the other (Purdy, 1978).

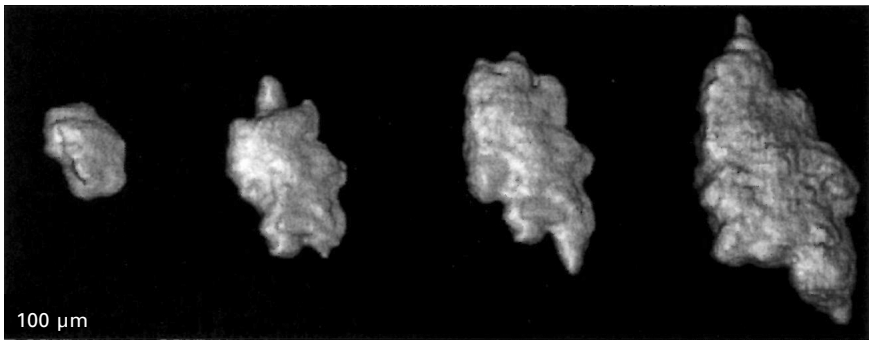
The development of combined focused ion beam (FIB)/electron back-scattered diffraction (EBSD) instruments and X-ray/neutron tomography recently allowed the true 3D shapes of grains and other features to be determined in a more continuous manner than serial sectioning. Studies of grains in various metallic alloy systems (Groeber *et al.*, 2006; Xu *et al.*, 2007; St-Pierre *et al.*, 2008; Ludwig *et al.*, 2009) have revealed a far greater shape complexity than expected from 2D sections (Fig. 6.7).

Beyond the geometry factors, the number density of critically sized embryos needs input of driving force and interfacial energy terms (also dependent

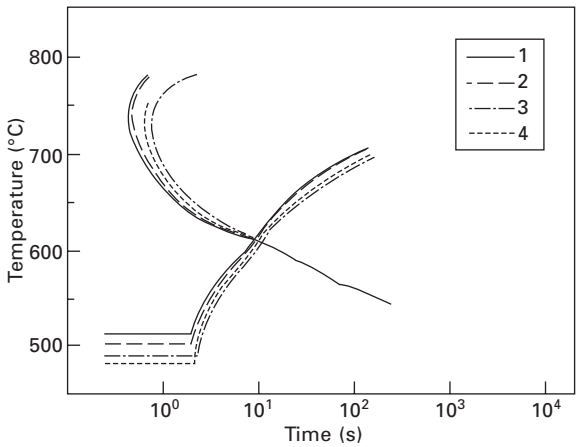


6.6 Elongated prior austenite grains from partially recrystallised Nb-containing steel deformed at 1150°C (courtesy of A. Kundu).

© Woodhead Publishing Limited, 2012



6.7 Snapshots of a growing grain determined using 3D-XRD (Ludwig *et al.*, 2009). Used with permission from Elsevier.



6.8 Comparison of predicted and experimental TTT curves for weld metal deposits with a range of C levels (0.029–0.1 wt%); 1: 0.029 wt% C, 2: 0.061 wt% C, 3: 0.080 wt% C, and 4: 0.1 wt% C (Bhadeshia *et al.*, 1985). Used with permission from Elsevier.

on the assumed shapes). In the dilute solution case (< 5 wt% total alloying addition), the Wagner interaction parameters, ε_{ij}, can be used to estimate the free energy of the parent and product phases. This approach has been used to predict the transformation start lines (formation of 5% ferrite) for low alloy steels (Kirkaldy *et al.*, 1978; Bhadeshia, 1982) with good success for grain boundary nucleation of ferrite (Fig. 6.8), using a modification of Russell's approach (Russell, 1969). The Wagner interaction parameters (Wagner, 1952) do indicate the general behaviour of alloying elements in terms of being austenite or ferrite stabilisers, but their derivation means that cross-element interaction must be limited and so they are only applicable to the low concentration limit, e.g. weld metals.

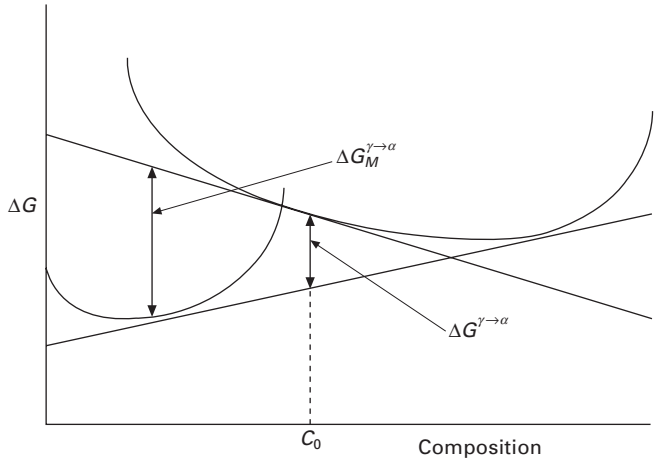
© Woodhead Publishing Limited, 2012

A wider range of compositions, including stainless steels, can be dealt with by using regular and sub-regular models as for Scientific Group Thermodata Europe (SGTE) and commercial packages such as MT-DATA, ChemSage and Thermo-Calc. The databases for these packages have been expanded, especially for Al-, Ti- and Ni-based systems, but also for a wider range of alloying elements and compositions ranges for ferrous systems (the model of Kirkaldy included seven elements, whilst ferrous databases now contain up to 22 elements including B and O). This continuing measurement of thermodynamic properties along with increased functionality of the energy minimisation software should improve the accuracy of predictions for ferrite formation, although, largely, the equations outlined above are utilised. The scope and use of computational thermodynamics have been reviewed recently by Costa e Silva *et al*. (2007). Thermodynamic models can be used to estimate the driving force for transformation per unit volume ($\Delta G_v^{\gamma\to\alpha}$), which, with an assumed shape for the ferrite and appropriate values for the prior austenite grain boundary ($\sigma^{\gamma\gamma}$) and ferrite/austenite interfacial ($\sigma^{\alpha\gamma}$) energies, will give the activation barrier for nucleation:

$$\Delta G^* \alpha \frac{(\sigma^{\alpha\gamma})^3}{(\Delta G_v^{\gamma\to\alpha})^2} \qquad [6.3]$$

The thermodynamic data used in computational modelling are derived by fitting models (such as the regular or sub-regular models) to experimental data (such as phase diagrams) (Hack, 1996). Continued measurement of these parameters by organisations such as the National Physical Laboratory (NPL) and Royal Institute of Technology is improving the fit and confidence that free energy differences predicted by these models are appropriate to the change in external parameters and so represent the system's response. In the ferrous and nickel-based alloy systems, data are well established; those in Ti- and Al-based systems, not so well. Thus, given composition, temperature (T) and pressure (P), the difference in free energy between parent (γ) and product (α) phases can be estimated. For equilibrium this would be the multi-dimensional equivalent of the 'common tangent' for a binary system. This equilibrium value of $\Delta G^{\gamma\to\alpha}$ is appropriate for the overall transformation, i.e. applies to growth (see below) and the final volume fraction of ferrite. In the initial stages of nucleation, then the volume fraction of product formed is very limited and so composition differences between the parent and the product region tend to zero. This leads to the concept of the 'parallel tangent' for the binary diagram and its multidimensional equivalents, which gives a much higher driving force, $\Delta G_M^{\gamma\to\alpha}$ (Fig. 6.9). During transformation, the driving force decreases from $\Delta G_M^{\gamma\to\alpha}$ to $\Delta G^{\gamma\to\alpha}$. Increased computational resources make the averaging of this behaviour during transformation possible (Hillert, 1998). Thermodynamics allows the driving force for nucleation to be determined

© Woodhead Publishing Limited, 2012



6.9 Schematic binary free energy composition diagram showing driving forces derived from 'common' and 'parallel' tangent constructions.

provided that the composition of the parent phase at the nucleation site and the composition of the product cluster are known. Both of these features will benefit from *ab initio* modelling, which is on the correct scale for nuclei and can rationalise aspects such as grain boundary segregation.

A number of elements, e.g. S and B, have low solubility in the bulk of the austenite grains with a strong tendency to segregate to prior austenite grain boundaries. Grain boundary segregation is driven by the strain energy of the distorted iron atom lattice around the mis-sized solute atom and any valence difference between iron and the solute atom. Partition from the bulk lattice to a grain boundary results in reduction in these two terms due to the more open structure of a high angle grain boundary (HAGB) where there is a higher density of unsatisfied metallic bonds. In the case of sulphur, this results in the localisation of electron density in the plane of the interface with a consequent reduction in that across the interface. The net result of this segregation and re-localisation of electron density reduces the strength of the interface leading to hot shortness, but, in terms of ferrite formation, the presence of S segregation will lower the interfacial energy (Messmer & Briant, 1982) of the prior austenite grain boundaries and so reduce their effectiveness as nucleation sites. The modification of interfacial energy terms by other segregants (e.g. B and P) would also then be expected to modify the potency of grain boundaries as nucleating sites for ferrite. As noted above, the determination of interfacial energies is not well established. Interfacial energies can be estimated from fracture studies, but these often sample ferrite–ferrite boundaries that may also be the sites for carbide formation during cooling so that the correlation has not been demonstrated.

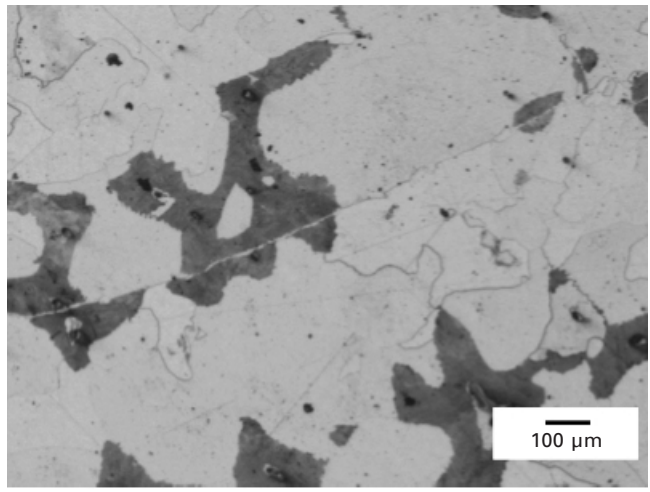
© Woodhead Publishing Limited, 2012

The equilibrium segregation behaviour to grain boundaries in binary alloys is well described by McLean (1956) using binding energies. Equilibrium segregation is established by isothermal holding at elevated temperatures where diffusion processes are not limited. The presence of a number of potential segregant species in steels and a finite number of sites for segregation in HAGBs leads to site competition so that attempts to apply the same binding energy approach to multi-component segregation have not been as successful (Guttmann, 1975; Misra, 2002). In cooling situations, non-equilibrium segregation can also occur (Anthony, 1969) where binding between solute atoms and vacancies can lead to solute atoms being dragged towards grain boundaries by vacancies. As the vacancy approaches the free energy well adjacent to a grain boundary, it accelerates causing it to break free from the solute atom leaving it in the bulk. This results in non-equilibrium segregation that extends over 10s–100s nm rather than the approximate monolayer coverage of the boundary for equilibrium segregation.

The precise composition at the grain boundary is a function of any reaustenitisation temperature (prior austenite grain size and segregation tendency – mainly equilibrium), but a species will show different tendencies to segregate depending on what other species are present. Site competition means that the segregated level of the segregant can also be time-dependent as, in the situation where site competition occurs, segregation may not depend just on the binding energy, but also on the rate at which atoms arrive at the grain boundaries. The use of increasingly complex steels and processing routes can lead to a variety of grain boundary compositions and hence nucleation potency, which may be manifested as scatter in the nucleation of ferrite. Historically, Auger and TEM-EDS studies have been used to determine grain boundary compositions, which would need to be carried out on samples from interrupted processes. In describing and modelling the nucleation of ferrite at grain boundaries, it will be necessary then to establish a thermodynamic and kinetic model for multi-component, multi-site segregation. 3D-POSAP (Sha *et al.*, 1993a; 1993b; 1993c; 1993d; Miller & Smith, 1995; Miller *et al.*, 2000; Pereloma *et al.*, 2006) has been used to investigate grain boundaries in maraging steels, but a systematic study of grain boundary segregation in engineering steels has not been reported. A study of this type would be possible using FIB to thin particular prior austenite grain boundaries for study by TEM/EELS linked to *ab initio* modelling as described above for grain boundary energies in the presence of B segregation.

A similar nucleation scheme applies for idiomorphs (Fig. 6.10), which often form on non-metallic inclusions, such as MnS and oxides. Intragranular ferrite formation has been more extensively studied for lower temperature products, such as acicular ferrite – needle-like ferrite present within the bulk of prior austenite grains originally seen in weld metals. In situations where

© Woodhead Publishing Limited, 2012



6.10 Example of ferrite idiomorph in as-cast Nb-containing steel (courtesy of A. Kundu).

ferrite, such as diffusional allotriomorphs, nucleates from inclusions, their action has been ascribed to:

- inert surface, i.e. a high-energy pre-existing interface offsetting the α/γ interfacial energy and acting as intragranular 'grain boundaries'
- lattice matching to reduce the energy barrier between ferrite and the inclusion
- strain energy due to differential thermal expansivity
- increased chemical driving force due to composition changes.

Of these, strain energy would be less operative for formation of idiomorphic ferrite due to the lower elastic modulus of the surrounding austenite at the formation temperature (see above). The adoption of an orientation relationship between an inclusion and idiomorphic ferrite would have to be accompanied by a KS, NW or GT orientation relationship between the idiomorph and the surrounding austenite. For some inclusions this would be achievable, namely those forming in the liquid, as these could nucleate delta-ferrite from the melt, which may give a similar orientation relationship to the later-forming ferrite. As the austenite that forms from delta will adopt a KS, NW or GT relationship, then it will have a specific crystallographic (low energy) relationship to the inclusion. On reversion to ferrite on idiomorph formation, the order is reversed so that linked orientation relationships could exist. If the inclusion were to act as an inert surface then the number density of idiomorphs would be related to the number density of active inclusions, which has not been demonstrated.

Chemical composition effects are potentially more powerful, e.g. the

© Woodhead Publishing Limited, 2012

'vanadium' effect (He & Edmonds, 2002) and the loss of alloying elements (γ-stabiliser) to inclusions (Strangwood & Bhadeshia, 1988). The latter will take place during inclusion formation, but fluid flow would be expected to remove any local chemical differences. In the solid state, however, loss of alloying element during cooling and subsequent heat treatment would not be so readily replenished by long-range diffusion so that higher local driving forces for ferrite formation would be present around inclusions leading to faster ferrite nucleation. The chemical composition variation could arise from segregation (as for grain boundary segregation noted above) or from absorption of alloying elements into the inclusion (as for C dissolution in TiO_x in weld metals).

Whatever the precise mechanism for inclusion nucleation of idiomorphs, the drive towards cleaner steels coupled with finer prior austenite grain sizes means that the formation of grain boundary allotriomorphs tends to swamp idiomorph formation so that the latter morphology is increasingly rare in commercial grades.

6.5 Growth

Once nucleated, growth of allotriomorphs and idiomorphs will take place by interstitial and/or substitutional diffusion under mixed diffusion and interface control. In pure iron there is no need for long-range diffusion and so most dissipation of the driving force occurs in the interface leading to interfacial control and generally high growth rates; Massalski (1976) reports interface speeds of 10–120 mm/s in non-ferrous massive transformations. Massive ferrite growth can occur readily under these conditions until impingement with other massive ferrite grains; soft impingement (the overlapping of diffusion fields ahead of α/γ interfaces to give non-Fickian conditions and a slowing of growth) does not occur in this situation due to the lack of long-range diffusion. The rapid growth rates of massive grains make quenching out during transformation difficult and so partial transformation in iron has not often been observed, although mixed massive–martensite structures can be obtained by quenching Fe-Ni alloys (Massalski *et al.*, 1975). In more complex systems, e.g. TiAl-based intermetallics (Zhang *et al.*, 1996) nuclei have been observed (by TEM of electron beam welded samples) nucleating with low energy interfaces on one side of the parent grain boundary, but growing into the adjacent grain, where the disordered interface has a higher mobility. This mechanism should be applicable for pure iron.

6.5.1 Diffusional vs interfacial control

In steels, rather than pure iron, the driving force for transformation can be dissipated in either transport of alloying element atoms to or from the

© Woodhead Publishing Limited, 2012

growing interface (long-range diffusion) so that this becomes rate controlling ('diffusional' control) or, as in pure iron, by diffusional movement within the interface (short-range and lateral to the growth direction) and incorporation of atoms into the interface. In the latter situation atom movement to and from the interface is rapid compared with incorporation into the interface so that this becomes rate determining and growth is under 'interface' control. The carbon content of microalloyed steels is now becoming very low and this has been associated with a change in the ferrite morphology from traditional equiaxed structures to more 'massive'-like structures (Rehman & Edmonds, 2000); these changes are not fully understood, but would be consistent with a change in growth control mode from diffusional to interfacial. As noted in the literature (Christian, 1975; Bhadeshia, 1985) mostly growth would be under 'mixed' control, but is dealt with as if one or other of the processes dominated.

The formation of ferrite at very low cooling rates is seen in meteorite structures (Fe-Ni-based alloys), which exhibit classical Widmanstätten structures. The slow cooling rates experienced in deep space (~ 50 K per million years; Weller & Wegst, 2009) mean that transformation is occurring under very low undercoolings and, hence, driving forces. Under these conditions, the increase in interfacial energy as the ferrite grows dominates the energy balance, requiring the α/γ interface to maintain a low energy configuration (e.g. $\{558\}_\gamma$). The transformation at the interface becomes military and under 'interface' control as the atoms (mostly Ni) must leave the ferrite from specific locations. This form of Widmastätten ferrite gives a low nucleation rate and slow growth to very large plates (visually resolvable) under local equilibrium conditions and so differs from that forming at the top of the lower 'C' curve (Fig. 6.3), when growth occurs under paraequilibrium (ParaE) conditions at rates between 50 and 550 $\mu m\ s^{-1}$ in low C weld metals (Bhadeshia *et al.*, 1985).

When long-range diffusion dominates energy dissipation, when ferrite growth would be considered to be under 'diffusion' control, a range of growth rates can occur depending on how closely interfacial compositions (for both interstitial and substitutional alloying elements) approach equilibrium values. Initial models (and the equations below) often simplified diffusion processes by assuming a dependence on temperature, but not on path and concentration. The concentration dependence of carbon diffusion has been covered in the classic work of Atkinson *et al.* (1973) and approaches similar to this could now be incorporated into nucleation and growth models, whilst the ability to extract specimens from quenched-in growing interfaces via FIB along with improved analysis tools should allow the concentration dependence to be determined and incorporated into transformation models. The enhanced diffusivity of C and N associated with interfaces has been investigated by Dirks and Meijering (1972, 1975) but the detailed effect of interfaces on

© Woodhead Publishing Limited, 2012

substitutional alloying element diffusion is an area that would benefit from greater study.

6.5.2 Partition-local equilibrium (P-LE)

At low driving forces only small deviations from equilibrium can be tolerated at the interface for both substitutional and interstitial elements. Long-range diffusion of the substitutional alloying element(s) take(s) place, which must keep pace with the faster moving interstital element(s). For multiple substitutional alloying elements then, the need to maintain equilibrium at the interface will mean that growth tends to be controlled by the slowest diffusing species, which requires that accurate diffusion data are available (e.g. Table 6.3) (Atkinson *et al.*, 1995). Mathematically, this is represented by the independent mass balances for each element being compatible with a single interface speed; these are given for carbon by:

$$J_1 = -D_{11}\nabla C_1 - \sum_j D_{1j}\nabla C_j \qquad [6.4]$$

where $j \neq 1$, J_1 = flux of carbon in austenite at the interface, D_{11} = diffusivity of carbon in austenite, C_1 = carbon concentration, D_{1j} = ternary diffusion coefficient for the effect of element j on carbon flux, and C_j = concentration of element j (Onsager, 1945–46).

The corresponding equations for the substitutional alloying elements are given by:

$$J_j = -\sum_k D_{jk}\nabla C_k - D_{jj}\nabla C_j \qquad [6.5]$$

where $j \neq 1$, $k \neq j$, J_j = flux of element j and D_{jk} = ternary diffusion coefficient between elements j and k.

In many cases, the only significant ternary diffusional interactions are assumed to be those between the substitutional alloying elements and carbon, i.e. $D_{jk} = 0$. Whilst this may be approximately true in the dilute limit, within the accuracy of transformation rate data, it is unlikely to hold in more highly concentrated alloys, e.g. stainless steels and tool steels, where the formation

Table 6.3 Example diffusivity values for carbon, manganese and silicon in austenite

Temperature (°C)	D^{γ}_{11} ($m^2\ s^{-1}$) (C)	D^{γ}_{22} ($m^2\ s^{-1}$) (Mn)	D^{γ}_{22} ($m^2\ s^{-1}$) (Si)
750	1.6×10^{-12}	3.5×10^{-19}	1.8×10^{-18}
800	3.5×10^{-12}	1.7×10^{-18}	8.4×10^{-18}
850	7.3×10^{-12}	7.0×10^{-18}	3.5×10^{-17}
900	1.4×10^{-11}	2.6×10^{-17}	1.3×10^{-16}

Source: Atkinson *et al.* (1995).

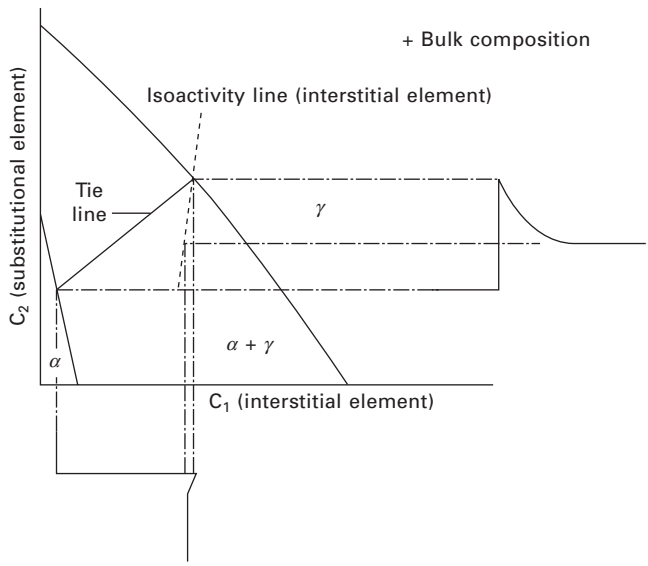
© Woodhead Publishing Limited, 2012

of intermetallics implies a stronger metal–metal bond and, hence, a stronger effect of one element on the flux of another. Overall, the conservation of mass at the α/γ interface, s^*, for a ternary system is given by:

$$(C_{i\alpha} - C_{i\gamma})\frac{ds^*}{dt} = -J_i\big|_{s=s^*} \qquad [6.6]$$

with further relationships of a similar format for higher order systems. These simultaneous equations can easily be solved using software such as MATLAB or commercial microstructural modelling packages.

Qualitatively the trends in composition and transformation temperatures can be described using a ternary (Fe-C substitutional alloying element, e.g. Mn) example. In the range where P-LE holds, the conservation of mass at the advancing interface is satisfied by reducing the driving force for carbon diffusion almost to zero (Fig. 6.11) (Onsager, 1945–46). In order to do this, the tie-line defining the interfacial composition and controlling the growth rate is diverted so that it does not pass through the bulk composition, but passes through the carbon isoactivity line instead. Isoactivity lines join points in both phases where the activity of carbon in solution is constant. The interface tie-line is defined as the one whose intersection at the $(\alpha + \gamma)/\gamma$ phase boundary coincides with the extrapolation of the carbon isoactivity line through the bulk composition to that phase boundary (Fig. 6.11). This reduces the flux of the interstitial element (carbon) to that of the substitutional element, which partitions between α and γ. The partition



6.11 Schematic isothermal ternary section with tie-line for P-LE diffusional growth.

© Woodhead Publishing Limited, 2012

of the substitutional alloying element generally gives a slow growth rate (10^{-6}–10^{-10} μm s^{-1}) (Liu & Ågren, 1989). These equations can be used in finite difference or finite volume models to predict the position of the moving interface with time and temperature. For shape-preserving particles (e.g. spheres, cylinders and ellipses), more analytical solutions are possible based on (Coates, 1972; 1973a; 1973b):

$$\frac{ds^*}{dt} = 0.5\eta_2 \sqrt{\left(\frac{D_{22}}{t}\right)} \qquad [6.7]$$

where the subscript 2 refers to the rate-controlling substitutional alloying element. The interface position is then given by:

$$s^* = \eta_1 \sqrt{D_{11} t} = \eta_2 \sqrt{D_{22} t} \qquad [6.8]$$

The appropriate tie-line and the resulting interstitial and substitutional alloying element compositions give the fractional compositions for different morphologies:

$$f_2^l = \frac{(C_2^0 - C_2^\gamma)}{(C_2^a - C_2^\gamma)} \qquad [6.9]$$

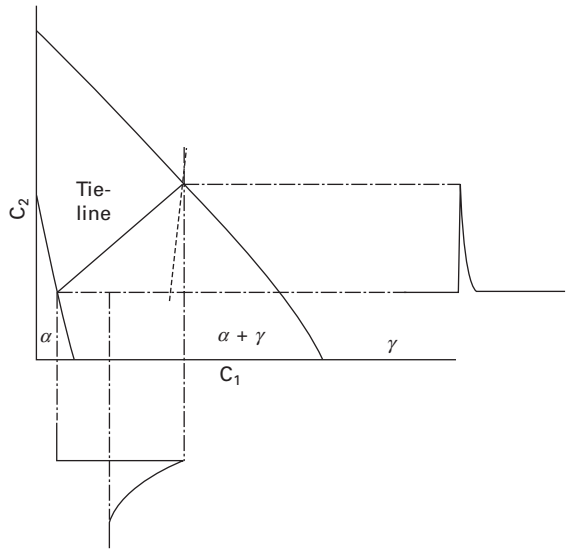
where $l = s$, c or p for spherical, cylindrical and planar morphologies. f_2^l equations are tabulated and plotted so that the appropriate growth rate can be obtained from:

$$f_2^l = f^l(\eta_2) \qquad [6.10]$$

6.5.3 Negligible partition-local equilibrium (NP-LE)

Transformation at lower temperatures increases the driving force, which allows for greater deviation of interfacial composition from full equilibrium, whilst ensuring parity of substitutional and interfacial fluxes across the moving interface. This is achieved by increasing the former's driving force effectively to infinity, which results in negligible long-range diffusion between ferrite and austenite and low diffusional drag. This occurs by maintaining the substitutional element concentration in α to levels close to the bulk value, which lies along that element's isoactivity line. In the dilute alloy limit (< ~7 wt% total alloying element in solution), the effect of carbon on the activity of the substitutional alloying element is low so that the isoactivity lines are effectively parallel to the interstitial axis (Fig. 6.12). The generally low driving force still means that equilibrium at the interface itself is maintained for as long as possible. In the case of the substitutional alloying element, equilibrium is achieved by a 'spike' at the interface. The spike requires

© Woodhead Publishing Limited, 2012



6.12 Schematic isothermal ternary section with tie-line for NP-LE diffusional growth.

short-range diffusion in the vicinity of the interface, but removes the need for long-range diffusion of the substitutional alloying element. As for P-LE, the tie-line does not pass through the bulk composition, but terminates at the intersection of the substitutional alloying element isoactivity line (through the bulk composition value) and the $(\alpha + \gamma)/\alpha$ phase boundary. Under these conditions the growth equations (represented by the interfacial speed, ds^*/dt) are given by (Coates, 1972; 1973a; 1973b):

$$\frac{ds^*}{dt} = 0.5\eta_1\sqrt{\frac{D_{11}}{t}} \qquad [6.11]$$

where η_1 is a growth constant (see below) and D_{11} is the diffusivity of the rate controlling species.

These rates are closer to those controlled by diffusion of the interstitial alloying element. As for P-LE the tie-line compositions give the fractional compositions, although the ternary diffusional interactions mean that:

$$f_1^l \neq f^l(\eta_1) \qquad [6.12]$$

but

$$f_1^l = f^l(\eta_1) - \frac{(C_2^\alpha - C_2^\gamma)}{(C_1^\alpha - C_1^\gamma)}\frac{D_{12}}{D_{11}}(1 - f^l(\eta_1)) \qquad [6.13]$$

For dilute solutions, within the range that the Wagner interaction parameters,

© Woodhead Publishing Limited, 2012

ε_{ij}, hold to represent the effects of alloying elements in solution on austenite/ferrite stability, irreversible thermodynamics (Kirkaldy, 1958; Brown & Kirkaldy, 1964) give:

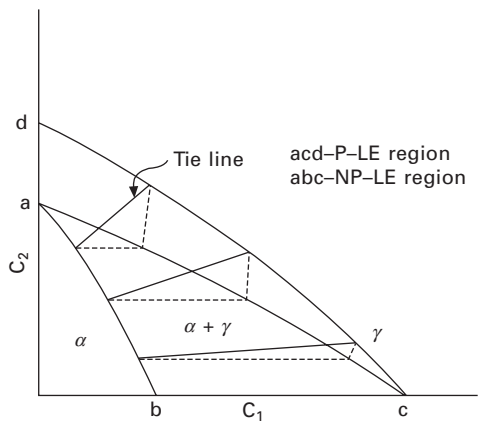
$$\frac{D_{12}}{D_{11}} = \frac{\varepsilon_{12} X_1}{(1 + \varepsilon_{11} X_1)} \qquad [6.14]$$

where X_1 is the mole fraction of carbon.

The phase diagram can now be separated into two regions (Fig. 6.13), one where P-LE dominates at low supersaturations and NP-LE at higher supersaturations. Both of these mechanisms are affected by soft impingement (interaction of diffusion fields), which reduces the activity gradient and hence the growth rate. This is manifested as a shift in the tie-line defining the interface towards the bulk composition; when the tie-line passes through the bulk composition, transformation ceases.

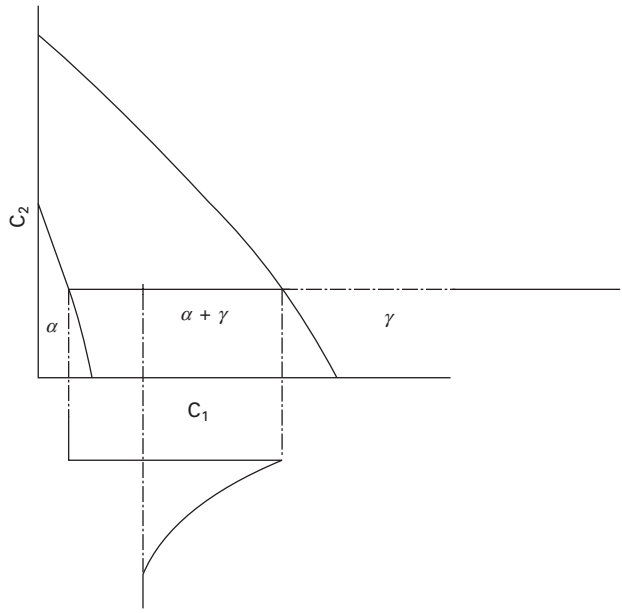
6.5.4 Paraequilibirium (ParaE)

Increasing driving force and growth rate compared with those correlating to NP-LE cause interfacial equilibrium to be abandoned leading to the third diffusional growth mode. In NP-LE, the 'spike' decreases in width as the growth rate increases. The 'spike' width decreasing below a lattice spacing is only possible mathematically, so in practice there is no change in substitutional alloying element concentration across the interface (Fig. 6.14). The resulting tie-line is parallel to the interstitial element axis and is a component ray of that element. The interstitials, having much higher diffusion rates, can redistribute so that equilibrium with respect to these



6.13 Schematic isothermal ternary section showing separation into regions where P-LE and NP-LE dominate diffusional growth.

© Woodhead Publishing Limited, 2012



6.14 Schematic isothermal ternary section with tie-line for ParaE diffusional growth.

elements across the interface is maintained subject to the constraint of constant substitutional alloying element/iron ratio. Paraequilibrium (ParaE) was first suggested by Hultgren (1947, 1951) and has subsequently been incorporated into thermodynamic and kinetic models, e.g. Thermo-Calc. This is the fastest of the diffusional growth modes (1 μm s^{-1}) (Liu & Ågren, 1989) and is controlled by the interstitial alloying element with a growth rate given by:

$$\frac{ds^*}{dt} = \frac{2D_{11}}{\Delta s} \qquad [6.15]$$

where Δs is the 'spike' width and was originally estimated using the Zener approximation (Zener, 1949). This is taken as a measure of the diffusion zone thickness with mass conservation being given by:

$$V_f^{\alpha}(C_1^{\alpha} - C_1^0) \approx 0.5A^{\alpha}\,\Delta s\,(C_1^0 - C_1^{\gamma}) \qquad [6.16]$$

where V_f^{α} = volume fraction of ferrite and A^{α} = ferrite interfacial area.

The growth modes and rates described above are extremes for true local equilibrium or ParaE and apply strictly to limited geometries. It is likely that growth forms a continuous spectrum from P-LE with negligible dissipation of driving force in interfacial processes through to ParaE with significant interfacial dissipation. The increased use of numerical modelling approaches

© Woodhead Publishing Limited, 2012

leads to greater fitting of models to the available experimental data, much of which has considerable scatter, e.g. TTT diagrams. In addition, although the 'spike' width can be estimated, it has not been verified experimentally; FIB could be used to extract an interface from a growing α/γ interface, quenched out during transformation. TEM-EDS should be able to reveal the enrichment of the interface in substitutional alloying elements. The first rather empirical limit suggested by Coates (1972) was for:

$\Delta s > 50$ Å Local equilibrium

$\Delta s < 10$ Å Paraequilibrium

Ågren's later treatment of the transition between LE and ParaE was based on a critical supersaturation at the interface so that the degree of LE or ParaE depended on diffusivity of the alloying element within the interface. This works well for Fe-C-Mn (Liu & Ågren, 1989) and expansion of this with clarification of the actual composition at and adjacent to growing interfaces (using the techniques mentioned above) would be useful. This rationalisation of the degree that ferrite growth deviates from the cases noted above for a range of compositions and processing parameters for higher order systems would allow ever more accurate prediction and control of ferrite fractions and morphology.

Application of nucleation and growth equations does allow good agreement with both the start and finish lines of TTT curves (Fig. 6.3), whilst other groups are continuing to develop models for transformation (e.g. Grong & Myhr, 2000; Gamsjäger *et al.*, 2005) using thermodynamic and kinetic data along with Johnson–Mehl–Avrami–Kolmogorov (JMAK) expressions (Kolmogorov, 1937; Avrami, 1939; Johnson & Mehl, 1939) between the start and finish temperatures.

6.6 Conclusions

The study of diffusional formation of ferrite at low undercoolings has established the basis of much phase transformation work. The understanding generated has been incorporated into good models for the behaviour of a range of alloyed steels. Improvements in this area are likely to be incremental, but the accuracy and generality of the models currently developed would benefit from the application of new experimental and modelling techniques. Principally these would be in the areas of grain boundary compositions, interfacial energies and composition-dependent diffusion.

6.7 References

Aaronson H I (1962), *Decomposition of Austenite by Diffusional Processes*, Zackay V F & Aaronson H I (eds), New York, Interscience, 387–546.

© Woodhead Publishing Limited, 2012

Aaronson H I (1969), *Mechanisms of Phase Transformations in Crystalline Solids*, Monograph 13, London, Institute of Metals.
Ackert R J & Parr J G (1971), 'Massive and martensitic transformation temperatures in very dilute iron-carbon alloys', *JISI*, **209**, 912–920.
Akselsen O M, Grong Ø & Kvaale P E (1986), 'A comparative study of the heat affected zone (HAZ) properties of boron-containing low carbon steels', *Metall. Trans A*, **17A**, 1529–1536.
Anthony T R (1969), 'Solute segregation in vacancy gradients generated by sintering and temperature changes', *Acta Metall.*, **17**, 603–609.
ASM International (1977), *Atlas of Isothermal Transformation and Cooling Transformation Diagrams*, Materials Park, OH, ASM.
Atkinson C, Aaron H B, Kinsman K R & Aaronson H I (1973), 'On the growth kinetics of grain boundary ferrite allotriomorphs', *Metall. Trans*, **4**, 783–792.
Atkinson C, Akbay T & Reed R C (1995), 'Theory for the reaustenitisation from ferrite/cementite mixtures in Fe-C-X steels', *Acta Metall. Mater.*, **43**, 2013–2031.
Avrami M (1939), 'Kinetics of phase change I – General theory', *J. Chem. Phys*, **7**, 1103–1112.
Babu S S & Bhadeshia H K D H (1991), 'A direct study of grain boundary allotriomorphic ferrite crystallography', *Mater. Sci. Engg*, **A142**, 209–219.
Bain E C (1924), 'The nature of martensite', *Trans AIMME*, **70**, 25–46.
Basinski Z S, Hume-Rothery W & Sutton A L (1955), 'The lattice expansion of iron', *Proc. Roy. Soc. London A,* **229**, 459–467.
Becker R & Döring W (1935), 'Kinetic treatment of germ formation in supersaturated water', *Annalen der Physik*, **24**, 719–752.
Bhadeshia H K D H (1982), 'Thermodynamic analysis of isothermal transformation diagrams', *Met. Sci.*, **16**, 159–165.
Bhadeshia H K D H (1983), 'Ferrite formation in heterogeneous dual-phase steels', *Scripta Metall.*, **17**, 857–860.
Bhadeshia H K D H (1985), 'Diffusional formation of ferrite in iron and its alloys', *Prog. Mats Sci.*, **29**, 321–386.
Bhadeshia H K D H, Svensson L-E & Gretoft B (1985), 'A model for the development of microstructure in low-alloy steel (Fe-Mn-Si-C) weld deposits', *Acta Metall.*, **33**, 1271–1283.
Boettinger W J, Kattner U R, Moon K-W & Perepezko J H (2007), 'DTA and heat-flux DSC measurement of alloy melting and freezing', *Methods for Phase Diagram Determination*, Zhou J-C (ed.), Oxford, Elsevier, 151–221.
Braithwaite J S & Rez P (2005), 'Grain boundary impurities in iron', *Acta Mater.*, **53**, 2715–2726.
Brown L C & Kirkaldy J S (1964), 'Carbon diffusion in dilute ternary austenites', *Trans TMS-AIME*, **230**, 223–226.
Choi S (2003), 'Model for estimation of transformation kinetics from the dilation data during cooling of hypoeutectoid steels', *Mater. Sci. Engg*, **A363**, 72–80.
Christian J W (1965), *Physical Properties of Martensite and Bainite*, Spec. Rep. 93, London, Iron and Steel Institute.
Christian J W (1975), *The Theory of Transformations in Metals and Alloys: Part 1*, 2nd edn, Oxford, Pergamon.
Coates D E (1972), 'Diffusion controlled precipitate growth in ternary systems I', *Metall. Trans*, **3**, 1203–1212.
Coates D E (1973a), 'Precipitate growth kinetics for Fe-C-X alloys', *Metall. Trans*, **4**, 395–396.

© Woodhead Publishing Limited, 2012

Coates D E (1973b), 'Diffusion controlled precipitate growth in ternary systems II', *Metall. Trans*, **4**, 1077–1086.

Cohen M, Machlin E S & Paranjpe V J (1949), *Thermodynamics in Physical Metallurgy,* Cleveland, OH, ASM.

Cooke G M E (1988), 'An introduction to the mechanical properties of structural steel at elevated temperatures', *Fire Safety Journal*, **13**, 45–54.

Costa e Silva A, Ågren J, Clavaguera-Mora M T, Djurovic D, Gomez-Acebo T, Lee B-J, Liu Z-K, Miodownik P & Seifert H J (2007), 'Applications of computational thermodynamics – the extension from phase equilibrium to phase transformations and other properties', *Computer Coupling of Phase Diagrams and Thermochemistry*, **31**, 53–74.

Dahmen U (1982), 'Orientation relationships in precipitation systems', *Acta Metall.*, **30**, 63–73.

Davenport E S & Bain E C (1930), 'Transformation of austenite at constant subcritical temperatures', *Trans AIME Chicago Meeting 1930*, reproduced in *Metall. Mater. Trans B,* **41B**, (2010), 1353–1390.

Dennis C A, Scott A J, Brydson R & Brown A P (2004), 'ELNES modelling of interfaces in steels', *Electron Microscopy and Analysis 2003,* McVitie S & McComb D (eds), Institute of Physics Conference Series 179, Bristol, IoPP, 397–400.

Denton A R & Ashcroft N W (1991), 'Vegard's Law', *Phys Rev. A*, **43**, 3161–3164.

Dingley D (2004), 'Progressive steps in the development of electron backscatter diffraction and orientation imaging microscopy', *Journal of Microscopy*, **213**, 214–224.

Dirks A G & Meijering J L (1972), 'Rapid Fe-Ni surface diffusion and rapid diffusion of N and C along an austenite/ferrite phase boundary', *Acta Metall.*, **20**, 1101–1107.

Dirks A G & Meijering J L (1975), 'Rapid diffusion of nitrogen and carbon along interphase interfaces in iron-base diffusion couples', *Acta Metall.*, **23**, 217–220.

Dubé C A (1948), PhD thesis, Carnegie Institute of Technology.

Duflos F & Cantor B (1982), 'The microstructure and kinetics of marteniste transformations in splat-quenched Fe and Fe-Ni alloys – I. Pure Fe', *Acta Metall.*, **30**, 323–342.

Dyson D J & Holmes B (1970), 'Effect of alloying additions on lattice parameter of austenite', *ISIJ Intl*, **208**, 469–475.

Edmonds D V (1979), 'Direct observations on the crystallography and morphology of grain boundary proeutectoid ferrite formation in a medium-carbon low-alloy steel', *Phase Transformations*, vol. 2, York Conference, London, Instn. Metall., II80–83.

Enomoto M & Aaronson H I (1986), 'Nucleation kinetics of proeutectoid ferrite at austenite grain boundaries in Fe-C-X alloys', *Metall. Trans A*, **17A**, 1385–1397.

Enomoto M, Lange III W F & Aaronson H I (1986), 'The kinetics of ferrite nucleation at austenite grain boundaries in Fe-C and Fe-C-X alloys', *Metall. Trans A*, **17A**, 1399–1407.

Eshelby J D (1957), 'The determination of the elastic field of an ellipsoidal inclusion and related problems', *Proc. Roy. Soc.*, **A 241**, 376–396.

Eshelby J D (1959), 'The elastic field outside an ellipsoidal inclusion', *Proc. Roy. Soc.*, **A 252**, 561–569.

Finnis M W & Sinclair J E (1984), 'A simple empirical N-body potential for transition-metals', *Philos. Mag. A*, **50**, 45–55.

Foiles S M, Baskes M I & Daw M S (1986), 'Embedded-atom-method functions for the fcc metals Cu, Ag, Au, Ni, Pd, Pt and their alloys', *Phys. Rev. B*, **33**, 7983–7991.

Gamsjäger E, Svoboda J & Fischer F D (2005), 'Austenite-to-ferrite phase transformation in low-alloyed steels', *Computational Mats Sci.*, **32**, 360–369.

© Woodhead Publishing Limited, 2012

Garcia de Andres C, Caballero F G, Capdevila C & Bhadeshia H K D H (1998), 'Modelling of isothermal ferrite formation using an analytical treatment of soft impingement in 0.37C-1.45Mn-0.11V microalloyed steel', *Scr. Mater.*, **39**, 853–859.

Garcia de Andres C, Caballero F G, Capdevila C & Alvarez L F (2002), 'Application of dilatometric analysis to the study of solid-solid phase transformations in steels', *Mater. Characterization*, **48**, 101–111.

Geng W T, Freeman A J, Olson G B, Tateyama Y & Ohno T (2005), 'Hydrogen-promoted grain boundary embrittlement and vacancy activity in metals: insights from *ab initio* total energy calculations', *Mater. Trans*, **46**, 756–760.

Gilbert A & Owen W S (1962), 'Diffusionless transformations in iron-nickel, iron-chromium and iron-silicon alloys', *Acta Metall.*, **10**, 45–54.

Goldschmidt H J (1962), *Advanced X-ray Analysis*, New York, Plenum Press.

Gorton A T. Bifsianes G & Joseph T L (1965), 'Thermal expansion coefficients for iron and its oxides from X-ray diffraction measurements at elevated temperatures', *Trans AIME*, **233**, 1519.

Greninger A B & Troiano A R (1949), 'The mechanism of martensite formation', *Trans AIME,* **185**, 590–598.

Groeber M, Haley B, Uchic M, Dimiduk D, Bhandari Y & Ghosh S (2006), 'Advances in computational modeling through the use of higher-level microstructure characterization', *High Performance Structures and Materials III*, Brebbia C A (ed.), **85**, Southampton, WIT Press/Computational Mechanics Publications, 331–341.

Grong Ø & Myhr O R (2000), 'Additivity and isokinetic behaviour in relation to diffusion controlled growth', *Acta Mater.*, **48**, 445–452.

Guttmann M (1975), 'Equilibrium segregation in a ternary solution – model for temper embrittlement', *Surf. Sci.*, **5**, 213–227.

Hack K (1996), *Thermodynamics at Work*, London, Institute of Materials.

Hackett M J, Busby J T & Was G S (2008), 'The mechanism of Zr and Hf in reducing radiation-induced segregation in 316 stainless steel', *Metall. Mater. Trans A*, **39A**, 218–224.

Hammond C (1989), 'The contribution of Henry Clifton Sorby to the study of reflected light microscopy of iron and steel', *Historical Metallurgy*, **23**, 1–8.

Harrison P & Farrar R (1987), 'Microstructure and toughness of C-Mn and C-Mn-Ni weld metal – Part 1', *Metal Constr.*, **7**, 392R–399R.

He K & Edmonds D V (2002), 'On the formation of acicular ferrite and the influence of vanadium alloying', *Mater. Sci. Technol.*, **18**, 289–296.

He Y, Godet S, Jacques P J & Jonas J J (2006), 'Crystallographic relations between face- and body-centred cubic crystals formed under near-equilibrium conditions: observations from the Gibeon meteorite', *Acta Mater.*, **54**, 1323–1334.

Higginson R L & Sellars C M (2003), *Worked Examples in Quantitative Metallography*, London, Maney.

Hillert M (1998), *Phase Equilibria, Phase Diagrams and Phase Transformations*, Cambridge, Cambridge University Press.

Homberg D (1996), 'A numerical simulation of the Jominy end-quench test', *Acta Mater.*, **44**, 4375–4385.

Honeycombe R W K (1976), 'Transformation from austenite in alloy steels', *Metall. Trans A*, **7A**, 915–936.

Honeycombe R W K (1979), 'Precipitation of alloy carbides in austenite and ferrite', *Scand. J. Metall.*, **8**, 21–26.

Hu X L, Zhang Y, Lu G H, Wang T M, Xiao P H, Yin P G & Xu H B (2009), 'Effect

© Woodhead Publishing Limited, 2012

of O impurity on structure and mechanical properties of NiAl intermetallics: a first principles study', *Intermetallics*, **17**, 358–364.

Hultgren A (1947), 'Isothermal transformation of austenite', *Trans AIME*, **39**, 915–1005.

Hultgren A (1951), 'Isoterm omvandling av austenit', *Jernkontorets Ann.*, **135**, 403–494.

Hummelshøj T S, Christiansen T L & Somers M A J (2010), 'Lattice expansion of carbon-stabilized expanded austenite', *Scripta Mater.*, **63**, 761–763.

Iron and Steel Institute (1956), *Atlas of Isothermal Transformation Diagrams of B.S. En Steels*, Iron and Steel Institute Special Report 56, London.

Johnson W A & Mehl R F (1939), 'Reaction kinetics in process of nucleation and growth', *Trans AIMME*, **135**, 416–422.

Kempen A T W, Sommer F & Mittemeijer E J (2002), 'The kinetics of the austenite-ferrite phase transformation of Fe-Mn: differential thermal analysis during cooling', *Acta Mater.*, **50**, 3545–3555.

Kirkaldy J S (1958), 'Diffusion in multicomponent metallic systems. 2. Solutions for 2-phase systems with applications to transformations in steel', *Can. J. Phys.*, **36**, 907–916.

Kirkaldy J S (1973), 'Prediction of alloy hardenability from thermodynamic and kinetic data', *Metall. Trans*, **4**, 2327–2333.

Kirkaldy J S (1991), 'Diffusion-controlled phase-transformations in steels – theory and applications', *Scand. J. Metall.*, **20**, 50–61.

Kirkaldy J S, Thomson B A & Baganis E (1978), 'Prediction of multicomponent equilibrium and transformation diagrams for low alloy steels', in *Hardenability Concepts with Applications to Steel*, Doane D V & Kirkaldy J S (eds), Warrendale, PA, TMS-AIME, 82–125.

Kitahara H, Ueji R, Ueda M, Tsuji N & Minamino Y (2005), 'Crystallographic analysis of plate martensite in Fe-28.5 at.% Ni by FE-SEM/EBSD', *Materials Characterization*, **54**, 378–386.

Kohlhaas R, Dünner Ph, Schmitz-Pranghe N & Angew A (1967), 'Über die Temperaturabhängigkeit der Gitterparameter von Eisen, Kobalt und Nickel im bereich hoher Temperaturen', *Z. Angewandte Phys.*, **23**, 245–249.

Kolmogorov A (1937), 'A statistical theory for the recrystallisation of metals', *Akad. nauk SSSR, Izv., Ser. Matem,* **1**, 355–359.

Kop T A, Sietsma J & van der Zwaag S (2001), 'Dilatometric analysis of phase transformations in hypo-eutectoid steels', *J. Mater. Sci.*, **36**, 519–526.

Kurdjumov G V & Sachs G Z (1930), 'Über den Mechanisms der Stahlhärtnung', *Z. Phys*, **64**, 518.

Lee J-L & Bhadeshia H K D H (1993), 'A methodology for the prediction of time-temperature-transformation diagrams', *Mat. Sci. Engg*, **A171**, 223–230.

Lee S-J & Lee Y-K (2005), 'Quantitative analyses of ferrite lattice parameter and solute Nb content in low carbon microalloyed steels', *Scripta Mater.*, **52**, 973–976.

Li C-M, Sommer F & Mittemeijer E J (2002), 'Characteristics of the $\gamma \rightarrow \alpha$ transformation in Fe-Mn alloys', *Mat. Sci. Engg*, **A325**, 307–319.

Liu W P & Bunge H J (1991), 'Variant selection in the martensitic-transformation of an Fe-30% Ni-alloy with cube texture', *Mater. Letters*, **10**, 336–343.

Liu Y C, Sommer F & Mittemeijer E J (2004), 'Calibration of the differential dilatometric measurements signal upon heating and cooling; thermal expansion of pure iron', *Thermochimica Acta*, **413**, 215–225.

© Woodhead Publishing Limited, 2012

Liu Z-K & Ågren J (1989), 'On the transition from local equilibrium to paraequilibrium during the growth of ferrite in Fe-Mn-C austenite', *Acta Metall.*, **37**, 3157–3163.

Lu G H, Deng S H, Wang T M, Kohyama M & Yamamoto R (2004), 'Theoretical tensile strength of an Al grain boundary', *Phys. Rev. B*, **69**, 134106.

Ludwig W, King A, Reischig P, Herbig M, Lauridsen E M, Schmidt S, Proudhon H, Forest S, Cloetens P, Rolland du Roscoat S, Buffiere J Y, Marrow T J & Poulsen H F (2009), 'New opportunities for 3D materials science of polycrystalline materials at the micrometer lengthscale by combined use of X-ray diffraction and X-ray imaging', *Mater. Sci. Engg A*, **524**, 69–76.

Malet L, Barnett M R, Jacques P J & Godet S (2009), 'Variant selection during the γ–to-α_b phase transformation in hot-rolled bainitic TRIP-aided steels', *Scripta Mater.*, **61**, 520–523.

Massalski T B (1976), 'Massive transformations', *Mater. Sci. Engg*, **25**, 119–125.

Massalski T B, Perepezko J H & Jaklovsky J (1975), 'A microstructural study of massive transformations in the Fe-Ni system', *Mater. Sci. Engg*, **18**, 193–198.

McLean D (1956), *Grain Boundaries in Metals*, Oxford, Oxford University Press.

McMahon C J (1980), 'The role of solute segregation in promoting the hardenability of steel', *Metall. Mater. Trans A*, **11**, 531–535.

Messmer R P & Briant C L (1982), 'The role of chemical bonding in grain boundary embrittlement', *Acta Metall.*, **30**, 457–467.

Miller M K & Smith G D W (1995), 'Atom-probe analysis of interfacial segregation', *Applied Surface Science*, **87–88**, 243–250.

Miller M K, Pareige P & Burke M G (2000), 'Understanding pressure vessel steels – an atom probe perspective', *Materials Characterization*, **44**, 159–176.

Misra R D K (2002), 'Temperature-time dependence of grain boundary segrgation of phosphorus in interstitial-free steels', *J. Mater. Sci. Letters*, **21**, 1275–1279.

Miyamoto G, Iwata N, Takayama N & Furuhara T (2010), 'Mapping the parent austenite orientation reconstructed from the orientation of martensite by EBSD and its application to ausformed martensite', *Acta Mater.*, **54**, 6393–6403.

Morimoto T, Yoshida F, Chikusi I, Kitahara H & Tsuji N (2007), 'Development of variant analysis program by using EBSD', *Tetsu-to-Hagane*, **93**, 591–599.

Nishiyama Z (1934), 'X-ray investigation of the mechanism of the transformation from face centred cubic lattice to body centred cubic', *Sci. Rep. Tohoku Univ.*, **23**, 637–644.

Offerman S E, van Dijk N H, Sietsma J, Lauridsen E M, Margulies L, Grigull S, Poulsen H F & van der Zwaag S (2005), '3DXRD microscopy for the study of solid-state phase transformation kinetics', *Nuclear Instruments and Methods in Physics Research B*, **238**, 107–110.

Olson G B (1987), 'Overview: science of steel', *Innovations in Ultrahigh-Strength Steel Technology*, Olson G B, Azrin M & Wright E S (eds), Sagamore Army Materials Research Conference Proceedings, vol. 34, 3–66.

Onink M, Brakman C M, Tichelaar F D, Mittemeijer E J, van der Zwaag S, Root J H & Konyer N B (1993), 'The lattice parameters of austenite and ferrite in Fe-C alloys as functions of carbon concentration and temperature', *Scripta Metall. Mater.*, **29**, 1011–1016.

Onsager L (1945–46), 'Theories and problems of liquid diffusion', *Ann. NY Acad. Sci.*, **46**, 241–265.

Paju M, Grabke H J & Hougady H P (1991), 'Effects of boron alloying on properties of a low-carbon low-alloyed steel. 2. Austenite decomposition', *Scand. J. Metall.*, **20**, 135–140.

© Woodhead Publishing Limited, 2012

Pereloma E V, Timokhina I B, Jonas J J & Miller M K (2006), 'Fine-scale microstructural investigations of warm rolled low-carbon steels with and without Cr, P and B additions', *Acta Mater.*, **54**, 4539–4551.

Piatti G & Schiller P (1986), 'Thermal and mechanical properties of the Cr-Mn-(Ni-free) austenitic steels for fusion reactor applications', *J. Nuclear Mats*, **141–143**, 417–426.

Pitsch W (1962), 'Der Orientierungszusammenhang zwischen Zementit und Austenit', *Acta Metall.*, **10**, 897–900.

Poulsen H F (2002), '3DXRD microscopy – a comparison with neutron diffraction', *App. Phys. A: Mat. Sci. Prod.*, **74**, s1673–s1675.

Purdy G R (1978), 'The dynamics of transformation interfaces in steels – I. The ferrite-austenite interface in Fe-C-Mo alloy', *Acta Metall.*, **26**, 477–486.

Raghunathan S L, Azeem M A, Collins D & Dye D (2008), '*In-situ* observation of individual variant transformations in polycrystalline NiTi', *Scripta Metall.*, **59**, 1059–1062.

Raju S, Ganesh B J, Banerjee A & Mohandas E (2007), 'Characterisation of thermal stability and phase transformation energetics in tempered 9Cr-1Mo steel using drop and differential scanning calorimetry', *Mat. Sci. Engg A*, **A465**, 29–37.

Raju S, Ganesh B J, Rai A K, Mythili R, Saroja S, Mohandas E, Vijayalakshmi M, Rao K B S & Raj B (2009), 'Measurement of transformation temperatures and specific heat capacity of tungsten added reduced activation ferritic-martensitic steel', *J. Nuclear Mats*, **389**, 385–393.

Randle V (2009a), 'Electron backscatter diffraction: strategies for reliable data acquisition and processing', *Materials Characterization*, **60**, 913–922.

Randle V (2009b), 'Applications of electron backscatter diffraction to materials science: status in 2009', *J. Mats Sci.*, **44**, 4211–4218.

Rehman A & Edmonds D V (2000), 'Ferrite morphologies in ultra-low carbon steels', *HSLA Steels 2000*, Liu G, Wang F, Wang Z & Zhang H (eds), Beijing, The Metallurgical Industry Press, 241–247.

Ridley N, Stuart H & Zwell L (1969), 'Lattice parameters of Fe-C austenites at room temperature', *Trans AIME*, **245**, 1834–1840.

Rios P R (2005), 'Relationship between non-isothermal transformation curves and isothermal and non-isothermal kinetics', *Acta Mater.*, **53**, 4893–4901.

Roberts G (2010), 'KAM as a method to further understand deformation in rail steels' 1st year PhD report, The School of Metallurgy and Materials, University of Birmingham.

Roitburd A L & Kurdjumov G V (1979), 'Nature of martensitic transformation', *Mater. Sci. Engg*, **39**, 141–167.

Russell K C (1969), 'Grain boundary nucleation kinetics', *Acta Metall.*, **17**, 1123–1131.

Scheil E (1935), 'Anlaufzeit de Austenittumwendlung', *Archiv für das Eisenhüttenwesen*, **12**, 564–567.

Schwingenschlogl U & Schuster C (2009), 'First-principles calculations of electronic states and self-doping effects at a 45° grain boundary in the high temperature $YBa_2Cu_3O_7$ superconductor', *Phys. Rev. L.*, **102**, 227002.

Sha W, Cerezo A and Smith G D W (1993a), 'Phase chemistry and precipitation reactions in maraging steels. 1. Introduction and study of Co-containing C-300 steel', *Metall. Trans A*, **24**, 1221–1232.

Sha W, Cerezo A & Smith G D W (1993b), 'Phase chemistry and precipitation reactions in maraging steels. 2. Co-free T-300 steel', *Metall. Trans A*, **24**, 1233–1239.

Sha W, Cerezo A & Smith G D W (1993c), 'Phase chemistry and precipitation reactions in maraging steels. 3. Model alloys', *Metall. Trans A*, **24**, 1241–1249.

© Woodhead Publishing Limited, 2012

Sha W, Cerezo A & Smith G D W (1993d), 'Phase chemistry and precipitation reactions in maraging steels. 4. Discussion and conclusions', *Metall. Trans A*, **24**, 1251–1256.

Shipway P H & Bhadeshia H K D H (1995), 'Mechanical stabilisation of bainite', *Mater. Sci. Tech.*, **11**, 1116–1128.

Speich G R & Warlimont H (1968), 'Yield strength and transformation substructure of low-carbon martensite', *J. Iron Steel Inst.*, **206**, 385–392.

St-Pierre L, Heripre E, Dexet M, Crepin J, Bertolino G & Bilger N (2008), '3D simulations of microstructure and comparison with experimental microstructure coming from OIM analysis', *Intl J. Plasticity*, **24**, 1516–1532.

Strangwood M (1987), 'The Prediction and Assessment of Weldmetal Microstructures', PhD thesis, Cambridge University.

Strangwood M & Bhadeshia H K D H (1986), 'The mechanism of acicular ferrite formation in steel weld deposits', *Advances in Welding Science and Technology*, David S A (ed.), Metals Park, OH, ASM, 209–213.

Strangwood M & Bhadeshia H K D H (1988), 'Nucleation of ferrite at ceramic steel interfaces', *Phase Transformations 87*, Ridley N (ed.), London, Institute of Metals, 466–470.

Takahashi N, Mizoguchi T, Tohei T, Nakamura K, Nakagawa T, Shibata N, Yamamoto T & Ikuhara Y (2009), 'First principles calculations of vacancy formation energies in sigma 13 pyramidal grain boundary of α-Al_2O_3', *Mater. Trans*, **50**, 1019–1022.

Tamura I & Wayman M C (1992), 'Martensitic transformations and mechanical effects', *Martensite*, Olson G B & Owen W S (eds), Materials Park, OH, ASM International, 227–242.

te Velthuis S G E, Root J H, Sietsma J, Rekveldt M Th & van der Zwaag S (1998), 'The ferrite and austenite lattice parameters of Fe-Co and Fe-Cu binary alloys as a function of temperature', *Acta Mater.,* **46**, 5223–5228.

Thivellier D, Maitrepierre P, Rofesvernis J & Tricot R (1978), 'Quenchability and microstructure of low alloy boron steels', *Memoires scientifiques de la revue de metalurgie*, **75**, 559–569.

Tian Z X, Yan J X, Hao W & Xiao W (2011), 'Effect of alloying additions on the hydrogen-induced grain boundary embrittlement in iron', *J. Physics – Condensed Matter*, **23**, 015501.

Tsai M C, Chiou C S, Du J S & Yang J R (2002), 'Phase transformation in AISI 410 stainless steel', *Mater. Sci. Engg*, **A332**, 1–10.

Umemoto M, Nishioka N & Tamura I (1982), 'Prediction of hardenability from isothermal transformation diagrams', *Trans ISIJ*, **22**, 629–636.

Underwood E E (1970), *Quantitative Stereology*, Reading, MA, Addison-Wesley.

US Steel (1963), *USS Atlas of Isothermal Transformation Diagrams*, Pittsburgh, PA, US Steel Company.

Volmer M (1939), *Kinetik der Phasenbildung*, Dresden, Steinkopf.

Wachowicz E & Kiejna A (2008), 'Effect of impurities on grain boundary cohesion in bcc iron', *Computational Mats Sci.*, **43**, 736–743.

Wagner C (1952), *Thermodynamics of Alloys*, Cambridge, Addison-Wesley.

Wasserman G (1933), *Arch. Eisenhuttenevesen*, **16**, 647.

Weller M & Wegst U G K (2009), 'Fe-C Snoek peak in iron and stony meteorites: metallurgical and cosmological aspects', *Mater. Sci. Engg A*, **521–522**, 39–42.

Xu X, Ferry M, Mateescu N, Cairney J M & Humphreys F J (2007), 'Techniques for generating 3-D EBSD microstructures by FIB tomography', *Mater. Characterization*, **58**, 961–967.

© Woodhead Publishing Limited, 2012

Yuan Y, Davenport A J & Strangwood M (2005), 'Interfacial control of β-phase precipitation in Al-Mg alloys', *Solid-Solid Phase Transformations in Inorganic Materials 2005,* Howe J M, Laughlin D E, Lee J K, Dahmen U and Soffa W A (eds), Warrendale, PA, TMS, 377–382.

Zener C (1949), 'Theory of growth of spherical precipitates from solid solution', *J. Appl. Phys*, **20**, 950–953.

Zhang X D, Godfrey S P, Weaver M, Strangwood M, Threadgill P L, Kaufman M J & Loretto M H (1996), 'The massive transformation in Ti-Al alloys: mechanistic observations', *Acta Metall. Mater.*, **44**, 3723–3734.

© Woodhead Publishing Limited, 2012

7

Proeutectoid ferrite and cementite transformations in steels

M. V. KRAL, University of Canterbury, New Zealand

Abstract: Proeutectoid ferrite and cementite are principal microconstituents of steels, and have received considerable attention over the years. A proeutectoid constituent is defined here as the first diffusional product to form from austenite upon cooling. The purpose of this chapter is to provide an updated, detailed description of the morphology and crystallography proeutectoid constituents, ferrite and cementite (mainly in slowly cooled or isothermally transformed steels). A significant task along the way is to augment the two-dimensional (2D) classification system with three-dimensional (3D) observations. Some insights gained from recent studies on the subject of nucleation and growth are provided.

Key words: proeutectoid, ferrite, cementite, allotriomorph, Widmanstätten, crystallography.

7.1 Introduction

More than 100 years have passed since H. C. Sorby, the father of metallography, first revealed the major phases that appear in steel microstructures (Sorby, 1887). The Davenport and Bain (1930) study on the kinetics of austenite decomposition is also regarded as groundbreaking, a watershed in the study of solid-state phase transformations. Another work bearing the hallmarks of a 'classic' is the Mehl *et al*. (1933) view on Widmanstätten structures in steels, which is only limited in retrospect by the experimental methods that could be brought to bear at the time. Progress in understanding phase transformations in steels has been rapid over the decades but perhaps never in such leaps forward as in the aforementioned work. Aaronson exhaustively reviewed the proeutectoid ferrite and cementite reactions in 1962 in *The Decomposition of Austenite by Diffusional Processes* (Aaronson, 1962). There have been several reviews of proeutectoid ferrite and cementite in the ensuing years. To name a few: Reynolds *et al*. reviewed proeutectoid ferrite in 1984 in *Phase Transformations in Ferrous Alloys* (Reynolds *et al*., 1984). In 2001, both proeutectoid ferrite and cementite were briefly reviewed in *The Encyclopedia of Materials* (Enomoto, 2001; Spanos and Kral 2001). Spanos and Kral provided a detailed review of proeutectoid cementite in 2009.

The number of scientific papers on the general subject of phase

© Woodhead Publishing Limited, 2012

transformations in steels (numbering in the thousands), and specifically involving the proeutectoid transformations (numbering in the hundreds), may be overwhelming but there should be no doubt that the driving force behind the interest in steel is engineering performance. The relationships between mechanical properties and microstructures (Rhines, 1977) are often inferred but sometimes directly studied. For example, Ichikawa *et al*. (1996) concluded that some allotriomorphic ferrite should be retained in steel weld microstructures (of fire-resistant steels) in order to improve high temperature mechanical properties, after showing that percent elongation dropped from 30% at room temperature to less than 10–15% at temperatures above 500°C without allotriomorphic ferrite. The presence of allotriomorphic proeutectoid ferrite on prior austenite grain boundaries has also been shown to be beneficial for resistance to zinc liquid metal embrittlement and impurity (e.g. phosphorus) controlled embrittlement. Especially in weld metals, the so-called acicular morphology is known to be a desirable microstructure (Bhadeshia, 1996). It is also known that elongated shapes, e.g. Widmanstätten, have lower toughness than equiaxed or blocky shapes (Huang and Yao, 1989). Likewise, proeutectoid cementite (whether as a continuous network on prior austenite grain boundaries or Widmanstätten) is known to embrittle high carbon steels (Krauss, 1978; Barrallier *et al*., 2005). Simple and unambiguous relationships between the various diverse microstructures of steels and the multiplicity of properties that relate to engineering performance will continue to be sought for direct application and as a guide to predictive models (Bhadeshia, 1996).

As a principal microconstituent of hypoeutectoid steels, proeutectoid ferrite has received considerable attention over the years. In recognition of its technological importance, the morphology, crystallography, growth kinetics, effects of alloying elements and so on have been studied experimentally in detail. Numerous models have been devised to predict and/or explain the development of proeutectoid ferrite. To name only a very few, see Mehl *et al*. (1933), Hillert (1957), Dubé *et al*. (1958), Aaronson (1962), Eichen *et al*. (1964), Townsend and Kirkaldy (1968), Simonen *et al*. (1973), Bradley *et al*. (1977), Purdy (1987), Spanos and Hall (1996), Jones and Bhadeshia (1997), Krielaart *et al*. (1997), Aaronson (1999) and te Velthuis *et al*. (2000).

Proeutectoid cementite has also been studied in detail for over 100 years, often used as a model for solid-state phase transformations. Iron carbide, usually referred to as cementite, is a brittle compound phase with the formula Fe_3C. There have been a series of detailed investigations of proeutectoid cementite morphology (e.g., Mehl *et al*. 1933; Greninger and Troiano, 1940; Heckel and Paxton, 1961; Ando and Krauss, 1981b; Spanos and Aaronson, 1988), followed by a series of papers by Kral, Spanos and co-workers (Kral and Spanos, 1997, 1999; Mangan *et al*., 1999; Kral and Fonda, 2000; Hung *et al*., 2002; Kral and Spanos, 2003), representing the most recent progress to date in the study of proeutectoid cementite.

© Woodhead Publishing Limited, 2012

Aaronson's original and definitive monograph on proeutectoid ferrite and cementite had a central theme of describing morphologies as a starting point for understanding microstructural evolution, mechanisms and kinetics of nucleation and growth. The idea, which is still completely valid, was that a morphological classification system would provide a simple framework for further discussion. The Dubé morphological classification system (Dubé *et al.*, 1958) was based upon two-dimensional observations of proeutectoid ferrite and later modified by Aaronson (1956). Heckel and Paxton (1961) found that the Dubé system also worked for classifying proeutectoid cementite. The Dubé morphological classification system was accepted, and the terminology has been employed consistently throughout the literature that followed and thus needs to be explained.

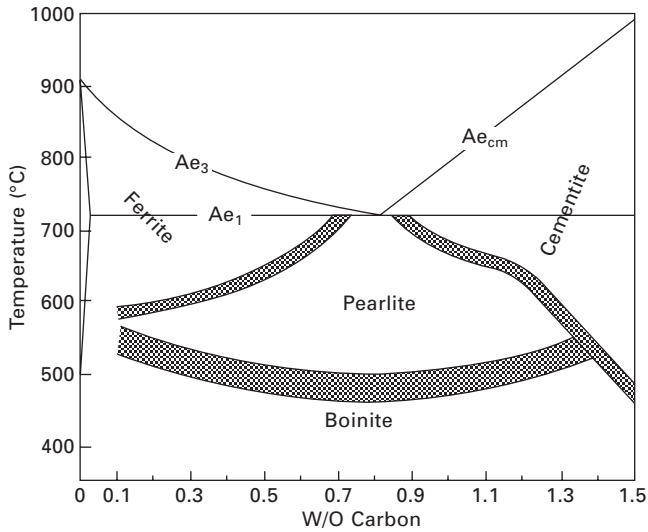
The purpose of this chapter is to provide an updated, detailed description of the morphology and crystallography proeutectoid constituents, ferrite and cementite (mainly in slowly cooled or isothermally transformed steels). A proeutectoid constituent is defined here as the first product to form from austenite upon cooling, thus various ferrite-carbide aggregates such as bainite, interphase boundary carbides and degenerate pearlite are outside the scope of this chapter. A significant task along the way is to augment the two-dimensional (2D) classification system with three-dimensional (3D) observations. Some insights gained from recent studies on the subject of nucleation/growth are provided. Kinetics and detailed growth mechanisms will be explained in other chapters.

7.2 Temperature-composition range of formation of proeutectoid ferrite and cementite

Proeutectoid ferrite can form in steels when the carbon content is lower than the eutectoid composition (hypoeutectoid steels). Likewise, proeutectoid cementite typically forms in steels when the carbon content is greater than that of the eutectoid composition (hypereutectoid steels) (see Fig. 7.1). For plain carbon steels, i.e. Fe-C-based alloys containing about 0.5% Mn and 0.25% Si,[1] the eutectoid composition corresponds to a carbon composition of about 0.8%, and the eutectoid temperature is approximately 725°C (Bain and Paxton, 1966). Considerable amounts of alloying elements can significantly change the eutectoid composition, the eutectoid temperature and can also change the number of phases present in the phase fields on the phase diagram. Bain and Paxton (1966) provided a number of pseudo-binary phase diagrams with effective eutectoid compositions and temperatures for various ternary and quaternary alloy steels. A review of the effects of alloying elements on

[1] All alloy percentages presented in this chapter are in wt%.

© Woodhead Publishing Limited, 2012



7.1 Temperature-composition regions in which the various diffusional products of austenite decomposition are dominant. The Ae_1 temperature is the equilibrium eutectoid temperature. The Ae_3 temperature for a specific carbon composition is given by the boundary between the single-phase austenite field and the two-phase austenite/ferrite field. The Ae_{cm} temperature is given by the boundary between the single-phase austenite field and the two-phase austenite/cementite field. This figure is slightly modified from Aaronson (1962).

the Fe-C phase diagram is not within the scope of this chapter, and there are many reports in the literature on this subject see, e.g., (Bain and Paxton, 1966; Hillert and Waldenstrom, 1977; Doane and Kirkaldy, 1978). Software packages and databases which can be used to calculate such phase diagrams are also now readily available (Sundmand *et al.*, 1985; Thermo-Calc, 2007). It is also worth mentioning that it has been shown recently that the presence of a strong magnetic field can shift the eutectoid point to higher carbon compositions and higher temperatures, thus reducing the driving force for and the composition-temperature range of the proeutectoid cementite transformation (Zhang *et al.*, 2006).

At equilibrium in hypoeutectoid steels, proeutectoid ferrite forms below the Ae_3 temperature (also known as the upper critical temperature) and above the eutectoid temperature (also known as Ae_1 or the lower critical temperature). The Ae_3 temperature for a specific carbon composition is given by the boundary between the single-phase austenite field and the two-phase austenite/ferrite field. Similarly, under equilibrium conditions in hypereutectoid steels, proeutectoid cementite forms below the Ae_{cm} temperature and above the eutectoid temperature. The Ae_{cm} temperature for a specific

© Woodhead Publishing Limited, 2012

carbon composition is given by the boundary between the single-phase austenite field and the two-phase austenite/cementite field. Both proeutectoid ferrite and cementite can form directly from the high temperature austenite phase *below* the eutectoid temperature, without pearlite or bainite formation (see the shaded boundaries, marking the lower extent of the appearance of proeutectoid phases below the Ae_1 temperature in Fig. 7.1).

In hypereutectoid steels, 'abnormal ferrite' has been described as large regions of ferrite covering coarse proeutectoid cementite (Hillert, 1962; Chairuangsri and Edmonds, 2000). This microstructure is not due to an effect or coarsening of pearlite, but is believed to be a characteristic microstructural constituent of hyper-eutectoid steels at transformation temperatures slightly below the eutectoid temperature. The occurrence of 'abnormal cementite' in hypo-eutectoid steels is thought to be unlikely.

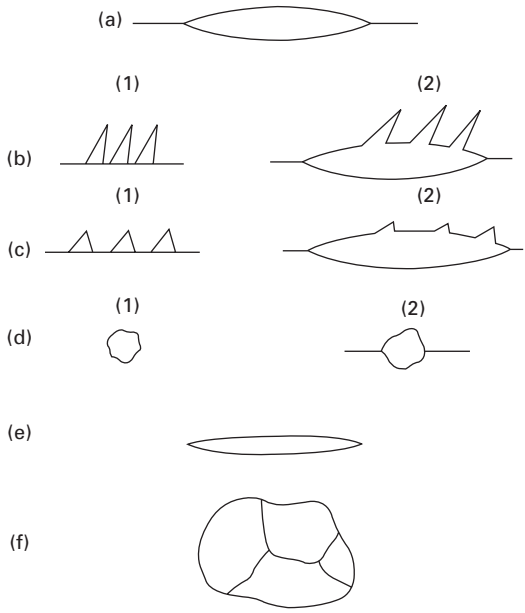
Studies of proeutectoid phase transformations generally involve heat treatment in three steps: (1) austenitization (e.g., holding at 1100–1200°C), (2) isothermal transformation in a molten salt or lead bath below Ae_3 or Ae_{cm} (e.g., 650–850°C, depending on alloy content) and (3) a quench to room temperature in water or iced brine. In the case of proeutectoid cementite, much of the work has involved high-Mn hypereutectoid alloys that remain austenitic at room temperature, to avoid the complexity of the martensitic transformation that occurs upon quenching. Unfortunately, the remaining austenite in alloys used to study the proeutectoid ferrite reaction invariably transforms to martensite, thus destroying the ferrite:austenite interface.

The major drawbacks to typical isothermal transformation experiments are the assumption of instantaneous cooling and quenching, as well as precluding direct observation of kinetics. Thermionic emission microscopy (Eichen *et al.*, 1964) or hot-stage TEM (Purdy, 1978) can allow *in situ* observations, although the kinetics of transformations may be too fast to make useful observations, and surface effects in thin foils may be misleading. Synchrotron experiments (e.g., Offerman *et al.*, 2002), offer the ability to study transformation kinetics in bulk materials in real time, although with a limited spatial resolution (*ca.* 2 microns).

7.3 The Dubé morphological classification system

Dubé (Dubé, 1948; Dubé *et al.*, 1958) determined that the cross-sectional shapes of individual proeutectoid ferrite fall into only a few general categories, based on many (single section) metallographic observations of proeutectoid ferrite grains in isothermally transformed alloy steels. Dubé thus developed a morphological classification system based on these observations. Aaronson (Aaronson, 1962; Aaronson *et al.*, 1970) subsequently modified Dubé's classification system (see Fig. 7.2) to distinguish between primary Widmanstätten precipitates, which grow directly from grain boundaries, and

© Woodhead Publishing Limited, 2012



7.2 The Dubé morphological classification system, slightly modified from Aaronson (1962).

secondary Widmanstätten precipitates, which nucleate upon and grow from other precipitates already formed at the grain boundaries.

Grain boundary allotriomorphs (Fig. 7.2(a)) are found at austenite grain boundaries and are often described as two abutting spherical caps. The mineralogical term 'allotriomorphic' refers to crystals with shapes not dictated by their own crystal structure but by adjacent crystals. *Widmanstätten sideplates or needles* (Fig. 7.2(b)) extend into austenite grains after nucleating either directly upon grain boundaries (b1, *primary sideplates*) or upon precipitates already formed at the grain boundaries (b2, *secondary sideplates*). Primary and secondary *Widmanstätten sawteeth* (Fig. 7.2(c)) are similar to sideplates, but have a larger apex angle. *Idiomorphs* (Fig. 7.2(d)) are equiaxed crystals that usually form within grains (d1), presumably at inclusions, but sometimes are found at grain boundaries (d2). The mineralogical term 'idiomorphic' refers to crystals with shapes that *are* dictated by their own crystal structure and not influenced by adjacent crystals. *Intragranular Widmanstätten plates or needles* (Fig. 7.2(e)) lie wholly within the matrix grains. *Massive*[2] *structures* (Fig. 7.2(f)) are aggregates of impinged precipitate crystals within the matrix grains. Aaronson (1962) proposed that these morphological classifications

[2] The term 'massive' does not mean origination by a massive transformation, but an agglomeration of impinged precipitates.

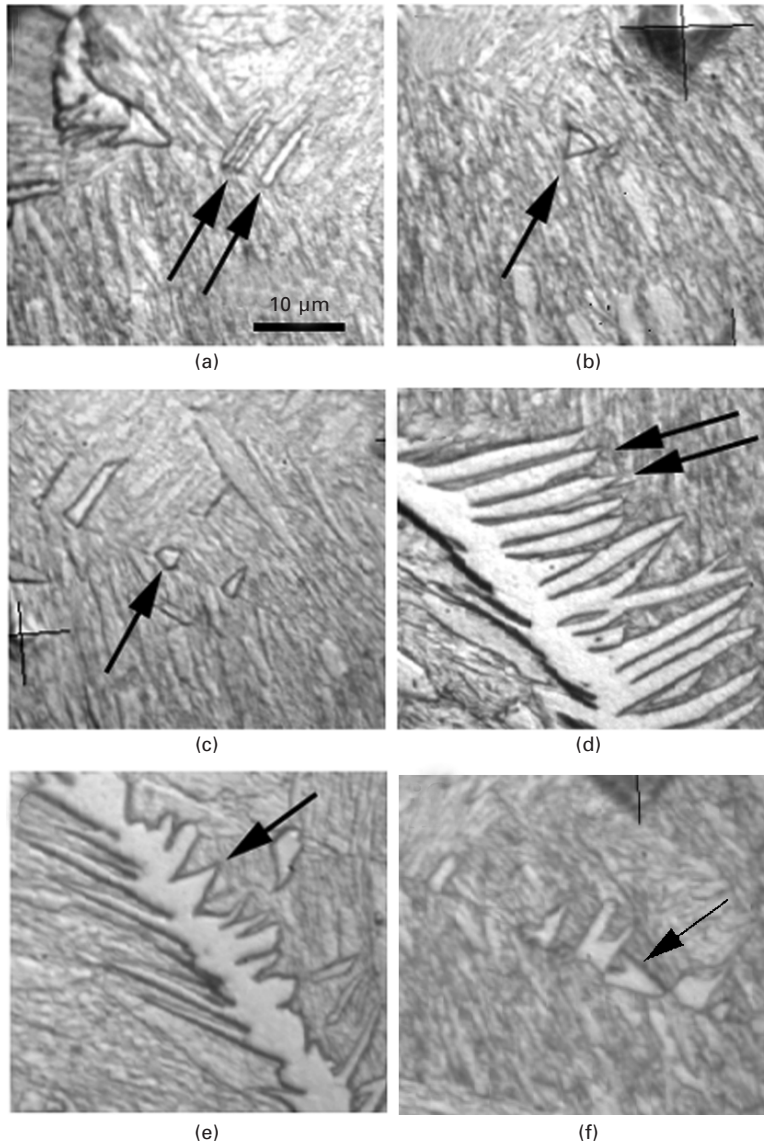
© Woodhead Publishing Limited, 2012

are general to products of diffusional nucleation and growth transformations in a wide variety of alloy systems. Heckel and Paxton (1961) suggested that Dubé's system could be applied specifically to proeutectoid cementite formed in hypereutectoid steels, again based upon many optical observations of single planes of polish. The schematic diagram of Fig. 7.2 can be compared to some actual microstructures of small, isolated precipitates in Fig. 7.3. The temperature and composition regions in which the various morphologies are dominant are shown in Fig. 7.4. It should be noted that the Widmanstätten-start temperature is a strong function of austenite grain size (Krahe *et al.*, 1972). Microstructures in industrial alloys are more complex, but contain the same micro constituents (see Fig. 7.5).

The term 'acicular ferrite' is sometimes used interchangeably with Widmanstätten ferrite (Wu *et al.*, 2004), but was discouraged by Honeycombe (Honeycombe, 1972) who stated that the term is 'inaccurate' and that Widmanstätten ferrite (see Fig. 7.6; Bramfitt and Lawrence, 2004) is more appropriate. Actually, it should be recognized that neither of these terms are necessarily more correct than the other, and refer to two different phenomena. The distinction is based upon nucleation site. Acicular ferrite (which has a Widmanstätten morphology, see Fig. 7.7; Babu, 2004) is associated with nucleation (at temperatures slightly higher than upper bainite; Thompson *et al.*, 1990) upon non-metallic inclusions (e.g. V(C,N), MnS, Al_2O_3) within prior austenite grains (Madariaga and Gutierrez, 1999; Bhadeshia and Honeycombe, 2006). Widmanstätten ferrite nucleates on prior austenite grain boundaries or upon grain boundary allotriomorphs. The confusion of terminologies may arise from the various requirements of descriptive metallography, and implications about the growth mechanism being displacive or diffusional.

Users of the Dubé system, where the term Widmanstätten dominates, often describe the products of carefully controlled isothermal transformation experiments on sets of small, individually processed samples, perhaps at early stages of transformation to avoid the confusion of impingement. In another (perhaps more pragmatic) group, there is a need to describe the more complex microstructures of bulk industrially processed materials, welds and castings, where higher volume fractions of ferrite and impingement are normal. The term acicular literally means narrow, long and pointed as a needle in 3D, whereas the term Widmanstätten is adopted from very early (*ca.* 1808) 2D observations of the cross-hatched shapes on etched cross sections of iron-nickel meteorites. The Dubé system leaves open the possibility that the Widmanstätten shapes could be plates or needles, but it has been shown that the true 3D shapes vary between lath and plate (Kral and Spanos, 1999). In the present work, to maintain consistency, the term Widmanstätten will be used to describe elongated shapes in ferrite and cementite. Similarly, the term 'polygonal ferrite' is sometimes used to describe an equiaxed ferrite grain nucleated within a prior austenite grain (Thompson *et al.*, 1990). In the

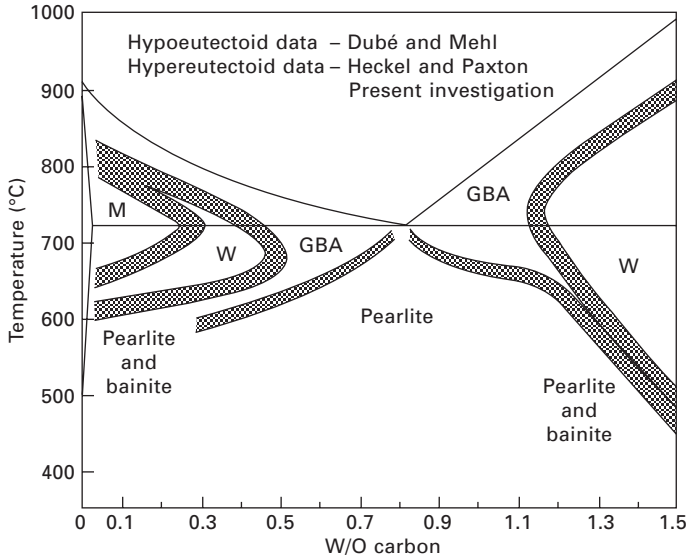
© Woodhead Publishing Limited, 2012



7.3 Optical micrographs of various 2D morphologies: (a) primary sideplates, (b) a primary sawtooth, (c) a grain boundary idiomorph, (d) secondary sideplates, (e) a secondary sawtooth (Kral and Spanos, 2005), (f) an allotriomorph (Cheng *et al.*, 2008).

present work, such morphologies will be described as intragranular idiomorphs. Polygonal ferrite is also used to describe a largely equiaxed ferrite structure in low alloy steels, which might, for example, be obtained from a ferrite allotriomorph impinging from a relatively small prior austenite grain size

© Woodhead Publishing Limited, 2012



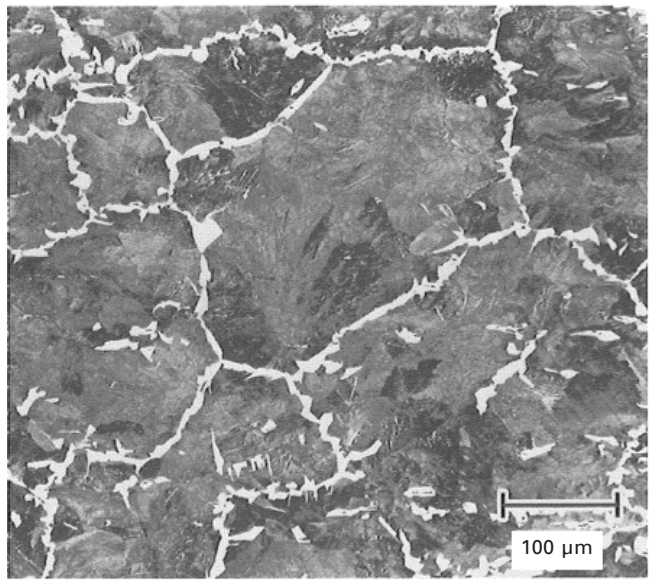
7.4 Temperature-composition regions in which the various morphologies of ferrite are dominant at late reaction times in coarse grain austenite (ASTM 0-1, average diameter ~250–350 microns). GBA = grain boundary allotriomorphs, W = Widmanstätten shapes and M = massive (i.e., impinged; see footnote in text) ferrite (Aaronson, 1962).

in low carbon steel. There is also a morphology described as 'degenerate' Widmanstätten ferrite (Aaronson, 1962; Goldenstein and Aaronson, 1990; Reynolds *et al*., 1990; Hackenberg *et al*., 2002b). It must be recognized that any attempt to categorize the shapes of individual grains in complex microstructures over a wide range of possible compositions and thermo-mechanical histories will fall short for one reason or another (Kennon, 1999), and that the present discussion presents a simplified approach to describe isothermally transformed model alloys.

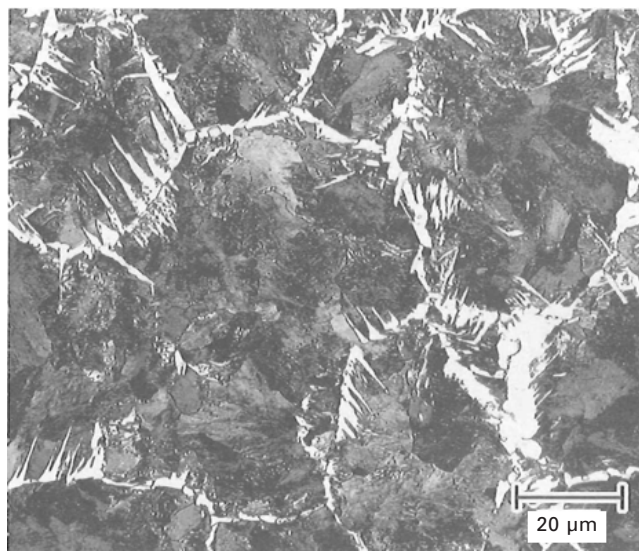
7.4 Three-dimensional morphological classifications

Recent work (Kral and Spanos, 1999, 2005) showed that 3D analysis is required to accurately characterize complex morphologies. Revisions of the Dubé morphological classification systems for proeutectoid ferrite (Kral and Spanos, 2005; Spanos *et al*., 2005) and proeutectoid cementite (Kral and Spanos, 1997, 1999; Hung *et al*., 2002) are described in detail below. There is a growing body of work in three-dimensional analysis of proeutectoid ferrite (Wu *et al*., 2007; Cheng *et al*., 2008, 2010a, 2010b; Wan *et al*., 2010), which so far shows consistency with previous descriptions (Kral and Spanos, 2005).

© Woodhead Publishing Limited, 2012



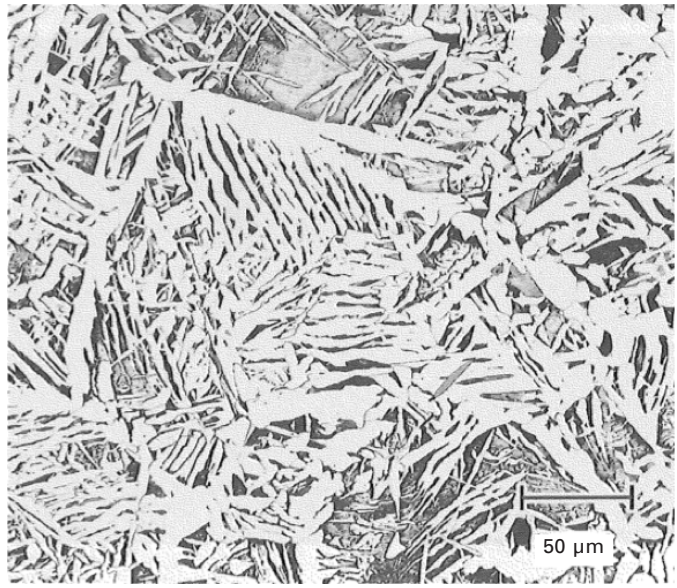
(a)



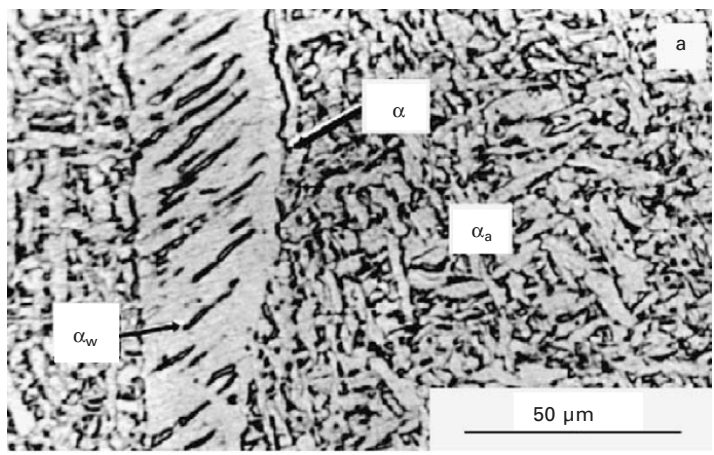
(b)

7.5 The microstructure of a continuously cooled plain carbon UNS G10400 (0.4%C) steel (a) with impinged grain boundary ferrite allotriomorphs along prior austenite grain boundaries (white), and (b) Widmanstätten ferrite extending either directly from prior austenite grain boundaries or from ferrite allotriomorphs. Dark etching constituent is pearlite (Bramfitt and Lawrence, 2004).

© Woodhead Publishing Limited, 2012



7.6 The microstructure of a continuously cooled plain carbon UNS G10200 steel (0.2%C), with impinged grain boundary ferrite and Widmanstätten ferrite (white). The minor dark etching constituent is pearlite (Bramfitt and Lawrence, 2004).



7.7 This optical micrograph shows the presence of grain boundary (α) and Widmanstätten ferrite (α_W) coexisting with acicular ferrite (α_a) microstructure in a low alloy steel (Fe-0.06C-0.51Si-1.11Mn-0.48Cr wt%) weld metal with small additions of aluminum, titanium and oxygen (Babu, 2004).

© Woodhead Publishing Limited, 2012

Note that the morphologies of ferrite and cementite are different enough to warrant separate classifications.

7.4.1 Ferrite morphologies

Prior investigations of proeutectoid ferrite in steels have typically been based on observations of 2D cross sections in the context of the Dubé morphological classification system, whether by optical microscopy (e.g., Dubé, 1948; Aaronson and Wells, 1956; Dubé *et al.*, 1958; Townsend and Kirkaldy, 1968), transmission electron microscopy (TEM) of thin foils (e.g., Purdy, 1978; Reynolds *et al.*, 1990; Spanos and Hall, 1996) or other techniques (e.g., Eichen *et al.*, 1964). The following section presents the three-dimensional shapes and distributions of grain boundary nucleated proeutectoid ferrite precipitates that were obtained by computer-aided 3D reconstruction of serial sections in an Fe-0.12 wt%C-3.28 wt%Ni alloy (Kral and Spanos, 2005).

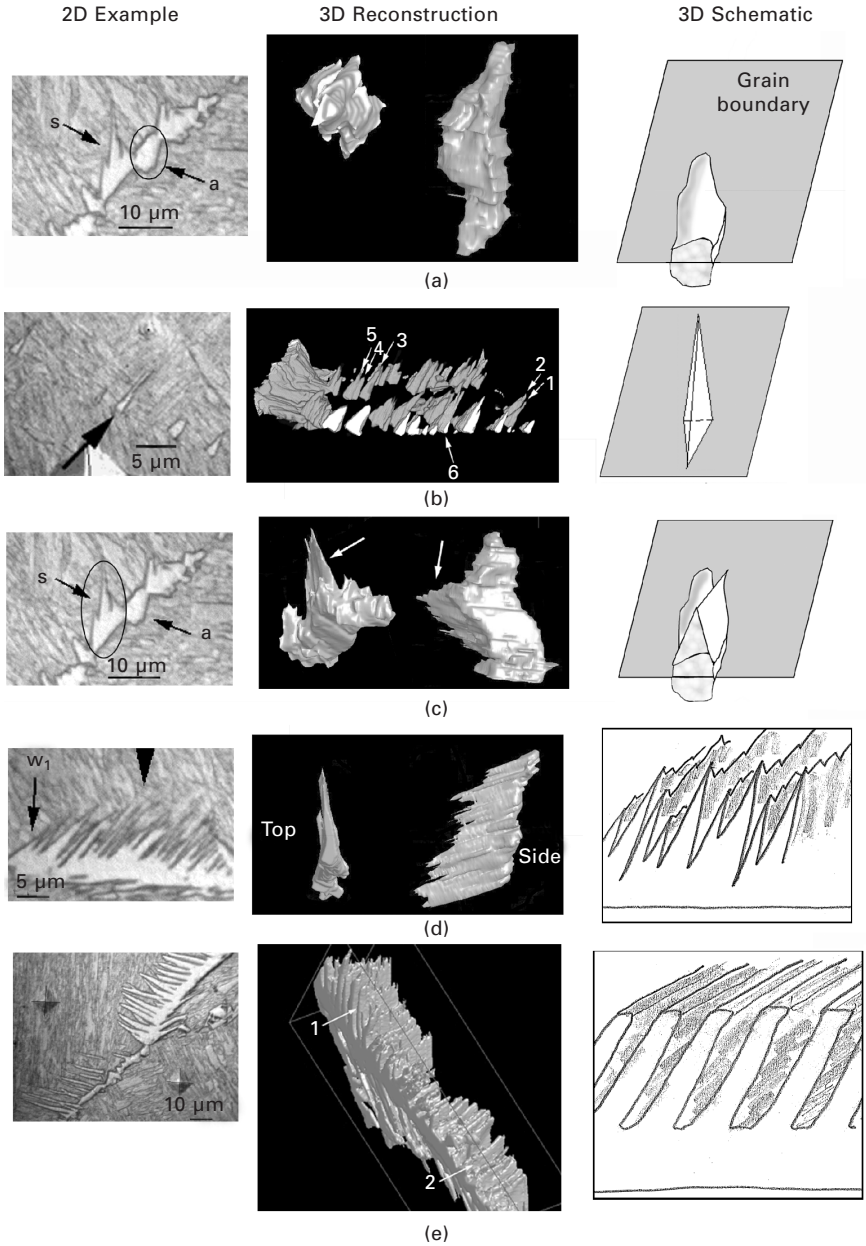
The proeutectoid ferrite morphologies shown in Fig. 7.3 can all be described reasonably well in 2D by the Dubé classification system (Fig. 7.2). It is important, however, to distinguish between primary precipitates and secondary precipitates. The former connect directly to austenite grain boundaries and the latter connect to grain boundary precipitates that had formed previously (allotriomorphs). The origins of secondary precipitates, whether due to a separate nucleation event or continued growth of perturbations on the ferrite allotriomorph/austenite interface, will be discussed subsequently. The relevant 2D classifications employed here thus include:

- primary ferrite sideplates, i.e. developed directly from austenite grain boundaries (Fig. 7.3(a)),
- primary ferrite sawteeth (Fig. 7.3(b)),
- grain boundary idiomorphs (Fig. 7.3(f)),
- secondary ferrite sideplates, connected to grain boundary allotriomorphic ferrite (Fig. 7.3(d)),
- secondary sawteeth (Fig. 7.3(e)), and
- grain boundary allotriomorphs (Fig. 7.3(f)).

Three-dimensional analysis of serial sections of these precipitates showed that the shape apparent from single 2D sections varied substantially for each precipitate. Viewing 3D reconstructions of each precipitate from different perspectives was necessary to understand the true shape. Figure 7.8 depicts a summary of the five different 3D morphologies that were observed:

- grain boundary allotriomorphs (Fig. 7.8(a)).
- primary ferrite ‘spike’, i.e. developed directly from austenite grain boundaries (Fig. 7.8(b)),

© Woodhead Publishing Limited, 2012



7.8 Three-dimensional reconstructions of proeutectoid ferrite shown in Fig. 7.3, modified from Kral and Spanos (2005).

© Woodhead Publishing Limited, 2012

- secondary Widmanstätten 'spike' or sawtooth (Fig. 7.8(c)),
- secondary Widmanstätten plate (Fig. 7.8(d)),
- secondary Widmanstätten lath (Fig. 7.8(e)).

The three-dimensional analysis revealed that several different Dubé morphologies (primary ferrite sideplates, i.e. developed directly from austenite grain boundaries (in Fig. 7.3(a)), primary ferrite sawteeth (in Fig. 7.3(b)), grain boundary idiomorphs (in Fig. 7.3(c)) were all obtained from different cross sections through the same primary spike morphology shown in Fig. 7.8(b)). In other words, specific classification of single precipitates in single planes of polish is likely to be incorrect in some cases. This will be more important for those wishing to measure and/or model the growth of precipitates at early stages (e.g., Townsend and Kirkaldy, 1968; Bradley *et al.*, 1977). This will be less important for those wishing to describe later stages of growth and/or industrial alloys. For instance, one could accurately describe the microstructure of Fig. 7.5(a) as impinged ferrite allotriomorphs on prior austenite grain boundaries and Fig. 7.5(b) as impinged ferrite allotriomorphs with primary and secondary Widmanstätten ferrite on prior austenite grain boundaries.

7.4.2 Ferrite allotriomorphs

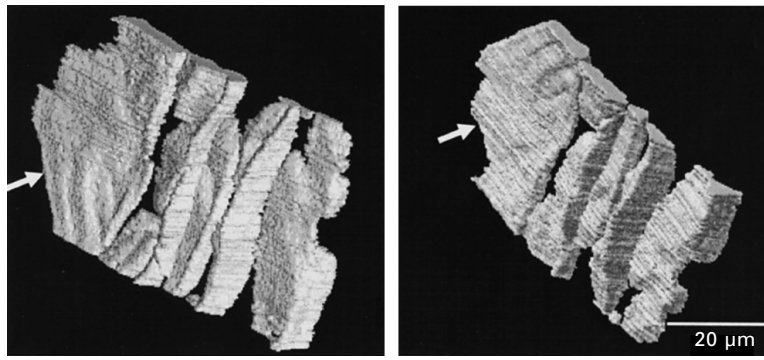
The true shape of allotriomorphs (see, e.g., Fig. 7.8(a)) in the Fe-0.12C-3.28Ni alloy is not well represented by double-spherical caps in most cases. Subsequent 3D analysis (Cheng *et al.*, 2008) of an Fe-0.09C-1.48Mn isothermally transformed at 690°C for approximately 5–15 seconds showed that the allotriomorphs are elongated in one direction, therefore more closely approximated by prolate ellipsoids rather than oblate ellipsoids. Furthermore, spike-like protrusions and facets were observed rather than the smooth curvature of an ellipsoid. Hard impingement was certainly a factor at this stage of growth (see Fig. 7.9 and Fig. 7.10). Again, this insight will be relevant to interpreting measurements and/or modeling the early stage growth of ferrite precipitates (e.g., Johnson *et al.*, 1975; Lee and Aaronson, 1975; Bradley and Aaronson, 1981; Jones and Bhadeshia, 1997; Aaronson, 1999; Militzer *et al.*, 2006).

7.4.3 Widmanstätten ferrite

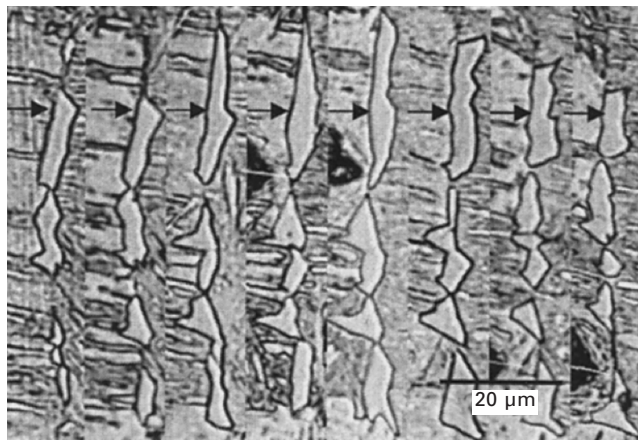
Widmanstätten shapes vary from 'spike', to lath and plate. Spikes, also described as triangular pyramids, can either be primary (directly on the prior austenite grain boundary; see Fig. 7.8(b)) or secondary (growing or nucleating atop grain boundary allotriomorphs; see Fig. 7.8(c)).

The leading growth edge of the plates (Fig. 7.8(d)) is sharp and has an

© Woodhead Publishing Limited, 2012



7.9 3D-reconstructed ferrite allotriomorphs viewed from opposite sides of the prior austenite grain boundary (Cheng *et al.*, 2008).



7.10 Eight serial sections spaced 8.2 m apart in depth; i.e., every 20th section from a large portion of 2D stack for the 3D reconstruction of Fig. 7.9 (Cheng *et al.*, 2008).

acute angle of taper. The observed plates are notched or undulated along their perimeter, such that the apex appears as a jagged ridge. It should be mentioned that fine details of 3D reconstructions are likely to be artifacts due to some combination of the individual sectioning thickness (0.3 μm), the computerized reconstruction algorithm and/or limitations of the resolution due to the thickness of the etched ferrite:martensite boundary.

Widmanstätten ferrite laths (Fig. 7.8(e)) have their long direction in contact with the grain boundary allotriomorph. The laths have a blunt or rounded leading edge, which is not as ragged as the leading edge of the plates previously described. Laths are roughly parallel to each other in groups connected by a common base, and some of the broad faces (or habit

© Woodhead Publishing Limited, 2012

planes) apparently curve, or rotate, as the laths extend away from the grain boundary (see arrow #1). There are also rotations of the habit planes amongst the different laths, e.g. repeated study from many viewing angles showed a change in the habit plane direction between the precipitate labeled #1 and that labeled #2 (and those in between) in Fig. 7.8(b). These rotations of the macroscopic habit planes, either along the length of a lath or amongst the different laths, appear to be about a common rotation axis roughly defined by the intersection of the broad faces (habit planes) of the precipitates and the grain boundary plane, and depicted by the direction of the arrows in the 3D reconstruction of Fig. 7.8(e).

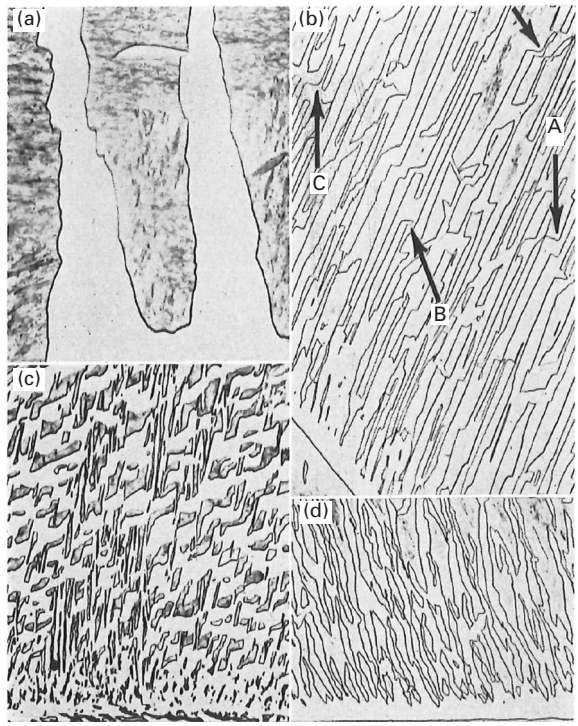
It should also be pointed out that these are only examples of 3D morphologies and that generality of these shapes is yet to be determined. Furthermore, a more complete, general description of proeutectoid ferrite in 3D would depend upon serial sectioning of specimens heat treated at several different isothermal transformation temperatures and times. Insights gained from morphology and crystallography on the subject of nucleation and growth will be discussed in a subsequent section. The present observations alone cannot definitively differentiate as to whether the actual mechanism of formation occurred by the initial formation of primary Widmanstätten crystals which filled in with ferrite at their bases later in the growth process, or by formation of Widmanstätten precipitates atop previously formed grain boundary allotriomorphs.

7.4.4 Non-classical ferrite morphologies

These are not covered in the Dubé classification system and so are being called non-classical. Zackay and Aaronson (1962) described 'degenerate ferrite' as differing from classical Widmanstätten sideplates by having 'appreciably lower symmetry' in 0.29%C-0.76%Mn steel, starting at transformation temperatures of 725°C and a major feature of proeutectoid ferrite formed in the range 675–575°C (see Fig. 7.11). Type A degeneracy retains the average growth direction of a Widmanstätten sideplate, but considerable irregularities are seen at the broad face. Type B appears as offset new plates originating from the broad faces of original plates, retaining the habit plane of the original and having a ladder-like appearance. Type C has a similar appearance to Type B but the new plates have a different habit plane to the original plates. Further study of these morphologies using 3D analysis and EBSD would elucidate the similarities or differences of the three described types, and would shed light on the mechanism of formation, which Aaronson suggested to be sympathetic nucleation.

Three-dimensional analysis revealed the morphology of degenerate morphologies in steels reacted at even lower temperatures (Hackenberg *et al.*, 2002a: in Fe-0.30C-6.3W isothermally transformed at 590°C for 10 min;

© Woodhead Publishing Limited, 2012

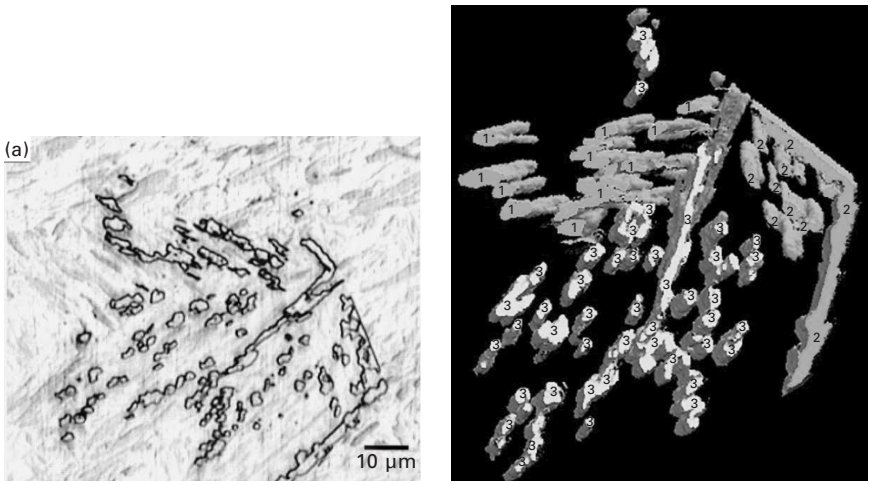


7.11 (a) Type A degenerate Widmanstätten proeutectoid ferrite sideplates; 0.29%C reacted 5 min at 700°C; original magnification 1000×. (b) Type B degenerate Widmanstätten proeutectoid ferrite sideplates; 0.29%C reacted 20 sec at 650°C; original magnification 500×. (c) Type C degenerate Widmanstätten proeutectoid ferrite sideplates; reacted 16 sec at 600°C; original magnification 500×. (d) Comparison with (a) shows the effect of temperature on Type A degeneracy; 0.29%C reacted 20 sec at 650°C; original magnification 500× (Zackay and Aaronson, 1962).

and Wu and Enomoto, 2002: in Fe-0.28C-3.0Mo isothermally transformed at 550°C for 10,000 seconds). As shown in Fig. 7.12, the morphology appears in 3D as groups of rods, rather than laths or plates. While the term degenerate ferrite implies a lack of adherence to crystallographic constraints, 3D analysis shows a more well-behaved shape than previously thought and allowed the observation that the growth directions was close to $<310>_{\alpha}$ (Hackenberg *et al.*, 2002b).

Three-dimensional analysis of acicular ferrite in a gas metal arc weld deposit (0.078C, 0.90Si, 1.57Mn, 0.03Ti, 0.0320O, 0.0050Ni, 0.0059S) isothermally transformed at 570°C for short times (1, 5 s) (Wu and Enomoto, 2005; Wu, 2006) clearly shows the nucleation site is on non-metallic inclusions and 3D morphology is that of a Widmanstätten Star (see Fig. 7.13). A better energetic

© Woodhead Publishing Limited, 2012

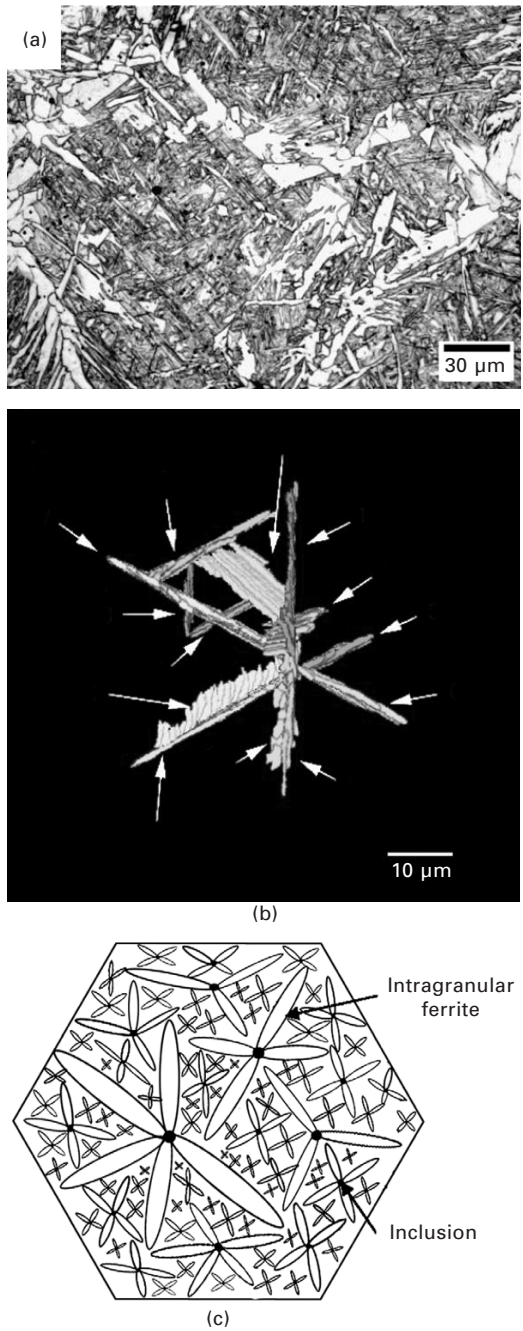


7.12 (a) A single section and (b) 3D isosurface view of a reconstructed ferrite sheaf. This rendering of the 3D body highlights the sidewalls as different shades of gray, depending on their orientation with respect to the light source (emanating from the top right). The numbered surfaces demarcate the plane of polish of the top most section, which truncates the intersecting subunits.

Each number represents a group or packet of subunits; note the three sets of differently aligned rod-like subunits. The 3D body from which this view was generated had its z-axis (depth, into the page) expanded relative to the true depth scaling. The x- and y-axes (aligned horizontally and vertically, respectively in the view), however, are correctly proportioned to each other. Two austenite twin boundaries (both covered with impinged subunits) run in the middle and on the right side of the image (Hackenberg *et al.*, 2002b).

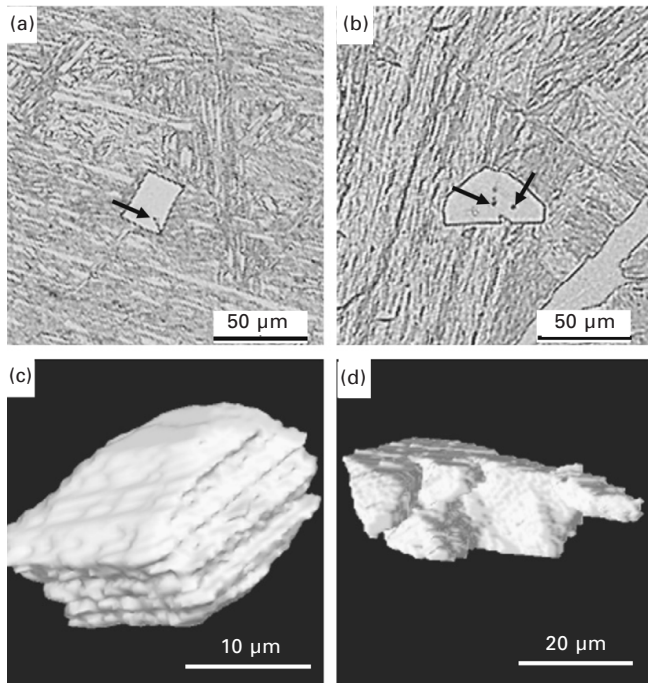
balance is obtained by replacing a high-energy interface between inclusion and austenite with a lower energy interface between inclusion and ferrite (Madariaga and Gutierrez, 1999). In a similar alloy at a higher transformation temperature (0.09C, 0.20Si, 1.48Mn, 0.01Al, 0.05V, isothermally transformed at 690°C for 40 s), ferrite developed as intragranular idiomorphs (see Fig. 7.14). The difference in morphology is related to the crystallographic orientation relationship. In idiomorphs, ferrite takes an orientation to obtain low misfit with the inclusion (Bhadeshia and Honeycombe, 2006). In acicular ferrite, the inclusion acts as a substrate for heterogeneous nucleation and a Kurdjumov–Sachs OR leads to the elongated shape with growth directions $<111>_\alpha // <110>_\gamma$ and habit plane $\{110\}_\alpha // \{111\}_\gamma$ (Wu *et al.*, 2004).

© Woodhead Publishing Limited, 2012



7.13 (a) Optical micrograph, (b) 3D reconstructed image of acicular ferrite plates in a specimen isothermally held at 570°C for 1 s (Wu *et al.*, 2004) and (c) schematic illustration showing the morphology of acicular ferrite (Cheng and Wu, 2009).

© Woodhead Publishing Limited, 2012



7.14 Optical micrographs and 3D reconstructed images of ferrite idiomorphs. (c and d) 3D reconstructed images of the ferrite idiomorphs in (a and b), respectively. The black dots arrowed are inclusions (Cheng and Wu, 2009).

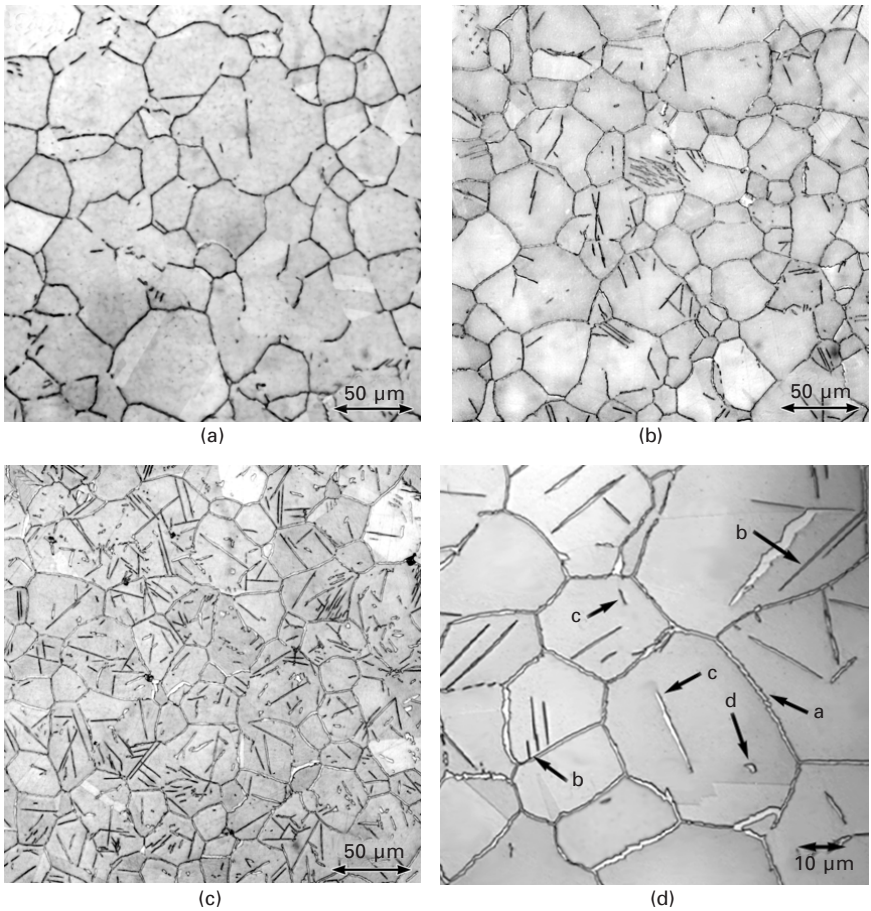
7.4.5 Proeutectoid cementite morphologies

The development of the proeutectoid cementite microstructure is, as shown in Fig. 7.15, nucleation and growth of allotriomorphs on austenite grain boundaries and eventual development of elongated Widmanstätten precipitates within austenite grains. The true 3D shape and connectivity of these cementite precipitates are not clear from single sections. The following 3D morphological observations are mainly based upon serial sectioning studies of a model alloy (Fe-1.34%C-13.1%Mn) in which the austenitic matrix is retained at room temperature (Kral and Spanos, 1999). Samples were isothermally transformed at various temperatures for specific times before being quenched.

Cementite grain boundary allotriomorphs

Sorby first observed networks of ferrite and cementite allotriomorphs during his early metallographic studies in 1887 (Sorby, 1887). It was later reported (Osmond, 1893; Howe, 1911) that these networks are formed by precipitation of the proeutectoid phase at the austenite grain boundaries (Aaronson,

© Woodhead Publishing Limited, 2012



7.15 Optical micrographs of isothermally transformed Fe-1.34 wt% C-13.1 wt% Mn show the effect of increasing isothermal transformation times on the morphology and distribution of cementite after: (a) 5 s at 650°C, (b) 15 s at 650°C and (c) 50 s at 650°C. (d) A higher magnification optical micrograph of a sample transformed for 50 s at 650°C illustrates various precipitate morphologies (Kral and Spanos, 1999).

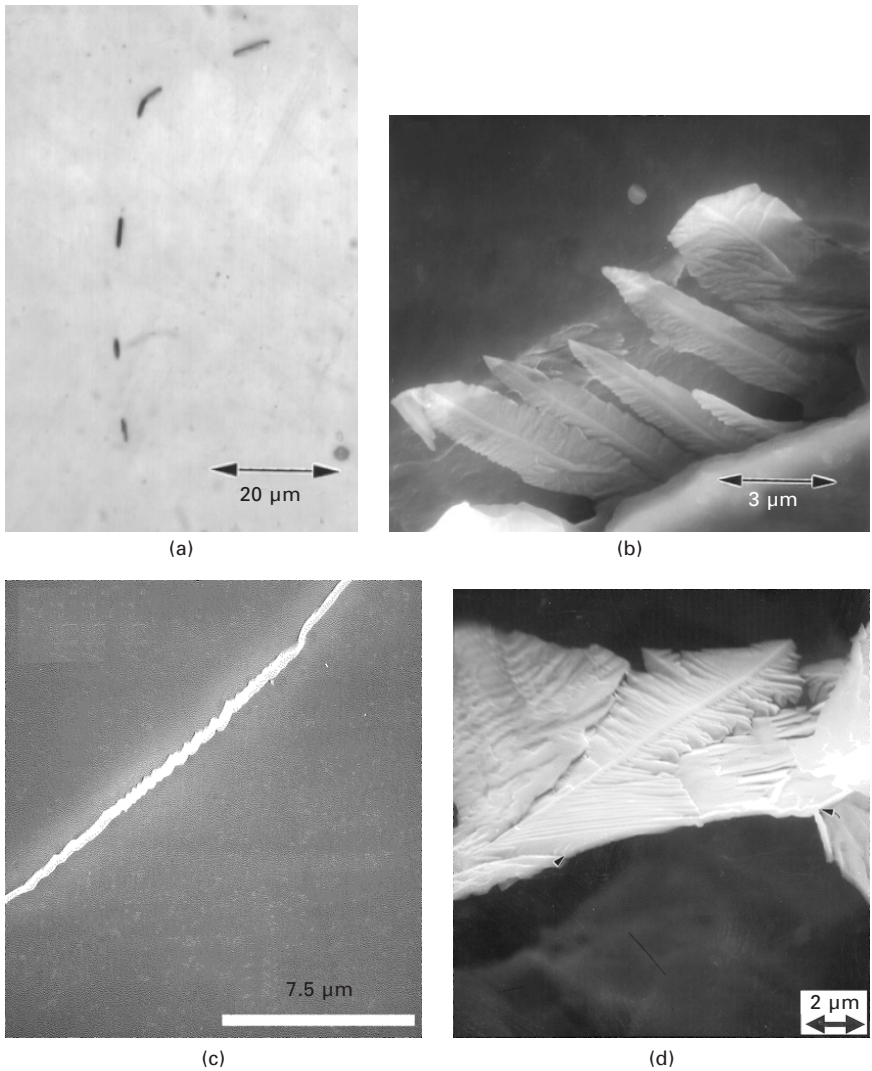
1962). Heckel and Paxton (1961) reported on observations of continuous proeutectoid cementite films completely outlining the prior austenite grain boundaries at all except precipitate temperatures close to the A_{cm}. Aaronson (1962) subsequently compared the observations of Heckel and Paxton on grain boundary cementite (Heckel and Paxton, 1960, 1961), to the findings of other researchers on grain boundary ferrite in steels (e.g., Aaronson, 1962), and grain boundary precipitates in many other alloys systems (e.g., Mehl and Marzke, 1931; Barrett *et al.*, 1941; Carter, 1955). It was suggested

© Woodhead Publishing Limited, 2012

that the grain boundary cementite films corresponded to the latter stages of impingement of individually nucleated cementite allotriomorphs and, based on 2D observations, that cementite allotriomorphs (like ferrite) at early stages often possessed a morphology corresponding to 'pancakes with slightly bulged centers' (Aaronson, 1962). Models approximated this shape as a double-spherical cap or oblate ellipsoid (Hawbolt and Brown, 1967; Bradley and Aaronson, 1977). Ando and Krauss subsequently used SEM and TEM in conjunction with optical microscopy to study the growth of proeutectoid cementite allotriomorphs in hypereutectoid steels containing 1%C and 1.5%Cr (AISI 52100), and in some cases with phosphorous additions up to 0.023% (Ando and Krauss, 1981a, 1981b, 1982). In these studies the grain boundary cementite morphology was similar to that observed by Heckel and Paxton, i.e. thin cementite films fully covering the austenite grain boundaries (Ando and Krauss, 1981b). Therefore, even at the earliest stages of transformation studied, the individual cementite crystals that had nucleated along the grain boundaries had already impinged to form essentially continuous films of cementite coating the prior austenite grain boundaries (Heckel and Paxton, 1960, 1961; Aaronson, 1962; Ando and Krauss, 1981a, 1981b; Wasynczuk *et al.*, 1986; Kral and Spanos, 1999).

As shown in Fig. 7.16, cementite indeed quickly coats the austenite grain boundaries during isothermal transformation of an Fe-1.34C-13.1Mn steel at 650°C (partially after 1 second and completely in less than 10 seconds). At shorter transformations times, the allotriomorphs can appear as individual grain boundary allotriomorphs, in a 2D morphology that could be interpreted as double-spherical caps (Fig. 7.16(a)). After a longer transformation time (10 seconds), the 2D optical appearance is that of a fairly uniform film of cementite covering the austenite grain boundaries (Fig. 7.16(c)). However, deep etching of the same samples revealed that the actual 3D shape is fern-like or dendritic (see Fig. 7.16(b) and Fig. 7.16(d)) (Kral and Spanos, 1997, 1999; Kral, 2000) along the austenite grain boundaries with no appreciable growth inward, i.e., toward the centre of the austenite matrix grains. Grain boundary carbide dendrites have been reported previously in stainless steels (Mahla and Nielsen, 1951; Kinzel, 1952; Wilson, 1971), where study was focused on stress corrosion cracking in sensitized stainless steels. It is interesting that the 3D morphology of grain boundary cementite in carbon steel had not been noted previously, but not surprising, since such morphologies can only be revealed by deep etching. There is emerging interest in alloying additions to inhibit the nucleation and growth of these thin grain boundary films of cementite. Hypereutectoid steels (also known as ultra-high carbon steels) with additions such as Al, Si and V obtain high strength coupled with adequate ductility for cold drawing, and show promise for rod/wire and rail track applications (Khalid and Edmonds, 1994; Lesuer *et al.*, 1999; Han *et al.*, 2001).

© Woodhead Publishing Limited, 2012



7.16 Images of grain boundary allotriomorphs (a and b) after 1 s isothermal transformation: (a) optical, (b) scanning electron micrograph of the same sample deep etched; (c and d) after 10 s isothermal transformation: (c) optical (d) scanning electron micrograph of the same sample deep etched in 10% nitric acid in methanol (Kral and Spanos, 1997).

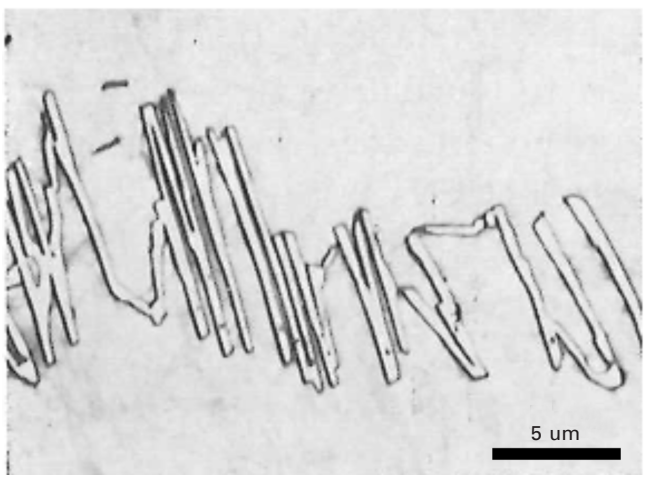
The dendritic grain boundary cementite morphology explains the previous observations of roughness, but further morphological evolution (longer transformations times) did not directly lead to the development of Widmanstätten cementite as had been previously thought (Heckel and

© Woodhead Publishing Limited, 2012

Paxton, 1961). Rather, the films appeared to become initially smoother, and after longer transformation times and higher transformation temperatures, developed the zig-zag morphology (Heckel and Paxton, 1961) (see Fig. 7.17). Grain boundary cementite films, and possibly parts of the austenite grain boundary, might migrate to minimize interfacial energies by maximizing the area of low energy facets, for whatever orientation relationship is obtained (Heckel and Paxton, 1961; Kral and Spanos, 2003). Initially, however, the growth of dendrites along the austenite grain boundaries originates from morphological instabilities (Mullins and Sekerka, 1963). There is no clear influence of the local crystallography on the outward shape, since no reproducible crystallographic direction could be identified with primary or secondary dendrite arms (Kral and Spanos, 2003).

Widmanstätten cementite

In 1933, Mehl *et al*. stated that 'Widmanstätten cementite is correctly understood as plate-like in outward form'. Their careful classical approach allowed pseudo-3D observations of large single austenite crystals via sectioning and polishing samples on three orthogonal planes. A complicated morphology was revealed at higher magnifications, including observations of surface corrugations, laminations and serrations, and these were attributed at least in part to the volume change during the transformation. Greninger and Troiano subsequently (1940) also suggested that proeutectoid Widmanstätten cementite possessed a plate morphology (Greninger and



7.17 The zig-zag grain boundary cementite morphology in an Fe-1.48C alloy, isothermally transformed 90 s at 900°C (Heckel and Paxton, 1961).

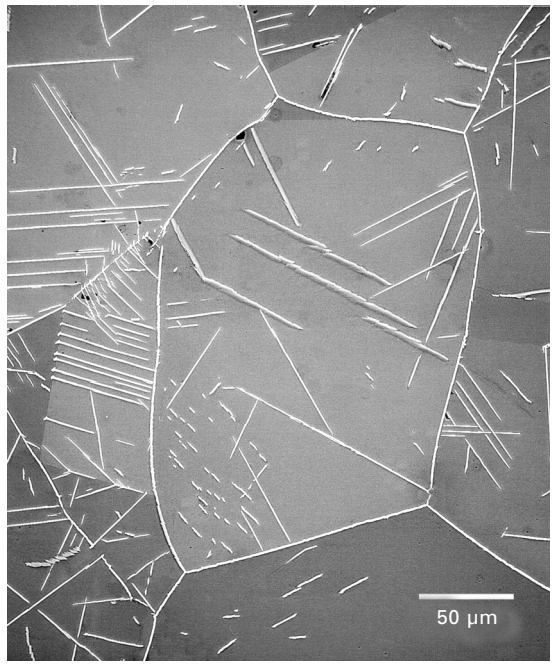
© Woodhead Publishing Limited, 2012

Troiano, 1940). Heckel and Paxton (1961) defined the Widmanstätten start temperature as the temperature below which Widmanstätten cementite first begins to appear, and above which allotriomorphs predominate (see Fig. 7.4) (Heckel and Paxton, 1961; Aaronson, 1962). Heckel and Paxton (1961) describe proeutectoid cementite morphologies as Widmanstätten sideplates and intragranular Widmanstätten plates. Degenerate cementite plates were also described as sometimes possessing a 'wavy' shape, but more often having a morphology which suggested that they were actually formed by the sympathetic nucleation (Aaronson, 1956; Aaronson and Wells, 1956; Aaronson *et al.*, 1995) of a number of smaller cementite crystals (Aaronson, 1962). Sympathetic nucleation is defined as the nucleation of a precipitate crystal at an interphase boundary of a crystal of the same phase when these two crystals differ in composition from their matrix phase throughout the transformation process (Aaronson *et al.*, 1995).

Thompson and Howell (1987, 1994) referred to the precipitates that they observed by thin foil TEM as intragranularly nucleated cementite plates. At about the same time, Spanos and Aaronson made a number of observations of the morphology, formation mechanism and crystallography of what they termed proeutectoid cementite plates, based on conventional thin foil TEM (2D) analyses in high Mn hypereutectoid steels (Spanos and Aaronson, 1988, 1990). The latter results included the suggestion and more detailed analysis of sympathetic nucleation (Aaronson, 1956; Aaronson and Wells, 1956; Aaronson *et al.*, 1995) of multiple plates on top of one another, both in face-to-face and edge-to-edge arrangements (Spanos and Aaronson, 1988). In five hypereutectoid high Mn steels containing 0.82–1.13%C, and 9.7–13.0%Mn, Khalid *et al.* (1993) observed long thin plates by optical microscopy, TEM, and limited deep etching SEM techniques, with further evidence of what they termed smaller plate segments (the latter observation was based predominantly on 2D optical microscopy). Figure 7.18 shows clear examples of plate morphologies and smaller segments with face-to-face and edge-to-edge arrangements. Further progress on the understanding of proeutectoid Widmanstätten cementite morphology required 3D analysis.

Mangan *et al.* (1997) were the first to apply modern 3D analysis techniques to cementite when they reconstructed serial sections of portions of Widmanstätten cementite precipitates within a single austenite grain in a 12.3%Mn-0.8%C steel. These precipitates were described as 'plates' in 3D, due to having only one relatively thin dimension and two relatively long dimension(s) (Mangan *et al.*, 1997) (i.e., a length to width aspect ratio ≈ 1, and length/width to thickness aspect ratio $>> 1$). Kral and Spanos (1999) subsequently performed serial sectioning and 3D reconstruction of over 200 Widmanstätten cementite crystals in an Fe-1.34%C-13%Mn alloy in 25 entire austenite grains. Evidence (see Fig. 7.18) suggested that there are actually two distinct Widmanstätten cementite morphologies: plate-like or lath-like

© Woodhead Publishing Limited, 2012

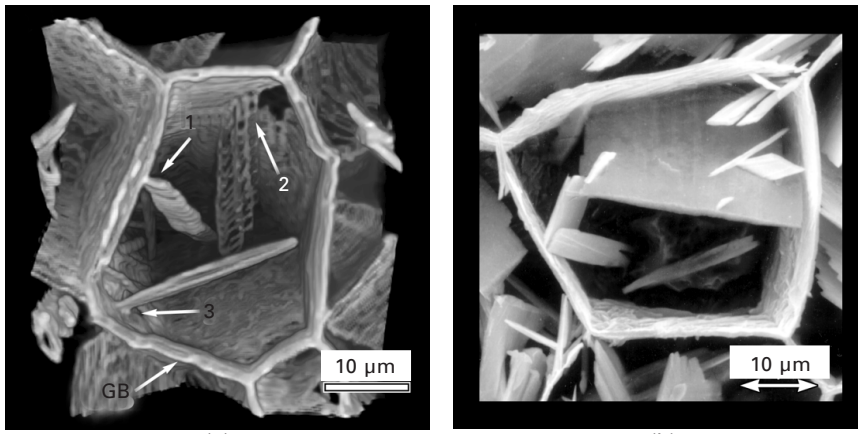


7.18 SEM micrograph of specimen isothermally reacted at 650°C shows Widmanstätten cementite precipitates in an austenitic matrix.

in three dimensions (Mangan *et al.*, 1999). The origins of this distinction are crystallographic and will be discussed in a subsequent section.

Due to the significant difference in etching properties of austenite and cementite, deep etching can be an effective way of revealing three-dimensional characteristics of cementite (Mehl *et al.*, 1933; Cowley and Edmonds, 1988; Khalid *et al.*, 1993; Kral and Spanos, 1997, 1999). High-resolution electron microscopy of deep etched specimens revealed that individual plates are monolithic, single crystals. They may appear as groups of parallel plates within an austenite grain, sometimes adjacent to a point where they may appear to be face-to-face, and often obtain different crystallographic orientation variants within a grain (see Figs 7.18 and 7.19). Laths, on the other hand, are relatively thin in two dimensions, and large in only one dimension. Laths may appear as groups that are arranged edge-to-edge, or only slightly offset within an austenite grain, so that they may seem to be sub-units of a single precipitate. Deep etching observations in SEM and TEM also showed that laths had many large striations on their broad faces and appeared to be made up of similarly oriented subunits. This led to the deduction that these laths might also be composed of multiple, finer, sympathetically nucleated crystals, as was suggested by earlier researchers for cementite plates (Spanos and Aaronson, 1988; Khalid *et al.*, 1993).

© Woodhead Publishing Limited, 2012



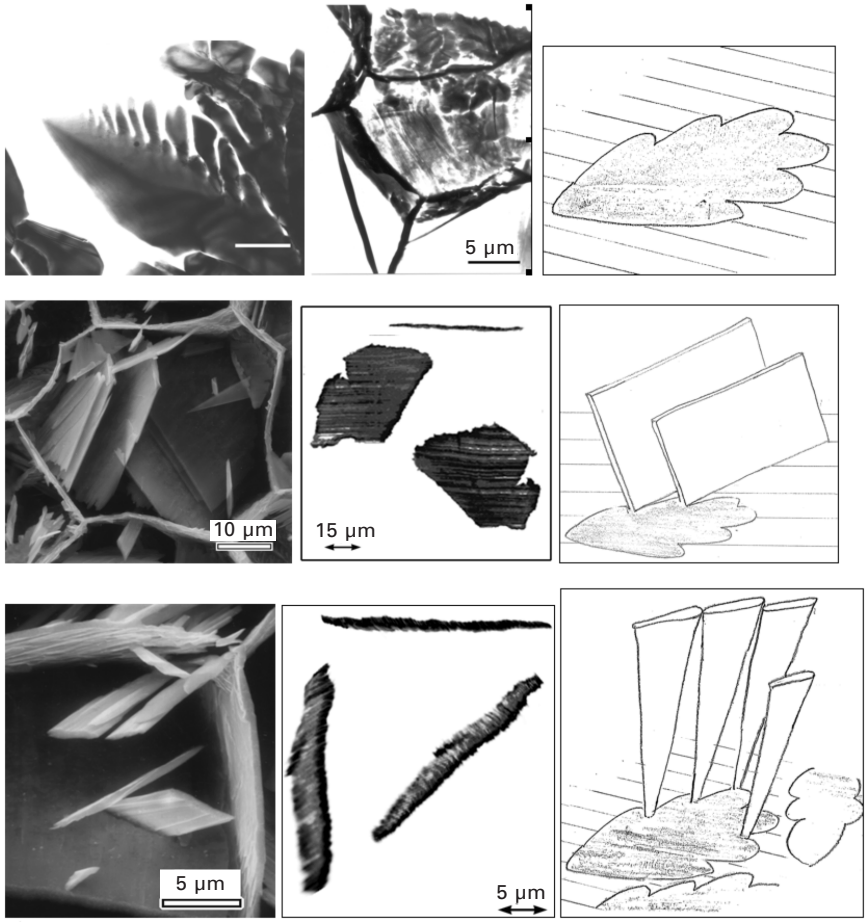
7.19 (a) Three-dimensional reconstruction of single austenite grain containing three cementite laths (50 s at 650°C). (b) SEM micrograph of a deeply etched specimen showing plates and laths within a similar austenite grain (50 s at 650°C) (Kral and Spanos, 1999).

Both plate and lath morphologies obtain different orientation variants within a single austenite grain, and the apparent habit plane for these variants is obviously different for plates and laths. Again, the origins of these different habit planes are crystallographic. Furthermore, it is interesting that only a few researchers characterized Widmanstätten cementite as laths (Krzanowski and Hruska, 1987; Cowley and Edmonds, 1988) prior to 3D analysis. Instead, when based on 2D observations alone, the majority of studies have referred to Widmanstätten cementite crystals almost exclusively as 'plates'. It is almost certain that, depending on the orientation at which they were sectioned in two dimensions, laths have been described as plates or idiomorphs.

In summary, 3D analysis reveals only three classifications for proeutectoid cementite: grain boundary dendrites ('allotriomorphs'), Widmanstätten plates and Widmanstätten laths. Figure 7.20 shows examples of the three morphologies in three different ways: pseudo-3D images of deep etched samples, 3D reconstructions of serial sections[3] and schematic diagrams (Kral and Spanos, 1999). Note that the schematic diagrams contain implications about nucleation site: even at very short transformation times, all Widmanstätten cementite in the subject volumes (Hung *et al.*, 2002) were connected at some point along their perimeter to grain boundary cementite. Examination of intact grain boundary cementite networks in deep-etched TEM specimens revealed that Widmanstätten laths originated from features such as boundaries

[3] The resolution to reveal dendritic features probably requires the use of electron microscopy, so TEM images of deep etched samples are shown rather than serial section reconstructions.

© Woodhead Publishing Limited, 2012



7.20 Electron micrographs, three-dimensional images and schematic diagrams of cementite grain boundary dendrites ('allotriomorphs', top row), secondary Widmanstätten plates (middle row) and secondary Widmanstätten laths (bottom row). Both secondary Widmanstätten morphologies are shown as nucleating at features on grain boundary dendrites (Kral and Spanos, 1999).

between grain boundary dendrites (allotriomorphs), and that these laths were only slightly misoriented from the cementite to which they connected (Kral, 2000). This is strong evidence for sympathetic nucleation, and one true opportunity to study unambiguous nucleation sites.

Comparison of ferrite and cementite morphologies

While there are similarities, the three-dimensional morphologies of proeutectoid ferrite are clearly more complex than for cementite. For proeutectoid ferrite, the

© Woodhead Publishing Limited, 2012

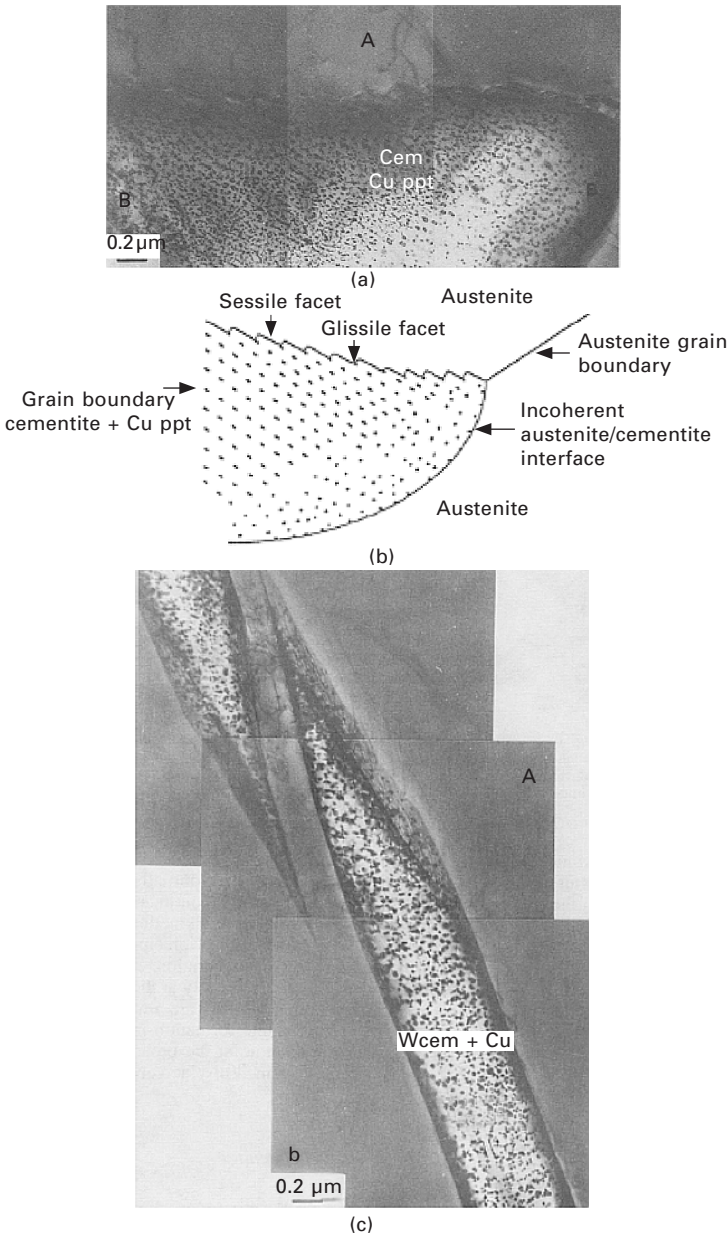
Dubé morphological classification system remains useful due to its simplicity and completeness. However, for proeutectoid cementite, three-dimensional analysis showed that the Dubé system is overly complex. Since there are only three different 3D morphologies (grain boundary dendrites, Widmanstätten plates and Widmanstätten laths), descriptions based on 2D observations using the Dubé classification could mask the actual 3D shape.

Unlike proeutectoid cementite in a hypereutectoid Mn steel (Kral and Spanos, 1999), Widmanstätten ferrite in the hypoeutectoid Fe-C-Ni alloy studied here clearly can nucleate directly upon austenite grain boundaries, and therefore formation of 'primary' Widmanstätten ferrite does occur. In the case of proeutectoid cementite, it was instead found that the Widmanstätten precipitates always nucleate in association with earlier formed solid state grain boundary cementite dendrites that coat the austenite grain boundaries (Kral and Spanos, 1997). On the other hand, the 3D observations presented here suggest that ferrite allotriomorphs do not grow in a dendritic fashion along austenite grain boundaries, at least based on the level of resolution of the serial sectioning techniques currently employed. As mentioned previously, the growth of cementite dendrites occurs via morphological instabilities while growth of ferrite allotriomorphs may be more heavily influenced by crystallography. It would be desirable to verify that ferrite allotriomorphs are not dendritic with higher resolution 3D observations, such as deep etching in conjunction with scanning electron microscopy (SEM) (Kral and Spanos, 1997), if a suitable alloy for such experiments could be identified.

One similarity between proeutectoid cementite and ferrite is that there were no intragranular precipitates observed in 3D in either case (Kral and Spanos, 1999, 2005; Hung *et al.*, 2002). This may not be a realistic impression of the 'normal' microstructures, and definitely has been influenced by the relatively high purity alloys used, the relatively small austenite grain size in the cementite study and the relatively small volumes visualized in the ferrite study.

It is also interesting to note the occurrence of interphase boundary precipitation of copper within grain boundary cementite and Widmanstätten cementite plates in isothermally transformed alloys containing approximately 0.8%C, 10–12%Mn and 1–3%Cu (Khalid and Edmonds, 1993). The copper was found to appear in rows and sheets, analogous to the interphase precipitation (see Fig. 7.21) found within ferrite in numerous hypoeutectoid steels (Davenport *et al.*, 1968; Davenport and Honeycombe, 1971) and some titanium-rare earth alloys (Kral *et al.*, 1997). In a TEM investigation of the effects of copper on proeutectoid cementite precipitation, the growth, morphology and internal structure of grain boundary cementite allotriomorphs in hypereutectoid Fe-1.43%C and Fe-1.49%C-4.9%Cu alloys (Wasynczuk *et al.*, 1986) was studied. At very early stages of the transformation (isothermal reaction at 825°C for one minute, followed by an iced brine quench),

© Woodhead Publishing Limited, 2012



7.21 (a) TEM photomontage of grain-boundary cementite showing interphase precipitation of copper in rows and ledges at the austenite/cementite interface and also randomly dispersed precipitates near a more irregular interface (region B); (b) schematic illustration of interphase precipitation of copper at the austenite/cementite interface migrating by a ledge mechanism; (c) TEM photomontage showing copper precipitation in a Widmanstätten cementite plate with a precipitate-free midrib (Khalid and Edmonds, 1993).

© Woodhead Publishing Limited, 2012

individual, separated cementite allotriomorphs could be resolved at prior austenite grain boundaries by optical microscopy, and the 2D shapes of these precipitates appeared at that resolution to correspond to the classic 'bulged pancake' allotriomorphic morphology described earlier by Aaronson (1962). These individual allotriomorphs very quickly impinged during growth, and at longer reaction times and temperatures studied the external morphology corresponded to thin films of proeutectoid cementite completely covering the austenite grain boundaries, as observed in the other studies (Heckel and Paxton, 1960, 1961; Ando and Krauss, 1981a, 1981b, 1982). TEM observations of these allotriomorphic films focused predominantly on the copper precipitation within the cementite, and made no further mention of the external morphology, or the presence of cementite:cementite grain boundaries within these films (i.e., internal morphology) (Wasynczuk *et al.*, 1986).

A subsequent TEM investigation of copper precipitation in cementite in Fe-0.8%C-10–11%Mn-1–2.5%Cu alloys (Khalid and Edmonds, 1993) provided observations of proeutectoid cementite allotriomorphs mostly at high levels of magnification, where it was difficult to infer their external morphology, although the TEM and optical micrographs presented are consistent with the impinged allotriomorphic film morphology reported by earlier investigators. These results show that the mechanism for formation of grain boundary and Widmanstätten cementite is analogous to that of ferrite, i.e., a ledge mechanism (see, e.g., Cahn, 1960; Gibbs, 1961; Zackay and Aaronson, 1962; Purdy, 1987; Spanos *et al.*, 1991, 1994).

It should be noted that austenite annealing twins have an influence on the morphology and crystallography of Widmanstätten proeutectoid precipitates. There is evidence that annealing twins are not strong nucleation sites of Widmanstätten cementite (Hung *et al.*, 2002). On the contrary, proeutectoid ferrite has been observed to nucleate on austenite twin boundaries (Inagaki, 1988; Aaronson *et al.*, 2004b). Hillert (1962) observed that Widmanstätten ferrite growth was either completely halted or resulted in a bulbous 'irregularly shaped head' upon impingement at a twin boundary while, on the other hand, Widmanstätten cementite was sometimes found to continue growth albeit with a different apparent habit plane. In either Widmanstätten ferrite (Hillert, 1962) or cementite (Yang and Choo, 1994), austenite twins should act as barriers to growth due to crystallographic constraint (Hackenberg and Shiflet, 2003).

7.5 Crystallographic orientation relationships with austenite

7.5.1 Proeutectoid ferrite: austenite

There are known to be at least five crystallographic orientation relationships between ferrite and parent FCC austenite (Headley and Brooks, 2002). The

© Woodhead Publishing Limited, 2012

three best known are the Bain, Kurdjumov–Sachs (K-S) and Nishiyama–Wassermann (N-W) correspondence relationships. The Bain orientation relationship (OR) between FCC austenite (γ) and BCC ferrite (α) can be expressed as:

$$(100)_\gamma \,//\, (100)_\alpha$$

$$[010]_\gamma \,//\, [01\bar{1}]_\alpha.$$

The Kurdjumov–Sachs (K-S) OR between austenite (γ) and ferrite (α) can be expressed as:

$$(111)_\gamma \,//\, (1\bar{1}0)_\alpha$$

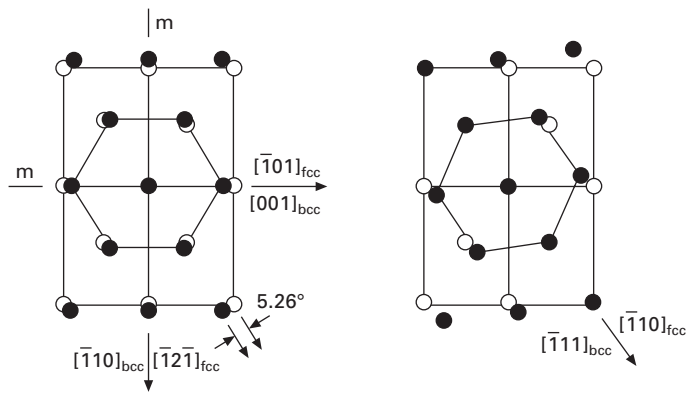
$$[\bar{1}10]_\gamma \,//\, [\bar{1}11]_\alpha.$$

The Nishiyama–Wassermann (N-W) OR between austenite (γ) and ferrite (α) can be expressed as:

$$(111)_\gamma \,//\, (1\bar{1}0)_\alpha$$

$$[\bar{1}01]_\gamma \,//\, [001]_\alpha.$$

The K-S and N-W ORs are the most frequently reported relationships for bcc-fcc systems, and they are the only ones that have been reported for ferrite-austenite microstructures. A continuous distribution of orientations between the exact K-S and N-W positions has been observed (He *et al.*, 2005). These two relationships differ from each other by a small relative rotation of 5.26° around $[111]_\gamma \,//\, [1\bar{1}0]_\alpha$. Figure 7.22 depicts the superimposed close-packed



(a) Nishiyama–Wassermann (b) Kurdjumov–Sachs

7.22 Atomic arrangement in close-packed planes for bcc (open circle) and fcc (solid circle) lattices as they are superimposed in (a) N-W OR, (b) K-S OR. The position of mirror planes in the 2D pattern symmetry is denoted by 'm', while arrows and indices denote real-lattice directions normal to the mirror planes (Dahmen, 1982).

© Woodhead Publishing Limited, 2012

planes in both phases. Both K-S and N-W have closest-packed planes parallel, and K-S also has closest-packed directions parallel.

7.5.2 Proeutectoid cementite: austenite

It is now known that there are at least two crystallographic orientation relationships between proeutectoid cementite and austenite. The first reproducible OR between proeutectoid cementite and austenite was found (Pitsch, 1962) and originally expressed as:

$$[100]_{cem}//[5\bar{5}4]_{\gamma}$$

$$[010]_{cem}//[110]_{\gamma}$$

$$[001]_{cem}//[\bar{2}25]_{\gamma}$$

The Pitsch OR was subsequently observed by a number of other researchers for various morphologies of proeutectoid cementite (Spanos and Aaronson, 1988, 1990; Farooque and Edmonds, 1990; Khalid and Edmonds, 1993; Howe and Spanos, 1999; Mangan *et al.*, 1999). There appear to be other orientation relationships that may be austenite twin-related (Thompson and Howell, 1987, 1988; Yang and Choo, 1994). However, based on an approach combining Δg (Zhang and Purdy, 1993a, 1993b) and O-line (Zhang and Purdy, 1993a) analyses, Zhang *et al.* (2000) suggested that these ORs are not simply variants of the Pitsch OR, and stated that: 'Corresponding to different ORs, the habit planes are distinct'.

Thompson and Howell (1988) expressed the Pitsch OR as:

$$(\bar{1}03)_{cem} // (\bar{1}1\bar{1})_{\gamma}$$

$$[010]_{cem} // [10\bar{1}]_{\gamma}$$

$$[\bar{3}0\bar{1}]_{cem} // [\bar{1}\bar{2}\bar{1}]_{\gamma}.$$

This expression is more physically significant because it emphasizes the potentially good atomic matching between the closest-packed planes, i.e. $(\bar{1}03)$ in cementite and $(\bar{1}1\bar{1})$ in austenite, and a direction of 'good fit', i.e. [010] in cementite and $[10\bar{1}]$ in austenite.

Farooque and Edmonds (1990) found a completely different orientation relationship for proeutectoid Widmanstätten cementite formed in an Fe-0.8%C-12%Mn steel, which will be referred to henceforth in this chapter as the Farooque–Edmonds OR, originally represented as:

$$[100]_{cem} // [112]_{\gamma}$$

$$[010]_{cem} // [02\bar{1}]_{\gamma}$$

$$[001]_{cem} // [\bar{5}12]_{\gamma}$$

© Woodhead Publishing Limited, 2012

Zhang and Kelly (1997, 1998) later used convergent beam electron diffraction (CBED) to study Widmanstätten proeutectoid cementite and described an orientation that was essentially the same as the Farooque–Edmonds OR but rotated 2.2° about the $[100]_{cem}$ // $[112]_{\gamma}$ axis:

$$(0\bar{2}2)_{cem} \text{ // } (\bar{1}\,\bar{1}1)_{\gamma}$$

$$[100]_{cem} \text{ // } [112]_{\gamma}$$

$$[011]_{cem} \text{ // } [\bar{1}10]_{\gamma}$$

The way Zhang and Kelly expressed the Farooque–Edmonds OR was more physically significant in that it describes parallel close-packed planes $(0\bar{2}2)_{cem}$ // $(\bar{1}\,\bar{1}1)_{\gamma}$ and a direction of 'good fit' $[100]_{cem}$ // $[112]_{\gamma}$.

Crystallographically, the Pitsch OR and the Farooque–Edmonds OR are quite different. The minimum angle of rotation to bring them into coincidence is actually 20° (Mangan *et al.*, 1999). Cementite holding the Farooque–Edmonds OR has been observed to occur along with the cementite holding the Pitsch OR in near equal numbers (Mangan *et al.*, 1999), although a predominance of F-E may be found at lower (<500°C) transformation temperatures (Zhang and Kelly, 1998). Despite the fact that the Pitsch OR was recognized many years before the Farooque–Edmonds OR, it is highly likely that both ORs co-exist in alloys containing proeutectoid cementite in an austenitic matrix.

7.6 Habit plane, growth direction and interfacial structure of proeutectoid precipitates

Predicting and modelling crystallographic orientation relationships and resultant precipitate morphologies are still rich with opportunities for research. Numerous papers provide excellent background on the relationships between crystallography and morphology (Dahmen, 1982; Dahmen and Westmacott, 1982; Liang and Reynolds, 1998; Kelly and Zhang, 1999; Zhang *et al.*, 2000; Nie, 2004; Zhang and Weatherly, 2005). Crystallographic considerations are also related to the details of nucleation sites, critical nucleus shapes, nucleation mechanisms, growth mechanisms (e.g., Aaronson *et al.*, 1997) and growth kinetics. These topics are covered in great detail elsewhere in this book. The scope of this discussion will be limited to the experimental evidence pertaining directly to the crystallography and morphology of proeutectoid ferrite and cementite.

7.6.1 Proeutectoid ferrite

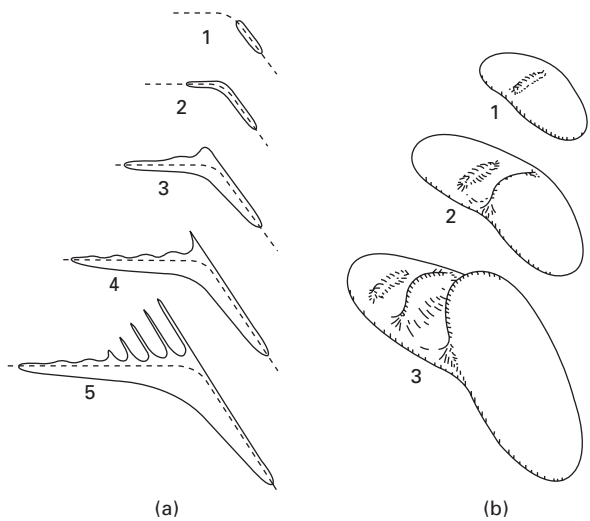
It is generally accepted that cooling below the A_{e3} in hypoeutectoid steel will result in ferrite nucleation preferentially at austenite grain corners, followed by edges and then boundaries (Cahn, 1956). Photoemission electron microscopy

© Woodhead Publishing Limited, 2012

of surfaces (Middleton and Edmonds, 1977; Edmonds and Honeycombe, 1978) showed that ferrite allotriomorphs predominantly nucleate at triple points, as expected, and tend to grow away from the austenite to develop a blocky structure with faceted interfaces. It is likely that each type of nucleation site would have a range of potency depending on crystallography (Enomoto and Yang, 2008).

The crystallographic constraints between the parent and precipitating phases are relatively complex at corners (interfaces develop between the precipitate and four matrix grains) and edges (where there are interfaces between the precipitate and three matrix grains). Taking the simplest case, it has been shown that grain boundary nucleated ferrite obtains a near K-S OR with only one of the austenite grains and an irrational/random OR with the opposite side (King and Bell, 1975). Nucleation of grain boundary precipitates is preferred when a low deviation from K-S can be obtained with both adjacent matrix grains (Lischewski and Gottstein, 2011). The deviation from the exact K-S OR is necessary to reduce the interfacial energy for both the adjacent austenite grains (Furuhara *et al*., 2010).

Mehl *et al*. (1933) confirmed the Kurdjumov–Sachs orientation relationship between austenite and Widmanstätten ferrite by trace analysis of etch pits, and that the outward form of Widmanstätten ferrite is plate-like by viewing orthogonal planes of polish through the same prior austenite grains. Serial sections confirmed the plate-like shape of Widmanstätten ferrite (Eichen *et al*., 1964). The development of Widmanstätten ferrite was thought to occur by the following sequence (Townsend and Kirkaldy, 1968) (see Fig. 7.23): nucleation of grain boundary ferrite with the conjugate habit plane

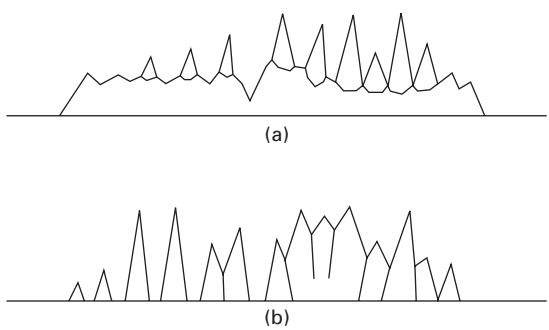


7.23 Sequence of developing Widmanstätten plates in (a) profile and (b) in perspective (adapted from Townsend and Kirkaldy, 1968).

© Woodhead Publishing Limited, 2012

of the K-S OR near the plane of the austenite grain boundary; followed by spread of the planar nucleus until a curvature in the austenite grain boundary causes a distortion; colonies of sideplates then develop by the point effect of diffusion at morphological instabilities (Sekerka, 1967). Alternatively, there is evidence that suggests that Widmanstätten ferrite forms by either (1) nucleation and growth of individual sideplates on the austenite grain boundary, followed by rapid impingement at the bases of thickening plates or (2) sympathetic nucleation atop grain boundary allotriomorphs. In the latter case, the deviations from the exact K-S OR could be corrected by small misorientations, and would explain the low angle grain boundaries observed between allotriomorphic ferrite and the adjacent Widmanstätten ferrite (Spanos and Hall, 1996; Spanos *et al*., 2005) (see Fig. 7.24).

Mehl *et al*. (1933) also concluded that Widmanstätten ferrite has a 'habit plane' corresponding to $\{111\}_\gamma//\{110\}_\alpha$. It is important now to distinguish between the 'apparent' habit plane, which can be observed optically or with electron microscopy, and the atomic habit plane, which can only be observed with some difficulty in ferrous alloys that contain retained austenite (Purdy, 1978; Rigsbee and Aaronson, 1979b). Evidence shows that there is considerable scatter in the apparent habit plane between precipitates and even within a single precipitate (King and Bell, 1976). However, at higher resolution it can be shown that the broad faces of ferrite plates contain coherent patches of good atomic matching, and that the spacing between coherent patches and curvature (apparent deviation from the atomic habit plane) is explained by the presence of structural ledges and misfit dislocations (Hall *et al*., 1972; Rigsbee and Aaronson, 1979a; Aaronson *et al*., 1997). High voltage electron microscopy showed that broad, planar facets of ferrite:austenite interfaces are essentially immobile and grow normal to their habit plane by the passage of growth ledges (Purdy, 1978; Spanos *et al*., 1991). In order to obtain a Widmanstätten structure from an allotriomorph (by perturbation or sympathetic



7.24 Schematic illustration of (a) sympathetic nucleation of plates atop pre-existing allotriomorphs, and (b) rapid impingement of primary sideplates (adapted from Spanos and Hall, 1996).

© Woodhead Publishing Limited, 2012

nucleation) or growth directly from the austenite grain boundary, the habit plane needs to obtain an appreciable angle from the austenite grain boundary, reported to be between 60–90° (Fong and Glover, 1982).

Specific studies of microconstituent growth kinetics showed that ferrite allotriomorphs thicken according to a parabolic growth rate ($\sim t^{1/2}$) (Zener, 1949; Purdy and Kirkaldy, 1963; Bradley *et al.*, 1977; Edmonds and Honeycombe, 1978), which agrees with the assumption that growth is controlled by the volume diffusion of carbon in austenite. The measured growth rates are smaller than calculations, which is explained by the development of large areas of partially coherent facets (Aaron and Aaronson, 1968; Bradley *et al.*, 1977). Researchers using a 3D X-ray diffraction microscope (3DXRD) at a synchrotron source (Offerman *et al.*, 2002) confirmed the parabolic model and interpreted their results to suggest three other fundamentally different types of growth are active and that the activation energy for grain nucleation is two orders of magnitude lower than calculated by previous thermodynamic models (Lange *et al.*, 1988). These findings have stimulated much discussion (e.g., Aaronson *et al.*, 2004a; Li *et al.*, 2007) and are still under investigation (Enomoto and Yang, 2008).

However, Widmanstätten ferrite thickening rates have been found to be 'highly variable' and thickening occurs with the passage of growth ledges, which have spacing and heights varying over two orders of magnitude (Kinsman *et al.*, 1975). Widmanstätten ferrite lengthening rates are found to be linear (Speich and Cohen, 1960; Townsend and Kirkaldy, 1968; Simonen *et al.*, 1973), and were successfully modelled by Trivedi (1970) and Bosze and Trivedi (1974).

7.6.2 Widmanstätten proeutectoid cementite

A breakthrough in the understanding of cementite:austenite crystallography was made in a study that directly related the 3D morphology of Widmanstätten proeutectoid cementite precipitates to their OR with the austenite matrix (Mangan *et al.*, 1999). Three-dimensional analysis of specific, individual cementite precipitates in austenite, coupled with identification of the cementite:austenite crystallographic OR for those same precipitates, conclusively showed that the monolithic plates (shown in Fig. 7.20 middle) always have the Pitsch OR and that laths (shown in Fig. 7.20 bottom) always have the Farooque–Edmonds OR.

This critical connection between crystallography and morphology cleared up confusion that was related to the incorrect belief (Mehl *et al.*, 1933; Greninger and Troiano, 1940; Heckel *et al.*, 1960) that there was no unique habit plane for cementite plates. The presence of a broad face corresponding to a plate-shaped precipitate is usually indicative of a habit plane of good fit between the precipitate and matrix lattices (Aaronson, 1969; Dahmen,

© Woodhead Publishing Limited, 2012

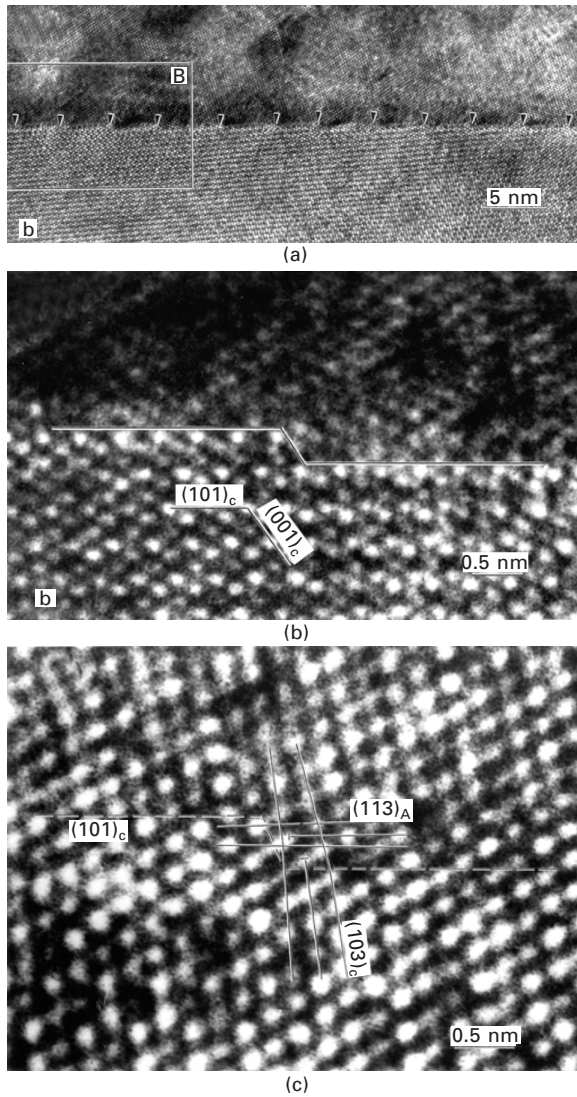
1982; Aaronson *et al*., 1990). So, the lack of a habit plane at the broad face of plates conflicted with most theories of precipitate shape (e.g., Mehl *et al*., 1933; Aaronson, 1962, 1969; Barrett and Massalski, 1980), as well as experimental observations in other alloys and alloy systems (e.g., Bowles and Barrett, 1952; Pitsch, 1962). The fact that there are (at least) *two* orientation relationships between Widmanstätten cementite was the origin of the confusion.

Ultimately, lattice matching analysis, TEM diffraction methods (Spanos and Aaronson, 1990) and atomic resolution of interfaces (Howe and Spanos, 1999), showed that the habit plane for monolithic plates adhering to the Pitsch OR is $(101)_{cem}$ // $(1\bar{1}3)_{\gamma}$ (see Fig. 7.25). This pair of parallel planes is consistent with the Pitsch OR, and contains two relatively 'good fit' directions, i.e. $[010]_{cem}$ // $[110]_{\gamma}$ and $[\bar{1}01]_{cem}$ // $[\bar{3}32]_{\gamma}$, the former of which were parallel to fine ledge traces. Zhang and Kelly (1998) applied 'edge-to-edge matching' analysis to Widmanstätten proeutectoid cementite precipitates in austenite. Edge-to-edge matching is a crystallographic approach to understanding habit planes and precipitate morphologies, based on the concept that interfacial energy is minimized when rows of atoms match across an interface. In cementite obeying the Pitsch OR with an austenite matrix, their analysis verified the best fit atomic habit plane, $\{101\}_{cem}$ // $\{1\bar{1}3\}_{\gamma}$, the good fit direction, $<010>_{cem}$ // $<110>_{\gamma}$, and even the secondary direction of good fit in the atomic habit plane, $[\bar{1}01]_{cem}$ // $<\bar{3}32>_{\gamma}$, that had been determined earlier (Spanos and Aaronson, 1990). Zhang and Kelly thus showed the usefulness of considering the edge-to-edge matching of close-packed planes in the two lattices, i.e. {103} or {022} for cementite, and {111} for austenite.

The growth direction, interfacial structure and crystallography of the 'other' Widmanstätten cementite morphology, i.e. the lath morphology, in an Fe-1.3C-13Mn alloy that had been isothermally transformed at 650°C for 50 seconds were revealed in a series of papers by Fonda and co-workers (Fonda and Kral, 2000; Kral and Fonda, 2000; Fonda *et al*., 2003). Deep etching of TEM specimens revealed that the lath growth direction is parallel to $[100]_{cem}$, as shown in Fig. 7.26(a). Transmission electron diffraction methods and high resolution TEM showed that cementite laths obeying the Farooque–Edmonds OR have a non-unique habit plane that varies from 10° to 15° from the $(001)_{cem}$ plane (see Figs 7.26(b) and (c)). The observed lath growth direction was consistent with the Farooque-Edmonds OR and parallel to the relatively 'good fit' direction, i.e. $[100]_{cem}$ // $[112]_{\gamma}$. The broad faces of the cementite laths were shown to contain a complex interfacial structure consisting of three types of features (not shown in Fig. 7.26):

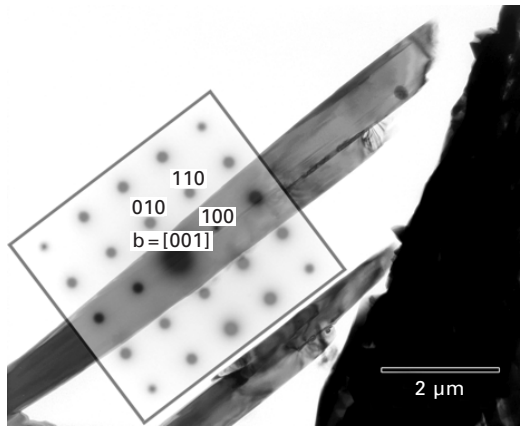
- direction steps (fine ledges which change the average direction of the habit plane),

© Woodhead Publishing Limited, 2012



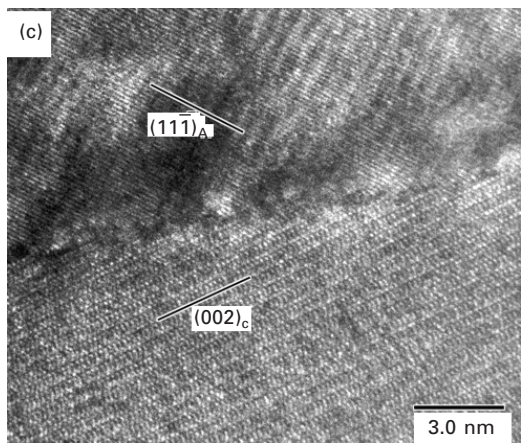
7.25 High resolution TEM micrographs taken from an Fe-1.34%C-13%Mn alloy isothermally reacted at 650°C for 100 s, showing: (a) a series of fine ledges (spaced about 3.7 nm apart) at the austenite:cementite interface (austenite on top, cementite on bottom) corresponding to the broad face of a proeutectoid cementite plate; (b) enlargement from one of the arrowed ledges in region B of Fig. 7.11(a), showing the $(001)_C$ ledge riser plane, which connects the upper and lower $(101)_C$ terrace planes; (c) high resolution image from another ledge in a very thin region of the TEM foil, showing, in addition to the positions of the $(101)_C//(1\bar{1}3)_A$ ledge terrace and the $(001)_C$ ledge riser planes, the exact positions of the terminating $(\bar{1}03)_C$ plane and a terminating $(1\bar{1}3)_A$ plane, corresponding to two edge dislocations associated with the ledge (Howe and Spanos, 1999).

© Woodhead Publishing Limited, 2012



(a)





7.26 (a) TEM image of a cementite lath in a deep etched sample, showing the growth direction is parallel to $[100]_{cem}$; (b) a thin foil specimen showing a cluster of laths viewed near the $[100]_{cem}//[112]\gamma$ direction, showing that there is no apparent habit plane; (c) a high-resolution TEM image of a 'typical' interface orientation (Fonda *et al.*, 2003).

© Woodhead Publishing Limited, 2012

- another set of compensating defects described as either misfit dislocations or structural ledges, and
- a coarser set of curved features which were interpreted as either growth ledges or intruder dislocations from the austenite matrix which intersect the austenite:cementite interface (Fonda *et al.*, 2003).

It is noted here that intruder dislocations that have a Burger's vector component normal to the interface can produce interfacial ledges that might then be adopted as growth ledges. A 3D near-coincidence analysis (Liang and Reynolds, 1998; Fonda *et al.*, 2003; Reynolds *et al.*, 2003) for cementite obeying the Zhang and Kelly refinement of the Farooque–Edmonds OR with the austenite showed that the good fit direction lies along $[100]_{cem}$ // $[112]_{\gamma}$, but it was noted that the coincidence was not 'continuous' in this direction, such that a direction analogous to an invariant line or O-line was not observed in the modelling. Nevertheless, the predicted $[100]_{cem}$ // $[112]_{\gamma}$ direction of good fit agreed very well with the experimental observation of the $[100]_{cem}$ lath growth direction (Kral and Fonda, 2000; Fonda *et al.*, 2003). On the other hand, in the Zhang and Kelly refinement of the Farooque–Edmonds OR, the 3D near-coincidence site modelling did not reveal a single moiré plane with significantly better atomic matching than all others, and it was suggested that this may be responsible for the experimental observation of the lack of a well-defined habit plane for the cementite laths obeying this OR. Zhang and Kelly (1998) also applied an edge-to-edge matching analysis to cementite precipitates obeying the Farooque–Edmonds OR to show that the good fit direction in this OR is $<112>_A//<100>_C$. Their TEM trace analysis techniques of Hadfield steels (e.g., Fe-1.2C-13.4Mn, aged at 400°C for 96 hours) showed an atomic habit plane for the Farooque–Edmonds OR that was within a few degrees of $\{421\}_A//\{015\}_C$. The relatively lower isothermal transformation temperature and longer transformation times could explain the disagreement in habit plane.

On a historical note, in 1933 Mehl *et al.* showed extracted Widmanstätten cementite 'plates' from a slowly cooled hypereutectoid steel, and remarked upon the appearance of 'striations' that were parallel with $[100]_{cem}$ as well as the good atomic matching between austenite and cementite along $[112]_{\gamma}//[100]_{cem}$. Therefore, the essence of the Farooque–Edmonds OR was anticipated in 1933, but apparently remained overlooked in detail until the Farooque and Edmonds paper in 1990. Note also that cementite intragranular idiomorphs and some Widmanstätten cementite originally described as Widmanstätten plates were likely to have been Farooque–Edmonds oriented Widmanstätten laths.

Proeutectoid cementite allotriomorph thickening and Widmanstätten plate lengthening and thickening were studied some time ago (Heckel and Paxton, 1960; Ando and Krauss, 1981b, 1982), using the same analytical

© Woodhead Publishing Limited, 2012

methods described earlier for proeutectoid ferrite. In all cases, the kinetics were much more sluggish than expected. This was explained at the time by the partially coherent ledge structure at the interface and/or partitioning of Cr and/or Si. The new distinction between plate and lath Widmanstätten proeutectoid cementite offers more scope for interpreting thickening and lengthening kinetics data. All of the available data (Heckel and Paxton, 1960) are based on the assumption of a single plate-like shape. The actual shapes are important because the crystallography, both apparent and atomic habit planes and tip radius of each shape are different for plates and laths. There must therefore be different lengthening and thickening rates for the two different types of Widmanstätten proeutectoid cementite.

There is also a strong tendency for allotriomorphs to facet. In the extreme, a zig-zag grain boundary morphology develops. Migration of the austenite:cementite interfaces occurs to satisfy the primary growth directions relevant to the orientation relationships obtained with austenite on either or both sides. As such migrations/rotations are occurring, the volume fraction of grain boundary cementite can increase without appreciable thickening. These morphological and crystallographic considerations have not yet been taken into account.

7.7 Future trends

New insights can be gained from 3D analysis methods that would have been very difficult from 2D (e.g., Mangan *et al*., 1999; Spanos *et al*. 2005). Two-dimensional observations of a limited number of cross sections are almost always a pragmatic necessity but now can be informed by the 3D classification system. In the future, morphological studies and measurements of nucleation and growth kinetics can be expressed in terms of the 3D morphologies, if not actually measured using 3D techniques such as focused ion beam (FIB). Models of growth should take 3D morphologies into consideration. Continuing investigation of phase transformations using 3DXRD methods will bring further advancement in this field.

7.8 Source of further information and advice

Aaronson, H.I. (ed.) 1962, *The Decomposition of Austenite by Diffusional Processes*, Interscience, New York.

Dahmen, U. 1982, 'Orientation relationships in precipitation systems', *Acta Metallurgica*, vol. 30, no. 1, pp. 63–73.

Mehl, R.F., Barrett, C.S. and Smith, D.W. 1933, 'Studies upon the Widmanstätten structure, IV – the iron-carbon alloys', *Trans. AIME*, vol. 105, pp. 215–258.

Samuels, L.E. 1999, *Light Microscopy of Carbon Steels*, revised edn., ASM, Materials Park, OH.

© Woodhead Publishing Limited, 2012

Smith, C.S. 1960, *A History of Metallography: The Development of Ideas on the Structure of Metals Before 1890*, University of Chicago Press, Chicago.

Sorby, H.C. 1887, 'The microscopical structure of iron and steel', *J. I. Steel Inst. (London)*, vol. 33, pp. 255–288.

Spanos, G. and Kral, M.V. 2009, 'The proeutectoid cementite transformation in steels', *International Materials Reviews*, vol. 54, no. 1, pp. 19–47.

Zhang, W.Z. and Weatherly, G.C. 2005, 'On the crystallography of precipitation', *Progress in Materials Science*, vol. 50, pp. 181–292.

7.9 Acknowledgements

The author expresses his appreciation to Robert E. Hackenberg (Los Alamos National Laboratory) for his many helpful suggestions.

7.10 References

Aaron, H.B. and Aaronson, H.I. 1968, 'Growth of grain boundary precipitates in Al-4% Cu by interfacial diffusion', *Acta Metallurgica*, vol. 16, no. 6, pp. 789–798.

Aaronson, H.I. 1956, 'Effects of nucleation site upon precipitate morphology', *The Mechanism of Phase Transformations in Metals*, vol. 18, pp. 47–56.

Aaronson, H.I. 1962, 'Proeutectoid ferrite and cementite reactions', in Zackay, V.F. & Aaronson, H.I. (eds), *The Decomposition of Austenite by Diffusional Processes*, Interscience, New York, pp. 387–546.

Aaronson, H.I. 1969, 'On the problem of the definitions and the mechanisms of the bainite reaction', in *The Mechanism of Phase Transformations in Crystalline Solids*, Institute of Metals, London, pp. 270–281.

Aaronson, H.I. 1999, 'Nucleation kinetics of grain boundary ferrite allotriomorphs at austenite grain faces during the proeutectoid ferrite reaction in Fe-C, Fe-C-X and Fe-C-Mn-X alloys', *Materials Forum*, vol. 23, pp. 1–22.

Aaronson, H.I. and Wells, C. 1956, *Trans. AIME*, vol. 206, pp. 1216–1223.

Aaronson, H.I., Laird, C. and Kinsman, K.R. 1970, 'Mechanisms of diffusional growth of precipitate crystals', in Aaronson, H.I. (ed.), *Phase Transformations*, ASM, Metals Park OH, pp. 313–396.

Aaronson, H.I., Furuhara, T., Rigsbee, J.M., Reynolds Jr., W.T. and Howe, J.M. 1990, 'Crystallographic and mechanistic aspects of growth by shear and diffusional processes', *Metallurgical Transactions A*, vol. 21A, pp. 2369–2409.

Aaronson, H.I., Spanos, G., Masumura, R.A., Vardiman, R.G., Moon, D.W., Menon, E.S.K. and Hall, M.G. 1995, 'Sympathetic nucleation – an overview', *Materials Science and Engineering*, vol. 32B, no. 3, pp. 107–123.

Aaronson, H.I., Howe, J.M., Hall, M.G., Furuhara, T. and Hirth, J.P. 1997, 'Mobility of structural ledges', *Scripta Materialia*, vol. 37, no. 9, pp. 1301–1307.

Aaronson, H.I., Lange, W.F. and Purdy, G.R. 2004a, 'Discussion to "Grain nucleation and growth during phase transformations"' by S.E. Offerman *et al., Science*, 298, 1003 (November 1, 2002)', *Scripta Materialia*, vol. 51, no. 9, pp. 931–935.

Aaronson, H.I., Reynolds, W.T. and Purdy, G.R. 2004b, 'Coupled-solute drag effects

© Woodhead Publishing Limited, 2012

on ferrite formation in Fe-C-X systems', *Metallurgical and Materials Transactions A*, vol. 35A, pp. 1187–1210.

Ando, T. and Krauss, G. 1981a, 'The effect of phosphorus content on grain boundary cementite formation in AISI 52100 steel', *Metall. and Mater. Trans. A*, vol. 12A, pp. 1283–1290.

Ando, T. and Krauss, G. 1981b, 'The isothermal thickening of cementite allotriomorphs in a 1.5Cr1C steel', *Acta Metallurgica*, vol. 29, no. 2, pp. 351–363.

Ando, T. and Krauss, G. 1982, 'Growth of grain boundary cementite allotriomorphs in ternary Fe-C-Cr alloys', in Aaronson, H. I., Laughlin, D. E., Sekerka, R. F. and Wayman, C. M. (eds), *Proceedings of an International Conference on Solid-Solid Phase Transformations*, TMS-AIME, Warrendale, PA, pp. 573–577.

Babu, S.S. 2004, 'The mechanism of acicular ferrite in weld deposits', *Current Opinion in Solid State and Materials Science*, vol. 8, no. 3–4, pp. 267–278.

Bain, E.C. and Paxton, H.W. 1966, *Alloying Elements in Steel*, ASM, Metals Park, OH.

Barrallier, L., Traskine, V. and Botchenkov, S. 2005, 'Morphology of intergranular cementite arrays in nitrided chromium-alloyed steels', *Materials Science and Engineering A*, vol. 393, no. 1–2, pp. 247–253.

Barrett, C.S. and Massalski, T.B. 1980, *The Structure of Metals*, 3rd edn, Pergamon Press, New York.

Barrett, C.S., Geisler, A.H. and Mehl, R.F. 1941, *Trans. AIME*, vol. 143, p. 134.

Bhadeshia, H.K.D.H. 1996, 'Models for the elementary mechanical properties of steel welds', in Cerjak, H. (ed.), *Mathematical Modelling of Weld Phenomena III*, Institute of Materials, Graz University of Technology, Austria, pp. 1–50.

Bhadeshia, H.K.D.H. and Honeycombe, R.W.K. 2006, *Steels – Microstructure and Properties*, 3rd edn, Butterworth-Heinemann, Oxford.

Bosze, W.P. and Trivedi, R. 1974, 'On the kinetic expression for the growth of precipitate plates', *Metallurgical Transactions*, vol. 5, no. 2, pp. 511–512.

Bowles, J.S. and Barrett, C.S. 1952, *Prog. Met. Phys.*, vol. 3, p. 1.

Bradley, J.R. and Aaronson, H.I. 1977, 'The stereology of grain boundary allotriomorphs', *Metallurgical Transactions*, vol. 8A, no. 2, pp. 317–322.

Bradley, J.R. and Aaronson, H.I. 1981, 'Growth kinetics of grain boundary ferrite allortiromorphs in Fe-C-X alloys', *Metallurgical Transactions*, vol. 12A, no. 10, pp. 1729–1741.

Bradley, J.R., Rigsbee, J.M. and Aaronson, H.I. 1977, 'Growth kinetics of grain boundary ferrite allotriomorphs in Fe-C alloys', *Metallurgical Transactions*, vol. 8A, no. 2, pp. 323–333.

Bramfitt, B.L. and Lawrence, S.J. 2004, 'Metallography and microstcutures of carbon and low-alloy steels', in VanderVoort, G.F. (ed.), *Metallography and Microstructures*, vol. 9, ASM International, Metals Park, OH, pp. 609–626.

Cahn, J.W. 1956, 'The kinetics of grain boundary nucleated reactions', *Acta Metall.*, vol. 4, pp. 449–459.

Cahn, J.W. 1960, 'Theory of crystal growth and interface motion in crystalline materials', *Acta Metallurgica*, vol. 8, no. 8, pp. 554–562.

Carter, A. 1955, *J. Inst. Met. (London)*, vol. 83, p. 481.

Chairuangsri, T. and Edmonds, D.V. 2000, 'Abnormal ferrite in hyper-eutectoid steels', *Acta Materialia*, vol. 48, no. 7, pp. 1581–1591.

Cheng, L. and Wu, K.M. 2009, 'New insights into intragranular ferrite in a low-carbon low-alloy steel', *Acta Materialia*, vol. 57, no. 13, pp. 3754–3762.

© Woodhead Publishing Limited, 2012

Cheng, L., Li, Z.G. and Wu, K.M. 2008, 'Serial sectioning and 3D-reconstruction of ferrite allotriomorphs nucleated at grain boundary faces in an Fe-C-Mn alloy', *ISIJ International*, vol. 48, no. 6, pp. 830–834.

Cheng, L., Wan, X.L. and Wu, K.M. 2010a, 'Three-dimensional analysis of ferrite allotriomorphs nucleated on grain boundary faces, edges and corners', *Materials Characterization*, vol. 61, no. 5, pp. 580–583.

Cheng, L., Wan, X.L. and Wu, K.M. 2010b, 'Three-dimensional morphology of grain boundary Widmanstätten ferrite in a low carbon low alloy steel', *Materials Characterization*, vol. 61, no. 2, pp. 192–197.

Cowley, S.A. and Edmonds, D.V. 1988, 'Proeutectoid cementite transformation in a 12Mn-0.8C steel', in Lorimer, G.W. (ed.), *Phase Transformations 87*, The Institute of Metals, London, p. 459.

Dahmen, U. 1982, 'Orientation relationships in precipitation systems', *Acta Metallurgica*, vol. 30, no. 1, pp. 63–73.

Dahmen, U. and Westmacott, K.H. 1982, 'Role of invariant line in the nucleation and growth of precipitates', in Aaronson, A.I., Laughlin, D.E., Sekerka, R.F. and Wayman, C.M. (eds), *Proceedings of an International Conference on Solid-Solid Phase Transformations*, TMS-AIME, Pittsburgh, PA, pp. 433–437.

Davenport, A.T. and Honeycombe, R.W.K. 1971, 'Precipitation of carbides at gamma-alpha boundaries in alloy steels', *Proc. R. Soc. London*, vol. A322, pp. 191–205.

Davenport, A.T., Berry, F.G. and Honeycombe, R.W.K. 1968, 'Interphase precipitation in iron alloys', *Metal Science Journal*, vol. 2, pp. 104–106.

Davenport, E.S. and Bain, E.C. 1930, 'Transformation of austenite at constant subcritical temperatures', *Trans. AIME*, vol. 90, pp. 117–154.

Doane, D.V. and Kirkaldy, J.S. 1978, *Hardenability Concepts with Applications to Steel*, TMS-AIME, Warrendale, PA.

Dubé, C.A. 1948, PhD dissertation, Carnegie-Mellon University.

Dubé, C.A., Aaronson, H.I. and Mehl, R.F. 1958, 'La formation de la ferrite proeutectoide dans les aciers au carbon', *Revue de Metallurgie*, vol. 55, no. 3, pp. 201–210.

Edmonds, D.V. and Honeycombe, R.W.K. 1978, 'Photoemission electron microscopy of growth of grain boundary ferrite allotriomorphs in chromium steels', *Metal Science*, vol. 12, no. 9, pp. 399–405.

Eichen, E., Aaronson, H.I., Pound, G.M. and Trivedi, R. 1964, 'Thermionic emission microscope study of the formation of ferrite sideplates', *Acta Metallurgica*, vol. 12, pp. 1298–1301.

Enomoto, M. 2001, 'Proeutectoid ferrite', in Buschow, K.H.J., Cahn, R.W., Flemings, M.C., Ilschner, B., Kramer, E.J. and Mahajan, S. (eds.), *Encyclopedia of Materials: Science and Technology*, 2nd edn, Elsevier Science, Oxford, pp. 7898–7903.

Enomoto, M. and Yang, J.B. 2008, 'Simulation of nucleation of proeutectoid ferrite at austenite grain boundaries during continuous cooling', *Metallurgical and Materials Transactions A: Physical Metallurgy and Materials Science*, vol. 39 A, no. 5, pp. 994–1002.

Farooque, M. and Edmonds, D.V. 1990, in Peachey, L.D. and Williams, B.D. (eds), *Proc. XIIth Intl. Congress for Electron Microscopy*, San Francisco, CA, p. 910.

Fonda, R.W. and Kral, M.V. 2000, 'The morphology of Widmanstätten cementite laths', *Microscopy & Microanalysis 2000*, vol. 6, supplement 2, pp. 342–343.

Fonda, R.W., Reynolds, W.T. and Kral, M.V. 2003, 'The interfacial structure of Widmanstätten cementite laths', in Damm, E.B. (ed.), *Symposium on Austenite Formation and Decomposition at Materials Science & Technology 2003*, TMS, Chicago. IL, pp. 425–436.

© Woodhead Publishing Limited, 2012

Fong, H.S. and Glover, S.G. 1982, 'Angle between grain-boundary Widmanstätten ferrite and grain boundaries in carbon steel', *Metal Science*, vol. 16, no. 5, pp. 239–244.

Furuhara, T., Saito, H., Miyamoto, G. and Maki, T. 2010, 'Crystallography of ferrite nucleation at austenite grain boundary in a low carbon steel', in *Materials Science Forum*, vol. 654–656, pp. 7–10.

Gibbs, J.W. 1961, *The Scientific Papers of J. Willard Gibbs*, Dover, New York.

Goldenstein, H. and Aaronson, H.I. 1990, 'Overall reaction kinetics and morphology of austenite decomposition between the upper nose and the Ms of a hypoeutectoid Fe-C-Cr alloy', *Metallurgical Transactions A*, vol. 21, no. 6, pp. 1465–1478.

Greninger, A.B. and Troiano, R. 1940, *Trans. AIME*, vol. 140, pp. 307–331.

Hackenberg, R.E. and Shiflet, G.J. 2003, 'The influence of morphology on grain-boundary and twin-boundary bainite growth kinetics at the bay in Fe-C-Mo', *Philosophical Magazine*, vol. 83, no. 29, pp. 3367–3385.

Hackenberg, R.E., Granada, D.G. and Shiflet, G.J. 2002a, 'Austenite decomposition to carbide-rich products in Fe-0.30C-6.3W', *Metall. Mater. Trans. A*, vol. 33, pp. 3619–3633.

Hackenberg, R.E., Nordstrom, D.P. and Shiflet, G.J. 2002b, 'Morphology and three-dimensional structure of ferrite formed below the bay in an Fe-C-W alloy', *Scripta Materialia*, vol. 47, no. 6, pp. 357–361.

Hall, M.G., Aaronson, H.I. and Kinsman, K.R. 1972, 'The structure of nearly coherent fcc:bcc boundaries in a Cu–Cr alloy', *Surface Science*, vol. 31, pp. 257–274.

Han, K., Edmonds, D.V. and Smith, G.D.W. 2001, 'Optimization of mechanical properties of high-carbon pearlitic steels with Si and V additions', *Metallurgical and Materials Transactions A: Physical Metallurgy and Materials Science*, vol. 32, no. 6, pp. 1313–1324.

Hawbolt, E.B. and Brown, L.C. 1967, 'Grain boundary precipitation in Ag-5.64 wt pct Al alloys', *Trans. AIME*, vol. 239, pp. 1916–1924.

He, Y., Godet, S., Jacques, P.J. and Jonas, J.J. 2005, 'Crystallographic relationships between FCC and BCC crystals: a study using EBSD techniques', *Diffusion and Defect Data Pt.B: Solid State Phenomena*, vol. 105, pp. 121–126.

Headley, T. and Brooks, J. 2002, 'A new bcc-fcc orientation relationship observed between ferrite and austenite in solidification structures of steels', *Metallurgical and Materials Transactions A*, vol. 33, no. 1, pp. 5–15.

Heckel, R.W. and Paxton, H.W. 1960, 'Rates of growth of cementite in hypereutectoid steels', *Trans. AIME*, vol. 218, pp. 799–806.

Heckel, R.W. and Paxton, H.W. 1961, 'On the morphology of proeutectoid cementite', *Trans. ASM*, vol. 53, pp. 539–554.

Heckel, R.W., Smith, J.H. and Paxton, H.W. 1960, 'On the Widmanstätten habit plane of proeutectoid cementite', *Trans. AIME*, vol. 218, pp. 566–568.

Hillert, M. 1957, 'Role of interfacial energy during solid state phase transformations', *Jernkont. Ann.*, vol. 141, pp. 757–789.

Hillert, M. 1962, 'The formation of pearlite', in Zackay, V.F. and Aaronson, H.I. (eds), *The Decomposition of Austenite by Diffusional Processes*, Interscience, New York, pp. 197–237.

Hillert, M. and Waldenstrom, M. 1977, 'A thermodynamic analysis of the Fe-Mn-C system', *Metallurgical Transactions A*, vol. 8A, pp. 5–13.

Honeycombe, R.W.K. 1972, 'Ferrite and bainite in alloy steels', *Metallurgical Transactions*, vol. 3A, no. 5, pp. 1099–1112.

Howe, H. 1911, *Proc. Am. Soc. Testing Materials*, vol. 11, p. 262.

© Woodhead Publishing Limited, 2012

Howe, J.M. and Spanos, G. 1999, 'Atomic structure of the austenite-cementite interface of proeutectoid cementite plates', *Philosophical Magazine A – Physics of Condensed Matter Structure Defects and Mechanical Properties*, vol. 79, no. 1, pp. 9–30.

Huang, Z. and Yao, M. 1989, 'Effect of arrangement of acicular ferrite in a Widmanstätten microstructure on the fracture of mild steel', *Materials Science and Engineering: A*, vol. 119, pp. 211–217.

Hung, C.Y., Spanos, G., Rosenberg, R.O. and Kral, M.V. 2002, 'Three-dimensional observations of proeutectoid cementite precipitates at short isothermal transformation times', *Acta Materialia*, vol. 50, no. 15, pp. 3781–3788.

Ichikawa, K., Horii, Y., Motomatsu, R., Yamaguchi, M. and Yurioka, N. 1996, 'Mechanical properties of weld metal for fire-resistant steel with large heat input submerged arc welding', *Yosetsu Gakkai Ronbunshu/Quarterly Journal of the Japan Welding Society*, vol. 14, no. 1, pp. 27–32.

Inagaki, H. 1988, 'Morphologies of the proeutectoid ferrite formed in the γ to α transformation of a low carbon steel', *Zeitschrift für Metallkunde/Materials Research and Advanced Techniques*, vol. 79, no. 11, pp. 716–724.

Johnson, W.C., White, C.L., Marth, P.E., Ruf, P.K., Tuominen, S.M., Wade, K.D., Russell, K.C. and Aaronson, H.I. 1975, 'Influence of crystallography on aspects of solid-solid nucleation theory', *Metallurgical Transactions A*, vol. 6, no. 4, pp. 911–919.

Jones, S.J. and Bhadeshia, H.K.D.H. 1997, 'Kinetics of the simultaneous decomposition of austenite into several transformation products', *Acta Materialia*, vol. 45, no. 7, pp. 2911–2920.

Kelly, P.M. and Zhang, M.X. 1999, 'Edge-to-edge matching – a new approach to the morphology and crystallography of precipitates', *Materials Forum*, vol. 23, pp. 41–62.

Kennon, N.F. 1999, 'Nomenclature of phases and constituents', in Samuels, L.E. (ed.), *Light Microscopy of Carbon Steels*, ASM, Materials Park, OH, pp. 5–27.

Khalid, F.A. and Edmonds, D.V. 1993, 'A transmission electron microscopy study of copper precipitation in the cementite phase of hypereutectoid alloy steels', *Metallurgical Transactions*, vol. 24A, pp. 781–793.

Khalid, F.A. and Edmonds, D.V. 1994, 'Effect of vanadium on the grain boundary carbide nucleation of pearlite in high-carbon steels', *Scripta Metallurgica et Materiala*, vol. 30, no. 10, pp. 1251–1255.

Khalid, F.A., Farooque, M. and Edmonds, D.V. 1993, 'The formation of Widmanstätten cementite plates in alloy steels', in Wayman, C.M. and Perkins, J. (eds), *The International Conference on Martensitic Transformations (1992)*, Montery Institute for Advanced Studies, Carmel, CA, pp. 431–437.

King, A.D. and Bell, T. 1975, 'Crystallography of grain boundary proeutectoid ferrite', *Metallurgical Transactions*, vol. 6A, no. 7, pp. 1419–1429.

King, A.H. and Bell, T. 1976, 'Observations on the morphology and crystallography of proeutectoid ferrite', *Metallography*, vol. 9, pp. 397–413.

Kinsman, K.R., Eichen, E. and Aaronson, H.I. 1975, 'Thickening kinetics of proeutectoid ferrite plates in Fe-C alloys', *Metallurgical Transactions*, vol. 6A, pp. 303–317.

Kinzel, A.B. 1952, 'Chromium carbide in stainless steel', *Trans. AIME*, vol. 194, pp. 469–488.

Krahe, P.R., Kinsman, K.R. and Aaronson, H.I. 1972, 'Influence of austentie grain size upon the Widmanstätten-start (Ws) temperature for the proeutectoid ferrite reaction', *Acta Metallurgica*, vol. 20, no. 9, pp. 1109–1121.

Kral, M.V. 2000, 'Transmission electron microscopy of deep etched cementite', *Materials Characterization*, vol. 45, no. 2, pp. 105–110.

© Woodhead Publishing Limited, 2012

Kral, M.V. and Fonda, R.W. 2000, 'The primary growth direction of Widmanstatten cementite laths', *Scripta Materialia*, vol. 43, no. 2, pp. 193–198.

Kral, M.V. and Spanos, G. 1997, 'Three dimensional morphology of cementite precipitates', *Scripta Materialia*, vol. 36, no. 8, pp. 875–882.

Kral, M.V. and Spanos, G. 1999, 'Three dimensional analysis of proeutectoid cementite precipitates', *Acta Materialia*, vol. 47, no. 2, pp. 711–724.

Kral, M.V. and Spanos, G. 2003, 'Crystallography of solid state grain boundary cementite dendrites', *Acta Materialia*, vol. 51, no. 2, pp. 301–311.

Kral, M.V. and Spanos, G. 2005, 'Three dimensional analysis of grain boundary nucleated proeutectoid ferrite precipitates', *Metallurgical and Materials Transactions A*, vol. 36, no. 5, pp. 1199–1207.

Kral, M.V., Hofmeister, W.H. and Wittig, J.E. 1997, 'Interphase boundary precipitation in a Ti-1.7 at. pct Er alloy', *Metallurgical and Materials Transactions A – Physical Metallurgy and Materials Science*, vol. 28, no. 12, pp. 2485–2497.

Krauss, G. 1978, 'The microstructure and fracture of a carburized steel', *Metallurgical Transactions A*, vol. 9, no. 11, pp. 1527–1535.

Krielaart, G.P., Sietsma, J. and van der Zwaag, S. 1997, 'Ferrite formation in Fe-C alloys during austenite decomposition under non-equilibrium interface conditions', *Materials Science & Engineering A*, vol. 237, no. 2, pp. 216–223.

Krzanowski, J.E. and Hruska, S.J. 1987, 'Internal structure of a new microconstituent observed in carburized 9310 steel', *Scripta Materialia*, vol. 21, 39–44.

Lange, W.F., Enomoto, M. and Aaronson, H.I. 1988, 'The kinetics of ferrite nucleation at austenite grain boundaries in Fe-C alloys', *Metallurgical Transactions A*, vol. 19, no. 3, pp. 427–440.

Lee, J.K. and Aaronson, H.I. 1975, 'Influence of faceting upon the equilibrium shape of nuclei at grain boundaries – II. Three-dimensions', *Acta Metallurgica*, vol. 23, no. 7, pp. 809–820.

Lesuer, D.R., Syn, C.K., Whittenberger, J.D. and Sherby, O.D. 1999, 'Microstructure-property relations in as-extruded ultrahighcarbon steels', *Metallurgical and Materials Transactions A: Physical Metallurgy and Materials Science*, vol. 30, no. 6, pp. 1559–1568.

Li, D.Z., Xiao, N.M., Lan, Y.J., Zheng, C.W. and Li, Y.Y. 2007, 'Growth modes of individual ferrite grains in the austenite to ferrite transformation of low carbon steels', *Acta Materialia*, vol. 55, no. 18, pp. 6234–6249.

Liang, Q. and Reynolds, W.T. 1998, 'Determining interphase boundary orientations from near-coincidence sites', *Metallurgical and Materials Transactions A: Physical Metallurgy and Materials Science*, vol. 29, no. 8, pp. 2059–2072.

Lischewski, I. and Gottstein, G. 2011, 'Nucleation and variant selection during the α-γ-α phase transformation in microalloyed steel', *Acta Materialia*, vol. 59, no. 4, pp. 1530–1541.

Madariaga, I. and Gutierrez, I. 1999, 'Role of the particle-matrix interface on the nucleation of acicular ferrite in a medium carbon microalloyed steel', *Acta Materialia*, vol. 47, no. 3, pp. 951–960.

Mahla, E.M. and Nielsen, N.A. 1951, 'Carbide precipitation in Type 304 stainless steel – an electron microscope study', *Trans. ASM*, vol. 43, pp. 290–322.

Mangan, M.A., Lauren, P.D. and Shiflet, G.J. 1997, 'Three-dimensional reconstruction of Widmanstatten plates in Fe-12.3Mn-0.8C', *Journal of Microscopy*, vol. 188, pp. 36–41.

Mangan, M.A., Kral, M.V. and Spanos, G. 1999, 'Correlation between the crystallography

© Woodhead Publishing Limited, 2012

and morphology of proeutectoid Widmanstätten cementite precipitates', *Acta Materialia*, vol. 47, no. 17, pp. 4263–4274.

Mehl, R.F. and Marzke, O.T. 1931, 'Studies upon the Widmanstätten Structure, II – Introduction. The beta copper-zinc and the beta copper-aluminum alloys', *Trans. AIME*, vol. 93, pp. 123–161.

Mehl, R.F., Barrett, C.S. and Smith, D.W. 1933, 'Studies upon the Widmanstatten Structure, IV – the iron-carbon alloys', *Trans. AIME*, vol. 105, pp. 215–258.

Middleton, C.J. and Edmonds, D.V. 1977, 'The application of photoemission electron microscopy to the study of diffusional phase transformations in steels', *Metallography*, vol. 10, pp. 55–87.

Militzer, M., Mecozzi, M.G., Sietsma, J. and van der Zwaag, S. 2006, 'Three-dimensional phase field modelling of the austenite-to-ferrite transformation', *Acta Materialia*, vol. 54, no. 15, pp. 3961–3972.

Mullins, W.W. and Sekerka, R.F. 1963, 'Morphological stability of a particle growing by diffusion or heat flow', *J. Appl. Phys.*, vol. 34, pp. 323–329.

Nie, J.F. 2004, 'Crystallography and migration mechanisms of planar interphase boundaries', *Acta Materialia*, vol. 52, no. 3, pp. 795–807.

Offerman, S.E., van Dijk, N.H., Sietsma, J., Grigull, S., Lauridsen, E.M., Margulies, L., Poulsen, H.F., Rekveldt, M.T. and van der Zwaag, S. 2002, 'Grain nucleation and growth during phase transformations', *Science*, vol. 298, no. 5595, pp. 1003–1005.

Osmond, F. 1893, *Trans. AIME*, vol. 22, p. 243.

Pitsch, W. 1962, 'Der Orientierungszusammenhang zwischen Zementit und Autenit', *Acta Metall.*, vol. 10, pp. 897–900.

Purdy, G.R. 1978, 'The dynamics of transformation interfaces in steels – i. the ferrite-austenite interface in Fe-C-Mo alloys', *Acta Met.*, vol. 26, pp. 477–486.

Purdy, G.R. 1987, 'On the direct observation of the formation of ferrite in steels', *Scripta Metallurgica*, vol. 21, no. 8, pp. 1035–1038.

Purdy, G.R. and Kirkaldy, J.S. 1963, 'Kinetics of the proeutectoid ferrite reaction at an incoherent inferface, as determined by a diffusion couple', *Trans. AIME*, vol. 277, no. 10, pp. 1255–1256.

Reynolds, W.T., Enomoto, M. and Aaronson, H.I. 1984, 'The proeutectoid ferrite reaction', in Marder, A.R. and Goldstein, J.I. (eds), *Phase Transformations in Ferrous Alloys*, TMS-AIME, Warrendale, PA, pp. 155–200.

Reynolds, W.T., Li, F.Z., Shui, C.K. and Aaronson, H.I. 1990, 'Incomplete transformation phenomenon in Fe-C-Mo alloys', *Metallurgical Transactions A*, vol. 21, no. 6, pp. 1433–1463.

Reynolds, W.T., Nie, J.F., Zhang, W.Z., Howe, J.M., Aaronson, H.I. and Purdy, G.R. 2003, 'Atomic structure of high-index $\alpha(2)$: $\gamma(m)$ boundaries in a Ti-46.54at% alloy', *Scripta Mater.*, vol. 49, no. 5, pp. 405–409.

Rhines, F.N. 1977, 'Microstructure-property relationships in materials', *Metallurgical Transactions*, vol. 8A, pp. 127–133.

Rigsbee, J.M. and Aaronson, H.I. 1979a, 'A computer modeling study of partially coherent f.c.c.:b.c.c. boundaries', *Acta Metallurgica*, vol. 27, pp. 351–363.

Rigsbee, J.M. and Aaronson, H.I. 1979b, 'The interfacial structure of the broad faces of ferrite plates', *Acta Metallurgica*, vol. 27, no. 3, pp. 365–376.

Sekerka, R.F. 1967, 'Application of the time-dependent theory of interface stability to an isothermal phase transformation', *Journal of Physics and Chemistry of Solids*, vol. 28, no. 6, pp. 983–994.

Simonen, E.P., Aaronson, H.I. and Trivedi, R. 1973, 'Lengthening kinetics of ferrite and bainite sideplates', *Metallurgical Transactions*, vol. 4, pp. 1239–1245.

© Woodhead Publishing Limited, 2012

Sorby, H.C. 1887, 'The microscopical structure of iron and steel', *J. I. Steel Inst. (London)*, vol. 33, pp. 255–288.

Spanos, G. and Aaronson, H.I. 1988, 'Morphology, crystallography and mechanism of sympathetic nucleation of proeutectoid cementite plates', *Scripta Metallurgica*, vol. 22, no. 9, pp. 1537–1542.

Spanos, G. and Aaronson, H.I. 1990, 'The interfacial structure and habit plane of proeutectoid cementite plates', *Acta Met.*, vol. 38, no. 12, pp. 2721–2732.

Spanos, G. and Hall, M.G. 1996, 'The formation mechanism(s), morphology, and crystallography of ferrite sideplates', *Metallurgical and Materials Transactions A*, vol. 27A, no. 6, pp. 1519–1534.

Spanos, G. and Kral, M.V. 2001, 'Proeutectoid cementite', in Buschow, K.H.J., Cahn, R.W., Flemings, M.C., Ilschner, B., Kramer, E.J. and Mahajan, S. (eds), *Encyclopedia of Materials: Science and Technology*, 2nd edn, Elsevier Science, Oxford, pp. 7893–7898.

Spanos, G. and Kral, M.V. 2009, 'The proeutectoid cementite transformation in steels', *International Materials Reviews*, vol. 54, no. 1, pp. 19–47.

Spanos, G., Reynolds, W.T. and Vandermeer, R.A. 1991, 'The role of ledges in the proeutectoid ferrite and proeutectoid cementite reactions in steel', *Metallurgical Transactions A*, vol. 22, no. 6, pp. 1367–1380.

Spanos, G., Masumura, R.A.,Vandermeer, R.A. and Enomoto, M. 1994, 'Evolution and growth kinetics of precipitate plates growing by the ledge mechanism', *Acta Metallurgica et Materialia*, vol. 42, no. 12, pp. 4165–4176.

Spanos, G., Wilson, A.W. and Kral, M.V. 2005, 'New insights into the Widmanstätten proeutectoid ferrite transformation: integration of crystallographic and three-dimensional morphological observations', *Metallurgical and Materials Transactions A*, vol. 36, no. 5, pp. 1209–1218.

Speich, G.R. and Cohen, M. 1960, 'The growth rate of bainite', *Trans. AIMME* vol. 218, no. 6, pp. 1050–1059.

Sundmand, B., Jansson, B. and Andersson, J.O. 1985, *Calphad*, vol. 9, pp. 153–190.

te Velthuis, S.G.E., van Dijk, N.H., Rekveldt, M.T., Sietsma, J. and van der Zwaag, S. 2000, 'Three-dimensional model for the development of the microstructure in steel during slow cooling', *Materials Science and Engineering A*, vol. 277, no. 1–2, pp. 218–228.

Thermo-Calc 2007, *Thermo-Calc Thermodynamics Software* http://www.thermocalc.com/.

Thompson, S.W. and Howell, P.R. 1987, 'The orientation relationship between intragranularly nucleated Widmanstätten cementite and austenite in a commercial hypereutectoid steel', *Scripta Metall.*, vol. 21, pp. 1353–1357.

Thompson, S.W. and Howell, P.R. 1988, 'A preliminary comparison of two apparently diverse cementite/austenite orientation relationships', *Scripta Metall.*, vol. 22, pp. 229–233.

Thompson, S.W. and Howell, P.R. 1994, 'The habit plane of cementite formed in austenite with a Pitsch-like orientation relationship', in Johnson, W.C., Howe, J.M., Laughlin, D.E. and Soffa, W.A. (eds), *Solid-solid Phase Transformations Proceedings*, TMS, Warrendale, PA, pp. 1127–1132.

Thompson, S.W., Colvin, D.J. and Krauss, G. 1990, 'Continuous cooling transformations and microstructures in a low-carbon, high-strength low-alloy plate steel', *Metallurgical Transactions A*, vol. 21, no. 6, pp. 1493–1507.

Townsend, R.D. and Kirkaldy, J.S. 1968, 'Widmanstatten ferrite formation in Fe-C alloys', *Trans. ASM*, vol. 61, pp. 605–619.

© Woodhead Publishing Limited, 2012

Trivedi, R. 1970, 'The role of interfacial free energy and interface kinetics during the growth of precipitate plates and needles', *Metall. Trans.*, vol. 1, no. 4, pp. 921–927.

Wan, X.L., Cheng, L. and Wu, K.M. 2010, 'Three-dimensional morphology and growth behavior of ferrite allotriomorphs formed at grain boundary edges', *Journal of Iron and Steel Research International*, vol. 17, no. 11, pp. 49–53.

Wasynczuk, J.A., Fisher, R.M. and Thomas, G. 1986, 'Effects of copper on proeutectoid cementite precipitation', *Metall. Trans. A*, vol. 17A, pp. 2163–2173.

Wilson, F.G. 1971, 'The morphology of grain- and twin-boundary carbides in austenitic steels', *Journal of Iron and Steel Institute*, vol. 209, pp. 126–130.

Wu, K.M. 2006, 'Three-dimensional analysis of acicular ferrite in a low-carbon steel containing titanium', *Scripta Materialia*, vol. 54, no. 4, pp. 569–574.

Wu, K.M. and Enomoto, M. 2002, 'Three-dimensional morphology of degenerate ferrite in an Fe-C-Mo alloy', *Scripta Materialia*, vol. 46, no. 8, pp. 569–574.

Wu, K.M. and Enomoto, M. 2005, 'Three-dimensional morphology of acicular ferrite in a low carbon steel weld', in *Materials Science and Technology 2005*, Pittsburgh, PA, pp. 95–104.

Wu, K.M., Inagawa, Y. and Enomoto, M. 2004, 'Three-dimensional morphology of ferrite formed in association with inclusions in low-carbon steel', *Materials Characterization*, vol. 52, pp. 121–127.

Wu, K.M., Guo, A.M. and Cheng, L. 2007, 'Three-dimensional observation and growth kinetics of proeutectoid ferrite formed at austenite grain boundary in a low carbon microalloyed steel', *Materials Science Forum*, vol. 539–543, pp. 4578–4583.

Yang, K.H. and Choo, W.K. 1994, 'The variants of the orientation relationship between austenite and cementite in Fe-30wt%Mn-1.0wt%C alloy', *Acta Metallurgica et Materialia*, vol. 42, no. 1, pp. 263–269.

Zackay, V.F. and Aaronson, H.I. (eds) 1962, *The Decomposition of Austenite by Diffusional Processes*, Interscience, New York.

Zener, C. 1949, 'Theory of growth of spherical precipitates from solid solution', *Journal of Applied Physics*, vol. 20, no. 10, pp. 950–953.

Zhang, M.X. and Kelly, P.M. 1997, 'A new orientation relationship between Widmanstätten cementite and austenite', *Scripta Materialia.*, vol. 37, pp. 2017–2024.

Zhang, M.X. and Kelly, P.M. 1998, 'Crystallography and morphology of Widmanstätten cementite in austenite', *Acta Materialia*, vol. 46, no. 13, pp. 4617–4628.

Zhang, W.Z. and Purdy, G.R. 1993a, 'O-lattice analyses of interfacial misfit. I. General considerations', *Phil. Mag.*, vol. 68A, pp. 279–290.

Zhang, W.Z. and Purdy, G.R. 1993b, 'O-lattice analyses of interfacial misfit. II. Systems containing invariant lines', *Phil. Mag.*, vol. 68A, pp. 291–303.

Zhang, W.Z. and Weatherly, G.C. 2005, 'On the crystallography of precipitation', *Progress in Materials Science*, vol. 50, pp. 181–292.

Zhang, W.Z., Ye, F., Zhang, C., Qi, Y. and Fang, H.S. 2000, 'Unified rationalization of the Pitsch and T-H orientation relationships between Widmanstätten cementite and austenite', *Acta Materialia*, vol. 48, no. 9, pp. 2209–2219.

Zhang, Y.D., Esling, C., Gong, M.L., Vincent, G., Zhao, X. and Zuo, L. 2006, 'Microstructural features induced by a high magnetic field in a hypereutectoid steel during austenite decomposition', *Scripta Materialia.*, vol. 54, pp. 1897–1900.

© Woodhead Publishing Limited, 2012

8

The formation of pearlite in steels

D. EMBURY, McMaster University, Canada

Abstract: In this treatment of the pearlite reaction, the classical approach of the coupled growth of ferrite and cementite into austenite controlled by carbon diffusion is outlined. This is followed by a consideration of the growth of pearlite in ternary systems and evidence is presented for both partitioned and non-partitioned growth. Attention is paid to the various reactions which can occur at lower transformation temperatures which compete with conventional pearlite. Finally, a brief section on the deformation of pearlite is included together with some suggestions for future areas of research.

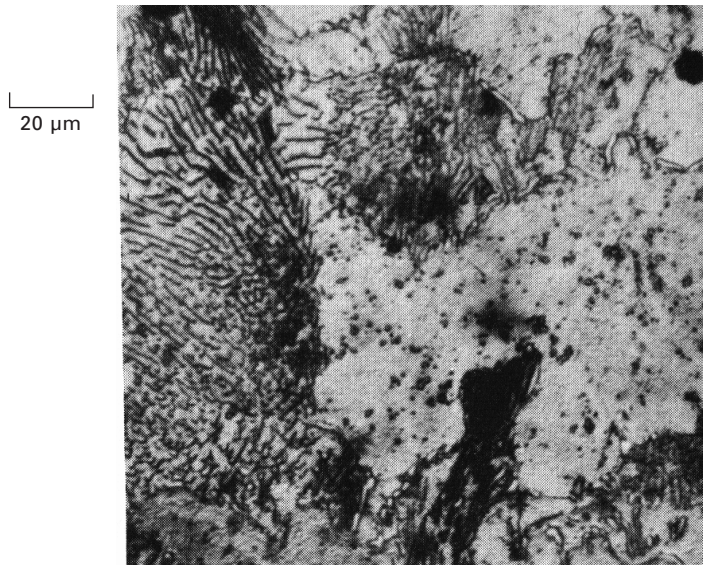
Key words: pearlite, eutectoid decomposition, diffusion control, co-operative growth, interlamellar spacing, orientation relationship, alloy partitioning, co-deformation.

8.1 Introduction

Pearlite is the product of the decomposition of austenite by a eutectoid reaction and comprises a lamellar arrangement of ferrite and cementite. The pearlite reaction provides an excellent example of the historical development of physical metallurgy and the importance of the interaction of experimental observations and the development of quantitative models. It is interesting to note that in the classical work *A History of Metallography*, Smith (1960) refers to Sorby's presentation of the first images of pearlite at the British Association meeting in September 1864 (Sorby, 1864). Smith comments that the images got little response or interest and speculates that this may have been because they lacked a theoretical interpretation at the time. A copy of one of Sorby's original images is reproduced in Fig. 8.1, in which the characteristic lamellar morphology of the two constituent phases, ferrite and cementite, of pearlite is evident.

The techniques of optical metallography improved greatly during the latter part of the 19th century and early 20th century and it was the work of Carpenter and Robertson (1932) that clearly established that pearlite colonies, as they became known, nucleated at prior austenite boundaries during cooling. Davenport and Bain (1930) produced pioneering work which provided a basis for the development of time-temperature-transformation (TTT) diagrams and the ability to quantify and rationalise the role of alloying elements in terms of hardenability and their influence on structure–property relationships in

© Woodhead Publishing Limited, 2012



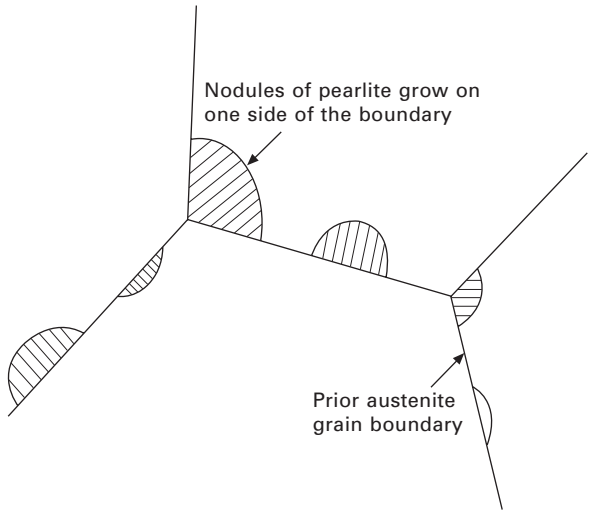
8.1 Reproduction of one of Sorby's original images of a pearlitic structure in a heat treated cast iron (Sorby, 1864).

steels. This was followed by the detailed microstructural approach of Mehl and Hagel (1956) who produced a basic quantitative description by measuring nucleation and growth rates and the interlamellar spacing of pearlite for both plain C and alloy steels.

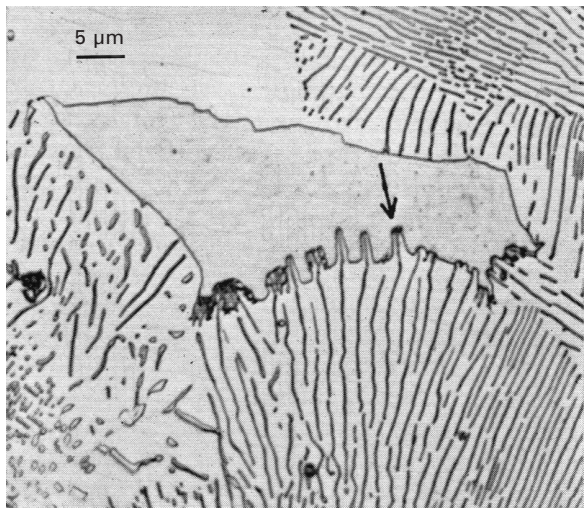
The proceedings of the 1962 AIME conference, edited by Zackay and Aaronson (1962), contain a number of seminal papers on the decomposition of austenite to pearlite, including the work of Cahn and Hagel (1962) which discusses in detail both the analytical and experimental aspects of describing the nucleation and growth kinetics of the pearlite reaction. In addition, the book contains an excellent paper by Kirkaldy (1962) on the theory of diffusional growth and a paper by Hillert (1962) which demonstrates clearly the ability to gather a basic description of a spatially complex three-dimensional structure from precise two-dimensional metallographic sections.

In reviewing the pearlite reaction, it is appropriate to begin with a simplified description of the reaction in Fe-C alloys and then examine in detail the various complexities which arise from the detailed chemical and microstructural features. Thus the simple schematic diagram in Fig. 8.2 indicates that pearlite grows as nodules on the prior austenite boundaries, that each nodule may have different colonies or orientations and that the nodules spread to cover the prior austenite boundaries. By changing the reaction temperature, the spacing or length scale of the pearlitic product can be changed by branching of cementite, as shown in Fig. 8.3.

© Woodhead Publishing Limited, 2012



8.2 Schematic diagram which indicates that pearlite grows as nodules on one side of the prior austenite boundaries and at grain corners.



8.3 Micrograph of a 0.6wt%C steel reacted at 713°C then held for 2 s at 645°C. The fine scale pearlite characteristic of the lower reaction temperature develops by branching of the cementite lamellae (Hillert, 1962).

8.2 An overview of the pearlite reaction

The pioneering work of Davenport and Bain (1930) led to an understanding of the isothermal transformation of austenite and to the development of

© Woodhead Publishing Limited, 2012

models of the kinetics of the transformation. In order to provide an overview of the pearlite reaction, we first need a simple description of the kinetics of the transformation followed by a model to describe the length scale, i.e. lamellar spacing of the pearlitic product and the velocity of the austenite/pearlite interface as a function of the undercooling below the eutectoid temperature.

The pearlite nucleates heterogeneously on one side of the prior austenite boundaries as shown schematically in Fig. 8.2, and ferrite and cementite grow in a co-operative manner as a series of colonies or nodules. The rate of pearlite formation dX/dt depends on the nucleation rate $\dot{N}$ which is the number of product nuclei formed per unit time per unit volume of the untransformed austenite and the rate of growth G (the rate at which the interface advances into the untransformed austenite). If we assume a reaction at constant temperature and let X be the volume fraction of pearlite formed in time t, then

$$\frac{dX}{dt} = GA_f \qquad [8.1]$$

where A_f is the area of the austenite/pearlite interface.

It is useful to define an extended volume fraction X_x and an extended interfacial area A_x. These are the hypothetical volumes and areas the pearlite nodules would have if nucleation and growth had continued with all the austenite still available for transformation. The fraction of A_x not inside other nodules is equal to the untransformed volume $1 - X$ so that $A_f = (1 - X)\, A_x$. We also have $dX_x/dt = GA_x$. Hence, combining these with Eq. [8.1],

$$\frac{dX}{dX_X} = 1 - X \qquad [8.2]$$

which integrates to

$$X = 1 - e^{-X_x} \qquad [8.3]$$

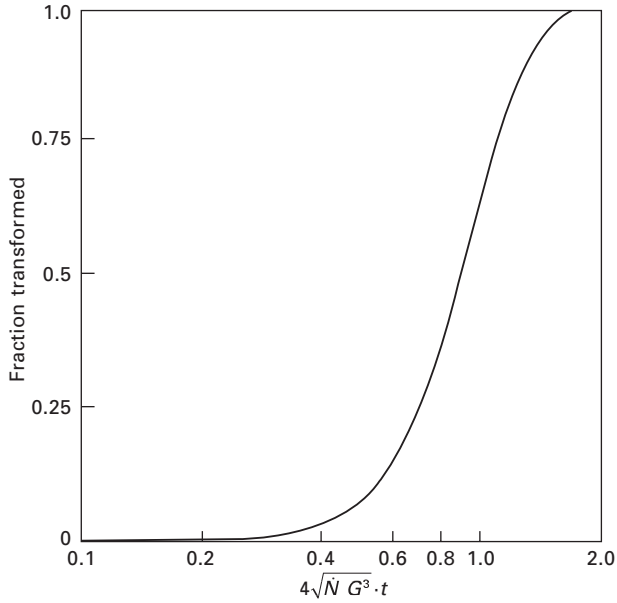
In detail, consideration can be given to a variety of nucleation sites at grain corners, edges, faces, etc. but one representative equation of the form [8.3] is the Johnson–Mehl equation (1939) where

$$X_x = \int_0^t \frac{4}{3}\pi(t - t')^3 G^3 \dot{N}\, dt' = \frac{\pi}{3} G^3 \dot{N} t^4 \qquad [8.4]$$

This gives a typical sigmoidal curve describing the fraction transformed as a function of time, as shown in Fig. 8.4.

The detailed crystallography of the product phases and the parent austenite will be considered in a later section. However, the establishment of a co-operative growth front requires time and thus the rate of colony nucleation increases with time.

© Woodhead Publishing Limited, 2012



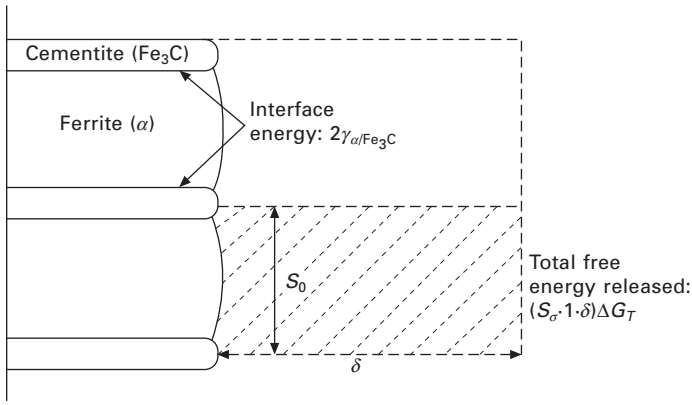
8.4 Typical reaction curve for the increase in volume fraction of pearlite as a function of time according to the Johnson–Mehl equation (Johnson and Mehl, 1939).

The growth of pearlite is a co-operative process which involves the two constituent phases, ferrite and cementite. This can be considered analogous to the growth of a lamellar eutectic from a liquid, and similar models can be applied to the process. However, in the case where the co-operative growth of a eutectic into a liquid occurs, the degree of undercooling is small because the motion of the interface is controlled by heat flow. In contrast, the rate of interface motion in solid state reactions can be controlled by diffusion and thus large undercoolings can occur. It is important to recognise that both volume diffusion and diffusion at the advancing interface are possible transport processes.

The elegant analysis developed by Verhoeven (1975) provides a very clear view of the analogue between eutectic solidification and the eutectoid reaction which produces pearlite, and this will be used here as a basis in order to relate the observed lamellar spacing and the velocity of the pearlite/austenite interface to the undercooling.

If we consider, as shown schematically in Fig. 8.5 which has a height of S_0 (= the pearlite spacing) and a depth of unity length (= 1), the region of pearlite advanced of a distance δ into the prior austenite, then the total free energy released is given by $[(S_0 \cdot 1 \cdot \delta)\Delta G_T]$. Here, ΔG_T is used both to provide the free energy needed to extend the planar interfaces between the ferrite

© Woodhead Publishing Limited, 2012



8.5 Schematic showing the free energy balance when free energy is provided by the transformation of austenite and consumed both by the provision of interfacial energy at the α/Fe_3C interfaces and the free energy required to drive diffusion at the advancing interface.

and cementite and the free energy needed to drive the lateral diffusion of C in austenite (γ phase) to allow the co-operative growth of ferrite (α phase) and cementite (Fe_3C phase). Thus the free energy balance is given by

$$\Delta G_T = \Delta G_s + \Delta G_d = \frac{2\gamma_{\alpha/Fe_3C}}{S_0} + \Delta G_d \qquad [8.5]$$

where ΔG_s and ΔG_d are the free energy per unit volume to create interfaces and to drive the diffusion, respectively; γ_{α/Fe_3C} is the surface energy per unit area at the interface α/Fe_3C.

The minimum spacing, $S_{\min}$, will arise if all the available free energy is used to extend the ferrite/cementite interfaces, thus ΔG_d will be zero and

$$S_{\min} = \frac{2\gamma_{\alpha/Fe_3C}}{\Delta G_T} \qquad [8.6]$$

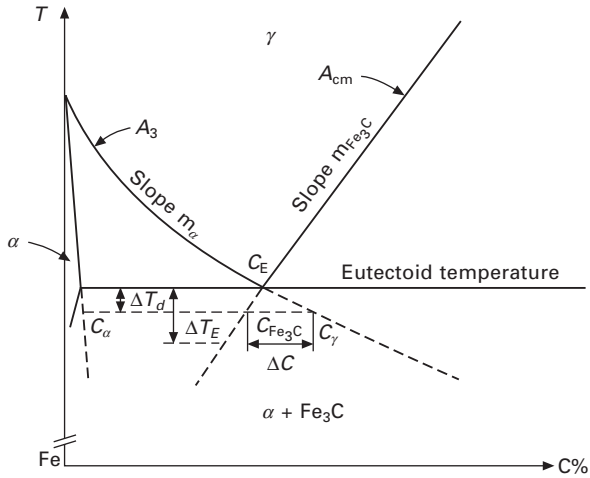
If the volume free energy released is proportional to the undercooling ΔT_E, then we can express ΔG_d approximately,

$$\Delta G_d = \Delta S_p \cdot \Delta T_d = \Delta S_p \cdot \Delta T_E \cdot \left[1 - \frac{S_{\min}}{S_0}\right] \qquad [8.7]$$

where ΔS_p is the entropy change per unit volume for the pearlite reaction.

Thus we can give the following expression for the composition difference ΔC_d to drive diffusion in terms of the undercooling ΔT_E, the pearlite spacings S_0 and $S_{\min}$ as well as the slopes m_α and m_{Fe_3C} of the A_3 and A_{cm} lines on the Fe-C phase diagram, as shown schematically in Fig. 8.6:

© Woodhead Publishing Limited, 2012



8.6 Schematic Fe-C diagram showing the relationship of the compositional difference driving diffusion ΔC_d to the total undercooling ΔT_E if it is assumed that the phase diagram at the eutectoid point can be approximated by linear extrapolations.

$$\Delta C_d = \Delta T_E \cdot \left[1 - \frac{S_{\min}}{S_0}\right] \cdot \left[\frac{1}{|m_\alpha|} + \frac{1}{m_{Fe_3C}}\right] \quad [8.8]$$

By relating the rate R of motion of the pearlite interface to ΔC_d as in

$$R = \frac{2D\Delta C_d}{S_0(C_\gamma - C_\alpha)} \quad [8.9]$$

where D is the diffusion coefficient of carbon, C_γ is the composition in γ phase and C_α is the composition in α phase, as defined in the Fig. 8.6, we can obtain an expression for the rate of motion:

$$R = \frac{2D\Delta T_E}{S_0(C_\gamma - C_\alpha)}\left[\frac{1}{|m_\alpha|} + \frac{1}{m_{Fe_3C}}\right]\left[1 - \frac{S_{\min}}{S_0}\right] \quad [8.10]$$

A simplified form of Eq. [8.10] is:

$$R = K \cdot \Delta T_E \cdot \left[1 - \frac{S_{\min}}{S_0}\right] \Big/ S_0 \quad [8.11]$$

where $K = \dfrac{2D}{(C_\gamma - C_\alpha)}\left[\dfrac{1}{|m_\alpha|} + \dfrac{1}{m_{Fe_3C}}\right]$ is a constant.

There has been much debate over the basis for determining the optimum spacing S_{opt} between two cementite plates. The proposition of Zener (1946) that the spacing is selected to give maximum growth rate is widely used,

© Woodhead Publishing Limited, 2012

although others, such as the maximum rate of entropy production, have also been used (Hashiguchi and Kirkaldy, 1984). Differentiating Eq. [8.11] with respect to S_0 for a given ΔT_E leads to the result $S_0 = 2S_{\min}$ as the optimum spacing, S_{opt}. By substituting into Eq. [8.11]

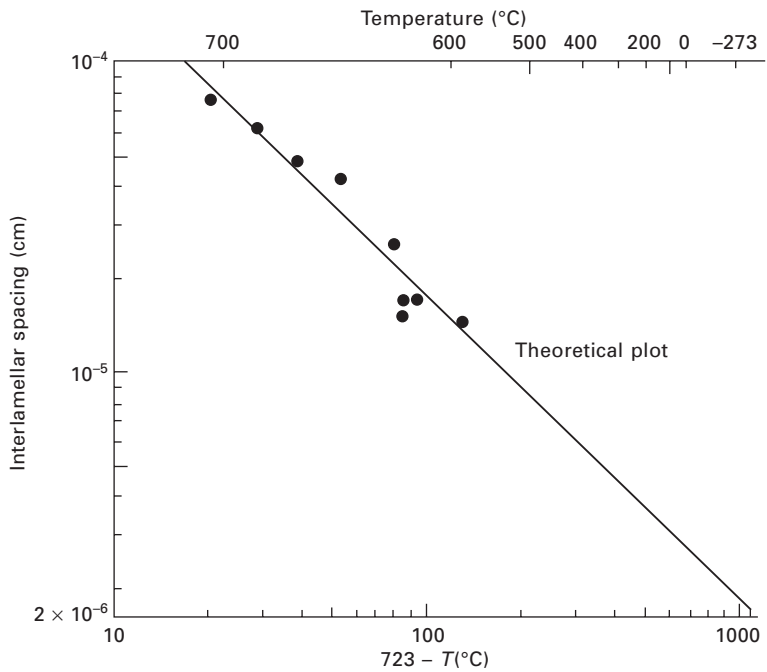
$$\Delta T_E = \frac{\Delta G_T}{\Delta S_P} = \frac{\dfrac{2\gamma_{\alpha/Fe_3C}}{S_{\min}}}{\Delta S_P} \text{ and } S_0 = 2S_{\min} = S_{\text{opt}},$$

we have now a rate equation in the simple form

$$R = \cdot \frac{K'}{S_{\text{opt}}^2} \qquad [8.12]$$

with the constant $K' = 2K/\Delta S_{\text{P}}$.

A great deal of careful experimental work by Brown and Ridley (1969) and others has been treated by Puls and Kirkaldy (1972) to include aspects such as the compositional dependence of the diffusion coefficient of C in austenite. In addition, the interlamellar spacing of the pearlite has been measured as a function of transformation temperature as shown in Fig. 8.7 (Hawkes *et al.*, 1942).



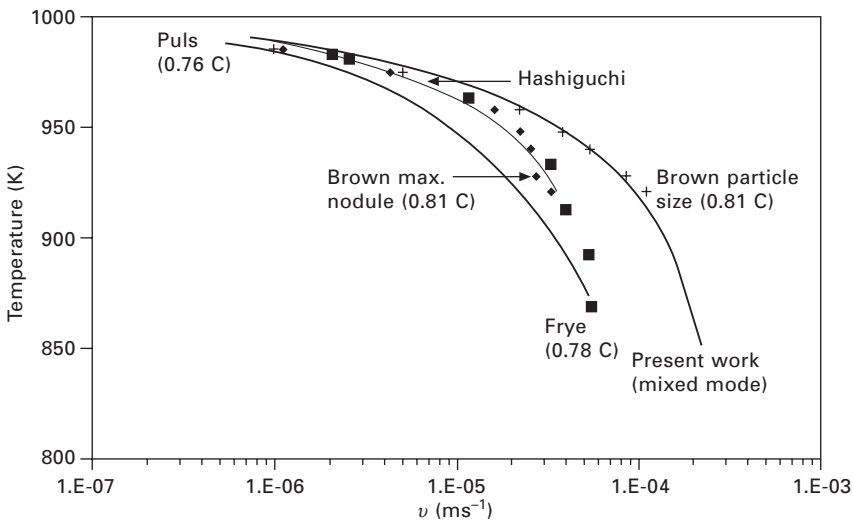
8.7 Classical data on the variation of interlamellar pearlite spacing as a function of the isothermal transformation (Hawkes *et al.*, 1942).

© Woodhead Publishing Limited, 2012

Much of the existing data suggests that the controlling diffusional mechanism during pearlite growth is volume diffusion of C in austenite. However, a number of other proposals have been made including an elegant model by Hashiguchi and Kirkaldy (1984) which envisaged simultaneous diffusion in the austenite and at the interface. Nakajima *et al*. (2006) have proposed a phase field model which incorporates thickening of the cementite plates behind the migrating interface by diffusion in the ferrite. A very recent paper by Pandit and Bhadeshia (2011) examines in detail the concept of mixed diffusional fluxes and appears to give good agreement with a range of experimental results, as shown in Fig. 8.8.

In addition to defining the detailed diffusion process, consideration is also needed of the surface energies both for the ferrite/cementite interfaces and the migrating pearlite/austenite interface. There is a considerable scatter in the values for the cementite/ferrite interface determined by a variety of techniques, but the value deduced for the austenite/pearlite interface is of the order 0.6 J/m^2 (Puls and Kirkaldy, 1972), which is consistent with that expected for the migration of an incoherent high angle grain boundary.

Although an excellent framework for the understanding of the pearlite reaction in plain C steels exists, the understanding of the detailed transport events at the interface still needs to be clearly defined including the role of interface diffusion and the possible effects of plastic strain at the growing



8.8 Influence of temperature on the rate of pearlite growth including a number of sources of experimental data and models of growth. The line termed 'present work' refers to the recent model by Pandit and Bhadeshia (2011).

© Woodhead Publishing Limited, 2012

interface at high growth rates, as opined by Verhoeven and Pearson (1984).

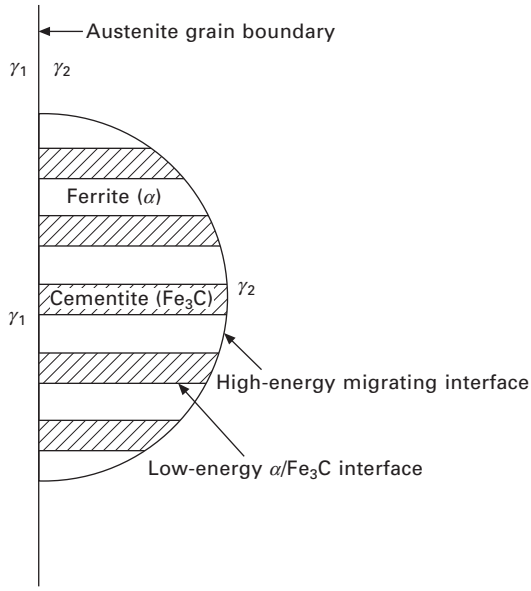
In addition to isothermal studies of pearlite growth, other methods have been used, such as continuous cooling with hot stage microscopy and more recently studies using a three-dimensional neutron depolarisation technique (Offerman *et al.*, 2003), which probes the volume fraction of the magnetic phase, the mean size of the magnetic phase and its spatial distribution. This technique provides valuable information about both the rate of formation and spatial distribution of the pearlite nuclei.

An alternative transformation method to isothermal transformation is to use an imposed temperature gradient to control the velocity of the pearlite transformation front. The technique, which is similar to the directional solidification of eutectics, was pioneered by Bolling and Richman (1970) and produces an austenite zone of the order of 1 cm in length which can be produced in a rod and moved at speeds in the range of 0.1–500 μm/s to produce a temperature gradient of the order of 2000°C/mm. This technique was also used by Chadwick and Edmonds (1973) to study directional growth of pearlite and extended to the study of a ternary Fe-0.8 wt%C-Co alloy (Mellor and Edmonds, 1977). In a subsequent series of two articles, Pearson and Verhoeven have compared data from isothermal experiments and those obtained by forced velocity growth (Pearson and Verhoeven, 1984; Verhoeven and Pearson, 1984). The agreement between the techniques is satisfactory and establishes a direct relationship between interface velocity and interlamellar spacing, suggesting that volume diffusion is controlling at higher temperatures and possibly interface diffusion is controlling at lower temperatures. These authors also observed that there appears to be a maximum growth rate of ~ 100 μm/s. Above this rate, the pearlite product becomes increasingly rod-like and degenerate. An interesting feature of the observations was that, unlike the case for eutectic solidification, the transformation does not yield colonies aligned with the growth direction and in addition there are changes in morphology of the growing pearlite when other prior austenite boundaries are encountered. Thus it is clear that there remain a number of aspects of the growing interface to be understood particularly at high growth rates.

8.3 Crystallographic aspects of the reaction

As pearlite grows by a co-operative process in which orthorhombic cementite and BCC ferrite grow from the grain boundaries of the prior austenite, there are a variety of crystallographic relationships between the participating phases to consider. These are illustrated schematically in Fig. 8.9. We need to consider the relationships between the lamellar product phases and the relationship of each of these phases with the austenite grain into which the colony grows and the austenite grain into which the pearlite does not

© Woodhead Publishing Limited, 2012



8.9 Schematic showing the various interfaces which need to be defined for a crystallographic description of the growing pearlite colony.

advance. In most steels, this task is complicated by the fact that, on cooling a partially transformed pearlite product from the reaction temperature, the untransformed austenite decomposes to martensite. The elegant experiments conducted by Dippenaar and Honeycombe (1973) used a steel containing 0.79 wt% C with 11.9 wt%Mn to ensure the stability of the untransformed austenite on cooling.

It is important to note that this steel is of a hypereutectoid composition, so that the formation of pearlite is preceded by the formation of proeutectoid grain boundary cementite, as isolated particles rather than as continuous films of cementite along the austenite boundaries. This microstructural dispersion allowed a more comprehensive analysis of the crystallographic relationships between the phases.

Dippenaar and Honeycombe (1973) were able to determine, in reference to Fig. 8.9:

- the ferrite-cementite relationship within various pearlite nodules,
- the ferrite-austenite relationship for both austenite grains γ_1 and γ_2,
- the cementite-austenite relationship for both austenite grains γ_1 and γ_2,
- the orientation relationship between the prior particles of grain boundary cementite and the cementite within the growing pearlite nodule,
- in agreement with a number of previous investigations (Bagaryatski, 1950;

© Woodhead Publishing Limited, 2012

Pitsch, 1962; Lupton and Warrington, 1972), the observed orientation relationships are summarised below:

– the Pitsch relationship:

$$(100)_{Fe_3C}2.6° \text{ from } [13\bar{1}]_\alpha \quad (010)_{Fe_3C}2.6° \text{ from } [113]_\alpha \quad (001)_{Fe_3C}//[5\bar{2}\,\bar{1}]_\alpha \qquad [8.13]$$

– the Bagaryatski relationship:

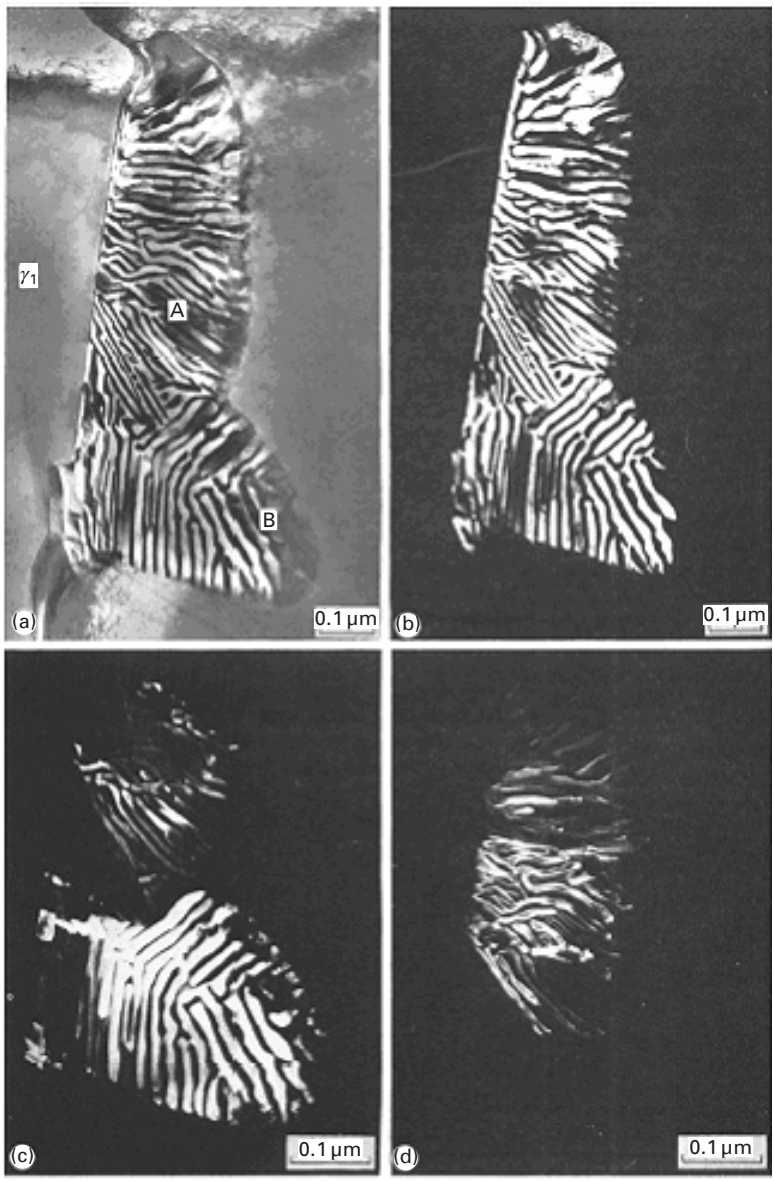
$$(100)_{Fe_3C}//[0\bar{1}1]_\alpha \quad (100)_{Fe_3C}//[1\bar{1}\,\bar{1}]_\alpha \quad (001)_{Fe_3C}//[211]_\alpha \qquad [8.14]$$

In all cases they found that both the pearlitic cementite and the ferrite were not related in a defined way to the austenite into which they were growing, which is consistent with a number of previous postulations and with the assumption that the migrating interface can be regarded as an incoherent high energy grain boundary.

It was established that the existence of the Pitsch relationship implied that nucleation occurred by direct contact of both the growing phases with the adjacent grain of prior austenite. In contrast, pearlite colonies exhibiting the Bagaryatski relationship appeared to nucleate on proeutectoid cementite pre-existing at the prior austenite grain boundaries. This observation is in agreement with the earlier conclusion by Hillert (1962) based on careful analysis of multiple sections by optical metallography. Thus the ferrite in the Bagaryatski related colonies has no crystallographic relationship with the adjacent austenite grain. However, the cementite both at the grain boundary and in the pearlite colony is related to the adjacent austenite grain γ_1 as defined in Fig. 8.9.

An additional important finding of Dippenaar and Honeycombe (1973) was the investigation of complex pearlite colonies of the type shown in Fig. 8.10. The selected area electron diffraction analysis showed that the ferrite has two different orientations. This can arise if, at different points on the original prior austenite boundary, the ferrite has formed with two different variants of the Kurdjumov–Sachs orientation relationship from the adjacent austenite, resulting in subsequent growth in two separate colonies. This observation has important implications because it implies that a variety of factors, such as solute segregation, local precipitation or plastic deformation at the prior austenite boundaries, may change the progress of the pearlite reaction. This topic is discussed later in relation to the effects of Si and V alloying additions. A number of contributions to the understanding of the important effects of V on the nucleation of grain boundary carbides and on precipitation at the migrating austenite boundaries have been made by Khalid and Edmonds (1993, 1994). This aspect is of importance not only in the understanding of the various processes which can occur at the austenite

© Woodhead Publishing Limited, 2012

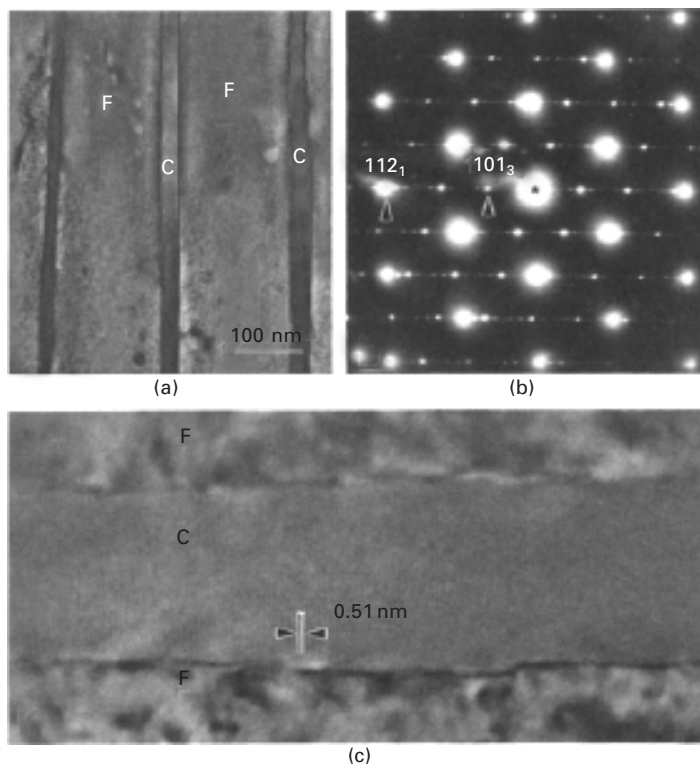


8.10 A TEM study showing a complex array of pearlite nodules in both a bright field image (a) and dark field images (b), (c) and (d). In image (b) the ferrite lamellae appear to have the same orientation. However, on tilting and imaging with reflections from areas A and B images (c) and (d) show that the ferrite has two different orientations. This suggests that ferrite nucleates at different points on the austenite grain boundary where two different variants of the Kurdjumov-Sachs relationships are operative (Dippenaar and Honeycombe, 1973).

© Woodhead Publishing Limited, 2012

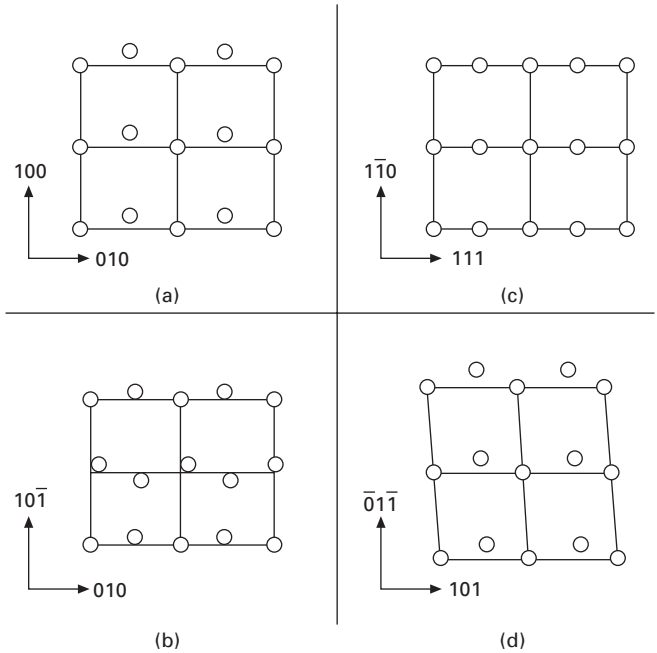
boundaries but from the practical viewpoint of improving the properties of pearlitic rail steels.

In addition to the overall crystallography of the pearlite colonies, it must be recognised that each colony is essentially a duplex single crystal in which the orthorhombic cementite and the BCC ferrite have conjugate interfacial planes which result from the co-operative growth process and are usually coherent or semi-coherent in nature. These interfacial planes or habit planes are not simple to investigate and a very elegant study by Zhou and Shiflet (1992) using large angle tilting and high resolution electron microscopy has provided a very clear picture of the process of atomic matching between the ferrite and cementite in individual pearlite colonies. Their studies showed that for the Bagaryatski relationship, the habit plane of the cementite was (001) where the planes have a spacing of 0.67 nm and appear to be very smooth (Fig. 8.11). In the Pitsch relationship the habit planes are (001) cementite and (215) ferrite. The atomic configurations of the various planes of cementite and ferrite are shown schematically in Fig. 8.12, where the



8.11 Detailed image of pearlite exhibiting the Bagaryatski relationship including a direct lattice image with the spacing of the (001) cementite planes revealed (Zhou and Shiflet, 1992).

© Woodhead Publishing Limited, 2012



8.12 Configurations of Fe atoms in the (001) (a) and (101) (b) planes of cementite and the similar atomic configurations on the (11$\bar{2}$) (c) and ($\bar{2}\bar{1}$5) (d) planes (Zhou and Shiflet, 1992).

Table 8.1 Orientation relationships and habit planes of ferrous pearlite

Number	Combination	Habit plane	Orientation relationship	Comment
1	a + c	$(001)_c//(11\bar{2})_f$	$[100]_c//[1\bar{1}0]_f$ $[010]_c//[111]_f$ $[001]_c//[11\bar{2}]_f$	Bagaryatsky
2	b + c	$(101)_c//(11\bar{2})_f$	$[010]_c//[111]_f$ $(101)_c//(11\bar{2})_f$	Isaichev
3	a + d	$(001)_c//(\bar{2}\bar{1}5)_f$	$[100]_c$ 2.6 deg from $[\bar{3}1\bar{1}]_f$ $[010]_c$ 2.6 deg from $[131]_f$ $[001]_c//[\bar{2}\bar{1}5]_f$	Pitsch–Petch
4	b + d	$(101)_c//(\bar{2}\bar{1}5)_f$	$[100]_c//[1\bar{2}5]_f$ $[010]_c//[131]_f$ roughly $[001]_c//[\bar{3}11]_f$	Unknown

open circles refer to the positions of only the iron atoms. The summary of observed orientation relationships and habit planes is given in Table 8.1 (Zhou and Shiflet, 1992).

Zhou and Shiflet (1991) have also described the curvature of the lamellae in pearlite in terms of the height and density of surface steps, as illustrated in

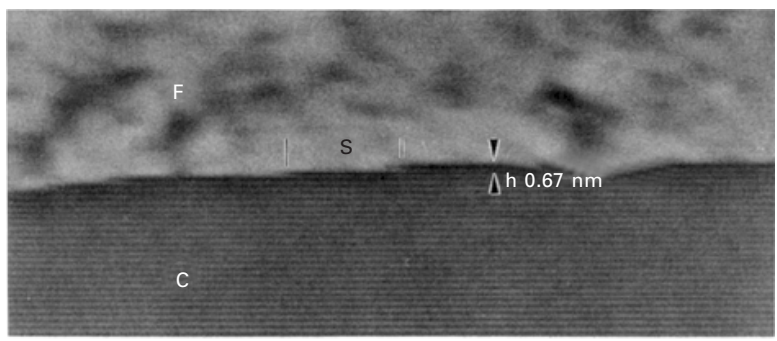
© Woodhead Publishing Limited, 2012

Fig. 8.13. These types of observation are of great importance in understanding the interfacial energy and detailed structure of the habit planes resulting from co-operative growth and the manner in which curvatures of the lamellar pearlite are accommodated. They may also be of value in understanding the various modes of co-deformation of the phases during plastic flow and the nature and distribution of slip events needed both to allow uniform thinning of the cementite during drawing and also co-operative kinking processes.

8.4 The role of alloying elements

Alloying elements X can influence the pearlite reaction in a variety of ways. The most direct consequence is that elements can be considered in terms of whether they stabilise the austenite (e.g. Mn, Ni) or the ferrite (e.g. Cr, Mo, Si) phases. This determines how they will influence the form of the Fe-C-X phase diagram so as to change the eutectoid temperature and the eutectoid composition. In addition, the substitutional elements can have different solubilities in the cementite and ferrite phases, i.e. they can partition between the phases. Furthermore, their rates of diffusion are much slower than that of C. Hence they are able to change the growth rate of pearlite and, thus, by moving the nose of the C-curve and changing the form of the TTT diagram, change the hardenability. This process will be discussed in detail in the section on pearlite growth in alloy steel systems.

Let us first consider ways in which alloying elements can influence the organisation and morphology of the pearlite reaction. Strong carbide formers such as Cr can enter into solid solution in the cementite. Entin (1962) observed that cementite in a 3.5 wt% Cr-0.4 wt% C steel could contain 20 wt% Cr in solid solution and in steels with higher Cr contents the lamellar colony form of the pearlite is maintained, but the cementite is replaced by the chromium carbide Cr_7C_3. Generally it is observed that the morphology of the alloy

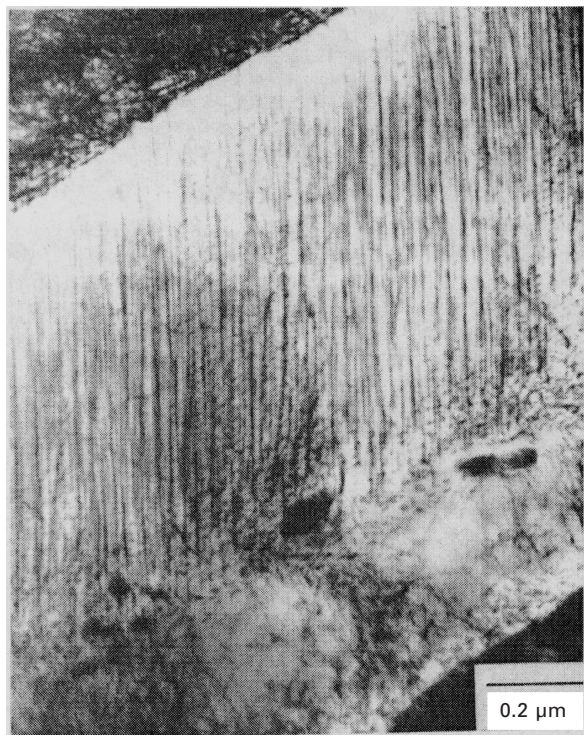


8.13 Lattice image of pearlitic cementite with the Bagaryatski relationship showing how surface steps take up the curvature of the lamellae (Zhou and Shiflet, 1992).

© Woodhead Publishing Limited, 2012

carbide phase is more branched and irregular than in Fe-C pearlite, and it is unlikely that there are simple planar habit planes between the carbide and ferrite constituents. In addition, in many isothermally transformed alloys a much finer arrangement of the alloy carbide phase can develop in which the alloy carbides are fibrous in form with a diameter of the order 30–50 nm. Although these structures grow in a co-operative manner between the fibrous carbide and the ferrite (Bungardt *et al.*, 1958), they do not grow as nodules but often as a planar front growing away from the prior austenite boundary, as shown in Fig. 8.14. Fibrous carbides of this type have been observed in a variety of alloy systems including alloys with Cr, Mo, Ti and V. In view of the fine scale of the fibrous carbides, it may well be that they are effectively whiskers, and thus developing techniques for control of these transformations may yield materials with attractive combinations of mechanical properties.

We can also consider the influence of alloying elements in terms of the competitive processes which can occur at the prior austenite boundaries. Bhadeshia and Honeycombe (2006) provide a concise and valuable comparison



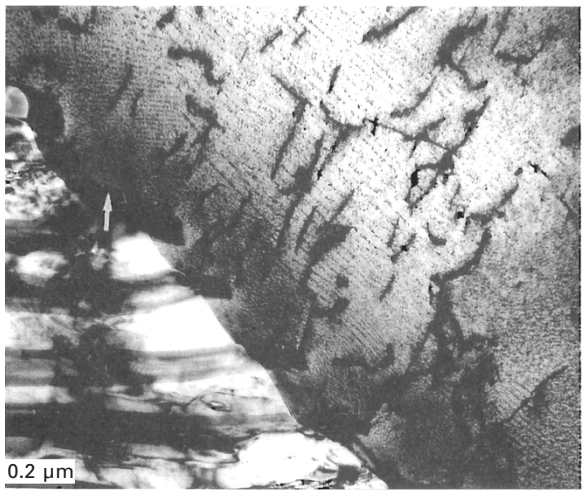
8.14 TEM image taken in an Fe-Mo-C alloy transformed at 650°C showing the coupled growth of an array of fine fibres of Mo_2C growing away from the prior austenite boundary (Honeycombe, 1976).

© Woodhead Publishing Limited, 2012

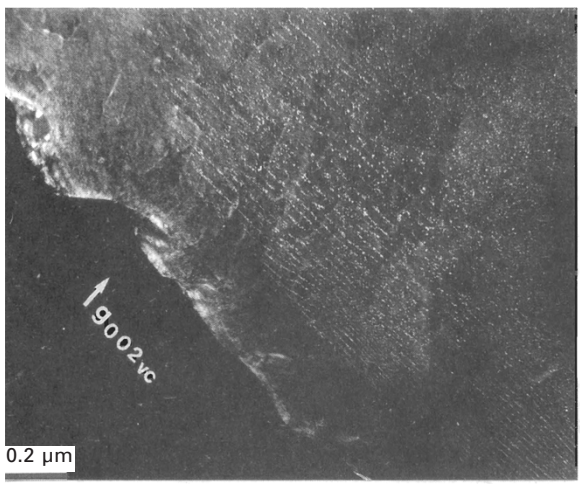
of the morphologies and distributions of alloy carbides. It is well known, in a variety of reactions including the tempering of martensite and in the bainite transformation, that the addition of Si retards cementite formation because Si is rejected by the carbide phase leading to an increase in the Si content of the surrounding matrix. A very interesting study of the combined effects of additions of Si and V was performed by Han *et al*. (1995) using a variety of hypereutectoid compositions and transformation temperatures in the range 550–650°C. They found that the alloy additions resulted in the preferential formation of a variety of non-lamellar products at the prior austenite boundaries. A number of reactions were observed at the prior austenite boundaries including the formation of discreet particles of cementite. In addition, films of grain boundary ferrite were observed, some of which contained rows of embedded VC formed at the migrating ferrite interface. Davenport and Honeycombe (1971) used the term 'interphase precipitation' to describe the distribution of carbides such as V_4C_3 which are nucleated at the austenite ferrite boundary at successive positions of the transformation front. This process has been observed in a wide range of alloy systems with much coarser distributions of alloy carbides formed in Cr and W containing steels. An example of these structures is shown in Fig. 8.15 and the interpretation of the structures is summarised in the schematic diagram in Fig. 8.16. Han *et al*. (1995) also observed that the presence of V also drastically reduced the austenite grain size. This increases the grain boundary area and may result in the formation of smaller, more isolated, cementite particles. The results suggest that the formation of either isolated cementite particles and films of grain boundary ferrite can frustrate the nucleation of the pearlite reaction resulting in an incubation stage prior to the development of the coupled growth required for pearlite formation.

In addition to the influence of alloying elements on competitive processes which can occur at the initial prior austenite boundaries, they can perturb events at the migrating pearlite interfaces, particularly at low transformation temperatures. Early metallographic studies of Cr-containing steels (Lyman and Troiano, 1946) showed the occurrence of fine scale decomposition products. The study by Kaya and Edmonds (1998) has clearly elucidated the drastic changes in the morphology of the transformation products in Fe-0.4 wt% C-Cr alloys with 3.6 to 10 wt% Cr. The TTT diagram for a steel with 3.5% Cr is shown in Fig. 8.17. If this alloy is isothermally transformed at 700°C, it forms a lamellar pearlite with M_7C_3 carbides by the migration of a coupled growth front. However, as the transformation temperature is lowered, the morphology becomes very irregular with a series of spikes protruding from the interface. These are composed of acicular structures with a central spine of alloy carbide surrounded by a sheath of ferrite, as illustrated in Fig. 8.18. The ferrite and alloy carbide appear to be related by the following relationship:

© Woodhead Publishing Limited, 2012



(a)



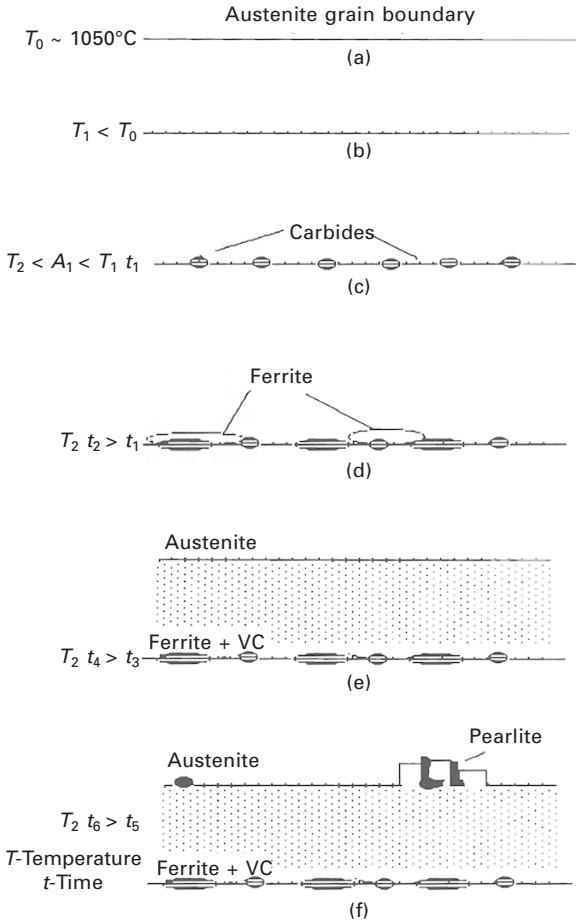
(b)

8.15 Micrograph showing the detailed nature of the grain boundary ferrite in an Fe-0.79 wt% C-0.62 wt% Mn-0.22 wt% Si-0.2 wt% V steel transformed at 650°C in TEM bright-field image (a) and dark-field image (b) showing small vanadium carbides in the grain boundary ferrite (Han *et al.,* 1995).

$$(100)_{\alpha}//[11.0]_{M_7C_3}$$
$$(001)_{\alpha}//[00.1]_{M_7C_3} \qquad [8.15]$$

The individual regions of ferrite thicken and may show interphase precipitation of fine scale carbides. In the alloys with higher Cr content, the conventional nodular pearlite was not observed, which suggests there are two competing

© Woodhead Publishing Limited, 2012



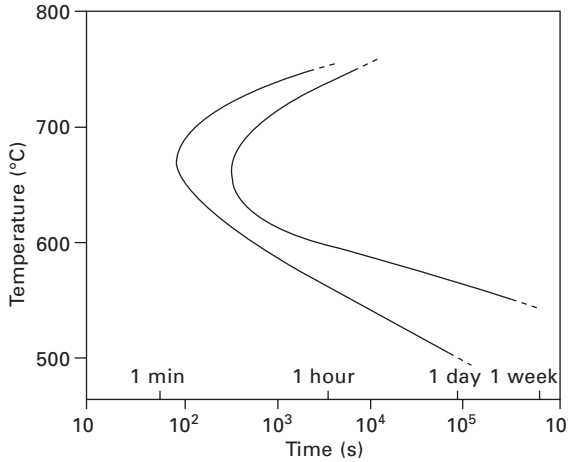
8.16 Sequence of events that can take place at an austenite boundary on cooling showing that a variety of structures can be formed prior to the establishment of conditions favourable to the co-operative growth of pearlite (Han *et al.,* 1995).

transformation mechanisms operative. These mechanisms not only differ in resultant morphology but the alloy partitioning is greater in the pearlitic regions and the growth rate is slower. These observations suggest that a variety of oriented growth processes can arise at lower transformation temperatures depending on both alloy content and the detailed structure of the migrating interface.

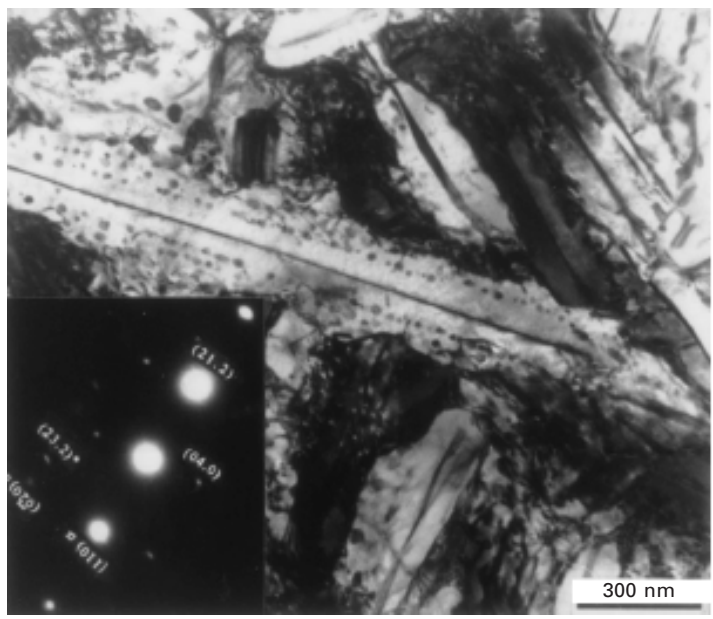
8.4.1 Alloy partitioning during pearlite growth

If consideration is given to the formation of pearlite in alloy systems Fe-C-X, where X is Mn, Ni, Cr ..., then the definition of the conditions at the

© Woodhead Publishing Limited, 2012



8.17 TTT diagram of an Fe-0.4 wt% C-3.5 wt% Cr steel reproduced after Kaya and Edmonds (1998).



8.18 TEM image of an Fe-0.4 wt% C-3.5 wt% Cr steel partially transformed at 650°C showing needles of ferrite with a central rib of carbide and interface precipitation of $M_{23}C_6$ within the ferrite needle (Kaya and Edmonds, 1998).

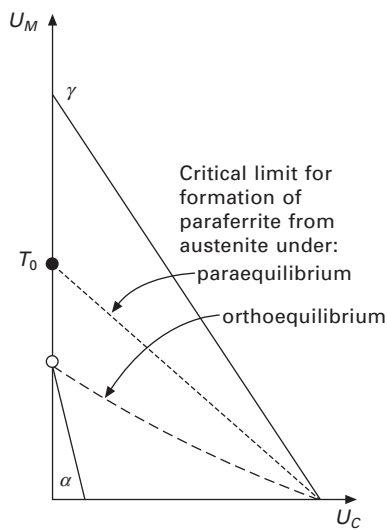
migrating interface is complicated by both the diffusivities of C and X in austenite, which may differ by several orders of magnitude and by the large solubilities of X in the parent and product phases. Thus, it is possible

© Woodhead Publishing Limited, 2012

to have bulk partitioning of X in the transformation products (Sharma *et al.*, 1979). Hultgren (1947) was the first to distinguish the case where the alloy element redistributes between the ferrite and carbide phases (which he termed ortho-pearlite) and the case where there is no redistribution (which he termed para-pearlite). He further suggested that the two types of pearlite formed under different conditions of local equilibrium at the pearlite austenite interface.

It was the seminal work of Hillert (1969, 1981) that provided the framework for the understanding of a number of phase transitions in alloy steels, which extended the concepts of Hultgren using the concepts of isoactivity lines on ternary diagrams of the type shown schematically in Fig. 8.19. Hillert was able to rationalise situations such as those observed by Cahn and Hagel (1962) where the pearlite growth velocity decreased and the pearlite spacing increased with time (Han *et al.*, 1995) due to the partition of the alloying elements. In addition, Hillert's models provide an understanding of the results of Pickelsimer *et al.* (1960) in which ortho-pearlite was formed at high transformation temperatures with full partitioning while a broad range of transition to para-pearlite occurred at lower transition temperatures. This is also in accord with the excellent early high-resolution microprobe studies by Al-Salman *et al.* (1979) who made *in situ* measurements of the partitioning of alloying elements between the ferrite and cementite phases.

There has been much experimental work to investigate the interfacial conditions governing pearlite growth using a comparison of experimental and



8.19 Comparative limit for the formation of para- and ortho-equilibrium in the binary Fe-Mn system. T_0 is the point of equal Gibbs free energy (Hillert, 1969).

© Woodhead Publishing Limited, 2012

calculated growth rates. However, advances in electron microscopy methods now enable local compositions and compositional profiles across the pearlite/austenite interface to be determined directly. The work by Hutchinson *et al*. (2004) provides an excellent example of the use of analytical transmission electron microscopy (TEM) to measure Mn profiles and was interpreted using the work of Hillert as a basis. An example of the use of analytical TEM to determine the Mn distribution across the austenite/pearlite interface and in the product phases is shown in Fig. 8.20.

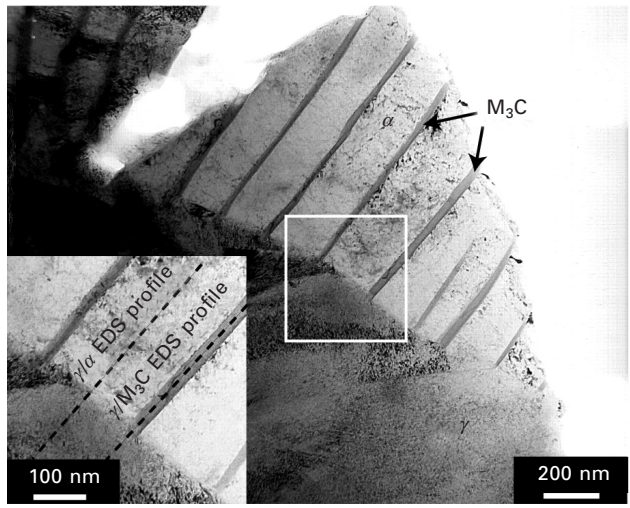
In the study by Hutchinson *et al*. (2004), a series of Fe-C-Mn alloys were designed using the Calphad method (Saunders and Miodownik, 1998) and isothermal reaction temperatures between 575°C and 650°C were chosen in order to have pearlite growth in either the (α +M_3C) field or in the (α + γ + M_3C) field. The evolution of the pearlite was followed by optical and scanning electron microscopy (SEM) observations plus analytical TEM. The TEM samples were carefully prepared by a combination of focused ion beam (FIB) milling and electro-polishing so that specific areas could be accurately located and analysed to establish the Mn concentration by energy dispersive X-ray analysis in the TEM, even for samples containing small volume fractions of pearlite.

The results clearly showed that pearlite grown in the (α + M_3C) field grew under steady-state conditions as illustrated in Figs 8.21 and 8.22. It can be seen in Fig. 8.21 that the pearlite has a time invariant interlamellar spacing. The associated analytical TEM image in Fig. 8.22 revealed that the Mn content of α and M_3C phases is constant indicative of steady-state growth conditions. In contrast, the pearlitic structures grown in the (α + γ + M_3C) field exhibited a lamellar spacing which increased with time, as shown in Fig. 8.23. The associated analytical TEM data (Fig. 8.24) shows that the Mn content of α and M_3C phases increases during the growth period. These results are thus consistent with growth under non-steady-state conditions.

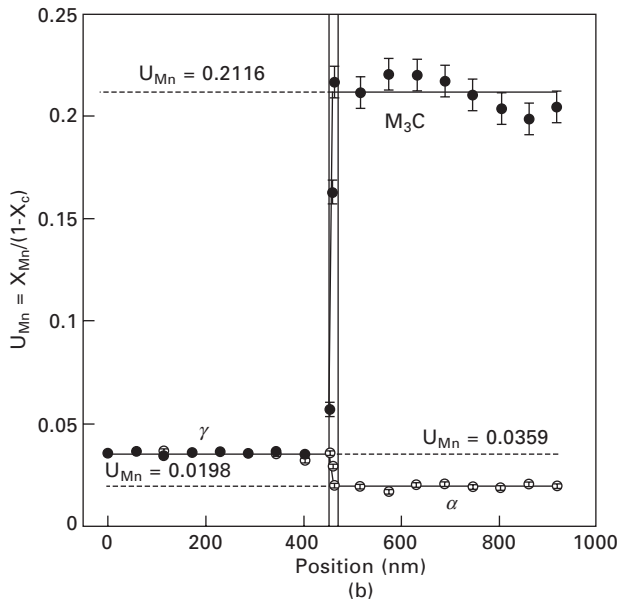
8.5 The deformation of pearlite

The current brief review is concerned largely with the detailed microstructural aspects of the transformation of austenite to pearlite. However, deformed pearlitic steels are the basis for important engineering applications such as bridge cables and high strength tyre cord and thus some comment on the deformation characteristics is deemed appropriate. In addition, the deformation of pearlite represents a classical case of the co-deformation of two interpenetrating structures and thus raises a number of important fundamental questions regarding the nature and spatial distribution of the plasticity processes which are operative. The deformation of pearlite is complicated by the fact that it requires the co-deformation of a directionally

© Woodhead Publishing Limited, 2012



(a)



(b)

8.20 Example of the use of analytical TEM to determine the Mn distribution across the γ/pearlite interface and in the product phases: (a) bright-field TEM image and (b) the Mn profile across the γ/α and γ/M_3C interfaces labelled in (a) (Hutchinson *et al.*, 2004).

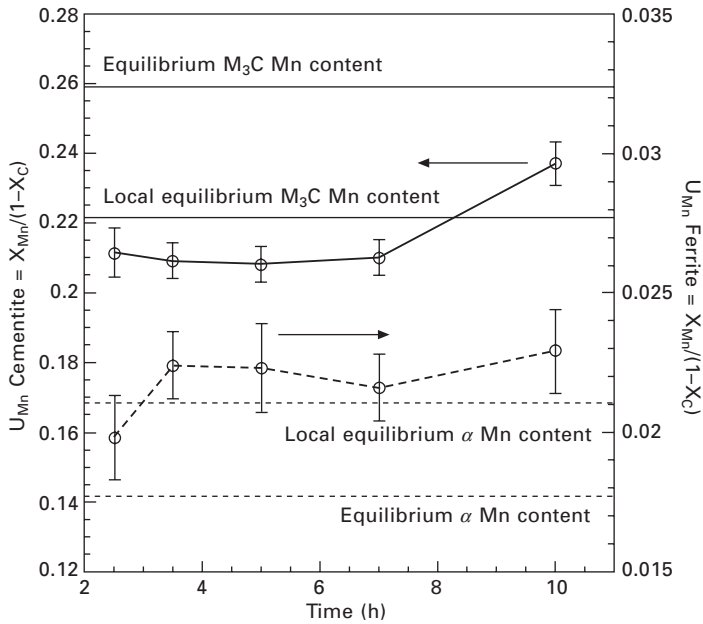
bonded carbide phase and BCC ferrite to very large plastic strains under a variety of stress states.

It is well established that in tensile deformation, cementite located at

© Woodhead Publishing Limited, 2012

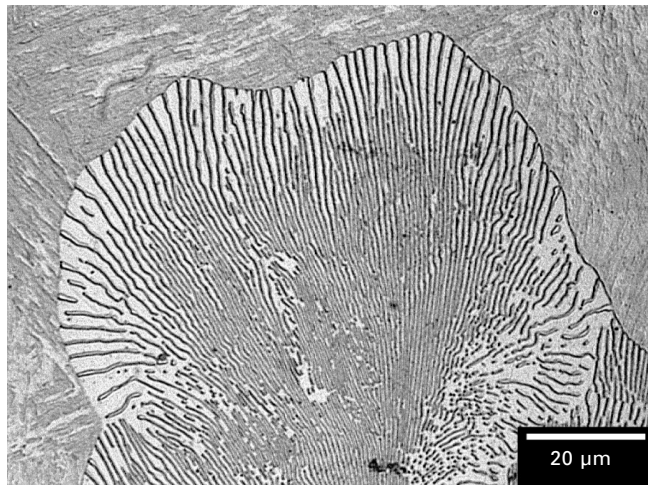


8.21 Optical micrograph showing the structure of an Fe-2.46%C-3.5%Mn steel isothermally transformed in the (α + M_3C region) at 625°C for 14 h. The interlamellar spacing is constant throughout consistent with steady-state growth but increases when colonies impinge (Hutchinson *et al.*, 2004).

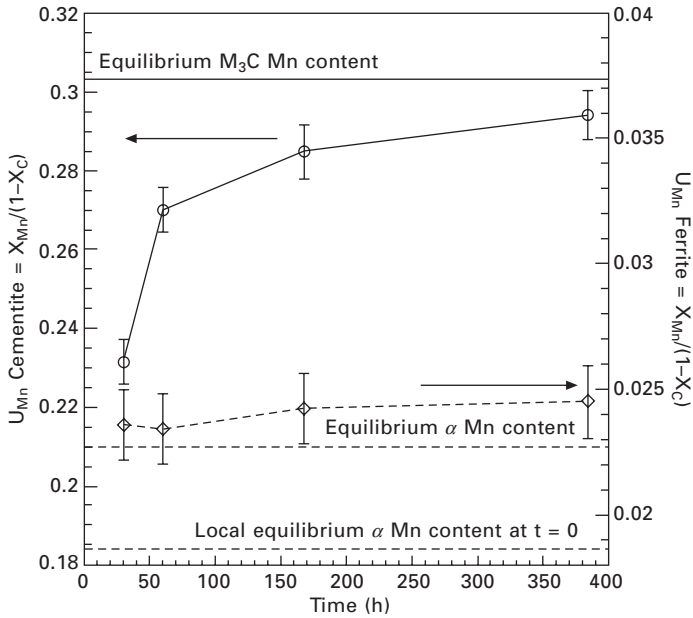


8.22 Plot of the measured Mn distribution for the steel shown in Fig. 8.21. The Mn contents in the ferrite and M_3C phases are consistent with local equilibrium values. The increase in Mn content of the M_3C after 10 h is due to colony impingement (Hutchinson *et al.*, 2004).

© Woodhead Publishing Limited, 2012



8.23 Alloys transformed in the (α + γ +M_3C) field exhibited non-steady-state growth characterised by a lamellar spacing which increased with time as shown for the colony in this optical micrograph (Hutchinson *et al.*, 2004).



8.24 Plot of the measured Mn distribution in the ferrite and M_3C phases as a function of reaction time for the steel shown in Fig. 8.23. The variations in composition with time are consistent with a model for non-steady-state growth (Hutchinson *et al.*, 2004).

© Woodhead Publishing Limited, 2012

grain boundaries fractures and serves as the heterogeneous site for cleavage cracks. In contrast, the detailed study by Langford (1977) shows that below a thickness of about 0.01 microns cementite plates do not fragment in a brittle manner but deform plastically. The early work on the deformation of pearlite by Maurer and Warrington (1967) postulated the existence of ½(111) partial dislocations in the cementite. The work of Inoue *et al*. (1977) on deformation of pearlitic over a wide range of temperatures showed that at room temperature slip occurred in Fe_3C on only (100) and (001), but at higher temperatures other slip planes were operative. Thus, as the cementite has limited slip modes, the associated deformation is complex and dislocations must be stored at the ferrite/cementite interfaces resulting in very high local elastic stresses. This is consistent with the neutron diffraction studies of van Acker *et al*. (1996). An excellent general account of the deformation of pearlitic steels during wire drawing has been presented by Zelin (2002). This comprehensive account includes discussion of textural changes and the evolution of the ferrite/cementite interfaces. The complex structure arising from wire drawing has, in cross section, a characteristic curly-grained structure described by Gil Sevillano (1991). However, by considering the axial structures, Embury and Fisher (1966) developed a simple similitude model to describe the evolution in tensile yield strength as a function of wire drawing strain and the initial pearlite spacing. By similitude, S_0 and external wire diameter D_0 are proportional:

$$\frac{S_0}{S_\varepsilon} = \frac{D_0}{D_\varepsilon} \qquad [8.16]$$

where S_ε and D_ε are the pearlite spacing and the wire diameter after strain. The imposed drawing strain is

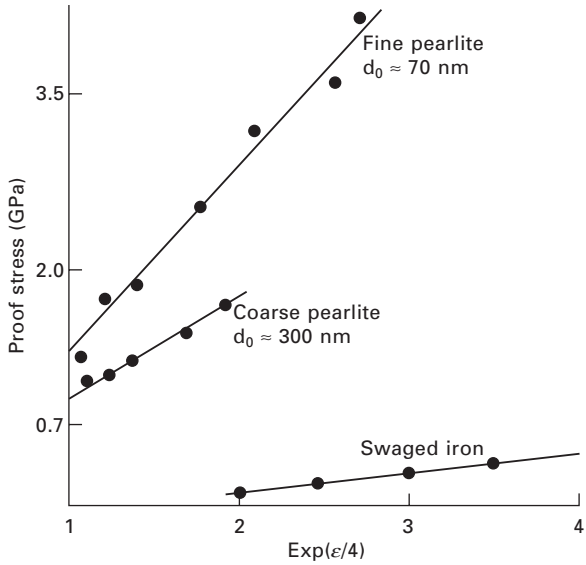
$$\varepsilon = 2\ln\left(\frac{D_0}{D_\varepsilon}\right) \qquad [8.17]$$

Thus the Hall–Petch scaling law gives

$$\sigma_y = \sigma_0 + \frac{k}{\sqrt{S_0}} \exp(\varepsilon/4) \qquad [8.18]$$

with σ_0 the friction stress of iron and k the Hall–Petch coefficient. This permits the strength to be predicted as a function of initial pearlite spacing and imposed wire drawing, as summarised in Fig. 8.25. More recent work using three-dimensional atom probe microscopy by Sauvage *et al*. (2002) has shown that the deformation and the thermodynamic stability of the carbide are linked as large plastic strains result in C being driven from the carbide into solid solution and a corresponding redistribution of carbide in the adjacent ferrite, as shown in Fig. 8.26. The dissolution of carbon from

© Woodhead Publishing Limited, 2012



8.25 Simple model based upon the Hall–Petch equation to describe the evolution of the proof stress σ_y as a function of wire drawing strain ε and the initial pearlite spacing S_0 (Embury and Fisher, 1966).

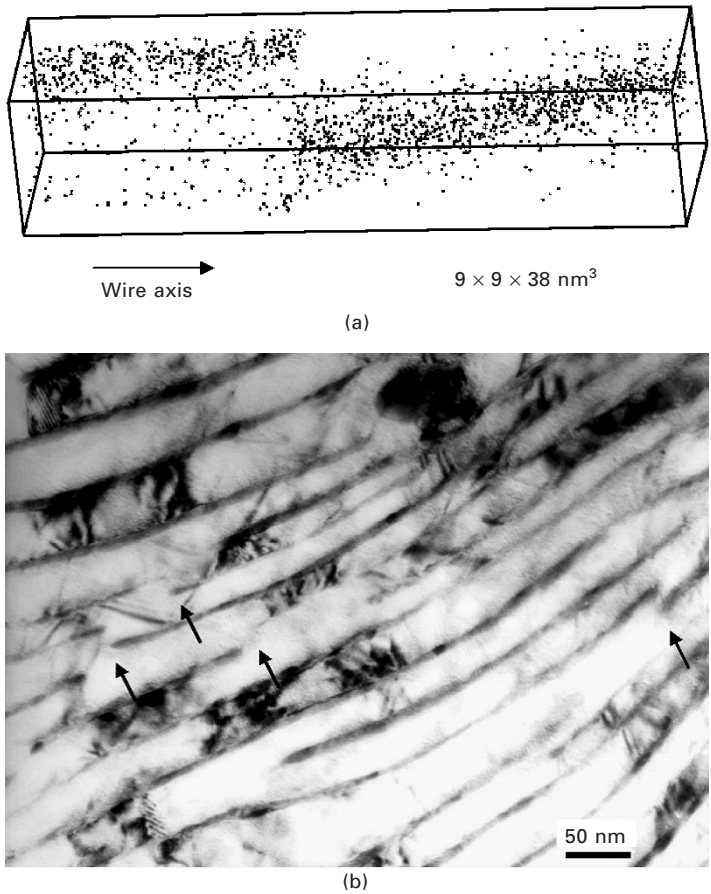
the cementite has also been studied extensively by Gavriljuk (2001, 2002) using a variety of techniques.

Thus, although the length scale in the spacing of the highly deformed pearlite is an important factor in controlling the strength, it does not represent a complete model and the continued study of a variety of deformed pearlitic structures will yield valuable new insights into the mechanism of strengthening in these ultra-high strength materials including the role of local elastic stresses. The residual elastic stresses in heavily deformed materials are usually determined by X-ray diffraction or stress relaxation, but the cylindrical geometry and small diameter of drawn pearlitic wire make these methods difficult to interpret. However, a recent paper by Yang *et al*. (2008) exploited a novel use of the FIB technique to cut grooves of controlled depth in the structure at various positions and by correlation imaging map the local residual stresses and their distribution in the wire diameter.

8.6 Future trends in pearlitic steels

It is clear from the material reviewed that there exists a very comprehensive understanding of the pearlite reaction due to careful studies by a variety of authors, particularly the many seminal contributions both experimental and theoretical by Hillert, who has given a quantitative understanding of the

© Woodhead Publishing Limited, 2012



8.26 (a) Carbon map obtained by three-dimensional atom probe showing the redistribution of C from the cementite lamellae due to the large imposed plastic strains which force C back into solid solution during deformation. (b) Bright-field TEM image indicating, with arrows, the areas probed (Sauvage *et al.*, 2002).

pearlite reaction but also considered its relation to other processes such as bainite formation.

In one sense, future work needs to be focused on the long-standing issue of what are the appropriate interfacial conditions during the growth of pearlite in a wide variety of alloy steels and what is the relationship between pearlite and other decomposition products.

Clearly new and developing analytical tools, such as analytical electron microscopy and three-dimensional atom probe microscopy, have an important role to play. However, advanced tomographic methods also have a role to play in understanding the spatial organisation of pearlitic reactions.

© Woodhead Publishing Limited, 2012

An important factor which remains to be understood is the process of diffusion ahead of a moving interface. It is certainly possible that the rates of diffusion are much higher than for static boundaries and it may also be that at lower transformation temperatures plasticity at the interface plays a role in the transformation. These aspects remain a challenge for the experimentalists.

There is also scope for extension of the Bolling and Richman technique (1970) of forced velocity growth, possibly by using rapid heating rates in collaboration with high thermal gradients during subsequent growth. It may be possible to design such experiments using wire samples with bamboo grain structures so that reactions at a well characterised single austenite boundary can be studied.

Much is known of the role of prior austenite grain size in regard to hardenability studies, but the possibility of producing nano-grained austenite by rapid heat treatment now exists (Tsuji *et al*., 2002) and these are of great interest, not simply from the viewpoint of their mechanical properties but in the study of the pearlite transformation also.

It is clear from the studies of Kaya and Edmonds (1998) that, in the lower regimes of the pearlite transformation in Cr steels, a variety of non-classical products with new forms of ferrite/carbide aggregates can occur with very fine intrinsic length scales. These certainly merit additional study from both the viewpoint of their microstructures and their related mechanical properties. Similarly, the work of Han *et al*. (1995) indicates that elements such as V and Si may change the progress and form of the pearlite reaction by changing the detailed nucleation events at the prior austenite grain boundaries. This opens a broad area for future work both in terms of having competitive and simultaneous reactions at the prior boundaries. An excellent illustration of such reactions is given by the work of Chairuangsri and Edmonds (2000) concerning the precipitation of copper in a number of hypereutectoid steels. These authors observed fine scale precipitation of copper both in abnormal ferrite and in the pearlitic structures. They also observed precipitation in rows characteristic of interphase precipitation at the pearlitic ferrite/austenite interface boundary and precipitation of copper within the pearlitic cementite. In addition, changes in the mode of the reaction can be accomplished by perturbing the prior austenite boundaries and by ausforming or other thermo-mechanical processing methods.

Finally, it is important to recognise that deformed pearlite in drawn steels reaches a strength level of $E/60$, where E is Young's modulus, ~210 GPa of steel. The detailed interfacial structure in the deformed condition in relation to the as-transformed condition is not well understood and alternative deformation paths and sequences may extend the range of application of pearlitic products. An important aspect of this concept is that the concept of the similitude principle for refining the scale of the pearlitic structure

© Woodhead Publishing Limited, 2012

during drawing can be applied to low C steels by varying the transformation temperature and cooling rate, as shown recently by Allain *et al*. (2011). It can also be applied to other lamellar structures such as the bainite retained austenite structure developed by Caballeros and Bhadeshia (2005) in order to achieve very high strength materials which exhibit large strains to failure.

Thus it is likely that the further understanding of the pearlite reaction and its relation to both heat treatment and plastic deformation of steels will remain a fruitful and challenging area for research in the future.

8.7 Sources of further information and advice

It is important to consider the pearlite reaction both in the context of the various ways in which austenite can decompose and the resultant properties of pearlitic and ferrite–pearlite steels. Thus general texts such as 'The comprehensive treatment' in the book *Steels: Microstructure and properties* by Bhadeshia and Honeycombe (2006) and the volume 7 of the VCH series Materials Science and Technology edited by Pickering (1992) provide a broad background of the microstructures and uses of pearlitic steels.

As outlined in this article, the understanding of the pearlite reaction has developed from the synergism of careful metallographic studies first by optical methods and in the last 50 years by more refined analytical electron microscopy methods. The AIME conference of 1962 edited by Zackay and Aaronson (1962) remains an invaluable guide to the development of the subject. It also clearly demonstrates the debt which current researchers owe to the pioneering work of Hillert (1962), Cahn and Hagel (1962) and Kirkaldy (1962) in developing an understanding of the complex problem entailed in describing the detailed thermodynamics and kinetics of migrating interfaces. These contributions themselves were built on the concepts developed by Zener (1946) and the initial comprehensive studies of Davenport and Bain (1930) and Mehl and Hagel (1956).

The central issue of understanding events, structures and detailed compositions at migrating interfaces links the pearlite reaction to other processes such as the formation of proeuctectoid ferrite and also the bainite reaction which are treated elsewhere in the current volume. It is also important to consider pearlite formation as a patterning process and this has been carefully reviewed in a recent comprehensive article (Brechet and Hutchinson, 2006).

This brief review has focused largely on the microstructural aspects of the pearlite reaction. However, as heavily deformed pearlite is the strongest bulk material made by man, it would be remiss not to refer to the seminal work done on the understanding of drawn pearlite by Gil Sevillano *et al*. (1980) and Gil Sevillano (1991, 2010) over a period of some 30 years. This, too, represents a literature of broad general value to the materials community.

© Woodhead Publishing Limited, 2012

8.8 Acknowledgements

The author is grateful to Yves Brechet, Olivier Bouaziz and Chris Hutchinson for advice and discussions, and to the Editors for a variety of insightful comments and criticisms. In addition, he is most grateful to Zhang Kui and Wang Xiang for their precious help and support in the preparation of this chapter.

8.9 References

Al-Salman, S.A., Lorimer, G.W. and Ridley, N. 1979. Pearlite growth kinetics and partitioning in a Cr-Mn eutectoid steel, *Metall. Trans. A*, 10A, pp. 1703–1709.

Allain, S., Goune, M., Bouaziz, O., Kassir, E., Barges, P. and Jantzen, L., 2011. Design and characterisation of a lamellar nanostructure in a low C steel. *J. Mat. Sci.*, 46, pp. 2764–2770.

Bagaryatski, Y.A., 1950. Likely mechanism for the tempering of martensite (Veroyatnue mechanezm raspada martenseeta). *Dokl. Akad. Nauk. SSSR.*, 73, pp. 1161–1164.

Bhadeshia, H.K.D.H. and Honeycombe, R.W., 2006. *Steel: Microstructure and Properties*, 3rd edn. London: Butterworth-Heinemann.

Bolling, G.F., and Richman, R.H., 1970. Forced velocity pearlite. *Metall. Trans.*, 1, pp. 2095–2104.

Brechet, Y. and Hutchinson, C., 2006. Defect induced dynamic pattern formation in metals and alloys. In: M. Ehrenreich and F. Spaepen (eds.) *Solid State Physics*, Cambridge, MA: Academic Press, pp. 182–285.

Brown, D. and Ridley, N., 1969. Kinetics of the pearlite reaction in high-purity nickel eutectoid steels. *J. Iron Steel Inst.*, 207, pp. 1232–1240.

Bungardt, K., Kunze, E. and Horn, E., 1958. Untersuchungen über den Aufbau des Systems Eisen-Chrom-Kohlenstoff. *Arch Eisenhüttenwes*, 29(3), pp. 193–203.

Caballeros, F.G. and Bhadeshia, H.K.D.H., 2005. Very strong bainite. *Current Opinion in Solid State and Materials Science*, 8, pp. 183–196.

Cahn, J.W. and Hagel, W.C., 1962. Theory of the pearlite reaction. In: V.F. Zackay and H.I. Aaronson (eds) *The Decomposition of Austenite by Diffusional Processes*, New York: Wiley, pp. 131–236.

Carpenter, C.H.C. and Robertson, J.M., 1932. The austenite↔pearlite Inversion. *J. Iron Steel Inst.*, 25, pp. 309–328.

Chadwick, G.A. and Edmonds, D.V., 1973. Unidirectional growth of pearlitic steels. In: *Chemical Metallurgy of Iron and Steel*. London: Iron and Steel Institute, pp. 264–267.

Chairuangsri, T. and Edmonds, D.V., 2000. The precipitation of copper in abnormal ferrite and pearlite in hyper-eutectoid steels. *Acta Mater.*, 48, pp. 3931–3949.

Davenport, A.T. and Honeycombe, R.W.K., 1971. Precipitation of carbides at γ/α boundaries in alloy steels. *Proc. R. Soc. London*, 322, pp. 191–205.

Davenport, E.S. and Bain, E.C., 1930. Transformation of austenite at constant subcritical temperatures. *Trans. AIME*, 90, pp. 117–54.

Dippenaar, R.J. and Honeycombe, R.W.K., 1973. The crystallography and nucleation of pearlite. *Proc. R. Soc. A*, 333, pp. 455–467.

Embury, J.D. and Fisher, R.M., 1966. The structure and properties of drawn pearlite. *Acta Mater.*, 14, pp. 147–159.

© Woodhead Publishing Limited, 2012

Entin, R.I., 1962. Elementary reactions in the austenite to pearlite and austenite to bainite transfortion. In: V.F. Zackay and H.I. Aaronson (eds) *The Decomposition of Austenite by Diffusional Processes*, New York: Wiley, pp. 295–311.

Gavriljuk, V.G., 2001. Comment on 'Effect of interlamellar spacing on cementite dissolution during wire drawing of pearlitic steel wires'. *Scripta Mater.*, 45, pp. 1469–1472.

Gavriljuk, V.G., 2002. Comment on 'Cementite decomposition in heavily drawn pearlite steel wire'. *Scripta Mater.*, 46, pp. 175–177.

Gil Sevillano J., 1991. Substructure and strengthening of heavily deformed single and two-phase metallic materials. *J. Physique III*, 1, pp. 967–988.

Gil Sevillano, J., 2010. A twist on heavily drawn wires, Mordica Lecture, New York: Wire Association International, pp. 926–930.

Gil Sevillano, J., Van Houtte, P. and Aernoudt, E., 1980. Large strain work hardening and textures. *Progress in Materials Science*, 25, pp. 69–134.

Han, K., Smith, G.D.W. and Edmonds, D.V., 1995. Pearlite phase transformation in Si and V steel. *Metall. Trans. A*, 26A, pp. 1617–1631.

Hashiguchi, K. and Kirkaldy, J.S., 1984. Pearlite growth by combined volume and phase boundary diffusion. *Scand. J. Metall.*, 13, pp. 240–248.

Hawkes, J., Johnson, W.A. and Mehl, R.F., 1942. The interlamellar spacing of pearlite, *Trans ASM*, 30, pp. 1049–1086.

Hillert, M., 1962. The formation of pearlite. In: V.F. Zackay and H.I. Aaronson (eds) *The Decomposition of Austenite by Diffusional Processes*, New York: Wiley, pp. 197–237.

Hillert, M., 1969. The role of interfaces in phase transformations. In: *The Mechanisms of Phase Transformations in Crystalline Solids*, Monograph and Report Series No. 33, London: Institute of Metals.

Hillert, M., 1981. An analysis of the effect of alloying elements on the pearlite reaction. *Proc. Int. Conf. on Solid-solid Phase Transformations*, Warrendale, PA: TMS, pp. 789–806.

Honeycombe, R.K.W., 1976. Transformation from austenite in alloy steels. Institute of Metals Lecture, *Metall. Trans. A*, 7A, pp. 915–936.

Hultgren, A., 1947. Isothermal transformation of austenite. *Trans. ASM*, 39, pp. 915–989.

Hutchinson, C.R., Hackenberg, R.E. and Shiflet, G.J., 2004. The growth of partitioned pearlite in Fe-C-Mn steels. *Acta Mater.*, 52, pp. 3565–3585.

Inoue, A., Ogura, T. and Masumoto, T., 1977. Microstructures of deformation and fracture of cementite in pearlitic C steels strained at various temperatures. *Metall. Trans.*, 8A, pp. 1689–1695.

Johnson, W.A. and Mehl, R.F., 1939. Reaction kinetics in processes of nucleation and growth. *Trans. AIME.*, 135, pp. 416–442.

Kaya, A.A. and Edmonds, D.V., 1998. Non-classical decomposition products of austenite in Fe-C-Cr Alloys. *Metall. Trans. A*, 29A, pp. 2913–2924.

Khalid, F.A. and Edmonds, D.V., 1993. Interphase precipitation in microalloyed engineering steels and a model alloy. *Mater. Sci. Technol.*, 9, pp. 384–396.

Khalid, F.A. and Edmonds, D.V., 1994. Effect of vanadium on the grain boundary carbide nucleation of pearlite in high-carbon steels. *Scripta Metall.*, 30, pp. 1251–1255.

Kirkaldy, J.S., 1962. Theory of diffusional growth in solid-solid transformations. In: V.F. Zackay and H.I. Aaronson (eds) *The Decomposition of Austenite by Diffusional Processes*, New York: Wiley, pp. 39–123.

Langford, G., 1977. Deformation of pearlite. *Metall. Trans. A*, 8A, pp. 861–875.

© Woodhead Publishing Limited, 2012

Lupton, D.F. and Warrington, D.H., 1972. The zero-misfit analysis of pearlite nucleation in a eutectoid steel. *Acta Metall.*, 20, pp. 1325–1333.

Lyman, T. and Troiano, A.R., 1946. Influence of carbon content upon the transformation in three percent chromium steel. *Trans. ASM*, 37, pp. 402–448.

Maurer, K.L. and Warrington, D.H., 1967. Deformation of cementite. *Phil. Mag.*, 15, pp. 321–327.

Mehl, R.F. and Hagel, W.C., 1956. The austenite-pearlite reaction. *Progress in Metal Physics*, 6, pp. 74–134.

Mellor, B.G. and Edmonds, D.V., 1977. The unidirectional transformation of Fe-0.8C-Co alloys: Part I: Process and structure relationships and the significance of interlamellar spacing measurements. *Metall. Trans*, 8A pp. 763–771.

Nakajima, K., Apel, M. and Steinbach, I., 2006. The role of C diffusion in ferrite on the kinetics of cooperative growth of pearlite: a multi-phase field study. *Acta Mater.*, 54, pp. 3665–3672.

Offerman, S.E., van Wilderen, L.J.G.W., van Dijk N.H., Sietsma J., Rekveldt M.Th., van der Zwaag, S., 2003. *In-situ* study of pearlite nucleation and growth during isothermal austenite decomposition in nearly eutectoid steel. *Acta Mater.*, 51, pp. 3927–3938.

Pandit, A.S. and Bhadeshia, H.K.B.D., 2011. Mixed diffusion-controlled growth of pearlite in binary steel, *Proc. R. Soc. A*, 467, pp. 508–521.

Pearson, D.D. and Verhoeven, J.D., 1984. Forced velocity pearlite in high purity Fe–C alloys: Part I. Experimental. *Metall. Trans. A*, 15A, pp. 1037–1045.

Pickelsimer, M.L., McElroy, D.L., Kegley, T.M., Stansbury, E.E. and Frey, J.H., 1960. Effect of manganese on the austenite-pearlite transformation. *Trans. TMS-AIME*, 218, pp. 473–480.

Pickering, F.B. (ed.), 1992. *Constitution and Properties of Steels*. In: R.W. Cahn, P. Haasen, and E.J. Kramer (eds) Materials Science and Technology: *A Comprehensive Treatment*, Vol. 7. Weinheim: VCH, pp. 339–399.

Pitsch, W., 1962. Der Orientierungszusammenhang zwischen Zementit und Ferrit im Perlit. *Acta Metall.*, 10(1), pp. 79–80.

Puls, M. and Kirkaldy, J.S., 1972. The pearlite reaction. *Metall. Trans.*, 3, pp. 2777–2796.

Saunders, N. and Miodownik, A.P., 1998. *Calphad Software*, New York: Pergamon Press.

Sauvage, X., Guelton, N. and Blavette, D., 2002. Microstructure evolutions during drawing of a pearlitic steel. *Scripta Mater.*, 46, pp. 459–464.

Sharma, R.C., Purdy, G.R. and Kirkaldy, J.S., 1979. Kinetics of the pearlite reaction in Fe-C-Cr. *Metall. Trans. A*, 10A, pp. 1129–1139.

Smith, C.S., 1960. *A History of Metallography*, Chicago, IL: University of Chicago Press.

Sorby, H.C., 1864. On microscopical photographs of various kinds of iron and steel. *Report of the 34th Meeting of British Assn. Adv. Science* (Bath), Part II.

Tsuji, N., Ueji, R., Minamino, Y. and Salto, Y., 2002. A new and simple process to obtain nano-structured bulk low-C steel with superior mechanical properties. *Scripta Mater.*, 46, pp. 305–310.

Van Acker, K., Root, J., Van Houtte, P. and Aernoudt, E., 1996. Neutron diffraction measurement of the residual stress in the cementite and ferrite phases of cold-drawn steel wires. *Acta Mater.*, 44, pp. 4039–4049.

Verhoeven, J.D. (ed.), 1975. *Fundamentals of Physical Metallurgy*, New York: Wiley.

Verhoeven, J.D. and Pearson, D.D., 1984. Forced velocity pearlite in high purity Fe–C alloys: Part II. Theoretical. *Metall. Trans. A*, 15A, pp. 1047–1054.

© Woodhead Publishing Limited, 2012

Yang, Y.S., Bae, J.G. and Park, C.G., 2008. Improvement of bending fatigue resistance of hyper-eutectoid steel wire by post process annealing. *Mat. Sci. & Eng A*. 488, pp. 554– 561.

Zackay, V.F. and Aaronson, H.I. (eds.), 1962. *The Decomposition of Austenite by Diffusional Processes*, New York: Wiley.

Zelin, M., 2002. Microstructure evolution in pearlitic steels during wire drawing. *Acta Mater.*, 50, pp. 4431–4447.

Zener, C., 1946. Kinetics of the decomposition of austenite. *Trans. AIME*, 167, pp. 550–595.

Zhou, D.S. and Shiflet G.J., 1991. Interfacial steps and growth mechanism in ferrous pearlites. *Metall. Trans. A*, 22, pp. 1349–1365.

Zhou, D.S. and Shiflet, G.J., 1992. Ferrite: cementite crystallography in pearlite. *Metall. Trans. A*, 23A, pp. 1259–1269.

© Woodhead Publishing Limited, 2012

9

Nature and kinetics of the massive austenite-ferrite phase transformations in steels

Y. LIU, Max Planck Institute for Intelligent Systems, Germany and Tianjin University, P. R. China, F. SOMMER, Max Planck Institute for Intelligent Systems, Germany and E. J. MITTEMEIJER, Max Planck Institute for Intelligent Systems, Germany and University of Stuttgart, Germany

Abstract: The nature and kinetics of the austenite (γ) to ferrite (α) phase transformation, and vice versa, in iron-based materials are dealt with. The focus is on the current understanding of the so-called 'abnormal' and 'normal' transformation kinetics, the (unusual) transition of diffusion-controlled growth to interface-controlled growth and effects of uniaxially applied stress. The so-called modular model of transformation kinetics can be applied successfully to interpret the kinetic data.

Key words: austenite-ferrite and ferrite-austenite phase transformation, kinetics, dilatometry, uniaxially applied stress, interface migration.

9.1 Introduction

The phase transformation from austenite (γ, fcc) to ferrite (α, bcc) in iron-based alloys is of cardinal importance in the steel industry, since this solid-state phase transformation controls the final microstructure of many components and consequently their performance. This transformation has been studied extensively both from a technological point of view and from a fundamental scientific point of view (e.g. Wilson 1984; Lange *et al*. 1988; Reed & Bhadeshia 1992; Honeycombe & Bhadeshia 1995: Zhao & Notis 1995; Huang & Hillert 1996; Van der Ven & Delaey 1996; Li *et al*. 2001; Chen *et al*. 2010).

Because the diffusion of substitutional solutes in Fe-based alloy is relatively slow (Honeycombe & Bhadeshia 1995), and the occurrence of the $\gamma \rightarrow \alpha$ transformation requires a large undercooling (Kempen *et al*. 2002a), the $\gamma \rightarrow \alpha$ transformation can take place without significant diffusion (i.e. redistribution) of substitutional solute. Therefore, the $\gamma \rightarrow \alpha$ transformation of the substitutionally alloyed Fe-based alloys can be considered as a partitionless, massive transformation: i.e. the parent γ-phase and the product α-phase have

© Woodhead Publishing Limited, 2012

the same composition and the transformation proceeds by the independent motion of individual atoms at and across the migrating α/γ transformation interface.

Massive transformations have been studied since the late 1950s, and the definition of this type of transformation is still a matter of some discussion (e.g. Christian 1975; Massalski *et al*. 1975; Massalski 1984, 2002, 2010; Borgenstam & Hillert 2000; Aaronson & Vasudevan 2002; Hillert 2004). It has been proposed that the massive transformation can be described as a composition-invariant nucleation-and-growth formation of one solid phase from another solid phase (Christian 1975). It has been argued that the massive transformation can be defined as the 'partitionless counterpart of the partitional precipitation of allotriomorphs' (Hillert 2004). The transformation has also been defined as 'a composition-invariant, interface-controlled diffusional phase transformation', leading to a characteristic patchy morphology, frequently exhibiting faceting and ledges, and not necessarily involving specific parent-product lattice orientation relationships (Massalski 2002, 2010). It appears that (at least) the following characteristics of the massive ($\gamma \rightarrow \alpha$) transformation are generally accepted:

- no specific lattice-orientation relationship between the parent and product phases,
- occurrence of nucleation and growth modes and
- partitionless nature, i.e. the compositions of the parent phase and the product phase are the same.

In general, the $\gamma \rightarrow \alpha$ phase transformation of steels comprises three overlapping mechanisms: nucleation, growth and impingement (Mittemeijer & Sommer 2002, 2011; Liu *et al*. 2007). Upon nucleation, a new interface is generated that separates the product ferrite phase from the parent austenite phase. This interface migrates into the surrounding parent phase during the subsequent growth. The migration rate of the interface is generally determined by the diffusion of alloying elements away from the interface and/or the mobility of the interface (Agren 1989; Van der Ven & Delaey 1996; Aaronson *et al*. 2002; Hillert 2002; Loginova *et al*. 2003). The resulting microstructure is strongly influenced by the (type of) impingement mode of the growing ferritic grains. Evidently, control (and thus variation) of the possibly operating nucleation, growth and impingement mechanisms would allow diversity in the resulting microstructure. The progress of transformation can be modeled as a function of time and temperature in a modular approach, which permits expression and hence exploration of the dependence on the nucleation, growth and impingement modes and thus the kinetic parameters to be quantitied (Kempen *et al*. 2002b; Mittemeijer & Sommer 2002, 2011; Liu *et al*. 2007; Mittemeijer 2010).

In order to understand the mechanism of the massive type of phase

© Woodhead Publishing Limited, 2012

transformation, it is important to consider the phase diagram. The temperature corresponding to equal Gibbs energies of the metastable product phase and the metastable parent phase of the same composition is called T_0, which is positioned in the two (α, γ)-phase field. The critical temperature for kinetic prevalence of a massive transformation, i.e. the temperature below which the transformation initiates upon cooling from the γ-phase field, has been a matter of considerable controversy over the years (Hillert 2004). The critical temperature of the Fe-Ni alloy system coincides with the $\alpha/\alpha + \gamma$ phase boundary, and moves into the $\alpha + \gamma$ two-phase field with increasing concentration of Ni. Furthermore the critical temperature never approaches the corresponding T_0 temperature (Swanson & Parr 1964). These results have been supported by computer simulations applying the phase-field method (Loginova *et al*. 2003). By performing isochronal high-resolution dilatometric measurements on ultra-low-carbon Fe-C alloys (Liu *et al*. 2006, 2008a, 2008c), it was shown that upon cooling, a transition from diffusion-controlled growth to interface-controlled growth can occur.

Recent experimental results revealed the importance of the (type of) nucleation process on the overall kinetics of the massive transformation. Two different kinds of transformation kinetics, normal and abnormal, were observed (and classified for the first time) in pure iron (Liu *et al*. 2004b), substitutionally alloyed Fe-Co alloys (Liu *et al*. 2003, 2004a) and interstitially alloyed Fe-N alloys (Liu *et al*. 2008b). Normal transformation behavior exhibits a single maximum in the ferrite-formation rate as a function of the degree of transformation, whereas abnormal transformation behavior is characterized by the occurrence of more than one maximum in the ferrite-formation rate as a function of transformed fraction (Liu *et al*. 2004a, 2004b, 2008b). Abnormal transformation behavior can be explained by repeated (i.e. autocatalytic) nucleation ahead of the migrating γ/α interface (Liu *et al*. 2003, 2004a, 2004b, 2008b).

In general, two (extreme) growth modes, volume diffusion-controlled growth and interface-controlled growth, can be distinguished (Liu *et al*. 2007; Mittemeijer 2010) and can be observed, for example, for the $\gamma \rightarrow \alpha$ transformation in Fe-C alloys (Liu *et al*. 2006). The redistribution of carbon by diffusion of carbon atoms in front of the advancing interface can lead to a diffusion-controlled growth mode, at relatively low γ/α interface velocity, whereas the redistribution/partitioning of carbon is obstructed if a massive transformation occurs, where the ferrite product phase has the same composition as the parent austenite phase, which represents an interface-controlled growth mode and implies a relatively high γ/α interface velocity.

Fe-based alloys used in practice are often subjected to (externally) applied or (internal) residual stresses. Thus, from both a fundamental and a practical point of view, it is of importance to investigate the influence of stress on the kinetics of the $\gamma \rightarrow \alpha$ and $\alpha \rightarrow \gamma$ transformations (Mohapatra *et al*.

© Woodhead Publishing Limited, 2012

2007; Liu *et al*. 2009, 2010). The energies corresponding with the elastic and plastic deformation associated with the accommodation of the volume misfit of austenite and ferrite upon phase transformation likely influence the interface process.

9.2 Kinetic information based on thermal analysis

Differential dilatometry is a powerful technique for precise measurements of the thermal dilatation behavior as a function of temperature/time during application of a specific heat-treatment cycle (Mittemeijer 2010). High-resolution dilatometers are required for the determination of kinetic data of the explored γ-α and α-γ phase transformations, both in the presence and in the absence of applied stress. The resistant heated Bähr DIL 802 dilatometer is such an instrument: it features a very high resolution of length change ($\pm$10 nm; for a specimen length of 10 mm this implies a relative accuracy of 10^{-4}%) while applying relatively low heating/cooling rates ($\leq$20 K min^{-1}). The inductively heated Bähr DIL 805 A/D dilatometer is characterized by its possibility to impose high heating/cooling rates (30 to about 1000 K min^{-1}), a length-change resolution of 20 nm, and application of uniaxial loading force (in the range of 10–5000 N). The majority of kinetic data on the $\alpha \rightarrow \gamma$ and $\gamma \rightarrow \alpha$ transformations reported in recent years have been obtained by application of such dilatometers.

Procedures have been developed for calibration of the (both length and temperature) differential dilatometric measurement signal both upon isochronal heating and cooling (for details, see Liu *et al*. 2004c, 2009). It has to be emphasized that the measured dilatation is a direct response to length change, as caused by the investigated transformation, because instrumental thermal lag effects, as pertain to differential thermal analysis (DTA) or differential scanning calorimetry (DSC) measurements of the heat-capacity changes, are negligible for dilatometry: a practically homogeneous temperature field can be maintained within the specimen.

For DSC/DTA analysis, an iterative procedure is possible leading simultaneously to values for both the heat of transformation and the degree of transformation as a function of temperature, as described by Kempen *et al*. (2002b). The measured thermal signal cannot follow a sudden heat release as well as a sudden length change can be traced by dilatometry. This can be exemplified by comparison of the (shape of the) the first two maxima in the ferrite-formation-rate curve of pure iron as a function of temperature measured using a dilatometer (cf. Fig. 9.4(b)) and the corresponding results as function of time measured using a DTA instrument (cf. Fig. 9.12). The first two maxima in the DTA recordings shown in Fig. 9.12 are smeared and overlapped. For a further comparative discussion of dilatometry and DSC/DTA, see Section 9.6.13 in Mittemeijer (2010).

© Woodhead Publishing Limited, 2012

9.3 Modular phase transformation model

The overall transformation generally is the result of, more or less, simultaneously occurring nucleation and growth processes. One strives for determination of the kinetic parameters of these processes from the overall kinetics. A general procedure for the quantitative, analytical/numerical description of phase transformation kinetics on the basis of nucleation, growth and impingement mechanisms has been proposed by Kempen *et al*. (2002b) and Mittemeijer & Sommer (2002) (see in particular the reviews given by Liu *et al*. 2007 and Mittemeijer 2010). The first step in this approach involves the calculation of the volume of all growing particles, assuming that all grains never stop growing and that new grains hypothetically nucleate also in the transformed material: the extended transformed volume. In a next step, the extended volume is corrected for, e.g., 'hard' or 'soft' impingement of the growing particles, and the real transformed fraction can be obtained.

9.3.1 Nucleation

An overview of the different modes of nucleation (e.g. continuous nucleation, possibly including a nucleation index, pre-existing nuclei ('site-saturation' at $t = 0$), Avrami nucleation and mixtures of nucleation modes) has been given by Liu *et al*. (2007). Here nucleation modes of special relevance for γ-α transformation will be considered.

Site saturation

The term site saturation is used for those cases where the number of nuclei (= supercritical particles) does not change during the transformation: all nuclei, of number N^* per unit volume (the size has to be specified for each application), are present at $t = 0$ and start to grow at time $t = 0$. The nucleation rate per unit volume can be given by:

$$N(t) = N^{*}\delta(t - 0) \qquad [9.1]$$

with δ denoting the Dirac function ($\delta(t - 0) = 0$ for $t \neq 0$ and $\int_0^t \delta(t - 0) = 1$).

Autocatalytic nucleation

Autocatalytic nucleation can be induced as a consequence of product-phase/parent-phase volume misfit, by the build-up of strain energy, possibly in association with plastic deformation, in the parent matrix in front of the advancing product/parent interface.

© Woodhead Publishing Limited, 2012

The $\gamma \rightarrow \alpha$ transformation is accompanied by accommodation of a considerable amount of volume misfit-strain energy: a growing ferrite grain may thus induce strain and generate defects in the surrounding austenite matrix. This deformed austenite, immediately in front of the growing ferrite, may allow easier nucleation of ferrite than un-deformed austenite. Thus occurrence of repeated nucleation of ferrite in front of the moving interface may be understood, leading to nucleation 'bursts' established by the appearance of multiple transformation rate maxima: so-called 'abnormal' transformation kinetics (Liu *et al*. 2003, 2004b), due to autocatalytic nucleation (Fisher 1953; Cohen 1958; Speich & Szirmae 1969). The phenomenon of autocatalytic nucleation has been considered before for martensitic transformation (Cohen 1958; Kaufman & Cohen 1958; Meng *et al*. 2006).

The repeated nucleation may be described by a variation of the number of nucleation sites, N, of the type $N = pf_p$ with p as autocatalytic factor (Fisher 1953; Speich & Szirmae 1969) (note that the subscript p to f indicates the product phase). However, this relation overestimates the total amount of nucleation sites at some stage of transformation, because (continued) growth of earlier nucleated grains consumes the new additionally (by autocatalytic nucleation) nucleated and growing ferrite grains. Thus the development of maxima in the transformation rate (due to the autocatalytically induced nucleation 'bursts', followed by consumption of the correspondingly generated ferrite grains upon growth of the 'older' ferrite grains) can be understood. This leads to the introduction of a correction factor in the expression for the nucleus density that depends on the degree of transformation and that in first order approximation may be taken as $\left(\frac{f_{tr} - f_p}{f_{tr} - f_{st}}\right)$, where f_{st} and f_{tr} denote the degrees of transformation at the start and finish of the nucleation 'burst' concerned, respectively. Thus, the number of growing particles per unit volume can be expressed as:

$$N = p(f_p - f_{st})\left(\frac{f_{tr} - f_p}{f_{tr} - f_{st}}\right) \qquad [9.2]$$

Mixed site saturation and autocatalytic nucleation

In practice, intermediate types of nucleation occur often: a significant amount of nuclei is present before the transformation starts and other nuclei are formed during the transformation. Thus, a mixed nucleation comprising site saturation and autocatalytic nucleation can be expressed according to Eqs [9.1] and [9.2] as (Mittemeijer & Sommer 2002; Liu *et al*. 2007):

$$N = N^* + p(f_p - f_{st})\left(\frac{f_{tr} - f_p}{f_{tr} - f_{st}}\right) \qquad [9.3]$$

© Woodhead Publishing Limited, 2012

9.3.2 Growth

Two (extreme) growth modes are considered; volume diffusion-controlled growth (i.e. 'parabolic' growth: growth rate proportional with $t^{1/2}$ at constant T) and interface-controlled growth (i.e. 'linear' growth: growth rate proportional with t at constant T).[1]

The diffusion-controlled and interface-controlled growth modes can be given in a compact form. At time t, the volume Y of a growing particle nucleated at time τ is given by (Mittemeijer & Sommer 2002; Liu *et al.* 2007):

$$Y(\tau, t) = g\left(\int_{\tau}^{t} v_p d\tau'\right)^{d/m} \qquad [9.4]$$

where g is a particle-geometry factor (for growth of cubical grains, $g = 1$; for spherical growth, $g = 4\pi/3$), v_p is the interface velocity, m is the growth-mode parameter (interface-controlled ('linear') growth: $m = 1$; diffusion-controlled ('parabolic') growth: $m = 2$) and d is the dimensionality of the growth.

For the case of interface-controlled growth, the interface velocity is given by (Christian 1975):

$$\begin{aligned} v_p(T(t)) &= M \exp\left(1 - \frac{\Delta G}{RT(t)}\right) \\ &= v_0 \exp\left(-\frac{\Delta G^a}{RT(t)}\right) \exp\left(1 - \exp\left(\frac{\Delta G}{RT(t)}\right)\right) \end{aligned} \qquad [9.5]$$

where M is the temperature-dependent interface mobility, v_0 is the pre-exponential factor for growth (also called temperature-independent interface velocity), ΔG^a is the activation energy for the transfer of atoms through the parent-phase/product-phase interface, and ΔG is the energy difference of the new phase and the parent phase.

For large undercooling or overheating, $|\Delta G|$ is large compared to RT, and the above equation becomes:

$$v_p(T(t)) = M = v_0 \exp\left(-\frac{Q_G}{RT(t)}\right) \qquad [9.6]$$

where Q_G ($= \Delta G^a$) is the activation energy for growth and v_0 is the temperature-independent interface velocity.

For small undercooling or overheating, the driving force $|\Delta G|$ is small as compared to RT, and Eq. [9.6] reduces to:

[1]It should be recognized that occurrence of 'linear' growth need not be interface-controlled growth: in special cases it may pertain to diffusion-controlled growth (e.g. of precipitate platelets; Trivedi 1970).

© Woodhead Publishing Limited, 2012

$$v_p(T(t)) = M\,(-\Delta G(T(t))) \qquad [9.7]$$

Note that ΔG in Eq. [9.7] depends on temperature and thus calculation of Y according to Eq. [9.4], after substitution of Eq. [9.7], is only possible by numerical integration. This has led to limited application of Eq. [9.7], as compared to Eq. [9.4]. However, for isothermal transformation or isochronal transformation controlled by site saturation, analytical analysis on the basis of Eq. [9.4] after substitution of Eq. [9.7] is possible. Such analysis has been applied to quantitatively describe successfully the kinetics of the massive $\gamma \rightarrow \alpha$ transformation in Fe-based alloys (Kempen *et al*. 2002a; Liu *et al*. 2004a, 2004b, 2006, 2008b, 2009, 2010). For the case of interface-controlled growth at large undercooling (e.g. regarding the $\gamma \rightarrow \alpha$ transformation by quenching from the high temperature austenite-phase field), the interface velocity is given by Eq. [9.6].

9.3.3 Numerical and analytical phase transformation models

For any combination of modes for nucleation, growth and impingement, the degree of transformation can in principle always be calculated, as function of time and temperature.

The extended volume, V^e, can be given as (see below):

$$V^e = \int_0^t V\,\dot{N}(T(\tau))Y(t,\,\tau)\,d\tau \qquad [9.8]$$

where $\dot{N}$ is the nucleation rate per unit volume, V is the sample volume, and Y is the volume of a single particle nucleated at time τ. The transformed fraction for randomly dispersed nuclei growing isotropically can then be given as (Liu *et al*. 2007; Mittemeijer 2010):

$$f_p = 1 - \exp\left(\frac{V^e}{V}\right) = 1 - \exp(-x^e) \qquad [9.9]$$

and for anisotropic growth as

$$\frac{df_p}{dx_e} = (1 - f_p)^{\xi} \qquad \text{with } \xi \geq 1 \qquad [9.10]$$

and for non-random nuclei distribution

$$\frac{df_p}{dx_e} = (1 - f_p^{\varepsilon}) \qquad \text{with } \varepsilon \geq 1 \qquad [9.11]$$

$$x_e(f_p) = \text{arctanh}(f_p) \qquad \text{with } \varepsilon = 2 \qquad [9.12]$$

where x^e is the extended transformed fraction ($= V^e/V$) and subscript p

© Woodhead Publishing Limited, 2012

represents α for the $\gamma \rightarrow \alpha$ transformation and γ for the $\alpha \rightarrow \gamma$ transformation, respectively.

The above recipes to calculate f_p generally are of numerical nature. Analytical models for f_p are only possible in specific cases. Analytical descriptions of f_p provide more direct insight into functional dependences, are often used in practice and are therefore briefly considered below.

Analytical model for isothermal transformation

Upon the isothermal $\gamma \rightarrow \alpha$ transformation in the interstitial Fe-C alloy, a transition from interface-controlled growth to diffusion-controlled growth occurs (for more details, see Section 9.8.1). Against this background the following analytic model can be proposed (Liu *et al*. 2008a).

For the case of the first, interface-controlled growth stage, lasting till $t = t_1$, with site-saturation nucleation, and adopting three-dimensional growth, the extended volume V_I^e developing for $0 \leq t \leq t_1$ can be calculated applying Eqs (9.8, 9.1, 9.4 and 9.6):

$$V_I^e = g \int_0^t V(N_{IS}^* \delta(\tau - 0)) \left(\int_\tau^t \nu_0 \exp\left(-\frac{Q_G}{RT} \right) dt \right)^3 d\tau$$

$$= VgN_{IS}^* \left(t\nu_0 \exp\left(-\frac{Q_G}{RT} \right) \right)^3 \quad (0 \leq t \leq t_1) \qquad [9.13]$$

where N_{IS}^* is the nucleus density for the first, interfaced-controlled growth stage.

The onset for the second, diffusion-controlled growth stage occurs at a time t_1 ($0 \leq t_1 \leq t$). The time t_1 is considered as a fit parameter (see Section 9.4.2). In the absence of advance knowledge on what kind of nucleation mode prevails during the second diffusion-controlled growth stage, the experimental isothermal transformation data can be fitted using different nucleation modes: site saturation, continuous nucleation and Avrami nucleation (Liu *et al*. 2007). For the case considered (see Section 9.8.1) the results show that only adopting site saturation leads to reasonable fits of the experimental data. Then, for the second diffusion-controlled growth stage, also adopting three-dimensional growth, the corresponding extended volume V_D^e developing for $t > t_1$, calculated by applying Eqs (9.8, 9.1, 9.4 and 9.6), satisfies:

$$V_D^e = g \int_{t_1}^t V(N_{DS}^* \delta(\tau - t_1)) \left(\int_\tau^t D_0 \exp\left(-\frac{Q_d}{RT} \right) dt \right)^{3/2} d\tau$$

$$= Vg \left[N_{DS}^* \left(D_0 \exp\left(-\frac{Q_d}{RT} \right) \right)^{3/2} (t - t_1)^{3/2} \right] (t > t_1) \qquad [9.14]$$

© Woodhead Publishing Limited, 2012

where N^*_{DS} is the nucleus density for the second, diffusion-controlled stage. Hence, for $t > t_1$ the total extended volume, $V^e(t) = V^e_I(t = t_1) + V^e_D(t)$ can be obtained by using Eqs [9.13] and [9.14].

Analytical model for isochronal transformation

For the isochronal $\gamma \rightarrow \alpha$ transformation in substitutional Fe-based alloys, it has been argued that decomposition of austenite into α and γ does not occur measurably in the $\alpha + \gamma$ two-phase region during cooling (Kempen *et al*. 2002a; Liu *et al*. 2004a). Yet, nucleation of ferrite can take place upon traversing the two-phase region (Vandermeer 1990; Vooijs *et al*. 2000). Thus, during subsequent decomposition occurring at the temperatures and compositions within the α single-phase region, the nucleation can be supposed to have been completed at the start of growth, i.e. 'site saturation' can be adopted as nucleation mode. Further, the diffusion of substitutional components needed to establish the solute enrichment of the remaining austenite matrix during growth of the solute depleted ferrite particles is very slow, such that this redistribution practically does not take place. At $T < T_0$ (for T_0, see Section 9.7) the $\gamma \rightarrow \alpha$ transformation can take place under release of energy even if no solute redistribution occurs. Thus the $\gamma \rightarrow \alpha$ transformation of the substitutional Fe-based alloys takes place as a partitionless transformation, i.e. without any occurring composition difference between the parent γ-phase and the product α-phase.

Based on site saturation, interface-controlled growth at modest undercooling, so that Eq. [9.7] can be adopted for v_p, and an impingement model that is an intermediate of the cases of ideally randomly and of ideally periodically dispersed growing particles (cf. Eq. [9.12]), the phase transformation model can be given as (Kempen *et al*. 2002a):

$$\frac{df_p}{dt} = 3(N^* g)^{1/3}(1 - f_p^2)\, v_p \ \text{arctanh}^{2/3}(f_p) \qquad [9.15]$$

Hence, for a known number density of nuclei per unit volume, N^*, and a known value of g, experimental values for the interface velocity, v_p, can be determined as a function of temperature, time, or transformed fraction, by using data of df_p/dt and f_p, as for example obtained from dilatometry or DTA, in isothermally and/or isochronally conducted experiments.

9.4 Characteristics of normal and abnormal transformations

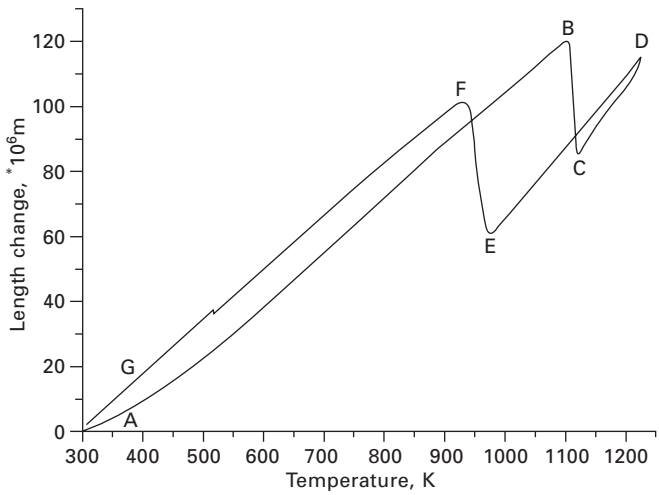
9.4.1 Normal transformation behavior

The length changes recorded for an Fe-2.26at%Mn alloy during one whole heating and cooling cycle, involving heating from room temperature up to

© Woodhead Publishing Limited, 2012

1223 K at a rate of 20 K min^{-1}, holding for 30 minutes at 1223 K and cooling down to 373 K at a rate of 20 K min^{-1}, are shown in Fig. 9.1. In the curve shown, segment AB corresponds with the normal thermal expansion of the specimen during continuous heating in the absence of a phase transformation. Segment BC represents the $\alpha \rightarrow \gamma$ transformation, during which a length contraction occurs due to the formation of austenite. Segments CD and DE represent the normal expansion and contraction of austenite, upon heating and subsequent cooling, respectively. Segment EF corresponds with the $\gamma \rightarrow \alpha$ transformation, associated with a length increase. After completion of the $\gamma \rightarrow \alpha$ transformation, the length of the sample decreases continuously down to room temperature due to normal thermal shrinkage (indicated by segment FG).

In the low temperature range (α phase) and the high temperature range (γ phase), the length-change values during heating (segments AB and CD) do not coincide exactly with those during cooling (segments FG and DE, see Fig. 9.1). As pointed out by Vandermeer (1990) and Offerman *et al*. (2004), the length change due to the $\gamma \rightarrow \alpha$ phase transformations in the substitutional Fe-based alloys is sensitive to the microstructure of the specimen (e.g. grain size, grain morphology). This may lead to the transformation taking place non-uniformly throughout the sample. As a result, the length of the specimen after one cycle is not expected to be exactly equal to the initial value. Further, the $\alpha \rightarrow \gamma$ phase transformation upon heating is associated with the (inhomogeneous) build-up of misfit-deformation energy. After



9.1 Measured length changes of an Fe-2.26at%Mn alloy during continuous heating (20 K min^{-1}) from room temperature to 1223 K and subsequent continuous cooling (20 K min^{-1}) interrupted by an isothermal annealing of 30 min at 1223 K (Liu *et al*. 2003).

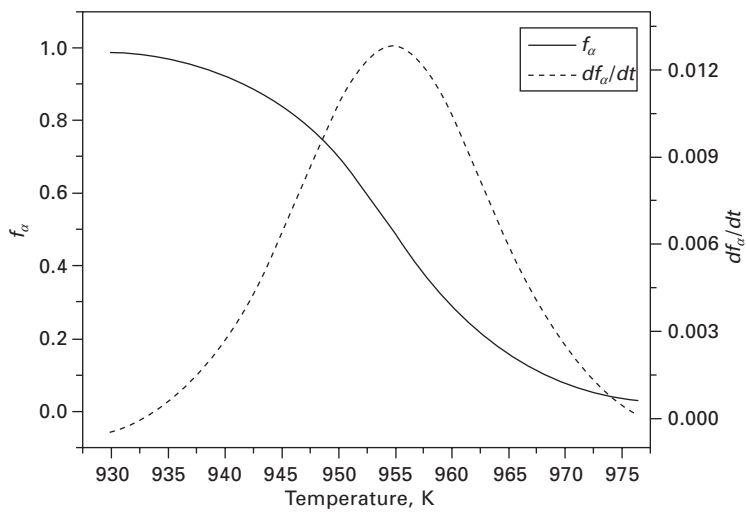
© Woodhead Publishing Limited, 2012

completion of the $\alpha \rightarrow \gamma$ phase transformation, this misfit-strain energy is relaxed which corresponds to modest length change. Therefore the slope of segment CD is not constant. During holding at 1223 K for 30 minutes (at point D) the misfit-strain energy becomes fully relaxed. Therefore, upon subsequent cooling only contraction due to thermal shrinkage occurs (constant slope: segment DE). A similar reasoning can explain the variable slope of segment FG during cooling directly after completion of the $\gamma \rightarrow \alpha$ phase transformation.

The values determined for f_α and df_α/dt of the Fe-2.26at%Mn alloy are shown in Fig. 9.2 as a function of temperature for the dilatometric measurement performed at a cooling rate of 20 K min^{-1}. Clearly, for the $\gamma \rightarrow \alpha$ transformation of the Fe-2.26at%Mn alloy the usual S-shaped curve is observed for f_α, and df_α/dt exhibits only one positive maximum (see the dashed line in Fig. 9.2). This type of transformation behavior is normally observed and is called here 'normal transformation behavior'.

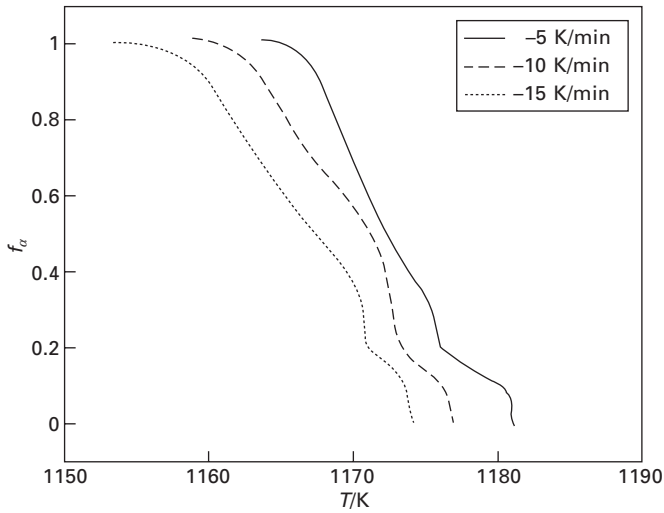
9.4.2 Abnormal transformation behavior

The development of the ferrite fraction in pure iron (with an initial average grain size of 439 μm, denoted by A in Fig. 9.7) is shown in Fig. 9.3 as a function of temperature for various cooling rates applied in the dilatometer. The curves in Fig. 9.3 are more or less parallel to each other. The higher



9.2 The ferrite fraction, f_α, and the ferrite-formation rate, df_α/dt, as a function of temperature of an Fe-2.26at%Mn alloy as determined from the length change measured at a cooling rate of 20 K min^{-1} (Liu *et al.* 2003).

© Woodhead Publishing Limited, 2012



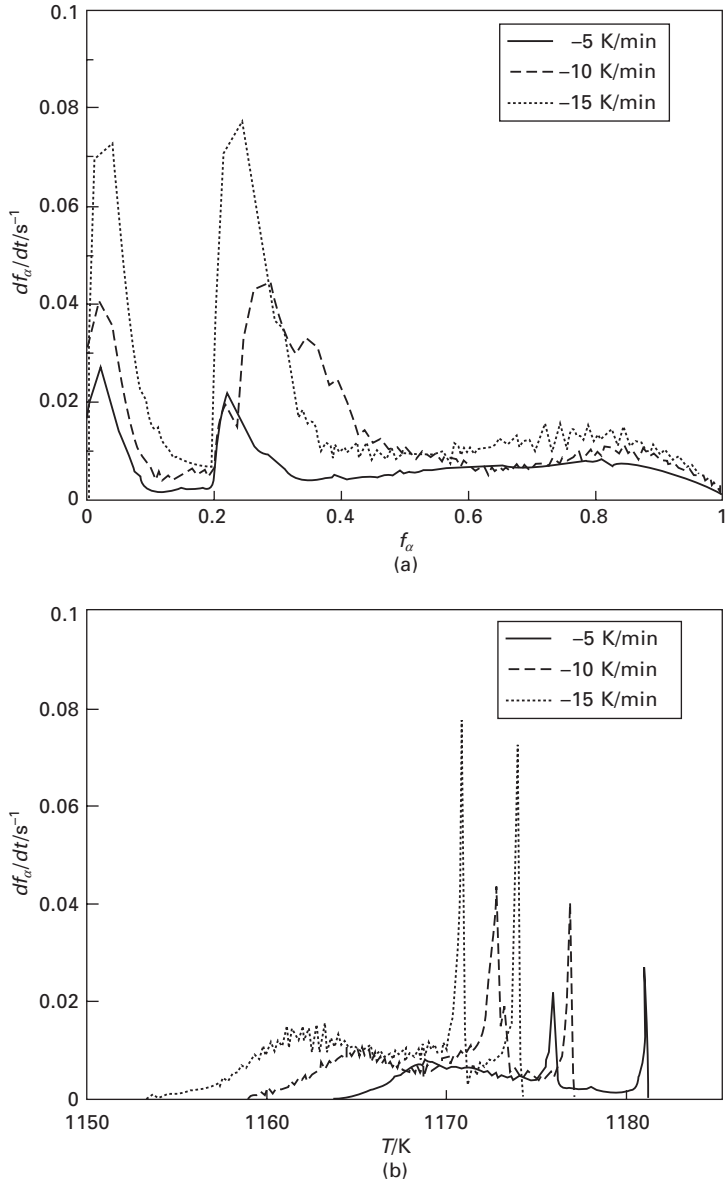
9.3 The ferrite fraction, f_α, as a function of temperature, T, as determined from isochronal dilatometric measurements of different fresh Fe specimens (A; cf. Fig. 9.7) subjected to cooling from the γ-phase field at rates of 5, 10 and 15 K min^{-1} (Liu *et al.* 2004b).

the cooling rate applied, the lower the start temperature of the $\gamma \rightarrow \alpha$ transformation.

The corresponding df_α/dt of the pure iron specimens are shown in Fig. 9.4, for different cooling rates applied, both as a function of ferrite fraction and as a function of temperature. In contrast with the normal transformation behavior as illustrated for the Fe-2.26at%Mn alloy (cf. Fig. 9.2), three maxima of the ferrite-formation rate occur for pure iron, with the value of the first df_α/dt maximum being distinctly larger than those of the subsequent two maxima. This multiply peaked nature for the ferrite-formation rate is called here 'abnormal transformation behavior'.

This abnormal $\gamma \rightarrow \alpha$ transformation behavior in Fe-based alloys has not been noticed until recently (Liu *et al.* 2003). This may have various causes. One reason could be the limited resolution of the experimental methods applied in the past. The resolution of the usually employed dilatometers is in the range of only about 1 μm, which can well obstruct detection of abnormal transformation behavior. Furthermore, in reported dilatometric or calorimetric analyses, the discussion has often been restricted to the average result from two or more successive runs, leading to distinct smoothing of the recorded effects. Upon close inspection of some recently published data of the $\gamma \rightarrow \alpha$ transformation, abnormal transformation behavior, as discussed above, can be discerned as well. For example, two transition stages can be detected in DTA results of Vooijs *et al.* (2000), and in neutron diffraction

© Woodhead Publishing Limited, 2012



9.4 The ferrite-formation rate, df_α/dt, as a function of (a) ferrite fraction, f_α, and (b) temperature, T, of pure iron specimens (A; cf. Fig. 9.7) for applied cooling rates of 5, 10 and 15 K min^{-1} (Liu *et al.* 2004b).

results of Velthuis *et al.* (1998), but the phenomenon was left undiscussed in these works.

The following observations have been made (Liu *et al.* 2004b). (i) Abnormal

© Woodhead Publishing Limited, 2012

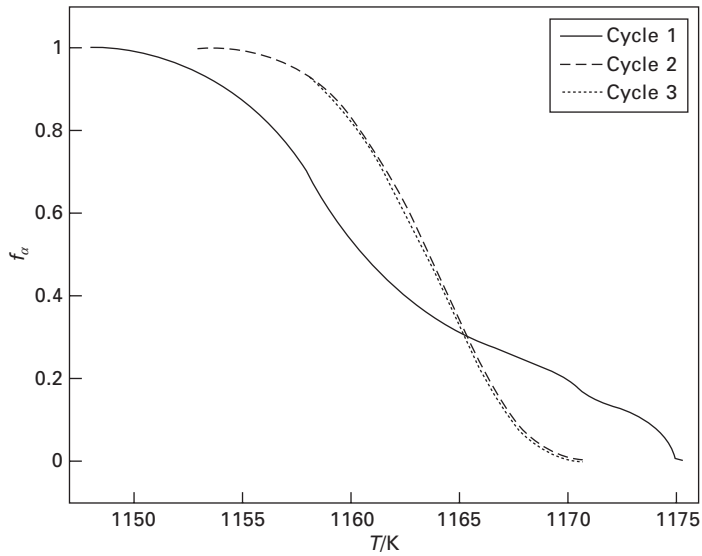
transformations, typified by the occurrence of more than one (here, in Fig. 9.4, three) maxima in the df_α/dt curve, occur for all pure iron specimens (A) for all applied cooling rates. (ii) A one-to-one relation exists between the locations of the first two maxima in the df_α/dt curve and the corresponding ferrite fractions; i.e. the location of the first two maxima in the df_α/dt curves as function of f_α is independent of the cooling rate. (Clearly no such one-to-one relation occurs for the ferrite-formation rate as a function of temperature.) For all applied cooling rates, the maximum df_α/dt values of the first and second peak appear around $f_\alpha = 0.04$ and $f_\alpha = 0.21$, respectively; the range of the ferrite fraction comprising the first two maxima ends at about $f_\alpha = 0.42$ (see Fig. 9.4a). Recognizing the fixed f_α values for the first two peaks in the ferrite-formation rate and that the absolute value of the ferrite-formation rate in the range of the first two peaks of the ferrite-formation rate increases with increasing the cooling rate applied, it follows that the first part of the transformation of pure iron is *not* thermally activated. Upon increasing the cooling rate, the absolute value of the third maximum in the ferrite-formation rate varies only a little and the position of this third maximum shifts in the direction of higher ferrite fraction (see Fig. 9.4a). This indicates that the last (second) stage of the transformation of pure iron (third maximum in the df_α/dt curve) is thermally activated.

The development of f_α and the variation of df_α/dt in an Fe-1.79at%Co alloy during the cooling parts of three successive heat treatment cycles are shown in Figs 9.5 and 9.6. It follows that in the first heat treatment cycle the $\gamma \rightarrow \alpha$ transformation shows an abnormal transformation behavior, in the sense of the above discussion for pure iron. The $\gamma \rightarrow \alpha$ transformations of the second and third heat treatment cycles exhibit only one df_α/dt maximum, start at a temperature below the starting temperature of the first cycle, and the temperature ranges for complete transformation of the second and third cycles are practically equal and shorter than that of the first cycle. Evidently a transition from abnormal to normal transformation behavior occurs in the Fe-1.79at%Co alloy upon increasing the number of heat treatment cycles.

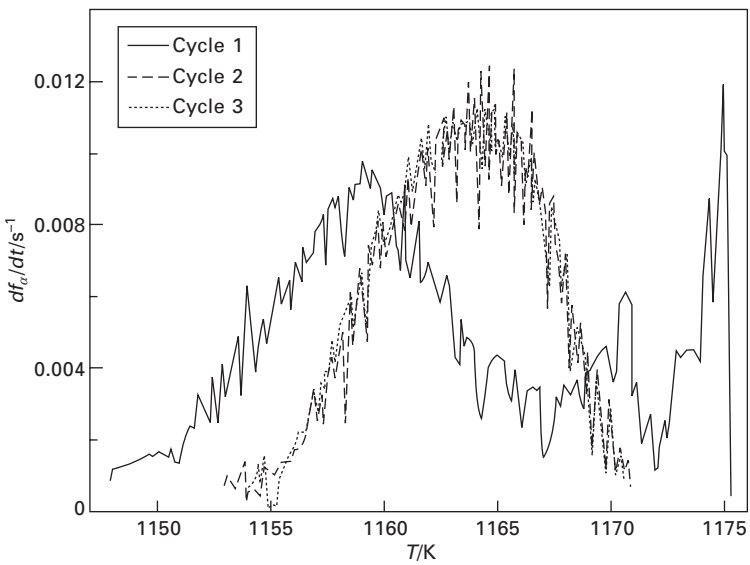
The observed change from abnormal to normal transformation behavior correlates with a decrease in grain size of the specimen. The Fe-1.79at%Co alloy exhibits a large decrease in average (α)-grain diameter upon increasing the number of heat treatment cycles: grain size decreases from 401.1 μm to 263.3 μm. Indeed, the average ferrite-grain diameter of the Fe-2.26at%Mn alloy, exhibiting only normal transformation behavior, is one order of magnitude smaller (24.8 μm) than that of the Fe-1.79at%Co alloy.

The role of grain size on the normal to abnormal transition has been demonstrated by experiments on pure iron. The transformation behavior of pure iron specimens at different initial grain size (A, B, C and D, cf. Fig. 9.7) was measured, employing a cooling rate of 10 K min^{-1}, and is shown in Figs 9.7 and 9.8. The two kinds of transformation kinetics, abnormal and

© Woodhead Publishing Limited, 2012

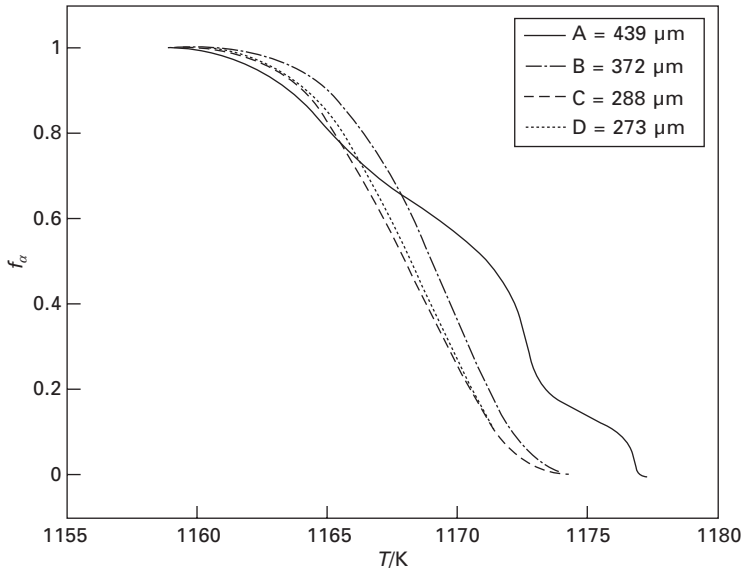


9.5 The ferrite fraction, f_α, as a function of temperature, T, as determined from isochronal dilatometric measurements of different fresh Fe-1.79at%Co alloy as determined from the length change measured at a cooling rate of 20 K min^{-1} for three subsequent heat treatment cycles; note that the results of the second and third cycle coincide (Liu *et al*. 2003).



9.6 The ferrite-formation rate, df_α/dt, as a function of temperature, T, of the Fe-1.79at%Co alloy as determined from the length change measured at a cooling rate of 20 K min^{-1} for three subsequent heat treatment cycles (Liu *et al*. 2003).

© Woodhead Publishing Limited, 2012



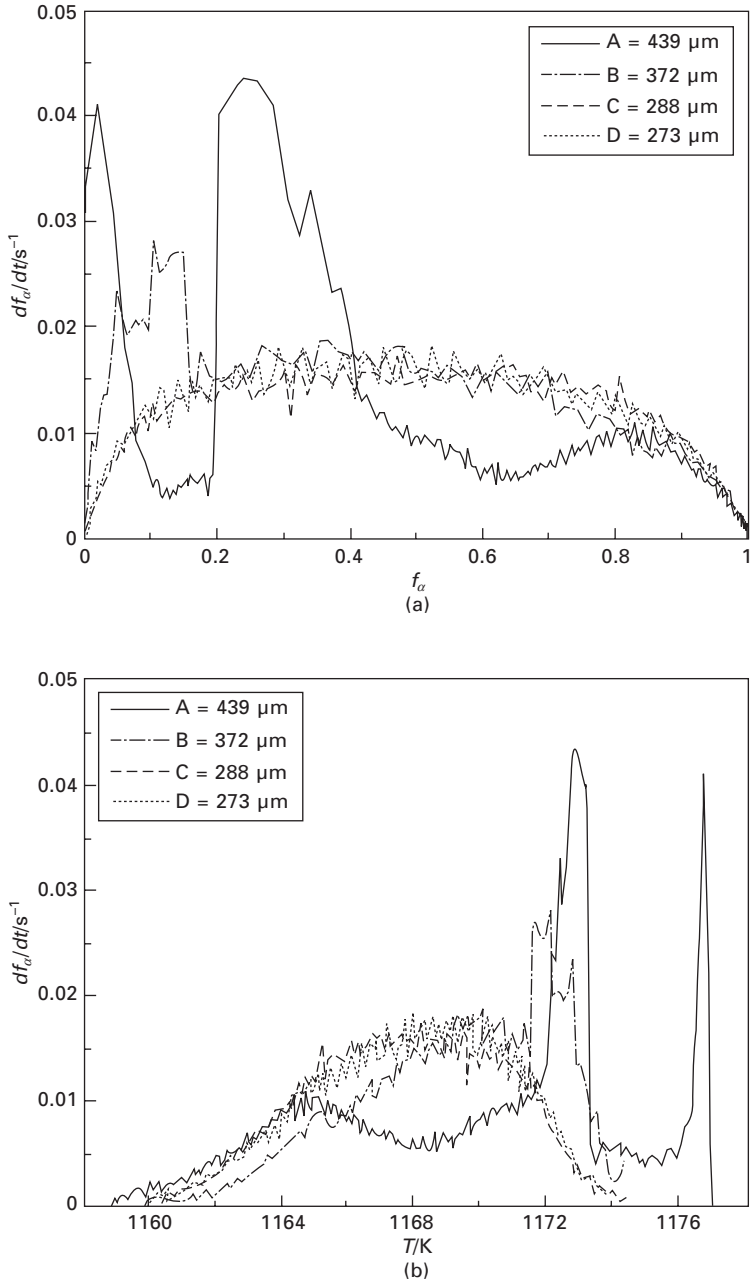
9.7 The ferrite fraction, f_α, as a function of temperature, T, as determined from isochronal dilatometric measurements of different Fe specimens (A, B, C and D exhibiting different grain sizes) subjected to cooling from the γ-phase field at a rate of 10 K min^{-1} (Liu *et al.* 2004b).

normal, are easily recognized. Specimen A, with the largest grain size, exhibits distinctly abnormal transformation behavior as revealed by the occurrence of three maxima in the df_α/dt curve. Specimens C and D, with the smallest grain size, exhibit only one maximum for the ferrite-formation rate, which is typical for normal transformation behavior. The starting temperature of the abnormal $\gamma \rightarrow \alpha$ transformation (specimen A) is slightly higher than that of the normal transformation (specimens C and D). The first maximum in the first part of the df_α/dt curve of specimen B corresponds to abnormal transformation behavior (Fig. 9.8).

The development of the ferrite fraction in Fe-0.005at%N alloy is shown for different cooling rates (5, 10 and 15 K min^{-1}; corresponding grain sizes: 219, 184 and 145 μm) in Fig. 9.9. The curves of the ferrite fraction, for 5, 10 and 15 K min^{-1}, are more or less parallel to each other. The higher the applied cooling rate, the lower is the onset temperature of the $\gamma \rightarrow \alpha$ transformation. The corresponding df_α/dt curves are shown in Fig. 9.10, both as a function of temperature and as a function of ferrite fraction. The following observations can be made:

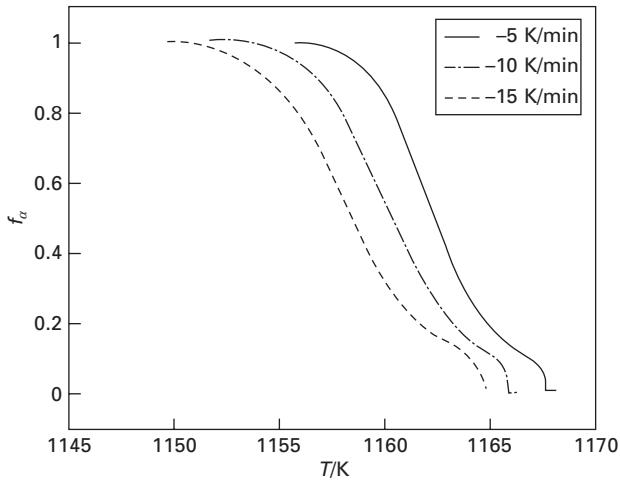
1. Abnormal transformation behavior, characterized by the occurrence of two maxima in the df_α/dt curve, occurs for all applied cooling rates.
2. The value of df_α/dt in the range of the first peak (abnormal transformation)

© Woodhead Publishing Limited, 2012



9.8 The ferrite-formation rate, df_α/dt, as a function of (a) ferrite fraction, f_α, (b) temperature, T, of different Fe specimens A, B, C and D (cf. Fig. 9.7) as determined from dilatometric measurements at a cooling rate of 10 K min^{-1} (Liu *et al*. 2004b).

© Woodhead Publishing Limited, 2012



9.9 The ferrite fraction, f_α, as a function of temperature, T, as determined from isochronal dilatometric measurements of different fresh Fe-0.005at%N alloy subjected to cooling from the γ-phase field at rates of 5, 10 and 15 K min^{-1} (Liu *et al*. 2008b).

increases strongly with increasing applied cooling rate. The first peak occurs at about the same value of f_α (= 0.02) independent of cooling rate. The range of the first peak ends at about $f_\alpha = 0.13$ (see Fig. 9.10a), which also represents the start of the last, main maximum (normal transformation).

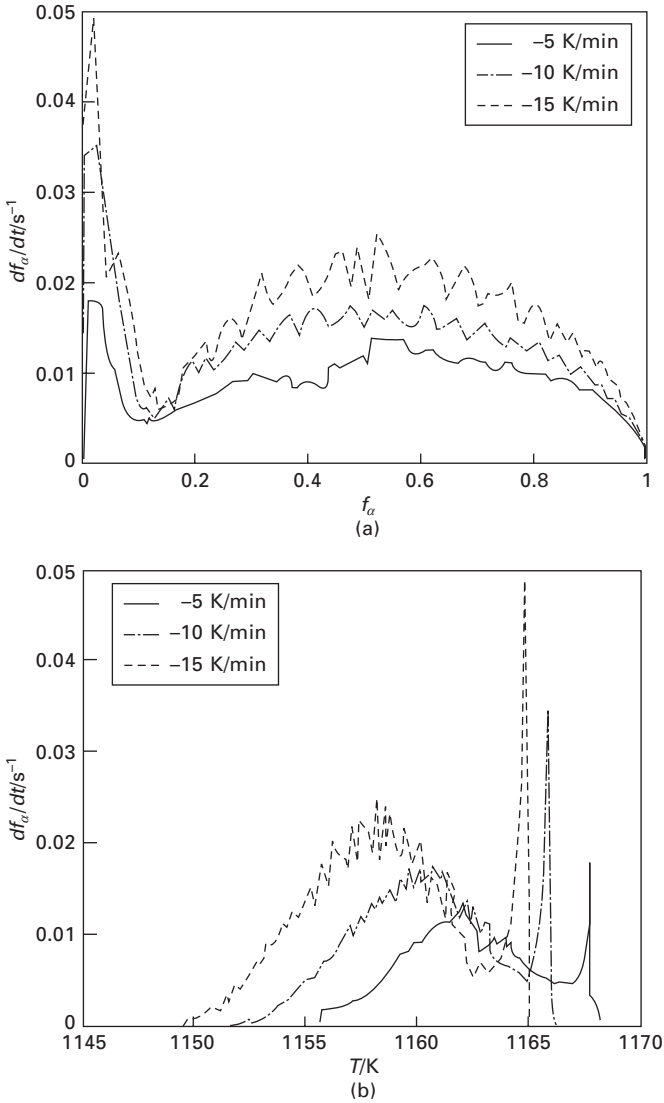
3. The value of df_α/dt in the range of the last, main maximum (normal transformation) increases slightly with increasing applied cooling rate.

The above observations for the $\gamma \rightarrow \alpha$ transformation in the Fe-0.005at%N alloy, resemble those pertaining to the abnormal transformation behavior observed for pure iron and the substitutional iron-based alloy as discussed above.

The experimentally determined onset temperatures T_{onset} for the $\gamma \rightarrow \alpha$ transformation in the Fe-0.005at%N alloy have been determined for all applied cooling rates (for more details, see Table 9.2 in Section 9.7). It follows that the temperatures at the onset of the transformation for all applied cooling rates are located in the single α-phase field (and the onset temperature decreases with increasing applied cooling rate). This result makes any effect of solute drag unlikely and is compatible with a massive, interface-controlled nature for the transformation.[2]

[2]It was recently shown by phase-field simulations and using available diffusional mobilities that solute drag effects can occur for binary Fe-C alloys below the T_0 line and above the α-solvus line. Below the α-solvus line the transformation is massive and the driving force (Gibbs energy difference) is used to move the interface and is not dissipated by diffusion of solutes to the interface and through the interface (Loginova *et al*. 2003).

© Woodhead Publishing Limited, 2012



9.10 The ferrite-formation rate, df_α/dt, as a function of (a) ferrite fraction, f_α, (b) temperature, T, of the Fe-0.005at%N alloy for applied cooling rates of 5, 10 and 15 K min^{-1} (Liu *et al.* 2008b).

The following general conclusion can be drawn: an abnormal nature of the $\gamma \rightarrow \alpha$ phase transformation occurs if the grain size is relatively large and the driving force is large (for the Fe-based alloys the last condition can be met if the transformation initiates in the single α-phase region independent of the alloying element being dissolved substitutionally or interstitially).

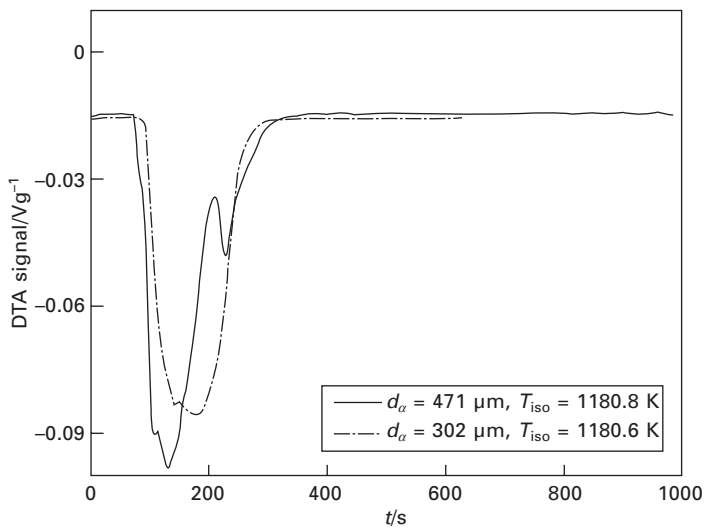
© Woodhead Publishing Limited, 2012

9.4.3 Isothermal versus non-isothermal transformation

In order to verify that abnormal transformation behavior is not limited to/caused by non-isothermal cooling, isothermal annealing experiments must be performed. The experimental accessibility of the massive $\gamma \rightarrow \alpha$ transformation in isothermally conducted experiments is not a trivial matter: the temperature window to observe the isothermal transformation of pure iron and substitutional Fe-based alloys within a practicable range of time is very narrow. For pure iron, the temperature window is about 0.6 K around 1180.7 K. Results for the rate of enthalpy release ($d\Delta H(t)/dt$) of pure iron specimens of different grain size due to the $\gamma \rightarrow \alpha$ transformation at constant temperature are shown as a function of time (t) in Fig. 9.11. (For DTA equipment applied in this experiment, the relative accuracy of temperature measurement is 0.1 K, and the absolute error (precision) is about ± 1 K; Liu *et al*. 2004b.) The results of the measured transformation enthalpy for repeated measurements were found to differ less than ± 0.4%. The corresponding df_α/dt data of the pure iron specimens of different grain size are shown as a function of annealing time in Fig. 9.12.

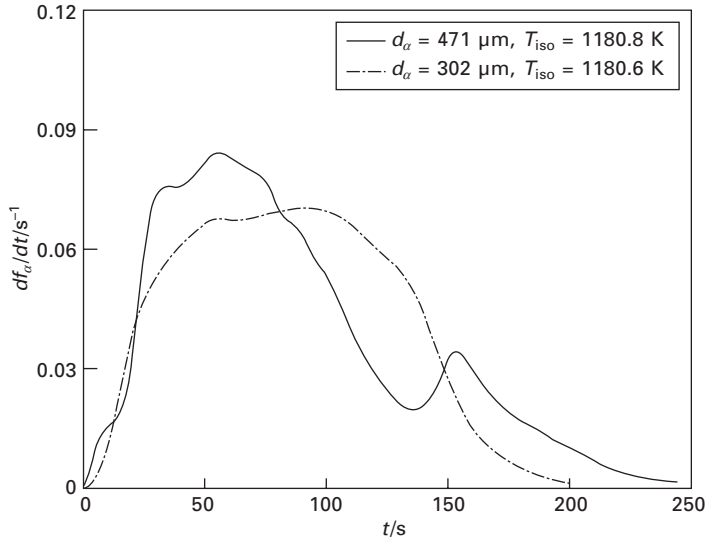
The following observations can be made:

1. Two maxima of the df_α/dt curve (abnormal transformation) occur for the specimen of relatively large grain size, as observed also in the isochronal dilatometric measurements (cf. Section 9.4.1).



9.11 The isothermally recorded DTA signal as a function of time, t, of pure iron (initially austenite) specimens of different grain size, d_α, at the indicated annealing temperatures, T_{iso} (Liu *et al*. 2004b).

© Woodhead Publishing Limited, 2012



9.12 The ferrite-formation rate, df_α/dt, as a function of time, t, of pure iron (initially austenite) specimen of different grain size, d_α, at the indicated annealing temperatures, T_{iso} (Liu *et al*. 2004b).

2. Only one distinct maximum (normal transformation) occurs for the Fe specimen of relatively small grain size (cf. Section 9.4.1).

Hence, both abnormal and normal $\gamma \rightarrow \alpha$ transformation behaviors are observed in both isochronally and isothermally conducted annealing experiments.

9.5 Kinetics of the normal transformation

9.5.1 Determination of the interface velocity

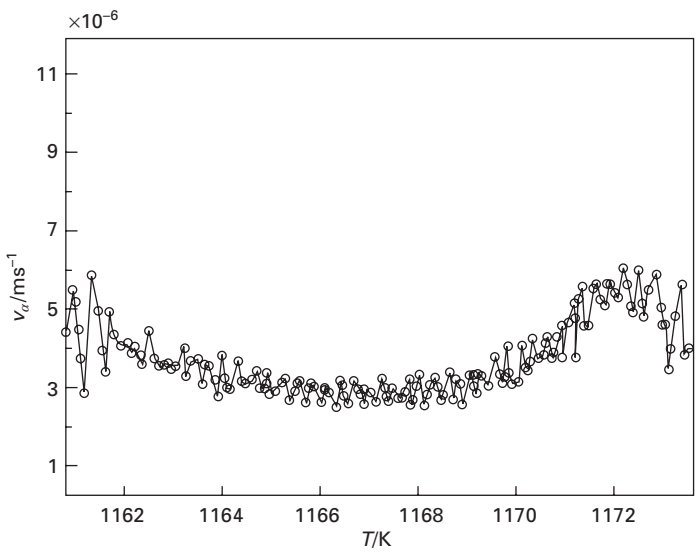
The ferrite-formation rate, according to Eq. [9.15], is proportional to the product of v_α and $(N^*)^{1/3}$. Hence, v_α and N^* cannot be determined independently from the experimentally obtained df_α/dt data. For example, the nucleus density, N^*, has to be determined separately.

For measurement of the nucleus density, different approaches have been proposed (Kempen *et al*. 2002a; Offerman *et al*. 2006). The nucleus density can be estimated from the number of final (product phase) grains, assuming (implicitly) that each grain derives from (only) one nucleus. The thus obtained nucleus density may be an underestimate of the real nucleus density due to possible grain coarsening at the higher temperatures during cooling after the $\gamma \rightarrow \alpha$ transformation of the Fe-based alloys. Because N^* occurs in Eq. [9.15] with an exponent of 1/3, an error in the nucleus density does not strongly influence the calculated values for the velocity of interface

© Woodhead Publishing Limited, 2012

migration. For the results presented below, all initial nucleus density values (recognizing the occurrence of site saturation; see discussion on page 316) were estimated from the product ferrite-grain size.

As an example, data for f_α and df_α/dt obtained upon isochronal $\gamma \rightarrow \alpha$ transformation of pure iron (specimen D), which exhibits an average grain size of 273 μm for the product (α) phase (see Liu *et al*. 2004b), were used for calculation of the interface velocity (v_α). The obtained result of v_α is shown as a function of temperature in Fig. 9.13. It is found that (the running average of) v_α is more or less constant during the whole $\gamma \rightarrow \alpha$ transformation. It is important to note that the observed fluctuations in the interface velocity are much larger than the experimental inaccuracy. The accuracy of the length change data is about ±10 nm (see Section 9.2), which causes a relative error of $\pm 3 \times 10^{-4}$ in the value determined for f_α. This uncertainly in f_α introduces a relative error of $\pm 1 \times 10^{-3}$ for the interface velocity calculated according to Eq. [9.15], which is much smaller than the observed fluctuations (of relative value 1×10^{-1}) of v_α (see Fig. 9.13). The interface density in these relatively large grained specimens is small, so that 'averaging out' does not occur in the dilatometric signal. The observed fluctuations of v_α can be interpreted as a succession of periods of acceleration and deceleration in the interface-migration process (due to the accumulation and relaxation (e.g. by the vacancy diffusion; Svoboda *et al*. 2005) of stress; see discussion at the end of Section 9.5.2), in correspondence with observations by *in-situ* transmission electron microscopy analysis (Onink *et al*. 1995).



9.13 The γ/α interface velocity, v_α, as a function of temperature, *T*, of pure iron (specimen D; 10 K min^{-1}), as derived from dilatometric data applying Eq. [9.15] (Liu *et al*. 2004b).

© Woodhead Publishing Limited, 2012

The interface velocity, v_α, can be expected to be constant during isothermal massive solid-state phase transformation. The observed constancy of v_α in the non-isothermal transformation can be understood considering the small temperature range (about 45 K) needed to complete the transformation.

9.5.2 Interface mobility and transformation strain

The growth velocity of the migrating interface can be given for large undercooling by Eq. [9.6] and for small undercooling by Eq. [9.7]. Small undercooling ($-\Delta G_{\gamma\alpha}$ small compared to RT), pertains to the massive γ/α transformation of pure iron (see Section 9.4.2).

Data for the interface mobility $M(T)$ generally are experimentally hardly available. With known values for the driving force and the interface velocity, the interface mobility can be calculated (see Eq. [9.7]). Mobility data obtained in this way for the grain growth of pure iron (ferrite) ($M = 0.035 \exp(-147000/RT)$ ($m^4J^{-1}s^{-1} = 4.9 \times 10^3 \exp(-147000/RT)$ mmol $J^{-1}s^{-1}$) (Hillert 1975) were adopted extensively for the kinetic analyses of the $\gamma \rightarrow \alpha$ and $\alpha \rightarrow \gamma$ transformations (e.g. Kempen *et al*. 2002a; Liu *et al*. 2004a; 2004b, Mohapatra *et al*. 2007). These values reflect the intrinsic mobility of an α/α interface: no phase change takes place upon grain growth, the chemical driving force is zero, and the elastic and plastic accommodation energy can be neglected; the only driving force is the (decrease of) interface energy. The mobility values for α/α and γ/α interfaces were discussed recently (Höglund & Hillert 2006) and it was stated that there is a strong indication from the evaluated γ/α mobilities (determined assuming only the difference in chemical Gibbs energy as driving force) that the γ/α mobility is much lower than that of the α/α interface boundaries, which is also stated by Krielaart & van der Zwaag (1998), Wits *et al*. (2000) and Gamsjäger *et al*. (2006). However, the effect of transformation-strain energy on the interface mobility was ignored in these works.

An estimate of the γ/α mobility, obtained in the way adopted by Höglund and Hillert (2006), can be obtained as well from the experimentally determined transformed fraction for the massive γ/α transformation of pure iron (samples C and D: normal transformation; see Section 9.4.2); as follows.

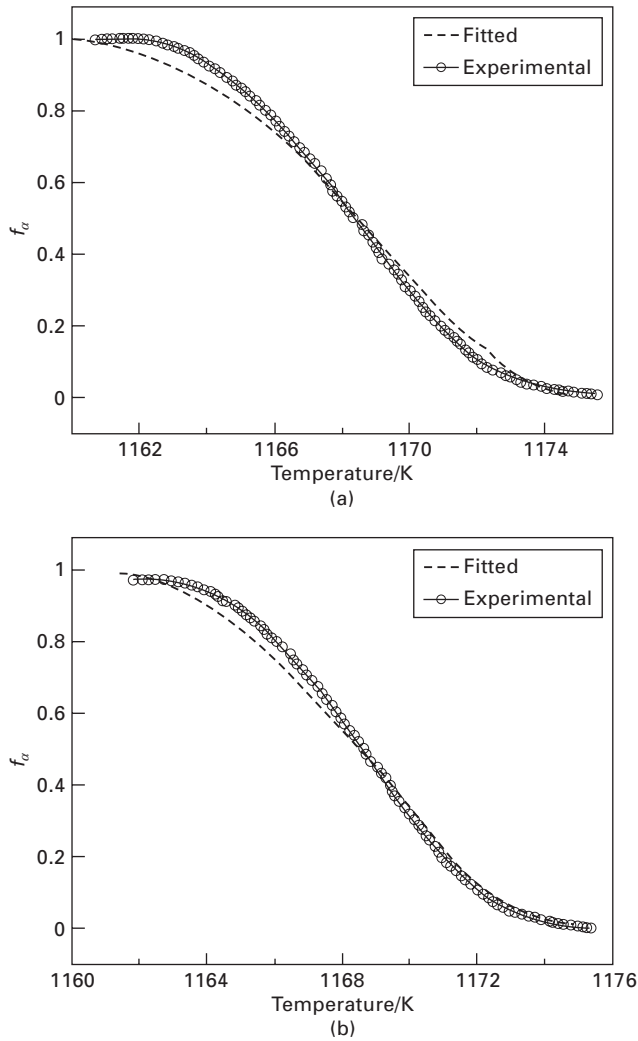
The combination of Eq. [9.7] with Eq. [9.15] results in:

$$\frac{df_\alpha}{dt} = 3(N^* g)^{1/3}(1 - f_\alpha^2) M_0 \exp\left(\frac{-Q}{RT}\right)(-\Delta G_{\alpha\gamma}^{\text{chem}}) \operatorname{arctanh}^{2/3}(f_\alpha) \quad [9.16]$$

The above equation can be used to determine M_0 values by fitting this model to the measured kinetic data by adopting the nucleus density as estimated from the measured grain size and using the experimental data of f_α and df_α/dt. The temperature dependence of the chemical driving force ($-\Delta G_{\alpha\gamma}^{\text{chem}}$)) of pure iron at atmospheric pressure was evaluated according to the Scientific Group

© Woodhead Publishing Limited, 2012

Thermodata Europe (SGTE) (Dinsdale 1991). The magnetic model given by Hillert and Jarl (1978) was adopted to evaluate the magnetic contribution to the ferrite Gibbs energy. M_0 was taken as the fitting parameter for the normal, main maximum in the explored $\gamma \rightarrow \alpha$ phase transformation rate curve of pure iron; the activation energy of M, Q, was taken the same as that for the grain growth of ferrite. A comparison of the experimental and fitted ferrite fractions can be made as a function of temperature in Fig. 9.14. The thus



9.14 Comparison of the experimental and fitted values for the ferrite fraction (f_α) as a function of temperature in pure iron specimens of different grain size: (a) sample C (grain size 288 μm) and (b) sample D (grain size 273 μm) (Liu *et al.* 2004b) (applied cooling rate: 10 K min^{-1}) (Liu *et al.* 2008b).

© Woodhead Publishing Limited, 2012

obtained M_0 values are 1.4 (C), and 1.3 (D) mmol $J^{-1}s^{-1}$. Thus, as a result, an average value is obtained for M_0 for the γ/α interface in pure iron: about 1.35 mmol $J^{-1}s^{-1}$, also very much lower than that for the α/α interface.

However, it should be emphasized in particular that the effect of the unknown elastic and plastic accommodation energies that occur in reality, but which are not recognized in Eq. [9.16] and not accounted for in the work of Hillert (1975), Krielaart and van der Zwaag (1998), Wits *et al*. (2000), Höglund and Hillert (2006) and Gamsjäger *et al*. (2006), for the $\gamma \rightarrow \alpha$ transformation of pure iron now are implicitly incorporated in the above obtained value for M_0. This may simply explain the difference, considered by Höglund and Hillert (2006), of such calculated M_0 values for the γ/α and α/α interfaces.

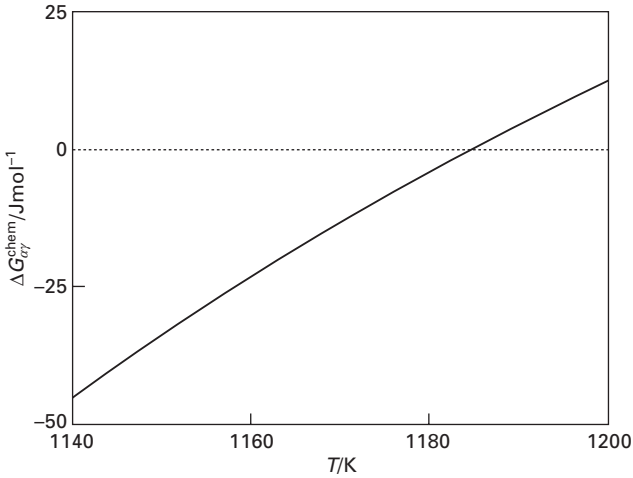
The transformation energy does have a direct implication for the resulting interface velocity. The negative of the driving force for the explored $\gamma \rightarrow \alpha$ transformation in the Fe-based alloys can be written as (Kempen *et al*. 2002a):

$$\Delta G_{\alpha\gamma}(T, f_\alpha) = \Delta G_{\alpha\gamma}^{\text{chem}}(T) + [\Delta G_{\alpha\gamma}^{\text{def}}(f_\alpha) + \Delta G_{\alpha\gamma}^{\text{int}}(f_\alpha)] \qquad [9.17]$$

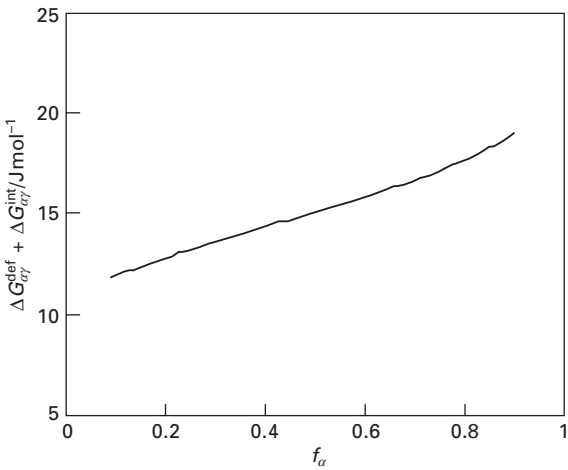
where $\Delta G_{\alpha\gamma}^{\text{chem}}$ is the molar chemical Gibbs energy difference of the ferrite and austenite, $\Delta G_{\alpha\gamma}^{\text{def}}$ is the summation of molar elastic and plastic accommodation energies resulting from the crystalline strain induced to accommodate the volume misfit of α and γ, and $\Delta G_{\alpha\gamma}^{\text{int}}$ is the molar free energy of the γ/α interface. The chemical driving force depends on temperature, and not on the fraction transformed, because the transformation is partitionless. Both $\Delta G_{\alpha\gamma}^{\text{def}}$ and $\Delta G_{\alpha\gamma}^{\text{int}}$ depend primarily on the fraction transformed (f_α) (and not directly on temperature). The driving force ($-\Delta G_{\alpha\gamma}$) consists of a positive term ($-\Delta G_{\alpha\gamma}^{\text{chem}}$) which favors the transformation, and two negative terms ($-\Delta G_{\alpha\gamma}^{\text{def}}$ and $-\Delta G_{\alpha\gamma}^{\text{int}}$) which counteract the transformation. Adopting an interface energy of 0.8 J m^{-2} (Zhan & Johnson 1993) for the α/γ interface and taking the number of growing particles as 4.2×10^{10} mol^{-1} (as determined for specimen C; Liu *et al*. 2004b), the energy dissipated by the formation of interface is estimated to be 0.2 J mol^{-1} at a stage of transformation of f_α = 0.5. Thus, $\Delta G_{\alpha\gamma}^{\text{int}}$ is negligible in comparison to $\Delta G_{\alpha\gamma}^{\text{def}}$ and can be neglected for the following determination of transformation-strain energy.

Adopting Eqs [9.7] and [9.17] and using the experimental data of interface velocity (Fig. 9.13) and nucleus density (as determined from the ferrite grain size after the transformation (cf. Fig. 9.7)), $\Delta G_{\alpha\gamma}^{\text{chem}}$ presented in Fig. 9.15, and the interface-mobility data of grain growth in Fe, ($\Delta G_{\alpha\gamma}^{\text{def}} + \Delta G_{\alpha\gamma}^{\text{int}}$) can be calculated. Thus determined results are shown in Fig. 9.16. As demonstrated above, $\Delta G_{\alpha\gamma}^{\text{int}}$ is negligible as compared to the $\Delta G_{\alpha\gamma}^{\text{chem}}$. Hence, the absolute value of $\Delta G_{\alpha\gamma}^{\text{def}}$ increases gradually with increasing the ferrite fraction and is of the same order of magnitude as $\Delta G_{\alpha\gamma}^{\text{chem}}$.

© Woodhead Publishing Limited, 2012



9.15 Chemical driving force, $\Delta G_{\alpha\gamma}^{chem}$, as a function of temperature, T, for the $\gamma \rightarrow \alpha$ transformation of pure iron (Liu *et al.* 2004b).



9.16 The sum of the misfit-accommodation energy and the interface energy, $\Delta G_{\alpha\gamma}^{def} + \Delta G_{\alpha\gamma}^{int}$, as a function of ferrite fraction, f_α, for the normal $\gamma \rightarrow \alpha$ transformation of pure iron (specimen D; 10 K min^{-1}) (Liu *et al.* 2004b).

A similar analysis can also be applied to the kinetic data obtained for the normal $\gamma \rightarrow \alpha$ transformation of the Fe-based alloys. Then, for these cases, one may question the applicability of the M_0 data of α/α grain boundaries in pure iron (see discussion in the beginning of this section). To investigate the sensitivity of the conclusion given at the end of the preceding paragraph for large variation in M_0, the above kinetic analysis has been performed for the normal $\gamma \rightarrow \alpha$ transformation of the Fe-1.79at%Co alloy for both

© Woodhead Publishing Limited, 2012

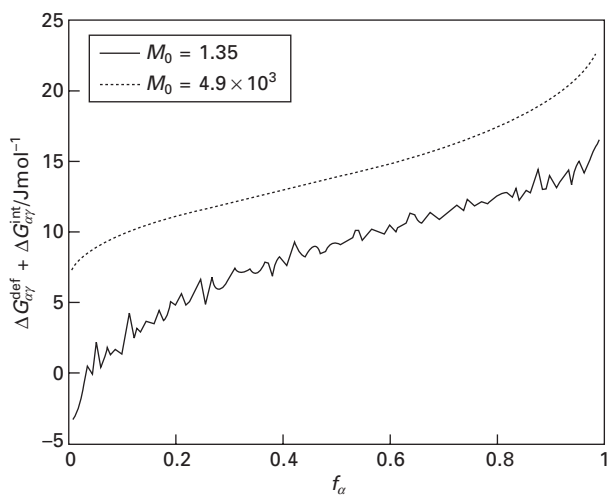
greatly different M_0 values discussed above. The results for $\Delta G_{\alpha\gamma}^{\text{def}}$ + ($\Delta G_{\alpha\gamma}^{\text{int}}$, which is negligible (see above)), are shown in Fig. 9.17 for both values of M_0. Although both M_0 values differ about a factor of 4000, the $\Delta G_{\alpha\gamma}^{\text{def}}$ values differ only about a factor of 2.

The above results substantiate the general validity of the conclusion that the misfit-induced deformation energy is of the same order of magnitude as the chemical driving force. This can be discussed as follows. Upon cooling, the transformation can proceed as long as a net driving force occurs ($\Delta G_{\alpha\gamma} < 0$). As soon as the deformation-induced strain energy has become equal to the chemical driving force, the transformation has to come to a halt. Upon continued cooling, a net driving force can occur again, because the chemical driving force increases with decreasing temperature (or, upon isothermal holding, strain relaxation may reduce $\Delta G_{\alpha\gamma}^{\text{def}}$ and a net driving force occurs again). The transformation then proceeds (again) until the deformation-induced energy (again) is equal to the chemical driving force. This leads to the irregular nature of the interface velocity (see Fig. 9.13).

9.6 Kinetics of the abnormal transformation

9.6.1 Origin of abnormal transformation kinetics: repeated nucleation

In the abnormal transformation, the first transformation stage (incorporating the first two maxima in df_α/dt of the pure iron and the Fe-1.79at%Co alloy,



9.17 The sum of the misfit-accommodation energy and interface energy as a function of ferrite fraction (f_α) for the normal $\gamma \rightarrow \alpha$ transformation of an Fe-1.79at%Co alloy (cooling rate: 10 K min^{-1}) by adopting different M_0 values (unit: mmol J^{-1}s^{-1}) (Liu *et al.* 2008b).

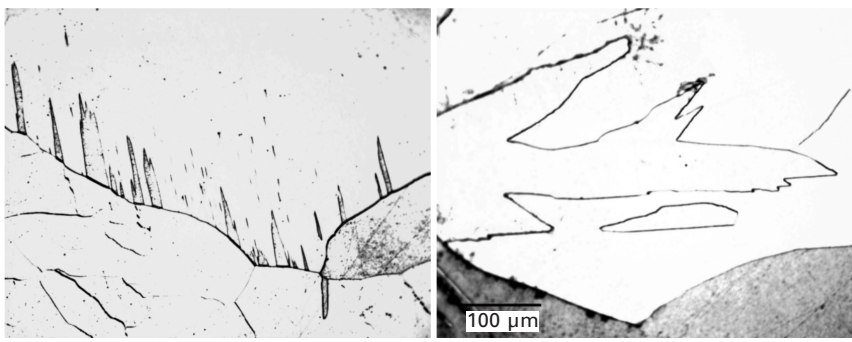
© Woodhead Publishing Limited, 2012

the first one maximum in df_α/dt of the ultra-low-nitrogen Fe-N alloy; cf. results gathered in Section 9.4.2) is not thermally activated. This can be discussed as follows.

The $\gamma \rightarrow \alpha$ transformation is accompanied by build-up of a considerable amount of volume misfit-strain energy, which, as shown in Section 9.5.2, is of the same order of magnitude as the chemical Gibbs energy driving the reaction. Thus it is likely that the volume misfit-strain energy largely influences the transformation kinetics (as demonstrated for the normal transformation in Section 9.5). A growing ferrite grain induces strain and defects in the surrounding austenite. This deformed austenite, immediately in front of the growing ferrite, may allow easier nucleation of ferrite than the original undeformed austenite. Hence, occurrence of repeated nucleation of the ferrite in front of the migrating interface may be understood: autocatalytic nucleation. The occurrence and extent of this repeated nucleation thus primarily depend on the degree of transformation and not on temperature (cooling rate), as observed.

The first ferrite phase nucleates at the original γ-grain boundaries and the α grains advance into the parent austenite grain. This interpretation is supported by the microstructure shown in Fig. 9.18. Evidently, a lot of ferrite subgrains formed along the original γ-grain boundaries (Fig. 9.18a). Branching is observed too (Fig. 9.18b), suggesting repeated nucleation of the ferrite in front of the migrating γ/α interface.

Obviously, a large amount of nuclei generated by autocatalytic nucleation would lead to grain refinement. The grain size measured corresponds to grains having high-angle grain boundaries. A lot of subgrains with small-angle grain boundaries can be observed in the ferrite grains, which may be indicative of



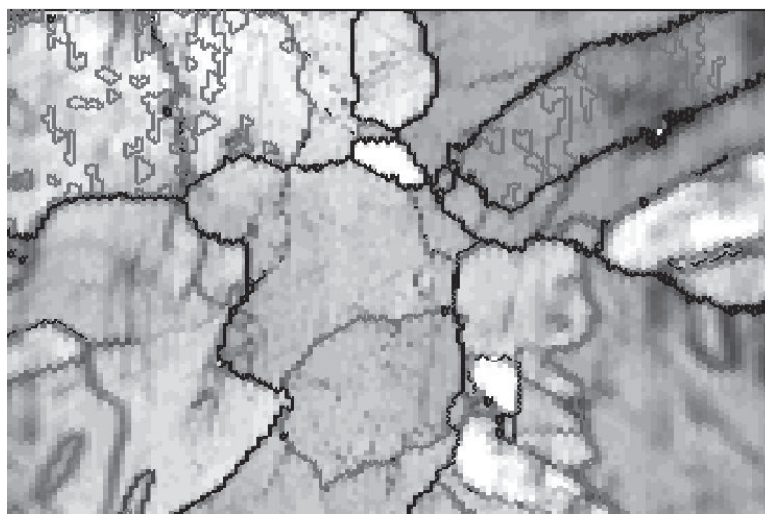
9.18 Ferrite-grain morphology of the Fe-1.79at%Co alloy after having experienced the abnormal $\gamma \rightarrow \alpha$ transformation (first cycle; see Section 9.4.2). (a) Needle-like ferrite subgrains have developed along the high-angle γ-grain boundaries and (b) ferrite subgrains with side branches (Liu *et al.* 2003).

© Woodhead Publishing Limited, 2012

the additional nuclei formed during the autocatalytic nucleation. Small-angle boundaries corresponding to differences in orientation of about 1°, 2°, 3° and 5° are shown in Fig. 9.19 by thin, grey lines. Thick, black lines in the figure correspond to high-angle grain boundaries representing orientation differences larger than 15°. It is suggested that the high-angle boundaries indicate the initial austenite-grain boundaries, and that the small-angle grain boundaries exhibit the subgrain structure caused by the autocatalytic nucleation.

Due to the autocatalytically induced nucleation 'bursts', followed by consumption of the correspondingly generated 'new' ferrite grains upon growth of the 'older' ferrite grains, the first (one, two or more) maxima in the ferrite-formation rate have to be modeled separately; i.e. the kinetic model must account for the extra nuclei, due to autocatalytic nucleation, to be practically swallowed by the advancing ferrite front originating from the original austenite-grain boundaries. This leads to the introduction of a correction factor in the expression for the nucleation density that depends on the degree of transformation: see Eq. [9.3].

Adopting mixed nucleation, comprising site saturation and autocatalytic nucleation (cf. page 316), the nucleation-density changes in the transformation ranges covered by, for example, the first and second peaks of df_α/dt of abnormal transformation of pure iron (see Fig. 9.3 and Section 9.4.2) can be given by: $N = N^* + p_1(f_\alpha - f_{st1})\left(\frac{f_{tr1} - f_\alpha}{f_{tr1} - f_{st1}}\right)$ for the first peak in the $df_\alpha/$



9.19 High-angle grain boundaries (the thick, black lines) and small-angle grain boundaries between subgrains (the thin, grey lines) in the pure iron (specimen A; cf. Fig. 9.8) after experiencing the abnormal $\gamma \rightarrow \alpha$ transformation (Liu *et al.* 2004b).

© Woodhead Publishing Limited, 2012

dt curve, and $N = N^* + p_2(f_\alpha - f_{st2})\left(\frac{f_{tr2} - f_\alpha}{f_{tr2} - f_{st2}}\right)$ for the second peak in the df_α/dt curve, where N^* is the initial nucleus density (contribution due to site saturation; as estimated from the measured ferrite-grain size), and where the subscripts 1 and 2 pertain to the first and second df_α/dt maxima in the first, not thermally activated, part of the transformation.

Thus, the nucleation rate $\dot{N}$ can eventually be expressed as:

$$\dot{N} = N^*\delta(t-0) + ap_1\frac{df_\alpha}{dt}\left(\frac{f_{tr1} - 2f_\alpha}{f_{tr1} - f_{st1}}\right) + bp_2\frac{df_\alpha}{dt}\left(\frac{f_{tr2} + f_{st2} - 2f_\alpha}{f_{tr2} - f_{st2}}\right)$$

with $a = 1$ for $f_\alpha \in [f_{st1}, f_{tr1}]$ and $a = 0$ for $f_a \notin [f_{st1}, f_{tr1}]$, $b = 1$ for $f_a \in [f_{st2}, f_{tr2}]$ and $b = 0$ for $f_\alpha \notin [f_{st2}, f_{tr2}]$.

Now, combining this nucleation model with the interface-controlled growth model (Eq. [9.4]), the extended volume can be expressed by Eq. [9.8]. Furthermore the impingement correction is desired for an intermediate of the cases of the ideally periodically and of the ideally randomly dispersed growing particles (Eq. [9.12]). Then it follows by substitution of Eqs [9.4] and [9.8] into Eq. [9.12]:

$$\operatorname{arctanh}(f_\alpha) = v_\alpha^3\left[\begin{array}{l} N^*t^3 + \dfrac{ap_1}{f_{tr1} - f_{st1}}\displaystyle\int_0^t \frac{df_\alpha}{d\tau}(f_{tr1} - 2f_\alpha)(t-\tau)^3 \\ \qquad + \dfrac{bp_2}{f_{tr2} - f_{st2}}\displaystyle\int_0^t \frac{df_\alpha}{d\tau}(f_{tr2} + f_{st2} - 2f_\alpha)(t-\tau)^3 d\tau \end{array}\right] \quad [9.18]$$

9.6.2 Variation of nucleus density

Using the known data of f_α and df_α/dt as a function of $T(t)$, as determined by isochronal dilatometric measurements of the pure iron specimen A (see Fig. 9.8), the value for the initial nucleus density (N^*) as estimated from the measured grain size, and the value for the γ/α interface velocity as determined from the kinetic analysis of the normal transformation (e.g. $v_\alpha = 3.05 \times 10^{-6}$ ms^{-1} (for pure iron; see Fig. 9.13)), the autocatalytic factors (p_1 and p_2) operating in the abnormal transformation can now be determined by fitting Eq. [9.18] to the experimental data for df_α/dt and f_α as a function of time. The thus obtained autocatalytic factors for pure iron have been listed in Table 9.1 for the various cooling rates applied. The corresponding variation of the nucleus density during the abnormal transformation of the pure iron (sample A), is shown as a function of ferrite fraction for different cooling rates in Fig. 9.20.

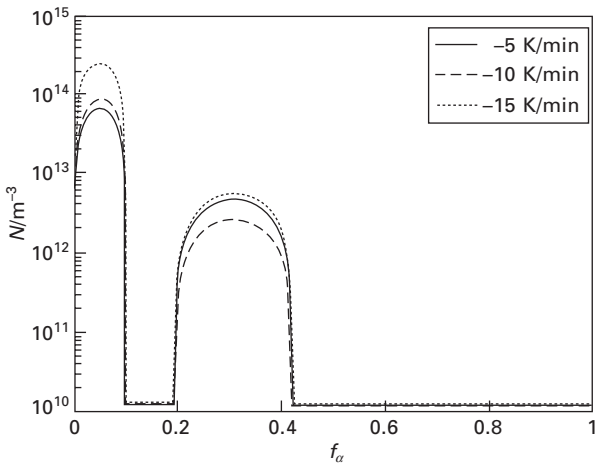
The values of the autocatalytic factor (p) for the first and second maxima in the abnormal transformation of pure iron are about 10^{15} and 10^{13} m^{-3},

© Woodhead Publishing Limited, 2012

Table 9.1 The autocatalytic factor, *p*, as determined for pure iron (grain size: 439 μm) from the first two transformation stages during the abnormal $\gamma \rightarrow \alpha$ transformation, at different applied cooling rates

Cooling rate, K min^{-1}	*p*, m^{-3}	
	First peak ($0 < f_\alpha < 0.10$)	Second peak ($0.19 < f_\alpha < 0.42$)
5	2.7×10^{15}	3.6×10^{13}
10	3.5×10^{15}	4.3×10^{13}
15	9.9×10^{15}	9.9×10^{13}

Source: Liu *et al.* (2004b).



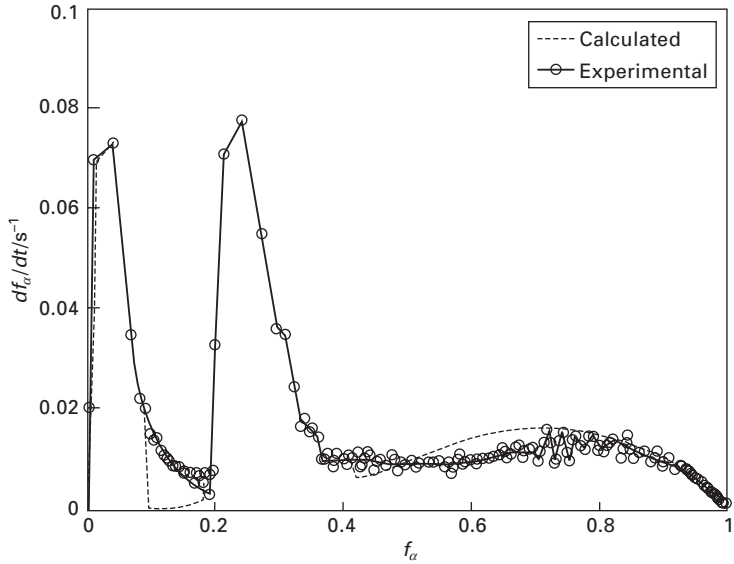
9.20 The nucleus density, *N*, as a function of f_α as determined for the $\gamma \rightarrow \alpha$ transformation by fitting the model for abnormal transformation kinetics (cf. Eq. [9.18]) to the dilatometric data observed for pure iron (grain size: 439 μm) for cooling rates of 5, 10 and 15 K min^{-1} (Liu *et al.* 2004b).

respectively. These autocatalytic factors are about two orders of magnitude smaller than those typical for the martensitic transformation of steels, which are of the order of 10^{17} m^{-3} (Saker *et al.* 1991).

A comparison of experimental df_α/dt data and those calculated by model fitting for the pure iron specimen is provided in Fig. 9.21. In view of the simplicity of the model (Eq. [9.18]), the calculated df_α/dt values agree reasonably well with the experimental data.

A relatively large austenite-grain size is required for the occurrence of abnormal transformation kinetics. Then it is interesting to consider the kinetic data obtained for a specimen of intermediate austenite grain size. Data for df_α/dt and f_α of a pure iron specimen B (grain size: 372 μm; see Fig. 9.8) were also analysed on the basis of Eq. [9.18]. A comparison of the

© Woodhead Publishing Limited, 2012



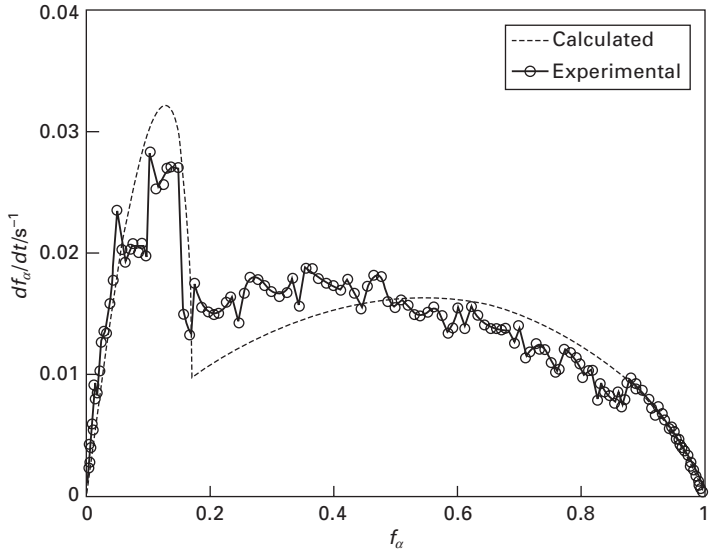
9.21 Comparison of the calculated (fitted) and experimental df_α/dt data as a function of ferrite fraction, f_α, for the abnormal transformation of pure iron (grain size: 439 μm) with a cooling rate of 15 K min^{-1} (Liu *et al.* 2004b).

measured and calculated (by model fitting) df_α/dt is provided in Fig. 9.22. The variation of nucleus density during the $\gamma \rightarrow \alpha$ transformation is given in Fig. 9.23 as a function of ferrite fraction. The nucleus density exhibits a maximum in the first part of the transformation ($f_\alpha < 0.19$), characterized by an autocatalytic factor of about 7.8×10^{13} m^{-3}. As compared to the abnormal transformation in the pure iron specimen A (grain size: 439 μm; Fig. 9.21), the influence of autocatalytic nucleation on transformation of the pure iron specimen B of smaller grain size is much smaller: the autocatalytic factor decreases with decreasing austenite grain size.

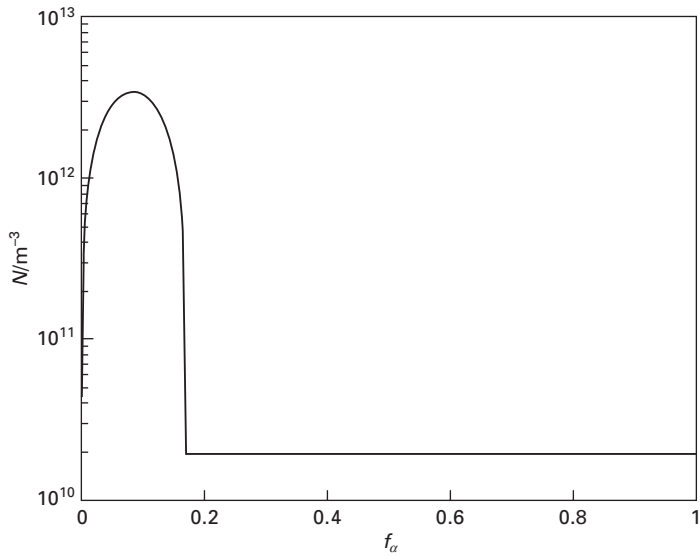
At a higher cooling rate the transformation starts at a lower temperature. Accordingly, the chemical driving force is correspondingly larger (cf. Fig. 9.15). Therefore more misfit-strain energy can be accommodated before the net driving force becomes nil. Consequently the autocatalytic effect is larger for larger cooling rates: indeed, the autocatalytic factors for both the first and the second maxima of df_α/dt increase with increasing cooling rate (see Table 9.1).

The results presented here for the abnormal transformation of pure iron are exemplary for the similar results obtained for Fe-1.79at%Co (Liu *et al.* 2004a) and Fe-0.005at%N (Liu *et al.* 2008b).

© Woodhead Publishing Limited, 2012



9.22 The ferrite-formation rate, df_α/dt, as a function of ferrite fraction, f_α, of pure iron (grain size: 372 μm) at 10 K min^{-1}. The dashed line represents the fit of the model for abnormal transformation behavior to the measured dilatometric data (Liu *et al*. 2004b).



9.23 The nucleus density, *N*, as a function of ferrite fraction, f_α, for the $\gamma \rightarrow \alpha$ transformation observed for the pure iron (grain size: 372 μm) at 10 K min^{-1}. Results obtained by fitting the model for abnormal transformation kinetics to the measured dilatometric data (Liu *et al*. 2004b).

© Woodhead Publishing Limited, 2012

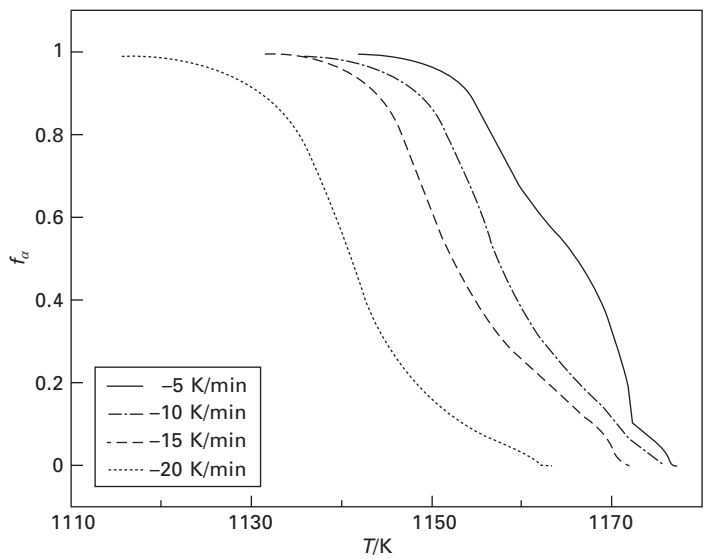
9.7 Transition from diffusion-controlled growth to interface-controlled growth

9.7.1 Isochronal $\gamma \rightarrow \alpha$ transformation in ultra-low-carbon alloys

The development of f_α and the corresponding df_α/dt is shown for ultra-low-carbon Fe-C alloy in Figs 9.24 and 9.25. The normal *S*-type transformation curve appears only for the f_α curve recorded for the largest cooling rate (20 K min^{-1}; Fig. 9.24) and, thus the corresponding df_α/dt data exhibits only one maximum (Fig. 9.25d). In this sense an abnormal transformation curve is observed for the smallest rate of 5 K min^{-1} (Fig. 9.24) and three maxima occur in the corresponding df_α/dt curve (Fig. 9.25a). The transformation curves recorded at cooling rates of 10 and 15 K min^{-1} take an intermediate position (Figs 9.24, 9.25b and 9.25c).

A direct comparison of the df_α/dt data for the Fe-0.01at%C alloy considered here and the abnormal transformation of pure iron (Section 9.4.2) reveals the following differences (see Fig. 9.26):

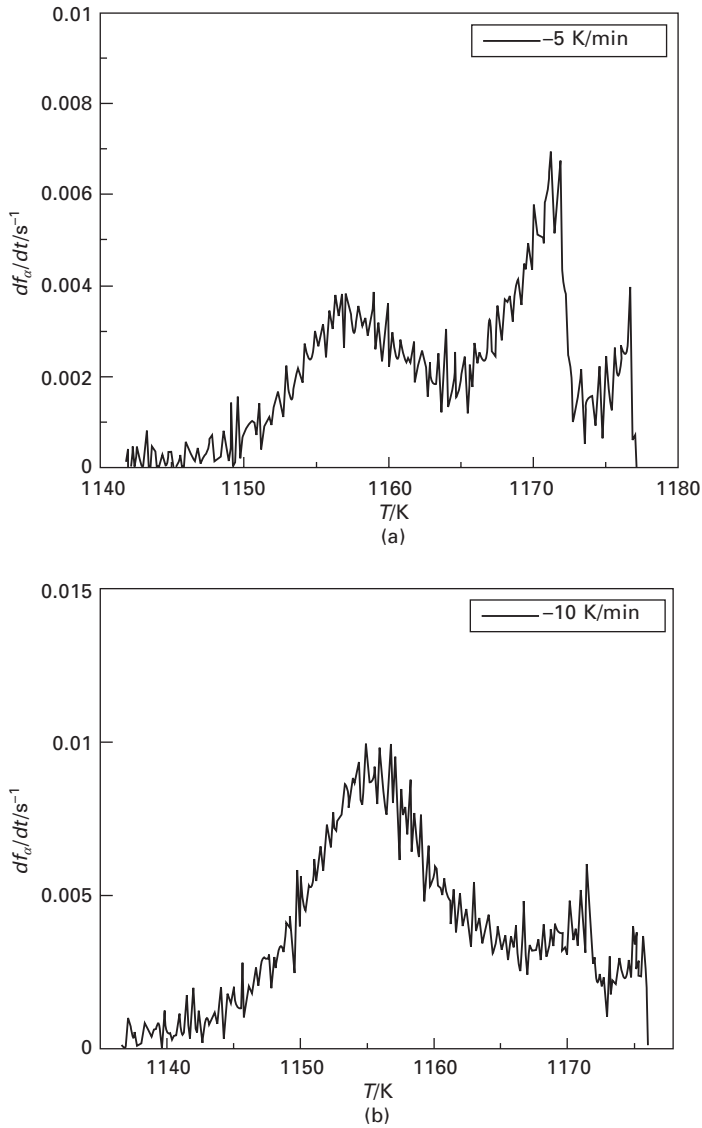
- The number of additional df_α/dt maxima in the first part of the transformation does not depend on cooling rate for pure iron, whereas for the Fe-0.01at%C alloy the number of additional df_α/dt maxima decreases with increasing cooling rate.



9.24 The ferrite fraction, f_α, as a function of temperature *T*, calculated from dilatometric measurements of different fresh Fe-0.01at%C alloy subjected to cooling from the γ-phase field at different rates (Liu *et al.* 2006).

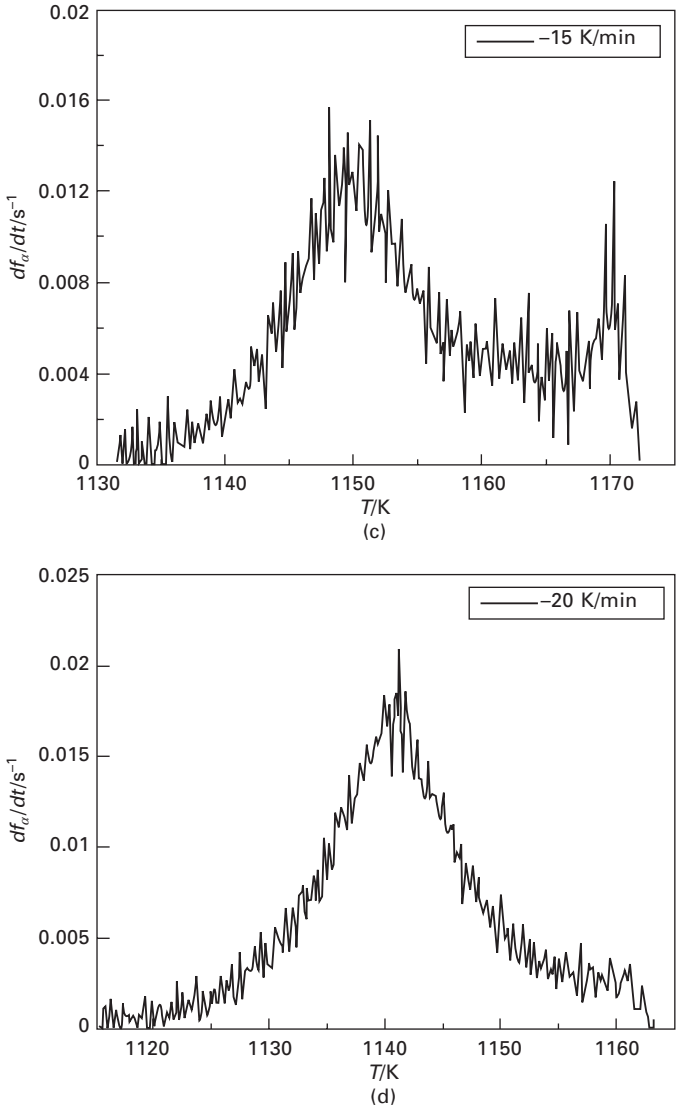
© Woodhead Publishing Limited, 2012

- For pure iron the additional df_α/dt maxima occur at approximately the same values of the degree of transformation and increase with cooling rate. This does not hold for the Fe-0.01at%C alloy.



9.25 The ferrite-formation rate, df_α/dt, as a function of temperature, T, of the Fe-0.01at%C alloy as determined from the length-change measurements at different cooling rates of (a) 5, (b) 10, (c) 15 and (d) 20 K min^{-1} (cf. Fig. 9.24) (Liu *et al.* 2006).

© Woodhead Publishing Limited, 2012

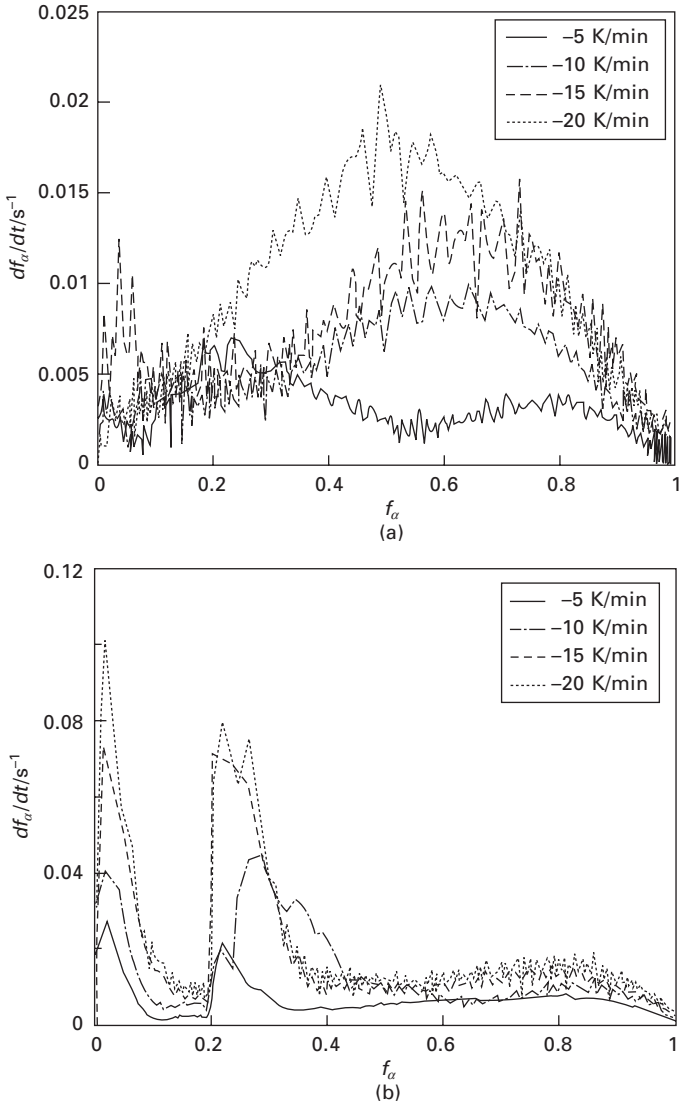


9.25 Continued

This discussion suggests that the transformation mechanism for the $\gamma \rightarrow \alpha$ transformation depends on the cooling rate applied for the Fe-0.01at%C alloy, whereas this is not the case for pure iron and the iron-based alloys considered in Section 9.4.2.

Microstructures (grain morphologies) of the Fe-0.01at%C alloy after completed $\gamma \rightarrow \alpha$ transformation are shown in the orientation-imaging micrographs (OIM) of Fig. 9.27. Thick, black lines in the figure correspond

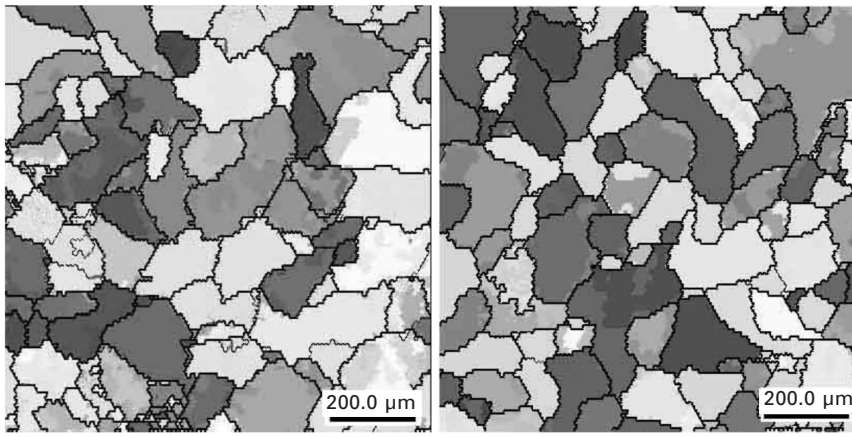
© Woodhead Publishing Limited, 2012



9.26 Comparison of the ferrite-formation rate, df_α/dt, as a function of the ferrite fraction, f_α, of (a) Fe-0.01at%C alloy (corresponding to the data shown in Fig. 9.25), and (b) pure iron for the applied cooling rates of 5, 10, 15 and 20 K min^{-1} (Liu *et al*. 2006).

to high-angle grain boundaries representing orientation differences larger than 15°; these boundaries represent the initial γ-grain boundaries. Subgrains with differences in orientation from 2° to 5° can be discerned in the figures by image (grey) contrast inside the high-angle grain boundary. In the Fe-0.01at%C alloy transformed upon cooling at a rate of 5 K min^{-1} (Fig. 9.27a),

© Woodhead Publishing Limited, 2012



9.27 Micrographs obtained by orientation imaging microscopy (OIM) showing large-angle grain boundaries (the thick, black lines) and subgrains (small-angle grain boundaries) indicated by image (grey) contrast inside the high-angle grain boundary in the Fe-0.01at%C alloy after the $\gamma \rightarrow \alpha$ transformation with applied cooling rates of (a) 5 K min^{-1} and (b) 20 K min^{-1} (Liu *et al.* 2006).

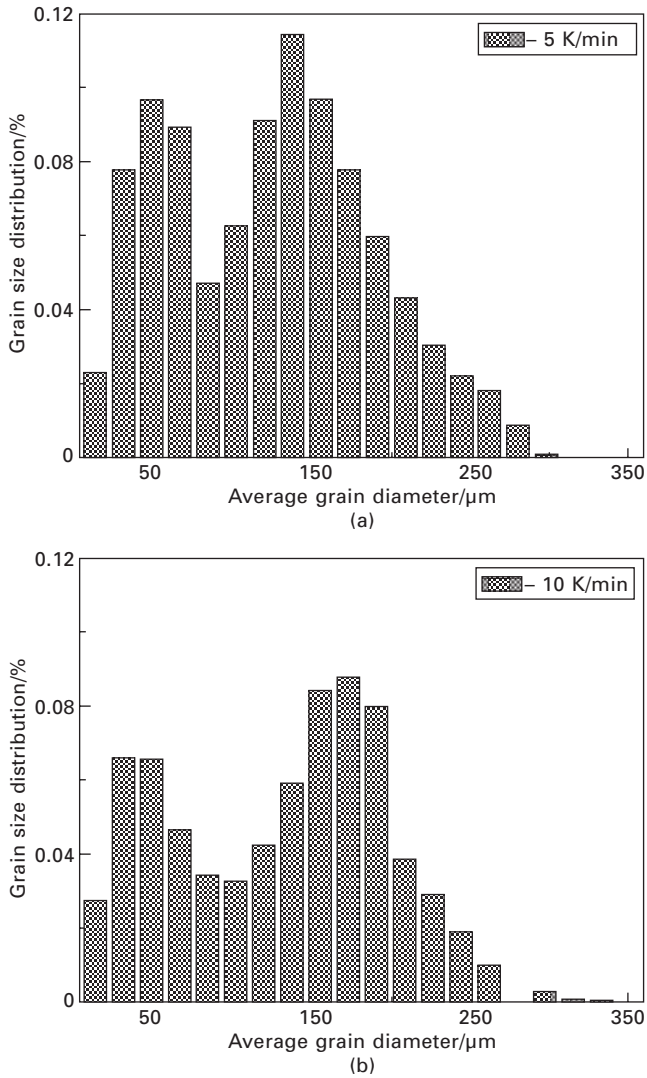
and as compared to the specimen transformed at 20 K min^{-1} (Fig. 9.27b), many subgrains have formed, mainly along the grain boundaries of the large (initially) γ grains.

Grain-size distributions (adopting the grain boundaries represented by the thick lines in Figs 9.27a and b) of the Fe-0.01at%C alloy, after completed $\gamma \rightarrow \alpha$ transformation and as measured at room temperature, are shown in Fig. 9.28. The average α-grain diameter of the transformed Fe-0.01at%C alloy increases upon increasing the cooling rate from 5 to 20 K min^{-1} (average grain size increases from 117 to 183 μm). Evidently, a bimodal distribution of grain size occurs for low cooling rates (see results for 5 and 10 K min^{-1} shown in Figs 9.28a and b), whereas a monomodal grain size distribution results for the high cooling rate (see result for 20 K min^{-1} shown in Fig. 9.28d).

Now consider the partial Fe-C phase diagram shown in Fig. 9.29. The so-called T_0 line (dotted line in the figure) is the locus of points where the Gibbs energy of the metastable γ phase equals that of the metastable α phase of the same carbon concentration. The experimentally determined onset temperatures, T_{onset}, for the $\gamma \rightarrow \alpha$ transformation of the Fe-0.01at%C alloy have been given in Table 9.2 together with the experimentally determined temperature, T_{tr}, indicating the starting temperature of the main (last) maximum in the df_α/dt curves shown in Fig. 9.26. With reference to the partial Fe-C phase diagram shown in Fig. 9.29, it follows that:

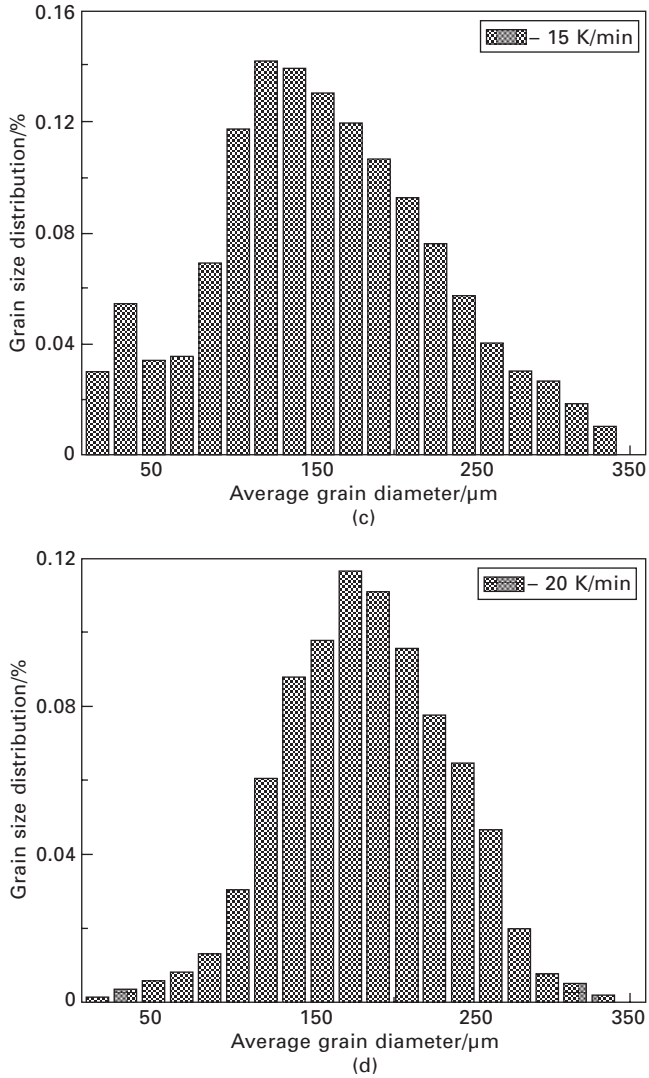
© Woodhead Publishing Limited, 2012

- the onset transformation temperatures for the cooling rates of 5, 10 and 15 K min^{-1} are located between the T_0 temperature and the solvus temperature, T_s
- the onset transformation temperature for the cooling rate of 20 K min^{-1} is located within the single α-phase field



9.28 The ferrite grain-size distribution of the Fe-0.01at%C alloy after experiencing the $\gamma \rightarrow \alpha$ transformation with different cooling rates: (a) 5 K min^{-1}, (b) 10 K min^{-1} (c) 15 K min^{-1} and (d) 20 K min^{-1} (Liu *et al.* 2006).

© Woodhead Publishing Limited, 2012

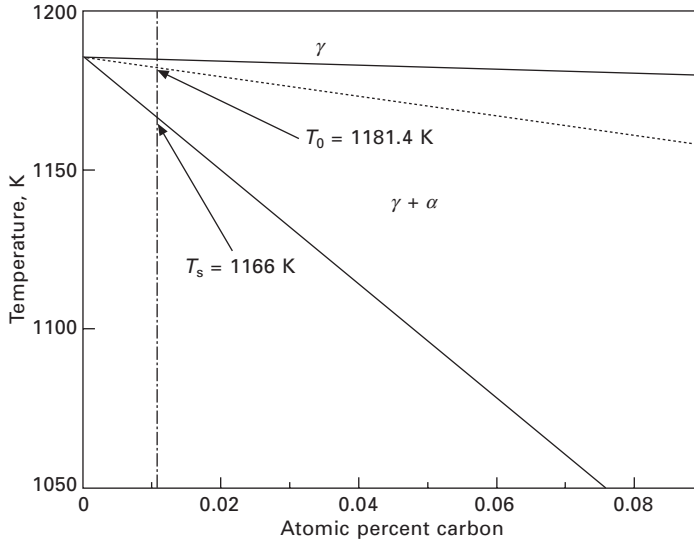


9.28 Continued

- the starting temperatures for the main (last) maximum in the df_α/dt curves, recorded for all cooling rates ($\geq$ 5 K min^{-1}) are located within the single α-phase field.

Recognizing the equality of the onset temperature for the $\gamma \rightarrow \alpha$ transformation of the Fe-0.01at%C alloy at a cooling rate of 20 K min^{-1} and the starting temperature for the process corresponding to the main rate maximum for the transformation at cooling rates $\geq$ 5 K min^{-1}, and because

© Woodhead Publishing Limited, 2012



9.29 Partial phase diagram of the Fe-C system with superimposed T_0 line (dotted line) calculated by equating the chemical Gibbs energies of the α and γ phases for the same composition. The values of T_0 and T_s (solvus temperature) have been indicated for the composition of the alloy investigated (see vertical dashed line) (Liu *et al.* 2006).

Table 9.2 The onset temperature, T_{onset}, for the $\gamma \rightarrow \alpha$ transformation and the temperature, T_{tr}, indicating the start of the main (last) maximum in the df_α/dt curve of the Fe-0.01at%C alloy subjected to different cooling rates. Note $T_{onset} = T_{tr}$ for the transformation at a cooling rate of 20 K min^{-1}

Cooling rates, K min^{-1}	T_{onset}, K	T_{tr}, K
5	1177 ± 1	1164 ± 2
10	1176 ± 1	1164 ± 2
15	1172 ± 1	1163 ± 2
20	1163 ± 1	1163 ± 1

Source: Liu *et al.* (2006).

this temperature is below the ferrite solvus temperature for the Fe-0.01at%C alloy, it is concluded that the parts of the transformations corresponding to the main rate maximum at low cooling rates (< 20 K min^{-1}) and the entire transformation at high cooling rate can be interpreted as a (normal) massive $\gamma \rightarrow \alpha$ transformation.

As a consequence of the above reasoning, the first parts of the transformation at low cooling rates, which occur in the two-phase, $\alpha + \gamma$ region of the Fe-C phase diagram between the onset temperature of the transformation and the ferrite-solvus temperature, pertain to decomposition of the austenite into

© Woodhead Publishing Limited, 2012

ferrite (of much lower carbon content than that of the initial austenite) and austenite (enriched in carbon, as compared to its initial carbon content). Hence, this first part of the transformation is carbon diffusion (in γ) controlled. In this regard, the occurrence of a number of rate maxima in the first part of the $\gamma \rightarrow \alpha$ transformation is ascribed to continued nucleation, recognizing that during cooling in the first part of the transformation the driving force for the decomposition in the untransformed part of the specimen increases with decreasing temperature.

This above qualitative interpretation can be quantitatively supported as follows. The decomposition of austenite, in the two-phase, $\alpha + \gamma$, region, is associated with build-up of carbon concentration in the austenite at the moving γ/α interface and thus is likely rate-controlled by the diffusion of carbon in the austenite away from the moving γ/α interface. According to the results of microstructural analysis presented above, many small grains formed in the specimens exhibiting multiply peaked transformation rates in the first part of transformation (i.e. at cooling rates <20 K min^{-1}; see the bimodal grain-size distributions shown in Figs 9.28a to c). It can now be suggested that the small grains had formed during the first part of the transformation (i.e. in the diffusion-controlled stage). Then, an estimate for the average interface velocity during the diffusion-controlled part of the transformation, $\bar{v}_d$, can be obtained from the average grain diameter of the *small* grains, d_s, and the time passed between the onset of the transformation and the start of the massive part of the transformation, t_d:

$$\bar{v}_d = d_s/t_d \qquad [9.19]$$

The thus calculated average interface velocities for the diffusion-controlled part of the $\gamma \rightarrow \alpha$ transformation have been indicated in Fig. 9.30 by the horizontal lines. Note that the value of $\bar{v}_d$ (~10^{-7} ms^{-1}) is about five times smaller than the interface velocity obtained for the (later) interface-controlled massive part of the transformation process (see Section 9.7.2).

If it is assumed that long-range diffusion of carbon in the austenite governs the growth of the ferrite particles, then the γ/α interface velocity v_d during the diffusion-controlled part of the transformation can be approximately expressed as (Cohen 1958):

$$v_d = (D/t)^{1/2} \qquad [9.20]$$

with D as the diffusion coefficient of carbon in the austenite. Adopting

$$D = 4.529 \times 10^{-7} \exp\left(-\left(\frac{1}{T} - 2.221 \times 10^{-4}\right) \times \left(17767 - \frac{26436 x_c}{1 - x_c}\right)\right)^{1/2} \text{ m}^2\text{s}^{-1}$$

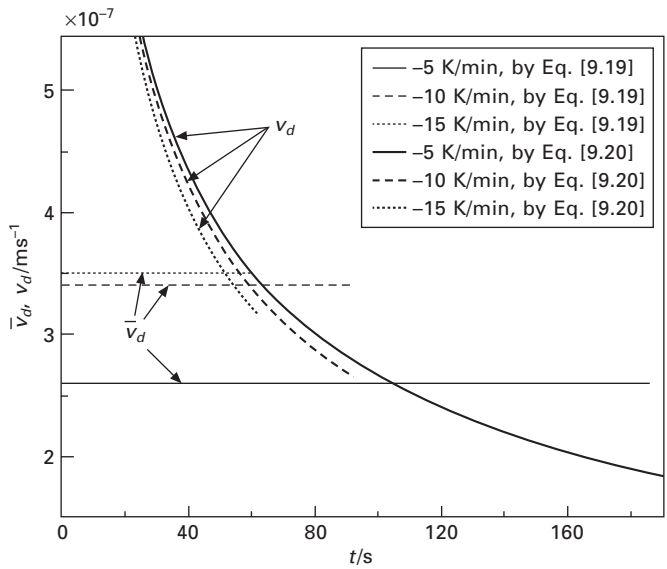
(where x_c is the atomic percentage of carbon) (Agren 1986), the interface velocity for the diffusion-controlled part of the transformation, v_d, can be obtained as a function of transformation time/temperature for the cooling

© Woodhead Publishing Limited, 2012

rates of 5, 10 and 15 K min^{-1}. These results are also shown in Fig. 9.30 (the curves). The time ranges indicated in Fig. 9.30 for $\bar{v}_d$ and v_d are equal to the times until the onset of the interface-controlled, massive part of the transformation (corresponding to the main maximum in the df_α/dt curves; see T_{tr} data in Table 9.2). It follows that the estimates for $\bar{v}_d$ obtained from the size of the small grains approximately agree with the average of v_d corresponding to the v_d curves calculated using the model represented by Eq. [9.20], thereby supporting the interpretation that the first part of the transformation is (carbon) diffusion-controlled.

Of course, for the first part of the transformation (occurring in the two-phase, $(\alpha + \gamma)$, region and dominated by diffusion-controlled growth) the very beginning of the transformation may yet be interface-controlled. However, on the time scale of the first part of the transformation discussed here, the initiation of the transformation can be ignored (according to the model by Sietsma & van der Zwaag 2004, interface control would prevail until a grain size of only about 2 μm, whereas the size of the small grains discussed here is of the order of 20 μm).

As suggested by the bimodal nature of grain size distribution, it appears likely that at start of the massive part of the transformation, new ferrite nuclei



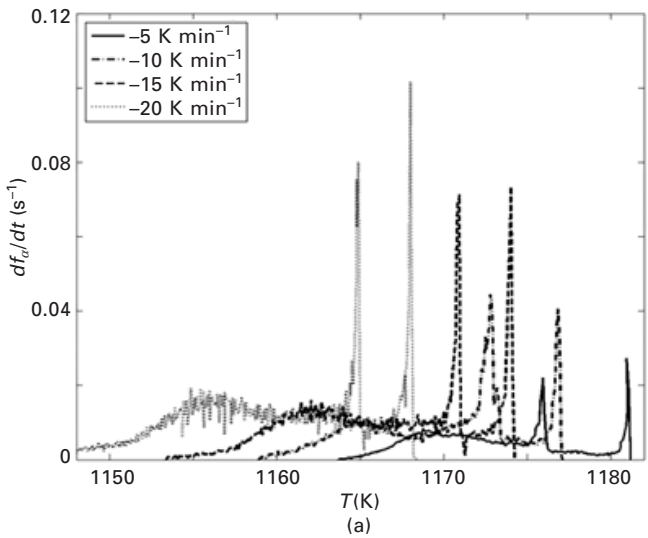
9.30 Comparison of the average interface velocity, $\bar{v}_d$, obtained from the measured average diameter of the small grains (Eq. [9.19]), with the calculated interface velocity, v_d, according to the diffusion-controlled growth model given by Eq. [9.20]. The time ranges given for $\bar{v}_d$ and v_d are equal to the times of transformation until the beginning of the massive part of the transformation characterized by the main maximum in the df_α/dt curves (Liu *et al.* 2006).

© Woodhead Publishing Limited, 2012

become active. Thereby the ferrite grains formed during the initial, diffusion-controlled part of the transformation do not grow further. These ferrite grains are discerned in the microstructure (after completed transformation) as the fraction of small grains in the grain-size distributions (Figs 9.28a–c).

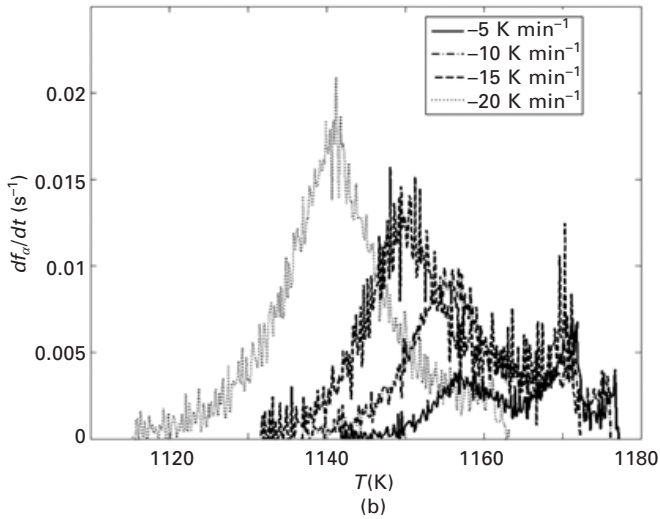
Similar results as shown and discussed here for the Fe-0.01at%C alloy were obtained upon cooling at specific cooling rates for a series of Fe-C alloys containing up to 0.05at%C. The recorded df_α/dt curves (as obtained by dilatometry) are shown in Fig. 9.31. Note that the alloy denoted by Fe-0.001at%C is in fact the 'pure iron' discussed in Section 9.4.2. The initial df_α/dt maxima observed for this 'pure iron' are ascribed to nucleation bursts in a fully massive transformation (Section 9.6.2), whereas the initial df_α/dt maxima in the Fe-C alloys with carbon content ≥0.01at%C are due to a first stage of diffusion-controlled transformation in the $\gamma + \alpha$, two-phase field. For detailed discussion, see Liu *et al*. (2008c).

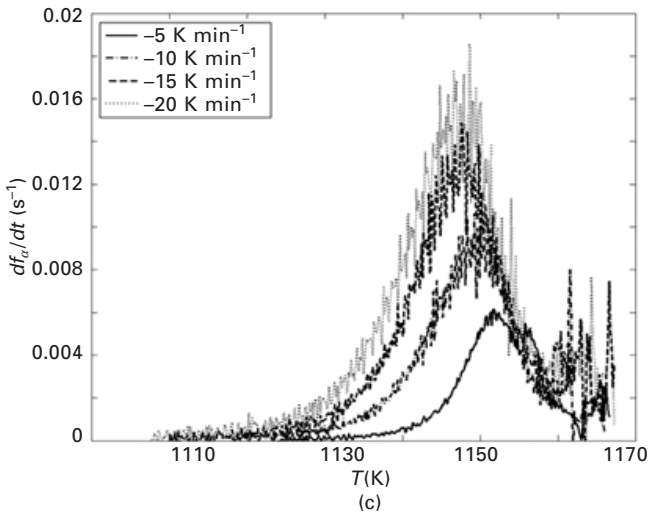
The onset temperature of the massive part of the transformation in the Fe-C alloys, T_{tr}, does not depend on cooling rate (see Table 9.2). These T_{tr} temperatures have been indicated in the partial Fe-C phase diagram (Fig. 9.32). The onset transformation temperatures for the massive part of the transformation, T_{tr}, in the explored Fe-0.001at%C (entire transformation is of massive nature) and Fe-0.01at%C alloys are located below the solvus temperature, T_s, of ferrite, whereas the onset temperatures for the massive part of the $\gamma \rightarrow \alpha$ transformation for the Fe-0.03at%C, Fe-0.04at%C and



9.31 The ferrite-formation rate, df_α/dt, as a function of temperature, T, of (a) Fe-0.001at%C (i.e. 'pure iron'), (b) Fe-0.01at%C, (c) Fe-0.03at%C, (d) Fe-0.04at%C and (e) Fe-0.05at%C alloy, subjected to cooling from the γ-phase field at rates of 5, 10, 15 and 20 K min^{-1} (Liu *et al*. 2008c).

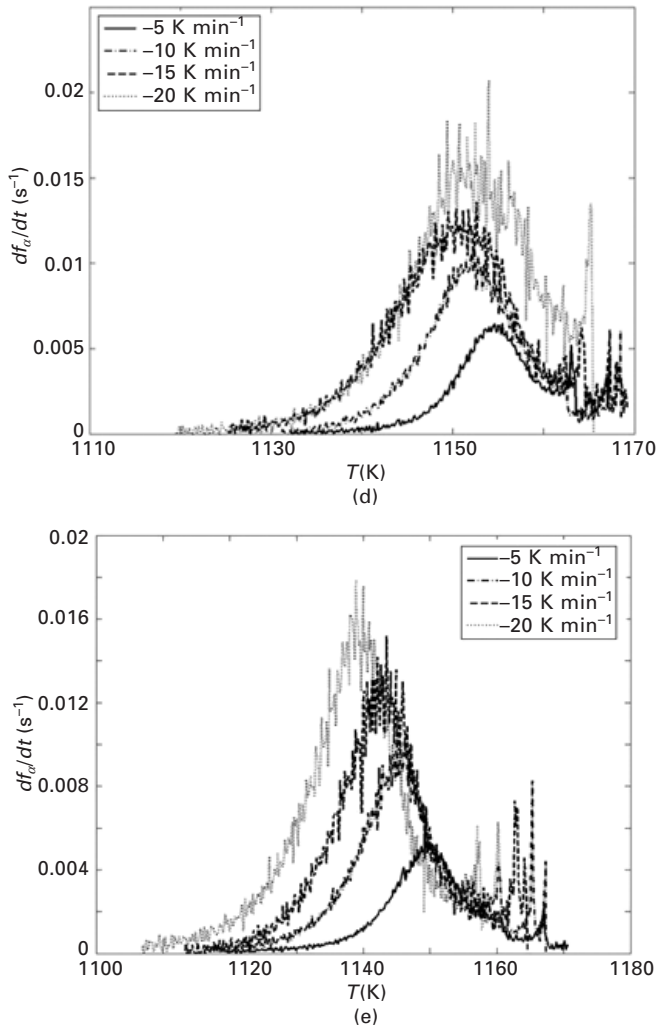
© Woodhead Publishing Limited, 2012





9.31 Continued

© Woodhead Publishing Limited, 2012



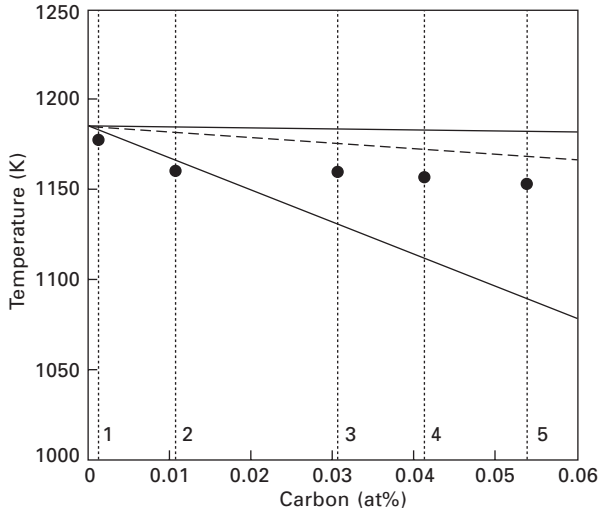
9.31 Continued

Fe-0.05at%C alloys are located between the T_0 temperature and the solvus temperature, T_s, of the ferrite (see discussion in Section 9.7.1).

9.7.2 Kinetic analysis of the massive, normal, interface-controlled part of the isochronal $\gamma \rightarrow \alpha$ transformation in ultra-low-carbon Fe-C alloys

For this part of the transformation a kinetic analysis can be performed that is largely similar to that of the normal massive transformation as discussed

© Woodhead Publishing Limited, 2012



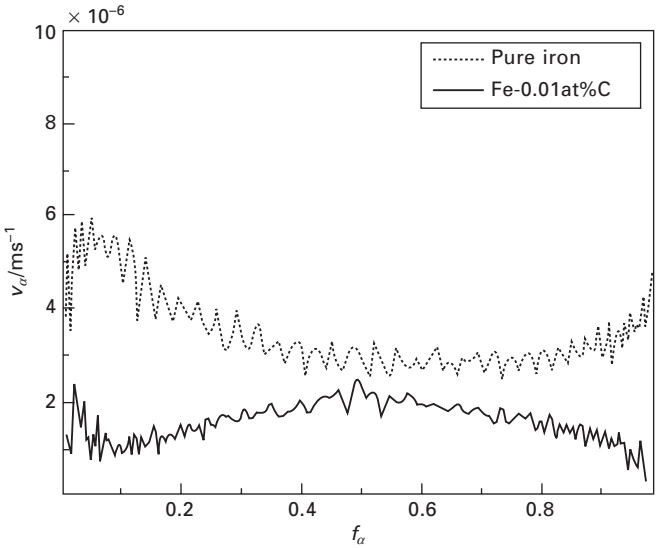
9.32 Partial phase diagram of the Fe-C system with superimposed T_0 line. The separate data points (bold) indicate the average of the experimental onset transformation temperatures for the massive part of the $\gamma \rightarrow \alpha$ transformation of the ultra-low-carbon Fe-C alloys (Liu *et al.* 2008c).

on page 320. Thus site saturation, interface-controlled growth and an impingement correction for an intermediate case of randomly distributed and ideally periodically distributed growing particles can be adopted. The interface velocity, v_α, can then be calculated directly using the measured experimental data for df_α/dt and f_α and by using Eq. [9.15] with the nucleus density, N^*, estimated from the average α-grain size.

The thus obtained v_α, for the ultra-low-carbon Fe-C alloys at a cooling rate of 20 K min^{-1} (then only one df_α/dt maximum; see Fig. 9.25d), is presented as a function of f_α in Fig. 9.33. The value of the interface velocity is practically constant during the whole normal transformation, which corresponds well to results obtained for the normal $\gamma \rightarrow \alpha$ transformations discussed in Section 9.5.1. The value of the average interface velocity for the $\gamma \rightarrow \alpha$ transformation of the Fe-0.01at%C alloy at a cooling rate of 20 K min^{-1} is about 1.6×10^{-6} ms^{-1} which is only slightly lower than that (3.9×10^{-6} ms^{-1}) for pure iron (see Fig. 9.33) (Liu *et al.* 2004b).

The same kinetic model (see Eq. [9.15]) can now be adopted for the massive part of the transformation as recorded for the cooling rates of 5, 10 and 15 K min^{-1} (i.e. pertaining to the main, large maximum in the df_α/dt vs. f_α curves). The average interface velocity, as obtained from the above kinetic analysis pertaining to a cooling rate of 20 K min^{-1} (1.6×10^{-6} ms^{-1}) can now be taken as a known parameter. The nucleus-density values, n_c, for

© Woodhead Publishing Limited, 2012



9.33 The interface velocity, v_α, as a function of the ferrite fraction, f_α, as determined by the phase transformation model (see Eq. [9.15]) applied to the dilatometric data recorded for the Fe-0.01at%C alloy and pure iron with an applied cooling rate of 20 K min^{-1} (Liu *et al.* 2006).

Table 9.3 Comparison of the values for the nucleus density (n_e) estimated from the experimentally determined values for the average size of the large grains, d_L, with values for the nucleus density, n_c, as determined by fitting according to Eq. [9.15] to the $\gamma \rightarrow \alpha$ transformation of the Fe-0.01at%C alloy

Cooling rates, K min^{-1}	d_L, μm	n_e, m^{-3}	n_c, m^{-3}
5	170	2.0×10^{11}	1.1×10^{10}
10	175	1.9×10^{11}	5.4×10^{10}
15	179	1.7×10^{11}	1.6×10^{11}

Source: Liu *et al.* (2006).

the interface-controlled part of the transformation process, as determined by fitting the kinetic model, have been collected in Table 9.3. The n_c values for the nucleus density can be compared with the n_e values for the nucleus density as estimated from the experimentally determined values for the average diameter of the large grains in the transformed Fe-0.01at%C alloy (see the grain-size distributions in Fig. 9.28). A fair agreement of n_c and n_e values occurs. This supports the interpretation (Section 9.3.1) that the last transformation stage is an interface-controlled, massive $\gamma \rightarrow \alpha$ transformation. The difference between the calculated, n_c, and estimated, n_e, nucleus density values increases with decreasing applied cooling rate (from 15 to 5 K min^{-1}).

© Woodhead Publishing Limited, 2012

This parallels the diminishing contribution of the interface-controlled, massive part of the transformation to the entire transformation for decreasing cooling rate (<50% for a cooling rate of 5 K min^{-1}), which hinders an accurate estimation of the nucleus density from the grain-size measurements (cf. Fig. 9.28).

9.7.3 Comparison of the $\gamma \rightarrow \alpha$ transformation in ultra-low-carbon Fe-C and ultra-low-nitrogen Fe-N alloys

Abnormal $\gamma \rightarrow \alpha$ transformation kinetics occur for Fe-0.005at%N alloy governed by interface-controlled growth without occurrence of a preceding diffusion-controlled growth (see Section 9.4.2). To understand this difference with the above discussed ultra-low-carbon Fe-C alloys, consider the partial phase diagrams of the Fe-N and Fe-C systems shown together in Fig. 9.34.

The experimentally determined onset temperatures T_{onset} for the $\gamma \rightarrow \alpha$ transformation in the ultra-low-nitrogen Fe-N alloy have been given for all applied cooling rates in Table 9.4. It follows that the onset transformation temperatures for the ultra-low-nitrogen Fe-N alloy for all applied cooling rates are located in the single α-phase field. Hence, this $\gamma \rightarrow \alpha$ transformation in the ultra-low-nitrogen Fe-N alloy is always massive and thus interface-controlled. Note that upon cooling the temperature range where α and γ can co-exist (in equilibrium) is much smaller for the Fe-N system than for the Fe-C system. Thus it is likely that, as compared to the Fe-N system, a much more distinct driving force for the $\gamma \rightarrow \alpha$ transformation already occurs for the Fe-C system in the $\alpha + \gamma$ two-phase region. Moreover, for the ranges of (ultra-low) interstitial content and temperature concerned, it always holds that the diffusion coefficient of carbon in the austenite is more than a factor of 2 larger than the diffusion coefficient of nitrogen in the austenite (Liu *et al*. 2008b).

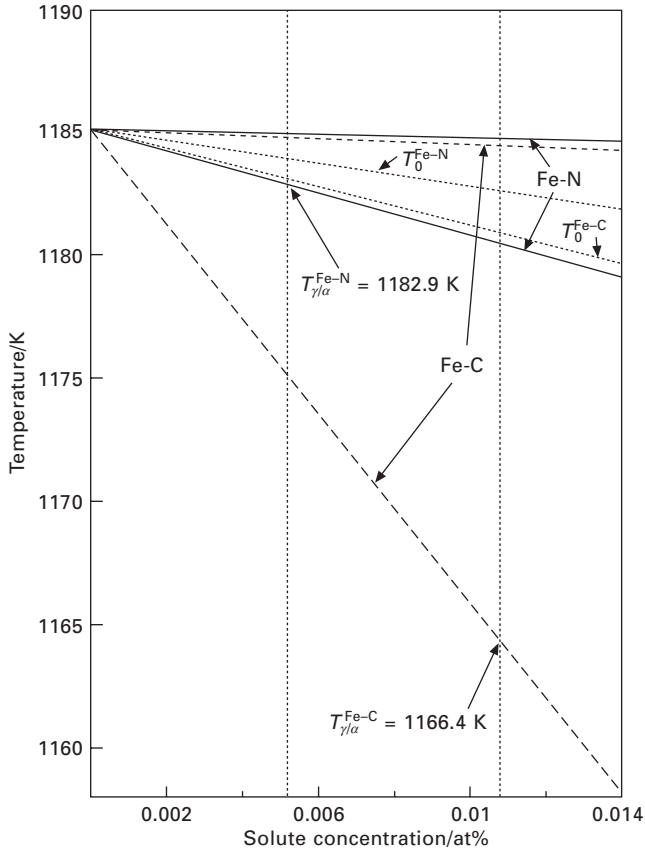
9.8 Transition from interface-controlled growth to diffusion-controlled growth

9.8.1 Isothermal $\gamma \rightarrow \alpha$ phase transformation in ultra-low-carbon Fe-C alloys

To observe and analyze a full isothermal $\gamma \rightarrow \alpha$ transformation in an iron-based alloy, it is important that the transformation initiates directly upon or after, and not before, the specimen has attained a constant temperature after quenching from the high-temperature γ-phase region.

Also recognizing the high velocity of the γ/α interface, this makes the available temperature window for such experiments very small. For example,

© Woodhead Publishing Limited, 2012



9.34 Superimposed partial phase diagrams of Fe-C and Fe-N. The vertical dash-dotted lines indicate the interstitial solute concentrations 0.0052 at%N and 0.0108 at%C pertaining to the alloys considered and the dotted lines indicate the $T_0^{Fe\text{-}N}$ and T_0^{Fe-C} lines (Liu *et al*. 2008b).

Table 9.4 The onset temperature, T_{onset}, for the $\gamma \rightarrow \alpha$ transformation of the Fe-0.005at%N alloy subjected to different applied cooling rates

Cooling rate, K min^{-1}	5	10	15
T_{onset}, K	1168	1166	1165

Source: Liu *et al.* (2008b).

upon performing series of test experiments with Fe-0.04at%C alloy with selected isothermal holding temperatures within the range of 1090–1120 K, i.e. below the α-solvus temperature for this alloy, it was found (Liu *et al*. 2008a) that isothermal $\gamma \rightarrow \alpha$ transformations initiating right after

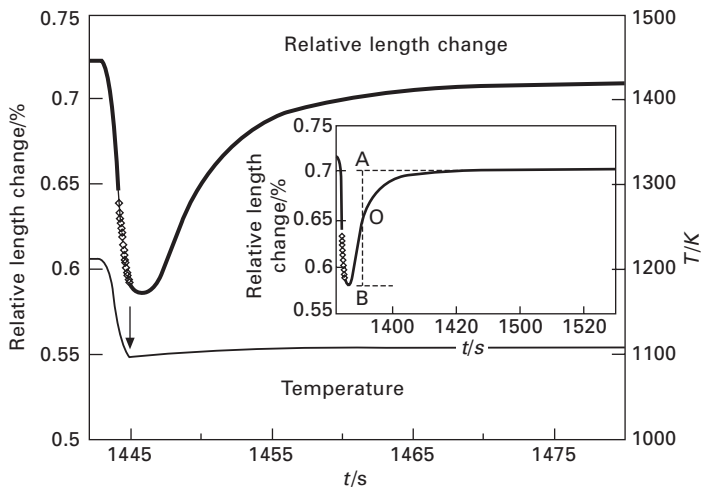
© Woodhead Publishing Limited, 2012

the isothermal holding stage starts were (only) obtained in a temperature range of < 2 K (thereby an isothermal holding temperature range for full transformation of about 15 K as reported by Kozeschnik & Gamsjäger 2006 cannot be confirmed); for pure iron, see Section 9.4.3.

The measured relative length change and the recorded temperature of a Fe-0.04at%C alloy during an isothermal holding at 1107.7 ± 0.2 K (Liu *et al*. 2008a) are shown as a function of time, t, in Fig. 9.35. The specimen attained the programmed isothermal temperature (as indicated by the arrow) before the onset of the $\gamma \rightarrow \alpha$ transformation which is associated with specimen length increase.

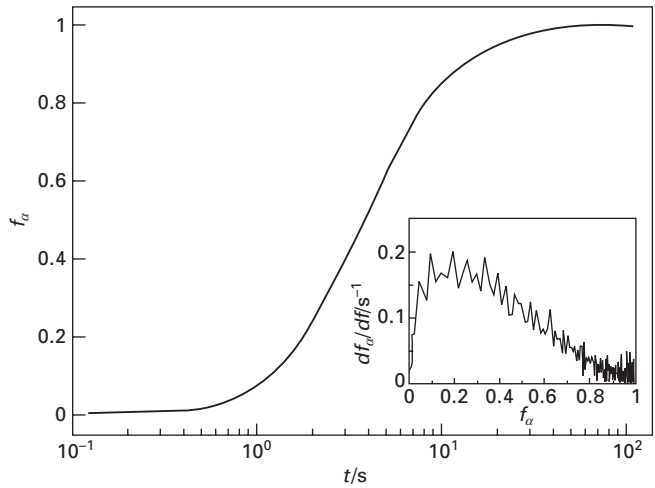
A lever rule can be used to calculate the ferrite fraction, f_α, from the recorded relative length change, $\Delta l/l_0$, data during the isothermal $\gamma \rightarrow \alpha$ transformation (as schematically illustrated in Fig. 9.35): $f_\alpha = |OB|/|AB|$. The thus determined developments of f_α as a function of t and of df_α/dt as a function of f_α are shown in Fig. 9.36. The transformation occurs in two stages: a first, extremely fast stage, with a maximum df_α/dt at about 2 seconds, followed by a second, sluggish stage characterized by a smaller and steadily decreasing df_α/dt. Such ferrite-formation rate behavior is indicative for a transition from interface-controlled growth to diffusion-controlled growth during the $\gamma \rightarrow \alpha$ transformation.

The grain-size distribution of the Fe-0.04at%C alloy, after completed isothermal $\gamma \rightarrow \alpha$ transformation and as measured at room temperature, is

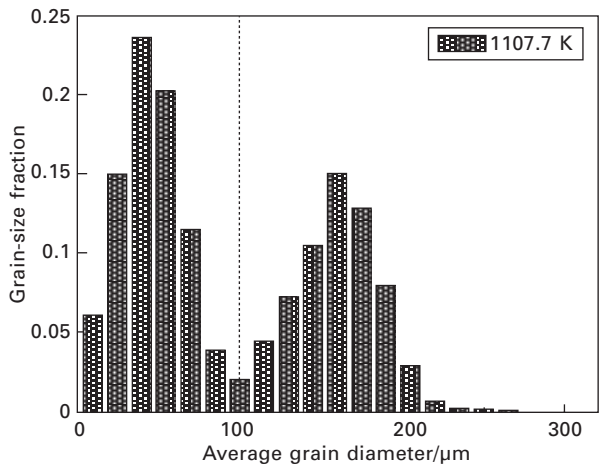


9.35 Both the measured relative length change and the actual temperature as a function of time, *t*, before and during an isothermal holding at 1107.7 ± 0.2 K of an Fe-0.04at%C alloy. The arrow indicates the start of isothermal holding and the inset illustrates the determination of f_α from the recorded relative length-change curve for the isothermal $\gamma \rightarrow \alpha$ transformation (Liu *et al*. 2008a).

© Woodhead Publishing Limited, 2012



9.36 The ferrite fraction, f_α, as a function of time t, as determined from isothermal dilatometric measurements (see Fig. 9.35) of the Fe-0.04at%C alloy at 1107.7 ± 0.2 K. The inset shows the ferrite-formation rate, df_α/dt, as a function of the ferrite fraction, f_α (Liu *et al.* 2008a).



9.37 Ferrite grain-size distributions of Fe-0.04at%C alloy after having experienced the isothermal $\gamma \rightarrow \alpha$ transformation at a holding temperature of 1107.7 K (Liu *et al.* 2008a).

shown in Fig. 9.37. Evidently, a distinctly bimodal grain-size distribution results for the isothermally-transformed Fe-C specimen. It is suggested that the bimodal nature of the grain-size distribution is a consequence of the two-stage nature of the isothermal transformation. Recognizing that most of the

© Woodhead Publishing Limited, 2012

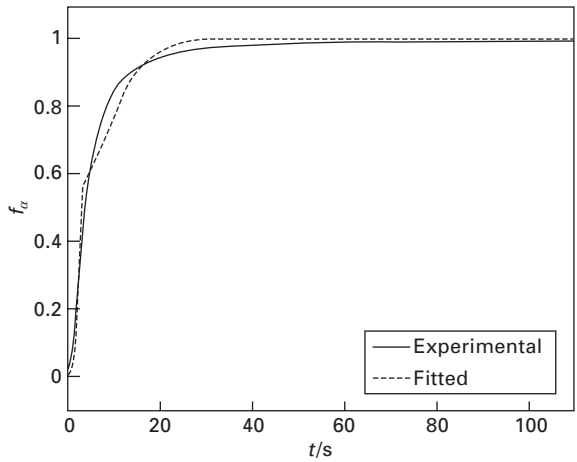
specimen has transformed before onset of the second, diffusion-controlled stage, it is likely that the fraction of large grains in the isothermally-transformed specimen has formed in the first interface-controlled stage and that the fraction of small grains has formed during the second, diffusion-controlled stage. An estimation of the nucleus density for the two transformation stages can be made on the basis of the average ferritic grain size of the large ($d_{\alpha,IS}$) and small ($d_{\alpha,DS}$) grains of the Fe-C specimens after the transformation ($d_{\alpha,IS}$ = 190.9 μm and $d_{\alpha,DS}$ = 54.5 μm for the transformation at 1107.7 K) and thus: $N^*_{IS} = d^{-3}_{\alpha,IS}$ and $N^*_{DS} = d^{-3}_{\alpha,DS}$. Site saturation nucleation was assumed for both stages of growth. Application of different nucleation modes (as continuous nucleation and Avrami nucleation) for the second, diffusion-controlled growth stage does not lead to a reasonable fit of the experimental data (Liu *et al*. 2008a).

The extended volume V^e can be separated into two contributions: V^e_I due to interface-controlled growth and V^e_D due to diffusion-controlled growth. Thus the total extended volume can be given as $V^e = V^e_I + V^e_D$, with V^e_I and V^e_D described by Eqs [9.13] and [9.14]. The transformed fraction then is obtained assuming randomly distributed nuclei by Eq. [9.9] (see Section 9.3). Admittedly, this transformation model is a crude one, but it allows a meaningful analysis of the kinetics of the two-stage isothermal transformation (see below). The transition from an interface-controlled growth to diffusion-controlled growth stage may be better described by adopting a 'mixed-mode growth' model (Sietsma & van der Zwaag 2004; Bos & Sietsma 2007).

The transformed fraction, f_α, can be calculated as a function of time during isothermal annealing on the basis of Eqs [9.9], [9.13] and [9.14]. Assuming growth of cubical grains ($g = 1$), adopting for the nucleus density the estimates derived from the measured ferritic grain size distributions after the $\gamma \rightarrow \alpha$ transformation (see above) and using the diffusion coefficient of carbon in γ given by Agren (1986) for the diffusion-controlled contribution, three independent parameters can be recognized: t_1, Q_G and v_0 in the model given by Eqs [9.9], [9.13] and [9.14]. Fitting of the model was performed such that the sum of the squared differences between the calculated data for f_α according to the model and the experimental data for f_α, as a function of time t, was minimized using a downhill-simplex fitting procedure, by varying the values for the model parameters t_1 (T dependent), Q_G (T independent) and v_0 (T independent). A 'reasonable' fit should provide both minimum error and physically realistic values for the fit parameters (see also the review by Liu *et al*. 2007).

A comparison of the experimental and fitted f_α values obtained in this way is provided in Fig. 9.38. In the model there is a discontinuous change of the df_α/dt at time t_1 when the second, diffusion-controlled stage initiates, because overlapping of the two growth modes is not incorporated in the model. Apart from the transition region around, $t = t_1$, the calculated f_α and

© Woodhead Publishing Limited, 2012



9.38 The transformed fraction f_α as measured and as fitted by the phase transformation model (see text) as a function of annealing time, t, for the $\gamma \rightarrow \alpha$ transformation of the Fe-0.04at%C alloy at an isothermal holding temperature of 1107.7 K (Liu *et al*. 2008a).

Table 9.5 Kinetic parameters as determined by fitting the phase transformation model to the isothermal $\gamma \rightarrow \alpha$ transformation of the Fe-0.04at%C alloy (site-saturation plus interface-controlled growth followed by site saturation and diffusion-controlled growth)

Isothermal holding temperature, K	1107.7
t_1, s	3.44
Q_G, kJ mol^{-1}	138.0
v_0, m s^{-1}	98.9
error, %	3.5

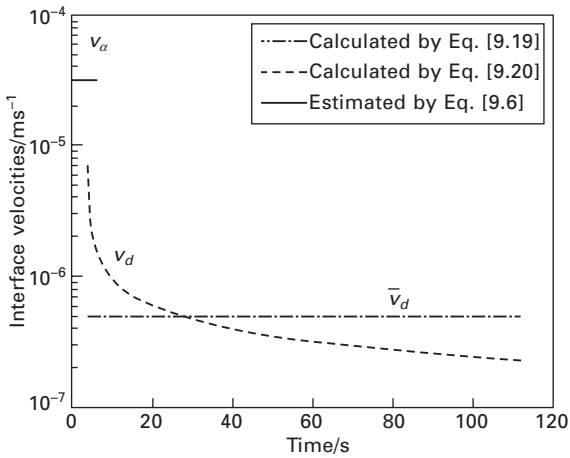
Note: The 'error' indicating the goodness of the fits was calculated as the sum of the squared differences of the measured and the fitted f_α values.
Source: Liu *et al*. (2008a).

df_α/dt values agree well with the experimental data. The results obtained for the kinetic parameters have been gathered in Table 9.5.

The value obtained for the activation energy Q_G for the first, interface-controlled growth stage is about 138 kJ mol^{-1}, which corresponds well with that obtained for the massive, interface-controlled $\gamma \rightarrow \alpha$ transformation of a binary Fe-Mn alloy (Krielaart & van der Zwaag 1998) and the one obtained for the grain-growth mobility of pure iron (Hillert 1975). The value obtained for the parameter v_0 for the interface-controlled growth stage (see Table 9.5) indicates fast interface migration at the first transformation stage, which is compatible with interface-controlled growth in this first transformation stage (see also below).

© Woodhead Publishing Limited, 2012

An estimate for the average interface velocity during the diffusion-controlled part of the transformation, $\bar{v}_d$, can be obtained from the average grain diameter of the fraction of small grains (cf. Fig. 9.37 and its discussion) and the period of time for the second diffusion-controlled stage by using Eq. [9.19] (see Section 9.7.2). The average interface velocities, $\bar{v}_d$, thus calculated for the diffusion-controlled part of the isothermal $\gamma \rightarrow \alpha$ transformation of the Fe-0.04at%C alloy are indicated in Fig. 9.39 by the short horizontal (dashed-dot) lines. Using the values for the fit parameters presented in Table 9.5, the corresponding interface velocity, v_α, for the interface-controlled stage has also been calculated, using Eq. [9.6], and are indicated in Fig. 9.39 by the short, horizontal full lines at the ordinates. Evidently the value of the interface velocity in the (second) diffusion-controlled stage is about 100 times smaller than the value of the interface velocity in the (first) interface-controlled massive part of the transformation process. If it is assumed that long-range diffusion of carbon in the austenite governs the growth of the α particles in the diffusion-controlled stage (see Section 9.7.2), then the γ/α interface velocity v_d during the diffusion-controlled growth stage could be approximately calculated by application of Eq. [9.20]. The thus calculated



9.39 Comparison of the average interface velocity, $\bar{v}_d$, as obtained from the measured average diameter of the small grains (Eq. [9.19]), with the calculated interface velocity, v_d, according to the diffusion-controlled growth stage (Eq. [9.20]). The interface velocity, v_α, for the interface-controlled growth model given by Eq. [9.6] is also shown. The time ranges given for $\bar{v}_d$ and v_d are equal to the time span for the second diffusion-controlled growth stage. The time range given for v_α is equal to the time span for the first interface-controlled stage. The results shown pertain to the $\gamma \rightarrow \alpha$ transformation of Fe-0.04at%C alloy at an isothermal holding temperature of 1107.7 K (Liu *et al.* 2008a).

© Woodhead Publishing Limited, 2012

interface velocity for diffusion-controlled growth, v_d, can be obtained as a function of transformation time (t–t_1), at the different isothermal holding temperatures, and is also shown in Fig. 9.39 (curved dashed lines). The time ranges indicated in Fig. 9.39 for $\bar{v}_d$ and v_d are equal to the time span between the end of first the interface-controlled part of the transformation and the end of second diffusion-controlled part of the transformation. It follows that the estimates for $\bar{v}_d$, as obtained from the size of the small grains (see above), agree well with the average of v_d corresponding to the v_d curves calculated using the model represented by Eqs [9.19] and [9.20]. This finding supports the interpretation that the second part of the isothermal transformation is of diffusion-controlled nature.

It is concluded that, in an ultra-low-carbon Fe-C alloy, the isothermal $\gamma \rightarrow \alpha$ transformation below but close to the ferrite solvus temperature proceeds by a succession of interface-controlled growth and diffusion-controlled growth stages, which is opposite to what is observed upon isochronal $\gamma \rightarrow \alpha$ transformation (see Section 9.7.1).

9.9 Massive transformation under uniaxial compressive stress

The energy uptake owing to the elastic and plastic deformation, associated with the accommodation of the volume misfit of austenite and ferrite upon phase transformation, likely has a significant influence on the interface-migration process (see Section 9.5.2). A considerable amount of work was performed in the past on the transformation kinetics of pre-strained austenite in iron-based alloys, in particular with a view to bainitic (Rees & Shipway 1997) and martensitic transformations (Greenwood & Johnson 1965); a few such studies dealt with the $\gamma \rightarrow \alpha$ phase transformation in pre-strained austenite (e.g. Han *et al*. 2007).

In this section the focus is on the influence of a uniaxial compressive stress applied during the massive $\alpha \rightarrow \gamma$ and $\gamma \rightarrow \alpha$ phase transformations. The imposed compressive stresses are below the yield stress of the phases concerned in the temperature ranges investigated (see Liu *et al*. 2009, 2010).

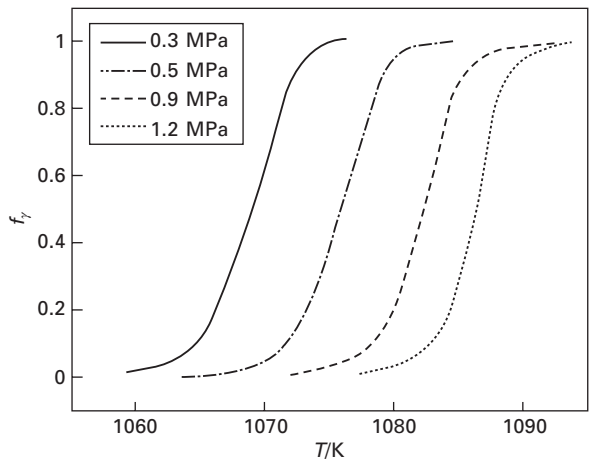
9.9.1 Characteristics of the isochronal massive $\alpha \rightarrow \gamma$ and $\gamma \rightarrow \alpha$ transformations under compressive stress

The $\alpha \rightarrow \gamma$ transformation is accompanied by a volume shrinkage. The austenite fraction, f_γ , and the austenite-formation rate, df_γ/dt, for an Fe-2.96at%Ni alloy, as determined by isochronal heating under applied compressive stress

© Woodhead Publishing Limited, 2012

of various values in a dilatometer,[3] are shown as a function of the temperature in Figs 9.40 and 9.41, respectively. It follows that, under the uniaxial compressive stresses below the yield limits of both austenite and ferrite, that the $\alpha \rightarrow \gamma$ transformation exhibits the following (kinetic) features: the onset transformation temperature, the temperature where the transformation reaches completion and the df_α/dt maximum increase with increasing applied uniaxial compressive stress. The transformation process exhibits one df_γ/dt maximum (see Fig. 9.41) indicating that a so-called normal transformation (see Section 9.3.2) takes place at all uniaxial compressive stresses applied.

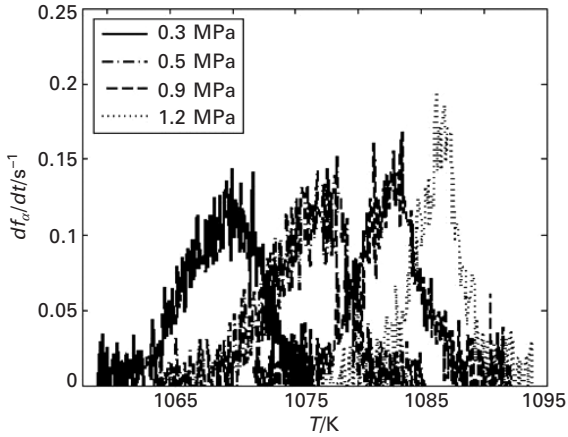
The $\gamma \rightarrow \alpha$ transformation is accompanied by a volume expansion. The ferrite fraction, f_α, and the ferrite-formation rate, df_α/dt, for an Fe-2.96at%Ni alloy, as determined by isochronal cooling under applied compressive stresses of various values in a dilatometer, are shown as a function of the temperature in Figs 9.42 and 9.43, respectively. It follows that, under the uniaxial compressive stresses below the yield limits of both austenite and ferrite, the $\gamma \rightarrow \alpha$ transformation exhibits the following kinetic features: the onset transformation temperature, the temperature where the transformation



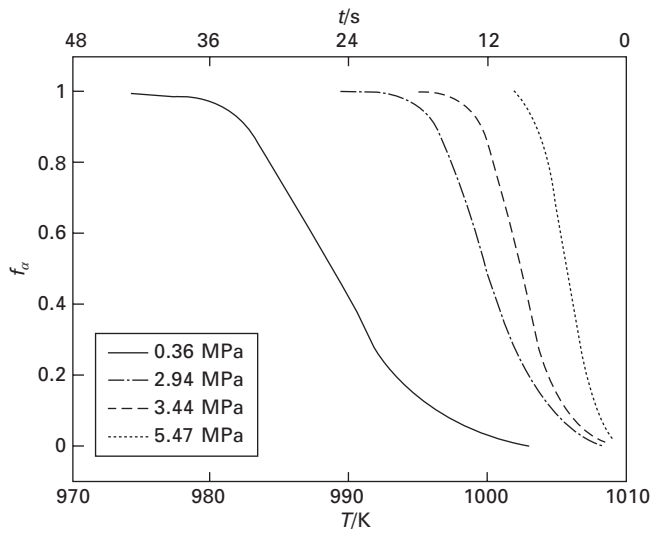
9.40 The austenite fraction, f_γ, as a function of temperature of different fresh Fe-2.96at%Ni alloy subjected to heating at a rate of 50 K min^{-1} from room temperature into the γ-phase field (up to 1223 K) under different uniaxial compressive stresses (Liu *et al.* 2010).

[3]In a dilatometer, the applied compressive stress can never be truly zero, which thus also pertains to the dilatometric measurements considered earlier in this chapter, because the length-change measuring part of the dilatometer has to be kept in direct contact with the specimen by applying a small force. Hence, the minimum applies stress, 0.30 MPa upon isochronal heating and 0.36 MPa upon isochronal cooling, corresponds to the case of a programmed zero load, which is considered as a case without applied stress.

© Woodhead Publishing Limited, 2012



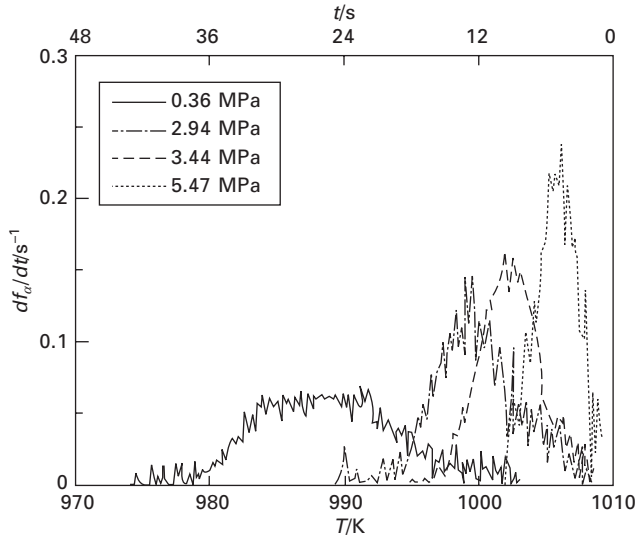
9.41 Comparison of the austenite-formation rate, df_γ/dt, as a function of temperature of different Fe-2.96at%Ni alloy subjected to heating at a rate of 50 K min^{-1} from room temperature into the γ-phase field (up to 1223 K) under different uniaxial compressive stresses (Liu *et al.* 2010).



9.42 The ferrite fraction, f_α, as a function of temperature of different fresh Fe-2.96at%Ni alloy subjected to cooling at a rate of 50 K min^{-1} from the γ-phase field under various applied uniaxial compressive stresses (Liu *et al.* 2009).

reaches completion and the df_α/dt maximum increase with increasing applied uniaxial compressive stress. Here, as for the above $\gamma \rightarrow \alpha$ transformation, a so-called normal transformation (see Section 9.3.2) takes place at all compressive stresses applied.

© Woodhead Publishing Limited, 2012



9.43 Comparison of the ferrite-formation rate, df_α/dt, as a function of temperature of different fresh Fe-2.96at%Ni alloy subjected to cooling at a rate of 50 K min^{-1} from the γ-phase field under various applied uniaxial compressive stresses (Liu *et al.* 2009).

Table 9.6 The average grain diameter of the Fe-2.96at%Ni alloy as measured at room temperature after a heat treatment cycle with, in the heating part of the heat treatment cycle, various applied uniaxial compressive stresses during the $\alpha \rightarrow \gamma$ transformation (initial grain size: 65.7 ± 3 μm)

Stress, MPa	Average grain diameter, μm
0.30	59.4 ± 3
0.50	57.9 ± 3
0.90	56.4 ± 3
1.20	54.8 ± 3

Source: Liu *et al.* (2010).

Independent of the values of applied compressive stress upon heating ($\alpha \rightarrow \gamma$ transformation) or upon cooling ($\gamma \rightarrow \alpha$ transformation), all heat-treated Fe-2.96at%Ni alloy specimens show a more or less log-normal type of grain-size distribution. The values of the average ferrite-grain size (d) as determined after one complete heat treatment cycle for the various cases of applied uniaxial compressive stress have been gathered in Tables 9.6 and 9.7. An overall slight decrease in average ferrite-grain size occurs with increasing applied uniaxial compressive stress during the $\alpha \rightarrow \gamma$ transformation, whereas an overall increase of average ferrite-grain size occurs with increasing applied uniaxial compressive stress during the $\gamma \rightarrow \alpha$ transformation. This

© Woodhead Publishing Limited, 2012

Table 9.7 The average grain diameter of the Fe-2.96at%Ni alloy as measured at room temperature after a heat treatment cycle with, in the cooling part of the heat treatment cycle, various applied uniaxial compressive stresses during the $\gamma \rightarrow \alpha$ transformation (initial grain size: 65.7 ± 3 μm)

Stress, MPa	Average grain diameter, μm
0.36	67.6 ± 3
2.94	73.6 ± 3
3.44	74.9 ± 3
5.47	79.4 ± 3

Source: Liu *et al.* (2009).

suggests that increasing the applied compressive stress increases the number of austenite nuclei in the $\alpha \rightarrow \gamma$ transformation and decreases the number of ferrite nuclei during the $\gamma \rightarrow \alpha$ transformation.

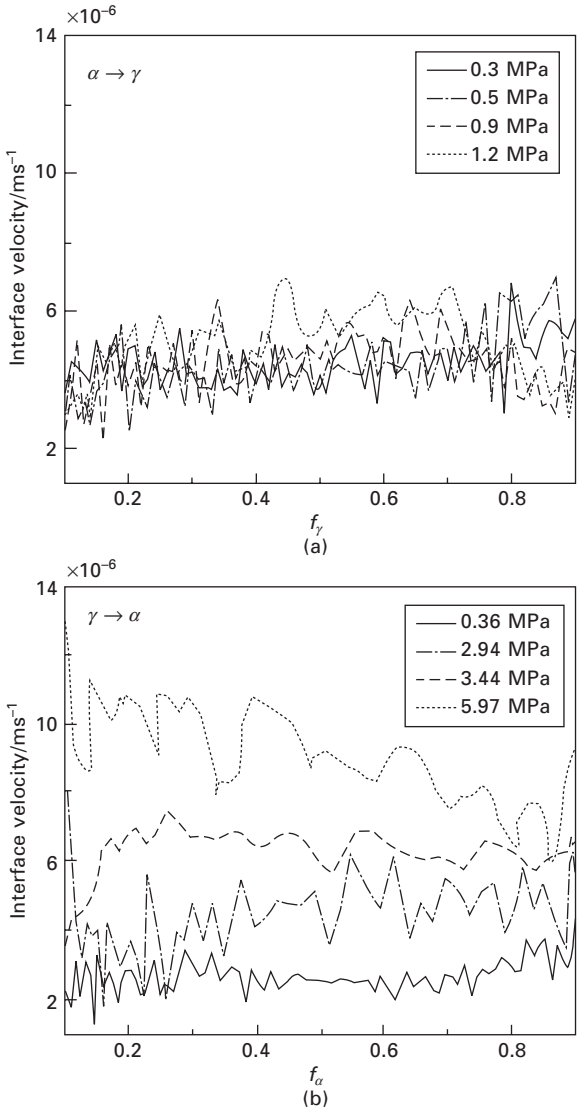
9.9.2 Kinetic analysis of the isochronal massive $\alpha \rightarrow \gamma$ and $\gamma \rightarrow \alpha$ transformations under applied compressive stress

The interface velocity

Following the same reasoning as given in Section 9.3, the $\alpha \rightarrow \gamma$ and $\gamma \rightarrow \alpha$ transformations of the substitutional Fe-based alloys can be considered as partitionless transformations, i.e. the parent and product phases have the same composition. Now, the interface velocities can be calculated according to Eq. [9.15] from the experimentally determined data for f_i, df_i/dt, N^* ($i = \alpha, \gamma$) and taking $g = 1$ (adopting growth of cubical grains). The initial nucleus density values can be estimated from the ferrite-grain size as measured after completed heat treatment cycles (see Tables 9.6 and 9.7). (To this end, in case of the specimen after completion of the $\alpha \rightarrow \gamma$ transformation, the specimen was quenched down to room temperature, in order to preserve the grain boundary morphology of the product (γ) phase; Liu *et al.* 2010.) For impingement correction, (again) a case intermediate of ideally periodical and ideally random dispersion of product particles (i.e. $\varepsilon = 2$ according to Eq. [9.12]) can be adopted. The thus obtained results for the $\alpha \rightarrow \gamma$ (v_γ) and $\gamma \rightarrow \alpha$ (v_α) interface velocities as a function of f_i are presented in Figs 9.44(a) and (b), respectively.

For the same alloy and for the same applied compressive stress, the interface velocity for the $\alpha \rightarrow \gamma$ transformation is larger than that determined for the $\gamma \rightarrow \alpha$ transformation. Recognizing the temperature dependence of the interface velocity, this positive difference of v_γ and v_α at similar applied compressive stress, might be due to the temperature (range) for the $\alpha \rightarrow \gamma$

© Woodhead Publishing Limited, 2012



9.44 (a) The α/γ interface velocity as a function of the austenite fraction, f_γ, determined by application of the phase transformation model (see Eq. [9.15]) during the $\alpha \rightarrow \gamma$ transformation of the Fe-2.96at%Ni alloy subjected to heating at a rate of 50 K min^{-1} from the α-phase field into the γ-phase field under different applied uniaxial compressive stresses (Liu *et al*. 2010). (b) The γ/α interface velocity as a function of the ferrite fraction, f_α, determined by application of the phase transformation model (see Eq. [9.15]) during the $\gamma \rightarrow \alpha$ transformation of the Fe-2.96at%Ni alloy subjected to cooling at a rate of 50 K min^{-1} from the γ-phase field into the α-phase field under various applied uniaxial compressive stresses (Liu *et al*. 2009).

© Woodhead Publishing Limited, 2012

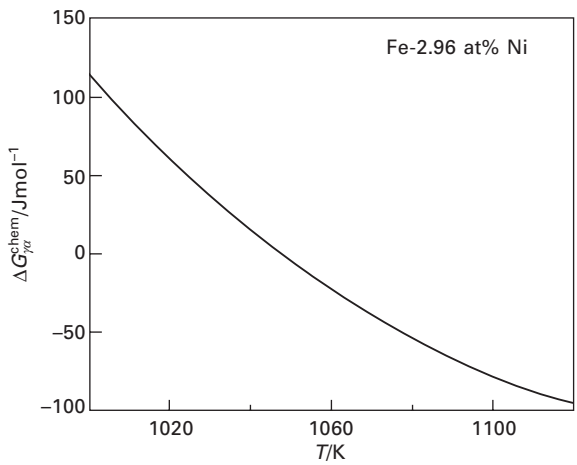
transformation being situated at somewhat higher temperatures than that for the $\gamma \rightarrow \alpha$ transformation.

The deformation energy

To extract values for the deformation energy, the approach presented in Section 9.5.2 can be used as follows. The temperature dependence of the interface velocity is dominated by the interface mobility according to Eq. [9.6]. The interface mobility obtained from the grain growth of pure iron will be adopted for further kinetic analysis (cf. the extensive discussion in Section 9.5.2).

The chemical Gibbs energy difference, $\Delta G_{\gamma\alpha}^{\text{chem}}(T) \equiv G_{\gamma}(T) - G_{\alpha}(T)$ driving the $\alpha \rightarrow \gamma$ transformation of the Fe-2.96at%Ni alloy, as determined using the CALPHAD assessment of the Fe-Ni system (Chuang *et al.* 1985), is presented as a function of temperature in Fig. 9.45. For the $\alpha \rightarrow \gamma$ transformation, a positive driving force ($-\Delta G_{\gamma\alpha}^{\text{chem}}(T)$) occurs for $T > 1047.2$ K; its value increases with increasing transformation temperature. For the case of the $\gamma \rightarrow \alpha$ transformation, the chemical driving force can be obtained as: $\Delta G_{\alpha\gamma}^{\text{chem}}(T) \equiv -\Delta G_{\gamma\alpha}^{\text{chem}}(T)$.

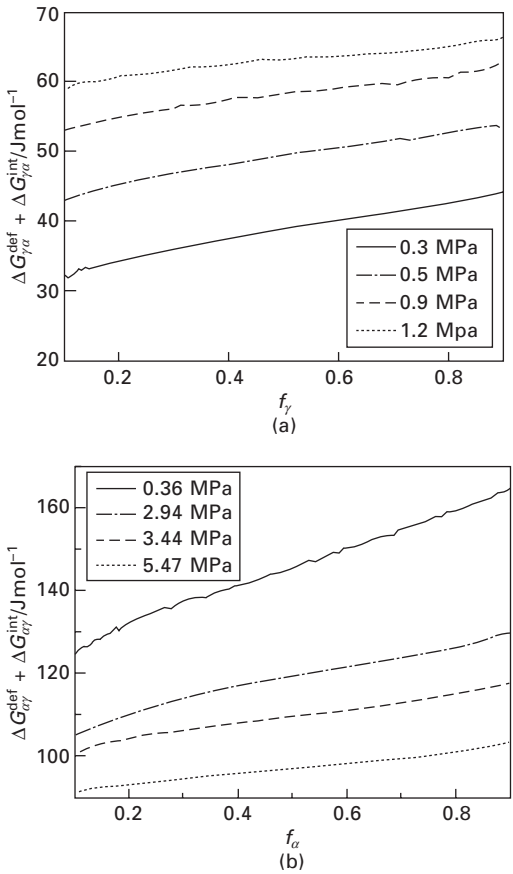
The negative of the driving forces, $\Delta G_{\gamma\alpha}(T, f_{\gamma})$ and $\Delta G_{\alpha\gamma}(T, f_{\alpha})$ can now be determined for the various applied uniaxial compressive stresses, on the basis of Eq. [9.17] using the experimental data of the interface velocities (see Figs 9.44a and b) and the interface mobility data (see above). By subtraction of the chemical Gibbs energy differences, $\Delta G_{\gamma\alpha}^{\text{def}}(f_{\gamma}) + \Delta G_{\gamma\alpha}^{\text{int}}(f_{\gamma})$



9.45 The chemical Gibbs energy difference, $\Delta G_{\gamma\alpha}^{\text{chem}} = G_{\gamma} - G_{\alpha}$, as a function of temperature for the $\alpha \rightarrow \gamma$ transformation of the Fe-2.96at%Ni alloy (Chuang *et al.* 1985).

© Woodhead Publishing Limited, 2012

and $\Delta G^{\text{def}}_{\alpha\gamma}(f_\alpha) + \Delta G^{\text{int}}_{\alpha\gamma}(f_\alpha)$ are obtained (see Figs 9.46a and b). As discussed in Section 9.5.2, the contributions of $\Delta G^{\text{int}}_{\gamma\alpha}(f_\gamma)$ and $\Delta G^{\text{int}}_{\alpha\gamma}(f_\alpha)$ are negligible in comparison with $\Delta G^{\text{def}}_{\gamma\alpha}(f_\gamma)$ and $\Delta G^{\text{def}}_{\alpha\gamma}(f_\alpha)$, respectively, and a possible difference between the α/γ and γ/α interface mobilities and the adopted α/α interface mobility does not distinctly influence the sum of the elastic and



9.46 (a) The sum of the elastic and plastic deformation energies, taken up by the specimen to accommodate the α/γ volume misfit, and the interface energy, $\Delta G^{\text{def}}_{\gamma\alpha} + \Delta G^{\text{int}}_{\gamma\alpha}$, as a function of f_γ, during the $\alpha \rightarrow \gamma$ transformation of the Fe-2.96at%Ni alloy upon heating at a rate of 50 K min^{-1} from room temperature into the austenite region under different applied uniaxial compressive stresses (Liu *et al.* 2010). (b) The sum of the elastic and plastic deformation energies, taken up by the specimen to accommodate the γ/α volume misfit, and the interface energy, $\Delta G^{\text{def}}_{\alpha\gamma} + \Delta G^{\text{int}}_{\alpha\gamma}$, as a function of f_α, during the $\gamma \rightarrow \alpha$ transformation of the Fe-2.96at%Ni alloy subjected to cooling at a rate of 50 K min^{-1} from the γ-phase field under various applied uniaxial compressive stresses (Liu *et al.* 2009).

© Woodhead Publishing Limited, 2012

plastic deformation energy, taken up by the specimen to accommodate the product/parent volume misfit, and the interface energy.

It follows that $\Delta G_{\gamma\alpha}^{\text{def}}(+\Delta G_{\gamma\alpha}^{\text{int}})$ and $\Delta G_{\alpha\gamma}^{\text{def}}(+\Delta G_{\alpha\gamma}^{\text{int}})$ during the $\alpha \rightarrow \gamma$ and $\gamma \rightarrow \alpha$ transformations, respectively, increase with increasing product fraction (γ phase for the $\alpha \rightarrow \gamma$ transformation and α phase for the $\gamma \rightarrow \alpha$ transformation), independent of the value of the compressive stress applied.

Clearly, $\Delta G_{\gamma\alpha}^{\text{def}}(f_\gamma)$ $(+\Delta G_{\gamma\alpha}^{\text{int}}(f_\gamma))$ is of the same order of magnitude as $-\Delta G_{\gamma\alpha}^{\text{chem}}(T)$ and thus has a pronounced influence on the driving force (similarly for the $\gamma \rightarrow \alpha$ transformation; see section 9.5.2). It is important to recognize that $\Delta G_{\gamma\alpha}^{\text{def}}(f_\gamma)$ increases pronouncedly with increasing applied uniaxial compressive stress during the $\alpha \rightarrow \gamma$ transformation upon isochronal heating, whereas the opposite holds for the $\gamma \rightarrow \alpha$ transformation under applied uniaxial compressive stress. This observation suggests that the applied uniaxial compressive stress hinders the $\alpha \rightarrow \gamma$ transformation and promotes the $\gamma \rightarrow \alpha$ transformation.

9.9.3 Anisotropic transformation specificities for the $\alpha \rightarrow \gamma$ and $\gamma \rightarrow \alpha$ transformations under uniaxial compressive stress

Regarding the energetics of the $\alpha \rightarrow \gamma$ and $\gamma \rightarrow \alpha$ transformations, two conclusions can be drawn. By increasing the uniaxial compressive load stress:

- the transformation-induced deformation energy taken up by the specimen increases for the $\alpha \rightarrow \gamma$ transformation, whereas it decreases for the $\gamma \rightarrow \alpha$ transformation (Fig. 9.46);
- a larger chemical driving force is needed to initiate the $\alpha \rightarrow \gamma$ transformation, and a smaller chemical driving force is needed to initiate the $\gamma \rightarrow \alpha$ transformation.

These two results for the $\alpha \rightarrow \gamma$ and $\gamma \rightarrow \alpha$ transformations under a compressive stress can be discussed as follows.

The $\alpha \rightarrow \gamma$ transformation leads to a volume decrease (about 1.2% for the Fe-2.96at%Ni alloy). Such a locally-induced volumetric strain, which occurs at many places in the specimen, cannot be accommodated elastically. Hence, although the applied compressive load stress is within the compressive yield limits for both the product phase and the parent phase, the transformation will induce plastic deformation, predominantly within the relatively weak ferrite phase. The compressive load stress acts along the longitudinal axis of the specimen and the associated negative strain can be relaxed by the transformation-induced length (specific volume) decrease of the specimen in this direction. Indeed, the length decrease of the specimen upon the $\alpha \rightarrow \gamma$ transformation decreases with increasing uniaxial compressive stress applied (see results shown in Liu *et al*. 2010, fig. 2).

© Woodhead Publishing Limited, 2012

The longitudinal axis is one of the three principal, orthogonal axes for the deformation process. The other two principal axes occur in radial directions of the specimen. Application of the compressive load stress along the longitudinal axis is associated with expansion along the radial directions (by means of the Poisson contraction effect) and thus counteracts the contraction by plastic deformation due to the transformation particularly in these radial directions. Thus, in only one principal direction is accommodation of the transformation strain facilitated, whereas in the other two principal directions the (negative) transformation strain is opposed. As a consequence, as compared to the unloaded case, an increase in the chemical driving force is needed to initiate the transformation and larger transformation-induced deformation energy is taken up by the specimen.

Secondary effects for the $\alpha \rightarrow \gamma$ transformation, which can be understood as consequences from the above, are that, within the scatter of data, the γ/α interface velocity is approximately constant (actually slightly increasing) for increasing the uniaxial compressive stress (Fig. 9.44a) as a result of compensation of the first effect by the second.

The reverse $\gamma \rightarrow \alpha$ transformation is associated with an increase in volume. Then the compressive loading stress acting along the longitudinal axis obstructs the transformation-induced expansion in this direction. Indeed, the length increase of the specimen upon the $\gamma \rightarrow \alpha$ transformation decreases with increasing compressive stress (see results shown in by Liu *et al*. 2010, fig. 4). Application of the compressive load stress along the longitudinal axis is associated with expansion along the radial directions and facilitates expansion by plastic deformation due to the transformation in these directions. Thus, as in only one principal direction is realization of the (positive) transformation strain is opposed, and in the other two principal directions the (positive) transformation strain promoted, it can be suggested that a uniaxially applied compressive stress promotes the $\gamma \rightarrow \alpha$ transformation. Indeed, as compared to the unloaded case, upon uniaxial compressive loading: (i) a smaller chemical driving force is needed to initiate the $\gamma \rightarrow \alpha$ transformation (i.e. the onset temperature is increased) and (ii) a smaller transformation-induced deformation energy is taken up by the specimen.

Secondary effects for the $\gamma \rightarrow \alpha$ transformation, which can be understood as consequences from the above, are that the ferrite-nucleus density decreases (see Table 9.7) with increasing uniaxial compressive load as a consequence of (i) and that the γ/α interface velocity increases (see Fig. 9.45b) with increasing uniaxial compressive load as a consequence of (ii).

It is interesting to observe that characteristics as discussed above for the $\alpha \rightarrow \gamma$ transformation (accompanied by volume shrinkage) under uniaxial *compressive* load correspond well with the $\gamma \rightarrow \alpha$ transformation (accompanied by volume expansion) under uniaxial *tensile* load (see Mohapatra *et al*. 2007).

© Woodhead Publishing Limited, 2012

Hence, the antagonistic effects observed for the $\alpha \rightarrow \gamma$ transformation and the $\gamma \rightarrow \alpha$ transformation upon uniaxial compressive loading can be rationalized considering the constraints for the transformation-induced dilatation along principal axes of the specimen. The primary effects of an uniaxially compressive load on the transformation with volume shrinkage are, with increasing uniaxial compressive load, an increase in the transformation-induced deformation energy taken up by the specimen and an increase in the chemical driving force needed to initiate the transformation, in contrast with the reverse transformation with volume expansion, under the applied uniaxial compressive load. For the transformation with volume shrinkage, the applied uniaxial compressive load facilitates accommodation of the transformation-induced strain in only one of the three principal directions; for the transformation with volume expansion this is the case for two of the principal directions. This is consistent with larger and smaller deformation energies taken up by the specimen and smaller and larger chemical driving forces needed to initiate the transformation, for the $\alpha \rightarrow \gamma$ transformation and the $\gamma \rightarrow \alpha$ transformation, respectively.

9.10 Conclusion

The formation of ferrite from austenite and vice versa, upon thermal and mechanical processing of steels, are phase transformations of great technological importance. Generally, these transformations comprise three overlapping mechanisms: nucleation, growth and impingement, subjected to internally and/or externally imposed states of stress. High quality experimental data on the transformation kinetics are obtained by application of high-resolution differential dilatometry. The so-called modular model of transformation kinetics can be applied successfully to interpret the kinetic data obtained. An overview has been presented of current understanding of the so-called 'abnormal' and 'normal' massive transformation kinetics, the (unusual) transition of diffusion-controlled growth to interface-controlled growth and effects of uniaxially applied compressive stress, below the yield stresses of γ and α. The occurrence of abnormal transformation is ascribed to repeated nucleation ahead of the migrating γ/α interface, as a consequence of the accommodation of transformation-induced product/parent deformation energy. The application of a uniaxially applied compressive stress leads to antagonistic effects on the $\alpha \rightarrow \gamma$ and $\gamma \rightarrow \alpha$ transformation kinetics, which can be discussed in terms of chemical and deformation energy changes.

9.11 References

Aaronson H I, Vasudevan V K (2002), General discussion session of the symposium on 'the mechanisms of the massive transformation', *Metal Mater Trans*, 33: 2445–2470.

© Woodhead Publishing Limited, 2012

Aaronson H I, Mahajan S, Purdy G R, Hall M G (2002), Origins of internal structure in massive transformation products, *Metall Mater Trans A*, 33, 2347–2351.

Agren J (1986), A revised expression for the diffusivity of carbon in binary Fe-C austenite, *Scripta Metall Mater*, 20, 1507–1509.

Agren J (1989), Simplified treatment of the transition from diffusion controlled to diffusion-less growth, *Acta Metal*, 37, 181–189.

Borgenstam A, Hillert M (2000), Massive transformation in the Fe-Ni system, *Acta Mater*, 48, 2765–2775.

Bos C, Sietsma J (2007), A mixed-mode model for partitioning phase transformations, *Scripta Mater*, 57, 1085–1088.

Chen H, Liu Y C, Yan Z S, Li Y L, Zhang L F (2010), Consideration of the growth mode in isochronal austenite-ferrite transformation of ultra-low-carbon Fe-C alloy, *Appl Phys A*, 98, 211–217.

Christian J W (1975), *The Theory of Transfomation in Metals and Alloys*, *Part 1 Equilibrium and General Kinetics Theory*, Pergamon Press, Oxford.

Chuang Y Y, Chang Y A, Schmid R, Lin J C (1985), Magnetic contributions to the thermodynamic functions of alloys and the phase equilibria of Fe-Ni system below 1200 K, *Metal Trans A*, 17A, 1361–1372.

Cohen M (1958), Thermodynamics and kinetics of martensitic transformations, *Trans AIME*, 212, 171–183.

Dinsdale A T (1991), SGTE data for pure elements, *Calphad*, 15, 317–425.

Fisher J C (1953), Application of nucleation theory to isothermal martensite, *Acta Metal*, 1, 32–35.

Gamsjäger E, Militzer M, Fazeli F, Svoboda J, Fischer F D (2006), Interface mobility in case of the austenite-to-ferrite phase transformation, *Comp Mater Sci*, 37, 94–100.

Greenwood G W, Johnson R H (1965), The deformation of metals under small stresses during phase transformations, *Proc R Soc London A*, 283, 403–422.

Han H N, Lee J K, Suh D W, Kim S J (2007), Diffusion-controlled transformation plasticity of steel under externally applied stress, *Philo Mag*, 87, 159–176.

Hillert M (1975), Diffusion and interface control of reactions in alloys, *Metal Trans A*, 6, 5–19.

Hillert M (2002), Critical limit for massive transformation, *Metall Mater Trans A*, 33, 2299–2308.

Hillert M (2004), Nature of massive transformation, *Metall Mater Trans A*, 35, 351–352.

Hillert M, Jarl M (1978), A model for alloying effects in ferromagnetic metals, *Calphad*, 2, 227–238.

Höglund L, Hillert M (2006), Mobility of α/γ phase interfaces in Fe alloys, *Scripta Mater*, 54, 1259–1263.

Honeycombe R W K, Bhadeshia H K D H (1995), *Steels Microstructure and Properties*, Edward Arnold, London, 7–33.

Huang W, Hillert M (1996), The role of grain corners in nucleation, *Metall Mater Trans A*, 27, 480–483.

Kaufman L, Cohen M (1958), Martensitic transformations, *Prog Metal Physics*, 7, 165–246.

Kempen A T W, Sommer F, Mittemeijer E J (2002a), The kinetics of the austenite-ferrite phase transformation of Fe-Mn: differential thermal analysis during cooling, *Acta Mater*, 50, 3545–3555.

© Woodhead Publishing Limited, 2012

Kempen A T W, Sommer F, Mittemeijer E J (2002b), Determination and interpretation of isothermal and non-isothermal transformation kinetics; the effective activation energies in terms of nucleation and growth, *J Mater Sci*, 37, 1321–1322.

Kozeschnik E, Gamsjäger E (2006), High-speed quenching dilatometer investigation of the austenite-to-ferrite transformation in a low to ultralow carbon steel, *Metall Mater Trans*, 37A, 1791–1797.

Krielaart G P, van der Zwaag S (1998), Kinetics of $\gamma \rightarrow \alpha$ phase transformation in Fe-Mn alloys containing low manganese, *Mater Sci Tech*, 14, 10–18.

Lange W F, Enomoto M, Aaronson H I (1988), The kinetics of ferrite nucleation at austenite grain boundaries in Fe-C alloys, *Metall Mater Trans A*, 19, 427–440.

Li C M, Sommer F, Mittemeijer E J (2001), Quantitative dilatometric analysis of the isothermal decomposition of hypereutectoid Fe-C austenite, *Z Metall*, 92, 32–36.

Liu F, Sommer F, Bos C, Mittemeijer E J (2007), Analysis of solid state phase transformations kinetics: models and recipes, *Inter Mater Rev*, 52, 193–212.

Liu Y C, Sommer F, Mittemeijer E J (2003), Abnormal austenite–ferrite transformation behavior in substitutional Fe-based alloys, *Acta Mater*, 51, 507–519.

Liu Y C, Sommer F, Mittemeijer E J (2004a), Kinetics of the abnormal austenite–ferrite transformation behavior in substitutional Fe-based alloys, *Acta Mater*, 52, 2549–2560.

Liu Y C, Sommer F, Mittemeijer E J (2004b), Abnormal austenite-ferrite transformation behavior of pure iron, *Phil Mag A*, 84, 1853–1876.

Liu Y C, Sommer F, Mittemeijer E J (2004c), Calibration of the differential dilatometric measurement signal upon heating and cooling; thermal expansion of pure iron, *Thermochimica Acta*, 413, 215–225.

Liu Y C, Sommer F, Mittemeijer E J (2006), The austenite-ferrite transformation of ultralow-carbon Fe-C alloy; transition from diffusion- to interface-controlled growth, *Acta Mater*, 54, 3383–3393.

Liu Y C, Wang D J, Sommer F, Mittemeijer E J (2008a), Isothermal austenite-ferrite transformation of Fe-0.04at.% C alloy: dilatometric measurement and kinetic analysis, *Acta Mater*, 56, 3833–3842.

Liu Y C, Sommer F, Mittemeijer E J (2008b), Abnormal austenite-ferrite transformation kinetics of ultra-low-nitrogen Fe-N alloy, *Metall Mater Trans*, 39A, 2306–2318.

Liu Y C, Sommer F, Mittemeijer E J (2008c), Critical temperature for massive transformation in ultra-low-carbon Fe-C alloys, *Inter J Mater Res*, 99, 925–932.

Liu Y C, Sommer F, Mittemeijer E J (2009), Austenite-ferrite transformation kinetics under uniaxial compressive stress in Fe-2.96 at.% Ni alloy, *Acta Mater*, 57, 2858–2868.

Liu Y C, Sommer F, Mittemeijer E J (2010), Kinetics of austenitization under uniaxial compressive stress in Fe-2.96 at% Ni alloy, *Acta Mater*, 2010, 58, 753–763.

Loginova I, Odqvist J, Amberg G, Agren J (2003), The phase-field approach and solute drag modeling of the transition to massive $\gamma \rightarrow \alpha$ transformation in binary Fe-C alloys, *Acta Mater*, 51, 1327–1339.

Massalski T B (1984), Distinguishing features of massive transformation, *Metall Mater Trans A* 15, 421–425.

Massalski T B (2002), Massive transformations revisited, *Metall Mater Trans A*, 33, 2277–2283.

Massalski T B (2010), Comments concerning some features of phase diagrams and phase transformations, *Mater Trans*, 51, 583–596.

Massalski T B, Perepezko J H, Jaglovsky J (1975), A microstructural study of massive transformations in the Fe-Ni system, *Mater Sci Eng A*, 15, 193–198.

© Woodhead Publishing Limited, 2012

Meng Q P, Rong Y H, Hse T Y (2006), Effect of internal stress on autocatalytic nucleation of martensitic transformation, *Metall Mater Trans A*, 37, 1405–1411.

Mittemeijer E J (2010), *Fundamentals of Material Science*, Springer, Heidelberg.

Mittemeijer E J, Sommer F (2002), Solid state phase transformation kinetics: a modular transformation model, *Z Metallkd*, 93, 352–361.

Mittemeijer E J, Sommer F (2011), Solid state phase transformation kinetics: evaluation of the modular transformation model, *Int J Mat Res*, 102, 784–795.

Mohapatra G, Sommer F, Mittemeijer E J (2007), The austenite to ferrite transformation of Fe-Ni under the influence of a uniaxially applied tensile stress, *Acta Mater*, 55, 4359–4367.

Offerman S E, van Dijk N H, Sietsma J, Lauridsen E M, Margulies L, Grigull S, Poulsen H F, van der Zwaag S (2004), Solid-state phase transformations involving solute partitioning: modeling and measuring on the level of individual grains, *Acta Mater*, 52, 4757–4766.

Offerman S E, van Dijk N H, Sietsma J, Lauridsen E M, Margulies L, Grigull D S, Poulsen H F, van der Zwaag S (2006), Phase transformations in steel studied by 3DXRD-microscopy, *Nuclear Instruments and Methods in Physics Research Section B*, 246, 194–200.

Onink M, Tichelaar F D, Brakman C M, Mittemeijer E J, van der Zwaag S (1995), An *in situ* hot stage transmission electron microscopy study of the decomposition of Fe-C austenites. *J Mater Sci*, 30, 6223–6234.

Plichta M R, Rigsbee J M, Hall M G, Russell K C, Aaronson H I (1976), Nucleation kinetics of the massive transformation in Cu-Zn in the presence and absence of special orientation relationships, *Scripta Metall*, 10, 1065–1070.

Reed R C, Bhadeshia H K D H (1992), Kinetics of reconstructive austenite to ferrite transformation in low alloy steels, *Mater Sci Tech*, 8, 421–435.

Rees G I, Shipway P H (1997), Modelling transformation plasticity during the growth of bainite under stress, *Mater Sci Eng A*, 223, 168–178.

Saker A, Leroy Ch, Michel H, Franz C (1991), Properties of sputtered stainless steel-nitrogen coatings and structural analogy with low temperature plasma nitrided layers of austenitic steels, *Mater Sci Eng A*, 140, 702–708.

Sietsma J, van der Zwaag S (2004), A concise model for mixed-mode phase transformations in the solid state, *Acta Mater*, 52, 4143–4152.

Speich G R, Szirmae A (1969), Formation of austenite from ferrite and ferrite-carbide aggregates, *Trans AIME*, 245, 1063–1074.

Svoboda J, Gamsjäger E, Fischer F D (2005), Relaxation of the elastic strain energy of misfitting inclusions due to diffusion of vacancies, *Phil Mag Let*, 85, 473–479.

Swanson W D, Parr J G (1964), Transformations in iron-nickel alloys, *J Iron Steel Inst*, 202, 104–106.

Trivedi R (1970), The role of interfacial free energy and interface kinetics during the growth of precipitate plates and needles, *Met Trans*, 1, 921–926.

van der Ven A, Delaey L (1996), Models for precipitate growth during the $\gamma \rightarrow \alpha + \gamma$ transformation in Fe-C and Fe-C-M alloys, *Progress in Materials Science*, 40, 181–264.

Vandermeer R A (1990), Modeling diffusional growth during austenite decomposition to ferrite in polycrystalline Fe-C alloys, *Acta Metal Mater*, 38, 2461–2470.

Velthuis S G E T, Root J H, Sietsma J, Rekveldt M Th, van der Zwaag S (1998), The ferrite and austenite lattice parameters of Fe–Co and Fe–Cu binary alloys as a function of temperature, *Acta Mater*, 46, 5223–5228.

© Woodhead Publishing Limited, 2012

Vooijs S I, Leeuwen YV, Sietsma J, van der Zwaag S (2000), On the mobility of the austenite-ferrite interface in Fe-Co and Fe-Cu, *Metall Mater Trans A*, 31, 379–385.

Wilson E A (1984), $\gamma \rightarrow \alpha$ transformation in Fe, Fe-Ni, and Fe-Cr alloys, *Metal Science*, 18, 471–484.

Wits J J, Kop T A, van Leeuwen Y, Seitsma J, van der Zwaag S (2000), Study on the austenite-to-ferrite phase transformation in binary substitutional iron alloys, *Mater Sci Eng A*, 283, 234–241.

Zhan Y, Johnson R A (1993), An EAM simulation of the α-γ iron interface, *Modelling & Simulation in Mater Sci & Eng*, 1, 707–716.

Zhao J C, Notis M R (1995), Continuous cooling transformation kinetics versus isothermal transformation kinetics of steels: a phenomenological rationalization of experimental observations, *Mater Sci Eng R*, 15, 135–207.

© Woodhead Publishing Limited, 2012

10
Mechanisms of bainite transformation in steels

S. B. SINGH, Indian Institute of Technology, Kharagpur, India

Abstract: The chapter deals with the mechanisms of bainite transformation. The essential features of the transformation are discussed in terms of the microstructure and transformation kinetics to highlight its similarity with ferrite and pearlite transformation in some cases and with martensite transformation in other cases. The characteristic features of the transformation are critically examined in the light of diffusion-controlled reconstructive and displacive mechanisms. Certain features of the transformation can perhaps be explained by both the proposed mechanisms. However, response of the transformation to external stress and strain can only be rationalised in terms of a displacive mechanism of transformation.

Key words: bainite transformation, reconstructive and displacive mechanisms, microstructure (bainite sheaf, sub-unit) and kinetics (TTT diagram), upper and lower bainite, carbide-free bainite, carbide precipitation, diffusion-controlled growth, solute drag, invariant plane strain shape deformation, incomplete reaction phenomenon, crystallography, transformation plasticity, mechanical stabilisation.

10.1 Introduction

Pure iron shows several allotropic transitions. Under equilibrium cooling conditions, liquid iron first solidifies with a body centred cubic (bcc) crystal structure at 1538 °C which then transforms to a face centred cubic (fcc) structure at 1394 °C; finally, this fcc solid transforms again into a bcc structure at 912°C which is stable right up to room temperature and below (Chipman, 1972). The three solid forms are known as δ-iron, γ-iron and α-iron, respectively. Addition of carbon and other alloying elements in steels leads to formation of solid solutions based on these structures or phases; in addition, C forms cementite (Fe_3C) and various other carbide phases. Solid solutions of C and other alloying elements in γ-iron and α-iron are known as austenite (γ) and ferrite (α), respectively. The presence of alloying elements affects the stability of different phases and alters the transition temperatures listed above. These details are mapped on phase diagrams which show the effect of temperature and concentration of the alloying elements on the stability of different phases (Chipman, 1972). Phase diagrams, however, do not show other metastable phases that can possibly form under non-equilibrium conditions.

© Woodhead Publishing Limited, 2012

Depending upon the composition and state (mainly grain size and density of various defects) of austenite before transformation and the temperature of transformation or cooling rate, it can transform to allotriomorphic (or idiomorphic) ferrite, pearlite, Widmanstätten ferrite, bainite or martensite. Some of these products form by a diffusion-controlled, reconstructive mechanism of transformation, while others form by a displacive shear mechanism. The transformation of austenite to these products is of immense technological importance because it determines the final microstructure of the material, which in turn decides its mechanical properties and performance during service. Moreover, the transformation of austenite provides a wide scope to study the fundamental aspects of transformation.

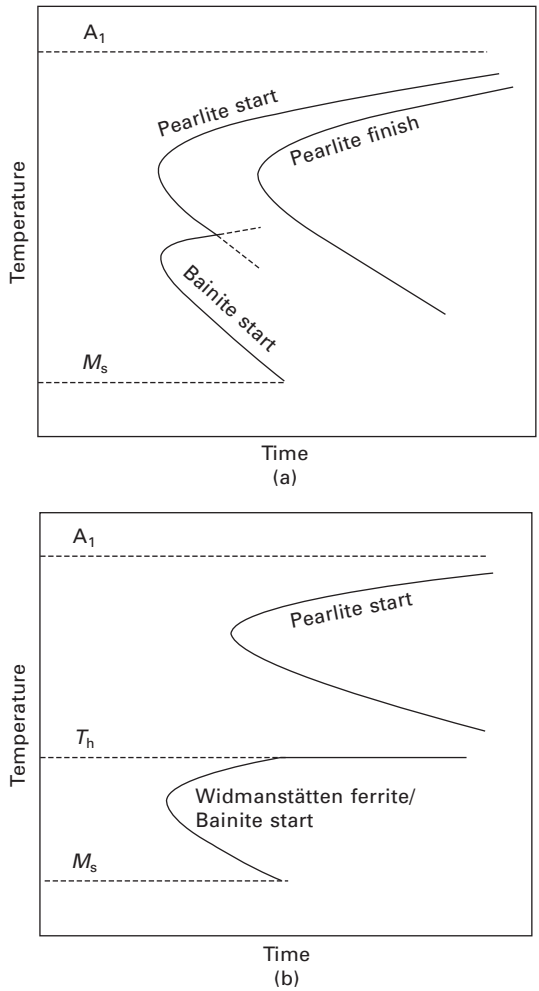
10.2 Bainite: general characteristics

The kinetics or the progress of transformation of austenite is represented on time-temperature-transformation (TTT) diagrams. In general, the TTT diagram of steels consists of two sets of 'C-curves' (Hehemann and Troiano, 1956; Reynolds *et al.*, 1990a; Bhadeshia and Honeycombe, 2006; Hillert, 2011), one for the transformation of austenite to ferrite, pearlite and/or carbides and one for its transformation to bainite. The upper and lower C-curves in these steels are separated by a bay region where the transformation of austenite is sluggish (Fig. 10.1). In many plain carbon steels, however, the two C-curves overlap to a large extent so that effectively only one set of C-curves is observed. Transformation to athermal martensite, on the other hand, is represented by lines parallel to the time axis of the diagram.

Bainite usually forms at temperatures that are intermediate between those of reconstructive pearlite and displacive martensite, even though in some cases there may be some overlap, and exhibits characteristic features of both pearlite and martensite transformation. As such, the mechanism of transformation of bainite has been the subject of intense debate ever since its discovery some 80 years ago (Robertson, 1929; Davenport and Bain, 1930). While one school of thought attempts to rationalise the experimental observations within the framework of diffusional, reconstructive mechanisms of transformation, the other school subscribes to a displacive, shear mode of transformation (Aaronson, 1969; Hehemann, 1970; Hehemann *et al.*, 1972; Christian and Edmonds, 1984; Aaronson *et al.* 1990; Bhadeshia and Christian, 1990; Bhadeshia, 2001).

In the most simple terms, bainite can be defined as a non-lamellar aggregate of lath- or plate-shaped ferrite and carbide (Davenport and Bain, 1930; Hehemann *et al.*, 1972; Bhadeshia, 1990). The details of the microstructure vary with composition and temperature of transformation, thus it is common to identify two varieties, namely upper bainite and lower bainite. These form over upper and lower temperature ranges and can be distinguished by

© Woodhead Publishing Limited, 2012



10.1 Schematic illustration of the TTT diagram when the C-curves for pearlite and bainite transformations overlap as in (a) or when they are completely separate as in (b) (adapted from Hehemann and Troiano, 1956; Bhadeshia, 2001).

their morphology, hence making the description quite useful (Mehl, 1939; Hehemann *et al.*, 1972; Christian and Edmonds, 1984). It is possible to suppress the carbide component of bainite in steels with sufficient concentration of alloying elements such as Si or Al. The microstructure and other features of this carbide-free variety are then very similar to the one with carbides but it consists of an aggregate of ferrite plates and untransformed austenite. It has therefore been thought justified to classify it as carbide-free bainite. Carbide-free bainite has also been reported in extremely low carbon steels containing

© Woodhead Publishing Limited, 2012

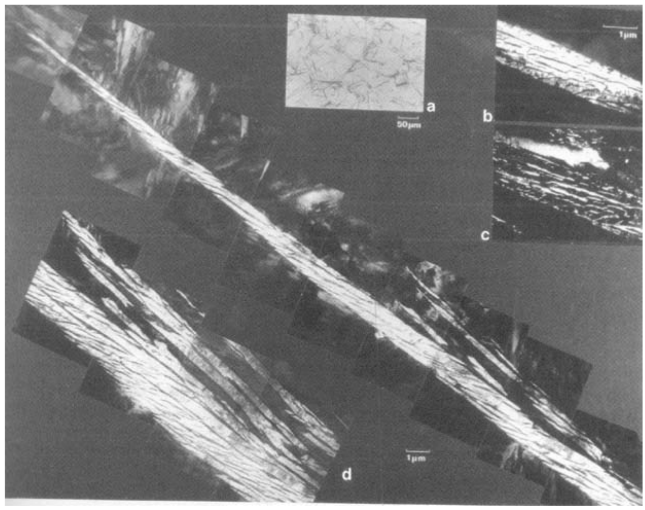
less than 0.02 wt% carbon (Fumimaru *et al.*, 2000). A simple corollary, if this is accepted, is that carbide is not essential to bainite (Hehemann, 1970; LeHouillier *et al.*, 1971; Hehemann *et al.*, 1972; Christian and Edmonds, 1984; Bhadeshia and Christian, 1990).

Aaronson and co-workers hold a slightly different view and define bainite as 'a non-lamellar, non-cooperative mixture of ferrite and carbides formed during eutectoid decomposition' (Reynolds *et al.*, 1990a,b; Aaronson *et al.*, 2006). There is no restriction on the morphology (acicular/plate or otherwise) of the ferrite component of bainite according to this view and the carbide-free variety is identified simply as proeutectoid ferrite (Reynolds *et al.*, 1990b).

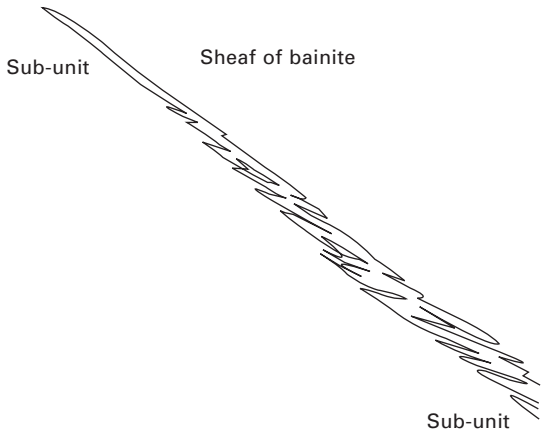
The bainitic ferrite nucleates at austenite grain boundaries and grows in the form of clusters of laths or plates that nucleate adjacent to each other by 'autocatalysis' or 'sympathetic nucleation'. These clusters are called sheaves (Aaronson and Wells, 1956; Goodenow *et al.*, 1963; Goodenow and Hehemann, 1965; Oblak and Hehemann, 1967) and their morphology on a macroscopic level is that of a wedge-shaped plate or lath in three dimensions with the thicker end originating at the grain boundary (Oblak *et al.*, 1964; Srinivasan and Wayman, 1968a; Ohtani *et al.*, 1990). The typical microstructure of a bainite sheaf and its schematic representation are shown in Fig. 10.2. The sheaves and the constituent platelets within them do not cross the austenite grain boundaries. The individual platelets, also known as the 'sub-units' of the sheaf, are much finer (typically less than 1 μm in thickness and about 10 μm in length) than the sheaf as a whole and therefore cannot be resolved in an optical microscope (Oblak and Hehemann, 1967). The thickness of the sub-units is known to decrease with decreasing transformation temperature, although the length is largely unaffected (Pickering, 1967; Chang and Bhadeshia, 1994). The sub-units in a sheaf are in approximately identical crystallographic orientation and are separated by small angle grain boundaries when they meet each other. Other phases such as cementite, untransformed austenite or martensite occupy the regions between the sub-units or sheaf. In the case of lower bainite, however, carbides are present within the sub-units as well and are aligned at an angle of about 55–60° to the long axis of the ferrite plate. The transition from upper bainite to lower bainite is usually observed to take place at around 350°C and is relatively insensitive to composition (Hehemann *et al.*, 1972; Christian and Edmonds, 1984). Similar behaviour was observed by Pickering in steels containing 0.5 wt% Mo when the carbon content was more than about 0.6 wt%; in lower C steels, however, the transition temperature was much higher (Pickering, 1967). The transition temperature is not sharp and both upper and lower bainite can form at intermediate temperatures.

The volume fraction of bainite at a given isothermal transformation temperature increases as a sigmoidal function of time and, accordingly, the

© Woodhead Publishing Limited, 2012



(a)



(b)

10.2 Microstructure of a sheaf of upper bainite: (a) optical and transmission electron micrographs under bright-field and dark-field illumination and (b) outline of the sub-units at the tip of the sheaf (Bhadeshia and Edmonds, 1980; Bhadeshia, 2001).

transformation kinetics are represented by a C-curve on the TTT diagram (Bhadeshia, 2001; Quirdort and Bréchet, 2002). The martensite transformation, on the other hand, occurs extremely rapidly and the amount of martensite formed in steels is independent of time. In terms of overall kinetics, therefore, the bainite transformation is similar to the ferrite or pearlite transformation (Kumar, 1968).

© Woodhead Publishing Limited, 2012

In many alloy steels, it is possible to study the progress of transformation to bainitic ferrite without any interference from other competing reactions such as carbide precipitation. In such steels, the transformation to bainitic ferrite is found to stop prematurely in the sense that it stops before austenite attains the paraequilibrium composition given by the extrapolated paraequilibrium $(\alpha + \gamma)/\gamma$ line (Ae_3'). The reaction is thus said to be incomplete and the phenomenon is called 'incomplete reaction phenomenon' or 'transformation stasis' (e.g. Bhadeshia and Christian, 1990). A direct consequence of this is that the maximum volume fraction of bainitic ferrite that can form at a given isothermal reaction temperature is less than that expected from application of the lever rule to the relevant paraequilibrium phase boundaries. The critical concentration of carbon where the reaction ceases decreases with increasing temperature so that the extent of transformation to bainite also decreases with increasing temperature and becomes zero at the bainite start (B_s) temperature (Christian and Edmonds, 1984). Obviously bainite cannot form above the B_s temperature. When cementite or other carbides precipitate out from austenite or bainitic ferrite, the carbon content of the austenite is less than the critical value and, therefore, the transformation can proceed to a greater extent. In alloys where Widmanstätten ferrite does not form and pearlite and bainite transformation ranges are separated by a bay, the B_s temperature should correspond to the top of the lower C-curve of the TTT diagram.

There are a number of other features of the transformation to bainite as summarised below. Formation of bainite leads to martensite-like invariant plane strain (IPS) surface relief on pre-polished surfaces (Ko and Cottrell, 1952). Bainite has a high dislocation density and the dislocation density of bainitic ferrite is higher than that in allotriomorphic ferrite formed at similar transformation temperatures (Oblak and Hehemann, 1967); moreover, the dislocation density of bainitic ferrite has been found to increase with decreasing transformation temperature (Pickering, 1967; Fondekar *et al.*, 1970). The effect of stress and strain on the bainite transformation is quite similar to that on martensite (Jepson and Thompson, 1949; Bhattacharyya and Kehl, 1955; Christian and Edmonds, 1984; Bhadeshia, 1999, 2001). Thus, when the transformation to bainite takes place in a plastically deformed austenite the extent of transformation is reduced (Bhadeshia, 2001), an effect similar to the mechanical stabilisation of martensite (Raghavan, 1992; Bhadeshia, 1999, 2001). Furthermore, effects similar to the thermal stabilisation of martensite have also been observed for bainite (Hehemann and Troiano, 1954).

Any transformation mechanism or model proposed for bainite should explain the features discussed above. In the next two sections we shall discuss these mechanisms in detail.

© Woodhead Publishing Limited, 2012

10.3 Diffusion-controlled growth mechanism

10.3.1 Morphology and surface relief

According to this view, the mechanism of formation of bainite is not fundamentally different from that of allotriomorphic ferrite that forms at relatively higher temperature and therefore they are treated in continuity. The theory of precipitate morphology has been invoked to explain the plate-shaped morphology of bainitic ferrite (Aaronson and Zackay, 1962; Aaronson, 1969; Aaronson *et al*., 1970). In a first order nucleation and growth type of transformation, the product phase grows by the movement of interfaces and the rate of growth depends, amongst other parameters, on the nature of interface. The precipitate phase (ferrite in this case) is bound by coherent or semi-coherent type interfaces at orientations where the matching between the parent and the product phase is better and by incoherent and disordered boundaries at orientations where the matching is poor. The coherent or semi-coherent interface poses a strong barrier to growth; the interface is thus immobile and cannot move normal to itself (Chattopadhayay, 1985). It is considered that it can, however, move in this direction by the lateral migration of steps or ledges that are present on the interface. The risers of the ledges are deemed to be incoherent so that atoms can freely attach on the face of the ledges resulting in migration of these ledges along the interface at rates governed by long-range diffusion. If a constant supply of ledges can be maintained, the precipitate will thicken in the direction normal to the interface when the ledges sweep across the interface. This indirect nature of growth results in slow and discontinuous growth. At low supercooling, when the driving force for growth is small, both kinds of interfaces grow with nearly the same velocity so that we get nearly equiaxed precipitate. At higher supercooling, however, the incoherent interface moves with higher growth rate because of the larger driving force available, but the semi-coherent interface moves slowly. The anisotropy of growth rate should therefore result in plate-shaped precipitates. Alternatively, when the precipitate phase is bound by coherent or semi-coherent interfaces only, a difference in inter-ledge spacing can give rise to anisotropic growth rates (Aaronson, 1969).

Liu and Aaronson (1970) have proposed that invariant plane strain (IPS) can form during diffusional transformation when all the ledges move in the same direction from sample interior to sample surface. It has been further argued that the volume expansion associated with austenite to ferrite transformation is constrained by the need to maintain coherency at the interface (Kinsman *et al*., 1975). Thus it is believed that the invariant plane strain shape and the associated surface relief arise because of this constrained volume change. The surface relief is further affected by arrival of successive waves of ledges at the free surface (Aaronson, 1969). Tent-shape relief is thought to occur by motion of the ledges in the reverse direction (Kinsman *et al*., 1975).

© Woodhead Publishing Limited, 2012

However, these mechanisms have been shown to be mutually inconsistent (Watson and McDougall, 1973; Christian and Edmonds, 1984; Bhadeshia, 1987).

10.3.2 Solute drag and transformation stasis

It has been argued that formation of bainite is not fundamentally different from that of other higher temperature varieties of ferrite and therefore it cannot have a separate C curve of its own on the TTT diagram. The bay in the TTT diagram and the incomplete reaction phenomenon are attributed to the 'special effect' of certain alloying elements and therefore it is argued that these phenomena are not the basic characteristics of the transformation (Aaronson, 1969). This special effect was termed the 'solute drag effect' drawing analogy with recrystallisation and grain growth kinetics where segregation of a very small amount of solute to grain boundaries retards these processes (Aaronson *et al.*, 1970). In the present case of bainite transformation, even though substitutional solute elements do not partition between austenite and ferrite, they segregate to the austenite-ferrite interface if they have a negative interaction energy with the interfaces and exert a drag force on the migration of disordered areas of the interface. This drag force decreases the interface mobility. The extent of segregation, and therefore the drag force, increases as the temperature is reduced. The ferrite growth kinetics slow down when the drag force becomes large compared with the chemical driving force for ferrite growth. Eventually, segregation reaches a saturation point but the driving force continues to rise as the temperature is reduced and it is able to overcome the drag force so that mobility of the interface is restored and the transformation bay appears in the TTT diagram. These alloying elements have also been shown to reduce the nucleation rate of ferrite (Aaronson, 1969), and this, together with lowering of the ferrite growth rate, is postulated to result in the incomplete reaction phenomenon. Strong carbide forming elements like Mo give rise to such special effects and the effectiveness of an alloying element in developing the bay depends on its effect on the activity of carbon in austenite.

The solute drag model described above was later modified to 'solute drag-like effect' (SDLE) by Bradley and Aaronson (1981) when it was realised that the diffusion of the substitutional atoms at the temperatures of interest is too slow to exert a drag force on the austenite-ferrite interface. SDLE denotes non-equilibrium segregation of substitutional and interstitial (carbon) solute atoms within the moving austenite-ferrite interface that leads to reduction in the chemical potential gradient of carbon ahead of the interface with concomitant reduction in the ferrite growth kinetics (Reynolds *et al.*, 1990a,b). These authors have argued that transformation stasis results when (i) SDLE is strong enough to stop ferrite growth and (ii) large-scale

© Woodhead Publishing Limited, 2012

carbide precipitation is absent so that carbon-enriched austenite is unable to support sympathetic nucleation of ferrite.

The most recent version of the solute effect that has been applied to understand the kinetic behaviour of bainite transformation is the coupled solute drag effect (C-SDE) (Aaronson *et al.*, 2004, 2006). Coupling refers to a mutual effect of substitutional solute like Mo and interstitial solute C on their concentration at the austenite-ferrite interface. Growth stasis results when the chemical potential of C at the interface becomes equal to that in the bulk austenite due to C-SDE. Growth stasis, together with cessation of nucleation, results in transformation stasis.

The incomplete reaction phenomenon and transformation bay have been found to be more general than described above. Thus they have been observed in alloy systems with elements such as silicon and nickel that increase the activity of C in austenite (Hehemann, 1970; Hehemann *et al.*, 1972; Tsuzaki and Maki, 1995). Moreover, Mo appeared to have no effect on the rate of growth of austenite from ferrite in an Fe-N-1 wt% Mo alloy at similar transformation temperatures (Paxton *et al.*, 1967). There are conflicting reports in the literature on direct experimental measurement of segregation at the transformation interface. While Bhadeshia and co-workers (Bhadeshia and Waugh, 1982; Bhadeshia, 1984) did not observe any segregation in Fe-Si-Mn steel using atom probe field ion microscopy, Humphreys *et al.* (2004) reported some segregation of Mo in Fe-C-Mo alloy studied using scanning transmission electron microscopy (STEM). Detailed high resolution analysis is obviously warranted to arrive at a firm conclusion. A critical analysis of the effect of solute drag on phase transformation in steels has been presented by Bhadeshia (1983).

10.3.3 Diffusion-controlled growth

A number of experimental studies on edgewise lengthening rates of bainite (and of Widmanstätten ferrite) have been carried out by *in-situ* hot stage optical microscopy or by thermionic emission microscopy and by indirect metallographic methods (Hillert, 1960; Speich and Cohen, 1960; Oblak and Hehemann, 1967; Townsend and Kirkaldy, 1968; Simonen *et al.*, 1973). The most comprehensive study is perhaps that of Hillert (1960) who measured the edgewise growth rate of bainite and Widmanstätten ferrite over the temperature range of 380–750°C in plain carbon and C-Ni steels containing 0.21–0.81 wt% C. In all the cases, the plates have been found to lengthen at a constant rate which increases with temperature in most cases and yields apparent activation energy values that are smaller for upper bainite and higher for lower bainite. It should be noted that these growth rates, in terms of the morphological descriptions above, refer to the growth of a bainite sheaf as a whole.

© Woodhead Publishing Limited, 2012

The experimentally measured lengthening rates can be compared with the diffusion-controlled lengthening rate equation of plates formulated first by Zener (1946) and subsequently modified by Hillert (1960, 1975). The lengthening rate is given by:

$$\frac{V}{D} = \frac{(x^{\gamma\alpha} - x_o)^2}{(x_o - x^{\alpha\gamma})} \cdot \frac{RT}{8\sigma V_m} \qquad [10.1]$$

where V is the (maximum) growth rate at temperature T, D is the diffusion coefficient of carbon in austenite, $x^{\gamma\alpha}$ and $x^{\alpha\gamma}$ are the equilibrium (or paraequilibrium) mole fraction of carbon in austenite and ferrite respectively, x_o is the mole fraction of carbon in the alloy, σ is the interfacial energy per unit area and V_m is the molar volume of ferrite.

Calculation of growth rates using the above equation is subject to certain uncertainties (Hillert, 1994, 2002). These are related to (i) choice of an appropriate value for the interface energy and the diffusion coefficient of C in austenite, the latter depending on the carbon content which varies with the distance from the interface, and (ii) extrapolation of thermodynamic and kinetic parameters to lower temperatures. When reasonable values are used for the calculations, the measured values are found to be lower than the calculated ones in most cases, although the temperature dependence is predicted rather well (Kaufman *et al*., 1962; Aaronson *et al*., 1970). These results have been interpreted to imply that the rate of growth of bainite is controlled by diffusion of carbon, the rates being too low to allow growth of ferrite plates with carbon supersaturation (Purdy and Hillert, 1984; Aaronson *et al*., 1990; Hillert, 1994). It is emphasised here that the growth rate calculations treat the entire bainite sheaf as a single entity and do not take into account successive nucleation and subsequent growth of individual sub-units that constitute the sheaf.

Growth rate: further analysis

Hillert has further analysed the growth rates using the Zener–Hillert equation (Hillert, 1960, 1975, 1994; Hillert *et al*., 2004). He concluded that experimental growth rates are continuous across the temperature ranges for Widmanstätten ferrite and bainite. He further argued that there is a thermodynamic barrier to growth that results in lower experimental growth rates than is predicted by the carbon diffusion-controlled growth given by Eq. [10.1]. This thermodynamic barrier represents dissipation of energy at the interface and indicates departure from local equilibrium at the interface. The thermodynamic barrier, Δ, for Fe-C alloys was evaluated in the following manner (Hillert *et al*., 2004): variation of the lengthening rate of the plates at a given transformation temperature was considered as a function of the initial

© Woodhead Publishing Limited, 2012

carbon content of the alloy in the light of Eq. [10.1]. The lengthening rate was extrapolated to zero to obtain the critical carbon content above which growth stops. The corresponding free energy change for the austenite to ferrite transformation under carbon partitioning was calculated and this value was taken to represent the energy required for interface movement. This procedure was followed for 700 and 300°C, the highest and the lowest temperatures for which growth rate data exist. For the intermediate temperature of 450°C, the critical carbon content was obtained from carbide-free retained austenite in an Fe-C-2.1 wt% Si alloy of Tsuzaki *et al.* (1994). The thermodynamic barrier was found to increase with decreasing temperature. A spline function was fitted to the free energy values thus obtained and was termed the 'Δ function'. This function was used to estimate a WB_s line as a function of temperature for Fe-C alloys; this line simply represents the Widmanstätten ferrite start (W_s) or the bainite start temperatures (B_s) on the Fe-C phase diagram (Hillert *et al.*, 2004). The WB_s line is below the Ae_3 line on the Fe-C diagram and therefore it explains the incomplete reaction phenomenon for carbide-free bainite, since the growth stops prematurely even before the carbon concentration of austenite reaches the Ae_3 value.

Similar 'Δ functions' were evaluated for Cr and Mo alloyed steels and it was found that the growth barrier is larger in these cases, which was interpreted to imply a strong solute drag effect. In both cases the barrier was found to be higher at higher temperatures.

10.3.4 Carbide precipitation

It is generally agreed that cementite in upper bainite precipitates from austenite. Direct observation of microstructure and an analysis of the orientation relationships between cementite and ferrite confirm this (Pickering, 1967; Shackleton and Kelly, 1967). In case of lower bainite, the picture is less clear. On the basis of the observation that the carbide particles are aligned in the ferrite plate and only a single variant is observed in many cases, it has been proposed that carbide precipitates from austenite at the austenite-ferrite interface and is eventually incorporated into the ferrite plate (Hehemann *et al.*, 1972; Honeycombe, 1976). Similarly, analysis of the data on average carbon content of retained austenite under several assumptions led to the conclusion that most of the carbide is precipitated from austenite (Hehemann *et al.*, 1972). The transition from upper to lower bainite is not clearly elucidated in this scheme.

Recently, Borgenstam *et al.* (2009) have re-analysed the classical microstructure of lower bainite from the early Oblak and Hehemann work (1967) and compared it with ledeburite formed during the solidification of white cast iron. They concluded that the general shape of the sub-units of lower bainite is the same as that of sub-colonies of ledeburite and therefore

© Woodhead Publishing Limited, 2012

the sub-units may be regarded as sub-colonies formed by 'cooperative growth of the eutectoid phases' (ferrite and cementite in this case). It was further suggested that the cooperative mode of growth indicates that the sub-units grow gradually rather than rapidly and the rate of growth is controlled by diffusion of carbon.

Further detailed examination of the published microstructures of lower bainite led to the conclusion that the plates initially grow along the length (edgewise growth) with sidewise diffusion of carbon into the parent austenite, and the initial plates do not contain any carbides. Subsequently, the plates thicken sideways by cooperative growth of ferrite and carbide after the nucleation of carbides which triggers thickening. It was therefore suggested that lower bainite be regarded as a eutectoid mixture. However, it was noted that the degree of cooperation to 'form a well developed eutectoid structure' is less in upper bainite for 'some reason' (Borgenstam *et al.*, 2009). It is also not clear as to why the degree of cooperation is less in the case of upper bainite which forms at intermediate temperatures while it is higher in the case of high temperature products like ledeburite and pearlite, on the one hand, and the low temperature product lower bainite, on the other.

10.4 Displacive mechanism of transformation

According to this view, bainite forms by a displacive, shear mechanism involving coordinated movement of many atoms across a glissile interface. The growth of bainite is accompanied by an invariant plane strain shape deformation with a large shear component (Bhadeshia and Christian, 1990). The strain energy of the shape deformation has been calculated and measured to be about 400 J mol^{-1} (Bhadeshia and Edmonds, 1980). The product phase takes the shape of plates to minimise the strain energy of shape deformation. Although carbon diffusion takes place during paraequilibrium nucleation, the growth is completely diffusionless (Bhadeshia and Christian, 1990; Christian and Edmonds, 1984). This makes it thermodynamically impossible for the transformation to take place above the T_o temperature at which both austenite and ferrite of the same composition have the same free energy. In fact, the transformation takes place at a finite supercooling below the T_o temperature to compensate for 400 J mol^{-1} of stored strain energy of transformation. This temperature is called the T_o' temperature. The loci of T_o and T_o' temperatures as a function of carbon concentration on the Fe-C phase diagram are called the T_o and T_o' curves, respectively. Nucleation of bainite usually occurs at austenite grain surfaces but the plates do not cross austenite grain boundaries or twin boundaries.

© Woodhead Publishing Limited, 2012

10.4.1 Nucleation

Experimental data indicate that the composition of a steel has a larger effect on the Widmanstätten ferrite start (W_s) or the bainite start temperatures (B_s) than on the Ae_3 temperature, and alloys with similar Ae_3 temperatures can have significantly different W_s or B_s temperatures. It is thus obvious that the effect of the alloying elements dissolved in austenite is more than just thermodynamic and warrants a kinetic analysis of the problem. The kinetics of transformation in steels, as already stated, is represented on time-temperature-transformation (TTT) diagrams. A TTT diagram for steels consists essentially of two C-curves, one for high temperature reconstructive transformations to allotriomorphic ferrite and pearlite, and the other for displacive transformations to Widmanstätten ferrite and bainite which occur at comparatively lower temperatures (Fig. 10.1). In steels where the transformation is very fast, the two curves overlap so that only a single curve may be detected in routine experiments.

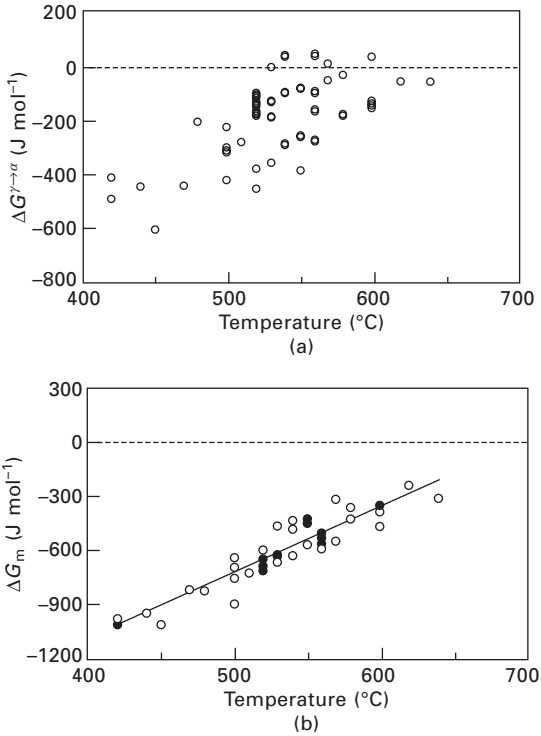
The lower C-curve has a characteristic flat top which represents the highest temperature T_h (equivalent to the WB_s temperature discussed earlier) at which displacive transformation to ferrite can take place. This transformation start temperature must be controlled by nucleation that is more difficult than growth, because of the disproportionate amount of energy spent in creating a new interface around a small particle. An analysis of the magnitude of the free energy change available at T_h provides useful clues to the mechanism of transformation and gives an indication of the amount of driving force necessary for nucleation to occur at a detectable rate (Bhadeshia, 1981a).

Steven and Haynes (1956) have measured T_h temperatures for a wide range of low-allow steels, all of which exhibited two distinct C-curves. For each of these steels, the driving force available at T_h was calculated assuming two possible nucleation mechanisms: (i) nucleation without the partitioning of any of the solute atoms including carbon ($\Delta G^{\gamma\rightarrow\alpha}$) and (ii) nucleation with paraequilibrium carbon partitioning (ΔG_m) (Bhadeshia, 1981a). The results of the analysis are plotted in Fig. 10.3 and reveal some important facts. Firstly, the nucleation of Widmanstätten ferrite or bainite occurs with the partitioning carbon atoms since the alternative hypothesis of diffusionless nucleation would lead to an increase in the free energy for some of the cases illustrated (Fig. 10.3(a)). Secondly, all the points, whether they correspond to Widmanstätten ferrite or to bainite, lie on the same straight line in Fig. 10.3(b). It can therefore be concluded that both phases originate from the same nucleus which develops into bainite or Widmanstätten ferrite depending on certain growth criteria which will be discussed later.

Figure 10.3(b) also shows that the driving force at which nuclei start to form at a detectable rate varies linearly with the temperature T_h:

$$G_N = B_1\, T_h - B_2 \text{ J mol}^{-1} \qquad [10.2]$$

© Woodhead Publishing Limited, 2012



10.3 The driving force for nucleation for a variety of steels at their respective T_h temperatures (Bhadeshia, 1981a). The driving force was calculated assuming (a) diffusionless nucleation ($\Delta G^{\gamma\to\alpha}$) and (b) paraequilibrium redistribution of carbon (ΔG_m).

where G_N is defined as the minimum free energy change required to obtain a detectable amount of Widmanstätten ferrite or bainite. For the best fit line, the values of B_1 and B_2 have been found to be 3.637 J mol^{-1}K^{-1} and 2540 J mol^{-1}, respectively, where T_h is expressed in °C (Ali and Bhadeshia, 1989). G_N is known as the 'universal nucleation function' and is applicable to all low-alloy steels in the temperature range 400–650°C. Nucleation of Widmanstätten ferrite or bainite becomes possible at a temperature at which the actual driving force for nucleation, ΔG_m (a negative quantity at the temperature of interest), becomes less than that given by the G_N function.

Although the above treatment appears empirical, it has been shown to be consistent with the theory of martensite nucleation (Bhadeshia, 1981a, 2001), where the activation energy for nucleation is expected to be directly proportional to the driving force (Magee, 1970; Raghavan and Cohen, 1971). This should be contrasted with the classical nucleation theory where a new phase forms by a random structural and composition fluctuation in the parent phase and the activation energy is inversely proportional to the square of the

© Woodhead Publishing Limited, 2012

driving force for nucleation. Such a relation cannot explain the behaviour obtained for Widmanstätten ferrite and bainite.

10.4.2 Growth of the nucleus

It was pointed out earlier that both Widmanstätten ferrite and bainite grow from the same nucleus and that the nucleation rate becomes appreciable when

$$\Delta G_m \leq G_N \qquad [10.3]$$

The nucleus can develop into Widmanstätten ferrite (i.e. $T_h = Ws$) if the driving force for paraequilibrium growth exceeds the stored energy of Widmanstätten ferrite which has been estimated to be 50 J mol^{-1} (Bhadeshia, 1981a) (even though the mechanism of transformation of Widmanstätten ferrite is displacive, carbon diffusion takes place during paraequilibrium nucleation and growth (Bhadeshia and Christian, 1990)).

$$\Delta G^{\gamma\rightarrow\gamma'+\alpha} \leq -50 \text{ J mol}^{-1} \qquad [10.4]$$

Alternatively, if the driving force for diffusionless growth is sufficient to allow for 400 J mol^{-1} of the stored energy of bainite, then transformation to bainite takes place and T_h is identified with the bainite-start temperature B_s,

$$\Delta G^{\gamma\rightarrow\alpha} \leq -400 \text{ J mol}^{-1} \qquad [10.5]$$

It should be noted that for all the steels included in the analysis of Fig. 10.3 and Eq. [10.2], the transformation start temperature (T_h) was controlled by the nucleation criterion; $\Delta G^{\gamma\rightarrow\gamma'+\alpha}$ was less than –50 J mol^{-1} at T_h in all cases so that the growth criterion for Widmanstätten ferrite was satisfied for all the steels. The Widmanstätten ferrite start temperature, W_s, or the bainite start temperature, B_s, is defined as the highest temperature at which both the nucleation and the growth criteria for the respective phase are first satisfied.

10.4.3 Growth of bainite

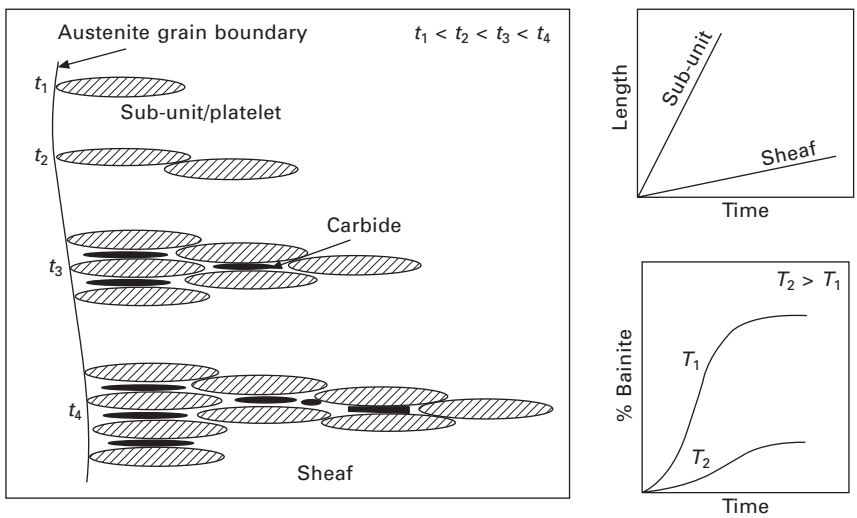
As pointed out in the previous section, the nucleus can grow as bainite plates if the magnitude of the free energy available for diffusionless growth of ferrite is more than 400 J mol^{-1}. Compared with martensite, bainite grows at relatively high temperatures when the austenite is weak and cannot accommodate the shape deformation elastically. Hence it undergoes plastic deformation in the region adjacent to the bainite plate to relieve the large shape strain. Atom force microscopic studies have confirmed the shape deformation and the concomitant plastic relaxation in regions adjacent to the parent austenite (Swallow and Bhadeshia, 1996). The resulting local increase in dislocation

© Woodhead Publishing Limited, 2012

density hinders the motion of the glissile transformation interface. The growth of the plate is eventually stifled by the build-up of dislocation debris so that each plate is usually much smaller than the austenite grain size. The reaction progresses further by the nucleation of new plates, also known as sub-units, particularly near the tips of the existing ones. This results in a sheaf-like structure shown in Fig. 10.1 and illustrated schematically in Fig. 10.4 (Hehemann, 1970; Bhadeshia, 2001). Sheaves grow by repeated nucleation and rapid growth of sub-units to a limiting size. A re-analysis of sheaf growth rate data showed that the lengthening rate is greater than expected from carbon diffusion-controlled growth (Ali and Bhadeshia, 1989). The kinetic aspects of the transformation have been reviewed further by Takahashi (2004).

Since the driving force for the bainite transformation is smaller than for martensite, and because of the plastic deformation caused by the shape change, bainite plates grow at a rate much slower than martensite plates. Nevertheless, the rate of lengthening of individual sub-units of bainite, as measured directly using hot-stage photoemission electron microscopy, is many orders of magnitude faster than expected from carbon diffusion-controlled growth under paraequilibrium conditions (Bhadeshia, 1984).

The mechanism of sheaf formation and growth outlined above make it obvious that the rate of lengthening of the sheaf as a whole is much less than that of an individual sub-unit and depends on the time taken by the



10.4 Schematic representation of formation of a bainite sheaf by repeated nucleation and limited growth of sub-units and its effect on overall transformation kinetics (adapted from Bhadeshia and Honeycombe, 2006).

© Woodhead Publishing Limited, 2012

sub-unit to reach its limiting size and the time interval that must elapse before a new sub-unit is nucleated. This slows down the overall kinetics of transformation with the result that the volume fraction of bainite formed at a given isothermal temperature is a sigmoidal function of time (Fig. 10.4) and a typical C-curve for bainite transformation is obtained on the TTT diagram.

Role of solutes and the incomplete reaction phenomenon

High resolution atom probe studies have shown that the substitutional atoms do not partition between austenite and bainitic ferrite during the transformation (Bhadeshia and Waugh, 1982). The ratio of substitutional to iron atoms is the same everywhere, including at the transformation interface.

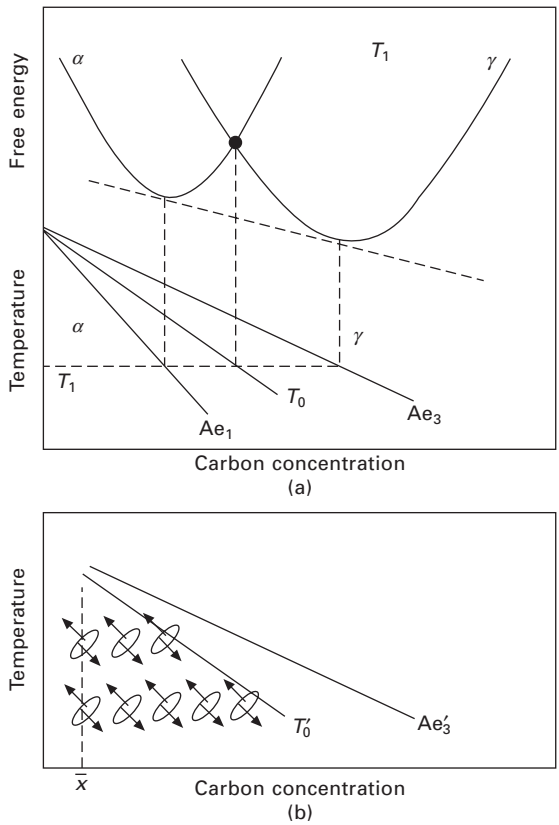
The role of carbon is somewhat different. The growth of the bainitic ferrite is diffusionless so that its composition is exactly the same as the parent austenite and it is completely supersaturated with carbon when first formed (Zener, 1946). In principle at least, the transformation should go to completion. However, as explained earlier, the entire austenite grain does not transform instantly. Given the relatively high temperatures at which bainite transformation takes place, the plate of bainitic ferrite formed first has sufficient time to reject its excess carbon into the residual austenite during the course of transformation. The next plate of bainite then grows from carbon-enriched austenite with a lower driving force. This continues until the carbon concentration of austenite reaches T'_o when the driving force for diffusionless shear transformation drops to zero and the reaction stops. The phenomenon is known as the 'incomplete reaction phenomenon' because the reaction stops before the austenite reaches its paraequilibrium concentration given by the Ae'_3, (Fig. 10.5). The maximum volume fraction of bainite that can form at any temperature increases with decreasing temperature.

Experimental measurement of the carbon content of residual austenite left untransformed after the cessation of the bainite reaction indeed confirms that it follows the T'_o line and the transformation stops prematurely (Bhadeshia, 1981b, 2001; Bhadeshia and Edmonds, 1980; Christian and Edmonds, 1984; Chang and Bhadeshia, 1994; Chupatanakul and Nash, 2006). Thus there is indirect evidence that the growth of ferrite is diffusionless. It is very difficult to obtain direct evidence to prove that the bainitic ferrite is initially supersaturated with carbon since it typically takes less than a second for the carbon to escape from ferrite at the usual reaction temperatures (Bhadeshia, 1988). Some measurements do, however, indicate that bainitic ferrite is supersaturated with carbon (Pickering, 1967; Bhadeshia and Waugh, 1982; Tsuzaki *et al.*, 1994), but these can be attributed to segregation of carbon to dislocations (Christian and Edmonds, 1984; Borgenstam *et al.*, 2009) and the evidence does not seem to be conclusive.

© Woodhead Publishing Limited, 2012

10.4.4 Upper and lower bainite

Bainite is usually distinguished into the upper and lower bainite morphologies. The difference between the two morphologies arises out of competition between the rate of carbide precipitation from supersaturated ferrite and the rate of carbon rejection from supersaturated ferrite to austenite (Matas and Hehemann, 1961). Upper bainite forms at relatively higher temperatures where the carbon can diffuse rapidly. The time taken for the decarburisation of a supersaturated ferrite plate is smaller than that required for precipitation of carbide within the plate. The excess carbon of the supersaturated ferrite is therefore rejected into the adjacent austenite. Cementite may eventually precipitate out of the enriched residual austenite. As the transformation temperature is lowered, the diffusion of carbon becomes slower and some



10.5 Schematic illustration of the (a) T_o concept where austenite and ferrite of the same composition have the same free energy and (b) incomplete reaction phenomenon where the reaction stops well before the paraequilibrium phase boundary Ae_3' (adapted from Bhadeshia and Honeycombe, 2006).

© Woodhead Publishing Limited, 2012

of the carbon is precipitated as fine carbide particles inside the ferrite plates. The remaining carbon escapes into the austenite and may precipitate as inter-plate carbide. This gives the lower bainite morphology.

The rate at which carbon diffuses away from the austenite-ferrite interface depends on the concentration gradient which in turn depends on the carbon content of austenite that is undergoing transformation and thus the transition temperature depends on the carbon content of the alloy as well (Pickering, 1967). The transition from upper to lower bainite is not observed in all alloys. For example, only lower bainite was found to form in an Fe-1.1C–7.9Cr (wt%) steel having a B_s temperature of 300°C (Srinivasan and Wayman, 1968b). Similar results have been reported by Okamoto and Oka (1986) in high purity steels containing 0.85–1.8 wt% C. On the other hand, only upper bainite has been observed in high purity plain carbon steels containing less than 0.4 wt% C (Ohmori and Honeycombe, 1971). A simple quantitative model for the transition has been developed by Takahashi and Bhadeshia (1990). The model elegantly explains the experimental observations that only lower bainite forms in high carbon steels whereas only upper bainite forms in low carbon steels (Bhadeshia, 2001).

It is important to note that ε-carbide as well as cementite have been reported to precipitate inside the ferrite plates in lower bainite; the nature of carbide depends on composition and transformation temperature (Matas and Hehemann, 1961; Kumar, 1968; Bhadeshia, 1980). The ε-carbide precipitate is observed in high carbon steels and has only a transitory existence and gives way to cementite at longer times; they persist for a longer time in steel containing high silicon content (Matas and Hehemann, 1961; Hehemann, 1970; Hehemann *et al.*, 1972; Bhadeshia, 1980). The presence of ε-carbide in bainitic ferrite indicates that it is supersaturated with carbon (Bhadeshia and Christian, 1990). The actual sequence depends on temperature, composition and dislocation density and is similar to the process of tempering of martensite (Bhadeshia, 1988).

10.4.5 Crystallography

It has been pointed out earlier that bainite grows in the form of sheaves. The sub-units within a sheaf have nearly the same crystallographic orientation and therefore abutting sub-units are separated by only a small angle boundary. The longitudinal direction of the ferrite sub-units is parallel to the closed packed direction $<111>_\alpha$ (Christian and Edmonds, 1984). In spite of morphological complexity of bainite (sheaf-like cluster of sub-units, presence of many phases, high dislocation density), it has been possible to rationalise the crystallographic features of the transformation in terms of the phenomenological theory of martensite transformation in a large number of cases. The results accumulated since the pioneering work of Srinivasan and

© Woodhead Publishing Limited, 2012

Wayman (1968c) have been compiled by Luo *et al*. (1992) and a brief review of the crystallographic aspects of the transformation has been presented by Ohmori (2002).

The relative orientation between bainitic ferrite and the parent austenite is close to the classic Kurdjumov–Sachs (1930) or Nishiyama–Wasserman (Nishiyama, 1934; Wasserman, 1933) (Table 10.1) where the close-packed planes in the two structures are parallel or nearly parallel. Srinivasan and Wayman (1968c) studied the crystallography of lower bainite sheaves in Fe-1.1C-7.9Cr wt% alloy. The habit plane of the sheaf was found to be close to $(254)_\gamma$. It was shown that the sheaf habit plane and the orientation relationship could be predicted using the phenomenological theory if one of the following two conditions is satisfied: (i) the habit plane is exactly an invariant plane and the lattice invariant shear is irrational in both plane and direction or (ii) the lattice invariant deformation is a double shear on

Table 10.1 Some common orientation relationships relevant to bainite transformation in steel (after Shackleton and Kelly, 1967). Please note that the indicated planes and direction need not be exactly parallel but may be within a few degrees of each other

Sl. No.	Relationship	Transformation	Phases involved	Crystallographic orientation relationship
1.	Kurdjumov–Sachs (1930)	Austenite to proeutectoid ferrite, bainitic ferrite or martensite	Proeutectoid ferrite, bainitic ferrite or martensite and austenite	$\{1\bar{1}1\}_\gamma \parallel \{1\bar{1}0\}_\alpha$ $\langle\bar{1}10\rangle_\gamma \parallel \langle\bar{1}\bar{1}1\rangle_\alpha$
2.	Nishiyama–Wasserman (Nishiyama, 1934; Wasserman, 1933)			$\{11\bar{1}\}_\gamma \parallel \{1\bar{1}0\}_\alpha$ $\langle\bar{1}12\rangle_\gamma \parallel \langle\bar{1}10\rangle_\alpha$
3.	Bagaryatski (1950)	Tempering or precipitation of cementite in ferrite, bainitic ferrite or martensite	Cementite and ferrite	$\{001\}_{Fe_3C} \parallel \{2\bar{1}1\}_\alpha$ $\langle100\rangle_{Fe_3C} \parallel \langle0\bar{1}\bar{1}\rangle_\alpha$ $[010]_{Fe_3C} \parallel [1\bar{1}\,1]_\alpha$
4.	Pitsch (1962)	Precipitation of cementite in austenite	Cementite and austenite	$\{001\}_{Fe_3C} \parallel \{\bar{2}2\bar{5}\}_\gamma$ $\langle100\rangle_{Fe_3C} \parallel \langle\bar{5}\bar{5}4\rangle_\gamma$ $\langle010\rangle_{Fe_3C} \parallel \{1\,\bar{1}\,10\}_\gamma$
5.	Isaichev (1947)	Precipitation of cementite in austenite or ferrite	Cementite and ferrite	$\{103\}_{Fe_3C} \parallel \{10\,\bar{1}\}_\alpha$ $\langle010\rangle_{Fe_3C} \parallel \langle11\,\bar{1}\rangle_\alpha$
6.	Jack (1951)	Precipitation of ε-carbide in lower bainitic ferrite or martensite	ε-carbide and ferrite	$\{10\bar{1}\}_\alpha \parallel \{10\bar{1}1\}_\varepsilon$ $\{2\bar{1}1\}_\alpha \parallel \{10\bar{1}0\}_\varepsilon$ $\langle100\rangle_\alpha \parallel \langle11\bar{2}0\rangle_\varepsilon$

© Woodhead Publishing Limited, 2012

the $(1\bar{1}1)_\gamma$ and $(101)_\gamma$ along the common $[\bar{1}01]_\gamma$ so that the habit plane is isotropically contracted by about 1.2%. The habit plane of martensite in the same alloy was found to be $(494)_\gamma$ which is 16° away from the bainite habit. The orientation relationship between the parent and the product phases was also found to be different for bainite and martensite and they attributed these differences to a possible difference in the deformation mode in the two cases.

Sandvik (1982) studied the structure and crystallography of bainite in an Fe-C-Si alloy containing a small amount of Mn and Cr and reported the mean habit plane of the individual sub-units to be $(0.37\ 0.66\ 0.65)_\gamma$ which is 6° from the sheaf habit plane of the alloys studied by Srinivasan and Wayman (1968c). Sandvik (1982) also observed twinning in the austenite adjoining bainitic ferrite and was able to estimate the direction and magnitude of shape strain from the displacement of twins and found them to be close to the values for $\{225\}_\gamma$ and $\{15\ 10\ 3\}_\gamma$ martensite. Hoekstra (1980), on the other hand, found that the crystallography of bainite formed in an Fe-C-Ni-Cr steel was inconsistent with the phenomenological theory of martensite. Luo *et al*. (1992) have, however, shown that much better agreement with the theory can be obtained in this case if a lattice invariant shear on the $(1\bar{1}1)_\gamma\ [\bar{1}01]_\gamma$ system is used in place of the $(101)_\gamma\ [\bar{1}01]_\gamma$ used originally by Hoekstra (1980). Thus they found very good agreement with the theory in their own study on carbide-free upper bainite in Fe-0.55C-1.35Si-0.8Mn-0.45Mo (wt%) alloy. The habit plane was determined to be $(5\ 12\ 7)_\gamma$ and it was found to be very close to the calculated habit plane of $(0.34\ 0.80\ 0.48)_\gamma$ (Luo *et al*., 1992).

The orientation relationship between ferrite and cementite has been studied in detail by Shackleton and Kelly (1967). The Bagaryatski relationship (1950), usually observed during tempering of martensite or during ageing of quenched ferrite, was also found to hold good for cementite precipitated within lower bainitic ferrite. In upper bainite, the Bagaryatski relationship was obeyed in only two-thirds of all the bainite plates examined. In the remaining cases the observed ferrite-cementite orientation relationship could be explained by combination of variants of the usual (i) Kurdjumov–Sachs relationship between ferrite and austenite and (ii) Pitsch relationship (1962) between cementite and austenite.

The results described above led Shackleton and Kelly (1967) to suggest that ferrite and cementite form independently from austenite in upper bainite with Kurdjumov–Sachs and Pitsch relationships respectively, and therefore the ferrite and cementite are related indirectly through their relationship with the common parent phase. In some fortuitous cases, combination of appropriate (Kurdjumov–Sachs and Pitsch) variants gives rise to the Bagaryatski relationship between ferrite and cementite. They further concluded that cementite always precipitates from supersaturated ferrite in lower bainite,

© Woodhead Publishing Limited, 2012

since the Bagaryatski relationship was the only cementite-ferrite orientation relationship observed in all the cases examined except one. These results are in broad agreement with the findings of Pickering (1967). Usually, only one variant of cementite precipitates inside the lower bainitic ferrite plate; however, more than one variant of the cementite habit plane has also been observed (Bhadeshia and Edmonds, 1979).

Isaichev's cementite-ferrite orientation relationship (1947), which differs from the Bagaryatski relationship by a rotation of about 4° around <111>, has also been reported for upper and lower bainite by a few workers (Ohmori and Honeycombe, 1971; Huang and Thomas, 1977; Ohmori, 1989; Ohmori *et al.*, 1996).

When ε-carbide precipitates out from the ferrite plates of lower bainite, its orientation relationship with ferrite is the same as that observed during low temperature tempering of martensite; the orientation relationship is the one given by Jack (1951). These results can be interpreted to imply, as mentioned already, that carbides in lower bainite form from supersaturated ferrite since they are similar to those observed during tempering of martensite (Bhadeshia and Christian, 1990). Various orientation relationships discussed above are summarised in Table 10.1.

As pointed out earlier, it has sometimes been suggested that cementite in lower bainite forms by interphase precipitation (Hehemann *et al.*, 1972; Honeycombe, 1976). The issue has been examined in detail using three-phase (lower bainitic ferrite-cementite-austenite) crystallographic data (Bhadeshia, 1980; Christian and Edmonds, 1984; Bhadeshia and Christian, 1990). It can justifiably be argued that a third-phase precipitate particle at the austenite-ferrite transformation interface would tend to match its lattice with both the adjacent phases. Therefore, in the light of the Bagaryatski orientation relationship between lower bainitic ferrite and cementite and the Kurdjumov–Sachs orientation relationship between lower bainitic ferrite and austenite, the three-phase crystallographic relationship is expected to be:

$$[100]_{Fe_3C} \parallel [0\bar{1}1]_\alpha \parallel [111]_\gamma$$

$$[010]_{Fe_3C} \parallel [1\bar{1}\bar{1}]_\alpha \parallel [\bar{1}01]_\gamma$$

Since the three-phase crystallographic data from lower bainite do not agree with these orientation relationships, it can be concluded that interphase precipitation does not take place during the formation of lower bainite, and cementite precipitates out from supersaturated lower bainitic ferrite (Bhadeshia, 1980).

10.4.6 Thermal stabilisation

Martensite is known to show thermal stabilisation, which refers to a temporary cessation of transformation and lower volume fraction of martensite when

© Woodhead Publishing Limited, 2012

cooling is interrupted (Mohanty, 1995). There is at least one report in the literature which indicates a similar result for bainite as well (Hehemann and Troiano, 1954). A sample first transformed to the maximum possible extent at 500°C was further cooled down to 425°C. The total amount of bainite formed (measured by both dilatometric and metallographic techniques) in this two-step experiment was less than the amount of bainite that formed when the sample was transformed directly at 425°C as in a regular isothermal experiment. This is similar to the thermal stabilisation seen in martensite, but perhaps more work is needed to draw a firm conclusion.

10.4.7 Stress and transformation plasticity

Displacive transformation can be viewed as a mode of deformation which is also accompanied by a change in crystal structure. The plastic strain associated with the transformation is called 'transformation plasticity' to distinguish it from the plastic deformation caused by slipping or twinning. The shear component of the applied stress can interact with the large shear component of the IPS shape deformation associated with the transformation and influence the transformation significantly (Wayman and Bhadeshia, 1996). The dilatational component of the shape strain is much smaller than the shear component and therefore it is expected to have only a small influence, and the overall effect of the applied stress is dominated by the shear component (Patel and Cohen, 1953). The deformation or strain energy can be regarded as an additional 'mechanical driving force', which can complement the chemical driving force in accomplishing the transformation (Patel and Cohen, 1953; Olson and Cohen, 1982). The effect of stress on the martensite transformation has been studied extensively particularly in the context of transformation induced plasticity (TRIP) or TRIP-aided steels where transformation plasticity leads to significant improvement in the properties and performance of the material (Olson and Cohen, 1975, 1982; Olson and Azirin, 1978; Mukherjee *et al.*, 2008).

Externally applied stress can induce martensite transformation at temperatures above the M_s temperature because it provides additional mechanical driving force (Wayman and Bhadeshia, 1996). It is usual to refer to an M_d temperature which is identified as the highest temperature at which stress can induce martensite transformation. Above the M_d temperature, the applied stress, limited by the yield stress of the parent austenite phase (which decreases with increasing temperature), cannot provide enough mechanical driving force to aid the chemical driving force and therefore the transformation cannot take place (Olson and Cohen, 1972).

Similar studies have not been carried out for bainite presumably because the parent austenite cannot sustain large stresses at the relatively high temperatures at which bainite forms. There are, however, reports which

© Woodhead Publishing Limited, 2012

suggest an acceleration of bainite transformation when it happens under the influence of stress (Cottrell, 1945; Jepson and Thompson, 1949; Bhattacharyya and Kehl, 1955; Shipway and Bhadeshia, 1995a). The volume fraction of bainite formed at a particular temperature has been found to increase with stress (Cottrell, 1945; Jepson and Thompson, 1949; Bhattacharyya and Kehl, 1955; Shipway and Bhadeshia, 1995a). Moreover, the steels studied by Bhattacharyya and Kehl included 4340 steel which exhibits the incomplete reaction phenomenon (see also Hehemann and Troiano, 1954). The effect of an externally applied stress of 415 MPa (equivalent to a mechanical driving force of 350 J mole^{-1}; Patel and Cohen, 1953) was to drive the transformation towards completion at 450°C. It can thus be argued that the mechanical driving force due to the applied stress was sufficient for the transformation to cross the T_o' barrier so that near-complete transformation could be obtained.

In addition to the above effects on the kinetics, the applied stress would also favour the formation of those variants which best comply with the stress, i.e., the variant for which the mechanical driving force is the highest. The variant selection changes the appearance of the microstructure which is expected to become more organised because of preferential orientation. Jepson and Thompson (1949) studied the effect of compressive stress on the transformation of austenite to low temperature bainite and found that, while certain grains showed a large degree of transformation, it was small or absent in others. They further noted the alignment of bainite 'needles' at 45° to the direction of applied stress in those favourably oriented grains which also showed a much higher degree of transformation than the others. The results indicate that even on a microscopic scale, the amount of transformation increases with resolved shear stress. The applied compressive stress resolves to give maximum shear stress on planes that are inclined at 45° to the stress axis. Even though austenite grains have a multiplicity of variants to choose from, some of them may be more favourably oriented with respect to the applied stress than others, so that the plane of maximum shear stress coincides (or nearly so) with one of the available habit planes. For these grains, the mechanical and hence the total driving force is the highest and hence the degree of transformation is higher and the plates are aligned along the plane of maximum shear stress. The driving force would be less for other grains that are not so favourably oriented and therefore the degree of transformation is much less. The results imply a large shear component of the shape deformation associated with displacive transformation which interacts strongly with the applied stress. Similar results on the effect of stress on alignment of microstructure have been reported by other investigators for bainite (Bhattacharyya and Kehl, 1955; Umemoto, *et al*. 1986; Bhadeshia *et al*., 1991; Mangal *et al*., 2009) as well as for martensite (Bhadeshia, 1982) and indicate the essential similarity between the two.

When displacive transformation takes place in an unstressed polycrystalline

© Woodhead Publishing Limited, 2012

sample where austenite grains are randomly oriented, the product has a choice of some 24 variants and they form with random orientation. The shear components of the shape strain of the randomly oriented plates cancel out so that only an isotropic volume strain is obtained which is recorded during routine dilatometer experiments. However, when the transformation takes place under the influence of an externally applied stress, variants which best comply with the applied stress are formed preferentially and the shear components of the aligned plates do not cancel out so that transformation strain is not isotropic (Bhadeshia *et al.*, 1991). The anisotropy of transformation strain is manifested as transformation plasticity. Similar results have been obtained when the parent austenite grains are crystallographically textured (Bhadeshia *et al.*, 1991). Transformation plasticity has been detected during bainite transformation and is directly related to the shear component of the shape deformation associated with displacive transformation (Bhadeshia *et al.*, 1991; Shipway and Bhadeshia, 1995a). These results are inconsistent with a reconstructive mechanism of transformation.

10.4.8 Strain and mechanical stabilisation

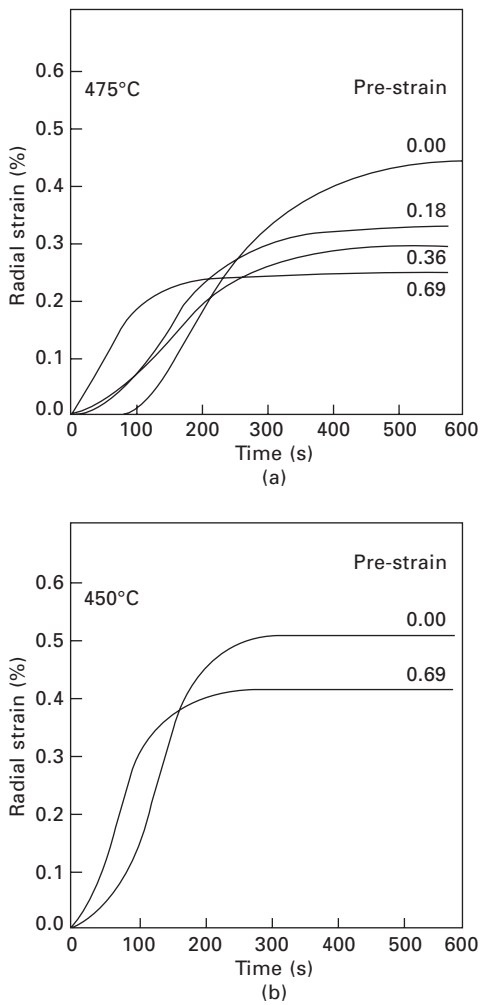
Displacive phase transformations and mechanical twinning involve the coordinated movement of atoms during the glide of glissile interfaces. Such movements cannot be sustained against strong structural barriers such as grain boundaries. Thus, martensite or mechanical twin plates cannot cross grain boundaries. Defects such as dislocations also hinder the progress of any glissile interface in much the same way that ordinary slip is made more difficult by the presence of dislocation forests.

It follows that displacive transformations can be suppressed by pre-straining the parent phase which has the effect of enhancing the defect density of the matrix. This effect is known as 'mechanical stabilisation' and is well established for martensitic transformations where transformation can be hindered by pre-straining the austenite (Raghavan, 1992; Mohanty, 1995). Prior deformation of metastable austenite at temperatures sufficiently above the M_s temperature lowers the transformation temperature and the amount of martensite formed at any subsequent temperature is reduced (Breedis and Robertson, 1963; Christian, 1975; Raghavan, 1992; Bhadeshia, 1999).

There is now sufficient evidence to show that bainite transformation also exhibits mechanical stabilisation (Freiwillig *et al.*, 1976; Fujiwara *et al.*, 1995; Shipway and Bhadeshia, 1995b; Yang *et al.*, 1996). Based on microstructural observations and microhardness measurements across non-uniformly deformed samples, Shipway and Bhadeshia (1995b) came to the conclusion that the bainite transformation is stabilised because of deformation of the austenite. Singh and Bhadeshia (1996) used a dilatometric technique to monitor the progress of transformation of pre-deformed austenite to bainite and came

© Woodhead Publishing Limited, 2012

to the same conclusion. Their results, shown in Fig. 10.6, indicate that the effect of pre-strain is first to accelerate the formation of bainite, but with an eventual reduction in the total amount of transformation. This is because there is an increase in the nucleation rate but each nucleus leads to a smaller degree of transformation in plastically deformed austenite. It was pointed out earlier that ferrite sub-units of bainite grow to a limited size only. Pre-straining has the effect of reducing this limiting size even further, so that the total amount of bainite can be reduced even though the nucleation rate might



10.6 Effect of austenite pre-strain (at 700°C) on the progress of bainite transformation at (a) 475°C and (b) 450°C. Radial strain refers to dilatation in the radial direction due to transformation (from Singh and Bhadeshia, 1996; used with permission from Maney Publishing).

© Woodhead Publishing Limited, 2012

be increased. The extent of stabilisation is less at a lower transformation temperature where the driving force for transformation is larger.

These results can be compared with reconstructive transformation to ferrite which is invariably accelerated when austenite is deformed. Deformation in this case not only increases the number density of nucleation sites of ferrite, it provides additional driving force for transformation since the defects generated by deformation are eliminated as the transformation front moves into the parent phase. The transformation thus resembles recrystallisation where strain energy stored in the material provides the driving force and is therefore accelerated when the strain is large. On the other hand, the defects are inherited by plates that grow by a displacive mechanism so that they do not contribute to the driving force. The displacive transformation is analogous to plastic deformation which shows work hardening where slip is made more difficult by the presence of dislocations introduced by prior deformation. Based on these arguments, Bhadeshia (1999, 2001) has suggested a very simple criterion to distinguish the two mechanisms of transformation: only displacive transformation shows mechanical stabilisation; reconstructive transformation cannot be retarded by plastic deformation. Judged on this criterion, it can be concluded that bainite forms by a displacive mechanism.

10.5 Summary and conclusion

Diffusion-controlled reconstructive and displacive mechanisms for the bainite transformation in steels have been discussed. Bainite grows in the form of sheaves comprising clusters of autocatalytically nucleated platelets or sub-units of ferrite that are separated by cementite, untransformed austenite or martensite. This morphological variety is commonly classified as upper bainite and is distinguished from lower bainite where carbides are present within the ferrite sub-units also.

According to the reconstructive mechanism of transformation, bainite is considered a non-lamellar mixture of ferrite and cementite formed as a result of eutectoid decomposition of austenite. Carbide-free bainite is viewed simply as proeutectoid ferrite. According to this view, the growth rate of bainitic ferrite is controlled by diffusion of carbon, and migration of coherent/semi-coherent transformation interface by ledge mechanism is believed to result in the plate-shaped morphology of ferrite. Movement of interface by ledge mechanism is also thought to be responsible for the observed surface relief. The kinetic features of the transformation, such as (i) a distinct B_s temperature above which bainite transformation does not take place, (ii) incomplete transformation, and (iii) existence of a separate 'C-curve' for bainite in the TTT diagram, are attributed to special solute drag-like effect of certain alloying elements that decrease the activity of carbon in austenite. These features are supposed to be alloy-specific and therefore not essential to bainite transformation.

© Woodhead Publishing Limited, 2012

A competing proposition for the transformation is that bainite forms by a displacive mechanism of transformation where the growth of the bainitic ferrite plate is diffusionless and is accompanied by an invariant plane strain shape deformation with a large shear component. Thus bainite transformation is not possible above the T_o temperature. Successive nucleation and rapid but limited growth because of accumulation of debris arising out of plastic accommodation of shape strain result in a sheaf-like structure. The ferrite plates are completely supersaturated with carbon when they first form, but because the temperature of transformation is relatively high (compared with martensite transformation), excess carbon diffuses out into the parent austenite during the course of transformation and may eventually precipitate out as cementite. It is possible to suppress the precipitation of cementite from austenite by suitable alloying and the resulting carbon enrichment of austenite ultimately leads to the 'incomplete reaction phenomenon'. The diffusion of carbon slows down at relatively lower temperatures in the bainite transformation range, and therefore carbon supersaturation of bainitic ferrite is at least partially relieved by precipitation of carbide with the ferrite plates itself giving rise to the lower bainite morphology.

The response of bainite transformation to externally applied stress and pre-strain is quite similar to that in the case of martensite transformation. Thus, transformation plasticity and alignment of bainitic ferrite plates along the planes of maximum shear stress are commonly observed when the transformation takes place under the influence of externally applied stress. The amount of bainite formed at a given temperature has been found to scale with the magnitude of the external stress. Similarly, mechanical stabilisation that is well established for martensite has also been observed for bainite transformation when the parent austenite phase is pre-strained. These findings provide very definite evidence in favour of a displacive mechanism of transformation for bainite.

10.6 References

Aaronson, H. I. (1969), *The Mechanism of Phase Transformations in Crystalline Solids*. The Institute of Metals, London, pp. 270–281.

Aaronson, H. I. and Wells, C. (1956), *Trans. AIME*, Vol. 206, pp. 1216–1223.

Aaronson, H. I. and Zackay, V. F. (eds) (1962), *Decomposition of Austenite by Diffusional Processes*. Interscience, New York.

Aaronson, H. I., Laird, C. and Kinsman, K. R. (1970), *Phase Transformations*, ASM, Metals Park, OH, pp. 313–396.

Aaronson, H. I., Reynolds, Jr., W. T., Shiflet, G. J. and Spanos, G. (1990), *Metall. Mat. Trans. A*, Vol. 21A, pp. 1343–1380.

Aaronson, H. I., Reynolds, Jr., W. T. and Purdy, G. R. (2004), *Metall. Mat. Trans. A*, Vol. 35A, pp. 1187–1210.

Aaronson, H. I., Reynolds, Jr. W. T. and Purdy, G. R. (2006), *Metall. Mat. Trans. A*, Vol. 37A, pp. 1731–1745.

© Woodhead Publishing Limited, 2012

Ali, A. and Bhadeshia, H. K. D. H. (1989), *Materials Science and Technology*, Vol. 5, pp. 398–402.
Bagaryatski, Y. A. (1950), *Doklady Akad. Nauk SSSR*, Vol. 73, pp. 1161–1164.
Bhadeshia, H. K. D. H. (1980), *Acta Metall.*, Vol. 28, pp. 1103–1114.
Bhadeshia, H. K. D. H. (1981a), *Acta Metall.*, Vol. 29, pp. 1117–1130.
Bhadeshia, H. K. D. H. (1981b), *International Conference on Solid-Solid Phase Transformations*, TMS-AIME, Warrendale, PA, pp. 1041–1048.
Bhadeshia, H. K. D. H. (1982), *Journal of Materials Science*, Vol. 17, pp. 383–386.
Bhadeshia, H. K. D. H. (1983), *Journal of Materials Science*, Vol. 18, pp. 1473–1481.
Bhadeshia, H. K. D. H. (1984), *Int. Conf. on Phase Transformations in Ferrous Alloys*, Marder, A. R. and Goldstein, J. I. (eds), ASM, Cleveland, OH, pp. 335–340.
Bhadeshia, H.K.D.H. (1987), *Scripta Metall.*, Vol. 21, pp. 1017–1022.
Bhadeshia, H. K. D. H. (1988), *Proc. Int. Cont. on Solid-Solid Phase Transformations*, Lorimer, G. W. (ed.), Institute of Metals, London, pp. 309–314.
Bhadeshia, H. K. D. H. (1990), *Metallurgy, Welding, and Qualification of Microalloyed (HSLA) Steel Weldments*, Hickey, J. T., Howden, D. G. and Randall, M. D. (eds), American Welding Society, Miami, FL pp. 34–69.
Bhadeshia, H. K. D. H. (1999), *Materials Science and Engineering A*, Vol. 273–275, pp. 58–66.
Bhadeshia, H. K. D. H. (2001), *Bainite in steels*, Institute of Materials, London.
Bhadeshia, H. K. D. H. and Christian, J. W. (1990), *Metall. Mat. Trans. A*, Vol. 21A, pp. 767–797.
Bhadeshia, H. K. D. H. and Edmonds, D. V. (1979), *Metall. Trans. A*, Vol. 10A, pp. 895–907.
Bhadeshia, H. K. D. H. and Edmonds, D.V. (1980), *Acta Metall.*, Vol. 28, pp. 1265–1273.
Bhadeshia, H. K. D. H. and Honeycombe, S. R. (2006), The bainite reaction. In *Steels: Microstructure and Properties*, 3rd edn, Butterworth-Heinemann, Oxford, pp. 129–154.
Bhadeshia, H. K. D. H. and Waugh, A. R. (1982), *Acta Metall.*, Vol. 30, pp. 775–784.
Bhadeshia, H. K. D. H., David, S. A., Vitek, J. M. and Reed, R. W. (1991), *Materials Science and Technology*, Vol. 7, pp. 686–698.
Bhattacharyya, S. and Kehl, G. L. (1955), *Trans. ASM*, Vol. 47, pp. 351–379.
Borgenstam, A., Hillert, M. and Ågren, J. (2009), *Acta Materialia*, Vol. 57, pp. 3242–3252.
Bradley, J. R. and Aaronson, H. I. (1981), *Metall. Mat. Trans. A*, Vol. 12A, pp. 1729–1741.
Breedis, J. F. and Robertson, W. D. (1963), *Acta Metall.*, Vol. 11, pp. 547–559.
Chang, L. C., Bhadeshia, H. K. D. H. (1994), *Materials Science and Engineering A*, Vol. 184, pp. L17–L19.
Chattopadhayay, K. (1985), *Materials Science Forum*, Vol. 3, pp. 231–246.
Chipman, J. (1972), *Metall. Mat. Trans. B*, Vol. 3, pp. 54–64.
Christian, J. W. (1975), *Theory of Transformations in Metals and Alloys, Part 1*, 2nd edn, Pergamon Press, Oxford.
Christian, J. W. and Edmonds, D. V. (1984), *Int. Conf. on Phase Transformations in Ferrous Alloys*, Marder, A. R. and Goldstein, J. I. (eds), ASM, Cleveland, OH, pp. 293–326.
Chupatanakul, S and Nash, P. (2006), *J. Mater Sci*, Vol. 41, pp. 4965–4969.
Cottrell, A. H. (1945), *JISI*, Vol. 15, pp. 93–104.

© Woodhead Publishing Limited, 2012

Davenport, E. S. and Bain, E. C. (1930), *Trans. Met Soc. AIME*, Vol. 90, pp. 117–154.
Fondekar, M. K., Rao, A. M. and Mallik, A. K. (1970), *Metall. Mat. Trans. A*, Vol. 1, pp. 885–890.
Freiwillig, R., Kudrman, J. and Chraska, P. (1976), *Metall. Mat. Trans. A*, Vol. 7A, pp. 1091–1097.
Fujiwara K., Okaguchi, S. and Ohtani, H. (1995), *ISIJ International*, Vol. 35, pp. 1006–1012.
Fumimaru, K., Toshiyuki, H. and Keniti, A. (2000), *La Rev. Metall.*, Vol. 97, pp. 1235–1244.
Goodenow, R. H. and Hehemann, R. F. (1965), *Trans. AIMME*, Vol. 233, pp. 1777–1786.
Goodenow, R. H., Matas, S. J. and Hehemann, R. F. (1963), *Trans. AIMME*, Vol. 227, pp. 651–658.
Hehemann, R. F. (1970), *Phase Transformations*, *ASM*, *Metals Park*, OH, pp. 397–432.
Hehemann, R. F. and Troiano, A. R. (1954), *Trans. AIME*, Vol. 200, pp. 1272–1279.
Hehemann, R. F. and Troiano, A. R. (1956), *Metal Progress*, Vol. 70, pp. 97–104.
Hehemann, R. F., Kinsman, K. R. and Aaronson, H. I. (1972), *Metall. Mat. Trans.*, Vol. 3, pp. 1077–1094.
Hillert, M. (1960), *The Growth of Ferrite*, *Bainite and Martensite*, Internal Report, Swedish *Inst. Met. Res.*, Stockholm, Sweden.
Hillert, M. (1975), *Metall. Mat. Trans. A*, Vol. 6A, pp. 5–19.
Hillert, M. (1994), *Metall. Mat. Trans. A*, Vol. 25A, pp. 1957–1966.
Hillert, M. (2002), *Scripta Materialia*, Vol. 47, pp. 175–180.
Hillert, M. (2011), *Metall. Mat. Trans. A*, Vol. 42, pp. 541–542.
Hillert, M., Höglund, L. and Ågren, J. (2004), *Metall. Mat. Trans. A*, Vol. 35A, pp. 3693–3700.
Hoekstra, S. (1980), *Acta Metall.*, Vol. 28, pp. 507–517.
Honeycombe, R. W. K. (1976), *Metall. Mat. Trans. A*, Vol. 7A, pp. 915–936.
Huang, D. H. and Thomas, G. (1977), *Metall. Mat. Trans. A*, Vol. 8A, pp. 1661–1674.
Humphreys, E. S., Fletcher, H. A., Hutchins, J. D., Garratt-Reed, A. J., Reynolds, W. T., Aaronson, H. I., Purdy, G. R. and Smith, G. D. W. (2004), *Metall. Mat. Trans. A*, Vol. 35, pp. 1223–1235.
Isaichev, I. V. (1947), *Zhur Tekhn. Fiziki.*, Vol. 17, pp. 835–838.
Jack, K. H. (1951), *JISI*, Vol. 169, pp. 26–36.
Jepson, M. D. and Thompson, F. C. (1949), *JISI*, Vol. 162, pp. 49–56.
Kaufman, L., Radcliffe, S. V. and Cohen, M. (1962), In *Decomposition of Austenite by Diffusional Processes*, Zackay, V. F. and Aaronson, H. I. (eds), Inderscience, New York, pp. 313–351.
Kinsman, K. R., Eichen, E. and Aaronson, H. I. (1975), *Metall. Mat. Trans. A*, Vol. 6, pp. 303–317.
Ko, T. and Cottrell, S. A. (1952), *JISI*, Vol. 172, pp. 307–313.
Kumar, R. (1968), *Physical Metallurgy of Iron and Steel*, Asia Publishing House, Bombay.
Kurdjumov, G. V. and Sachs, G. (1930), *Z. Phys.*, Vol. 64, pp. 325–343.
LeHouillier, R. Begin, G. and Dubé, A. (1971), *Metall. Mat. Trans. A*, Vol. 2, pp. 2645–2653.
Liu, Y. C. and Aaronson, H. I. (1970), *Acta Metall.*, Vol. 18, pp. 845–856.
Luo, C.P. Weatherly, G.C. and Liu, Z.-Y. (1992), *Metall. Mat. Trans. A*, Vol. 23A, pp. 1403–1411.

© Woodhead Publishing Limited, 2012

Magee, C. L. (1970), *Phase Transformations*, ASM, Metals Park, OH, pp. 15–156.
Mangal, A., Kundu, S. and Singh, S. B. (2009), *Unpublished Research*.
Matas, S. J. and Hehemann, R. F. (1961), *Trans. Met Soc. AIME*, Vol. 221, pp. 179–185.
Mehl, R. F. (1939), In *Hardenability of Alloy Steels*, ASM, Cleveland, OH, pp. 1–65.
Mohanty, O. N. (1995), *Materials Science and Engineering B*, Vol. 32, pp. 267–278.
Mukherjee, M., Singh, S. B. and Mohanty, O. N. (2008), *Metall. Mat. Trans. A*, Vol. 39A, pp. 2319–2328.
Nishiyama, Z. (1934), *Sci. Rep. Tohoku Univ.*, Vol. 23, pp. 637–664.
Oblak, J. M. and Hehemann, R. F. (1967), In *Transformations and Hardenability in Steels*, Climax Molybdenum, Ann Arbor, MI, pp. 15–30.
Oblak, J. M., Goodenow, R. H. and Hehemann, R. F. (1964), *Trans-TMS AIME*, Vol. 230, pp. 258–259.
Ohmori, Y. (1989), *Mater. Trans.*, *JIM*, Vol. 30, pp. 487–497.
Ohmori, Y. (2002), *Scripta Materialia*, Vol. 47, pp. 201–206.
Ohmori, Y. and Honeycombe, R. W. K. (1971), *Trans. ISIJ*, Vol. 11, pp. 1160–1164.
Ohmori, Y., Jung, Y. C., Ueno, H., Nakai, K. and Ohtsubo, H. (1996), *Mater. Trans.*, *JIM*, Vol. 37, pp. 1665–1671.
Ohtani, H., Okaguchi, S., Fujihiro, Y. and Ohmori, Y. (1990), *Metall. Mat. Trans. A*, Vol. 21A, pp. 877–888.
Okamoto, H. and Oka, M. (1986), *Metall. Mat. Trans. A*, Vol. 17A, pp. 1113–1120.
Olson, G. B. and Azrin, M. (1978), *Metall. Mat. Trans. A*, Vol. 9, pp. 713–721.
Olson, G. B. and Cohen, M. (1972), *J. Less Common Met.*, Vol. 28, pp. 107–118.
Olson, G. B. and Cohen, M. (1975), *Metall. Mat. Trans. A*, Vol. 6, pp. 791–795.
Olson, G. B. and Cohen, M. (1982), *Metall. Mat. Trans. A*, Vol. 13, pp. 1907–1914.
Patel, J. R. and Cohen, M. (1953), *Acta Metall.*, Vol. 1, pp. 531–538.
Paxton, H. W., Kinsman, K. R. and Aaronson, H. I. (1967), In *Transformation and Hardenability in Steels*, Climax Molybdenum., Ann Arbor, MI, pp. 3–14.
Pickering, F. B. (1967), In *Transformations and Hardenability in Steels*, Climax Molybdenum, Ann Arbor, MI, pp. 109–132.
Pitsch, W. (1962), *Acta Metall.*, Vol. 10, p. 897–900.
Purdy, G. R. and Hillert, M. (1984), *Acta Metall.*, Vol. 32, pp. 823–828.
Quirdort, D. and Bréchet, Y. (2002), *Scripta Materialia*, Vol. 47, pp. 151–156.
Raghavan, V. (1992), In *Martensite*, *a tribute to Morris Cohen*, Olson, G. B. and Owen, W. S. (eds), *ASM International*, Materials Park, OH, pp. 197–226.
Raghavan, V. and Cohen, M. (1971), *Metall. Trans.*, Vol. 2, pp. 2409–2418.
Reynolds, JR., W. T., Li, F. Z., Shui, C. K. and Aaronson, H. I., (1990a), *Metall. Mat. Trans. A*, Vol. 21A, pp. 1433–1463.
Reynolds, JR., W. T., Liu, S. K., Li, F. Z., Hartfield, S. and Aaronson, H. I. (1990b), *Metall. Mat. Trans. A*, Vol. 21A, pp. 1479–1491.
Robertson, J. M. (1929), *JISI*, Vol. 119, pp. 391–426.
Sandvik, B. P. J. (1982), *Metall. Mat. Trans. A*, Vol. 13, pp. 777–787.
Shackleton, D. N. and Kelly, P. M. (1967), *Acta Metall.*, Vol. 15, pp. 979–992.
Shipway, P. H. and Bhadeshia, H. K. D. H. (1995a), *Materials Science and Engineering A*, Vol. 201A, pp. 143–149.
Shipway, P. H. and Bhadeshia, H. K. D. H. (1995b), *Materials Science and Technology*, Vol. 11, pp. 1116–1128.
Simonen, E. P., Aaronson, H. I. and Trevedi, R. (1973), *Metall. Mat. Trans. A*, Vol. 4, pp. 1239–1245.

© Woodhead Publishing Limited, 2012

Singh, S. B. and Bhadeshia, H. K. D. H (1996), *Materials Science and Technology*, Vol. 12(7), pp. 610–612.
Speich, G. R. and Cohen, M. (1960), *Trans. Met Soc. AIME*, Vol. 218, pp. 1050–1059.
Srinivasan, G. R. and Wayman, C. M. (1968a), *Trans. Met Soc. AIME*, Vol. 242, pp. 79–81.
Srinivasan, G. R. and Wayman, C. M. (1968b), *Acta Metall.*, Vol. 16, pp. 609–620.
Srinivasan, G. R. and Wayman, C. M. (1968c), *Acta Metall.*, Vol. 16, pp. 621–636.
Steven, W. and Haynes, A. J. (1956), *JISI*, Vol. 183, pp. 349–359.
Swallow, E. and Bhadeshia, H. K. D. H. (1996), *Materials Science and Technology*, Vol. 12, pp. 121–125.
Takahashi, M. (2004), *Current Opinion in Solid State and Materials Science*, *V*ol. 8, pp. 213–217.
Takahashi, M. and Bhadeshia, H. K. D. H. (1990), *Materials Science and Technology*, Vol. 6, pp. 592–603.
Tsuzaki, K. and Maki, T. (1995), *Journal de Physique IV*, Vol. 5, pp. 61–70.
Tsuzaki, K., Kodai, A. and Maki, T. (1994), *Metall. Mater. Trans. A*, Vol. 25A, pp. 2009–2016.
Townsend, R. D. and Kirkaldy, J. S. (1968), *Trans ASM*, Vol. 61, pp. 605–619.
Umemoto, M., Bando, S. and Tamura, I. (1986), *Proc. Int. Conf. on Martensitic Transformations (ICOMAT '86)*, Japan Institute of Metals, Tokyo, pp. 595–600.
Wasserman, G. (1933), *Aron. Bisenhuttenw*, Vol. 6, pp. 347–351.
Watson, J. D. and McDougall, P. G. (1973), *Acta Metall.*, Vol. 21, pp. 961–973.
Wayman, C. M. and Bhadeshia, H. K. D. H. (1996), In *Physical Metallurgy*, Cahn R. W. and Hassen, P. (eds), Elsevier Science, Amsterdam, pp. 1507–1554.
Yang, J. R., Huang, C. Y., Hsieh, W. H. and Chiou, C. S., (1996), *Materials Transactions, JIM*, Vol. 37, pp. 579–585.
Zener, C. (1946), *Trans. AIME*, Vol. 167, pp. 550–591.

© Woodhead Publishing Limited, 2012

11
Carbide-containing bainite in steels

T. FURUHARA, Tohoku University, Japan

Abstract: Bainite ordinarily refers to the ferrite-carbide aggregates that form in an intermediate temperature range overlapped by pearlite transformation and proeutectoid ferrite or cementite precipitation at higher temperatures and martensite transformation at lower temperatures. (More recently it has become acceptable to refer to carbide-free bainite when carbide formation is suppressed by alloying.) In the original 1939 paper on high carbon steels by Davenport and Bain, microstructure which corresponds to present 'carbide-containing bainite' was termed 'troostite' when formed just below pearlite transformation temperatures and 'martensite-troostite' when formed at lower temperatures just above the martensite transformation start temperature (M_s). However, it should be mentioned that complexity in morphology of the ferrite and cementite components subsequently led to a wide variety of microstructure definitions proposed by different researchers, sometimes in relation to transformation mechanisms. In this chapter, several kinds of definitions of the carbide-containing bainite structure are reviewed. Then characteristics of each of the ferrite and carbide (mainly cementite) components are described.

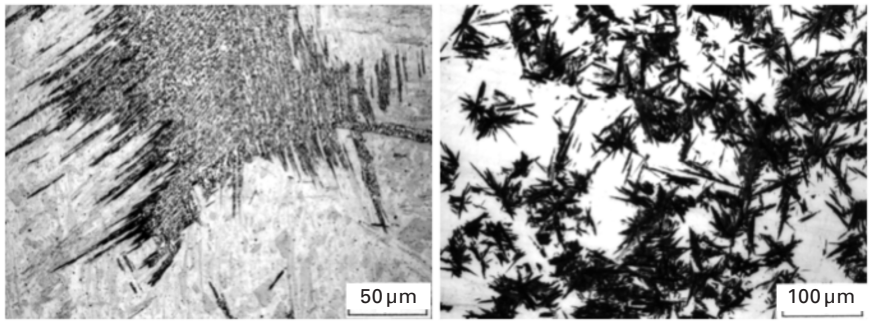
Key words: bainite, ferrite, austenite, carbide, eutectoid transformation, crystallography, dislocation.

11.1 Definitions of bainite structure

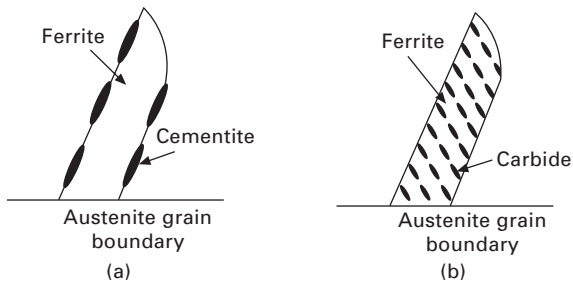
There are two classical terms describing bainite structures proposed by Mehl based upon microstructure as observed by light optical microscopy; upper bainite and lower bainite (Mehl, 1939), relating to formation at higher or lower temperatures, respectively. Upper bainite shows a feather-like morphology as seen in Fig. 11.1(a). Each ferrite crystal is acicular and grows from the austenite matrix grain boundaries in the form of needles or laths. This kind of bainite develops characteristic aggregates of ferrite crystals, 'packet' and 'block', as in lath martensite (Furuhara *et al.*, 2006). On the other hand, lower bainite consists of fine platelets and forms both at austenite grain boundaries and apparently within grain interiors (see Fig. 11.1(b)). Anisotropy of ferrite morphology such as needle, lath or plate arises from a specific crystallographic orientation relationship held with respect to its parent austenite as described later. Hereafter the ferrite component is denoted as bainitic ferrite (BF).

Hehemann proposed a clear definition of the bainite structure based upon

© Woodhead Publishing Limited, 2012



11.1 Optical micrograph of bainite microstructures in Fe-Ni-C alloys: (a) upper bainite in Fe-7Ni-0.2C (mass%), transformed at 681 K for 120 s, (b) lower bainite in Fe-7Ni-0.8C (mass%), transformed at 423 K for 32 h (Sawada *et al.*, 1994).



11.2 Classification of bainite based upon carbide precipitation: (a) upper bainite, (b) lower bainite (Hehemann, 1970).

carbide distribution or formation site (Hehemann, 1970). Figure 11.2 shows schematically the distinction between upper bainite and lower bainite proposed. In upper bainite, carbide precipitates at ferrite/austenite interphase boundaries to give an interlath dispersion, whilst, on the other hand, carbide is contained inside ferrite crystals in the lower bainite structure. This terminology is conventionally used because of significant effects of carbide morphology on the toughness of bainitic steels (Pickering, 1967). As transformation temperature is lowered, the bainitic ferrite grain size is decreased. In the upper bainite temperature range, the strength is correspondingly increased whereas the toughness is degraded. However, for lower bainite, strength still continues to increase, but because of the morphological change in carbide precipitation from upper bainite to lower bainite, toughness is improved remarkably. Due to this change in the strength/toughness balance, the classification in Fig. 11.2 is most widely used in industry.

There is another way to define bainite structure focused more upon ferrite morphology. Thus Ohmori *et al.* (1971) characterized bainite in low-alloy,

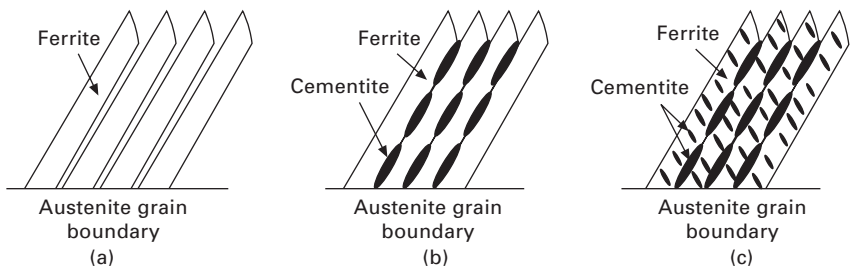
© Woodhead Publishing Limited, 2012

low-carbon steels showing that upper bainite consists of lath-shaped ferrite, whereas lower bainite structure contains plate-like ferrite. Upper bainite is classified into three types: BI, BII and BIII. BI-type (Fig. 11.3(a)) is lath-shaped ferrite without carbide precipitation. Carbon is enriched in the untransformed austenite between neighbouring bainitic ferrite crystals, leading upon cooling to formation of high carbon martensite and retained austenite as secondary phases or a mixture of those two phases, i.e., martensite-austenite (MA) constituent as it has generally become known. BII-type (Fig. 11.3(b)) is a mixture of lath-shape ferrite with cementite precipitation along the lath boundaries. In BIII-type (Fig. 11.3(c)), cementite precipitates at interlath boundaries and also inside the laths. Lower bainite contains cementite within plate-like bainitic ferrite. So the 'lower bainite' defined by Hehemann corresponds to the BIII-type upper bainite of Ohmori *et al.*, whereas Hehemann's 'upper bainite' corresponds to B II-type upper bainite in the classification by Ohmori *et al*. Ohmori *et al.*, however, have accounted for bainitic microstructure which does not contain carbide precipitation.

Figure 11.4 shows microstructures observed in Fe-C-2Si-1Mn alloys (Tsuzaki *et al.*, 1991). Bainite start temperature based on microstructural observation is just below 873 K. Based upon the ferrite morphology, upper bainite is dominant at the lower carbon and higher transformation temperature ranges. Plate-like bainitic ferrite was recognized below 673 K in a high-C alloy.

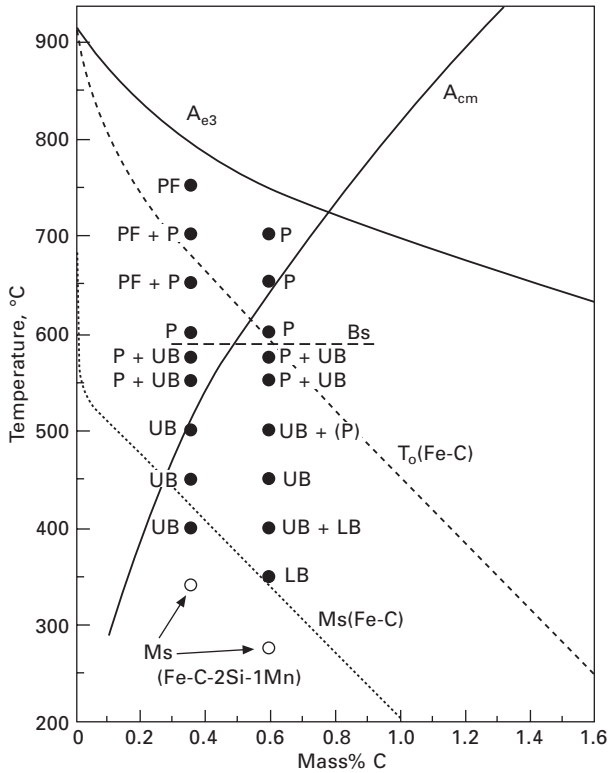
Bramfitt and Speer (1990) proposed another alternative classification based on secondary phases but without distinction between lath and plate morphologies of the ferrite, as in the following:

- Class 1 (B_1): acicular ferrite with intralath (plate) precipitation.
- Class 2 (B_2): acicular ferrite with interlath (plate) particle or film constituent.
- Class 3 (B_3): acicular ferrite with 'discrete islands' of retained austenite or secondary transformation product.



11.3 Three types of upper bainite distinguished by carbide precipitation: (a) BI-type (carbide-free), (b) BII-type (cementite precipitation along lath boundaries) and (c) BIII-type (cementite precipitation inside lath-shaped ferrite) (Ohmori *et al.*, 1971).

© Woodhead Publishing Limited, 2012



11.4 Microstructures observed in Fe-C-2Si-1Mn alloys isothermally transformed at different temperatures. PF: proeutectoid ferrite; P: pearlite; UB: upper bainite; LB: lower bainite (Tsuzaki *et al.*, 1991).

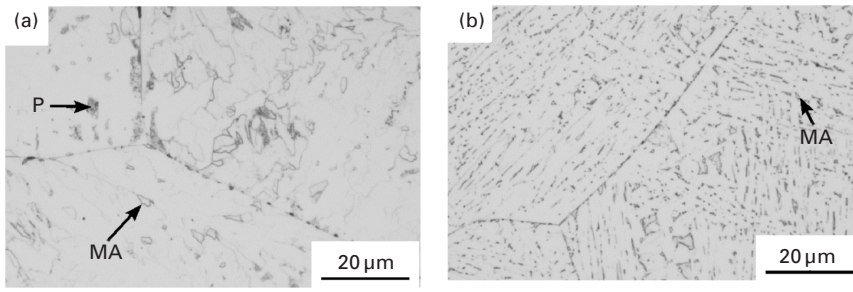
In addition to those major definitions, use of superscripts listed below was proposed to describe minor constituent phases.

- a: austenite
- c: cementite
- ε: epsilon carbide
- m: martensite
- p: pearlite.

All of the above-mentioned three definitions are for an acicular morphology of ferrite as the leading phase. However, there are more derivative and complex microstructures referred to as 'bainite'.

'Granular' bainite has been described in continuously cooled low-carbon, low-alloy steels (Habraken and Economopoulos, 1967) and high-carbon steels. Figure 11.5 shows optical microstructures of bainite formed in an ultra-low carbon steel containing Mn by continuous cooling (Takahashi *et al.*, 2007). Because of a small amount of secondary transformation product,

© Woodhead Publishing Limited, 2012



11.5 Optical microstructure of bainite with MA constituent formed in 0.05mass%C-1.5mass%Mn steels microalloyed with B during continuous cooling at (a) 0.1 K/s and (b) 5 K/s (Takahashi *et al.*, 2007).

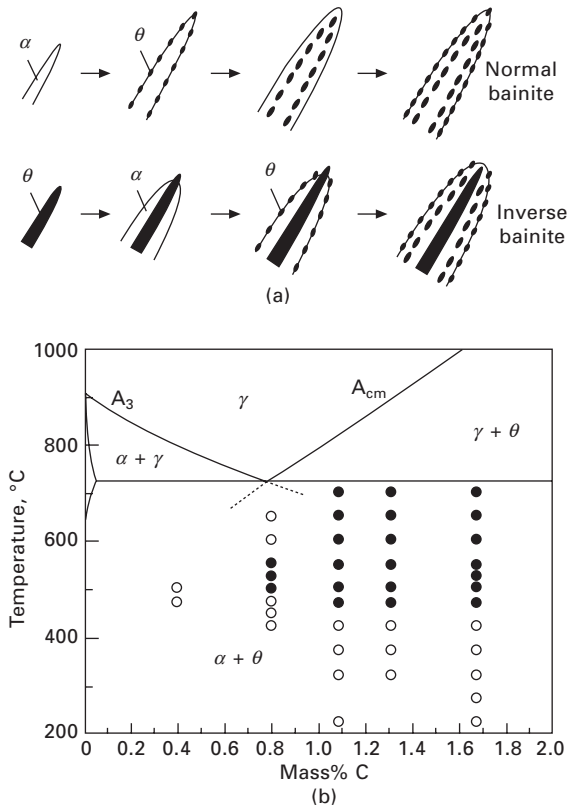
mainly MA constituent, an aggregate of lath-shaped bainitic ferrite exhibits a blocky morphology as observed by optical microscopy. Particularly in the case of a slow cooling rate, i.e., a higher transformation temperature, this microstructure contains lath-shaped ferrite with a relatively high dislocation density characteristic of bainitic ferrite as observed by transmission electron microscopy (TEM).

Intermediate transformation products in high-carbon steels can be even more complex, especially in cases of hypereutectoid compositions. Thus various nomenclatures are reviewed by several investigators (Bhadeshia, 2001: 277–284; Spanos *et al.*, 1990b; Borgenstam *et al.*, 2011).

One of the most distinctive morphologies is 'nodular bainite', originally reported by Greninger and Trioano (1940). This type of microstructure is also denoted as 'columnar bainite' or 'fan structure'. The external morphology of the 'nodule' is subdivided into several 'fans', which correspond to ferrite crystals of different crystallographic variants. It was confirmed that each fan-like ferrite region contains elongated but non-lamellar cementite (Borgenstam *et al.*, 2011). Nodular bainite was characterised also by a rough interface with respect to austenite, whereas pearlite, containing cementite lamellae and formed at higher temperatures, showed smooth interfaces.

Another distinctive morphology is 'inverse bainite'. Modin and Modin (1955) reported this kind of morphology in a hypereutectoid Fe-C alloy. A Widmanstätten cementite plate forms first, and is then surrounded by ferrite in inverse bainite, as described schematically in Fig. 11.6(a), unlike normal bainite where acicular ferrite formation is followed by cementite precipitation. Kinsman and Aaronson (1970) defined the composition-temperature conditions where inverse bainite is formed (Fig. 11.6(b)). In this figure, inverse bainite is formed at higher temperatures in the hypereutectoid composition region. As transformation proceeds, the austenite region between inverse bainite is replaced by normal bainite or nodular bainite (Kinsman and Aaronson, 1970; Borgenstam *et al.*, 2011). Figure 11.7 shows that, as carbon content

© Woodhead Publishing Limited, 2012



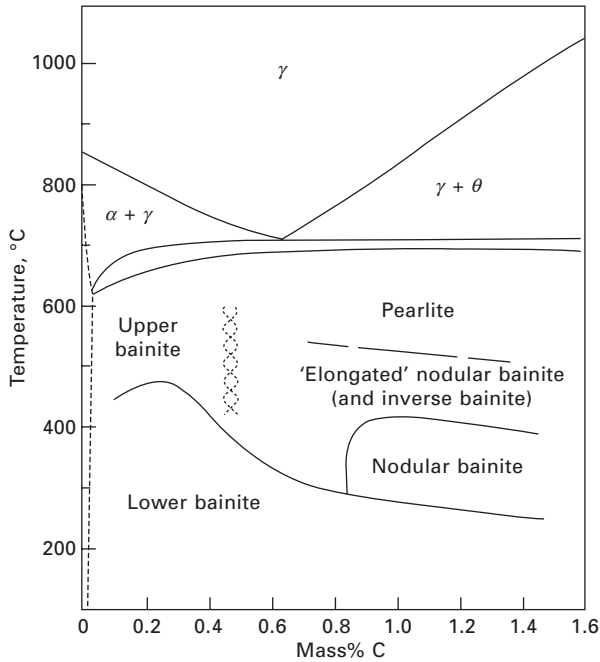
11.6 (a) Morphological difference between normal bainite and inverse bainite. (b) Formation condition of inverse bainite on a composition–temperature map of Fe-C binary system (Kinsman and Aaronson, 1970).

or transformation temperature is lowered, the bainite morphology changes to nodular bainite and lower bainite.

Aaronson and co-workers made a clear distinction between bainite and pearlite as a eutectoid transformation product based on the concept of diffusion-controlled mechanism (Lee *et al.*, 1988). According to them, both pearlite and bainite are formed by nucleation and growth of two constituent phases. In pearlite, ferrite and cementite both grow cooperatively, i.e., at the same rate. On the other hand, two phases grow independently in bainite. Cementite is overgrown by ferrite and re-nucleates at the ferrite/austenite interphase boundary.

Degenerate pearlite is a microstructure observed in hypoeutectoid Fe-C alloys (Ohmori and Honeycombe, 1971). Proeutectoid ferrite grows preferentially into the austenite matrix grain from the grain boundary below the eutectoid temperature, causing enrichment of carbon in austenite which promotes

© Woodhead Publishing Limited, 2012



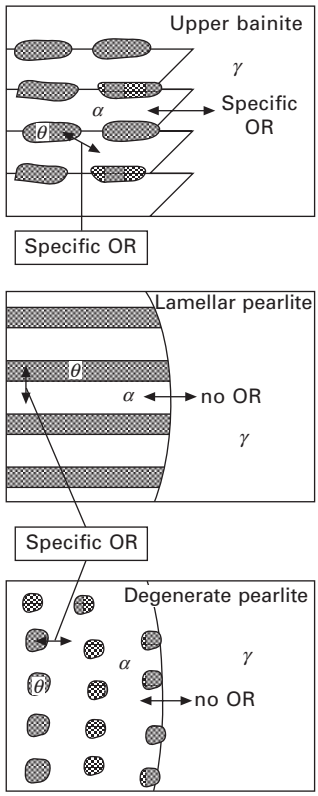
11.7 Morphology map of bainite in Fe-C-2Mn ternary alloys (Spanos *et al.,* 1990b).

cementite precipitation at the ferrite/austenite boundary. By repetition of this sequence, a fine dispersion of cementite in proeutectoid polygonal ferrite is obtained. In the definition by Lee *et al*., degenerate pearlite is categorised as 'bainite'. However, it was implied that the ferrite component of degenerate pearlite does not have a rational orientation relationship (Furuhara *et al*., 2007). As described schematically in Fig. 11.8, this characteristic is quite different from that of ordinary bainite structure and resembles that of ordinary lamellar pearlite. Such a crystallographic constraint in transformation should be one of the most important factors to characterise the bainite structure, as described in the following section.

11.2 Crystallography and related characteristics of ferrite in bainite

Initial studies on morphology and crystallography of bainitic ferrite (BF) were briefly summarised by Bhadeshia (2001: 58–59). Sandvik (1982) made the most systematic study, by means of transmission electron microscopy (TEM), on the crystallography of BF in Fe-Si-C alloys in which the austenite matrix is retained by suppression of cementite precipitation. The ferrite/

© Woodhead Publishing Limited, 2012



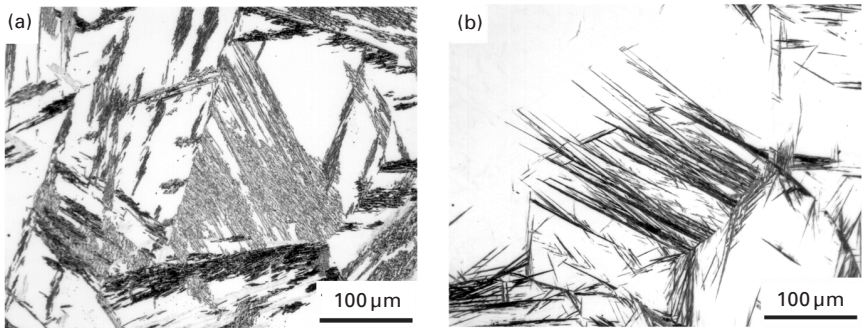
11.8 Schematic illustrations of crystallography of three types of eutectoid transformations.

austenite orientation relationship (OR) deviates slightly from the well-known Kurdjumov–Sachs (K-S) relationship, $(111)\gamma // (011)\alpha$, $[\bar{1}01]\gamma // [\bar{1}\,\bar{1}1]\alpha$, and is closer to the Nishiyama–Wasserman (N-W) relationship, $(111)\gamma // (011)\alpha$, $[110]\gamma // [\bar{1}00]\alpha$. The average OR was expressed as $(111)\gamma // (011)\alpha$, $[\bar{1}01\gamma \sim 4 \pm 1°$ from $[\bar{1}\,\bar{1}1]\alpha$.

Figure 11.9 shows optical micrographs of BF formed at different temperatures in an Fe-0.6C-2Si-1Mn (mass%) alloy (Moritani, 2003). As reported by Tsuzaki *et al*. (1991), aggregates of lath-shaped BF, defined as upper bainite, are formed at 723 K (Fig. 11.9(a)) whereas thin plate-type BF, denoted as lower bainite, is observed at 623 K (Fig. 11.9(b)).

Figures 11.10(a)–(c) show TEM micrographs of the BF formed at 723 K in this Fe-0.6C-2Si-1Mn alloy observed from three different orientations (Moritani, 2003). In (a), the cross section of BF roughly exhibits the shape of a parallelogram. On the other hand, those in (b) and (c) are largely elongated. From these micrographs, the lath morphology of BF was confirmed. Figure

© Woodhead Publishing Limited, 2012

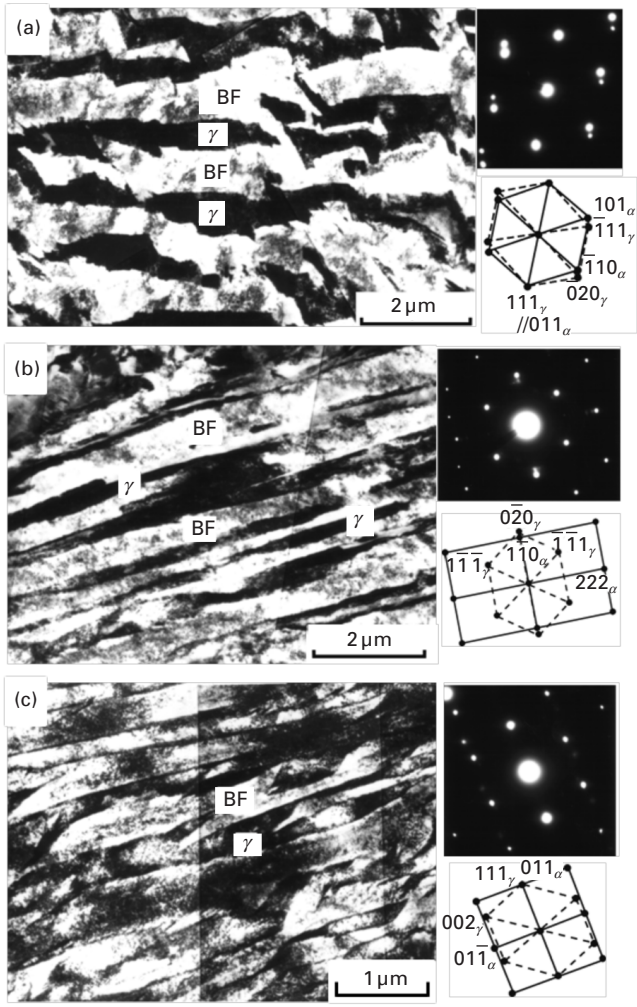


11.9 Optical micrographs of BF in an Fe-0.6C-2Si-1Mn (mass%) alloy transformed at (a) 723 K and (b) 623 K (Moritani, 2003).

11.11 illustrates the 3D morphology of BF schematically. BF is lath-shaped and its ORs with respect to the parent austenite are similar to those reported by Sandvik (1982). It is noted that there are small deviations between close-packed planes. The macroscopic habit plane of the broad face deviates slightly from the parallel close-packed planes ($(111)\gamma//(011)\alpha$). Each BF lath seems to be elongated preferentially along the near-parallel close-packed directions ($[\bar{1}01]\gamma// [\bar{1}\,\bar{1}1]\alpha$) which lie on the plane of Fig. 11.10(b). It has been reported that the macroscopic BF lath is composed of many subunits (Oblak and Hehemann, 1967; Bhadeshia and Edmonds, 1980) which can be particularly recognised as extremely fine ferrite crystals in Fig. 11.10(a). The macroscopic habit plane reported as nearly $(111)\gamma$ is achieved by coalescence of needle-like subunits (Ohmori *et al.*, 1996). The size of BF was decreased with decreasing transformation temperature which was attributed to the higher driving force promoting more nucleation of BF and an increase in difficulty of plastic accommodation in austenite with increasing strength (Singh and Bhadeshia, 1998).

Figure 11.10 also indicates clearly that the orientations (variants) of neighbouring BF crystals are almost identical. Such a grouping of variants leads to development of characteristic substructures of the bainite structure. Figure 11.12 shows the substructure of upper bainite schematically (Furuhara *et al.*, 2006). A prior austenite grain is divided into packets each of which consists of a group of laths with the same parallel close-packed plane relationship as the Kurdjumov–Sachs (K-S) orientation relationship. In general, a bainite packet is partitioned into several blocks each of which contains laths of a single variant of the K-S relationship. This kind of hierarchy in the substructure is quite similar to those of lath martensite (Morito *et al.*, 2003b). Blocks and packets are refined with an increase in carbon content. More interestingly, preferential formation of specific variant pairs which are misoriented by a relatively low angle (*ca.* 10 degrees) in a packet was revealed for low carbon alloys. Such a tendency was observed in upper

© Woodhead Publishing Limited, 2012

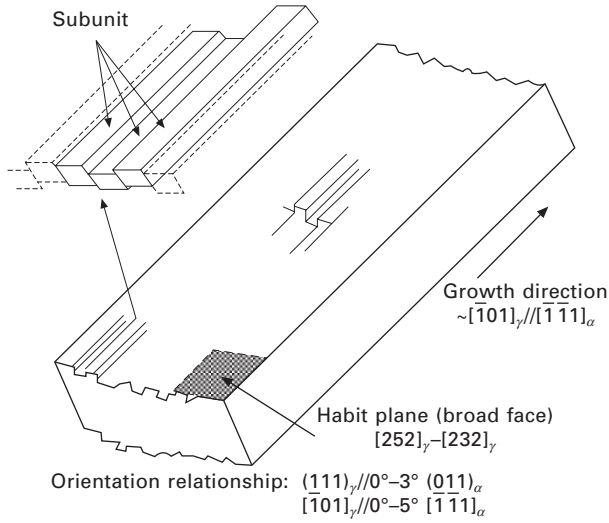


11.10 TEM micrographs of BF formed at 723 K in an Fe-2Si-1Mn-0.6C alloy: (a) beam direction ~ $[\bar{1}01]\gamma//[\bar{1}\,\bar{1}1]\alpha$, (b) beam direction ~ $[101]\gamma//[112]\alpha$, (c) beam direction ~ $[110]\gamma//[\bar{1}00]\alpha$ (Moritani, 2003).

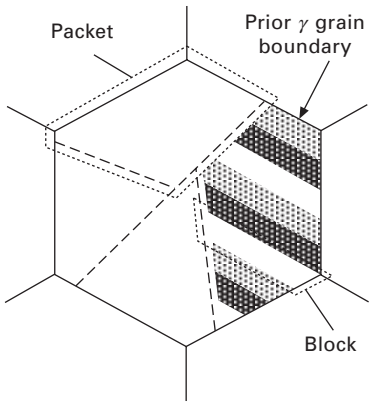
bainite structures of Fe-Ni-C alloys in the cases of higher transformation temperature or higher carbon content (Furuhara *et al.*, 2006).

Figure 11.13 shows a TEM micrograph of BF formed at 623 K in the Fe-0.6C-2Si-1Mn alloy (Moritani, 2003). The macroscopic shape of BF is plate-like seen in Fig. 11.9(b) classified into lower banite in Ohmori *et al.*'s definition. It is clear that each plate is again composed of a number of fine subunits as previously reported (Oblak and Hehemann, 1967). There is no systematic investigation on the orientation relationship between BF and

© Woodhead Publishing Limited, 2012



11.11 Schematic illustration of BF crystallography at 723 K (Moritani, 2003).



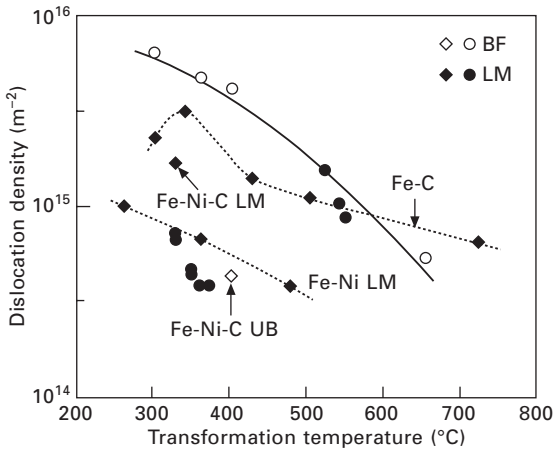
11.12 Schematic illustration of substructure of upper bainite (Furuhara *et al.*, 2006).

austenite for lower bainite. Srinivasan and Wayman (1968) reported that the close-packed planes are about 0.5 of a degree apart and a deviation between the close-packed directions is about 4° for the lower bainite transformation of an Fe-Cr-C alloy. There are some remarks reporting the existence of the near N-W OR (Bhadeshia, 1980), and the near K-S OR (Oka *et al.*, 1989), implying that some small deviations could exist from those ORs. According to Srinivasan and Wayman (1968), the habit plane of lower bainite plates was reported to be (254)γ which is different from the habit plane of upper

© Woodhead Publishing Limited, 2012



11.13 Bright field TEM micrograph of lower bainite formed at 623 K in the Fe-0.6C-2Si-1Mn alloy (Moritani, 2003).



11.14 Dislocation densities in bainitic ferrite (BF) and lath martensite (LM). UB represents upper bainite (Moritani, 2003; Takahashi and Bhadeshia, 1990, Morito *et al.*, 2003).

bainite. The complex arrangement of subunits, as seen in Figs 11.10 and 11.13, contributes to such a difference in the macroscopic habit plane between upper and lower bainite.

BF in both the upper and lower bainite structure contains a high density of dislocations. Figure 11.14 summarises the data measured by TEM for lath martensite and bainitic ferrite (Moritani, 2003; Takahashi and Bhadeshia, 1990, Morito *et al.*, 2003a). As temperature is lowered, the dislocation density becomes higher. However, depending upon alloy composition and heat treatment, the measured data are scattered with a maximum of one order of magnitude. In martensite, by increasing carbon content or decreasing M_s temperature, transformation twins are introduced. Bainitic ferrite does

© Woodhead Publishing Limited, 2012

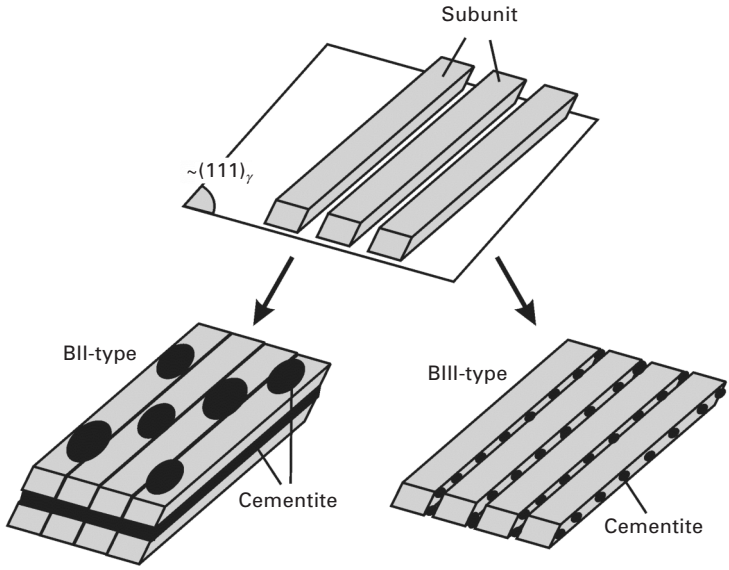
not usually contain such twins either in upper or lower bainite. However, Okamoto and Oka reported a unique morphology of lower bainite in which thin plate martensite formed isothermally above the M_s temperature is sandwiched as 'midrib' by ordinary lower bainite containing carbides in high C hypereutectoid Fe-C alloys (Okamoto and Oka, 1986). This morphology resembles lenticular martensite observed typically in Fe-Ni-C alloys with M_s temperature much lower than room temperature. In the formation process of lenticular martensite, the midrib is first formed and subsequently the thickening of the outer region occurs athermally during cooling (Kakeshita *et al.*, 1980). In this unique morphology, a similar mechanism might be operative. In fact, it was deduced that the midrib region coresponds to thin plate martensite isothermally formed for the lower bainite case (Okamoto and Oka, 1986).

11.3 Characteristics of carbide precipitation in bainite structure

Precipitation of carbide is the other important feature of bainite structure in most cases. As described in Section 11.1, dispersion of carbide in bainite is important in terms of its definition, its identification and also for the mechanical properties of bainitic steels. It has long been known, as previoiusly mentioned, that finer dispersions of carbide, in most cases cementite, lead to a better strength–toughness balance in low-carbon low-alloy bainitic and martensitic steels (Pickering, 1967; Bowen *et al.*, 1986; Ohtani *et al.*, 1990). In ordinary upper bainite (Hehemann, 1970) or BII-type upper bainite (Ohmori *et al.*, 1971), or B_2-type bainite (Bramfitt and Speer, 1990), interlath cementite precipitates clearly at the austenite/BF interphase boundary. In order to accomplish such cementite precipitation, carbon should be enriched in austenite by rejection from BF up to the extrapolated A_{cm} line, i.e., the $\gamma/(\gamma+\theta)$ phase boundary (see Fig. 11.4) below the eutectoid temperature. Figure 11.15 shows schematic illustrations of the development of two kinds of the upper bainite structure proposed by Ohmori *et al.* (1996). First, neighbouring BF subunits are formed by development from an austenite grain boundary. Enrichment of carbon in the untransformed austenite between subunits results in cementite precipitation at the austenite/BF boundaries. At high temperature, cementite is formed along the macroscopic habit plane near $(111)\gamma$ after coalescence of the subunits (BII-type). As transformation temperature is lowered, cementite can nucleate at the side facets of BF before their coalescence, leading to the intralath cementite dispersion of the BIII-type structure.

Shackleton and Kelly (1965) made a systematic study of the crystallography of cementite precipitation in both upper and lower bainite. Cementite mostly holds the Bagaryatski orientation relationships, $(11\bar{2})\alpha//(001)\theta$, $[\bar{1}10]\alpha//[100]\theta$, $[111]\alpha//[010]\theta$, typically observed in tempered martensite, whereas

© Woodhead Publishing Limited, 2012



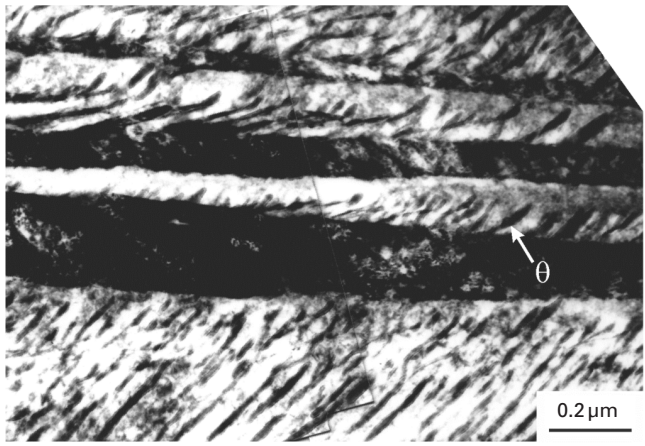
11.15 Schematic illustrations of carbide precipitation in association with BF subunit formation in upper bainite (Ohmori *et al.,* 1996).

the orientation relationship for upper bainite was interpreted as precipitation of cementite with constraint from austenite. Subsequently, a three-phase orienation relationship was considered in the upper bainite structure of an Fe-Ni-C alloy (Ohmori *et al.*, 1996) where cementite clearly nucleates at the austenite/BF boundary: $(111)\gamma//(011)\alpha//(\bar{1}03)\theta$, $[\bar{1}01]\gamma//[\bar{1}\bar{1}1]\alpha//[010]\theta$.

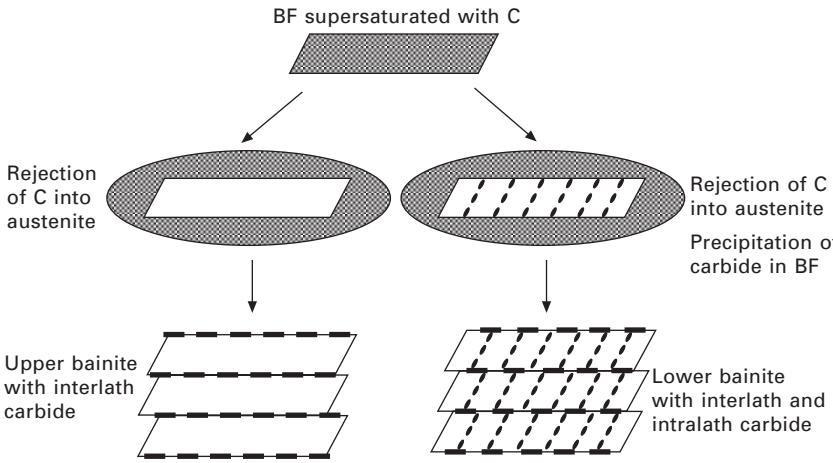
Curiously, cementite precipitates contained in a single BF crystal in lower bainite also exhibited a similar morphology by holding the same unique three-phase orientation relationship with respect to both austenite and BF (Srinivasan and Wayman, 1968).

Figure 11.16 shows the microstructure observed by TEM of lower bainite formed in Fe-9Ni-0.8C (mass%) alloy (Sawada *et al.*, 1994). Cementite precipitates are seen inside BF plates. The habit plane of cementite is inclined to that of BF by large angles as reported previously (Shimizu *et al.*, 1964). The carbide phase is usually cementite but in some cases, where the alloy contains Si, an element which effectively suppresses cementite precipitation, ε-carbide was observed in the lower bainite structure (Matas and Hehemann, 1961). The presence of such a transition carbide has been considered as evidence in support of a large supersaturation of carbon (Bhadeshia, 2001: 68–71), since it was observed in an alloy containing carbon of more than 0.25 mass% in tempered martensite (Roberts *et al.*, 1957). Similarity in the cementite/ferrite orientation reationship in lower bainite to that in the tempered martensite case also led to the same deduction, and proposal of a diffusionless/

© Woodhead Publishing Limited, 2012



11.16 TEM micrograph showing lower bainite in Fe-9Ni-0.8C transformed at 473 K for 32 h (Sawada *et al.*, 1994).



11.17 Schematic illustrations describing the formation mechanism of upper and lower bainite based on a diffusionless/displacive transformation concept (Takahashi and Bhadeshia, 1990).

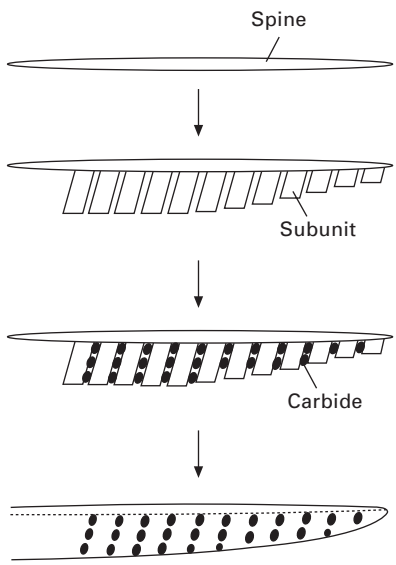
displacive transformation mechanism (Takahashi and Bhadeshia, 1990) as summarised schematically in Fig. 11.17. First, BF fully supersaturated with carbon forms as in the martensite transformation. Carbon starts to escape from BF into the surrounding untransformed austenite matrix. At higher transformation temperature, carbon diffusion in ferrite and austenite is fast enough to decrease the carbon level in BF sufficiently to prevent carbide precipitation inside BF. As a result, carbide precipitates preferentially at the austenite/BF boundary, forming the conventional upper bainite structure

© Woodhead Publishing Limited, 2012

with interlath carbide. As transformation temperature is lowered, diffusion becomes more difficult so that carbide starts to precipitate inside BF as well as at the interphase boundary. In such a case, the lower bainite structure with intralath carbide is developed.

However, there is some difficulty in explaining why the orientation of cementite (variant) is restricted to be unique in BF for lower bainite, unlike multivariant cementite precipitation in tempered martensite. Such a characteristic alignment of cementite was often explained in terms of internal defects introduced by lattice invariant deformation, which is analogous to martensite (Srinivasan and Wayman, 1968; Shimizu *et al.*, 1964). For example, Srinivasan and Wayman (1968) reported that the habit plane of cementite is $(112)\alpha$ which corresponds to $(101)\gamma$ in the Bain system. They noted that this plane coincides with the probable lattice invariant shear plane and thus presumably affects the variant selection of cementite. This does not explain the presence of multivariant cementite in martensite. On the other hand, Ohmori (1971) proposed that cementite particles nucleate at steps on the austenite/BF boundary introduced by the lattice invariant deformation.

Spanos *et al*. studied the morphology of lower bainite in Fe-2Mn-C alloys in detail and proposed an alternative sequence for lower bainite formation described in Fig. 11.18 (Spanos *et al*., 1990a). First, a thin ferrite plate called a 'spine' is formed and, subsequently, sympathetic nucleation, which is nucleation occuring at the pre-existing matrix/product interphase boundary, of secondary ferrite subunits takes place at one side of the ferrite spine. In



11.18 Schematic illustrations of carbide precipitation in association with subunit formation in lower bainite (Spanos *et al.,* 1990a).

© Woodhead Publishing Limited, 2012

the austenite between these subunits, cementite precipitates due to enrichment of carbon. Then the remaining gap is filled by ferrite growth and cementite precipitaion during further holding. Since secondary subunits are inclined to the ferrite spine by a large angle, cementite precipitates aligned in the same manner are achieved naturally by this sequence. Spanos (1994) confirmed later that there are fine dispersions of retained austenite between subunits in lower bainite in an alloy with Si additions which suppress cementite precipitation. Figure 11.13 shows direct evidence of the aggregation of BF subunits in the lower bainite plate. Without Si, retained austenite might be diminished by fast cementite precipitation and simultaneous ferrite growth. Further investigation is needed for clarification of formation mechanism, in particular of lower bainite.

11.4 Future trends

Carbide-containing bainite structures remain important in practical high-strength steels. Increasing attention has been paid to complex transformation structures containing ferrite, martensite, bainite and retained austenite, particularly recently for automotive applications (Sugimoto, 2009). One of the most important factors is carbon content of retained austenite, which is significantly affected by formation kinetics of both BF and carbide, and which is often non-uniform during intermediate stages of bainite transformation. Despite such uncertainty, advanced and sophisticated processing has been applied for better mechanical properties. Careful control of phase constituents in fraction (Suzuki *et al*., 2011) and stability of retained austenite to stress-induced martensite transformation (Matsuda *et al*., 2010) become more important for further improvement of ductility at higher strength levels. Thus, systematic investigations should be continued for the improvement of advanced high-strength steels by controlling transformation kinetics and microstructure through careful alloying in cooperation with appropriate thermomechanical processing.

11.5 References

Bhadeshia H K D H (1980), 'The lower bainite transformation and the significance of carbide precipitation', *Acta Metallurgica*, 28, 1103–1114.

Bhadeshia H K D H (2001), *Bainite in Steels*, 2nd edn, London, IOM Communications.

Bhadeshia H K D H and Edmonds D V (1980), 'The mechanism of bainite formation in steels', *Acta Metallurgica*, 28, 1265–1273.

Borgenstam A, Hedstrom P, Hillert M, Kolmskog P, Stormvinter A, Ågren J (2011), 'On the symmetry among the diffusional transformation products of austenite', *Metallurgical and Materials Transactions A*, 42A, 1558–1574.

Bowen P, Druce S G, Knott J F (1986), 'Effects of microstructure on cleavage fracture in pressure-vessel steel', *Acta Metallurgica*, 34, 1121–1131.

© Woodhead Publishing Limited, 2012

Bramfitt B L, Speer J G (1990), 'A perspective on the morphology of bainite', *Metallurgical Transactions A*, 21A, 817–829.

Davenport E S, Bain E C (1939), 'Transformation of austenite at constant subcritical temperatures', *Transactions AIME*, 90, 117–144.

Furuhara T, Kawata H, Morito S, Maki T (2006), 'Crystallography of upper bainite in Fe-Ni-C alloys', *Materials Science and Engineering A*, 431, 228–236.

Furuhara T, Moritani T, Sakamoto K, Maki T (2007), 'Substructure and crystallography of degenerate pearlite in an Fe-C binary alloy', *Materials Science Forum*, 539–543, 4832–4837.

Greninger A B, Troiano A R (1940), 'Crystallography of austenite decomposition', *Transactions AIME*, 140, 307–331.

Habraken L J, Economopoulos M (1967), 'Bainitic microstructures in low-carbon alloy steels and their mechanical properties' in *Transformation and Hardenability in Steels*, Ann Arbor, MI, Climax Molybdenum, 69–108.

Hehemann R F (1970), 'The bainite transformation', in *Phase Transformations*, Metals Park, OH, ASM, 397–432.

Kakeshita T, Shimizu K, Maki T, Tamura I (1980), 'Growth behavior of lenticular and thin plate martensite', *Scripta Metallurgica*, 14, 1067–1070.

Kinsman K R, Aaronson H I (1970), 'Inverse bainite reaction in hypereutectoid Fe-C alloys', *Metallurgical Transactions*, 1, 1485–1488.

Lee H J, Spanos G, Shiflet G J, Aaronson H I (1988), 'Mechanisms of the bainite (non-lamellar eutectoid) reaction and a fundamental distinction between the bainite and pearlite (lamellar eutectoid) reactions', *Acta Metallurgica*, 36, 1129–1140.

Matas S J, Hehemann R F (1961), 'The structure of bainite in hypoeutectoid steels', *Transactions AIME*, 221, 179–185.

Matsuda H, Noro H, Nagataki Y, Hosoya Y (2010), 'Effect of retained austenite stability on mechanical properties of 590 MPa grade TRIP sheet steels', *Materials Science Forum*, 638–642, 3374–3379.

Mehl R F (1939), 'The physics of hardenability – The mechanism and the rate of the decomposition of austenite', in *Hardenability of Alloy Steels*, Cleveland, OH, ASM, 1–65.

Modin H, Modin S (1955), 'Pearlite and bainite structures in a eutectoid carbon steel: an electron microscopic investigation', *Jernkont. Ann.*, 139, 481–515.

Moritani T (2003), PhD thesis, Kyoto University.

Morito S, Nishikawa J, Maki T (2003a), 'Dislocation density within lath martensite in Fe-C and Fe-Ni alloys', *ISIJ International*, 43, 1475–1477.

Morito S, Tanaka H, Konishi R, Furuhara T, Maki T (2003b), 'The morphology and crystallography of lath martensite in Fe-C alloys', *Acta Materialia*, 51, 1789–1799.

Oblak J M and Hehemann R F (1967), 'Structure and growth of Widmanstätten ferrite and bainite', in *Transformation and Hardenability in Steels*, Ann Arbor, MI, Climax Molybdenum, 15–38.

Ohmori Y (1971), 'Crystallography of lower bainite transformation in a plain carbon steel', *Transactions ISIJ*, 11, 95–101.

Ohmori Y, Honeycombe R K W (1971), 'The isothermal transformation of plain carbon austenite', in *Proceedings of International Conference on the Science and Technology of Iron and Steel*, Tokyo, The Iron and Steel Institute of Japan, Supplement of *Transactions ISIJ*, 11, 1160–1165.

Ohmori Y, Ohtani H, Kunitake T (1971), 'Bainite in low carbon low alloy high strength steels', *Transactions ISIJ*, 11, 250–259.

© Woodhead Publishing Limited, 2012

Ohmori Y, Jung Y-C, Ueno H, Nakai K, Ohtsubo H (1996), 'Crystallographic analysis of upper bainite in Fe-9%Ni-C alloys', *Materials Transactions, JIM*, 37, 1665–1671.
Ohtani H, Okaguchi S, Fujishiro Y, Ohmori Y (1990), 'Morphology and properties of low-carbon bainite', *Metallurgical Transactions A*, 21A, 877–888.
Oka M, Okamoto H, Ishida K (1989), 'Transformation of lower bainite in hypereutectoid steels', *Metallurgical Transactions A*, 21A, 845–851.
Okamoto H, Oka M (1986), 'Lower bainite with midrib in hypereutectoid steels', *Metallurgical Transactions A*, 17A, 1113–1120.
Pickering F B (1967), 'The structure and properties of bainite in steels', in *Transformation and Hardenability in Steels*, Ann Arbor, MI, Climax Molybdenum, 109–132.
Roberts C S, Averbach B L, Cohen M (1957), 'The mechanism and kinetics of the 1st stage of tempering', *Transactions ASM*, 45, 576–604.
Sandvik B P J (1982), 'The bainite reaction in Fe-Si-C alloys: the primary stage', *Metallurgical Transactions A*, 13A, 777–787.
Sawada M, Tsuzaki K, Maki T (1994), Unpublished research, Kyoto University.
Shackleton D N and Kelly P M (1965), 'Morphology of bainite', in *Physical Properties of Martensite and Bainite*, Special Report 93, The Iron and Steel Institute, London, 126–134.
Shimizu K, Ko T, Nishiyama Z (1964), 'Transmission electron microscope observation of the bainite of carbon steel', *Transactions JIM*, 5, 225–230.
Singh S B, Bhadeshia H K D H (1998), 'Estimation of bainite plate-thickness in low-alloy steels', *Materials Science and Engineering A*, 245A, 72–79.
Spanos G (1994), 'The fine-structure and formation mechanism of lower bainite', *Metallurgical Transactions A*, 25A, 1967–1980.
Spanos G, Fang H S, Aaronson H I (1990a), 'A mechanism for the formation of lower bainite', *Metallurgical Transactions A*, 21A, 1381–1390.
Spanos G, Fang H S, Sarma D S, Aaronson H I (1990b), 'Influence of carbon concentration and reaction temperature upon bainite morphology in Fe-C-2 Pct Mn alloys', *Metallurgical Transactions A*, 21A, 1391–1411.
Srinivasan G R, Wayman C M (1968), 'The crystallography of the bainite transformation – I', *Acta Metallurgica*, 16, 621–636.
Sugimoto K-I (2009), 'Fracture strength and toughness of ultra high strength TRIP aided steels', *Materials Science and Technology*, 25, 1108–1117.
Suzuki K, Ono Y, Miyamoto G, Furuhara T (2011), 'Microstructure and mechanical properties of austempered medium carbon steels', *Tetsu-to-Hagané*, 97, 26–33.
Takahashi M, Bhadeshia H K D H (1990), 'Model for transition from upper to lower bainite', *Materials Science and Technology*, 6, 592–603.
Takahashi K, Miyamoto G, Furuhara T (2007), Unpublished research, Tohoku University.
Tsuzaki K, Nakao C, Maki T (1991), 'Formation temperature of bainitic ferrite in Si-containing steels', *Materials Transactions, JIM*, 32, 658–666.

© Woodhead Publishing Limited, 2012

12
Carbide-free bainite in steels

F. G. CABALLERO, National Center for Metallurgical Research (CENIM-CSIC), Spain

Abstract: The present chapter focuses upon bainite in steels where the bainitic microstructure is devoid of carbides. The precipitation of cementite during bainitic transformation can be suppressed by alloying the steel with silicon. The carbon that is rejected from the bainitic ferrite enriches the residual austenite, thereby stabilising it down to ambient temperature. The microstructure obtained consists of bainitic ferrite laths interwoven with thin films of untransformed retained austenite. The suppression of carbide precipitation has allowed more direct experimental examination of the carbon distribution during the bainite reaction and any plastic relaxation accompanying the transformation.

Key words: carbide-free bainite, high silicon steels, carbon partitioning, plastic accommodation.

12.1 Introduction

Although there has been much interest and progress in recent decades, bainite transformation remains the least understood of all the decomposition reactions of the high temperature austenitic phase in steels. This is because of the complexities of its formation mechanism and kinetics, and the apparent diversity in its microstructural appearance, which created earlier disagreements even in identifying its correct definition (Aaronson, 1968: 270; Hehemann *et al.*, 1972). However, the well-known difference in carbide distribution between bainite formed at high and low temperatures, namely interlath and intralath, respectively, appears to exist in a majority of steels and makes the classical nomenclature of upper and lower bainite useful, both in describing the microstructural appearance and in classifying the overall reaction mechanism. In upper bainite, the carbides precipitate from the carbon-enriched residual austenite between the developing laths. Upper bainitic ferrite itself is thus generally free from intralath precipitates. The precipitation of carbides in upper bainite is a secondary process, not essential to the mechanism of formation of bainitic ferrite except where any precipitation from austenite will deplete its carbon content, thereby promoting further transformation. In contrast, there are many observations that reveal that lower bainitic cementite nucleates and grows within supersaturated bainitic ferrite in a process identical to the tempering of martensite (Bhadeshia, 1980). The slower diffusion associated

© Woodhead Publishing Limited, 2012

with the reduced transformation temperature provides an opportunity for some of the carbon to precipitate in the supersaturated bainitic ferrite. A fine dispersion of plate-like carbides is then found inside the bainitic ferrite, which also has a plate morphology, with a single crystallographic variant within a given bainitic ferrite plate, although it is possible to observe more than one variant of carbide precipitation in a lower bainite sub-unit (Bhadeshia, 1980; Chang, 2004).

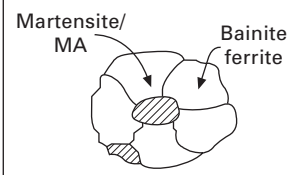
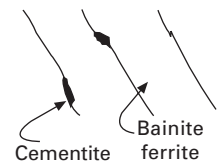
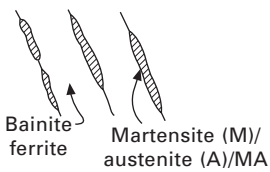
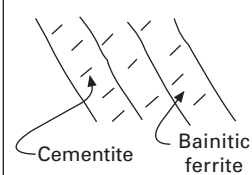
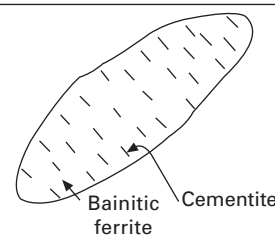
In the literature other categorisation schemes for the description of bainite have been proposed (Ohmori *et al*., 1971; Bramfitt and Speer, 1990; Ohtani *et al*., 1990; Krauss and Thomson, 1995; Zajac *et al*., 2005). These additional classifications can be useful in describing the form of the microstructure, especially in commercial steels using light optical microscopy, but the mechanisms of all the bainitic transformations are the same among all the morphologies. Ohmori and co-workers (Ohmori *et al*., 1971; Ohtani *et al*., 1990) claimed that, from the view of a crystallographic definition of bainite, the classification of bainite should be upon bainitic ferrite morphology but not cementite dispersion i.e. the shape of bainitic ferrite is lath-like or plate-like. They proposed a broader classification of bainitic-type microstructures for low carbon and alloy carbon steels, where cementite is not associated with intermediate-temperature austenite transformation. Following Ohmori's description, the bainitic ferrite of upper bainite in low-carbon steels will always have a lath-like morphology, but the bainite may be carbide-free (Type I), with austenite retained between laths, or have cementite particles in layers between the bainitic ferrite laths (Type II), or have fine platelets lying parallel to a specific bainitic ferrite plane in the austenite grain interior (Type III). As martensite, bainite would change its morphology from lath-like to plate-like with increasing carbon content.

Bramfitt and Speer (1990) proposed a new classification system encompassing both isothermally transformed and continuously cooled bainitic microstructures. Bainite morphologies are classified as B1, B2, or B3, depending on whether the lath of bainitic ferrite is associated with (i) intralath precipitates, (ii) interlath particles/films, or (iii) discrete regions of retained austenite and/or secondary transformation product (e.g., martensite or pearlite), respectively. Krauss and Thompson (1995) qualified the Bramfitt and Speer (1990) bainite classification system as the most compressive proposal to date for bainite morphologies, but they also showed that this system does not describe all of the ferritic microstructures observed in continuously cooled low-carbon steels. For instance, granular bainite, consisting of dispersed retained austenite or martensite/austenite (M/A) constituent with a granular or equiaxed morphology in a featureless matrix which may retain the prior austenite grain boundary structure, is incorporated into the Bramfitt–Speer classification system by including a category of bainite consisting of lath-like bainitic ferrite with discrete-island constituent (B3). However, it is difficult

© Woodhead Publishing Limited, 2012

to see how secondary phases can assume equiaxed morphologies in a matrix of lath-like bainitic ferrite.

More recently, Zajac *et al*. (2005) provided a unified terminology, which may be applied for both low carbon and high carbon bainite. In this new classification (Fig 12.1), bainite is divided into three main groups depending on bainitic ferrite morphology and the type and distribution of second phases:

Bainite	Morphology	Bainite description
Granular bainite	Irregular ferrite with M/A	
Lath-like upper bainite	Lath-like ferrite with cementite on lath boundaries	
Cementite-free lath-like bainite	Lath-like ferrite with M/A on lath boundaries	
Lath-like lower bainite	Lath-like ferrite with cementite inside the ferrite laths	
Plate-like lower bainite	Plate-like ferrite with cementite inside the ferrite plates	

12.1 Morphological classification used in this chapter based on Zajac *et al.*'s categorisation scheme (Zajac *et al.*, 2005) and microstructural observations, including optical microscopy and scanning electron microscopy.

© Woodhead Publishing Limited, 2012

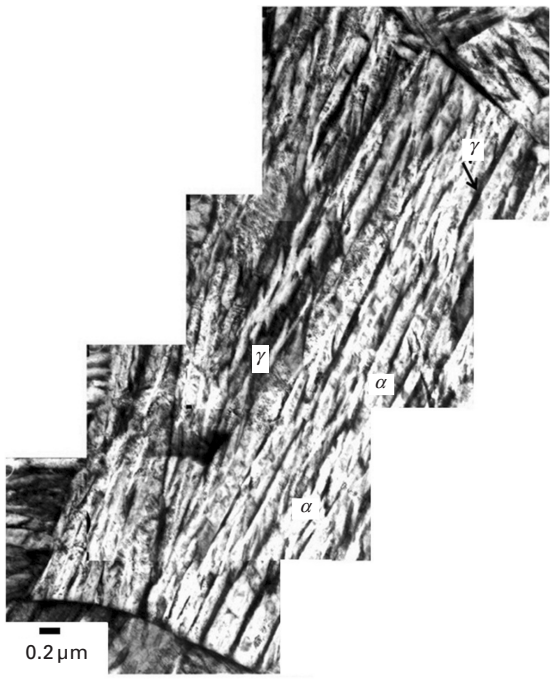
- granular bainite with irregular bainitic ferrite;
- upper bainite with lath-like bainitic ferrite and the second phases on lath boundaries; and
- lower bainite, lath-like or plate-like, with cementite within the bainitic ferrite laths or plates.

The microstructure of low carbon high strength steels, composed of bainitic ferrite with M/A constituent is called cementite-free bainite in the Ohmori *et al*. (1971) classification. The upper bainite which does not contain carbides but the M/A constituent is called degenerate upper bainite by Zajac *et al*. (2005). Lower bainite having cementite forming within the ferrite crystals is divided into two groups which have either lath morphology, typical for low carbon steels, or plate morphology which is typical for lower bainite in steels with higher carbon levels.

It is important to remark that granular bainite microstructure under the optical and scanning electron microscopes is observed as coarse granular-shaped bainitic ferrite plates with islands of retained austenite and martensite. However, coarse granular-shaped ferrite plates do not really exist. In fact, they are sheaves of bainitic ferrite with very thin regions of austenite between the sub-units because of the low carbon concentration of the steels involved (Josefsson and Andren, 1989). The definition of granular bainite given by Zajac *et al*. (2005) is based on microstructural observations, including optical microscopy and scanning electron microscopy, which are not of sufficient resolution to reveal the fine structure within the granular bainite. The granular bainite is, however, similar to the cementite-free bainite at the micro-scale.

Zajac *et al*.'s morphological classification (Zajac *et al*., 2005) is used in the present chapter, although this chapter deals specifically with a microstructural form, generally accepted also as bainite, but which can be totally free of carbide. The precipitation of cementite during bainitic transformation can be suppressed in low carbon steel using controlled rolling followed by multi-stage cooling processes (Ohtani *et al*., 1990) and alloying the steel with silicon (>1%), a well-known carbide inhibitor in steels (Petty, 1970). The carbon that is rejected from the bainitic ferrite enriches the residual austenite, thereby stabilising it (partially or totally) down to ambient temperature. A microstructure of a carbide-free bainite is presented in Fig. 12.2; instead of the classical structure of bainitic ferrite laths with interlath carbide, it consists of bainitic ferrite laths interwoven with thin films of untransformed retained austenite. This does not contravene the classical understanding and description of the primary austenite decomposition reaction, which is to a bainitic ferrite structure; it simply expands this to allow for suppression of the secondary carbide precipitation reaction which otherwise removes carbon from solution. By remaining in solution, the carbon stabilises the untransformed

© Woodhead Publishing Limited, 2012



12.2 Transmission electron micrograph of carbide-free bainitic microstructure formed by air cooling after forging in Fe-0.30C-1.50Si-3.50Ni-1.44Cr-0.25Mo wt% steel. α is bainitic ferrite and γ is austenite.

austenite to give the microstructure of Fig. 12.2. Importantly, this has allowed more direct experimental examination of the essential process of the bainite transformation, which is the decomposition of parent austenite to bainitic ferrite, uncluttered by the interjection of carbide precipitation reactions. In consequence, some commentary on some of the more important observations is made below. However, of equal importance is that a multiphase bainitic ferrite-austenite microstructure such as shown in Fig. 12.2 has led to some interesting and novel developments in steel design and application.

High silicon bainitic steels originally emerged as laboratory alloys useful in experiments designed to study the decomposition of austenite to bainitic ferrite without the added complication of secondary reactions to precipitate carbides, but subsequently have proved interesting subjects for developing multiphase microstructures which can enhance performance in certain applications (Bhadeshia and Edmonds, 1983a, 1983b; Miihkinen and Edmonds, 1987a, 1987b, 1987c; Caballero *et al.*, 2001a, 2001b, 2006, 2009a; Caballero and Bhadeshia, 2004). The importance of a silicon addition in this respect is that it inhibits the formation of cementite, which is still a critical event in the progress of the bainite reaction since it removes carbon

© Woodhead Publishing Limited, 2012

from the austenite or bainitic ferrite. Thus, despite being classified as a ferrite forming element, the presence of silicon during the bainite reaction can contribute to incomplete transformation. This is not just due to the suppression of bainitic carbides because carbon partitioning to untransformed austenite will eventually stabilise it against further decomposition. Further, addition of Mn to impart sufficient hardenability for heat treatment in the bainitic temperature range also helps to stabilise untransformed austenite at room temperature. The presence of this metastable austenite subsequently led also to enhanced mechanical behaviour on which to base commercial steel compositions, e.g. transformation induced plasticity (TRIP) steels.

Since bainite forms in the temperature range dividing the reconstructive ferrite/pearlite reactions and the displacive martensitic reaction, there was a natural desire to relate bainite to one or other of these phases which led to much debate concerning the mechanism of its formation (Oblak and Hehemann, 1967; Hehemann *et al.*, 1972; Huang and Thomas, 1977; Christian and Edmonds, 1984; Christian, 1994). One school of thought considered that the ferritic component of bainite develops over the whole bainitic temperature range by a diffusional ledge mechanism analogous to the proposal made to account for the formation of Widmanstätten proeutectoid ferrite (Hehemann *et al.*, 1972). The carbon content of this ferrite was considered to be between the $\alpha/\alpha+\theta$ and the extrapolated $\alpha/\alpha+\gamma$ phase boundaries, and the bainitic carbides considered to form primarily at the austenite/ferrite interface (Hehemann *et al.*, 1972). Detailed electron diffraction studies of the carbide precipitation reactions were interpreted to give support to this hypothesis (Huang and Thomas, 1977). In addition, a solute drag model was invoked to explain the bay in the temperaturature-time-transformation (TTT) curve at the B_s temperature (Kinsman and Aaronson, 1967) and thus, the incomplete reaction characteristic of the bainite transformation (Hehemann, 1970; Hehemann *et al.*, 1972) claimed not to be a general phenomenon (Hehemann *et al.*, 1972).

Another school of thought considered the bainite reaction to be a separate displacive transformation, involving an atomic correspondence, controlled essentially by carbon partitioning between supersaturated bainitic ferrite and retained austenite (Speer *et al.*, 2004), i.e. the rate at which composition change is accomplished by carbon removal to the surrounding parent austenite, or by some other rate controlling process such as strain energy relaxation (Oblak and Hehemann, 1967; Hehemann, 1970; Hehemann *et al.*, 1972). It was expected that the austenite/ferrite interface should exhibit the same characteristics as in the martensitic transformations. The ferritic component of bainite was thus thought to form with a carbon supersaturation (Oblak and Hehemann, 1967; Hehemann, 1970; Le Houiller *et al.*, 1971) which in lower bainite can be relieved by carbide precipitation within the bainitic ferrite. This reaction is thus analogous to autotempered martensite. The existence

© Woodhead Publishing Limited, 2012

of a metastable eutectoid reaction controlling the carbide precipitation event has also been postulated (Hehemann, 1970), a concept also extended to support the idea of a discontinuous change from upper to lower bainite at a temperature of 350°C virtually independent of the steel composition. The B_s temperature is considered to be due to the intersection of C-curves for two separate reactions (namely, Widmanstätten ferrite and upper bainite) occurring by fundamentally different mechanisms (Hehemann *et al.*, 1972; Kennon, 1978).

The formation of a carbide-free bainite allows some attempts at validation of these ideas. The presence of retained austenite and the slower progress of the overall bainite reaction allow a more thorough study of features critically relevant to understanding the atomic mechanisms controlling bainitic ferrite growth, such as the incomplete transformation phenomenon and the carbon supersaturation of bainitic ferrite.

12.2 Influence of silicon on cementite precipitation in steels

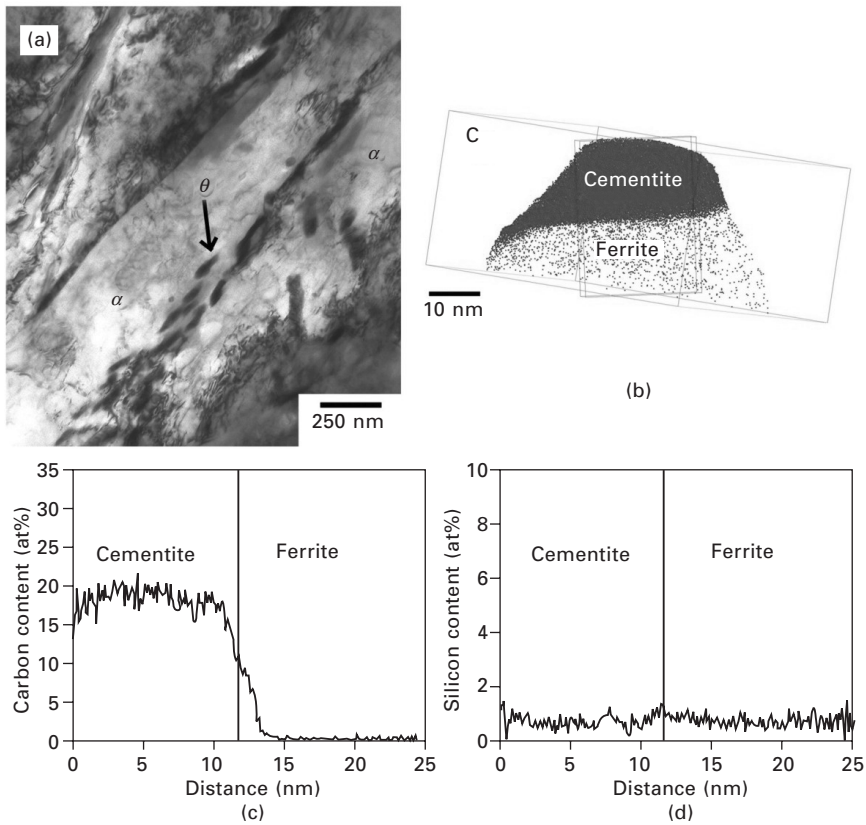
It has long been known that silicon inhibits the precipitation of cementite; concentrations of ~2 wt% silicon can change a brittle, cementite-rich white cast iron into a ductile graphite-rich grey cast iron (Petty, 1970). In high strength tempered martensitic steels, silicon can be used to control the tempering reactions in the martensite (Bain, 1939; Allten and Payson, 1953; Owen, 1954; Keh and Leslie, 1963; Gordine and Codd, 1969; Lorimer *et al.*, 1972). Indeed, this is the basis of the successful aerospace alloy 300M, containing ~1.6 wt%Si; in this case the rate at which cementite precipitates from supersaturated martensite is significantly reduced when compared with a corresponding steel without the silicon (Pickering, 1978). Silicon also retards the precipitation of cementite from austenite (Matas and Hehemann, 1961; Entin, 1962; Sandvik, 1982a, 1982b; Bhadeshia and Edmonds, 1983b).

12.2.1 Cementite precipitation from austenite

The retardation of precipitation from austenite is only valid when the cementite is forced by circumstance to inherit the silicon concentration of the matrix from which it precipitates. Silicon has a negligible solubility in cementite, which can form rapidly if diffusion permits the silicon to partition into the parent phase during growth. This is only possible when transformation occurs at elevated temperatures. However, the decomposition of austenite into a mixture of cementite and ferrite during the formation of bainite is at temperatures where the mobility of substitutional atoms is limited. The silicon then becomes trapped in the cementite during its para-equilibrium growth as the atom probe tomography (APT) results in Fig. 12.3 illustrate.

© Woodhead Publishing Limited, 2012

The transmission electron microscopy (TEM) image in Fig. 12.3(a) shows the distribution of cementite particles between the bainitic ferrite platelets in upper bainite formed at 500°C for 180 s in Fe-0.3C-0.25Si-1.22Mn-0.14Cr wt% steel. The carbon atom map (Fig. 12.3(b)) and concentration profiles (Fig. 12.3(c) and (d)), allow identification of the type of carbide (carbon content of ~25 at% for cementite and ~30 at% for ε-carbide) precipitated from carbon enriched austenite. Besides the apparent low carbon concentration of cementite, it is clear from these results that para-cementite is observed. This underestimation of the carbon concentration of cementite is due to the assignment of the carbon peak at mass-to-charge state ratio of 12 Da to be exclusively C^+ rather than containing some C_2^{++} ions. This will lead to a



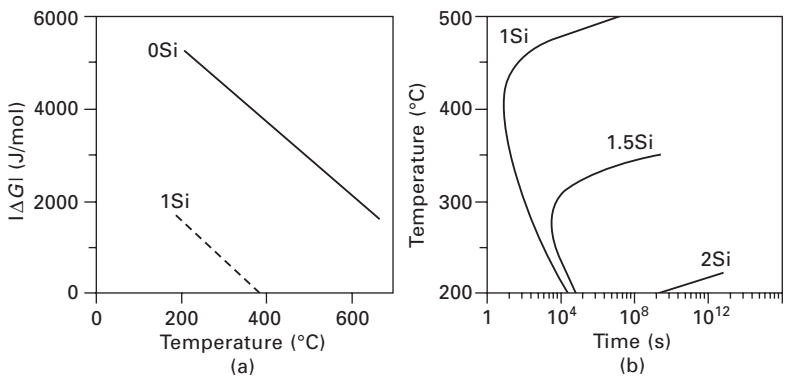
12.3 (a) Transmission electron micrograph of cementite particles between the bainitic ferrite platelets in upper bainite formed at 500°C for 180 s in Fe-0.3C-0.25Si-1.22Mn-0.14Cr wt% steel (Fe-1.4C-0.49Si-1.22Mn-0.15Cr (at%) steel); (b) carbon atom map and concentration profiles showing distribution of (c) carbon and (d) silicon across a cementite/ferrite interface during bainite transformation. α is bainitic ferrite and θ is cementite.

© Woodhead Publishing Limited, 2012

small undervalue of the true carbon level. Although the carbon concentration changes at the cementite-ferrite interface, silicon does not change at all through the interface, indicating that the concentration of silicon is uniform throughout both phases.

The trapping of silicon in cementite dramatically reduces the free energy change associated with precipitation, with a corresponding large reduction in precipitation kinetics (Bhadeshia, 2003; Bhadeshia *et al.*, 2003), as Fig. 12.4 illustrates. The magnitude of free energy change accompanying the $\gamma \rightarrow \gamma + \theta$ reaction for para-equilibrium conditions as a function of silicon concentration of austenite is represented in Fig. 12.4(a). This graph shows the significant reduction in $|\Delta G|$ when the silicon is trapped in the cementite structure. ΔG is the free energy change associated with the formation of a minute quantity of product phase such that it hardly affects the composition of the remaining parent phase, and the composition of the product phase is that which ensures that $|\Delta G|$ is maximised. A time-temperature-precipitation diagram for para-equilibrium cementite in the system Fe-1.2C-Si-1.5Mn (wt%), which corresponds to the typical composition of residual austenite after bainite transformation (Bhadeshia, 2001; Caballero *et al.*, 2001b; De Cooman, 2004; Jacques, 2004) is plotted in Fig. 12.4(b); the transformation temperature range of interest from the point of view of bainitic steels is between about 300 and 400°C and the time periods are hours or days at silicon concentrations higher than 1.5 wt%, making it possible to prevent cementite precipitation from austenite during the course of the routine heat treatment used to produce bainitic steels.

Kozeschnik and Bhadeshia (2008) utilised theory on the kinetics of precipitation processes and provided a quantitative framework for the



12.4 (a) Free energy change accompanying $\gamma \rightarrow \gamma + \theta$ reaction for para-equilibrium conditions as a function of silicon concentration of austenite; (b) time-temperature-precipitation diagram for para-equilibrium cementite in the system Fe-1.2C-Si-1.5Mn (wt%).

© Woodhead Publishing Limited, 2012

formation of cementite from supersaturated austenite. It was confirmed that one condition for the retardation of cementite precipitation from austenite is that the latter must grow under para-equilibrium conditions, i.e. the silicon must be trapped in the cementite. However, this seems not to be a sufficient condition in that it can only be effective in retarding the transformation rate if the overall driving force for the $\gamma \rightarrow \gamma + \theta$ reaction is not large.

Jacques *et al.* (2001) deliberately designed both low and high silicon TRIP steels and reported experimental data for comparison against theory. The chemical compositions of the two steels are Fe-0.16C-0.38Si-1.3Mn (wt%) and Fe-0.29C-1.41Si-1.42Mn (wt%), respectively, and the carbon concentrations of the retained austenite were reported to be 0.8 and 1.0 wt%, respectively. TEM examination of the low silicon alloy transformed at 370°C for 180 s revealed cementite precipitation from the austenite between the bainitic ferrite platelets, consistent with calculations, which showed time periods of a few seconds for para-equilibrium cementite precipitation.

In contrast, Jacques *et al.* (2001) did not find any cementite in the high silicon alloy treated at 360°C for time periods up to 4000 s. Calculations showed that para-equilibrium precipitation in the austenite (with a concentration of 1 wt% C) was thermodynamically impossible at that temperature due to the lack of sufficient driving force. The cementite can then only form with the partitioning of silicon, which may take an inordinately long time. Calculations confirmed the need for unrealistically long time (up to 10^{11} s) for equilibrium cementite precipitation from austenite containing Fe-1.0C-1.41Si-1.42Mn (wt%) held at 360°C.

12.2.2 Cementite precipitation from bainitic ferrite

Kozeschnik and Bhadeshia (2008) also conducted calculations on the kinetics of cementite precipitation from supersaturated bainitic ferrite for the so-called 4340 steel with a chemical composition Fe-0.4C-0.7Mn-0.28Si-0.8Cr-1.8Ni-0.25Mo (wt%) and the alloy 300M with essentially the same composition but with the silicon concentration boosted to 1.6 wt%. The 4340 steel is a high quality, strong steel used in the quenched and tempered condition but, to avoid the 350°C tempered martensite embrittlement (Honeycombe and Bhadeshia, 1995), it is somewhat over tempered at 425°C for 1 h, giving a yield strength of 1350 MPa. Tempered martensite embrittlement is associated with the formation of coarse cementite which reduces toughness in such a high strength matrix. It manifests as a minimum in a plot of toughness versus tempering temperature when the latter is 350°C. To avoid this difficulty, the alloy 300M was developed with a higher silicon concentration to retard tempering so that the minimum in toughness is shifted to higher tempering temperatures; therefore, 300M can be tempered at just 315°C without embrittlement, leading to a much greater strength in excess of 1650 MPa.

© Woodhead Publishing Limited, 2012

The experimental evidence clearly shows, therefore, that silicon retards the para-equilibrium precipitation of cementite from carbon supersaturated bainitic ferrite. Calculations by Ghosh and Olson (2002) suggested, however, that precipitation is too rapid to have a perceptible effect. Kozeschnik and Bhadeshia's (2008) calculations on the kinetics of cementite precipitation from supersaturated bainitic ferrite confirmed that the cementite precipitates rapidly during tempering at 315°C, with little meaningful difference between the silicon-rich 300M and low silicon 4340 steels. Calculation also showed that a significant influence of silicon in retarding tempering only occurs when the carbon concentration is substantially reduced from 0.4 wt% down to 0.01 wt%. The reason for this is that even at the lowest carbon concentrations, the driving force for the $\alpha \rightarrow \alpha + \theta$ reaction at 315°C in the silicon-rich steel remains large, a reflection of the fact that the solubility of carbon in ferrite in equilibrium or para-equilibrium with cementite is negligible at the tempering temperature of 315°C.

One probable explanation of the discrepancy between Ghosh and Olson's (2002) and Kozeschnik and Bhadeshia's (2008) calculations and experimental observations on the tempering of martensite comes from the earlier classic work by Kalish and Cohen (1970). They proposed that in the presence of dislocations, carbon prefers to be segregated to dislocations rather than precipitate as cementite or ε-carbide. Although they did not consider other defects, such as the high density of interfaces present in the microstructure of martensite, these would also be expected to tie up the carbon that is normally available for precipitation.

The defects can effectively be thought of as a separate phase which is a greater attractor for carbon than cementite. In these circumstances, the carbon available for precipitation as cementite is reduced. The rate of precipitation then depends on the 'dissolution' of the defects during annealing, making carbon available for cementite formation (Bigg *et al.*, 2011). This must greatly retard tempering kinetics and, because of the reduced carbon concentration in the perfect lattice, lead to a smaller driving force for precipitation and hence a larger difference between the silicon-rich and silicon-poor steels.

12.3 Carbon distribution during the carbide-free bainite reaction

The excellent mechanical properties of carbide-free bainite are intimately related to the thermal and mechanical stability of untransformed austenite. One of the most important factors governing austenite stability is the carbon enrichment which can be attained after transformation. Thus, it is important to understand the partitioning of carbon between parent austenite and potential bainitic products – bainitic ferrite, carbides and untransformed residual austenite – in order to relate to the potential carbide reactions and stabilisation

© Woodhead Publishing Limited, 2012

of austenite that lead to the final condition of the microstructure. But it is impossible to measure experimentally the carbon concentration of bainitic ferrite during growth because it has long been recognised (Winchell and Cohen, 1962) that the time taken for any carbon to diffuse into austenite can be extremely short. However, enabled by the development of Si-containing steels, the carbon levels in newly formed bainitic ferrite were determined indirectly by early atom probe analysis of the carbon concentration in the retained austenite at the end of the bainite reaction (Bhadeshia and Waugh, 1982; Stark *et al.*, 1990). Interpretations of these early results were that carbon concentrations in the residual austenite indicated that bainitic ferrite formed initially with a supersaturation of carbon. This also has implications for ideas about the 'incomplete reaction phenomenon' associated with the formation mechanism of bainitic ferrite: this incomplete reaction is defined as the temporary cessation of ferrite formation before the fraction of austenite transformed to ferrite, allowed by the lever rule in the absence of carbide precipitation at ferrite/austenite boundaries, is reached (Hehemann *et al.*, 1972). The fact that bainitic ferrite formation ceases such that untransformed austenite remains, which is stabilised to room temperature, is clearly crucial to the establishment of the carbide-free austenite-ferrite microstructure.

12.3.1 Carbon content in retained austenite at the end of the bainite reaction

Over the last 25 years, the incomplete reaction phenomenon has been an important issue for the definition of bainite transformation mechanisms. The various theories proposed for the incomplete reaction phenomenon have recently been reviewed (Aaronson *et al.*, 2004, 2006). According to Aaronson and co-workers, the currently most promising theories involve the cessation of growth induced by the coupled-solute drag effect, accentuated by the overlap of carbon diffusion fields associated with nearby ferrite crystals, although they also state that additional experimental-based isothermal transformation studies on the incomplete reaction phenomenon and bainite formation are needed, especially for Fe-C-Mn alloys with a lower strength of the coupled-solute drag effect upon ferrite formation than that in widely reported Fe-C-Mo alloys.

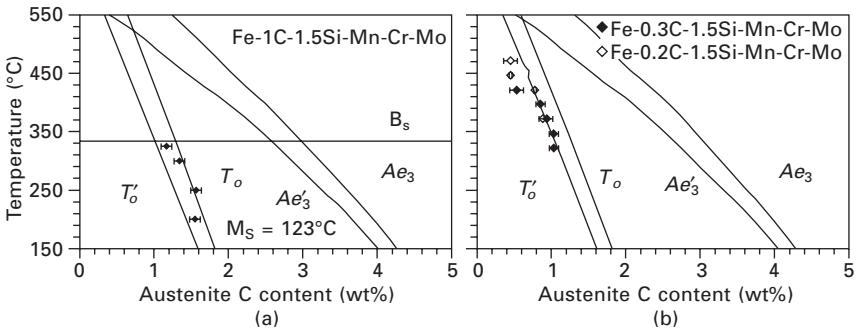
On the other hand, Bhadeshia and Edmonds (1980) explained this phenomenon as a manifestation of the formation of essentially supersaturated bainitic ferrite so that the original bainitic ferrite retains much of the carbon content of the parent austenite. The partitioning of carbon into the residual austenite occurs immediately after formation. In that case, the bainite reaction is expected to cease as soon as the austenite carbon content reaches the T_o' curve. The T_o curve is the locus of all points, on a temperature versus carbon concentration plot, where austenite and ferrite of the same chemical

© Woodhead Publishing Limited, 2012

composition have the same free energy. The T_o' curve is defined similarly, but taking into account the stored energy of the ferrite due to the displacive mechanism of the transformation (400 J/mol) (Bhadeshia, 1981).

New measurements of the carbon content of the austenite remaining after the isothermal formation of bainitic ferrite has ceased and before any carbide has formed, using X-ray diffraction (XRD) were recently presented for medium and high carbon manganese steels with enhanced silicon addition (Pereloma *et al.*, 2008; Caballero *et al.*, 2009b). As mentioned above, silicon alloying inhibits the formation of cementite in the progress of the classical bainite reaction, essential to study the incomplete reaction phenomenon. Interestingly, the T_o' curve was validated on an Fe-1C-1.5Si-1.9Mn-1.3Cr-0.3Mo (wt%) steel, a new generation of nanostructured carbide-free bainite known as Nanobain, that transforms to bainite at abnormally low temperatures (123–335°C), temperatures at which the diffusion of iron atoms is inconceivable during the course of the transformation (Caballero and Bhadeshia, 2004).

The carbon content of the austenite measured by XRD at the termination of phase transformation for Nanobain is shown in Fig. 12.5(a). The calculated values for T_o' and paraequilibrium Ae_3' phase boundaries are also plotted. Likewise, the same type of calculation, but not considering the stored energies of the related phases, is presented as T_o and Ae_3. The measured carbon concentrations in austenite lie closer to the T_o' or T_o value boundaries and far from the paraequilibrium phase boundaries (Ae_3 and Ae_3' lines) for Nanobain that transforms at abnormally low temperatures. The results were considered to be consistent with a mechanism whereby excess carbon partitions into austenite soon after bainitic ferrite formation. The reaction is



12.5 Calculated phase boundaries together with X-ray experimental data representing the carbon concentration of the austenite which is left untransformed after cessation of the carbide-free bainite reaction: (a) for an Fe-1C-1.5Si-1.9Mn-1.3Cr-0.3Mo (wt%) steel that transforms to bainite at abnormally low temperatures (123–335°C); and (b) for two Fe-C-1.5Si-1.6Mn-1.5Cr-0.3Mo (wt%) steels with different average carbon contents (0.2 and 0.3 wt%).

© Woodhead Publishing Limited, 2012

said to be incomplete therefore, since transformation stops before the phases achieve their equilibrium compositions.

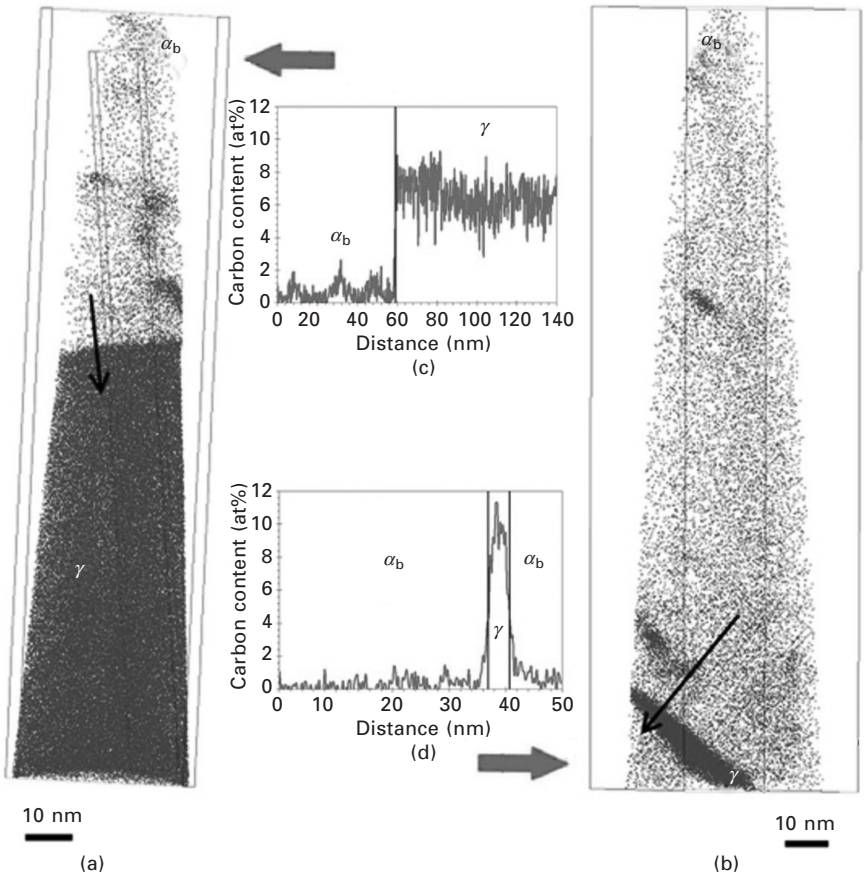
Quidort *et al*. (2003) reported a strong influence of the carbon content of the steel on the carbon concentration of the austenite at bainite stasis (i.e., when the bainite transformation ends) in three high silicon steels with an average carbon content ranging between 0.12 and 0.43 wt%. They proposed that plastic resistance of austenite is responsible for incomplete transformation and evaluated the implications of the process of plastic accommodation in the austenite matrix, considering plastic deformation as an additional source of Gibbs energy dissipation during bainite transformation.

However, a comparison of the carbon concentration in austenite measured by XRD at the termination of bainite transformation for different temperatures in two Fe-C-1.5Si-1.6Mn-1.5Cr-0.3Mo (wt%) steels with different average carbon content (0.2 and 0.3 wt%) is presented in Fig. 12.5(b). It is clear that there is no dependence in these steels on the average carbon content, but rather, that this result is consistent with T_o' calculations, as both steels exhibit the same T_o' curve. In consequence, the simplest explanation for the results in Fig. 12.5(b) is that the driving force for the formation of new plates decreases as the carbon concentration in the untransformed austenite approaches the T_o' composition, at which point the free energy of ferrite and austenite phases of the same composition become identical, leading to bainite stasis (Zener, 1946; Bhadeshia and Edmonds, 1980).

In certain cases, the measured carbon concentrations were observed to exceed the T_o concentration (Bhadeshia and Edmonds, 1980; Caballero *et al*., 2009b). This can be explained as a consequence of the fact that the austenite films entrapped between neighbouring sub-plates of bainitic ferrite have a higher carbon content than the blocks of residual austenite located between the sheaves of bainite, which may transform to martensite during the subsequent quench (Bhadeshia and Edmonds, 1980). This inhomogeneous distribution of carbon would allow the transformation to proceed to an extent somewhat greater than that allowed by the thermodynamic conditions based on a uniform carbon assumption.

Self *et al*. (1981) proved quantitatively the existence of non-uniform distributions of carbon in retained austenite by measuring the austenite lattice parameter from TEM lattice fringes. Atom probe tomography (APT) can also be employed to determine directly the distribution of carbon in austenite. Carbon atom maps obtained from Fe-0.3C-1.5Si-2Mn-0.4Cr-0.3Mo (wt%) steel (Fe-1.3C-2.9Si-2Mn-0.4Cr-0.2Mo in at%) isothermally transformed at 325°C for 1350 s are shown in Fig. 12.6. The distribution of carbon atoms in the analysis volume (Fig. 12.6(a) and (b)) is not uniform and carbon-enriched and carbon-depleted regions are clearly distinguishable. As no crystallographic information is available, the carbon-enriched regions of the atom maps are assumed to represent a region of austenite as the carbon

© Woodhead Publishing Limited, 2012



12.6 (a) and (b) Carbon atom maps; (c) and (d) corresponding concentration profiles across austenite-ferrite interfaces in Fe-0.3C-1.5Si-2Mn-0.4Cr-0.3Mo (wt%) steel alloy (Fe-1.3C-2.9Si-2Mn-0.4Cr-0.2Mo in at%) transformed at 325°C for 1350 s. α_b is bainitic ferrite and γ is austenite.

content is higher than the average value of 1.32 at%, whilst the low carbon (< 1 at%) regions indicate the ferrite phase. Figures 12.6(a) and (b) show two examples of an austenite-ferrite interface for two different sizes of austenite regions. The corresponding carbon concentration profiles are also presented in Figs 12.6(c) and (d). The average carbon content in the 80 nm thick austenite region (sub-micron blocky austenite) is 6.4 ± 1.8 at% C, similar to the corresponding XRD (6.0 ± 0.3 at% C) and T_o (5.5 at%) values, whereas the average carbon content in the 3.5 nm thick austenite film is 9.8 ± 0.4 at% C, well beyond the T_o (5.5 at%) curve, but less than the para-equilibrium Ae_3 boundary (17.3 at%). In general, the APT results confirm

© Woodhead Publishing Limited, 2012

that finer austenite films accumulate higher amounts of carbon during bainite formation. The local carbon content in blocky austenite must be lower than the average given by XRD analysis; unfortunately, coarse features observed in scanning electron micrographs, such as blocky austenite, are not readily observed in APT without special lift-out specimen preparation methods due to the more limited volume of analysis.

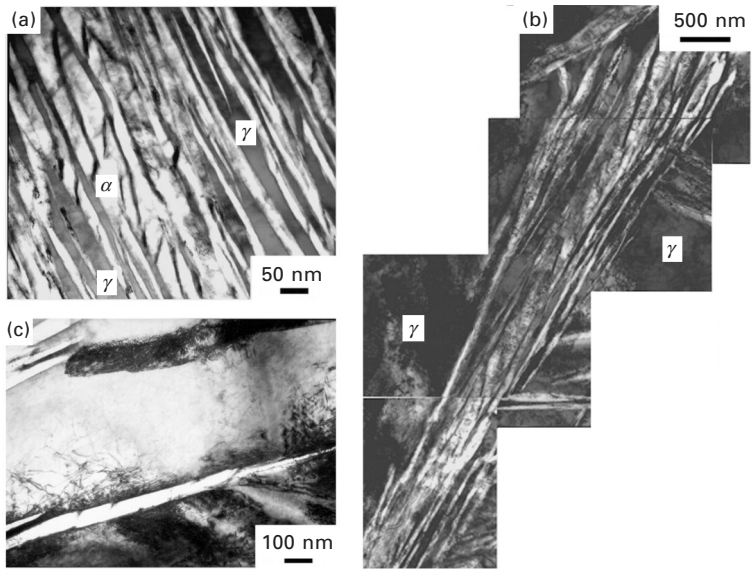
12.3.2 Carbon supersaturation of bainitic ferrite in carbide-free bainite

Slow reaction rates can be advantageous for determining the carbon content of the bainitic ferrite during growth (Caballero *et al.*, 2010), which are important, as mentioned above for example, in trying to understand the partitioning of carbon between parent austenite and bainitic products and thus to distinguish between a reconstructive or displacive reaction mechanism. However, the rate at which bainite forms will slow down dramatically as the transformation temperature is reduced. There is, in principle, no lower limit to the temperature at which bainite can be generated, but, it may take hundreds or thousands of years at room temperature (Garcia-Mateo *et al.*, 2003). One theory of the bainite transformation (Bhadeshia, 1981) has allowed the estimation of the lowest temperature at which bainite can be formed in a reasonable time. This led to the design of the Nanobain steel, Fe-1C-1.5Si-1.9Mn-1.3Cr-0.3Mo (wt%) (Fe-4.3C-2.8Si-1.8Mn-1.3Cr-0.1Mo in at%), which on transformation at 200°C for 144 h, leads to a remarkable microstructure consisting of slender crystals of ferrite (35 ± 2 nm thick) separated by retained austenite (Fig. 12.7), essentially a refined microstructure of the carbide-free bainite presented above in Fig. 12.2. According to XRD, the volume fraction of the retained austenite was 29 ± 2% and was enriched in carbon to 6.69 ± 0.44 at% (Caballero and Bhadeshia, 2004).

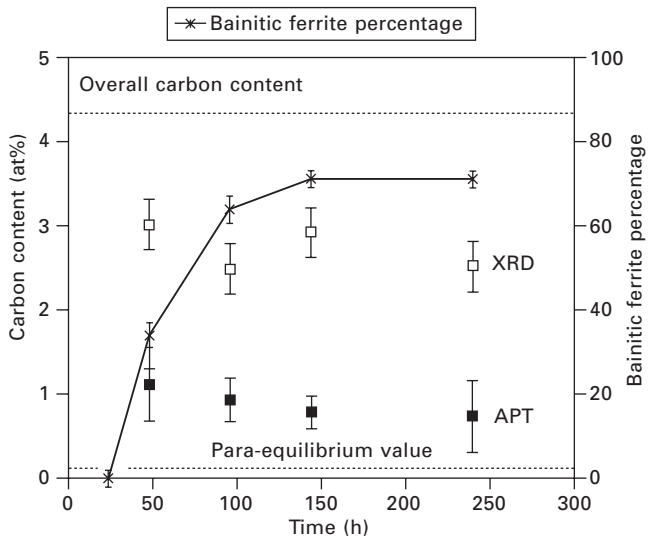
The evolution of the carbon content in bainitic ferrite, as determined from XRD analysis and APT as bainite transformation progresses at 200°C in Nanobain steel (Caballero *et al.*, 2010), is shown in Fig. 12.8. Both XRD and APT values proved the presence of a high level of carbon in bainitic ferrite, which was well above that expected from para-equilibrium with austenite (0.12 at% C). APT estimates are from selected volumes of bainitic ferrite that did not contain any carbon-enriched regions, such as dislocations and boundaries, whereas the higher XRD estimates are average estimates of larger volumes of bainitic ferrite that include such regions expected to be carbon-enriched. The difference between XRD and APT analysis was attributed to the trapping of carbon at the dislocations in the bainitic ferrite (Caballero *et al.*, 2007).

What is remarkable is that, for the first time (Caballero *et al.*, 2010), it proved possible by using these novel alloys, to monitor effectively the

© Woodhead Publishing Limited, 2012



12.7 Transmission electron micrographs of microstructure obtained at 200°C after 144 h in Fe-1C-1.5Si-1.9Mn-1.3Cr (wt%) steel. α is bainitic ferrite and γ is retained austenite.



12.8 Evolution of carbon content in ferrite as carbide-free bainite transformation progresses at 200°C in Fe-1C-1.5Si-1.9Mn-1.3Cr-0.3Mo (wt%) steel (Fe-4.3C-2.8Si-1.8Mn-1.3Cr-0.1Mo in at%).

© Woodhead Publishing Limited, 2012

carbon supersaturation of bainitic ferrite and the partitioning of carbon into the residual austenite as the transformation progressed (Fig. 12.8). Thus it was claimed that the new APT results then provided clear evidence of carbon supersaturation in bainitic ferrite at the early stage of transformation, it is believed, putting beyond question, that the bainite transformation is essentially displacive in nature.

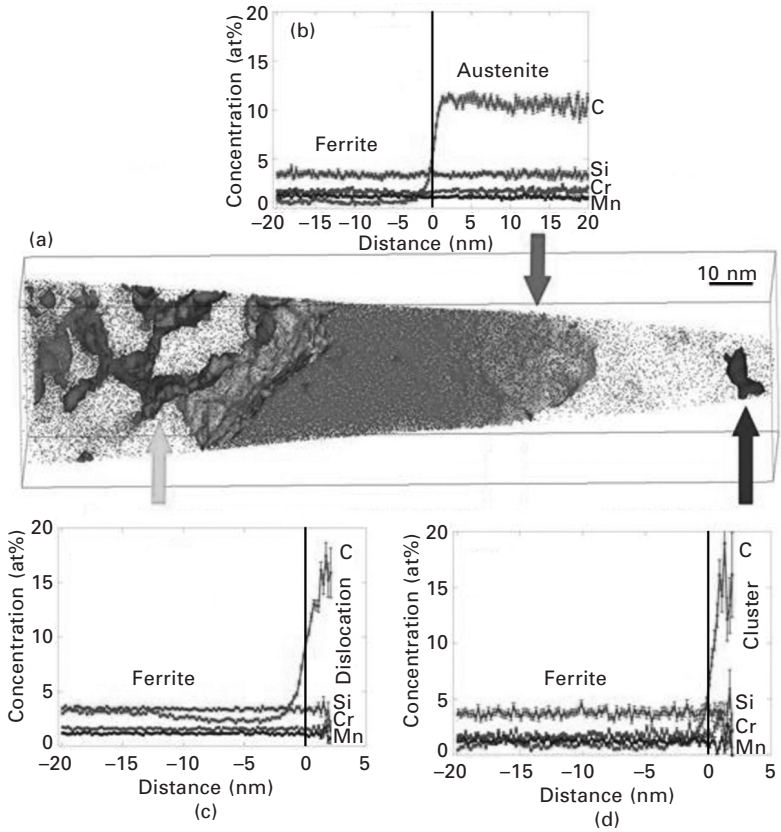
12.3.3 Carbon trapped at defects

Apart from carbon partitioning from supersaturated bainitic ferrite to austenite, other competing reactions, such as carbon segregation to dislocations and twins, were reported to be activated during carbide-free bainite formation at low temperature (Caballero *et al.*, 2007). A carbon atom map with superimposed isoconcentration surfaces obtained from Nanobain steel transformed at 200°C for 240 h is shown in Fig. 12.9(a). The analysis volume encompasses a central carbon-enriched (10.4 ± 0.6 at% C) austenite film bounded by two bainitic ferrite plates (<1 at% C) and dislocation tangles in the vicinity of a bainitic ferrite-austenite interface at the left of the volume and a carbon-enriched cluster, small features with a carbon content of ~14 at% and chromium and manganese contents too low to be identified as refractory M_6C carbide (Caballero *et al.*, 2011). The proximity histogram (Miller and Forbes, 2009) across the bainitic ferrite-austenite interface in Fig. 12.9(b) demonstrates that there was no significant segregation of either substitutional elements or carbon to the austenite-ferrite interface. The quantitative data also confirmed the absence of any partitioning of the substitutional elements between the phases involved. The results are again fully consistent with early atom probe investigation (Bhadeshia and Waugh, 1982), demonstrating that in a variety of steels, none of the substitutional atoms, Mn, Si, Ni, Mo or Cr, partitions during transformation, even on the finest conceivable scale.

Smith (1984) estimated a mean dislocation density of 4×10^{14} m^{-2} in bainitic ferrite using TEM images in an Fe-0.07C-0.23Ti wt% alloy when isothermally transformed to bainite at 650°C. The relatively high dislocation density associated with bainitic ferrite can be attributed to a shape change accompanying the transformation which is accommodated at least partially by plastic relaxation (Bhadeshia and Edmonds, 1979a). Then the resulting dislocation debris introduced into the austenite can be inherited by any bainite that forms subsequently (Bhadeshia and Christian, 1990). Dislocation debris is evident in bainitic microstructure shown in Fig. 12.7(c). The dislocation density in bainitic ferrite and austenite of Nanobain steel transformed at 300°C was determined by TEM to be $5.1 \pm 2.7 \times 10^{14}$ m^{-2} and $1.8 \pm 0.2 \times 10^{14}$ m^{-2}, respectively (Cornide *et al.*, 2011).

It is clear from the proximity histograms across the dislocations in bainitic ferrite (Fig. 12.9(c)) that dislocations only trap the carbon atoms,

© Woodhead Publishing Limited, 2012



12.9 (a) Carbon iso-concentration surfaces at 8 at% C superimposed with the carbon atom map, and proximity histograms across (b) a ferrite/austenite interface, (c) a dislocation network in the vicinity of the ferrite/austenite interface, and (d) a carbon cluster in bainitic ferrite after transformation at 200°C in Fe-1C-1.5Si-1.9Mn-1.3Cr (wt%), Fe-4.3C-2.8Si-1.8Mn-1.3Cr (in at%) steel.

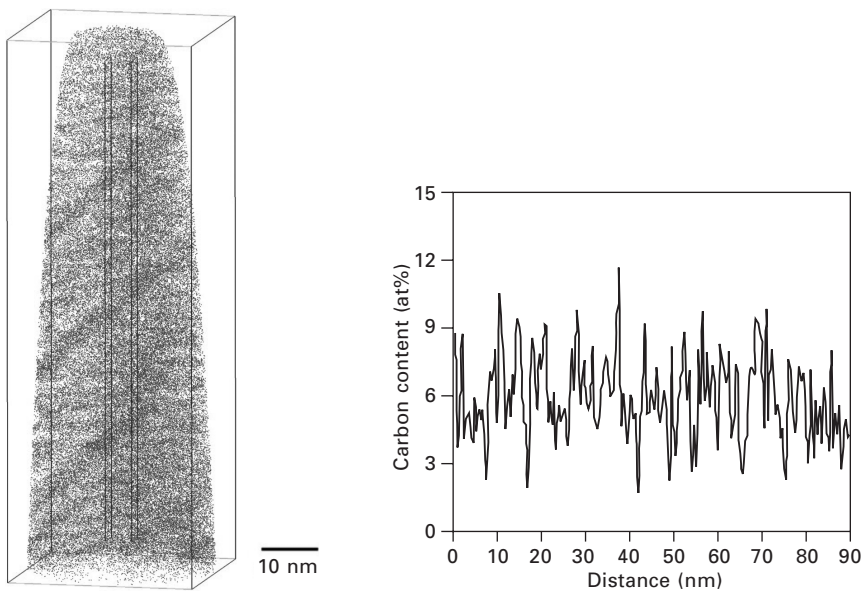
as originally suggested by Kalish and Cohen (1970). The lateral extent of the Cottrell atmosphere in the vicinity of a dislocation was estimated to be ~5 nm. The average carbon level of the Cottrell atmosphere in this example was estimated to be 13.4 ± 0.8 at% C. This value is higher than former experimental evidence of carbon trapped at dislocations in the vicinity of a bainitic ferrite/austenite interface estimated to be 7.4 ± 0.1 at% C (Caballero *et al*., 2007). Pereloma *et al*. (2006) found that the extent of solute segregation to a dislocation depends on its position relative to other defects.

Sandvik and Nevalainen (1981) also observed that the austenite adjacent to the bainitic ferrite contains fine twins, which divide the austenite into small blocks. The twin density was highest in the austenite between parallel, closely spaced bainitic ferrite plates, and increased with decreasing transformation

© Woodhead Publishing Limited, 2012

temperature. It is known that impurities such as phosphorous, calcium and silicon can segregate on incoherent twin boundaries with a high free volume (Ogura *et al.*, 1978, 1987; Swiatnicki *et al.*, 1995). The concentration profile in Fig. 12.10 shows a very fine-scale modulation normal to the parallel carbon-enriched regions of the carbon atom map for Nanobain steel transformed at 300°C for 4 h. It was speculated that carbon might also be segregated at nano-twins in retained austenite (average carbon content of 5.3 at%). APT evidence on carbon segregation to microtwins in retained austenite was also reported in TRIP steels after intercritical annealing (Timokhina *et al.*, 2010).

Carbon segregation to defects has become an important issue with respect to stabilisation of austenite (Bigg *et al.*, 2011), since it is expected to prevent or hinder the carbon atoms from diffusing out of the ferrite lattice. Extensive TEM examination of Nanobain microstructures failed to reveal carbide particles inside the bainitic ferrite (Caballero and Bhadeshia, 2004; Hodgson *et al.*, 2008). This is indeed an interesting observation, as at these temperatures, steel with such high carbon levels might be expected to transform to a lower bainitic microstructure. As mentioned already above, the difference between upper and lower bainite has been ascribed to competition between the rate at which carbides can precipitate from bainitic ferrite and the rate at which



12.10 Carbon atom map and concentration profile showing carbon segregation to nano-twins in retained austenite for a sample transformed at 300°C in Fe-1C-1.5Si-1.9Mn-1.3Cr (wt%), Fe-4.3C-2.8Si-1.8Mn-1.3Cr (in at%), steel.

© Woodhead Publishing Limited, 2012

carbon is partitioned from super-saturated bainitic ferrite into austenite (Takahashi and Bhadeshia, 1990).

The carbon segregation to defects and the absence of carbides in low temperature bainite helps to explain the high level of carbon that exists in the bainitic ferrite after transformation in Nanobain steel (as shown by Fig. 12.8). Moreover, it can then be argued that the excess of carbon in bainitic ferrite at low transformation temperatures is consistent with the fact that the dislocation density of bainitic ferrite is higher for lower reaction temperatures (Fondekar *et al.*, 1970).

Finally, the presence of fine carbon-rich clusters and Fe-C carbides with a wide range of compositions in bainitic ferrite was reported to be revealed by APT (Caballero *et al.*, 2007; Hodgson *et al.*, 2011). The proximity histogram across the ~3 nm thick cluster in Fig. 12.9(d) shows a maximum carbon content of ~15 at%, higher than that associated with dislocations, but with chromium and manganese contents too low (less than 2 at%) to be identified as a carbide. In addition, silicon does not change at all through the interface, indicating that the concentration of silicon is uniform throughout both phases. These features resemble those carbon clusters in a modulated matrix structure consisting of alternating carbon-rich and carbon-poor bands reported for Fe-Ni-C martensite after natural ageing (Miller *et al.*, 1981; Taylor *et al.*, 1989). It is likely that these carbon-enriched regions may signify the onset of the transition carbides observed during subsequent tempering of Nanobain microstructure (Caballero *et al.*, 2008).

12.4 Microstructural observations of plastic accommodation in carbide-free bainite

Plastic relaxation in the austenite adjacent to the bainitic ferrite may control the final size of the bainitic ferrite plates (Chang and Bhadeshia, 1995). The defects generated in this process resist the advance of the bainitic ferrite-austenite interface, the defect density being highest for lower transformation temperatures (Fondekar *et al.*, 1970). The plastic relaxation of the shape change was examined a long time ago using *in-situ* hot-stage TEM and pre-polished samples of austenite transforming to bainite. Observations revealed that the growth of bainite is accompanied by the formation of dislocations in and around the bainite (Nemoto, 1974).

The retained austenite was also found to have the appearance of multiple planar faults/twins, often with one dominant fault plane (Bhadeshia and Edmonds, 1979a). When the fault plane was approximately normal to the foil plane, the faults could be seen to terminate at slip steps in the austenite/ferrite interface indicative of accommodation slip on $\{111\}_\gamma$ planes during displacive transformation (Bhadeshia and Edmonds, 1979a).

The shape deformation associated with a displacive transformation

© Woodhead Publishing Limited, 2012

of austenite in steel can be described as an invariant plane strain with a relatively large shear component. Christian (1958) demonstrated that when the shape strain is elastically accommodated, the aspect ratio (thickness/length) of the plate adjusts so that the strain energy is equal to the driving force. In ideal circumstances, where the transformation interface remains glissile throughout, and where there is no friction opposing the motion of the interface, thermoelastic equilibrium occurs (Kurdjumov and Khandros, 1949).

The thermoelastic equilibrium has been widely demonstrated for martensite (Kurdjumov and Khandros, 1949), but it has not been straightforward for bainite. One reason for this is that the bainite transformation occurs at higher temperatures than those of martensite, where the austenite is mechanically weaker. The shape deformation therefore causes plastic deformation, and the resulting debris from dislocations eventually blocks the transformation interface, which loses coherency. Consequently, platelets of bainitic ferrite are arrested in their growth even when their size is much smaller than the austenite grain size. In this scenario, the plates are expected to become thicker at high temperatures because the yield strength of the austenite will then be lower.

Experimental data on the thickness of bainitic ferrite plates in silicon-rich steels were analysed (Singh and Bhadeshia, 1998) in order to develop a quantitative model for the plate thickness. It was confirmed that the strength of the austenite, and the chemical free energy change accompanying transformation, are by far the most important factors influencing plate thickness. The transformation temperature does not have any independent effect within the limits of the analysis.

12.4.1 Distribution of dislocations in carbide-free bainite

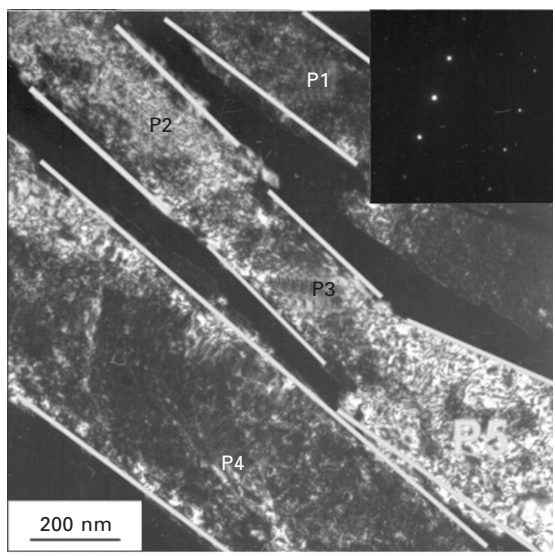
Moritani *et al*. (2002) compared the characters of accommodation dislocations on two kinds of interphase boundaries: lath-like bainitic ferrite/austenite interphase boundary in Fe-0.6C-2Si-1Mn steel and lath martensite/austenite interphase boundary in Fe-20Ni–5.5Mn steel. Both laths exhibited the macroscopic habit plane scattered around $(121)_\gamma$ which contains monoatomic steps with the $(111)_\gamma \,||\, (011)_\alpha$, terrace (transformation dislocations/structural ledges). Similar accommodation dislocations, with pure-screw characters on $(111)_\gamma \,||\, (011)_\alpha$, were also observed in both cases. This study clearly indicated that similar boundary structures can be formed during martensitic and bainite transformations in steels.

Cornide *et al*. (2011) determined by TEM the distribution of dislocations in bainitic ferrite and austenite in Nanobain steel, Fe-1C-1.5Si-1.9Mn-1.3Cr-0.3Mo (wt%), transformed at 300°C. Local dislocation density quantification was performed for eight different bainitic ferrite plates, as illustrated in Fig.

© Woodhead Publishing Limited, 2012

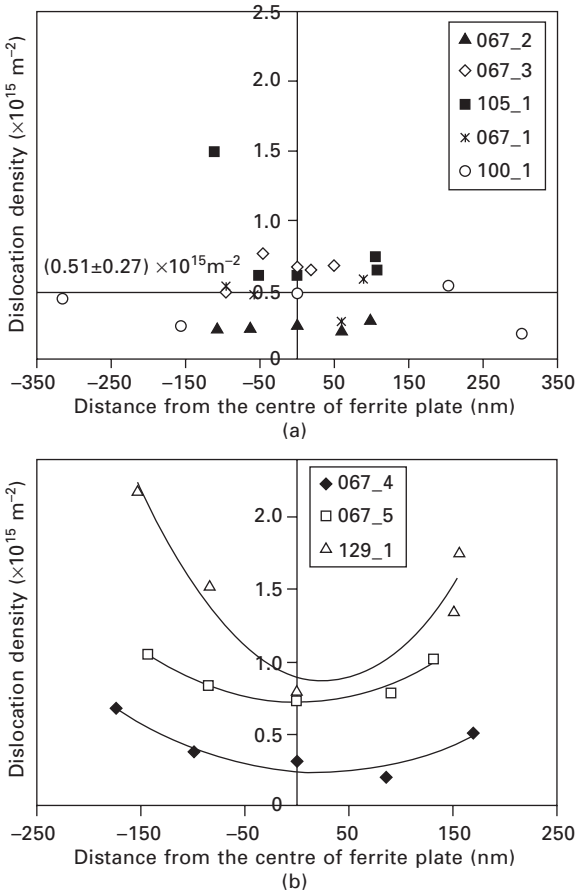
12.11 along the intercept lines parallel to the closest austenite/ferrite interface at multiple distances from the interface. Results are presented in Fig. 12.12 as a function of the distance from the central axis of the corresponding bainitic ferrite plate to the closest austenite/ferrite interface. Different data series correspond to various bainitic ferrite plates (1, 2, 3, … etc.) observed in different dark field TEM images (micrograph numbers 067, 129, … as summarised in Fig. 12.12) as in the example shown in Fig. 12.11.

Results on the local distribution of dislocations shown in Fig. 12.12(a) indicate that five out of eight bainitic ferrite plates show a homogeneous dislocation density distribution with average dislocation density values of $(0.51 \pm 0.27) \times 10^{15}$ m^{-2}, which is lower than those measured by other authors for bainitic and martensitic microstructures as listed in Table 12.1 (Takahashi and Bhadeshia, 1990; Morito *et al*., 2003; Garcia-Mateo and Caballero, 2005; Garcia-Mateo *et al*., 2009). The observed difference is likely to be due to the measurement technique used. For instance, XRD measurements (Garcia-Mateo and Caballero, 2005; Garcia-Mateo *et al*., 2009) include the effects of low-angle grain boundaries because such boundaries can be composed of arrays of dislocations. However, three of the eight bainitic ferrite plates, as shown in Fig. 12.12(b), exhibited a progressive increase in the dislocation density as the interface is approached. Dislocations in the central region of these three bainitic ferrite plates could indicate a lattice-invariant deformation at the



12.11 Dark-field transmission electron microscopy image revealing dislocation debris in bainitic ferrite in Fe-1C-1.5Si-1.9Mn-1.3Cr (wt%) steel transformed at 300°C. Lines indicate interface positions. P# indicates the bainitic ferrite plates analysed in the micrograph.

© Woodhead Publishing Limited, 2012



12.12 (a) Homogeneous and (b) non-homogeneous distribution of dislocation densities within eight different bainitic ferrite plates as a function of the distance from the central axis of the corresponding ferrite plate to the closest austenite/ferrite interface in Fe-1C-1.5Si-1.9Mn-1.3Cr (wt%) steel transformed at 300°C. The data series name in both graphs indicates the TEM number and an individual bainitic ferrite plate.

earlier stage of bainite growth. The higher dislocation density at the vicinity of the austenite/ferrite interface can be related to the plastic deformation occurring in the surrounding austenite to accommodate the transformation strain as growth progresses and the inheritance of these dislocations by the expansion of the growing bainitic ferrite plate. It is reasonable to assume that bainitic ferrite plates exhibiting different dislocation density distribution are formed at different stages of transformation. Bainitic ferrite in the early stage transforms from austenite free of dislocations, whereas bainitic ferrite

© Woodhead Publishing Limited, 2012

Table 12.1 Average dislocation density values for bainitic and martensitic microstructures reported in this work and in the literature

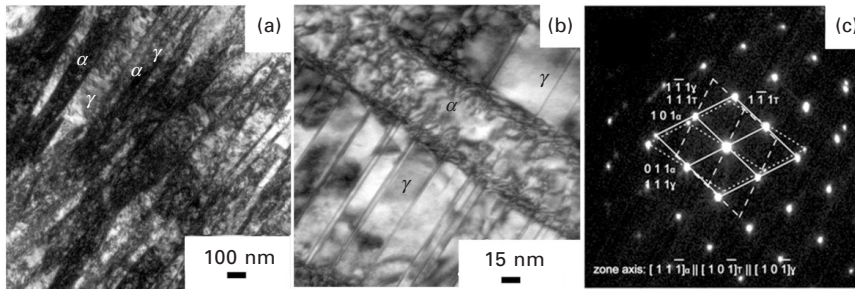
Phase/ Microstructure	Dislocation density [m^{-2}]	Temperature	Technique	Reference
Retained austenite	$(0.18 \pm 0.02) \times 10^{15}$	300°C	TEM	Cornide *et al.*, 2011
Bainitic ferrite	$(0.51 \pm 0.27) \times 10^{15}$	300°C	TEM	Cornide *et al.*, 2011
Bainite	$(4.50 \pm 1.71) \times 10^{15}$ $(3.97 \pm 1.63) \times 10^{15}$ $(3.24 \pm 1.49) \times 10^{15}$ $(3.24 \pm 1.49) \times 10^{15}$ $(2.15 \pm 1.22) \times 10^{15}$ $(1.55 \pm 1.03) \times 10^{15}$ $(1.07 \pm 0.15) \times 10^{16}$ $(7.43 \pm 1.12) \times 10^{15}$ $(4.11 \pm 0.71) \times 10^{15}$ $(3.29 \pm 0.58) \times 10^{15}$	200°C 200°C 250°C 250°C 300°C 300°C 250°C 300°C 350°C 375°C	XRD	Garcia-Mateo and Caballero, 2005 Garcia-Mateo *et al.*, 2009
Martensite	3.01×10^{15} 4.11×10^{15}	300°C 357°C	TEM	Morito *et al.*, 2003
Bainite + Martensite	7.46×10^{15} 7.40×10^{15} 3.77×10^{15}	200°C 300°C 400°C	Empirical model	Takahashi and Bhadeshia, 1990

transformed in the later stage inherits a higher density of dislocations from austenite.

12.4.2 Accommodation twinning in carbide-free bainite

Accommodation twinning (Chang and Bhadeshia, 1995) in austenite, so called in order to distinguish these mechanical twins from the transformation twins observed in martensite due to the lattice invariant strain (Bhadeshia and Edmonds, 1979b), is further microstructural evidence of plastic relaxation of the shape change occurring during carbide-free reaction. Accommodation twinning is apparent in TEM micrographs of an Fe-0.8C-2.0Si-1.5Mn-0.3Mo-1.3Cr-0.1V (wt%) steel transformed at 200°C for 10 days shown in Fig. 12.13 (Chen *et al.*, 2007). The bright field image in Fig. 12.13(b) illustrates the austenite in contact with a bainitic ferrite plate exhibiting, apart from dislocation debris associated with the austenite/ferrite interface, extensive twinning. These twins are lenticular in shape with a thickness of approximately 2–10 nm. The corresponding diffraction pattern of Fig. 12.13(c) confirms that the bainitic ferrite obeys the Kurdjumov–Sachs orientation relationship with the austenite and inheriting twins from austenite. Zhang and Kelly (2006) obtained similar results for a carbide-free bainitic steel (Fe-0.8C-1.6Si-2.0Mn-1.0Al-0.2Mo-1.0Cr-1.5Co-0.002P in wt%) using a convergent

© Woodhead Publishing Limited, 2012



12.13 Transmission electron micrographs of Fe-0.8C-2.0Si-1.5Mn-0.3Mo-1.3Cr-0.1V (wt%) steel transformed at 200°C for 10 days: (a) general microstructure; (b) nanoscale twins in retained austenite; (c) corresponding diffraction pattern (Chen *et al.*, 2007). α is bainitic ferrite and γ is austenite.

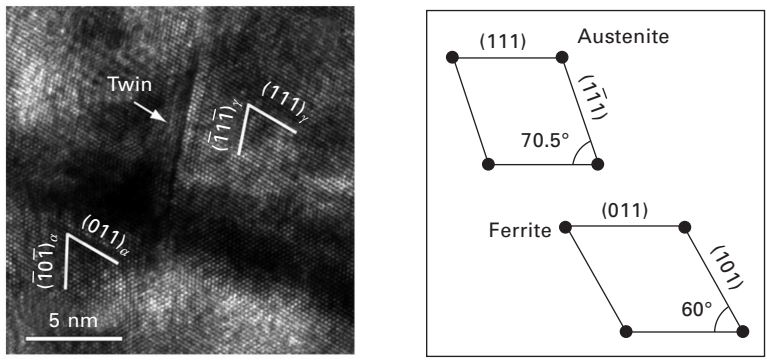
beam Kikuchi line diffraction technique. Nanoscale twinning austenite was also observed on Fe-0.8C-1.6Si-2.0Mn-0.3Mo-1.3Cr-0.1V (wt%) steel after isothermal transformation at 200°C for 10 days and tempering at 400°C for 30 min (Chen *et al.*, 2007). The trace of the twinning was displaced by an angle of 9–12° after crossing the austenite/ferrite interface verifying that a pre-existing twin caused by the shape strain of bainitic transformation was displaced by the shape strain of another plate of transforming bainitic ferrite (Sandvik, 1982a).

A high resolution transmission electron microscopy (HR-TEM) image of a nanoscale twin formed at the austenite/bainitic ferrite interface holding nearly the Kurdjumov–Sachs (K-S) orientation relationship is shown in Fig. 12.14(a). HR-TEM images of mechanical twins often contain Moiré fringes parallel to the twinning plane because it is often embedded in the austenite matrix due to its lenticular shape. The lattice shear from $\{111\}_\gamma$ to $\{101\}_\alpha$ with a shear angle of 10.5° is identified at the interface in the HR-TEM image shown in Fig. 12.14(a). The schematic in Fig. 12.14(b) illustrates that the lattice deformation results in a 10.5° displacement from austenite to ferrite under the K-S orientation relationship. This angle is comparable to that observed for twinning at the interface. Moreover, Figs 12.14(a) and (b) show the twinning shear to be identified as a $\{1\bar{1}1\}<\{121\}>$ mode. It was suggested that these defects are indicative of accommodation slip on $\{1\bar{1}1\}_\gamma$ planes (Bhadeshia and Edmonds, 1979a). Kang *et al.* (2006) also found $\{1\bar{1}1\}_\gamma$ defects during bainite transformation by *in-situ* TEM observations using a specimen heating stage.

12.5 Conclusions

Bainite microstructure is examined in silicon-containing steels. Instead of the classical structure of bainitic ferrite laths with interlath carbide, it

© Woodhead Publishing Limited, 2012



12.14 (a) High resolution transmission electron micrograph of a nanoscale twin at the austenite/bainitic ferrite interface in Fe-0.8C-2.0Si-1.5Mn-0.3Mo-1.3Cr-0.1V (wt%) steel transformed at 200°C for 10 days; (b) schematic of the lattice correspondence of austenite in $[10\bar{1}]$ projection and bainitic ferrite in $[11\bar{1}]$ projection (Chen *et al.,* 2007).

consists of bainitic ferrite laths interwoven with thin films of untransformed retained austenite. This does not contravene the classical understanding and description of the primary austenite decomposition reaction, which is to a bainitic ferrite structure; it simply enlarges this to allow for suppression of the secondary carbide precipitation reaction which otherwise removes carbon from solution. This has allowed more direct experimental examination of the essential process of the bainite transformation without the interjection of carbide precipitation reactions. In consequence, microstructure characterisation at the atomic scale of a new generation of carbide-free bainitic steels, that slowly transform to bainite at abnormally low temperatures (123–335°C), has provided experimental evidence on carbon partitioning during the bainite reaction and the plastic relaxation of the shape change accompanying the transformation, subjects critically relevant to understanding the atomic mechanisms controlling bainite transformation. However, there are other aspects of bainite transformation that remain unknown, including the type of dislocation associated with the austenite/bainitic ferrite interface and the nature of the carbon atom clustering processes indicative of a stage of ageing prior to precipitation of ε-carbide in bainitic steels.

12.6 Acknowledgement

It is a special pleasure to acknowledge Professor H.K.D.H. Bhadeshia for his support on bainite phase transformation research. Three-dimensional atom probe analysis was performed in collaboration with Dr M.K. Miller from Oak Ridge National Laboratory (ORNL) and sponsored by the Office of Basic Energy Sciences, US Department of Energy and by ORNL's Shared

© Woodhead Publishing Limited, 2012

Research Equipment (SHaRE) User Facility, which is sponsored by the Office of Basic Energy Sciences, US Department of Energy.

12.7 References

Aaronson H I (1968), *The Mechanism of Phase Transformations in Crystalline Solids*, London, Institute of Metals.

Aaronson H I, Reynolds Jr W T and Purdy G R (2004), 'Coupled-solute drag effects on ferrite formation in Fe-C-X systems', *Metall Mater Trans*, 35A, 1187–1209.

Aaronson H I, Reynolds Jr W T and Purdy G R (2006), 'The incomplete transformation phenomenon in steel'. *Metall Mater Trans* 2, 37A, 1731–1746.

Allten G and Payson P (1953), 'The effect of silicon on the tempering of martensite', *Trans. ASM*, 45, 498–532.

Bain E C (1939), *Alloying Elements in Steel*, Cleveland, OH, American Society of Materials.

Bhadeshia H K D H (1980), 'The lower bainite transformation and the significance of carbide precipitation', *Acta Metall*, 28, 1103–1114.

Bhadeshia H K D H (1981), 'A rationalisation of shear transformations in steels', *Acta Metall*, 29, 1117–1130.

Bhadeshia H K D H (2001), *Bainite in Steels*, 2nd edn, London, Institute of Materials.

Bhadeshia H K D H (2003), 'Advances in the kinetic theory of carbide precipitation', *Mater Sci Forum*, 426–432, 35–42.

Bhadeshia H K D H and Christian J W (1990), 'The bainite transformation in steels', *Metall Trans*, 21A, 767–797.

Bhadeshia H K D H and Edmonds D V (1979a), 'The bainite transformation in a silicon steel', *Metall. Trans*, 10A, 895–907.

Bhadeshia H K D H and Edmonds D V (1979b), 'A direct analysis of twinning in a low-alloy martensite', in *Phase Transformations*, York Conference, The Institution of Metallurgists, Series 3, No. 11, Vol. 2, pp. IV-4–IV-8.

Bhadeshia H K D H and Edmonds D V (1980), 'The mechanism of bainite formation in steels', *Acta Metall*, 28, 1265–1273.

Bhadeshia H K D H and Edmonds D V (1983a), 'Bainite in silicon steels: a new composition-property approach. Part I', *Met Sci*, 17, 411–419.

Bhadeshia H K D H and Edmonds D V (1983b), 'Bainite in silicon steels: a new composition-property approach. Part II', *Met Sci*, 17, 420–425.

Bhadeshia H K D H and Waugh A R (1982), 'Bainite: an atom-probe study of the incomplete-reaction phenomenon', *Acta Metall*, 30, 775–784.

Bhadeshia H K D H, Lord M and Svensson L-E (2003), 'Silicon-rich bainitic steel welds', *Trans JWRI*, 32, 91–96.

Bigg T D, Matlock D K, Speer J G and Edmonds D V (2011), 'Dynamics of the quenching and partitioning (Q&P) process', *Solid State Phenomena*, 172–174, 827–832.

Bramfitt B L and Speer J G (1990), 'A perspective on the morphology of bainite', *Metall Trans*, 21A, 817–829.

Caballero F G and Bhadeshia H K D H (2004), 'Very strong bainite', *Curr Opin Solid State Mater Sci*, 8, 251–257.

Caballero F G, Bhadeshia H K D H, Mawella K J A, Jones D G and Brown P (2001a), 'Design of novel high strength bainitic steels. Part 1', *Mater Sci Technol*, 17, 512–516.

© Woodhead Publishing Limited, 2012

Caballero F G, Bhadeshia H K D H, Mawella K J A, Jones D G and Brown P (2001b), 'Design of novel high strength bainitic steels. Part 2', *Mater Sci Technol*, 17, 517–522.

Caballero F G, Santofimia M J, Capdevila C, García-Mateo C and García de Andrés C (2006), 'Design of advanced bainitic steels by optimization of TTT diagrams and T_0 curves', *ISIJ Int*, 46, 1479–1488.

Caballero F G, Miller M K, Babu S S and Garcia-Mateo C (2007), 'Atomic scale observations of bainite transformation in a high carbon high silicon steel', *Acta Mater*, 55, 381–390.

Caballero F G, Miller M K, Garcia-Mateo C, Capdevila C and Babu S S (2008), 'Redistribution of alloying elements during tempering of a nanocrystalline steel', *Acta Mater*, 56, 188–199.

Caballero F G, Santofimia M J, García-Mateo C, Chao J and García de Andrés C (2009a), 'Theoretical design and advanced microstructure in super high strength steels', *Materials and Design*, 30, 2077–2083.

Caballero F G, Garcia-Mateo C, Santofimia M J, Miller M K and García de Andrés C (2009b), 'New experimental evidence on the incomplete transformation phenomenon in steel', *Acta Mater*, 57, 8–17.

Caballero F G, Miller M K and Garcia-Mateo C (2010), 'Carbon supersaturation of ferrite in a nanocrystalline bainitic steel', *Acta Mater*, 58, 2338–2343.

Caballero F G, Miller M K and Garcia-Mateo C (2011), 'Atom probe tomography analysis of precipitation during tempering of a nanostructured bainitic steel', *Metall Mater Trans A*, 42, 3660–3668.

Chang L C (2004), 'Microstructures and reaction kinetics of bainite transformation in Si-rich steels', *Mater Sci Eng A*, 368A, 175–182.

Chang L C and Bhadeshia H K D H (1995), 'Metallographic observations on the mechanism of the bainite transformation', *Mater Sci Technol*, 11, 105–108.

Chen C Y, Yen H W and Yang J R (2007), 'Nanostructure investigation on a tempered super bainitic steel', in *The 1st International Symposium on Steel Science*, Kyoto, *ISIJ Int*, 123–126.

Christian J W (1958), 'Accommodation strains in martensite formation, and the use of a dilatation parameter', *Acta Metall*, 6, 377–379.

Christian J W (1994), 'Crystallographic theories, interface structures, and transformation mechanisms', *Metall Mater Trans A*, 25A, 1821–1839.

Christian J W and Edmonds D V (1984), 'The bainite transformation', in Marder A R and Goldstein J I, *Phase Transformations in Ferrous Alloys*, Warrendale, PA, TMS-AIME, 293–325.

Cornide J, Miyamoto G, Caballero F G, Furuhara T, Miller M K and Garcia-Mateo C (2011), 'Distribution of dislocations in nanostructured bainite', *Solid State Phenomena*, 172–174, 117–122.

De Cooman B C (2004), 'Structure–properties relationship in TRIP steels containing carbide-free bainite', *Curr Opin Solid State Mater Sci*, 8, 285–303.

Entin R (1962), 'The elementary reactions in the austenite → pearlite, bainite transformations', in Zackay V F and Aaronson H I, *Decomposition of Austenite by Diffusional Processes*, New York, Interscience, 295–304.

Fondekar M K, Rao A M and Mallik A K (1970), 'Strain tempering of bainite', *Metall Trans*, 1, 885–890.

Garcia-Mateo C and Caballero F G (2005), 'Ultra-high-strength bainitic steels', *ISIJ Int*, 45, 1736–1740.

© Woodhead Publishing Limited, 2012

Garcia-Mateo C, Caballero F G and Bhadeshia H K D H (2003), 'Development of hard bainite', *ISIJ Int*, 43, 1238–1243.

Garcia-Mateo C, Caballero F G, Capdevila C and Garcia de Andres C (2009), 'Estimation of dislocation density in bainitic microstructures using high-resolution dilatometry', *Scripta Mater*, 61, 855–858.

Ghosh G and Olson G B (2002), 'Precipitation of paraequilibrium cementite: experiments, and thermodynamic and kinetic modeling', *Acta Mater*, 50, 2099–2119.

Gordine J and Codd I (1969), 'The influence of Si up to 1.5 wt% on the tempering of a spring steel', *J. Iron Steel Inst*, 207, 461–467.

Hehemann R F (1970), 'The bainite transformation', in Aaronson H I and Zackay V F, *Phase Transformations*, Metals Park, OH, ASM, 397–432.

Hehemann R F, Kinsman K R and Aaronson H I (1972), 'A debate on the bainite reaction', *Met Trans*, 3, 1077–1093.

Hodgson P D, Timokhina I B, Beladi H, Sabirov I and Pereloma E V (2008), 'Nanostructural engineering of steel', in *SimPro'08*, Ranchi, India, 223–236.

Hodgson P, Timokhina I, Adachi Y and Beladi H (2011), 'Understanding of bainite transformation in nano-structured bainitic steel', *Solid State Phenomena*, 172–174, 123–128.

Honeycombe R W K and Bhadeshia H K D H (1995), *Steels: Microstructure and Properties*, 2nd edn, London, Butterworth-Heinemann.

Huang D H and Thomas G (1977), 'Metallography of bainitic transformation in silicon containing steels', *Met Trans A*, 8A, 1661–1674.

Jacques P J (2004), 'Transformation-induced plasticity for high strength formable steels', *Curr Opin Solid State Mater Sci*, 8, 259–265.

Jacques P J, Girault E, Harlet P H and Delannay F (2001), 'The developments of cold-rolled TRIP-assisted multiphase steels. Low silicon TRIP-assisted multiphase steels', *ISIJ Int*, 41, 1061–1067.

Josefsson B and Andren H O (1989), 'Microstructure and thermodynamic behaviour of a chromium molybdenum submerged arc weld metal in the as welded state', in David S A and Vitek J, *Advances in the Science and Technology of Welding,* Metals Park, OH, ASM, 243–247.

Kalish D and Cohen M (1970), 'Structural changes and strengthening in the strain tempering of martensite', *Mater Sci Eng*, 6, 156–166.

Kang M K, Zhang M X and Zhu M (2006), '*In situ* observation of bainite growth during isothermal holding', *Acta Mater*, 54, 2121–2129.

Keh S and Leslie W C (1963), *'Materials Science Research', Vol. 1*, New York, Plenum Publishing.

Kennon N F (1978), 'The morphology and mechanical. properties of bainite formed from deformed austenite', *Met Trans* A, 9A, 57–66.

Kinsman K R and Aaronson H I (1967), 'Influence of molybdenum and manganese on the kinetics of the proeutectoid ferrite reaction' in *Transformations and Hardenability in Steels*, Ann Arbor, MI, Climax Molybdenum Company, 39–56.

Kozeschnik E and Bhadeshia H K D H (2008), 'Influence of silicon on cementite precipitation in steels', *Mater Sci. Technol*, 24, 343–347.

Krauss G and Thomson S W (1995), 'Ferritic microstructures in continuously cooled low- and ultralow-carbon steels', *ISIJ Int*, 35, 937–945.

Kurdjumov G V and Khandros L G (1949), 'On the "thermoelastic" equilibrium on martensitic transformations', *Dokl. Akad. Nauk SSSR*, 66, 211–214.

Le Houiller R, Begin G and Dubé A (1971), 'A study of the peculiarities of austenite during the formation of bainite', *Met Trans*, 2, 2645–2653.

© Woodhead Publishing Limited, 2012

Lorimer G W, Hobbs R M and Ridley N (1972), 'Effect of silicon on the microstructure of quenched and tempered medium carbon steels', *J Iron Steel Inst*, 210, 757–764.
Matas S J and Hehemann R F (1961), 'The structure of bainite in hypoeutectoid steels', *Trans TMS AIME*, 221, 179–185.
Miihkinen V T T and Edmonds D V (1987a), 'Microstructural examination of two experimental high-strength bainite low-alloy steels containing silicon', *Mater Sci Technol*, 3, 422–431.
Miihkinen V T T and Edmonds D V (1987b), 'Tensile deformation of two experimental high-strength bainitic low-alloy steels containing silicon', *Mater Sci Technol*, 3, 432–440.
Miihkinen V T T and Edmonds D V (1987c), 'Fracture toughness of two experimental high-strength bainitic low-alloy steels containing silicon', *Mater Sci Technol*, 3, 441–449.
Miller M K and Forbes R G (2009), 'Atom probe tomography', *Mater Charact*, 60, 461–469.
Miller M K, Beaven P A and Smith G D W (1981), 'A study of the early stages of tempering of iron-carbon martensites by atom probe field ion microscopy', *Metall Mater Trans*, 12A, 1197–1204.
Moritani T, Miyajima N, Furuhara T and Maki T (2002), 'Comparison of interphase boundary structure between bainite and martensite in steel', *Scripta Mater*, 47, 193–199.
Morito S, Nishikawa J and Maki T (2003), 'Dislocation density within lath martensite in Fe-C and Fe-Ni alloys', *ISIJ Int*, 43, 1475–1477.
Nemoto M (1974), *High Voltage Electron Microscopy*, New York, Academic Press.
Oblak J M and Hehemann R F (1967), *Transformations and Hardenability in Steels*, Ann Arbor, MI, Climax Molybdenum Company.
Ogura T, McMahon C J, Feng H C and Vitek V (1978), 'Structure-dependent intergranular segregation of phosphorus in austenite in a Ni-Cr steel', *Acta Metall*, 26, 1317–1330.
Ogura T, Watanabe T, Karashima S and Masumoto T (1987), 'Dependence of phosphorus segregation on grain boundary crystallography in an Fe-Ni-Cr alloy', *Acta Metall*, 35, 1807–1814.
Ohmori Y, Ohtani H and Kunitake T (1971), 'The bainite in low carbon low alloy high strength steels', *Trans Iron Steel Inst Jpn*, 11, 250–259.
Ohtani H, Okaguchi S, Fujishiro Y and Ohmori Y (1990), 'Morphology and properties of low-carbon bainite', *Metall Trans A*, 21, 877–888.
Owen W S (1954), 'The effect of silicon on the kinetics of tempering', *Trans ASM*, 46, 812–829.
Pereloma E V, Timokhina I B, Jonas J J and Miller M K (2006), 'Fine-scale microstructural investigations of warm rolled low-carbon steels with and without Cr, P, and B additions', *Acta Mater*, 54, 4539–4551.
Pereloma E V, Timokhina I B, Hodgson P D and Miller M K (2008), 'Nanoscale characterisation of advanced high strength steels using atom probe tomography', in *SimPro'08*, Ranchi, India, 256–266.
Petty E R (1970), *Physical Metallurgy of Engineering Materials*, London, George Allen and Unwin.
Pickering F B (1978), *Physical Metallurgy and the Design of Steels*, London, Applied science.
Quidort D, Bouaziz O and Brechet Y (2003), 'The role of carbon on the kinetics of bainite

© Woodhead Publishing Limited, 2012

transformation in steels', in Buddy D E and Merwin M J *Austenite Formation and Decomposition*, Warrendale, PA, TMS.

Sandvik B J P (1982a), 'The bainite reaction in Fe-Si-C alloys: the primary stage', *Metall Trans A*, 13A, 777–787.

Sandvik B J P (1982b), 'The bainite reaction in Fe-Si-C alloys: the secondary stage', *Metall Trans A*, 13A, 789–800.

Sandvik B P J and Nevalainen H P (1981), 'Structure-property relationships in commercial low alloy bainitic-austenitic steel with high strength', *Met Technol*, 15, 213–220.

Self P, Bhadeshia H K D H and Stobbs W M (1981), 'Lattice spacings from lattice fringes', *Ultramicroscopy*, 6, 29–40.

Singh S B and Bhadeshia H K D H (1998), 'Estimation of bainite plate-thickness in low-alloy steels', *Mater Sci Eng A*, 245, 72–79.

Smith G M (1984), 'The microstructure and yielding behaviour of some Ti steels', Cambridge, University of Cambridge.

Speer J G, Edmonds D V, Rizzo F C and Matlock D K (2004), 'Partitioning of carbon from supersaturated plates of ferrite, with application to steel processing and fundamentals of the bainite transformation', *Curr Opin Solid State Mater Sci*, 8, 219–237.

Stark I, Smith G D W and Bhadeshia H K D H (1990), 'The distribution of substitutional alloying elements during the bainite transformation', *Metall Trans A*, 21A, 837–844.

Swiatnicki W, Lartigue-Korinek S and Laval J Y (1995), 'Grain boundary structure and intergranular segregation in Al_2O_3', *Acta Metall Mater,* 43, 795–805.

Takahashi M and Bhadeshia H K D H (1990), 'A model for the transition from upper to lower bainite', *Mater Sci. Technol*, 6, 592–603.

Taylor K A, Chang L, Olson G B, Smith G D W, Cohen M and Van der Sande J B (1989), 'Spinodal decomposition during aging of Fe-Ni-C martensites', *Metall Mater Trans*, 20A, 2717–2737.

Timokhina I B, Pereloma E V, Ringer S P, Zheng R K and Hodgson P D (2010), 'Characterization of the bake-hardening behavior of transformation induced plasticity and dual-phase steels using advanced analytical techniques', *ISIJ Int*, 50, 574–582.

Winchell P G and Cohen M (1962), 'The strength of martensite', *Trans ASM*, 55, 347–361.

Zajac S, Komenda J, Morris P, Dierickx P, Matera S and Penalba Diaz F (2005), 'Quantitative structure-property relationship for complex bainitic microstructures', Report EUR 21245EN, Luxembourg, Technical Steel Research, European Commission.

Zener C (1946), 'Kinetics of the decomposition of austenite', *Trans AIME*, 167, 550–595.

Zhang M X and Kelly P M (2006), 'Crystallography of carbide-free bainite in a hard bainitic steel', *Mater Sci Eng A*, 438, 272–275.

© Woodhead Publishing Limited, 2012

13

Kinetics of bainite transformation in steels

A. BORGENSTAM and M. HILLERT,
Royal Institute of Technology (KTH), Sweden

Abstract: The main kinetic features of the formation of bainite are discussed, firstly in relation to two incompatible hypotheses for the growth mechanism of bainitic ferrite. One is based on diffusionless growth of bainitic ferrite but diffusional growth of Widmanstätten ferrite. The other is based on the assumption that there is only one kind of acicular ferrite and it grows under simultaneous diffusion of carbon into the interior of the parent austenite. The kinetics of the first stage of bainite formation, the growth of acicular ferrite, is treated in detail because it has been subject to the more intensive research. The kinetics of the reactions by which cementite forms and the subsequent reactions, by which the transformation to bainite is completed, have been subject to less research.

Key words: bainite, kinetics, diffusion controlled, diffusionless, TTT diagrams, B_s lengthwise growth, nucleation.

13.1 Introduction

The iron-rich part of the Fe-C phase diagram has a eutectoid character, i.e., it illustrates that the high temperature phase, austenite, should transform to a eutectoid mixture of ferrite and cementite on cooling below the eutectoid temperature, 1000 K. However, it is well known that there are two very different eutectoid microstructures, pearlite and bainite. The difference is due to different formation mechanisms. Ferrite and cementite cooperate quite well in pearlite by forming parallel lamellae. Bainite can form in a wide range of temperatures. It forms in two steps, at least in the upper part of this range where the result is so-called upper bainite. Acicular ferrite forms first, often arranged in groups of parallel plates. Secondly, cementite will appear and the austenite that remains in between the plates will transform to a mixture of ferrite and cementite. Ferrite is thus regarded as the leading phase. In this chapter, the term 'bainite' will always mean an acicular microstructure composed of ferrite and cementite. Without any carbide it will be regarded either as bainitic ferrite or Widmanstätten ferrite.

It is often stated as a fact that bainite forms by a displacive mechanism which implies that each lattice atom, mainly iron atoms, ends up in a prescribed site in the ferrite lattice. The transfer of iron atoms across the phase interface occurs with a coordinated mechanism and those atoms do not

© Woodhead Publishing Limited, 2012

cross the phase interface by diffusion. In that sense, a displacive mechanism is diffusionless. It is frequently implied that the transfer of carbon atoms should then also be diffusionless, which should mean that the first step, the formation of acicular ferrite, takes place with very rapid growth that forces the ferrite to inherit all the carbon atoms of the parent austenite. That is not justified, demonstrated by the general agreement that Widmanstätten ferrite is also displacive but diffusional with respect to carbon. When it is assumed that there is no diffusion of carbon during the formation of acicular ferrite, it should be regarded as a separate assumption. There are thus two matters that are subject to debate. One concerns the mechanism by which the lattice atoms, mainly iron, are transferred across the moving phase interface; the other concerns the possible diffusion of interstitial atoms, mainly carbon.

Before discussing the information on the reaction kinetics, some attempt must first be made to rationalize any potential conflicting ideas which arise from these two separate views of the mechanism. The first idea to examine concerns the explanation of the surface relief observed on an initially flat surface when a unit of Widmanstätten ferrite or bainite forms. It has often been taken as an indication that the change of the lattice from the fcc lattice of austenite to the bcc or bct lattice of ferrite occurs by a displacive mechanism, as for martensite. However, it has also been proposed that a ledge mechanism could be the cause of the surface relief (Laird and Aaronson, 1967). That created a debate (Hehemann *et al*., 1972) but the issue now seems to be less important because some agreement has been reached that not only a displacive mechanism can give rise to surface relief (Cahn, 1994; Christian, 1994). This question will not be further discussed here and attention will be concentrated on two hypotheses, one stating that the ferritic constituent of bainite forms with a rapid diffusionless growth mechanism, the other stating that it grows under diffusion of carbon. They were recently (Borgenstam *et al*., 2009) tested for their ability to explain microstructural features of the transformation to bainite with the conclusion that the diffusionless hypothesis is less useful. They will now be tested on kinetic features. For the model developed from the diffusionless hypothesis the present account is based on a monograph by Bhadeshia (2001) and a recent discussion (Borgenstam and Hillert, 2011).

The term acicular will be used simply to characterize the shape and will be applied to what is usually called Widmanstätten ferrite and also to the ferrite that forms in the first step of bainite formation, often called bainitic ferrite. The term will not imply any particular mechanism of formation. In the field of welding technology the term 'acicular ferrite' has been applied exclusively to acicular ferrite nucleated inside the austenite grains in welds. Here we will maintain the traditional definition of the term acicular that means needle-like and simply refers to the shape observed in metallographically prepared sections of steel specimens. The real shape is more or less plate-like. If it is

© Woodhead Publishing Limited, 2012

much longer in one direction, it is often described as lath. However, in this chapter only the term plate will be used. It should be emphasized that there is full agreement that Widmanstätten ferrite grows with low carbon content due to diffusion of carbon away from the advancing phase interface during growth.

13.2 Transformation diagrams

13.2.1 Principles of time-temperature-transformation (TTT) diagrams

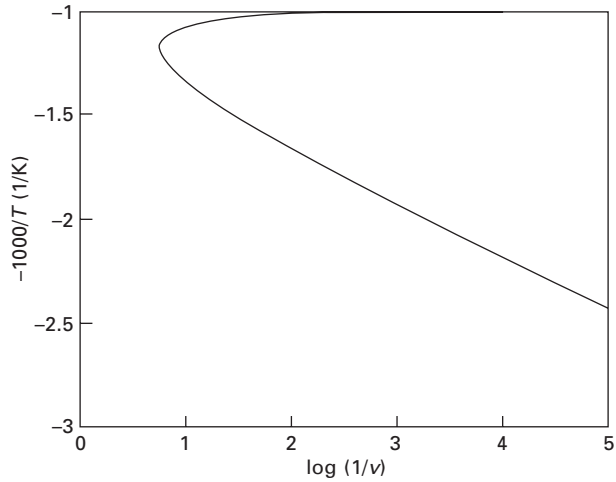
A very important aspect of the kinetics of a transformation is how the rate of formation of various microstructures varies with time and temperature. A wealth of careful metallographic observations, coupled with transformation diagrams, across a vast range of Fe-C alloys and steels exists and so it is constructive to try and distil useful information from this rich source of data. Experimental information is generally presented in TTT diagrams (from time, temperature, fraction of transformation product). The character of TTT diagrams can be illustrated with simple model calculations. Two cases will be considered here. The first may apply to pearlite which transforms the volume gradually without affecting the remaining part of the parent austenite. It will finally cover the whole volume. A rate equation could be formulated as

$$v = K(f) \cdot (T_{cr} - T)^n \cdot \exp(-Q/RT) \qquad [13.1]$$

where T_{cr} is a critical temperature below which the driving force turns positive. It is here assumed that the driving force is proportional to the undercooling, $T_{cr} - T$, and n is an exponent that may depend on the particular rate determining process. It is common to use $n = 1$ for a simple process, such as grain boundary migration, and $n = 2$ may be typical for a diffusion-controlled phase transformation. Q is the activation energy of the rate limiting process. $K(f)$ depends on the degree of transformation, f, and one may hope that it will be independent of temperature. Figure 13.1 illustrates a simple case, e.g. 5% transformation to pearlite. It was calculated with $K = 1$, $T_{cr} =$ 1000 K, $n = 2$ and $Q/R = 10{,}000$ K. The abscissa is logarithmic and represents a measure of time, expressed as $1/v$. Temperature is plotted as $1/T$ and the slope at low temperatures should then represent $-(Q/R)$ ln 10. It should thus be possible to evaluate the activation energy of the rate limiting process by plotting experimental information in this kind of diagram. It should also be useful for extrapolating experimental data to lower temperatures.

Fe-C austenite should transform to ferrite and cementite below 1000 K according to the Fe-C phase diagram. One could thus expect a eutectoid transformation austenite → ferrite + cementite. Two eutectoid mixtures of ferrite and cementite have been known for a long time, pearlite and bainite.

© Woodhead Publishing Limited, 2012

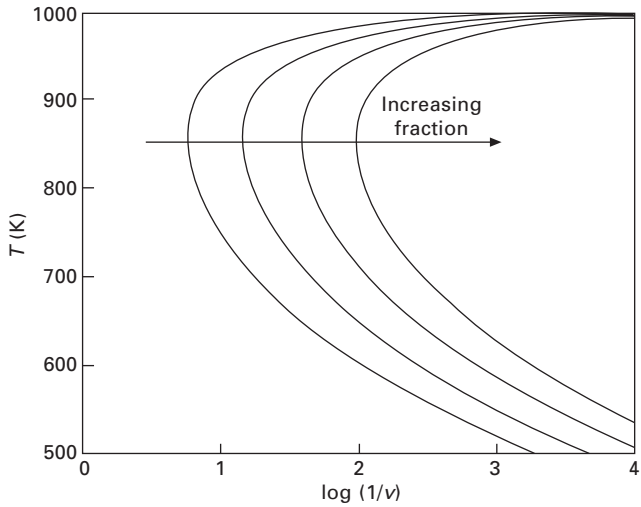


13.1 Schematic TTT diagram with a C curve, for example, representing 5% pearlite. The logarithmic abscissa represents decreasing rates.

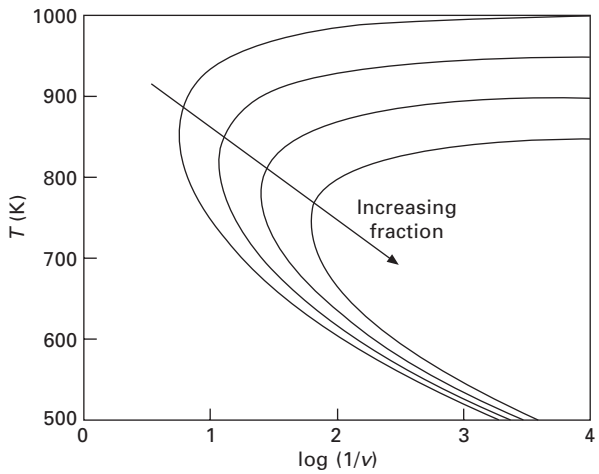
Pearlite is known to form by a cooperative process where the two new phases grow side by side and form more or less well-defined lamellae. Nucleation occurs at austenite grain boundaries and, after cooperation between the two new phases has been established, growth under isothermal conditions takes place under constant rate and coarseness of the lamellar microstructure. The growth rate is believed to be controlled primarily by the rate of carbon diffusion and, hence, on a driving force that is related to the difference in the carbon content between the two interfaces, austenite/ferrite and austenite/cementite. That difference starts from zero at the eutectoid equilibrium temperature, 1000 K. The driving force may thus be roughly proportional to 1000 – T. The slope of the asymptote at low temperatures may represent the activation energy of carbon diffusion in the austenite, the ferrite or the pearlite/austenite interface, depending on the predominant diffusion path. Curves for larger fractions of pearlite should be very similar but displaced towards longer times. All the curves have the same horizontal asymptote at 1000 K. This is illustrated in Fig. 13.2 where a linear temperature scale has been used. Such transformation curves are called C curves.

A typical set of C curves for proeutectoid ferrite, which grows under rejection of carbon into the parent austenite, is quite different. Figure 13.3 illustrates C curves for various fractions of proeutectoid ferrite in a eutectoid Fe-C alloy. Contrary to pearlite, the horizontal asymptote here depends on the volume fraction transformed. Any particular fraction of ferrite should have a horizontal asymptote at a temperature where the equilibrium phase diagram predicts that fraction of ferrite. This diagram may serve as a guideline for the construction of C curves for bainite, in particular for upper bainite

© Woodhead Publishing Limited, 2012



13.2 Schematic TTT diagram with C curves representing different volume fractions of pearlite.

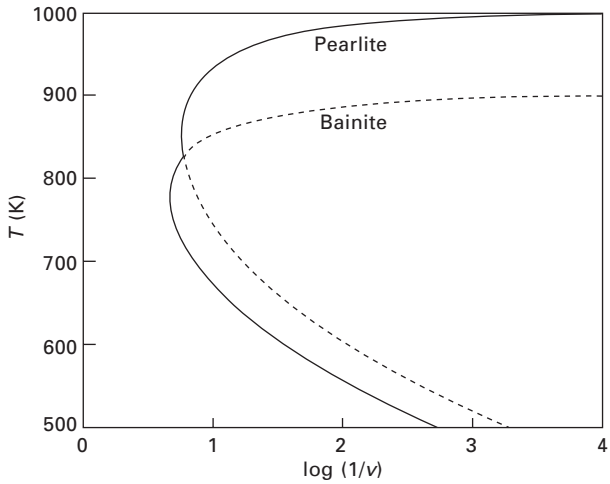


13.3 Schematic TTT diagram with C curves representing different volume fractions of proeutectoid ferrite.

in which the initial formation of ferrite is most pronounced. Of course, it will usually be followed by the formation of cementite, which will have a decisive influence on the progress of the transformation.

Naturally, a TTT diagram should show how various microstructures can occur in competition with each other. Each transformation is generally delayed by the competition and the modelled curves should thus be modified behind their intersection. See Fig. 13.4 where those parts have been continued with

© Woodhead Publishing Limited, 2012



13.4 Schematic TTT diagram with C curves for the beginning of the pearlitic and bainitic transformations when they have different upper temperature limits.

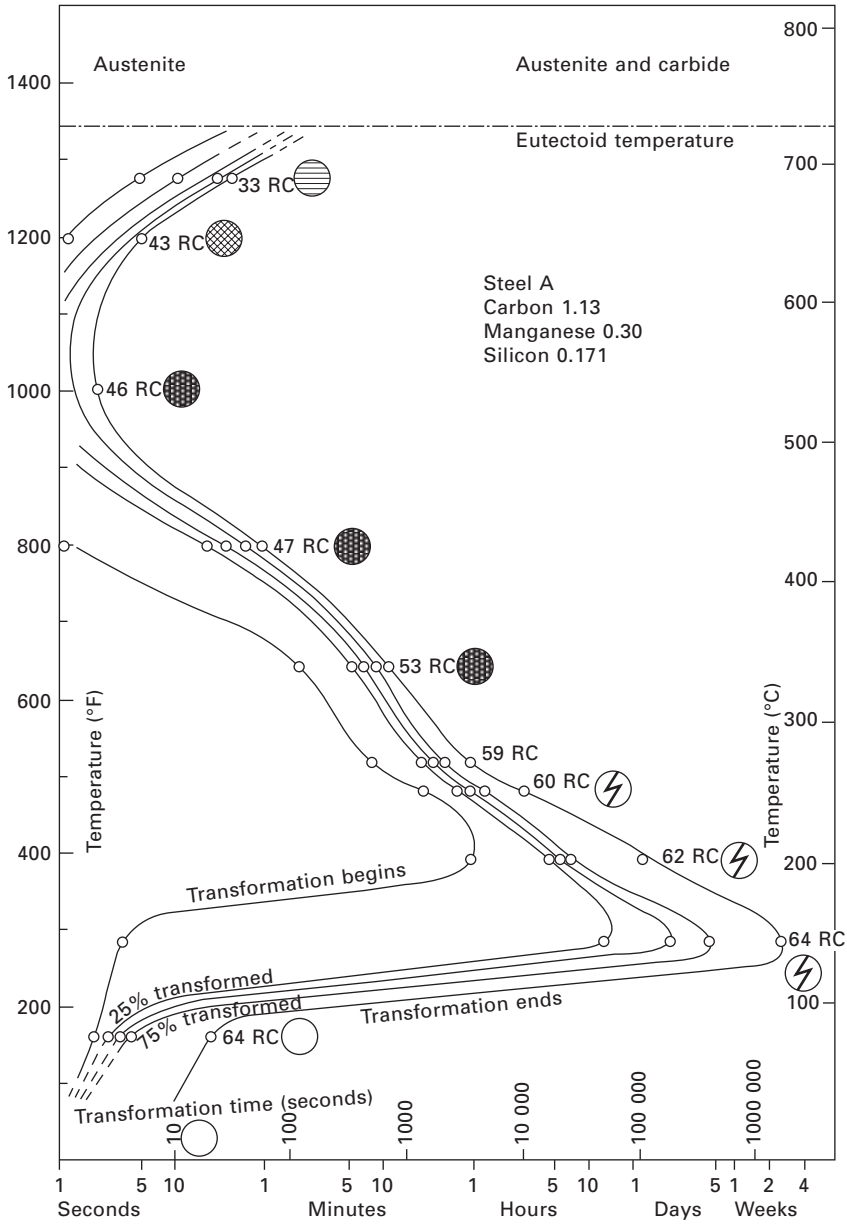
dashed lines to indicate that they should be modified. The transformations may compete for favourable nucleation sites but, for simplicity, it may be assumed that one kind of transformation is not affected by the progress of another transformation until a substantial fraction of the volume has been transformed. In order to make the curves in Fig. 13.4 intersect, the horizontal asymptote of bainite was supposed to fall well below 1000 K. That would happen in steels with hypereutectoid compositions.

Following this theory, it may be emphasized that Widmanstätten ferrite and bainite should each have their own set of C curves according to the diffusionless hypothesis because it is based on the assumption that acicular ferrite grows under diffusion of carbon for Widmanstätten ferrite but without diffusion for bainitic ferrite. According to the diffusional hypothesis, there should be only one kind of acicular ferrite and one set of C curves before cementite appears.

13.2.2 Examples of actual TTT diagrams

Davenport and Bain (1930) were the first to use TTT diagrams and one of their original diagrams is reproduced in Fig. 13.5. Their curves represented the total volume fraction of transformation products but symbols were used to identify the various products. They did not try to draw separate curves for pearlite and bainite. In low-alloy steels both transformations should occur simultaneously in an appreciable range of temperatures. The fast growing product at low temperatures was martensite and it should be realized that

© Woodhead Publishing Limited, 2012



13.5 One of the original TTT diagrams by Davenport and Bain (1930).

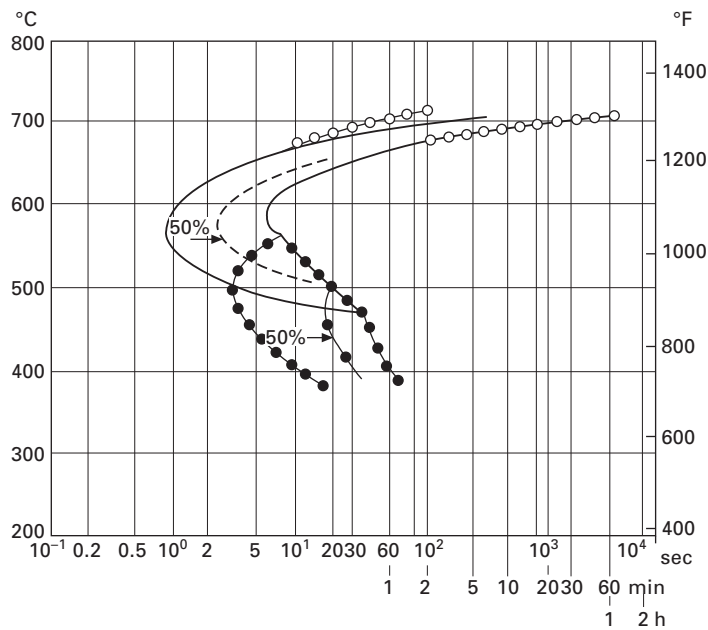
those authors were not aware of the fact that martensite forms athermally and does not progress with time. In modern TTT diagrams, the curves representing various fractions of martensite are horizontal lines.

Many TTT diagrams are based on continuous measurements of some

© Woodhead Publishing Limited, 2012

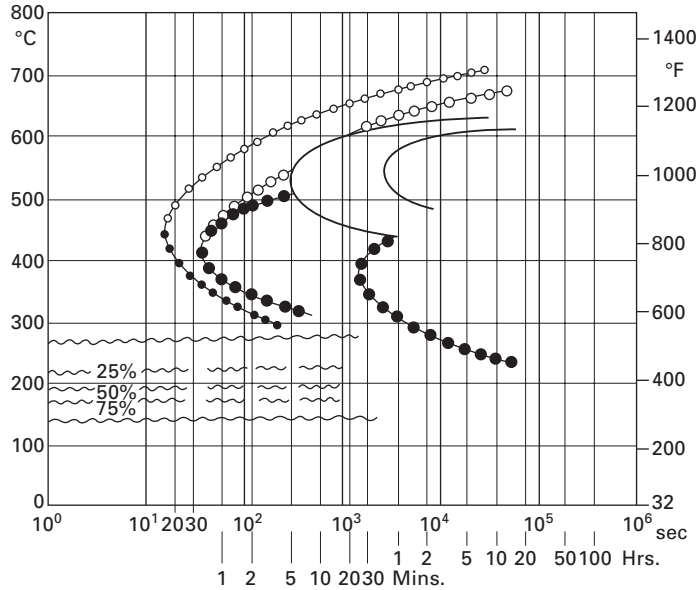
physical quantity and they are published without identifying the various transformation products by microscopic examination. However, TTT diagrams with individual C curves for various transformation products are available. Figure 13.6 from Hultgren *et al*. (1953) is an example with C curves for proeutectoid ferrite, pearlite and bainite. C curves are given for 1 and 50 vol% of the transformation products and finally for the end of the transformation of austenite. The diagram does not distinguish between allotriomorphic ferrite and Widmanstätten ferrite but the latter certainly dominates more as the temperature is lowered.

Figure 13.7 is an earlier example from Hultgren (1947). For the start of the transformations, Hultgren here plotted a common curve and indicated that it represented ferrite above the nose and bainite below the nose. This diagram is particularly interesting because it illustrates a close relation between the lower part of the C curve for 50% ferrite, i.e. certainly Widmanstätten ferrite, and the corresponding C curve for bainite. Down to the nose he gave separate curves for 50% transformation, probably to indicate that it takes longer for the cementite constituent to appear than for ferrite. In agreement with the definition of bainite as a eutectoid microstructure, he did not identify a microstructure as bainite until it was composed of both phases. From



13.6 TTT diagram by Hultgren (1951) showing separate C curves for pearlite (plain lines), Widmanstätten ferrite (lines with open circles) and bainite (lines with filled circles) in a steel with 0.68 C, 0.22 Si, and 0.34 Mn, in mass%. Reprinted with permission from Jernkontoret, Sweden.

© Woodhead Publishing Limited, 2012



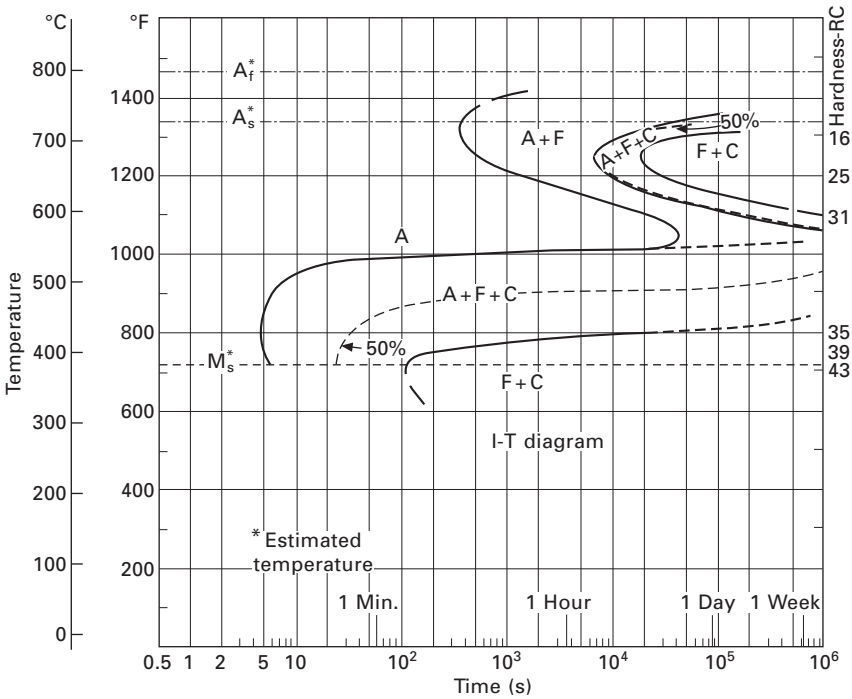
13.7 TTT diagram by Hultgren (1947) showing one continuous curve for start of Widmanstätten ferrite and bainite in a steel with 0.52 C and 3.23 Mn, in mass%. Plain lines represent pearlite, lines with open circles Widmanstätten ferrite and filled circles bainite. Reprinted with permission of ASM International. All rights reserved. www.asminternational.org

published micrographs it is evident that Hultgren observed how a group of parallel Widmanstätten plates transformed to upper bainite by the appearance of cementite and that is why he did not believe in a difference between two kinds of acicular ferrite.

Accepting the diffusionless hypothesis, one would probably have identified the ferrite up to at least 500°C as bainitic ferrite and thus consider Hultgren's curves for ferrite as representing bainite. In that range of temperature one would probably not have shown his curves for bainite. At higher temperatures there would be a problem of selecting the transition between the starts of bainite and Widmanstätten ferrite. Presumably, one would have to find a sharp change of the substructure which Oblak and Hehemann (1967) suggested should reveal subunits characteristic of bainite. That would require examination by transmission electron micrography (TEM).

Figure 13.8 is from a steel alloyed with Cr, Mo and V and it has two groups of C curves (Vander Voort, 1991). The first curve in the upper group is for proeutectoid ferrite and not yet transformed austenite (A+F) and the last curve is for pearlite (F+C). The lower group is for bainite and not yet transformed austenite (A+F+C) and for 100% bainite (F+C), respectively. Whether the proeutectoid ferrite in the high temperature region is Widmanstätten ferrite or

© Woodhead Publishing Limited, 2012



13.8 TTT diagram for a commercial steel with C curves for pearlite and bainite with a bay in between in a steel with 0.27 C, 0.84 Mn, 0.60 Ni, 0.73 Cr, 0.9 Mo and 0.11 V, in mass% (Vander Voort, 1991). Reprinted with permission of ASM International. All rights reserved. www.asminternational.org

grain boundary allotriomorphic ferrite or a mixture of them is not indicated and the answer may vary with the temperature. This may be a case where there are separate C curves for Widmanstätten ferrite and bainite and it could then be used as an argument for a difference between the two kinds of acicular ferrite in accordance with the diffusionless hypothesis. This question will again be discussed in Section 13.5 on the effects of alloying elements.

13.3 Nucleation and growth of bainite

13.3.1 Nucleation

Each C curve only represents a particular overall fraction of a transformation product without consideration of its distribution in the volume. The time to form that fraction at any particular temperature is a complicated result of nucleation and growth processes and both are usually too complicated to be modelled without assumptions and serious approximations. As an example,

© Woodhead Publishing Limited, 2012

there are fairly strict theories about so-called homogeneous nucleation but the main transformations in steel are nucleated at preferred sites that have different potency. The most potent sites are situated at austenite grain corners, edges and boundaries. Growth is also preferred along grain edges and boundaries, although most of the growth must eventually occur into the interior of the grains. The effects of various nucleation events will thus be different. Here we will only discuss specific details of this complicated reality.

A transformation cannot start without nucleation and, in order to learn something about the nucleation process, Bhadeshia (1981) evaluated the available chemical driving force at the start of bainite formation, B_S, in a large number of steels. He plotted the results versus the start temperature and found that all the data could be fairly well represented by a single straight line when the driving force had been evaluated from the decrease of Gibbs energy for one mole of ferrite with the equilibrium carbon content. This was not possible when the driving force had been evaluated for the diffusionless formation of a nucleus of ferrite, i.e., a nucleus with the same carbon content as the parent austenite. The scatter was too large. It was thus proposed that the nucleus of bainitic ferrite forms under diffusion of carbon. It was further found that the evaluated driving force under the diffusionless conditions was negative for some of the alloys which should imply that diffusionless growth is not possible. It was thus concluded that the reported B_S temperatures of some of the steels must have concerned the start of Widmanstätten ferrite, which has a higher driving force due to the diffusional growth mechanism.

Since Bhadeshia had been able to represent all the data with a single line in the first diagram, he regarded the line as representing a universal nucleation function, valid for both Widmanstätten ferrite and bainitic ferrite. It should then represent a barrier for nucleation of acicular ferrite under diffusion of carbon. However, only four of the 45 steels had a driving force larger than the assumed barrier for growth of bainite, which he estimated to be 400 J mol^{-1}. Only a few of the steels could thus have transformed to bainite if the diffusionless hypothesis applies. But there is an alternative conclusion. Rather than indicating that all the acicular ferrite had nucleated with the same mechanism, it seems that the data could indicate that it is the mechanism of growth that is the same and the thermodynamic results prove that it must then be diffusional growth. In this case it seems that the diffusionless hypothesis does not apply to bainite but it is the barrier for diffusional growth that has caused the single straight line in Bhadeshia's diagram.

Nevertheless, accepting that all kinds of acicular ferrite nucleate with the same mechanism made it necessary to provide an explanation of how bainite and Widmanstätten ferrite can have different start temperatures. Bhadeshia (1981) emphasized that one should not be able to observe a microstructure unless the driving force is sufficient for nucleation as well as growth and the growth conditions are different for the two kinds of acicular ferrite. He

© Woodhead Publishing Limited, 2012

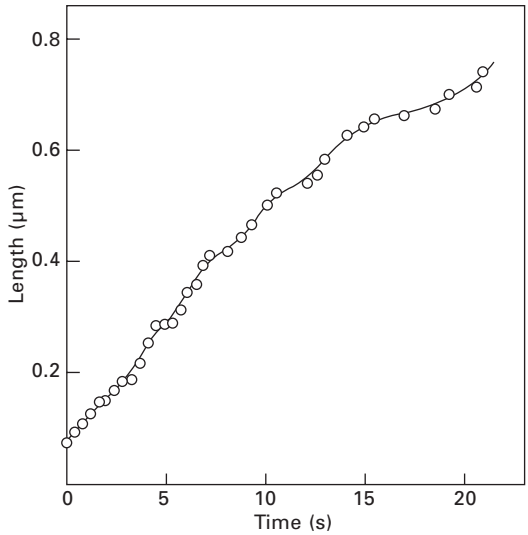
thus evaluated possible barriers for growth by estimating the stored energy caused by the transformation strains, obtaining 50 J mol^{-1} for Widmanstätten ferrite and, as already mentioned, 400 J mol^{-1} for bainitic ferrite. If the conditions for nucleation and growth are satisfied for both kinds of acicular ferrite, then diffusionless growth should predominate, i.e. bainitic ferrite should form because of its higher growth rate. If a nucleus would then start to grow under diffusion, the growth should spontaneously develop into the diffusionless mode. It was concluded that Widmanstätten ferrite would never form in a steel if the driving force for diffusionless growth is sufficient when nucleation starts. If it is not sufficient but the driving force for diffusional growth is, then Widmanstätten ferrite could form and that would happen down to the temperature where the driving force for diffusionless growth is large enough, the B_S temperature. Below that temperature, Widmanstätten ferrite could never form. With this reasoning it was possible to maintain the ideas of different growth mechanisms and different start temperatures, B_S and W_S. On the other hand, it is not evident how one should explain why the diffusionless growth of bainitic ferrite, when it is stopped by the gradually increasing carbon content in the remaining austenite during isothermal treatment, does not continue as diffusional growth which should yield Widmanstätten ferrite.

13.3.2 Lengthwise growth of plates

The lengthening rate of acicular ferrite illustrates the difference between the two hypotheses. It was expected to be very much higher than observed experimentally if it is controlled by the diffusionless mechanism. This discrepancy was explained by Oblak and Hehemann (1967) through the suggestion that diffusionless growth will build up strains that eventually will stop the growth and the result will be only a subunit. Further growth will have to wait for a new nucleation event. The rate controlling factor should then be the rate of nucleation of new subunits and their final lengths, not the very high growth rate of each subunit. The subunits have been identified with a substructure observed by electron microscopy of thin foils. Different estimates have been made and it has, for instance, been mentioned that a typical size of a subunit may be $0.2 \times 10 \times 10\ \mu m^3$ (Bhadeshia and Waugh, 1982). Smaller sizes have also been reported. However, alternative observations have also been made. Figure 13.9 reproduces an *in-situ* observation of gradual growth of bainite made by Nemoto (1974) using TEM. The data show that, if there had been a succession of rapidly growing steps, their lengths must have been less than 0.1 μm which is much shorter than expected. This may be taken as an indication that stepwise growth does not occur.

Growth rate equations have been proposed for both hypotheses. For the diffusionless hypothesis, expressions have been suggested that have two

© Woodhead Publishing Limited, 2012



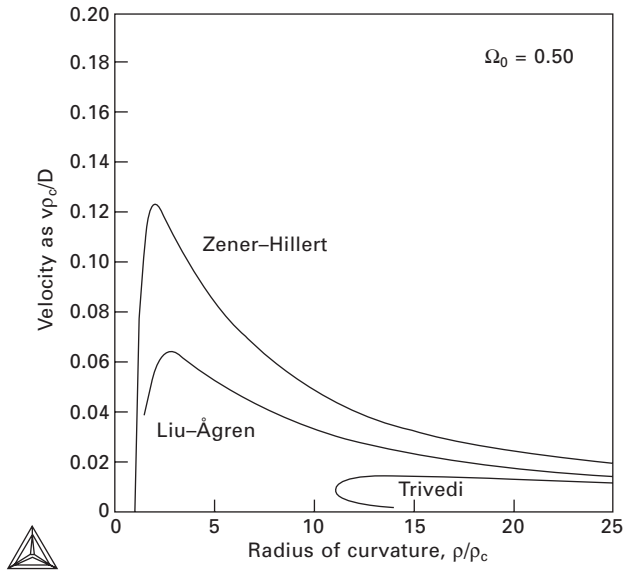
13.9 Measured length of bainite at 380°C as a function of time by Nemoto (1974) showing that the growth of bainite is continuous in a steel with 0.51 mass%C and 9.1 mass% Ni.

or three fitting parameters, one governing the rate of nucleation of a new subunit at the tip of the preceding one and another representing the length of the subunits (e.g. Matsuda and Bhadeshia, 2004). It can thus be used for representing experimental data after fitting the parameter values to selected experimental information on growth rates. From the diffusional hypothesis, expressions have been derived for the edgewise growth rate of a plate based on the rate of diffusion of carbon in austenite and with various degrees of sophistication (Zener, 1946; Hillert, 1957; Trivedi, 1970; Liu and Ågren, 1989). These were recently compared (Hillert *et al.*, 2003) and objections were raised against the treatment by Trivedi. The comparison is illustrated in Fig. 13.10 and it is demonstrated that the sharpness of the edge, expressed as a radius of curvature, ρ, is not defined in any of the treatments. Hillert (1960) obtained an equation of the following form by modifying Zener's equation and applying Zener's criterion of maximum growth rate,

$$v_{\max} = \frac{RTD(x_{eq}^{\gamma/\alpha} - x^{\gamma o})^2}{8\sigma V_m^{\alpha}(x^{\gamma o} - x^{\alpha})} \cong \frac{RTD(x_{eq}^{\gamma/\alpha} - x^{\gamma o})^2}{8\sigma V_m^{\alpha} x^{\gamma o}} \qquad [13.2]$$

where D is the diffusion coefficient for carbon in austenite, σ is the specific interfacial energy, V_m^{α} is molar volume of ferrite and x represents the various mole fractions of carbon and, in particular, $x^{\gamma o}$ is the initial carbon content.

© Woodhead Publishing Limited, 2012



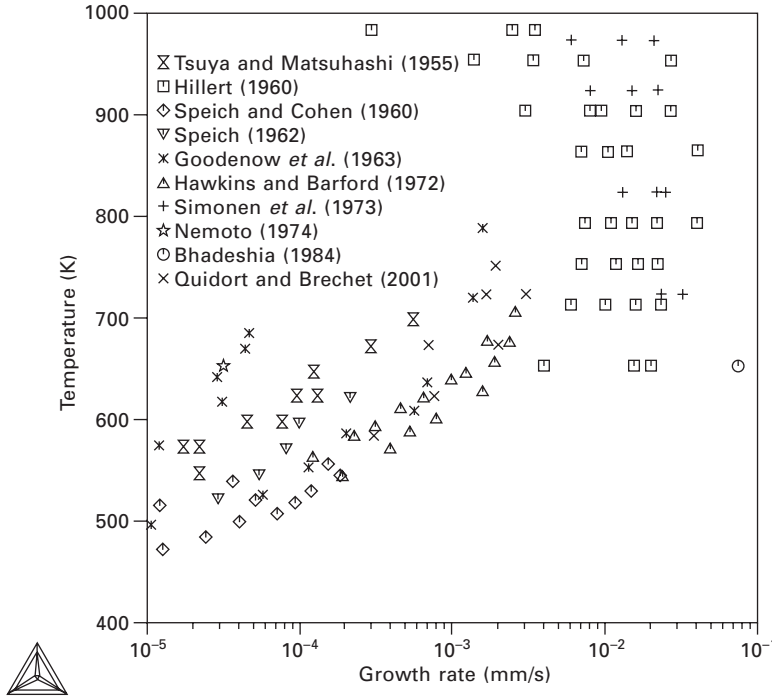
13.10 Lengthening rate at a supersaturation of Ω = 0.5 according to three different treatments (Hillert *et al.*, 2003).

13.3.3 Experimental lengthening of Widmanstätten ferrite and bainite

The lengthening rate of bainite and acicular ferrite has been measured in several studies (see Fig. 13.11). Tsuya and Mitsuhashi (1955) measured the growth rate of bainite in some steels using hot stage microscopy, observing that the surface relief revealed gradual growth of bainite. The same technique was used by Speich and Cohen (1960), Speich (1962), Goodenow *et al.* (1963), Yada and Ooka (1967) and Hawkins and Barford (1972). Hillert (1960) determined lengthening rates of acicular microstructures from 700 down to 380°C going from Widmanstätten ferrite down to lower bainite. The rates were determined by measuring the length of the plates after different isothermal holding times. The same technique was used by Simonen *et al.* (1973) and by Quidort and Brechet (2001) in a more recent study. These results are similar to those obtained using hot stage microscopy.

The high temperature data in Fig. 13.11 concern Widmanstätten ferrite and the rest concerns upper or lower bainite, but the boundary depends on alloying elements, in particular Si and Al. The majority of the publications concern the temperature dependence of a single alloy and each set of such data can be reasonably well represented by a smooth curve. They are fairly parallel with each other but displaced horizontally due to different compositions. It is to be expected that the carbon content has a major effect. Hillert studied a series of plain carbon steels with 0.21 to 0.81 mass% C. His data are probably

© Woodhead Publishing Limited, 2012



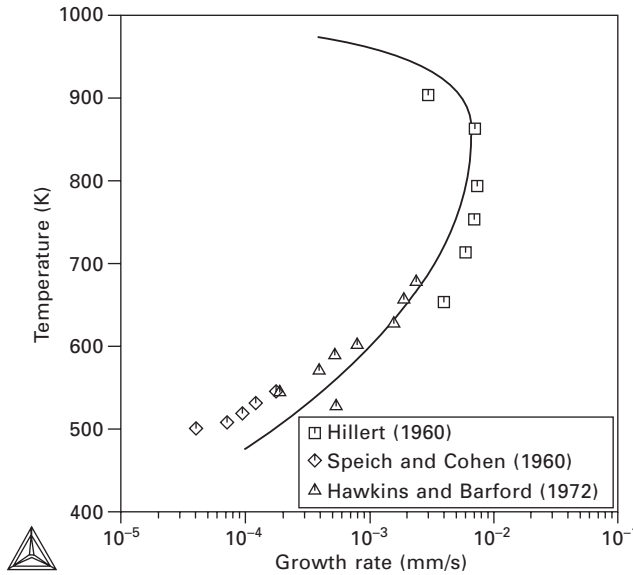
13.11 Experimental edgewise growth rates of Widmanstätten ferrite or bainite in some steels as a function of temperature.

less accurate but he could demonstrate the dependence of the carbon content by combining the information from each temperature.

In order to demonstrate the temperature dependence in a wider range of temperatures, Fig. 13.12 includes information on a plain carbon steel with 0.81 mass% C (Hillert, 1960) and Fe-C alloys with 0.96 and 0.91 mass% C, respectively (Speich and Cohen, 1960; Hawkins and Barford, 1972). This diagram covers the whole range of microstructures from Widmanstätten ferrite to lower bainite. It seems possible to describe all this information fairly well with a common C curve, which is inverted in comparison with previous C curves because growth data are here plotted as rate instead of time of transformation. Expressed in this way, the data set is not inconsistent with the idea that there is no main difference between Widmanstätten ferrite and the primary stage of bainite formation.

The diffusionless hypothesis can be tested in this way because it does not seem to have any predictive capacity for lengthening rates. It contains fitting parameters which have to be evaluated for agreement with a selected set of experimental growth rates. On the other hand, the diffusional hypothesis should be capable of predicting lengthening rates from basic information, although there are severe uncertainties. Accepting that Eq. [13.2] has been

© Woodhead Publishing Limited, 2012

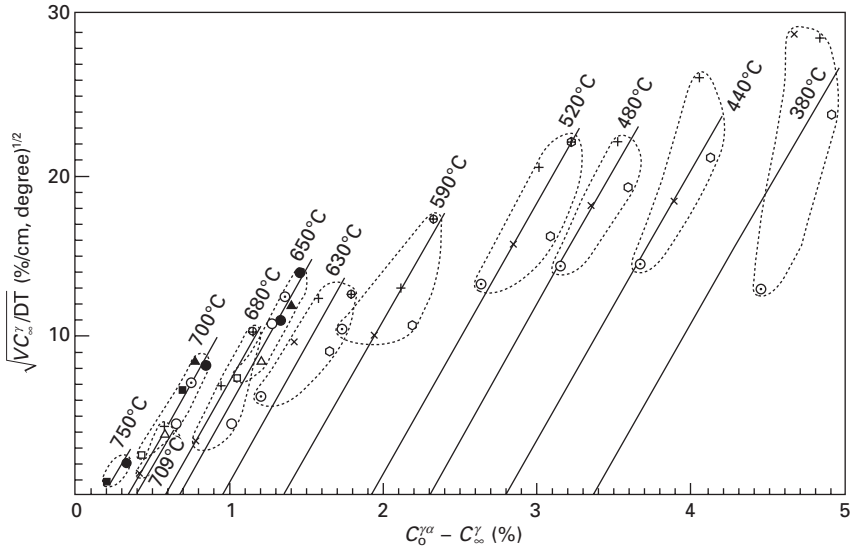


13.12 Experimental edgewise growth rate, in steels with about 0.85 mass% C, as a function of temperature showing a continuous change going from bainite to Widmanstätten ferrite at high temperatures. A calculated line using Eq. 12.2 is included.

derived with several approximations, it will now be applied to examine the experimental results compiled in Fig. 13.12.

Several uncertainties are connected to the interfacial energy. In the more ambitious derivations mentioned above, it was assumed that the specific interfacial energy is constant around the whole interface. However, the flatter sides should really have lower specific interfacial energy than the curved edge because the plate is supposed to be somewhat coherent with the parent austenite along the sides. That should give particularly good atomic matching along the sides of the plate but not so much at the edge. This effect should severely influence the shape of the edge. Rather than being parabolic, it may be abruptly truncated or have a very sharp edge like a knife if both sides can deviate somewhat from the direction of ideal matching without the specific interfacial energy increasing too much. In any case, since it is the specific interfacial energy of the sides that puts the material just inside the edge under an increased pressure, it seems reasonable to use that energy in Eq. [13.2]. Unfortunately, there is no reliable information of this kind and instead Hillert (1960) attempted to evaluate the effective interfacial energy from his growth rate data by applying Eq. [13.2]. The evaluation is illustrated by Fig. 13.13 where he fitted straight lines to his data for each temperature, making them parallel for all temperatures assuming that the interfacial energy is independent of temperature. From the slope he obtained

© Woodhead Publishing Limited, 2012



13.13 Lengthening rates by Hillert (1960) plotted as $\sqrt{vc^{\gamma o}/DT}$ versus $c_{eq}^{\gamma/\alpha} - c^{\gamma o}$. Each line was supposed to represent the data from the given temperature but were drawn under the constraint that they should be parallel. The slope represents the specific surface energy.

the specific interfacial energy as 0.23 J m^{-2}, which may seem a reasonable value for a phase interface with a coherent character. That value will be used here.

Another problem is connected to the diffusion coefficient of carbon in austenite which is known to vary strongly with the carbon content. Trivedi and Pound (1967) considered a somewhat similar case and proposed that one should use an efficient value that is regarded as constant. It is defined as

$$D = \int_{x^{\gamma o}}^{x^{\gamma/\alpha}} D\,\mathrm{d}x/(x^{\gamma/\alpha} - x^{\gamma o}) \qquad [13.3]$$

Yet another important problem is revealed by the parallel lines in Fig. 13.13 which, when extrapolated to zero growth rate, do not give the ferrite/austenite equilibrium carbon content. Hillert concluded that the growing acicular ferrite, being highly coherent with the parent austenite, is not under full local equilibrium with austenite and from the intersections with the abscissa in Fig. 13.13 he evaluated an energy barrier for growth, finding that it varied with temperature. It may be mentioned here that it is a common observation and a generally accepted fact that the broad sides of Widmanstätten plates are highly immobile. The magnitude of Hillert's barrier for edgewise growth

© Woodhead Publishing Limited, 2012

has more recently been reassessed (Hillert *et al.*, 2004) as described in the next section.

One may also mention the uncertain role of diffusion of carbon through the ferrite from the edge to the austenite at the sides of the plate. Considering all uncertainties, it is natural to raise doubts about the predictive capacity of the growth equations for the diffusional hypothesis. Nonetheless, a C curve for a carbon content of 0.85 mass% was calculated from Eq. [13.2] using an interfacial energy of 0.23 J m^{-2}, the reassessed barrier and diffusion data for carbon in austenite from the MOB2 database in the DICTRA software (Andersson *et al.*, 2002). The result is included in Fig. 13.12 and the curve has a shape that reflects all the data in Fig. 13.12 rather well. Considering the wide temperature range, this is a result that may be taken as support for the diffusional hypothesis, because it implies that there is no difference between Widmanstätten ferrite and bainitic ferrite. But it should be emphasized that the reasonable fit to the information from Hillert (1960) is natural because the specific interfacial energy was fitted to that piece of information.

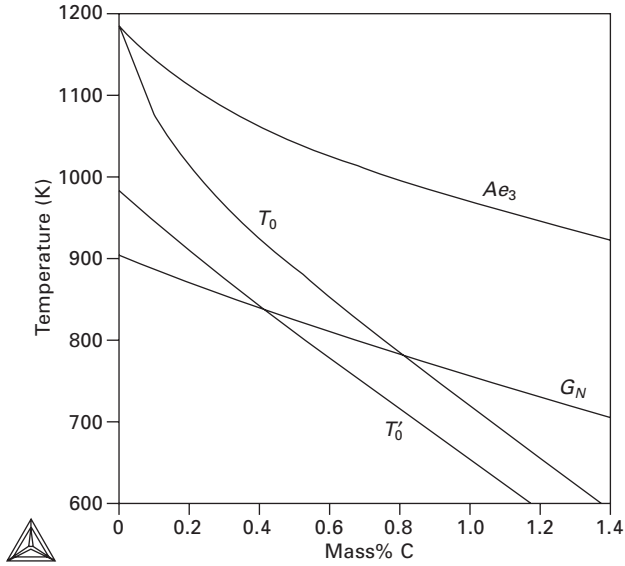
It should be noted that there is a single experimental point in Fig. 13.11 that falls at a higher growth rate than would be expected from the rest of the points. It was obtained by Bhadeshia (1984) at 380°C for a steel containing 0.43 C, 2.02 Si, 3 Mn, all in mass%. It represents a growth rate that is four times higher than the closest point at similar temperatures, which is for a steel with 0.42 C, 0.08 Si, 0.28 Mn, all in mass%. It has been argued that the growth rate obtained in this experiment is many orders of magnitude higher than the diffusional hypothesis can account for (Bhadeshia, 2001). It is worthwhile mentioning, however, that this result may be due to the use of Trivedi's (1970) growth equation. In any case, the primary concern should be the difference of this growth rate from what could be expected from other information in Fig. 13.11.

13.4 Start temperature of bainite

13.4.1 Prediction of the start temperature for bainite formation in Fe-C alloys

In order to overcome the barrier for growth of bainite, it is necessary to cool the austenite down to a temperature where the driving force for the austenite transformation to ferrite is larger than this barrier. From the barrier for growth one can thus predict a critical line in the Fe-C phase diagram inside which the thermodynamic properties make the transformation to bainite possible. Bhadeshia (1981) presented such a prediction based on the suggestion by Zener (1946) of diffusionless growth of bainitic ferrite. The thermodynamic evaluation itself yields the so-called T_o line where austenite and ferrite of the same composition have the same Gibbs energy (Fig. 13.14). The driving

© Woodhead Publishing Limited, 2012



13.14 Schematic diagram of barriers for the formation of bainitic ferrite according to the diffusionless hypothesis. B_s is predicted to be controlled by nucleation above the intersection of G_N and T'_o and by growth below that point.

force for the diffusionless transformation to bainite does not turn positive until below that line. Since Bhadeshia had estimated that a barrier of 400 J mol^{-1} must be overcome during growth (see Section 13.3.1), he calculated the line where the driving force would be of that magnitude. See the T_o' line in Fig. 13.14. According to the diffusionless hypothesis, it should represent the start of bainite formation, B_S, except for the possibility that the barrier for nucleation is higher. In order to predict B_S, it would thus be necessary also to plot the critical line for nucleation. For demonstration, a possible line for the nucleation barrier, G_N, was added to Fig. 13.14 and on each side of the intersection of the lines for T_o' and G_N one should accept the line that represents the lowest carbon content. B_S should thus depend on nucleation on one side of the intersection and on growth on the other side, and the B_S curve should thus be a broken line according to the diffusionless hypothesis. As explained in Section 13.3.1, the critical line for nucleation was based on information on B_S but it is now evident that only part of the B_S line can represent the barrier for nucleation and the remainder should not be used for evaluating the barrier for nucleation. There may be a practical problem to identify those steels and exclude them from the evaluation of the barrier.

Hillert *et al*. (2004) examined experimental information on the start of bainite and Widmanstätten ferrite in steels with supposedly small effects of alloying elements. In agreement with an earlier suggestion (Hillert, 1960)

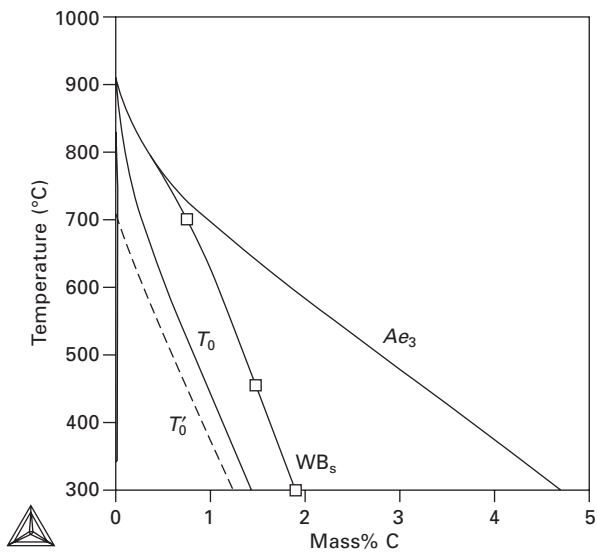
© Woodhead Publishing Limited, 2012

they assumed that there is a common line for the two acicular microstructures. Finally, they selected three pieces of experimental information and constructed a line through them using a spline function. See the three points and the WB_S line in Fig. 13.15. Admittedly, the exact position of this line may be questioned but, in principle, it represents experimental information and its distance from the predicted B_S as T_o' is huge. If these constructs have any substance then they raise an interesting question, although there is copious experimental evidence in support of the T_o' concept as applied to the bainite reaction in Fe-C alloys or plain carbon steels.

In the same way as the distance between T_o' and T_o is related to the assumed barrier for diffusionless growth, the distance between the WB_S line and the line for the ferrite/austenite equilibrium, Ae_3, should be related to the barrier for diffusional growth. The result is presented in Fig. 13.16. Line (a) is from a recent evaluation based on the WB_S line in Fig. 13.15 (Hillert *et al.*, 2004), line (d) is from the preceding evaluation (Hillert, 1960) and lines (b) and (c) are taken from Bhadeshia (1981, 2001) although, as mentioned in Section 13.3.1, it was instead proposed that those lines should represent a universal nucleation function.

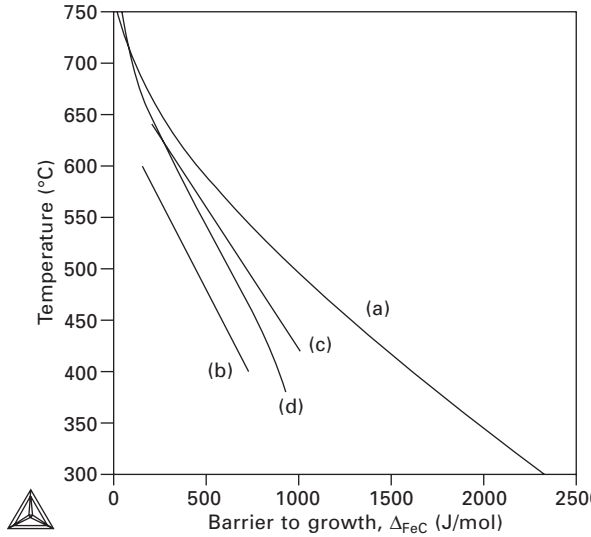
13.4.2 Second stage of transformation

Depending on the composition of the steel, there may be a high temperature region where Widmanstätten ferrite forms, sometimes observed as single



13.15 The Fe-C phase diagram with the WB_S, T_0 and T'_o lines included (from Hillert *et al.*, 2004).

© Woodhead Publishing Limited, 2012



13.16 Comparison of different estimates of the barrier for acicular growth of ferrite in Fe-C by Hillert *et al.* (2004). (a) is from Hillert *et al.* (2004), (b) is from Bhadeshia (1981), (c) is from Bhadeshia (2001) and (d) is from Hillert (1960).

plates inside the austenite grains. As the temperature is lowered, these plates seem to develop into so-called sheaves of ferrite and this has been explained as the result of repeated sympathetic nucleation of new plates starting from the first one (Aaronson and Wells, 1956). An alternative explanation is that the plates are outgrowths from the first plate, stimulated by cementite after it has appeared in the ferrite/austenite interface (Borgenstam *et al.*, 2009).

In any case, at longer times or at lower temperatures cementite may appear in the austenite enriched in carbon, either by the rejection of carbon from the supersaturated ferrite plates, according to the diffusionless hypothesis, or by carbon escaping from the moving ferrite/austenite interface, according to the diffusional hypothesis. A second stage of transformation will be initiated by the appearance of cementite on the sides of ferrite plates. According to the diffusional hypothesis, it will simply be transformed by simultaneous growth of cementite and ferrite and the result will be a mixture of ferrite and relatively coarse cementite. This complex microstructure is called upper bainite. It does not seem to be clearly stated whether the model based on the diffusionless hypothesis predicts that the ferritic constituent, which finally fills the gap between primary plates of ferrite, has formed by displacive and diffusionless growth or under diffusion of carbon.

Hillert (1957) pointed out that wider spaces between the primary plates may transform to a mixture that is somewhat organized and he proposed that this would gradually be more frequent and better organized at lower

© Woodhead Publishing Limited, 2012

temperatures. That could be how lower bainite forms. The primary plates of ferrite are then thinner and will be covered with a thickening layer of ferrite and cementite which grows with a cooperative mechanism, even somewhat resembling pearlite (Borgenstam *et al.*, 2009).

On the other hand, according to the diffusionless hypothesis lower bainite forms by precipitation of cementite inside the supersaturated ferrite, similar to what happens during the tempering of martensite. It is generally agreed that the fairly flat austenite/ferrite interfaces on the sides of ferrite plates are rather immobile, and Kinsman and Aaronson (1967) described how carbon could be rejected from supersaturated ferrite into the surrounding austenite without the austenite/ferrite interface moving. That was in accordance with Zener's (1946) original proposal in which he explained that the increasing carbon content of the remaining austenite should make further formation of bainite units more difficult and it should cease completely when the carbon content has increased to the T_o line at the experimental temperature. With a growth barrier 400 J mol^{-1}, the T_o' line should play that role as well as defining the condition for starting the bainite formation. On the other hand, the carbon content should approach the WB_S line according to the diffusional hypothesis. In both cases, the fraction of ferrite does not approach what is predicted by the lever rule based on the Ae_3 line. That phenomenon has been called 'stasis' by Reynolds *et al.* (1990b).

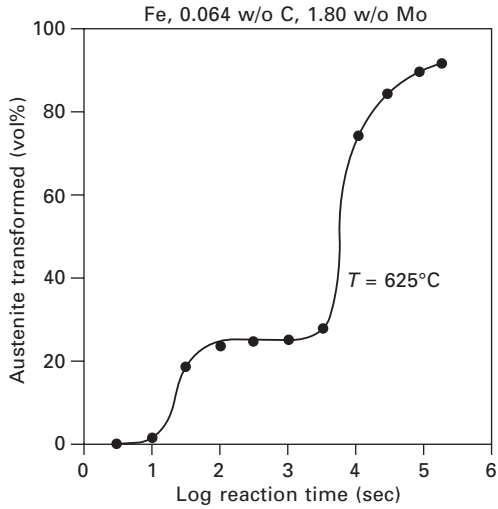
However, one should expect the transformation to continue to completion if the rejected carbon does not enrich the austenite but precipitates as cementite at the ferrite/austenite interface and initiates the growth of a mixture of ferrite and cementite, yielding the eutectoid microstructure called bainite. The stage before cementite has appeared may be regarded as incomplete reaction, or transformation to bainite if one includes carbide-free bainite in the definition of bainite, although it just consists of acicular ferrite and is the result of a proeutectoid reaction for which one must expect that the reaction terminates before 100% of the volume has been transformed. That was illustrated in Fig. 13.3. Sometimes the term stasis is used as synonymous with incomplete transformation (Reynolds *et al.*, 1990b).

Incomplete transformation has not been observed in pure Fe-C alloys, probably because cementite will appear too soon. Figure 13.17 from Reynolds *et al.* (1990a) is a typical example of the isothermal transformation curve displaying the so-called incomplete transformation to bainite in an alloyed steel.

13.4.3 The problem of defining B_S

In this connection, the uncertainty how to define bainite should be emphasized. According to the diffusional hypothesis, there is no difference between Widmanstätten ferrite and bainitic ferrite, whereas bainite is the final product

© Woodhead Publishing Limited, 2012



13.17 Diagram showing the degree of transformation as a function of time in an alloy with incomplete transformation (from Reynolds *et al.,* 1990a).

when the second step has completed the eutectoid transformation. One should then define only one temperature for the start of acicular ferrite and, possibly, a lower temperature for the start of bainite as a eutectoid microstructure. At low temperatures this does not create any practical difficulty because cementite appears soon after the acicular ferrite. However, for isothermal reaction below B_S one simply regards the primary plates of ferrite, protruding in front of the advancing bainite, as an indication that ferrite is the leading phase in bainite formation and it is thus considered as part of the bainite. On the other hand, at high temperatures there may be an appreciable time difference and above the eutectoid temperature, 1000 K in the pure Fe-C system, Widmanstätten ferrite may appear without ever being succeeded by cementite.

It should also be mentioned that there are at least two other definitions of bainite. One says that bainite is any non-lamellar eutectoid decomposition product (Aaronson, 1969) and another is based on the overall kinetics (Hehemann and Troiano, 1956). Reynolds *et al*. (1990b) referred the term bainite to 'the transformation product expected to follow the overall reaction kinetics definition: this product consists of ferrite with or without carbides but excludes pearlite'. It may also be mentioned that the metallographic terms of various microstructures in steel are based on optical microscopy. The only exception is that carbide-free bainite cannot be distinguished from Widmanstätten ferrite without the use of TEM.

Apart from the different methods of defining the B_S temperature, there is a practical problem of measuring it for a given steel. The observation of

© Woodhead Publishing Limited, 2012

at what temperature bainite appears requires a number of specimens heat treated with sufficiently close temperature intervals. Another possibility is to study the growth rate at a series of times or temperatures and to extrapolate to zero growth rate.

13.5 Effect of alloying elements

Experimental information on the effect of alloying elements on B_S has several times been compiled and described with analytical expressions. The most popular one is the expression by Steven and Haynes (1956):

$$B_S = 830 - 270\text{w\%C} - 90\text{w\%Mn} - 37\text{w\%Ni} - 70\text{w\%Cr} - 83\text{w\%Mo} \ (^\circ\text{C}) \quad [13.4]$$

where w% stands for mass% in the austenite. The coefficients were evaluated for the composition range; 0.1–0.55w%C, 0.1–0.35w%Si, 0.2–1.7w%Mn, 0.0–5.0w%Ni, 0.0–3.5w%Cr, 0.0–1.0w%Mo. This type of empirical relation, like similar empirical relations for M_S, is usually limited to rather small composition intervals. For this reason, it should be of considerable interest to have models based on physical principles as the ones based on the diffusional or diffusionless hypothesis. Only some aspects of the effects of alloying elements on the kinetics of bainite will now be discussed, but it should first be emphasized that any model for the effect of alloying elements should be based on a reasonable model for bainite in the binary Fe-C system. On the other hand, information from alloyed steels may help to clarify questions raised in the work with a binary model and justify modifications to it.

It was postulated by Hultgren (1947) and found by Kuo and Hultgren (1953) that the alloying elements do not partition between ferrite and cementite when bainite forms. Hultgren coined the term paraequilibrium for the local conditions at phase interfaces yielding this result. It implies that the alloy content, relative to Fe, is the same on both sides of the moving phase interface but there is local equilibrium for C. Today it is generally agreed that bainite forms under paraequilibrium, or without any diffusion according to the diffusionless hypothesis. One may then expect that the mechanism of bainite formation is not much affected by alloying elements. It is as if the Fe atoms were replaced by a new kind of element with different thermodynamic properties. The effect of alloying should thus be essentially thermodynamic. Two thermodynamic consequences will now be discussed.

According to Kuo and Hultgren (1953), the cementite constituent of bainite will gradually lose its Si content to ferrite under prolonged heat treatments, and it is generally accepted that the equilibrium contents of both Si and Al in cementite are very low. It is thus evident that paracementite with its higher contents of Si and Al must have considerably higher Gibbs energy

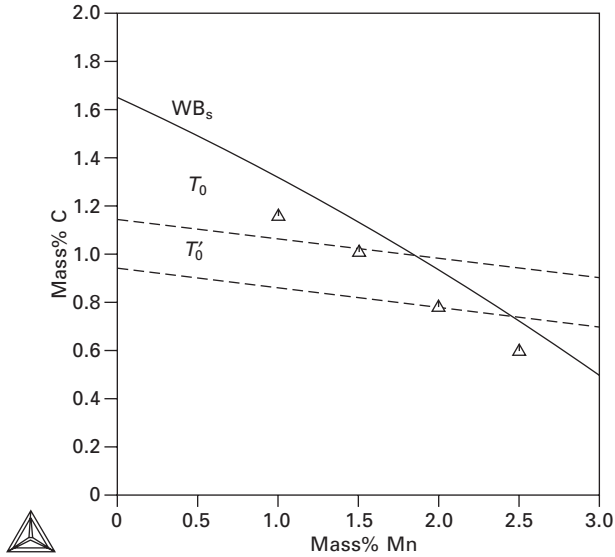
© Woodhead Publishing Limited, 2012

than cementite under full equilibrium. The tendency to form cementite is thus decreased by the addition of Al or Si to a steel and with sufficient contents it is possible to prevent the formation of cementite completely. The result is often regarded as carbide-free bainite. Of course, it is just a proeutectoid precipitate of acicular ferrite. Whether it will be regarded as Widmanstätten ferrite or bainitic ferrite depends on whether the diffusional or diffusionless hypothesis is accepted. In reality it makes no difference because in both cases it is assumed that most of the carbon will eventually be partitioned to the remaining austenite where it suppresses the martensitic transformation on cooling to room temperature. This microstructure of fine, acicular ferrite and retained austenite gives the steel very useful mechanical properties and is the basis of new TRIP (transformation induced plasticity) sheet steels (DeCooman, 2002). Lower contents of Al and Si will only delay the formation of cementite and will then contribute to the kind of transformation curve illustrated in Fig. 13.17. That is an example of a temporarily incomplete transformation where the carbide particles do not appear until after prolonged heat treatment. The plateau represents the completion of the formation of so-called carbide-free bainite. Since no more carbide-free bainite can form in the remaining austenite, one can apply the carbon content in the austenite at the plateau in combination with the heat treatment temperature to define a point on the B_S or WB_S line, depending on which hypothesis one accepts. That carbon content is easily found by applying the lever rule to the volume fraction of ferrite on the plateau. This is one way of determining the B_S or WB_S temperature experimentally, and it will apply to a steel with that carbon content and the initial alloy content.

The effect of alloying elements on the bainite start temperature is of considerable technical importance and it was analysed by Hillert *et al.* (2004) based on binary models. As an example, Fig. 13.18 illustrates the effect of Mn at 400°C. Experimental results (Usui *et al.*, 1990) are compared with thermodynamic predictions from the two hypotheses. The predicted WB_S line has the same slope as a line drawn through the experimental data and it may be concluded that the diffusional hypothesis can predict the effect of Mn, although there is a slight parallel displacement. The predicted T_o' line is fairly independent of the Mn content and it seems that the diffusionless hypothesis cannot explain the effect of Mn. It is interesting that the predicted T_o' line approaches the experimental data as Mn is added to the Fe-C system and at about 2 mass% Mn there seems to be reasonable agreement. It appears that two shortcomings of the diffusionless hypothesis, the incorrect predictions for the pure Fe-C system and the prediction of a weak effect of the Mn content, happen to compensate each other at about 2 mass% Mn.

When Hillert (1960) introduced the barrier for growth, he treated it as dependent of temperature, evidently assuming that it was independent of the carbon content. When Bhadeshia (1981) proposed a barrier for nucleation, the

© Woodhead Publishing Limited, 2012

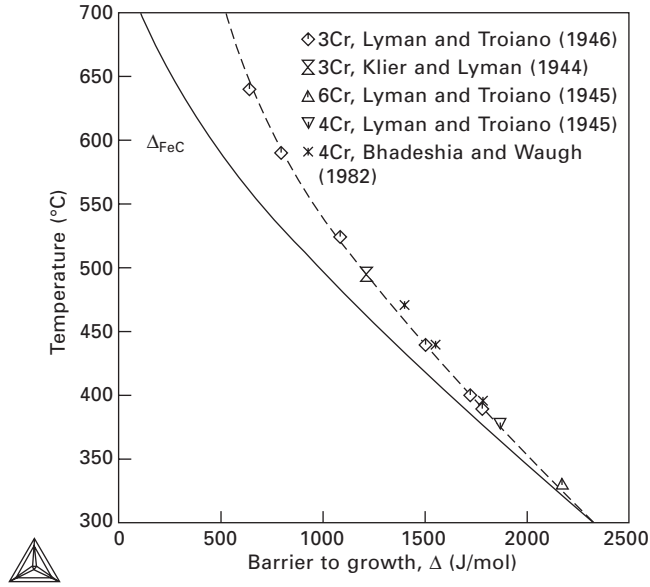


13.18 The effect of Mn on the critical carbon content of bainite at 400°C for steels with 1.5% Si. The WB_s, T_o and T'_o lines are included. From Hillert *et al.* (2004). Experimental information by Usui *et al.* (1990).

universal nucleation function, he also assumed that it should be a function of temperature and independent of composition. It has here been interpreted as a barrier for growth and was thus included in Fig. 13.16. Furthermore, Bhadeshia treated his barriers for growth as independent of composition. When Hillert's analysis was revised (Hillert *et al.*, 2004) the independence of the carbon content was still accepted and applied when the effect of Mn was analysed. The successful result may be taken as an indication that the barrier is also independent of the Mn content. However, when the experimental information on Cr and Mo was analysed, it was found that the barrier increased with the alloy content. Figure 13.19 shows the evaluated effect for 3 mass% Cr and the effect of Mo was similar. The quantity Δ_{FeC} represents the barrier for the Fe-C system which yielded the WB_S line in Fig. 13.15. It was then proposed that carbide-forming elements may have an effect that is proportional to the content and it was suggested that the effect is due to some solute drag effect but no specific mechanism was presented. A similar 'impurity drag effect' was proposed by Kinsman and Aaronson (1967) and Aaronson (1969). It is now known as solute drag-like effect (SDLE) (Reynolds *et al.*, 1990b).

Hillert *et al.* (2004) discussed the possibility that the proposed solute drag effect of strong carbide formers, which was illustrated for Cr in Fig. 13.19, may decrease at higher temperatures, which may give rise to a second C

© Woodhead Publishing Limited, 2012



13.19 The evaluated barrier for acicular growth of ferrite with 3 mass% Cr. Δ_{FeC} represents the driving force for the Fe-C system (from Hillert *et al.*, 2004).

curve for Widmanstätten ferrite at high temperatures. That possibility should be considered in connection with TTT diagrams with a bay between two separated regions of rapid reactions as in Fig. 13.8.

13.6 Overall kinetics

13.6.1 TTT and CCT diagrams

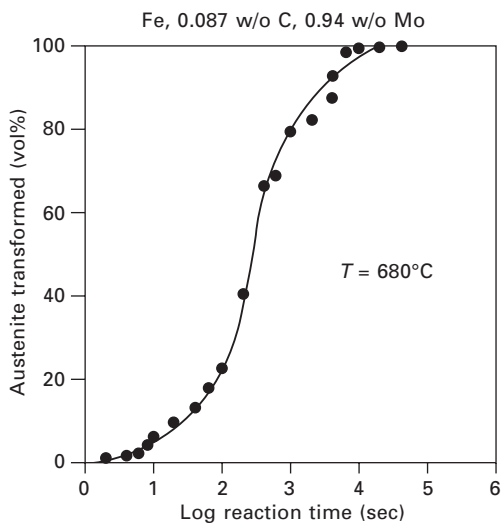
Steels are austenitized as the first stage in most practical heat treatments and the final result depends on the method of cooling or quenching. It is thus essential to have information on how the austenite reacts when the temperature is decreased and such information is represented in transformation diagrams. Basically, such diagrams are constructed for continuous cooling, so-called continuous cooling transformation (CCT) diagrams, in which the progress of transformation is illustrated with curves in a log(time) vs temperature coordinate system. It is necessary to illustrate the cooling method by also including cooling curves. However, there is an infinite number of cooling methods depending on the initial temperature, the cooling medium, the method of stirring, the size and shape of the piece of steel, the position inside the piece that is of primary interest and the heat of transformation, just to mention a few complications. On the other hand, in principle there is only one diagram illustrating the progress of transformation under constant

© Woodhead Publishing Limited, 2012

temperature, the so-called TTT diagram. That kind of diagram is also important for analysing the mechanisms and kinetics of transformation and that is why only TTT diagrams have been discussed in the present chapter. However, it should be realized that in practice one can achieve isothermal conditions only approximately. The limitation depends on the rate of transformation relative to the efficiency of the extraction of heat. Fortunately, diffusion of carbon limits the rate of the austenite to ferrite transformation and also the formation of carbides in Fe-C alloys and with sufficient carbon content one may achieve almost isothermal conditions if the piece of steel is not too large. However, the carbon content is not sufficient in many low carbon steels and the transformation may start before the isothermal condition is established. In practice, it may not always be possible to produce a realistic TTT diagram even if very thin specimens are used.

13.6.2 Progress of isothermal transformations

Already in Fig. 13.17 it was illustrated that more detailed information on the kinetics of phase transformations can be represented in diagrams of the degree of transformation as a function of annealing time during isothermal annealing of austenite. Figure 13.20 gives a simpler example (Reynolds *et al.*, 1990a). There have been many attempts to represent such transformation curves with a simple mathematical expression. A useful basis for such equations was given by an exact expression derived by Kolmogorov (1937) for a very well-defined case. He considered the growth of spherical units that had been



13.20 Diagram showing the degree of transformation as a function of time (from Reynolds *et al.,* 1990a).

© Woodhead Publishing Limited, 2012

nucleated randomly in the system with a constant rate of nucleation per unit of untransformed volume, $\dot{N}$, and constant growth rate, G:

$$\ln(1-f) = -(\pi/3)\dot{N}G^3t^4 \qquad [13.5]$$

Johnson and Mehl (1939) independently derived the same equation in a manner that was more complicated because they considered impingement explicitly.

Evidently, the formation of bainite is far from satisfying the conditions for this equation. The bainite units do not grow into spherical shapes and they do not nucleate independently, nor at random, especially not according to the idea that the new units, called subunits, nucleate in contact with preceding subunits that stopped growing. Furthermore, the equation was derived under an assumption which, when applied to plate-like precipitations, implies that a plate does not completely stop growing when it impinges on another plate but continues on the other side of the impinged plate.

Nevertheless, there is a considerable need for this kind of equation to represent the overall rate of a reaction. Avrami (1939, 1940, 1941), who also derived the same equation, suggested that the shape of the expression could still have practical use if one would consider the time exponent as a fitting parameter. The result was the Kolmogorov–Johnson–Mehl–Avrami (KJMA) equation:

$$\ln(1-f) = -Kt^n \qquad [13.6]$$

where K and n are two fitting parameters. However, it must be emphasized that there is a theoretical basis for the derivation only for spheres. Equation [13.6] should thus be regarded as an empirical equation that has been found to be useful in some cases. Primarily, Eq. [13.6] describes the progress of the transformation with time and, by regarding the fitting parameters as temperature dependent, it has been possible to fit the equation to the formation of the fractions of pearlite and bainite in a number of steels and then use the result for predicting TTT diagrams for similar steels. As an example, Matsuda and Bhadeshia (2004) designed programs for predicting TTT diagrams based on this approach.

13.6.3 Effect of carbon content on C curves

Finally, an example will be given of how a rather simple kinetic equation can be applied without fitting it to the dependence on carbon content and with only one fitting parameter for the temperature dependence. The primary interest is to test the effect of the carbon content by comparing with information from a series of plain carbon steels with carbon contents from 0.18 to 1.65 mass%. The secondary purpose of presenting such results is to indicate how the effect of alloying elements may be expressed. The model is based on Eq.

© Woodhead Publishing Limited, 2012

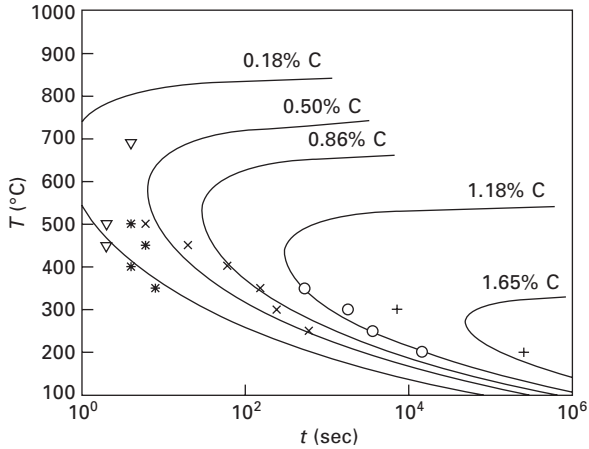
[13.1] that was used to evaluate the curves in Figs 13.1–13.4. It will first be modified to account for the need for carbon diffusion according to the diffusional hypothesis. With inspiration from Eq. [13.2] and assuming that the time to achieve a certain degree of transformation is inversely proportional to the velocity, one may write

$$t = \frac{K\,(c^o - c^\alpha)}{(\mathrm{WB_s} - T)^2} \exp(Q/RT) \qquad [13.7]$$

where c^o and c^α are the mass% C in the initial austenite and in the growing ferrite, respectively. $\mathrm{WB_s}$ is the upper temperature limit for the formation of acicular ferrite, i.e. Widmanstätten or bainitic ferrite, T is the isothermal temperature and K is a new constant of proportionality that depends on the degree of transformation and may also depend on the composition of the steel. It is essential to know how K and the activation energy Q depend on the carbon content. There does not seem to be sufficient experimental information from the binary Fe-C system, and even the information from plain carbon steels is limited as far as bainite is concerned, partly because of the influence from pearlite and martensite and also from allotriomorphic ferrite. In most cases it may thus be necessary to accept a predicted value of the B_S temperature, here generalized to $\mathrm{WB_S}$. The method presented by Hillert *et al*. (2004) will be used because the method based on the T_o' temperature does not seem to apply to low alloy steels. Instead of relying on published TTT diagrams, which are based on smoothed information, Borgenstam *et al*. (2011) decided to evaluate the time to form about 15–20 vol% of bainite or Widmanstätten ferrite by inspecting micrographs from five plain carbon steels presented by Modin (1958) and Modin and Modin (2000). Naturally, such data will not be very precise but may be adequate for the present purpose.

The data from steels with 0.86 and 1.18 mass% C extend over the largest range of temperature and, in particular, down to low temperatures due to their low M_S temperatures. They were first plotted in a diagram of log(time) vs $1/T$ after removing the assumed effects of T and c^o according to Eq. [13.7]. A straight line with a slope representing an activation energy of $Q = 75$ kJ mol^{-1} and with a constant value of $K = 8$ could represent much of the information. Curves for the five carbon contents were then calculated using these parameter values, and the predicted $\mathrm{WB_S}$ values were plotted in Fig. 13.21 together with the experimental values. The experimental points for the steel with 1.18 mass% C fall very close to its curve. For the other steels there is usually one point that deviates from the respective curve but the deviations seem to be random. Evidently, the data are based on limited information and crude estimates. Considering this fact, it is encouraging that the general tendency of the data, which cover five decades and a wide range of temperatures, is so well described in Fig. 13.21.

© Woodhead Publishing Limited, 2012



13.21 Calculated C curves for the formation of 15–20 vol% of bainite for five steels compared with experimental data evaluated from micrographs by Modin (1958) and Modin and Modin (2000). Carbon contents in mass% were ∇ – 0.18, ✳ – 0.5, × – 1.18 and + – 1.65.

One may only speculate about the physical mechanism behind the activation energy, which predicts the increasing transformation time as the temperature is lowered. Its value seems too low for diffusion of carbon in austenite unless the strong increase in the equilibrium carbon content in austenite at lower temperatures and the strong increase in the diffusivity with the carbon content can provide an explanation. Another possibility may be that the transport of carbon away from the advancing edge is controlled mainly by diffusion inside the ferrite plate from the edge to its sides. On the other hand, if growth is diffusionless, then the explanation may be quite different and it will be necessary to replace Eq. [13.7] with a completely different expression.

Since the effect of carbon seems to come mainly through the thermodynamic properties represented by the effect of the WB_s temperature and the presence of c^o in Eq. [13.7], it should be interesting to examine how the alloying elements affect the values of WB_s and K and if most of their effect can be accounted for in that way. It may be mentioned that Borgenstam and Hillert (1997) tried a similar approach on alloyed steels without first examining the Fe-C system. They concluded that the effect of alloying elements on the activation energy is small and recommended $Q = 80$ kJ mol^{-1}. For Mn they found that the effect on K was small but for Cr it had to be taken into account.

In conclusion, it seems that a major part of the effect of alloying elements on the C curves for bainite may be explained by their thermodynamic effect on the WB_s temperature. A crude method of predicting C curves for bainite may be based on Eq. [13.7] after the alloying effects on the WB_S

© Woodhead Publishing Limited, 2012

temperature and the single, adjustable parameter, K, have been evaluated from experimental information.

13.7 Conclusions

The main features of the kinetics of bainite formation have been discussed and compared to predictions based, as much as can be accomplished from available data on carbon diffusion and thermodynamic properties, on two hypotheses formulated for the growth mechanism of bainitic ferrite. It is stressed that a model for bainite formation should first of all apply to the binary Fe-C system. Most of the experimental information concerns alloyed steels and better information from binary or close to binary Fe-C alloys is badly needed as support for efforts to improve the modelling. It is concluded that some kinetic features are difficult to account for with the diffusionless hypothesis.

It should be mentioned that there have been many attempts to measure the carbon content of bainitic ferrite with the hope of proving that it is supersaturated in accordance with the diffusionless hypothesis. Appreciable carbon contents have indeed been found on several occasions but not corresponding to the carbon content of the parent austenite. Furthermore, the specimens have been kept at high temperature long enough to allow carbon to equilibrate. It seems that the observed carbon contents represent some kind of equilibrium, maybe modified by many defects in the bainitic ferrite that may attract carbon atoms, as proposed by Kalish and Cohen (1970). This is an important topic for future studies.

13.8 Acknowledgement

This chapter has naturally been influenced by the authors' opinions which were further developed in a project on bainite transformation within the VINN Excellence Center Hero-m, financed by VINNOVA, the Swedish Governmental Agency for Innovation Systems, Swedish Industry and KTH (Royal Institute of Technology).

13.9 References

Aaronson H I (1969), *The Mechanisms of Phase Transformations in Crystalline Solids*, Institute of Metals, London.

Aaronson H I and Wells C (1956), *Trans AIME*, 206, 1216.

Andersson J O, Helander T, Höglund L, Shi P F and Sundman B (2002), *CALPHAD*, 26, 273.

Avrami M (1939), *J. Chem. Phys.*, 7, 1103.

Avrami M (1940), *J. Chem. Phys.*, 8, 212.

Avrami M (1941), *J. Chem. Phys.*, 9, 177.

© Woodhead Publishing Limited, 2012

Bhadeshia H K D H (1981), *Acta Metall.*, 29, 1117.
Bhadeshia H K D H (1984), *Int. Conf. Phase Transf. Ferrous Alloys*, eds. Marder A R and Goldstein J I, ASM, Cleveland, OH, 335.
Bhadeshia H K D H (2001), *Bainite in Steels*, The Institute of Materials, London.
Bhadeshia H K D H and Waugh A R (1982), *Acta Metall.*, 30, 775.
Borgenstam A and Hillert M (1997), *Acta Mater.*, 45, 651.
Borgenstam A and Hillert M (2011), Report, Department of Materials Science and Engineering, KTH (Royal Institute of Technology), Stockholm, Sweden.
Borgenstam A, Hillert M and Ågren J (2009), *Acta Mater.*, 57, 3242.
Borgenstam A, Kolmskog P and M Hillert (2011), Unpublished work.
Cahn J W (1994), in General Discussion Session of the Pacific Rim Conference on the Roles of Shear and Diffusion in the Formation of Plate-Shaped Transformation Products, eds. Aaronson H I, Hirth J P, Rath B B and Wayman C M, *Metall. Mater. Trans.*, 25A, 2656.
Christian J W (1994), in General Discussion Session of the Pacific Rim Conference on the Roles of Shear and Diffusion in the Formation of Plate-Shaped Transformation products, eds. Aaronson H I, Hirth J P, Rath B B and Wayman C M, *Metall. Mater. Trans.*, 25A, 2657.
Davenport E S and Bain E C (1930), *Trans. AIME*, 117.
DeCooman B C (ed) (2002), *International Conference on TRIP-Aided High Strength Ferrous Alloys*, Technologisch Instituut VZW, Antwerp.
Goodenow R H, Matas S J and Hehemann R F (1963), *Trans. AIME*, 227, 651.
Hawkins M J and Barford J (1972), *J. Iron Steel Inst.*, 97.
Hehemann R F and Troiano A R (1956), *Met. Prog.*, 70, 97.
Hehemann R F, Kinsman K R and Aaronson H I (1972), *Metall. Trans.*, 3, 1077.
Hillert M (1957), *Jernkontorets. Annaler.*, 141, 757.
Hillert M (1960), Internal Report, Swedish Institute for Metals Research, Stockholm. Printed in Thermodynamics and Phase Transformations – The Selected Works of Mats Hillert, eds. Ågren J, Bréchet Y, Hutchinson C, Philibert J and Purdy G, EDP Sciences, Les Ulis, 2006, 9.
Hillert M, Höglund L and Ågren J (2003), *Acta Mater.*, 51, 2089.
Hillert M, Höglund L and Ågren J (2004), *Metall. Mat. Trans.*, 35A, 3693.
Hultgren A (1947), *Trans ASM*, 39, 915.
Hultgren A (1951), *Jernkontorets Annaler*, 135, 403.
Hultgren A (1953), *Isothermal Transformation of Austenite and Partitioning of Alloying Elements in Low Alloy Steels*, Kungliga Vetenskapsakademiens Handlingar, Stockholm, 4th Ser., Vol. 4, No. 3.
Johnson W A and Mehl R F (1939), *Trans. AIME*, 135, 416.
Kalish D and Cohen M (1970), *Mater. Sci. Eng.*, 6, 156.
Kinsman K R and Aaronson H I (1967), *Transformation and Hardenability in Steels*, Climax Molybdenum Ann Arbor, MI, 33.
Klier E P and Lyman T (1944), *Trans. AIME*, 158, 394.
Kolmogorov A N (1937), *Izv. Akad. Nauk SSR Ser. Fiz. Mat. Nauk.*, 355.
Kuo K and Hultgren A (1953), in *Isothermal Transformation of Austenite and Partitioning of Alloying Elements in Low Alloy Steels*, Kungliga Vetenskapsakademiens Handlingar, Stockholm, 4th Ser., Vol. 4, No. 3, pp. 22–34.
Laird C and Aaronson H I (1967), *Acta Metall.*, 15, 73.
Liu Z-K and Ågren J (1989), *Acta Metall.*, 37, 3157.
Lyman T and Troiano A R (1945), *Trans AIME*,162, 196.

© Woodhead Publishing Limited, 2012

Lyman T and Troiano A R (1946), *Trans AIME*, 37, 402.
Matsuda H and Bhadeshia H K D H (2004), *Proc. Roy. Soc. Lond. A*, 460, 1707.
Modin S (1958), *Jernkontorets Annaler*, 142, 37.
Modin H and Modin S (2000), *Microstructures in Three Isothermally Transformed Carbon Steels with High Carbon Content*, Meritförlaget, Stockholm.
Nemoto M (1974), in *High Voltage Electron Microscopy*, eds Swann P R, Humphrey C J and Goringe M J, Academic Press, London.
Oblak J M and Hehemann R F (1967), *Transformation and Hardenability in Steels*, Climax Molybdenum Ann Arbor, MI, 15.
Quidort D and Brechet Y J (2001), *Acta Mater.*, 49, 4161.
Reynolds W T Jr, Li F Z, Shui C K and Aaronson H I (1990a), *Metall. Trans.*, 21A, 1433.
Reynolds W T Jr, Liu S K, Li F Z, Hartfield S and Aaronson H I (1990b), *Metall. Trans.* 21A, 1479.
Simonen E P, Aaronson H I and Trivedi R (1973), *Metall. Trans.*, 4, 1239.
Speich G R (1962), *The Decomposition of Austenite by Diffusional Processes*, eds Aaronson H I and Zackay V F, Interscience, New York.
Speich G R and Cohen M (1960), *Trans. AIME*, 218, 1050.
Steven W and Haynes A J (1956), *JISI*, 183, 349.
Trivedi R (1970), *Metall. Trans.*, 1, 921.
Trivedi R and Pound G M (1967), *J Applied Phys.*, 38, 3569.
Tsuya K and Mitsuhashi T (1955), *J. Mech. Lab. J.*, 1, 42.
Usui N, Sugimoto E, Nishida M, Kobayashi M and Hashimoto S (1990), *CAMP-ISIJ*, 3, 2013.
Van der Voort G F (1991), *Atlas of Time-Temperature Diagrams for Iron and Steels*, ASM International, Cleveland, OH.
Yada H and Ooka T (1967), *J. Japan Inst. Met.*, 31, 766.
Zener C (1946), *Trans. AIME*, 167, 550.

© Woodhead Publishing Limited, 2012

14

Nucleation and growth during the austenite-to-ferrite phase transformation in steels after plastic deformation

J. SIETSMA, Delft University of Technology, The Netherlands and Ghent University, Belgium

Abstract: High temperature plastic deformation of austenite prior to the austenite-to-ferrite phase transformation during cooling can significantly influence the evolution of the microstructure during this transformation. This forms the basis for the formation of ultra-fine ferrite in steels. The basic processes of the phase transformation and the way in which these are affected by deformation defects in the parent structure are discussed in this chapter. Both experimental and modelling studies indicate the dominant influence of prior plastic deformation on the nucleation process. Since the nucleus density is found to increase more strongly than the defect density before the transformation, a distinct increase in the nucleation potency is identified.

Key words: phase transformation, plastically deformed microstructure, nucleation, grain boundaries.

14.1 Introduction

Phase transformations in metallic microstructures are governed primarily by the free-energy difference between the parent phase and potential new phases. The origin of the free-energy difference is primarily in the chemical and structural state of the phases involved. In the decomposition of austenite, the relative stability of austenite is determined by the free-energy difference between the austenite and the types of BCC-iron and carbide possible, which constitute more stable configurations at lower temperatures. According to the cooling conditions and the initial state of the austenite, the types of BCC-iron that can form may vary from proeutectoid ferrite plus pearlite to martensite. In the case where the austenitic phase has undergone plastic deformation, the free energy of this phase is influenced, normally increased, by defects, modified grain structure and internal stress. As a consequence, the austenitic state becomes more unstable due to plastic deformation, leading to an increase in the A_3-temperature, defined as the lowest temperature at which the austenite does not start to transform into the BCC-phase.

However, the actual development of the phase transformation is not fully

© Woodhead Publishing Limited, 2012

governed by the average free-energy difference, but is strongly dependent on the variations in the free-energy distribution, primarily because locally enhanced stored defect energy determines the nucleation behaviour of the phase transformation. At a temperature below the A_3-temperature for the deformed austenitic microstructure the deformed microstructure is relaxed through recovery and recrystallisation, but at the same time the onset of the phase transformation takes place. If the ferrite formation occurs before complete relaxation of the austenite, the phase transformation will evolve more rapidly and at higher temperatures during cooling due to the effect of deformation. The plastic deformation increases the defect density in the parent structure, which will affect both the nucleation and the growth stages of the phase transformation. As a consequence not only the transformation kinetics, but also the resulting microstructure are affected by prior deformation.

This phenomenon has been the subject of several experimental and modelling studies in the past (Umemoto *et al.*, 1983, 1992; Aaronson *et al.*, 1988; Bengochea *et al.*, 1998; Hanlon *et al.*, 2001; Lan *et al.*, 2005; Xiao *et al.*, 2006; Fazeli and Militzer, 2006). As will be discussed in this chapter, considerable insight has been obtained on the underlying physical processes, and overall agreement reached that the main influence of plastic deformation is on the nucleation of ferrite, influenced by locally stored defect energy. Nevertheless, more specific experimental evidence is needed to further enhance this understanding.

In the present chapter, the physical background of the influence of prior deformation on the phase transformation of austenite to ferrite will be discussed. The degree to which the deformed state of the austenitic parent phase is relaxed by recovery and recrystallisation will not be a topic for this chapter; rather, it concentrates on the characteristics of the phase transformation given a certain deformed state of the parent austenite. The physical background of structural defects and of the phase transformation, in terms of both nucleation and growth, being affected by prior plastic deformation, will be presented in Section 14.2. In Section 14.3 the main studies describing experimental observations of the deformation effect, causing enhanced transformation kinetics and altering the resulting microstructure, will be presented, as well as modelling approaches to unravel the underlying processes. Section 14.4 presents conclusions and a brief outlook on the understanding of these phenomena.

14.2 Background

14.2.1 Deformation defects and free energy

Plastic deformation of a metallic microstructure is normally accomplished through the motion and production of dislocations. Alternative processes such as plasticity-induced twinning or martensite formation will not be

© Woodhead Publishing Limited, 2012

considered in this chapter, since these are less relevant for the subsequent phase transformation. The structural effects of plastic deformation can be classified into three main categories:

- increased dislocation density;
- deformed grain morphology;
- modified grain-boundary character.

The vacancy concentration can also be increased by plastic deformation, but this effect is normally considered of minor importance.

The dislocation density increases by several orders of magnitude due to plastic deformation, which gives rise to the well-known and highly important phenomenon of work hardening. The relationship between the flow stress σ_f of a metallic structure and the average dislocation density ρ is given by (Taylor, 1934):

$$\sigma_f = \sigma_0 + \alpha\mu b\rho^{1/2}, \qquad [14.1]$$

where σ_0 is the sum of contributions to the flow stress from other hardening mechanisms than work hardening, α a constant, μ the shear modulus and b the length of the Burgers vector. For steel deformed in the austenitic state at, for instance, a temperature of 900°C, this equation implies a typical flow-stress increase from 100 MPa to 300 MPa due to plastic deformation if the dislocation density increases to 4×10^{14} m^{-2}. Dislocation densities can be determined experimentally by means of several techniques, such as X-ray diffraction, transmission electron microscopy (TEM) or electrical resistivity, but unfortunately a very accurate determination is not feasible. The effect of the dislocation density on the free energy of the structure is even more difficult to determine. Whereas the dislocation density is unambiguously defined as the dislocation-line length per unit of volume, the dislocation structure is of prominent importance for the dislocation contribution to the free energy of the microstructure of the material. Several processes occur due to which the spatial distribution of dislocations is not random. During plastic deformation dislocations formed by a Frank–Read source can collect into pile-ups when an obstacle such as a precipitate or grain boundary is encountered. During recovery, substructures of dislocations can form, in which the majority of the dislocations are concentrated in sub-grain walls, thus reducing their stress fields and consequently their defect energy. The simplest example of these sub-grain walls is formed by low-angle tilt or twist boundaries, for which it can be readily shown that the defect energy of the constituent dislocations is reduced by a factor of 3–4 due to their specific arrangement in which stress fields with opposite signs overlap. Because of the difficulties of accurate observation and characterisation of the dislocation structure, in general the defect free-energy density g_d due to a dislocation density ρ is commonly known to be estimated by:

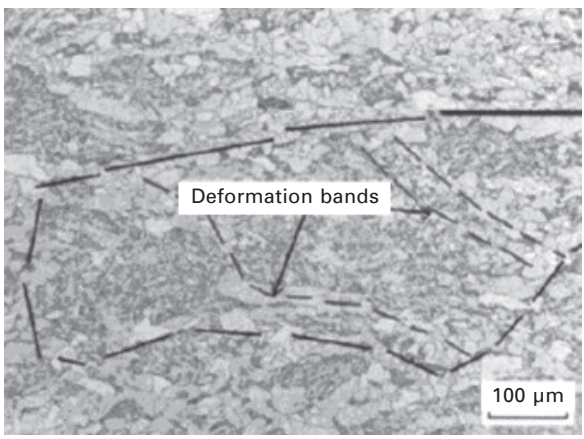
© Woodhead Publishing Limited, 2012

$$g_d = \frac{1}{2}\mu b^2 \rho \qquad [14.2]$$

Following the assumption of a homogeneous spatial distribution of dislocations, which is used in the derivation of Eq. [14.2], the free energy due to dislocations is assumed to be homogeneously dispersed in the microstructure, which is relevant for the description of grain growth during the phase transformation. In the conditions mentioned above (following Eq. [14.1]), this results in a defect energy of 1 MJ/m^3, which is of a comparable magnitude to the chemical driving force typically acting during ferrite formation from austenite (as can be derived by Thermo-Calc calculations).

Plastic deformation of the austenitic state can result in the formation of shear bands, regions in which relatively strong deformation takes place. Yin *et al*. (2010) have shown the relevance of these shear bands for the phase transformation to ferrite (see Fig. 14.1): nucleation of ferrite grains takes place at grain boundaries and at shear bands (indicated in Fig. 14.1 as deformation bands).

The grain morphology in the microstructure can be significantly affected by plastic deformation, of which the best known example is formation of pancake-shaped grains during rolling. Since the stress conditions are normally not hydrostatic, plastic deformation will increase the anisotropy of the grain morphology, which is usually quantified by means of the aspect ratio, defined as the ratio between the largest and smallest dimensions of grains in two-dimensional microscopic observations. This anisotropic distortion of grains leads to an increase in the free energy of the structure due to an increase in the specific grain boundary area. An estimation of the morphological effect on the free energy due to grain boundaries can be obtained by applying the



14.1 Nucleation of ferrite on deformation bands in deformed austenite (Yin *et al.,* 2010).

© Woodhead Publishing Limited, 2012

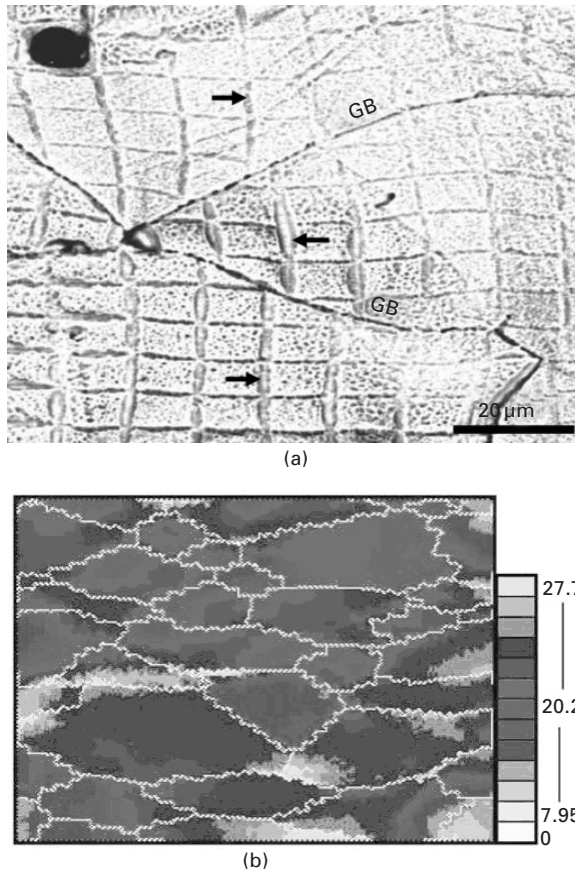
equation proposed by Sun *et al.* (2005) for the relative increase of the density of grain boundary area as a function of plastic deformation:

$$S = \frac{1}{3}(1 + \exp(-\varepsilon) + \exp(\varepsilon))S_0\,, \qquad [14.3]$$

in which ε is the strain, S is the density of grain boundary area, i.e. the total area of grain boundaries per unit of volume, and S_0 is the density of grain boundary area at $\varepsilon = 0$. This approximation shows that the increase in grain boundary area is limited for conventional deformation (e.g. 30% at $\varepsilon = 0.9$). For the larger strains effectuated in specialised severe plastic deformation techniques, such as torsion deformation (Horita *et al.*, 1996), equal-channel angular pressing (Segal, 1999) or accumulated roll bonding (Saito *et al.*, 1999), the relative increase of grain boundary area is nearly exponential (e.g. by a factor of approximately 50 at $\varepsilon = 5$). However, when relating this increase to the reduction of the resulting ferrite grain size through nucleation at grain boundaries, it should be realised that a factor 50 in the three-dimensional nucleus density leads to a reduction of less than a factor of approximately four in the grain size. The spatial distribution of the contribution of grain boundaries to the free energy is not homogeneous; the additional free energy is concentrated in grain boundaries. Therefore, this free-energy contribution is more relevant for the nucleation process, as will be discussed later in this section.

Finally, the grain boundary character is significantly affected. Plastic deformation causes significant changes in the defect structure close to and in grain boundaries. Dislocations accumulate near grain boundaries, which form an obstacle to their motion. Due to the difference in the orientation of neighbouring grains, and thus differently oriented slip systems, the local plastic deformation causes mismatch effects, leading to internal stresses and geometrically necessary dislocations in the grain boundary regions. Due to these processes, local increases in deformation defects can be expected near grain boundaries. Although the accumulation of defects near grain boundaries has been observed in, for instance, dual-phase steels (e.g. Calcagnotto *et al.*, 2010), detailed experimental observations following plastic deformation are scarce. An observation by means of the micro-grid technique (Hernandez-Castillo, 2005) is shown in Fig. 14.2(a). Local concentration of plastic deformation has also been reported on the basis of simulations, for which an example is given in Fig. 14.2(b) (Xiao *et al.*, 2006). This phenomenon has been widely acknowledged to occur, but quantification is not straightforward. An effective way to account for the change in grain boundary character is to assume the value of the specific interfacial energy γ to be affected by plastic deformation. By its localised character of this free-energy contribution, the grain boundary character will significantly affect the nucleation process.

© Woodhead Publishing Limited, 2012



14.2 Local strain in metallic microstructure. (a) Experimental observation with the micro-grid technique with GB indicating grain boundaries (Hernandez-Castillo, 2005). The arrows indicate a vertical grid line that is strongly affected across the grain boundaries; (b) Crystal-plasticity simulations, the grey scale indicating the local stored energy in J/mol (Xiao *et al.*, 2006). Used with permission from Elsevier.

14.2.2 Nucleation

The austenite decomposition is initiated by a nucleation event. Although classical nucleation theory (e.g. Christian, 1981) is widely accepted as a valid theoretical description of this process, detailed understanding and quantification of the nucleation process is still far from complete. The basis of the classical theory of nucleation is to consider the change in free energy ΔG of a metallic microstructure due to a nucleation event. If this event takes place at a defect in the microstructure, the change in free energy is given by:

© Woodhead Publishing Limited, 2012

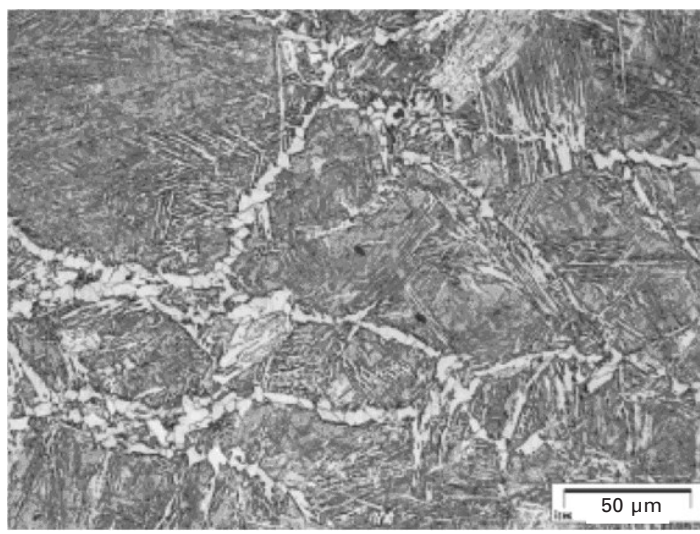
$$\Delta G = -V\Delta g_{\alpha\gamma} + A\gamma_{\alpha\gamma} - \Delta G_{\mathrm{d}} \quad [14.4]$$

in which V and A are respectively the volume and surface area of the nucleus, $\Delta g_{\alpha\gamma}$ is the difference in free-energy density between the parent γ-phase and the forming α-phase, $\gamma_{\alpha\gamma}$ is the interfacial energy of the interface between nucleus and parent phase and ΔG_{d} is the reduction in the defect energy due to the nucleation event.

For the nucleation of ferrite from austenite, the austenite/austenite grain boundaries act as the most efficient nucleation sites (see e.g. Fig. 14.3). The reduction in defect free energy ΔG_{d} can then be given by:

$$\Delta G_{\mathrm{d}} = \gamma_{\gamma\gamma}\Delta A_{\gamma\gamma}, \quad [14.5]$$

where $\gamma_{\gamma\gamma}$ is the interfacial energy of the grain boundary and $\Delta A_{\gamma\gamma}$ is the grain boundary area that is annihilated by the formation of the nucleus. Both quantities can be complex in their nature, for instance, if nucleation takes place at a corner point involving four γ-grains. The classical nucleation theory considers the existence of spontaneously forming atomic clusters of the α-phase, which can grow or shrink according to free-energy development with size of the nucleus. Evaluation of Eqs [14.4] and [14.5] leads to the concept of an activation energy for nucleation, ΔG^*, governing the nucleation rate. The activation energy is due to the fact that for small nucleus size, ΔG in Eq. [14.4] is positive and increasing due to the dominant effect of the nucleus area A. With increasing nucleus size, a maximum in ΔG is



14.3 Nucleation of allotriomorphic ferrite at grain boundaries of deformed austenite (Suwanpinij *et al.,* 2009). Used with permission from Wiley.

© Woodhead Publishing Limited, 2012

reached because of the increasing influence of the negative volume term in Eq. [14.4]. The maximum in ΔG as a function of the nucleus size is the activation energy ΔG^*. The activation energy is crucial for the nucleation rate, which, according to the classical theory of nucleation, can be given by (Porter and Easterling, 1992):

$$\frac{\partial n}{\partial t} \propto n_0 \beta \exp\left(-\frac{\Delta G^*}{kT}\right) \qquad [14.6]$$

In Eq. [14.6] the nucleus density is given by n, time by t, the density of potential nucleation sites by n_0, a frequency factor representing the atomic mobility by β, while k is Boltzmann's constant and T is temperature.

For homogeneous nucleation, not involving a structural defect, the nucleus will assume a spherical shape in order to minimise the ratio of surface area over volume, and the activation energy for nucleation is given by:

$$\Delta G^* = \frac{\gamma_{\alpha\gamma}^3}{\Delta g_{\alpha\gamma}^2} \qquad [14.7]$$

This equation expresses the balance between the driving force for the nucleation event ($\Delta g_{\alpha\gamma}$) and the effect of extra free energy introduced into the structure by the formation of a new grain boundary ($\gamma_{\alpha\gamma}$).

For heterogeneous nucleation at grain boundaries, there is no obvious and generally applicable solution for the optimal nucleus shape (Lange *et al.*, 1988; Landheer, 2010). A simple suggestion is a spherical-cap geometry for a nucleus at a perfectly flat grain boundary forming an incoherent grain boundary with the parent phase (Porter and Easterling, 1992). This concept falls short if coherent boundaries can be formed with at least one of the parent grains, inducing orientation relationships, or if nucleation takes place at grain edges, involving three parent grains, at grain corners, involving four parent grains, or at local disruptions of the grain boundary, as is likely to be introduced by plastic deformation of the parent phase (Hernandez-Castillo *et al.*, 2005). In order to take this into account, it has been proposed (Offerman *et al.*, 2002) to express the activation energy for nucleation analogously to Eq. [14.7], but in a more generally applicable form, as:

$$\Delta G^* = \frac{\Psi}{\Delta g_{\alpha\gamma}^2}, \qquad [14.8]$$

in which the factor Ψ in the numerator represents the effect of the net formation or annihilation of interfacial energy. The factor Ψ contains positive terms due to the formation of new interface area between parent phase and nucleus, and negative terms due to annihilation of interfaces of the parent phase (Offerman *et al.*, 2004). Its value can be calculated on the basis of

© Woodhead Publishing Limited, 2012

geometrical assumptions for the nucleus shape, which yields an estimated value $\Psi = 2 \times 10^{-6}$ J^3/m^6 for the pill-box nucleus suggested by Lange *et al.* (1988), but was experimentally determined to be much lower: a value of $\Psi = 5 \times 10^{-8}$ J^3/m^6 was found for ferrite formation during cooling of undeformed austenite (Offerman *et al.*, 2002). When comparing the value of $\Psi^{1/3}$ ([5×10^{-8} J^3/m^6]$^{1/3}$ = 4 mJ/m^2) to realistic values of the interfacial energy (of the order of 10^2 mJ/m^2), it is clear that Ψ is strongly dependent on the interfacial energies involved in the process. Thus, the factor Ψ is strongly dependent on the character of the grain boundary, for instance, after plastic deformation. The higher the interfacial energy $\gamma_{\gamma\gamma}$, the lower the factor Ψ will be, since more interfacial energy can be annihilated by the nucleation event.

Equation [14.8] can be used to classify defects in the parent microstructure according to their nucleation potency. Considering the driving force for nucleation, $\Delta g_{\alpha\gamma}$, as constant throughout the microstructure (and thus neglecting composition variations), variations in the activation energy will occur due to variations in Ψ. Thus, a distribution $p(\Psi)$ of Ψ-values exists in the microstructure, and the overall nucleation rate can be derived from Eq. [14.6] to be given by:

$$\frac{\partial n}{\partial t} \propto \Omega^{-1} \int_{\Omega} n_0(\Psi)\beta \exp\left(-\frac{\Delta G^*(\Psi)}{kT}\right) \mathrm{d}V'. \qquad [14.9]$$

In this equation, Ω represents the microstructural volume considered and V' is the integration variable. It is clear that the density of potential nucleation sites with a certain Ψ-value, $n_0(\Psi)$, depends on the occurrence and character of defects in the microstructure.

The distribution $p(\Psi)$ is strongly affected by plastic deformation of the microstructure. When considering the prior-austenite grain boundaries, the dominant sites for nucleation, it was argued in the previous subsection that plastic deformation changes the distribution $p(\Psi)$ because of (i) change in the overall density of grain boundary area and (ii) change in the grain boundary energies $\gamma_{\gamma\gamma}$. The density of grain boundary area can be expected to increase during plastic deformation, due to shape changes of the grains. This is reflected in an increase in the density of potential nucleation sites, the factor n_0 in Eq. [14.9]. Increases in the grain boundary energy will lead, as argued in this subsection, to a decrease in the parameter Ψ. This will substantially increase the nucleation rate, since it enters into the exponential factor in Eq. [14.9]. Although some authors (e.g. Lan *et al.*, 2005; Xiao *et al.*, 2006) argue that the driving force for nucleation, $\Delta g_{\alpha\gamma}$ (Eqs [14.4] and [14.8]) is affected by the defect energy g_d due to dislocations (Eq. [14.2]), this *average* free-energy contribution does not represent the *local* free energy at a potential nucleation site. During the nucleation event, the defect energy annihilated by the nucleus is not necessarily proportional to the nucleus volume, for instance in the case of nucleation at two-dimensional grain boundaries

© Woodhead Publishing Limited, 2012

or shear bands, but also for nucleation at one-dimensional dislocations. Therefore, deformation defects, including increased grain boundary energy, will primarily affect the activation energy for nucleation through a decrease in the parameter Ψ. In applying Eq. [14.9], the effect of plastic deformation should thus be accounted for by the parameters n_0 and Ψ.

14.2.3 Growth

During the phase transformation of austenite into BCC α-iron, in most cases (except for ultra-low carbon steel and for martensite formation) carbon has to partition from the newly forming phase into the austenite. The lattice formed by iron and substitutional alloying elements also changes its crystal structure from FCC to BCC in a diffusional process. The kinetics of the latter process results in an α/γ-interface velocity v that can be described by (see e.g. Christian, 1981):

$$v = M\Delta g. \qquad [14.10]$$

In this equation, Δg is the driving force for the phase transformation acting at the interface and M is the interface mobility. The relevant driving force is acting at the location of the interface, and is therefore not necessarily the same value as $\Delta g_{\alpha\gamma}$ in the Eqs [14.7] and [14.8] for nucleation. In fact, the local driving force is directly dependent on the local concentration, and thus related to the long-range carbon diffusion into the parent austenite ahead of the interface (Sietsma and van der Zwaag, 2004; see also Chapter 4 in this volume).

In the case of plastically deformed austenite, the parent austenitic phase will have a higher free energy than in the undeformed case, due to the increased dislocation density. In principle this results in faster transformation kinetics, which can be expressed by:

$$v = M(\Delta g + g_d), \qquad [14.11]$$

for which the dislocation defect energy g_d can be approximated by Eq. [14.2]. This equation, however, does not account for the effect of an inhomogeneous spatial distribution of dislocations, e.g. due to pile-ups at grain boundaries.

A second influence of the deformed structure on the growth kinetics of the phase transformation is due to enhanced diffusion kinetics because of the increased dislocation density. On the other hand, the increased vacancy concentration can lead to a reduction in the carbon diffusivity (Sluiter, 2010). A second effect increasing the carbon diffusion rate is the expected increase in the equilibrium carbon concentration in the austenite due to the increased free energy of this phase (Xiao *et al.*, 2006). An increase in the carbon diffusivity will, however, not lead to a proportional increase in the

© Woodhead Publishing Limited, 2012

transformation kinetics, since the relative influence of the interface mobility on the transformation kinetics will become stronger; in other words, the mixed-mode character of the transformation is shifted in the direction of interface control (Sietsma and van der Zwaag, 2004; Chapter 4, this volume).

14.2.4 Combined effects

A widely studied consequence of the ferrite formation being affected by prior plastic deformation is the formation of a very fine-grained ferritic microstructure (see e.g. Beladi *et al.*, 2007; Chapter 15, this volume). The basic requirement for grain refinement is enhanced nucleation, whereas an increase in the growth rate due to prior plastic deformation in principle reduces the effectiveness of any grain refining. Successful formation of fine-grained ferrite after deformation of the austenite therefore indicates that nucleation is the dominant mechanism, and that growth is either less enhanced or becoming effective only when the major part of the nucleation has already taken place. Indeed, in the discussion in Sections 14.2.2 and 14.2.3, it has been argued that the effect of plastic deformation on nucleation is much stronger than that on growth.

Plasticity-induced ferrite formation does not only occur statically, i.e. after plastic deformation, but also dynamically, during plastic deformation (Chung *et al.*, 2010; Basabe and Jonas, 2010; Hsu, 2005). During plastic deformation a mechanical stress is exerted on the austenitic phase, which causes an increase in the free energy by an elastic-stress contribution (Hsu, 2005). This free-energy contribution for the austenite can form an additional term in the driving force for the nucleation of ferrite, since the ferrite nucleus forms while this stress is acting, and can therefore accommodate (part of) the atomic-scale distortion. The result is an increase in the driving force for nucleation $\Delta g_{\alpha\gamma}$ and a corresponding increase in the nucleation rate according to Eqs [14.8] and [14.9] (Hsu *et al.*, 2005). Experimental quantification of this phenomenon is extremely difficult due to the well-known difficulties to quantify the nucleation behaviour in general, let alone during plastic deformation at elevated temperature. Nevertheless, evidence for the occurrence of this phenomenon results from the formation of ferrite during the application of a mechanical stress at temperatures above the A_3 temperature that relates to the unloaded condition. Chung *et al.* (2010) investigated a low-alloy steel containing 0.15 wt% C, 0.15 wt% Si and 1.10 wt% Mn during high-temperature plastic deformation. These treatments resulted in strain-induced ferrite formation at temperatures up to more than 50°C higher than the T_0 temperature. Local concentration measurements by electron-probe microanalysis indicated the formed ferrite to be of a massive character. Basabe and Jonas (2010) performed torsion tests on a micro-alloyed steel containing 0.09 wt% C and 0.036 wt% Nb at temperatures above the A_3

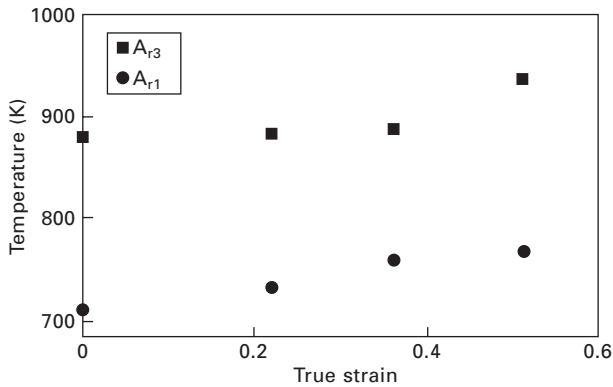
© Woodhead Publishing Limited, 2012

temperature. Dynamic formation of ferrite was found to take place at strains higher than a critical value, which depended on strain rate and temperature. The ferrite formed with a grain size of 2.0–3.5 μm.

14.3 Experiments and simulations on the effect of plastic deformation on ferrite formation

Much attention has been paid in the literature to the formation of ultra-fine grained ferrite and the corresponding mechanical properties; for a review see Beladi *et al*. (2007) and Chapter 15 in this volume. In this section a discussion will be given of experimental and modelling studies focusing on the influence of plastic deformation on the phase transformation of austenite into ferrite. This includes both experimental studies and microstructural modelling simulations.

Yin *et al*. (2010) investigated the phase transformation kinetics after plastic deformation of the austenite in a Nb-containing high-strength low-alloy (HSLA) steel. Figure 14.4 shows the increase in the temperature range for the transformation of austenite into ferrite during cooling, indicating enhanced transformation kinetics. Note that during cooling both the start and the finish temperature of the austenite-to-ferrite transformation increase with increasing degree of prior deformation, with the width of the temperature range in which the transformation takes place being smaller after deformation of the austenite than without prior deformation (strain zero in Fig. 14.4). In the same study it was shown that the phase transformation kinetics are also enhanced with increasing strain rate. The effect of decreasing the deformation temperature was found to be a slight decrease in the transformation temperatures, which was characterised by the authors as 'surprising', since increased defect energy



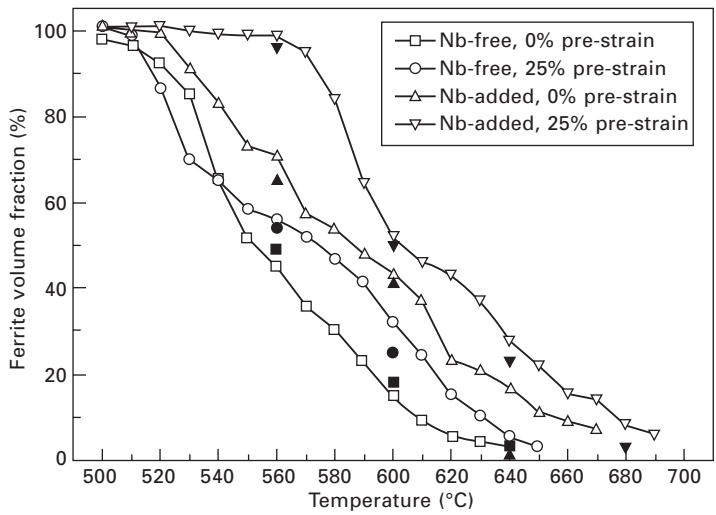
14.4 Strain dependence of the phase transformation temperature range; A_{r3} indicates the transformation-start temperature during cooling, A_{r1} the transformation-finish temperature (Yin *et al.*, 2010).

© Woodhead Publishing Limited, 2012

is expected after deformation at lower temperature. A possible explanation was suggested to be in the formation of bainite at lower temperatures, after initial formation of ferrite occupying possible nucleation sites for bainite formation (Yin *et al*., 2010).

Experimental observations on the evolution of the ferrite fraction as a function of temperature during cooling of deformed austenite have been reported by Xu *et al*. (2006). This study concerns 0.19 wt% C-1.96 wt% Mn steels with and without 0.03 wt% niobium. The phase fraction of ferrite was determined *in situ* during cooling at a rate of 5°C/min by means of neutron diffraction. The resulting ferrite fractions as a function of temperature are presented in Fig. 14.5. The distinct effect of the plastic deformation and of the addition of niobium is primarily ascribed by the authors to the increase in grain boundary area in both cases. After plastic deformation at 700°C the specimens were held at the same temperature for 900 s, but no detailed picture of the degree to which recrystallisation has taken place prior to the phase transformation is given (Xu *et al*., 2006). Comparing the two steels, the degree of recrystallisation can be expected to be higher in the Nb-free steel, which is in line with the smaller effect of strain seen in Fig. 14.5. The kinetics of ferrite formation after 25% pre-strain is slower in the more recrystallised Nb-free steel.

Hanlon *et al*. (2001) have also presented an experimental study of the effect of deformation on the austenite-to-ferrite transformation, but in



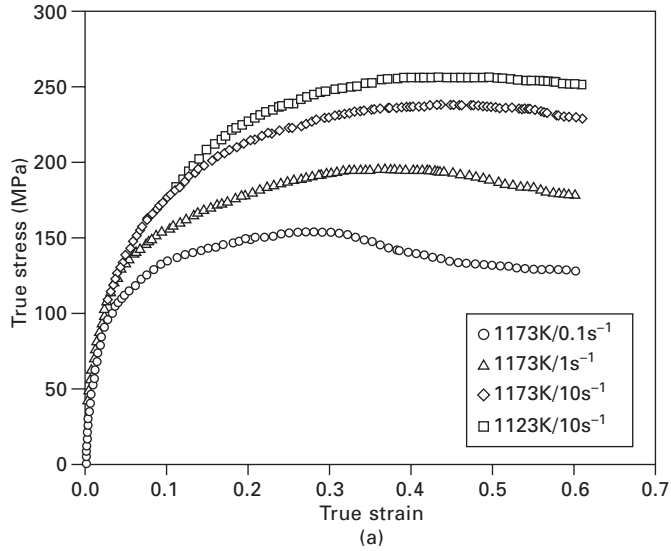
14.5 Ferrite fraction as a function of temperature during cooling for a plain C-Mn steel and a Nb-containing steel, with or without prior plastic deformation of the austenite (Xu *et al.*, 2006). The open symbols are determined by means of neutron diffraction, the closed symbols by optical microscopy. Used with permission from Elsevier.

© Woodhead Publishing Limited, 2012

this study the authors also discuss the observed phenomena in terms of the underlying mechanisms. The experimental evidence shows a distinct acceleration of ferrite formation during cooling of plastically deformed austenite. Figure 14.6 shows the ferrite + pearlite fraction derived from dilatometry during cooling of steel samples (composition 0.19 wt% C, 1.46 wt% Mn, 0.445 wt% Si) at 15 K/s after compression deformation to a true strain of 0.6 in the austenitic state. The deformation conditions (temperature and strain rate) were chosen such that the degree of dynamic recovery and recrystallisation varied between the experiments. This is clearly visible in the deformation curves in Fig. 14.6(a). A higher deformation temperature and a lower strain rate allow more dynamic recovery and recrystallisation, resulting in a lower dislocation density, and therefore defect energy, in the material after deformation, visible as a lower flow stress at the end of the deformation (see Fig. 14.6(a), cf. Eqs [14.1] and [14.2]). Upon cooling, the fully austenitic microstructure transforms into ferrite and pearlite, and it can be seen in Fig. 14.6(b) that the transformation kinetics are faster with higher defect energy: the order in the four fraction curves agrees with the order in the flow stress in Fig. 14.6(a). The resulting average ferrite grain size did not show strong differences within this series of experiments (the average grain size ranged between 11 and 15 μm; Hanlon *et al.*, 2001). It was also investigated (Hanlon *et al.*, 2001) by microstructural simulations which of three microstructural processes correlated best with the observed transformation kinetics: growth, nucleation density or nucleation potency. In the description in the present chapter, these three processes relate to Eq. [14.11], n_0 in Eq. [14.9] and ΔG^* in Eq. [14.9], respectively. The solid lines in Fig. 14.6(b) show that reasonable agreement is achieved when the increased nucleation potency is taken into account in the modelling as a decreasing undercooling necessary for nucleation. Therefore, the conclusion is drawn that the acceleration of the transformation due to prior plastic deformation, out of the three aforementioned processes, corresponds most closely to the simulated effect of enhanced nucleation potency (Hanlon *et al.*, 2001).

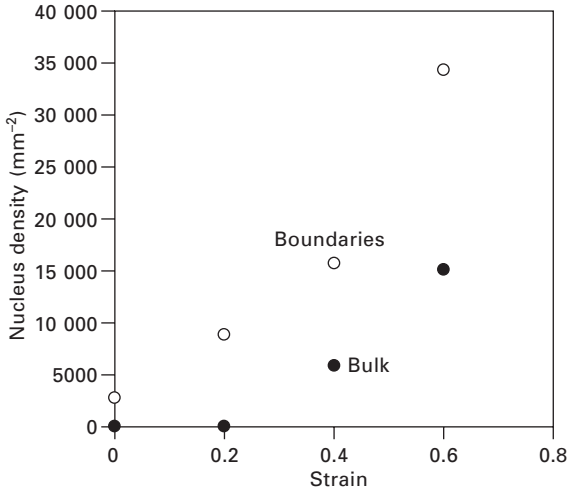
More extensive microstructural modelling of the austenite-to-ferrite phase transformation after plastic deformation of the austenite has been presented by Suwanpinij *et al.* (2009), who employed two-dimensional phase-field modelling in combination with experimental observations on the phase fractions (by means of dilatometry) and the microstructures (by means of optical microscopy). The experimentally determined density of ferrite nuclei as a function of the strain applied to the austenite is given in Fig. 14.7. The authors make a distinction between ferrite grains nucleated on grain boundaries and in the grain interiors. Although it can be argued that this distinction is not unambiguous when considering only two-dimensional representations of the microstructures, both densities, as well as the total nucleus density, increase nearly exponentially with the applied strain, with an increase by a

© Woodhead Publishing Limited, 2012



14.6 Compression deformation and subsequent accelerated ferrite formation during cooling of deformed austenite (Hanlon *et al.*, 2001): (a) stress–strain curves, with the temperature and strain rate of the deformation parameters given in the key; (b) the fraction of austenite that is transformed during cooling after deformation of the austenite at the conditions given in the key. The symbols give experimental results, the solid lines give results of microstructural simulations, applying an undercooling for nucleation of [1] 60 K; [2] 55 K; [3] 40 K; [4] 30 K.

© Woodhead Publishing Limited, 2012



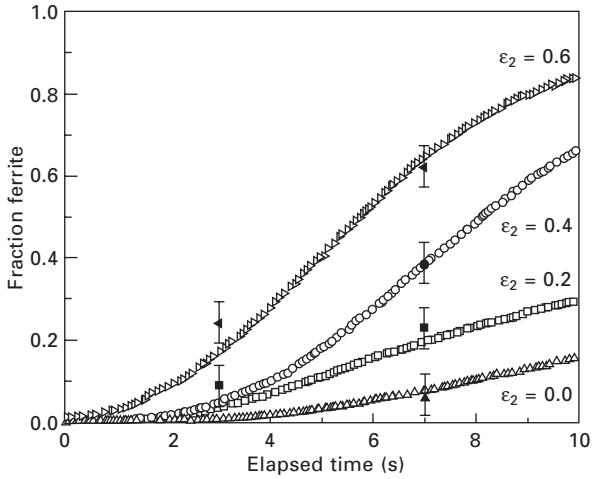
14.7 Ferrite-nucleus density as a function of plastic strain applied to the austenite, determined from optical microscopy (Suwanpinij *et al.*, 2009). Used with permission from Wiley.

factor of nearly 20 for a strain of 0.6. In the same study, the authors estimate the increase in the relative increase of the grain boundary area to be less than 10% for the maximum strain of 0.6 (Eq. [14.3]) (Sun *et al.*, 2005). These experimental data on the nucleus density form a clear indication that the increase in grain boundary is not sufficient to account for the much stronger increase in the nucleus density due to prior deformation.

Suwanpinij *et al.* (2009) have performed microstructural simulations of the phase transformation by means of two-dimensional phase-field modelling. Phase-field modelling (Steinbach *et al.*, 1996) is a simulation technique that can be used for grain growth; the nucleation behaviour of the microstructure must be accounted for on different grounds. In the phase-field modelling, Suwanpinij *et al.* (2009) have related the nucleation behaviour as a function of annealing time during the isothermal transformation at 680°C to their experimental data. The grain growth was simulated by using a driving force that consisted of three contributions: (i) the chemical driving force, derived from Thermo-Calc; (ii) defect energy due to the dislocation density; and (iii) defect energy due to the grain boundaries.

The evolution of the ferrite fraction during cooling that resulted from the simulations of Suwanpinij *et al.* (2009) is shown in Fig. 14.8. The modelling results agree very well with the experimentally determined phase fractions. By suitably choosing the simulated nucleation behaviour in the phase-field modelling with MICRESS® code, introducing nuclei at grain edges, grain boundaries and in the grain interior, satisfactory agreement in the nucleation behaviour was also found. The assignment of nuclei at the

© Woodhead Publishing Limited, 2012



14.8 Phase-field modelling results compared to experimental phase fractions during isothermal annealing at 680°C. The closed symbols give experimental results, the open symbols the simulation results (Suwanpinij *et al.,* 2009). Used with permission from Wiley.

different locations in the microstructure could, however, not be compared with experimental observations, since the nucleus positions could not be distinguished with sufficient accuracy. The authors reached the conclusion that phase-field modelling is an effective tool to investigate the underlying mechanism for the influence of plastic deformation on the austenite-to-ferrite phase transformation, and that the influence on the nucleation behaviour is more significant than that on the growth behaviour.

Microstructural modelling has also been performed by Lan *et al.* (2005) and by Xiao *et al.* (2006). In both studies the defect energy due to the plastic deformation has been introduced into the modelled microstructure by applying a crystal-plasticity model. In both studies local concentrations of stored defect energy in the microstructure result from modelling of the plastic deformation. These regions of high defect energy primarily appear close to grain boundaries, but to some extent also in grain interiors (Lan *et al.*, 2005). Lan *et al.* applied a simulated true strain of 0.6 at 850°C to the CMn-steel with 0.19 wt% C and 1.46 wt% Mn in order to make a comparison with the experimental results reported by Hanlon *et al.* (2001). Lan *et al.* also adopted the value $\Psi = 5 \times 10^{-8}$ J^3/m^6 (Offerman *et al.*, 2002) to simulate the nucleation behaviour. The effect of the defect energy on nucleation has been implemented by adding the maximum defect energy to the driving force $\Delta g_{\alpha\gamma}$, and considering only sites with at least 75% of the maximum defect energy as potential nucleation sites. For the simulation of growth a cellular-automaton method was employed by Lan *et al.* (2005). In the cellular-automaton model (Lan *et al.*, 2004), microstructural volume

© Woodhead Publishing Limited, 2012

elements at the α/γ interface are transformed in subsequent time steps according to transformation rules representing the assumed nucleation and growth behaviour. Both for nucleation and for growth, the effect of plastic deformation of the austenite was incorporated into the driving force by adding the stored energy g_d, derived according to Eqs [14.1] and [14.2], to the driving force for the phase transformation. In the growth behaviour, both carbon diffusion and interface mobility were taken into account during the phase transformation from deformed austenite to ferrite occurring during cooling from 850°C at a rate of 15 Ks^{-1}. Very good agreement was obtained with the experimental data for the ferrite fraction during cooling that was reported by Hanlon *et al*. (2001). The authors derived from this agreement that the nucleation of ferrite in deformed austenite is highly non-uniform, taking place at grain boundaries and on localised deformation regions in grain interiors. The effect of plastic deformation on carbon diffusion and on the interface mobility M was not taken into account in this study.

Xiao *et al*. (2006) presented a similar study, but the growth behaviour was now simulated by a Monte-Carlo (MC) method. Similar to the previously discussed cellular-automaton method, the phase transformation is simulated by transforming microstructural volume elements. The criterion for transformation in the MC method is based on the changes in the Hamiltonian of the system, in which the stored energy is added to the driving force for the transformation. Also ferrite nucleation is implemented in the MC scheme and 'is dominated by the interaction among the chemical free energy, interface energy and stored energy' (Xiao *et al*., 2006). The crystal-plasticity simulations lead to an increase in the grain boundary area, which is approximately twice as large as predicted by Eq. [14.3] (i.e. 80% increase at $\varepsilon = 0.9$). The phase transformation to ferrite after deformation of an Fe-0.2 wt% C alloy is modelled during isothermal annealing at 1070 K, at which temperature the equilibrium fraction of ferrite is 0.45. Due to the increased free energy of the austenitic phase, the equilibrium fraction of ferrite increases to approximately 0.56 after plastic deformation to $\varepsilon = 0.9$. In addition, the transformation kinetics are enhanced by a factor of approximately 3. Recovery and recrystallisation have not been included in the simulations.

The faster transformation kinetics are partly ascribed by the authors to the higher nucleation rate and density occurring after plastic deformation, and partly to accelerated growth due to a higher driving force and enhanced carbon diffusion. The relative increase in the nucleus density due to plastic deformation is observed to be distinctly higher than the relative increase in grain boundary area, again indicating enhanced nucleation potency. The authors relate the enhanced carbon diffusion to an increase in the equilibrium carbon concentration in the austenite due to the increased free energy of this phase and to the reduction in the activation energy for diffusion due to structural defects, although it does not become entirely clear as to how this

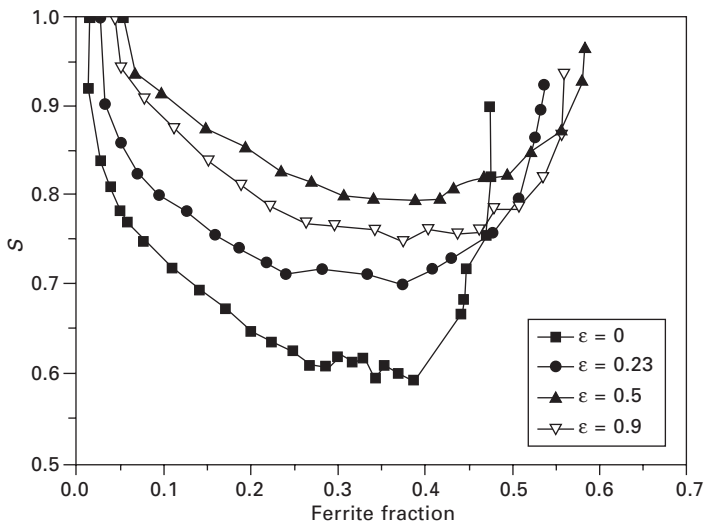
© Woodhead Publishing Limited, 2012

latter effect has been quantified in the simulations. The enhanced diffusion kinetics result in a shift in the mixed-mode character of the transformation (Sietsma and van der Zwaag, 2004; Chapter 4, this volume), which is shown in Fig. 14.9. The parameter S in this figure is a measure of the mixed-mode character, and is linearly scaling with the carbon concentration in the austenite at the austenite/ferrite interface. For $S = 0$ this concentration is equal to the equilibrium concentration and the transformation is diffusion controlled (local equilibrium); for $S = 1$ the transformation is interface controlled (Sietsma and van der Zwaag, 2004; Bos and Sietsma, 2007).

The clear shift of the transformation character towards interface control is primarily caused by enhanced carbon diffusion due, as argued before, to the increased equilibrium concentration in the austenite and structural defects, but also to the higher area-over-volume ratio for smaller ferrite grains (due to enhanced nucleation), which will contribute to the observed shift (Sietsma and van der Zwaag, 2004).

14.4 Future trends and conclusion

Experimental evidence on the effect of plastic deformation of austenite on the nucleation and growth processes during the subsequent ferrite formation



14.9 Mixed-mode character of the austenite-to-ferrite phase transformation after plastic deformation. A value $S = 1$ for the mixed-mode parameter represents fully interface-controlled behaviour; $S = 0$ indicates diffusion control. The increase in S towards the end of the transformation is most likely due to impingement affecting the reference values of S (Xiao *et al.*, 2006). Adapted and used with permission from Elsevier.

© Woodhead Publishing Limited, 2012

is limited; more specific information can be obtained from the reported simulation studies. All authors agree that the nucleation process is much more strongly affected than the growth process, and this should also be considered the basis for the grain-refining effect and the consequent possibility to form (ultra-)fine ferrite (see Chapter 15). The increase in nucleus density is generally found to be larger than the increase in the density of potential nucleation sites, and an essential contribution is therefore attributed to the increased nucleation potency of nucleation sites such as grain boundaries. Although the modelling studies in the literature described in this chapter do take nucleation into account in a physical manner, experimental evidence underpinning the relevance of the approaches used is still too limited. Simulation results do show good agreement with the available experimental data, but this agreement is based on average data on the development of the phase transformation, e.g. the overall ferrite fraction, rather than on specific local information. Although the results are consistent, it proves difficult to elucidate the essentials and the values of the parameters involved, especially in the nucleation behaviour. Thus, in general, in this specific topic the nucleation process deserves more specific and more detailed attention, especially in experimental studies. *In-situ* application of newly developed techniques such as electron backscatter diffraction and diffraction with synchrotron radiation, as well as 3D atom-probe tomography, can greatly enhance the experimental evidence that can form a more demanding benchmark to test the presently developed simulation approaches.

14.5 References

Aaronson, H.I., Enomoto, M., Furuhara, T. and Reynolds, W.T. 1988, *Thermec 88, International conference on physical metallurgy of thermomechanical processing of steels other metals, vol. 1*. Tokyo: Iron and Steel Institute of Japan, 80.

Basabe, V.V. and Jonas, J.J. 2010, The ferrite transformation in hot deformed 0.036 % Nb austenite at temperatures above the Ae_3, *ISIJ International* 50, 1185.

Beladi, H., Kelly, G.L. and Hodgson, P.D. 2007, Ultrafine grained structure formation in steels using dynamic strain induced transformation processing, *International Materials Review* 52, 14.

Bengochea, R., Lopez, B. and Gutierrez, I. 1998, Microstructural evolution during the austenite-to-ferrite transformation from deformed austenite, *Metall. Trans.* 29A, 417.

Bos, C. and Sietsma, J. 2007, A mixed-mode model for partitioning phase transformations, *Scr. Mater.* 57, 1085.

Calcagnotto, M., Ponge, D., Demir, E. and Raabe, D. 2010, Orientation gradients and geometrically necessary dislocations in ultrafine grained dual-phase steels studied by 2D and 3D EBSD, *Mat. Sci. Eng.* A 527, 2738.

Christian, J.W. 1981, The Theory of Transformations in Metals and Alloys, Oxford: Pergamon.

Chung, J.H., Park, J.K., Kim, T.H., Kim, K.H. and Ok, S.Y. 2010, Study of deformation-

© Woodhead Publishing Limited, 2012

induced phase transformation in plain low carbon steel at low strain rate, *Mater. Sci. Eng. A*, 527, 5072.

Fazeli, F. and Militzer, M. 2006, Modeling the transformation kinetics from work-hardened austenite in a TRIP-steel, *Mater. Sci. Forum* 539–543, 4339.

Hanlon, D.N., Sietsma, J. and van der Zwaag, S. 2001, The effect of plastic deformation of austenite on the kinetics of subsequent ferrite formation, *ISIJ Int.* 41, 1028.

Hernandez-Castillo, L.E. 2005, Determination of micro-scale strain distribution in hot-worked steel microstructures, PhD thesis, Sheffield University.

Horita, Z., Smith, D.J., Furukawa, M., Nemoto, M., Valiev, R.Z. and Landon, T.G. 1996, An investigation of grain boundaries in submicrometer-grained Al-Mg solid solution alloys using high-resolution electron microscopy, *J. Mat. Res.* 11, 1880.

Hsu, T.Y. 2005, Additivity hypothesis and effects of stress on phase transformations in steel, *Curr. Opinion in Solid State and Mater. Sci.* 9, 256.

Lan, Y.J., Li, D.Z. and Li, Y.Y. 2004, Modelling austenite decomposition into ferrite at different cooling rate in low-carbon steel with cellular automaton method, *Acta Mater.* 52, 1721.

Lan, Y.J., Xiao, N.M., Li, D.Z. and Li, Y.Y. 2005, Mesoscale simulation of deformed austenite decomposition into ferrite by coupling a cellular automaton method with a crystal plasticity finite elements model, *Acta Mater.* 53, 991.

Landheer, H. 2010, Nucleation of ferrite in austenite, PhD thesis, Delft University of Technology.

Lange III, W.F., Enomoto, M. and Aaronson, H.I. 1988, The kinetics of ferrite nucleation at austenite grain boundaries in Fe-C alloys, *Metall. Trans. A* 19, 427.

Offerman, S.E., van Dijk, N.H., Sietsma, J., Grigull, S., Lauridsen, E.M., Margulies, L., Poulsen, H.F., Rekveldt M.Th. and van der Zwaag, S. 2002, Grain nucleation and growth during phase transformations, *Science* 298, 2003.

Offerman, S.E., van Dijk, N.H., Sietsma, J., van der Zwaag, S., Lauridsen, E.M., Margulies, L., Grigull, S. and Poulsen, H.F. 2004, Reply to the discussion by Aaronson *et al.* to 'Grain nucleation and growth during phase transformations', *Scr. Mater.* 51, 937.

Porter, D.A. and Easterling, K.E. 1992, *Phase Transformations in Metals and Alloys*, 2nd edn, London: Chapman & Hall.

Saito, Y., Utsunomiya, H., Tsuji, N. and Sakai, T. 1999, Novel ultra-high straining process for bulk materials: development of the accumulated roll-bonding (ARB) process, *Acta Mater.* 47, 579.

Segal, V.M. 1999, Equal-channel angular extrusion: from macromechanics to structure formation, *Mat. Sci. Eng. A* 271, 322.

Sietsma, J. and van der Zwaag, S. 2004, A concise model for mixed-mode phase transformations in the solid state, *Acta Mater.* 52, 4143.

Sluiter, M.H.F. 2010, private communication.

Steinbach, I., Pezzolla, F., Nestler, B., Seeßelberg, M., Prieler, R., Schmitz, G. and Rezende, J. 1996, A phase field concept for multi-phase systems, *Physica* D94, 135.

Sun, X., Liu, Q. and Dong, H. 2005, Deformation-induced ferrite transformation and grain refinement in low-carbon steel, *1st Int. Conf. Proc. Super-High Strength Steels*, Rome, November, article 35 (CD-ROM).

Suwanpinij, P., Rudnizki, J., Prahl, U. and Bleck, W. 2009, Investigation of the effect of deformation on γ-α phase transformation kinetics in hot-rolled dual-phase steel by phase-field approach, *Steel Research Intern.* 80, 616.

Taylor, G.I. 1934, The mechanism of plastic deformation of crystals, *Proc. Royal Society* A145, 362.

© Woodhead Publishing Limited, 2012

Umemoto, M., Ohtsuka, H. and Tamura, I. 1983, Transformation to pearlite from work-hardened austenite, *Trans ISI Japan* 23, 775.

Umemoto, M., Hiramatsu, A., Moriya, A., Watanabe, T., Nanba, S. and Nakajima, N. 1992, Computer simulation of phase transformation from work-hardened austenite, *ISIJ Int*. 32, 306.

Xiao, N.M., Tong, M.M., Lan, Y.J., Li, D.Z. and Li, Y.Y. 2006, Coupled simulation of the influence of austenite deformation on the subsequent isothermal austenite-ferrite transformation, *Acta Mater*. 54, 1265.

Xu, P.G., Tomota, Y., Lukas, P., Muransky, O. and Adachi, Y. 2006, Austenite-to-ferrite transformation in low alloy steels during thermomechanically controlled process studied by *in-situ* neutron diffraction, *Mater. Sci. Eng. A* 435–436, 46.

Yin, S.B., Sun, X.J., Liu, Q.Y. and Zhuang, Z.B. 2010, Influence of deformation on transformation of low carbon and high Nb-containing steel during continuous cooling, *J. Iron and Steel Res. Intern*. 17, 43.

© Woodhead Publishing Limited, 2012

15

Dynamic strain-induced ferrite transformation (DSIT) in steels

P. D. HODGSON and H. BELADI, Deakin University, Australia

Abstract: The goal in the heat treatment or thermomechanical processing of steel is to improve the mechanical properties. For structural steel applications the general aim is to refine the ferrite grain size as this is the only method that improves both the strength and toughness simultaneously. For conventional hot rolling and accelerated cooling processes, it is difficult to refine the grain size below 5 μm without extensive alloying. However, it has been found that inducing transformation during deformation (i.e. dynamic transformation) can lead to grain sizes of the order of 1 μm, even in very simple steel compositions. The exact mechanism(s) for this transformation process are still being debated, and this has also been complicated by recent studies where such grain sizes can be obtained by static transformation from austenite that has been heavily deformed at low temperatures prior to the transformation. This chapter reviews the various major studies related in particular to dynamic transformation and considers the contributions from the deformed austenite structure developed prior to the transformation and the potential for dynamic recrystallisation of the ferrite. A key factor is proposed to be the early three-dimensional impingement of the ferrite which also provides an insight into cases where ultrafine grains are achieved statically.

Key words: strain-induced transformation, ultrafine ferrite, dynamic transformation, steel, grain size, thermomechanical processing, dynamic recrystallisation.

15.1 Introduction

Grain size refinement is the only way to simultaneously improve strength and toughness in metals. Therefore, the development of structural steel products has focused for the past 50 years on methods to refine the ferrite grain size. Thermomechanical controlled processing (TMCP) has been largely based around the concept of grain refinement with the need for extra heat treatments. Prior to the development of TMCP, structural plate steels were generally normalised, which is a very costly process for large products. In TMCP the rolling schedule and post-rolling cooling are optimised to produce the required level of refinement. Controlled rolling, where the steel is finish rolled in the non-recrystallisation region, flattens the austenite grains and introduces internal defects that increase the number of nucleation sites for

© Woodhead Publishing Limited, 2012

ferrite. Increasing the cooling rate after rolling plays two roles: firstly, it can lead to greater undercooling and, thereby, a higher nucleation density and, secondly, as the steel cools the growth rate of the ferrite is reduced.

These approaches have enabled the production of steels with grain sizes in the range of 5–10 μm depending on the exact processing routes and composition. In hot strip mills, it is possible to further refine the microstructure due to the higher cooling rate and the ability to isothermally transform in the coil. In the latter case, the microstructures have a much higher internal dislocation density and are less equiaxed, and hence appear more like a mixture of ferrite and bainite/acicular ferrite. In general, for a classic proeutectoid ferrite, a grain size of ~5 μm is the limit.

Steel has an abnormally high Hall–Petch slope compared to other metals, which is believed to be linked to very small amounts of interstitial C at the grain boundaries (Honeycombe and Bhadeshia, 1995). Therefore, a typical slope is of the order of 20 MPa/mm$^{0.5}$. Decreasing the grain size from 5 to 1 μm should thereby increase the strength by 350 MPa, and from other models it is predicted that the ductile to brittle transition temperature could reduce to below the liquid nitrogen temperature. With such a major potential improvement in properties, it was the case that the 1 μm grain size was the dream for all steel metallurgists. However, all attempts to achieve such a grain size failed until early work in the late 1980s from Japan (Yada *et al.*, 1984, 1988) that was largely forgotten about until the mid-1990s when research commenced again with large national programmes in Japan, Korea and China, which all showed that it is possible to achieve such grain sizes through dynamic transformation (i.e. during deformation) of the austenite to ferrite.

This chapter will explore the various aspects related to the formation of what is now termed 'ultrafine ferrite (UFF)'. Firstly, the reason why it is believed that this cannot occur statically under typical industrial conditions is discussed. However, the real focus of this chapter is on dynamic strain induced transformation (DSIT) of ferrite and the areas to be covered here include the general observations of this phenomena and the effect of process variables, followed by a deeper insight into the role of the deformed state of the austenite and the nature of the transformation. A recent descriptive model will be presented along with attempts to model mathematically the transformation. The final section explores the mechanical properties and how these may be improved by developing more complex microstructures.

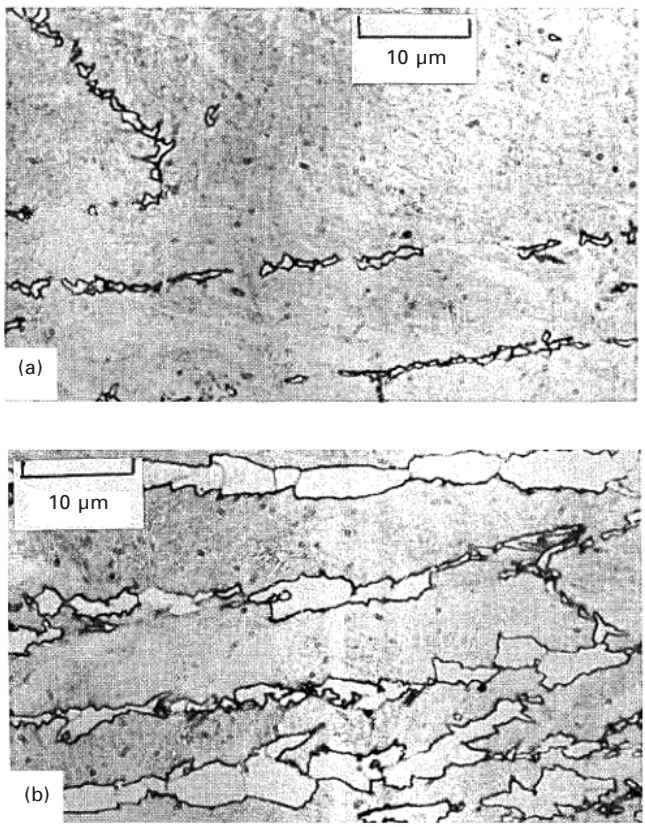
15.2 What limits grain refinement in conventional static transformation?

The nature of the austenite to ferrite transformation has been covered elsewhere in this book (see Part II) and involves a nucleation and growth stage. Grain

© Woodhead Publishing Limited, 2012

refinement is achieved by increasing the nucleation density and/or slowing the growth rate. In theory, if the steel was to have a very fine austenite grain (say 20 μm) that was reduced in a hot strip mill by 90% followed by heavy cooling, then the prior austenite boundaries are at most 2 μm away from each other and with an optimum cooling you would imagine that you could produce a microstructure where the grain size was at most 2 μm just through grain boundary nucleation, assuming that nucleation sites along the prior austenite boundary could be refined in spacing to this level.

In fact, it is possible to refine the potential sites along the prior austenite grain boundary for nucleation of ferrite to 1 μm, even at much lower strains. This is due to the roughening of the austenite boundary because of the intersection of slip systems with the boundary. Figure 15.1(a) shows an example of a steel deformed in torsion with an initial austenite grain size of 35 μm and a retained strain (i.e. the strain in the non-recrystallisation



15.1 The microstructure of 0.18C, 0.015Si-1.32Mn, 0.035Nb (in wt%) steel deformed at 810°C followed by cooling at 1°C/s and quenched from 750°C (a) and 720°C (b) (after Priestner and Hodgson, 1992).

© Woodhead Publishing Limited, 2012

region) of 1.25 at an early stage of deformation (Priestner and Hodgson, 1992). Two features are clear in this: firstly, there are regions where the ferrite has impinged and where the spacing between ferrite grain centres is of the order of 1 μm and, secondly, there are austenite grain boundaries with no ferrite. These local areas of ferrite were termed rafts and the grains within them were studied as the transformation progressed. After the stage of full impingement within a raft, the aspect ratio of the ferrite grains did not change markedly and hence any growth of ferrite into the austenite must have been balanced by a reduction in the number of ferrite boundaries along the prior austenite boundary (Fig. 15.1(b)). Hence, the microstructure was coarsening during transformation.

A simple measure of coarsening (Eq. [15.1]) is to consider the final grain size and to then collapse this grain back to 0 assuming the simple relationship (Priestner and Hodgson, 1992):

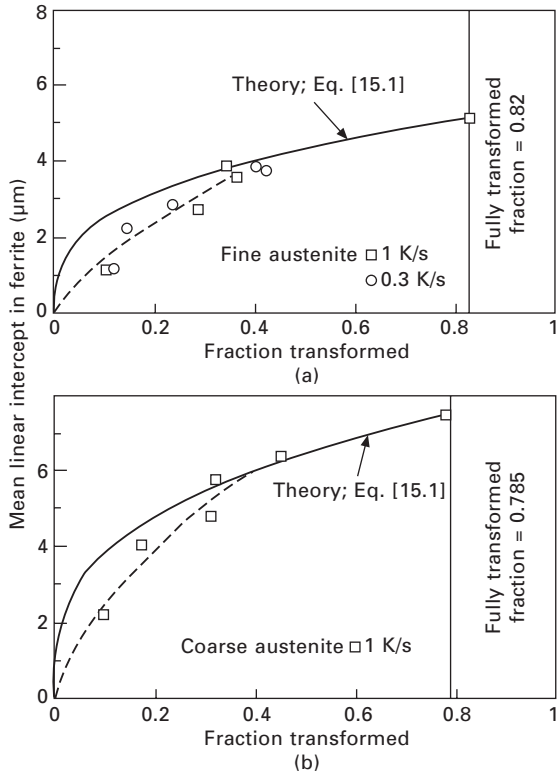
$$d_i = d_c(V_i/V_c)^{1/3} \qquad [15.1]$$

where d_c is the mean linear intercept grain size of ferrite after complete transformation; V_c represents the volume fraction of ferrite at the end of transformation (the remainder being pearlite, martensite and/or carbide); and d_i, V_i are corresponding quantities at any instant during incomplete transformation. This assumes that each grain represents an initial nucleus that has grown to the final grain size. Figure 15.2 illustrates quite clearly that for up to 40% of the transformation the data lie below this line, meaning there were more grains/nuclei than required to form the final microstructure. It appears that coarsening even occurs when there is no retained strain, although the degree of coarsening would appear to decrease as the retained strain increases. Similarly, cooling rate and composition are expected to play a role.

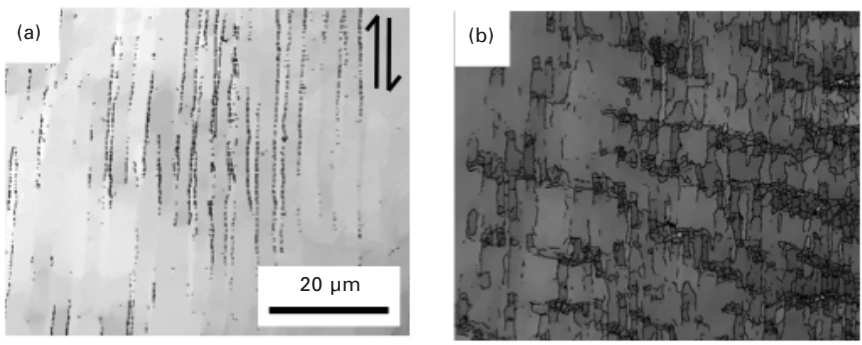
The other feature, that rafts were formed in different areas, is due to a number of factors. The most important is that the prior austenite grains will have different orientations with respect to the deformation and hence will deform differently. Figure 15.3 shows an electron back scattered diffraction (EBSD) map of ausenite grains in Ni-30Fe with different orientations after deformation to a strain of 0.5. It is clear that the level of deformation and the internal structure within the grains is significantly different for A-type crystallographically orientated grains developing much less internal structure, which in turn affects the grain boundary roughening as well as the development of internal nucleation sites. Another factor for locally different transformation rates is the local composition fluctuations. Through microsegregation there can be differences in Mn and other elements, which is why banding is a common feature in low to medium carbon steels.

Priestner and Hodgson (1992) proposed that the ferrite rafts will continue to grow until they directly impinge upon another ferrite raft or by overlapping

© Woodhead Publishing Limited, 2012



15.2 Mean linear intercept in ferrite phase during transformation with a retained strain of 1.25 for two prior austenite grain sizes: (a) fine (35 μm) and (b) coarse (65 μm) (after Priestner and Hodgson, 1992).



15.3 A comparison between the substructure developed in Ni-30Fe alloy within the deformed matrix grains having orientation A, (1-11)[110], (a) and orientation C, (001)[110], (b) in shear deformation mode for a deformation temperature of 1000°C, strain rate of 1 s^{-1} and strain of 0.5. The black lines represent $\theta > 0.5°$ boundaries in both EBSD maps. The double arrow in (a) indicates the macroscopic shear direction (after Beladi *et al.*, 2010).

© Woodhead Publishing Limited, 2012

diffusion fields (i.e. soft impingement). They stated for the first time that to obtain an ultrafine microstructure required 3D impingement, almost instantaneously, across the microstructure. As will be shown later in this chapter, the current authors still believe that this is the key to obtaining an ultrafine microstructure either dynamically or even statically.

Novillo *et al.* (2004) explored the reasons for the observation by Priestner and Hodgson (1992) using a detailed EBSD study of the evolving microstructure. Behind the transformation front (i.e. within what Priestner and Hodgson (1992) termed a raft) their work suggested that the grain coarsening resulted from a mixture of normal grain growth and coalescence. The latter occurs if there is a low misorientation between neighbouring ferrite grains. They also found that, as the retained strain was raised, in general the misorientation between neighbouring ferrite grains increased and coarsening was dominated by normal growth. In later modelling (Li *et al.*, 2007) using both cellular automata (CA) and Monte Carlo (MC) approaches, the role of curvature driven growth in the coarsening behaviour of an undeformed austenite was also shown.

In summary, it is possible to produce a microstructure consisting of ultrafine ferrite grains through heavy deformation of the austenite. However, as this happens only in local regions, the subsequent filling of space by the growing transformation front also results in coarsening and the potential level of refinement appears to saturate such that only grain sizes of the order of 5 μm are possible.

15.3 Ultrafine ferrite formation in steels

15.3.1 Early observations

In the late 1980s a series of papers appeared by researchers from Nippon Steel Corporation (NSC) where grain sizes of the order of 1 μm were reported for the first time through transformation (Yada *et al.*, 1984, 1988). The only other time that such a fine grain size had been obtained was in early work on the Hall–Petch relationship in steel by Morrison (1972), where he obtained even finer grain sizes by careful control of cold rolling and annealing. For some reason this early work did not attract a large amount of attention, even though NSC appeared to have been able to produce full-scale trials as part of its patents (Yada *et al.*, 1984).

The essence of the work was to deform the steel just above the Ar_3 (i.e. the continuous cooling ferrite transformation start temperature). The deformation appeared to do two things: raise the Ar_3 so that the transformation was accelerated and occurred during deformation, and induce dynamic recrystallisation of the ferrite in subsequent passes. Most of this work was performed using plane strain compression with very large strains per pass.

© Woodhead Publishing Limited, 2012

The NSC group also developed multiphase steels consisting of ultrafine ferrite and retained austenite, where this austenite would then transform to martensite (i.e. by transformation induced plasticity – TRIP) during deformation at room temperature, thus providing high strength and good ductility.

There was also even earlier work on intercritical rolling (Priestner and de los Rios, 1980) where patches of very fine ferrite grains could be seen in the microstructure. Mintz and Jonas (1994) also showed in hot ductility tests that, when the test temperature was just near the Ar_3, ferrite grains much finer than generally observed could be obtained. In this case they were not ultrafine but even at the very low strain rates and moderate strains there appeared to be significant refinement if the transformation occurred dynamically (i.e. during deformation).

In a multipass hot torsion study of the transformation behaviour of a microalloyed steel under high rates of cooling and short inter-deformation times, Beynon *et al.* (1992) also showed that for some conditions the ferrite was remarkably refined and that small changes in temperature either way led to either ultrafine, coarsened or work hardened ferrite. So again this suggested that deformation near the Ar_3 was important to obtain very fine grain sizes.

However, systematic research on ultrafine ferrite did not really begin until the late 1990s. The first driver was the large national programme called the 'Ultra Steel Project' in Japan to develop the next generation of steels (Sato, 2000), which was soon matched by similar programmes in Korea (Lee, 2000) and China (Weng, 2000). The second was the work by the authors' group, which arose out of studies initially related to the rolling of strip cast steels (Hodgson *et al.*, 2000) while Hodgson was at BHP Research, that then moved into more basic research. Most of the work focused on understanding and trying to control the dynamic transformation process while also trying to separate out the important factors and physical phenomena. Even now there are still a number of remaining questions as will be discussed later.

The work in Japan, Korea and China was largely based around hot compression studies to map conditions where an ultrafine ferrite microstructure could be obtained and the effect of process variables and composition. There has been a large amount of debate as to whether the dynamic transformation can even occur above the Ae_3 (Matsumura and Yada, 1987; Yada *et al.*, 1997; Basabe and Jonas, 2010). One of the key issues that has arisen from this is that the strains required to obtain a large fraction of ultrafine ferrite are very high – much higher than those easily achieved in hot rolling. So, as will be shown later, the next stage was to develop multi-deformation strategies to obtain a greater fraction of ultrafine grains.

The early work by Hodgson and co-workers (Hickson *et al.*, 1999; Hodgson *et al.*, 2000; Hurley *et al.*, 2001) involved the rolling of thin strip with a large austenite grain size under conditions where there is a high level of shear in

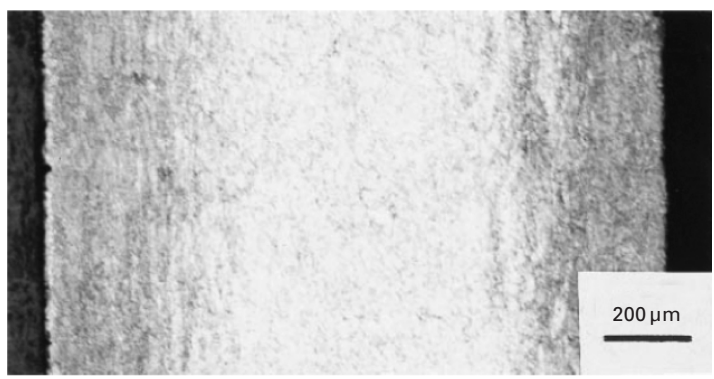
© Woodhead Publishing Limited, 2012

certain regions of the strip and where the rolls also rapidly cool the strip. Inducing shear means that the effective strain in the near surface regions is much higher than the nominal strain from the reduction in thickness (Hickson *et al.*, 1999; Hurley *et al.*, 2001). They found that steels with compositions ranging from 0.04 to 0.77 wt%C could all be rolled to obtain an ultrafine layer on the top and bottom of the strip with a coarser microstructure in the middle (Hickson *et al.*, 1999). For the rest of this chapter this will be referred to as 'shear strip rolling'.

15.3.2 Shear strip rolling

The concept for shear strip rolling arose from work related to the thermomechanical processing of directly cast strip steels. While some studies of direct rolling from a laboratory strip caster were performed, most of the work involved reheating thin 2 mm strip to produce a large austenite grain size followed by hot rolling. In these experiments the effect of temperature was considered at it was found that the large austenite grain size substantially reduced the Ar_3 relative to the Ae_3 and hence it was possible to roll at high undercoolings. This was accentuated by the quenching effect of the cold rolls. The overall effect of this (Hodgson *et al.*, 1998) was that an ultrafine grained ferrite surface layer was formed on both the top and bottom surfaces of the strip while the centre of the strip formed much coarser ferrite (Fig. 15.4). This result on the surface contradicted all views related to ferrite refinement: one pass, instead of heavy accumulated deformation, and air cooling after rolling, rather than intense quenching.

Further investigation (Hodgson *et al.*, 1999) showed that the key factors were the high level of undercooling combined with a shear zone caused by



15.4 Layered microstructure after single pass rolling of a low carbon steel consisting of surface UFF (dark) and coarse centre grains (light) (after Hodgson *et al.,* 1999).

© Woodhead Publishing Limited, 2012

friction between the thin strip and the work roll. In other experiments (Hickson and Hodgson, 1999) the strip was rolled with the work rolls closed and an intense water curtain directed into the roll gap. As the strip was rolled it was then instantaneously quenched on the exit side of the rolls. This produced a different layered structure, in this case an ultrafine ferrite on the surface and a quenched martensite core, suggesting that the ferrite formed dynamically during the very short time in the roll gap.

A wide range of steel compositions was then tested and a common picture emerged of this layered structure, with relatively little difference in the ferrite grain size in the surface layer (Hickson *et al.*, 1999). Finally, a model Fe-Ni alloy (discussed later) was used to show the nature of the deformation structure in the austenite. The centre of the strip consisted of conventional relatively low angle microbands. There was then a transition zone, while the surface layer consisted of high angle cells and evidence of a very complex deformed structure due to the high shear. It was proposed that these regions could be suitable nucleation sites (Hurley *et al.*, 2001), which, combined with the high undercooling and the rapid quenching, gave full 3D impingement within these zones. Such deformation features are less sensitive to composition which would then explain the relatively constant grain size in the sheared zone. However, this process offered little control and also could not produce a fully transformed ultrafine strip, and so most work since has focused on more conventional deformation processes.

15.3.3 Effect of process parameters

From all of the laboratory studies to date, it is clear that the strain, strain rate and temperature play major roles in determining the extent of transformation to ultrafine ferrite. Strain is the dominant factor as there is generally a critical strain required to start the dynamic transformation process (Beladi *et al.*, 2004a,b). This can be inferred from the stress–strain curves (Choi *et al.*, 2003) in a similar way to the detection of the onset of dynamic recrystallisation (Poliak and Jonas, 2003). Increasing the strain enhances the volume fraction of ultrafine grains until a strain is reached where there is no further transformation. This is most clearly seen using a hot torsion test, as the strain range over which this happens is much larger than in compression. The reason for this is that in torsion the number of active slip systems is much lower than other modes of deformation (Davenport and Higginson, 2000) and this difference appears to increase with decreasing temperature.

The deformation temperature affects the level of undercooling of the austenite and so plays a strong role in the rate of transformation (Matsumura and Yada, 1987; Yada *et al.*, 1988; Hanlon *et al.*, 2001; Hurley and Hodgson, 2001; Beladi *et al.*, 2004c). Whether it is possible to have strain-induced transformation above the Ae_3 (Matsumura and Yada, 1987; Yada *et al.*,

© Woodhead Publishing Limited, 2012

1997; Basabe and Jonas, 2010) is still an area of debate. In early work it was unclear if this was a result from transformation during the quench, but more recent work (Basabe and Jonas, 2010) does suggest that it is possible. However, the amount of transformation will be low and higher levels of undercooling are required to form a significant volume fraction of ultrafine ferrite.

While temperature affects the volume fraction of ultrafine ferrite, it does not appear to have a major effect on the ferrite grain size. In the early shear strip process, Hodgson and co-workers rolled a wide range of steel compositions and in all cases obtained a grain size of approximately 1 μm (Hurley and Hodgson, 2001). Other work has also shown a relatively constant ferrite grain size over a wide range of compositions as well, except in microalloyed steels where it does appear that Nb offers further refinement (Hickson and Hodgson, 1999; Dong, 2001). In other words, if the temperature and strain (and composition) are such that they lead to dynamic transformation to ferrite, then they do not have a great effect on the actual grain size, although they will affect the volume fraction.

The effect of strain rate is much more complex with different authors claiming that increasing strain rate can lead to a finer structure (Mintz and Jonas, 1994; Seo *et al.*, 1999; Hurley and Hodgson, 2001; Beladi *et al.*, 2004b), whereas others (Seo *et al.*, 2001; Tong *et al.*, 2004a,b) state that it is detrimental to obtaining a uniformly fine microstructure. This is probably not unexpected and it is likely that the role of strain rate will depend upon the composition and the level of undercooling. Increasing the strain rate can produce deformation heating and reduce the time available for transformation, and these two factors will work against an ultrafine structure being formed. However, at higher levels of undercooling an increase in strain rate is likely to refine the microstructure through dynamic recrystallisation. As will be discussed elsewhere, there is evidence that the microstructure involves both transformation and dynamic recrystallisation. If so, then increasing the strain rate is known to have a strong effect in refining the grain size during dynamic recrystallisation (Dehghan-Manshadi *et al.*, 2008).

15.4 Nature of the transformation

15.4.1 Mechanism

There has been speculation over the years as to whether this is a conventional austenite to allotriomorphic ferrite transformation or some other form, such as a massive transformation (Yada *et al.*, 2000). The latter has largely been based upon the insensitivity of ferrite formation during deformation to the strain rate up to 250 s^{-1}. It was concluded that there would not be long range carbon diffusion taking place during transformation, limiting the carbon

© Woodhead Publishing Limited, 2012

partitioning between ferrite and adjacent austenite. A possible contribution of massive transformation in the dynamic strain-induced phase transformation was then suggested (Yada *et al.*, 2000).

Hurley *et al.* (1999) showed that the transformation appears to produce the conventional Kurdjumov–Sachs orientation relationship between the austenite and the ferrite. There is also clear evidence of carbon rejection to the ferrite grain boundaries due to the large number of carbides observed at triple points. There are also some reports of carbides within the grains, although whether they form during the transformation or cooling is not clear.

There is also debate about the role of dynamic recrystallisation in the ferrite refinement. It has been suggested that the transformation initially leads to a slightly coarser grain size and that this is then refined through dynamic recrystallisation (Hong *et al.*, 2003). It would appear that this is through a fragmentation process, rather than the bulge process in conventional discontinuous dynamic recrystallisation (Dehghan-Manshadi *et al.*, 2008). Ferrite is known (Eghbali *et al.*, 2006; Oudin *et al.*, 2008) to undergo continuous dynamic recrystallisation at high temperatures and moderate strain rates. This involves the build-up of substructure inside the grains eventually leading to high angle boundaries. As will be shown in a later section, if the ultrafine grains are allowed to grow, then they clearly show this structural evolution. However, this takes a large strain, whereas after the formation of the ultrafine grains through transformation, there may not be sufficient strain for this to occur. As will be discussed, this is an area where more systematic work is required.

As most evidence points to a conventional austenite to ferrite transformation, it is clear that it is necessary to be able to introduce a high density of nucleation sites into the austenite.

15.4.2 Nucleation sites

Ferrite preferentially nucleates at austenite grain boundaries. The density of potential nucleation sites for ferrite transformation, S_v, is expressed as the surface area of high angle austenite boundaries per unit volume of material. With the absence of recrystallisation, the deformation can enhance the number of ferrite nucleation sites through both direct and indirect geometry changes in the austenite. The indirect geometry effect of deformation can be seen in the reduction in the distance between adjacent austenite grain boundaries. The large flattening of the austenite grains through deformation means smaller separation between them, which may limit the size of ferrite growing from each of the boundaries through soft impingement resulting in a smaller ferrite grain size.

The primary effect of deformation is to introduce serrations in the austenite

© Woodhead Publishing Limited, 2012

grain boundary, which then act as nucleation sites for the transformation. Indeed, the strain enhances the number of nuclei per unit length of austenite grain boundary. The coherent twin boundaries also lose their low energy characteristics with strain, transforming to high angle grain boundaries, which may also become appropriate sites for ferrite nucleation (Tamura, 1988). The role of deformation in ferrite grain refinement becomes more pronounced when it activates intragranular defects (i.e. deformation bands (Bengochea *et al*., 1999), and dislocation arrays (Umemoto *et al*., 1992)), with relatively high angle internal structures. These intragranular features can be suitable sites for ferrite nucleation, consequently leading to more refinement of the ferrite grain size.

Early work revealed that the strain enhances the deformation band density more rapidly than the austenite grain boundary area (Tamura *et al*., 1988; Kvackaj and Mamuzic, 1998). It was then proposed that the ferrite grain refinement resulting from deformation with the absence of recrystallisation is due mainly to an increase in the deformation band density rather than an increase in the austenite grain boundary area. Kozasu *et al*. (1977), however, argued that not all deformation bands have the same potential as grain boundaries to act as nucleation sites for ferrite. Bae *et al*. (2004) later studied the effect of the surface area of prior austenite grain boundaries and deformation bands on DSIT ferrite nucleation using a high strength low alloy steel (0.15C-0.04Nb). Samples were deformed either in the recrystallisation region or in the non-recrystallisation region to achieve two different austenite conditions (i.e. equiaxed austenite grains and elongated austenite grains, respectively) with the same effective surface area. Then, the samples were deformed at a strain of 0.6 just above the Ar_3 followed by water quenching. The microstructural study revealed that the volume fraction of DSIT ferrite nucleated from the elongated prior austenite grains was higher than that nucleated from the equiaxed austenite grains. It was concluded that the diffusional transformation was accelerated by the presence of deformation bands formed in the non-recrystallisation region.

A recent study by Beladi *et al*. (2004c) confirmed that dynamic strain induced transformation initially occurred at prior austenite grain boundaries at an early stage of deformation followed by intragranular nucleation, as in controlled rolling. It was proposed that the extra grain refinement through the DSIT route compared with controlled rolling (i.e. static transformation) is largely due to the absence of a delay between deformation and transformation in this mechanism (Priestner and de los Rios, 1980). This effectively eliminates the possibility for recovery to occur within the austenite, thus enhancing the effectiveness of intragranular defects (i.e. deformation bands) in nucleating ferrite. This idea was supported by some researchers (Amin and Pickering, 1982; Yoshi *et al*., 1988) who concluded that recovery of the dislocation substructure within deformation bands decreases the potential for ferrite

© Woodhead Publishing Limited, 2012

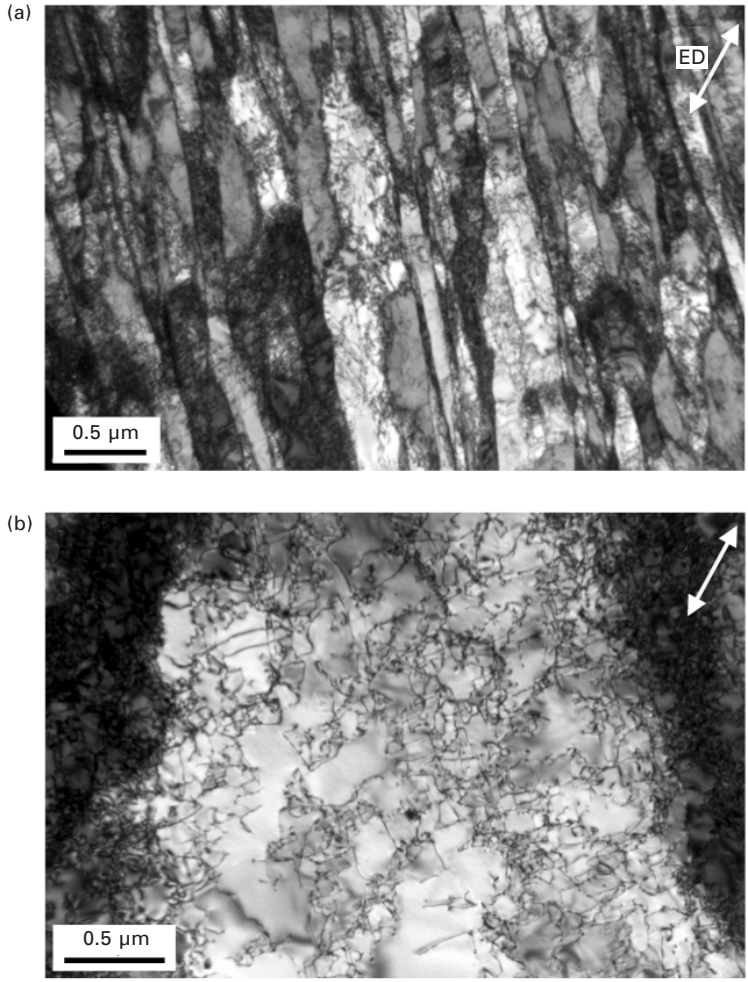
nucleation on these bands. Hurley (1999) also suggested that if recovery takes place between the deformation and the transformation, then the level of refinement is not as great, which would support the need for concurrent deformation.

More recently, Adachi *et al*. (2007) performed critical experiments in which they successfully produced a ferrite grain size of ~1.5 μm through static transformation. The main difference between this process and controlled rolling is the deformation temperature. They deformed a 0.2C-2Mn-2Si (in wt%) steel with a large austenite bay at a temperature of 570°C followed by reheating to 750°C and controlled cooling to room temperature, whereas the deformation temperature is generally above 800°C in controlled rolling. Although the rate of recovery could be different for both techniques, it appeared that the recovery did not affect the nucleation potential of the intragranular defects. Rather, it was reported that the low temperature deformation induced organised microband structures with high misorientation angle and a sufficiently fine spacing to form the ultrafine ferrite. This was determined by studying the nature of intragranular defects in Ni-30Fe alloys that have a similar stacking fault energy to low alloy steels (Charnock and Nutting, 1967) as these alloys maintain their austenitic microstructure to room temperature.

Besides the deformation temperature, the substructure characteristics (i.e. morphology, size and misorientation angle) strongly depend upon the grain crystallographic orientation (Cizek *et al*., 2005), grain size (Adachi *et al*., 2007) and deformation mode (Beladi *et al*., 2011; Inoue *et al*., 2001), which may alter the ferrite nucleation sites and consequently grain refinement. More recent work related to the plane-strain compression technique revealed that the substructure formed within grains relating to the copper, S, brass, goss and rotated goss texture components was relatively homogeneous and appeared to display similar general character (Cizek *et al*., 2005). The quantitative substructure characteristics, however, differed significantly between the different orientations. Whereas microbands were the common dislocation feature in non-cube orientated grains, in cube orientation, the grains were split into coarse deformation bands containing large, low misorientation subgrains (Fig. 15.5) (Cizek *et al*., 2005). This produces a more heterogeneous deformation structure.

The austenite grain size also appeared to affect the nature of intragranular defects. In coarse austenite grains, the substructure developed in the grain interior tends to differ from that in the vicinity of grain boundaries, enhancing inhomogeneity of ferrite grain distribution (Beladi *et al*., 2011). In the grain interior, the microbands are the dominant intragranular feature. However, the substructure in the vicinity of prior austenite grain boundaries is characterised as complex cell/subgrain morphologies, rather than microband, with comparably higher misorientation angles across them. The extent of

© Woodhead Publishing Limited, 2012



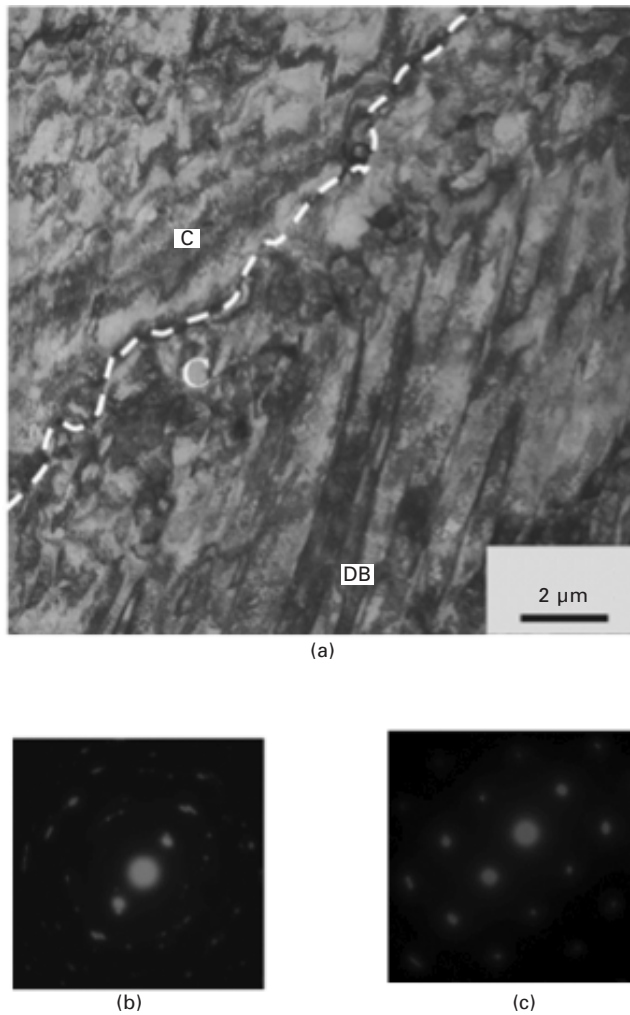
15.5 TEM bright-field micrographs of the interior of grains oriented close to the goss texture component (a) and the cube texture component (b) in the Ni-30%Fe alloy deformed in plane strain compression at 800°C to a strain of 0.5. The arrows indicate the sample extension direction ED.

this complex region changes with grain size as well as the thermomechanical condition (e.g. strain).

The distinct difference in intragranular features developed in grain interiors and near grain boundaries is known to be due to the disparity in the number of operating active slip systems (Kashyap and Tangri, 1997; Beladi *et al.*, 2010). The interior of a grain is generally deformed through a restricted number of active slip systems leading to the formation of an organised banded structure with a systematic alternation in the misorientation across the band

© Woodhead Publishing Limited, 2012

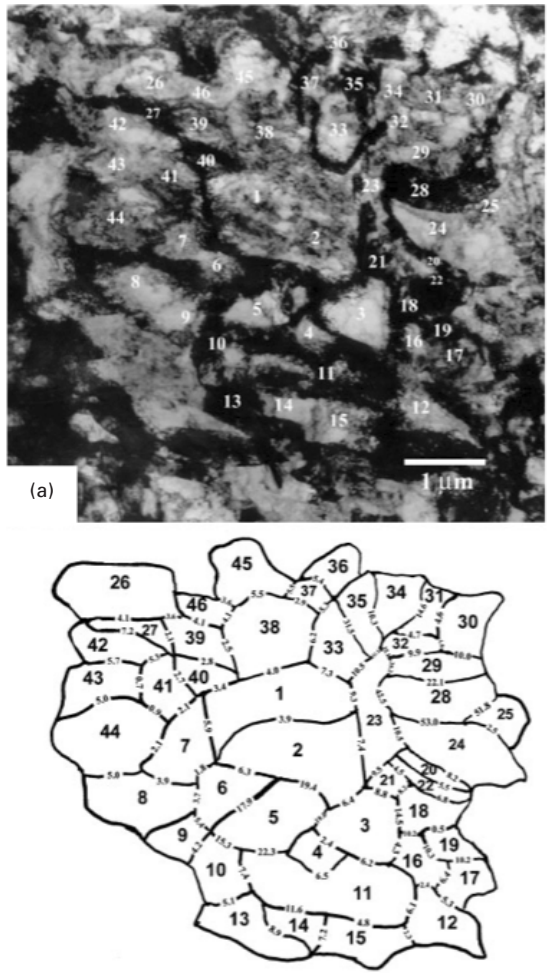
width (Fig. 15.6). However, the regions close to the grain boundary enhance the activation of multiple slip due to the strain compatibility requirements, resulting in the formation of a subgrain/cell substructure, locally having higher misorientation angles compared with the microband formed in the grain interiors (Kashyap and Tangri, 1997; Beladi *et al.*, 2010) (Fig. 15.6). Similarly, a heavily dislocated, equiaxed cell substructure was also reported



15.6 (a) TEM bright-field image of Ni-30%Fe alloy deformed at 570°C at a strain of 1. (b) and (c) show diffraction patterns of areas close to the grain boundary (i.e. C) and grain interior (i.e. DB), respectively. The dashed line represents the prior austenite grain boundary (after Beladi *et al.*, 2011).

© Woodhead Publishing Limited, 2012

in the surface layer of hot rolled austenite using the shear strip process (Fig. 15.7) (Hurley *et al.*, 2001). The formation of complex substructure in the surface layer of the rolled strip can be explained due to simultaneous operation of shear and compression deformation modes at the surface region, which similarly enhance the activation of multiple slip systems. The boundaries between most pairs of dislocation cells showed relatively high misorientation angles and their size closely corresponded with the size of ultrafine ferrite grains (i.e. spacing between nuclei) produced on the surface of the strip



15.7 (a) TEM bright-field image showing substructure within surface zone of Ni-30Fe strip rolled at 800°C and (b) schematic representation of cell structure observed in (a), with angles of misorientation across individual cell boundaries superimposed (after Hurley *et al.,* 2001).

© Woodhead Publishing Limited, 2012

through the DSIT process (Hurley *et al*., 2001). The mode of deformation can also play an important role in establishing the type of intragranular defects and consequently the level of grain refinement. A multi-axis deformation technique has been employed by others to establish these features and successfully refine ferrite grain size at lower strains (Inoue *et al*., 2001).

15.5 Modelling

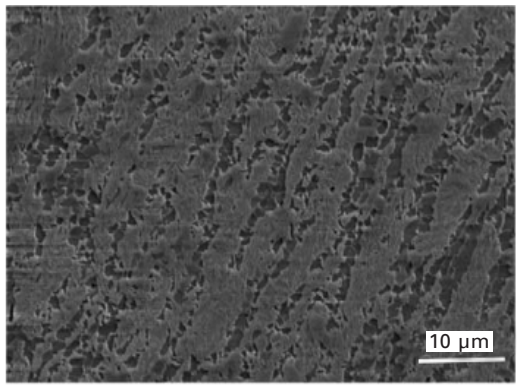
15.5.1 A descriptive model

The authors have proposed (Hodgson *et al*., 2008) a descriptive model in an attempt to bring together the key elements of what we believe is occurring, although also acknowledging there are still a number of gaps. The key element of this is that the austenite has a regular spacing of internal high angle boundaries that will act as the nucleation sites and that the aim is to obtain 3D impingement as rapidly as possible. In Fig. 15.3 there is a regular spacing of planar defects in the austenite that will act as potential nucleation sites. In the first instance, rafts of ferrite will form along these defects (Fig. 15.8(a)), similar to the static transformation results of Priestner and Hodgson (1992). If transformation is incomplete then those rafts will coarsen and consume other 'potential' nucleation sites (Fig. 15.8(b)). However, if the cooling rate is high, then it may be possible to activate these sites before they are consumed during cooling. This explains why a complete ultrafine microstructure can be formed, even if there is incomplete strain induced transformation (Fig. 15.8(c)).

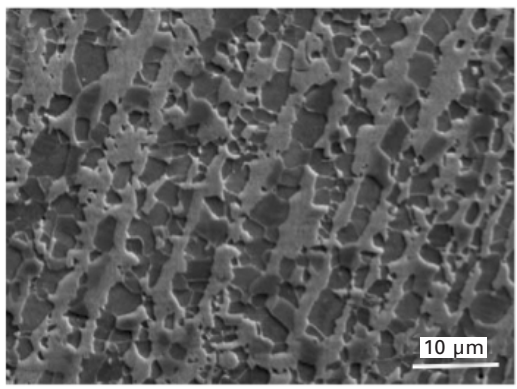
However, to form the ultrafine microstructure during deformation only, other factors must come into play. Firstly, if the deformation rate is reasonably high and the strain is sufficient, then all of the potential nucleation sites will have become activated within a very short time. With little time for growth to have occurred, either during the deformation or very soon after they will all grow and 3D impingement will be achieved.

These two scenarios do not fully cover all of the observations, though. In the case of the hot torsion tests at a moderate strain rate, the transformation occurs over a very large strain and hence time scale. In this case, the transformation progress can be clearly followed and there are some important observations. First, the grains remain equiaxed throughout, even though some will have formed very early in the deformation and could have experienced strains of over 1 which would be expected to elongate these grains. Secondly, there is no evidence of coarsening (i.e. growth of grains formed earlier in the deformation). This is one aspect that is not completely understood. To maintain an equiaxed grain shape would suggest dynamic recrystallisation, because in dynamic recrystallisation the grains formed early in the process do maintain an equiaxed shape. This is presumably through

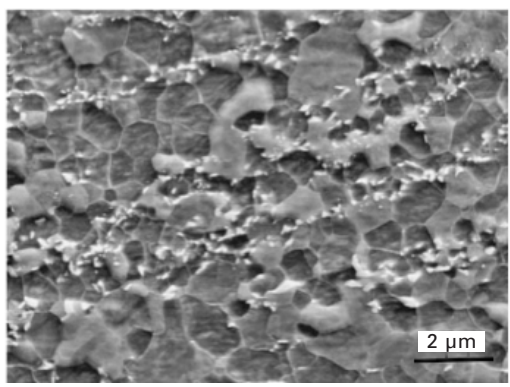
© Woodhead Publishing Limited, 2012



(a)



(b)



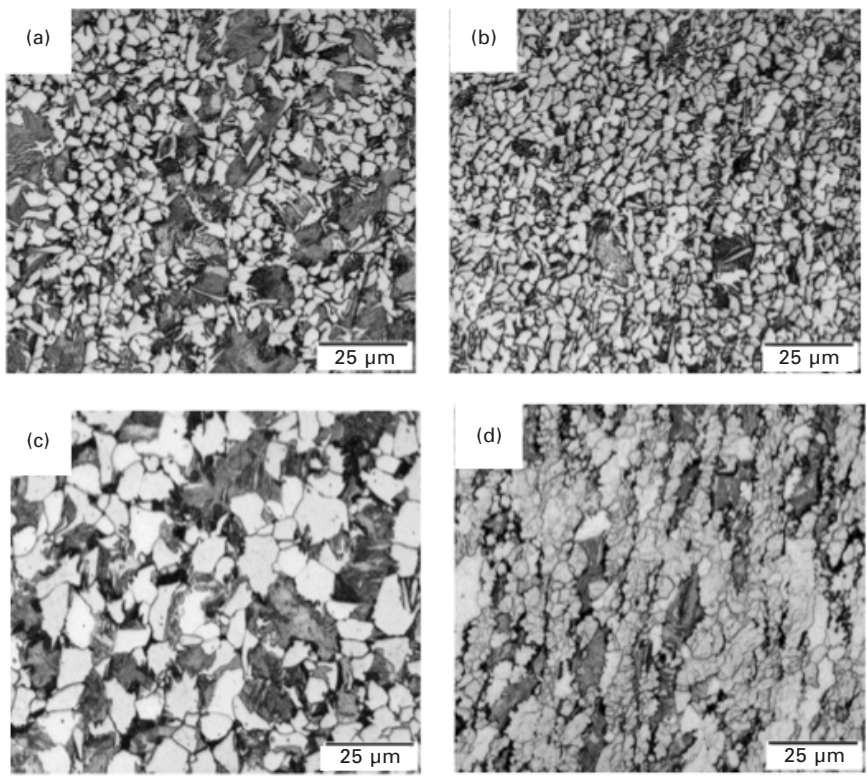
(c)

15.8 The microstructures of 0.17C-1.5Mn-0.02V (in wt%) steel after deformation at 775°C for different quench temperatures: (a) 775°C and (b) 710°C (after Beladi *et al.,* 2004c); (c) UFF structure formed in 1020 plain carbon steel through DSIT route (after Beladi *et al.,* 2004a).

© Woodhead Publishing Limited, 2012

repeated recrystallisation. What is different here, though, is that the ferrite grains will often be surrounded by austenite and therefore it is more difficult to imagine a recrystallisation process occurring. Rather, it may be a grain rotation process, even though this is happening at such high strain rates and low temperatures.

This is not to say dynamic recrystallisation is not occurring. Shokouhi and Hodgson (2009) examined this by using multi-deformation torsion tests. In these the first deformation was used to obtain a given fraction of strain induced ferrite. Then the inter-deformation time was varied before a second deformation was performed, followed by a quench. It was found that during the inter-deformation time, there was coarsening. However, if the second deformation was activated before the grain size had doubled then the ultrafine microstructure was maintained (Figs 15.9(a,b)). In contrast, if the microstructure had coarsened during the second deformation, there was elongation of the grains, the development of an internal substructure



15.9 (a) DSIT ferrite coarsened to <2 times its size, then (b) deformed to a strain of 2. (c) DSIT ferrite coarsened to >2 times its size, then (d) deformed to a strain of 1 (after Hodgson *et al.*, 2008).

© Woodhead Publishing Limited, 2012

and eventually the formation of high angle boundaries at large strains (Figs 15.9(c,d)). This is typical of continuous dynamic recrystallisation, commonly observed in ferrite (Eghbali *et al.*, 2006; Oudin *et al.*, 2008). Interestingly, the final grain size (as defined by the spacing of the high angle boundaries in both cases) was the same.

Therefore, this suggests that the grain size in the ultrafine ferrite is linked to that which would form under continuous dynamic recrystallisation and that this is the stable unit size under the given deformation conditions. This would also explain the slight refinement seen in Nb microalloyed steels (Hickson and Hodgson, 1999; Dong, 2001).

15.5.2 Mathematical models

From the early papers dealing with ultrafine ferrite there have been a number of attempts to develop mathematical models to describe the phenomenon and potentially provide greater insight into the mechanism(s).

The early models attempted to relate the nucleation rate to the stored energy induced by the deformation (Umemoto *et al.*, 1992). On the surface this would seem reasonable. However, if this is correct then why is there a limit in controlled rolling? For example, the strain levels where ultrafine ferrite is observed are of the order of 0.6–1.0 in uniaxial compression. In a hot strip mill producing 2 mm strip, the accumulated strains can therefore be as high as 2.5. While there is some recovery between passes, most of the deformation energy is still stored in the austenite and yet the final grain size is only 5 μm. As already noted above, the real reason for this is that conventional rolling at typical rolling temperatures does not create high angle features within the austenite grains to then act as nuclei.

Recently, Militzer and Brechet (2009) developed a phenomenological model that captures most of the work described above and leads to predictions that match experimental data. Their model assumes intragranular defects set up by deformation providing suitable nucleation sites (i.e. corner points of the dislocation substructure of microshear bands) for ferrite nucleation. The UFF formation was predicted to be independent of the steel chemistry in low carbon steels and would be promoted by the strain rate.

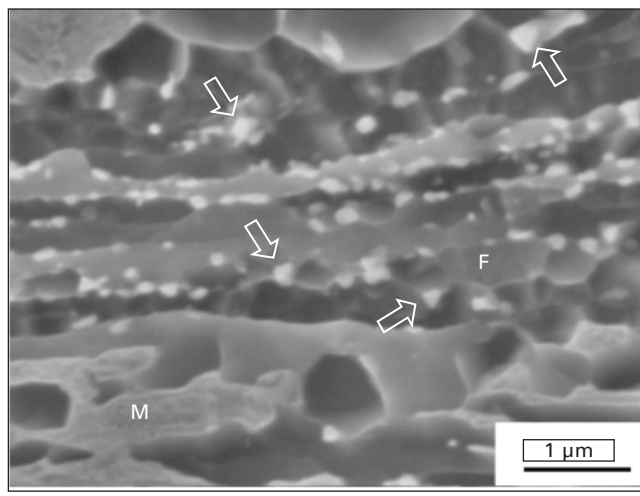
15.6 Can grain sizes less than 1 μm be achieved?

The above sections have all demonstrated that the grain size saturates towards a minimum of 1–2 μm. This would appear to be related to the typical spacing between internal high angle deformation features in the austenite grains and the size expected if dynamic recrystallisation of the ferrite is operating. Recently Yokota *et al.* (2004) considered the formation of nanoscale microstructures in steel by phase transformation. Using a thermodynamics approach, they

© Woodhead Publishing Limited, 2012

showed that the grain size for two classes of C-Mn steels (low and high Mn) as a function of the free energy change was much greater than predicted in the ideal case. In this ideal case, it should have been possible to achieve grain sizes below 100 nm with relatively small free energy changes, whereas even at very large free energy changes, the grain size was almost independent of the free energy change and remained close to 1 μm. While there were a number of simplifying assumptions, the authors were able to show that recalescence will lead to large temperature rises and that if this temperature rise was then used to create a recalescence corrected curve, then there was much better agreement with the data. Their overall conclusion was that very large undercoolings are required to obtain much finer grain sizes, but that this then leads to recalescence which essentially cancels this factor out and that there needs to be a process developed where isothermal transformation can be maintained at such high undercoolings.

This seems quite reasonable and supports nearly all of the observations in this chapter. However, in the section on the nature of nucleation sites, it was shown that, in a steel deformed at a low temperature, near the prior austenite grain boundaries there were areas of intense deformation and very small cell sizes (Fig. 15.6). This was also the steel where the static transformation behaviour could be studied. In this case the region near the prior austenite boundary did, in fact, transform at 650°C to much finer ferrite (Fig. 15.10) of the order of 200–800 nm, again with numerous carbides located between



15.10 The microstructure of 0.3C-2Mn-2Si-0.28Mo steel deformed at 570°C, strain rate of 0.1 s^{-1} and strain of 1 followed by reheating to 650°C held for 15 minutes before quenching in water. Arrows show the carbides (i.e. white particles). M and F represent martensite and ferrite, respectively (after Beladi *et al.*, 2011).

© Woodhead Publishing Limited, 2012

the ferrite grains (Beladi *et al.*, 2011). Hence, while there is no doubt that coalescence will reduce the refinement effect, a factor widely known in trying to industrially control pearlite refinement, there is an underlying issue related to the density of nucleation sites and the rapid 3D impingement.

15.7 Industrial implementation

From the above it is clear that the deformation conditions to produce a significant volume fraction of ultrafine ferrite are quite extreme. High reductions and significant undercooling are difficult to achieve in conventional processes as it is more typical in hot rolling for the later passes to be relatively small for good shape control. However, there are a number of reports of attempts at industrial implementation. As mentioned in Section 15.3.1, Nippon Steel Company undertook full-scale mill trials, described in their early patents of this process (Yada *et al.*, 1984). There was also another approach to make very tough plate where the surface of the plate was quenched prior to the final pass(es) so that the surface region was then rolled to form an ultrafine layer. This was then shown to significantly improve the toughness (Ishikawa *et al.*, 2001; Tsuchida *et al.*, 2004).

In China and Korea there are reports of large-scale laboratory and industrial trials. In Korea this involved making plate using a large-scale laboratory mill (Lee and Um, 2008) where tight control of temperature and deformation conditions was possible. In China there appears to have been a large number of products produced in this way, including bar and plate (Dong *et al.*, 2008). However, in most cases the grain sizes they are reporting are closer to 3 μm and sometimes more in the range 3–5 μm. This does represent a major refinement over the typical grain size for the given process but it is unclear whether it is a real strain induced ferrite or not.

There has been an attempt to develop, on a large laboratory scale, a concept mill specifically to implement ultrafine ferrite production. The spacings between the stands and having cooling immediately after the last stand have led to the production of bulk material with a grain size of around 1 μm (Miyata *et al.*, 2007). It is also possible with this process to produce more complex mixed microstructures, such as dual-phase steels with ultrafine ferrite and martensite. In essence, this mill captures the key elements discussed above where an ultrafine microstructure can be built up over a number of passes as long as there is insufficient time for coarsening both between the deformations and after the final deformation.

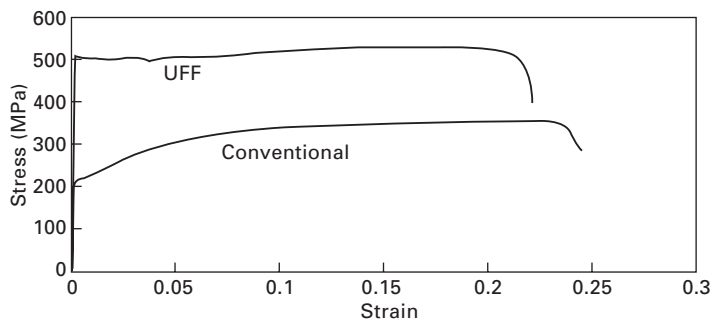
15.8 Future trends

Despite significant research performed so far, there are still a number of areas which require further work including the role of dynamic recrystallisation of

© Woodhead Publishing Limited, 2012

ferrite in the production of UFF by DSIT. This arises from the complexity of the DSIT process as the deformation is being applied in the two-phase region beyond the onset of DSIT ferrite formation. Therefore, while some ferrite grains are formed during deformation, those that formed at an earlier strain are being deformed at the same time. It is expected that the level of deformation of the ferrite could be quite high as the strain will be more concentrated in the ferrite phase, because the ferrite is much softer than the work hardened austenite. Therefore, the DSIT ferrite grains should be noticeably elongated along the deformation direction, but they mainly maintain their equiaxed morphology. This leads to different hypotheses such as the occurrence of continuous dynamic recrystallisation of ferrite, otherwise the size of DSIT ferrite would be close to the steady-state subgrain size obtained in ferrite for a given deformation condition.

Another issue that has become apparent is that a fully ultrafine ferrite structure can lead to a yield stress close to the value of the tensile strength. This produces flatter stress–strain curves (Fig. 15.11), offering a high yield ratio (i.e. the proportion of yield strength to ultimate tensile strength), varying between 0.7 and 1 (Beladi *et al.*, 2007). Such unstable plasticity is a common feature of such steels and severely limits the prospects for their utilisation. This undesired property motivates a search for new approaches to design UFF microstructure having optimum mechanical properties. The yield ratio can nevertheless be decreased through improvements in the microstructure. There were some attempts to overcome this barrier through inducing a second phase such as martensite into the UFF microstructure (Fujioka *et al.*, 2001; Um *et al.*, 2001). It appeared that the presence of martensite islands in UFF structure significantly reduces the yield ratio to ~0.6–0.7 through a continuous yielding phenomena (i.e. low yield strength and high work hardening rate) (Beladi *et al.*, 2007). The other alternative as a second phase is bainite, which can play the same role as martensite, but offering higher toughness.



15.11 Tensile behaviour of steels with ultrafine (1 μm) and coarse (10 μm) grained microstructures (after Hodgson, 1999).

© Woodhead Publishing Limited, 2012

15.9 Conclusions

This chapter reviewed the status of the production of ultrafine grained steels through relatively simple thermomechanical processing, in which the deformation is applied within the Ae_3 to Ar_3 temperature range for a given alloy. Here, the formation of ultrafine ferrite involves the transformation of a significant volume fraction of the austenite to ferrite during the course of deformation (i.e. dynamic transformation). This kind of phase transformation arises from the introduction of extensive intragranular nucleation sites, which are not present in the conventional controlled rolling process (i.e. static phase transformation). The DSIT route has the potential to be adjusted to suit current industrial infrastructure. However, there are a number of significant issues that have been raised, both as gaps in our understanding and as obstacles to industrial implementation. One of the critical issues is that this process requires very large strains. Another problem that has also become apparent is that fully ultrafine grained structure can lead to low work hardening rate (i.e. low ductility). Hence, there have been some attempts to introduce a second phase (e.g. martensite) to provide the required ductility. There is also a debate between researchers whether the dynamic recrystallisation of ferrite takes place in the production of ultrafine grained structure through the DSIT route or whether other mechanisms are operating during concurrent deformation and ferrite phase transformation.

15.10 Acknowledgements

Much of the work described here by the authors has been supported by the Australian Research Council, including a Federation Fellowship and an Australian Laureate Fellowship to Professor Hodgson. The authors also acknowledge the contributions from students and postdoctoral fellows to this work, particularly Drs P. Hurley, G. L. Kelly, A. Shokuohi, A. Taylor and P. Cizek.

15.11 References

Adachi, Y., Wakita, M., Beladi, H. and Hodgson, P.D., 2007, The formation of ultrafine ferrite through static transformation in low carbon steels, *Acta Mater.*, **55**, 4925–4934.

Amin, R.K. and Pickering, F.B., 1982, Ferrite formation from thermomechanically processed austenite, *Proc. Conf. on Thermo. Proc. of Micr. Aust.*, TMS-AIME, Pittsburgh, PA, 377–403.

Bae, Y.H., Lee, J.S., Choi, J.K., Choo, W.Y. and Hong, S.H., 2004, Effect of austenite/ferrite phase transformation of HSLA steel, *Mater. Trans.*, **45**, 137–142.

Basabe, V.V. and Jonas, J.J., 2010, The ferrite transformation in hot deformed 0.036%Nb austenite at temperatures above the Ae_3, *ISIJ Int.*, **50**, 1185–1192.

Beladi, H., Kelly, G.L. and Hodgson, P.D., 2004a, Formation of ultrafine grained

© Woodhead Publishing Limited, 2012

structure in plain carbon steels through thermomechanical processing, *Mater. Trans.*, **45**, 2214–2218.

Beladi, H., Kelly, G.L., Shokouhi, A. and Hodgson, P.D., 2004b, Effect of thermomechanical parameters on the critical strain for ultrafine ferrite formation through hot torsion testing, *Mater. Sci. Eng. A*, **367**, 152–161.

Beladi, H., Kelly, G.L., Shokouhi, A. and Hodgson P.D., 2004c, The evolution of ultrafine ferrite formation through dynamic strain induced transformation, *Mater. Sci. Eng. A*, **371**, 343–352.

Beladi, H., Kelly, G.L. and Hodgson, P.D., 2007, Ultrafine grained structure formation in steels using dynamic strain induced transformation, *Inter. Mater. Rev.*, **52**, 14–28.

Beladi, H., Cizek, P. and Hodgson, P.D., 2010, On the characteristics of substructure development through dynamic recrystallization, *Acta Mater.*, **58**, 3531–3541.

Beladi, H., Timokhina, I.B., Mukherjee, S. and Hodgson P.D., 2011, Ultrafine ferrite formation through isothermal static phase transformation, *Acta Mater.*, **59**, 4186–4196.

Bengochea, R., Lopez, B. and Gutierrez, I., 1999, Influence of the prior austenite microstructure on the transformation products obtained for C-Mn-Nb steels after continuous cooling, *ISIJ Int.*, **39**, 583–591.

Beynon, J.H., Gloss, R. and Hodgson, P.D., 1992, The production of ultrafine equiaxed ferrite in a low carbon microalloyed steel by thermomechanical treatment, *Mater. Forum*, **16**, 37–42.

Charnock, W. and Nutting, J., 1967, The effect of carbon and nickel upon the stacking fault energy of iron, *Met. Sci. J.*, **1**, 123–127.

Choi, J.K., Seo, D.H., Lee, J.S., Um, K.K. and Choo, W.Y., 2003, Formation of ultrafine ferrite by strain induced dynamic transformation in plain low carbon steel, *ISIJ Int.*, **43**, 746–754.

Cizek, P., Bai, F., Palmiere, E.J. and Rainforth, W.M., 2005, EBSD study of the orientation dependence of substructure characteristics in a model Fe-30wt%Ni alloy subjected to hot deformation, *J. of Micros.*, **217**, 138–151.

Davenport, S.B. and Higginson, R.L., 2000, Strain path effects under hot working: an introduction, *J. of Mater. Proc. Tech.*, **98**, 267–291.

Dehghan-Manshadi, A., Barnett, M.R. and Hodgson, P.D., 2008, Hot deformation and recrystallization of austenitic stainless steel: Part I. Dynamic recrystallization, *Metall. Mater. Trans. A*, **39**, 1359–1370.

Dong, H., 2001, Ultrafine grained steels and properties, *Proc. Int. Symp. on Ultrafine Grained Steels*, The Iron and Steel Institute of Japan, Fukuoka, Japan, 18–25.

Dong, H., Sun, X., Hui, W., Zhang, S., Shi, J. and Wang, M., 2008, Grain refinement in steels and the application trials in China, *ISIJ Int.*, **48**, 1126–1132.

Eghbali, B., Abdollah-Zadeh, A., Beladi, H. and Hodgson, P.D., 2006, Characterization on ferrite microstructure evolution during large strain warm torsion testing of plain carbon steel, *Mater. Sci. Eng. A*, **435–436**, 499–503.

Fujioka, M., Abe, Y. and Aihara, S., 2001, Refining ferrite grains in steel by recrystallization induced by heavy deformation, *Proc. Int. Symp. on Ultrafine Grained Steels*, The Iron and Steel Institute of Japan, Fukuoka, Japan, 274–277.

Hanlon, D.N., Sietsma, J. and van der Zwaag, S., 2001, The effect of plastic deformation of austenite on the kinetics of subsequent ferrite formation, *ISIJ Int.*, **41**, 1028–1036.

Hickson, M.R. and Hodgson, P.D., 1999, Effect of preroll quenching and post-roll quenching on production and properties of ultrafine ferrite in steel, *Mater. Sci. Technol.*, **15**, 85–90.

© Woodhead Publishing Limited, 2012

Hickson, M.R., Gibbs, R.K. and Hodgson, P.D., 1999, The effect of chemistry on the formation of ultrafine ferrite in steel, *ISIJ Int.*, **39**, 1176–1180.

Hodgson, P.D., 1999, The evolution of ferrite grain size in structural steels, *Mater. Forum*, **23**, 105–115.

Hodgson, P.D., Hickson, M.R. and Gibbs, R.K., 1998, The production and mechanical properties of ultrafine ferrite, *Mater. Sci. Forum*, **35**, 63–72.

Hodgson, P.D., Hickson, M.R. and Gibbs, R.K., 1999, Ultrafine ferrite in low carbon steel, *Scr. Mater.*, **40**, 1179–1184.

Hodgson, P.D., Hickson, M.R. and Gibbs, R.K., 2000, Strain-induced transformation of ultrafine microstructure in steel, US Patent No. 6,027,587.

Hodgson, P.D., Shokouhi, A. and Beladi, H., 2008, A descriptive model for the formation of ultrafine grained steels, *ISIJ Int.*, **48**, 1046–1049.

Honeycombe, R.W.K. and Bhadeshia, H.K.D.H., 1995, *Steels: Microstructures and Properties*, 2nd edn, Arnold, London.

Hong, S.C., Lim, S.H., Lee, K.L., Shin, D.H. and Lee, K.S., 2003, Effect of undercooling of austenite on strain induced ferrite transformation behaviour, *ISIJ Int.*, **43**, 394–399.

Hurley, P.J., 1999, Production of Ultra-Fine Ferrite during Thermomechanical Processing of Steels, PhD Thesis, Monash University, Melbourne, Australia.

Hurley, P.J. and Hodgson, P.D., 2001, Effect of process variables on formation of dynamic strain induced ultrafine ferrite during hot torsion testing, *Mater. Sci. Technol.*, **17**, 1360–1368.

Hurley, P.J., Hodgson, P.D. and Muddle, B.C., 1999, Analysis and characterisation of ultrafine ferrite produced during a new steel strip rolling process, *Scr. Mater.*, **40**, 433–438.

Hurley, P.J., Muddle, B.C., Hodgson, P.D., 2001, Nucleation sites for ultrafine ferrite produced by deformation of austenite during single pass strip rolling, *Metall. Mater. Trans. A*, **32**, 1507–1517.

Inoue, T., Torizuka, S. and Nagai, K., 2001, Formation of uniformly fine grained ferrite structure through multidirectional deformation, *Mater. Sci. Technol.*, **17**, 1329–1338.

Ishikawa, T., Inoue, T., Nomiyama, Y. and Yajima, H., 2001, Improvement of brittle crack arrest toughness by ultrafine grained microstructure in surface layers of steel plate, *Proc. Int. Symp. on Ultrafine Grained Steels*, The Iron and Steel Institute of Japan, Fukuoka, Japan, 236–239.

Kashyap, B.P. and Tangri K., 1997, Hall–Petch relationship and substructural evolution in boron containing type 316L stainless steel, *Acta Mater.*, **45**, 2383–2395.

Kozasu, I., Ouchi, C., Sanpei, T. and Okita, T., 1977, Hot rolling as a high temperature thermomechanical process, *Microalloying 75*, Union Carbide Corp., New York, 120–135.

Kvackaj, T. and Mamuzic, I., 1998, A quantitative characterization of austenite microstructure after deformation in nonrecrystallization region and its influence on ferrite microstructure after transformation, *ISIJ Int.*, **38**, 1270–1276.

Lee, H.C. and Um, K.K., 2008, Ferrite transformation during deformation of super cooled austenite, *ISIJ Int.*, **48**, 1050–1055.

Lee, W.P., 2000, Development of high performance structural steels for 21st century in Korea, *Proc. Int. Workshop on the Innov. Struc. Mater. for Infr. in 21st Century*, Tsukuba, Japan, 33–64.

Li, D.Z., Xia, N.M., Lan, Y.J., Zheng, C.W. and Li, Y.Y., 2007, Growth modes of individual ferrite grains in the austenite to ferrite transformation of low carbon steels, *Acta Mater.*, **55**, 6234–6249.

© Woodhead Publishing Limited, 2012

Matsumura, Y. and Yada, H., 1987, Evolution of ultrafine grained ferrite in hot successive deformation, *Trans. ISIJ*, **27**, 492–498.

Militzer, M. and Brechet, Y., 2009, Phenomenological model for deformation induced ferrite transformation, *Metall. Mater. Trans. A*, **40**, 2273–2282.

Mintz, B. and Jonas, J.J., 1994, Influence of strain rate on production of deformation induced ferrite and hot ductility of steels, *Mater. Sci. Technol.*, **10**, 721–727.

Miyata, K., Wakita, M., Fukushima, S., Eto, M., Sasaki, T. and Tomida T., 2007, Ultrafine grained steels due to super short interval multi-pass rolling in stable austenite region, *Mater. Sci. Forum*, **539–543**, 4698–4703.

Morrison, W.B. 1972, Recrystallisation in a low C steel in the austenite range, *J. Iron and Steel Inst.*, **210**, 618–623.

Novillo, E., Hernandez, D., Gutierrez, I. and Lopez, B., 2004, Analysis of ferrite grain growth mechanisms during γ-to-α transformation in a niobium alloyed steel using EBSD, *Mater. Sci. Eng. A*, **385**, 83–90.

Oudin, A., Hodgson, P.D. and Barnett, M.R., 2008, EBSD analysis of a Ti-IF steel subjected to hot torsion in the ferritic region, *Mater. Sci. Eng. A*, **486**, 72–79.

Poliak, E.I. and Jonas, J.J., 2003, Initiation of dynamic recrystallization in constant strain rate hot deformation, *ISIJ Int.*, **43**, 684–691.

Priestner, R. and de los Rios, E., 1980, Ferrite grain refinement by controlled rolling of low carbon and microalloyed steel, *Met. Tech.*, **7**, 309–316.

Priestner, R. and Hodgson P.D., 1992, Ferrite grain coarsening during transformation of thermomechanically processed C-Mn-Nb austenite, *Mater. Sci. Technol.*, **8**, 849–854.

Sato, A., 2000, Research Project on Innovative Steels in Japan (STX-21 Project), *Proc. Int. Workshop on the Innov. Struc. Mater. for Infr. in 21st Century*, Tsukuba, Japan, 1–10.

Seo, D.H., Lee, S.W. and Choo, W.Y., 1999, Ferrite grain refinement through heavy deformation in plain carbon steels, *Proc. 2nd Joint Korea-Australia Workshop on Manufac. Tech. and Steel Processing, POSTECH*, Pohang, Korea, 52–61.

Seo, D.H., Um, K.K., Lee, J.S., Choi, J.K. and Choo, W.Y., 2001, Fine ferrite formation by strain induced dynamic transformation in low carbon steel, *Proc. Int. Symp. on Ultrafine Grained Steels*, The Iron and Steel Institute of Japan, Fukuoka, Japan, 104–107.

Shokouhi, A. and Hodgson, P.D., 2009, Effect of transformation mechanism (static or dynamic) on final ferrite grain size, *Mater. Sci. Technol.*, **25**, 29–34.

Tamura, I., 1988, A role of thermomechanical processing of austenite on ferrite grain refinement, *Proc. Conf. Thermec '88*, The Iron and Steel Institute of Japan, Tokyo, Japan, **1**, 1–10.

Tamura, I., Sekine, H., Tanaka, T. and Ouchi, C., 1988, *Thermomechanical Processing of High-Strength Low-Alloy Steels*, Butterworth, London.

Tong, M., Li, D., Li, Y., Ni, J. and Zhang, Y., 2004a, Monte Carlo-method simulation of the deformation induced ferrite transformation in the Fe-C system, *Metall. Mater. Trans. A*, **35**, 1565–1577.

Tong, M., Ni, J., Zhang, Y., Li, D. and Li, Y., 2004b, Temporal oscillatory behaviour in deformation induced ferrite transformation in an Fe-C binary system, *Scr. Mater.*, **50**, 909–913.

Tsuchida, N., Tomota, Y. and Nagai, K., 2004, Tensile deformation behavior at high strain rate for ultrafine-grained ferrite cementite steels, *Testu-to-Hagane*, **90**, 1043–1049.

Um, K.K., Choi, J.K. and Choo, W.Y., 2001, Mechanical behaviours of fine dual

© Woodhead Publishing Limited, 2012

microstructures produced by dynamic austenite/ferrite transformation and accelerated cooling, *Proc. Int. Symp. on Ultrafine Grained Steels*, The Iron and Steel Institute of Japan, Fukuoka, Japan, 302–305.

Umemoto, M., Hiramatsu, A., Moriya, A., Watanabe, T., Nanba, S., Nakajima, N., Anan, G. and Higo, Y., 1992, Computer modelling of phase transformation from work hardened austenite, *ISIJ Int.*, **32**, 306–315.

Weng, Y.Q., 2000, New generation of iron and steel material in China, *Proc. Int. Workshop on the Innov. Struc. Mater. for Infr. in 21st Century*, Tsukuba, Japan, 11–32.

Yada, H., Matsumura, Y. and Nakajima, K., 1984, Ferrite steel having ultrafine grains and a method for producing the same, US Patent No. 4,466,842.

Yada, H., Matsumura, Y. and Senuma, T., 1988, A new thermomechanical heat treatment for grain refining in low carbon steels, *Proc. Conf. Thermec '88*, The Iron and Steel Institute of Japan, Tokyo, **1**, 200–207.

Yada, H., Li, C.M., Yamagata, H. and Tanaka, K., 1997, Dynamic γ-to-α transformation during hot deformation in low carbon steels, *Proc. Conf. Thermec '97*, TMS, Warrendale, PA, 765–770.

Yada, H., Li, C.M. and Yamagata, H., 2000, Dynamic γ-to-α transformation during hot deformation in iron-nickel-carbon alloys, *ISIJ Int.*, **40**, 200–207.

Yokota, T., Meteo, C.G. and Bhadeshia, H.K.D.H., 2004, Formation of nanostructured steels by phase transformation, *Scr. Mater.*, **51**, 767–770.

Yoshi, A., Fujioka, M., Morikawa, H. and Onoe, Y., 1988, Estimation model for evaluation of microstructural and mechanical properties of Nb bearing steel plates produced by thermo-mechanical control process, *Proc. Conf. Thermec '88*, The Iron and Steel Institute of Japan, Tokyo, **1**, 799–806.

© Woodhead Publishing Limited, 2012

16

The effect of a magnetic field on phase transformations in steels

Y. ZHANG and C. ESLING, Université de Lorraine, France

Abstract: The chapter deals with the effects of a magnetic field on austenitic decomposition (from diffusional transformation to non-diffusional transformation), and martensite decomposition in steels. The principal field effect mechanisms are introduced and microstructural influences related to the thermodynamic, kinetic and magnetic interaction among atomic magnetic moments are outlined.

Key words: magnetic field, phase equilibrium, phase transformation, microstructure, texture.

16.1 Introduction

As an important thermodynamic parameter like temperature and pressure, magnetic field has been introduced to phase transformations of metallic materials, especially Fe-C based alloys, for the purpose of microstructure control. In these transformations, either the transformation is accompanied by a magnetic state (magnetic nature) transition, such as for martensitic, bainitic, ferritic or pearlitic transformation, or several new phases with different magnetization behavior precipitate, such as, for example, carbide precipitation during martensitic decomposition. In the former cases, the parent phase is of low magnetization whereas the product phases are of high magnetization. Therefore, the introduction of a magnetic field to such phase transformation induces thermodynamic and kinetic changes of the transformation and gives rise to corresponding microstructural modification, whereas in the latter case, the precipitation becomes selective.

These field related microstructure modification potentials were recognized in the 1950s. After an insightful survey of the influence of the magnetic properties of constituent atoms on the various properties of metals and alloys, Zener became aware of the important role that magnetism will play in the future development of metallurgy (Zener, 1955). The practice of applying a magnetic field during phase transformations in ferrous alloys or steels was first realized for the martensitic transformation. The early investigations were conducted by the research group of Sadovskii *et al.* (Sadovskii *et al.*, 1961; Krivoglaz and Sadovskii, 1964; Fokina *et al.*, 1965; Malinen and Sadovskii, 1966) in the former USSR. They studied the effect of a magnetic field on

© Woodhead Publishing Limited, 2012

martensitic transformation and obtained convincing results that the magnetic field could increase the transformation start temperature (*Ms*) and thus promote the transformation, thereby enhancing the final strength of the material. As there were no powerful superconducting magnets available at that time, the intensity of the magnetic field obtained was limited (<2 Tesla) and hence many other effects remained undetectable. However, from the 1980s, with the progress in high field generating techniques, magnetic fields greater than 10 Tesla became available, rejuvenating such studies (e.g. Kakeshita *et al.*, 1990). Consequently, additional results were obtained on the influence of magnetic field on *Ms* temperature, the amount of martensite obtained and the martensite morphology, as well as the time-temperature-transformation (TTT) diagram of athermal martensitic transformation. However, diffusional phase transformations in steels, such as proeutectoid or eutectoid transformation and precipitation from supersaturated martensite, happen at relatively high temperatures, with large chemical driving forces compared to the magnetic driving force (depending on the induced magnetization difference between the parent and the product phase).

For any effect of magnetic field on these transformations, a much higher magnetic field is required. For some time, there existed technical difficulties in incorporating high temperature furnaces that irradiate heat to elevate the temperature inside field generating superconducting magnets that work at cryogenic temperatures. But from the late 1980s and early 1990s, installation of high temperature heat treatment equipment inside superconducting magnets became available, thus enabling research on high temperature phase transformations under high magnetic field. Since then, extensive examinations of the effect of a high magnetic field on diffusional decomposition of austenite in steels have flourished. Many valuable microstructure phenomena have been revealed. On the basis of experimental investigations, theoretical exploration aimed at quantifying the field effect has also been elaborated.

16.2 Evolution of the magnetic field generators

In parallel to the exploration of the magnetic field effect, and also driven by the requirement for higher field intensity, dedicated high field facilities have been developed in many countries including the United States, France, The Netherlands, Japan, Poland and Russia (Brooks *et al.*, 1998; Motokawa *et al.*, 1998; Brandt *et al.*, 2001; Jones *et al.*, 2001; Klamut *et al.*, 2001; Watanabe *et al.*, 2004). The most notable facilities were provided by the Francis Bitter Nation Magnet Laboratory at MIT, Cambridge, MA, USA. The High Magnetic Field Laboratory at Grenoble, France; the High Field Laboratory at Tohoku University, Sendai, Japan and the High Magnetic Field Laboratory at Radboud University Nijmegen, Netherlands offer free access to external users. Later, new international facilities were opened in

© Woodhead Publishing Limited, 2012

the USA and Japan: the high magnetic field laboratories established and operated by Florida State University, Tallahassee, the University of Florida, Gainesville, and the Los Alamos National Laboratory, New Mexico, and the Tsukuba Magnet Laboratory operated by the National Research Institute of Metals, Japan.

In parallel with the opening of these new facilities, and driven by increasing demands for powerful magnetic fields, new investments were made to upgrade the existing facilities in Grenoble, France, in Nijmegen, the Netherlands and in Sendai, Japan, targeting the enhancement of the continuous field to a range of 30–45 Tesla and prolonging the machine time by improving magnet materials and design, upgrading the power systems and conceiving new cooling systems. These facilities provide continuous fields with either water-cooled, powered resistive magnets or with hybrid magnets (a superconducting outer magnet and a water-cooled powered inner resistive magnet). In addition to these continuous field facilities, there are also pulsed magnetic field generating facilities extending the availability of field intensity up to 80 Tesla with a pulse duration from the order of several hundreds to several tens of microseconds (Boebinger *et al.*, 2001; Kindo, 2001; Frings *et al.*, 2002). Alongside the development of this high field technology, experimental platforms incorporating magnetic field generator and X-ray or even neutron diffraction facilities have been constructed in the USA, France and Japan to realize *in-situ* structure characterization during field induced phase or structure transitions, which further extend the capacity of both the field treatment and the characterization technique (Nojiri *et al.*, 1998).

16.3 Basic mechanisms of field influence on a phase transformation in steels

All matter is magnetic, but some is much more magnetic than other matter. The origin of magnetism lies in the orbital and spin motions of electrons and the way in which the electrons interact with one another. The magnetic behavior of materials can be classified into five major groups: diamagnetism, paramagnetism, ferromagnetism, ferrimagnetism and antiferromagnetism (http://www.irm.umn.edu/hg2m/hg2m_b/hg2m_b.html).

The diamagnetic substances are composed of atoms that have no net magnetic moments (i.e. all the orbital shells are filled and there are no unpaired electrons). However, when they are exposed to a field, a negative magnetization is produced and thus the susceptibility is negative.

For paramagnetic substances, the atoms possess individual magnetic moments but they do not interact magnetically in the absence of a magnetic field. When the field is introduced, the atomic magnetic moments partially align in the field direction, thus resulting in a net positive magnetization (Fig. 16.1(a)).

© Woodhead Publishing Limited, 2012



16.1 Magnetic ordering in paramagnetism, ferromagnetism, ferrimagnetism and antiferromagnetism.

Like paramagnetic materials, the ferromagnetic materials also possess atomic magnetic moments but the atomic moments exhibit very strong interactions. The atomic magnetic moments are parallel (Fig. 16.1(b)) within a microscopic volume (the so-called magnetic domain), resulting in large net magnetization – spontaneous magnetization – even in the absence of a magnetic field. When a magnetic field is applied, the magnetic moment of the domains tends to align in the field direction, thus a much higher magnetization can be induced. This induced magnetization reaches saturation when all the domain magnetic moments align in the field direction. Although electronic exchange forces in ferromagnetic materials are very large, thermal agitation that randomizes the magnetic alignment eventually overcomes the exchange. This occurs at the Curie temperature (Tc). Below Tc, the magnetic moments are ordered and above it, disordered.

For ferrimagnetic materials, the magnetic moments of the atoms on different sublattices are antiparallel (Fig 16.1(c)). However, the opposing moments are unequal and a resolved spontaneous magnetization remains. If the opposing moments are exactly equal, the net moment is zero. This type of magnetic ordering is called antiferromagnetism (Fig. 16.1(d)).

The transition element, Fe, possesses unpaired 3d electrons and hence unbalanced magnetic spins that give rise to atomic magnetic moment. Pure Fe and many of its alloys are ferromagnetic below the Curie temperature Tc. The Tc for the pure Fe and ferrite is 770°C. For steels, there are three equilibrium phases of importance to engineering properties located within different carbon composition and temperature ranges. One is high temperature austenite, which is the parent phase for proeutectoid and eutectoid transformation, and the other two are ferrite and cementite that are products of decomposition of this austenite. Austenite is paramagnetic; ferrite is ferromagnetic below 770°C (so are its non-equilibrium counterparts, bainite and martensite) and cementite is paramagnetic at the formation temperature (≥ eutectoid temperature). It becomes ferromagnetic below 210°C.

Due to the natural magnetic difference of these phases, the transformation process and the resultant microstructure could be modified by an external magnetic field. Qualitatively, the magnetic field 'helps' the transformation from a low magnetization phase to a high magnetization phase, such as the proeutectoid ferrite transformation. Quantitatively, when an external magnetic

© Woodhead Publishing Limited, 2012

field is applied, the phases under the magnetic field will be magnetized and their Gibbs free energy will be lowered by an amount $V\int_0^M \mu_0 H_0 \mathrm{d}M$, where V is the volume of the phase, μ_0 the permeability of free space (vacuum), H_0 the magnetic field strength in free space and M the induced magnetization per unit volume. $V\int_0^M \mu_0 H_0 \mathrm{d}M$ is the so-called intrinsic magnetization energy, that is, the work provided to the phase by raising the level of its magnetization under a fixed magnetic field. It is also denoted the 'magnetic Gibbs free energy', if we specify the Gibbs free energy of a phase with a certain chemical composition in the absence of a magnetic field as 'chemical Gibbs free energy'. Therefore, for a transformation from austenite to ferrite in the presence of a magnetic field, the total Gibbs free energy change ${}^M\Delta G^{\gamma->\alpha+\gamma}$ will contain two terms: the 'chemical Gibbs free energy difference' ΔG^C and the 'magnetic Gibbs free energy difference' ΔG^M as follows:

$$\begin{aligned} {}^M\Delta G^{\gamma->\alpha+\gamma} &= \Delta G^C + \Delta G^M \\ \Delta G^M &= -\left(\int_0^{M^\alpha} H_0 \mathrm{d}(\mu_0 M_\alpha) - \int_0^{M^\gamma} H_0 \mathrm{d}(\mu_0 M_\gamma)\right) \\ &= -H_0\mu_0\left(\int_0^{M^\alpha} \mathrm{d}M_\alpha - \int_0^{M^\gamma} \mathrm{d}M_\gamma\right) \end{aligned} \quad [16.1]$$

where superscript and subscript α and γ denote ferrite and austenite and M the magnetization. As the magnetization of ferrite is higher than that of austenite at all the transformation temperature concerned, ΔG^M has the same sign as ΔG^C. The absolute value of the Gibbs free energy difference between the two phases is increased. In this context, the effect of the field on the transformation can be both thermodynamic and kinetic.

It is known that transformation thermodynamics deals with phase equilibrium and phase stability, whereas transformation kinetics with the rate. When two phases are in equilibrium, their Gibbs free energy difference is zero. By adding the different magnetic Gibbs free energy of the two phases, the magnetic field changes the equilibrium temperature. In this way, the field effect is thermodynamic. The Gibbs free energy difference is also denoted the transformation driving force. The higher the driving force, the faster the overall transformation proceeds. Therefore by introducing the additional magnetic driving force, the magnetic field changes the overall transformation time, demonstrating a kinetic effect.

In addition to the thermodynamic and kinetic effects, there also exist the magnetization and demagnetization effects of the magnetic field resulting from the strong magnetic interaction among the magnetic moments of Fe atoms when placed in a magnetic field. This is called magnetic dipolar interaction. Each Fe atom can be treated as a magnetic dipole. When an

© Woodhead Publishing Limited, 2012

external magnetic field is applied, the atomic moments tend to align along the field direction, as illustrated in Fig. 16.2. This gives rise to a dipolar interaction between neighboring atoms. If m is the magnetic moment of an iron atom and r the distance between two neighboring atoms, as shown in Fig. 16.2, then the dipolar interaction energy E_D is:

$$E_D = -\frac{\mu_0 m^2}{4\pi} \cdot \frac{3\cos^2\theta - 1}{r^3} \qquad [16.2]$$

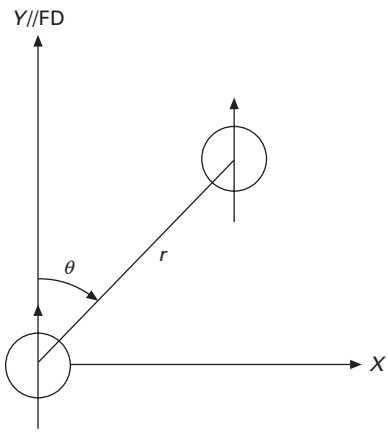
E_D depends on θ and r. When $\theta = 0°$, i.e. the magnetic moments align along the field direction, E_D is minimum (negative), whereas when $\theta = 90°$, i.e. the moments align along the transverse field direction, E_D is maximum (positive). Therefore, the atoms attract each other along the field direction (magnetization) but repel each other in the transverse field direction (demagnetization). This dipolar interaction has mainly a microstructural effect. It accompanies the growth process of the product phases. By minimizing the demagnetization energy (repulsion between magnetic moments), it may bring about grain shape anisotropy by preferential grain growth in the field direction or crystallographic texture by selective grain nucleation or growth (see pages 571–3).

16.4 Effect of magnetic field on phase equilibrium and transformation

16.4.1 Phase equilibrium in a magnetic field

Prediction of martensitic transformation start temperature Ms

In steels, martensitic transformation decomposes austenite with a face-centered-cubic (fcc) crystal structure to carbon-supersaturated martensite with a body-



16.2 A pair of magnetic dipoles in a magnetic field. FD: magnetic field direction.

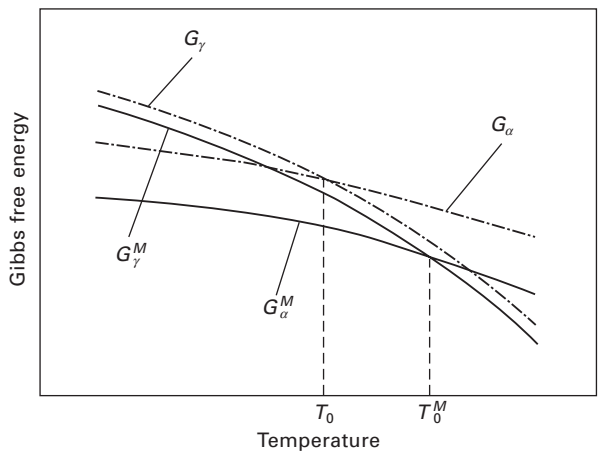
© Woodhead Publishing Limited, 2012

centered-tetragonal (bct) crystal structure depending on the degree of carbon supersaturation. In this transformation, the parent austenite is paramagnetic, whereas the martensite product is ferromagnetic. The induced magnetization of the two phases is different, that of martensite being much higher than that of austenite. Thus, the Gibbs free energy of austenite does not change much but that of martensite is greatly lowered. As illustrated in Fig. 16.3, magnetic field moves the Gibbs free energy curve of martensite from G_α to G_α^M, whereas that of austenite changes only a little from G_γ to G_γ^M, so that the equilibrium temperature of the two phases T_0 is raised to T_0^M, the martensitic transformation temperature *Ms* being raised accordingly.

Krivoglaz and Sadovskii (1964) formulated the magnetization energy of a magnetized phase as $M \cdot H$ (M and H in CGS[1] units). By assuming that the Gibbs chemical free energies of austenite and martensite are linear with temperature, they derived a simple formula of the shift of the equilibrium temperature between austenite and martensite under a magnetic field ΔT to represent the shift of *Ms*:

$$\Delta T = \Delta M \cdot H \cdot T_0/q, \qquad [16.3]$$

where T_0 is the temperature of the thermodynamic equilibrium for the austenite and martensite without a magnetic field, ΔM is the magnetization difference between the product and the parent phases at the equilibrium temperature under the magnetic field ($T_0 + \Delta T$), and q is the latent heat of transformation.



16.3 Schematics of the Gibbs free energy of austenite and martensite without and with a magnetic field. α = martensite; γ = austenite; M = magnetic field.

[1] CGS = centimetre-gram-second system of units.

© Woodhead Publishing Limited, 2012

The calculated shift of *Ms* fitted well with experimental results in some Fe-Ni alloys (Sadovskii *et al*., 1961; Fokina *et al*., 1965). It should be noted, however, that the calculation of the magnetization energy is quite approximate. The magnetization energy is not simply a bi-linear product of magnetization with the magnetic field, if we consider that magnetization of a substance in a magnetic field is a process during which the magnetization changes from M_{initial} to M_{final}. M_{initial} is either zero (paramagnetic state) or of a certain value (the spontaneous magnetization in the ferromagnetic state). As Eq. [16.3] was derived based on the experimental results in low magnetic field, the uncertainty due to this approximation was not significant. Consequently, this formula has been widely accepted. However, when a high magnetic field (>10 T) is applied, the discrepancy between the experimental observation and the calculated value becomes significant.

Thus, Kakeshita *et al*. (1985) further extended Eq. [16.3] by adding a term for the high field susceptibility energy of austenite: $(1/2) \cdot \chi_{h\gamma} \cdot H^2$. Furthermore, they observed another effect that occurs in a high magnetic field, namely the volume change with increase in the magnetic field. They defined the related energy change as forced volume magnetostriction energy. In addition, they introduced a more realistic formulation for the chemical Gibbs free energy change between the austenite and the martensite. A general expression incorporating all these effects and considering that, experimentally, there exists a critical field strength H_C at which the martensitic transformation starts, was proposed (Kakeshita *et al*., 1985):

$$\Delta G(Ms) - \Delta G(Ms') = -\Delta M(Ms') \cdot H_c - (1/2) \cdot \chi_{h\gamma} \times H_c^2 + \varepsilon_0 \cdot (\partial w/\partial H) \cdot H_c \cdot B \qquad [16.4]$$

in which $\Delta G(Ms)$ and $\Delta G(Ms')$ represent the difference in the Gibbs chemical free energy between the austenite and martensite at temperatures *Ms* and *Ms′* (*Ms* and *Ms′* are the martensitic transformation start temperatures, without and with a magnetic field respectively); $\Delta M(Ms')$ is the difference in magnetization between the austenite and the martensite at temperature *Ms′*, *H* the strength of the magnetic field, $\chi_{h\gamma}$ is the high field susceptibility of the parent austenite, ε_0 is the transformation strain, $(\partial w/\partial H)$ is the forced volume magnetostriction and *B* is the bulk modulus. It was shown that the calculated *Ms′* under a magnetic field agrees well with the experimental values in a variety of alloy systems (Kakeshita *et al*., 1990).

Fe-C phase diagrams

In the Fe-C binary phase diagram, the lower left corner containing proeutectoid and eutectoid transformations has a particular importance as it provides comprehensive constitutional and instructive information on microstructure

© Woodhead Publishing Limited, 2012

formation for a variety of steel heat treatments (annealing, normalizing, etc.). The Gibbs free energy difference between the parent and the product phases is modified in a magnetic field. In consequence, phase boundaries in the phase diagram are shifted.

We know that the A_{e3} line is the austenite/ferrite+austenite or $\gamma/\alpha + \gamma$ equilibrium boundary and the A_{ecm} line austenite/cementite+austenite or $\gamma/cem + \gamma$ equilibrium boundary. The eutectoid point is the intersection of the two, and the A_{e1} boundary is horizontal intersecting this point. The A_{e3} line, the A_{ecm} line and the A_{e1} line mark the onset of the proeuctoid ferrite transformation, the proeutectoid cementite transformation and the eutectoid transformation, respectively. The $\alpha + \gamma/\alpha$ boundary marks the finish of the austenite to ferrite transformation. These equilibrium boundaries can be calculated using the equations of Gibbs free energy change accompanying the corresponding transformation.

A_{e3} line or the $\gamma/\alpha + \gamma$ boundary

The Gibbs free energy change for proeuctectoid ferrite formation is:

$$\Delta G^{\gamma\to\alpha+\gamma} = RT\left[x^{\gamma}\ \ln\frac{a_C^{\gamma/\alpha+\gamma}}{a_C^{\gamma}} + (1-x^{\gamma})\ln\frac{a_{Fe}^{\gamma/\alpha+\gamma}}{a_{Fe}^{\gamma}}\right] \qquad [16.5]$$

where x^{γ} is the mole fraction of carbon in the initial austenite, R the gas constant, T absolute temperature, $a_j^{\gamma/\alpha+\gamma}$ is the activity of C or Fe in austenite on the $\gamma/\alpha+\gamma$ boundary and a_j^{γ} the activity of C or Fe in the initial austenite. The additional Gibbs free energy change induced by a magnetic field is:

$${}^{M}\Delta G^{\gamma\to\alpha+\gamma} = -\left(\int_0^{M^{\alpha}} \mu_0 H\cdot dM - \frac{1}{2}\chi^{\gamma}H^2\right) \qquad [16.6]$$

Assume that under the magnetic field, the $\gamma/\alpha + \gamma$ boundary $x^{\gamma/\alpha+\gamma}$ (mol fraction of carbon in austenite on $\gamma/\alpha + \gamma$ boundary or on A_{e3} line) moves to ${}^{M}x^{\gamma/\alpha+\gamma}$. The activity of C or Fe in austenite at the new $\gamma/\alpha + \gamma$ boundary is ${}^{M}a_j^{\gamma/\alpha+\gamma}$, thus the total driving force under the magnetic field for the austenite-to-proeutectoid ferrite transformation can be expressed as:

$$\Delta G^{\gamma\to\alpha+\gamma} + {}^{M}\Delta G^{\gamma\to\alpha+\gamma} = RT\left[x^{\gamma}\ln\frac{{}^{M}a_C^{\gamma/\alpha+\gamma}}{a_C^{\gamma}} + (1-x^{\gamma})\ln\frac{{}^{M}a_{Fe}^{\gamma/\alpha+\gamma}}{a_{Fe}^{\gamma}}\right] \qquad [16.7]$$

Substituting Eq. [16.5] into Eq. [16.7] and letting x^{γ} represent the equilibrium carbon content $x^{\gamma/\alpha}$ at the $\gamma/\alpha + \gamma$ boundary without a magnetic field, we obtain:

© Woodhead Publishing Limited, 2012

$$^{M}\Delta G^{\gamma\rightarrow\alpha+\gamma} = RT\left[x^{\gamma/\alpha+\gamma}\ln\frac{^{M}a_C^{\gamma/\alpha+\gamma}}{a_C^{\gamma/\alpha+\gamma}} + (1-x^{\gamma/\alpha})\ln\frac{^{M}a_{Fe}^{\gamma/\alpha+\gamma}}{a_{Fe}^{\gamma/\alpha+\gamma}}\right] \quad [16.8]$$

Using the appropriate statistical thermodynamic equations for $a_j^{\gamma/\alpha+\gamma}$ summarized in (Hsu (X) and Mou, 1984; Mou and Hsu (X), 1986), $^{M}x^{\gamma/\alpha+\gamma}$ can be calculated.

A_{ecm} line or the γ/cem + γ boundary

For the proeutectoid cementite transformation, the parent phase is austenite and the product phase is cementite. The magnetization of austenite and cementite phases is very close (Zhang *et al.*, 2006b, 2007). The magnetic Gibbs free energy difference between the two phases is very small and can be neglected compared with their chemical Gibbs free energy difference. Thus, it can be considered that this phase boundary line remains unchanged, even under a high magnetic field (>10 T).

α + γ/α boundary

The Gibbs free energy change associated with the transformation from austenite to stress-free ferrite of the same carbon content, $\Delta G^{\alpha+\gamma\rightarrow\alpha}$ would be expressed as (Hsu (X) and Mou, 1984):

$$\Delta G^{\gamma+\alpha\rightarrow\alpha} = (1-x^{\gamma})\Delta G_{Fe}^{\gamma-\alpha} + RT\left[x^{\gamma}\ln\frac{a_C^{\alpha+\gamma/\alpha}}{a_C^{\gamma}} + (1-x^{\gamma})\ln\frac{a_{Fe}^{\alpha+\gamma/\alpha}}{a_{Fe}^{\gamma}}\right] \quad [16.9]$$

where $\Delta G_{Fe}^{\gamma-\alpha}$ is the Gibbs free energy difference between pure γ-*Fe* and α-*Fe*, $a_j^{\alpha+\gamma/\alpha}$ is the activity of C or Fe in austenite on the $\alpha + \gamma/\alpha$ boundary. Similar to the case of the proeutectoid ferrite transformation, the Gibbs free energy change under a magnetic field is:

$$\Delta G^{\gamma+\alpha\rightarrow\alpha} + {}^{M}\Delta G^{\gamma+\alpha\rightarrow\alpha} = (1-x^{\gamma})\Delta G_{Fe}^{\gamma-\alpha} + RT\left[x^{\gamma}\ln\frac{^{M}a_C^{\alpha+\gamma/\alpha}}{a_C^{\gamma}} + (1-x^{\gamma})\ln\frac{^{M}a_{Fe}^{\alpha+\gamma/\alpha}}{a_{Fe}^{\gamma}}\right] \quad [16.10]$$

Substituting Eq. [16.9] into Eq. [16.10] and with x^{γ} representing the equilibrium carbon content at the $\alpha + \gamma/\alpha$ boundary without a magnetic field, we obtain:

© Woodhead Publishing Limited, 2012

$$^{M}\Delta G^{\alpha+\gamma\rightarrow\alpha} = (1 - x^{\alpha+\gamma/\alpha})\Delta G_{Fe}^{\gamma-\alpha}$$

$$+ RT\left[x^{\alpha+\gamma/\alpha}\ln\frac{^{M}a_{C}^{\alpha+\gamma/\alpha}}{a_{C}^{\alpha+\gamma/\alpha}} + (1-x^{\alpha+\gamma/\alpha})\ln\frac{^{M}a_{Fe}^{\alpha+\gamma/\alpha}}{a_{Fe}^{\alpha+\gamma/\alpha}}\right] \qquad [16.11]$$

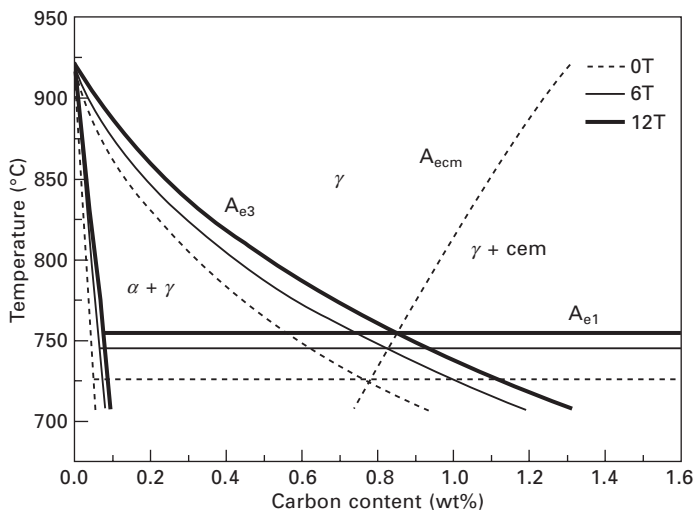
By applying the appropriate activity equations, Eq. [16.11] can be solved for the $\alpha + \gamma/\alpha$ boundary.

Figure 16.4 shows an example of the calculated part of the Fe-C phase diagram under various field intensities. The clear effect is that the magnetic field shifts the A_{e3} line and the eutectoid point towards higher carbon and higher temperature.

16.4.2 Phase transformation under a magnetic field

Martensitic transformation

As explained above, by enlarging the Gibbs free energy difference between austenite and martensite, the magnetic field both thermodynamically and kinetically affects the transformation. This was revealed in the 1960s. The observation of the acceleration of the transformation and the elevation of the *Ms* is well known in a variety of Fe-based alloys and steels exhibiting either isothermal or athermal transformation behavior, even at relatively low field intensities. Recently, San Martin *et al*. (2008, 2010) have studied the kinetics of the isothermal martensitic transformation of maraging steels under a high magnetic field by *in situ* experiments (San Martin *et al*., 2008)



16.4 Fe-C diagram under various field intensities.

© Woodhead Publishing Limited, 2012

and with time resolved magnetization measurements (San Martin *et al.*, 2010). Their study showed that the isothermal martensite formation can be accelerated by several orders of magnitude when a high magnetic field of up to 30 T is applied (San Martin *et al.*, 2010). The transformation at T = 233 K took about two months to complete without a magnetic field, whereas it reached the finishing state (about 80% martensite) in only a few minutes under a magnetic field of 30 T.

In addition, the influence of the magnetic field on the morphology of martensite has been investigated in a variety of ferroalloys. Many studies showed that the morphology including the internal structure of the magnetic field-induced martensite was not affected by the magnetic field (Kakeshita *et al.*, 1985, 1990). Given that the mechanical properties of materials are determined directly by their microstructure, any increase in the amount of martensite under a magnetic field should surely result in further strengthening, as martensite is a hard phase whereas austenite is soft. This has been demonstrated by early studies: Bernshteyn *et al.* (1965) applied a magnetic field of 4000 Oe (0.4 T) to the martensitic transformation in Fe-Ni-C steels and found that the transformation was greatly enhanced, resulting in an increase in the yield point by 10–15%.

Bainitic transformation

The principal effect of a magnetic field on the bainite transformation in steels is similar to the case for martensitic transformation. The parent austenite is paramagnetic and the bainitic product is ferromagnetic. By enlarging the Gibbs free energy difference between the two phases, the magnetic field enhances the transformation. Similar influences on transformation start temperature, transformation rate and transformation amount have been recorded. Grishin (1988) imposed a magnetic field during the austenitic decomposition of different structural steels in the bainitic transformation zone. He found that the magnetic field promotes the bainitic transformation and enhances the dispersion of carbide precipitates. Later, Fokina *et al.* (1995) applied a magnetic field to the bainitic transformation of several structural steels. They found that the magnetic field shortens the incubation time and enhances the transformation amount. Similar phenomena were also found in bearing steels 9SiCr (C: 0.95–0.85; Si: 1.2–1.6; Cr: 0.95–1.25; Mn: 0.3–0.6) (Ren *et al.*, 1993). In addition, they found that the bainite obtained was obviously refined by the magnetic field. The refinement is due to the fact that the magnetic field lowers the Gibbs free energy of the ferromagnetic phase and thus decreases the nucleation barrier and increases the nucleation rate.

© Woodhead Publishing Limited, 2012

Diffusional austenitic decomposition

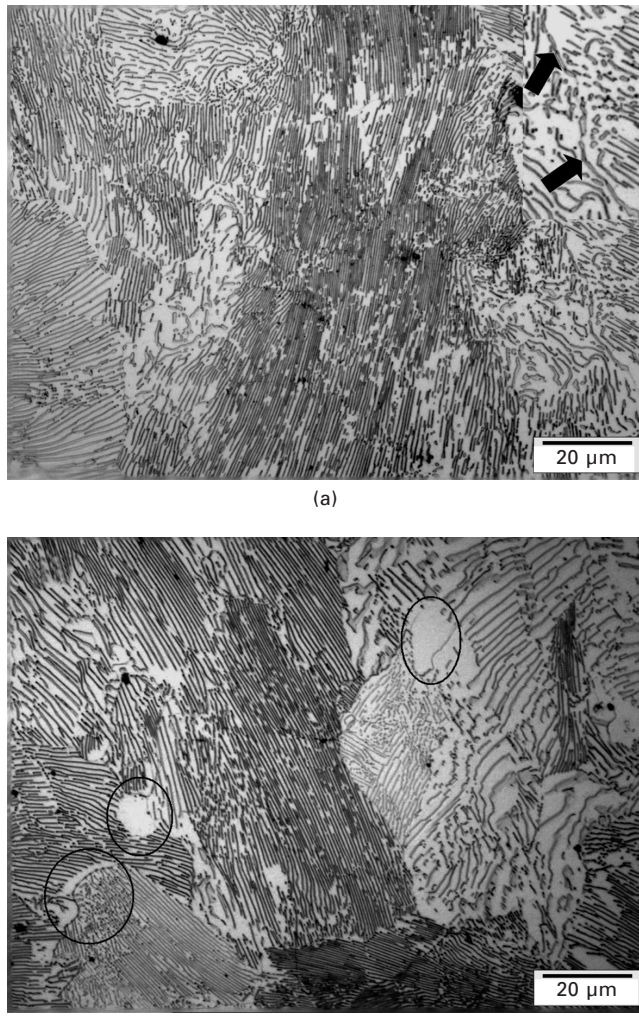
As seen in Fig. 16.4, the magnetic field shifts the A_{e3} line to the high carbon content side and high temperature side, whereas the A_{ecm} line does not change much. Thus, the eutectoid point is raised to the high temperature and high carbon content side and the A_{e1} line is raised accordingly in temperature. There have been constant attempts to investigate experimentally the rise of the transformation temperatures and the shift of the eutectoid point. Rivoirard *et al*. (2009) and Garcin *et al*. (2010) have conducted *in situ* dilatation measurements to follow austenite decomposition of pure Fe and several steels and observed enhancement of transformation by a magnetic field.

The shift of the eutectoid point under an applied magnetic field has been observed experimentally (Zhang *et al*., 2007), as shown in Fig. 16.5 for a marginal hypereutectoid carbon steel (Fe-0.81C wt%) austenitized at 840°C for 42 min and cooled at 2°C/min. The difference between the two microstructures is that, in the non-field treated specimen, a small amount of proeutectoid cementite (indicated by arrows in the magnified image in the top right corner of Fig. 16.5(a)) was observed, which characterizes the hypereutectoid nature of the microstructure, while in the field treated specimen some proeutectoid ferrite between pearlite colonies (white areas circled in Fig. 16.5(b)) appears. The unexpected formation of proeutectoid ferrite, the typical component of a hypoeutectoid microstructure, in the slightly hypereutectoid composition demonstrated, illustrates the shift of the eutectoid point in the Fe-C system. Examination shows that under the 12 T magnetic field, the eutectoid shifts from 0.77%C to 0.83%C.

With the shift of the eutectoid point to a higher carbon content, the proeutectoid ferrite transformation occurs over a larger range of carbon content. In such a context, the amount of proeutectoid ferrite is increased. This has been shown in many magnetic field treated steels (Zhang *et al*., 2005c; Wang *et al*., 2007, Garcin *et al*., 2010) and the phenomenon can be interpreted using the Lever Rule (Zhang *et al*., 2005c).

As the eutectoid point in the Fe-C system is also raised to higher temperatures, the eutectoid transformation, or austenite to pearlite transformation, occurs at higher temperature. It is known that the austenite to pearlite transformation is diffusional and involves the cooperative formation of carbon-depleted ferrite and carbon-enriched cementite. The interlamellar spacing of the pearlite then depends on the diffusion distance of the carbon. The higher formation temperature allows greater carbon diffusion and thus, when a high magnetic field is applied, the interlamellar spacing is increased. Statistical examination by Zhang *et al*. (2006a) shows that, in a hypereutectoid steel (Fe-1.0C (wt%)) austenitized at 840°C for 50 min and cooled at 2°C/min without and with a 12 T magnetic field, the average lamellar spacing is increased by about 9–10% under the magnetic field.

© Woodhead Publishing Limited, 2012



16.5 Optical micrographs of Fe-0.81C specimens austenitized at 840°C for 42 min and cooled at 2°C/min without (a) and with (b) a 12 T magnetic field. The magnified image in the right-hand corner of Fig. 16.5(a) shows some proeutectoid cementite, as indicated by the arrows. The circles in Fig. 16.5(b) mark out the proeutectoid ferrite between pearlite colonies (Zhang *et al.,* 2007).

It is known that for austenitized steels, the decomposition of austenite can be either diffusional or diffusionless with respect to interstitial carbon, depending on the cooling rate. It has been revealed that the magnetic field can enlarge the attainable cooling rate range for diffusional transformation, demonstrating a positive kinetic effect on the decomposition of austenite,

© Woodhead Publishing Limited, 2012

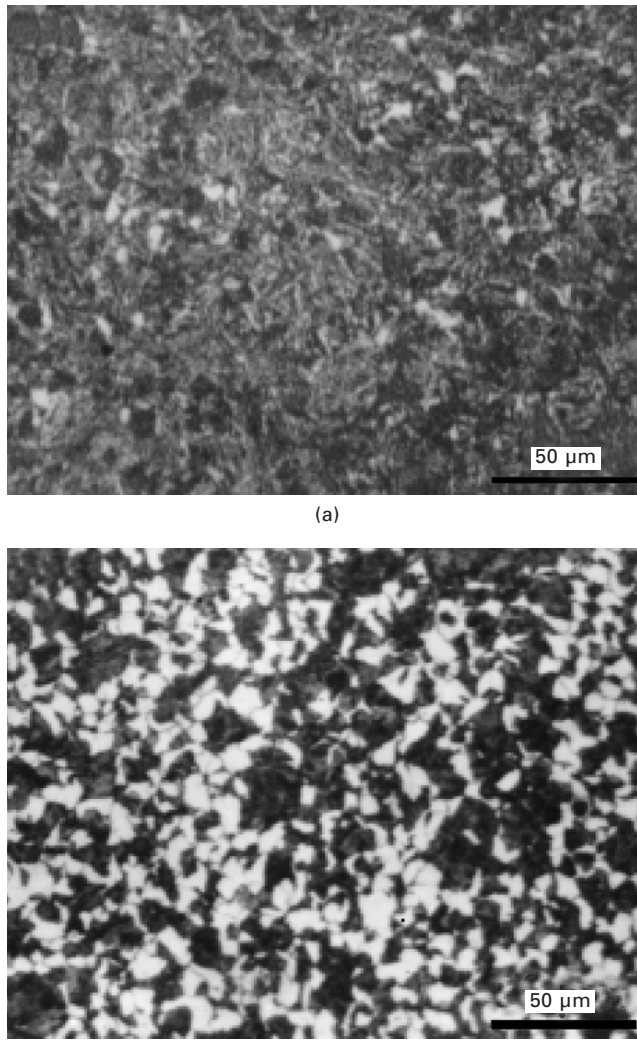
as found in the 42CrMo low alloy high strength steel (Zhang *et al*., 2005c) and in novel bainitic steels (Jaramillo *et al*., 2005). The former 42CrMo designation is a medium carbon low alloy steel. When the steel was cooled from its austenitic state at a relatively fast cooling rate (46°C/min) under a 14 T magnetic field, the microstructure obtained was composed of proeutectoid ferrite and pearlite, characteristic of an equilibrium microstructure, whereas that obtained without the magnetic field was described as bainitic structure, as shown in Fig. 16.6. Similarly, the formation of bainite was prevented when the novel bainitic steels (0.75C-1.63Si-195Mn-0.28Mo-1.48Cr wt% and 0.78C-1.60Si-2.02Mn-0.24Mo-1.01Cr-3.87Co-1.37Al wt%) were continuously cooled at 1°C/s, under a 30 T magnetic field. The diffusional transformation of austenite was accelerated and formation of pearlite with an incredibly fine spacing (50 nm) took place.

In addition to the thermodynamic and kinetic influence of the magnetic field on the proeutectoid and eutectoid transformation of austenite, the magnetic field also imposes significant microstructural modification to the product phases. The microstructure modification manifests itself in several ways depending on the materials and the heat treatment conditions.

The magnetic field lowers the amount of low angle misorientation of the ferrite and increases the frequency of low Σ boundaries, especially Σ3, of both proeutectoid and eutectoid ferrite, as shown in Fig. 16.7 (Zhang *et al*., 2006a) and Fig. 16.8 (Zhang *et al*., 2005d). The influence of the magnetic field on the amount of low angle misorientation in pearlitic ferrite is related to its effect on the transformation strain. It is known that the transformation from austenite to pearlite involves the formation of ferrite and cementite that present different hardnesses and volume changes. This gives rise to transformation stress and further transformation strain through formation of dislocations in the softer ferrite phase, when the stress accumulates to a sufficient level. The magnetic field applied may affect this transformation strain in the following two ways. One is elevation of the transformation temperature. As the field shifts the eutectoid transformation point to higher temperature, the formation of pearlite occurs at higher temperature and the transformation stress could be lowered. The other is the direct influence of the magnetic field on dislocation activity. It has been found that during deformation of a 30CrMnSi steel, a magnetic field decreases the dislocation density in the ferrite matrix near carbide particles (Tang *et al*., 2000), and lowers the internal stress (Prasad *et al*., 1996). These effects on dislocation behavior could also occur when dislocations form during phase transformation. Therefore, the transformation strain could be reduced.

The effect of the magnetic field on the occurrence of coincidence site lattice (CSL) boundaries is mainly related to the increase in the transformation temperature. It is known that different types of grain boundaries have different energy and mobility. Random high-angle boundaries have high

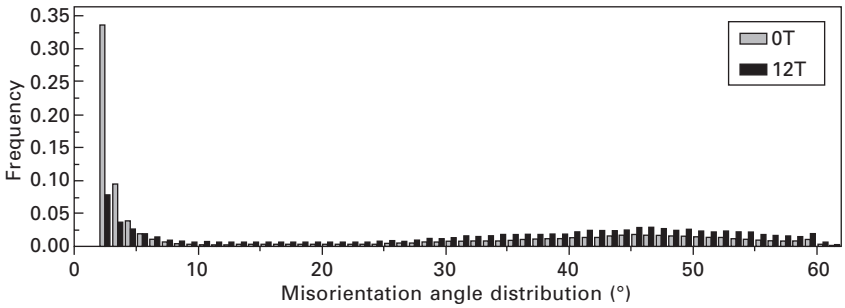
© Woodhead Publishing Limited, 2012



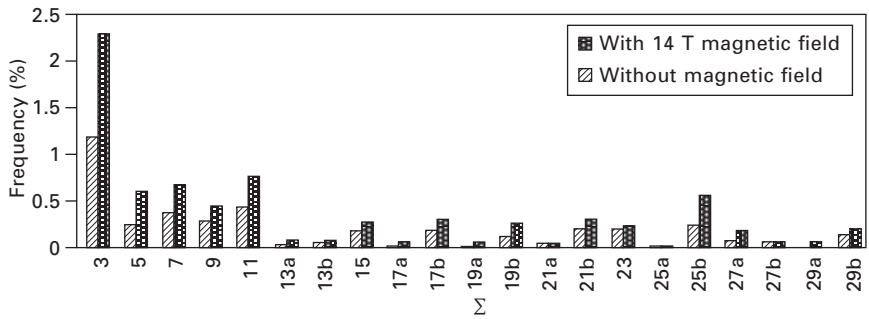
16.6 Microstructure of 42CrMo specimen austenitized at 880°C for 33min and cooled at 46°C/min without (a) and with (b) a 14 T magnetic field (Zhang *et al.,* 2005c).

energy and high mobility, while some low Σ boundaries, especially Σ3 boundaries, have low energy and low mobility. For a grain enclosed with different types of boundaries, grain growth through boundary migration will lead the lower mobility types to enlarge their boundary areas while the high mobility types will tend to shrink. Hence, after growth, the proportion of low mobility boundaries increases. As the magnetic field increases the austenite to proeutectoid ferrite and pearlite transformation temperatures,

© Woodhead Publishing Limited, 2012



16.7 Misorientation angle distribution of Fe-1.0wt%C specimens austenitized at 880°C for 33 min and cooled at 10°C/min without and with a 12 T magnetic field (Zhang *et al.*, 2006a).

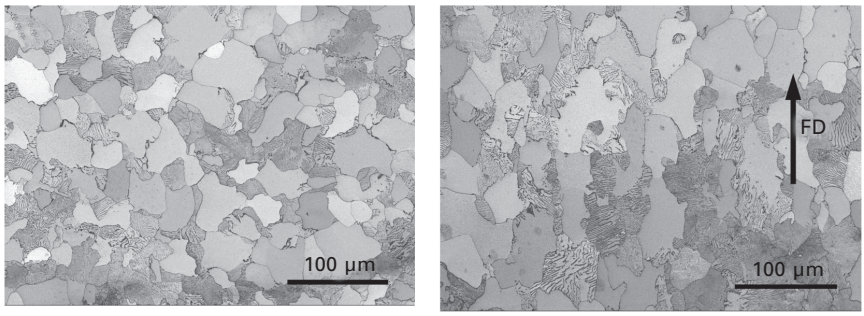


16.8 Distribution of CSL (coincidence site lattice) boundaries in 42CrMo specimens austenitized at 880°C for 33 min and cooled at 10°C/min without and with a 14 T magnetic field (Zhang *et al.*, 2005d).

the proeutectoid and eutectoid ferrite undergo a wider temperature range for growth. As a result, the proportion of low Σ boundaries, especially Σ3, obtained under a magnetic field is increased. In this case, the high occurrence of Σ boundaries is by the increase of their surface area (Zhang *et al.*, 2005a, 2005d).

For hypoeutectoid steels, elongation of proeutectoid ferrite grains in the magnetic field direction is commonly observed (Shimotomai *et al.*, 2003; Zhang *et al.*, 2005a). As was found in Fe-0.49wt%C medium carbon steel (Zhang *et al.*, 2005b), the 12 T magnetic field applied during austenite decomposition (cooling rate 2°C/min) promotes the proeutectoid ferrite grains to grow along the field direction and results in an elongated grain microstructure, as shown in Fig. 16.9 (Zhang *et al.*, 2005b). This field effect can be qualitatively explained by the dipolar interaction between the atomic magnetic moments carried by the iron atoms in the ferrite grains. As described in Section 16.3, each iron atom carries a magnetic moment

© Woodhead Publishing Limited, 2012



16.9 EBSD band contrast micrographs of Fe-0.49wt%C specimens austenitized at 870°C for 12 min and cooled at 2°C/min (a) without, and (b) with a 12 T magnetic field. FD: magnetic field direction.

due to the unpaired spin of its 3d electrons. Under the magnetic field, the atomic magnetic moments align along the field direction. The interaction among those atomic magnetic moments makes them attract each other along the field direction but repel along the direction perpendicular to the field direction. Therefore, elongation along the field direction is energetically favorable. However, this elongation of the grain changes the shape of the grain from equiaxed to ellipsoidal. With the same volume, the surface area of an ellipsoid is larger than that of a sphere (representing the equiaxed grain), hence the total grain boundary energy increases, and this opposes the elongation. Considering these two opposite effects, the total Gibbs free energy difference ΔG_{tot} resulting from grain elongation can be expressed as (Zhang *et al.*, 2005b):

$$\Delta G_{tot} = (E_D^e - E_D^s)V + \sigma(A^e - A^s)$$

$$= -\frac{2\pi}{3}a^3 r \mu_0 \left(\frac{1}{3} - N_{//}\right)(M^2 - M_s^2)$$

$$+ 2\pi a^2 \sigma \left(1 + \frac{r^2 arcsin\sqrt{r^2 - 1}/r}{\sqrt{r^2 - 1}} - 2r^{2/3}\right) \qquad [16.12]$$

where the superscripts e and s represent ellipsoidal and spherical shape of the grain, E_D the total dipolar interaction energy density, V the volume of the grain, A its surface area, σ the energy density of the interface between the ferrite grain and the parent austenite, a the radius of the shortest axis of the ellipsoid, r is the aspect ratio of the ellipsoid, $N_{//}$ the demagnetization factor, M the induced magnetization of ferrite and Ms its spontaneous magnetization. Differentiating Eq. [16.12] with respect to r gives the equilibrium shape (or r_0) of the grain:

© Woodhead Publishing Limited, 2012

$$\left.\frac{\partial(\Delta G_{tot})}{\partial r}\right|_{r=r_0} = 0 \qquad [16.13]$$

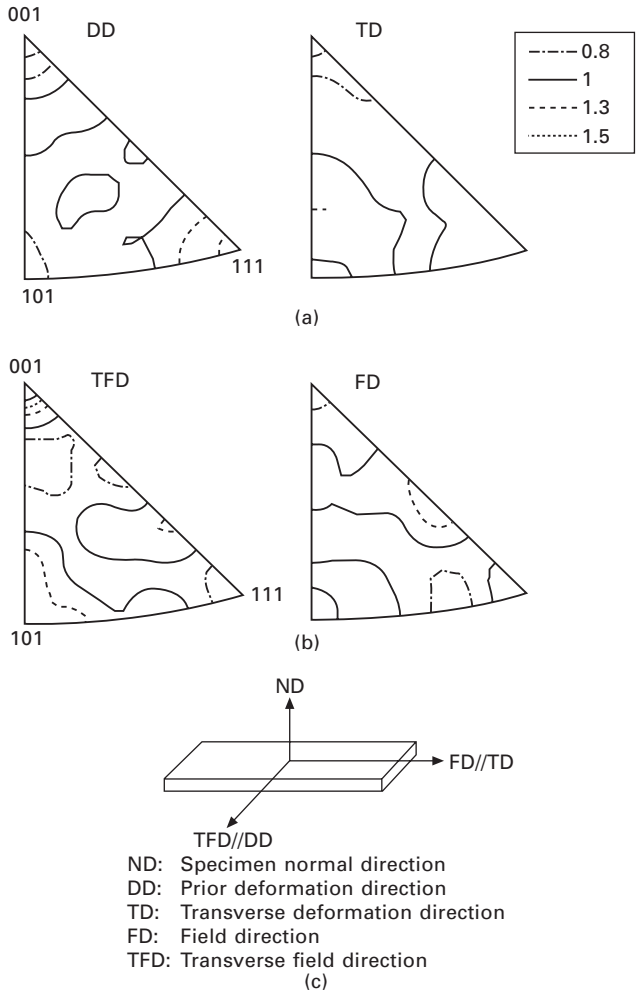
In addition to the anisotropic grain growth induced by the magnetic field, the magnetic field also has a clear effect on crystallographic orientation of proeuctectoid ferrite and eutectoid ferrite when the thermal treatment condition is appropriate for texturation. As found in a medium carbon steel (Fe-0.49C wt%) cooled at 23.5°C/min under a 12 T magnetic field from the austenitic state (Zhang *et al.*, 2005a), the applied magnetic field enhances the <001> fiber texture component along the transverse field direction (TFD), as displayed in the inverse pole figures of the ferrite (Fig. 16.10). This field effect is related to the magnetostriction due to the dipolar interaction among magnetic moments of Fe atoms. As the atoms attract each other along the field direction (FD) but repel each other along the TFD, correlatively, the distance between neighboring atoms tends to decrease along FD and increase along TFD to minimize the total interaction energy of the system.

For ferrite, the carbon atoms are located in the octahedral interstices, as shown in Fig. 16.11. The interstices are shorter in the <001> direction (indicated in Fig. 16.11). The occupation of this interstice by a carbon atom exerts an expansion force on the neighboring iron atoms along the <001> direction. This gives rise to the lattice distortion and creates distortion energy. If this <001> direction of a grain is parallel to the TFD, the lattice distortion energy would be reduced through increasing the atomic spacing in this <001> direction by the magnetic field. Therefore, the nucleation and growth of the grains having their <001> parallel to the TFD are most energetically favored by the magnetic field. In this way, the TFD <001> component is enhanced.

Precipitation

Precipitation of carbides from martensite during tempering processes is a very important phase transformation that generally reduces brittleness of quenched steel. This martensite decomposition takes place in a wide temperature range with characteristic microstructural changes at specific temperatures. In a customary high temperature tempering process, the carbon precipitates from the quenched martensite to form cementite, restoring the crystal distortion induced by carbon supersaturation, and the matrix starts to recover and eventually to recrystallize. At lower tempering temperatures (low temperature tempering), the carbon precipitates to form a refined dispersion of metastable carbides, and the matrix also retains a higher density of crystal defects formed during quenching. It was found that a high magnetic field (14 T) demonstrates remarkable influence on both high temperature (Zhang

© Woodhead Publishing Limited, 2012

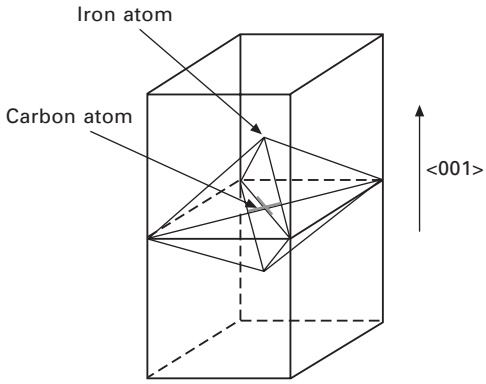


16.10 EBSD inverse pole figures of 0.49C-Fe specimens austenitized at 870°C for 10 min and cooled at 23.5°C/min without and with a 12 T magnetic field and corresponding sample coordinates: (a) 0 T; (b) 12 T (Zhang *et al.,* 2005a).

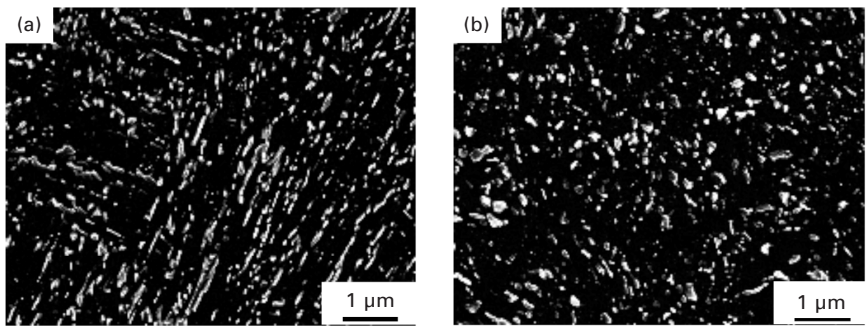
et al., 2004) and low temperature tempering behaviors (Zhang *et al*., 2005e) of a hot rolled 42CrMo after it was water quenched.

For high temperature tempering, it was found that without the magnetic field, the cementite precipitates are in long plates and distributed along martensite plate boundaries, whereas with the 14 T magnetic field, they are in a form of spherical shape and distributed homogeneously, as shown in Fig. 16.12 (Zhang *et al*., 2004). This spheroidization effect of magnetic

© Woodhead Publishing Limited, 2012



16.11 Octahedral interstice occupied by a carbon atom in bcc Fe.

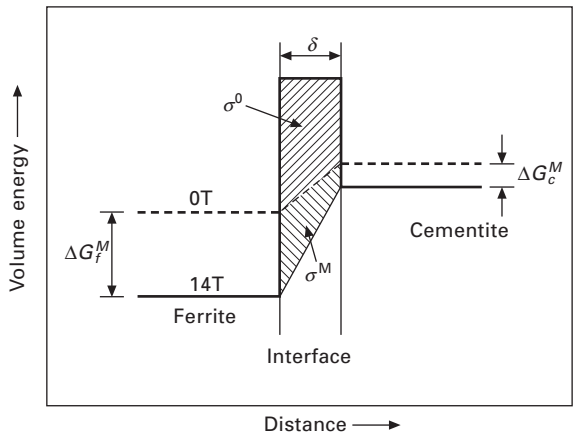


16.12 SEM micrographs of carbide obtained in 42CrMo specimen tempered at 650°C for 1 h (a) without magnetic field; (b) with a 14 T magnetic field (Zhang *et al.*, 2004).

field is attributed to a change in the interfacial energy and magnetostrictive energy by the magnetic field (Zhang *et al.*, 2004).

As both ferrite and cementite can be magnetized to some extent, their Gibbs free energies are lowered by the magnetic field. As the interface between these two phases is highly disordered, its energy level remains unchanged. Consequently, the relative interfacial energy is increased as schematically illustrated in Fig. 16.13. So a shape of cementite that has minimum interface area becomes advantageous to minimize the final total interfacial energy. Therefore, a spherical or particle shaped cementite is most favorable. In addition, the magnetostriction of the cementite and ferrite is also different. In the case of hard cementite growing within the soft ferrite matrix, directional growth of cementite will cause a large increase in strain energy and is thus not favorable. Under these two effects of the magnetic field, the shape of cementite particles that have minimum total interfacial area and minimum magnetostriction strain energy is energetically more favorable and consequently occurs under a magnetic field.

© Woodhead Publishing Limited, 2012



16.13 Cementite/ferrite interfacial energy without and with a magnetic field (Zhang *et al.*, 2004). In the figure, δ is the thickness of the interface; σ^0 and σ^M are the relative interfacial energy without and with a magnetic field; ΔG_f^M and ΔG_c^M are the magnetic Gibbs free energy change of ferrite and cementite induced by a magnetic field.

Moreover, the magnetic field also affects the recovery of the ferrite matrix. Statistical analysis of the measured EBSD map with the 'Recrystallized Fraction' of 'Channel 5' software showed that the area percentages of the 'distortion-free' zones are 7.24% without and 5.42% with the 14 T magnetic field and the percentages in the number of the 'distortion-free' zones are 55.41% without and 51.64% with the 14 T magnetic field for the analyzed area (Zhang *et al.*, 2004). This indicates that a magnetic field has an obvious effect of retardation on the formation and growth of the 'distortion-free' regions.

It has been proposed by Martikainen and Lindroos (1981) that the magnetic field lowers the mobility of the grain boundaries either by atomic diffusion through magnetic ordering or by the obstructive effect of domain walls. As the formation and growth of the 'distortion-free' zones need atom diffusion and boundary migration, the recovery could be retarded by the application of a magnetic field. In this way recovery of the matrix is retarded by the magnetic field.

When the 14 T magnetic field was applied to the low temperature tempering process (200°C; 1 h) of water quenched 42CrMo steel, the 14 T magnetic field showed a strong effect, changing the precipitation sequence of the metastable transition carbides (Zhang *et al.*, 2005e). The carbide formed during non-magnetic tempering is typically orthorhombic η-Fe_2C. However, the carbide precipitating in the magnetic field is the monoclinic χ-Fe_5C_2. Normally, χ-Fe_5C_2 precipitates at higher temperature after η-Fe_2C dissolves. The change to this precipitation sequence results in an improvement in the

© Woodhead Publishing Limited, 2012

impact toughness of the steel. When treated with a magnetic field, the toughness is increased by around 9% (Zhang *et al*., 2005e). This precipitation sequence change is related to the magnetization difference of the related carbides. Based on this observation, *ab initio* calculations have been performed to calculate the magnetic properties of the two carbides (Faraoun *et al*., 2006). It was found that η-Fe_2C, and χ-Fe_5C_2 are both ferromagnetic at 200°C, but the magnetization of χ-Fe_5C_2 is higher than that of η-Fe_2C. As mentioned above, the magnetic field lowers the Gibbs free energy of the magnetized phase according to their induced magnetization. Thus, its total Gibbs free energy may go lower than that of η-Fe_2C under a 14 T magnetic field, so that it precipitates before η-Fe_2C.

16.5 Future trends and conclusions

Through several decades of intensive study on the effects of a magnetic field, especially a high magnetic field, on phase transformations in steels, the origins of the field influences have been clarified in a variety of steel compositions and heat treatment conditions. This shows that a magnetic field could be a useful tool to modify the microstructures of steels during phase transformations.

Although the use of magnetic fields demonstrates possibilities for microstructural modification, there are still many challenges in the practical application of magnetic fields during phase transformations, especially high magnetic field. For the present, high magnetic field is always generated by superconducting magnets. The field operation cost is very high and its application remains exotic even for academic purposes. Moreover, to obtain a sufficient effect of the magnetic field in diffusional or diffusionless transformations in the solid-state in steels, a high magnetic field is always required. To secure high intensity, the uniform field zone is very small with a bore range of several tens of millimeters; therefore the acceptable volume of the materials is quite limited. The possibility of field application in practical use depends on the attainability of high field with low cost and large material treatment space.

16.6 References

Bernshteyn M. L., Granik G. I. and Dolzhanskiy P. R. (1965) 'Effect of magnetic field on the phase transformations in nickel steels', *Fiz. Metal. Metalloved*., vol. 19, no. 6, pp. 77–83.

Boebinger G. S., Lacerda A. H., Schneider-Muntau H. J. and Sullivan N. (2001) 'The National High Magnetic Field Laboratory's pulsed magnetic field facility in Los Alamos', *Physica B*, vol. 294–295, pp. 512–518.

Brandt B. L., Hannahs S., Schneider-Muntau H. J., Boebinger G. and Sullivan N. S. (2001) 'The National High Magnetic Field Laboratory', *Physica B*, vol. 294–295, pp. 501–511.

© Woodhead Publishing Limited, 2012

Brooks J. S., Crow J. E. and Moulton W. G. (1998) 'Science opportunities at high magnetic fields', *J. Phys. Chem. Solids*, vol. 59, pp. 569–590.

Faraoun H., Zhang Y. D., Esling C., Zuo L. and Aourag H. (2006) 'Crystalline, electronic and magnetic structures of θ-Fe_3C, χ-Fe_5C_2 and η-Fe_2C from first principle calculation', *J. Appl. Phys.*, vol. 99, pp. 093508 (8 pages).

Fokina Y. A., Smirnov L. V., Sadovskiy V. D. and Peikul A. F. (1965) 'Effect of a permanent magnetic field on the martensitic transformation in steel', *Fiz. Metal. Metalloved.*, vol. 19, no. 6, pp. 121–122.

Fokina E. A., Kaletin A. Y., Olesov V. N., Smirnov L. V. and Kaletina Y. V. (1995) 'Influence of permanent magnetic field on pearlitic transformation and reversible temper brittleness in steels', *Fiz. Metal Metalloved*, vol. 79, pp. 110–118.

Frings P., Huang Y. and Hennes E. (2002) 'Pulsed-high-field technology, close to the edge', *Physica B*, vol. 319, pp. 330–338.

Garcin T., Rivoirard S., Elgoyhen C. and Beaugnon E., (2010) 'Experimental evidence and thermodynamics analysis of high magnetic field effects on the austenite to ferrite transformation temperature in Fe-C-Mn alloys', *Acta Mater.*, vol. 58, pp. 2026–2032.

Grishin S. A. (1988) 'Structure and properties of structural steels after isothermal treatment in a magnetic field', *Metal Science and Heat Treatment*, vol. 29, pp. 882–886.

Hsu T. Y. (Xu Z.) and Mou Y. (1984) 'Thermodynamics of the bainitic transformation in Fe-C alloys', *Acta Metall.*, vol. 32, pp. 1469–1481.

Jaramillo R. A., Babu S. S., Ludtka G. M., Kisner R. A., Wilgen J. B., Mackiewicz-Ludtka G., Nicholson D. M., Kelly S. M., Murugananth M. and Bhadeshia H. K. D. H. (2005) 'Effect of 30 T magnetic field on transformations in a novel bainitic steel', *Scripta Materialia*, vol. 52, pp. 461–466.

Jones H., Siertsema W. J., Richens P. E., Newson M., Saleh P. M. and Hickman A. L. (2001) 'An update on the Oxford high magnetic field facilities', *Physica B*, vol. 294–295, pp. 598–604.

Kakeshita T., Shimizu K., Funada S. and Date M. (1985) 'Composition dependence of magnetic field-induced martensitic transformations in Fe-Ni alloys', *Acta Metall.*, vol. 33, no. 8, pp. 1381–1389.

Kakeshita T., Shimizu K., Ono M. and Date M. (1990) 'Magnetic field-induced martensitic transformations in a few ferrous alloys', *J. Magn. Magn. Mat.*, vol. 90&91, pp. 34–36.

Kindo K. (2001) '100T magnet developed in Osaka', *Physica B*, vol. 294–295, pp. 585–590.

Klamut J., Palewski T., Suski W. and Nizhankovskii V. I. (2001) International Laboratory of High Magnetic Fields and Low Temperatures in Wroclaw (Poland), *Physica B*, vol. 294–295, pp. 547–550.

Krivoglaz M. A. and Sadovskii V. D. (1964) 'Effect of strong magnetic fields on phase transformations', *Fiz. Metal. Metalloved.*, vol. 18, no. 4, pp. 23–27.

Malinen P. A. and Sadovskii V. D. (1966) 'Effect of a magnetic field on the α→γ transformation in iron-nickel alloys', *Fiz. Metal. Metalloved.*, vol. 21, no. 5, pp. 139–140.

Martikainen H. O. and Lindroos V. K. (1981) 'Observations on the effect of magnetic field on the recrystallization in Ferrite', *Scand. J. Metall.*, vol. 10, pp. 3–8.

Motokawa M., Watanabe K., Miura S., Awaji S., Nojiri H. and Mogi I. (1998) 'Recent developments at the high-field laboratory of Tohoku University', *Physica B*, vol. 246–247, pp. 360–363.

© Woodhead Publishing Limited, 2012

Mou Y. and Hsu T. Y. (Xu Z.) (1986) 'C-C interaction energy in Fe-C alloys', *Acta Metall*., vol. 34, pp. 325–331.

Nojiri H., Takahashi K., Fukuda T., Fujita M., Arai M. and Motokawa M. (1998) '25T repeating pulsed magnetic fields system for neutron diffraction experiments', *Physica B*, vol. 241–243, pp. 210–212.

Prasad S. N., Singh P. N. and Singh V. (1996) 'Influence of pulsating magnetic field on softening behaviour of cold rolled AISI 4340 steel at room temperature', *Scripta Mater*., vol. 34, pp. 1857–1860.

Ren F. D., Xu B. J., Peng H. F. and Gu N. J. (1993) *Heat Treatment of Metals*, vol. 5, pp. 23–26.

Rivoirard S., Garcin T., Beaugnon E. and Gaucherand F. (2009) 'High temperature dilatation measurements by *in situ* laser interferometry under high magnetic field', *Review of Scientific Instruments*, vol. 80, pp. 103901.

Sadovskii V. D., Rodigin N. M., Smirnov L. V., Filonchik G. M. and Fakidov I. G. (1961) 'The question of the influence of magnetic field on martensitic transformation in steel', *Fiz. Metal. Metalloved*., vol. 12, pp. 131–133.

San Martin D., van Dijk N. H., Bruck E. and van der Zwaag S. (2008) 'The isothermal martensite formation in a maraging steel: a magnetic study', *Mater. Sci. Eng. A*, vol. 481–482, pp. 757–761.

San Martin D., van Dijk N. H., Jiménez-Melero E., Kampert E., Zeitler U. and van der Zwaag S. (2010) 'Real-time martensitic transformation kinetics in maraging steel under high magnetic fields', *Mater. Sci. Eng. A*, vol. 527, pp. 5241–5245.

Shimotomai M., Maruta K., Mine K. and Matsui M. (2003) 'Formation of aligned two-phase microstructures by applying a magnetic field during the austenite to ferrite transformation in steels', *Acta Mater*. vol. 51, no. 10, pp. 2921–2932.

Tang G., Lu A., Chen X., Zhou H. and Tang F. (2000) 'Effect of a pulsed magnetic treatment on the dislocation substructure of a commercial high strength steel', Proc. 3rd International Symposium on Electromagnetic Processing of Materials, *ISIJ*, Nagoya, vol. 9, pp. 606–611.

Wang S. J., Zhao X., Zhang Y. D., Zuo L. and Esling C. (2007) 'Effect of a high magnetic field on the formation of Widmanstätten ferrite in Fe-0.52C', *Materials Transactions*, vol. 48, pp. 2816–2820.

Watanabe K., Nishijima G., Awaji S., Takahashi K., Koyama K., Motokawa M., Ishizuka M., Hasebe T. and Sakuraba J. (2004) 'Advances in the first cryogen-free hybrid magnet', *IEEE Trans. Appl. Superconductivity*, vol. 14, pp. 388–392.

Zener C. (1955) 'Impact of Magnetism Upon Metallurgy', *Journal of Metals*, vol. 7, pp. 619–630.

Zhang Y. D., Gey N., He C. S., Zhao X., Zuo L. and Esling C. (2004) 'High temperature tempering behaviors in a structural steel under high magnetic field', *Acta Mater*., vol. 52, no. 12, pp. 3467–3474.

Zhang Y. D., Esling C., Lecomte J. S., He C. S., Zhao X. and Zuo L. (2005a) 'Grain boundary characteristics and texture formation in a medium carbon steel during its austenitic decomposition in a high magnetic field', *Acta Mater*., vol. 53, pp. 5213–5221.

Zhang Y. D., Esling C., Muller J., He C. S., Zhao X. and Zuo L. (2005b) 'Magnetic-field-induced grain elongation under a high magnetic field in medium carbon steel in its austenitic decomposition', *Appl. Phys. Lett*., vol. 87, pp. 212504.

Zhang Y. D., He C. S., Zhao X., Zuo L., Esling C. and He J. C. (2005c) 'Thermodynamic and kinetic characteristics of high temperature cooling phase transformation under high magnetic field', *J. Magn. Magn. Mater*., vol. 294, pp. 267–272.

© Woodhead Publishing Limited, 2012

Zhang Y. D., Vincent G., Dewobroto N., Germain L., Zhao X., Zuo L. and Esling C. (2005d) 'The effect of thermal processing in a magnetic field on grain boundary characters of ferrite in a medium steel', *J. Mater. Sci.*, vol. 40, pp. 905–908.

Zhang Y. D., Zhao X., Bozzolo N., He C. S., Zuo L. and Esling C. (2005e) 'Low temperature tempering behaviors in a structural steel under high magnetic field', *ISIJ Int.*, vol. 45, pp. 913–917.

Zhang Y. D., Esling C., Gong M. L., Vincent G., Zhao X. and Zuo L. (2006a) 'Microstructural features induced by a high magnetic field in a hypereutectoid steel during austenitic decomposition', *Scripta Mat.*, vol. 54, pp. 1897–1900.

Zhang Y. D., Faraoun H., Esling C. and Aourag H. (2006b) 'Paramagnetic susceptibility of ferrite and cementite obtained from *ab initio* calculations', *J. Magn. Magn. Mater.*, vol. 299, pp. 64–69.

Zhang Y. D., Esling C., Calcagnotto M., Gong M. L., Zhao X., Zuo L. (2007) 'Shift of the eutectoid point in the Fe-C binary system by a high magnetic field', *Journal of Physics D: Applied Physics*, vol. 40, pp. 6501–6506.

© Woodhead Publishing Limited, 2012

17

The effect of heating rate on reverse transformations in steels and Fe-Ni-based alloys

YU. YA. MESHKOV, Institute for Metal Physics, National Academy of Sciences, Ukraine and E. V. PERELOMA*, University of Wollongong, Australia

Abstract: An overview of the mechanisms, kinetics and crystallography of austenite formation in rapidly heated steels and Fe-Ni-based alloys is given. A particular focus is on the morphology of austenite microstructure and the conditions under which the phenomenon of structural inheritance takes place. The possible reasons for it are listed and discussed. The effects of rapid heat treatments on the mechanical properties of steels are briefly addressed and some examples of industrial applications are provided.

Key words: rapid heating, mechanism, kinetics, structural heredity, austenite morphology.

17.1 Introduction

Since the 1930s, first high frequency induction surface treatments (Vologdin, 1939), then direct resistance electric heating of steel parts have gained attention as successful techniques for hardening and improving the strength-ductility balance of steels (Gridnev, 1948; Sadovskiy and Sazonov, 1951; Kidin, 1969; Gridnev *et al.*, 1973; Sadovskiy, 1973). More recently, the surface treatment of steels using a high-energy laser beam, where heating rates can reach about 10^4–10^5 K s^{-1} and more, has become widely applied (Lyasotskiy and Shtanskiy, 1991; Yakovleva *et al.*, 1993, 1995; Mioković *et al.*, 2006; Lefevre-Schlick *et al.*, 2008).

Rapid heat treatment technologies not only provide the opportunity for improvements in mechanical properties, but also offer the economic advantage of much shorter processing times. In order to fully realize the potential of rapid heat treatments, in-depth understanding of the phase transformations, which control the microstructural changes under these conditions, is essential. Temperature and time are the main parameters determining phase transformation kinetics. They are also key factors influencing the kinetics of diffusion processes, which accompany phase transformations in heterogeneous

* Note that Pereloma is formerly Emchenko-Rybko.

© Woodhead Publishing Limited, 2012

alloys. In alloys with various microstructures and chemistry, these factors affect differently the resultant phases and their compositions after heat treatment. Therefore, the use of various heating rates makes possible the production of a wide range of microstructures in Fe alloys and steels, leading to an expansion of the range of their mechanical properties.

In view of the technological importance of rapid heat treatment, investigations of the mechanism and kinetics of phase transformations taking place in rapidly heated alloys have received considerable attention. Whereas the majority of initial studies were carried out using *ex-situ* techniques, the high temperature nature of the investigated phenomena resulted in the necessity to develop a special package of physical methods to investigate *in-situ* the mechanism and kinetics of phase transformations during rapid heating. These methods allow the determination of the main process parameters and material properties as a function of heating rate: temperature, time, volume change (dilatometry) (Gridnev and Kocherzinsky, 1953), electrical resistivity (Gridnev *et al.*, 1965b), magnetization (Gridnev *et al.*, 1965a), and lattice parameters of alpha and gamma phases (Gridnev *et al.*, 1964b). Later on, a rapid method for the X-ray recording of Laue patterns in the course of the $\alpha(\alpha') \rightarrow \gamma$[1] transformation was added to these methods (Oshkaderov *et al.*, 1989). Although with some limitations on heating rates, for microstructure observations *in-situ* special methodologies of transmission electron microscopy (TEM) (Singh and Wayman, 1986) and electron back scattering diffraction (EBSD) (Lischewski *et al.*, 2008) are utilized.

In this chapter the current viewpoints on the mechanisms, kinetics and crystallography of austenite formation during rapid heating of Fe-C-based and Fe-Ni-based alloys and steels are discussed.

17.2 Effect of heating rate on austenite formation in steels

17.2.1 Kinetics of austenite formation

Reverse transformation start (A_s) and finish (A_f) temperatures are important parameters, which depend on several variables, such as alloy composition, initial microstructure and heating rate. For Fe-C alloys these critical temperatures are A_{c1} and A_{c3}, respectively. The dependence of the austenite formation temperatures on heating rate provides the first indication of the possible mechanism of its formation. Similarly to the transformations taking place on cooling, the reverse transformations could occur by two main mechanisms:

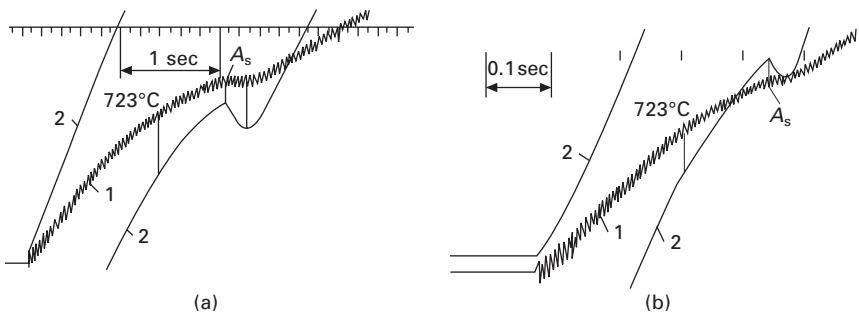
[1]Here α denotes ferrite (body cubic centred, bcc), α' denotes martensite and γ denotes austenite (face cubic centred, fcc).

© Woodhead Publishing Limited, 2012

1. diffusional or reconstructive, and
2. displacive via coordinated movement of atoms by shear.

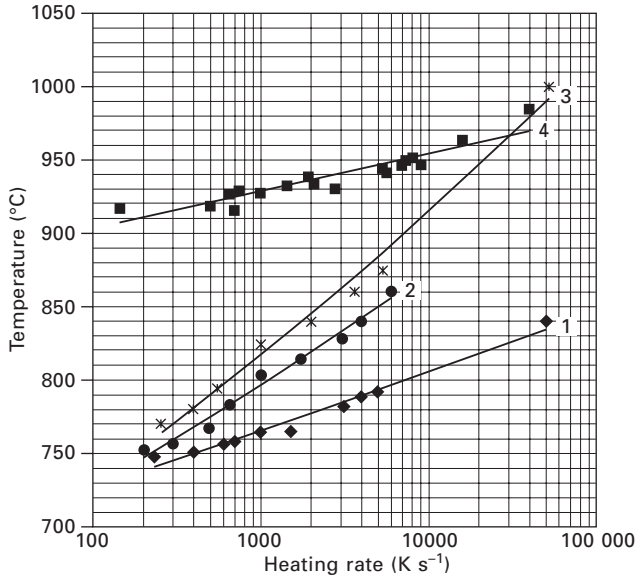
The latter is time independent due to the extremely high nucleation and growth rate of the new phase resulting in transformation temperature independence of heating rate, as shown for non-ferrous (Cu-Al-(Mn)) and Fe-Ni alloys (Gridnev, 1989). This will be discussed in more detail in Section 17.4.

The first mechanism is time dependent and under isothermal conditions takes place based on local equilibrium concepts. However, rapid heating changes the conditions to non-equilibrium ones and exerts a pronounced effect on nucleation and growth of austenite formed by a diffusion-controlled mechanism. Although both nucleation rate and growth rate are temperature dependent, the dependence is more pronounced for the former. With increase in heating rate the time allowed for diffusion decreases, whereas the diffusivity increases with increase in temperature. Thus, for rapid heating the limited rate of nucleation and growth of austenite nuclei in the ferrite matrix lags behind the rate of temperature increase, resulting in superheating above the equilibrium phase transformation start and finish temperatures, A_1 and A_3. This manifests itself in a continuous rise of transformation temperature with increasing heating rate (Figs 17.1 and 17.2). The recorded temperature and dilatometry curves with time on heating of 0.8 wt% C steel clearly indicate the occurrence of phase transformation at higher temperatures with increased heating rate from 110 K s^{-1} to 1080 K s^{-1} (cf. Figs 17.1(a) and (b)). However, care should be taken in accounting for the possible thermocouple lag when studying the effect of rapid heating on critical temperatures, otherwise instrumental errors may lead to erroneous conclusions about the mechanism of austenite formation. The initial steel microstructure also affects the reverse transformation temperatures: in 0.8 wt% C steel with a lamellar pearlite structure, the temperature of austenite formation reaches 800°C at a heating



17.1 Temperature (1) and dilatometric (2) curves for 0.8 wt% carbon steel heated at (a) 110 K s^{-1} and (b) 1080 K s^{-1}. A_s is start temperature of phase transformation. Reprinted from Gridnev *et al.* (1973) with copyright permission from Naukova Dumka.

© Woodhead Publishing Limited, 2012



17.2 Effect of heating rate on the start of reverse transformation temperature in the steel with 0.8 wt% C (curves 1–3) and in pure α-iron (curve 4). Initial conditions of 0.8 wt% C steel are: 1, as-quenched (martensite); 2, normalized (lamellar pearlite); 3, annealed (degenerated pearlite).

rate of about 10^3 K s^{-1}, whereas in the same steel in the quenched martensite state, this temperature is about 760°C (Fig. 17.2).

Gridnev *et al*. (1973) found that the law governing increase of A_s with heating rate (V_H) in carbon and alloyed steels is given by:

$$\Delta A_s = KV_H^{1/3} \qquad [17.1]$$

where ΔA_s is the superheat (in °C) above the equilibrium transformation start temperature A_s, which for eutectoid steel is 723°C, and K is a constant which depends on the fineness of the pearlite starting microstructure.

There are no diffusion processes associated with carbon transport to γ-iron nucleation sites in pure iron, thus the austenite formation kinetics are sharply accelerated (Gridnev *et al*., 1964a). As a result, there is a less pronounced dependence of the phase transformation temperatures on heating rates, and the rise of A_{c3} above the equilibrium temperature at heating rates, $V_H \approx 10^4$ K s^{-1} is only ~40 K compared to 100 K rise for eutectoid steel heated at ~10^3 K s^{-1} (Fig. 17.2).

© Woodhead Publishing Limited, 2012

17.2.2 Mechanism of austenite formation on the fast heating of Fe-C-base alloys

Austenite formation in quenched steels with martensite microstructure

The main characteristics of displacive (martensitic type) phase transformations include the specific crystallographic orientation relationships between the parent and product phase, appearance of a distinct surface relief and the preservation of the chemical composition of the parent phase, including both interstitial and substitutional elements, in the transformation product. As the first two features could also be characteristics of diffusional-displacive phase transformations (Muddle *et al.*, 1994; Christian, 1997; Aaronson and Nie, 2000), the examination of chemical compositions of parent phase and of austenite is important for judging the nature of the reverse phase transformations. Carbon has the fastest diffusion rate in ferrous materials out of all elements. Thus, for reverse displacive (diffusionless) transformation to take place, the diffusion of carbon needs to be suppressed. Although with increased heating rates the tempering temperature ranges in quenched steels increase continuously, even at a heating rate of 60 000 K s^{-1}, the first and third tempering stages were detected in hardened steel with 0.8 wt% C, i.e. martensite decomposition takes place (Gridnev, 1989). This means that during rapid heating the following sequence of events takes place:

$$\alpha' \rightarrow \alpha_{\text{C-depleted}} + \alpha_{\text{C-rich}} \rightarrow \alpha_{\text{C-depleted}} + Fe_3C \rightarrow \gamma \qquad [17.2]$$

However, there is no experimental evidence on the formation of low carbon austenite from tempered martensite on rapid heating ($V_H \sim 3–4 \times 10^3$ K s^{-1}); instead the concentration of carbon in freshly formed austenite is close to the eutectoid one (Gridnev, 1989). This means that when even at high heating rates the processes of martensite decomposition take place, the diffusion of carbon is necessary in order to obtain high-carbon austenite from such heterogeneous microstructure. In comparison with carbon steels, in alloy steels the process of martensite decomposition could be further inhibited, but not completely eliminated. The indirect collaboration of the diffusion-controlled mechanism of austenite formation in low alloy steel with 0.4 wt% C (AISI 4140) subjected to laser treatment has been obtained by Mioković *et al.* (2006). It was shown that in the heat affected zone of the laser beam, homogeneous austenite is formed at a depth of 0.42 mm at a local heating rate of 10^3 K s^{-1} and at a depth of 0.05 mm at a local heating rate of 10^4 K s^{-1}.

Thus, the formation of austenite on rapid heating in quenched steels occurs by a diffusional mechanism owing to high carbon diffusivity. However, in general, this might only be true on a macroscale, as during ultra-rapid heating the decomposition of martensite may be prevented in very small micro-volumes where the dislocation substructure is still maintained. In these areas the concentration of carbon will be high due to the carbon atmospheres

© Woodhead Publishing Limited, 2012

at dislocations, and the conditions of austenite formation will significantly deviate from the equilibrium ones, leading to the possibility of displacive formation of lath-like austenite at the nucleation stage of reverse transformation (Gridnev *et al.*, 1979). The formation of lath-like/acicular austenite was observed between the laths of martensite (Judd and Paxton, 1968), where the carbon concentration could be higher due to the preservation of the lath boundary dislocation structure up to the transformation temperatures. A discussion on the crystallography of reverse transformation and austenite morphology is presented in Section 17.3.

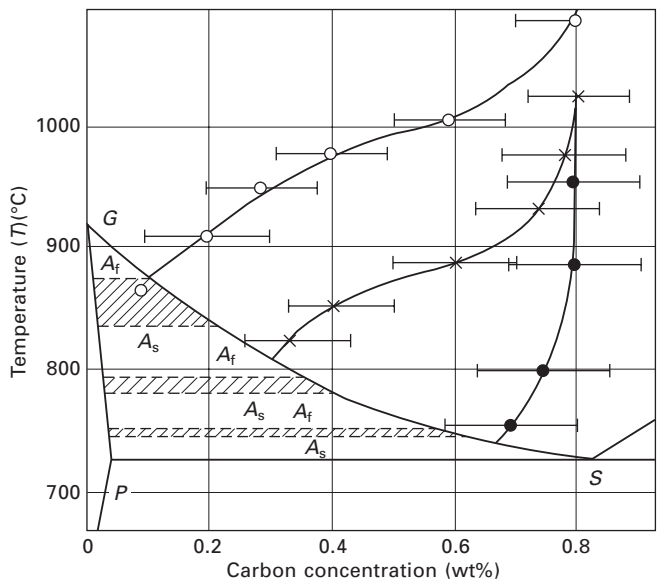
Austenite formation in normalized steels containing pearlite or a ferrite/globular carbide mixture

Three possible mechanisms of reverse phase transformation, depending on heating conditions, have been put forward: (i) diffusional; (ii) displacive (martensitic-like) and (iii) massive. Here we discuss the main reasons for this.

The traditional view on the mechanism of diffusional formation of austenite in rapidly heated eutectoid steels involves formation of volumes of concentration fluctuations, in which carbon concentration could reach the levels above the equilibrium one (Gridnev, 1967). Such micro-volumes could be found in the vicinity of ferrite/cementite interfaces due to the dissolution of cementite leading to the formation of austenite nuclei in such regions (Gridnev, 1967). For austenite growth the necessary condition is diffusion of carbon to the interface, which is also easily achieved by the dissolution of cementite. Observation of the early nucleation stage in rapidly heated steel containing carbides (Lefevre-Schlick *et al.*, 2008) has confirmed the preferential nucleation of γ phase at ferrite/carbide interfaces. Initial formation of austenite at pearlite colony boundaries and pearlite/ferrite interfaces of Fe-0.15C-0.25Si-1.06Mn (wt%) steel containing proeutectoid ferrite and pearlite heated at 10 K s^{-1} was also evident (Park *et al.*, 2007). Contrarily, austenite was formed first in the ferrite lamellae of pearlite in the same steel under similar heating conditions, but containing ultrafine grained microstructure produced by severe plastic deformation. The change in the austenite nucleation site is associated with a significant enrichment of the pearlitic ferrite in carbon (0.2–3.0 at%) due to partial or full decomposition of cementite following different severe plastic deformation methods (Hono *et al.*, 2001; Ivanisenko *et al.*, 2003; Sauvage *et al.*; 2004). This also leads to a reduction in the A_{c1} temperature compared to that of coarse grained pearlitic steels, by more than 10–20°C (Ivanisenko *et al.*, 2006; Park *et al.*, 2007). These results support a diffusion-controlled mechanism of austenite formation in regions supersaturated with carbon, and the larger the degree of supersaturation the lower the start temperature of reverse transformation.

© Woodhead Publishing Limited, 2012

The carbon concentration of freshly formed austenite is an important indication of the mechanism of its formation. Based on the determination of the martensite formation start temperature on quenching (M_s) the first fractions of austenite formed on reverse transformation, the carbon content of this austenite could be estimated. For a pearlitic 0.8 wt% C steel heated at 2000 K s^{-1}, the $\alpha \rightarrow \gamma$ transformation start temperature A_s was 850 ± 10°C and the corresponding M_s, measured by high-speed magnetometry on quenching after 10–15% austenite formation, was ~600°C (Gridnev *et al.*, 1973). This M_s corresponds to an equilibrium concentration of about 0.1–0.15 wt% C in austenite (Fig. 17.3). At a heating rate of 150 K s^{-1}, $A_s \approx 815 \pm 10$°C and the M_s for freshly formed and quenched austenite is ~400°C, corresponding to an homogeneous composition of austenite with ~0.3–0.4 wt% C (Fig. 17.3). High temperature XRD studies of austenite lattice parameter (with an accuracy of ±0.0002 nm) also confirmed that after heating at 200–500 K s^{-1}, the initially formed austenite in eutectoid steel contains ~0.8 wt% C (Gridnev *et al.*, 1973), which corresponds to a carbon content in austenite formed by a diffusion-controlled mechanism according to the equilibrium Fe-Fe_3C phase diagram. Thus, the carbon concentration in the first portion of austenite



17.3 Dependence of austenite composition on the temperature of its formation in rapidly electric heated steel with 0.8 wt% C, plotted on equilibrium Fe-Fe_3C diagram. ○ degenerated pearlite (V_H = 2000 K s^{-1}), × degenerated pearlite (V_H = 150 K s^{-1}), ● martensite (V_H = 150 K s^{-1}), A_S and A_f are the start and end temperatures of equilibrium $\alpha \rightarrow \gamma$ transformation. Adapted from Gridnev *et al.* (1973) with copyright permission from Naukova Dumka.

© Woodhead Publishing Limited, 2012

formed in the case of rapid heating always corresponds to its equilibrium composition at the particular $\alpha \rightarrow \gamma$ transformation temperature.

Equiaxed, relatively fine grained austenite microstructure is formed on heating of ferrite/pearlite steels (Fig. 17.4). With increase in heating rate, the grain size becomes finer (Televich and Prikhod'ko, 1994e; Ivasishin and Teliovich, 1999), which correlates with a shift of diffusion-controlled transformation to higher temperatures. For these microstructures, no clearly defined $\gamma \rightarrow \alpha \rightarrow \gamma$ phase transformation texture was observed by *in-situ* XRD experiments with heating rates up to 50 K s^{-1} (Televich and Prikhod'ko, 1994e).

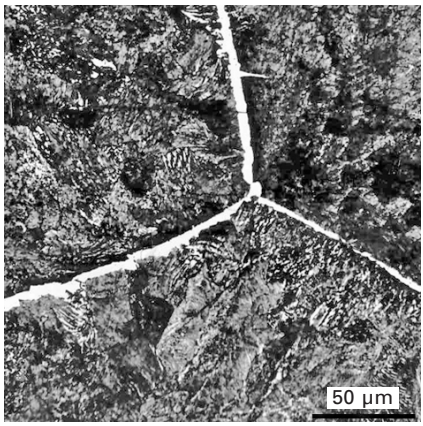
Thus, the carbon concentration of the first portion of austenite, the absence of specific crystallographic relationships and the dependence of transformation temperatures and austenite grain size on heating rate support a diffusional mechanism of austenite formation in normalized steels on heating at $V_H < 10^3$ K s^{-1}.

However, Yakovleva *et al*. (1993, 1995) argue that a critical heating rate exists above which the formation of austenite in eutectoid steel will take place by a displacive mechanism. Such a critical heating rate was estimated earlier to be ~30 000 K s^{-1} (Gridnev *et al*., 1973). In support of this hypothesis, Yakovleva *et al*. show the absence of cementite dissolution until the start of the $\alpha + Fe_3C \rightarrow \gamma$ transformation in laser heated 0.8 wt% C steel and existence of crystallographic orientation relationships close to Kurdjumov–Sacks orientation relationships (K-S OR) (Kurdjumov and Sachs, 1930) between ferrite and reverted austenite:

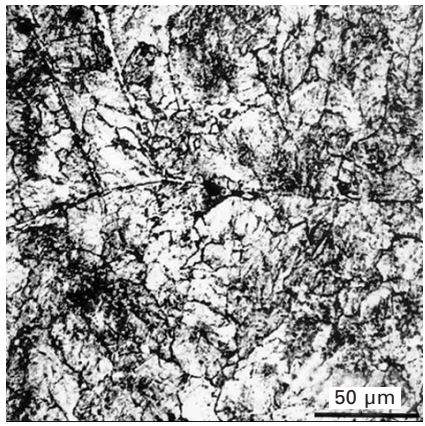
$$(111)_\gamma // (011)_\alpha,\ [01\bar{1}]_\gamma // [11\bar{1}]_\alpha \qquad [17.3]$$

In addition, electron microscopy studies of quenched austenite after ultra-rapid laser heating (10^3–10^4 K s^{-1}) into the intercritical temperature interval have shown that initially lath austenite is formed within one ferrite lamella (Fig. 17.5(a)) and that the rate of austenite growth is faster in the centre of the ferrite lamellae than in regions adjacent to the neighbouring cementite lamellae. This contradicts diffusion-controlled α/γ interface movement, as the higher carbon concentration near the cementite/ferrite interface would be expected to assist its faster movement in the adjacent area. The transformation of this austenite into ferrite on quenching also indicates its low carbon content. When austenite is quenched at a slightly later stage of transformation, martensite formed from the transformed austenite is localized within one ferrite lamella (Fig. 17.5(b)). Based on these observations, a model of austenite formation in eutectoid steel at ultrahigh heating rates was proposed (Yakovleva *et al*., 1993, 1995): (i) the first fractions of lath austenite formed from ferrite by a displacive mechanism are low in carbon, and (ii) immediately after formation of austenite the dissolution of cementite starts at these temperatures and concentration of carbon in austenite rapidly increases.

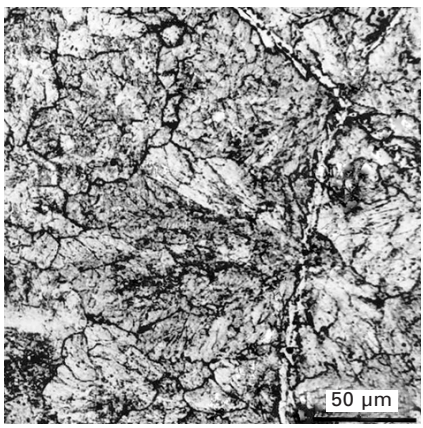
© Woodhead Publishing Limited, 2012



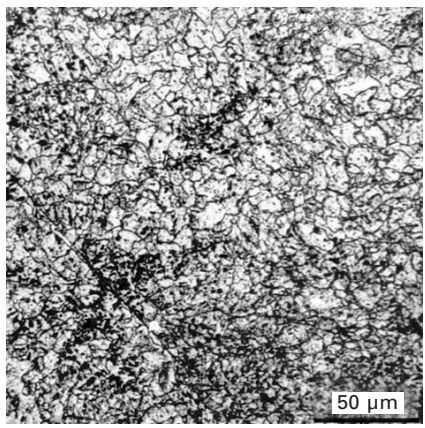
(a)



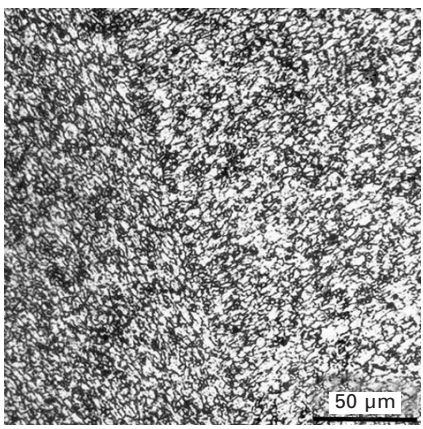
(b)



(c)



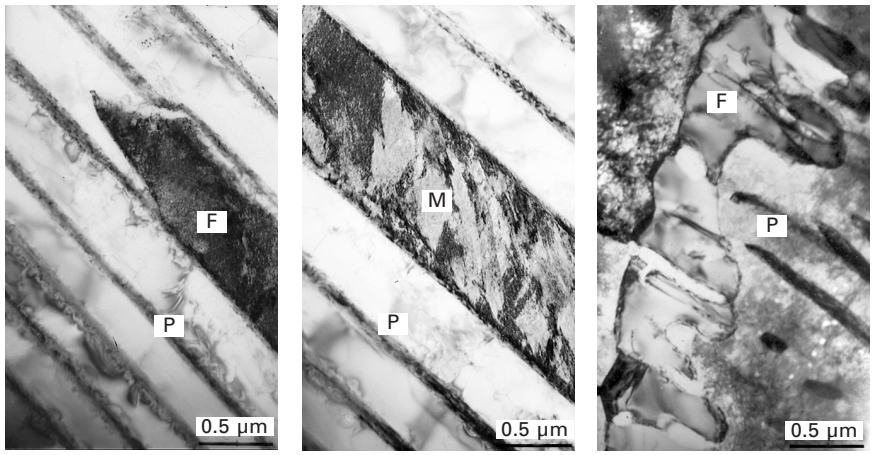
(d)



(e)

17.4 Formation of austenite in ferrite/pearlite matrix of 0.38 wt% C steel heated to A_{c3}:
(a) initial microstructure after isothermal transformation at 480°C; (b) V_H = 0.016 K s^{-1}; (c) V_H = 3 K s^{-1}; (d) V_H = 50 K s^{-1}; (e) V_H = 200 Ks^{-1}. From Televich and Prikhod'ko (1994e). Copyright permission from original publisher Metallofizika i Noveishie Tekhnologii.

© Woodhead Publishing Limited, 2012



(a) (b) (c)

17.5 TEM observations of microstructure after laser heating and quenching of eutectoid steel with pearlite microstructure: (a) sharp growing front of austenite within ferrite lamella and displacement of cementite; (b) martensite formed from austenite within one initial ferrite lamella and (c) massive formation of austenite. P is pearlite, F is newly formed on quenching from austenite ferrite and M is formed on quenching from austenite martensite. Courtesy of Dr I.L. Yakovleva, Institute of Physics of Metals, Russian Academy of Sciences.

However, the evidence presented is not fully convincing, as the quenching rate might have been low resulting in ferrite formation instead of martensite and the heating rates achieved are still below the predicted critical one for the change of mechanism of the phase transformation. It should also be noted that the orientation relationships between ferrite and austenite in pearlitic steel may be maintained at the nucleation stage; at high temperatures the movement of the interface is not sensitive to the crystallographic orientation of crystal lattices and its movement has a non-conservative component, e.g. thermally activated climb of misfit dislocations.

Formation of lath-like austenite at ferrite boundaries at the very early stages of transformation (time is shorter than the incubation period for reconstructive (diffusional) austenite formation) in 0.69% C, 0.72% Mn, 0.24% Cr, 0.24% Si carbon steel, containing globular cementite, was also observed at heating rates in the range of 200–2000 K s^{-1} (Kaluba *et al.*, 1998). As transformation progresses, further austenite growth takes place according to the equilibrium conditions, e.g. diffusion-controlled growth. On water quenching the freshly formed austenite, some of the austenite laths remained untransformed to martensite indicating their high carbon content, 0.9–1.3% C, contrary to the results of Yakovleva *et al.* (1995). Similar untransformed austenite was also detected at cementite particles. This lath-like austenite

© Woodhead Publishing Limited, 2012

exhibited orientation relationships which deviated from the K-S ORs (Eq. [17.3]) by several degrees. These crystallographic and morphological features fuelled a debate on the similarities of this lath-austenite to the upper bainite formed on cooling and whether they indicate the nature of the mechanism of its formation being reconstructive or displacive at the nucleation stage (Kaluba *et al.*, 1998, 2000; Aaronson and Nie, 2000; Hillert, 2000). Further research on this issue would thus be warranted.

It should be noted that, at heating with such ultrahigh rates during laser treatment, the temperature of austenite formation might reach 860–870°C, which is the temperature of polymorphous formation in pure iron. Thus, the active participation of carbon in the phase transformation under such conditions is not a mandatory one and formation of austenite could proceed via a massive transformation mechanism (Gridnev, 1967; Speich and Szirmae, 1969; Televich and Prikhod'ko, 1994e). If austenite forms according to this mechanism, the movement of the austenite/ferrite interface is expected to progress uniformly at the front, as seen in Fig. 17.5(c). Thus, the current experimental evidence suggests that under laser heating different heating rates may be achieved and *nucleation* of austenite could take place either by a massive (Speich and Szirmae, 1969; Lyasotskiy and Shtanskiy, 1991) or a displacive (Yakovleva *et al.*, 1993, 1995) mechanism. At lower heating rates austenite forms in normalized steels by a diffusion-controlled mechanism (Gridnev, 1967; Gridnev *et al.*, 1973; Televich and Prikhod'ko, 1994e).

17.2.3 Chemical inhomogeneity of austenite

Due to the different solubility of alloying elements in low and high temperature phases, their redistribution accompanies formation of a new phase on heating. The lattice and compositional changes during phase transformation on heating are shifted to higher temperatures with increase in heating rate. The diffusion-controlled compositional changes are completed later than the crystallographic ones, and the higher the heating rates the more delayed is the chemical homogenization. As a result, a variety of microstructural conditions with different degrees of inhomogeneity could be produced, resulting in various mechanical properties. For 0.8% C steel, with an initial microstructure of degenerate pearlite, the decomposition of carbides takes place in austenite and complete carbon homogenization of the austenite microstructure is achieved at ~1000°C at 150 K s^{-1} heating rate, but delayed to ~1100°C when the steel is heated at 2000 K s^{-1} (Fig. 17.3). When the initial microstructure is martensite, carbon homogenization is completed earlier, at ~900°C at a heating rate of 150 K s^{-1}, as no coarse carbides are present in such microstructure. Contrarily, in alloy steel with 0.3% C heated at 100 K s^{-1}, homogenization of austenite is not finalized up to 1000°C (Gridnev *et al.*, 1964b), and in steel containing 0.4 wt% C and 1.5 wt% Mn with a coarse

© Woodhead Publishing Limited, 2012

pearlite microstructure, evidence of austenite inhomogeneity is retained up to 1100°C even when heated at 1000 K s^{-1} (Shutts, 2004). High carbon steel with 1.2 wt% C also remains very inhomogeneous at 1200°C when heated at 450 K s^{-1}, because it retains a significant fraction of undissolved cementite in austenite (Gridnev *et al.*, 1965a). Controlled austenite inhomogeneity in rapidly heated 0.3% C martensitic structural steel, when fine alloy carbides remained undissolved at 900°C, resulted in the achievement of an attractive combination of strength, ductility and fracture toughness (Ivasishin and Teliovich, 1999).

17.3 Effect of heating rate on austenite microstructure after $\gamma \rightarrow \alpha(\alpha') \rightarrow \gamma$ phase transformations in quenched steels

Irrespective of the nature of initial microstructure (Widmanstätten ferrite, bainite or martensite) the austenite microstructure formed on heating displays two distinctive arrangements of grains: (i) restoration of the original coarse austenite grain structure (see Figs 17.6(a) and (c)) or (ii) a fine grained microstructure (Fig. 17.6(b)). The former process takes place either at very slow heating rates $<\sim 1$ K min^{-1} or at rapid ones, whereas the latter process occurs at intermediate heating rates. These two characteristic austenite microstructures are observed in both plain carbon and alloy steels. The exact ranges of heating rates at which formation of these austenite microstructures occurs depend on steel composition.

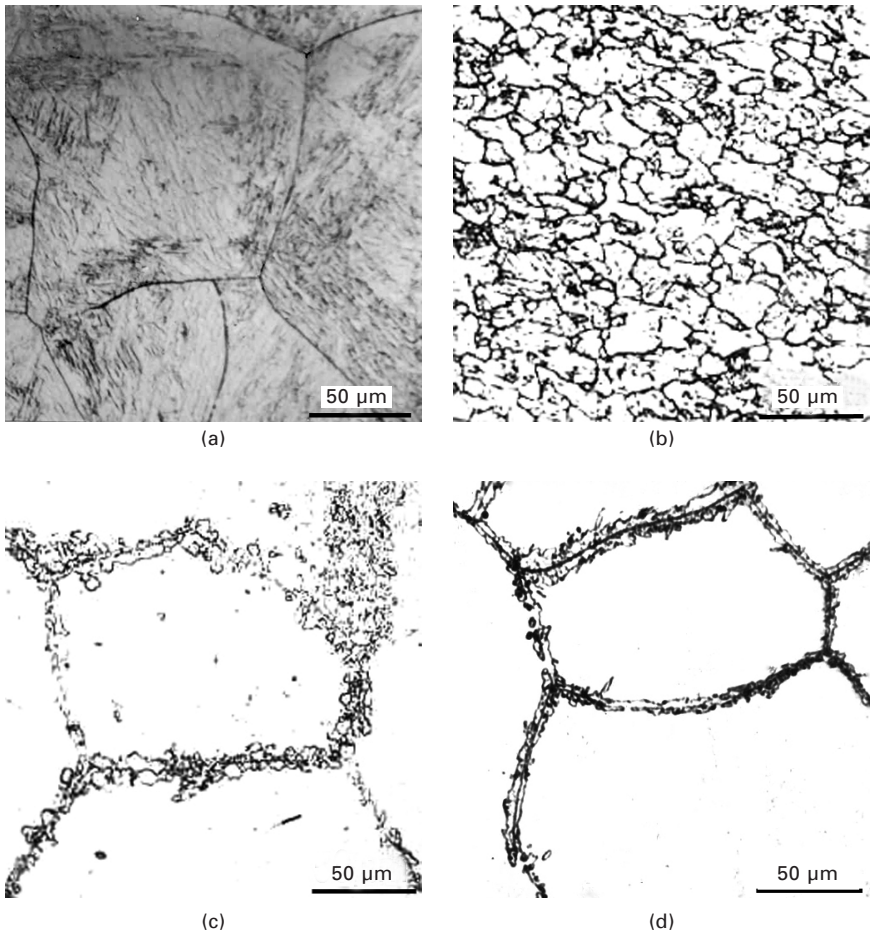
17.3.1 Fine grained austenite microstructure formation

There has been a long-standing debate concerning the mechanism and crystallography of the formation of the fine grained austenite microstructure on heating at intermediate heating rates. It was suggested that such austenite forms by a mechanism which is

- disordered (Sadovskiy, 1976),
- ordered, but grain refinement takes place by recrystallization, which also proceeds at the same temperatures as phase transformation, whose start temperature falls into phase transformation temperatures interval (D'yachenko, 1982; Sadovskiy, 1984) and
- crystallographically ordered, but which does not result in restoration of the prior austenite grain structure due to the realization of multiple orientation variants different from the original (Ozhiganov *et al.*, 1974).

Due to the high temperature nature of reverse $\alpha \rightarrow \gamma$ transformations, the above hypotheses were based on experimental evidence obtained by indirect methods. More recent results of work carried out by *in-situ* XRD observation

© Woodhead Publishing Limited, 2012



17.6 Effect of heating rate on austenite microstructure of quenched 0.35C-0.5Mn-0.25Si-3Ni-0.4Mo-1.2Cr-0.1V-0.02S-0.02P (wt%) steel: (a) as-quenched from 1200°C; (b) heating rate 3 K s^{-1}, (c) heating rate ~300 K s^{-1}, (d) heating rate 4400 K s^{-1}. Courtesy of Dr R.V. Televich, Institute for Metal Physics, National Academy of Sciences, Ukraine.

of austenite formation in one packet of martensite crystals in both plain carbon and alloy steels provided further insight into the mechanism of fine grained austenite formation (Oshkaderov *et al.*, 1992; Televich and Prikhod'ko, 1994a, 1994c). It was confirmed that in plain carbon steels (Oshkaderov *et al.*, 1992; Televich and Prikhod'ko, 1994a) the fine grained austenite has a pronounced texture corresponding to the realization of six variants of the Greninger–Troiano orientation relationship (G-T OR) (Eq. [17.4]), which are within a few degrees of the K-S OR, in a martensite packet on quenching, and predominantly four out of 24 possible variants on heating, accompanied by

© Woodhead Publishing Limited, 2012

the additional four twin variants. A good correlation was achieved between the experimental pole figures and the theoretically calculated ones based on the assumption that these twin variants are formed by twinning of all four G-T variants on the {111} planes not appearing in the G-T variant (Televich and Prikhod'ko, 1994a):

$$(111)_\gamma // (011)_\alpha,\ [01\bar{1}]_\gamma \approx 2.5°[11\bar{1}]_\alpha \qquad [17.4]$$

The crystallographic behaviour is more complex in alloyed steels containing Cr, Ni, Mo and V. Although the formation of austenite microstructure was according to specific crystallographic orientations, two types of relationships were observed (Televich and Prikhod'ko 1994c): the G-T one and the additional one (Eq. [17.5]):

$$\{211\}_\gamma // \{110\}_\alpha,\ <0\bar{1}1>_\gamma // <\bar{1}12>_\alpha \qquad [17.5]$$

The orientation relationship described by Eq. [17.5] was first reported by Mehl and Smith (1934) in quenched steels and confirmed later in other studies (Gridnev *et al.*, 1980b; Vovk *et al.*, 1987) with respect to the orientation relationships between eutectoid ferrite (in a pearlite colony) and austenite. During heating to the temperatures of the start of reverse transformation, the decomposition of martensite (Gridnev *et al.*, 1979) takes place according to the following reaction:

$$\alpha' \rightarrow \alpha + Fe_3C \qquad [17.6]$$

It was suggested that an OR such as Eq. [17.5] could be associated with the following reaction:

$$\alpha + Fe_3C \rightarrow \gamma \qquad [17.7]$$

However, this OR might also be the product of the reaction: $Fe_3C \rightarrow \gamma$, as direct formation of austenite in cementite was previously observed after laser heating of steels (Lyasotskiy and Shtanskiy, 1991, 1993; Kaluba *et al.*, 1998). However, further work is required to confirm this.

Among the variants of the G-T OR (Eq. [17.4]) the same variants as for plain carbon steel were the dominant ones. No such variant dominance was detected for the second OR of Eq. [17.5]. In steels with quenched bainite microstructure, the realization of OR (Eq. [17.5]) was not observed. It was also found that carbon content is critical for the occurence of this OR.

If, before rapid heating, the martensite is tempered at low temperatures (<300°C, 0.4 wt% C steel) there is no effect on the crystallography of fine grained austenite formation, e.g. the same variants of the ORs are realized as in the case of rapid heating without preliminary tempering (Televich and Prikhod'ko, 1994d). When the tempering takes place at higher temperature (~600°C) the formation of fine austenite grains with new variants of the same G-T OR was observed. These results indicate that the preservation of

© Woodhead Publishing Limited, 2012

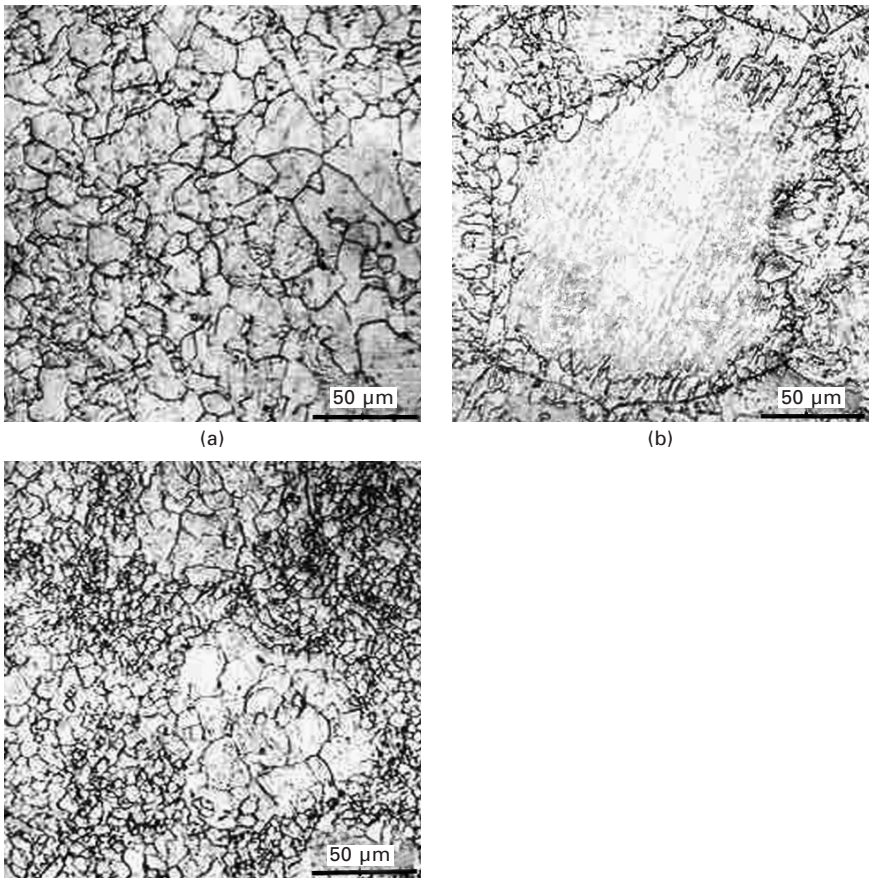
the dislocation structure formed in martensite may be important in order to maintain crystallographic reversibility of the phase transformations, as at both tempering temperatures the shape and boundaries of martensite grains are preserved, whereas the degree of degradation of dislocation substructure is significantly higher at higher tempering temperatures. The decomposition of martensite with formation of ferrite and carbides during high temperature tempering introduces an additional factor (e.g. carbides), which may also be affecting the crystallography of reversed austenite formation. On further heating above A_{c3}, the recrystallization of fine grained austenite microstructure takes place (Televich and Prikhod'ko, 1994b).

17.3.2 Structural inheritance in quenched steels

The restoration of the size, shape and orientation of prior austenite grains is called 'structural heredity', 'structural inheritance' or 'structural memory' and has become the focus of research since the 1970s in two major research centres in the former Soviet Union led by Professors Sadovskii and Gridnev, respectively (Sadovskiy, 1973, 1976; Gridnev, 1978; Gridnev *et al.*, 1980a). However, at fast heating rates the restoration of prior austenite grain microstructure is not complete due to grain boundary effects, e.g. formation of the network of very fine grains along the prior austenite grain boundaries (Fig. 17.6(c)). This grain boundary effect decreases with increase in heating rate (Fig. 17.6(d)). These fine grains, located along boundaries, differ in orientation from the coarse restored austenite grains, and their appearance was originally associated with recrystallization (Umova and Sadovsky, 1977) or random transformation development due to the additional near-boundary lattice distortions (Sadovskii, 1973). However, Televich *et al.* (1993) have shown by *in-situ* rapid XRD studies of $\alpha' \rightarrow \gamma$ transformation in quenched martensitic structural alloy steels that the fine grain boundary austenite is formed according to the crystallographic orientation relationships (Eq. [17.5]).

Alloying elements have influence not only on the grain boundary effect, but on the critical heating rate above which the phenomenon of structural inheritance is observed. In plain carbon steels the structural inheritance takes place at heating rates above 3000–4000 K s^{-1}, whereas the addition of 1 wt% Co to 0.8 wt% C plain carbon steel shifts the critical heating rate to 8000 K s^{-1}. On the other hand, addition of Cr leads to reduction in critical heating rate (Gridnev *et al.*, 1980a). Studies of Fe-3% Cr alloys with various carbon contents also highlighted the role of carbon; the reduction in C content from 0.08 to 0.008% C leads to prevention of the restoration of original austenite grains, even at very rapid heating (>12 000 K s^{-1}), whereas it takes place at 300 K s^{-1} heating rate in the higher carbon alloy (Fig. 17.7; Televich, 1995). If structural steels alloyed with Mo, V and/or Ti are subjected to long

© Woodhead Publishing Limited, 2012



17.7 Effect of carbon content on structural heredity in Fe-3%Cr alloys: (a) 0.08% C, V_H = 50 K s^{-1}; (b) 0.08% C, V_H = 300 K s^{-1}; (c) 0.008% C, V_H = 12 000 K s^{-1}. Courtesy of Dr R.V. Televich, Institute for Metal Physics, National Academy of Sciences, Ukraine.

austenitizing times at temperatures above 1300°C, followed by quenching, they display a structural inheritance at any experimentally achieved heating rate. It could be assumed that the role of these alloying elements, associated with their concentration in solid solution, affects the degree of martensite decomposition during rapid heating and preserves the volumes of unchanged substructure until the start of reverse transformation (Televich, 1995). However, further studies are required to confirm this hypothesis.

17.3.3 Mechanism of structural heredity

Based on the observed restored morphology of austenite, the crystallographic reversibility of the $\alpha \rightarrow \gamma$ transformation was considered. Crystallographically,

© Woodhead Publishing Limited, 2012

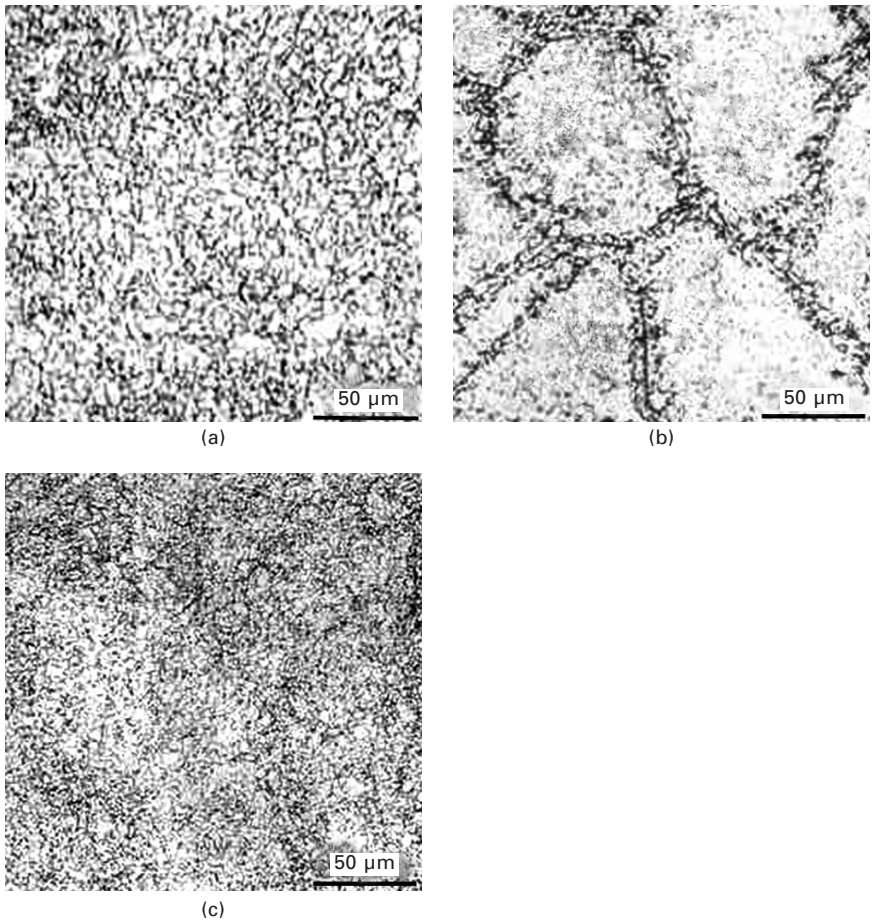
the phenomenon of structural inheritance is a restriction of all possible orientation variants to a single one during the $\alpha \rightarrow \gamma$ transition. Although there are several hypotheses regarding the reasons for this, to date there is no unified and experimentally proven theory. The majority of these hypotheses are based on the assumption that new γ grains grow epitaxially under the influence of the substrate. This substrate may be (i) the retained austenite (Kunz, 1965; Sadovskii, 1976), (ii) the boundaries between martensite crystals (Schastlivtsev and Koptseva, 1976; Sadovskiy, 1984), (iii) the interfaces between the phases (Lipchin, 1969), or (iv) the dislocation structure (Vovk *et al.*, 1987; Gridnev, 1989; Televich, 1995). In the majority of situations all or some of the microstructural features listed above are present simultaneously, thus making it difficult to exclude their competitive influence from consideration.

Although based on the assumption that the dislocation substructure formed in each martensite crystal may be associated with its orientation variant, it was suggested (Gridnev, 1989; Televich, 1995) that, out of all factors, the dislocation substructure plays the dominant role in the formation of restored austenite microstructure. This approach is similar to that suggested for the case of heterogeneous nucleation on dislocations during diffusional phase transformation and precipitation reactions, when effective accommodation of the transformation strain by the strain field of dislocations occurs, leading to the variant selection in which the direction of the maximum misfit is nearly parallel to the Burgers vector of the dislocations (Furuhara and Maki, 2001). Indirect support for this hypothesis was obtained by investigating the effects of conditions under which $\alpha \rightarrow \gamma \rightarrow \alpha$ and $\gamma \rightarrow \alpha \rightarrow \gamma$ phase transformations occurred in austenite structural memory (Umova and Sadovsky, 1977; Vovk *et al.*, 1987; Televich *et al.*, 1994).

Deformation of martensite before rapid heating (<15%) delays the structural heredity effect until higher heating rates (>21 000 Ks^{-1}, see Figs 17.8(a) and (b)). With increase in degree of deformation to 30%, no restoration of prior austenite microstructure is achieved at a heating rate of 21 000 K s^{-1} (Fig. 17.8(c)). The formation of fine grained austenite microstructure in steels deformed after quenching is associated with realization of many crystallographic variants of OR in a martensite packet instead of a single one (Televich, 1995).

Whereas short rapid tempering of martensite or tempering at low temperatures in various steels did not affect the subsequent restoration of prior austenite microstructure on rapid heating (Fig. 17.9), longer tempering times and/or higher tempering temperatures or slow heating rates (<300 K s^{-1}) led to the formation of fine grained austenite microstructure (Gridnev *et al.*, 1979; Televich *et al.*, 1994). Thus, different degrees of degradation in the original dislocation substructure, resulting from either applied deformation or tempering delays, could eliminate completely the structural heredity in

© Woodhead Publishing Limited, 2012

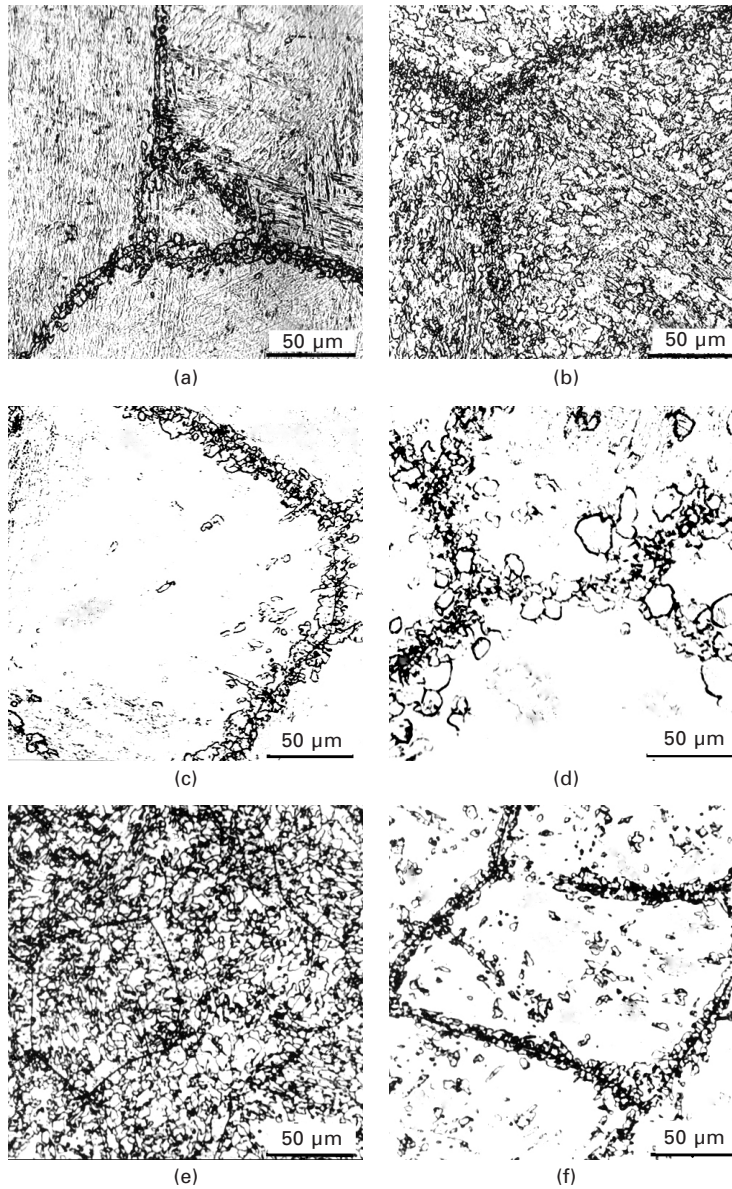


17.8 Effect of cold deformation on the structural memory in 0.11C-1.0Cr-3.5Ni-0.6 Mn-0.05V (wt%) alloy steel: (a) 0.15ε, heating rate 3000 K s^{-1}; (b) 0.15ε, heating rate 21 000 K s^{-1} and (c) 0.3ε, heating rate 21 000 K s^{-1}. Courtesy of Dr R.V. Televich, Institute for Metal Physics, National Academy of Sciences, Ukraine.

the range of heating rates studied (up to 50 000 Ks^{-1}) (Gridnev *et al.*, 1979; Televich *et al.*, 1994).

These findings showed that the presence of retained austenite is not necessary for the phenomenon of structural heredity, as retained austenite generally decomposes during long tempering times at around 250°C, while the restoration of prior austenite microstructure is still achieved at increased heating rates. Although it was stipulated that preservation of the microstructure similar to that existing in martensite after tempering below 200–250°C at the start of reverse phase transformation is a necessary condition for structural

© Woodhead Publishing Limited, 2012



17.9 Effect of tempering on structural heredity in 0.35C-0.5Mn-0.25Si-3Ni-0.4Mo-1.2Cr-0.1V-0.02S-0.02P (wt%) steel: rapid tempering at heating rate of 120 K s^{-1} to 390°C (a) and 530°C (b) followed by quenching and rapid heating at 4500 K s^{-1} above A_{c3}; rapid tempering at 2500 K s^{-1} at 400°C (c) and 660°C (d) followed by rapid heating at 4500 K s^{-1} above A_{c3}; 1 h tempering at 250°C followed by rapid heating at 350 K s^{-1} (e) and 4400 K s^{-1} (f). Courtesy of Dr R.V. Televich, Institute for Metal Physics, National Academy of Sciences, Ukraine.

© Woodhead Publishing Limited, 2012

inheritance (Sadovskii, 1973), the restoration of prior austenite microstructure was observed even after rapid heating of completely decomposed martensite into a ferrite/carbide mixture (Gridnev *et al.*, 1979). This is associated with the presence, even in decomposed microstructure, of micro-volumes of incompletely decomposed martensite associated with carbon enrichment at dislocations. Such micro-inhomogeneities could satisfy the conditions for metastable martensite phase and have a pronounced effect both on the kinetics and crystallography of austenite formation. Thus, the necessary conditions for structural heredity is conservation, even in micro-volumes, of the dislocation structure associated with the crystallographic variant of martensite formation and a critical concentration of carbon (Gridnev *et al.*, 1979; Televich *et al.*, 1994; Televich, 1995).

17.4 Effect of rapid heating on mechanical properties of steels and its applications

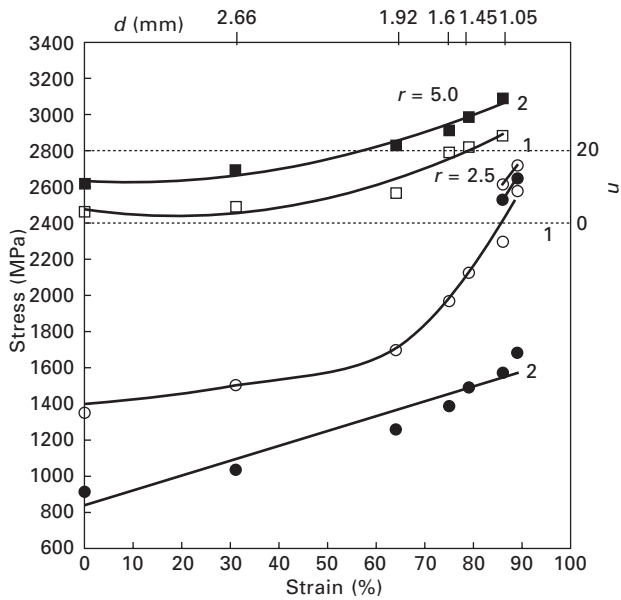
As a result of the peculiarities of austenite formation on rapid heating discussed above (e.g. very fast formation of the appropriate morphology and compositional state of austenite), a unique microstructural state is formed in the steel. The formation of fine grained austenite with uniform grain size after quenching and rapid annealing allows the realization of a very advantageous combination of mechanical properties in finished products: 30–40% higher strength and 10–20% higher ductility and impact toughness are achieved compared to those of steel produced by traditional processing (Lerinman and Sadovsky, 1951; Gridnev and Meshkov, 1961). For example, after rapid heat treatment the ultimate tensile strength of 0.8% C steel has increased from 1100 MPa to 1500 MPa whereas elongation of 10% was maintained. The difference between strength and fracture strength determines the ductility reserve of metals. On this basis, a powerful technological trend in metallurgy and manufacturing, so-called high-rate electro-thermal treatment process (HRETTP), quickly found implementation in the Soviet Union in the 1960s (Gridnev *et al.*, 1973, 1977). The HRETTP method involved: (i) fast contact electro-resistivity heating of a wire blank of 5–6 mm diameter during the drawing process followed by quenching using a water spray, (ii) rapid tempering at 550–600°C again using electro-resistivity heating and (iii) subsequent cold drawing of the wire to the finished product, such as cold-drawn wire for cables, springs or reinforcement, with upgraded service properties. Rapid tempering also produces a unique microstructure containing fine-grained ferrite/cementite mixtures due to rapid decomposition of martensite with the prevention of coagulation and coarsening of cementite, which takes place during traditional isothermal tempering in furnaces or salt baths. Moreover, in the case of rapid tempering, the crystallographic order in the orientation of fine carbide precipitates is retained (Gridnev and Petrov, 1968), which

© Woodhead Publishing Limited, 2012

enables cold drawing of wire to high reduction ratios. Another advantage of rapid tempering is prevention of alloying element segregation typically occurring during long traditional tempering treatments and leading to temper embrittlement (Meshkov *et al.*, 1994). Figure 17.10 shows a comparison of the properties of a wire blank and drawn wire of 0.5% C steel with those of wire made by the standard patenting technology. However, application of the HRETTP method resulted not only in the improvement in properties of steels with pearlite microstructures suitable for patenting. It allowed the manufacturing of steel cable wire from steels unsuitable for patenting, i.e. low carbon 0.3% C steel instead of eutectoid steel. Such steel had the same strength and improved ductility, which led to increased cable life (Gridnev *et al.*, 1977).

Heat treatment of automotive parts is generally performed by induction heating and electrical resistivity tempering to improve surface properties (Gridnev *et al.*, 1973). Application of rapid heating to produce refined microstructure and improved mechanical properties is discussed in more detail elsewhere (Gridnev *et al.*, 1973; Ivasishin and Teliovich, 1999; Teliovich *et al.*, 1999).

Thus, the understanding of martensite decomposition and specific features



17.10 Change in the properties of cold-drawn wire of steel 50 with increase in draw reduction: ■, □ ultimate tensile strength, σ; ○, ● bending ductility (*n* is a number of reverse bending on cylindrical support of 5 mm radius); 1 (□, ○) after rapid tempering at 550°C, V_H = 850 Ks^{-1}; 2 (■, ●) after patenting; *d* is wire diameter.

© Woodhead Publishing Limited, 2012

of the kinetics and mechanisms of phase transformation in steels at high heating rates allowed a promising new technology for steel strengthening, HRETTP, to be developed. This technology possesses many technical and economic advantages over traditional heat treatments. However, social and economic problems in the Soviet Union and then in the countries of the former Soviet Union did not permit the potential of this new technology to be realized in full. Recently, this processing route has gained attention again (Lefevre-Schlick *et al.*, 2008). Furthermore, it has been proposed that nanocrystalline microstructure could be achieved under high current density electropulsing (Zhou *et al.*, 2002). This could lead to further applications in this area.

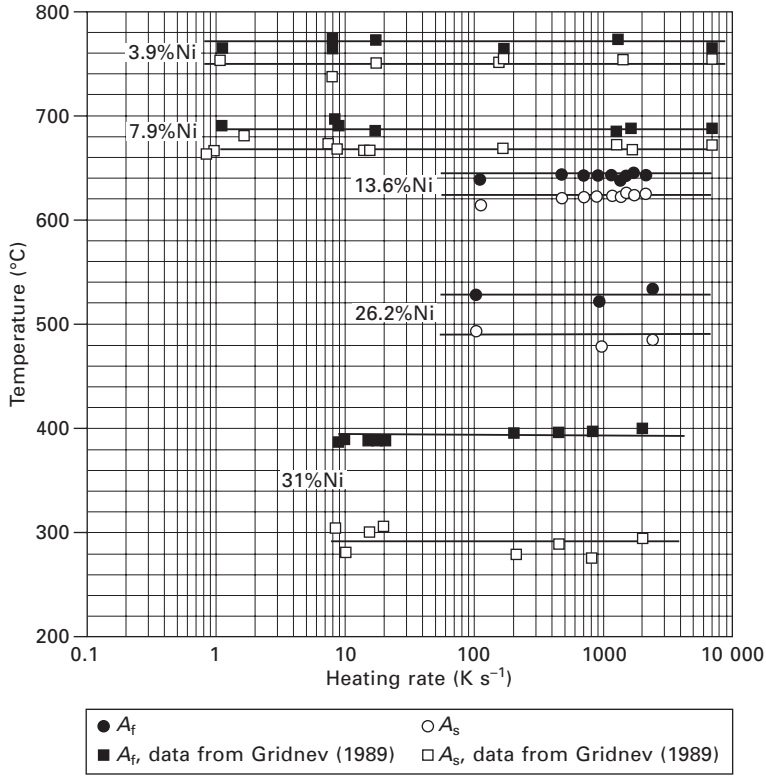
17.5 Effect of heating rate on the reverse austenite transformation in Fe-Ni-based alloys

17.5.1 Mechanism and kinetics

The possibility of reversibility of phase transformation in Fe-Ni alloys was demonstrated nearly 80 years ago (Wassermann, 1932/33; Gridnev, 1941). The possibility of diffusionless formation of austenite on heating at 2.5 K s^{-1} was suggested for the first time for Fe-Ni alloys containing 10, 15 and 23% Ni by Gridnev in 1941. Since then, extensive research on the effect of heating rates revealed that, contrary to the behaviour of Fe-C-based alloys, the start and finish temperatures of austenite formation in binary Fe-Ni alloys are independent of heating rate within the range from ~1 K s^{-1} to 8000 K s^{-1} (Krauss and Cohen, 1962; Kessler and Pitsch, 1967; Gridnev 1978, 1989; Servant and Lacombe, 1977; Sagaradze *et al.*, 2002). Such temperature independent behaviour (Fig. 17.11), similar to that of non-ferrous materials, indicates the diffussionless mechanism of $\alpha' \rightarrow \gamma$ transformation without significant concentration rearrangements within the martensite before the start of the transformation. Being a substitutional element, the diffusion of nickel is much more sluggish in comparison to carbon, and is even slower under conditions of accelerated or rapid heating.

The decomposition of Fe-Ni solid solutions, with formation of Ni-rich and Ni-depleted regions, takes place during slow heating or isothermal ageing (Zel'dovich and Sadovsky, 1968; Sagaradze and Shabashov, 1984) as well as with addition of various alloying elements or carbon. Thus, in binary Fe-Ni alloys containing less than 12% Ni, the mechanism of reverse transformation is diffusional or massive, depending on the conditions of slow heating, leading to the decomposition of martensite (Golovchiner, 1951; Kardonskiy and Roschina, 1978; Allen and Earley, 1950). In Fe-Ni alloys containing 15–27% Ni the reverse transformation is diffusion controlled at slow heating rates, whereas at intermediate heating rates the process exhibits two steps: (i) at

© Woodhead Publishing Limited, 2012



17.11 Effect of heating rate on reverse transformation temperatures in quenched Fe-Ni alloys. A_s = austenite formation start temperature; A_f = austenite formation finish temperature.

low temperatures (~300–400°C) γ-phase is formed according to a displacive mechanism and (ii) with subsequent heating to higher temperatures the redistribution of Ni between phases takes place leading to stabilization of untransformed martensite and reverse transformation is completed at a later stage by a diffusion-controlled mechanism. Finally, in binary Fe-Ni alloys with Ni content above 15%, the reverse transformation at rapid heating is diffusionless (Golovchiner, 1951; Kardonskiy and Roschina, 1978; Kessler and Pitsch, 1967). In Fe-Ni alloys containing above 30% Ni the displacive mechanism of reverse transformation is realized even at heating with rates just faster than 0.15 K s^{-1} (Gilbert and Owen, 1962; Apple and Krauss, 1972; Gridnev, 1978; Sagaradze *et al.*, 2002). In Fe-Ni-C alloys at carbon contents exceeding 0.05% C, the mechanism of $\alpha' \rightarrow \gamma$ transformation is diffusional; however, at low carbon content (~0.004 wt%) and very high heating rates (above 1500 K s^{-1}) it changes to diffusionless (Apple and Krauss, 1972).

Depending on the level of supersaturation of solid solution, the nature of

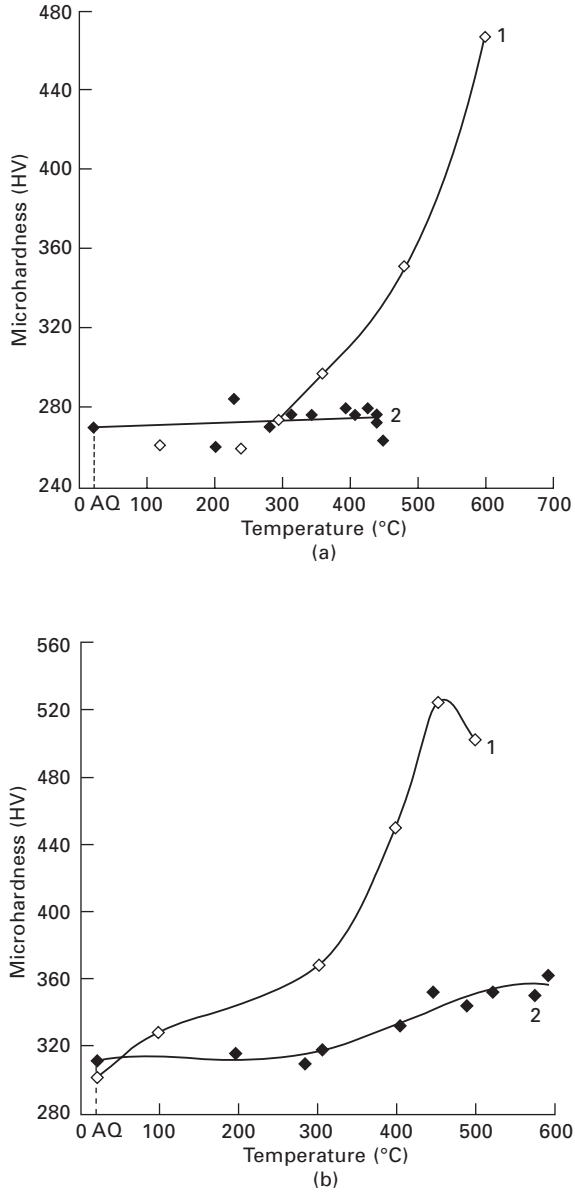
© Woodhead Publishing Limited, 2012

alloying elements and heating conditions, there are two possible scenarios for the reverse transformation in Fe-Ni-based maraging alloys. In the first one, at accelerated heating rates, but slow enough for short-range diffusion of substitutional elements to take place, the decomposition of martensite with formation of clusters or precipitates takes place followed by the transformation to austenite. For details on precipitation behaviour during ageing of maraging steels, readers are referred to Chapter 11 in Volume 2 of this publication. Hardness measurements, transmission electron microscopy, Mössbauer spectroscopy, dilatometry and atom probe tomography (Goldberg and O'Connor, 1967; Emchenko-Rybko *et al.*, 1985a, 1985b; Gavrilyuk *et al.*, 1990; Kapoor and Batra, 2004; Pereloma *et al.*, 2004; Shekhter *et al.*, 2004) indicated alloying element redistribution before the start of reverse transformation to austenite at heating rates at or below 100 K s^{-1} for a variety of maraging alloys (Figs 17.12 and 17.13). At higher heating rates the decomposition of martensite is generally suppressed, but this is not the case for the Fe-Ni alloys containing a significant amount of Mn (4–7%) in addition to Ti, although the extent of the martensite decomposition was reduced and the ageing behaviour was slightly retarded under very rapid heating conditions (>1000 K s^{-1}) (Figs 17.12(b), (c) and 17.13(b)).

In all of these situations the formation of austenite starts in martensite regions depleted by Ti, Ni, Mn and other alloying elements forming clusters or intermetallics. This correlates with high temperatures of reverse transformation at accelerated heating rates and even rises in these temperatures with increase in heating rate for maraging alloys containing high amounts of Mn in addition to Ti and Al (Fig. 17.14). This tendency, which is similar to that observed for Fe-C-based alloys and steels, is a clear indication of the diffusional component of reverse transformation. The diffusional events corresponding to the decomposition of martensite and precipitation could either take place before the start of diffusionless reverse transformation or also proceed during the reverse transformation. In both cases they affect the start temperature of reverse transformation due to the various degrees of martensite depletion in micro-volumes. Although it has been suggested earlier that displacive transformation of the α lattice into the γ lattice could be accompanied by the exchange of alloying elements at the interface (Zel'dovich and Sadovskiy, 1972), studies by Kapoor and Batra (2004) indicate that at slow heating rates (<6 K s^{-1}), the reverse transformation occurs by a diffusional mechanism.

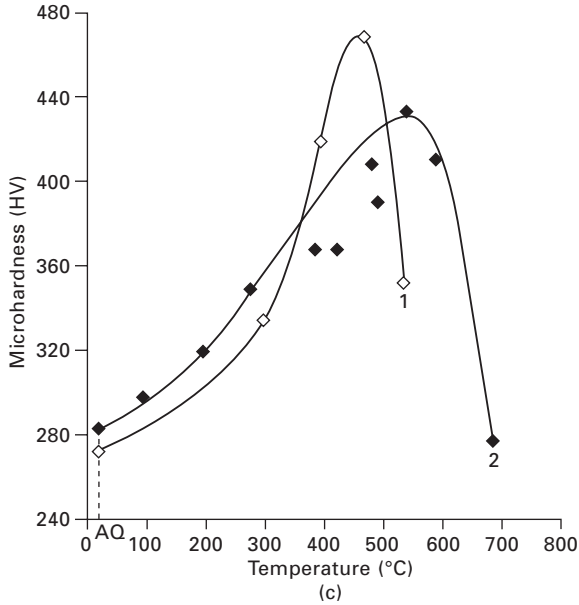
Reduction in reverse transformation temperatures with increase of heating rates above 100 K s^{-1}, eventually plateauing (Figs 17.14(a) and 17.15), indicates a change in the mechanism of reverse transformation, as the stability of transformation temperatures in the range of heating rates is evidence for a displacive mechanism. Depending on the steel composition, there is a critical heating rate above which the decomposition of martensite is suppressed and formation of austenite takes place by shear (Fig. 17.14; Emchenko-Rybko *et*

© Woodhead Publishing Limited, 2012



17.12 Effect of heating rate on microhardness of martensite quenched from various temperatures before the start of reverse transformation: (a) Fe-28%Ni-2%Ti, (b) Fe-21%Ni-1.7%Ti-1%A-0.16%Mn and (c) Fe-16.2Ni-3.7%Mn-1.9%Ti-15Al. Curves 1 (◇), heating rate 1 K s^{-1} and 2(◆) are 1500 K s^{-1} in (a) and 1300 K s^{-1} in (b, c). Adapted from Emchenko-Rybko *et al.* (1985a, 1985b).

© Woodhead Publishing Limited, 2012



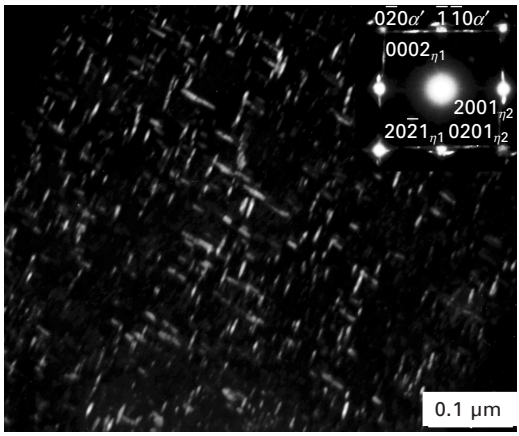
17.12 Continued

al., 1985a, 1985b). For Fe-18%Ni-9%Co-5%Mo, heating rates just above 17 K s^{-1} result in a displacive mechanism of reverse transformation (Thevenin *et al*., 1971), whereas for 300 grade maraging steel this rate is 40 K s^{-1} (Goldberg and O'Connor, 1967). However, for some maraging alloys this critical heating rate is above 3000 K s^{-1}. The activation energies of 248 and 904 kJ mol^{-1} obtained by Kapoor and Batra (2004), for the reverse transformation process in maraging steels also indicate that at slow and fast heating rates, the mechanism is diffusion controlled and displacive shear, respectively.

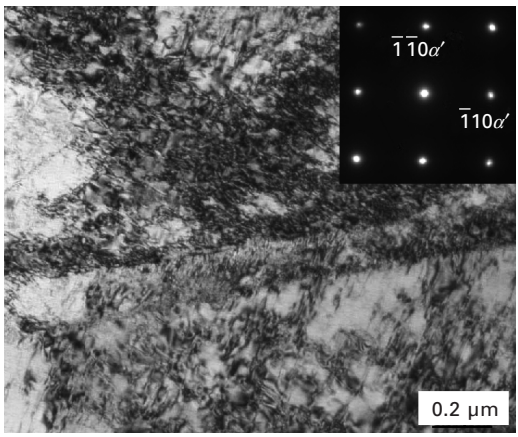
17.5.2 Austenite morphology in Fe-Ni-based alloys

At accelerated heating with rates exceeding the critical rate for a particular composition (for Fe-23%Ni, V_H = 5 K s^{-1}, whereas for Fe-32%Ni V_H is ~7 × 10^{-3} K s^{-1}), the formation of relatively coarse, plate-like austenite is observed. These plates start to form at martensite lath boundaries and interfaces with retained austenite. Similar to Fe-C alloys, the restoration of prior austenite morphology, size and orientation is observed in Fe-Ni alloys at these conditions (Wassermann, 1932/33; Grewen and Wassermann, 1961; Zel'dovich *et al*., 1977; Sagaradze *et al*., 2002). However, some austenite crystals of twin orientations were also observed (Krauss and Cohen, 1962). This structural memory of austenite also indicates that the reverse transformation follows

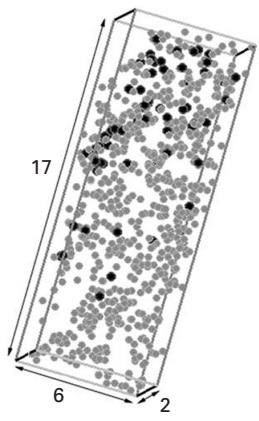
© Woodhead Publishing Limited, 2012



(a)



(b)



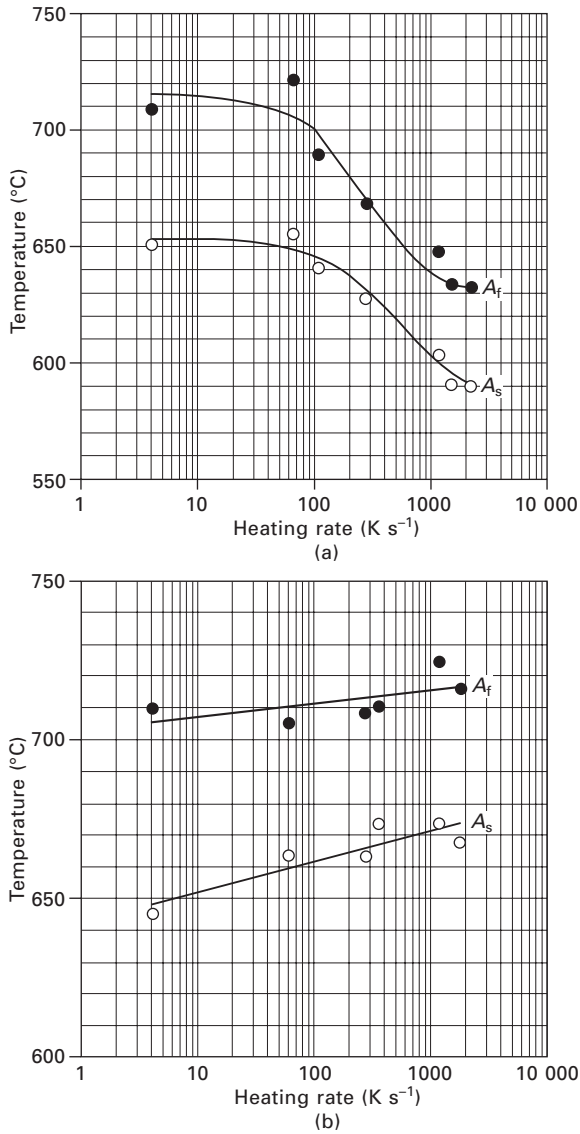
(c)

17.13 TEM micrographs of Fe-27.4%Ni-1.94%Ti alloy heated at 1 K s^{-1} to 580°C (a) and at 1500 K s^{-1} to 410°C (b) with corresponding selected area diffraction patterns. Formation of η-phase Ni_3Ti precipitates with zone axis $\mathbf{g}(0001)_\eta$ // $[001]_{\alpha'}$ visible in (a) and is suppressed in (b). Zone axis is $[001]_{\alpha'}$ in inset (b). Atom map in (c) shows cluster formation after heating of Fe-25.3%Ni-1.7%Ti-0.1%Al alloy at ~150 K s^{-1} to 550°C and 5 s hold. Grey are Ni atoms and black are Ti atoms. Dimensions of the box are in nm. Part (c) is reprinted from A. Shekhter *et al.* (2004), copyright © 2004, with permission from Springer.

© Woodhead Publishing Limited, 2012

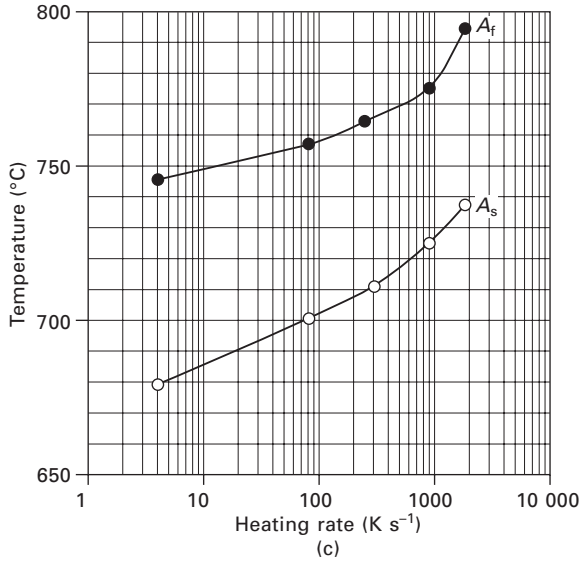
the same crystallographically ordered phase transition as a direct $\gamma \rightarrow \alpha$ transformation (Sorokin, 1966; Sagaradze and Sorokin, 1976).

Finely dispersed, so-called γ-martensite, in the form of laths oriented in many directions, is produced after reverse transformation at very slow



17.14 Reverse transformation start (A_s) and finish (A_f) temperatures of austenite as a function of heating rates for (a) Fe-21%Ni-1.7%Ti-1%A-0.16%Mn, (b) Fe-16.2%Ni-3.7%Mn-1.9%Ti-1%Al and (c) Fe-13.6%Ni-7.05%Mn-1.95%Ti-1%Al. Adapted from Emchenko-Rybko *et al.* (1985a).

© Woodhead Publishing Limited, 2012



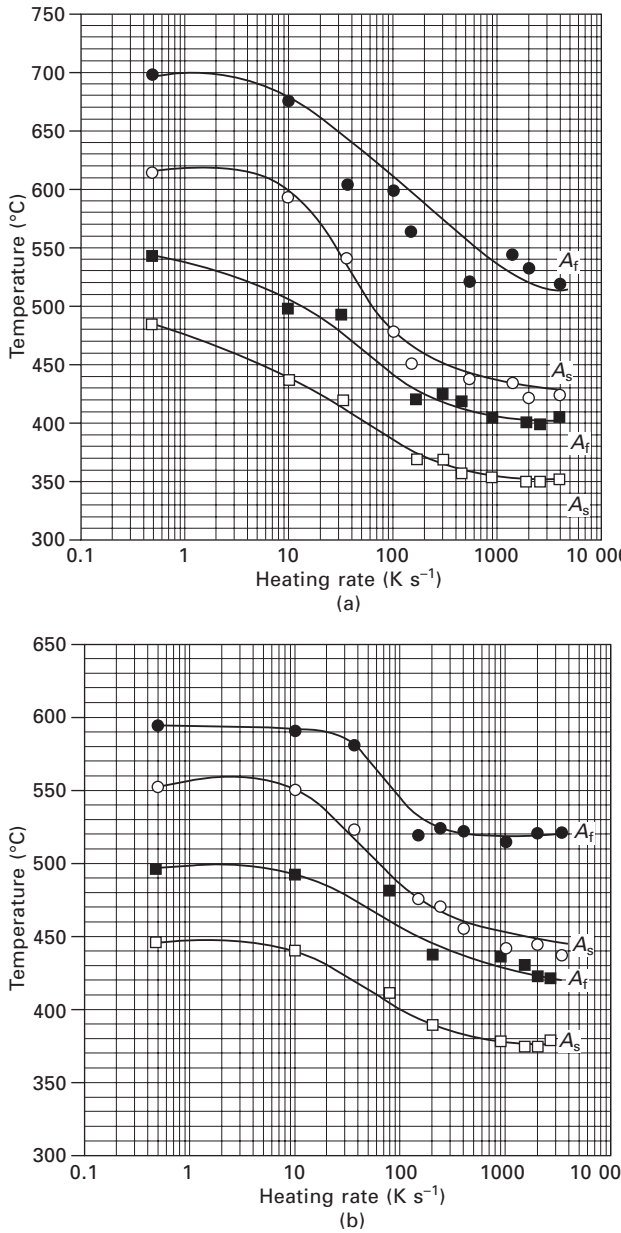
17.14 Continued

heating rates (Krauss and Cohen, 1962; Sagaradze *et al.*, 1974, 1975). These fine γ-laths are enriched in Ni, which leads to Ni depletion in the surrounding untransformed martensite (Sagaradze and Shabashov, 1984) and inhibition of nucleation and growth of γ-phase crystals on retained austenite as substrate. This results in significant grain refinement and steel strengthening, especially in the case of $\gamma \rightarrow \alpha' \rightarrow \gamma$ transformation cycling (Krauss and Cohen, 1962; Sagaradze and Kabanova, 1999; Sagaradze *et al.*, 2002). Finally, at higher temperature, within the reverse transformation interval at slow heating, the formation of globular austenite takes place both in remaining untransformed martensite, and newly formed austenite which could be related to a recrystallization process (Krauss and Cohen, 1962; Singh and Wayman, 1986; Sagaradze *et al.*, 1974, 1975). The observed habit planes in reversed γ crystals of many alloys did not differ much (close to/within 10° $\{110\}_\alpha$) and were close to the orientation of the α/γ interface (Sagaradze and Vaseva, 1976; Southwick and Honeycombe, 1980; Kabanova and Sagaradze, 1980). This, and the observation of the reverse movement of the α/γ interface during heating (Kajiwara and Kikuchi, 1983), provide additional support to the diffusionless mechanism of reverse transformations in Fe-Ni based alloys.

17.5.3 Structural heredity in Fe-Ni-based alloys

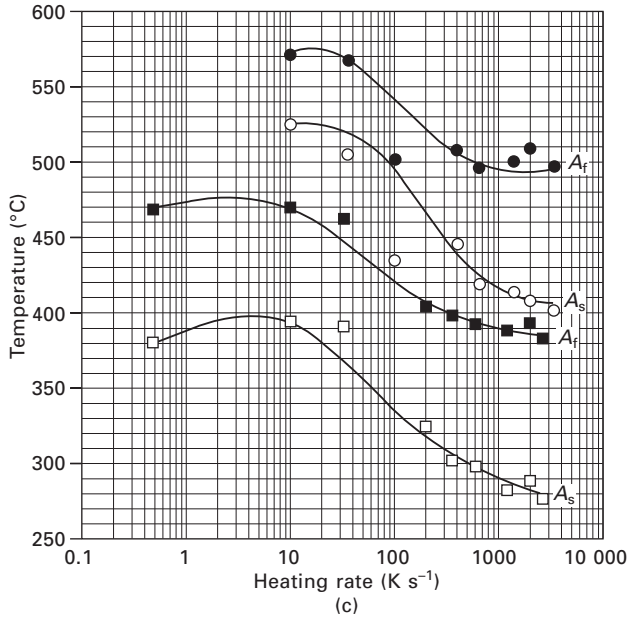
Similar suggestions to those for Fe-C alloys regarding microstructural factors, which are responsible for the structural inheritance phenomenon, have been put forward:

© Woodhead Publishing Limited, 2012

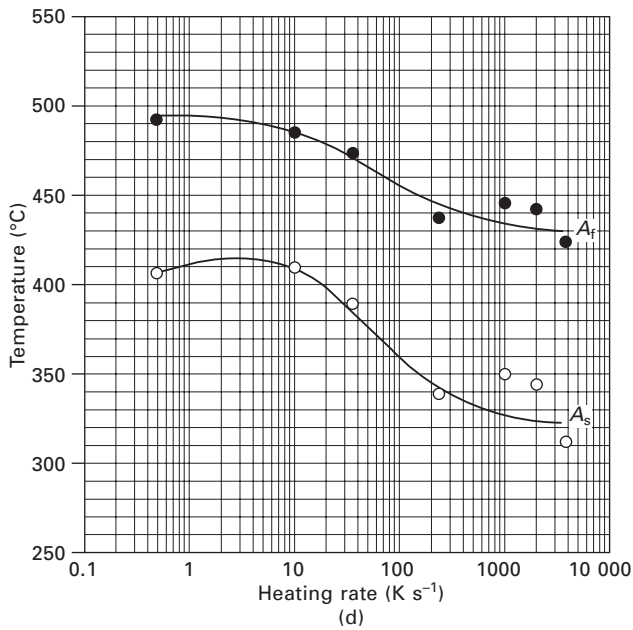


17.15 $\alpha' \rightarrow \gamma$ transformation start and finish temperatures as a function of heating rate in (a) Fe-27.4%Ni-1.94%Ti (○, ●) and Fe-26.1Ni-1.94%V (□, ■); (b) Fe-29%Ni-2%Al (○, ●) and Fe-24.4%Ni-1.45%Mn (□, ■); (c) Fe-28%Ni-2%Si (○, ●) and Fe-28.1%Ni-1.96%W (□, ■); (d) Fe-26.9%Ni-3.74%Mo. A_s-austenite formation start temperature; A_f – austenite formation finish temperature. Adapted from Emchenko-Rybko *et al*. (1985b).

© Woodhead Publishing Limited, 2012



(c)



(d)

17.15 Continued

- the epitaxial influence of retained austenite (Wassermann, 1932/33; Grewen and Wassermann, 1961) or interfaces between the martensite crystals or twins (Sorokin and Sagaradze, 1978; Sagaradze *et al*., 1975; Singh and Wayman, 1986; Schastlivtsev and Koptseva, 1976);

© Woodhead Publishing Limited, 2012

- intermetallic particles inherited from the austenite (Kokorin *et al.*, 1986);
- the contribution of carbides formed during tempering to the variant selection (Webser and Allen, 1962) and
- internal stresses in martensite resulting from the shear mechanism of its formation (Sorokin, 1966).

However, restoration of the prior austenite morphology has been observed without any presence of retained austenite (Schastlivtsev *et al.*, 1986) and the formation of γ-crystals on martensite lath boundaries or twin boundaries would lead only to the restriction of the possible austenite orientations to six according to the K-S OR (Schastlivtsev *et al.*, 1986), or to two for the G-T OR if realized (Sorokin and Sagaradze, 1978). Structural inheritance was observed in quenched Fe-32%Ni and Fe-26%Ni-Cr-Ti alloys heated at 2 K s^{-1}, whereas ~10% tensile deformation before heating led to the formation of austenite crystals with different crystallographic variants of both K-S and G-T ORs (Emchenko-Rybko *et al.*, 1988). In addition, a detailed analysis of these crystallographic variants showed no evidence of the effect of either martensite or twin boundaries on variant selection. It is well known that small amounts of plastic deformation do not affect the boundary structure, but can induce some changes in martensite substructure. This led to the suggestion that the dislocation substructure related to a particular crystallographic variant of martensite plays an important role in austenite variant selection and structural memory (Emchenko-Rybko *et al.*, 1988; Gridnev, 1989).

Nevertheless, the same difficulty of conducting *in-situ* investigations of high temperature phase formation and the inability to separate completely the individual effects of the factors listed above, result in issues of structural inheritance remaining unresolved.

17.6 Conclusions

Although a significant body of knowledge exists in regard to the kinetics and mechanisms of reverse austenite formation, several unanswered questions remain. In particular, the hierarchy of the microstructural factors affecting structural heredity and crystallographic variant selection in both Fe-C and Fe-Ni-based alloy needs clarification, as well as whether the mechanism changes from diffusional to displacive in Fe-C alloys at ultrahigh heating rates (>30 000 K s^{-1}). With advances in *in-situ* experimental techniques, both in process simulations and materials characterization, it might be possible now to elucidate the state of martensite or ferrite/carbide mixtures before the start of reverse transformation during rapid heating and how its changes affect the formation of austenite.

Whereas the current research efforts to produce ultrafine grained steels in order to improve strength are focused mainly on utilization of various

© Woodhead Publishing Limited, 2012

severe plastic deformation techniques, the benefits of rapid annealing and $\gamma \rightarrow \alpha \rightarrow \gamma$ cycling to improve the mechanical properties of steels by refining the microstructure have been clearly shown. Despite a significant slowdown in research carried out in this area since the 1990s, as can be seen from this overview, there is still scope for work to be done both on fundamental and applied aspects of reverse austenite formation during rapid heating.

17.7 References

Aaronson H I and Nie F G (2000), 'Discussion to "The Bainitic Mechanism of Austenite Formation during Rapid Heating"', *Scripta Mater.*, 42, 505–509.

Allen N P and Earley C C (1950), 'The Transformations $\alpha \rightarrow \gamma$ and $\gamma \rightarrow \alpha$ in Iron-Rich Binary Iron-Nickel Aloys', *J. Iron Seel Inst.*, 166, 281–288.

Apple C A and Krauss G (1972), 'The Effect of Heating Rate on the Martensite to Austenite Transformation in Fe-Ni-C Alloys', *Acta Metall.*, 20, 849–856.

Christian J W (1997), 'Lattice correspondence, atomic site correspondence and shape change in "diffusional-displacive" phase transformations', *Prog. Mater. Sci.*, 42, 101–108.

D'yachenko S S (1982), *Austenite Formation in Iron-Carbon Alloys*, Metallurgia, Moscow, (in Russian).

Emchenko-Rybko E V, Oshkaderov S P and Televich R V (1985a), 'Reverse Martensitic Transformations in Rapidly Heated Aging Iron-Nickel Alloys', *Phys. Metals*, 5(6), 1119–1125.

Emchenko-Rybko E V, Oshkaderov S P, Televich R V and Ziss G (1985b), 'The Effect of Manganese on the Stability of Martensite in Rapidly Heated Maraging Steels', *Phys. Metals*, 6(3), 495–502.

Emchenko-Rybko E V, Oshkaderov S P and Televich R V (1988), 'Effect of Deformation of Martensite on the Orientation of γ-Phase on Heating of Fe-Ni Alloys', *Metalofizika*, 10, 77–80 (in Russian).

Furuhara T and Maki T (2001), 'Variant Selection in Heterogeneous Nucleation on Defects in Diffusional Phase Transformation and Precipitation', *Mater. Sci. Eng.*, A312, 145–154.

Gavrilyuk V G, Emchenko-Rybko E V, Nadutov V M, Oshkaderov S P and Televich R V (1990), 'Alloying-Element Redistribution in Fast Heating for Quenched Martensite-Ageing Steels Containing Mn', *Phys. Metals*, 9(2), 191–198.

Gilbert W and Owen W S (1962), 'Diffusionless Transformation in Iron-Nickel, Iron-Chromium and Iron-Silicon Alloys', *Acta Mater.*, 10, 45–54.

Goldberg A and O'Connor D G (1967), 'Influence of Heating Rate on Transformations in an 18 per cent Nickel Maraging Steel', *Nature*, 213, 170–172.

Golovchiner Ya M (1951), 'Investigation of "Reversible" Transformations in Iron-Nickel Alloys', *Prob. Metallogr. Phys. Met.*, 2, 119–128 (in Russian).

Grewen J and Wassermann G (1961), 'Einfluβ von Umwandlung und Rekristallisation auf die Textur von Drähten aus seiner Eisen-Nickel-Ligierung mit 20% Ni', *Arch. Eisenhüttettenw*, 32, 863–866.

Gridnev V N (1941), 'Diffusionless Transformations in Iron-Nickel Alloys', *J. Theor. Physics*, 11, 1226–1231 (in Russian).

Gridnev V N (1948), 'Phase and Concentration Changes during Heating of Steels', in

© Woodhead Publishing Limited, 2012

Jubilee Procedings of Kiev Politechnical Institute (1898–1948), Kiev, KPI, 41–79 (in Russian).

Gridnev V N (1967), 'Kinetics and Mechanisms of Phase and Structural Changes under Continuous Electric Heating of Carbon Steels', *Ukranian Physics Journal*, XII(10), 1608–1817.

Gridnev V N (1978), 'Mechanism and Kinetics of Phase Transformations under Rapid Heating', *in Proc. Int. Conf. on Martensitic Transformations*, *ICOMAT-77*, Naukova Dumka, Kiev, USSR, 246–251 (in Russian).

Gridnev V N (1989), 'Evolution and Modern Ideas of Martensitic Transformations Reversibility', *Sov. Sci. Rev. A. Phys.*, 10, 133–165.

Gridnev V N and Kocherzinsky Yu A (1953), 'Dilatometer for Investigations of Transformation during Electro-heating', *Zavodskaya Laboratory*, 19, 493–494 (in Russian).

Gridnev V N and Meshkov Y Y (1961), 'Electro-tempering of Cr-containing Steel', *Metallovedenie i Termicheskaya Obrabotka Metallov*, 6, 2–4 (in Russian).

Gridnev V N and Petrov Yu N (1968), 'Possible Mechanisms of Carbide Formation during the Tempering of High Carbon Steels', *Izv. AN SSSR*, *Metally*, 1, 138–141 (in Russian).

Gridnev V N, Meshkov Yu Ya and Oshkaderov S P (1964a), 'Austenite Transformation Point in Rapidly Heated Steel and Iron', *Phys. Met. Metall.*, 18, 135–136.

Gridnev V N, Minakov V N and Trefilov V I (1964b), 'On the Mechanism of Austenite Formation on Rapid Heating', *Voprosy Fiziky Metallov i Metallovedenia*, 18, 107–114 (in Russian).

Gridnev V N, Gavrillyuk V G, Meshkov Yu Ya and Oshkaderov S P (1965a), 'On the Formation of Austenite during Electro-Heating of Hypoeutectoid Steels', in *Phase Transformations in Metals and Alloys*', Naukova Dumka, Kiev, USSR, 69–71 (in Russian).

Gridnev V N, Meshkov Yu Ya and Oshkaderov S P (1965b), 'Magnitometer for Investigation of Transformations during Ultra-rapid Heating', *Machiny i Pribory dlya Ispytania Metalov I Platmass (Devices and Equipment to Study Metals and Plastics*), Mashgiz, Moscow, 87–89 (in Russian).

Gridnev V N, Meshkov Yu Ya, Oshkaderov S P and Trefilov V I (1973), *Physical Principles of Electo-Thermal Strengthening of Steels*, Naukova Dumka, Kiev (in Russian).

Gridnev V N, Meshkov Yu Ya, S.P. Oshkaderov S P and Chernenko N F (1977), *Technological Principles of the Electro-Thermal Treatment of Steels*, Naukova Dumka, Kiev (in Russian).

Gridnev V N, Oshkaderov S P and Televich R V (1979), 'Formation of Austenite in Overheated Quenched Structural Steels', *Metallofizika*, 1, 92–100 (in Russian).

Gridnev V N, Oshkaderov S P and Televich R V (1980a), 'On Recovery of the Austenite Grain during Rapid Heating of Quenched Carbon Steels', *Phys. Met. Metall.* 49, 200–202.

Gridnev V N, Vovk Ya N, Oshkaderov S P and Televich R V (1980b), 'On the Orientation of Ferrite in Pearlite Relative to Austenite', *Phys. Met. Metall.*, 49, 190–193.

Hillert M (2000), 'Comments on "The Bainite Mechanism of Austenite Formation during Rapid Heating"', *Scripta Mater.*, 43, 1045–1046.

Hono K, Ohnuma M, Murayama M, Nishida S, Yoshie A and Takahashi T (2001), 'Cementite Decomposition in Heavily Drawn Pearlite Steel Wire', *Scripta Mater.*, 44, 977–983.

Ivanisenko Y, Lojkowski W, Valiev R Z and Fecht H-J (2003), 'The Mechanism of

© Woodhead Publishing Limited, 2012

Formation of Nanostructure and Dissolution of Cementite in a Pearlitic Steel during High Pressure Torsion', *Acta Mater.*, 51, 5555–5570.

Ivanisenko Y, MacLaren I, Sauvage X, Valiev R Z and Fecht H-J (2006), 'Shear-Induced $\alpha \rightarrow \gamma$ Transformation in Nanoscale Fe–C Composite', *Acta Mater.*, 54 1659–1669.

Ivasishin O M and Teliovich R V (1999), 'Potential of Rapid Heat Treatment of Titanium Alloys and Steels', *Mater. Sci. Eng.*, A263, 142–154.

Judd R R and Paxton H W (1968), 'Kinetic Studies of Austenite Formation from a Spheroidized Ferrite-Carbide Aggregate', *Trans. TMS-AIME*, 242, 206–215.

Kabanova I G and Sagaradze V V (1980), Theoretical Analysis of Crystal Geometry of the Reverse α-γ Martensite Transformation, *Fiz. Metal Metalloved*, 50(3), 588–601.

Kajiwara S and Kikuchi T (1983), 'Reversible Movement of Austenite-Martensite Interface and Dislocation Structures in Reverse-Transformed Austenite in Fe-Ni-C Alloys', *Phil. Mag.*, A48, 509–516.

Kaluba W J, Taillard R and Foct J (1998), 'The Bainitic Mechanism of Austenite Formation during Rapid Heating', *Acta Mater.*, 46, 5917–5927.

Kaluba W J, Taillard R and Foct J (2000), 'A reply to "comments on 'the bainitic mechanism of austenite formation during rapid heating'"', *Scripta Mater.*, 42 (2000), 1047–1049.

Kapoor R and Batra I S (2004), 'On the α' to γ Transformation in Maraging (Grade 350), PH 13-8 Mo and 17-4 PH Steels', *Mater. Sci. Eng.*, A 371, 324–334.

Kardonskiy V M and Roschina T V (1978), '$\alpha \rightarrow \gamma$ Transformation in Alloys with 0-32%Ni', *in Proc. Int. Conf. on Martensitic Transformations*, *ICOMAT-77*, Naukova Dumka, Kiev, USSR, 252–256 (in Russian).

Kessler H and Pitsch W (1967), 'On the Nature of Martensite to Austenite Reverse Transformation', *Acta Metall.*, 15, 401–405.

Kidin I N (1969), *Physical Foundations of Electrothermal Treatment of Metals and Alloys*, Metallurgiya, Moscow, (in Russian).

Kokorin V V, Gunjko L P and Kozlova L E (1986), 'Thermoplastic Martensitic Transformation in Fe-Co-Ni-Ti Alloy', *Doklady Academii Nauk SSSR*, 286, 883–886 (in Russian).

Krauss G and Cohen M (1962), 'Strengthening and Annealing of Austenite Formed by the Reverse Martensitic Transformation', *Trans. AIME*, 224, 1212–1221.

Kunz F (1965), 'Die Austenitisierung von martensitisch-austenitischen Gefungen', *Neue Hutte*, 10, 615–618 (in German).

Kurdjumov G and Sachs G (1930), 'Über der Mechanismus der Stahlhartung', *Z. Phys.*, 64, 325–343.

Lefevre-Schlick F, Wang X and Embury D (2008), 'The Production of Fine-Scale Microstructures by Rapid Annealing', *Mater. Sci. Eng. A*, 483–484, 258–261.

Lerinman M and Sadovsky V D (1951), 'Effect of High Heating Rates During Electro-tempering on the Impact Toughness of Structural Steels', *Proc. IFM UFAN AN SSR*, 13, 32–46 (in Russian).

Lipchin N N (1969), 'The Mechanism of Occurrence and Elimination of Structural Heredity in Steel', in *Structural and Phase Transformations on Heating in Steels and Alloys*, Perm Polytechnical Institute. Perm (in Russian).

Lischewski I, Kirch D M, Ziemons A and Gottstein G (2008), 'Investigation of the α-γ-α Phase Transformation in Steel: High-Temperature *In Situ* EBSD Measurements', in *Texture, Stress, and Microstructure*, Hindawi Publishing Corporation, Cairo.

Lyasotskiy I V and Shtanskiy D V (1991), 'Change of Structure in Unalloyed Steels with Platelike Pearlite Structure during Laser Heating', *Phys. Met. Metall.*, 71, 116–122.

© Woodhead Publishing Limited, 2012

Lyasotskiy I V and Shtanskiy D V (1993), 'Experimental Investigation of the Kinetics of Austenization of Pearlite during Laser Heating of Alloyed Steels Type ShKh15', *Phys. Met. Metall.*, 72, 107–114.

Mehl R F and Smith D W (1934), 'Orientation of Ferrite in Pearlite', *Trans. AIME*, 116, 330–341.

Meshkov Y Y, Statsenko I S and Bezbach V D (1994), 'Reasons for the Suppression of Temper Brittleness in Steels with Rapid Electric Tempering', *Metal Science and Heat Treatment*, 2, 84–87.

Mioković T, Schulse V, Voringer O and Löhe D (2006), 'Prediction of Phase Transformations during Laser Surface Hardening of AISI 4140 Including the Effects of Inhomogeneous Austenite Formation', *Mater. Sci. Eng. A*, 435–436, 547–555.

Muddle B C, Nie J F and Hugo G R (1994), 'Application of the Theory of Martensite Transformations to Displacive Phase Transformations in Substitutional Nonferrous Alloys', *Metall. Trans.*, 25A, 1841–1856.

Oshkaderov S P, Prichod'ko S V and Televich R V (1989), 'High Temperature X-ray Diffraction Camera', *Zav. Labor.*, 7, 45–46 (in Russian).

Oshkaderov S P, Prikhod'ko S V, Televich R V and Yakushechkin E I (1992), 'Crystallography of Fine-Grained Austenite Formed in Packet Martensite in Rapidly Heated Low-Carbon Steel', *Phys. Metals*, 11(2)(1992), 166–176.

Ozhiganov A V, Schastlivtsev V M, Polyakova A M and Sadovskiy V D (1974), 'Influence of Heating Rate on the Formation of Austenite in a Quenched and Tempered Steel', *Phys. Met. Metall.*, 37, 148–158.

Park K-T, Lee E J and Lee C S (2007), 'Reverse Austenitic Transformation Behavior of Equal Channel Angular Pressed Low Cabon Ferrite/Pearlite Steel', *ISIJ Int.*, 47, 294–298.

Pereloma E V, Shekhter A, Miller M K and Ringer S P (2004), 'Ageing Behaviour of Fe-20Ni-1.8Mn-1.6Ti-0.59Al(wt%) Maraging Steel', *Acta Mater.*, 52, 5589–5602.

Sadovskii V D (1973), *Structural Inheritance in Steels*, Metallurgiya, Moscow (in Russian).

Sadovskii V D (1976), *Structural Mechanisms of Phase Transformations in Metals and Alloys*, Nauka, Moscow (in Russian).

Sadovskiy V D (1984), 'The Origin of Structure Inheritance in Steels', *Phys. Met. Metall.*, 57, 1–10.

Sadovskiy V D and Sazonov B G (1951), 'Discussion on the Effect of Heating Rate on the Positions of Critical Points during Heating of Steel', *Journal of Theoretical Physics* (ŻTF), 21(6), 693–703 (in Russian).

Sagaradze V V and Kabanova I G (1999), 'Formation of a Nanocrystalline Structure during Direct and Reverse Martensitic Transformations', *Mater. Sci. Eng. A*, 273–275, 457–461.

Sagaradze V V and Shabashov VA (1984), 'Causes of Active Low-temperature Redistribution of Nickel in Iron-Nickel Alloys', *Phys. Met. Metall.*, 57, 113–118.

Sagaradze V V and Sorokin I P (1976), 'Crystallographic Features of the Reverse Martensitic Transformation in Alloys with Twinned Martensite', *Phys. Met. Metall.*, 42, 132–143.

Sagaradze V V and Vaseva Yu A (1976), 'Strengthening of Fe-Ni Alloys by Disperse Crystals of the γ-phase', Fiz. Met. Metalloved, 42(2), 397–405.

Sagaradze V V, Malyshev K A, Vaseva Yu A and Smirnov LV (1974), 'Formation Conditions of Finely Dispersed γ-Martensite in an Iron-Nickel-Titanium Alloy', *Phys. Met. Metall.*, 37, 141–148.

© Woodhead Publishing Limited, 2012

Sagaradze V V, Vaseva Yu A and Malyshev K A (1975), 'Recrystallisation of the γ-Phase in the Alloy Fe-Ni-Ti after the Direct and Reverse Martensitic Transformation', *Phys. Met. Metall.*, 40, 118–126.

Sagaradze V V, Danilchenko V E, L'Heritier P and Shabashov V A (2002), 'The Structure and Properties of Fe-Ni Alloys with a Nanocrystalline Austenite Formed under Different Conditions of $\gamma \rightarrow \alpha \rightarrow \gamma$ Transformations', *Mater. Sci. Eng. A*, 337, 146–159.

Sauvage X, Dacosta G and Valiev R Z (2004), '3D Atom Probe Investigation of Cementite Dissolution in a Pearlitic Steel Processed by High Pressure Torsion', in *Ultrafine Grained Materials III*, ed. by Y T Zhu, T G Langdon, R Z Valiev, S L Semiatin, D H Shin and T C Lowe, TMS, Warrendale, PA, 31–36.

Schastlivtsev V M and Koptseva N V (1976), 'Electron Microscopic Investigation of the Formation of Austenite during the Heating of an Engineering Steel', *Phys. Met. Metall.*, 42, 143–152.

Schastlivtsev V M, Kaletina Yu V, Yakovleva I L and Sadovskiy V D (1986), 'Peculiarities of Austenite Formation in Martensite-Ageing Steels with 18% Ni', *Phys. Met. Metall.*, 62(5), 150–158.

Servant C and Lacombe P (1977), 'Structure Transformations Produced during Tempering of Fe-Ni-Co-Mo Aloys', *J. Mater. Sci.*, 12, 1807–1826.

Shekhter A, Aaronson H I, Miller M K, Ringer S P and Pereloma E V (2004), 'Effect of Aging and Deformation on the Microstructure and Properties of Fe-Ni-Ti Maraging Steel', *Metall. Mater. Trans.*, 35A, 973–983.

Shutts A (2004), *Effects of Heating Rate and Prior Microstructure on SAE 1541 Forging Steel*, Report to Forging Industry Educational and Research Foundation, Advanced Steel Processing and Products Research Center, Colorado School of Mines, USA.

Singh J and Wayman C M (1986), 'Reverse Martensitic Transformation in Fe-Ni-Mn Alloy', *Metallography*, 20, 485–490.

Sorokin I P (1966), 'Crystallographic Ordering of the $\alpha \rightarrow \gamma$ Transformation in the Alloy Fe-30 per cent Ni', *Phys. Met. Metall.*, 22, 78–84.

Sorokin I P and Sagaradze V K (1978), 'Distribution of Austenite Orientations after Double Martensitic Transformation $\gamma \rightarrow \alpha \rightarrow \gamma$', *Phys. Met. Metall.*, 45, 62–74.

Southwick P D and Honeycombe R W K (1980), 'Decomposition of Ferrite to Austenite in 26%Cr-5%Ni Stainless Steel', *Metal Science*, 14, 253–261.

Speich G R and Szirmae A (1969), 'Formation of Austenite from Pearlite and Ferrite-Carbide Aggregates', *Trans. AIME*, 245, 1063–1074.

Televich R V (1995), *Structural Genetics of Austenite on Heating of Structural Steels*, D. Techn. Sci. Thesis summary, National Academy of Sciences, Ukraine, Institute for Metal Physics, Kiev.

Televich R V and Prikhod'ko S V (1994a), 'Crystallography of Austenite Formation in Quenched Carbon Steel', *Phys. Metals*, 13(4), 332–344.

Televich R V and Prikhod'ko S V (1994b), 'Recrystallization of Austenitic Fine-Grained Complex of Carbon Steel', *Phys. Metals*, 13(8), 325–333.

Televich R V and Prikhod'ko S V (1994c), 'Formation of Austenite Structure in Prequenched Alloy Steels', *Phys. Metals*, 13(8), 749–757.

Televich R V and Prikhod'ko S V (1994d), 'Crystallographic Features of $\alpha \rightarrow \gamma$ Transformation in a Tempered Structural Steel. II The Effect of Preliminary Tempering on the Crystallography of Fine-Grained Austenite', *Phys. Metals*, 13(12), 1126–1132.

Televich R V and Prikhod'ko S V (1994e), 'Crystallography of Austenite Formation in Hypoeutectoid Steel with Ferrite-Pearlite Microstructure', *Metal Phys. Adv. Techn.*, 16, 28–33.

© Woodhead Publishing Limited, 2012

Televich R V, Kocherga O V, Prikhod'ko S V and Yakushechkin E I (1993), 'Crystallographic Pattern of Near-Interface Austenite Formation', *Phys. Metals*, 11, 1160–1167.

Televich R V, Prikhod'ko S V and Kocherga O V (1994), 'Crystallographic Features of $\alpha \rightarrow \gamma$ Transformation in a Tempered Structural Steel. I The Effect of Preliminary Tempering of Martensite on Structural Heredity on Rapid Heating', *Phys. Metals*, 13(1), 984–991.

Teliovich R V, Ivasishin O M, Yakushechkin Ye I and Nikonenko D I (1999), 'Employment of Rapid Heat Treatment of Rolled Steel Products for Shipbuilding Application', in *Materials for Transportation Technology, Euroma 1999, vol. 1*, ed. P.J. Winkler, Wiley-VCH, Weinheim, 352–357.

Thevenin J, Cizeron G and Lacombe P (1971), 'Etude de la reversion de a vitesse de chauffage rapid de la martensite de l'acier maraging a 18% de nickel, 9% de cobalt et 5% molybdene', *Met. Scient. Rev. Metallurg.*, LXYIII, 215–222.

Umova V M and Sadovsky V D (1977), 'Morphology and Structural Composition of Austenite Formed during the Heating of a Quenched Steel', *Phys. Met. Metall.*, 45 112–120.

Vologdin V P (1939), *Induction Surface Quench Hardening of Steels*, Metallurgizdat, Moscow (in Russian).

Wassermann G (1932/33), 'Einfluß das $\alpha \rightarrow \gamma$ Umwandlung eines irreversible Nickelstahles und Kristallorientierung und Zugfestigheit', *Arch. Eisenhüttettenw*, 8, 347–359.

Vovk Ya N, Emchenko-Rybko E V, Oshkaderov S P and Televich R V (1987), 'Role of Dislocations in the Formation of Inherited Structure in Steel', *Phys. Metals*, 7, 6–75.

Webster D and Allen G B (1962), 'Grain Growth in Vanadium steels', *J. Iron Steel Inst.*, 200, 520–526.

Yakovleva I L, Schastlivtsev V M and Tabatchikova T I (1993), 'Experimental Observation of Diffusionless Formation of Austenite in a Steel with Pearlitic Structure upon Laser Heating', *Phys. Met. Metall.*, 76, 179–187.

Yakovleva I L, Schastlivtsev V M, Tabatchikova T I, Mirsaev D A and Osintseva A L (1995), 'A Diffusionless Martensite-like Mechanism of Formation of Austenite in a Pearlitic Steel during Laser Heating', *Phys. Met. Metall.*, 79, 576–580.

Zel'dovich V I and Sadovsky V D (1968), 'Redistribution of Components between the α- and γ- Phases during $\alpha \rightarrow \gamma$ Transformation in Iron-Nickel Alloys', *Phys. Met. Metall.*, 28, 147–155.

Zel'dovich V I and Sadovskiy V D (1972), 'Study of the $\alpha \rightarrow \gamma$ Transformation and Recrystallization of Martensite-Ageing Steel', *Phys. Met. Metall.*, 34, 66–75.

Zel'dovich V I, Shadrina O S, Sadovskiy V D and Yelokhina L V (1977), 'On the Structural Mechanism of γ-Phase Formation in an Iron-Nickel Alloy with Lath Martensite', *Phys. Met. Metall.*, 43, 136–146.

Zhou Y, Zhang W, Sui M, D Li D, He G and Guo J (2002), 'Formation of a Nanostructure in a Low-Carbon Steel under High Current Density Electropulsing', *J. Mater. Res.*, 17, 921–924.

© Woodhead Publishing Limited, 2012

Index

A_3-temperature, 505
A-type grains, 530
abnormal cementite, 229
abnormal ferrite, 229
abnormal transformation
  behaviour, 322–30
    Fe-Co alloy ferrite-formation rate vs temperature, 326
    Fe-Co alloy ferrite fraction vs temperature, 326
    Fe-N alloy ferrite-formation rate vs fraction and temperature, 330
    Fe specimens of different grain sizes ferrite fraction vs temperature, 327
    ferrite formation rate vs temperature and ferrite fraction, 328
    fresh Fe-N alloy ferrite fraction vs temperature, 329
    fresh Fe specimens ferrite fraction vs temperature, 323
    pure Fe formation rate vs ferrite fraction and temperature, 324
  kinetics, 338–41
    Fe-Co alloy ferrite-grain morphology, 339
    ferrite-formation rate vs ferrite fraction at 10K min^{-1}, 344
    ferrite-formation rate vs ferrite fraction at 15K min^{-1}, 343
    high- and small-angle grain boundaries, 340
    nucleus density vs ferrite fraction, 342
    nucleus density vs ferrite fraction for $\gamma \rightarrow \alpha$ transformation, 344
    pure iron autocatalytic factor, 342
    pure iron ferrite-formation rate vs ferrite fraction, 344
accommodation twinning, 460–1
accumulated roll bonding, 509
acicular ferrite, 159, 226, 231, 241, 469
active nucleus, 31
activity coefficient, 80
AISI 4140 alloy, 585
allotriomorphic, 386
allotriomorphic ferrite, 475
allotriomorphs, 238
Allotropist theory, 12, 14
allotropy, 4
  iron thermal analysis, 11–15
  phase change, 14
300M alloy, 442, 446
alloy partitioning
  pearlite growth, 295–8
    alloys transformed in the $(\alpha+\gamma+M_3C)$ field, 301
    isothermally transformed structure of a Fe-2.46%C-3.5%Mn steel, 300
    measured Mn distribution in the ferrite and M3C phases, 301
    Mn contents in the ferrite and M_3C phases, 300
    Mn distribution across the γ/pearlite interface and in the product phases, 299
    transformation of para- and ortho-equilibrium in the binary Fe-Mn system, 297
alloying elements
  role, 291–8
    alloy partitioning during pearlite growth, 295–8
    Fe-0.4 wt% C-3.5 wt% Cr steel partial transformation, 296
    Fe-Mo-C alloy transformation, 292
    nature of the grain boundary ferrite, 294
    sequence of events at an austenite boundary, 295
    TTT diagram of a Fe-0.4 wt% C-3.5 wt% Cr steel, 296
α–ferrites, 4
α-iron, 385
α′–martensite, 4
antiferromagnetism, 558
athermal martensitic transformation, 556
atom bonding, 7
atom probe field ion microscopy, 393
atom probe tomography, 443, 447, 449, 451, 453, 524, 604

© Woodhead Publishing Limited, 2012

atomic structure, 158–63
classification of phase boundary, 158–9
edge-to-edge matching model, 161–3
ledge structure of phase boundary, 159–61
atomistic model, 98–101
austenite, 18, 20, 161, 281
crystallographic orientation relationships, 255–8
atomic arrangement in close-packed planes for bcc and fcc lattices, 256
proeutectoid cementite, 257–8
proeutectoid ferrite, 255–7
austenite-ferrite transformation, 151, 189–90
abnormal transformation kinetics, 338–44
nucleus density variation, 341–4
repeated nucleation, 338–41
diffusion- to interface-controlled growth transition, 345–60
Fe-C alloys isochronal γ→α transformation kinetic analysis, 357–60
Fe-C vs Fe-N alloys γ→α transformation, 360
ultra-low-carbon alloys isochronal γ →α transformation, 345–57
interface- to diffusion-controlled growth transition, 360–7
Fe-C alloys isothermal γ→α transformation, 360–7
kinetic information from thermal analysis, 314
massive transformation under uniaxial compressive stress, 367–77
α→γ and γ→α transformations anisotropic specificities, 375–7
isochronal massive α→γ and γ→α transformation, 367–71
isochronal massive α→γ and γ→α transformation analysis, 371–5
modular phase transformation model, 315–20
growth, 317–18
nucleation, 315–16
numerical and analytical phase transformation models, 318–20
nature and kinetics in steels, 311–77
normal transformation kinetics, 332–8
interface mobility and transformation strain, 334–8
interface velocity determination, 332–4
nucleation and growth in steels after plastic deformation, 505–24
background, 506–16
future trends, 523–4
plastic deformation effects on ferrite formation, 516–23
transformations characteristics, 320–32
abnormal transformation behaviour, 322–30
isothermal vs non-isothermal transformation, 331–2
normal transformation behaviour, 320–2
austenite formation
heating rate effect, 582–92
austenite chemical inhomogeneity, 591–2
kinetics, 582–4
0.8 wt%C steel temperature and dilatometric curves, 583
heating rate effect on start temperature, 584
mechanisms on Fe-C alloys fast heating, 585–91
austenite composition dependence on formation temperature, 587
austenite formation in ferrite/pearlite matrix, 589
normalised steels with pearlite or ferrite carbide mixture, 586–91
pearlite microstructure after laser heating, 590
quenched steels with martensite microstructure, 585–6
austenite/pearlite interface, 279, 280
austenite phase (γ–Fe), 132
austenite-to-pearlite transformation, 567, 569
austenite zone, 285
austenitic microstructure, 506
austenitisation, 229
autocatalysis, 388
autocatalytic factor, 341–2
autocatalytic nucleation, 315–16
Avrami coefficient, 128, 129
Avrami nucleation, 319

Bagaryatski relationship, 287, 405–6, 429
Bähr DIL 802, 314
Bain orientation relationship, 256
Bain system, 432
bainite, 30, 31
bainite finish time (BF), 194
bainite start temperature, 485–91
B_s definition, 489–91
Fe-C alloy bainite formation prediction in Fe-C alloys, 485–7
Fe-C phase diagram, 487
ferrite growth barrier estimates, 488
formation barriers diagram, 486
second stage of transformation, 487–9
transformation degree vs time, 490
bainite start time, 194
bainite transformation
alloying elements effect, 491–4
ferrite acicular growth barriers, 494
Mn effect on the critical carbon content, 493
bainite characteristics, 386–90

© Woodhead Publishing Limited, 2012

pearlite and bainite TTT diagrams, 387
upper sheaf microstructure, 389
bainite growth and nucleation, 477–85
bainite length at 380ºC vs time, 480
bainite lengthening rate at supersaturation, 481
lengthwise growth of plates, 479–80
nucleation, 477–9
Widmanstätten ferrite and bainite experimental lengthening, 481–5
bainite start temperature, 485–91
B_s definition, 489–91
Fe-C alloy bainite formation prediction in Fe-C alloys, 485–7
second stage of transformation, 487–9
diffusion-controlled growth mechanism, 391–6
carbide precipitation, 395–6
diffusion-controlled growth, 393–5
morphology and surface relief, 391–2
solute drag and transformation stasis, 392–3
displacive transformation mechanism, 396–411
kinetics in steels, 468–99
mechanisms in steels, 385–412
overall kinetics, 494–9
15-20% bainite formation C curves, 498
carbon content effect on C curves, 496–9
isothermal transformations progress, 495–6
transformation degree vs time, 495
TTT and CCT diagrams, 494–5
transformation diagrams, 470–7
TTT diagram examples, 473–7
TTT diagram principles, 470–3
bainitic ferrite, 417
Baker–Nutting orientation relationship, 162
barrier-free nucleation, 136, 139
BCC ferrite, 285
bearing steels, 566
Bessemer–Kelly pneumatic process, 6
BII-type, 419
BIII-type, 419
binary *A-B* system, 109
binary systems
lattice-fixed frames, 109–10
number-fixed frames, 109–10
volume-fixed frames, 112–13
body-centred cubic (bcc), 4, 132, 147, 159, 189
body-centred tetragonal (BCT), 4
Boltzmann statistics, 98
Boltzmann's constant, 74–5
Bos–Sietsma mixed-mode model, 140
boundary migration
phase boundary, 171–7
growth kinetics of ledged boundary, 171–4
ledgewise growth *vs*. disordered growth, 174–6
mechanism, 171
motion of disconnections, 176–7
Bramfitt–Speer classification system, 437
Bronze Age, 6
Burgers vector, 177, 507, 597

C-curves, 386, 411, 471
Calphad method, 74–80, 124
activity and reference states, 79–80
modeling of disorder and entropy, 74–6
regular solution type models, 76–7
substitutional and interstitial components phases, 77–9
carbide-containing bainite, 417–33
bainite structure definition, 417–23
bainite with MA constituent microstructure, 421
BI-, BII, and BIII- types bainite illustration, 419
Fe-C-2Mn ternary alloys bainite morphology map, 423
Fe-Ni-C alloys microstructures micrograph, 418
Fe-2Si-1Mn-0.6C alloy BF micrographs, 426
isothermally transformed Fe-C-2Si-1Mn alloys microstructures, 420
normal vs inverse bainite and inverse bainite formation, 422
upper and lower bainite illustration, 418
carbide precipitation, 429–33
precipitation with subunit formation in lower bainite, 432
precipitation with subunit formation in upper bainite, 430
transformed Fe-9Ni-0.8C lower bainite micrograph, 431
upper and lower bainite formation mechanism, 431
crystallography and bainite characteristics in ferrite, 423–9
BF and LM dislocation densities, 428
BF crystallography illustration, 427
eutectoid transformations illustration, 424
Fe-0.6C-2Si-1Mn alloy micrographs, 425
lower bainite micrograph, 428
upper bainite substructure illustration, 427
future trends, 433
carbide-free bainite, 387–8, 411, 436–62, 490, 492
carbon distribution during reaction, 446–56
austenite carbon concentration plots, 448

© Woodhead Publishing Limited, 2012

austenite-ferrite interfaces carbon concentration profiles, 450
bainitic ferrite carbon supersaturation, 451–3
carbon content evolution in ferrite, 452
carbon map and concentration profile showing carbon segregation, 455
carbon trapped at defects, 453–6
dislocation proximity histograms, 454
Fe-1C-1.5Si-1.9Mn-1.3Cr steel micrographs, 452
retained austenite C content after bainite reaction, 447–51
plastic accommodation microstructural observations, 456–61
accommodation twinning, 460–1
bainitic and martensitic microstructures dislocation density values, 460
dislocation debris micrographs, 458
dislocation distribution, 457–60
dislocation distribution densities, 459
Fe-0.8C-2.0Si-1.5Mn-0.3Mo-1.3Cr-0.1V steel micrographs, 461
Fe-0.8C-2.0Si-1.5Mn-0.3Mo-1.3Cr-0.1V steel TEM and lattice schematic, 462
Si influence on steel cementite precipitation, 442–6
Fe-1.2C-Si-1.5Mn time-temperature-precipitation diagram, 444
precipitation from austenite, 442–5
precipitation from bainitic ferrite, 445–6
carbon, 197–8
state, 10–11
supersaturation, 441–2, 451–3
carbon-depleted ferrite, 567
carbon-enriched cementite, 567
Carbonist theory, 14
cellular-automaton model, 521–2, 532
'cement carbon,' 11–12
cementite, 161, 279, 280, 287
cementite-austenite relationship, 286
cementite-free bainite, 439
central-force many-body potential, 200
Channel 5 software, 576
chemical energy
coherent phase boundary, 163–7
comparison of coherent fcc/fcc boundary energies, 167
nearest neighbour atoms to atom A across the *((hkl)* type phase boundary, 163
variation with temperature of Wulff equilibrium shape, 165
chemical potential, 89
χ–Fe_5C_2 precipitate, 576–7
classical nucleation theory, 135–6, 510–11
closed system, 57–8
co-deformation, 298–9
coherent phase boundary, 158, 171
chemical energy, 163–7
coincidence site lattice boundary, 569
columnar bainite *see* nodular bainite
combined law, 63
different forms, 64–6
composition variable
concentration use, 110–12
lattice-fixed frame use, 110–11
volume-fixed frame use, 111–12
compressive load stress, 375–6
continuous cooling transformation (CCT), 193–7
homogenised and non-homogenised weld metal, 196
continuous cooling transformation diagram, 494
continuous nucleation, 129, 319
continuum diffusional growth rate theories, 33
correlation effect, 101–2
Cottrell atmosphere, 454
coupled solute drag effect, 393, 447
crystal-plasticity model, 521
crystallinity, 7
crystallographic behaviour, 592, 594
crystallography, 189–92, 403–6
aspect of the reaction, 285–91
complex array of pearlite nodules, 288
configurations of Fe atoms, 290
interfaces for a crystallographic description of the growing pearlite colony, 286
orientation relationships and habit planes of ferrous pearlite, 290
pearlite exhibiting the Bagaryatski relationship, 289
pearlitic cementite with the Bagaryatski relationship, 291
orientation relationship (OR), 191–2
volume change, 189–91
alloying elements in solution on lattice parameters of austenite and ferrite, 189

Daltonian chemistry, 7
decomposition-chain, 21, 28
deformation energy, 373–5
degenerate ferrite, 240
degenerate pearlite, 422
degenerate upper bainite, 439
δ–ferrites, 4
δ-iron, 385
demagnetisation energy, 560
diamagnetic substances, 557
DICTRA software, 485
differential dilatometry, 314, 320
differential scanning calorimetry (DSC), 145–7, 197, 314

© Woodhead Publishing Limited, 2012

calculated fractions of pro-eutectoid ferrite and pearlite, 146
heat capacities of high purity Fe-C alloys, 146
differential thermal analysis, 197, 314, 320
diffusion
atomistic model, 98–101
diffusionless transformation trapping and transition, 119–23
driving forces of simultaneous processes, 96–8
frame of reference, 101–13
fundamentals in phase transformations in steels, 94–124
future trends, 123–4
mobilities evaluation, 113–19
boundary conditions at phase interfaces, 118–19
interstitials, 114–18
diffusion coefficients, 95
diffusion-controlled growth, 391–6, 585–6, 591
carbide precipitation, 395–6
growth rate analysis, 394–5
morphology and surface relief, 391–2
solute drag and transformation stasis, 392–3
transition from interface-controlled growth, 360–7
average vs calculated interface velocity, 366
Fe-C alloy ferrite fraction vs time, 363
Fe-C alloy grain-size distributions, 363
Fe-C alloy length change and temperature vs time, 362
Fe-C and Fe-N superimposed partial phase diagrams, 361
Fe-N alloy $\gamma \rightarrow \alpha$ transformation onset temperature, 361
kinetic parameters from phase transformation model, 365
transformed fraction from phase transformation model, 365
transition to interface-controlled growth, 345–60
average vs calculated interface velocity, 354
Fe-C alloy and pure Fe ferrite formation rate vs ferrite fraction, 348
Fe-C alloy experimental vs theoretical nucleus density values, 359
Fe-C alloy ferrite-formation rate vs temperature, 346–7
Fe-C alloy ferrite fraction vs temperature, 345
Fe-C alloy $\gamma \rightarrow \alpha$ transformation T_{onset} and T_{tr}, 352
Fe-C alloy grain-size distribution, 350–1
Fe-C alloys and pure Fe ferrite-formation rate vs temperature, 355–7
Fe-C system partial phase diagram, 352, 358
interface velocity vs ferrite fraction, 359
large-angle grain boundaries micrographs, 349
diffusion-controlled lengthening rate, 394
diffusional austenitic decomposition, 567–73
coincidence site lattice boundaries distribution, 571
42CrMo specimen microstructure, 570
Fe-0.81C specimens micrographs, 568
Fe-0.49wt%C specimens band contrast micrographs, 572
Fe-1.0wt%C specimens misorientation angle distribution, 571
diffusional control, 208–10
diffusional-displacive transformation, 585
diffusional formation
crystallography, 189–92
ferrite fundamentals in steels, 187–216
growth, 208–16
nucleation, 198–208
overview, 187–8
Fe-C phase diagram and vertical isopleth for Fe-C-Ni, 188
transformation ranges, 193–8
carbon and iron steels, 197–8
pure iron, 197
TTT and CCT diagrams, 193–7
diffusional solid-solid nucleation theory, 33
diffusional transformation, 473, 482, 485, 489, 491, 497, 586
diffusionless growth, 399
diffusionless transformation, 469, 476–8, 482, 486, 488, 491
trapping and transition, 119–23
flux composition across phase interface, 122–3
volume local change at phase interface, 121–2
dilatometry, 143–5
dilatometer and dilation signal for linear cooling, 144
Dirac function, 315
direct resistance electric heating, 581
disconnections
motion, 176–7
broad face of a γ' plate in Al-Ag alloy, 178
ledges containing an edge dislocation, 176
discrete lattice plane nearest neighbour broken bond (DLP-NNBB), 165, 166, 178–9
discrete nucleation, 130

© Woodhead Publishing Limited, 2012

dislocation arrays, 538
disordered growth, 174–6
displacive transformation, 396–411, 441, 456–7, 468, 585–6
  bainite growth, 399–401
    solutes role and incomplete reaction phenomenon, 401
    T_o concept and incomplete reaction phenomenon illustration, 402
  crystallography, 403–6
    orientation relationship in bainite transformation, 404
  nucleation, 397–9
    bainite sheaf formation representation, 400
    driving force for different steels, 398
  nucleus growth, 399
  strain and mechanical stabilisation, 409–11
    austenite pre-strain effect on bainite transformation, 410
  stress and transformation plasticity, 407–9
  thermal stabilisation, 406–7
  upper and lower bainite, 402–3
downhill-simplex fitting procedure, 364
driving force, 336, 338, 375
  evaluation, 68–9
  frame of reference, 103–5
  simultaneous processes, 96–8
dual-phase steels, 548
Dubé classification system, 198, 229–33
  illustration, 230
  microstructure of a continuously cooled plain carbon UNS G10200, 235
  microstructure of a continuously cooled plain carbon UNS G10400, 234
  optical micrographs of various 2D morphologies, 232
  presence of grain boundary, 235
  temperature-composition regions, 233
dynamic recrystallisation, 543
dynamic strain-induced ferrite transformation, 527–50
  achieving grain sizes less than 1μm, 546–8
    deformed 0.3C-2Mn-2Si-0.28Mo steel microstructure, 547
  future trends, 548–9
    ultrafine and coarse grained steels tensile behaviour, 549
  grain refinement limits in conventional static transformation, 528–32
    0.18C, 0.015Si-1.32Mn, 0.035Nb microstructure steel, 529
    ferrite phase mean linear intercept, 531
    Ni-30Fe alloy substructures, 531
  industrial implementation, 548
  modelling, 543–6
    0.17C-1.5Mn-0.02V steel microstructure after deformation, 544
    descriptive model, 543–6
    dynamic recrystallisation experiment images, 545
    mathematical model, 546
  transformation nature, 536–43
    mechanism, 536–7
    nucleation sites, 537–43

edge-to-edge matching, 161–3, 262
  illustration, 162
EELS line near-edge structure (ELNES), 201
electrical resistivity analysis, 507
electron backscatter diffraction, 192, 199, 202, 524, 530, 582
electron microscopy, 5
embedded atom, 200
embedded atom model (EAM), 169
end member, 78
entropy, 74–6
ε–carbide, 403, 430, 462
equal-channel angular pressing, 509
equiaxed ferrite, 159
equilibrium, 60–2
  conditions, 67–8
    functions to be minimised for various external condition, 67
  fluctuations thermodynamics, 91–2
  Gibbs energy change during phase transformation, 61
  metastable and unstable, 61
  thermodynamics properties calculation under fixed *T, P* and composition, 72–4
  value of internal variable ξ that gives lowest Gibbs energy, 61
equilibrium cooling, 385
η–Fe_5, 576–7
eutectoid temperature-composition
  range of formation of proeutectoid ferrite amd cementite, 227–9
    dominance of diffusional products of austenite decomposition, 228
excess energy, 76
extended transformed volume, 315
extensive variables, 59–60
external action, 58
external variables, 57–60
  action and reaction, 57–9
    phase diagram of pure iron, 58
  extensive and intensive variables, 59–60
extrapolated paraequilibrium, 390

f surface tension, 86
face-centred cubic (fcc), 4, 132, 147, 159, 189
fan structure *see* nodular bainite
Farooque–Edmond orientation relationship, 161, 258, 262, 265
FCC -BCT lattice, 25
Fe-C-M phase diagram, 16

© Woodhead Publishing Limited, 2012

Fe-C phase diagram, 15, 17, 18, 468, 562–3
Fe-C-2Si-1Mn alloy, 419
Fe-Cr alloys, 595
Fe-Cr-C alloy, 427
Fe-2Mn-C alloys, 432
Fe-N-1 wt% Mo alloy, 393
Fe-Ni-based alloys, 535
austenite morphology, 602–6
$\alpha' \rightarrow \gamma$ transformation start and finish temperatures vs heating rates, 610–11
heated Fe-27.4%Ni-1.94%Ti alloy micrographs, 607
reverse transformation start and finish temperatures vs heating rates, 608–9
heating rate effect on reverse austenite transformations, 602–12
heating rate effect on reverse transformations, 581–613
mechanism and kinetics, 602–6
quenched Fe-Ni alloy heating rate vs temperature, 603
quenched martensite heating rate vs microhardness, 605–6
structural heredity, 609–12
ferrite, 279, 280, 281, 287, 386
allotriomorphs, 238
3D-reconstruction from opposite sides of the prior austenite grain boundary, 239
eight serial sections from a large portion of 2D stack for the 3D reconstruction, 239
crystallography, 189–92
formation fundamentals in steels, 187–216
growth, 208–16
morphologies, 236–8
three-dimensional reconstructions of proeutectoid ferrite, 237
non-classical morphologies, 240–4
optical micrograph, 3D reconstructed image and morphology of acicular ferrite, 243
optical micrographs and 3D reconstructed images of ferrite idiomorphs, 244
single section and 3D isosurface view of a reconstructed ferrite sheaf, 242
Type A, B, and C degenerate Widmanstätten proeutectoid ferrite, 241
nucleation, 198–208
overview, 187–8
Fe-C phase diagram and vertical isopleth for Fe-C-Ni, 188
transformation ranges, 193–8
ferrite-austenite relationship, 286, 424
ferrite/carbide aggregates, 305
ferrite-cementite relationship, 286
ferrite finish time (FF), 194
ferrite growth, 139–41, 208–16
diffusional vs interfacial control, 208–10
dilatation signal and transformation curve for cyclic transformation, 142
negligible partition-local equilibrium (NP-LE), 212–14
paraequilbirium (ParaE), 214–16
partition-local equilibrium (P-LE), 210–12
ferrite phase (α–Fe), 132, 138
ferrite spine, 432
ferrite start time, 194
ferromagnetic substances, 558
ferrous alloys
historical development of phase transformations, 3–40
first period, recognition (1880-1925), 8–21
overview, 3–5
second period, consolidation (1880-1925), 21–37
technology and characterisation, 5–8
Fick's law, 98, 101
fine-scale Guinier–Preston zones, 27
fire-substance *see* carbon
fluctuations, 91–2
focused ion beam (FIB), 202, 298
forced coherency, 158
42CrMo steel, 569, 576
4340 steel, 408, 445–6
14T magnetic field, 576–7
frame of reference, 101–13
alternative method, 106
concentration use as composition variable, 110–12
driving force, 103–5
lattice- and number-fixed frames application for binary systems, 109–10
lattice- and number-fixed frames diffusivities, 106–8
volume-fixed frames application to a binary system, 112–13
Frank-Read source, 507
free energy, 163–71, 281
atomistic calculation of phase boundary structure, 169–71
polar plot of K-S related α/γ phase boundary energy, 170
chemical energy of coherent phase boundaries, 163–7
ledged boundary, 168–9
misfit dislocation boundaries, 167–8
free-energy difference, 505

γ/α mobility, 334
γ–austenite, 4
γ-iron, 385
γ laths, 609

© Woodhead Publishing Limited, 2012

G-T relationship, 594, 612
geometric packing, 7
geometry
  kinetics, 129–32
    Avrami rate constant, 131
    JMA fit parameters, 131
    spherical and tetrakaidecahedron model calculated transformation curves, 130
    tetrakaidecahedron representation and partial transformation of austenite grain, 130
Gibbs energy, 72, 73–4, 75, 88–9, 96, 97, 98, 100, 101, 105, 107, 120, 133–4, 137, 336, 373
  phases in steel, 74–80
Gibbs Phase Rule, 15
Gibbs thermodynamics, 96
Gibbs–Duhem relation, 66–7, 71, 104, 119
grain boundary allotriomorphs, 230
  cementite, 244–8
    illustration, 247
    optical micrographs of isothermally transformed Fe, 245
    zig-zag grain boundary morphology, 248
grain boundary carbide dendrites, 246
grain boundary cementite, 286
grain boundary cementite dendrites, 247–8
grain rotation, 545
granular bainite, 420, 439
growth kinetics, 171–4

Hall-Petch relationship, 528, 532
Hall–Petch scaling law, 302
hardening carbon, 11–12
hardening problem, 10
hardenite, 14
heat capacity, 70
heating rate
  effect in quenched steels after $\gamma \rightarrow \alpha(\alpha') \rightarrow \gamma$ phase transformation, 592–600
    C content effect on structural heredity, 596
    fine grained austenite microstructure formation, 592–5
    structural heredity mechanism, 596–600
    structural inheritance, 595–6
  effect on austenite formation in steels, 582–92
    austenite formation kinetics, 582–4
    austenite microstructure in quenched steel after heating, 593
    Fe-C based alloys austenite formation mechanism, 585–91
  steels and Fe-Ni-based alloys reverse transformations, 581–613
heterogeneous deformation structure, 539
heterogeneous nucleation, 512
high-angle grain boundary, 205, 206, 340
high-energy laser beam, 581
high frequency induction surface treatment, 581
high-rate electro-thermal treatment method, 600–2
high resolution transmission electron microscopy (HRTEM), 157, 159
high silicon bainitic steels, 440
homogeneous nucleation, 478, 512
hot stage microscopy, 481
hot stage TEM, 198
hot torsion test, 535
hypereutectoid Fe-C alloy, 421
hypereutectoid steels, 227, 246
hypoeutectoid steels, 227, 571

idiomorphic *see* allotriomorphic
idiomorphs, 230
impingement correction, 341, 371
incoherent phase boundaries, 158, 171
incomplete reaction phenomenon, 390, 401, 412, 447
incomplete transformation, 489
indirect metallographic method, 393
intensive variables, 59–60
  examples obtaines by normalising extensive quantities to system size, 60
interface-controlled growth
  transition from diffusion-controlled growth, 360–7
  transition to diffusion-controlled growth, 345–60
interface mobility, 334–8
  chemical driving force vs temperature, 337
  experimental vs fitted values of ferrite fraction vs temperature, 335
  Fe-Co alloy $\Delta G^{def} + \Delta G^{int}$ vs ferrite fraction, 338
  pure iron $\Delta G^{def} + \Delta G^{int}$ vs ferrite fraction, 337
interface velocity, 371–3
  determination, 332–4
    γ/α interface velocity vs temperature, 333
interfaces
  effect, 85–90
    phase equilibria, 88–90
    surface energy and surface stress, 85–8
interfacial control, 208–10
interfacial energy, 483
internal variables, 57–60
  action and reaction, 57–9
    phase diagram of pure iron, 58
  extensive and intensive variables, 59–60
interphase precipitation, 35, 175–6
interstitial atoms, 77–8
interstitial sublattice, 114–15

© Woodhead Publishing Limited, 2012

interstitials
diffusion in phases, 114–18
applications, 117–18
lattice-fixed frame use, 115–16
number-fixed frame use, 116–17
intragranular defect, 538–9
intragranular nucleation, 538
intragranular Widmanstätten needles, 230
intragranular Widmanstätten plates, 230
intrinsic magnetisation energy, 559
invariant plane strain, 390–1
inverse bainite, 421
iron
technological history, 5–6
thermal analysis and allotropy, 11–15
critical points (thermal arrests) in the Fe-C binary system, 13
Iron Age, 5–6
iron steel, 197–8
Isaichev orientation relationship, 406
isothermal transformation, 29, 32, 229, 278–9, 285, 331–2, 495–6
pure iron DTA signal vs time, 331
pure iron ferrite formation rate vs time, 332

Johnson–Mehl equation, 279
Johnson–Mehl–Avrami equation, 126, 127
Johnson–Mehl–Avrami–Kolmogorov (JMAK), 127, 128, 216

Kikuchi line diffraction technique, 461
Kirkendall markers, 102, 103
Kirkendall shift, 102, 103, 104, 105, 108, 119, 120
Kolmogorov – Johnson – Mehl – Avrami equation, 496
Kurdjumov–Sachs orientation relationship, 159, 192, 256, 287
Kurdjumov–Sachs relationship, 405–6, 424–5, 460–1, 537, 588, 612

laser ultrasonics, 148
lath, 470
lath-like bainitic ferrite/austenite interphase boundary, 457
lath-like martensite/austenite interphase boundary, 457
lattice-fixed frames
application for binary systems, 109–10
diffusivities, 106–8
dependent composition variable elimination, 107–8
direct approach, 107
use, 110–11, 115–16
Laue patterns, 582
Le Chatelier's Principle, 72
illustration, 73
ledge
mechanism, 469
structure of phase boundary, 159–61
Kurdjumov–Sachs orientation relationship, 160
ledged boundary
energy, 168–9
growth kinetics, 171–4
relationship between the step velocity and supersaturation, 174
terrace-ledge-kink mechanism, 172
variation of isoconcentration contour with time, 173
ledgewise growth, 174–6
lever rule, 362
light optical microscopy, 6, 12, 16, 17, 28, 29, 417, 437
local equilibrium (LE), 34, 140, 141
longitudinal axis, 375–6
low Σ boundaries, 571
lower bainite, 396, 402–3, 417–19

magnetic dipolar interaction, 559
magnetic field
effect on phase equilibrium and transformation, 560–77
phase equilibrium in magnetic field, 560–5
phase transformation in magnetic field, 565–77
effect on phase transformations in steels, 555–77
future trends, 577
evolution of generators, 556–7
phase transformation influence mechanisms, 557–60
magnetic ordering illustration, 558
magnetic model, 335
magnetic state transition, 555
magnetic transitions, 35–6
magnetisation energy, 562
martensite, 14, 18, 20, 22, 25–6
martensite-autenite (MA) constituent, 419
martensite formation, 506–7
martensitic transformation, 560–2, 565–6
start temperature prediction, 560–2
Gibbs free energy schematic, 561
magnetic dipoles illustration, 560
massive transformation, 312, 586
mechanical stabilisation, 409–11
mechanical twinning, 409
metal
microstructure, 7–8
structure, 7–8
metal alloy, 15–16
metastable eutectoid reaction, 442
metastable parent phase, 313
metastable product phase, 313
MICRESS code, 520
micro-grid technique, 509
microbands, 539

© Woodhead Publishing Limited, 2012

microstructural modelling, 519, 521
microstructural modification, 577
microstructure
  kinetics, 129–32
    Avrami rate constant, 131
    JMA fit parameters, 131
    spherical and tetrakaidecahedron model calculated transformation curves, 130
    tetrakaidecahedron representation and partial transformation of austenite grain, 130
midrib morphology, 429
Militzer and Brechet phenomenological model, 546
misfit dislocation boundary, 167–8
mixed diagrams, 82–4
  metastable Fe-C phase diagram, 83, 84
mixed-mode growth model, 364
mixed-mode model, 140
MOB2 database, 485
modular phase transformation model, 315–20
  growth, 317–18
  nucleation, 315–16
    autocatalytic nucleation, 315–16
    mixed site saturation and autocatalytic nucleation, 316
    site saturation, 315
  numerical and analytical phase transformation models, 318–20
    isochronal transformation analytical model, 320
    isothermal transformation analytical model, 319–20
Moiré fringes, 461
molar diagrams, 82–4
  metastable Fe-C phase diagram, 83, 84
molar volume, 115
Monte-Carlo method, 522, 532
Mössbauer spectroscopy, 604
MT-DATA, 204
multi-axis deformation technique, 543
multi-deformation torsion test, 545

Nanobain steel, 448, 451, 453, 455–7
nanoscale twinning, 461
natural variables, 63–4
negligible partition-local equilibrium (NP-LE), 212–14
  isothermal ternary section showing P-LE and NP-LE dominate diffusional growth, 214
  isothermal ternary section with tie-line for diffusional growth, 213
negligible-partitioning, 140, 141
net transportation, 102
neutron depolarisation (ND), 148, 150
Ni-30Fe alloys, 539
Nippon Steel Corporation, 532, 548
Nishiyama–Wassermann relationship, 159, 162, 168, 192, 256, 424, 427
nodular bainite, 421
non-isothermal transformation, 331–2
normal transformation behaviour, 320–2
  Fe-Mn alloy length changes during heating, 321
  ferrite fraction and formation rate vs temperature, 322
nucleation, 132–9, 198–208, 312
  dependence of n and γ on the parameters α, 135
  development of γ as a function of the number of atoms n, 134
  morphology and interface, 198–201
    Dubé classification, 199
  rates, 201–8, 341
    binary free energy composition diagram, 205
    elongated austenite grains from partially recrystallised Nb steel, 202
    ferrite idiomorph in as-cast Nb-containing steel, 207
    growing grain determined using 3D-XRD, 203
    predicted vs experimental TTT curves, 203
  thermodynamics, 92–3
  type as a function of the undercooling, 138
nucleation and growth (N&G)
  kinetic theories, 32–4
nucleation sites, 537–43
  equiaxed cell substructure, 542
  interior grain micrographs, 540
  intragranular features images, 541
number-fixed frames
  application for binary systems, 109–10
  diffusivities, 106–8
    dependent composition variable elimination, 107–8
    uses, 108
  use, 116–17

O-lattice theory, 167–8, 179
octahedral interstices, 573
order-disorder, 35–6
orientation relationship (OR), 192, 286–7
  austenite orientation relationships in iron and steels, 192
  Bain strain, 191
ortho-pearlite, 297
orthorhombic cementite, 285
osmondite, 18, 20

para-cementite, 443
paraequilbirium (ParaE), 214–16
  isothermal ternary section with tie-line for diffusional growth, 215

© Woodhead Publishing Limited, 2012

paraequilibrium carbon partitioning, 397
paraequilibrium conditions, 491
paraequilibrium growth, 399
paramagnetic substances, 557
parent pre-straining, 409
particle-geometry factor, 317
partition-local equilibrium (P-LE), 210–12
  diffusivity values for carbon, manganese and silicon in austenite, 210
  isothermal ternary section with tie-line for diffusional growth, 211
partitionless transformation, 371
pearlite, 16, 17, 18, 20, 386, 471
  alloying elements role, 291–8
  crystallographic aspect of the reaction, 285–91
  deformation, 298–303
    Hall–Petch equation describing the evolution of proof stress, 303
    redistribution of C from the cementite lamellae, 304
  formation in steels, 276–307
  future trends, 303–6
  overview, 276–8
    lower reaction temperature develops by branching of the cementite lamellae, 278
    nodule growth on side of austenite boundaries and grain corners, 278
    reproduction of images of a pearlitic structure in a heat treated cast iron, 277
  reaction, 278–85
    classical data on the variation of interlamellar spacing, 283
    Fe-C showing relationship of drving diffusion to total undercooling, 282
    free energy balance, 281
    influence of temperature on the rate of pearlite growth, 284
    typical reaction curve for the increase in volume fraction, 280
Peclet number, 172
phase boundary
  atomic structure, 158–63
  free energies, 163–71
  future trends, 177–9
  migration, 171–7
  steels, 157–79
phase diagrams, 80–5
  molar and mixed, 82–4
  potential diagrams, 81–2
    metastable Fe-C, 82
  sections, 84–5
    isopleth, 85
phase equilibrium, 88–90
  magnetic field, 560–5
    $\alpha+\gamma+\alpha$ boundary, 564–5
    A_{e3} line or $\gamma/\alpha+\gamma$ boundary, 563–4
    A_{ecm} line or γ/cem boundary, 564
    Fe-C diagrams under various field intensities, 565
    Fe-C phase diagram, 562–3
    martensitic transformation start temperature prediction, 560–2
  metal alloy additions, 15–16
phase-field method, 313, 519–20
phase interface
  boundary conditions, 118–19
  flux composition, 122–3
  volume local change, 121–2
phase rule, 66–7
phase stoichiometry, 7
phase transformations
  Calphad method, 74–80
  combined first and second law
    different forms of combined law, 64–6
    driving force evaluation, 68–9
    equilibrium conditions, 67–8
    Gibbs–Duhem relation and the phase rule, 66–7
    Le Chatelier's Principle, 72
    natural variables, 63–4
    stability conditions, 69–72
  diffusion atomistic model, 98–101
  diffusionless transformation trapping and transition, 119–23
  driving forces of simultaneous processes, 96–8
  experimental methods, 141–50
    differential scanning calorimetry (DSC), 145–7
    dilatometry, 143–5
    laser ultrasonics, 148
    neutron depolarisation (ND), 148, 150
    X-ray diffraction, 147–8
  external and internal variables, 57–60
  ferrite growth, 139–41
  ferrous technology and characterisation, 5–8
    iron and steel, 5–6
    metal structure, 7–8
    metallographic studies, 6–7
  first period, recognition (1880–1925), 8–21
    carbon state, 10–11
    constituents, microstructure and reaction sequences, 16–21
    iron thermal analysis and allotropy, 11–15
    perspective, 21
    phase quilibria and alloy additions, 15–16
    second-generation ferrous phase transformations, 19
    steel hardening, 8–9
  fluctuations thermodynamics in equilibrium systems, 91–2
  frame of reference, 101–13

© Woodhead Publishing Limited, 2012

fundamentals of diffusion in steels, 94–124
future trends, 123–4
general kinetic models, 128–9
geometric/microstructure, 129–32
historical development in ferrous alloys, 3–40
industrial relevance, 150–1
interfaces effect, 85–90
kinetics in steels, 126–51
magnetic field, 565–77
bainitic transformation, 566
diffusional austenitic decomposition, 567–73
martensitic transformation, 565–6
precipitation, 573–7
magnetic field effect in steels, 555–77
field influence mechanisms, 557–60
future trends, 577
magnetic field generators evolution, 556–7
phase equilibrium and transformation, 560–77
mobilities evaluation, 113–19
boundary conditions at phase interfaces, 118–19
interstitials, 114–18
nucleation, 132–9
overview, 3–5
ferrous alloys importance and variety, 3–4
scope, 4–5
thermodynamics use, 56–7
phase diagrams, 80–5
second period, consolidation (1925-1970), 21–37
kinetic theories of diffusional nucleation and growth, 32–4
martensite, 22, 25–6
microconstituents and kinetics involving diffusion, 28–9
morphology and crystallography involving diffusion, 29–31
overview, 21–2
perspective, 36–37
precipitation and tempering, 26–7
spinodal decomposition, order-disorder and magnetic transitions, 35–6
third-generation ferrous phase transformations researchers, 23–4
unusual kinetic behaviour and morphologies, 34–5
state of equilibrium, 60–2
thermodynamics in steels, 56–93
thermodynamics of nucleation, 92–3
thermodynamics properties calculation and equilibrium, 72–4
phenomenological *L* coefficient, 99, 100, 101, 105
phenomenological theory, 404–5
Phenomenological Theory of Martensite Crystallography (PTMC), 25
photo-emission electron microscopy, 400
physical metallurgy, 21
pill-box nucleus, 513
Pitsch relationship, 161, 192, 257, 287, 405
plastic deformation
background, 506–16
combined effects, 515–16
growth, 514–15
nucleation, 510–14
deformation defects and free energy, 506–10
ferrite nucleation on deformation bands, 508
metallic microstructure local strain, 510
effect on ferrite formation experiments and analysis, 516–23
austenite-to-ferrite phase transformation mixed-mode character illustration, 523
ferrite fraction vs temperature during cooling, 517
ferrite-nucleus density vs plastic strain on austenite, 520
phase-field modelling vs experimental phase fractions, 521
phase transformation temperature range strain dependence, 516
strain effect on degree of recrystallisation, 518
steels nucleation and growth during austenite-to-ferrite phase transformation, 505–24
future trends, 523–4
mixed-mode character illustration, 523
plasticity-induced ferrite formation, 515
plasticity-induced twinning, 506–7
plate, 470
plate-like ferrite *see* acicular ferrite
plumbago *see* carbon
polygonal ferrite, 232
porous cementite, 35
pre-strained austenite, 367
precipitate phase, 391
precipitation, 26–7, 573–7
bcc Fe C atom in octahedral interstice, 575
0.49C-Fe specimens inverse pole figures, 574
42CrMo specimen carbide micrograph, 575
interfacial energy with and without magnetic field diagram, 576
proeutectoid cementite, 286, 287
austenite crystallographic orientation relationships, 255–8
Dubé morphological classification system, 229–33
ferrite transformations in steels, 225–67
future trends, 266

© Woodhead Publishing Limited, 2012

habit plane, growth direction and interfacial structure of precipitate, 258–66
temperature-composition range of formation, 227–9
three-dimensional morphological classifications, 233–55
ferrite allotriomorphs, 238
ferrite morphologies, 236–8
morphologies, 244–55
non-classical ferrite morphologies, 240–4
Widmanstatten ferrite, 238–40
vs proeutectoid ferrite morphologies, 252–5
EM photomontage of grain-boundary cementite, 254
proeutectoid ferrite, 258–61, 388, 423–4
austenite crystallographic orientation relationships, 255–8
cementite transformations in steels, 225–67
Dubé morphological classification system, 229–33
future trends, 266
habit plane, growth direction and interfacial structure of precipitate, 258–66
temperature-composition range of formation, 227–9
three-dimensional morphological classifications, 233–55
ferrite allotriomorphs, 238
ferrite morphologies, 236–8
non-classical ferrite morphologies, 240–4
proeutectoid cementite morphologies, 244–55
Widmanstatten ferrite, 238–40
vs proeutectoid cementite morphologies, 252–5
EM photomontage of grain-boundary cementite, 254
proeutectoid precipitate
habit plane, growth direction and interfacial structure of, 258–66
proeutectoid ferrite, 258–61
sequence of developing Widmanstätten plates, 259
sympathetic nucleation of plates and rapid impingement of primary sideplates, 260
Widmanstätten proeutectoid cementite, 261–6
Pt/Pt-Rh thermocouple, 12
pure iron, 197

R-parameter, 168
rafts, 530
random high-angle boundary, 569–70
Raoultian activity, 79
Raoultian reference, 79
rapid heat treatment technology, 581
rapid tempering, 600, 601
recalescence corrected curve, 547
reconstructive transformation, 411
recrystallisation behaviour, 592, 595
Redlich–Kister polynomial, 77
reflected light microscopy, 6
reverse transformation
heating rate effect in steels and Fe-Ni-based alloys, 581–613
austenite transformation in steels, 582–92
Fe-Ni based alloys reverse austenite transformation, 602–12
quenched steels transformation, 592–600
rapid heating effect on steel properties and applications, 600–2

scanning electron microscopy (SEM), 298
scanning transmission electron microscopy, 393
Scientific Group Thermodata Europe, 204, 335
second law of thermodynamics
first law, 62–72
semi-coherent phase boundary, 159, 171
sheaf, 388, 400, 488
shear strip rolling, 534–5
Siemens–Martin open hearth process, 6
site saturation, 129, 315
small-angle grain boundary, 339–40
solid mechanics, 8
solute atom partitioning, 397
solute drag, 392–3, 441, 493
sorbite, 18, 20
spheroidisation effect, 574–5
spinodal decomposition, 35–6
spontaneous magnetisation, 558
stable element reference (SER), 80
stable equilibrium, 69
stable system, 69–72
static transformation, 539
steady-state nucleation, 135
steels
austenite-ferrite transformations nature and kinetics, 311–77
abnormal transformation kinetics, 338–44
diffusion- to interface-controlled growth transition, 345–60
interface- to diffusion-controlled growth transition, 360–7
kinetic information from thermal analysis, 314
massive transformation under uniaxial compressive stress, 367–77
modular phase transformation model, 315–20
normal transformation kinetics, 332–8
transformations characteristics, 320–32

© Woodhead Publishing Limited, 2012

bainite transformation kinetics, 468–99
alloying elements effect, 491–4
bainite growth and nucleation, 477–85
bainite start temperature, 485–91
overall kinetics, 494–9
transformation diagrams, 470–7
bainite transformation mechanisms, 385–412
bainite characteristics, 386–90
diffusion-controlled growth mechanism, 391–6
displacive transformation mechanism, 396–411
carbide-containing bainite, 417–33
bainite structure definition, 417–23
carbide precipitation, 429–33
crystallography and bainite characteristics in ferrite, 423–9
future trends, 433
carbide-free bainite, 436–62
carbon distribution during reaction, 446–56
microstructure micrograph, 440
morphological classification, 438
plastic accommodation microstructural observations, 456–61
dynamic strain-induced ferrite transformation, 527–50
achieving grain sizes less than 1μm, 546–8
future trends, 536–43
grain refinement limits in conventional static transformation, 528–32
industrial implementation, 548
modelling, 543–6
transformation nature, 536–43
ferrite formation fundamentals, 187–216
crystallography, 189–92
growth, 208–16
nucleation, 198–208
overview, 187–8
transformation ranges, 193–8
formation in pearlite, 276–307
alloying elements role, 291–8
crystallographic aspect of the reaction, 285–91
deformation, 298–303
future trends, 303–6
overview, 276–8
reaction, 278–85
fundamentals of diffusion in phase transformations, 94–124
atomistic model, 98–101
diffusionless transformation trapping and transition, 119–23
driving forces of simultaneous processes, 96–8
frame of reference, 101–13
future trends, 123–4
mobilities evaluation, 113–19
growth, 514–15
hardening, 8–9
first-generation ferrous phase transformations researchers, 9
heating rate effect on reverse transformations, 581–613
austenite formation, 582–92
austenite microstructure after $\gamma \rightarrow \alpha(\alpha') \rightarrow \gamma$ phase transformation, 592–600
influence of Si on cementite precipitation, 442–6
paraequilibrium growth illustration, 443
kinetics of phase transformations, 126–51
experimental methods, 141–50
ferrite growth, 139–41
general kinetic models, 128–9
geometric/microstructure, 129–32
industrial relevance, 150–1
nucleation, 132–9
magnetic field effect on phase transformations, 555–77
field influence mechanisms, 557–60
future trends, 577
magnetic field generators evolution, 556–7
phase equilibrium and transformation, 560–77
nucleation, 510–14
allotriomorphic ferrite nucleation at grain boundaries, 511
nucleation and growth during austenite-to-ferrite phase transformation, 505–24
background, 506–16
future trends, 523–4
plastic deformation effect on ferrite formation, 516–23
phase boundary, 157–79
atomic structure, 158–63
free energies, 163–71
future trends, 177–9
migration, 171–7
proeutectoid ferrite and cementite transformations, 225–67
austenite crystallographic orientation relationships, 255–8
Dubé morphological classification system, 229–33
future trends, 266
habit plane, growth direction and interfacial structure of precipitate, 258–66
temperature-composition range of formation, 227–9
three-dimensional morphological classifications, 233–55
rapid heating effect on mechanical properties, 600–2

© Woodhead Publishing Limited, 2012

cold-drawn steel wire property changes, 601
technological history, 5–6
thermodynamics of phase transformation, 56–93
Calphad method, 74–80
combined first and second law, 62–72
external and internal variables, 57–60
fluctuations in equilibrium systems, 91–2
interfaces effect, 85–90
nucleation, 92–3
overview, 56–7
phase diagrams, 80–5
properties calculation and equilibrium under fixed *T, P* and composition, 72–4
state of equilibrium, 60–2
ultrafine ferrite formation, 532–6
early observations, 532–4
microstructure after single pass rolling, 534
process parameters effect, 535–6
shear strip rolling, 534–5
structural heredity, 595–600
C content effect on structural heredity, 596
mechanism, 596–600
effect of cold deformation, 598
effect of tempering, 599
substitutional atoms, 77–8
substitutional solute, 311
superbainite, 151
superconducting magnets, 556
supersaturate martensite, 556
surface energy, 85–8
surface stress, 85–8
thin-film experiment measurement between liquid and atmosphere, 87
sympathetic nucleation, 249, 388
synchrotron radiation, 524

temperature-time-transformation diagram, 441
tempering, 26–7
tensile deformation, 299–300
tetrakaidecahedron model, 129
thermal analysis, 11–15
thermal arrests, 12
thermal expansion, 71
thermal expansion coefficient, 190
thermal stabilisation, 406–7
thermionic emission microscopy, 393
Thermo-Calc, 58, 520
thermodynamics
Calphad method, 74–80
combined first and second law, 62–72
different forms of combined law, 64–6
driving force evaluation, 68–9
equilibrium conditions, 67–8
Gibbs–Duhem relation and the phase rule, 66–7
Le Chatelier's Principle, 72
natural variables, 63–4
stability conditions, 69–72
external and internal variables, 57–60
fluctuations in equilibrium systems, 91–2
interfaces effect, 85–90
nucleation, 92–3
overview
use in phase transformations, 56–7
phase diagrams, 80–5
phase transformation in steels, 56–93
properties calculation and equilibrium under fixed *T, P* and composition, 72–4
state of equilibrium, 60–2
thermoelastic equilibrium, 457
thermomechanical controlled processing, 527, 550
three-dimensional neutron depolarisation, 285
three dimensional X-ray diffraction (3D-XRD), 194
three-phase relationship, 430
time-temperature-precipitation diagram, 444
time-temperature transformation (TTT), 28, 193–7, 276
agreement between predicted and experimental curves, 195
time-temperature-transformation (TTT) diagrams, 386
T_o' curve, 448, 487, 489
torsion deformation, 509
transformation diagram, 470–7
TTT examples, 473–7
commercial steel TTT diagram, 477
Davenport and Bain TTT diagrams, 474
Hultgren diagram with separate C curves, 475
Hultgren diagram with single continuous C curves, 476
TTT principles, 470–3
5% transformation to pearlite schematic, 471
pearlitic and bainitic beginning transformations schematic, 473
proeutectoid ferrite C curves schematic, 472
various pearlite amount schematic, 472
transformation-induced deformation energy, 375, 377
transformation induced plasticity, 37, 407, 492
transformation kinetics
experimental methods, 141–50
differential scanning calorimetry (DSC), 145–7
dilatometry, 143–5
laser ultrasonics, 148
neutron depolarisation (ND), 148, 150

© Woodhead Publishing Limited, 2012

X-ray diffraction, 147–8
ferrite growth, 139–41
general kinetic models, 128–9
geometric/microstructure, 129–32
industrial relevance, 150–1
modular model, 377
nucleation, 132–9
phase transformations in steels, 126–51
transformation plasticity, 407–9
transformation stasis, 392–3, 489
transformation strain, 334–8
transition, 119–23
transmission electron microscopy, 22, 194, 198, 298, 333, 421, 423, 443, 458, 461, 476, 479, 507, 582, 604
transmitted light microscope, 6–7
trapping, 119–23
troostite, 18, 20
two-phase region, 320, 353, 360

ultra-high carbon steels *see* hypereutectoid steels
Ultra Steel Project, 533
ultrafine ferrite, 528
ultrarapid laser heating, 588
uniaxial compressive stress, 367–77
isochronal massive $\alpha \rightarrow \gamma$ and $\gamma \rightarrow \alpha$ transformation, 367–71
Fe-Ni alloy austenite-formation rate vs temperature, 369
Fe-Ni alloy austenite fraction vs temperature, 368
Fe-Ni alloy average grain diameters during heating, 370
Fe-Ni alloy ferrite-formation rate vs temperature, 370
Fe-Ni alloy ferrite fraction vs temperature, 369
Fi-Ni alloy average grain diameters during cooling, 371
isochronal massive $\alpha \rightarrow \gamma$ and $\gamma \rightarrow \alpha$ transformation kinetic analysis, 371–5
deformation energy, 373–5
elastic and plastic deformation energies sums, 374
Gibbs energy difference vs temperature, 373
interface velocity, 371–3
interface velocity vs austenite fraction, 372
massive $\alpha \rightarrow \gamma$ and $\gamma \rightarrow \alpha$ transformation anisotropic specificities, 375–7
uniaxial tensile load, 376
universal nucleation function, 398, 478, 493
upper bainite, 402–3, 417–19, 468, 488

vacancy concentration, 514
vector method, 164
Vienna *ab-initio* simulator package (VASP), 200
volume-fixed frames
application to a binary system, 112–13
use, 111–12
volumetric strain, 375

water quenching, 590
Widmanstätten bainite
experimental lengthening, 481–5
0.85 %C steels edgewise growth rate vs temperature, 483
edgewise growth rate vs temperature, 482
lengthening rates by Hillert, 484
Widmanstätten ferrite, 158, 198, 209, 226, 238–40, 253, 386, 397–9, 441, 469–70, 475
experimental lengthening, 481–5
0.85 %C steels edgewise growth rate vs temperature, 483
edgewise growth rate vs temperature, 482
lengthening rates by Hillert, 484
Widmanstätten needles, 230
Widmanstätten proeutectoid cementite, 248–52, 253, 258, 261–6
cementite lath in a deep etched sample, 264
Fe-1.34%C-13%Mn alloy isothermally reacted at 650°C, 263
precipitates in an austenitic matrix, 250
three-dimensional images of cementite grain boundary dendrites, 252
three-dimensional reconstruction of single austenite grain, 251
Widmanstätten sawteeth, 230
Widmanstätten sideplates, 230
W_s temperature, 159

X-ray, 5
X-ray diffraction, 5, 21–2, 29, 147–8, 189, 448, 451, 507
diffractograms half way during the transformation, 149

Zeldovich factor, 136
Zener–Hillert equation, 394
Zener's equation, 480

© Woodhead Publishing Limited, 2012